Geotechnical Safety and Risk IV

Editors: L.M. Zhang, Y. Wang, G. Wang and D.Q. Li

CRC Press
Taylor & Francis Group
A BALKEMA BOOK

GEOTECHNICAL SAFETY AND RISK IV

This page intentionally left blank

PROCEEDINGS OF THE FOURTH INTERNATIONAL SYMPOSIUM ON GEOTECHNICAL SAFETY AND RISK – 4TH ISGSR, HONG KONG, 4–6 DECEMBER 2013

Geotechnical Safety and Risk IV

Editors

L.M. Zhang
The Hong Kong University of Science and Technology, HKSAR

Y. Wang
City University of Hong Kong, HKSAR

G. Wang
The Hong Kong University of Science and Technology, HKSAR

D.Q. Li
Wuhan University, China

CRC Press
Taylor & Francis Group
Boca Raton London New York Leiden

CRC Press is an imprint of the
Taylor & Francis Group, an **informa** business

A BALKEMA BOOK

CRC Press/Balkema is an imprint of the Taylor & Francis Group, an informa business

Typeset by V Publishing Solutions Pvt Ltd., Chennai, India
Printed and bound in Great Britain by CPI Group (UK) Ltd, Croydon, CR0 4YY

Published by: CRC Press/Balkema
P.O. Box 11320, 2301 EH Leiden, The Netherlands
e-mail: Pub.NL@taylorandfrancis.com
www.crcpress.com – www.taylorandfrancis.com

ISBN: 978-1-138-00163-3 (Hbk + CD-ROM)
ISBN: 978-1-315-79734-2 (eBook PDF)

Geotechnical Safety and Risk IV – Zhang et al. (eds)
© 2014 Taylor & Francis Group, London, ISBN 978-1-138-00163-3

Table of contents

This page intentionally left blank

Geotechnical Safety and Risk IV – Zhang et al. (eds)
© 2014 Taylor & Francis Group, London, ISBN 978-1-138-00163-3

Preface

The 4th International Symposium on Geotechnical Safety and Risk (4th ISGSR) was organised by the Hong Kong University of Science and Technology under the auspices of the Geotechnical Safety Network (GEOSNet; Chair, Daniel Straub; Co-chair Limin Zhang), Technical Committee TC304 on Engineering Practice of Risk Assessment and Management (Chair, K.K. Phoon) and Technical Committee TC205 on Safety and Serviceability in Geotechnical Design (Chair, Brian Simpson) of the International Society of Soil Mechanics and Geotechnical Engineering (ISSMGE). The Symposium was also supported by Hong Kong Geotechnical Society, the Geotechnical Division of the Hong Kong Institution of Engineers, Chinese Institution of Soil Mechanics and Geotechnical Engineering, the Engineering Risk and Insurance Branch of China Civil Engineering Society, and American Society of Civil Engineers—Hong Kong Section.

The 4th ISGSR was a continuation of a series of symposiums and workshops on geotechnical risk and reliability starting with LSD2000 in Melbourne, Australia, IWS2002 in Tokyo and Kamakura, Japan, LSD2003 in Cambridge, USA, Georisk2004 in Bangalore, India, Taipei2006 in Taipei, 1st ISGSR in Shanghai, China in 2007, 2nd ISGSR in Gifu, Japan in 2009 and 3rd ISGSR in Munich, Germany in 2011.

Safety, reliability, and risk assessment and management have attracted growing interests of the geotechnical community in recent years due to the frequent occurrences of natural and man-made disasters and the needs for safe and cost-effective design, construction and operations of infrastructures. At the same time there is an increasing expectation of the general public that requires the engineering community to provide quantitative information concerning risks posed by geotechnical hazards. The 4th ISGSR provided an excellent opportunity to better understand the geotechnical safety and risk management issues in engineering practices and research. The proceedings contain seven invited keynotes and 69 accepted papers from 28 countries and regions. Each accepted paper in the conference proceedings was subject to review by two peers. These papers cover six themes: (1) geotechnical uncertainty and variability, (2) geohazards such as landslides, earthquakes and climate changes, (3) reliability and risk analysis, (4) reliability-based design and limit-state design in geotechnical engineering, (5) risk assessment and management in geotechnical engineering and infrastructural projects, and (6) practical applications.

One of the highlights of this symposium was the 3rd Wilson Tang Lecture. The lecture was inaugurated during the 2nd ISGSR in Gifu to recognize and honor the significant contributions of the late Professor Wilson Tang, who was one of the founding researchers in geotechnical reliability and risk. The first lecture was given by Prof. T. H. Wu of the Ohio State University and the second lecture by Prof. Y. Honjo of Gifu University. The 3rd lecture was given by Prof. Suzanne Lacasse of Norwegian Geotechnical Institute during the 4th ISGSR.

The credit for the proceedings goes to the authors and reviewers. The publication of the proceedings was financially supported by the National Basic Research Program of China (Grant No. 2011CB013500) and the National Natural Science Foundation of China's Oversea Collaborative Research Program (Grant No. 51129902).

Limin Zhang
Chairman of the Regional Organising Committee
August 2013, The Hong Kong University of Science and Technology, HKSAR

This page intentionally left blank

Geotechnical Safety and Risk IV – Zhang et al. (eds)
© 2014 Taylor & Francis Group, London, ISBN 978-1-138-00163-3

Organisation

REGIONAL ORGANISING COMMITTEE

Limin Zhang, *Chairman of the Committee and Conference*
Y.C. Chan and Dianqing Li, *Co-Chairs of the Technical Subcommittee*
Yu Wang and Gang Wang, *Secretaries*
J.P. Wang, *Treasurer*

Members

Ivan S.K. Au
K.T. Chau
Tony C.T. Cheung
John Endicott
Albert Ho
Jinhui Li
Jack Pappin
L.G. Tham
Jun Yang
Kelvin K.V. Yuen

INTERNATIONAL ADVISORY COMMITTEES

GEOSNet Executive Board Members

Daniel Straub (Chair)
Limin Zhang (Co-chair)
Yusuke Honjo (Past Chair)
Richard Bathurst
Andrew Bond
Samuel Paikowsky
Iason Papaioannou (Secretary)
Dongmei Zhang

ISSMGE-TC304 Members

K.K. Phoon (Chair)
Gordon Fenton (Vice Chair)
Jianye Ching (Secretary)
Y. Ashkey
Gregory Baecher
Hansgeorg Balthaus
Robert Berkelaar
Laura Caldeira
Paul Cools
Federica Cotecchia
Guillermo Espin
P. Ganne
Anthony TC Goh
Vaughan Griffiths
Ken Ho
Hongwei Huang
Mark Jaksa
Rafael Jiménez
Leena Korkiala-Tanttu
Kishor Kumar
Giuseppe Lanzo
Dianqing Li
B.K. Low
Dagang Lu
Farrokh Nadim
Laszlo Nagy
Shin-ichi Nishimura
Ali Noorzad
Lars Olsson
Lance Roberts
Adrian Rodriguez-Marek
Nick Sartain
Bernd Schuppener
Timo Schweckendiek
V.I. Sheinin
Kenichi Soga
Abdul-Hamid Soubra
M. Suzuki
Pavlos Tyrologou
Martin van Staveren
Yu Wang
Jianfeng Xue
Limin Zhang

ISSMGE-TC205 Members

Brian Simpson (Chair)
Colin Smith (Secretary)
Sam Clarke (Secretary)
Tony M. Allen
Maria J. Avecillas
Lech Bałachowski
Richard Bathurst
Andrew Bond
Luigi Callisto
Peter Day
Franco Francisca
Roger Frank
Takashi Hara
Yusuke Honjo
Hongwei Huang
Petr Koudelka
Kristian Krabbenhoft
Anders Kullingsjö
Tim Länsivaara
Kerstin Lesny
Iacint Manoliu
Trevor Orr
Sam Paikowsky
K.K. Phoon
Agustin Popa
W.K. Pun
Rodrigo Salgado
Bernd Schuppener
Adriaan van Seters
Masahiro Shirato
Antonio Soriano
Jørgen S. Steenfelt
Marco Uzielli
Balazs Vasarhelyi
Aida S. Zhakulin
Limin Zhang

Geotechnical Safety and Risk IV – Zhang et al. (eds)
© 2014 Taylor & Francis Group, London, ISBN 978-1-138-00163-3

Acknowledgements

MANUSCRIPT REVIEWERS

The editors are grateful to the following people who helped to review the manuscripts and hence assisted in improving the overall technical standard and presentation of the papers in these proceedings:

Patrick Arnold
M.W. Bari
N. Bergman
Zijun Cao
Y.C. Chan
Dongsheng Chang
Hongxin Chen
R.H. Chen
Jianye Ching
Jozsef Danka
Haijian Fan
Roozbeh Geraili Mikola
Duruo Huang
Shuihua Jiang
Rafael Jimenez
Suzanne Lacasse
Andy Y.F. Leung
A.J. Li
Chao Li
Dianqing Li
Jinhui Li
Victor Li
Xu Li
Jinchi Lu
Gang Ma
S.H. Marques
Madhusudhan Murthy
Farrokh Nadim
T. Namikawa
I.T. Ng
Y. Otake
Iason Papaioannou
K.K. Phoon
Nick Sartain
Timo Schweckendiek
Masahiro Shirato
H.W. Sun
Alex Tang
Gang Wang
J.P. Wang
Yu Wang
Jianfeng Xue
Ryan W.M. Yan
Jun Yang
Zhaohui Yang
K.V. Yuen
Jie Zhang
Limin Zhang
Lulu Zhang
Shuai Zhang
Zhenhua Zhang
Jidong Zhao
W.H. Zhou
Hong Zhu

This page intentionally left blank

1 *Wilson Tang lecture*

This page intentionally left blank

Geotechnical Safety and Risk IV – Zhang et al. (eds)

An homage to Wilson Tang: Reliability and risk in geotechnical practice—how Wilson led the way

S. Lacasse, K. Høeg, Z.Q. Liu & F. Nadim
Norwegian Geotechnical Institute, Oslo, Norway

ABSTRACT: The paper is in homage to Professor Wilson Tang for his inspiration to fellow engineers in the area of geotechnical engineering. The role of statistics, probability and reliability in geotechnical engineering is first outlined. Examples of solutions based on Wilson Tang's pioneering work are presented: uncertainties in soil parameters; Bayesian updating applications; reliability of tailings dam; model uncertainty and calibration of safety factor. Two aspects of special interest to Wilson Tang are also briefly discussed: improving the cost-effectiveness of site investigations and the reliability of offshore structures.

1 INTRODUCTION

This paper is in homage to Professor Wilson Tang (1943–2012) for his inspiration to fellow engineers to pursue his pioneering work in the application of reliability and risk in geotechnical engineering. The paper illustrates how the work initiated by Wilson Tang led the way to further developments by his colleagues, research partners, friends and practitioners in the geotechnical profession. Case studies based on Wilson Tang's learnings are provided for several geotechnical applications.

Wilson Tang's work covered a wide range of expertise areas within statistics, probability and reliability. These include: characterization of soil properties and random field models, reliability methods, structural reliability-based design, Bayesian updating and decision-making. Wilson applied reliability concepts to, for example, site investigation and geotechnical anomaly characterization, the analysis of slopes and offshore structures, earthquake hazard, the analysis of foundation solutions, model uncertainty and the calibration of safety factors. Wilson's work also covered the reliability of landfill systems, accident hazard analysis and prediction, and road network reliability.

Wilson Tang was a graduate student of the second author, post-doctoral fellow at NGI, the external doctoral examiner for the third author, and an inspiration and friend to all four authors. This is only a random cross-section of three generations of engineers at NGI. His radius of influence is so much wider, as he touched the lives of many in so many ways.

Examples of Wilson Tang's lasting influence are the invited papers for the 2013 ISGSR. The keynote speakers come from three continents, have very different backgrounds and different career profiles and are at different stages in their engineering profession. Yet, each of these recognized keynote lecturers has been influenced by Wilson's work, as witnessed by the list in Table 1.

After introductory comments on the role of statistics, probability and reliability in geotechnical engineering, the paper emphasizes four topics with solutions in large part developed thanks to the foundations laid by Wilson Tang:

- Uncertainties in soil parameters in practice.
- New applications for Bayesian updating.
- Reliability of containment facility.
- Model uncertainty and calibration of safety factors.

Table 1. Keynote contributions at ISGSR 2013.

Author	Title of keynote paper
Gilbert et al. (2013)	Advances in geotechnical risk and reliability for offshore applications
Griffiths et al. (2013)	Homogenization of geomaterials using the random finite element method
Huang et al. (2013)	Selecting optimal probability models for geotechnical reliability analysis
Juang et al. (2013)	Robust design of geotechnical barriers—A new design perspective
van Staveren (2013)	Integrated geo risk management: crossing boundaries
Wong (2013)	Is landslide risk quantifiable and manageable?

Furthermore, two additional aspects of special interest to Wilson Tang are briefly discussed: the use of probabilistic concepts to improve the cost-effectiveness of site investigations and to estimate the reliability of offshore structures.

2 ROLE OF STATISTICS, PROBABILITY AND RELIABILITY IN GEOTECHNICAL ENGINEERING

Wilson Tang and his co-author A. H-S Ang firmly believed that the best and most effective way for engineers to learn the concepts of probability, statistics and risk was through applications of the principles to engineering problems. It was important for them to be able to show the usefulness of the method in physically meaningful terms.

The motivation for probabilistic and statistical decision theory is multi-fold: uncertainties are unavoidable, and they need to be considered and reduced where possible; the need for a systematic development of design criteria for engineering designs; and quantitative risk assessment offers a logical framework for decision-making and documentation of the steps towards the decisions. In light of uncertainties, the role of probability and statistics ranges from the description of the basic information to the development of formulations as basis for design and decision-making (Ang & Tang 2007). Especially in geotechnical engineering, our knowledge is imperfect.

As part of design and decision-making under uncertainty (Høeg 1996), the properties of inherently inhomogeneous and highly variable soil materials must be considered. Natural deposits typically have irregular layers of clay, silt, sand, gravel or a combination thereof. The soil properties that affect strength and compressibility often have a wide range of variation. The information comes from the local geology, and limited soil or rock sampling and limited coverage of the area of concern with *in situ* tests.

The calculated bearing capacity (stability) can vary widely according to the analysis parameters and the calculation method selected. The calculation will therefore involve some possibility of overestimating the actual resistance provided by the soil, or leading to unnecessarily high costs due to overly conservative design. There will therefore always be a finite probability that the forces on a structure founded on or in soil or rock can cause damage, or the total collapse, of the structure.

Statistics, probability, reliability and the decisions made on the basis of these concepts offer remarkable tools that can quantify the trade-off between cost and tolerable probability of non-performance (failure) and risk (sentence slightly modified from Ang & Tang 2007). Such considerations, and as exemplified by Wilson Tang's long list of publications, can be extended to the entire chain of geotechnical design steps, from site investigation and soil testing, selection of design parameters to design calculations, reliability of a design method and selection of required safety factor(s).

The examples presented in this paper illustrate the role of statistics, probability and reliability in geo-engineering.

In the books "Probability concepts in engineering, planning and design" (Volume I and II 1975; 1984) and "Probability concepts in engineering—Emphasis on applications to civil and environmental engineering" (2nd ed. of Volume I–2007), Ang and Tang published two of the first books that made the probability concepts easily accessible to geotechnical engineers.

From an engineering standpoint, the Ang and Tang books, together with Benjamin & Cornell (1970) were instrumental in pointing the way for most users, including the authors of this paper. As a doctoral student at Stanford University, the young Wilson Tang greatly benefitted from the lectures and discussion with Professor Jack Benjamin.

Later books, especially Baecher & Christian (2003) and Fenton & Griffiths (2008) are of special relevance for geotechnical engineers. Vick (2002) and Jordaan (2008), for example, published books on decisions under uncertainty and continue the legacy of Wilson Tang. Yet, the first Ang and Tang's books have the far-reaching influence of being the pioneers for geotechnical engineers.

3 UNCERTAINTIES IN SOIL PARAMETERS IN PRACTICE

The terms 'aleatory' uncertainties (those associated with natural randomness) and 'epistemic' uncertainties (those associated with uncertainties in prediction and estimation) are known today. The terms 'aleatory' and 'epistemic' were first used by Hacking (1975) and Cornell, C.A (1982, Personal comm., Pau, France).

The importance of quantifying the variability in geotechnical design parameters is not adequately recognized in practice. Quantifying variability is a positive contribution as its consistent modelling and utilization lead, with limited additional effort, to more rational and economic designs. The modelling of soil variability belongs to one of two categories: (a) geostatistics, focusing on the interpolation of available data to estimate other values at the same location; and (b) reliability-based engineering, focusing on characterization for reliability/risk assessment.

A soil variability analysis can include three steps, each with increasing level of complexity:

1. statistical analysis of mean, variance (standard deviation) and probability density function;
2. analysis of spatial correlation describing the variation of the soil property in space; and
3. spatial averaging and variance reduction when averaging over a volume.

Integrated approaches making use of Monte Carlo simulation, finite element analysis and the results of high-level soil variability investigations have gained interest over recent years. These approaches allow enhanced modelling of the behavior of geotechnical systems, where spatial heterogeneity of soil properties invariably plays an important role.

Two aspects are described in more detail below: the statistical analysis of a random variable (level 1) and the analysis of spatially random variables (level 3). An example is then described for Troll clay offshore Norway.

3.1 *Level 1: Statistical analysis of random variable*

Following the precepts in Ang and Tang (1975), Figure 1 illustrates the phases leading to the probabilistic modelling of a random variable. The descriptive part includes the calculation of sample moments and visual inspection of data and histograms. The inferential part includes the selection of a probability density function type and the distribution parameters, and goodness-of-fit testing. The dashed lines indicate that the results of the descriptive analysis can be used in the inferential analysis; however, inference could also be performed without prior statistical description.

Different Probability Density Functions (PDF) have been used. The distributions are site- and parameter-specific. Based on cone penetration data from artificial and natural deposits (Fig. 2), Popescu et al. (1998) observed that the distribution of soil strength in shallow layers were prevalently positively skewed, while for deeper soils the corresponding distributions tended to follow more symmetric distributions.

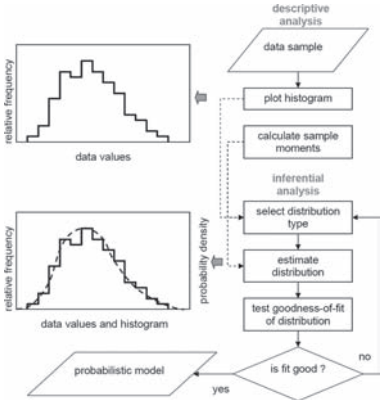

Figure 1. Descriptive and inferential analysis of a random variable (Uzielli et al. 2006b).

The resulting PDF's are in all cases close to the normal or lognormal PDF's. Lacasse & Nadim (1996) reviewed the probability distribution for several soil properties (Table 2).

3.2 *Level 2: Spatial correlation analysis*

Second-moment statistics alone are unable to describe the spatial variation of soil properties, whether measured in the laboratory or in-situ. Two sets of measurements may have similar second-moment statistics (i.e. mean and standard deviation) and statistical distributions, but could display substantial differences in spatial distribution.

As part of spatial averaging effect and variance reduction due to spatial averaging, scale of fluctuation and the spatial coefficient of variation of inherent variability are descriptors of a random field. Uzielli et al (2006b) provided a review of the calculation methods for such parameters.

3.3 *Level 3: Modelling of spatially random variables*

The description of a random field through a mean, standard deviation, a scale of fluctuation and a spatial correlation function is useful to characterize a spatially variable soil property (e.g. Vanmarcke 1977, 1983; Elkateb et al. 2003; and Jaksa 2006).

If spatial variability of soil properties is included in an engineering model, stresses and/or displacements may change compared to the homogeneous case. A design that does not take spatial variability into account is biased towards the conservative side and therefore will lead to more costly solutions. One of the most important benefits of random field modelling is the capacity to simulate data series. By using sets of random field simulations and implementing the variability in non-linear finite element meshes, the Monte Carlo technique, for example, can be used to predict reliability of geotechnical systems with spatially variable properties.

Recent studies have focused on combining random fields, non-linear finite element analysis and Monte Carlo simulation to investigate the reliability of geotechnical systems including the variability of soil properties. The studies suggest that:

– When soils are modelled as spatially variable, the failure mechanisms seem different and more complex than in the case of deterministic properties.

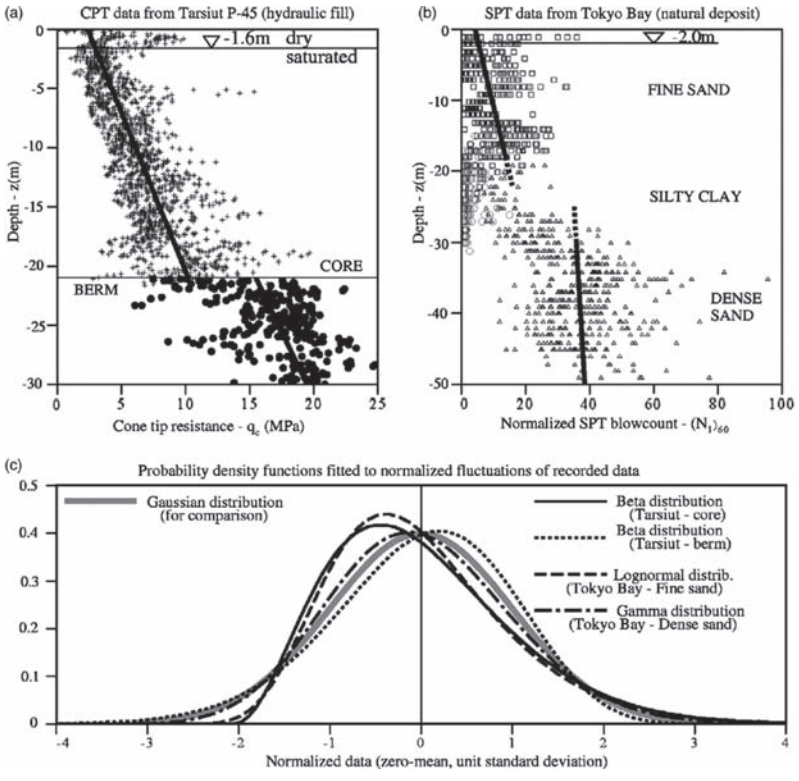

Figure 2. Probability distributions for Cone Penetration (CPT) and Standard Penetration (SPT) Tests (Popescu et al 1998).

Table 2. Probability distributions for different soil properties (adapted from Lacasse & Nadim 1996).

Soil property	Soil type	PDF
Cone resistance	Sand, clay	N/LN
Undrained shear strength	Clay (triaxial tests)	LN
	Clayey silt	N
Normalized undrained shear strength	Clay	N/LN
Plastic limit	Clay	N
Submerged unit weight	Clay, silt, sand	N
Friction angle	Sand	N
Void ratio, porosity	Clay, silt, sand	N
Overconsolidation ratio	Clay	N/LN

– There generally exists a critical correlation distance which corresponds to a minimum reliability.
– Phenomena governed by highly non-linear behavior laws are affected the most by spatial variations.

Variance reduction alone cannot convey a comprehensive picture of the implications of spatial variability on the behavior of a geotechnical system. Both statistical variability (i.e. second-moment) and spatial variability (i.e. spatial correlation) of soil properties affect the reliability of geotechnical systems.

The number of studies making use of random field simulation, finite elements and Monte Carlo simulation is still limited. The importance of the results so far, however, should be a stimulus for the transposition of results to practice.

Popescu et al. (2005) investigated the differential settlements and bearing capacity of a rigid strip foundation on an overconsolidated clay layer. The undrained strength of the clay was modelled as a non-normal random field. The deformation modulus was assumed to be perfectly correlated to undrained shear strength. The settlements (uniform and differential settlements) were computed with non-linear finite elements in a Monte Carlo simulation framework. Anisotropy in spatial correlation was addressed, with the horizontal scale of fluctuation exceeding the vertical scale of fluctuation by a factor of 10.

Figure 3a shows the contours of maximum shear strain for a uniform soil deposit with undrained strength of 100 kPa and for a normalized

vertical displacement at the center of foundation δ/B = 0.1. Different sample realizations of soil properties corresponded to fundamentally different failure surfaces. Figure 3b shows one sample realization where the spatial distribution of undrained strength is not symmetric with respect to the foundation. The configuration at failure, shown in Figure 3c, involves a rotation as well as vertical settlement. The repeated finite-element analysis allows an appreciation of the combined settlement and rotation of the footings, which could not be inferred from deterministic bearing capacity calculations (i.e. neglecting spatial variability). In general, the failure surfaces were not variations around the deterministic failure surface. There was also a significant reduction in the bearing capacity compared to the deterministic case. Figure 3d shows that the pressure required to induce a given settlement is always higher in the deterministic case.

Fenton and Griffiths (2005) investigated the reliability of shallow foundations against serviceability limit state failure, in the form of excessive and differential settlement, both for a single footing and for two footings. Figure 4 (left) shows cross-sections through finite element meshes of the single footing and the two footings. Figure 4 (right) provides the 3-D finite element mesh for the two-footings case. The elastic modulus of the soil was modelled as a lognormal random field with an isotropic correlation structure.

Fenton et al. (2005) investigated the failure and the reliability of a two-dimensional frictionless wall retaining a cohesionless drained backfill. Soil friction angle and unit weight are modelled as spatially variable properties using lognormal random fields with single exponential-type correlation structures. Figure 5 shows the active earth displacements for two realizations of the finite element mesh. The

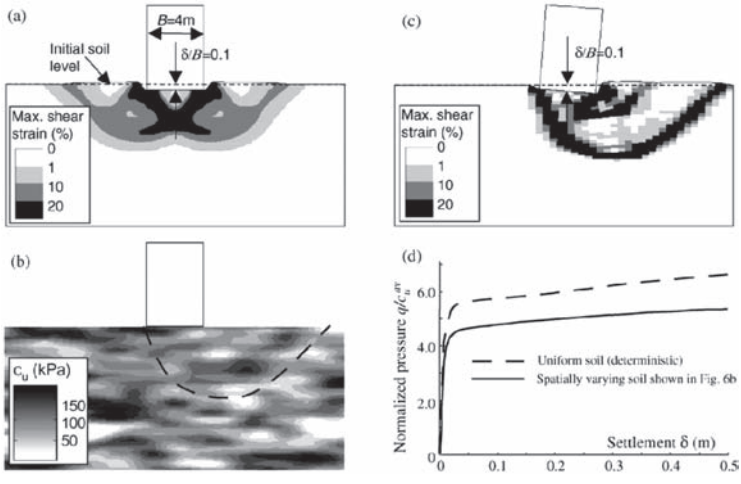

Figure 3. Results of investigation on homogeneous and spatially random foundation soil (Popescu et al. 2005).

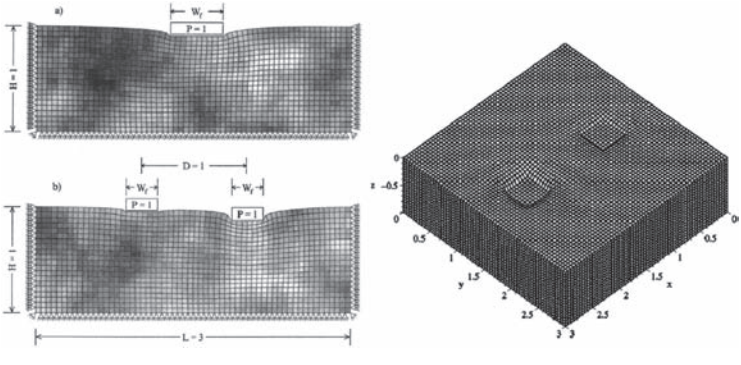

Figure 4. *Left:* Single footing and two footings founded on a spatially heterogeneous soil; *Right:* 3D finite element mesh of spatially heterogeneous soil volume supporting two footings (Fenton & Griffiths 2005).

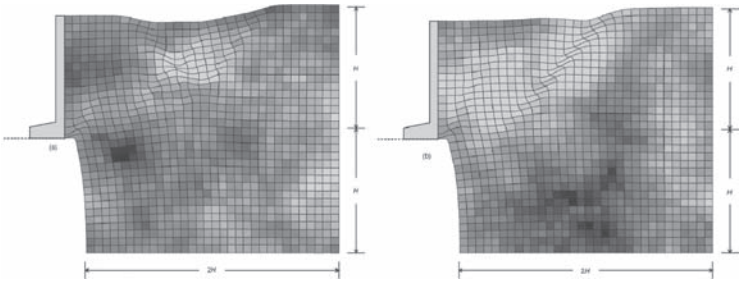

Figure 5. Active earth displacements for two realizations with same correlation distance and coefficient of variation of the random field of soil friction angle (Fenton et al. 2005).

location and shape of the failure surface is strongly related to the presence of weaker soil zones (shown in lighter colors) and is, in both cases, markedly different from the shapes assumed in earth pressure theory.

Griffiths et al. (2013) brings new developments on soil variability and random finite element analysis.

3.4 *Application to Troll clay*

Uzielli et al. (2006a) did an uncertainty-based geotechnical characterization of the Troll clay, a site offshore Norway for the world's largest gravity structure. Second-moment statistics were obtained from laboratory and *in situ* tests. Bayesian updating combined the values of undrained shear strength resulting from triaxial compression tests and piezocone tests. Some of the results are presented herein.

The authors believe that the approach followed would have been close to what Wilson Tang would have done himself, if he had been asked to interpret and calculate the uncertainty in the Troll data.

The characterization consisted of four steps: (a) visual inspection of data by soil unit and preliminary second-moment data analysis; (b) identification of a deterministic trend function and decomposition; (c) identification of a suitable uncertainty model; and (d) quantification of the uncertainty (mean, variance, standard deviation or coefficient of variation). The Kendall's tau statistic test (Uzielli et al. 2006b) was run to check whether or not the data were statistically independent. A trend function was obtained by regression analysis (Ang & Tang 2007). An uncertainty model was used to merge the different uncertainty components to estimate the total uncertainty.

3.4.1 *Laboratory data*

The results of anisotropically Consolidated Undrained Triaxial Compression (CAUC) and constant volume (undrained) Direct Simple Shear (DSS) tests were used (Fig. 6). No outliers were evident from visual inspection. The data from depths 0 to 5 m were excluded for this analysis. The following model for the total Coefficient of Variation (COV_{tot}) was used:

$$COV_{tot}^2 = COV_{\omega}^2 + COV_m^2 + COV_{se}^2 \quad (1)$$

where COV_{ω} is the coefficient of variation of inherent variability, representative of aleatory uncertainty; COV_m is the coefficient of variation of measurement error; and COV_{SE} is the coefficient of variation of statistical estimation uncertainty.

Figures 7 (CAUC data) and 8 (DSS data) and Table 3 present the second-moment estimates of

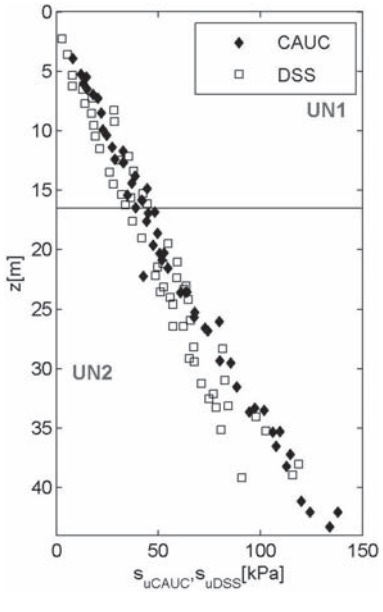

Figure 6. Undrained shear strength versus depth from CAUC and DSS for Troll clay (Unit 1 and Unit 2).

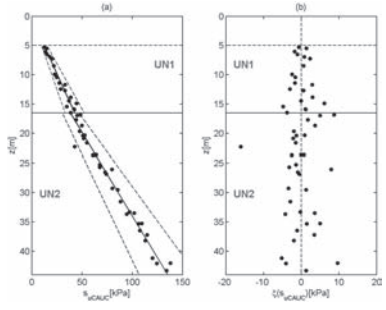

Figure 7. CAUC undrained shear strength: (a) trends and standard deviations; (b) residuals of detrending (Uzielli et al. 2006a).

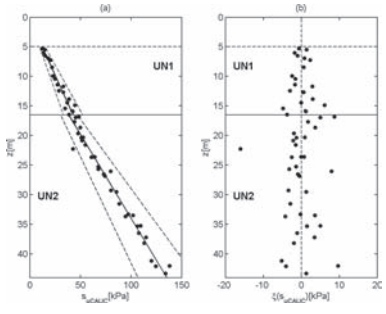

Figure 8. DSS undrained shear strength: (a) trends and standard deviations; (b) residuals of detrending (Uzielli et al. 2006a).

Table 3. Uncertainty components and total uncertainty for undrained shear strength (Uzielli et al. 2006a).

Lab test	CAUC		DSS	
Clay unit	Unit 1	Unit 2	Unit 1	Unit 2
μ_t (kPa)*	28.4	80.5	25.8	69.2
COV_ω	0.09	0.06	0.21	0.11
COV_m	0.20	0.20	0.20	0.20
COV_{SE}	0.02	0.01	0.04	0.02
COV_{tot}	0.22	0.21	0.29	0.23

*μ_t is the mean value of the trend.

the uncertainty components and total uncertainty for the laboratory data. The data show a discontinuity at the interface between the two units, the higher undrained shear strength being in the upper unit. This was consistent with the results for the plasticity index.

The total uncertainty in Unit 2 is smaller than in Unit 1, due to the smaller aleatory uncertainties. Uzielli et al. (2006a) suggested that for both tests; the effect of measurement uncertainty is significant. Aleatory uncertainty is directly related to the selected trend function. Hence, it is important to report trends and testing method explicitly when presenting the results.

3.4.2 *Piezocone measurements*

Five piezocone soundings (CPTU) were available for the Unit 1 clay (Uzielli et al. 2006a). Figure 9 indicates the locations of the CPTU soundings from the 2005 site investigation and Figures 10 and 11 the measured cone resistance and pore pressure. The water depth was between 305 and 313 m. The profiles show a considerable regularity and smoothness. Despite the distances between the

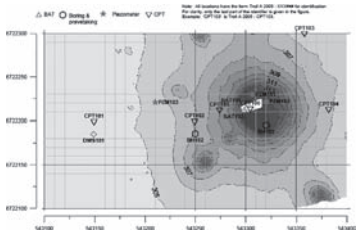

Figure 9. Map showing piezocone locations at Troll site (2005).

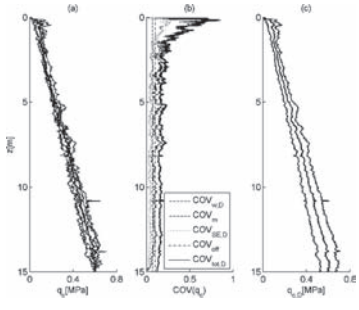

Figure 10. Statistics of cone resistance from 5 CPTU tests: (a) measured data. (b) coefficients of variation, (c) mean and standard deviation (Uzielli et al. 2006a).

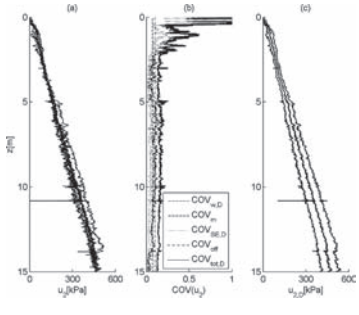

Figure 11. Statistics of pore pressure from 5 CPTU tests: (a) measured data, (b) coefficients of variation, (c) mean and standard deviation (Uzielli et al. 2006a).

sounding locations, there is considerable overlap between the soundings.

The lack of variability suggests homogeneity in the horizontal direction. Spatial correlation in the horizontal direction could not be investigated reliably due to the limited number of soundings and the considerable spacing between the soundings themselves.

At each measurement depth from the common zero-depth, the sample mean and standard deviation of the measurements from the 5 soundings were calculated.

The scatter in the data constituting each sample can be ascribed to the inherent variability of the penetrated soil and to measurement error. Phoon & Kulhawy (1999) suggested a coefficient of variation of 0.07 for the measurement error in cone resistance.

The total coefficient of variation for the cone resistance q_c and pore pressure u_2 at each measurement depth was obtained from the following model:

$$COV_{tot,D}^2 = COV_{\xi,D}^2 + COV_m^2 + COV_{SE,D}^2 + COV_{off}^2 \quad (2)$$

in which $COV_{\xi,D}$ is the coefficient of variation of the aleatory uncertainty; COV_m is the coefficient of variation of the cone resistance measurement error; $COV_{SE,D}$ is the coefficient of variation of the statistical uncertainty and COV_{off} is an additional uncertainty term to account for the artificial offsetting of CPTU soundings at different water depths.

The Harr's (1987) "rule of thumb" guidelines with a value of 0.20 was used for COV_{off}. While aleatory uncertainty and statistical uncertainty were depth-dependent, the measurement error and the offset-related uncertainty were assumed were non-depth dependent (subscript 'D'). The depth factor was included because inherent variability is variable with depth and a different number of measurements may be available at greater depths (some soundings are deeper than others).

Figures 10 and 11 illustrate, for cone resistance and pore pressure measured by the CPTU, the average value at each measurement depth and the coefficients of variation for each component of total uncertainty and for the total uncertainty.

The undrained shear strength is usually derived from cone penetration test through the net cone resistance (e.g. Lunne et al. 1997) defined as:

$$q_{net} = q_c + (1 - a_c)u_2 - p_0 \quad (3)$$

in which q_c is the measured cone resistance; u_2 the pore pressure measured behind the cone; p_0 the total vertical overburden stress; and a_c the cone area ratio. The cone area ratio for the cone used was $a_c = 0.75$. Uzielli et al. (2006a) estimated uncertainty in the undrained shear strength from piezocone tests with the first-order second moment (FOSM) approach (Ang & Tang 2007).

Figure 12 presents the profile of second-moment undrained shear strength derived from the CPTU data. The Coefficient of Variation (COV) varied from 21 to 26%, with an average of 24%. The COV is close to the COV from the laboratory CAUC data of 22%.

The classical statistical approach does not allow for the combination of subjective and observed data or the merging of data from different sources. However, Bayesian updating can be used to include different sets of data (see also Section 4 below).

Bayesian updating was done for the 17 CAUC measurements s_{uCAUC}. The second-moment parameters of each CAUC measurement of s_{uCAUC} were used as prior information. The second-moment parameters of the $s_{uCPTU\text{-}CAUC}$ values obtained from CPTU data at the same nominal depth of each CAUC measurement were taken as the likelihood function. The updated undrained shear strength was denoted s_{uB}. The details of the analysis are presented in Uzielli et al. (2006a).

Figure 12 compares the means of the prior, likelihood and updated (posterior) undrained shear strength. Table 4 lists the coefficients of variation obtained for each. For each data point, the standard deviation of the updated date (s_{uB}) was always smaller than that of s_{uCAUC} and $s_{uCPTU\text{-}CAUC}$. The COV of the posterior (updated) undrained shear strength is much lower than that of the likelihood. This is a general and beneficial result of Bayesian updating.

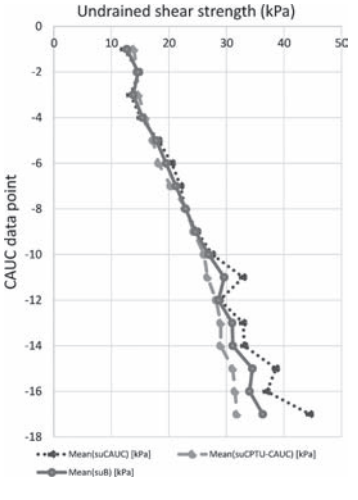

Figure 12. Bayesian updating CAUC undrained shear strength from CPTU data.

Table 4. COV's for the prior, likelihood and posterior undrained shear strength.

Undrained shear strength, s_u	Range	Ave $COV_{17\ points}$
Prior COV (s_{uCAUC})	0.19–0.21	0.20
Likelihood COV ($s_{uCPTU\text{-}CAUC}$)	0.21–0.26	0.24
Posterior COV (s_{uB})	0.15–0.16	0.15

The results obtained for the Troll data should not be uncritically exported to data from other sites.

The components of uncertainty depend on trend functions which may be strictly site- or case-specific. Perhaps most importantly, geotechnical expertise and engineering judgment were found to be essential in every phase of the uncertainty characterization: in the preliminary examination of data; in the evaluation of second-moment statistics of the measured data; in the formulation of uncertainty models for each parameter and in the selection of appropriate transformation models to obtain parameters useful for design.

3.5 *Summary*

Wilson Tang published more than 30 papers on site characterization, uncertainties in soil properties and spatial variability. Newer design codes recognize uncertainties in soil properties and engineering models, and soil variability then assumes an increasingly important role in practice and research. Ang & Tang (2007) and Uzielli et al. (2006b) provided an overview of techniques for modelling the variability of soils and highlight the benefits and limitations of the approaches. A first step towards an uncertainty-based approach in geotechnical practice could be the wider reporting of data statistics. However, both the simple and more powerful modelling technique can yield unreliable results if the input data are insufficient in quantity and quality.

Research is on-going to simplify the use of variability-modelling techniques. Research efforts focus on advanced simulation techniques, enhanced capabilities of computing tools and use of sophisticated integrated methodologies to model with increasing realism the behavior of complex geotechnical systems. Geotechnical practice, on the contrary, still largely relies on deterministic approaches.

The gap between geotechnical research and practice should be narrowed: research should make the mathematical techniques more readily usable and practice should recognize the importance of addressing uncertainty and variability. There is a necessity to acquire additional competence regarding the statistical treatment of data. At the same time, a shift towards an uncertainty-based perspective is taking place in practice. In these two respects, the learnings from Wilson Tang, from his books and papers, are a most useful and effective source of information.

4 BAYESIAN UPDATING AND BAYESIAN NETWORKS

Wilson Tang showed a keen interest for Bayesian updating, and more so in the latter years of his career, with, among others, excellent oral contributions in Xian & Oslo in 2008 and the work summarized in Cheung & Tang (2005) and Zhang et al. (2009 a; b). Wilson Tang also had a close collaboration as Kwang-Hua Chair Professor at Tongji University in Shanghai. He was important in moving the application of Bayesian updating forward.

Wilson Tang said that the Bayesian method was "a natural tool for processing geotechnical information". He presented applications to obtain improved estimates of anomaly occurrence probability, anomaly size, pile capacity, model uncertainty, failure probability, liquefaction probability, slope stability, and even the value of added information from additional tests. Bayesian updating can be assimilated to "the past as a guidebook for the future", as for instance illustrated by Folayan et al. (1970) for settlement predictions. Bayesian work continues in Wilson's spirit, e.g. Liu & Nadim (2013) suggest a three-level framework for multi-risk assessment, the third level using the Bayesian approach.

Two examples of work that have pursued Wilson's ideas are presented below: the use of Bayesian networks for (1) the assessment of risk for earthquake-triggered landslides and (2) the stability assessment of talus slopes during road construction works.

4.1 *Earthquake-triggered landslides*

Strong earthquakes in mountainous regions usually trigger many landslides. Earthquake-triggered landslides represent some of the most common secondary disasters caused by earthquake in mountainous areas. In the Wenchuan earthquake of May 2008, more than 15,000 landslides were triggered in the steep mountain slopes (Huang 2008), causing over 20,000 fatalities (Yin et al. 2009) and destroying housing and settlements and irrigation channels (Tang et al. 2011). Landslide dams blocking natural rivers create a new hazard that can be devastating unless the impounded water may be released in a controlled manner.

The assessment of the risks associated with multi-hazards requires the consideration of

the interactions among the hazards and the vulnerabilities of the elements at risk. Zhang et al. (2013) did an assessment of the loss of lives due to sequential or concurrent landslides, rock fall and debris flows hazards. They proposed approaches to estimate the vulnerability factors for loss of life in multi-risk assessment. For sequential hazards, the method considers the gradual reduction of the elements at risk in earlier hazard events. For concurrent hazards, the method estimates the lower and higher bounds of the vulnerability. The occurrence of one or two hazards at an early time can cause redistributions of the elements at risk and change the risk profile under subsequent hazards.

In earthquake-triggered landslide risk assessment, complex interactions are present between the earthquake and landslide threats. The vulnerabilities of the elements at risk can also be correlated to the threats. To date, the risk assessment involving multiple hazards neglects possible cascade effects of multiple hazards (Marzocchi et al. 2012; Kappes et al. 2012).

A study separating the two hazards (earthquake and landslide) as single hazard processes might lead to a misjudgment of the risks associated with such cascading hazards. The assessment and mitigation of the risks require a multi-risk analysis approach that can account for the interactions among the threats and among the vulnerabilities to these threats.

The risk assessment for earthquake-triggered landslides using Bayesian network is illustrated with a sensitivity analysis identifying the most appropriate risk reduction strategy in a multi-hazard perspective. Nadim & Liu (2013a) looked at risk to the buildings exposed to the threat of earthquake-triggered landslides using Bayesian network.

4.1.1 *Bayesian network for earthquake-triggered landslide risk assessment*

Nadim & Liu (2013a) provided a brief review of Bayesian networks. Figure 13 presents graphically a simple Bayesian network with five nodes and five arcs. The nodes are: Magnitude (*M*), Distance (*D*), Seismic severity (*S*), Landslide severity (*L*), and Building damage (*B*). These nodes are connected via the arcs: *M*-*S*, *D*-*S*, *S*-*L*, *S*-*B* and *L*-*B*. The user enters evidence, and the information propagates through the network. The probabilities in the network are updated when new information becomes available. The posterior probabilities and joint probabilities are calculated on the basis of Bayes' theorem (Ang & Tang 2007).

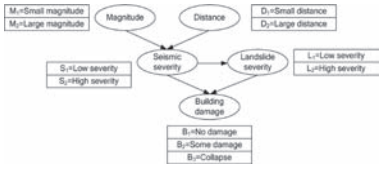

Figure 13. Simple Bayesian network (Nadim & Liu 2013a).

The network in Figure 14 estimates the risk to buildings under an earthquake-triggered landslide. One counts 11 nodes and 16 arcs. Each node has several discrete states (Table 5). Management includes options of 'no action', 'active' and 'passive' countermeasures, and 'warning systems' (a form of passive measure). Active measures, such as retaining walls and drainage result in lower probability of failure and reduced risk. Passive countermeasures, such as rock fall nets or protective sheds, reduce the vulnerability.

4.1.2 *Quantifying the network*

4.1.2.1 Seismic hazard

Figure 15 shows the distribution of the calculated distances to the seismic source taken as a line source. The annual probabilities as a function of the earthquake magnitude M_w (Fig. 16) used the recurrence relationship from Gutenberg & Richter

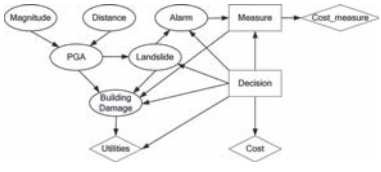

Figure 14. Decision making Bayesian network for earthquake-triggered landslide risk assessment (after Einstein et al. 2010).

Table 5. Nodes and their possible states in the Bayesian network in Figure 2 (after Nadim & Liu 2013a).

Node	# of states	Possible discrete states
Magnitude (M_w)	6	4.0–4.5–5.0–5.5–6.0–6.5–7.0
Distance (km)	6	22–25–28–31–34–37–40
PGA (g)	6	0–0.08–0.16–0.24–0.32–0.40–0.48
Landslide	2	Happens; does not happen
Building damage	3	No damage; some damage; collapse
Alarm	2	On; off
Measure	2	Yes; no
Decision	4	Passive; active; no action; warning on
Cost measure, cost, utilities	---	

(1994). The conditional probabilities of the Peak Ground Acceleration (PGA), given the magnitude and distance to epicenter, were calculated with the ground motion equation from Ambraseys et al. (2005) and a Monte Carlo simulation. Figure 17 illustrates the joint probabilities of the PGA inferred from the Bayesian network.

4.1.2.2 Landslide hazard

The approaches developed to assess the stability of slopes during earthquake fall into three analysis categories: (1) pseudo-static, (2) stress-deformation, and (3) permanent displacement. The dynamic slope performance was modelled with the permanent displacement analysis by Newmark (1965). The critical acceleration of a landslide block was:

$$a_c = (FS - 1) \cdot g \cdot sin\alpha \quad (4)$$

where FS is the static factor of safety; g the acceleration of gravity; and α the angle of the sliding surface. For an infinite slope, FS then becomes:

$$FS = c'/(\gamma z \cdot \sin\alpha \cdot \cos a) + (1 - m\gamma_w/\gamma)\tan\varphi'/\tan\alpha \quad (5)$$

where c' and φ' are the effective cohesion and friction angle; z the depth of the failure surface; α the slope angle; γ the total unit weight of the soil; and γ_w the unit weight of water. Table 6 gives the properties used in the Nadim & Liu (2013a) study. The probability of slope failure (P_f) as a function of Newmark displacement (Jibson et al 2000) was estimated from:

$$P_f = 0.335 \cdot [1 - exp(-0.048 \cdot D_n^{1.565})] \quad (6)$$

where D_n is the Newmark displacement (cm).

The calculated probabilities of slope failure for different ranges of PGA are listed in Table 7. As mentioned above, countermeasures made to landslide can reduce risk. The probability of slope failure when active actions were used are also listed Table 7.

For a building subjected to a multi-hazard situation involving additive load effects (e.g. earthquake and landslide), the damage was increased. For the

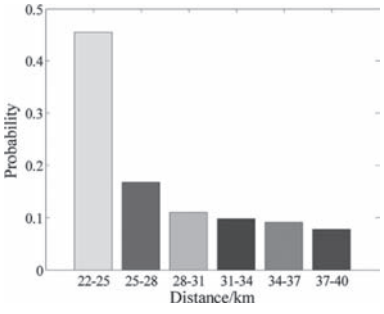

Figure 15. Discrete probabilities of distance to the seismic source (Nadim & Liu 2013a).

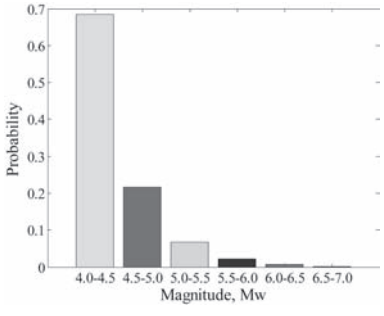

Figure 16. Discrete probabilities of earthquake magnitude (Nadim & Liu 2013a).

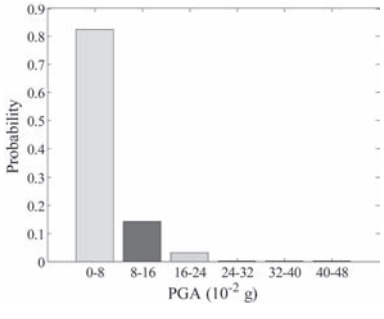

Figure 17. Discrete probabilities of peak ground acceleration (Nadim & Liu 2013a).

Table 6. Soil and slope properties (Nadim & Liu 2013a).

Variable	Mean	Standard deviation
c' (N/m^2)	10,000	2,000
φ' (degree)	30	2
z (m)	2.5	0
α (degree)	35	0
γ (N/m^3)	27,500	0
γ_w (N/m^3)	10,000	0
M	0.4	0

Table 7. Computed probability of failure (Nadim & Liu 2013a).

PGA (10^{-2} g)	0–8	8–16	16–24	24–32	32–40	40–48
$P_{f\ no\ action}$	0.124	0.256	0.305	0.328	0.339	0.346
$P_{f,\ active\ actions}$	0.025	0.03	0.035	0.04	0.045	0.05

other nodes, Nadim & Liu (2013a) adopted the Einstein et al (2010) probability approach and presented the results in tabular form. Table 8 gives an example for conditional probabilities of 'Building Damage'.

4.1.3 *Results*

Mitigation measures influence the outcome of multi-risk analyses. The results from the Bayesian network of the entire risk assessment and decision are shown in Figure 18 and compared to Einstein et al. (2010).

Different mitigation measures result in different utilities. The warning system, showing the lowest (negative) utility, is the most optimal mitigation measure. The expected losses for the four mitigation options increase due to the cascade probability triggered by the earthquake. Neglecting the cascade effect could therefore underestimate the risks.

The parameters in the analysis, e.g. the costs, the probability of slope failure or the reliability of the warning system, can vary. Sensitivity analyses were therefore conducted to assess the effects of these variations on the results.

Figure 19 shows the effect of changing the probability of landslide occurrence. In this graph, the best mitigation measure is the one having the less negative utility. For low failure probabilities (P[landslide] < 0.15), no action is preferable, as expected; otherwise, active measures are preferred, except for probabilities between 0.15 to 0.25 where warnings system are slightly preferable to active measures or no action. This is only an example. The sensitivity of the decision to other factors needs to be similarly studied.

As a further application, one can assume that the average unit rebuilding cost for the "collapse" damage state is €200,000, and the average repair costs for the "yielding" damage state as 50% (€100,000) of the unit rebuilding cost (Nadim and Liu 2013b). Figure 20 presents comparative risk curves with and without the cascade effect. The mean expected loss increases for the same return period of the hazard(s) when the cascade effects are included.

The results are still a preliminary step in furthering the earthquake-triggered landslide risk and multi-hazard risk assessment. The approach follows the philosophy of the recent work carried out by Wilson Tang, and the decision-making principles described in the Ang and Tang Part II (1984) book.

4.2 *Stability of talus*

Liu (2011) did a similar Bayesian network study as part of his doctoral dissertation for talus

Table 8. Conditional probabilities of 'Building Damage' for PGA = 0–0.08 g (Nadim & Liu 2013a, after Einstein et al. 2010).

Parent nodes	Measure	Passive		Active	
	Landslide	Yes	No	Yes	No
Building damage	No damage	0.4	0.1	0.52	0.1
	Some damage	0.3	0.1	0.43	0.1
	Collapse	0.3	0.8	0.05	0.8

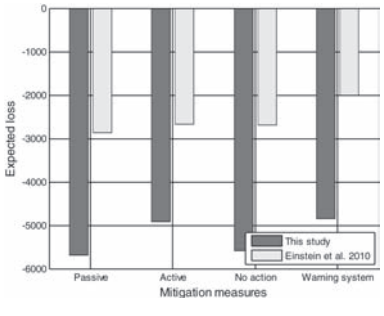

Figure 18. Losses for 'no action', 'active measures', 'passive measures' and 'warning system' (after Nadim & Liu 2013a).

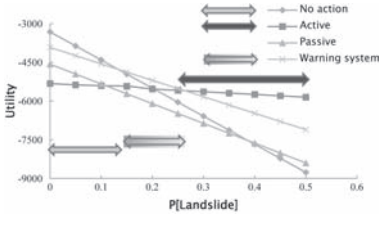

Figure 19. Sensitivity analysis of the risk as a function of the probability of slope failure for different mitigation actions—horizontal arrows indicate range where type of mitigation measure is the optimum (after Nadim & Liu 2013a).

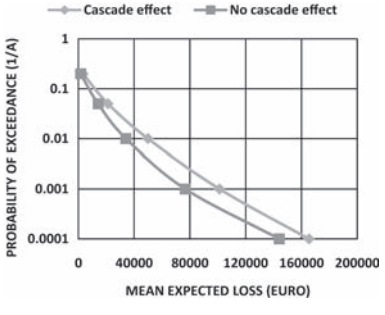

Figure 20. Example of risk curve with and without cascade effect (Nadim & Liu 2013b).

landslides. He investigated the characteristics of talus landslides and the factors affecting talus stability from existing talus failures in China and implemented geotechnical engineering risk analysis with the observed failure mechanism of talus slopes.

Talus landslides are common during the construction of highways in mountainous regions and may lead to construction delay and cause fatalities and large economic and environmental losses. A talus is a slope formed by an accumulation of mainly rock debris or broken rock fragments at the base of mountain cliffs or valley shoulders (talus can also be called "screes"). Talus often have a concave upwards shape and the maximum inclination corresponds to the angle of repose of the mean debris size. The deformation and failure mechanism of talus slope is different from those of natural soil and rock slopes.

The study area is along the Shuifu-Maliuwan Highway, which is located in the area adjacent to the Yungui Plateau and Liangshan Mountain, in northeast of Yunnan Province in China. The area has high mountains, steep gorges prone to heavy erosion, rapidly moving rivers and saw-cuts. Many talus slides have occurred along this highway due to cuts and excavations. Figure 21 provides examples of some to the structural damage encountered.

The characteristics of and factors affecting failure of talus were studied from the analysis of typical talus slides. In addition, to evaluate the input parameters for the Bayesian network, the composition (grain size) and structure of talus material were analyzed in the laboratory and by *in situ* investigations. Extensive laboratory direct shear tests were also conducted to study the effects of rock content, rock shape, and soil properties on the shear resistance of the talus. Model tests investigated the effect of construction procedure on the deformation of talus slopes.

Building the Bayesian network of talus landslide risk is complex. The network was built by assembling relevant expert knowledge. The nodes were divided into three classes: hazard factor node, event node and loss node (Fig. 22). Each node was characterized by several discrete states (Table 9). The prior probabilities of the six root nodes (lithology, soil type, gravel content, vegetation type, slope angle and time of landslide) were quantified from a study of 51 talus landslide cases. The conditional probability of each node could be determined by expert knowledge and interrelationship of each information source.

The Bayesian network was constructed using logic relationships among triggering factors, vulnerability factors, and consequence factors. The nodes (factors) and arcs (inter-relationships) of the network were quantified with historical data, empirical models and experimental results. The risk value, given the probabilities of the root factors and vulnerabilities, were calculated based on the networked interrelationships.

In the application of Bayesian networks along the Shuifu-Maliuwan Highway adjacent to the Yungui Plateau and Liangshan Mountain in northeast of Yunnan Province in China, the following steps were used: (1) the lithology of rock, soil type, gravel content, slope angle and vegetation cover

Figure 21. Structural damage after talus slide: damaged bridge piers (left) and crack in retaining wall (right) (Liu 2011).

Figure 22. Prior Bayesian network for assessment of talus landslide risk (Liu 2011).

Table 9. Examples of nodes and their states in the Bayesian network of Figure 21 (Liu 2011).

Node	State 1	State 2
Lithology	Sandstone	Mudstone
Soil type	Silty clay	Clay
Gravel content	≤50%	>50%
Veget. cover	Dry land	Mostly woods
Slope angle	≤30°	>30°
Travel length	≤60 m	>60 m
Volume	$\leq 10^6$ m^3	$>10^6$ m^3
Intensity	Weak	Strong
Time	06:00~18:00	18:00~0:00
Fatalities	Badly injured ≤ 3 or death ≤ 1	Badly injured > 3 or death > 1
Economic loss	<3% of investment	>3% of investment
Time overrun	≤30 days	>30 days

*States for marlite (3) and limestone (4) are not shown.

types were obtained through a geological survey; (2) to predict the scale of landslides, a stochastic model for generating the talus was developed based on Monte Carlo simulation and realized using the AutoCAD VBA program, accounting for gravel distribution, shape, position, size and content (Fig. 23 left). The finite element software ABAQUS was used to analyze the most likely slip surface and travel length (Fig. 23 right).

Using past failure and the spatial model developed, a decision-making Bayesian network was built to predict the potential economic loss, construction delay and time overrun and fatalities due to a talus slide.

Figure 24 presents the posterior probabilities of the Bayesian network together with the available evidence. The zones in red in the monitor windows indicate the parameters that have complete certainty due to the information acquired. If one compares Figures 22 and 24, the risk for losses and casualties for State 2, after updating, increased as expected for this specific talus landslide in light of the landslides that have occurred. The states of the fatalities and losses as well as the corresponding probabilities are listed in Table 10. Such Bayesian network could serve as an effective tool to manage talus landslide risk, provided that the information for the prior is available.

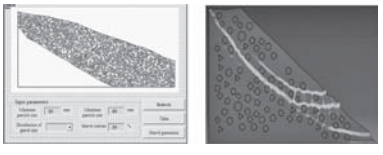

Figure 23. Bayesian network for estimating talus landslide risk: (left) stochastic model to generate talus; (right) slope failure calculation with ABAQUS software (Liu 2011).

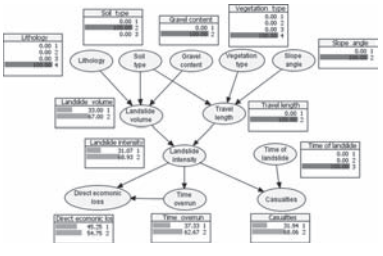

Figure 24. Posterior (updated) Bayesian network for estimating specific talus landslide risk (Liu 2011).

5 RISK OF TAILINGS DAM BREACH

In mid-career, Wilson Tang published 10 contributions on the safety of dams (e.g. Tang & Yen 1991; Cheng et al. 1993)). Although he did not work on this aspect in his later years, his colleagues at HKUST distinguished themselves in this area, perhaps also inspired by the work of Wilson (e.g. Xu & Zhang 2009).

The case study below is a hazard and risk analysis performed by NGI to estimate the probability of non-performance of a tailings management facility designed for gold mine development in Romania (www.gabrielresources.com/prj-rosia.htm). The analyses were to establish whether or not the dam would provide acceptable safety against release of tailings and toxic water, and whether or not additional hazard reducing measures were needed. The project lies within the existing Roşia Montană mining district north-east of the town of Abrud in the Apuseni Mountains of Transylvania.

The project should mitigate the consequences of the historic and future mining operations with the interception and containment of contaminated water currently entering the system, treatment of the contaminated waters and isolation and recovery of the waste rock piles within the project boundary. The operation of the project will generate tailings for approximately 17 years, producing tailings from the processing of a total of approximately 215 Mt of ore. The Tailings Management Facility (TMF) in the valley includes a Starter Dam as a first stage of the Completed Dam, a Secondary Containment Dam, a tailings delivery system, a reclaim water system and a waste rock stockpile (Fig. 25). The TMF is to provide the required design storage capacity for the life of the mine, plus an additional contingency capacity.

Table 10. Results of Bayesian updating of risk associated with talus landslide along the Shuifu-Maliuwan highway.

	Economic loss*		Time overrun*		Casualties*	
State	Prior	Posterior	Prior	Posterior	Prior	Posterior
1	60%	45%	52%	37%	38%	32%
2	40%	55%	48%	63%	62%	68%

*See Table 9 for definition.

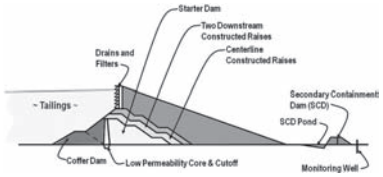

Figure 25. Cross-section of tailings dam in Romania (Corser, P. 2009. Personal comm. MWH Americas Inc. Bucharest, Romania).

To establish whether the dam provides acceptable safety against "uncontrolled" release of tailings and water during its life, an event tree approach was used to do the hazard analyses. This technique identified potential failure mechanisms and followed how a series of events leading to non-performance of a dam might unfold. The probability of each scenario, given a triggering event, was quantified.

The event tree hazard analyses considered the dam at different stages of its life and estimated the probability of non-performance. A non-satisfactory performance of the dam was defined as an uncontrolled release of tailings and water from the dam over a period of time. The release could be due to a breach of the dam or overtopping without breach of the dam. The analyses looked at critical scenarios, including all potential modes of non-performance under extreme triggers such as a rare, unusually strong earthquake and extreme rainfall in a 24-hour period.

5.1 *Design considerations*

The most significant requirements that influenced the probabilities in the hazard analyses include:

- Operational freeboard at all times of one meter above storage level for maximum reclaim pond and 2 PMP (probable maximum precipitation); the requirement leads to a storage volume capacity of two 1/10,000-yr rainfall within the same 24 hours.
- Gentle slopes for the Starter Dam (≈2H:1V upstream and ≈2H:1V downstream).
- Gentle downstream slopes for the Completed Dam (3H:1V).
- Good quality rockfill for the Starter Dam construction and the Completed Dam.
- "Well drained" tailings beach at the upstream face of the dam, where equipment can move in for repairs, in case of movement or partial breach.
- Secondary Containment Dam (SCD) with about 50,000 m^3 containment capacity after 16 years.
- Diversion channels along the sides of the valley to divert excess rainfall runoff away from the TMF pond to minimize the risk of overtopping.
- Emergency spillway to control any excess water released.
- Comprehensive geotechnical monitoring system for safety surveillance.
- Careful control of construction by owner and contractor/engineer.

5.2 *Event tree analysis*

To establish whether the dam provides acceptable safety against "uncontrolled" release of tailings and water during its life, an event tree analysis was done. A workshop was organized to develop the event trees and reach a consensus when quantifying the hazards. The analysis involved breaking down the complex system into its fundamental components, and determining the potential "failure" mechanisms leading to non-performance of the dam and the physical processes that could cause such mechanisms.

The key factors considered in the analyses included: dam configuration (Starter Dam, dam during construction and Completed Dam), and triggers, including earthquake shaking, extreme rainfall or snowmelt, natural terrain landslide in the valley or failure of the waste stockpile into the tailings reservoir.

Acts of war or sabotage, impact by meteorites or other extreme events of this type were not considered, as they would result in so low probabilities of non-performance that they are not realistic to consider.

The non-performance modes considered included:

1. Foundation failure, due to, e.g. excess pore pressures or weak layer in foundation leading to cracking, instability and breach of the dam.
2. Dam slope instability downstream or upstream, due to e.g., construction pore pressure in core of Starter Dam, excessive pore pressures caused by static or earthquake loads or instability due to inertia forces.
3. Unravelling of downstream toe and slope, due to e.g. overtopping or excessive leakage through or under the dam. This can be caused by a slide into the reservoir, dam crest settlement due to deformations of the Starter Dam, piping, internal erosion and sinkhole formation, or excessive deformations (slumping) of the top vertical part of the Completed Dam during earthquake shaking.
4. Dam abutment failure followed by breach, due to e.g. slide close to and/or under part of the dam.
5. Liquefaction of the tailings.

Figure 26 presents some of the configurations and examples of the non-performance modes analyzed. Overtopping without breach of the dam, including under-capacity or damage of the

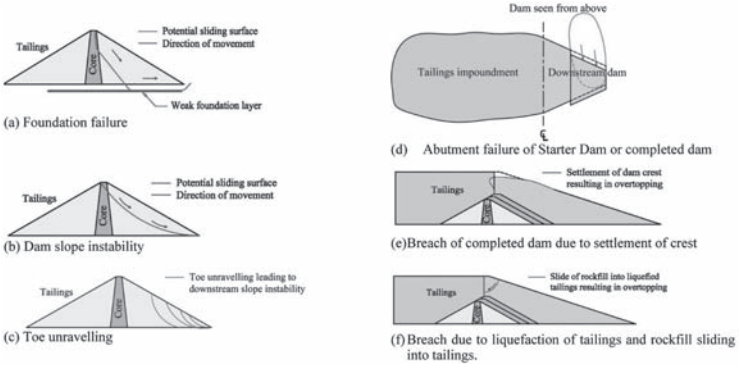

Figure 26. Examples of non-performance modes.

Secondary Containment Dam was also considered, not as a separate non-performance, but as one of the events in the sequence of events in the trees.

Different conditions can affect the probability of a hazard occurring or severity of a consequence, for example construction deficiencies or inadequate response of the field control team at the site when warning signals may appear. The analyses also looked into construction deficiencies, e.g. inadequate filters leading to uncontrolled internal erosion, inadequate drainage, very weak construction layers or zones in the embankment, inadequate types of material(s) in the embankment fill, or insufficient quality control and unforeseen construction schedule changes. These conditions were also integrated in the event trees as separate events during the course of the construction of the Starter Dam and Completed Dam.

5.3 *Probability of non-performance*

At the event tree workshop, the critical times in the life of the TMF were defined: during construction of the Starter Dam, during the downstream construction stages, during the centerline construction of the dam, and/or in the early years after the Completed Dam is built. A matrix of dam configuration versus time was prepared. The modes seen as most critical and susceptible to lead to the highest probabilities of non-performance were listed. As part of the mode screening, the following considerations were subjected to a consensus decision: extreme and critical precipitation (rainfall, flood and snowmelt), likelihood of failure of the waste stockpile, critical situations after construction of the dams, and geo-environmental considerations.

Event trees were developed for each dam configuration and trigger, with each non-performance mechanism looked at separately. In some cases, two non-performance mechanisms were considered successively. The total probability of non-performance is the sum of all contributing probabilities to the non-performance for each of the dam configurations. Table 11 presents the total probabilities for each configuration of the dam (all triggers included). The probabilities were presented as a function of the release of tailings and water associated with the non-performance of the dam. The highest annual probability of non-performance was 10^{-6}.

Table 11. Total probabilities of non-performance.

Configuration	P [non-performance]
Starter dam (t = 1.5 yr, internal erosion)	1.3×10^{-6} /yr
Completed dam (t = 16 yrs)	1.3×10^{-6}/yr
Intermediate stage (t = 4 yrs)	6.5×10^{-7}/yr
Intermediate stage (t = 9–12 yrs)	1.3×10^{-6}/yr

The highest probabilities of non-performance were associated with earthquake shaking of the completed dam and the static liquefaction of the tailings at time 9 to 12 years after the start of construction. The non-performance scenarios would result in some material damage and some contamination, but only in the vicinity downstream of the dam. For the Starter Dam, no reasonable expected scenario lead to a significant release of tailings and water because of the limited quantity of water available and the reserve capacity provided (2 PMP's). Internal erosion may cause, with an annual probability of 10^{-6}, a small escape of tailings and water. The escape would cause only modest contamination of the immediate vicinity downstream. Essentially all material released could be contained by the Secondary Containment Dam.

The analyses showed (1) no plausible events result in an annual probability of non-performance

greater than 10^{-6}. The probabilities are lower than the values considered as acceptable criteria for dams and other containment structures around the world and lower than probabilities of non-performance for most other engineered structures.

ICOLD (the International Commission on Large Dams) presented statistics of dam incidents where the mean probability of failure is between 10^{-4} and 10^{-5} per year (Londe 1993; ICOLD 1995; Foster et al. 2000; Høeg 2001). Peck (1980), based on work by Baecher et al. (1980a; b) who used the ICOLD database plus other data, reported that the probability of failure of dams in the United States and worldwide, was between 2 and 7×10^{-4} per year. Foster et al. (2000) reported annual probabilities of an accident due to downstream slope instability of 1 to 5×10^{-4} and an annual probability of failure of 1.5×10^{-5}.

Historical data are available for embankment dams that provide failure frequency per dam-year of operation. Figure 27 shows internal erosion failure frequencies for US dams. The annual probability of failure associated with internal erosion of earth dams is between 10^{-4} and 5×10^{-4} per year. Internal erosion failures tend to occur more frequently in the first 5 years reflecting first-filling failures. The data suggest significantly higher probabilities of failure than what was computed for the TMF at Roşia Montană.

For tailings dams, the probability of failure is significantly higher than the average annual probability of 10^{-4} and 10^{-5} reported above. Most of the tailings dams are dams entirely made of tailings, whereas the Roşia Montană TMF is made up of the Starter Dam (a regular type rockfill embankment dam), and when completed to top grade, has a downstream slope made of rockfill with gentle inclination of 1:3.

The probabilities of failure in Figure 27 are higher than the probability of non-performance computed for the TMF at Roşia Montană. The event tree analyses show that the probability of non-performance of the TMF is about 100 times lower than the probability of failure of containment dams, based on the performance observed for dams around the world.

The factors that contribute to the low probability of non-performance of the TMF include the use of good quality rock fill for the downstream shell of the dam, gentle downstream slopes for both the Starter and the Completed Dam, dam capacity to store extreme precipitation and/or snowmelt events, spillway to release excess water in a controlled manner, the safety monitoring and early warning of early signs of unexpected performance, and the proposed preparedness to remediate, given any unexpected behavior.

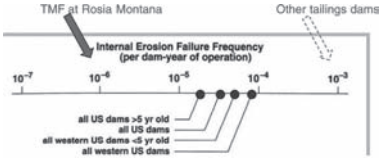

Figure 27. Annual probability of dam failure by internal erosion for different dams in the USA (Von Thun, 1985; Vick 2002).

5.4 *Environmental impact*

The physical impact in terms of damage to the environment was also studied, if a breach in the dam should occur. The analysis suggested that the released tailings' volume would be limited, and would only flow 100 to 200 m (Fig. 28). Studies were also conducted to determine possible pollution of the river downstream. The levels of pollution may be above surface water discharge standards for a limited period of time and in the immediate neighborhood of the tailings dam, but only under the worst case conditions (low flow in the downstream river). However, monitoring, early warning and emergency procedures are to be implemented to contain damage to a minimum. The weather and flow conditions for this to occur combined with the probability of dam breach occurring at the same time resulted in the probability of occurrence would reduce to 10^{-7}/year (Whitehead, P. 2009. Personal comm. Aquatic Environments Research Centre, Univ. of Reading, UK).

5.5 *Risk assessment of dams in practice*

The example illustrates that the event tree analysis is a systematic application of engineering judgment. Its application does not require the prior existence of extensive statistics or the application of complex mathematics. The process may provide meaningful and systematic estimates and outcomes on the basis of subjective probabilities (Vick 2002).

With increasing frequency, society demands that some form of risk analysis be carried out for activities involving risks imposed on the public. At the same time, society accepts or tolerates risks in terms of human life loss, damage to the environment and financial losses in a trade-off between extra safety and enhanced quality of life.

The role of the dam engineering profession is to explain the uncertainties involved in the

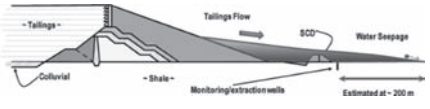

Figure 28. Physical impact of TMF dam breach at Roşia Montană (Corser, P. 2009. Personal comm. MWH Americas, Inc. Bucharest, Romania).

construction and operation of dams and to present the likelihood of incidents and failure in informative and meaningful terms. The conventional use of a factor of safety just does not do that, and concepts from probability theory and reliability analyses should be applied.

The key to making the risk analysis of dams effective begins with a detailed overview of all potential failure modes. If shortcuts are taken, the results could be misleading. Once the potential failure modes are understood, the screening process will identify the critical modes. A variety of tools are available for making the quantitative risk estimates. The event tree approach is useful and illustrative. It is recognized that risk estimates and risk assessment guidelines are only approximate, but they are useful for choosing among alternatives, comparing risk levels, and making decisions.

Høeg (2001) presented the basics of systematic risk analysis for dams. He concluded that after several years of optimism in the profession with developing and performing meaningful quantitative probabilistic risk analyses for dams, there now seems to be a trend towards increased use of the qualitative FMECA approach, or the Failure Modes, Effects and Criticality Analysis (BSI 1991). However, there is increased pressure on the decision-makers to quantify risk level so that it can be compared to acceptable or tolerable risk or public protection guidelines. In The Netherlands, the development in this direction is quite advanced and used in the safety evaluation and upgrading of dikes and storm surge barriers (Vrijling 2001).

Scott (2011) summarized the practice of risk assessment of dam safety of the US Bureau of Reclamation. Aging infrastructure, population growth downstream and limited resources render risk assessment of dam safety a reasonable and transparent method for risk management. Key to making the process effective is starting with a detailed analysis of the potential failure modes. Scott described a variety of tools available to do quantitative risk estimates. Such estimates and risk assessment guidelines are only approximate. In each case, it is essential to build the argumentation for the ability of the structure to withstand future loadings. If done diligently and openly, risk assessment is a very effective tool for managing the risks associated with containment facilities (Hartford & Baecher 2004).

6 MODEL UNCERTAINTY AND CALIBRATION OF SAFETY FACTORS

In an early paper, Høeg & Murarka (1974) studied the balanced, yet optimum, design of a gravity retaining wall by relating conventional factors of safety (load and resistance factors) to estimated probabilities of failure. Wilson Tang reviewed and commented on the manuscript, and he was really the first who worked systematically with model uncertainty. He wrote comprehensive reports for the American Petroleum Institute (e.g. Tang 1988) and several papers and discussions (e.g. Tang & Gilbert 1993b). His efforts were crowned in May 2013 with the induction in the Hall of Fame of the paper by Tang et al. (1990) on the performance reliability of offshore piles.

Wilson Tang was always concerned with two aspects: (1) the models used to quantify model uncertainty should duplicate as closely as possible the problem situation actually being calculated (Tang & Gilbert 1992), and (2) the profession should improve its ability to use experimental results to determine the uncertainties in its engineering models.

Today, work on this topic is still on-going. Lacasse et al. (2013 a; b; c) made a contribution which follows and expands on Wilson Tang's principle. The ultimate aim of the work was to obtain the appropriate factor of safety to use when designing offshore installations. To illustrate this, Gilbert et al. (2013) present at this conference the case of three actual offshore structures, presently under final design, where such calibration of the load and resistance safety factors was done. Only the approach and the conclusions are briefly reported herein.

The study was undertaken to document that the pile foundations were designed according to governing regulations. The goal was to make a recommendation on the appropriate resistance factor and minimum pile penetration depth to use for the design of the piles on an offshore jacket. The safety factors (load and resistance factors) for three case studies were calibrated for a target annual probability of failure, P_f, of 10^{-4}.

The reliability analyses of the axial pile capacity methods included seven steps:

- Establish the mean, standard deviation and Probability Density Function (PDF) of the soil parameters. Include correlations among parameters.
- Establish the model uncertainty for the different pile capacity calculation methods used.
- Establish the effect of cyclic loading on the axial pile capacity and determine whether the piles in compression or in tension govern the design.
- Develop a model for the statistics of the static (permanent) and environmental loads on the top of the piles.
- Do deterministic analysis of the ultimate axial pile capacity, Q_{ult}.

– Do probabilistic analyses of axial pile capacity and obtain the PDF of the ultimate capacity, Q_{ult}.
– Calculate the annual probability of failure by combining the loads and the probabilistic description of Q_{ult}.
– Calibrate the load and resistance factors required for an annual $P_f = 10^{-4}$.

When doing an axial pile capacity analysis, the following aspects should be included: (1) a careful selection of the characteristic soil parameters used for design; (2) the effect of cyclic loading on the characteristic shear strength or ultimate pile capacity, for both piles loaded in compression and in tension; (3) the effect of gapping and/or erosion at the top of the piles on the axial pile capacity; and (4) a decision on whether or not to account for the effect of time after pile installation on the axial capacity.

The calibration analyses showed that:

– The calibration of the safety factors demonstrate that the annual probability of failure vary with the axial pile capacity calculation method.
– The values of model uncertainty used in the analyses have an overwhelming influence on the resulting annual probability of failure and therefore on the required resistance factor for a target annual probability of failure.
– The current state-of-the-art design still relies heavily on qualified engineering judgment to assess and ensure a consistent safety level.
– The resistance factors calibrated suggest that the newer CPT-methods of pile design are as reliable as the current API method.
– The findings on margin of safety and the definition of the characteristic shear strength have important implications for the design of piles offshore and can result in significant savings.

As illustrated in Gilbert et al. (2013), the pile length could be considerably reduced through the study of a safety level corresponding to an annual probability of failure of 10^{-4}. Table 12 reproduces the final results, comparing pile penetration depths. The first number is the penetration depth from the deterministic analyses with a resistance factor of 1.5 on the CPT-methods. The second number is the penetration depth ensuring that the annual probability of failure is less than 10^{-4}.

The significant reduction in the required pile penetration depth was possible because one could demonstrate that the annual probability failure was less than the target P_f of 10^{-4}/year for the piles originally designed with a resistance factor of 1.5. It was then possible to use a resistance factor of 1.3, as for the current API method, instead of the *a priori* resistance factor of 1.5 set for the newer CPT design methods. A load factor of 1.3 or 1.35 was used.

Table 12. Pile penetration depth for design (Lacasse et al. 2013c).

Site A (clay)	Site B (sand)	Site C (clay and sand)
90 m to 75 m	51 m to 27 m	45 m to 38 m

The analyses demonstrated the importance of how the characteristic shear strength parameters are defined. Lacasse et al (2013a) recommended that the characteristic strength be defined in specific terms, e.g. setting the characteristic shear strength for the deterministic design of axial pile capacity at a value equal to the mean minus ½ or one standard deviation.

The importance of model uncertainty was pointed out early by Wilson Tang. This confirms the actuality of even his early papers. Here again, Wilson Tang led the way in his study of model uncertainty and calibration of safety factors in the early days of his career.

7 MORE OF WILSON TANG'S LEGACY

7.1 *Cost-effectiveness of site investigation*

Wilson Tang worked on the cost-effectiveness of site investigations, a central aspect of our profession. His contribution (Tang, 1987), published in the journal Structural Safety, may have passed unnoticed.

In general, more extensive site investigations and laboratory testing programs reduce the uncertainties in the soil characteristics and design parameters. At a certain point however, as Wilson Tang (1987) pointed out, the benefit obtained from further site investigations and testing may not yield sufficient added value (read: increase in the reliability of the performance) to the geotechnical system, and hence may not justify the additional cost (e.g. Folayan et al. 1970).

Soil investigations, in the way they are planned, represent a risk-based decision. The complexity of a soil characterization is based on the level of risk of a project. Lacasse & Nadim (1998; 1999) illustrated this graphically. A low risk project involves few hazards and has limited consequences. Simple *in situ* and laboratory testing and empirical correlations would be selected to document geotechnical feasibility. In a moderate risk project, there are concerns for hazards, and the consequences of non-performance are more serious than in the former case. Specific *in situ* tests and good quality soil samples are generally planned. For a high-risk project involving frequent hazards and potentially risk to life or substantial material or environmental

damage, high quality *in situ* and laboratory tests are required, and higher costs are involved.

The decision-making process for selecting the appropriate soil investigation methods, although subconscious, is risk-based. It involves consideration of requirements, consequences and costs.

Uncertainty analysis can help optimize site investigations. The uncertainty in a geotechnical calculation is often related to the possible presence of an anomaly, e.g. boulders, soft clay pockets or drainage layer. Probability approaches can be used to establish the cost-effectiveness of additional site investigations to detect anomalies. Figure 29 presents an example where the presence of a drainage layer was determinant on the resulting post-construction building settlements. A settlement of less than 50 cm would mean an important reduction in costs. With drainage layer detectability for each boring of 50% or 80% (Fig. 28), and assuming a given drainage layer extent, 3 to 6 borings were required in this case to establish whether the drainage layer was present or not.

7.2 *Reliability of offshore structures*

Wilson Tang started working with offshore structures (Høeg & Tang 1977) when he came to NGI on the Guggenheim research fellowship. Wilson was very much indebted to the John Simon Guggenheim Memorial Foundation for making possible his research stay first at the Imperial College of Science and Technology in London and then at NGI in Oslo, Norway.

From there on, he continued his research and became a recognized figure in offshore circles, especially with respect to model uncertainties and the reliability of pile foundations offshore (e.g. Tang & Gilbert 1992; 1993a). Noteworthy are his studies for the American Petroleum Institute, which conclusions are still in use today.

Gilbert et al. (2013), at this conference, give an overview of the advances in geotechnical risk and reliability for offshore applications. The lessons learned from Wilson Tang are now also used to calculate the reliability of offshore wind energy turbines (Stuyts et al. 2013). Lacasse & Nadim (2007) also summarized the applications of statistics, reliability and risk in offshore geotechnical engineering based on the original work by Wilson Tang.

The methods for assessing hazards offshore can vary from approximate estimates to more complex calculations. Applications include piled foundations, jack-up structures, gravity foundations and underwater slopes. The applications demonstrate that probabilistic analyses complement the conventional deterministic safety factor and/or deformation-based analyses, and contribute to achieving a safe and optimum design. The probabilistic approach adds value to the results with a modest additional effort. Engineering judgment is still necessary to achieve reliable results in both hazard and risk assessment.

8 SUMMARY AND CONCLUSIONS

Wilson Tang's work was an inspiration to move forward in the area of statistics, probability and reliability. He quickly saw the potential of these concepts in geotechnical engineering. He published his first book, together with Professor A.H-S Ang, one of the most useful and influential sources of information on the topic for geotechnical engineers, only six years after completing his PhD at Stanford University. With Ang and Tang's two volumes, one can find all the essential concepts and very many applications.

This paper presented only a few examples of how geotechnical engineers have taken the learnings of Wilson Tang and carried on with further applications in practice. The quantification of the natural and anthropogenic risks that can affect an area or engineering structures is today an essential component of a sustainable environment, land-use planning, and risk mitigation. To this development, Wilson Tang was a pioneer and before his time!

Wilson Tang was quick to see the importance and possible repercussions of using Bayesian updating in geotechnical engineering.

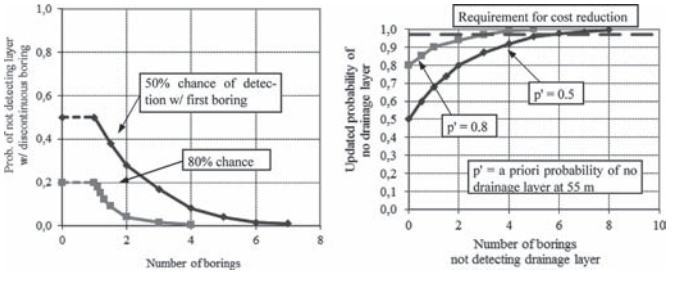

Figure 29. Cost reduction with increased number of borings (Lacasse & Nadim 1998 based on Tang 1987).

The advantages of the Bayesian approach include: (1) it is a probabilistic model instead of a deterministic model. The uncertainties in the parameters and their inter-relationships are represented by probabilities; (2) a large number of parameters and their inter-relationships can be considered in a systematic structure. The probabilities of one parameter can be updated via available information. The change in one parameter will influence the others in the network through their inter-relationships; and (3) physical mechanisms, previous studies, and statistical data can be accounted for. All three aspects are key to good geotechnical design.

The profession only gains by implementing, more systematically than before, probabilistic-based thinking and risk-based methodology. The geotechnical probabilistic approach still has major needs, including reducing uncertainty in the calculation model by obtaining and analyzing performance data of high quality, quantifying acceptable and tolerable hazard and risk levels, and convincing stakeholders of the value added in uncertainty-based analyses.

With the changes in climate and the occurrence of more extreme natural phenomena than before (e.g. storms and precipitation), one cannot only use data from existing experience to evaluate safety, but one should also include events and triggers that are not covered by e.g. 100- or 1000-year return periods. Another keyword is the importance of multi-disciplinarity, meaning wider expertise teams than before when evaluating hazard and risk to society, and the need to document cost-effectiveness of different mitigation measures.

Bayesian updating and hazard and risk analysis are important and necessary. Hazard and risk assessment present an opportunity to look at the bigger picture and seek out designs that meet not just some arbitrary idea of acceptable/tolerable risk but an unknown risk. The engineer should concentrate on exploiting the good features of the approach. As contributor to the profession's goals of documentation, continuity, high-quality and innovation, and the ever increasing requirement of globalization, hazard and risk assessment and the management of risk serve as communication vehicle among geo-specialists and other sectors of expertise. The authors are convinced that Wilson Tang would have appreciated working on these emerging aspects and would have contributed with his usual innovation, elegance and wisdom.

After a special workshop on Reliability Methods for Risk Mitigation in Geotechnical Engineering at Irvine in 1992, Tang & Duncan (1994) concluded that probability methods should be part of the geotechnical engineer's toolbox. Although every successful geotechnical engineer has learned to cope with uncertainty by applying lessons learned by the profession over decades of practice, the probabilistic toolbox provides a complement to deterministic analyses, and should be used for several reasons, including (in Wilson Tang's own words):

- "(…) Society is demanding more explicit assessment of risk. (…) To work effectively with the public and (…) regulatory agencies, geotechnical engineers must have some knowledge of probability theory and probability methodologies, as well as traditional geotechnical expertise."
- "Probabilistic methods are useful as a basis for making economic decisions. [For example,] in areas such as dam rehabilitation, landslide hazards mitigation, environmental remediation, and infrastructure rehabilitation, effective allocation of funds relies on quantifying the trade-offs between benefits and risks (…). Probabilistic methods provide a quantitative basis through which the relative contribution of risk can be systemically analyzed and communicated. In this way, decisions can be made more rationally and justified more logically."
- "(…) There is a risk in risk analyses and probability analyses, if the analyses are performed improperly. This possibility can be minimized by expanding knowledge of probabilistic methods among geotechnical engineers and by expanding knowledge of geotechnical engineering practice among probability specialists."
- "(…) With a working knowledge of probability theory, geotechnical engineers will be better equipped to deal with the many uncertainties that pervade geotechnical engineering practice."

In closing, the authors wish to express their gratitude to Wilson, not only for his competence and invaluable scientific contribution, but also for his friendship, his kindness, thoughtfulness and help with articles, discussions, workshops and presentations, over many years. One example: when NGI decided in the early 80's to offer an internal education program on the practice of statistics and probability in geotechnical engineering, we chose Ang & Tang Part I (1975) as textbook. Hearing this, Wilson immediately sent NGI his book of worked out solutions to all the problems in the book, which turned out to be a godsend. We still use this booklet of solved examples!

REFERENCES

Ambraseys, N.N., Douglas, J., Sarma, S.K. & Smit, P.M. 2005. Equations for the estimation of strong ground motions from crustal earthquakes using data from Europe and the Middle East: horizontal peak ground acceleration and spectral acceleration. *Bulletin of earthquake engineering* 3:1–53.

Ang, A.H-S. & Tang, W.H. 1975. *Probability concepts in engineering planning and design. Volume I Basic principles*. John Wiley & Sons. 409 p.

Ang, A.H-S. & Tang, W.H. 1984. Probability concepts in engineering planning and design. Volume II. *Decision, risk and reliability*. John Wiley & Sons. 562 p.

Ang, A.H-S. & Tang, W.H. 2007. *Probability concepts in engineering. Emphasis on applications to civil & environmental engineering*. 2nd Ed., John Wiley & Sons. 406 p.

Baecher, G.B. & Christian, J.T. (2003). *Reliability and statistics in geotechnical engineering*. Wiley & Sons. 605 p.

Baecher, G.B., Paté, M.-E. & de Neufville, R.1980a. Dam Failure in Benefit/Cost Analysis. *ASCE Jour. Geot. Eng. Div*. 106 (GT1): 101–116.

Baecher, G., Paté, M.-E. & de Neufville, R. 1980b. Risk of Dam Failure in Benefit-Cost Analysis. *Water Resources Research* 16(3): 449–456.

Benjamin, J.R. & Cornell C.A. 1970. *Probability, statistics and decision for civil engineers.* McGraw Hill Book Company. New York. 684 p.

BSI 1991. *BS 5760 Part 5: Guide to failure modes, effect and criticality analysis (FMEA and FMECA)*. British Standards Institution. London.

BSI 2001. British Standard Association. *BS 5760 Part 5: Guide to failure modes, effects and criticality analysis (FMEA and FMECA)*. London.

Cheng, S.T., Yen, B.C. & Tang, W.H. 1993. Stochastic Risk Modeling of Dam Overtopping, *Reliability and Uncertainty Analyses in Hydraulic Design.* B.C. Yen and Y.K. Tung, eds. ASCE Special Publication, 123–132.

Cheung, R.W.M. & Tang, W.H. 2005. Realistic Assessment of Slope Reliability for Effective Landslide Hazard Management. *Geotechnique* 55(1): 85–94.

Einstein, H.H., Sousa, R.L., Karam, K., Manzella, I. & Kveldsvik, V. 2010. Rock slopes from mechanics to decision making. *Rock Mechanics in Civil and Environmental Engineering*, J. Zhao, V. Labiouse, J.P. Dudt and J.F. Mathier (eds). London: CRC Press, 3–13.

Elkateb, T., Chalaturnyk, R. & Robertson, P.K. 2003. An overview of soil heterogeneity: quantification and implications on geotechnical field problems. *Canadian Geotechnical Journal* 40(1): 1–15.

Fenton, G.A. & Griffiths, D.V. 2005. Three-dimensional probabilistic foundation settlement. *Journal of Geotechnical and Geoenvironmental Engineering*, ASCE 131(2): 232–239.

Fenton, G.A. & Griffiths, D.V. 2008. *Risk assessment in geotechnical engineering*. Wiley and Sons. 461p.

Fenton, G.A., Griffiths, D.V. & Williams, M.B. 2005. Reliability of traditional retaining wall design. *Geotechnique* 55(1): 55–62.

Folayan, J.I., Høeg, K. & Benjamin, J.R. 1970. Decision theory applied to settlement prediction, ASCE J. *of the Soil Mechanics and Foundation Division* 96 (SM4) 1127–1141.

Foster, M., Fell, R. & Spannagle, M. 2000. The statistics of embankment dam failures and accidents. *Canadian Geotechnical Journal* 37(5): 1000–1024.

Gilbert, R.B., Lacasse, S. & Nadim, F. 2013. Advances in geotechnical risk and reliability for offshore applications. Keynote Lecture. *4th Intern. Symp. Geotechnical Safety and Risk*. ISGSR 2013. 4–6 Dec. Hong Kong Univ. Science & Technology.

Griffiths, D.V., Paiboon, J., Huang, J.S. & Fenton, G.A. 2013. Homogenization of geomaterials using the random finite element method. Keynote Lecture. *4th Intern. Symp. Geotechnical Safety and Risk*. ISGSR 2013. 4–6 Dec. Hong Kong Univ. Science & Technology.

Gutenberg, B. & Richter, C.F. 1944. Frequency of earthquakes in California. *Bulletin of the Seismological Society of America* 34: 185–188.

Hacking, I. 1975. *The emergence of probability*. Cambridge University Press. 209 p.

Harr, M.E. 1987. *Reliability-based design in civil engineering*. New York: McGraw-Hill. 290 p.

Hartford, D.N.D. & Baecher, G.B. 2004. Risk and uncertainty in dam safety. Thomas Telford London. 390 p.

Huang, H.W., Su, W.W. & Zhang, J. (2013). Selecting optimal probability models for geotechnical reliability analysis. Keynote Lecture. *4th Intern. Symp. Geotechnical Safety and Risk*. ISGSR 2013. 4–6 Dec. Hong Kong Univ. Science & Technology.

Huang, R.Q. 2008. Preliminary analysis of the development, distributions, and mechanisms of the geohazards triggered by the Great Wenchuan Earthquake *State Key Laboratory of Geohazards Prevention and Geological Environment Protection, Chengdu University of Technology.* Chengdu, China.

Høeg, K. 1996. Performance evaluation, safety assessment and risk analysis for dams. *Int. Journal on Hydropower and Dams* 3(6): 51–57.

Høeg, K. 2001. Embankment-dam engineering, safety evaluation and upgrading. *Proc. 15th ICSMGE*. Istanbul. 4 2491–2504.

Høeg, K. & Murarka R.P. (1974). Probabilistic analysis of a retaining wall. *ASCE J. of the Geotechnical engineering Division* 100 (GT3): 349–370.

Høeg, K. & Tang, W.H. 1977. Probabilistic Considerations in the Foundation Engineering for Offshore Structures. Proc. *2nd Intern. Conf. on Structural Safety and Reliability*, Munich, Germany, 267–296.

ICOLD 1995. Dam failures—statistical analysis, *Bulletin No. 99*. ICOLD, Paris, France.

Jaksa, M.B. 2006. Modeling the natural variability of an over-consolidated clay in Adelaide, South Australia. *2nd International Workshop on Characterization and Engineering Properties of Natural Soils.* Singapore, pp. 2721–2751.

Jordaan, I. (2008). *Decisions under uncertainty. Probabilistic analysis for engineering decisions*. Cambridge Univ. Press. 672 p.

Juang, CH., Wang, L. & Atamturktur, S. (2013). Robust design of geotechnical barriers—A new design perspective. Keynote Lecture. *4th Intern. Symp. Geotechnical Safety and Risk*. ISGSR 2013. 4–6 Dec. Hong Kong Univ. Science & Technology.

Kappes, M.S., Keiler, M., von Elverfeldt, K. & Glade, T. 2012. Challenges of analyzing multi-hazard risk: a review. *Natural Hazards* 64:1925–1958.

Lacasse, S. & Nadim, F. 1996. Uncertainties in characterizing soil properties. *Uncertainty in the Geologic Environment: From Theory to Practice*, ASCE Geotechnical Special Publication No. 58: 49–75.

Lacasse, S. & Nadim, F. 1998. Risk and Reliability in Geotechnical Engineering. State-of-the-Art paper. *4th International Conference on Case Histories in Geotechnical Engineering.* St-Louis MO USA. pp. 1172–1192.

Lacasse, S. & Nadim F. 1999. Risk analysis in geoengineering. *Rocksite 1999 Intern. Conf. on Rock Engineering Techniques for Site Characterization*, Bangalore, India, pp. 1–15.

Lacasse, S. & Nadim. F. 2007. Probabilistic geotechnical analyses for offshore facilities. *Georisk* 1(1): 21–42,

Lacasse, S., Nadim, F., Andersen, K.H., Knudsen, S., Eidsvig, U.K., Yetginer, G., Guttormsen, T.R. & Eide, A. 2013a. Reliability of API, NGI, ICP and Fugro Axial Pile Capacity Calculation Methods. *Offshore Technology Conference*. OTC-24063. Houston, Texas. 22 p.

Lacasse, S., Nadim, F., Langford, T., Knudsen, S., Yetginer, G., Guttormsen, T.R. & Eide, A. 2013b. Model Uncertainty in Axial Pile Capacity Design Methods. *Offshore Technology Conference.* OTC-24066. Houston, Texas. 10 p.

Lacasse, S., Nadim, F., K.H., Knudsen, S., Eidsvig, U.K., Liu, Z.Q., Yetginer, G. & Guttormsen, T.R. 2013c. Reliability of axial pile capacity calculation methods. *GeoMontréal 67th Canadian Geotechnical Conference.* Paper 699. Montréal Canada, 30 Sept–3 Oct 2013. 8 p.

Liu, Z.Q. 2011. Study on stability mechanism and risk decision making for talus slope. PhD dissertation submitted to Tongji University. March 2011. 169 p *(in Chinese)*.

Liu, Z.Q. & Nadim, F. 2013. A three-level framework for multi-risk assessment. *4th Intern. Symp. Geotechnical Safety and Risk*. ISGSR 2013 Dec 4–6. Hong Kong Univ. Science & Technology.

Londe, P. 1993. Safety evaluation using reliability analysis. *Proc. Workshop on Dam Safety Evaluation.* Grindelwald, Switzerland. 4: 171–188.

Lunne, T., Robertson, P.K. & Powell, J.J.M. 1997. *Cone penetration testing in geotechnical practice*. London: Spon Press. 312p.

Marzocchi, W., Garcia-Aristizabal, A., Gasparini, P., Mastellone, M.L. & Di Ruocco, A. 2012. Basic principles of multi-risk assessment: a case study in Italy. *Natural Hazards* 62: 551–573.

Nadim, F. & Liu, Z.Q. 2013a. Quantitative risk assessment for earthquake-triggered landslides using Bayesian network. Proc. 18th ICSMGE. Paris. Sept 2013.

Nadim, F. & Liu, Z.Q. 2013b. Framework for multi-risk assessment, Deliverable D5.2. New methodologies for multi-hazard and multi-risk assessment methods for Europe. MATRIX FP7 EU-project. With Garcia-Aristizabal, A., Woo, G., Aspinall, W., Fleming, K., Vangelsten, B.V., and van Gelder P. Contract No. 265138.

Newmark, N.M. 1965. Effects of earthquake on dams and embankments. *Geotechnique* 15(2): 139–160.

Peck, R.B. 1980. Where has all the judgment gone? The Fifth Laurits Bjerrum Memorial Lecture. *Canadian Geotechnical Journal* 17(4): 584–590.

Phoon, K.K. & Kulhawy, F.W. 1999. Characterisation of geotechnical variability. *Canadian Geotechnical Journal* 36: 612–624.

Popescu, R., Deodatis, G. & Nobahar, A. 2005. Effects of random heterogeneity of soil properties on bearing capacity. *Probabilistic Engineering Mechanics* 20: 324–341.

Popescu, R., Prevost, J.H. & Deodatis, G. 1998. Spatial variability of soil properties: two case studies. *Geotechnical Earthquake Engineering and Soil Dynamics*, ASCE Geotechnical Special Publication 75: 568–579.

Scott, G.A. 2011. The practical application of risk assessment to dam safety. *ASCE Geo-Risk 2011*, Atlanta. Keynote lecture. 129–168.

Staveren, M.Th. van (2013). Integrated geo risk management: crossing boundaries. Keynote Lecture. *4th Intern. Symp. Geotechnical Safety and Risk*. ISGSR 2013. 4–6 Dec. Hong Kong Univ. Science & Technology.

Stuyts, B., Gilbert. R. & Cathie, D. 2013. A reliability-based interpretation framework for pile-supported wind turbines. *Offshore Technology Conference*. OTC-24011. Houston, Texas. 10 p.

Tang, C., Zhu, J. & Qi, X. 2011. Landslide hazard assessment of the 2008 Wenchuan earthquake: a case study in Beichuan area. *Canadian Geotechnical Journal* 48: 128–145.

Tang, W. & J.M. Duncan 1994. Role of reliability methods in geotechnical engineering, Geotechnical News. June. pp. 12–13.

Tang, W.H. 1987. Updating anomaly statistics—single anomaly case. *Structural Safety* 4: 151–163.

Tang, W.H. 1988. Offshore axial pile design reliability. *Research Report for Project PRAC 86-29B,* American Petroleum Institute. Washington DC.

Tang, W.H. and Gilbert, R.B. 1992. Offshore piles system reliability. Research Report Project PRAC 89–29. American Petroleum Institute (API).

Tang, W.H. & Gilbert, R.B. 1993a. Case study of offshore pile system reliability. OTC 7196 *25th Annual Offshore Technology Conference*. Houston TX. 677–686.

Tang, W.H. & Gilbert, R.B. 1993b. Discussion Model Uncertainty Representation in Geotechnical Reliability Analyses, *J. Geotechnical Engineering* ASCE. 119(GT11) 1859–1861.

Tang, W.H., Woodford, D.L. & Pelletier, J.H. 1990. Performance Reliability of Offshore Piles. OTC 6379 *22nd Annual Offshore Technology Conference*. Houston TX. 299–308.

Tang, W.H. & Yen, B.C. 1991. Dam Safety Inspection Scheduling, Journal of Hydraulic Engineering, *ASCE Special publication*, 214–229.

Uzielli, M., Lacasse, S., Nadim, F. & Lunne, T. 2006a. Uncertainty-based characterisation of Troll marine clay. *2nd International Workshop on Characterisation and Engineering Properties of Natural Soils*, Singapore. 4: 2753–2782.

Uzielli, M., Lacasse, S., Nadim, F. & Phoon, K.K. 2006b. Soil variability analysis for geotechnical practice. *2nd International Workshop on Characterisation and Engineering Properties of Natural Soils*, Singapore, 3: 1653–1752.

Vanmarcke, E.H. 1977. Probabilistic modeling of soil profiles. *J. Geotechnical Engineering Division ASCE* 103(11): 1227–1246.

Vanmarcke, E.H. 1983. *Random Fields: analysis and synthesis.* Cambridge: MIT Press. 382p.

Vick, S. 2002. *Degrees of belief: Subjective probability and engineering judgment*. ASCE Press. Reston, VA. 455p.

Von Thun, J. 1985. *Application of statistical data from dam failure and accidents to risk-based decision analysis on existing dams*. U.S. Bureau of Reclamation, Engineering and Research Center, Denver, Colorado.

Vrijling, J.K. 2001. Safe dams and dykes—How safe?—Proc. *Symp. Dams and dykes in development*. ICOLD-ICID. Delft, The Netherlands. March 2001.

Wong, H.N. (2013). Is landslide risk quantifiable and manageable? Keynote Lecture. *4th Intern. Symp. Geotechnical Safety and Risk*. ISGSR 2013. 4–6 Dec. Hong Kong Univ. Science & Technology.

Xu, Y. & Zhang, L.M: 2009. Breaching parameters for earth and rockfill dams. *ASCE J. of Geotechnical and Geoenvironmental Engineering* 135(12): 1957–1970.

Yin, Y.P., Wang, F.W. & Sun, P. 2009. Landslide hazards triggered by the 2008 Wenchuan earthquake, Sichuan, China. *Landslides* 6: 139–152.

Zhang, J., Zhang, L.M. & Tang, W.H. 2009a. Bayesian framework for characterizing geotechnical model uncertainty. *J. Geotechnical and Geoenvironmental Engineering,* ASCE 135(7): 932–940.

Zhang, L.L., Tang, W.H. & Zhang, L.M. 2009b. Bayesian model calibration using geotechnical centrifuge tests. *J. Geotechnical and Geoenvironmental Engineering,* ASCE 135(2): 291–299.

Zhang, L.M., Nadim F. & Lacasse S. 2013. Multi-risk assessment for landslide hazards. *Proc. Pacific Rim Workshop on Innovations in Civil Infrastructure Engineering*, S.S. Chen, A.H-S. Ang and I.T. Yang (eds.), National Taiwan University of Science and Technology, Taipei, 321–329.

2 *Keynote lectures*

This page intentionally left blank

Geotechnical Safety and Risk IV – Zhang et al. (eds)
© 2014 Taylor & Francis Group, London, ISBN 978-1-138-00163-3

Advances in geotechnical risk and reliability for offshore applications

R.B. Gilbert
The University of Texas at Austin, Austin, Texas, USA

S. Lacasse & F. Nadim
Norwegian Geotechnical Institute (NGI), Oslo, Norway

ABSTRACT: This paper describes recent advances in geotechnical reliability and risk for offshore applications. The topics addressed include spatial variability, model uncertainty, hazard characterization, reliability-based design, system reliability and risk management. Conclusions from the evolution of reliability and risk approaches include that practical implementation is key, that assessment is best considered in the context of decision making, and that collaboration of multiple disciplines and stakeholders is important to managing risk effectively.

1 INTRODUCTION

The offshore oil and gas industry has been a leader in considering risk and reliability explicitly in developing and implementing designs. This industry has constantly pushed further the frontiers for design and technology, with facilities being developed at present in 3,000 m of water. The consequences of a failure can be severe, and the costs associated with mitigating risks can be enormous. Therefore, there is a strong need to avoid both under-conservatism and over-conservatism.

One of the first reliability-based design guidance documents was developed for offshore facilities (API 1993a). A sampling of the work that led to implementing reliability-based approaches in offshore geotechnical practice includes Bea (1983), Lacasse & Goulois (1989), Wu et al. (1989), Tang et al. (1990), Nadim & Lacasse (1992) and Tang & Gilbert (1993). In addition, the offshore industry has had the opportunity to learn from experience as the performance of facilities subjected to extreme operation conditions has been observed.

The objective of this paper is to describe recent advances in geotechnical reliability and risk for offshore applications. The following areas are highlighted:

1. Accounting for spatial variability in geotechnical properties;
2. Characterizing model uncertainty in design methods;
3. Representing loads and hazards in geotechnical systems;
4. Implementing reliability-based design in practice;
5. Considering the reliability of systems as well as components; and
6. Including a wide variety of perspectives, consequences and hazards in managing risks.

These advances are inevitably motivated by practical needs in offshore applications. However, the advances are general and fundamental, and therefore relevant to a wide variety of geotechnical applications. Case histories are presented to illustrate the recent advances. The paper concludes with recommendations for continuing the development and application of reliability and risk approaches in geotechnical engineering.

2 SPATIAL VARIABILITY

Accounting for spatial variability in geotechnical properties poses a significant challenge offshore for the following reasons:

1. The locations for offshore developments are not readily accessible;
2. The cost and time required to conduct offshore site investigations are orders of magnitude greater than for onshore site investigations[1]; and
3. The facilities on the seafloor for a single development, including foundations for structures, wells, manifolds and valves and pipelines, can extend many kilometers.

1. However, the costs of the geotechnical site investigations for offshore installations represent on y a very small fraction of the total development costs (less than 2%).

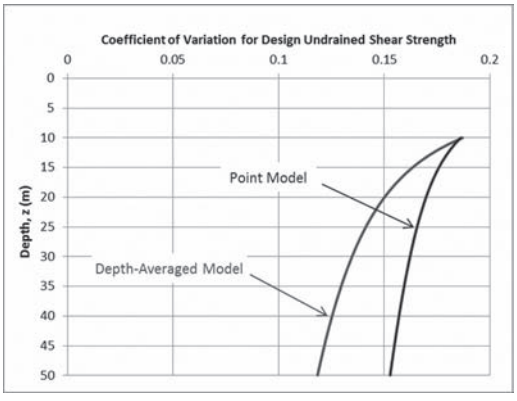

Figure 1. Coefficient of variation versus depth for point and depth-averaged values of design undrained shear strength in random field model (from Cheon & Gilbert 2013).

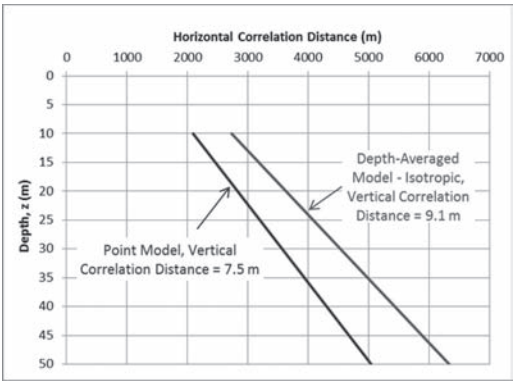

Figure 2. Horizontal correlation distance[2] versus depth for point and depth-averaged values of design undrained shear strength in random field model (from Cheon & Gilbert 2013).

Consequently, it is not feasible to gather 100 percent knowledge of the geotechnical properties at the location of or along every foundation element.

Recent advances have been made in developing realistic models of spatial variability to account for it in designing foundations and optimizing site investigation programs (e.g., Keaveny et al., 1990, Gambino & Gilbert 1999 and Valdez-Llamas et al., 2003).

An example of a random field model for the design capacity of deep foundations is shown in Figures 1 to 4. The geologic setting is normally to slightly overconsolidated marine clays in 1,500 to 3,000 m deep water in the Gulf of Mexico. The random field model represents spatial variations in the design shear strength. The design strength is the strength selected by a designer for the purposes of foundation design based on all available laboratory and field test data and geologic information at a given location. The available data for this geologic setting included over 100 design profiles of undrained shear strength from site investigations with soil borings, jumbo piston cores, field vane tests and Cone Penetration Tests (CPT). These design profiles are located as close as 100's of meters to as far as 1,000's of kilometers from one another.

The three-dimensional random field model consists of two cross-correlated models for the design undrained shear strength: one for the design strength at a particular depth below the sea floor (to calculate end bearing) and one for the depth-averaged design strength from the sea floor to that depth (to calculated side shear). The model incorporates means and standard deviations that increase with depth, an anisotropic spatial correlation structure, and horizontal correlations that increase with depth. Details for this model and its calibration are provided in Cheon (2011) and Cheon & Gilbert (2013).

The model shows that the influence of the spatial variability relative to the mean decreases with depth (Fig. 1), possibly reflecting the increasing overburden stress damping variations in mineralogy or depositional history. The effect of spatial averaging in reducing variability for the depth-averaged strength increases with averaging length (Fig. 1).

The horizontal correlation distance[2] obtained was between 2 and 6 km, and is therefore hundreds of times greater than the vertical correlation distance (Fig. 2). Note that the correlation distance is much greater for the design undrained shear strength compared to that for individual measurements of undrained shear strength since the design profile implicitly averages out small-scale variations (either real or due to measurement methods) and reflects larger-scale variations. Both the horizontal and vertical correlation distances are greater for the depth-averaged versus the point strength (Fig. 2). The horizontal correlation structure is best modelled as anisotropic, with a longer horizontal correlation distance moving away from the continental shelf (in the direction of depositional flow) compared to moving along the continental shelf (Fig. 3).

This model of spatial variability can be used to support design decisions. An example application

2. Correlation distance was defined here as the separation distance at which the correlation coefficient is equal to 0.37 for an exponentially decreasing correlation coefficient with separation distance. This correlation distance is one-half the scale of fluctuation defined by Vanmarcke (1983).

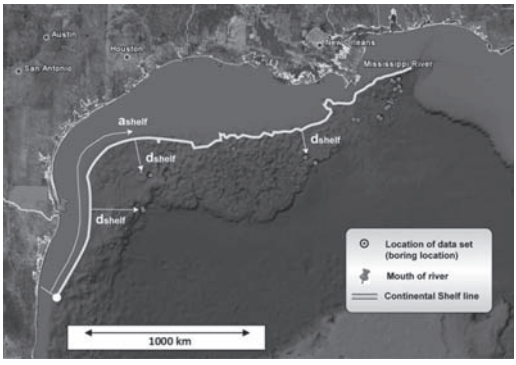

Figure 3. Coordinate system describing horizontal distances along and off the continental shelf for horizontally anisotropic correlation model (from Cheon & Gilbert 2013).

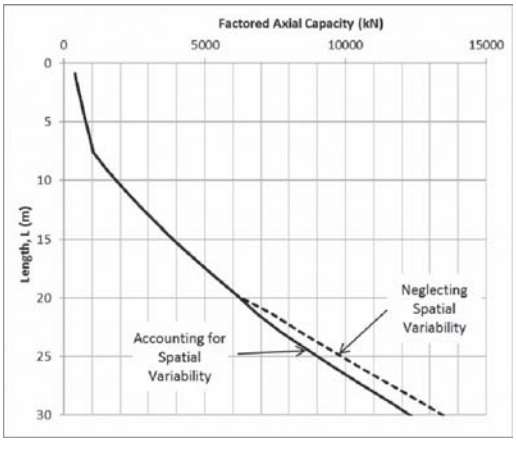

Figure 4. Factored design axial capacity for 5.5-m diameter suction caisson foundation (from Cheon & Gilbert 2013).

is for the design of a suction caisson that will need to penetrate below the depth of an available design profile for strength obtained from a jumbo piston core. Figure 4 shows the factored axial capacity (i.e., the nominal design axial capacity reduced by the resistance factor for a Load and Resistance Factor Design check).

The available design profile at this location extends to a depth of 20 m. For a caisson longer than 20 m, there is additional uncertainty in the axial capacity due to spatial variability. The curve labeled "Accounting for Spatial Variability" in Figure 4 incorporates an additional partial resistance factor to provide the same level of reliability as if a design profile were available. If the factored design load is 10,000 kN, then the required caisson length is 27 m. If an additional site investigation was conducted to develop a design profile at this location below a depth of 20 m, then the expected value of this additional information is a reduction in required caisson length of about 2 m (obtained by comparing the curves labeled "Accounting for Spatial Variability" and "Neglecting Spatial Variability" in Figure 4). The expected cost savings can be compared against the cost of obtaining the additional information and can be determinant for the decision-making on whether or not to do additional site investigations.

An important point in Figure 4 is that the added conservatism required to account for spatial variability, a reduction in capacity less than ten percent, is small compared to a typical resistance factor of 0.8 or material factor of 1.25. Therefore in this geologic setting, the additional (aleatory) uncertainty due to not having site-specific geotechnical data is small compared to the (epistemic) uncertainty in selecting a design shear strength that represents the actual strength mobilized when the foundation is loaded.

3 MODEL UNCERTAINTY

Model uncertainty, which is defined as variations between the actual performance and that predicted by a design method, can be one of the largest sources of uncertainty in offshore geotechnical design. For example, the coefficient of variation for model uncertainty in the axial capacity of a pile foundation is typically greater than 0.2, while the coefficient of variation due to spatial variability is less than 0.2 (Fig. 1).

Recent advances have been made in better characterizing model uncertainty for offshore applications. One advance has been related to the axial capacity of driven piles in sand. Based on several large-scale load testing programs and additional data, several newly developed design methods could be verified (e.g., Randolph 2003, Jardine et al., 2005, Lehane et al., 2005, Clausen et al., 2005, Kolk et al., 2005, Schneider et al., 2008 and Lacasse et al., 2013c).

In addition to pile load tests, recent advances have been made by studying the performance of actual offshore structures loaded to or beyond their calculated capacities. Five major hurricanes moved through the oil and gas infrastructure in the Gulf of Mexico between 2004 and 2008. Figure 5 shows an example of new information on the predicted versus measured axial capacity of driven piles at large capacity in normally consolidated clays. The data point with the largest measured capacity is for a 1,220 mm diameter by 70 m long pile that failed in tension when a tripod jacket was loaded beyond its ultimate capacity in Hurricane Ike (2008). It

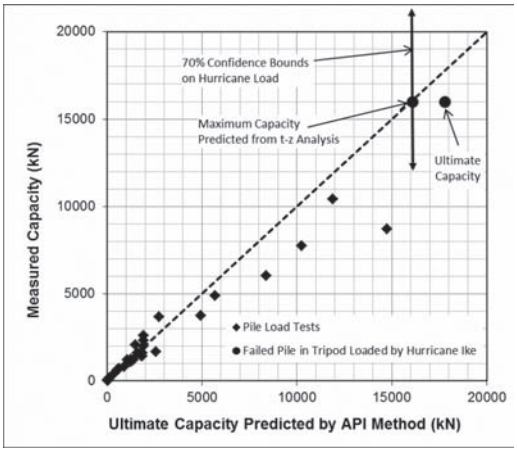

Figure 5. Comparison of measured with calculated axial capacity based on API current guidelines for driven piles in normally consolidated clays (adapted from Chen et al., 2013).

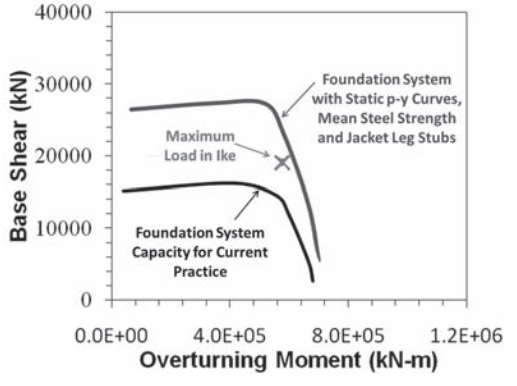

Figure 6. Comparison of measured and calculated pile system capacity for eight-pile jacket that survived Hurricane Ike (adapted from Gilbert et al., 2010).

is the largest published failure load to date for a driven pile in normally consolidated clay. The pile failed five years after installation under cyclic and rapid loading during a hurricane. It is notable because the predicted capacity, when a t-z analysis that accounts for strain-softening in side shear and an axial flexibility of the pile, matches very well with the most likely load at failure based on the hurricane hindcast.

Figure 6 shows an example of a pile system for an eight-leg jacket that survived Hurricane Ike. In this case, the piles are 920 to 1,070 mm in diameter, 52 m long, driven through layers of clay and sand, and tipped in sand. The estimated load in Hurricane Ike exceeded the calculated capacity of

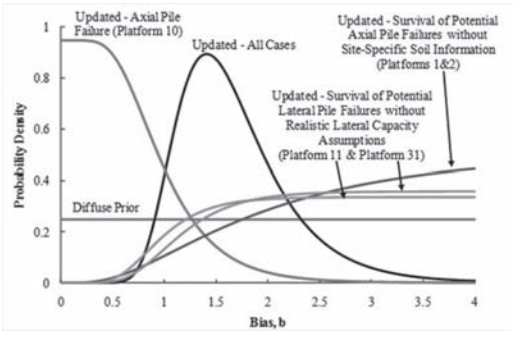

Figure 7. Probability distributions for bias on calculated ratio of pile system capacity to pile system load (reserve strength ratio) (from Chen & Gilbert 2013).

the foundation system, represented by the "Base Case" interaction curve in Figure 6. However, the calculated capacity of the foundation system is potentially conservative because it assumes a nominal rather than an average yield strength for the steel piles; the lateral resistance of the soil was reduced to account for cyclic loading when the piles are pushed into undisturbed soil at ultimate failure of the entire system; and the effect of jacket leg stubs extending below the mudline was assumed as negligible. When more realistic assumptions are used to model the pile system, the calculated capacity is equal to or greater than the estimated hurricane load (Fig. 6).

Figure 7 shows how the performance of individual platforms (e.g., Figs. 5 and 6) can be used to update model uncertainty with Bayes' theorem. The bias is defined as a multiplicative correction factor on the calculated ratio of capacity to load, defined as the reserve strength ratio, where the capacity is calculated using the existing API design method and the load is calculated using the hurricane hindcast. Variations between the actual and calculated reserve strength ratio could occur due both to errors in the calculated capacity or in the load. The updated probability distribution for this ratio is shown in Figure 7 for individual platforms that survived or failed in a hurricane. In addition, the results from these individual platforms are combined together into an overall result, labeled "Updated—All Cases," by assuming independence between platform performances. The overall result indicates that while there is possibly a conservative bias in the calculated reserve strength ratio, there is also considerable uncertainty (Fig. 7). The results in Figure 7 should be used with caution because they are based on a small data set and subsequently treat similarly a variety of different failure mechanisms, including lateral and axial pile failures.

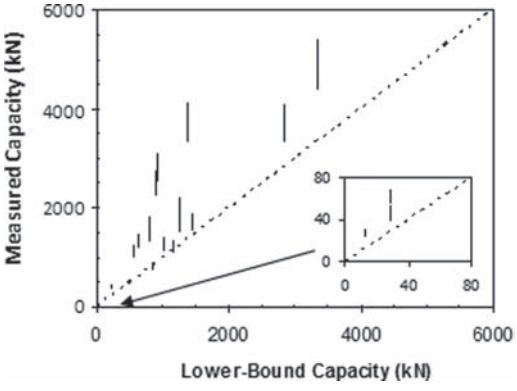

Figure 8. Comparison of measured axial capacity for driven piles in clay soils with estimated lower-bound capacity calculated assuming the side shear equal to the remolded undrained shear strength of the clay (adapted from Najjar 2005).

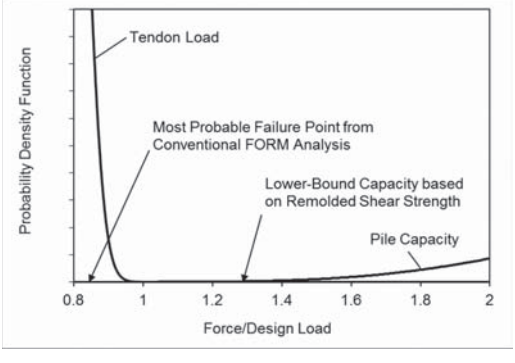

Figure 9. Probability distributions for load and capacity for a Tension Leg Platform foundation (adapted from Gilbert et al., 2010).

Another recent advance has been in refining models of the left-hand tail of capacity, which is the region of interest for reliability. Figure 8 shows an example of establishing a lower-bound on the axial capacity of a driven pile in clay based on the remolded undrained shear strength. This calculated lower-bound is less than the measured capacity in every load test. Figure 9 illustrates the physical significance of such a lower bound on the reliability of a Tension Leg Platform (TLP) foundation: the most probable point from a First Order Reliability Method (FORM) analysis, in which a conventional lognormal distribution is assumed for capacity, is well below the lower bound, which is unreasonable.

If a lower bound is incorporated into the probability distribution for capacity, then the reliability can be governed by this lower bound as opposed to

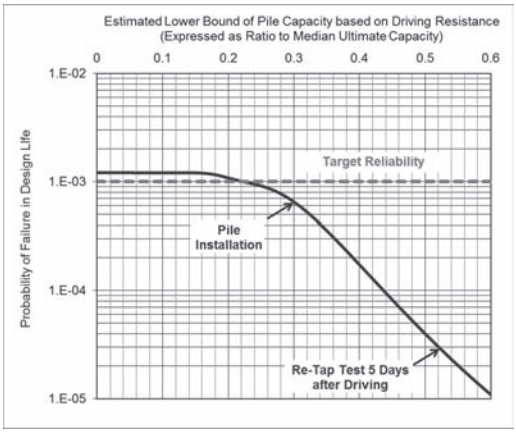

Figure 10. Effect of lower-bound on probability of failure for TLP foundation (adapted from Gilbert et al., 2010).

the mean or standard deviation (Najjar & Gilbert 2010). A lower bound on the capacity is particularly significant to the reliability in cases with relatively small uncertainty in the load or large factors of safety. In addition, a lower bound can be influential even when its exact value is uncertain. The application of this idea in practice is shown in Figure 10. The incorporation of a lower bound, which can be verified with pile driving monitoring during or after installation (i.e., a re-strike analysis), reduces the probability of failure for this foundation to within tolerable levels (Fig. 10).

4 HAZARD CHARACTERIZATION

The load or hazard is as important as the capacity in analyzing the reliability of a geotechnical system. In many cases, a thoughtful analysis of reliability can lead to advances in how the hazard is characterized.

Reliability-based design and the decision making processes in risk management often require an assessment of the failure probability during a reference time period, e.g., the annual failure probability or the failure probability during the lifetime of a project. The assessment of this probability requires a probabilistic description of the annual maximum environmental loads for foundation design, or a probabilistic description of frequency and intensity of trigger(s) for assessment of impact of geohazards on sea floor installations. Using this information, the probability of foundation failure or slope instability can be computed for all relevant scenarios and return periods in order to derive the annual or lifetime failure probability. However, including all possible scenarios can be

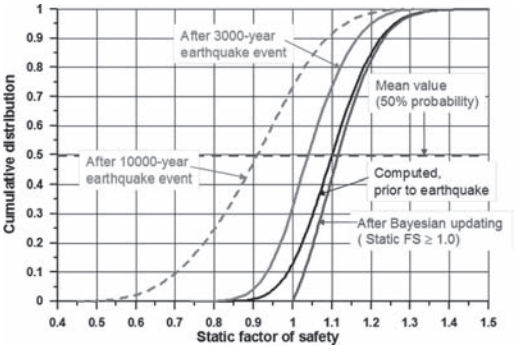

Figure 11. Results of probabilistic analyses of static undrained stability, prior to (black), updated (blue) and after the 3,000-year and 10,000-year earthquake (red) (from Nadim 2011).

time-consuming and impractical, and often only the few scenarios that contribute most to the failure probability are needed for a sound assessment.

Recent advances have been made in developing practical means to calculate the annual probability of earthquake-induced slope failure (Nadim 2002 and 2011). This work was supported by a number of joint-industry research projects and offshore geohazards studies in the North Sea, the Caspian Sea, the Black Sea, offshore Indonesia, and the Gulf of Mexico. The multi-step approach uses FORM, Monte Carlo simulation and Bayesian updating and is described in detail by Lacasse et al. (2013d). Nadim (2011) presents an example case study for a slightly overconsolidated clay slope in a moderately seismic area. Prior analyses showed that the earthquake events with return periods between 1,000 and 10,000 years contribute most to the annual probability of slope failure. The dynamic response analyses were therefore done for earthquake events with return periods of 3,000 and 10,000 years. Each of these events was represented by four sets of properly scaled acceleration time histories. Figure 11 shows the computed and the updated cumulative distribution functions for the static safety factor under undrained loading prior to the earthquake, and after the possible impact of 3,000-year and 10,000-year earthquake events.

To estimate the annual probability of slope failure, Nadim (2011) developed a simplified model similar to that suggested by Cornell (1996). The limit state function for the seismic resistance of the slope was defined as: G = Seismic resistance—Earthquake load = $A_{resist} - \varepsilon \cdot A_{max}$ where A_{max} is the annual peak ground acceleration representing the earthquake load, A_{resist} is the resistance of the slope to earthquake loading in terms of the peak ground acceleration causing slope failure, and ε describes the variability of the peak ground acceleration at a given return period.

The probability distribution of A_{max} was obtained from the site-specific Probabilistic Seismic Hazard Assessment (PSHA). A Pareto distribution provided a good fit for A_{max} with return periods greater than 100 years. The resistance parameter A_{resist} and the variability parameter ε were respectively assigned lognormal and normal distributions, and the parameters of the distribution functions were calibrated to match the conditional failure probabilities for the 3,000-year and the 10,000 year earthquake events (Fig. 11). With this limit state function, the annual probability of earthquake-triggered slope failure was computed using FORM to be $P_{f,annual} = 4 \times 10^{-4}$.

In some situations, such as offshore geohazards studies, it can be extremely difficult to identify the trigger(s) for submarine slides and a reference time frame. One must then rely on the identification and dating of recent (in geological sense) slide events in the area. The dating results and other relevant geological evidence can then be used in a Bayesian framework to establish the annual probability of slope instability (e.g., Nadim 2002). In performing these analyses, it is very important to consider the relevancy of the conditions present in the historical record, such as the sea level, to the conditions that may be present during the reference time period of interest.

Hazard characterization has also provided insight into physical mechanisms. As an example, a recent advance was made in assessing the hazard for wave-induced mudslides in the Mississippi River delta. For most fixed facilities in shallow water, such as jacket platforms, the loads are governed by the wave height and not the wave period. Therefore, the hazard has conventionally been described by a wave height in combination with an associated wave period that corresponds to the strong (right-hand in the northern hemisphere) side of a hurricane.

However, the wave period is an important consideration for wave-induced mudslides. Figure 12 shows how the factor of safety for a slope failure is affected by the wave height and the wave period at one location in the Mississippi River Delta. Wave-induced mudslides occurred at this location in both Hurricane Ivan (2004) and Hurricane Katrina (2005). While the maximum wave height in Ivan was significantly smaller than that during Katrina, the factor of safety was smaller in Ivan because of a relatively large wave period (Fig. 12). The Delta was about 150 km to the left of the eye of Hurricane Ivan, meaning that it was on the weak side of the storm. However, the wave periods on the weak side were similar to those for the much larger wave heights on the strong side

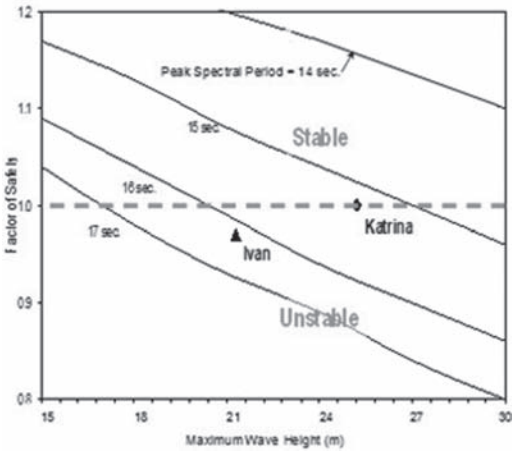

Figure 12. Factor of safety for slope failure versus wave height and period at one location in Mississippi River Delta (from Gilbert et al., 2010).

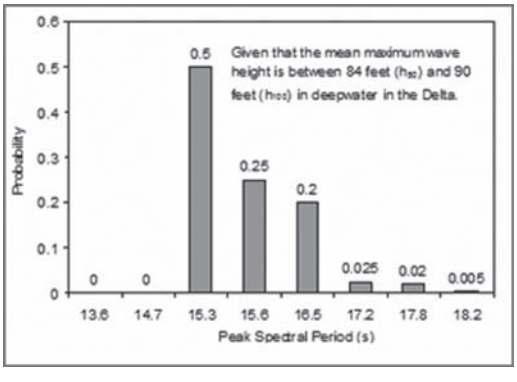

Figure 13. Conditional probability distribution for wave period in the Mississippi River Delta given a maximum wave height for a hurricane in the Gulf of Mexico (adapted from Nodine et al., 2009).

of the storm. Therefore, both large wave heights on the strong side of a storm (i.e., Katrina in Fig. 12) and smaller wave heights with longer periods on the weak side of a storm (i.e., Ivan in Fig. 12) contribute to the risk for wave-induced mudslides.

Based on this experience, an updated hazard representation was developed for wave-induced mudslides in the Delta. The approach utilized the Theorem of Total Probability to account for the possibilities that the maximum wave height in the Delta corresponds to the strong side of a storm with the largest waves in the storm or to the weak side of a storm with larger wave heights outside of the Delta (Nodine et al., 2009). An example of the conditional probability for wave period given

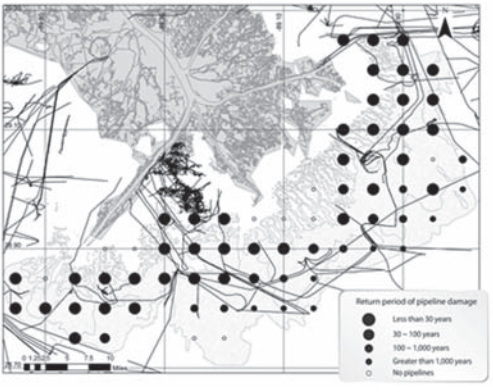

Figure 14. Return period for wave-induced mudslides impacting exiting pipelines in Mississippi River Delta (from Nodine et al., 2009).

a maximum wave height in the Delta is shown in Figure 13: the most probable combination of wave height and period represents hurricanes with their strong side over the Delta, while the other combinations represent hurricanes with their weak side over the Delta.

An example result from using this hazard characterization in assessing the hazard of wave-induced mudslides in the Delta is shown in Figure 14. This map incorporates the wave hazard with the water depth, bottom slope, geotechnical properties and pipeline locations.

5 RELIABILITY-BASED DESIGN

A significant benefit of a reliability-based design approach is to promote designs that efficiently achieve target levels of reliability. Recent advances have been made in implementing this principle in practice.

Lacasse et al. (2013a, 2013b and 2013c) describe a case study concerning the reliability of axially-loaded piles in sands. The API RP 2GEO (2011) and ISO 19902 (2007) guidelines included recently four CPT-methods for calculating the axial capacity of piles in sands. The design guidelines require that if newer methods are to be implemented in design, the same level of safety shall be documented for new methods as for existing methods.

Ensuring adequate reliability under severe loading is a necessary consideration, and the calculated safety margin depends on the uncertainty in the parameters used in the analyses and the model uncertainty. The design engineer attempts to compensate for the uncertainties by introducing appropriate (partial) "safety factor(s)" in design.

Table 1. Design methods considered in reliability analysis for axial capacity of driven piles.

Method	Methods in clay	Methods in sand
API	API-RP2 A 20th ed.1993	API-RP2 A 20th ed. 1993
NGI-05	Karlsrud et al. 2005	Clausen et al. 2005
ICP-05	Jardine et al. 1996; 2005	Jardine et al. 2005; API 2011; 2007
Fugro-96/05	Kolk and v.d.Velde 1996	Kolk et al. 2005
UWA-05	–	Lehane et al. 2005; Schneider et al. 2008

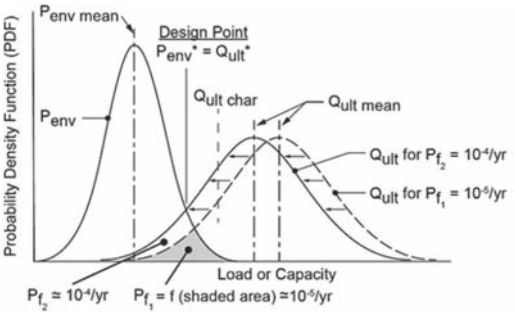

Figure 15. Simplified representation of reliability-based design calibration process (from Laasse et al., 2013a).

To evaluate the required resistance factor, Lacasse et al. (2013a, 2013b and 2013c) calculated the annual probability of failure for piles on offshore jackets designed with the API method and with the newer CPT-based methods. The goal was to make a recommendation on the appropriate resistance factor and minimum pile penetration depth to use for the design of the piles on an offshore jacket. Table 1 lists the axial pile capacity methods considered.

The reliability analyses of the axial pile capacity methods included a statistical analysis of the soil parameters; statistical analysis of the model uncertainty for the different pile capacity calculation methods used; statistical analysis of the static (permanent) and environmental loads on the top of the piles; deterministic analysis of the ultimate axial pile capacity, Q_{ult}; probabilistic analyses of axial pile capacity to obtain the PDF of the ultimate capacity, Q_{ult}; calculation of the annual probability of failure by combining the statistics of the loads and the probabilistic description of Q_{ult}; and calibration of the safety factors (load and resistance factor) for each pile capacity design method, for a target annual probability of failure of 10^{-4}.

Three sites, where jackets are currently under design, were analyzed. For Jacket A, the soil conditions are characterized by mainly clay layers with intermittent thin sand and silt layers. For Jacket B, the soil consists of mainly dense to very dense sand layers, with rather thin clay layers in between. For Jacket C, the soil profile consists of alternating very dense sand and very stiff clay units. The parameters were estimated with statistical analyses of the soil data, combined with well-documented correlations and experience (bias factors).

An extended study of the model uncertainty was carried out for the different axial pile capacity calculation methods (Lacasse et al., 2013c). The model uncertainty was expressed as a bias (mean), standard deviation, coefficient of variation and Probability Density Function (PDF). The model uncertainty was obtained by comparing the predicted to the measured axial pile capacity from relevant and reliable pile model tests. The NGI database of "super pile" load tests NGI (2000; 2001) was used.

The calibration used (1) the results of the deterministic analyses giving the ultimate axial pile capacity with the characteristic strength parameters ($Q_{ult\ char}$); (2) the probabilistic analyses giving the PDF of the ultimate axial pile capacity ($Q_{ult\ mean}$); and (3) the results of the probabilistic analyses giving the annual probability of failure, P_f.

Figure 15 is a simplification in two dimensions of the overlap of the probabilistic ultimate pile capacity (Q_{ult}) and probabilistic environmental load (P_{env}). The probability density function for the P_{env} was taken as the same for P_{f1} and P_{f2} in the calculations. The calibration of the resistance factor was coordinated with the definition of characteristic design load and the characteristic soil strength profile used for the calculation of axial pile capacity. The calibration details are described in Lacasse et al., 2013a.

Table 2 presents the results of the calibration of the resistance factor for the case study jackets to achieve an annual probability of failure of 10^{-4}. The resistance factor was obtained based on the axial pile capacity calculated with the characteristic undrained shear strength ($Q_{ult\ char}$). The load factors were maintained at the recommended values in the design guidance, although the load factor at the design point was smaller.

For a given pile length, the calibrated resistance factor varied with the pile design method. The factors reflect the varying influence of the uncertainty in the soil parameters and of the model uncertainties for the different methods. The results are generally consistent, where the axial pile capacity

Table 2. Calibrated resistance factors related to characteristic ultimate axial capacity.

Method	Site A (clay) 90-m pile	Site B (sand) 26-m pile	Site C (clay & sand) 40-m pile
NGI	1.23	1.35	1.20
ICP	1.52	1.45	1.32
Fugro	1.31	1.72	1.55
UWA	–	–	1.50
API	1.35	2.36	1.93

methods predicting higher axial pile capacity require a higher resistance factor to ensure that the annual probability of failure does not exceed 10^{-4}. The calibrated resistance factors apply to these case study jackets only, and cannot be transferred to other sites or structures without site-specific reliability studies.

These calibrated resistance factors allowed for a significant reduction in the required pile penetration depth because one could demonstrate that a target reliabilility could be achieved using lower resistance factors than the *a priori* values in the design guidance. The pile lengths could be reduced by 15 to 20 percent for Cases A and C and nearly 50 percent for Case B. A reliability analysis can therefore have important implications for the design of piles and result in significant savings.

This reliability study gave insight in the required resistance factor for different design methods of axial pile capacity to achieve the same annual P_f for a given pile penetration depth. The study is not meant to favor an approach. More case studies are needed on a variety of soil profiles to enable one to draw non site-specific recommendations on the resistance factor for each of the methods. The calibration analyses showed that:

1. The calibration of the safety factors demonstrates that the annual probability of failure varies with the axial pile capacity calculation method.
2. The values of model uncertainty used in the analyses have an overwhelming influence on the resulting annual probability of failure and therefore on the required resistance factor for a target annual probability of failure.
3. The current state-of-the-art design still relies heavily on qualified engineering judgment to assess and ensure a consistent safety level.
4. The resistance factors calibrated show that the newer CPT-methods of pile design are as reliable as the current API method.
5. The selection of the characteristic shear strength was also a significant parameter that influences the calibrated resistance coefficient.

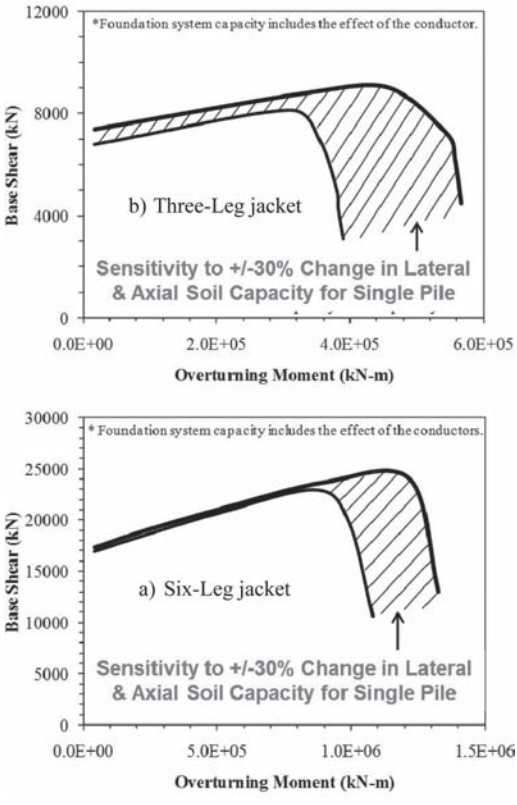

Figure 16. Interaction curves of pile system capacity exhibiting a robustness check (adapted from Chen et al., 2010).

6. The selection of the characteristic parameters to use in the deterministic analysis is often a source of uncertainty, and can be very subjective, varying from one engineer to the other. Lacasse et al. (2013a) provide recommendations for minimizing this variability.

6 SYSTEM RELIABILITY

Design checks are typically conducted on a component by component basis. However, the performance reliability of the entire system is generally of greatest interest in managing risk. Recent advances have been made in assessing system reliability for both fixed and floating offshore facilities.

Figure 16 shows a system robustness check for fixed jacket platforms. This idea was motivated by the performance of platforms in hurricanes in the Gulf of Mexico over the past decade. The check involves considering the capacity of the system when the lateral or axial capacity of any individual

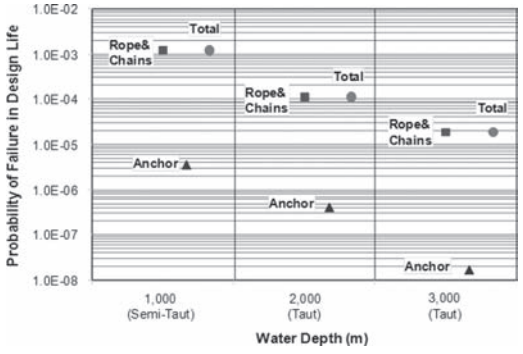

Figure 17. Comparison of probabilities of failure in design life for different components in the most heavily loaded line of a mooring system (from Clukey et al., 2013).

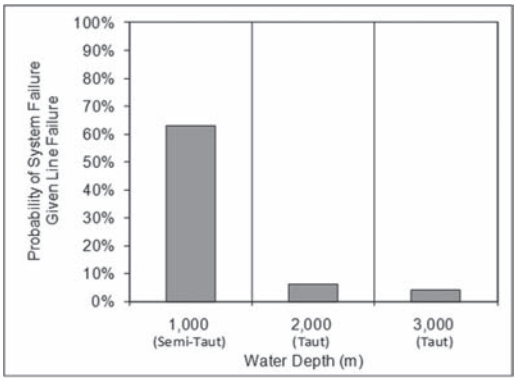

Figure 18. Conditional probability of failure given failure of the most heavily-loaded line for a mooring system in a hurricane (from Clukey et al., 2013).

pile is reduced. For the three-leg jacket, the system capacity in overturning is essentially proportional to the axial capacity of the most heavily-loaded pile (Fig. 16b). For the six-leg jacket (Fig. 16a), the system capacity in overturning is less sensitive, reducing by about 10% for a 30% reduction in the axial capacity of the most heavily-loaded pile. For both cases, the system capacity in shear is much less sensitive to the lateral capacity of an individual pile. This proposed design check is to maintain a minimum system capacity when reducing the axial and lateral capacities of individual piles in order to achieve a consistent level of reliability for a wide variety of pile systems.

Figure 17 shows the results from reliability analyses for the mooring system of a floating production system located in three different water depths (Clukey et al., 2013). The probability of failure for the suction caisson foundation (anchor) is orders of magnitude smaller than those for the ropes and chains in the mooring line. In addition, the probability of failure for individual components depends on the water depth, with the smallest probabilities of failure associated with the deepest water because the uncertain environmental loads are smaller relative the certain pre-tension loads as the water depth increases.

Figure 18 shows how the redundancy in this mooring system is sensitive to whether a semi-taut or taut[3] system is used. The redundancy in the taut system is greater than in the semi-taut system because the loads are re-distributed more evenly to the remaining lines when a single line fails (Fig. 18). Therefore, design checks based on single components in these mooring systems will not necessarily provide either a consistent or representative reliability with the system. This type of information is currently being considered in work to update the design guidance documents for mooring systems.

7 NEW TRENDS IN RISK MANAGEMENT

Disasters like the Maconda Well blowout, which caused the Deepwater Horizon oil spill in the Gulf of Mexico in May 2010, can catalyze moments of change in risk management aims, policy and practice. The population living along the coastline who might be affected by offshore accidents are demanding that their opinions are respected in the critical risk management decisions.

Quantitatively, risk is the expected consequence of an adverse event, where the consequences are obtained from the elements at risk and their vulnerabiltiy. Mitigation of risk can be accomplished by reducing the probabilty of the adverse event or by reducing the vulnerability and/or exposure of the elements at risk, or even by reducing both hazard and consequence (Fig. 19).

Designing participatory processes for stakeholder involvement the risk management decision making process is a new area of research. An example of this type of research was provided in the SafeLand Project (www.safeland-fp7.eu), a large collaborative project on landslide risk management within the European Commission's 7th Framework Programme. The SafeLand project developed and tested a public communication and participatory process for mitigating the risks of landslide in the highly at-risk community of Nocera Inferiore in southern Italy (SafeLand 2012). The pilot study demonstrated the potential

3. In a semi-taut mooring system there is moderate catenary in the mooring lines, while in a taut mooring system there is small catenary in the mooring lines.

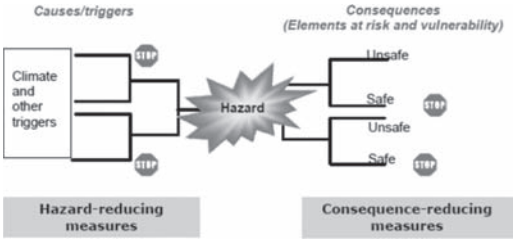

Figure 19. "Bow tie" diagram illustrating components in risk management (from Lacasse & Nadim 2009).

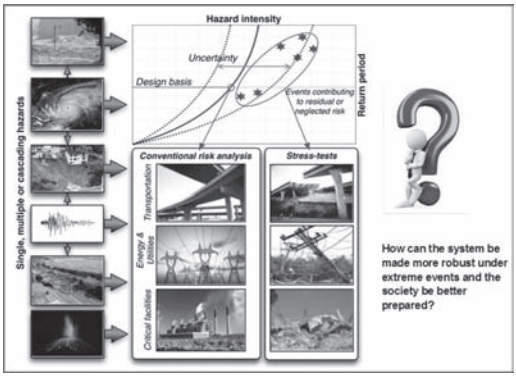

Figure 20. Stress testing as a tool to deal with residual or neglected risk for critical infrastructure (Nadim & Sparrevik, 2013).

and challenges of public participation in decisions characterized by high personal stakes and intricate technical, economic and social considerations. It should prove useful in informing similar processes, as stakeholders in Europe increasingly demand a voice in choosing landslide mitigation measures.

The results of the pilot study in SafeLand showed that it is feasible to organize an expert-informed participatory process that respects and builds on conflicting citizen perspectives and interests, and demonstrates spheres of policy consensus as well as policy dissent. Increasingly public interventions to reduce the risk of landslides and other hazards are moving from "expert" decisions to include the public and other stakeholders in the decision process. Variations in the role of science and scientists, governance structures and interest groups, legislation, availability of economic and political instruments, social learning, facilitation of communication and trust, media intervention, access to information, and external pressures and shocks were some of the issues identified by the SafeLand research that impact the cognition and management of risk practice in a society.

Another new trend in risk management is stress testing. Stress testing is a procedure used to determine the stability of a system or entity. It involves testing the said system or entity to beyond its normal operational capacity, often to a breaking point, in order to observe its performance/reaction to a pre-defined internal or external effects (pressure/force). Stress tests have been used for many years in air traffic safety, in particular for airplanes and helicopters. In recent years, stress testing has often been associated with methodologies to assess the vulnerability of a financial system or specific components of it, such as banks. A number of analytical tools have been developed in this area and have been frequently used since the late 1990's (e.g., Borio et al., 2012).

More recently, stress testing has been applied to the comprehensive safety and risk assessment of nuclear power plants, in particular in the aftermath of the 11th March 2011 East Japan earthquake and tsunami leading to the Fukushima Dai-ichi accident. Many aspects of the accident devastating the Fukushima Dai-ichi nuclear power plant are still uncertain. However, the accident highlighted three areas of potential weakness in the existing safety approaches:

1. Inadequacy of safety margins in the case of extreme external events, especially natural hazards.
2. Lack of robustness with respect to events that exceed the design basis.
3. Ineffectiveness of current emergency management under highly unfavourable conditions.

These issues were the focus of the stress tests imposed on all nuclear power plants in Europe in 2011 and 2012 (WENRA, 2011).

A stress test is an examination of the safety of a system under those particularly unfavourable scenarios that fall outside the design basis specified by the regulatory regime, by the operational institution or by the stakeholders. A stress test can test the system to assess its response to scenarios expected to be in the residual and neglected risk areas (Fig. 20). In this respect, stress testing is not a substitute for "conventional" risk or safety assessments, but it provides additional valuable insight under extreme situations. What stress tests and "conventional" risk or safety assessments have in common is that they both rely on a description of the system of interest, which helps to associate the state of the system and a set of consequences under any given or potential scenario.

Several multi-national research projects in Europe are starting up in 2014 to develop guidelines for stress testing of critical infrastructure under the action of natural hazards (Nadim & Sparrevik, 2013). The premises are that a critical

infrastructure is designed to withstand the impact of natural hazards according to regulations in codes and standards or specifications from the owner and/or stakeholders. The regulations are often set through probabilistic evaluations with the objective of reducing risk to an acceptable level. This evaluated risk will be in accordance with what society will tolerate in terms of loss of life, environmental damages and the loss of assets through the definition of acceptance criteria that are incorporated into regulations.

The design rules that result from such regulations implicitly accept that there is a residual risk associated with rare, extreme events that is neglected because of the (objectively calculated or perceived) very low probability of occurrence. However, the Fukushima accident showed that as a consequence of this neglect, a system that is quite robust as long as events remain within its design basis can abruptly shift to complete failure when that threshold is passed. Stress tests can help detect such "cliff-edge effects" and identify ways to introduce some robustness in the system without any change in the acceptable level of risk.

Most risk evaluations are based on probability estimates using historical data, observations and/or experience and engineering judgment, and consequence models that try to estimate the impact of unwanted future hazard situations. For natural hazards, historical data may in some cases be sparse or highly uncertain. There is also generally little experience with extreme events, because of their nature. Furthermore, simplified models of highly complex situations yield predictions of system response that contain significant uncertainty. The scarcity of data and model uncertainty may lead to optimistic evaluations that neglect the risks associated with extreme events. Stress testing provides a framework to address these neglected risks.

Stress tests have not yet been applied in offshore projects. However, the safety philosophy and premises for design of offshore structures are quite similar to those for onshore critical infrastructure. In the future, stress tests could complement the present risk assessment approaches for many offshore projects.

8 SUMMARY

This paper has described recent advances in geotechnical reliability and risk for offshore applications. The areas addressed include spatial variability, model uncertainty, hazard characterization, reliability-based design, system reliability and risk management. Case histories from real-world applications were described to illustrate the practical motivation for and usefulness of these advances.

The following conclusions are drawn from the evolution of reliability and risk approaches to their current state for offshore applications:

1. Applying the theory of reliability and risk in practice is critical to obtaining useful insights from the theory and to developing practical means to implement the theory. While the application of reliability and risk approaches has matured, each major practical application still involves a significant element of research and development to best suit that particular problem.
2. Assessing reliability and risk is most valuable if it is considered in the context of helping stakeholders make decisions. Opportunities in decision making exist both to mitigate risk as well as to reduce the cost required to achieve a target level of risk
3. Managing risk effectively requires the collaboration of multiple disciplines and the involvement of stakeholders at all stages of the process, from assessment to decision making.

While offshore applications have provided wonderful opportunities to advance these approaches, the results of these advances are relevant to a wide variety of geotechnical problems.

The future for reliability and risk approaches is bright. Public and private stakeholders will always welcome, seek and value help in making better and more defensible decisions. The following recommendations are offered to guide the continued advancement of these approaches:

1. Develop means and methods to implement reliability and risk approaches that are as simple as possible while still capturing the important characteristics that describe hazards, consequences and the performance of engineered systems. Simplicity is important both to make implementation practical and to make the approaches as transparent as possible for the stakeholders.
2. Encourage the application of reliability and risk approaches in the earliest stages of project development when the greatest opportunities exist to impact decisions and to proactively plan to acquire valuable data for future decisions.
3. Continuously strive to update knowledge about hazards, consequences and performance based on historical information. Reliability and risk approaches provide the link between this information and the assessment and management of risk for future applications.
4. Increase awareness and understanding about reliability and risk approaches for technical professionals and colleagues in the other disciplines such as social sciences, as well as the general public.

REFERENCES

API 1993a. Recommended Practice for Planning, Designing and Constructing Fixed Offshore Platforms—Load and Resistance Factor Design. API RP2 A-LRFD, 1st Ed. Washington.

API 1993b. Recommended Practice for Planning, Designing and Constructing Fixed Offshore Platforms—Working Stress Design. API RP2 A-WSD, 20th Ed. Washington.

API 2007. Recommended Practice for Planning, Designing and Construction Fixed Offshore Platforms—Working Stress Design. API RP 2 A-WSD, 21st Ed. Washington.

API 2011. Geotechnical and Foundation Design Considerations. ANSI/API RP 2GEO, 1st Ed. Washington.

Bea, R.G. 1983. Characterization of the reliability of offshore piles subjected to axial loadings. Structural Congress, American Society of Civil Engineering, New York, pp. 1–20.

Borio, C., Drehmann, M., and Tsatsaronis, K. 2012. Stress-testing macro stress testing: Does it live up to expectations? BIS Working Papers, No 369, January.

Chen, J-Y., Gilbert, R.B., Murff, J.D., Young, A. and Puskar, F. 2010. Structural factors affecting the system capacity of jacket pile foundations. Proceedings, International Symposium on Frontiers in Offshore Geotechnics, Perth, Australia.

Chen, J-Y., Gilbert, R.B., Puskar, F. and Verret, S. 2013. Case study of offshore pile system failure in Hurricane Ike. Journal of Geotechnical and Geoenvironmental Engineering, ASCE, in press.

Chen, J-Y. and Gilbert, R.B. 2013. Insights into the performance reliability of offshore piles based on experience in hurricanes. Principles and Practices in Geotechnical Engineering, A Geotechnical Special Publication honoring Roy Olson, American Society of Civil Engineers, Reston, Virginia, in press.

Cheon, J.Y. 2011. Analysis of spatial variability in geotechnical data for offshore foundations. Ph.D. Dissertation, The University of Texas at Austin, Austin, Texas, 2011, p. 212.

Cheon, J.Y. and Gilbert, R.B. 2013. Modeling spatial variability in offshore geotechnical data for reliability-based foundation design. Structural Safety, in press.

Clausen, C., P.M. Aas and K. Karlsrud 2005. Bearing Capacity of Driven Piles in Sand, the NGI Approach. Proceedings, International Symposium on Frontiers in Offshore Geotechnics, Perth, Australia.

Clukey, E.C., Gilbert, R.B., Andersen, K.H. and Dahlberg, R. 2012. Reliability of suction caissons for deep water floating facilities. Foundation Engineering in the Face of Uncertainty, Geotechnical Specialty Publication Honoring Dr. Fred H. Kulhawy, ASCE. Reston, Virgina.

Cornell, C.A. 1996. Calculating building seismic performance reliability: A basis for multi-level design norms, Proc. 11th World Conf. on Earthquake Eng., Acapulco, Mexico.

Gambino, S.J. and Gilbert, R.B. 1999. Modeling spatial variability in pile capacity for reliability-based design. Analysis, Design, Construction and Testing of Deep Foundations, Roesset Ed., ASCE Geotechnical Special Publication No. 88, pp. 135–149.

Gilbert, R.B., Murff, J.D. and Clukey, E.C. 2010. Risk and reliability on the frontier of offshore geotechnics. Proceedings, International Symposium on Frontiers in Offshore Geotechnics, Perth, Australia.

ISO 19902 2007. Petroleum and natural gas industries—Fixed Steel Offshore Structures. 1st ed., Switzerland.

Jardine, R.J. and Chow, F.C. 1996. New design procedures for offshore piles. Marine Technology Directorate. Publ. 96/103, London, UK.

Jardine R.J., F.C. Chow, R.F. Overy and J.R. Standing 2005. ICP design methods for driven piles in sands and clays. Imperial College, Thomas Telford Publishing, London.

Karlsrud, K., Clausen, C.J.F. and Aas, P.M. 2005. Bearing capacity of driven piles in clay, the NGI approach. Proceedings, International Symposium on Frontiers in Offshore Geotechnics, Perth, Australia.

Keaveny, J.M., Nadim, F. and Lacasse, S. 1990. Autocorrelation functions for offshore geotechnical data. Proceedings, International Conference on Structural Safety and Reliability, 5. ICOSSAR '89. San Francisco, California, pp. 263–270.

Kolk, H.J., A.E. Baaijens and M. Senders 2005. Design criteria for pipe piles in silica sands. Proceedings, International Symposium on Frontiers in Offshore Geotechnics, Perth, Australia.

Kolk, H.J. and Velde, E. v.d. 1996. A Reliable Method to Determine Friction Capacity of Piles Driven into Clays. Proceedings, Offshore Technology Conference, Houston, Texas, OTC 7993.

Lacasse, S. and Goulois, A. 1989. Uncertainty in API parameters for predictions of axial capacity of driven pile in sand. Proceedings, Offshore Technology Conference, Houston, Texas, Houston, Texas, pp. 353–358.

Lacasse, S. and Nadim, F. 2009. Landslide risk assessment and mitigation strategy, Chapter 3 in Landslides—Disaster Risk Reduction, Springer-Verlag, Berlin.

Lacasse, S., Nadim, F., Andersen, K.H., Knudsen, S., Eidsvig, U.K., Yetginer, G., Guttormsen, T.R. and Eide, A. 2013a. Reliability of API, NGI, ICP and Fugro Axial Pile Capacity Calculation Methods. Proceedings, Offshore Technology Conference, Houston, Texas, OTC-24063-MS.

Lacasse, S., Nadim, F., K.H., Knudsen, S., Eidsvig, U.K., Liu, Z.Q., Yetginer, G. and Guttormsen, T.R. 2013b. Reliability of Axial Pile Capacity Calculation Methods. Proceedings, GeoMontréal 67th Canadian Geotechnical Conference. Montréal Canada, Paper 699.

Lacasse, S., Nadim, F., Langford, T., Knudsen, S., Yetginer, G., Guttormsen, T.R. and Eide, A. 2013c. Model uncertainty in axial pile capacity design methods, Proceedings, Offshore Technology Conference, Houston, Texas, OTC 24066.

Lacasse, S., Nadim, F., Vanneste, M., L'Heureux, J.S., Forsberg, C.F. and Kvalstad, T. 2013d. Case Studies of Offshore Slope Stability. Keynote Lecture. Proceedings, ASCE GeoCongress 2013—Stability and Performance of Slopes and Embankments III, San Diego, California, pp 2379–2418.

Lehane, B.M., J.A. Schneider and X. Xu 2005. A Review of Design Methods for Offshore Driven Piles in Siliceous Sand. UWA Report No. GEO 05358, The

University of Western Australia, Perth, Australia, Sept. 2005.
Nadim, F. 2002. Probabilistic methods for geohazards problems: State-of-the-Art. Proceedings, Probabilistics in Geotechnics: Technical and Economic Risk Estimation, Graz, Austria, September 15–19, p. 18.
Nadim, F. 2011. Risk Assessment for Earthquake-Induced Submarine Slides. Keynote Lecture, 5th International Symposium on Submarine Mass Movements and Their Consequences, ISSMMTC, Kyoto, Japan, 24–26 October, Springer.
Nadim, F. and Lacasse, S. 1992. Probabilistic bearing capacity analysis of jackup structures. Canadian Geotechnical Journal, 29, pp. 580–588.
Nadim, F., and Sparrevik, M. 2013. Managing unlikely risks posed by natural hazards to critical infrastructure. Proceedings, 22nd SRA Europe Conference, Trondheim, Norway, 17–19 June.
Najjar, S.S. 2005. The importance of lower-bound capacities in geotechnical reliability assessments. Ph.D. Dissertation, The University of Texas at Austin, p. 347.
Najjar, S.S., and Gilbert, R.B. 2009. Importance of lower-bound capacities in the design of deep foundations. Journal of Geotechnical and Geoenvironmental Engineering, ASCE 135 (7): 890–900.
NGI 2000. Bearing Capacity of Driven Piles in Clay. Report 525211–1. 23 March 2000.
NGI 2001. Bearing Capacity of Driven Piles in Sand. Report 525211–2. 21 Jan. 2001.
Nodine, M.C., Gilbert, R.B., Cheon, J.Y., Wright, S.G. and Ward, E.G. 2009. Risk analysis for hurricane wave-induced submarine mudslides. Proceedings, Submarine Mass Movements and Their Consequences, 4th International Symposium, Springer, pp. 335–352.
Randolph, M.F. 2003. Science and empiricism in pile foundation design. Geotechnique 44 (3): 427–448.
SafeLand 2012. Deliverable D5.7: Design and testing: a risk communication strategy and a deliberative process for choosing a set of mitigation and prevention measures. http://www.safeland-fp7.eu/results/Documents/D5.7.pdf
Schneider, J.A., X. Xu and B.M. Lehane 2008. Database assessment of CPT-based design methods for axial capacity of driven piles in siliceous sands. Journal of Geotechnical and Geoenvironmental Engineering, ASCE 34 (9): 1227–1244.
Tang, W.H. and Gilbert, R.B. 1993. Case study of offshore pile system reliability. Proceedings, Offshore Technology Conference, Houston, Texas, pp. 677–686.
Tang, W.H., Woodford, D.L. and Pelletier, J.H. 1990. Performance reliability of offshore piles, Proceedings, Offshore Technology Conference, Houston, Texas, OTC 6379.
Valdez-Llamas, Y.P., Auvinet, G. and Nunez, J. 2003. Spatial variability of the marine soil in the Gulf of Mexico. Proceedings, Offshore Technology Conference, Houston, Texas, OTC 15266.
Vanmarcke, E.H. 1983. Random fields: analysis and synthesis. The MIT Press, Boston, Massachusetts.
WENRA (West European Nuclear Regulators Association) 2011. "Stress tests" specifications—Proposal by the WENRA Task Force, 21 April 2011. http://www.oecd-nea.org/nsd/fukushima/documents/WENRA20110421StressTestsSpecifications2011–04–21.pdf.
Wu, T.H., Tang, W.H., Sangrey, D.A., and Baecher, G.B. 1989. Reliability of offshore Foundations—state of art. Journal of Geotechnical Engineering, ASCE 115 (2): 157–178.

Geotechnical Safety and Risk IV – Zhang et al. (eds)
© 2014 Taylor & Francis Group, London, ISBN 978-1-138-00163-3

Homogenization of geomaterials using the random finite element method

D.V. Griffiths
Colorado School of Mines, Golden, CO, USA
University of Newcastle, NSW, Australia

Jumpol Paiboon
Colorado School of Mines, Golden, CO, USA

Jinsong Huang
University of Newcastle, NSW, Australia

Gordon A. Fenton
Dalhousie University, Halifax, NS, Canada

ABSTRACT: The homogenized stiffness of geomaterials that are highly variable at the micro-scale has long been of interest to geotechnical engineers. The purpose of this study is to investigate the influence of porosity and void size on the homogenized or effective properties of geomaterials. A Random Finite Element Method (RFEM) has been developed enabling the generation of spatially random voids of given porosity and size within a block of geomaterial. Following Monte-Carlo simulations, the mean and standard deviation of the effective property can be estimated leading to a probabilistic interpretation involving deformations. The probabilistic approach represents a rational methodology for guiding engineers in the risk management process. The influence of block size and the Representative Volume Elements (RVE) are discussed, in addition to the influence of anisotropy on the effective Young's modulus.

1 INTRODUCTION

The motivation of this work is to investigate the influence of porosity and void size on the stiffness of 3D geomaterials using a statistical approach. Even if the expected porosity of a site can be conservatively estimated, the location of the voids may be largely unknown such as in geological regions dominated by karstic deposits. This makes a statistical approach appealing. The work presented in this paper is developed from a study of 2D model homogenization of geomaterials containing voids by random fields and finite elements (Griffiths et al. 2012) and 3D random finite element methods (Fenton & Griffiths, 2005). The classic problem of homogenization of heterogeneous materials with variable micro-structure has long been of practical interest to engineers. In the current study, the influence of voids on effective elastic properties is investigated. The goal of homogenization is to predict the effective property of a heterogeneous material, where the effective value is defined as the property that would have led to the same response if the geomaterial had been homogeneous. A useful concept in this homogenization process is the Representative Volume Element (RVE). An RVE is an element of the heterogenous material that is large enough to represent the microstructure but small enough to achieve computational efficiency (e.g. Liu, 2005; Zeleniakiene et al. 2005).

Since the concept of the RVE was first introduced by Hill (1963), several theoretical models have been proposed for dealing with scale effects. Hazanov & Huet (1994) derived results involving mixed boundary conditions, which locate between the static and kinematic uniform boundary conditions for specimens smaller than the size of the RVE. Orthogonal mixed boundary conditions have also been proposed (e.g. Hazanov & Amieur, 1995; Havanov, 1998; Khisaeva & Ostoja-Starzewski, 2006). Numerical methods such as the Finite Element Method (FEM) have also been used to validate the RVE size of random heterogeneous materials. Kanit et al. (2003) used Monte-Carlo simulations to investigate RVE and effective properties, while Zohdi & Wriggers (2001) and Ostoja-Starzewski (2006) investigated the RVE size using a statistical computational approach. Although there are many models developed to investigate the effective properties of a material containing voids, there is no model that works for all problems

(e.g. Böhm, 1998, 2013). See also the reviews published by Torquato (2002), Kachanov (2005) and Klusemann & Svendsen (2009).

In this paper, the Random Finite Element Method (RFEM) (e.g. Griffiths & Fenton 2007), which combines finite element analysis with random field theory, will be used in conjunction with Monte-Carlo simulations, to examine the effective elastic properties of materials with randomly distributed voids. A 3D cube of material, discretized into a relatively fine mesh of 8-node hexahedral elements, forms the basis of the model. Random field theory will be used to generate a material containing intact material and voids with controlled porosity and size. The RFEM can vary the size of the voids through control of the spatial correlation length and excursion theory (see e.g. p.141 in Fenton & Griffiths 2008). For each simulation of the Monte-Carlo process, elements in the mesh are assigned either an intact stiffness value or a much lower stiffness value corresponding to a void. A deterministic analysis follows leading to effective values of the elastic parameters E and υ. Monte-Carlo analyses are typically repeated numerous times until the output statistics of the effective elastic properties (mean and SD) stabilize.

The first part of the paper investigates the size of the RVE for different input void properties. The second part of the paper investigates the statistics of the effective Young's modulus and Poisson's ratio in 3D as a function of porosity and void size, and compares results with numerical and analytical studies by other investigators. Effective properties in 3D are also compared with anisotropic results.

2 FINITE ELEMENT MODEL

Examples of the model which combines elastic material and voids are shown in Figure 1.

The finite element mesh for this study consists of a cubic block of material of side length $L = 50$ modeled by $50 \times 50 \times 50$ 8-node cubic elements of side length $\Delta x = \Delta y = \Delta z = 1.0$. Any consistent system of units could be combined with the dimensions and properties described in this paper. Since a mesh such as this involves rather large global matrices, equation solution in the runs described in this paper will be performed using a Preconditioned Conjugate Gradient (PCG) technique with element-by-element products as described by Smith and Griffiths (2004) which avoids entirely the need to assemble the global stiffness matrix. The model in Figure 2 is subjected to a vertical force $Q = L \times L$ on the top face leading to an average unit pressure on the top face of 1.0. The boundary conditions of the block involve the use of "tied freedoms" that allow analysis of an "ideal" block and direct evaluation of the effective Young's modulus and Poisson's ratio. Tied freedoms

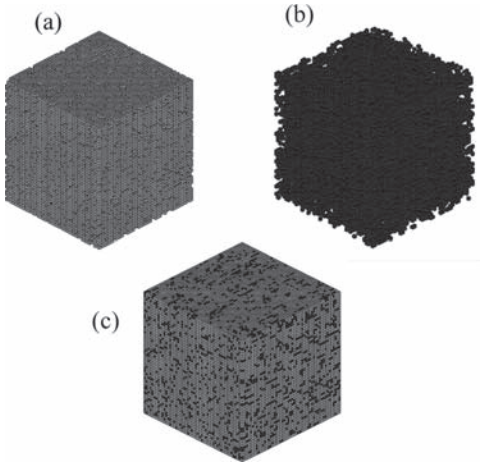

Figure 1. The 3D finite element model of ideal cubic blocks: (a) the solid material, (b) the voids, and (c) the combined model which show dark and light regions indicating voids and solid material respectively.

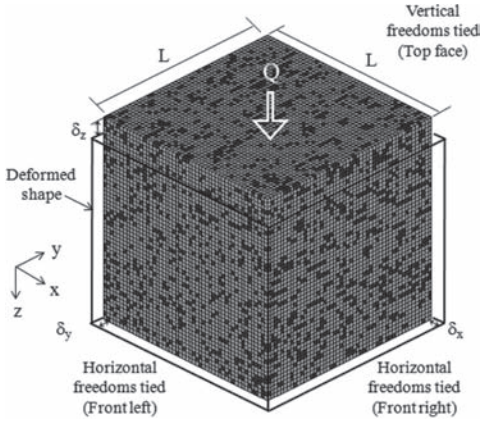

Figure 2. Analysis of tied freedom in a "cubic element test" model with voids. A vertical force is applied on the top side. Rollers are fixed at the bottom and two back sides. The top and the two front sides are tied. The dark and grey elements represent, respectively, void and intact solid elastic material.

are forced to move by the same amount in the analysis. The boundary conditions are such that the cubic block remains a regular hexahedron after deformation. Other methods may give similar outcomes (see e.g. the effects of tied freedom boundary condition from Huang et al. 2013). From this idea, the effective Young's modulus and Poisson's ratio easily be back-figured as will be described.

In particular, the boundary conditions are such that nodes on the base of the block can move only

in the $x - y$ plane. The back left and back right faces are constrained to move only in the $y - z$ and $z - x$ planes respectively. All z-freedoms on the top plane are tied, as are the y-freedoms on the front left plane and the x-freedoms on the front right plane. A consequence of these constraints is that the top surface remaining horizontal and the two front sides remaining vertical following deformation.

These specific boundary conditions enable more direct comparison to be made with experimental results, where displacements may be applied without friction on all sides of the specimen. Periodic boundary conditions have also been used in homogenization studies of heterogeneous media, (e.g. Garboczi & Day, 2005).

3 CONTROLLING POROSITY

The random field generator in the RFEM model known as the Local Average Subdivision method (LAS) (Fenton & Vanmarcke 1990) is used in this paper to model spatially varying voids properties. The target mean porosity n is obtained by using the standard normal distribution shown in Figure 3. A single value of the random variable Z is initially assigned to each element of the finite element mesh. Once the standard normal random field values have been assigned, cumulative distribution tables Φ (suitably digitized in the software) are then used to estimate the value of the standard normal variable $z_{n/2}$ for which

$$\Phi\left(z_{n/2}\right) - \Phi(0) = n/2 \tag{1}$$

where Φ is the cumulative normal distribution function, and n is the target porosity as shown in Figure 3.

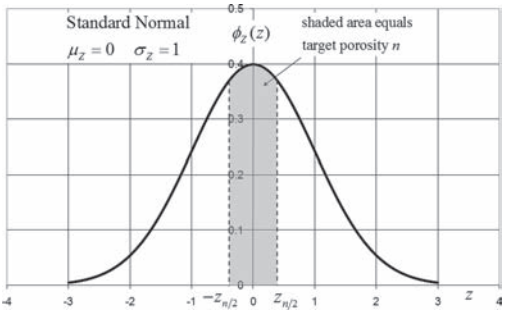

Figure 3. Target porosity area in standard normal distribution of random field. Any element assigned a random field value in the range $|Z| > z_{n/2}$ is treated as intact material a Young's modulus and Poisson's ratio given by $E_0 = 1$ and $\upsilon_0 = 0.3$, respectively.

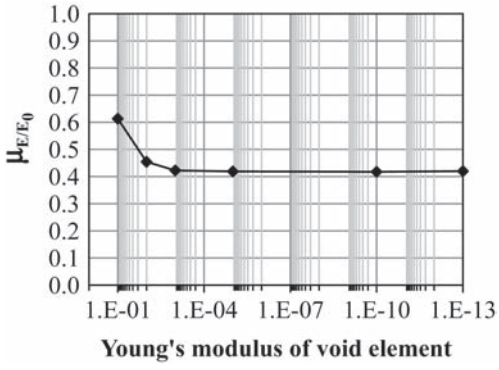

Figure 4. Influence of void element stiffness on the mean effective Young's modulus (intact material, $E_0 = 1$).

Thereafter, any element assigned a random field value in the range $|Z| > z_{n/2}$ is treated as intact material with a Young's modulus and Poisson's ratio given by $E_0 = 1$ and $\upsilon_0 = 0.3$, while any element where $|Z| \le z_{n/2}$ is treated as a void element with Young's modulus and Poisson's ratio given by $E_0 = 0.01$ and $\upsilon_0 = 0.3$ (100 times smaller than the surrounding intact material). As can be seen in Figure 4, for the case when $n = 0.2$, the results show a small influence of the arbitrarily selected Young's modulus of the void elements. In the current work, a void stiffness one hundred times less than the surrounding intact material gave reasonable (and stable) results. The nature of random fields is that the mean porosity is under the user's control, but the porosity of each individual simulation processed by the Monte-Carlo method will vary from one simulation to the next.

4 CONTROLLING OF VOID SIZE

As mentioned previously, two materials with the same average porosity could have quite different void sizes. One model could have frequent small voids, while the other could have less frequent larger voids. The void size in this study is controlled by the random field spatial correlation length θ which incorporates a "Markov" spatial correlation structure as follows

$$\rho = \exp\left(-2|\tau|/\theta\right) \tag{2}$$

where ρ = the correlation coefficient; $|\tau|$ = absolute distance between points in the field; and θ = scale of fluctuation or spatial correlation length. Larger values of θ will lead to larger voids and vice versa.

The Markov equation delivers a spatial correlation that reduces exponentially with distance. For example, from Eq. (3), $\tau < \theta$, the correlation coefficient $\rho > 0.13$. In the current study, the range

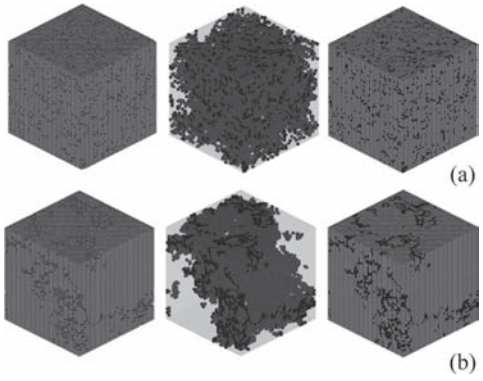

Figure 5. Typical simulations showing generation of voids at (a) low and (b) high spatial correlation lengths θ ($n = 0.2$ in both cases).

of ρ varies from 0 to 1. Points close together are strongly correlated and therefore likely to belong to the same void. In the limiting case of $\theta \to 0$, the random field value changes rapidly from point to point delivering numerous small voids. At the other extreme as $\theta \to \infty$, the random on each simulation becomes increasingly uniform with some simulations representing entirely intact material and other consisting entirely of voids. For example as shown in Figure 5, the models show typical simulations of different void clustering for two materials with the same mean porosity.

5 MONTE-CARLO SIMULATIONS

A "Monte-Carlo" process is combined with the RFEM and repeated until stable output statistics are achieved. The primary outputs from each elastic analysis are the vertical and horizontal deformations of the block δ_z, δ_x and δ_y. Although all simulation use the same θ and n, the spatial location of the voids will different each time. In some cases, the voids may be located just below the top of the block leading to a relatively high δ_z. While in others, the voids may be buried in the middle of the block leading to a relatively low δ_z. Following each simulation, the computed displacements δ_z, δ_x and δ_y are converted into the "effective" values of Young's modulus and Poisson's ratio as follows

Based on Hooke's law,

$$\varepsilon_x = \frac{1}{E}(\sigma_x - \upsilon(\sigma_y + \sigma_z))$$
$$\varepsilon_y = \frac{1}{E}(\sigma_y - \upsilon(\sigma_z + \sigma_x)) \quad (3)$$
$$\varepsilon_z = \frac{1}{E}(\sigma_z - \upsilon(\sigma_x + \sigma_y))$$

Given that L is the side length of cubic block, and assume stress boundary conditions.

$$\sigma_x = 0.0,\ \sigma_y = 0.0\ ,\ \sigma_z = -Q/L^2 \quad (4)$$

$$\varepsilon_x = \frac{\delta_x}{L},\ \varepsilon_y = \frac{\delta_y}{L},\ \varepsilon_z = \frac{\delta_z}{L} \quad (5)$$

hence after substitution into equation (3), the effective elastic properties can be written as

$$E = \frac{Q}{L\delta_z} \quad (6)$$

$$\upsilon_x = \frac{\delta_x}{\delta_z} \quad (7)$$

$$\upsilon_y = \frac{\delta_y}{\delta_z} \quad (8)$$

where E = the effective elastic Young's modulus, Q = stress loading at the top side, υ_x and υ_x = the effective Poisson's ratios based on the displacement in the x- and y-directions respectively.

In each simulation, the effective Young's modulus is normalized as E/E_0 by dividing by the intact Young's modulus E_0. In the current study, following some numerical experiments as shown in Figure 6, it was decided that 1000 simulations for each parametric combination would deliver reasonably repeatable results. In this study, we have expressed the spatial correlation length in dimensionless form

$$\Theta = \frac{\theta}{L} \quad (9)$$

where L is the width of the loaded element ($L = 50$).

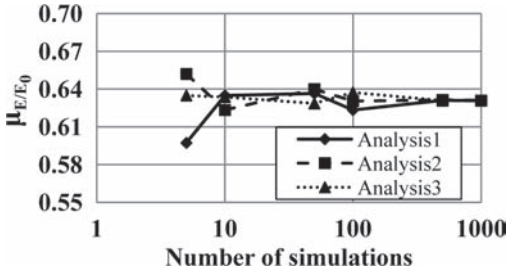

Figure 6. Sensitivity of the mean effective Young's modulus as a function of the number of simulations for $n = 0.2$ and $\Theta = 0.4$. It was decided that 1000 simulations would deliver reasonably repeatability.

6 REPRESENTATIVE VOLUME ELEMENT

An RVE is an element of the heterogeneous material that is large enough to represent the microstructure, but small enough to achieve computational efficiency. The RVE of four cases using the random field 3D finite element model have been considered as shown in Table 1.

Figure 7 shows a sequence of five blocks contained within and including the largest block of $50 \times 50 \times 50$ cubic elements. The different block sizes will indicate the optimal RVE for the given input conditions. When the RVE is "big enough", we expect the standard deviation of the effective Young's modulus to be reduced and its mean essentially constant as shown in Figures 8(a) and 8(b). While the mean values plotted in Figure 8(a) are fairly constant for different block sizes, it could be argued that the block size of $20 \times 20 \times 20$ led to essentially constant values for the low Θ cases (1 and 3), while a larger block, say $30 \times 30 \times 30$ would be needed for stable mean values with the larger Θ cases (2 and 4). The standard deviation shown in Figure 8(b) displays more variability with block size and tends to zero as the blocks get bigger, but at a slower rate for higher values of Θ. In both Figures 8, it is noted that the influence of Θ on block statistics is greater than that of n. The RVE depends more on spatial correlation length than porosity.

Table 1. Different input void properties.

Case	Target porosity (n)	Θ
1	0.2	0.2
2	0.2	0.7
3	0.7	0.2
4	0.7	0.7

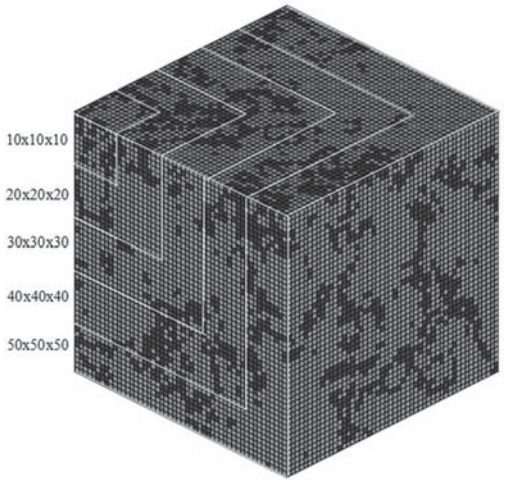

Figure 7. Different block sizes for computing the effective elastic properties of a material with random voids.

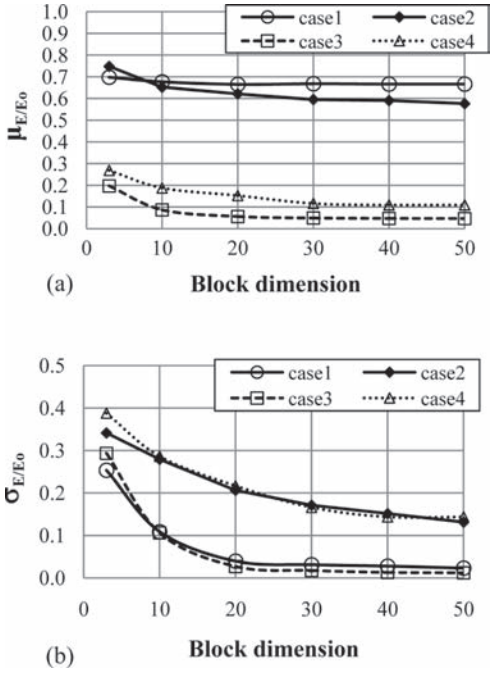

Figure 8. Effective Young's modulus (a) mean and (b) standard deviation following 1000 simulations for different block sizes.

7 RESULTS OF RFEM

Following each set of 1000 Monte-Carlo simulations, the mean and standard deviation of the normalized effective Young's modulus were computed for a range of parametric variations of n and Θ, with results shown in Figures 9 and 10, respectively.

It can be noted from Figure 9 that the mean normalized effective Young's modulus drops towards zero with increasing porosity n and that Θ does not have much influence. Figure 10 shows that Θ has more influence on the standard deviation of the effective Young's modulus σ_{E/E_0}. The standard deviation values as $n \to 0$ (intact stiffness material) and $n \to 1$ (very low stiffness material) show low variance since almost all simulations are the same and model essentially uniform material. The standard deviation was observed to reach a maximum value at around $n \approx 0.4$.

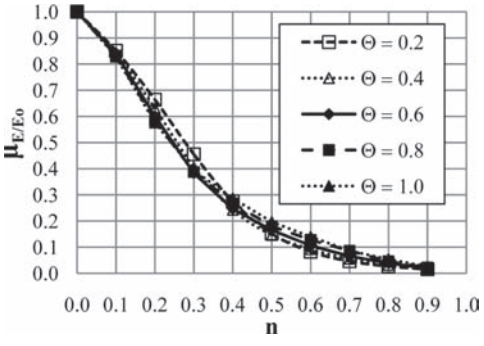

Figure 9. μ_{E/E_0} vs. n for $0.2 \le \Theta \le 1.0$.

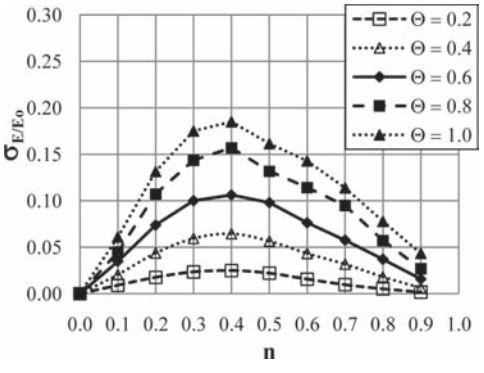

Figure 10. σ_{E/E_0} vs. n for $0.2 \le \Theta \le 1.0$.

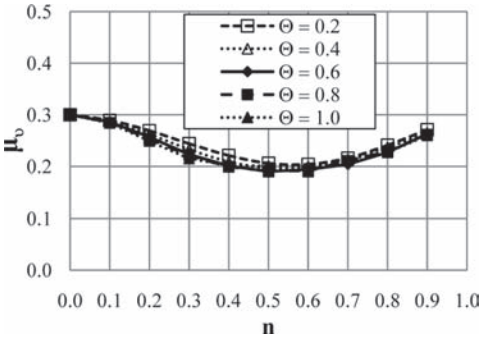

Figure 11. μ_υ vs. n for $0.2 \le \Theta \le 1.0$.

The result obtained from Equations 7 and 8 for the effective Poisson's ratio were in good agreement as expected for the range of n and Θ considered. In the isotropic material model, the two Poisson's ratios are essentially identical after Monte-Carlo simulation; however the results are based on an average to account for any small differences. The plots shown in Figures 11 and 12 give the mean

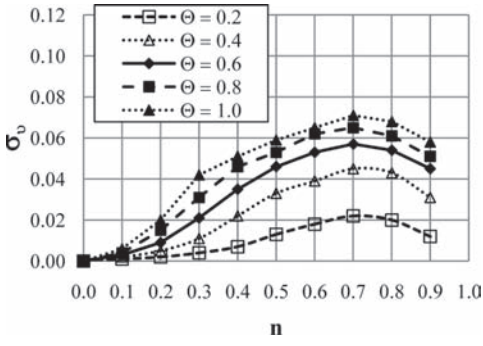

Figure 12. σ_υ vs. n for $0.2 \le \Theta \le 1.0$.

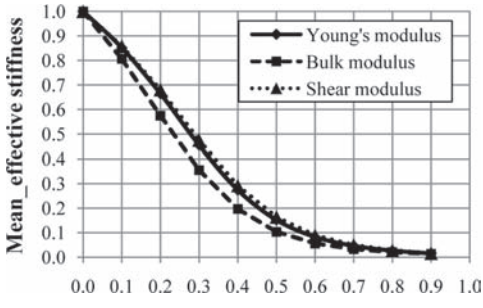

Figure 13. Mean effective values vs. n using $\Theta = 0.2$.

and standard deviation of the effective Poisson's ratio. Figure 11 shows that the mean effective Poisson's ratio μ_υ displays a minimum at around $n = 0.5$. On the other hand, as shown in Figure 12, the standard deviation of Poisson's ratio displays a maximum at $n = 0.7$ which is a similar trend to that observed for Young's modulus in Figure 10. For all values of Θ considered however, the standard deviations were quite small.

Although this paper has focused on Young's modulus and Poisson's ratio, other stiffness moduli may be of interest depending on the context. Figure 13 combines results from Figures 9 and 11 to show the variation of the mean effective shear modulus and bulk modulus using Eqns. (10 and 11). They display a similar trend to that observed for Young's modulus.

$$\mu_K = \frac{\mu_E}{3(1-2\mu_\upsilon)} \tag{10}$$

$$\mu_S = \frac{\mu_E}{2(1+\mu_\upsilon)} \tag{11}$$

where μ_K = the mean effective bulk modulus, μ_S = the mean effective shear modulus.

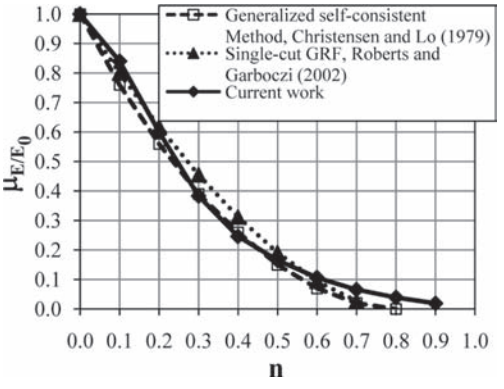

Figure 14. Comparison of the effective Young's modulus obtained from RFEM and other approaches.

8 COMPARISON OF RFEM AND OTHER RESULTS

The theoretical results based on the Generalized Self Consistent Method of Christensen & Lo (1979) and the numerical results based on the single-cut GRF model of Roberts & Garboczi (2002) are compared in Figure 14, with results from the current study using $\Theta = 0.6$ from Figure 9. The Generalized Self Consistent Method involved embedding an inclusion phase directly into an infinite medium. It was demonstrated that the method could also solve the spherical inclusion problem. The single-cut GRF model assigns a random number to each point in space. From Figure 14, it can be observed that the current method gives similar values of the mean effective Young's modulus

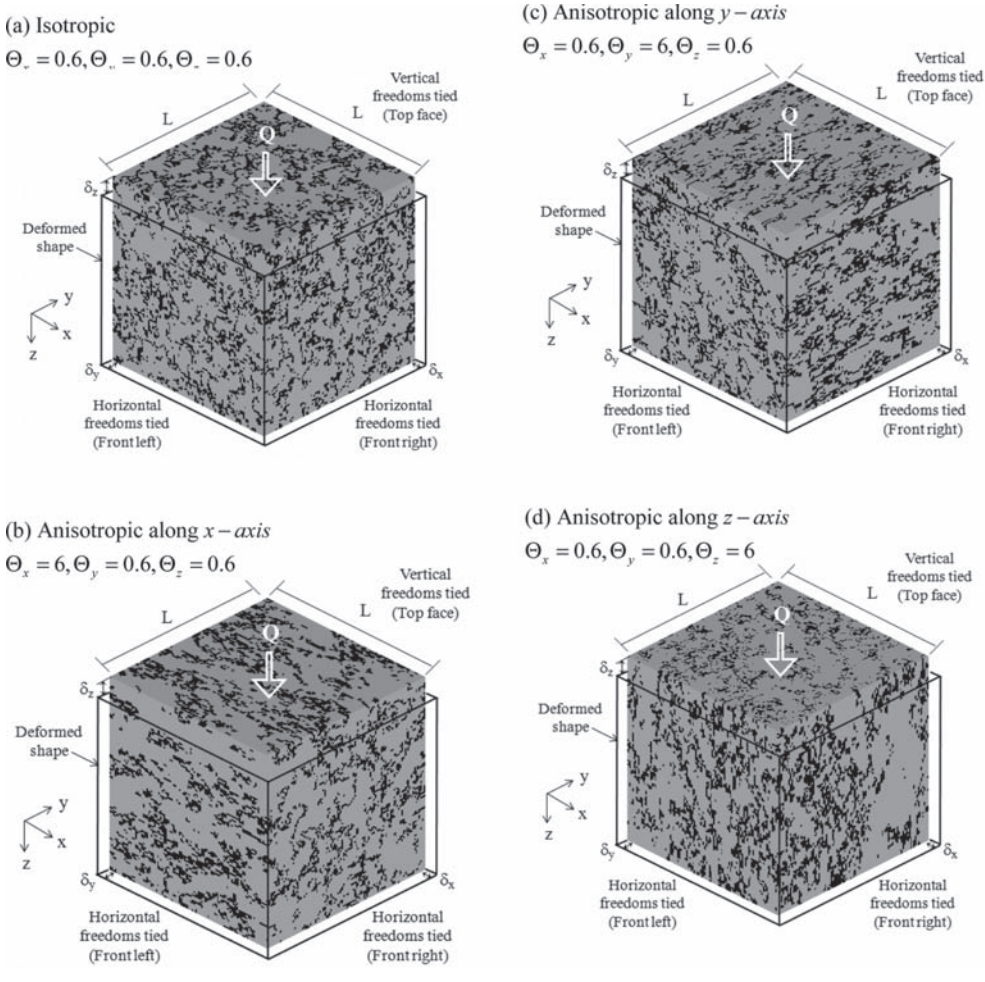

Figure 15. Analysis of tied freedom in four "cubic element test" models with voids: (a) isotropic model, (b) anisotropic model along *x-axis*, (c) anisotropic model along *y-axis* and (d) anisotropic model along *z-axis*.

to those given by the theoretical and numerical methods for all values of n.

9 COMPARISON OF ISOTROPIC AND ANISOTROPIC MODELS

Anisotropic models are performed with different spatial correlation lengths in different directions. Figure 15(a) shows a model of isotropic spatial correlation length at $\Theta_x = \Theta_y = \Theta_z = 0.6$. The voids tend to disperse in all directions within the material. In Figure 15(b), where $\Theta_x = 6$ and $\Theta_y = \Theta_z = 0.6$, and Figure 15(c) where $\Theta_y = 6$ and $\Theta_x = \Theta_z = 0.6$, voids are in horizontally elongated in the x- and y-directions, respectively. On the other hand, in Figure15(d) where where $\Theta_z = 6$ and $\Theta_x = \Theta_y = 0.6$, voids are in vertically elongated in the z-direction. The tied freedom approach described previously continued to be used in all 3D anisotropic models.

Following the Monte-Carlo simulations of the anisotropic models shown in Figure 15, the mean of the effective normalized Young's modulus was compared with isotropic results for a range of n, as shown in Figure 16. It was noted that similar results were obtained when the elongated direction of the anisotropic models was in the x- and y-directions, but the effective Young's modulus was noticeably higher when the elongations were in the z-direction (the direction of loading).

The isotropic 3D results from the current study using $\Theta = 0.6$ are also compared in Figure 16 with 2D (plane strain) for the same spatial correlation length as published previously by Griffiths et al. 2012. The mean normalized effective Young's modulus in 3D is obviously higher than in 2D for the same porosity. A direct comparison between 2D and 3D may not be justified, however, because voids in 2D (plane strain) are like "tunnels" that continue indefinitely into the 3rd dimension, while voids in 3D are isotropic, finite in size, and fully contained within the surrounding material. Thus, it might be explained that the 2D model is actually a 3D model with an infinite spatial correlation length in the 3rd direction.

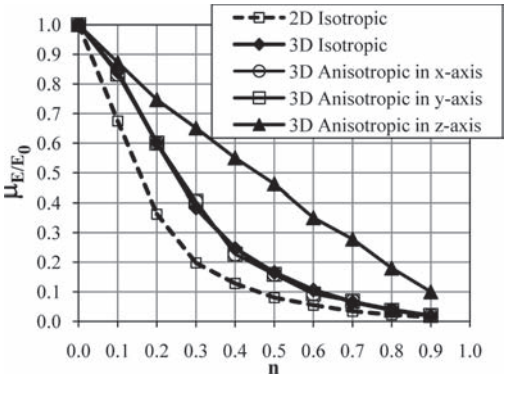

Figure 16. Comparison of the effective Young's modulus obtained from RFEM and other approaches.

10 CONCLUSIONS

A 3D RFEM with "tied freedoms" has been used in this study to investigate the influence of porosity and void size on homogenized elastic properties E and υ. It was observed that while porosity had a significant effect on both the mean and standard deviation of E and υ, the void size had little influence on the mean but more influence on the standard deviation. The study also investigated the RVE needed to capture the essential properties of a heterogeneous material containing voids. It was found that for the same porosity, the larger the size of the voids, the greater the size of the RVE. Finally, the paper presented favorable comparisons of the effective elastic properties in 3D with those obtained analytically and numerically by other investigators. In addition, the effective Young's modulus of the anisotropic system depends on the direction of voids elongation. The stiffest case was observed when the direction of void elongation was in the same direction as the loading. The RFEM approach to homogenization described in this paper shows much promise, and opens the possibility of making probabilistic statements about engineering performance of heterogeneous geomaterials. The probabilistic aspect has not been discussed in the current paper, but remains an area of continued research.

ACKNOWLEDGEMENT

The authors wish to acknowledge the support of (i) NSF grant CMMI-0970122 on "GOALI: Probabilistic Geomechanical Analysis in the Exploitation of Unconventional Resources", and (ii) The Royal Thai Government for their support of the second author.

REFERENCES

Böhm, H.J. 1998, 2013. A short introduction to basic aspects of comtinuum micromechanics, TU Wien, Vienna.

Christensen, R.M. and Lo, K.H. 1979. Solutions for effective shear properties in three phase sphere and cylinder models. *J. Mech. Phys. Solids* 27: 315–330.

Fenton, G.A. & Griffiths, D.V. 2005. Three-Dimension Probabilistic Foundation Settlement. *J. Geotech. Geoenviron. Eng.* 131 (2): 232–239.

Fenton, G.A. & Griffiths, D.V. 2008. Risk Assessment in Geotechnical Engineering, John Wiley & Sons, Hoboken, NJ.

Fenton, G.A. & Vanmarcke, E.H. 1990. Simulation of random fields via local average subdivision. *J Eng. Mech. 1*16 (8): 1733–1749.

Garboczi, E.J. & Day, A.R. 2005. An algorithm for computing the effective linear elastic properties of heterogeneous materials: three-dimensional results for composites with equal phase Poisson ratios. *J. Mech. Phys. Solids* 43 (9): 1349–1362.

Griffiths, D.V. & Fenton, G.A. 2007. Probabilistic Methods in Geotechnical Engineering, CISM Courses and Lectures No. 491, Pub. Springer, Wien, New York.

Griffiths, D.V., Paiboon, J., Huang, J. & Fenton, G.A. 2012. Homogenization of geomaterials containing voids by random fields and finite elements. *Int. J. Solids Structure* 49: 2006–2014.

Hazanov, S. & Huet, C. 1994. Order Relationships for Boundary-Conditions Effect in Heterogeneous Bodies Smaller Than the Representative Volume. *Journal of the Mechanics and Physics of Solids* 42 (12): 1995–2011.

Hazanov, S. & Amieur, M. 1995. On overall properties of elastic heterogeneous bodies smaller than the representative volume. *International Journal of Engineering Science* 33 (9): 1289–1301.

Hazanov, S. 1998. Hill condition and overall properties of composites. *Archive of Applied Mechanics* 68 (6): 385–394.

Hill, R. 1963. Elastic properties of reinforced solids: some theoretical principles. *J. Mech. Phys. Solids* 11: 357–372

Huang, J.S., Krabbenhoft, K. & Lyamin, A. 2013. Statistical homogenization of elastic properties of cement paste based on X-ray microtomography images. *Int. J. Solids Structure* 50: 699–709.

Kachanov, M. & Sevostianov, I. 2005. Onquantitative characterization of microstructures and effective properties. *Int. J. Solids Struct.* 42: 309–336.

Kanit, T., Forest, S., Galliet, I., Mounoury, V. & Jeulin, D. 2003. Determination of the size of the representative volume element for random composites: statistical and numerical approach. *Int. J. Solids Structure* 40 (13–14): 3647–3679.

Khisaeva, Z.F. & Ostoja-Starzewski, M. 2006. On the size of RVE in finite elasticity of random composites. *Journal of Elasticity* 85 (2): 153–173.

Klusemann, B. & Svendsen, B. 2009. Homogenization methods for multi-phase elastic composites: Comparisons and benchmarks. *Technische Mechanik* 30 (4): 374–386.

Liu, C. 2005. On the minimum size of representative volume element: an experimental investigation. *Exp. Mech. 4*5 (3): 238–243.

Ostoja-Starzewski, M. 2006. Material spatial randomness: From statistical to representative volume element. *Probabilistic Engineering Mechanics* 21 (2): 112–132.

Roberts, A.P. & Garboczi, E.J. 2002. Computation of the linear elastic properties of random porous materials with a wide variety of microstructure. *Proc. Royal Soc. of London* 458 (2021): 1033–1054.

Smith, I.M. & Griffiths, D.V. 2004. *Programming the finite element method*, John Wiley and Sons, Chichester, New York, 4th edition

Torquato, S. 2002. Random heterogeneous materials: microstructure and macroscopic properties. Springer-Verlag, NY.

Zeleniakiene, D. Griskevicius, P. & Leisis, V. 2005. The comparative analysis of 2D and 3D microstructural models stresses of porous polymer materials. ISSN 1392-1207. Mechanika, Nr. 3 (53).

Zohdi, T.I. & Wriggers, P. 2001. Aspects of the computational testing of the mechanical properties of microheterogeneous material samples. *International Journal for Numerical Methods in Engineering* 50 (11): 2573–2599.

This page intentionally left blank

Geotechnical Safety and Risk IV – Zhang et al. (eds)
© 2014 Taylor & Francis Group, London, ISBN 978-1-138-00163-3

Selecting optimal probability models for geotechnical reliability analysis

H.W. Huang, W.W. Su & J. Zhang
Department of Geotechnical Engineering, Tongji University, Shanghai, China
Key Laboratory of Geotechnical and Underground Engineering of Ministry of Education, Tongji University, Shanghai, China

ABSTRACT: The cohesion and friction angle of soil are two common random variables encountered in geotechnical reliability analysis. Its joint distribution can be fully specified with marginal distributions and a copula function. In this study, a probabilistic framework is suggested to construct, calibrate and rank probability models for failure probability estimation. It is shown that calibrating the marginal distributions and copula function may miss the optimal model parameters. The optimal probability model is problem specific, and the commonly adopted models based on the Gaussian copula function may not be optimal. When copula function is used to specify the joint distribution of cohesion and friction angle, many existing algorithms such as the first order reliability method cannot be directly used for failure probability calculation. Monte Carlo simulation can be applied to general performance functions and hence is superior to the existing one-dimensional integration method. Both the marginal distribution and copula function could significantly affect the failure probability calculation. If the probability model is arbitrarily chosen, the failure probability may be severely overestimated or underestimated. In general, the effect of probability model on failure probability estimation is more obvious when the failure probability is small. The effect of probability model on failure probability calculation also depends on the deterministic model and the available data. Increasing the amount of the measured data is likely to provide more constraint to the marginal distributions and hence reduce its effect on failure probability estimation. The effect of copula function on failure probability calculation decreases as there is less correlation between the cohesion and the friction angle.

1 INTRODUCTION

To address the uncertainties in geotechnical design, probabilistic methods in which uncertain variables are modeled as random variables have been widely employed in geotechnical analysis (Vanmarcke 1977, Tang 1979, Low & Tang 1997, Cherubini 2000, Duncan 2000, Whitman 2000, Baecher & Christian 2003, Zhang 2004, Honjo & Amatya 2005, Uzielli et al. 2005, Sivakumar Babu et al. 2006, Fenton & Griffiths 2008, Huang et al. 2010, Wang 2011, Luo et al. 2011, Xue & Gavin 2007, Zhang et al. 2011, Ching & Phoon 2012, Juang & Wang 2013, Zhang et al. 2013). The cohesion and friction angle are two commonly encountered important uncertain variables in many geotechnical problems. In many cases, the probability model for the shear strength parameters is the fundamental input for a geotechnical reliability analysis. If the probability model for the shear strength parameters is biased, the estimated failure probability will also be biased. Lumb (1970) and Chen et al. (2005) studied the marginal distributions of the cohesion and the friction angle. In practice, the cohesion and the friction angle are often modeled as normal or lognormal variables. A correlation coefficient is often used to describe the dependence between the cohesion and the friction angle (e.g., Harr 1987, Cherubini 1997). It is generally believed that the cohesion and friction angle are negatively correlated. Nevertheless, a positive correlation between the cohesion and the friction angle was also reported (e.g., Wolff 1985).

Recently, it has been found the marginal distributions and the correlation coefficient are insufficient to characterize a joint distribution (e.g. Durrleman et al. 2000, Cherubini et al. 2004, Nelsen 2006). Rather, a multivariate distribution can be fully specified by the marginal distributions and a copula function. It is increasingly aware in the field of structural reliability that a joint distribution should be modeled based on the copula theory (e.g. Goda 2010, Lebrun & Dutfoy 2009). In geotechnical engineering, Li and his coauthors pioneered the application of copula theory in a number of geotechnical reliability problems (Li et al. 2013, Tang et al. 2013). It was found that the estimated failure probability could be severely biased if the copula function is wrongly chosen.

Despite these substantial progresses, several important questions still remain in calibrating and selecting probability models for the shear strength parameters. Firstly, the marginal distributions and copula functions of the soil strength parameters were often determined separately, assuming there is no interaction between the optimal marginal distributions and the optimal copula function, which may not be true. Secondly, many existing methods for reliability analysis are implicitly based on probability models with the Gaussian copula function, which may not be directly applicable to a probability model with a general copula function. Thirdly, when and how the probability model will have significant impact on the failure probability estimation are still not well-understood.

The objectives of this paper include: (1) providing a systematical framework to calibrate and rank probability models for the shear strength parameters; (2) suggesting a method to evaluate the failure probability when a general performance function is involved; and (3) investigating when and how the probability model can have significant impact on failure probability estimation.

This paper is organized as follows. First, the copula theory is briefly introduced, followed by how various probability models can be calibrated and compared for modeling the shear strength data. Then, how the failure probability can be calculated when a general performance function is involved is presented. Finally, three examples are worked out to illustrate the proposed method and also to investigate the effect of probability model of soil strength parameters on failure probability calculation.

2 PROBABILITY MODELS FOR SHEAR STRENGTH PARAMETERS

Let c and φ denote the cohesion and friction angle, respectively. Let $F_1(c)$ and $F_2(\varphi)$ denote the Cumulative Distribution Function (CDF) of c and φ, respectively. Let $F(c, \varphi)$ denote the CDF of $\{c, \varphi\}$. It is reasonable to assume c and φ are both continuous variables. Based on Sklar's theorem (Sklar 1959), $F(c, \varphi)$ can be written as follows

$$F(c, \varphi) = C\left[F_1(c), F_2(\varphi), \theta\right] \tag{1}$$

where $C(u_1, u_2, \theta)$ is the copula function, $u_1 = F_1(c)$, $u_2 = F_2(\varphi)$, and θ is a parameter of the copula function. Eq. (1) shows that the joint distribution of c and φ can be decomposed into two parts, i.e. (1) the marginal distributions, i.e. $F_1(c)$ and $F_2(\varphi)$, and (2) the copula function that characterize the dependent structure of c and φ, i.e. $C(u_1, u_2, \theta)$. As an example, Table 1 shows several commonly used copula models.

Based on Eq. (1), the Probability Density Function (PDF) of c and φ can be written as

$$f(c,\varphi) = c\left[F_1(c), F_2(\varphi), \theta\right] f_1(c)\, f_2(\varphi) \tag{2}$$

where $c(u_1, u_2, \theta)$ is the density of the copula function $C(u_1, u_2, \theta)$ defined as follows

$$c(u_1, u_2, \theta) = \frac{\partial C(u_1, u_2, \theta)}{\partial u_1 \partial u_2} \tag{3}$$

Based on the definition of correlation coefficient, the correlation coefficient between c and φ can be written as follows

$$\rho_{12} = \frac{\int\int (c - \mu_c)(\varphi - \mu_\varphi) f(c,\varphi)\mathrm{d}c\mathrm{d}\varphi}{\sigma_c \sigma_\varphi} \tag{4}$$

where μ_c and μ_φ are the mean values of c and φ, respectively, and σ_c and σ_φ are the standard deviations of c and φ, respectively.

Comparing Eq. (3) with (4), we can see that the correlation coefficient is a function of the copula model. Previously, the Gaussian copula is often

Table 1. Summary of several commonly used copula functions.

Copula	$C(u_1, u_2, \theta)$	$c(u_1, u_2, \theta)$
Gaussian	$\phi_G(\phi^{-1}(u_1), \phi^{-1}(u_2); \theta)$	$\frac{1}{\sqrt{1-\theta^2}} \exp\left[-\frac{\theta^2 \cdot \phi^{-1}(u_1)^2 - 2\theta \cdot \phi^{-1}(u_1) \cdot \phi^{-1}(u_2) + \theta^2 \cdot \phi^{-1}(u_2)^2}{2(1-\theta^2)}\right]$
Clayton	$(u_1^{-\theta} + u_2^{-\theta} - 1)^{-\frac{1}{\theta}}$	$(1+\theta)(u_1 u_2)^{-\theta-1}(u_1^{-\theta} + u_2^{-\theta} - 1)^{-2-\frac{1}{\theta}}$
Frank	$-\frac{1}{\theta}\ln\left[1 + \frac{(e^{-\theta u_1} - 1)(e^{-\theta u_2} - 1)}{e^{-\theta} - 1}\right]$	$\frac{-\theta(e^{-\theta} - 1)e^{-\theta(u_1+u_2)}}{[(e^{-\theta u_1} - 1)(e^{-\theta u_2} - 1) + (e^{\theta} - 1)]^2}$
FGM	$u_1 u_2 (1 + \theta(1-u_1)(1-u_2))$	$1 + \theta(1-2u_1)(1-2u_2)$

used to construct the joint distribution. As shown in Table 1, Gaussian copula is only one of the possible options for constructing the probability models. Different copula functions can result in the same correlation coefficient. However, when different copula functions are used, the failure probability could be very different (Tang et al. 2013). The commonly adopted Gaussian copula may not always be the optimal copula function to construct probability models for shear strength parameters.

Sklar's theory provides the modeler ample chances to model the real data more realistically. For instance, if one assumes the marginal distributions are normal and that copula function is Clayton, the PDF of c and φ can be written as follows

$$f(c,\varphi) = (1+\theta)\left[F_1(c)\cdot F_2(\varphi)\right]^{-\theta-1} \times \left\{\left[F_1(c)\right]^{-\theta} + \left[F_2(\varphi)\right]^{-\theta} - 1\right\}^{-1-\frac{1}{\theta}} f_1(c) f_2(\varphi) \quad (5)$$

where $f_1(c)$ and $F_1(c)$ in this case are respectively the PDF and CDF of a normal variable with a mean of μ_c and a standard deviation of σ_c, and $f_2(\varphi)$ and $F_2(\varphi)$ are respectively the PDF and CDF of a normal variable with a mean of μ_φ and a standard deviation of σ_φ. As an example, $f_1(c)$ and $F_1(c)$ can be written as follows

$$f_1(c) = \frac{1}{\sqrt{2\pi}\sigma_c}\exp\left[-\frac{(x-\mu_c)^2}{2\sigma_c^2}\right] \quad (6)$$

$$F_1(c) = \int_{-\infty}^{c} f_1(z)\,\mathrm{d}z \quad (7)$$

Sklar's theory implies that the structure of a probability model for cohesion and friction angle can be constructed in two steps: (1) determining the marginal distributions of c and φ, and (2) determining the copula function between c and φ. After the structure of the probability model is determined, the next step is how to calibrate the model parameters of the probability model, as described in the following section.

3 MAXIMUM LIKELIHOOD CALIBRATION OF PROBABILITY MODELS

In the probability model for shear strength parameters, the parameters to be calibrated include μ_c, μ_φ, σ_c, σ_φ and θ. Let $\mathbf{d} = \{d_1, d_2\}$ denote a measurement of c and φ. Let $\mathbf{d}^1$, $\mathbf{d}^2$, $\mathbf{d}^3$, …, $\mathbf{d}^n$ denote n measurements of c and φ. For ease of presentation, let $\mathbf{\Theta} = \{\mu_c, \mu_\varphi, \sigma_c, \sigma_\varphi, \theta\}$ and $\mathbf{D} = \{\mathbf{d}^1, \mathbf{d}^2, \mathbf{d}^3, \ldots, \mathbf{d}^n\}$. Supposing the measurements are statistically independent, the chance to observe $\mathbf{D}$ when the values of $\mathbf{\Theta}$ are known can be written as

$$l(\mathbf{\Theta}\,|\,\mathbf{D}) = \prod_{i=1}^{n} f\left(\mathbf{d}^i\,|\,\mathbf{\Theta}\right) \quad (8)$$

where $f(\mathbf{d}^i|\mathbf{\Theta})$ is the chance to observe $\mathbf{d}^i$. If the density function in Eq. (5) is used, $f(\mathbf{d}^i|\mathbf{\Theta})$ can be written as

$$f\left(\mathbf{d}^i\,|\,\mathbf{\Theta}\right) = (1+\theta)\left[\left[F_1\left(d_1^i\right)\right]^{-\theta}\cdot\left[F_2\left(d_2^i\right)\right]^{-\theta}\right]^{-\theta-1} \times \left\{\left[F_1\left(d_1^i\right)\right]^{-\theta} + \left[F_2\left(d_2^i\right)\right]^{-\theta} - 1\right\}^{-1-\frac{1}{\theta}} f_1\left(d_1^i\right) f_2\left(d_2^i\right) \quad (9)$$

where $d_1^{\,i}$ and $d_2^{\,i}$ are the first and second elements of $\mathbf{d}^i$, respectively.

Based on the principle of maximum likelihood, the optimal values of $\mathbf{\Theta}$ can be obtained by maximizing the likelihood function, or equivalently, by maximizing the logarithm of the likelihood function as follows

$$L(\Theta\,|\,\mathbf{D}) = \sum_{i=1}^{n} \ln f\left(\mathbf{d}^i\,|\,\mathbf{\Theta}\right) \quad (10)$$

If Eq. (10) is used to find the optimal values of $\mathbf{\Theta}$, the marginal distributions and the copula function are calibrated simultaneously. Thus, if there is any interaction between the optimal marginal distributions and copula function, such interaction can be readily considered. Nevertheless, estimating the values of Θ using Eq. (10) requires solving the optimization problem in a five-dimensional space, which could be non-trivial. To reduce the computational challenge involved in the optimization work, one can assume there is no interaction between the optimal marginal distributions and the copula function. In such a case, the marginal distributions and copula function can be calibrated separately (Joe & Xu 1996). For the shear strength probability model studied here, the optimal values of μ_c, σ_c, μ_φ, σ_φ, and θ can be obtained by respectively maximizing the following three likelihood functions

$$l(\mu_c, \sigma_c\,|\,\mathbf{D}) = \prod_{i=1}^{n} f_1\left(d_1^i\,|\,\mu_c, \sigma_c\right) \quad (11)$$

$$l(\mu_\varphi, \sigma_\varphi\,|\,\mathbf{D}) = \prod_{i=1}^{n} f_2\left(d_2^i\,|\,\mu_\varphi, \sigma_\varphi\right) \quad (12)$$

$$l(\theta\,|\,\mathbf{D}) = \prod_{i=1}^{n} f\left(\mathbf{d}^i\,|\,\mu_c^*, \sigma_c^*, \mu_\varphi^*, \sigma_\varphi^*, \theta\right) \quad (13)$$

where in Eq. (13) μ_c* and σ_c* are optimal values of μ_c and σ_c determined based on Eq. (11), and μ_φ* and σ_φ* are optimal values of μ_φ and σ_φ determined based on Eq. (12). While no interaction between the marginal distributions and copula function is a convenient assumption to reduce the computational work, its accuracy needs to be verified. The accuracy of this approximate method will be studied later in this paper.

4 RANKING OF PROBABILITY MODELS

Considering the possible marginal distributions of cohesion and friction angle as well as the possible copula function, there could be more than one probability models that can be used to fit the measured data. When multiple probability models are available, the probability models can be compared using various information criteria available in the statistics literature, such as the Akaike Information Criterion (AIC) (Akaike 1974), the Bayesian Information Criterion (BIC) (Schwarz 1978), and the Kullback Information Criterion (KIC) (Cavanaugh 1999), as listed below:

$$\mathrm{AIC} = -2L(\Theta^* \mid \mathbf{D}) + 2k \tag{14}$$

$$\mathrm{BIC} = -2L(\Theta^* \mid \mathbf{D}) + k\ln n \tag{15}$$

$$\mathrm{KIC} = -2L(\Theta^* \mid \mathbf{D}) + 3k \tag{16}$$

where $\boldsymbol{\Theta}$* is the point where the likelihood function is maximized; k = number of parameters to be calibrated; and n = number of observed data. An information criterion generally has two components, i.e. a term related to the value of the maximum likelihood, and a term related to the number of parameters in the model. The term related to the likelihood function measures the degree of fit of the data to the model. The term related to the number of parameters measures the complexity of the model. Based on the information criterion, a model should be both accurate and concise to avoid over-fitting. The above criteria have different theoretical background and differ in the weight applied to the complexity of the model. The smaller the criterion is, the more the model is supported by the data. When the models to be compared have the same number of parameters, the model ranking result based on different information criteria is the same. In this study, the models to be compared all have five parameters, i.e. $k = 5$. Thus, the model ranking result will not be affected by the information criterion adopted. As an illustration, AIC will be used for model ranking. Note to obtain the AIC value of the model calibrated based on Eqs. (11)–(13), one simply needs to substitute the optimal values found for $\boldsymbol{\Theta}$ based on Eqs. (11)–(13) into Eq. (10) to obtain $L(\boldsymbol{\Theta}^*|\mathbf{D})$, based on which the AIC value can be conveniently calculated.

5 GEOTECHNICAL RELIABILITY ANALYSIS BASED ON COPULA MODELS

Considering the simple case where there is only one soil layer involved. Let $\mathbf{x} = \{c, \varphi\}$. Let $g(\mathbf{x}) = 0$ denote the limit state function with $g(\mathbf{x}) < 0$ implying failure. The probability of failure can be written as

$$p_f = \iint I\left[g(\mathbf{x})\right] f(c,\varphi)\,\mathrm{d}c\mathrm{d}\varphi \tag{17}$$

where I is the indictor function characterizing the failure domain defined as follows

$$I\left[g(\mathbf{x})\right] = \begin{cases} 1 & g(\mathbf{x}) < 0 \\ 0 & g(\mathbf{x}) \geq 0 \end{cases} \tag{18}$$

The First Order Reliability Method (FORM) (Ang & Tang 1984) is widely used in geotechnical engineering. However, as it is derived for probability models constructed based on the Gaussian copula function, it is not directly applicable when other copula functions are used. Tang et al. (2013) illustrated that the double integration in Eq. (17) can be simplified into a one-dimensional integration problem analytically if the performance function is relatively simple. However, such a method may not be applicable when the performance function is complex or when there are several soil layers involved. In this study, we used the Monte Carlo simulation to calculate the failure probability. The advantages of this method include: (1) it does not require that the double integration in Eq. (17) should be simplified into a single integration problem analytically; and (2) it is applicable even when the performance function is complex. Let $\mathbf{x}_i$ denote the ith sample of $\mathbf{x}$. The failure probability as indicated in Eq. (17) can be calculated as

$$p_f = \frac{1}{N}\sum_{i=1}^{N} I\left[g\left(\mathbf{x}_i\right)\right] \tag{19}$$

where N = number of samples. For a bivariate distribution constructed based on the Clayton, Frank and FGM function, the following conditional sampling algorithm can be used (Trivedi et al. 2005).

1. Draw two independent random variables (v_1, v_2) from a uniform distribution bounded between 0 and 1.
2. Set $u_1 = v_1$.

3. Set $t = C_2(u_2|u_1 = v_1) = \partial C(u_1,u_2)/\partial u_1 = C_u(v)$.
4. Set $u_2 = C^{-1}{}_u(v, t)$.
5. Let $x_1 = F^{-1}{}_1(u_1)$, and $x_2 = F^{-1}{}_2(u_2)$. $\{x_1, x_2\}$ will be samples of $\{c, \varphi\}$, where $F^{-1}{}_2(u_2)$ and $F^{-1}{}_2(u_2)$ are the inverse of the CDF of c and φ, respectively.

For a probability model constructed based on the Gaussian copula, the following algorithm can be used (Trivedi et al. 2005).

1. Generate two independent distributed samples from the standard normal distribution which are denoted as v_1 and v_2 here, respectively.
2. Set $y_1 = v_1$.
3. Set $y_2 = v_1 \cdot \theta + v_2 \cdot (1 - \theta^2)^{1/2}$.
4. Set $u_i = \Phi(y_i)$ for $i = 1, 2$ (Φ is the cumulative distribution function of the standard normal distribution).
5. Let $x_1 = F^{-1}{}_1(u_1)$, and $x_2 = F^{-1}{}_2(u_2)$. $\{x_1, x_2\}$ is a sample of $\{c, \varphi\}$.

6 AN ILLUSTRATIVE EXAMPLE

The suggested method is used to analyze the data as shown in Table 2, which was also studied previously in Tang et al. (2013). In this example, 16 possible probability models for c and φ are considered, as shown in Table 3. The 16 models are first calibrated based on Eq. (10) where the possible interaction between optimal marginal distributions and copula function is considered. The calibration results are also summarized in Table 3. From Table 3 the following phenomena can be observed.

1. When marginal distributions are both normal and when the copula function is Clayton, the mean and standard deviation of c is 152.3 kPa

Table 2. Test data from Ankang Hydropower site (Adapted from Tang et al. 2013).

Test no.	c (kPa)	φ (°)	Test no.	c (kPa)	φ (°)
1	165	11.86	14	85	20.81
2	127	14.04	15	18	25.64
3	253	13.50	16	15	22.29
4	427	10.20	17	78	24.70
5	106	11.31	18	12	26.10
6	242	12.95	19	34	22.78
7	209	12.41	20	70	19.80
8	328	13.50	21	20	17.74
9	98	12.95	22	20	20.81
10	10	15.64	23	217	20.30
11	213	16.17	24	221	20.30
12	365	17.22	25	254	27.47
13	324	20.81			

Table 3. Calibrated parameters of 16 probability models based on the given data (model parameters calibrated simultaneously).

Model no.	Copula	Marginal distributions*	AIC	θ	μ_c	σ_c	μ_φ	σ_φ
1	Gaussian	n,n	468.28	–0.407	156.440	122.229	18.052	5.014
2		l,n	462.58	–0.443	188.762	326.223	18.052	5.013
3		n,l	467.26	–0.421	156.440	122.186	18.058	5.253
4		l,l	461.70	–0.453	188.762	326.223	18.064	5.274
5	Clayton	n,n	466.27	–0.439	152.337	124.067	17.848	5.364
6		l,n	463.84	–0.273	196.685	351.868	18.110	4.849
7		n,l	466.34	–0.389	155.700	119.413	18.100	5.613
8		l,l	462.24	–0.299	195.782	351.356	18.070	5.027
9	Frank	n,n	468.62	–2.264	152.609	121.861	17.963	4.984
10		l,n	462.15	–2.712	180.607	302.962	18.157	4.973
11		n,l	468.04	–2.233	154.026	121.839	17.981	5.211
12		l,l	461.72	–2.552	183.182	307.764	18.157	5.243
13	FGM**	n,n	468.35	–1.000	154.310	122.118	18.042	4.956
14		l,n	462.22	–1.000	184.965	309.786	18.172	4.924
15		n,l	467.71	–1.000	155.206	121.928	18.084	5.222
16		**l,l**	**461.51**	**–1.000**	**186.422**	**311.737**	**18.201**	**5.217**

*n,n: both c and φ follow the normal distribution; l,n: c and φ follow the lognormal and normal distributions, respectively; n,l: c and φ follow the normal and lognormal distributions, respectively; l,l: both c and φ follow the lognormal distributions.
**For the FGM copula, the value of $\boldsymbol{\theta}$ is bounded between –1 and 1 (Trivedi et al. 2005). This constraint is considered in the maximum likelihood method.

Table 4. Calibrated parameters of 16 probability models based on the data shown in Table 2 (model parameters calibrated separately).

Model no.	Copula	Marginal distribution	AIC	θ	μ_c	σ_c	μ_φ	σ_φ
1	Gaussian	n,n	468.28	–0.407	156.440	122.229	18.052	5.014
2		l,n	462.58	–0.443	188.762	326.223	18.052	5.014
3		n,l	467.26	–0.423	156.440	122.229	18.064	5.274
4		l,l	461.70	–0.453	188.762	326.223	18.064	5.274
5	Clayton	n,n	457.89	–0.500	156.440	122.229	18.052	5.014
6		l,n	463.92	–0.273	188.762	326.223	18.052	5.014
7		n,l	466.50	–0.369	156.440	122.229	18.064	5.274
8		l,l	462.38	–0.298	188.762	326.223	18.064	5.274
9	Frank	n,n	468.67	–2.241	156.440	122.229	18.052	5.014
10		l,n	462.18	–2.740	188.762	326.223	18.052	5.014
11		n,l	468.07	–2.227	156.440	122.229	18.064	5.274
12		l,l	461.74	–2.647	188.762	326.223	18.064	5.274
13	FGM	n,n	468.37	–1.000	156.440	122.229	18.052	5.014
14		l,n	462.27	–1.000	188.762	326.223	18.052	5.014
15		n,l	467.71	–1.000	156.440	122.229	18.064	5.274
16		**l,l**	**461.57**	**–1.000**	**188.762**	**326.223**	**18.064**	**5.274**

and 124.1 kPa, respectively. However, when the marginal distribution of c is changed to be lognormal, the mean and standard deviation of c is changed to be 196.7 kPa and 351.9 kPa, respectively. The optimal model parameters are sensitive to the assumed marginal distribution.

2. When the marginal distributions of cohesion and friction angle are both normal distributions but when the copula function is assumed to be Gaussian and Clayton, respectively, the mean values of c and φ are both changed, indicating that the optimal marginal distribution is also affected by the copula function. Hence, it may not be appropriate to calibrate the marginal distribution and copula function separately. To verify this conclusion, Table 4 shows the calibration results of the 16 models when marginal distributions and the copula function are calibrated separately based on Eqs. (11)–(13). For the same model the AIC value in Table 4 is generally larger than that in Table 3, indicating that the model calibrated ignoring the interaction between marginal distributions and copula function is less supported by the data.
3. When the copula function is Gaussian, the four probability models with different marginal distributions have different AIC values, indicating that the validity of each probability model is affected by the marginal distributions. Also, when the marginal distributions are the same, the AIC values of the model vary with the copula function, indicating the validity of each model is also affected by the copula function.
4. For a given copula structure, the model assu-ming c and φ are lognormally distributed is most supported by the data. Comparing models with different copula functions, Model 16 with the FGM copula function has the smallest AIC, and hence is most supported by the data. Models based on the commonly used Gaussian copula function are not the optimal probabilistic models.

7 IMPACT OF PROBABILITY MODELS ON FAILURE PROBABILITY CALCULATION

7.1 *Example 1*

To investigate the effect of probability model on failure probability calculation, consider an infinite slope as shown in Figure 1. Its factor of safety can be calculated as follows:

$$F_s = \frac{c + \gamma H \cos^2 \alpha \tan \phi}{\gamma H \sin \alpha \cos \alpha} \tag{20}$$

where H = thickness of soil layer; α = slope angle; γ = unit weight of the soil. In this example, $H = 5$ m and $\gamma = 17$ kN/m^3.

Monte Carlo simulation is first used to calculate the failure probability of the slope when different probability models are adopted and as the slope angle varies. In the Monte Carlo simulation, 1,000,000 samples are generated. The obtained failure probabilities are summarized in Table 5.

For comparison, the failure probabilities calculated using the one-dimensional integration method suggested by Tang et al. (2013) are also shown. We can see that the failure probability calculated using Monte Carlo simulation and that calculated using the one-dimensional integration method is practically the same, thus verifying the validity of the suggested method for failure probability calculation.

Figures 2(a)–2(d) compare the calculated failure probability of the slope calculated when the marginal distributions vary but the copula function is fixed. In Figure 2(a), although there are four probability models involved, only two curves can be clearly identified. This is because the predictions from models 1 and 3 are very similar, and also the predictions from models 2 and 4 are very similar, as can be found in Table 5. It seems that the calculated failure probability is more sensitive to the marginal distribution of c than that of φ. Also, there is a trend that the difference between predicted failure probability increases as the calculated failure probability decreases, i.e. the small failure probability is more sensitive to the selection of probability model. Similar phenomena can also be found in Figures 2(c) and (d). Comparing Figures 2(a)–(d), the effect of marginal distribution is most obvious in Figure 2(b) for the case of $\alpha = 20^{o}$. In such a case, the failure probability calculated based on Model 5 is almost four orders of magnitude larger than that calculated based on Model 6.

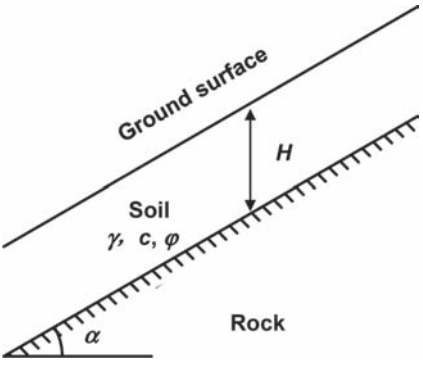

Figure 1. Infinite slope analyzed in example 1.

Figures 3(a)–(d) compare the calculated failure probability of the slope when the marginal distributions are the same but the copula function is different. In Figures 3(a) and (c), the effect of copula function on failure probability calculation is not very obvious. However, the copula function could significantly affect the calculated failure probability, as shown in Figures 3(b) and (d). Indeed, in Figure 3(b) the failure probability calculated based on Model 10 is more than two orders of magnitude larger than that calculated based on Model 6, implying the copula function can also significantly affect the failure probability calculation. Comparing Figures 3(b) and (d), the effect of copula function is also more obvious for small failure probability problems.

Table 5. Failure probability calculated based on different probability models (example 1).

			p_f					
			$\alpha = 30^{o}$		$\alpha = 25^{o}$		$\alpha = 20^{o}$	
Model no.	Copula	Marginal distribution	1-D integration	Monte Carlo simulation	1-D integration	Monte Carlo simulation	1-D integration	Monte Carlo simulation
1	Gaussian	n,n	0.119	0.120	0.110	0.109	0.098	0.098
2		l,n	0.038	0.038	0.011	0.011	0.001	0.001
3		n,l	0.119	0.119	0.109	0.109	0.098	0.098
4		l,l	0.039	0.039	0.012	0.012	0.002	0.002
5	Clayton	n,n	0.119	0.130	0.108	0.112	0.097	0.108
6		l,n	0.048	0.050	0.012	0.013	9.0×10^{-6}	7.0×10^{-6}
7		n,l	0.121	0.116	0.110	0.105	0.099	0.094
8		l,l	0.048	0.051	0.012	0.014	7.0×10^{-6}	7.0×10^{-6}
9	Frank	n,n	0.121	0.126	0.110	0.116	0.099	0.104
10		l,n	0.044	0.043	0.016	0.015	0.004	0.004
11		n,l	0.118	0.124	0.108	0.113	0.098	0.102
12		l,l	0.046	0.045	0.017	0.017	0.004	0.004
13	FGM	n,n	0.120	0.124	0.109	0.114	0.099	0.103
14		l,n	0.049	0.046	0.018	0.017	0.003	0.003
15		n,l	0.121	0.122	0.099	0.112	0.099	0.101
16		l,l	0.051	0.047	0.020	0.018	0.004	0.003

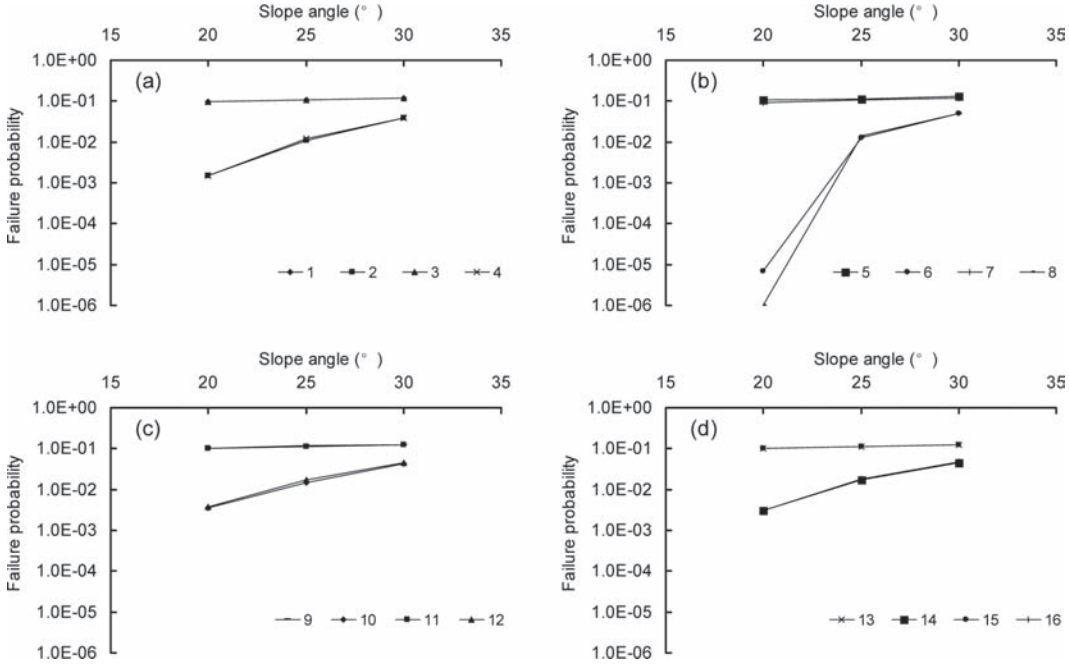

Figure 2. Effect of marginal distributions on failure probability calculation (example 1): (a) models 1, 2, 3, 4; (b) models 5, 6, 7, 8; (c) models 9, 10, 11, 12; (d) models 13, 14, 15, 16.

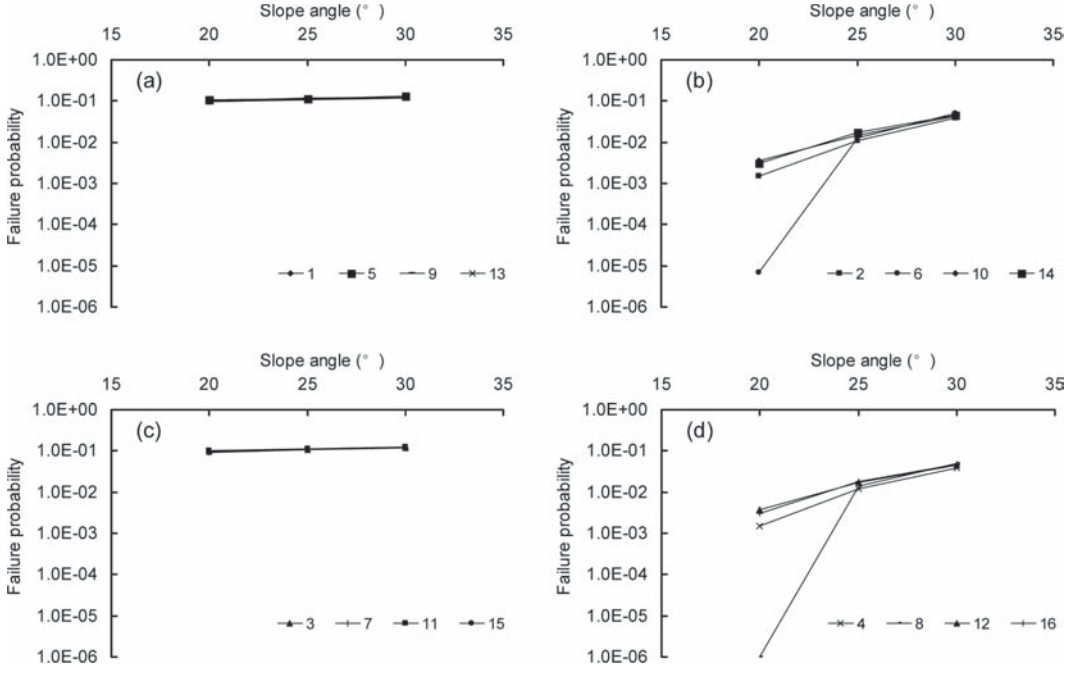

Figure 3. Effect of copula function on failure probability calculation (example 1) (a) models 1, 5, 9, 13; (b) models 2, 6, 10, 14; (c) models 3, 7, 11, 15; (d) models 4, 8, 12, 16.

To understand how the marginal distributions affect the failure probability calculation, Figures 4(a)–(d) compare the distribution of samples together with the limit state function when Models 1–4 are employed, respectively. In each figure, there are 1,000,000 simulated samples. For comparison, the measured data are also shown in these figures. We can see that the assumption on the marginal distribution could significantly affect the distribution of samples. For instance, when cohesion is assumed to be normal, a large portion of samples will lie in the failure region, indicating a relatively larger failure probability. However, when cohesion is assumed to be lognormal, the number of samples in the failure region is significantly reduced, making the calculated failure probability small. In this example, the distribution of samples is very sensitive to the assumed marginal distributions.

To investigate how the copula function affects the failure probability calculation, Figures 5(a)–(d) compare the distribution of samples together with the limit state functions when Models 2, 6, 10 and 14 are used for failure probability calculation. All the four models have the same marginal distributions but differ in the copula function. We could see that the distribution of samples is also affected by the copula function. The limit state functions are all close to the edge of the region where simulated samples are concentrated. As shown in Figure 3(b), the failure probabilities estimated based on these four models are quite large, implying the tail of the joint distribution is sensitive to the copula function used.

As mentioned previously, the FGM copula with c being lognormal and φ being lognormal is most supported by the data. Currently, the Gaussian copula is often used in practice. As shown in Table 5, when the marginal distributions of c and φ are both lognormal, the failure probability calculated from the Gaussian copula function is generally larger than that obtained based on the FGM copula function. In such a case, the failure probability will be overestimated if the Gaussian copula is used.

7.2 *Example 2*

In Example 1, the performance function is relatively simple, which can be solved by both the one-

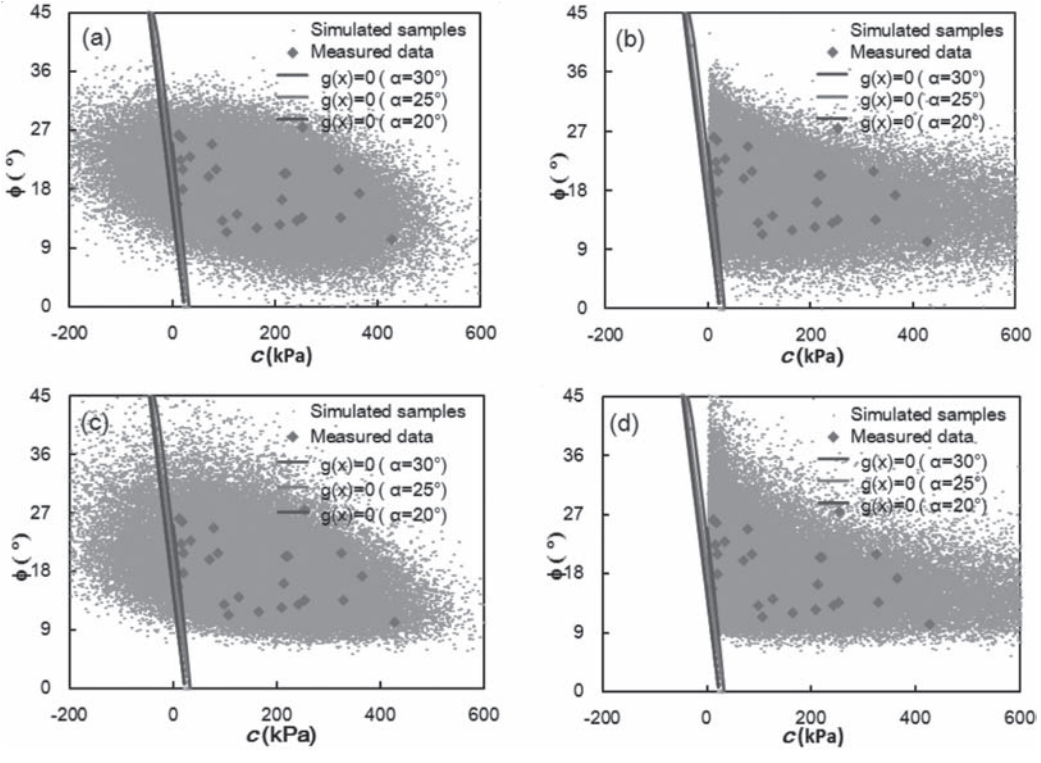

Figure 4. Effect of marginal distributions on the distribution of samples (example 1): (a) model 1; (b) model 2; (c) model 3; (d) model 4.

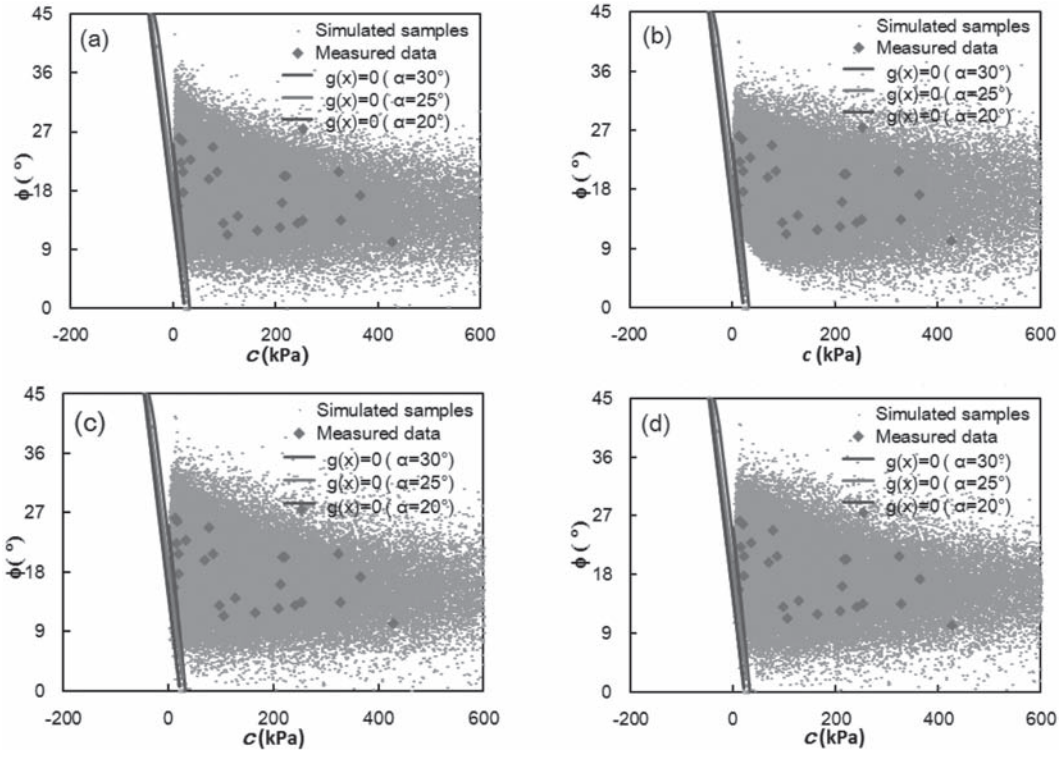

Figure 5. Effect of copula function on the distribution of samples (example 1): (a) model 2; (b) model 6; (c) model 10; (d) model 14.

dimensional integration method and Monte Carlo simulation. To illustrate the advantage of the Monte Carlo simulation algorithm, a strip footing subjected to a load of q (kPa) resting on a horizontal ground is analyzed (Fig. 6).

The bearing capacity of the strip footing Q_u can be calculated using the following equations (Cherubini 2000)

$$Q_u = 0.5 \cdot \gamma_1 \cdot B \cdot N_\gamma + c \cdot N_c + \gamma_2 \cdot D_f \cdot N_q \tag{21}$$

$$N_q = e^{\pi \tan\phi} \cdot \left(\tan\left(\frac{\pi}{4} + \frac{\phi}{2} \right) \right)^2 \tag{22}$$

$$N_\gamma = 1.8 \cdot (N_q - 1) \cdot \tan\phi \tag{23}$$

$$N_c = \frac{N_q - 1}{\tan\phi} \tag{24}$$

where D_f = embedded depth of foundation (m); B = foundation width (m); γ_1 = unit weight of the soil below the foundation bottom and γ_2 = unit weight of the soil above the foundation

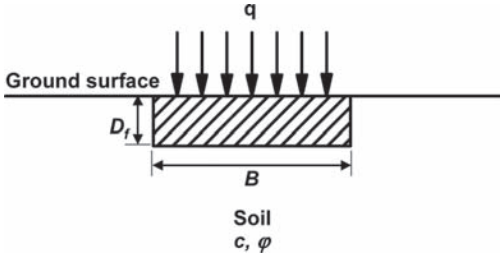

Figure 6. Strip footing analyzed in example 2.

bottom. In this example, $D_f = 0.5$ m, and $B = 2$ m, $\gamma_1 = \gamma_2 = 19.5$ kN/m^3.

As the performance function here is complex, the one-dimensional integration method can hardly be applied. However, the Monte Carlo simulation algorithm is still applicable. Table 6 summarizes the failure probability calculated using 16 different probability models (N = 1,000,000). Similar to Figures 2, 3 and Figures 7, 8 show the effect of marginal distribution and copula function on failure probability calculation in this example,

Table 6. Failure probability predicted based on different probability models (example 2).

Model no.	Copula	Marginal distribution	p_f		
			$q = 50$ kPa	$q = 80$ kPa	$q = 110$ kPa
1	Gaussian	n,n	0.091	0.094	0.096
2		l,n	0	0	2.7×10^{-4}
3		n,l	0.091	0.093	0.096
4		l,l	0	0	2.7×10^{-4}
5	Clayton	n,n	0.100	0.103	0.106
6		l,n	0	0	0
7		n,l	0.087	0.090	0.092
8		l,l	0	0	0
9	Frank	n,n	0.096	0.099	0.102
10		l,n	3.0×10^{-5}	3.2×10^{-4}	0.001
11		n,l	0.094	0.097	0.100
12		l,l	2.0×10^{-5}	2.5×10^{-4}	0.001
13	FGM	n,n	0.094	0.096	0.100
14		l,n	1.0×10^{-5}	1.0×10^{-4}	8.9×10^{-4}
15		n,l	0.093	0.095	0.098
16		l,l	0	1.1×10^{-4}	9.2×10^{-4}

*0 denotes that no failure sample is found during the conditional sampling with 1,000,000 samples.

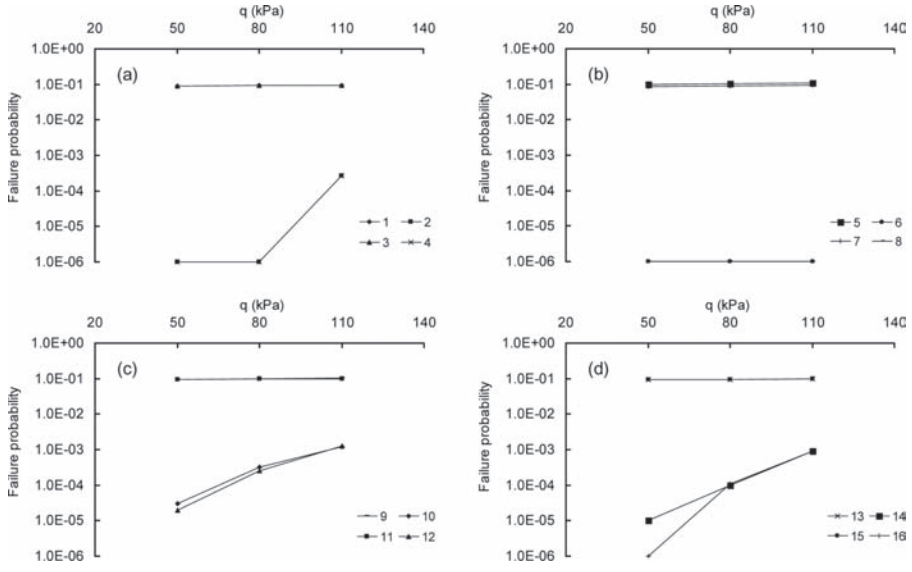

Figure 7. Effect of marginal distributions on failure probability calculation (example 2): (a) models 1, 2, 3, 4; (b) models 5, 6, 7, 8; (c) models 9, 10, 11, 12; (d) models 13, 14, 15, 16. (failure probability of 0 in Table 6 is plotted as 1.0×10^{-6}).

respectively. The phenomena observed in Figures 7 and 8 are generally similar to those observed in Figures 2 and 3, i.e. the effect of marginal distributions and copula functions on failure probability calculation is more obvious when the failure probability is small.

Figures 9(a) and (b) show the calculated failure probabilities based on 16 models for Example 1 and Example 2, respectively. The difference between calculated failure probabilities based on the 16 probability models in Example 2 is even larger than that observed in Example 1, indicating

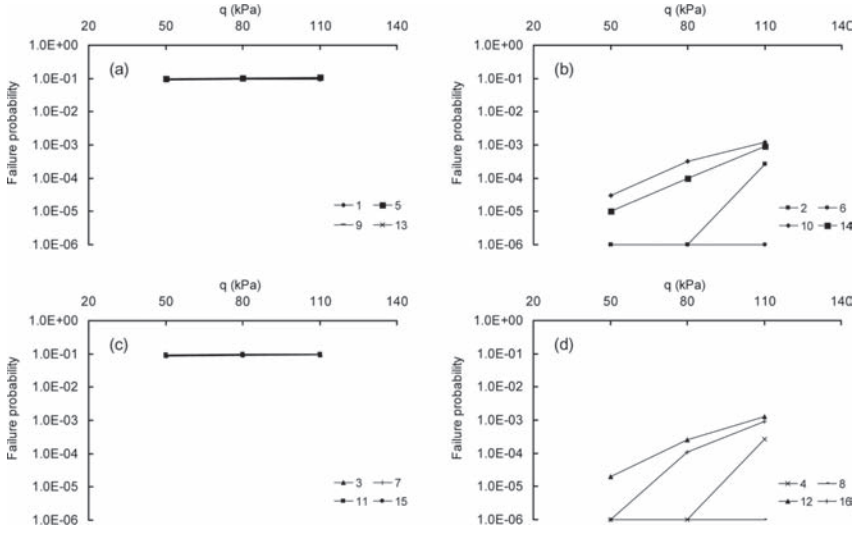

Figure 8. Effect of copula function on failure probability calculation (example 2): (a) models 1, 5, 9, 13; (b) models 2, 6, 10, 14; (c) models 3, 7, 11, 15; (d) models 4, 8, 12, 16. (failure probability of 0 in Table 6 is plotted as 1.0×10^{-6}).

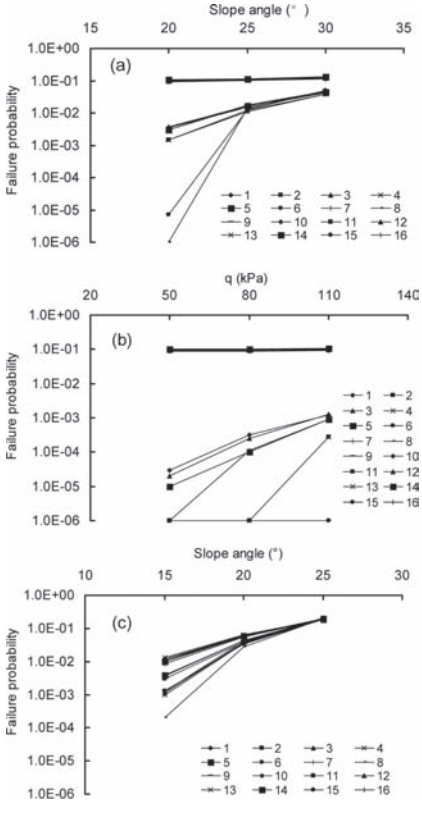

Figure 9. Failure probabilities calculated based on 16 models: (a) example 1; (b) example 2; (c) example 3. (Failure probability of 0 in Table 6 is plotted as 1.0×10^{-6}).

that the effect of probability model on failure probability calculation is also affected by the deterministic model. In other words, even for the same set of data and for the same probability models considered, the effect of probability model on failure probability calculation changes with the reliability problem considered.

7.3 *Example 3*

In the above two examples, the probability models have important effect on the failure probability. The third example shows a case where such an effect is less obvious. In this example, the data are adopted from Xu & Yang (1998) about the shear strength parameters of clay in Shanghai, as shown in Table 7. In this example, there are 81 measurements, compared to only 25 measurements in Example 1. The same 16 models are considered in this example, and the calibration results are shown in Table 8.

Among the 16 models considered, Model 8 has the smallest AIC value and hence is the optimal one, in which both c and φ are assumed to be lognormal and the copula function is Clayton. The optimal model in this example is different from that found in Example 1, indicating the optimal probability model is problem specific.

Using the calibrated samples, the failure probability of the infinite slope in Example 1 is calculated again. Figure 10 shows the effect of marginal distribution on failure probability calculation. The difference between failure probabilities calculated based on different probability models is generally

Table 7. Soil data analyzed in example 3 (Adapted from Xu & Yang 1998).

Test no.	c (kPa)	φ (°)	Test no.	c (kPa)	φ (°)	Test no.	c (kPa)	φ (°)	Test no.	c (kPa)	φ (°)
1	30	15.8	22	35	15.6	43	20	15.1	64	13	13.5
2	14	24.8	23	20	10.8	44	15	14.0	65	15	17.0
3	38	20.9	24	29	19.5	45	27	14.2	66	9	15.0
4	19	18.8	25	25	10.9	46	15	13.2	67	13	13.5
5	43	19.5	26	25	18.8	47	26	14.7	68	7	19.0
6	13	20.6	27	30	15.8	48	11	12.7	69	12	13.5
7	13	24.6	28	28	14.6	49	35	12.4	70	13	14.0
8	24	25.5	29	30	9.6	50	15	20.4	71	14	10.0
9	7	25.9	30	32	15.6	51	33	15.4	72	16	22.0
10	27	19.3	31	30	14.7	52	17	10.9	73	19	15.3
11	26	15.1	32	24	19.5	53	25	17.2	74	8	13.6
12	19	22.3	33	34	21.3	54	34	17.8	75	12	18.5
13	22	19.8	34	29	18.8	55	17	12.2	76	16	14.0
14	13	17.7	35	35	13.3	56	32	14.0	77	13	12.5
15	15	19.5	36	21	13.5	57	20	11.6	78	15	19.2
16	17	16.0	37	30	19.8	58	33	15.6	79	12	17.5
17	20	17.2	38	15	17.2	59	20	15.7	80	10	14.0
18	7	14.8	39	18	14.4	60	21	11.5	81	11	14.0
19	19	16.8	40	16	14.5	61	25	21.5			
20	18	10.8	41	25	13.0	62	30	17.4			
21	10	21.8	42	17	10.4	63	28	12.4			

Table 8. Calibrated parameters of 16 probability models based on the data in Table 7.

Model no.	Copula	Marginal distribution	AIC	θ	μ_c	σ_c	μ_φ	σ_φ
1	Gaussian	n,n	1028.57	–0.005	20.852	8.405	16.236	3.746
2		l,n	1025.20	–0.040	20.966	9.472	16.235	3.747
3		n,l	1022.83	–0.014	20.852	8.405	16.236	3.767
4		l,l	1019.60	–0.009	20.966	9.472	16.232	3.750
5	Clayton	n,n	1028.56	–0.030	20.852	8.401	16.237	3.747
6		l,n	1025.04	–0.084	20.945	9.463	16.231	3.750
7		n,l	1022.81	–0.036	20.844	8.399	16.236	3.767
8		**l,l**	**1019.18**	**–0.088**	**20.945**	**9.463**	**16.236**	**3.767**
9	Frank	n,n	1028.48	0.182	20.875	8.405	16.235	3.743
10		l,n	1025.34	0.092	20.966	9.472	16.231	3.747
11		n,l	1022.71	0.226	20.862	8.404	16.232	3.750
12		l,l	1019.58	0.150	20.975	9.501	16.232	3.750
13	FGM	n,n	1028.48	0.101	20.877	8.405	16.234	3.744
14		l,n	1025.33	0.049	20.966	9.472	16.225	3.745
15		n,l	1022.70	0.123	20.866	8.405	16.232	3.750
16		l,l	1019.58	0.094	21.008	9.491	16.216	3.746

no more than two orders of magnitude, which are less than those observed in Example 1, indicating the effect of marginal distribution is less obvious in this example. Figure 11 shows the effect of copula function on failure probability calculation. This is possibly because there are more measurements in this example, which provide more constraint on the shape of the marginal distributions. The maximum difference between failure probabilities calculated based on different copula functions occurs in Figure 11(d), which is less than one order of magnitude and is also significantly than that observed in Example 1. Note the copula function measures the dependence relationship between the cohesion and the friction angle. To find out the reason why the effect of copula is less obvious in example, the

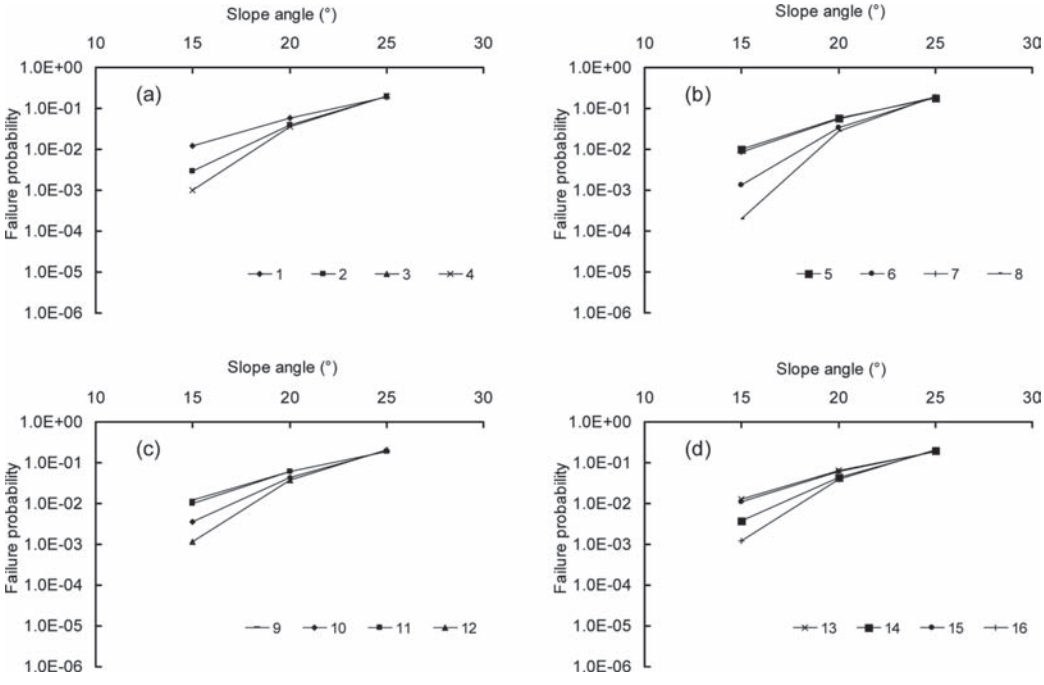

Figure 10. Effect of marginal distributions on failure probability calculation (example 3): (a) models 1, 2, 3, 4; (b) models 5, 6, 7, 8; (c) models 9, 10, 11, 12; (d) models 13, 14, 15, 16.

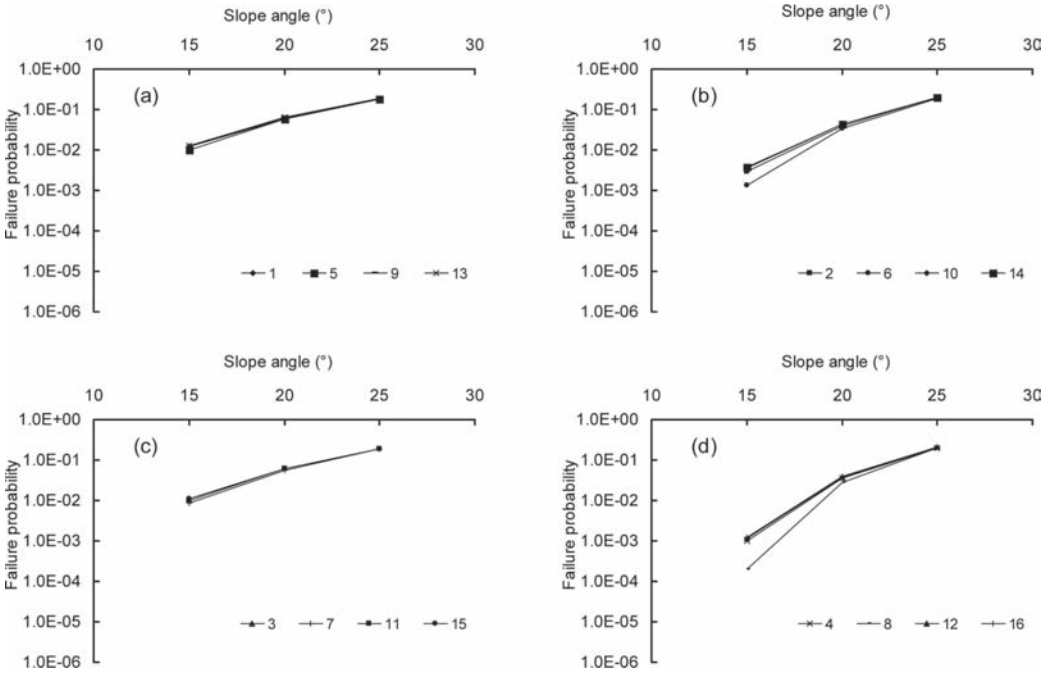

Figure 11. Effect of copula function on failure probability calculation (example 3) (a) models 1, 5, 9, 13; (b) models 2, 6, 10, 14; (c) models 3, 7, 11, 15; (d) models 4, 8, 12, 16.

correlation coefficients between c and φ in Example 1 and Example 3 are both calculated, which are –0.407 and –0.005, respectively. Although the correlation coefficient is not an accurate measure of dependence, it does show that the dependence relationship between c and φ is much weaker in Example 3. Thus, it is reasonable to expect that in Example 3 the effect of copula function is less obvious.

Figure 9(c) shows the calculated failure probability based on 16 models, which also shows that the effect of probability model on failure probability calculation is less obvious in this example than that in Example 1. As analyzed previously, this is due to the combined effect of more measured data and less correlation between c and φ. When there are more data for constructing the probability model, the probability model may have less effect on the failure probability calculation.

8 SUMMARY AND CONCLUSIONS

The joint distribution of the cohesion and the friction angle can be fully specified by the marginal distributions and a copula function. The model parameters can be calibrated simultaneously by the maximum likelihood method. Calibrating the model parameters separately can enhance the computational efficiency, but may miss the optimal model parameters. Different models could be ranked based on the information criteria available in statistics which are capable of considering the trade-off between model accuracy and model complexity. The examples studied in this paper indicate that the probability models constructed based on the Gaussian copula, which are widely used in the literature, may not be the optimal probability model. The optimal probability model depends on the data available and is problem specific.

Many existing reliability methods such as the first order reliability method are developed for probability models constructed based on the Gaussian copula, and can not be directly applied when other copula functions are used. Monte Carlo simulation, however, are generally applicable, even when the performance function is complex. Monte Carlo simulation can be applied to general performance function and hence is superior to the existing one-dimensional integration method when the performance function is complex or when there are several pairs of cohesion and friction angle in the geotechnical reliability analysis.

Both the marginal distribution and copula function could significantly affect the failure probability calculation. The failure probabilities calculated based on different probability models could vary by several orders of magnitude. In general, the effect of probability model on failure probability estimation is more obvious when the failure probability is small. The effect of probability model on failure probability estimation depends on the deterministic model and also the data available for constructing the probability models. Increasing the amount of measured data may provide more constraint to the theoretical model and hence reduce the effect of marginal distributions on failure probability estimation. As the correlation between the cohesion and friction angle decreases, the effect of copula function on failure probability calculation also decreases.

ACKNOWLEDGEMENTS

This research was substantially supported by the NSFC/ANR Joint Research Scheme (51161130523), National Basic Research Program of China (973 Program 2011CB013800) and Shanghai Outstanding Academic Leaders Program (12XD1405100). The authors also wish to thank Prof. Dianqing Li from Wuhan University for helpful discussions of the work presented.

REFERENCES

Akaike H. 1974. A new look at the statistical model identification. *IEEE Trans Autom Control* 19(6): 761–723.

Ang, A.H-S. & Tang, W.H., 1984. Probability concepts in engineering planning and design: design, risk and reliability, Vol. 2. Wiley, New York.

Baecher, G.B. & Christian, J.T. 2003. Reliability and Statistics in Geotechnical Engineering, Wiley, Chichester, United Kingdom.

Cavanaugh, J.E. 1999. A large-sample model selection criterion based on Kullback's symmetric divergence. *Statistics & Probability Letters* 42(4): 333–343.

Chen, L.H., Chen, Z.Y. & Liu, J.M. 2005. Probability distribution of soil strength. *Rock and Soil Mechanics* 26(1): 37–40, 45. (In Chinese).

Cherubini, C. 1997. Data and considerations on the variability of geotechnical properties of soils. *In Proceedings of the International Conference on Safety and Reliability (ESREL)* 97, Lisbon, Vol. 2, pp. 1583–1591.

Cherubini, C. 2000. Reliability evaluation of shallow foundation bearing capacity on c', φ' soils. *Canadian Geotechnical Journal* 37: 264–269.

Cherubini, U., Luciano, E. & Vecchiato,W. 2004. Copula Methods in Finance. Wiley Finance Series. Wiley, Chichester.

Ching, J.Y. & Phoon, K.K. 2012. Establishment of generic transformations for geotechnical design parameters. *Structural Safety* 35: 52–62.

Duncan, J.M. 2000. Factors of safety and reliability in geotechnical engineering. *ASCE Journal of Geotechnical and Geoenvironmental Engineering* 126(4): 307–316.

Durrleman, V., Nikeghbali, A., & Roncalli, T. 2000. Which copula is the right one? Groupe de Recherche Opérationnelle, France: Crédit Lyonnais *Working paper*.

Fenton, G.A. & Griffiths, D.V. 2008. Risk Assessment in Geotechnical Engineering. John Wiley & Sons, New York.

Goda K. 2010. Statistical modeling of joint probability distribution using copula: Application to peak and permanent displacement seismic demands. *Structural Safety* 32(2): 112–123.

Harr, M.E. 1987. Reliability-based design in civil engineering. McGraw-Hill Book Company, New York.

Honjo. Y. & Amatya, S. 2005. Partial factors calibration based on reliability analyses for square footings on granular soils. *Géotechnique*, 55(6): 479–491.

Huang, J., Griffiths, D.V. & Fenton, G.A. 2010. System reliability of slopes by RFEM. *Soils and Foundations* 50(3): 343–353.

Joe, H. & Xu, J.J. 1996. The estimation method of inference functions for margins for multivariate models. Department of Statistics. University of British Columbia, *Technical Report*, 166.

Juang, C.H. & Wang, L. 2013. Reliability-based robust geotechnical design of spread foundations using multi-objective genetic algorithm. *Computers and Goetechnics* 48: 96–103.

Lebrun R. & Dutfoy A. 2009. A generalization of the Nataf transformation to distributions with elliptical copula. *Probabilistic Engineering Mechanics 2009* 24(2):172–178.

Li, D.Q., Tang, X.S., Phoon, K.K., Chen, Y.F. & Zhou, C.B. 2013. Bivariate simulation using copula and its application to probabilistic pile settlement analysis. *International Journal for Numerical and Analytical Methods in Geomechanics* 37(6): 597–617.

Low, B.K. & Tang, W.H. 1997. Efficient reliability evaluation using spreadsheet. *Journal of Engineering Mechanics* 123(7): 749–752.

Lumb, P. 1970. Safety factors and the probability distribution of soil strength. *Canadian Geotechnical Journal* 7: 225–242.

Luo, Z., Atamturktur, H.S., Juang, C.H., Huang, H. & Lin, P.S. 2011. Probability of serviceability failure in a braced excavation in a spatially random field: Fuzzy finite element approach. *Computers and Geotechnics* 38: 1031–1040.

Nelsen R.B. 2006. An introduction to copulas. 2nd ed. *Springer*: New York.

Schwarz, G. 1978. Estimating the dimension of a model. *Ann. Statist.* 6: 461–464.

Sivakumar Babu, G.L., Srivastava, A. & Murthy, D.S.N. 2006. Reliability analysis of the bearing capacity of a shallow foundation resting on cohesive soil. *Canadian Geotechnical Journal* 43: 217–223.

Sklar, A. 1959. Fonctions de répartition à n dimensions et leurs marges. Publications de l'Institut de Statistique de l'Université de Paris 8, pp. 229–231.

Tang, W.H. 1979. Probabilistic evaluation of penetration resistances. *Journal of Geotechnical Engineering* 105(10): 1173–1191.

Tang, X.S., Li, D.Q., Rong, G., Phoon, K.K. & Zhou, C.B. 2013. Impact of copula selection on geotechnical reliability under incomplete probability information. *Computers and Geotechnics* 49: 264–278.

Trivedi, P.K. & Zimmer, D.M. 2005. Copula Modeling: An Introduction for Practitioners. *Foundations and Trends in Econometrics* 1(1): 1–111.

Uzielli, M., Vannucchi, G. & Phoon, K.K. 2005. Random field characterisation of stress-normalised cone penetration testing parameters. *Géotechnique* 55(1): 3–20.

Vanmarcke, E.H. 1977. Probabilistic modeling of soil profiles. *ASCE Journal of Geotechnical Engineering* 103(GT11): 1227–1246.

Wang, Y. 2011. Reliability-based design of spread foundations by Monte Carlo simulations. *Géotechnique* 61(8): 677–685.

Whitman, R.V. 2000. Organizing and evaluating uncertainty in geotechnical engineering. *ASCE Journal of Geotechnical Engineering* 125(6): 583–593.

Wolff, T.H. 1985. Analysis and design of embankment dam slopes: a probabilistic approach. Ph.D. thesis, Purdue University, Lafayette, Ind.

Xu, C. & Yang, L.D. 1998. Test of goodness of fit of random variables and Bayesian estimation of distribution parameters. *Journal of Tongji University* 26(3): 340–344. (In Chinese).

Xue, J.F. & Gavin, K. 2007. Simultaneous determination of critical slip surface and reliability index for slopes, ASCE *Journal of Geotechnical and Geoenvironmental Engineering* 133(7): 878–886.

Zhang, J., Zhang, L.M. &Tang, W.H. 2011. Kriging numerical models for geotechnical reliability analysis. *Soils and Foundations* 51(6): 1169–1177.

Zhang, L.L., Zuo, Z.B., Ye, G.L., Jeng, D.S. & Wang, J.H. 2013. Probabilistic parameter estimation and predictive uncertainty based on field measurements for unsaturated soil slope. *Computers and Geotechnics* 48: 72–81.

Zhang, L.M. 2004. Reliability verification using proof pile load tests. *Journal of Geotechnical and Geoenvironmental Engineering* 130(11): 1203–1213.

Geotechnical Safety and Risk IV – Zhang et al. (eds)
© 2014 Taylor & Francis Group, London, ISBN 978-1-138-00163-3

Robust design of geotechnical systems—a new design perspective

C. Hsein Juang, Lei Wang & Sez Atamturktur
Glenn Department of Civil Engineering, Clemson University, Clemson, SC, USA

ABSTRACT: This paper presents a new geotechnical design concept, called Robust Geotechnical Design (RGD). The new design methodology seeks to achieve design robustness and economics, in addition to meeting safety requirements. Here, a design is considered robust if the variation in the system response (i.e., failure probability) is insensitive to the statistical characterization of noise factors, such as uncertain geotechnical parameters. It can be shown that when safety requirements are met, cost and robustness are conflicting objectives with a trade-off, meaning that a single best design may be unattainable. In such a case, a multi-objective optimization considering cost and robustness can be performed to obtain *a suite of best designs* within the solution space in which safety is guaranteed. To this end, the suite of best designs forms the Pareto Front, which is a useful tool to aid in the design decision making within the RGD methodology. The new design methodology is illustrated with examples of spread foundation designs and rock slope designs, through which the significance of the RGD methodology is demonstrated.

1 INTRODUCTION

It is well recognized that uncertainty in geotechnical parameters is usually unavoidable in the geotechnical design (Whitman 2000). The uncertainty in the geotechnical parameters, as well as the uncertainty in the adopted geotechnical model, can lead to the uncertainty in the predicted response of a system. In a deterministic approach, the engineer uses an experience-calibrated factor of safety to cope with the uncertainty in the predicted response. Of course, the factor of safety adopted in a particular design depends not only on the degree of uncertainties but also on the consequence of failure; in other words, it depends on the "calculated risk" (Casagrande 1965). To account for the uncertainty in geotechnical parameters explicitly, the probabilistic or reliability-based approaches are often used (e.g., Harr 1987; Wu et al. 1989; Tang & Gilbert 1993; Christian et al. 1994; Lacasse & Nadim 1996; Duncan 2000; Phoon et al. 2003; Chalermyanont & Benson 2004; Fenton & Griffiths 2008; Najjar & Gilbert 2009; Wang et al. 2011; Zhang et al. 2011).

In a traditional reliability-based geotechnical design process, multiple candidate designs are first checked against safety requirements (in terms of probability of failure), and then the acceptable designs are optimized for cost, which yields the final design. The reliability-based design is quite straightforward if the results of the reliability analysis are accurate and precise so that there will be no question whether a given design satisfies the safety requirement. The accuracy and precision of a reliability analysis, however, depends on how well the random soil parameters are characterized. If the knowledge of the statistical distribution of soil parameters is "perfect," the results of reliability analysis will be sufficiently accurate and the reliability-based design can be easily implemented by selecting the least cost design constrained with the failure probability requirement.

In a typical project in geotechnical practice, the statistical characterization of geotechnical parameters is uncertain due to lack of data, measurement error, transformation error, etc. The variation range of geotechnical parameters is usually considerably large (Harr 1987; Phoon & Kulhawy 1999 a & b; Lee et al. 2012) and thus, the variation can be either overestimated or underestimated. Such overestimation or underestimation of the variation of geotechnical parameters can lead to over-design or under-design (Juang and Wang 2013).

While reduction of the uncertainty in geotechnical parameters is important, which should be pursued whenever it is deemed cost-effective, in this paper, we focus on a different approach by achieving robustness in the design without eliminating the sources of uncertainty. Here, a design is considered robust if the variation in the system response is insensitive to (or robust against) the variation of uncertain geotechnical parameters (called noise factors in this paper). The essence of a robust design is to select a design that yields a minimal variation in the system response without eliminating the sources of uncertainty or reducing the level of uncertainty.

In this paper, a Robust Geotechnical Design (RGD) methodology is proposed to fulfill the goal

of minimizing the effects of the uncertainty of soil parameters. Robust design concept is first proposed by Taguchi (1986) for improving product quality and reliability in Industry Engineering. Early applications of robust design are closely related to product and mechanical design to avoid the effects of the uncertainty from environmental and operating conditions (Taguchi 1986; Phadke 1989). The more recent applications are found in various fields such as mechanical, structural and aeronautical design (e.g., Chen et al. 1996; Chen et al. 1999; Lee & Park 2001; Doltsinis et al. 2005; Kang 2005; Park et al. 2006; Brik et al. 2007; Lagaros & Fragiadakis 2007; Kumar et al. 2008; Marano et al. 2008; Lee et al. 2010). Robust design attempts to adjust design parameters (i.e., the so-called "easy to control" factors) so that the system response of the design is insensitive to, or robust against, the variation of noise factors (i.e., "hard to control" factors). In a geotechnical design, the noise factors mainly refer to the uncertain geotechnical parameters, although model bias may also be considered. Thus, in a robust design, regions in the solution space that yield low variation in the system response are sought.

It should be noted that Robust Geotechnical Design (RGD) is a design strategy to complement the traditional methods. With the RGD approach, the focus is to satisfy three design requirements, namely safety, cost, and robustness (against the variation in system response caused by noise factors). The safety requirement is usually implemented through constraints of reliability, and hence the design becomes a bi-objective optimization problem. For the bi-objective problem examined in this paper, it is very likely that no single best solution exists that is most optimal with respect to both objectives (cost and robustness). In such a situation, a detailed study of the trade-offs between these objectives can lead to a more informed design decision.

In this paper, the RGD approach is demonstrated with two design examples: one on spread foundation designs and the other on rock slope designs. The significance and versatility of the RGD approach is demonstrated through these examples.

2 ROBUST GEOTECHNICAL DESIGN METHODOLOGY

In reference to Figure 1, the Robust Geotechnical Design (RGD) methodology conceptually consists of five steps outlined below (Juang et al. 2013a):

Step 1 is to define the geotechnical design problem of interest. For a given problem, the deterministic model (limit state or performance function) of the intended geotechnical system is first established, which can be in the form of either an analytical model or a numerical model. For all the input parameters of the adopted geotechnical model, the design parameters and the noise factors are then classified.

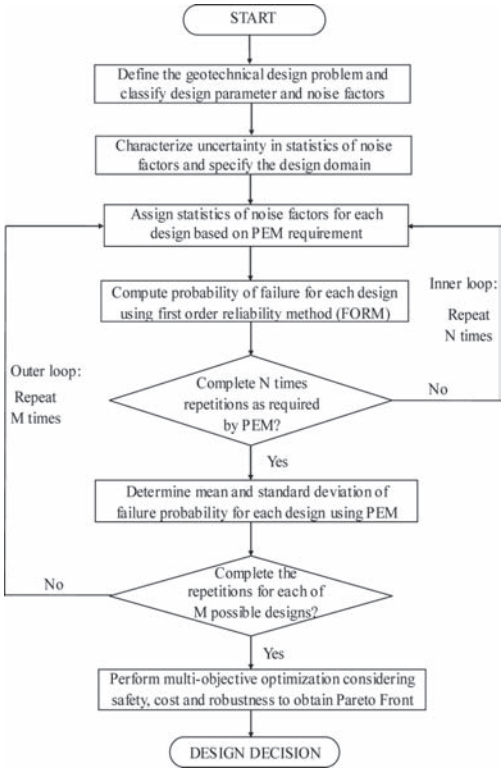

Figure 1. Flowchart for robust geotechnical design (modified after Juang et al. 2013a).

Step 2 is to characterize the uncertainty in statistics of noise factors and specify the design domain. For the design of geotechnical systems, the key uncertain geotechnical parameters are usually identified as noise factors. The uncertainty in the statistics (e.g., coefficient of variation) of the noise factors may be estimated based on published literature guided by engineering judgment or the bootstrapping method based on limited data. The design domain (space) of the design parameters are prescribed based on their typical ranges, augmented with local experiences. The design parameters are usually specified in discrete space for construction convenience. Thus, the design space will consist of a finite number (M) of designs.

Step 3 is to assess the variation of the system response as a measure of robustness for a given design. In this paper, the variation of system response (e.g., failure probability) caused by

uncertain statistics of noise factors is used as a measure of robustness, and a smaller variation of system response indicates a greater robustness. The variation of the failure probability is determined using the advanced Point Estimate Method (PEM) developed by Zhao & Ono (2000) based on the estimated variation in statistics of noise factors. The PEM evaluates the failure probability for a given design at selected values (say N sets of values) of statistical parameters of noise factors, and then the mean and standard deviation of the failure probability can be computed based on the PEM formulation. For a given set of statistical parameters, the failure probability is determined using the traditional reliability method, such as the first-order reliability method (FORM; Ang & Tang 1984). Thus, in this step, for a given design in the design space, the mean and standard deviation in the failure probability is computed by PEM integrated with FORM procedure, as represented by the inner loop shown in Figure 1.

Step 4 is to repeat the procedure in Step 3 for each design in the design space. The mean and standard deviation of the failure probability for all the M designs in the design space are obtained by M repetitions of the PEM integrated with FORM procedure in Step 3, as represented by the outer loop shown in Figure 1.

Step 5 is a key step in RGD for choosing the most preferred design. A multi-objective optimization is carried out considering three distinct criteria including safety, cost and robustness. Through the multi-objective optimization, a Pareto Front is established, which serves as a guide for selecting the most preferred design.

In the implementation of optimization, the mean failure probability is set as the safety constraint to screen out the unsatisfactory designs, and cost (in terms of construction cost for the geotechnical system) and robustness (in term of standard deviation of the failure probability) are set as two objectives for optimization.

Note that the multi-objective optimization seldom leads to a single best solution (or design). With conflicting objectives, it leads to a set of non-dominated solutions that collectively form a Pareto Front. For a minimization problem with two objectives, the solution A dominates solution B when no objective value of B is less than A, and at least one objective value of B is strictly greater than A (Ghosh & Dehuri 2004). By screening designs or solutions in the solution space and eliminating the solutions that are dominated by others, a set of solutions that are non-dominated by any other solution can be obtained, which collectively form a Pareto Front as shown in Figure 2 (Wang et al. 2013).

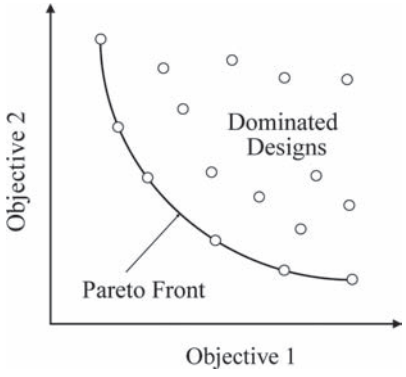

Figure 2. Illustration of Pareto Front (modified after Wang et al. 2013).

In this paper, the Non-dominated Sorting Genetic Algorithm version II (NSGA-II), developed by Deb et al. (2002) is used to establish the Pareto Front. The obtained Pareto Front can then be used for as a design aid for choosing the most preferred design when a specific cost range or a target robustness level is selected (Juang et al. 2013a&b).

It should be noted that when the number of candidate designs in the design space is large, the process for evaluating the mean and standard deviation of failure probabilities for all designs may be computationally prohibitive. In such cases, NSGA-II can be directly applied with PEM and FORM as its integrated components. In this scenario, the NSGA-II will automatically search for the "non-dominated designs" and only a limited number of selected designs in the design space that has potential to be on the Pareto Front require the full PEM and FORM procedures, which makes it more efficient.

3 RGD APPLICATION I: DESIGN OF SPREAD FOUNDATION

3.1 *Illustrative example*

A design example of a spread foundation subjected to the combined axial compressive loads and moment loads is first used to demonstrate the application of the proposed RGD approach. The axial loads are applied at the center of foundation with a permanent load component G of 900 kN and a random variable load component of Q with a mean of 458.7 kN and a Coefficient of Variation (COV) of 0.15. The moment load is applied at the center of foundation in the direction of the length of foundation with a deterministic value $M = 500$ kN · m.

The spread foundation is to be installed in a stiff till with a deterministic total unit weight of 22 kN/m^3, a mean effective friction angle ϕ' of 36.4° (c' = 0), a mean undrained shear strength c_u of 235.3 kPa and a mean coefficient of volume compressibility m_v of 0.01875 m^2/MN. The unit weight of concrete foundation is 24 kN/m^3. The foundation is founded at just above the ground water table with a foundation depth of D = 0.8 m. The deterministic model for computing the ULS capacity of spread foundation subjected to both vertical and moment loads is the "effective area" method (Meyerhoff 1953). For the Serviceability Limit State (SLS) capacity, the deterministic model defined in Eurocode 7 is adopted in this study (Orr & Farrell 1999; Orr & Breysse 2008). The ULS failure is said to occur when the computed bearing capacity is smaller than the total combined loads. The SLS failure is said to occur if the computed total settlement exceeds the maximum allowable settlement of 25 mm.

3.2 *Uncertainty modeling*

For the spread foundation design in a stiff till, the uncertain soil parameters are considered as noise factors, including ϕ', c_u and m_v.

In geotechnical practice, the sample size (i.e., number of specimens tested) of the geotechnical parameters is usually small due to the budget constraints, so the statistics of geotechnical parameters derived from a few testing results may not reflect the statistics of the real geotechnical properties. Generally, the "population" mean can be adequately estimated based on the sample mean even with a small sample size (Wu et al. 1989). However, the estimation of variation of "population" is likely to be subjected to error when the sample size is small. With insufficient data, the variation of soil parameters in terms of Coefficient of Variation (COV) is usually estimated based on the prior knowledge from local experiences or published literature (e.g., Phoon & Kulhawy 1999a). For example, Orr and Breysse (2008) provided typical ranges for COV of three soil parameters ϕ', c_u and m_v for this spread foundation example. The COV of ϕ', denoted as $COV[\phi']$, typically ranges from 4% to 11%; the COV of c_u, denoted as $COV[c_u]$, typically ranges from 20% to 40%; and the COV of m_v, denoted as $COV[m_v]$, typically ranges from 20% to 40%. Thus, the COVs of ϕ', c_u and m_v should be treated as random variables.

As an example to illustrate the robustness concept presented herein, $COV[\phi']$ is assumed to have a mean of 0.08 and a COV of 25% (roughly to cover the typical range of $COV[\phi']$). Similarly, $COV[m_v]$ is assumed to have a mean of 0.30 and a COV of 17%; $COV[m_v]$ is assumed to have a mean of 0.30 and a COV of 17%.

The robustness of a reliability-based design is achieved if the probability of failure of a design is insensitive to the variation of the estimated COVs of the input soil parameters. For a given set of fixed COVs of soil parameters (ϕ', c_u and m_v in this example), the failure probability determined from FORM procedure (Hasofer & Lind 1974) will be a fixed value. If the COVs of these soil parameters are treated as random variables, the resulting failure probability will also be a random value. Thus, the variation of the failure probability has to be evaluated.

3.3 *RGD of spread foundation*

In this example, the footing width B and footing length L are considered as design parameters, the design domain of which should be specified. Here, B and L are assumed to vary from a minimum value of 1.0 m to a maximum value of 4.0 m, with an increment of 0.1 m for construction convenience. Thus, the number of possible designs in the design pool (or solution space) is 961. For a typical rectangular footing, the range of the length-to-width ratio (L/B) is between 1 and 10 (Akbas 2007). When screened with this geometry constraint for the length-to-width ratio, the design pool is reduced to 496 designs.

For the safety requirements, the reliability requirements defined in Eurocode 7 are adopted for this foundation design (Wang 2011). The target failure probability for ULS is set as 0.000072 (corresponding to a reliability index of 3.8) and the target failure probability for SLS is set as 0.067 (corresponding to a reliability index of 1.5). A sensitivity study indicates that the ULS failure probability requirement is always more stringent than the SLS failure probability requirement and the ULS controls the design of spread foundations, which is consistent with those reported by other investigators (e.g., Wang & Kulhawy 2008; Wang 2011). Indeed, in all analyses performed in this study, the ULS requirement is more stringent than the SLS requirement for this shallow foundation problem. Therefore, in the subsequent analysis only the ULS failure probability is considered.

Following the flowchart of the RGD methodology presented in Figure 1, the mean and standard deviation of the ULS failure probability, denoted as μ_p and σ_p, can be obtained for all designs in the design pool using PEM integrated with FORM procedure. The cost for each design in the design pool can be determined using the cost estimation procedure for spread foundation proposed by Wang & Kulhawy (2008). The cost of spread foundation construction includes the costs for

excavation, formwork, concrete, reinforcement and compacted backfill, respectively based on U.S. average unit price for construction of spread foundation (Wang & Kulhawy 2008). In this paper, the total cost for spread foundation is therefore a function of design parameters B and L.

Then the multi-objective optimization using NSGA-II may be achieved considering safety, cost and robustness in the design. Safety is generally assured through a constraint that the computed mean failure probability is less than the target failure probability. Thus, the design can be optimized with two objectives, robustness and cost, subjected to the safety constraint and any additional constraint such as geometry. This optimization scheme can be set up as shown in Figure 3.

The design parameters (B and L in this case) are generated in the discrete space using NSGA-II. The population size is arbitrarily set at 100 individuals. For this example, a converged Pareto Front is obtained at 30th generation, meaning that Pareto Front has already reached a "stable" condition and negligible improvement can be made at further generations. For this spread foundation design, 80 "unique" designs are selected into the final Pareto Front, as shown in Figure 4. Thus, the RGD approach yields a set of optimal designs, called Pareto Front, which describes an obvious trade-off relationship between cost and robustness. The designer can select a design with greater robustness (i.e., the failure probability is insensitive to the statistical characterization of soil parameters) only at the expense of a higher cost. The least cost design on the Pareto Front is design with B = 2.1 m and L = 2.5 m with a construction cost of 1522.2 USD.

The obtained Pareto Front can then be used as a design aid in decision making for choosing the "best" design based on the target cost or robustness level. For example, if the allowable budget for the spread foundation construction is set at

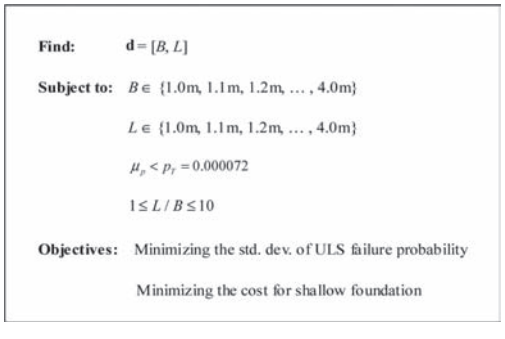

Figure 3. Formulation of multi-objective optimization for design of spread foundation.

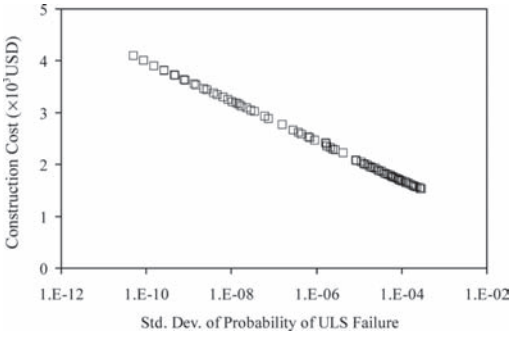

Figure 4. Pareto Front for design of spread foundation.

1700 USD, the design with the least standard deviation of failure probability (meaning greatest robustness) within this budget constraint has the design parameters of B = 2.2 m and L = 2.7 m with a construction cost of 1694.6 USD.

Although the Pareto Front with a specified trade-off relationship offers a valuable tool for decision-making, it may be desirable to further refine the decision-making use a more user-friendly index for robustness assessment. The *feasibility robustness* is defined as the confidence probability that the actual failure probability satisfies the target failure probability in the face of uncertainty, which is expressed as follows (Parkinson et al. 1993; Juang et al. 2013a):

$$\Pr[(p_f - p_T) < 0] = \Pr[(\beta_T - \beta) > 0] = \Phi(\beta_\beta) > P_0 \quad (1)$$

where p_f is the computed failure probability, which is a random variable affected by uncertainty in statistical characterization of noise factors; p_T is the target failure probability; $\Pr[(p_f - p_T) < 0]$ is the confidence probability that the requirement of target failure probability is satisfied; and P_0 is an acceptable level of the confidence probability specified by the designer. Thus, the feasibility robustness index β_β can be used as a measure for feasibility robustness, which corresponds to different confidence probability P_0 that the actual failure probability meets the requirement of target failure probability under the uncertainty in statistical characterization of noise factors.

The feasibility robustness index β_β for each of 80 designs on the Pareto Front of Figure 4 can be computed, the results of which are shown in Figure 5. As expected, a design with higher feasibility robustness (higher β_β) costs more. By selecting a desired target feasibility robustness level, the least-cost design among all on the Pareto Front can

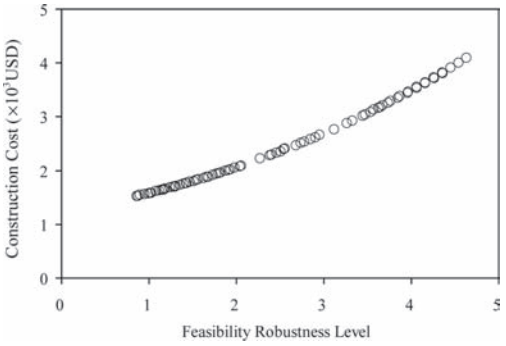

Figure 5. Cost versus feasibility robustness for design of spread foundation.

readily be identified. For example, when the feasibility robustness level is set at $\beta_\beta = 1$, which corresponds to a confidence probability of 84.13%, the least-cost design is $B = 2.2$ m and $L = 2.5$ m. The cost for this design is 1583.9 USD. When the feasibility robustness level is set at $\beta_\beta = 2$, the least-cost design is $B = 2.5$ m and $L = 3.0$ m, which corresponds to a confidence probability of 97.72%. The cost for this design is 2077.1 USD. The feasibility robustness Pareto Front offers an easy-to-use measure for a more informed decision-making considering cost and robustness after satisfying the safety requirement.

4 RGD APPLICATION III: DESIGN OF ROCK SLOPE

The example presented in this section is a summary of the prior work by the authors (Wang et al. 2013), and the reader is referred to this manuscript for additional details.

4.1 *Illustrative example*

The design of rock slope is used to further demonstrate the proposed RGD methodology. The case history of Sau Mau Ping rock slope in Hong Kong is used to illustrate the RGD of the rock slope. The rock mass of the Sau Mau Ping slope is un-weathered granite with sheet joints. The sheet joints are formed by the exfoliation processes during cooling of granite. Initial study by Hoek (2006) led to a simplification of Sau Mau Ping slope as a slope composed by a single unstable block with a water-filled tension crack, which involves only a single failure mode. Following Hoek (2006), the slope before remediation has a height H of 60 m and a slope angle θ of 50°. The potential failure plane is inclined at 35°. The unit weight of rock is assumed as 2.6 ton/m^3. For shear strength properties of rock discontinuity (along the failure plane), mean cohesion c is 10 ton/m^2 and mean friction angle ϕ is 35°.

A deterministic model with single failure mode developed by Hoek & Bray (1981) is employed herein for case study of Sau Mau Ping slope in Hong Kong. The model is a two dimensional limit equilibrium analytical model for plane failure, in which the rock slope is assumed with a 1-meter thick slice through slope. The factor of safety is expressed as follows (Hoek & Bray 1981; Hoek 2006):

$$F_S = \frac{cA + [W(\cos\psi - \alpha\sin\psi) - U - V\sin\psi]\tan\phi}{W(\sin\psi + \alpha\cos\psi) + V\cos\psi} \quad (2)$$

where F_S denotes the factor of safety for rock slope; c is the cohesion of the rock discontinuity (or joint surface) (ton/m^2); A is the base area of the wedge (m); W is the weight of rock wedge resting on the failure surface (°); ψ is angle of failure surface measured from horizontal level (°); α is ratio of horizontal earthquake acceleration to gravitational acceleration; U is the uplift force due to water pressure on the slip surface (ton); V is horizontal force due to water in tension crack (ton); ϕ is the friction angle of the rock discontinuity (°). Additional details for computing the factor of safety F_S can be found in Hoek (2006). The slope failure is said to occur if the factor of safety computed from a deterministic model (such as Eq. 2) is less than 1.

In this example, the slope height H and the slope angle θ are considered as design parameters for the rock slope, typical ranges for which should be specified based on the design situation in hand.

4.2 *Uncertainty modeling*

In a routine practice of rock slope design, only a small sample of data will be available for determining shear properties of the rock discontinuities. The mean value of these rock properties can usually be adequately estimated even with a small size of data. However in often cases, the Coefficients of Variation (COV) of uncertain rock properties and the coefficients of correlation (ρ) among these properties can only be estimated with engineering judgment, guided by published literature (for example, see Hoek 2006 and Lee et al. 2012). Hence, these estimates are subjected to error.

In the rock slope design discussed herein, cohesion and friction angle of rock discontinuity are treated as noise factors. Both parameters are assumed to follow normal distribution as per Hoek (2006). The COVs of c and ϕ, denoted as $COV[c]$

and $COV[\phi]$, as well as the correlation coefficient (ρ) of c and ϕ, denoted as $\rho_{c,\phi}$, are treated herein as random variables. In addition, the horizontal distance to tension crack b is assumed to follow normal distribution with a mean of 15.3 m and a COV of 21%.

According to Low (2007), the ratio of the depth of water in the tension crack (z_w) over the depth of tension crack (z), denoted as i_w, is assumed as an exponential distribution with a mean of 0.5, truncated to [0, 1]. Besides, the ratio of the horizontal earthquake acceleration over the gravitational acceleration, denoted as α, is assumed as an exponential distribution with a mean of 0.08, truncated to [0, 0.16]. As noted by Low (2007), b is likely to have a positive correlation with i_w. Thus, in addition to the variation in rock properties, the correlation of b and i_w, denoted as $\rho_{b,iw}$, is also considered as a random variable.

Based on the typical ranges for the above uncertain statistical parameters reported in literature (e.g., Low 2007; Lee et al. 2012), $COV[c]$ is assumed to have a mean of 0.20 and a COV of 17%; $COV[\phi]$ is assumed to have a mean of 0.14 and a COV of 12%; $\rho_{c,\phi}$ is assumed to have a mean of –0.50 and a COV of 25%; $\rho_{b,iw}$ is assumed to have a mean of 0.50 and a COV of 25%.

4.3 *RGD of rock slope*

As noted previously, the slope height H and the slope angle θ are treated as design parameters and the design space should first be specified for rock slope design. The slope height H may typically range from of 50 m to 60 m, and slope angle θ may typically range from 44° to 50°. For convenience in construction, slope height H may be rounded to nearest 0.2 m and slope angle θ may be rounded to nearest 0.2°. Thus, H can take 51 discrete values in its typical range, while and θ can take 31 discrete values. Thus, 1581 designs (pairs of H and θ) are possible, which define the entire design space.

For the safety consideration, the rock slope is designed to meet a target reliability index β_T of 2.5 (Low 2008), which corresponds to a target failure probability p_T of 0.0062. A simple cost estimation method is used in this paper for illustration of the RGD of rock slope. The cost of a given rock slope design is simplified as the volume of rock mass that needs to be excavated (Duzgun et al. 1995). It should be noted that cost estimation for the rock slope design is not the focus of this paper, and the proposed RGD method is not dependent on any particular cost estimation method. In fact, any reasonable cost estimation method can be adopted.

Following the RGD procedure outlined in Figure 1, the mean and standard deviation of the failure probability, denoted as μ_p and σ_p, can be computed for all possible designs in the design space using PEM integrated with FORM procedure. Then, a multi-objective optimization approach can be adopted for identifying the designs optimal to both objectives, robustness (minimizing the standard deviation of the failure probability) and cost (minimizing the construction cost), while subjected to the safety constraint that μ_p is less than the target failure probability. The scheme of this optimization is set up as shown in Figure 6.

The multi-objective optimization is performed here with the NSGA-II algorithm, in which the designs optimal to both objectives (cost and robustness) are searched iteratively in the discrete design space. With the NSGA-II algorithm, 89 "unique" designs are selected into the final Pareto Front as shown in Figure 7.

In Figure 7, an apparent trade-off relationship between cost and robustness is evident. In this case, greater design robustness can only be attained at the expense of a higher cost. The trade-off relationship in Figure 7 can be used as a design guide for choosing the preferred design when a desired

Find: $\mathbf{d} = [H, \theta]$

Subject to: $H \in \{50\text{m}, 50.2\text{m}, 50.4\text{m}, \ldots, 60\text{m}\}$

$\theta \in \{44°, 44.2°, 44.6°, \ldots, 50°\}$

$\mu_p < p_T = 0.0062$

Objectives: Minimizing the std. dev. of failure probability

Minimizing the cost for rock slope

Figure 6. Formulation of multi-objective optimization for design of rock slope.

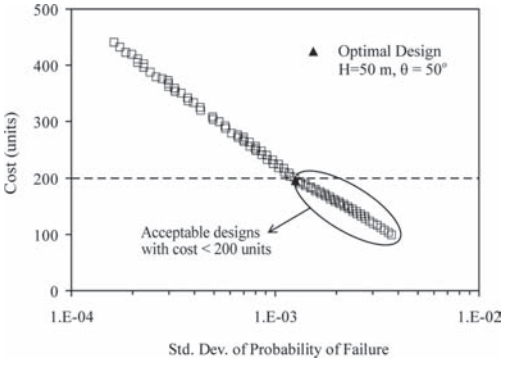

Figure 7. Pareto Front at convergence for design of rock slope.

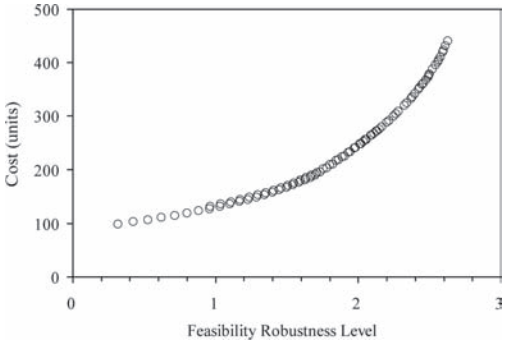

Figure 8. Cost versus robustness for design of rock slope.

cost level or a robustness level is specified. For example, when the maximum acceptable cost for the designer is 200 units [note: 1 unit = unit cost ($) of excavated volume of rock mass in m^3/m], then the design with the least σ_p while in the acceptable cost range will be the best design. In this scenario, it is a design with $H = 50$ m and $\theta = 50°$.

Furthermore, for each of the 89 designs on Pareto Front, the feasibility robustness index β_β can be determined. The β_β value for each of the 89 designs in the Pareto Front is plotted against the corresponding cost as shown in Figure 8. As expected, a design with higher feasibility robustness has a higher cost. When a desired feasibility robustness level (in terms of β_β) is selected, the least-cost design among those on the Pareto Front can readily be identified. The feasibility robustness can be used as a valuable design aid for decision making. For example, when the target feasibility robustness level is set at $\beta_\beta = 1$, which corresponds to a confidence probability of 84.13%, the least-cost design is $H = 52.8$ m, $\theta = 50°$ with a cost of 132.0 units. Similarly, when the target feasibility robustness level is set at $\beta_\beta = 2$, which corresponds to a confidence probability of 97.72%, the least-cost design is $H = 50.4$ m and $\theta = 48.4°$ with a cost of 247.6 units. The feasibility robustness provides an easy-to-use quantitative measure for more informed decision making from designs on the Pareto Front.

It should be noted that in this paper, the robustness within the proposed RGD framework is measured by the variation of the system response (in terms of standard deviation of failure probability). Of course, this is not the only measure for design robustness; alternative measures for robustness have been reported in the fields of structural and industry engineering. For example, measures such as signal-to-noise ratio (Phadke 1989), vulnerability function (Brik et al. 2007), and reliability sensitivity (Zhang et al. 2005) have been reported. Finally, the RGD methodology presented in this paper is equally applicable to other geotechnical design problems such as drilled shafts and braced excavations, and the reader is referred to Juang et al. (2013a&b) for additional details.

5 CONCLUDING REMARKS

In this paper, a new design methodology, called Robust Geotechnical Design (RGD), is presented and illustrated with applications in several geotechnical problems including design of spread foundations and rock slopes. In a geotechnical reliability-based design, the statistics of the noise factors, including the Coefficient of Variation (COVs) of the noise factors (mainly referring to uncertain geotechnical properties herein) and the coefficients of correlation between noise factors, are often difficult to ascertain. When these statistics are overestimated or underestimated, the design obtained from the traditional reliability based design can be cost-inefficient or unsafe. The proposed RGD approach aims at reducing the effect of uncertainties associated with the estimated statistics of noise factors by carefully adjusting the design parameters. Within the RGD framework, a multi-objective optimization is performed to identify designs optimal in both cost and robustness, while satisfying the safety requirements. Through this optimization, a Pareto Front is derived, which typically describes a trade-off relationship between cost and robustness at a given safety level. This trade-off relationship offers a design aid that can assist in selecting the most suitable design. The effectiveness and significance of the proposed RGD framework is demonstrated through two design examples presented in this paper.

ACKNOWLEDGMENTS

The study on which this paper is based has been supported in part by National Science Foundation through Grant CMMI-1200117 and the Glenn Department of Civil Engineering, Clemson University. The results and opinions expressed in this paper do not necessarily reflect the view and policies of the National Science Foundation.

REFERENCES

Akbas, S.O. 2007. Deterministic and probabilistic assessment of settlements of shallow foundations in cohesionless soils. *Ph.D. thesis*, Cornell Univ., Ithaca, New York.

Ang, A.H.-S. & Tang, W.H. 1984. *Probability concepts in engineering planning and design: decision, risk, and reliability.* Vol. 2. New York: Wiley.

Brik, B.A., Ghanmi, S., Bouhaddi, N. & Cogan, S. 2007. Robust design in structural mechanics. *International Journal for Computational Methods in Engineering Science and Mechanics* 8 (1): 39–49.

Casagrande A. 1965. The role of the "calculated risk" in earthwork and foundation engineering. *Journal of the Soil Mechanics and Foundations Division* 91 (4):1–40.

Chalermyanont, T. & Benson, C. 2004. Reliability-based design for internal stability of mechanically stabilized earth walls. *Journal of Geotechnical and Geoenvironmental Engineering* 130 (2): 163–173.

Chen, W., Allen, J.K., Mistree, F. & Tsui, K.L. 1996. A procedure for robust design: minimizing variations caused by noise factors and control factors. *Journal of Mechanical Design* 118 (4): 478–485.

Chen, W., Wiecek, M.M. & Zhang, J. 1999. Quality utility: a compromise programming approach to robust design. *Journal of Mechanical Design* 121 (2): 179–187.

Christian, J.T., Ladd, C.C. & Baecher, G.B. 1994. Reliability applied to slope stability analysis. *Journal of Geotechnical Engineering* 120 (12): 2180–2207.

Deb, K., Pratap, A., Agarwal, S. & Meyarivan, T. 2002. A fast and elitist multi-objective genetic algorithm: NSGA-II. *IEEE Transactions on Evolutionary Computation* 6 (2): 182–197.

Doltsinis, I., Kang, Z. & Cheng, G. (2005). Robust design on non-linear structures using optimization methods. *Computer Methods in Applied Mechanics and Engineering* 194: 1779–1795.

Duncan, M.J. 2000. Factors of safety and reliability in geotechnical engineering. *Journal of Geotechnical and Geoenvironmental Engineering* 126 (4): 307–316.

Duzgun, H.S.B., Pasamehmetoglu, A.G. & Yucemen, M.S. 1995. Plane failure analysis of rock slopes: a reliability approach. *International Journal of Surface Mining, Reclamation and Environment* 9 (1): 1–6.

Fenton, G.A. & Griffiths, D.V. 2008. *Risk assessment in geotechnical engineering*. New York: Wiley.

Ghosh, A. & Dehuri, S. 2004. Evolutionary algorithms for multi-criterion optimization: a survey. *International Journal of Computing and Information Sciences* 2 (1): 38–57.

Harr, M.E. 1987. *Probability-based design in civil engineering*. New York: McGraw-Hill Book Company.

Hasofer, A.M., & Lind, N.C. 1974. Exact and invariant second-moment code format. *Journal of the Engineering Mechanics Division* 100 (1): 111–121.

Hoek, E. (2006). *Practical rock engineering. Chapter 7: A slope stability problem in Hong Kong; and Chapter 8: Factor or safety and probability of failure.* In: http:// www.rocscience.com/hoek/PracticalRockEngineering.asp.

Hoek, E. & Bray, J. 1981. *Rock slope engineering. 3rd ed.* London: Institution of Mining and Metallurgy.

Juang, C.H. & Wang, L. 2013. Reliability-based robust geotechnical design of spread foundations using multi-objective genetic algorithm. *Computers and Geotechnics* 48: 96–106.

Juang, C.H., Wang, L., Liu, Z., Ravichandran, N., Huang, H. & Zhang, J. 2013a. Robust Geotechnical Design of drilled shafts in sand—A new design perspective, *Journal of Geotechnical and Geoenviromental Engineering*, doi: http://dx.doi.org/10.1061/(ASCE)GT.1943-5606.0000956.

Juang, C.H., Wang, L., Hsieh, H.S., & Atamturktur, S. 2013b. Robust geotechnical design of braced excavations in clays. *Structural Safety*, doi:http://dx.doi.org/10.1016/j.strusafe.2013.05.003.

Kang, Z. 2005. *Robust design optimization of structures under uncertainties.* Aachen, Germany: Shaker Verlag.

Kumar, A., Nair, P.B., Keane, A.J. & Shahpar, S. 2008. Robust design using bayesian monte carlo. *International Journal for Numerical Methods in Engineering*, 73: 1497–1517.

Lacasse, S. & Nadim, F. 1996. Uncertainties in characterizing soil properties. *In ASCE Uncertainties'96 Conference Proceedings*, C.H. Benson, Ed., Madison, WI, pp. 49–75.

Lagaros, N.D. & Fragiadakis, M. 2007. Robust performance based design optimization of steel moment resisting frames. *Journal of Earthquake Engineering* 11 (5): 752–772.

Lee, K.H. & Park, G.J. 2001. Robust optimization considering tolerances of design variables. *Computers and Structures* 79 (1): 77–86.

Lee, M.C.W., Mikulik, Z., Kelly, D.W., Thomson, R.S. & Degenhardt, R. 2010. Robust design-a concept for imperfection insensitive composite structures. *Composite Structures* 92 (6): 1469–1477.

Low, B.K. 2007. Reliability analysis of rock slopes involving correlated nonnormals. *International Journal of Rock Mechanics and Mining Sciences* 44 (6): 922–935.

Low, B.K. 2008. Efficient probabilistic algorithm illustrated for a rock slope. *Rock Mechanics and Rock Engineering* 41 (5): 715–734.

Marano, G.C., Sgobba, S., Greco, R. & Mezzina, M. 2008. Robust optimum design of tuned mass dampers devices in random vibrations mitigation. *Journal of Sound and Vibration* 313 (3–5): 472–492.

Meyerhof, G.G. 1953. The bearing capacity of foundations under eccentric and inclined loads. In *Proceedings, Third International Conference on Soil Mechanics and Foundation Engineering*, Zurich, Vol.1, pp. 440–445.

Najjar, S.S. & Gilbert, R.B. 2009. Importance of lower-bound capacities in the design of deep foundations. *Journal of Geotechnical and Geoenvironmental Engineering* 135 (7): 890–900.

Orr, T.L.L. & Farrell, E.R. 1999. *Geotechnical design to Eurocode 7*. Berlin: Springer.

Orr, T.L.L. & Breysse, D. 2008. Eurocode 7 and reliability-based design. In: *Reliability-based design in geotechnical engineering: computations and applications* (ed. Phoon KK), ch. 8, pp. 298–343. London: Taylor & Francis.

Park, G.J., Lee, T.H., Lee, K.H. & Hwang, K.H. 2006. Robust design: an overview. *AIAA Journal* 44 (1): 181–191.

Parkinson, A., Sorensen, C. & Pourhassan, N. 1993. A general approach for robust optimal design. *Journal of Mechanical Design* 115 (1): 74–80.

Phadke, M.S. 1989. *Quality engineering using robust design*. Englewood Cliffs: Prentice Hall.

Phoon K.K. & Kulhawy, F.H. 1999a. Characterization of geotechnical variability. *Canadian Geotechnical Journal* 36 (4): 612–624.

Phoon, K.K. & Kulhawy, F.H. 1999b. Evaluation of geotechnical property variability. *Canadian Geotechnical Journal* 36 (4): 625–639.

Phoon, K.K., Kulhawy, F.H. & Grigoriu, M.D. 2003. Development of a reliability-based design framework for transmission line structure foundations. *Journal of Geotechnical and Geoenvironmental Engineering* 129 (9): 798–806.

Taguchi, G. 1986. *Introduction to quality engineering: designing quality into products and processes.* New York: Quality Resources.

Tang, W.H. & Gilbert, R.B. 1993. Case study of offshore pile system reliability. *Proc., 25th Offshore Technology Conference*, Society of Petroleum Engineers, Houston, Texas, pp. 677–686.

Wang, L., Hwang, J.H., Juang, C.H. & Atamturktur, S. 2013. Reliability-based design of rock slopes—a new perspective on design robustness. *Engineering Geology* 154: 56–63.

Wang, Y. & Kulhawy, F.H. 2008. Economic design optimization of foundations. *Journal of Geotechnical and Geoenvironmental Engineering* 134 (8): 1097–1105.

Wang, Y. 2011. Reliability-based design of spread foundations by Monte Carlo Simulations. *Géotechnique* 61 (8): 677–685.

Wang, Y., Au, S.K. & Kulhawy, F.H. 2011. Expanded reliability-based design approach for drilled shafts. *Journal of Geotechnical and Geoenvironmental Engineering* 137 (2): 140–149.

Whitman, R.V. 2000. Organizing and evaluating uncertainty in geotechnical engineering. *Journal of Geotechnical and Geoenvironmental Engineering* 126 (7): 583–593.

Wu, T.H., Tang, W.H., Sangrey, D.A. & Baecher, G.B. 1989. Reliability of offshore foundations—State-of-the-art. *Journal of Geotechnical Engineering* 115 (2): 157–178.

Zhang, J., Zhang, L.M. & Tang, W.H. 2011. Reliability-based optimization of geotechnical systems. *Journal of Geotechnical and Geoenvironmental Engineering* 137 (12): 1211–1221.

Zhang, Y., He, X., Liu, Q. & Wen, B. 2005. Robust reliability design of Banjo flange with arbitrary distribution parameters. *Journal of Pressure Vessel Technology* 127 (4): 408–413.

Zhao, Y.G. & Ono, T. 2000. New point estimates for probability moments. *Journal of Engineering Mechanics* 126 (4): 433–436.

Geotechnical Safety and Risk IV – Zhang et al. (eds)
 ISBN 978-1-138-00163-3

Integrated geo risk management: Crossing boundaries

M.Th. van Staveren
VSRM Research and Development, Breda, The Netherlands

ABSTRACT: Any engineering and construction project involves dealing with risk, which has often a geotechnical origin. Therefore, the objective of applying Geotechnical Risk Management (GeoRM) is contributing to the engineering, construction, and maintenance of successful projects, despite the inherently uncertain character of its ground conditions. However, for realizing these projects in an effective and cost-efficient way, GeoRM has to be well-integrated within Project Risk Management (ProjectRM). As ISSMGE TC304 Task Force 3 revealed, a complete GeoRM application that is integrated with ProjectRM, seems not yet common practice in a lot of project phases, in a lot of projects, in a lot of countries. This requires crossing often hidden boundaries between risk concepts, disciplines, project phases, scopes, project types and even boundaries between industries and countries. Finally and perhaps first of all, we have to cross our own mental boundaries. Within this paper these boundaries are highlighted and crossed, for catching benefits of learning, effectiveness, and cost-efficiency. The promise of well-integrated GeoRM in ProjectRM, by crossing the mentioned boundaries, is substantially contributing to successful construction projects from a geotechnical engineering and construction perspective, with fewer cost overruns, less delays, less non-conformances of safety and quality, and therefore happier project participants and stakeholders.

1 INTRODUCTION

1.1 *Risk is pervasive*

Beck (1992) classifies our modern societies as *risk societies*. As mentioned by van Staveren and Halman (2013), over the last 25 years several risk research topics were awarded with Nobel Prices, including Markowitz and Sharpe in 1990 for their project portfolio theory, Nash in 1994 for his game theory, Kahneman and Tversky in 2002 for their prospect theory, and rather recently Sargent and Sims in 2011 for their cause and effect theory.

Especially civil engineering and construction projects are inherently risky, due to numerous uncertainties of many types. Examples are political uncertainties, financial uncertainties, market uncertainties, stakeholder uncertainties, technical uncertainties and, not to forget, *ground* uncertainties. The resulting challenges, such as ever-increasing operational complexity and serious safety and integrity concerns are widely acknowledged (e.g. Bea 2006, Beal 2007, Blockley & Godfrey 2000, Brandl 2004, Schinzinger & Martin 2000, Sowers 1993).

Each type of construction project, either large or small, involves several phases of feasibility, design, contracting, construction, and finally maintenance. Often, it takes a lot of years before a substantial project is actually realized. Over those years, the project circumstances may change dramatically. Therefore, effectively dealing with risks and underlying uncertainties will make the difference between project success and failure for all parties involved. These include clients, government agencies, engineering firms, main contractors, subcontractors, suppliers, end-users, the public and sometimes social pressure groups.

1.2 *Risk management as solution*

Well-structured and explicitly dealing with risk, including its key element of risk analysis, is by many researchers and practitioners seen as a mean for effectively and cost-efficiently dealing with project uncertainties (e.g. Boothroyd & Emmet 1996, Chapman & Ward 2011, Edwards 1995, Edwards & Bowen 2005, Flanagan and Norman 1993, Godfrey 1996, Smith 2003, Thompson & Perry 1992, and Weatherhead et al. 2005).

In many sectors and organizations several types of risk management are already in use, including enterprise risk management, project risk management, and discipline-based risk management. Examples of this latter type are financial risk management, IT risk management, and also geotechnical risk management. Several research results confirm the anticipated effects and benefits of risk management. One example is provided by

Raz et al. (2002), who discovered a statistically significant correlation between the application of several project risk management practices and success in meeting schedule and budget objectives. Another example gives Cooke-Davies (2002), who derived a correlation between on-time performance and organizational risk management characteristics, such as company-wide risk management education, processes for assigning risk ownership, using a risk register, and keeping an up-to-date risk management plan.

1.3 *Or failure of risk management application?*

Nevertheless, despite these promising research results, this available risk management knowledge apparently does not prevent a lack of effective risk management application. For instance, a longitudinal project management analysis over the years 1998–2003, which has been initiated by the Project Management Institute (PMI), shows that organizations consistently fail to apply risk management across projects (Mullaly, 2006). Researchers and practitioners, such as Hillson (2002), Hillson and Murray-Webster (2007), Olsson (2006), and Power (2009) confirm similar failures of risk management application and its effectiveness.

This application gap may be a root cause of failure in a lot of (construction) projects, which seems to be in line with the assessments of failure costs in the construction industry, typically ten to thirty percent of the total construction costs, as for instance raised by Barber et al. (2000), Egan (1988), and Latham (1994). In conclusion, many managers and engineers in the construction industry would agree that risk management is not always producing the expected results. Or positively stated: there are lots of opportunity for further risk management development and implementation within the construction industry.

1.4 *The geotechnical root cause of project risk*

As mentioned before, many of these adverse effects of risks and uncertainties in civil engineering and construction projects have geotechnical risk drivers with causes in the subsoil. Examples are unforeseen weak, hard, or organic soil layers, variations of groundwater tables, boulders, collapsible soils or sinkholes in calcareous rock. These unforeseen differing ground conditions can have a serious impact on the project. For instance, according to the US National Committee on Tunnelling Technology, poor site investigations result in different site conditions claims averaging 28% of the entire contract price (Smith, 1996). A recent survey including ten countries (van Staveren 2013a) once again confirmed the serious stake of the subsoil and ground conditions in the overall risk profile of civil engineering and construction projects.

A probably well-known example is that of a contractual risk that is caused by the occurrence of differing ground conditions during construction. This may generate an expensive and time consuming contractual dispute, due to an apparent poor site investigation program in the early project phase. These differing ground conditions can have several manifestations. Examples are harder rock than expected during excavation, which requires the mobilization of additional equipment to the site, softer soil layers, which require unforeseen, expensive, and time consuming ground improvement, or much more groundwater inflow during tunnel boring activities that demands for additional grouting measures. All of these situations will create additional costs and delay within the project, with one major question: which party is going to bear these unfavourable effects, by paying the costs? Is it the client, the contractor, the government or perhaps an insurance company?

1.5 *Integrated risk management: A better solution?*

This paper aims to take a new risk management development route, that of integrated risk management. In particular, this paper will focus on the integration of Geotechnical Risk Management (GeoRM) in Project Risk Management (ProjectRM), in all types of civil engineering and construction projects in the international construction industry. Integrated risk management aims to combine and synthesize these different types of risk management, in order to minimize the adverse effects of uncertainties and maximize their potential benefits, for all project participants and stakeholders.

As the Dutch Geo-Impuls program on reducing geotechnical failures teaches, the integration of GeoRM in ProjectRM seems to be promising. In this development program over 40 Dutch organizations, including ministries, city councils, other public clients, contractors, engineering consultants, universities, and research institutes are involved. Within the Geo-Impuls, over 200 professionals and managers work together in 12 Working Groups on the development and implementation of GeoRM within (project) organizations (Cools 2011, van Staveren et al. 2013a).

Also within the International Society of Soil Mechanics and Geotechnical Engineering, Technical Committee 403, Task Force 3 (TC304-TF3), this risk management integration topic has been worked out. Geotechnical representatives of ten countries reported the degree of application and integration of ProjectRM and GeoRM in their countries. The participating countries

are, in alphabetical order, Austria, China, Czech Republic, Finland, Germany, Japan, Netherlands, Sweden, Switzerland and United Kingdom.

The segregation of Geotechnical Risk Management (GeoRM) and Project Risk Management (ProjectRM) within project organizations is likely to obstruct the catchment of all potential risk management benefits, in terms of improved safety and quality, cost and time savings and strengthening of reputations. In addition, potential synergies of scale and learning of risk management remain unused. This resulted in the following TC304-TF3 research focus:

> *Contributing to the integration of GeoRM in ProjectRM, by evaluating existing international knowledge and lessons.*

By applying this international knowledge and lessons, geotechnical professionals and project managers, contract managers, safety managers, and quality managers worldwide are facilitated by jointly managing serious project risks with geotechnical risk drivers, in a cost-efficient way. In the resulting TC304-TF3 State of the Art Report (van Staveren 2013a), the status of ProjectRM and GeoRM application and integration has been analysed and summarized. These valuable results are included in this paper.

1.6 *Paper set up*

This necessarily rather extensive introduction resulted in the following paper set up. First, the main types of risk and risk management are presented in some more detail and with tight definitions. These definitions are essential for the rather abstract concept of risk and its management, of which each individual has his or her own, often hidden, perceptions.

A shared language between users of project risk management and geotechnical risk management, with similar definitions of uncertainty, risk, hazard, risk analysis and risk management proves to be essential for integrating geotechnical risk management in project risk management. In particular the positioning of (geotechnical) risk analysis within (geotechnical) risk management, as well as its difference with risk management, needs to be clarified.

Next, four distinguished degrees of GeoRM and Project RM application and integration are worked out in more detail. This provides the foundation for the next section on exploring and crossing GeoRM boundaries, for providing effective and cost-efficient risk management. These boundaries, which seem to be often quite hidden, are between risk concepts, disciplines, project phases, scopes, project types and even boundaries between industries and countries. But perhaps we have to cross first another one: our own mental boundary.

This paper ends with conclusions and recommendations for further and deeper integrating GeoRM and ProjectRM. This aims to support civil engineering and construction projects, in each project phase, for serving all project participants and stakeholders.

2 RISK: WHAT ARE WE TALKING ABOUT?

2.1 *Introduction*

Due to their rather abstract character, the terms risk and risk management have a lot of meanings and definitions. For instance, the words uncertainty and risk are often intermingled (Van Asselt & Vos 2006, van Staveren 2009b), as are the words risk and hazard (Waring & Glendon 1998).

Also the ten countries participating in the TC304-TF3 research reveal that there is not yet uniform and widely accepted risk terminology (van Staveren 2013a). Regarding definitions for project risk management (ProjectRM), in the majority of seven out of the ten countries (70%), no specific and widely accepted ProjectRM definitions are in use. In the remaining three countries ProjectRM definitions are slightly different, with also different origins. China reports their own ProjectRM definition, Netherlands refers to the RISMAN definition (van Well-Stam 2004), and Sweden uses the definition of ISO 73:2009 (ISO 2009b).

Within the TC304-TF3 research, the same situation has been observed for definitions of Geotechnical Risk Management (GeoRM). In the majority of eight out of the ten participating countries (80%) no specific and unified GeoRM definitions are in use. In Sweden GeoRM is not specifically defined, because it is considered an overall part of risk management. The remaining two countries, China and Netherlands, do have their slightly different GeoRM definitions.

Therefore, a starting point for effective risk management in general, and for effective ProjectRM and GeoRM in particular, is to provide clarity about the core definitions. When aiming to integrate GeoRM in more generic ProjectRM, which is the purpose of this paper, the specific geotechnical parts of the common risk terminology should be clarified as well. For this reason, pragmatic definitions five sets of risk-related terminology are presented. Generic risk terms are presented together with their geotechnical counterparts, in order to

create a common, uniform, and shared risk management language:

1. Project uncertainty & geotechnical uncertainty
2. Project risk & geotechnical risk
3. Hazard & geotechnical hazard
4. Risk analysis & geotechnical risk analysis
5. Risk management, ProjectRM & GeoRM.

This should minimize the usual confusion when talking about and dealing with risk and is management. The following definitions follow as much as possible the KISS approach: Keep It Simple, Stupid. The presented definitions are selected from the abundant definitions, as found in the literature, and proved their value in the practice of geotechnical engineering and construction in The Netherlands (van Staveren 2013b).

2.2 *Uncertainty*

According to the pragmatic approach of Ward and Chapman (2011), *uncertainty* is simple a *lack of certainty*. Within construction projects there is a lack of certainty in many ways, such as funding uncertainty in the feasibility phase of a project, price uncertainty of construction materials during construction, and uncertainty about the required degree of maintenance in after realization of for instance a tunnel or bridge.

2.3 *Geotechnical uncertainty*

Building forward on the pragmatic uncertainty definition by Ward and Chapman (2011), *geotechnical uncertainty* is simple a *lack of geotechnical certainty*. It may be helpful for geotechnical engineering purposes to distinguish between four types of uncertainty: (1) randomness, (2) fuzziness, (3) incompleteness and (4) incorrectness (Blockley & Godfrey 2000, van Staveren 2006).

2.4 *Risk*

Amongst the many definitions of *risk*, the one by the ISO 31000 Risk Management Guideline (ISO 2009a) proves to be useful in practice: risk is the *effect of uncertainty on realizing objectives*. Within this definition, the effect of uncertainty can be negative, which is the traditional meaning of risk. However, its neutral approach allows also a positive meaning, being the positive effect of uncertainty or in other words an opportunity. By this ISO definition, fruitless debates about differences and similarities between uncertainty and risk, initiated already by Knight (1921) and for instance critically judged by Hubbard (2009), can be omitted.

2.5 *Geotechnical risk*

By using the mentioned ISO 31000 risk definition, *geotechnical risk* can be simply defined as the *effect of geotechnical uncertainty on realizing objectives*, such as settlements or horizontal deformations within pre-set limits. A geotechnical risk has a probability of occurrence and one or more geotechnical causes. Moreover, and very important for non-geotechnical professionals and managers, if occurring, geotechnical risks have usually a number of unfavourable effects. These stretch far beyond geotechnical engineering into the arena of project management, such as physical damage to properties, injured persons or even dead victims, cost overruns and delay. By also including the positive side of risk, geotechnical uncertainty may also cause favourable effects. Examples are the presence of less settlement sensitive ground layers than expected below a road foundation under construction, or a lower ground water inflow than foreseen in the design phase at the executing a deep excavation. These in fact positive risks or opportunities may result for instance in cost savings for the contractor, and, depending on the type of contract, also for the client. Obviously, these benefits can only be materialized if the project is flexible enough to absorb these opportunities in the construction phase.

2.6 *Hazard*

When considering the provided definitions on uncertainty, risk and geotechnical risk, what could be the added value of a definition for the widely used term *hazard*? Remarkably, while the word hazard is deep-lee embedded in our daily language, it seems not explacidly defined in a lot of standard literature on risk and its management, including Bernstein (1996), Ewards & Bowen (2005), Chapman and Ward (2011), and Hillson (2010). Amongst the many available definitions, hazards can be defined as threats to people and the things they value (Van Staveren 2006). Therefore, hazards and risks seem closely coupled terms with a more or less similar meaning. This seems consistent with the definition in the on-line version of the Oxford Dictionary, which defines hazard as danger or risk. Therefore, for the sake of clarity, *hazard* is here defined simply as *risk*.

2.7 *Geotechnical hazard*

Given the above discussion about a workable definition of a hazard, the most pragmatic definition of a *geotechnical hazard* seems to be that of a *geotechnical risk*, as previously defined.

2.8 *Risk analysis*

Risk analysis is another term that is widely used in our day to day communication. Not seldom however, risk analysis and risk management are intermingled (van Staveren 2013b). ISO31000 (ISO 2009) defines risk analysis as a *process in order to understand the characteristics of a risk to determine the risk level*. The latter risk level, or risk profile, is the assessment of the probability of a risk, together with its expected consequences. Ideally, these risk consequences, or risk effects, are for construction projects expressed in key performance indicators, such as cost, time, quality, safety and reputation.

Any risk analysis should include at least risk identification and risk classification. Risk classification, often also called *risk assessment*, can be subdivided in a qualitative and a quantitative approach. The latter one is usually preferred by engineers, because it allows them to *calculate* probabilities and effects.

However, not seldom there are not sufficient reliable data available to allow calculations with a statistical acceptable accuracy. In these cases necessarily qualitative assessments have to be made, for instance based on expert judgment. Obviously, these qualitative assessments can be transformed into numbers by using expert judgment, for calculation purposes. However, sensitivity analyses are of utmost importance in these cases, to catch an understanding of the effects of the uncertain input data on calculated results.

Finally, it is of utmost importance to understand that risk analysis and risk assessment are an essential part of, yet not similar to, risk management.

2.9 *Geotechnical risk analysis*

By building on the foregoing definition, *a geotechnical risk analysis* can be defined as the *process in order to understand the characteristics of geotechnical risk to determine the project risk level*. As mentioned before, geotechnical risks, such as excessive settlements or even collapse of ground embankments or bored tunnels can have very severe effects on the project manager's key performance indicators costs, time, safety, quality, as well as reputation of all parties involved in the project. For this reason, the outcomes of geotechnical risk analyses should be compared with those of the usually more generic project risk management analyses. This is already one main reason for integrating GeoRM within ProjectRM, however without losing the specific degree of detail of geotechnical risk analyses.

2.10 *Risk Management (RM)*

Worldwide, there are many *Risk Management* (RM) definitions and related frameworks available.

Apart from the ISO 31000 Risk Management, well-known generic frameworks are for instance the COSO Enterprise Risk Management and the frame-work of the Institute of Risk Management (IRM). Nevertheless, most frameworks are more or less similar, with often somewhat different terminology. The ISO31000 (ISO 2009a) defines risk management simply as the *coordinated activities to direct and control an organization with regard to its risks*. This straightforward risk management definition will be used in this paper.

2.11 *Project Risk Management (ProjectRM)*

Well-known frameworks for *project risk management* are for instance those from the Project Management Institute (PMI) and the International Project Management Association (IPMA). In the Netherlands the RISMAN method is widely used in construction projects (van Well-Stam et al. 2004). Within this method, in each project phase the following subsequent steps need to be performed at least once:

1. Setting project objectives: what information?
2. Identifying risks: what risks?
3. Classifying risks: how serious?
4. Remediation risks: what actions?
5. Evaluating risks: effective remediation?
6. Reporting risks: to the next project phase!

Most risk management literature provides risk management processes with distinct risk management steps that are more or less equal to these six steps while the names of the steps may be slightly different (van Staveren 2013b). Therefore, are there any relevant differences between risk management and project risk management? This question was raised during a project risk management lecture that the author of this paper provided.

A literature scan learned that the majority of the literature considers project risk management implicitly as being risk management for projects (Chapman and Ward 2011, Edwards & Bowen 2005, van Well-Stam et al. 2004, Hopkinson 2011). Some literature does explicitly distinguish project risk management, from risk management, such as Hopkin (2012).

However, some specific points of attention for project risk management surfaced, because projects are one-off and always new to some extent. Also, projects have a start and an end with several project phases, while the decisions in earlier phases have an irreversible effect on the later phases. Moreover, many projects have a variety of stakeholders, often with different and even conflicting interests.

Finally, projects need to be realized within the pre-set limitations of budget and time, with usually specified criteria for safety and quality. All these

project characteristics give a specific flavour to risk management within projects, when compared to enterprise-wide risk management in organizations.

Nevertheless, the correct answer remains to be no, there are no significant methodological differences identified between risk management and project risk management. Therefore, the ISO31000 (ISO 2009a) definition will be used as well for defining for project risk management: *the coordinated activities to direct and control a project organization with regard to its project risks*.

2.12 *Geotechnical Risk Management (GeoRM)*

Finally we arrive at *geotechnical risk management*. First, what is it not? GeoRM is not about guaranteeing with 100% certainty that all geotechnical risks are eliminated. Nor is it about predicting the future. Its theory is also not difficult, and the GeoRM application is not necessarily expensive, when executed properly in accordance with the geotechnical risk profile and geotechnical risk acceptance within a project. Furthermore, while it may certainly be valuable in particular complicated construction projects, probabilistic calculations or finite element geotechnical modelling is by far *not automatically always* required for adequate geotechnical risk management (Van Staveren 2013b).

So what is geotechnical risk management? Similar to all the previously presented terminology, the literature presents many definitions, and different people often have a different view on it. For the sake of simplicity, geotechnical risk management is defined here as *explicitly communicating about continuously dealing with geotechnical risk, in a structured manner*.

Explicitly means completely describing all of the aspects of geotechnical risks and underlying uncertainties. *Communicating* means that geotechnical risks are discussed with and reported to the persons and parties involved, in order to share different perceptions of the causes, probabilities, and effects of risks. *Dealing* indicates that risk management is not only about reducing or eliminating risk. Also, opportunities may emerge from uncertainty. Basically, it is about making choices regarding the best way to handle a geotechnical uncertainty in view of the project objective. This can also mean simply accepting a risk. *Continuously* means that risk management steps are cyclic and therefore repeated after a predefined time of project phase. This is necessary because of the inherently dynamic character of risks. Due to the fact that circumstances and perceptions change, risks will change over time as well. Finally, *structured* indicates the importance of using of a defined process of discrete steps, which are presented in the next section.

In summary, geotechnical risk management, GeoRM, is an explicitly structured and well-communicated way of dealing with geotechnical risk that is executed in all construction project phases, in order to achieve project objectives effectively and cost-efficiently. Herewith, GeoRM is in fact a new name for the GeoQ process for geotechnical risk management (van Staveren 2006).

The process of geotechnical risk management is similar to the process of project risk management or even enterprise-wide risk management. It involves the same sequence of risk management steps as presented for ProjectRM. Therefore, GeoRM fits perfectly well in any sort of ProjectRM. The only main difference is that GeoRM is a more detailed and in-depth geotechnical approach of project risk management, for giving geotechnical risk the attention it requires in all phases of engineering and construction projects (van Staveren 2013b).

3 INTEGRATING GeoRM & ProjectRM

3.1 *Introduction*

While considering integrated GeoRM, what is *integration* anyway? According to conventional dictionaries and several definitions on the Internet, the verb integration can be defined as forming, coordinating, or blending elements into a functioning or unified whole. Related meanings are uniting with something else and *incorporating into a larger unit*. This latter definition seems appropriate for integrating GeoRM within ProjectRM.

As raised earlier, lot of serious *project* risks have their origin in ground or groundwater conditions and can be adequately controlled by sound *geotechnical* risk management. However, in the day-to-day practice of construction projects the two complementary types of risk management, GeoRM and ProjectRM, are either (1) *not* applied at all, (2) quite *separately* applied, (3) somewhat *blurred* into each other, or (4) fully *integrated*. In the next sections these four options are worked out in some more detail, supported by the results of the TC304-TF3 research.

3.2 *No GeoRM & ProjectRM applied*

In the introduction has been discussed that while risk management is promising in supporting the completion of successful civil engineering and construction projects, this promise is by far not always realized. Substantial failure costs in the construction industry demonstrate this situation. One of the causes may be that risk management, either ProjectRM or GeoRM, is *not applied at all* in the subsequent phases of construction projects.

A real-life project that seems to demonstrate no application of GeoRM and ProjectRM is the Heathrow Express Line in London. In October 1994, three tunnels of this project collapsed over a period of three days. There were surprisingly no injuries. Nevertheless, the tunnel collapses gave widespread disruption at Heathrow airport. Moreover, it seriously delayed the project, as well as the Jubilee extension project, on which the same New Austrian Tunnelling Method (NATM) was used. According to Clayton (2008), investigation of the collapses revealed a lack of risk awareness within the project.

The British newspaper The Guardian published an article with the title "Managers 'overlooked risk' in airport tunnel collapse" (Harper 2000). According to this article, a report by the health and safety executive concluded that warning signs had not been recognised. The problem would not have occurred if safety had been put before results. According to the executive's chief inspector of construction: "The collapses could have been prevented but for a cultural mindset which focused attention on the apparent economies and the need for production rather than the particular risks." The direct cause of the collapses was a chain of events, which started with substandard construction, inadequate repairs, and the construction of another tunnel in failing ground. The collapses have therefore been classified as an organisational incident. Regarding the impact on the project parties, the principal contractor was fined £1,2 million after pleading guilty to offences under the Health and Safety Act. Austrian advisers got a fine of £0.5 million (Harper 2000). The costs of recovery were £150 million, with a project delay of 6 months (Clayton 2008).

In the TC304-TF3 research Austria, Czech Republic, Germany, Switzerland and United Kingdom reported explicitly that no standardized ProjectRM is applied in all construction projects. Similar findings were reported about GeoRM. The following examples illustrate this situation.

Austria, Germany, Switzerland report that theoretically GeoRM should be applied in every construction project. Norm DIN4020 (DIN, 2010) describes the requirements on sharing the geotechnical risk in construction projects. The risk of unexpected geotechnical aspects is born by the owner (Sondermann and Trunk 2008). In practice however, GeoRM has not been applied in all projects. The share of projects where it is used is increasing and GeoRM application is mostly promoted by the construction companies.

In the Czech Republic GeoRM is in general a new approach. For example, the Czech State Mining Authority has accepted the concept of risk just recently. Before that, admitting any risk or hazard would mean stopping of the works, which motivated all involved parties including construction companies to hiding potential problems. Also in the Netherlands applying GeoRM in projects is relatively new.

In Japan it becomes a common view that it is important to study geotechnical risks during the construction stage of projects, especially those risks that could lead to some serious troubles or accidents.

In the United Kingdom GeoRM is not applied to all projects. It is a generalization, but the evidence suggests that the smaller the financial value of a project the less likely that GeoRM will be applied. Also the Geo-Impuls participants in the Netherlands notice this point regularly. At the smaller projects, or in the smaller work packages of larger projects, often executed by subcontractors like piling firms or dewatering firms, the application of ProjectRM and GeoRM seems quite underdeveloped.

The situation of no application, and therefore also no integration, of ProjectRM and GeoRM is symbolized in Figure 1 by the empty and separated circles, with GeoRM and ProjectRM put in between brackets.

3.3 *Separated GeoRM and ProjectRM application*

The second option of GeoRM and ProjectRM application is that both are applied, however still in a *separated* way. Examples of such a separated application are separated risk files for geotechnical risks and project risks, no communication between the project risk manager and geotechnical engineers, geotechnical risk remediation measures that are not related to quality control, and so on.

A real-life example of separated risk files have been encountered on a 0.5 billion euro tunnel project in a city in the Netherlands. The city government asked a Review Board to execute an independent risk identification and classification, in order to reveal the main risks with an impact on safety and hindrance for the inhabitants of the city.

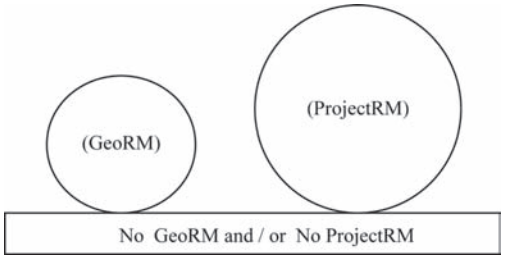

Figure 1. No application of GeoRM and ProjectRM.

In total sixteen top risks were identified by The Review Board, including five with geotechnical or geohydrological causes.

These results were compared with two other risk files of the project, a project management risk file, including the project phases of design, construction, and use of the tunnel, and a risk register focussing on contractual risks. Both of these files did also include geotechnical risks. Two main conclusions could be drawn from this comparison.

First, two out of the three risk files did present each risk as independent ones, without providing inter-relationships. The relationship between for instance geotechnical risks and contractual risks, including remediation measures, was not explicitly made. In other words, GeoRM was separated from ProjectRM.

Second, some 50% of the top risks, identified by the Review Board from a local government perspective, were not found in the two other risks files. The latter two were compiled with merely a project management and contractual focus. This case learns that separated application of risk management, from different perspectives, may lead to incomplete and suboptimal risk management. The good news is that after the review the project organization was able to combine the three risk registers, in order to strengthen its overall risk management.

Figure 2 presents the situation of separated GeoRM and ProjectRM application. Contrary to the previous Figure 1 with the empty circles, in Figure 2 the circles are shaded, but yet separated. This symbolizes separated application of GeoRM and/or ProjectRM.

The TC304-TF3 survey did not reveal many examples of fully separated but applied GeoRM and ProjectRM. The participating countries report either *no* application of GeoRM and ProjectRM, or a somewhat *blurred* version of GeoRM and ProjectRM integration, which is explained in the next section.

3.4 *Blurred GeoRM and ProjectRM integration*

In the third option of the relationship between the two complementary types of risk management,

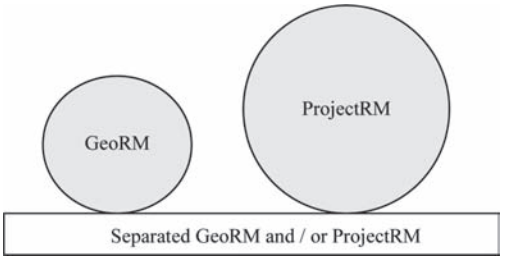

Figure 2. Separated GeoRM and ProjectRM.

GeoRM and ProjectRM, these are somewhat *blurred* towards each other. The definitions of both are not explicit, as well as the scopes and relationships. Examples are vague and incomplete descriptions of geotechnical risks in the project risk register, such as simply stated by words as "settlements" or "poor soil conditions". These poorly described geotechnical risks are not explicitly analysed, classified, and managed. In addition, geotechnical risk remediation measures, such as (additional) risk-driven site investigations, contractual geotechnical risk allocation by the Geotechnical Baseline Report (GBR) (e.g. Essex 1997), or geotechnical monitoring programs are not explicitly related to key performance indicators of project risk management, such as costs, budget, quality and safety.

A real-life example of rather blurred GeoRM and ProjectRM application has been identified during a redevelopment project of existing infrastructure in the Netherlands. In the project risk register some geotechnical risks were identified. However, their risk descriptions incomplete, with fuzzy causes and effects. Also non-geotechnical risks were often poorly described. Furthermore, risk management in this project consisted mainly of rather instrumental risk analyses, which stopped at risk management step 4 of taking risk remediation actions. Also step 5 of risk evaluation was not done in a well-structured way. Therefore, any effectiveness and cost-efficiencies of risk remediation measures, if performed, remained hidden. This obstructed learning from and improving of integrated risk management. Also, a geotechnical risk did occur, leakage of groundwater in a construction pit, yet without serious consequences for the project.

This situation, together with an increase of project complexity and disputes with the contractor, triggered to project manager to pay more attention to improving the risk management on her project. After a period with no or not so experienced risk managers, a well-experienced risk manager was appointed for 2–3 days a week. His task was improving integrated ProjectRM for contributing to project success, by making risk management useful and attractive for the project team members. He was supported by a risk consultant, who provided risk management training and guidance to the project team.

Figure 3 illustrates the blurred GeoRM and ProjectRM integration. Both ways of risk management are touching each other and GeoRM is even partly integrated in ProjectRM. However, the dotted circles of both indicate the vagueness and incomplete execution of GeoRM and ProjectRM.

The TC304-TF3 survey identified that this type of blurred GeoRM and ProjectRM integration seems to be common practice in at least 80% of

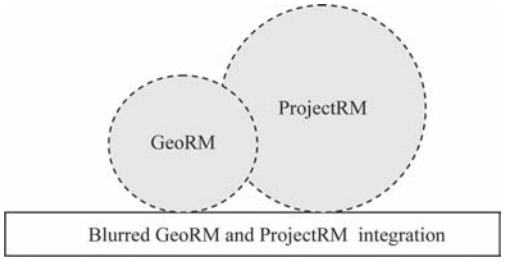

Figure 3. Blurred GeoRM and ProjectRM integration.

the ten participating countries. For instance, in Austria, Germany, and Switzerland, ProjectRM is obliged in the large construction firms, and GeoRM is required normatively as well. Nevertheless, integration of GeoRM and ProjectRM is not perfect and both are yet too much focused on only contractual allocation of risk. In China and the Netherlands, GeoRM fits theoretically well in ProjectRM, however more integration in practice, by more cooperation between ProjectRM and GeoRM professionals, may help to reduce too general and therefore inefficient and ineffective GeoRM approaches.

3.5 *Complete GeoRM and ProjectRM integration*

Finally, there is the fourth option of *complete* GeoRM and ProjectRM integration. In case of complete integration the definitions of ProjectRM and GeoRM are explicit and shared, as well as their respective scopes and relationships.

Examples are explicit and complete descriptions of geotechnical risks in the project risk register. Simply stated geotechnical risks by words as "settlements" or "poor soil conditions" are avoided. Moreover, well-described geotechnical risks are explicitly analysed, classified, and managed. In addition, geotechnical risk remediation measures, such as (additional) risk-driven site investigations, contractual geotechnical risk allocation by the Geotechnical Baseline Report (GBR) (e.g. Essex 1997), by geotechnical monitoring programs are explicitly related to key performance indicators of project risk management, such as costs, budget, quality and safety.

Also, there is close cooperation between geotechnical professionals, contract managers, quality managers, safety managers, planners, cost managers and so on, in order to optimize geotechnical risk management in line with the key performance indicators of the civil engineering or construction project.

A real-life example of complete GeoRM and ProjectRM integration is one of the largest motorway expansion projects ever in The Netherlands. This multi-billion Design, Build, Finance, and Maintenance (DBFM) project, includes 60 km of very busy motorways in one of the most densely populated areas, with soft soil conditions and high groundwater tables. The construction works have to be executed with a minimum of hindrance to the daily motorway users, for avoiding unacceptable mega-traffic jams.

For this and other large infrastructure projects, the client developed project-specific risk management flyers. The target groups for these flyers are technical managers, contract managers, and entire project teams. These flyers summarize the proven benefits of well-integrated GeoRM and ProjectRM for these specific project management roles within the project. An example of these benefits for the technical manager are the execution of additional risk-driven site investigations in the mentioned motorway expansion project in The Netherlands, which proved the feasibility of embankments in a conventional way and saved a lot of money. An example of GeoRM benefits for the contract manager is the application of a geotechnical baseline report in a large bridge project, which settled the occurrence of differing site investigation effectively and efficiently, without delaying the project. The entire project team gained for instance from the results of a GeoRiskScan (Bles et al. 2009) in a project for broadening a canal, which revealed just in time a gap in essential, yet lacking, ground information which has been filled by hiring specific geotechnical expertise (van Staveren et al. 2013c).

Figure 4 presents *complete* GeoRM and ProjectRM integration. While GeoRM is absorbed by ProjectRM, the clear lines of both circles symbolizes the explicit scopes of GeoRM and ProjectRM. While being an integral part of ProjectRM, GeoRM has keeps its own explicit and structured way of dealing with geotechnical risk, with its own risk remediation tools.

In the TC304-TF3 survey only the Scandinavian countries Finland and Sweden, which form 20% of the participating countries, indicate almost full integration of GeoRM and ProjectRM.

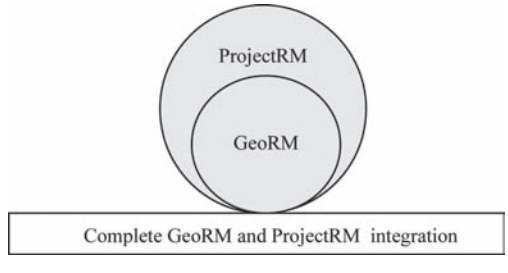

Figure 4. Complete GeoRM and ProjectRM integration.

Sweden adds that ProjectRM is applied in most projects, but not always exactly following standards or guidelines such as ISO31000 (ISO 2009a). ProjectRM following these standards is applied mainly in large projects.

The United Kingdom reported that full integration of GeoRM and ProjectRM is provided by the UK Highways Agency.

In the Czech Republic GeoRM and ProjectRM integration depends currently on the construction phase and type of project. The Czech Republic reports that GeoRM is well-integrated in ProjectRM during the construction phase for particularly tunnel projects. However, in the planning phase of these type of projects, risk management is often still missing. Moreover, GeoRM seems more advanced than Project RM in the Czech Republic, because application of GeoRM is mostly driven by the experts in geotechnics and was motivated by geotechnical failures.

3.6 *Benefits of GeoRM and ProjectRM integration*

The previous section presented some examples of completely integrated GeoRM and Project RM. However, what are the benefits of it?

Within the TC304-TF3 survey ProjectRM success examples were provided by 60% of the participating countries. The reported ProjectRM benefits seem mainly realized in large expressway and tunnel projects. Benefits include sensible risk allocation, no serious risks and losses happening, improved safety, prevention of conflicts, finding innovative solutions in unexpected conditions, perseverance of public project acceptance and ease and facilitation of design and construction.

However, as Sweden noticed, ProjectRM successes are quite difficult to find and not readily available. Moreover, the ProjectRM benefits as presented in all examples were qualitatively, rather than quantitatively. ProjectRM successes are not expressed in figures of the usual performance indicators for project success, such as cost, time, safety, and quality.

Also GeoRM success examples were provided by 60% of the participating countries by the TC304-TF3 survey. As the Czech Republic noticed, severe problems may be a trigger to start with GeoRM. Similar to the ProjectRM examples, also in the provided GeoRM success the examples, the results are qualitatively, rather than quantitatively. Also GeoRM successes are not expressed in figures of the usual performance indicators for project management, such as cost, time, safety, and quality.

The reported GeoRM benefits are derived from mainly tunnel projects and rail projects and include successful risk-driven operations in city areas, close to tunnels in use, which avoided leakage, deformations and resulting damage of adjacent structures. Also timely identification of site contaminations, efficiently reacting on unexpected geotechnical conditions, and transparent dialogues about geotechnical risk with the public were reported as GeoRM successes.

Motivated by these successes, the contribution of GeoRM to ProjectRM has also been identified within the TC304-TF3 survey. From the ten country reports in total ten specific types of contribution of GeoRM to ProjectRM have been derived, by using data triangulation (Patton 1987, Yin 2003). This involved comparing and clustering similar GeoRM contributions, as reported by the ten countries.

GeoRM contributions to ProjectRM, as raised by 40% of the ten participating countries, were (1) managing the crucial role of geotechnical uncertainties that have a major influence on construction projects, (2) increasing the safety during the works and of the final constructions and (3) combining systematic gathering of geotechnical information with construction performance and costs, for improving know-how and fostering learning from past performance.

The remaining seven GeoRM contributions were each identified by 20% or 10% of the countries, which means by one or two countries. This implies that the views on the GeoRM contributions vary considerably amongst several countries, which allows learning from each other. One country may adopt one or more GeoRM contributions from other countries for strengthening its ProjectRM.

For instance, China and the Netherlands remediate geotechnical risk in projects by involving QA/QC professionals, for aligning processes and achieving economies of scale and learning. This approach could be valuable for the remaining eight countries that participated in this survey.

Another example, the United Kingdom suggests that GeoRM may influence the choice of which risk responses to adopt. Some responses may be able to deal not only with geo-risks, but also with other project risks at the same time, which also may result in economies of scale and learning. This benefit may be attractive for some other countries as well.

Finally, all of the ten types of contribution of GeoRM to ProjectRM are again quite general and qualitative, rather than proven and quantitative contributions expressed in money, time, safety records and so on. Nevertheless, all presented examples of benefits by applying ProjectRM and GeoRM seem to confirm the value of more well-integrated ProjectRM and GeoRM. However, this

requires crossing a number of boundaries, which is the topic of the next chapter.

4 CROSSING GeoRM BOUNDARIES

4.1 *Introduction*

Despite the promising success examples of the previous chapter, complete and integrated GeoRM and ProjectRM seems not yet common practice in a lot of project phases, in a lot of projects, in a lot of countries. More complete and integrated GeoRM and ProjectRM seems to require the crossing of several boundaries. This may support faster learning how to increase GeoRM and ProjectRM completeness and integration, which is expected to pay off in effectiveness and cost-efficiency within projects. Within this chapter, the following eight boundaries are explored and crossed:

1. Boundaries between risk concepts
2. Boundaries between disciplines
3. Boundaries between phases
4. Boundaries of scope
5. Boundaries between project types
6. Boundaries between industries
7. Boundaries between countries
8. Boundaries within our minds.

By awareness of, and even better, crossing these boundaries, we can avoid to re-inventing the wheel in our own discipline of geotechnical engineering and construction. Outside this discipline there appear to be abundant readily available concepts, methods, tools, and approaches that geotechnical engineers can use for strengthening the impact of their valuable geotechnical activities within civil engineering and construction projects.

4.2 *Crossing boundaries between risk concepts*

This first boundary separates conventional *rule-based* risk management from more modern *principle-based* risk management. These are basically the two main routes of doing risk management. The first approach is using rules and gives apparently one best way for managing risk. This is not appropriate for GeoRM, because of the large diversity of engineering and construction projects in complexity, size, location, and ground conditions. For this reason, the Dutch participants of the earlier mentioned Geo-Impuls development program for reducing geotechnical failures and related costs, take the principle-based route for allowing fit-for-purpose GeoRM. Based on the eleven generic risk management principles from ISO31000 (2009a), eight specific geotechnical or GeoRM principles have been defined by a team of representative of Geo-Impuls participants.

By definition, principles are always abstract and need a translation into activities. Such a translation can be done for specific projects, and even for specific project phases, again in a fit-for-purpose way. By this approach GeoRM is a *mean* for realizing project objectives, and not an *end* in itself. Table 1, derived from van Staveren et al. (2013b) presents the eight GeoRM principles, together with a number of examples of related actions. The table can be used as a GeoRM checklist, simply by completing the column Done Yes/No.

Table 1. GeoRM principles in a checklist format.

No.	GeoRM principles	Examples of GeoRM actions	Done Yes	Done No
1	Generate and protect value	Make all geotechnical risks in each project phase explicit, with risk effects remediation measures		
2	Participate in decision making in all project phases	Make a geotechnical risk file from the start of the project, use it for decisionmaking		
3	Make geotechnical uncertainty explicit	Include geotechnical sensitivity analyses with margins in project reports		
4	Work systematically, structured, and in time	Include GeoRM explicitly in the project planning and reserve resources for it		
5	Use all available information	Work from a general level to a detailed level, from using geological maps to geotechnical monitoring		
6	Work transparently together with all stakeholders	Indicate and communicate any dependencies of geotechnics with other disciplines in the project		
7	Include the role of the human factor	Make differences in organizational culture of all involved project parties visible and feasible		
8	Use experiences and lessons for continuous improvement	Use all available and relevant project evaluations, risk checklists, and experiences from professionals		

Another example of using a "one-size-fits-all" *rule-based* risk management approach: the foundation design of a three-story building. Let us assume that it is common practice to execute one borehole for every fifty square meter for assessing and remediating the foundation risks of differential settlement, independent of the anticipated ground conditions. By adopting a *principle-based* risk management approach, the number of boreholes will be defined in a project-specific way. The site investigations depends on the anticipated ground conditions, the structural design of the building and resulting settlement tolerances, as well as of the degree of risk tolerance of the client and contractor and future inhabitants.

Therefore, the main results of crossing the boundaries of conventional rule-based to more modern principle-based risk management concepts is delivering more project-specific geotechnical risk management, that fits the specific risk tolerances of the parties involved, against reasonable costs. Effectiveness and cost-efficiency are the main anticipated benefits of crossing the rule-based-principle-based boundary of geotechnical risk management.

The TC304-TF3 survey reveals that in seven out of the ten countries (70%) principle-based standards, are mentioned. However, in three of these seven countries the ISO 31000 (ISO 2009a) Guideline for risk management is not yet well known (Czech Republic, Germany), or mentioned in only one project (Finland). Principle-based ISO standards seems rather well incorporated in Austria, Netherlands, Sweden and United Kingdom.

Finally, principle-based approaches are not limited to the discipline of risk management. For instance, the principle-based concept of High Reliability Organizations (HRO) (Weick and Sutcliffe 2007) has been developed in the discipline of *safety management*. The five HRO principles include reluctance to simplification, sensitivity to operations, and respect for expertise. Organizations that work in high risk environments according to these principles proved to have substantially better safety records than similar organizations that did not adopt these principles in their operations. Examples of typical HRO organizations are nuclear power stations and aircraft carriers. In the Netherlands, the HRO approach in winning popularity within other types of organizations, including healthcare and construction. This confirms the value of crossing borders between disciplines, as explored in the next section.

4.3 *Crossing boundaries between disciplines*

The second boundary separates several different disciplines. Let us start with the disciplines of *risk* management and *safety* management. The TC304-TF3 survey revealed that in a number of countries, such as Switzerland, risk management is quite safety-driven. Other discipline boundaries to cross are those between the *technical* disciplines, such as civil engineering and geotechnical engineering, and the *managerial* disciplines, including project management, organization sciences, and organizational change management. For instance, because effectively, cost-efficiently and routinely applying GeoRM requires and appropriate organizational structure and culture within all of the organizations that are involved in construction projects. The good news is that an appropriate organizational culture for *risk* management has a lot in common with an effective organizational culture for *quality* management and *Health, Safety and Environment (HSE)* management. Therefore, risk managers, quality managers and HSE managers can join their forces in order to establish organizational cultures within their projects that support risk management, rather than frustrate it.

Van Staveren (2013b) derived seven key conditions for an effective geotechnical and project risk management culture. These are derived from research on implementing risk management in organizations in the construction sector (van Staveren 2009). These key conditions are (1) *shared understanding* of the geotechnical risks in a project facilitated by speaking the same "risk management language" in the organization, (2) acknowledgement that dealing with geotechnical risk is driven by a combination of *rationality* and (often unconscious) *emotion*, specifically with regard to the assessments of risk probabilities and effects, (3) understanding of *differences in risk perception* by individual engineers and managers, which has a close relationship with the second cultural condition, (4) understanding that geotechnical risk management goes beyond geotechnical engineering and has *close relationships* with planning, cost control, safety, and quality, (5) *sharing* of geotechnical risk knowledge is common practice, (6) acknowledgement of *differences in motivation* to apply geotechnical risk management amongst engineers and managers, and finally (7) *cooperation* on geotechnical risk management with other disciplines within and outside the organization.

An example of the latter condition is that one party reduces the probability of a risk, while another partner reduces the risk effects in case of occurrence. For instance, an engineer makes a robust geotechnical design for a deep excavation in a city centre, while the contractor works out a fall-back scenario in case, despite the robust design, horizontal deformations exceed pre-set values. For avoiding confusion, a robust geotechnical design is here defined as one that reduces the probability

of failure or unacceptable deformation to a well-defined and agreed-upon risk level.

An additional way of joining forces by risk managers, quality managers, and HSE managers is the execution and control of risk remediation measures by quality and safety engineers. For instance, the risk of the placement of filter materials with inappropriate grain sizes at a dam site can be reduced by taking regularly bulk samples by the QA/QC team members. Moreover, the risk of slope instability during excavation works adjacent to an existing motor-way can be monitored by HSE engineers, because this concerns the safety of the workers as well as of the users of the motorway.

These are just two simple examples of crossing the boundaries of the risk, quality and safety disciplines on construction sites. For being effective, the delegation of risk remediation measures need to be formalized within the organizational project structure.

Therefore, the main benefits of crossing the boundaries between the disciplines of risk management, quality management and health, safety and environmental management are creating cost and time efficiencies, because risk remediation measures are combined with quality and safety controls.

Finally and obviously, integrating GeoRM and ProjectRM requires also crossing the boundaries between discipline-based risk management, such as GeoRM, and ProjectRM, which is in fact part or project management. Therefore, by crossing this border the border between a rather technical approach (geotechnical engineering) and managerial approach (project management) is also crossed. Both approaches complement each other and are fundamental for realizing successful civil engineering and construction projects.

4.4 *Crossing boundaries between phases*

The third border separates commonly distinguished project phases in civil engineering and construction projects. Conventional project phases for these type of projects are feasibility, pre-design and final design, contracting, construction, maintenance and finally decommissioning. Obviously, these phases have slightly different names in different countries. Also the sequence of these phases may be different, due to the type of contract. In case of Design and Build or Design and Construct contracts for example, the contracting phase will be before the design phase, because design is part of the contract to be executed by a construction company.

Table 2 is derived from the TC304-TF3 survey and shows in which project phases ProjectRM and GeoRM are applied in the ten participating countries (if applied at all, which is not yet a routine, as explained in the previous chapter).

Table 2. Project phases, GeoRM and ProjectRM.

Project phases	ProjectRM in countries	GeoRM in countries
Feasibility	60%	50%
Final design	70%	50%
Contracting	80%	50%
Construction	90%	90%
Maintenance	10%	10%
Decommissioning	10%	0%

In Table 2 the conventional order of subsequent project phases is presented, from feasibility to and including decommissioning. The table shows that ProjectRM is in particular applied during the construction phase (in 90% of the participating countries) and in the contracting phase (in 80% of the participating countries). If applied, then in a majority of countries ProjectRM is even executed during the feasibility phase and design phases.

Only the United Kingdom reports that ProjectRM is sometimes even executed during maintenance and decommissioning. Nevertheless, as explicitly indicated by the United Kingdom, is should not be excluded that ProjectRM is mainly applied in only one or two project phases of individual projects, rather than in all project phases, as ProjectRM theories do recommend (e.g. van Well-Stam 2004).

From Table 2 it can also be concluded that GeoRM is in particular applied during the construction phase, in 90% of the participating countries. In 50% of the ten participating countries GeoRM is applied in the feasibility, design and contracting phases. Nevertheless, as indicated by the United Kingdom, it is likely that also GeoRM is mainly applied in only one or two phases, rather than in all phases as GeoRM theories do recommend (van Staveren 2013b). For instance Austria, Czech Republic, Germany, and Switzerland reported that geotechnical risks are typically not well analysed, communicated, and managed during the project planning phase. Therefore, once again, Table 2 presents only in which project phases ProjectRM and GeoRM are applied, if applied at all.

When compared with ProjectRM, GeoRM seems to be applied to a lesser extent in the distinguished project phases than ProjectRM. The exception is the construction phase. In total 90% of the countries report that ProjectRM as well as GeoRM is executed during construction. However, the presented data does not reveal whether ProjectRM and GeoRM are both performed in the same projects or not. In other words, it is possible

that in some projects only ProjectRM is executed, and on other projects only GeoRM.

Table 2 and the previous remarks demonstrate that ProjectRM and GeoRM are not yet cyclic applied in the entire sequence of project phases, as highly recommended by the risk management theories (e.g. van Well-Stam 2004). This is simply demonstrated by the following example. A decision to apply the observational method as a risk remediation measure during construction should be taken already during design, because it requires a certain degree of design flexibility that allows changes during construction, if the ground properties encountered require changes in order to satisfy the specifications (van Staveren 2006).

In conclusion, crossing the boundaries of project phases may become an important step in developing the effectiveness of both GeoRM and ProjectRM.

4.5 *Crossing boundaries of scope*

The forth border is about scope. In particular, this border explores the *scope of communication* about geotechnical uncertainty, risk and the potential consequences for project parties and external stakeholders. While geotechnical calculations are obviously of key importance for successful projects, clear communication of the calculation results, their expected accuracy, as well as the need for reliable input parameters (to derive from site investigations) should also be part of the scope of the geotechnical engineer, once he or she aims to work according the principles of GeoRM.

For example, many geotechnical engineers complain from time to time about the lack of interest of clients in site investigations. Who of us is not familiar with a site investigation report for a project that is too limited with regard to the number of Cone Penetration Tests (CPTs), boreholes, and laboratory tests? Apparently, in those cases geotechnical engineers are not able to communicate clear about the geotechnical risk profile of the project and its potential consequences for the client and other project parties and stakeholders. As indicated by the United Kingdom in the TC304-TF3 report (van Staveren 2013a):

> *"Technical people often struggle to present information in a non-technical manner, reverting to techno-speak and jargon that simply turns others off."*

The *risk language issue* is made explicit by a number of countries that participated in the TC304-TF3 research. For instance, Austria, Germany, Switzerland report that communication of risks in general is quite limited. This is mainly due to cultural specifics that do not motivate open admission of potential problems. Especially in the technical field, engineers highly rely on standards and norms and they are not used to analyse possible deviations from an ideal standardized state or progress. Therefore, risks are typically not communicated to the public in advance. It has been common practice to present the project as a safe and certain action. However, this paradigm seems to be changing. There has been a rising debate about the number of sever cost overruns in large construction projects and about the fact, that uncertainty of the cost estimates should not be neglected in the planning phase.

In the Czech Republic many serious accidents and cost overruns occurred over the last years. Now the public is generally suspicious about the large construction projects. Open communication of geotechnical risks in future projects can thus cause exaggerated reactions of the affected inhabitants.

In the Netherlands it is for many clients and contractors quite a dilemma to either communicate about geotechnical risk before starting the project (which may make the public feeling uncomfortable about the project), or only once the geotechnical problems occur (for instance damage due to settlements) which would make the public not only feeling uncomfortable, but quite angry as well.

Switzerland demonstrates that public involvement in decisions about the large projects pays off. For example, the Gotthard base tunnel showed the benefits of public involvement into the process. This included three referenda on realization of the project on for instance its financing, ensured a general acceptance of the project amongst people, in spite of large time and cost overruns and even fatalities during its construction.

All of these examples invite geotechnical engineers to jump over the boundary that separates the area of geotechnical calculations with results in numbers from the area with convincing stories, graphs and other visual presentation means about the need for sound and risk-driven geotechnical engineering, in order to realize successful and safe engineering and construction projects.

This type of communication should start within the project team inside projects, should expands towards the public and other stakeholders in the external project environment. An example of within-the-team risk communication that is proposed in the TC304-TF3 survey is simply including geotechnical risk communication within all coordination and common practices inside the project, as done in Finland. Another example is presenting the consequences of identified geotechnical risks in terms that can be more widely understood by non-geotechnical project team members and managers, such as their impact to meeting business objectives

and the 'balance' to be achieved between risk and reward, as practiced in the United Kingdom.

Examples for geotechnical risk communication with the public outside the project are organizing workshops, evening meetings, door knocking, promoting in the local press, having a question & answer kiosk or information centre outside the site and manned by trained staff, and Open Doors Days for the project, as occasionally done in for example Czech Republic and in the United Kingdom. In the Netherlands, information centres for the public are common for large tunnel and railway projects in city centres, such as bored and cut and cover tunnels under construction and other works in the cities of Amsterdam, Delft and Utrecht.

In conclusion, crossing the boundaries of scope by geotechnical engineers concerns in particular *communication* from only numbers towards convincing stories in a language that can be easily understood by non-geotechnical managers, clients, and public.

4.6 *Crossing boundaries between project types*

The fifth boundary of concern is that between different project types. Civil engineering projects can be divided by several criteria, for instance by function or by size. The ten countries participating in the TC304-TF3 survey were asked in which type of projects ProjectRM and GeoRM are applied, if applied. The results are summarized in Table 3.

Table 3 shows for instance that ProjectRM is applied in underground construction in 70% of the ten participating countries, and in major highway projects in 60% of these countries. In the remaining types of projects ProjectRM is applied in a minority of the participating countries. GeoRM is applied in underground construction in 40% of the participating countries, and in major highway projects in 40% of these countries. In the remaining types of projects, GeoRM is applied in 30% or less of the participating countries.

Table 3. Project types, GeoRM and ProjectRM.

Types of projects	ProjectRM in countries	GeoRM in countries
Underground construction: tunnels, subway (metro) stations, parkings	70%	40%
Major highways	60%	40%
Large, multidisciplinary and complex infrastructure	40%	30%
Railways	40%	30%
Harbours	30%	20%
Bridges	30%	10%
Large dams	30%	10%
Dikes & slopes	10%	10%
Windfarms	00%	10%
Building foundations	00%	10%

When compared with ProjectRM, GeoRM seems to be applied to a lesser extent than ProjectRM. For example, in underground construction projects, ProjectRM is used in 70% of the countries, against GeoRM in 40% of the countries. Remarkably, for building foundations ProjectRM and GeoRM are not or almost not applied.

In conclusion, the TC304-TF3 survey results confirm that for certain types of project ProjectRM and sometimes also GeoRM is more common than for other types of project. This implies that professionals concerned with project types for which risk management is not yet common practice, may be able to learn a lot from engineers and managers who are already more familiar with applying ProjectRM and GeoRM in their projects. The same applies of course for larger projects, like highways, where risk management is rather common practice and smaller road projects, which may also benefit from applying risk management practices. For these reasons, crossing the border of project types may pay off.

4.7 *Crossing boundaries between industries*

The sixth boundary is about crossing boundaries between different industries. The introduction of this paper started with the statement that especially construction projects are inherently risky, due to numerous uncertainties of many types. While true, the construction industry is not the *only* industry facing challenges of high uncertainty. For instance, projects within the chemical, energy, offshore, oil, gas, military and space industry do also have their specific high uncertainty challenges.

There are a number of striking similarities between the space industry and the under-ground construction industry, involving tunnels works for instance. Quality and safety are key issues in the space industry, because once a rocket with a satellite is launched, repair is very difficult, if possible at all. Moreover, there is time and cost pressure in the space industry, because of increasing competition and governments cutting budgets.

Similar situations occur in the construction sector. Especially in Europe, there is severe price competition and government budgets are under pressure, due to the financial crises. Moreover, when returning to underground construction, once a tunnel is bored and completed, it is often very expensive to repair in case of for instance excessive groundwater inflow by cracks in the tunnel lining. The same applies to deep foundations.

Therefore, the need for adequate risk management in the construction sector may match well with the need for effective and cost-efficient risk management in the space industry. For instance, the NASA Risk Management Handbook (NASA 2011), free to download from the Internet, provides a wealth of risk management knowledge that may be of particular use for the construction industry.

A learning example is the rigorous relationship between risk and opportunity management that the NASA applies. Therefore, all uncertainties are perceived from the conventional risk side (the negative down-side), as well as from an opportunity perspective (the positive upside). Apart from the possibilities of financial gains from this approach, is much more fun for all professionals and managers involved, because they are not only looking for potential problems.

Other lessons from space, derived from a risk management implementation case in The Netherlands, are (1) paying more attention to interdisciplinary teamwork in all project phases, (2) explicitly discussing mistakes made in order to learn from them in other projects and (3) evaluating the effectiveness and cost efficiency of project risk management. The latter is done by assessing the Total Cost of Risk (TCoR) in projects, with is the sum of all risk management process costs, the costs of all risk remediation measures and the costs of all risks that occurred, despite the measures taken (which again requires a high degree of openness and trust within the organization).

Exploring the boundaries between industries for the benefits of learning about risk management was also part of the TC304-TF3 survey. In total five out of the ten participating countries (50%) suggested in total seven sectors outside the construction industry, where valuable lessons for more effective and cost-efficient GeoRM can be found. These suggested industries are presented in Table 4.

All of the suggestions in Table 4 demonstrate that there is probably a wealth of proven concepts, methods, techniques, tools, and approaches waiting for adoption in well-integrated ProjectRM and GeoRM. This may save a lot of time, energy and money by avoiding to re-invent the wheel by keeping considering ProjectRM and GeoRM as separated disciplines, as indicated by the United Kingdom in TC304-TF3.

In conclusion, the main benefits of crossing the boundaries between the different industries are cost-effective organizational learning and consequently costs savings. A lot of risk management experiences and lessons from other industries are ready to be applied within the construction industry, obviously in the earlier discussed principle-based and project specific way.

4.8 *Crossing boundaries between countries*

The seventh boundary is about different countries We are living in an ever more globalizing world, in which millions of professionals in different countries are interconnected by different kinds of social media. For instance, the professional LinkedIn network has currently globally more than 225 million users (per June 2013). With regard to risk management, there are numerous user-groups with participants from different countries, who can easily learn from each other.

When focusing on the construction sector, over the last fifteen years Dutch engineering firms and contractors imported for instance successfully soft soil tunnel boring expertise from abroad to The Netherlands. In return, Dutch technology for

Table 4. Project and GeoRM lessons from other industries.

Industry	Lessons for ProjectRM and GeoRM
Mechanical industry	How to increase productivity, despite the unique character of construction projects and the related risks.
IT-industry	How to use simulation tools for optimizing construction processes under risky conditions.
Space industry	How to integrate risk management in systems engineering in construction projects. How to develop risk management as part of continuous organizational improvement programs.
Insurance industry	How construction insurance claims can be avoided or reduced, by using qualified and competent people.
Chemical and nuclear industry	How to develop clear risk benchmarks How to combine risk and safety management
Financial services industry	How to consider risk in a holistic and integral way by applying Enterprise Risk Management (ERM).
Consulting industry	How to apply proven project management techniques within ProjectRM and GeoRM processes.

flood protection, gained during the Delta Works, is exported for tens of years all over the world, from northern America to south-east Asia. With regard to geotechnical risk management, the concept of the Geotechnical Baseline Report (GBR), as originally developed in the United States (Essex 1997) has been introduced in The Netherlands (van Staveren 2006). The same applies for the Observational Method (OM), as developed by Peck (1969) in the 1930s. The OM is currently starting up a successful second live in the Netherlands, in particular for major tunnel projects. It proves to be a valuable geotechnical risk control tool that has been made very efficient by using the latest sensor and information technology.

The ten countries participating in the TC304-TF3 survey provided in total 19 different recommendations for (further) integrating GeoRM and ProjectRM. These recommendations have been derived, by using data triangulation (Patton 1997, Yin 2003), which involved comparing and clustering largely similar recommendations, as reported in the ten country reports. All of the recommendations have been classified in three types: (1) recommendations that are primarily realized by changes in the organization structure of (project) organizations involved in construction projects, (2) those primarily realized by changing the culture within these organizations, and (3) recommendations primarily involving technical measures. Measures for changing organizational structure and culture seem often closely coupled. In total 13 out of the 19 recommendations (68%) have an organizational cause, either structural (47%) or cultural (21%). In total six technical recommendations have been identified (32%).

The top five recommendations for integrating GeoRM and ProjectRM, reported by 60% to 50% of the ten countries, involved *education* of applying ProjectRM and GeoRM, *communication* of their effects and successes, as well as *learning* from past performance of projects. All of these recommendations are classified as of an organization structure type, because the education should be structurally organized. In other words, the proposed ProjectRM and GeoRM education should not stay voluntary for engineers and managers. It should become a *formalized* part of their individual professional development. This results into professional development of organizations, either of clients, engineering firms, contractors, knowledge institutes and universities in the discipline of risk management.

Other recommendations, reported by 40% to 30% of the countries, involve increasing the *interest of public clients* in risk, to provide *standards for risk management processes* in public investments projects that would be broadly accepted by the community, and *increasing risk awareness and open communication*, which would likely increase their acceptance both in society and amongst practitioners.

The remaining eleven recommendations, were reported by 10% or just one of the ten countries. Examples of these recommendations are adopting new investigation methods or technologies, such as GPS and GIS in GeoRM to provide sufficient geotechnical information for minimizing the uncertainty in ProjectRM (suggested by China), and making an effort to involve people who are directly involved in risk handling to adopt those parts of risk management that they can benefit from (proposed by Sweden). Because these recommendations are suggested by just one country, they may be of particular interest for other countries, where these recommendations may be unknown to date. This makes it worthwhile to consider crossing boundaries of countries, either virtual just by surfing over the Internet, or real by participating in international conferences and by actually visiting organizations and construction projects in countries.

Similar to crossing the boundaries of industries, the main benefit of crossing the boundaries between countries is fostering cost-effective organizational learning. This is expected to result in substantial costs savings, because a lot of risk management experiences and lessons from other countries with more or less similar ground conditions can be applied, without paying the money of learning by mistake.

Finally, as mentioned before, six out of the nineteen recommendations (32%) made by the ten countries for integrating and developing ProjectRM and GeoRM were *technical* recommendations. However, in the same TC304-TF3 survey also the main *hurdles* for applying ProjectRM and GeoRM have been investigated. Of all hurdles investigated, in total 5% of the ProjectRM hurdles and 18% of the GeoRM hurdles were of *technical* origin. All remaining hurdles, i.e. 95% for ProjectRM and 82% for GeoRM seem to have an *organizational* cause.

Therefore, it seems that there is a tendency to solve *organizational* problems with *technical* solutions, rather than with organizational solutions. This should be a point of attention, when one is trying to reduce ProjectRM and GeoRM hurdles for (further and deeper) integrating both types of risk management. Here we return to the area of the human mind, which is the last border to cross.

4.9 *Crossing our mental boundaries*

Finally, we may have to cross some of our mental boundaries, in particular the one between different

risk perceptions. This requires a few rather philosophical and psychological reflections.

Understanding of differences in risk perception, the fact that people judge and classify the same factual risk data in a different way, is a key success factor for effective risk management (van Staveren 2006). Individual risk perception is the result of an (often hidden) mixture of ratio and emotion. This has been thoroughly investigated by for instance the Nobel laureates Kahnemann and Tversky (1979) in their prospect theory about how people make choices under uncertainty.

Dealing with different risk perceptions is by far not simple. Prof. Frans Barends (2005), emeritus professor at the Delft Technical University in The Netherlands, concluded in 2005 during his Terzaghi Oration:

> *'The effects of subjective individual interpretation of facts and data are underestimated.'*

This firm statement was illustrated with a geohydrological example about the interpretation of an observed porewater response, caused by changing water levels. This interpretation proved to be highly *subjective*, as six different geohydrological models could be applied to interpret the same data, obviously with different outcomes. Awareness of our own subjective expert judgment is a therefore a first step towards effective dealing with risk perceptions.

The next step is trying to understand the risk perceptions of *other* people: colleagues, geotechnical engineers, other engineers involved in the project, project managers, technical managers, contract managers, site managers, procurement managers, financial managers, quality and safety managers, our clients, the public, and other external stakeholders. Trying to understand their risk perceptions, and comparing these with our own perceptions, is a prerequisite for effective decision making under uncertainty. This applies also to geotechnical risks.

Explicit and open communication is required to identify and discuss any differences in risk perception between ourselves and other persons. It is likely to result in a more shared risk understanding, which opens doors towards less confusion, less misunderstanding, and consequently more successful engineering and construction projects, despite their inherent geotechnical and project risks. Therefore, understanding our own and other risk perceptions can be seen as crossing our mental boundary from unaware dealing towards well-aware dealing with risk.

In addition, as mentioned in the previous section, more effective and cost-efficient risk management seems often not so much a matter of only more and better risk management tools. Practice teaches that it seems often the result of better organizing the required expertise for dealing at the right time and place with geotechnical uncertainties.

For instance, research by van Tol (2008) of 40 failed excavation pits in the Netherlands proved that these failures were not caused by a lack of geotechnical expertise. For 80% of these cases the geotechnical expertise was readily available in the Netherlands, but not organized at the right time at the right place in the project. Therefore, these failures seem more of an *organizational* problem than an *geotechnical* problem. This stresses the need to pay more attention to (project) *organization design approaches*, including their structures and cultures (van Staveren 2009b).

Effective design of project organizations requires another approach than conventional technical design. For instance, *technical design* of constructions like a bridge or tunnel uses conventional *algorithmic* technological rules, which guarantee that a solution *will* be found. However, suitable *organizational design*, necessary for well-integrated and completely applied GeoRM and ProjectRM, needs so-called *heuristic* technological rules (Roozenburg & Eekels 1995). Contrary to the algorithmic ones, heuristic technological rules do not guarantee that a solution can or will be found. A heuristic rule facilitates *finding* of a solution. This aligns with a hermeneutic ontological view, which considers the world as a social construct with inherent subjectivities (Gumesson 1988).

Accepting these facts for developing GeoRM and ProjectRM implementation is another example of crossing a mental boundary. Moreover, it helps to keep a realistic and pragmatic view on developing risk management in civil engineering and construction projects.

5 CONCLUSIONS

Based on the previous chapters, and in particular the results of the TC304-TF3 survey, the following main conclusions are made.

First, abundant literature, and the TC304-TF3 survey provide evidence that integrated Geotechnical Risk Management (GeoRM) and Project Risk Management (ProjectRM) may considerably *contribute* to successful civil engineering and construction projects for all involved project parties and stakeholders.

Second, from a *methodological* point of view, there seem to be no objections for (further) integrating GeoRM and ProjectRM in all project phases, because their pragmatic definitions and processes fit well and complement each other.

Third, considerable failures and resulting additional costs in civil engineering and construction projects, often with a geotechnical root cause, as found in the literature, has been confirmed by the TC304-TF3 survey. In at least 80% of the participating countries GeoRM and/or ProjectRM are (1) *not* applied at all in all phases of civil engineering and construction projects, are (2) *incompletely and separately* applied, or are (3) applied in a rather *blurred* way. Only two out of the ten countries (20%) reported (4) rather *complete and integrated* application of GeoRM and ProjectRM in most projects, however not always performed according to standards and guidelines. Therefore, the degree of implementation of integrated ProjectRM and GeoRM varies considerably between and within the participating countries. Similar variations in the degree of GeoRM and ProjectRM application and integration are identified between different types of projects, between different project phases, and between different sizes of projects.

Forth, in total eight *boundaries* have been explored. Crossing these boundaries will probably improve the degree of GeoRM and ProjectRM application and integration within civil engineering and construction projects. These boundaries concern (1) risk concepts, (2) disciplines, (3) project phases, (4) scopes, (5) project types, (6) industries and (7) countries. For learning how to cross these seven boundaries, we may have to cross first some (8) mental boundaries.

Therefore, the final conclusion of this paper could be that in theory there are *no objections* for a full integration of GeoRM and ProjectRM, that the *awareness* of the need for and potential benefits of such an integration is growing, but that the integrated application of both types of risk management, for realizing real project success in practice, has still a lot of room for *development* and *improvement*. For this reason, the next and final chapter presents some main recommendations for further and deeper integrating GeoRM and ProjectRM.

6 RECOMMENDATIONS

Throughout this paper already many examples and recommendations for further and deeper integrating GeoRM and ProjectRM have been presented. Nevertheless, two main recommendations need considerable more attention, because these are considered as key success factors for developing complete and well-integrated execution of GeoRM and ProjectRM, in all project phases of civil engineering and construction projects.

First, improving the quality and quantity of *education* of geotechnical professionals, other engineers, and managers participating in projects. This education should focus on the concepts and practices of uncertainty, risk and its management in general, and on ProjectRM and GeoRM in particular. These professionals and managers should then become more capable of raising risk awareness and providing acceptable risk solutions for their projects and organizations, their clients, the public, and other stakeholders of civil engineering and construction projects.

Second, expand the degree multi-disciplinary and inter-disciplinary *research* and *development* of GeoRM and ProjectRM. This research should in particular focus on the interfaces with project management, with engineering and construction management, and with safety and quality management. A perhaps extreme relevant research topic is measuring the GeoRM and ProjectRM effectiveness and cost-efficiency, in relation the project management key performance indicators such as safety, quality, costs, time, and even reputation. Case study research may be an effective research methodology. In particular quantitative research results of risk management effectiveness are highly welcome, in order to convince sceptical professionals, clients, and the public about the added value of risk management within civil engineering and construction projects. Depending on the research results, further developing and fine-tuning of GeoRM and ProjectRM can be realized.

Execution of these recommendations will allow us to follow Deming's widely accepted and applied *Plan-Do-Check-Act* (PDCA) cycle, specifically for risk management improvement in engineering and construction. Plan equals providing *education*, do concerns *application* of integrated GeoRM and ProjectRM in projects, check is about *evaluation* by research of the risk management performance of projects, and finally act is about further *developing* and fine-tuning risk management theories and practices. Here emerges an important task for universities and other knowledge institutes.

The follow up of these recommendations, preferably in close cooperation with many countries, may realize the promise of well-integrated and completely applied GeoRM and ProjectRM. The ultimate objective remains substantially contributing to successful construction projects, by applying risk-driven geotechnical engineering and construction, which give us less cost overruns, less delays, less non-conformances of safety and quality, and therefore happier project participants, client, public and other stakeholders.

ACKNOWLEDGEMENTS

The author is grateful to the ISSMGE TC304-TF3 participants, who prepared their country reports

that made it possible to compare and analyse the degree of GeoRM and ProjectRM application and integration in ten different countries. These professionals are, in alphabetical order by first names, Alexander Rozsypal, Annina Peisa, Hongwei Huang Joost van der Schrier, Lars Olsson, Kati Kaskiala, Leena Korkiala-Tanttu Markku Tavi, Makoto Kimura, Martin Srb, Matti Kokkinen, Miroslav Matousek, Olga Spackova, Paul Cools, Paul Maliphant, Pentti Salo, Tadashi Hashimoto, Tobias Nevrly, Qunfang Hu and the members of the Swedish Geotechnical Society Committee on Risk Assessment.

Furthermore, the author is grateful to all professionals, engineers and managers, he met personally over the years during lectures, workshops, conferences, and consultancy activities in many organizations, inside and outside the construction industry. Without their open sharing of experiences and insights, this paper could not have been realized.

REFERENCES

Barber P., Graves A., Sheath D. & Tomkins, C. 2000. Quality failure costs in civil engineering projects. *International Journal of Quality & Reliability Management* 17(4/5): 479–492.

Barends, F.B.J. 2005. Associating with advancing insight: Terzaghi Oration 2005. In: *Proceedings 16th International Conference on Soil Mechanics and Geotechnical Engineering*, 12–16 September, Osaka, Japan, pp. 217–48. Rotterdam: Millpress.

Barends, F.B.J. 2009. Over Onzekerheid en Duurzaamheid in de Geotechniek [About Uncertainty and Sustainability in Geotechnics]. *Geotechniek Special* Nov.: 28–33.

Bea, R.G. 2006. Reliability and human factors in geotechnical engineering. *Journal of Geotechnical and Geoenvironmental Engineering* 132(5): 631–44.

Beal, A.N. 2007. CDM Regulations: 12 years of pain but little gain. *New Civil Engineer International August*: 82–8.

Beck, U. 1992. *Risk Society: Towards a New Modernity*. London: Sage.

Bernstein, P.L. 1996. *Against the Gods: The Remarkable Story of Risk*. New York: John Wiley & Sons.

Bles, T.J., van Staveren, M.Th., Litjens, P.P.T. & Cools, P.M.C.B.M. 2009. Geo Risk Scan: Getting grips on geotechnical risks. In *Y. Honjo et al. (eds) Geotechnical Safety and Risk*: 339–346. Leiden: CRC Press.

Blockley, D. & Godfrey, P. 2000. *Doing It Differently: Systems for Rethinking Construction*. London: Thomas Telford.

Boothroyd, C. & Emmet, J. 1996. *Risk Management: A Practical Guide for Construction Professionals*. London: Witherby.

Brandl, H. 2004. *The Civil and Geotechnical Engineer in Society: Ethical and Philosophical Thoughts, Challenges and Recommendations*. The Deep Foundations Institute, Hawthorne.

Chapman, C.B. & Ward, S. 2011. *How to Manage Project Opportunity and Risk: Why Uncertainty Management can be a Much Better Approach than Risk Management, 3rd Edition*. Chichester: John Wiley & Sons.

Clayton, C.R.I. 2008. The Heathrow Tunnel Collapse. *Advanced Course on Risk Management in Civil Engineering* LNEC Lisbon November 17–22 2008. URL: http://riskmanagement.lnec.pt/pdf/papers/Nov21_apresentacoes/20_presentation_Clayton.pdf.

Cooke-Davies, T. 2002. The "real" success factors on projects. *International Journal of Project Management* 20(3): 185–90.

Cools, P.M.C.B.M. 2011. The Geo-Impuls Programme reducing geotechnical failure in the Netherlands. In *N. Vogt et al. (eds), Geotechnical Safety and Risk*: 191–198. Karlsruhe: Bundesanstalt fur Wasserbau (BAW).

DIN Deutsches Institut für Normung. 2010. *DIN 4020: Geotechnische Untersuchungen für bautechnische Zwecke* [Geotechnical Investigations for Civil Engineering Purposes]. Berlin: Beuth-Verlag.

Egan, J. 1998. *Rethinking Construction: The Report of the Construction Task Force*. London: Department of the Environment, Transport and the Regions, HMSO.

Edwards, L. 1995. *Practical Risk Management in the Construction Industry*. London: Thomas Telford.

Edwards, P.J. & Bowen, P.A. 2005. *Risk Management in Project Organisations*. Oxford: Butterworth-Heinemann.

Essex R.J. (ed.). (1997). *Geotechnical Baseline Reports for Underground Construction.* Technical Committee on Geotechnical Reports of the Underground Technology Research Council. Danvers: ASCE.

Flanagan, R. & Norman, G. 1993. *Risk Management and Construction*. Oxford: Blackwell Scientific Publications.

Godfrey, P.S. 1996. *Control of Risk: A Guide to the Systematic Management of Risk from Construction*. CIRIA Special Publication 125. London: CIRIA.

Gummesson, E. 1988. *Qualitative Methods in Management Research*. Lund: Studentlitteratur.

Harper, K. 2000. Managers 'overlooked risk' in airport tunnel collapse. *The Guardian*, Thursday 6 July 2000 01.46 BST.

Hillson, D. 2002. *Risk Management Maturity Level Development*. Risk Management Specific Interest Group. Newton Square, PA: Project Management Institute.

Hillson, D.A. 2010. *Exploring Future Uncertainty: Creating Value From Risk*. Farnham: Gower.

Hillson, D.A. & Murray-Webster, R. 2007. *Understanding and Managing Risk Attitude,* 2nd edition. Aldershot: Gower.

Hopkin, P. 2012. *Fundamentals of Risk Management: Understanding, Evaluating and Implementing Effective Risk Management*, 2nd edition. London: Kogan Page.

Hopkinson, M. 2011. *The Project Risk Maturity Model: Measuring and Improving Risk Management Capability*. Farnham: Gower.

Hubbard, D.W. 2009. *The Failure of Risk Management: Why It's Broken and How to Fix It*. New Jersey: John Wiley & Sons.

ISO 2009a. *ISO 31000:2009 Risk management—Principles and guidelines*. Geneva: International Organization for Standardization.

ISO 2009b. *ISO Guide 73:2009 Risk management—Vocabulary*. Geneva: International Organization for Standardization.

Kahneman, D. & Tversky, A. 1979. Prospect theory: An analysis of decision under risk, *Econometrica* 47: 263–291.

Knight, F.H. 1921. *Risk, Uncertainty, and Profit*. Boston, MA: Houghton Mifflin.

Latham, M. 1994. *Constructing the Team: Joint Review of Procurement and Contractual Arrangements in the UK Construction Industry*. London: Department of the Environment, HMSO.

Mullaly, M. 2006. *Longitudinal Analysis of Project Management Maturity*. Newton Square, PA: Project Management Institute.

NASA 2011. *NASA Risk Management Handbook*., NASA/SP 2011-3422, Version 1.0 November 2011. Washington: National Aeronautics and Space Administration. URL: http://www.hq.nasa.gov/office/codeq/doctree/NHBK_2011_3422.pdf.

Olsson, R. 2006. *Managing Project Uncertainty by using and Enhanced Risk Management Process*. Ph.D. thesis, Mälardalen University Dissertations No. 34. Västerås: Mälardalen University Press.

Patton, M.Q. 1987. *How to Use Qualitative Methods in Evaluation*. Newbury Park, CA: Sage.

Peck, R.B. 1969. Advantages and limitations of the observational method in applied soil mechanics. *Géotechnique* 19: 171–87.

Power, M. 2009. The risk management of nothing. *Accounting, Organizations and Society* 34(6–7): 849–55.

Raz, T., Shenhar, A.J. and Dvir D. 2002. Risk management, project success, and technological uncertainty. *R & D Management* 32(2): 101–9.

Roozenburg, N.F.M. & Eekels, J. 1995. *Product Design: Fundamentals and Methods*. Chichester: Wiley.

Schinzinger, R. & Martin, M.W. 2000. *Introduction to Engineering Ethics*. New York: McGraw-Hill.

Smith, N. 2003. *Appraisal, Risk and Uncertainty*. London: Thomas Telford.

Smith R. 1996. Allocation of risk: the case for manageability. *The International Construction Law Review* 4:549–69.

Sondermann, W. & Trunk, U., 2008. Spezialtiefbau und risikomanagement: gibt es einen gemeinsamen Weg? [Deep constructions and risk management: is there a joint way?] In: *Beiträge Zum 7. Geotechnik-Tag in München. Risiko Und Sicherheit in Der Geotechnik*, 15.02.2008 München (Deutschland). Presented at the 7th Geotechnik-Tag, München, pp. 3–16.

Sowers, G.F. 1993. Human factors in civil and geotechnical engineering failures. *Journal of Geotechnical Engineering* 119(2): 238–56.

Thompson, P. & Perry, J. 1992. *Engineering Construction Risks*. London: Thomas Telford.

Van Asselt, M.B.A. & Vos, E. 2006. The precautionary principle and the uncertainty paradox. *Journal of Risk Research* 9(4): 313–36.

van Staveren, M.Th. 2006. *Uncertainty and Ground Conditions: A Risk Management Approach*. Oxford: Butterworth Heinemann.

van Staveren, M.Th. 2009a. Extending to geotechnical risk management. *Georisk* 3(3): 174–183.

van Staveren, M.Th. 2009b. *Risk, Innovation & Change: Design Propositions for Implementing Risk Management in Organizations*. Köln: Lambert Academic Publishing.

van Staveren, M.Th. 2013a. *International State of the Art Report on Integration of Geotechnical Risk Management and Project Risk Management*. Draft version 1 of July 2013 (in review process of TC304-TF3 members). ISSMGE TC304-TF3.

van Staveren, M.Th. 2013b. Geotechnics on the move: guidance for a risk-driven way of working. *Georisk* (accepted, ready for publication).

van Staveren, M.Th. & Halman, J.I.M. 2013. Key conditions for risk management implementation. *Risk Analysis* (paper in preparation).

van Staveren, M.Th., Litjens, P.P.T. & Cools, P.M.C.B.M. 2013a. Embedding geo risk management: The GeoImpuls approach. In: *Proceedings of the 18th International Conference on Soil Mechanics and Geotechnical Engineering* Paris (in press).

van Staveren, M.Th., Litjens, P.P.T. & Cools, P.M.C.B.M. 2013b. Implementing geo risk management in the construction industry. In: *Proceedings of the 4th International Symposium on Geotechnical Safety and Risk ISGSR2013,* Hong Kong (in press).

van Staveren, M.Th., Litjens, P.P.T. & Heerema, J.J. 2013c. Implementing geo risk management in a client organization. In: *Proceedings of the 4th International Symposium on Geotechnical Safety and Risk ISGSR2013,* Hong Kong (in press).

van Tol, A.F. 2008. Schadegevallen bij bouwputten [Failure Cases of Construction Pits] *Cement* 6: 6–13.

van Well-Stam, D., Lindenaar, F., Van Kinderen, S. & Van den Bunt, B.P. 2004. *Project Risk Management: An Essential Tool for Managing and Controlling Projects*. London: Kogan Page.

Waring A.E. & Glendon, A.I. 1998, *Managing Risk,* 1st edition. London: International Thomson Business Press.

Weatherhead, M., Owen, K. & Hall, C. 2005. *Integrating Value and Risk in Construction*. London: CIRIA.

Weick, K.E. & Sutcliffe, K.M. 2007. *Managing the Unexpected: Resilient Performance in an Age of Uncertainty*, 2nd edition. San Fransisco: John Wiley & Sons.

Yin, R.K. 2003. *Case Study Research: Design and Methods*, 3rd edition. Thousands Oaks: Sage.

This page intentionally left blank

Geotechnical Safety and Risk IV – Zhang et al. (eds)
 ISBN 978-1-138-00163-3

Is landslide risk quantifiable and manageable?

H.N. Wong
Civil Engineering and Development Department, Geotechnical Engineering Office, Government of the Hong Kong Special Administrative Region, Hong Kong, China

ABSTRACT: Quantitative Risk Assessment (QRA) enables decision-makers to exercise informed and rational judgement in evaluating and managing risk. It is commonly acknowledged that Hong Kong has showcased not only the state-of-the-art in, but also the practicability of, quantification and management of landslide risk. The author would caution that this is a simplistic view. With reference to Hong Kong's experience, it is highlighted that there are different categories of landslide problems, each with its own factors that combine to give rise to risk. As to whether the risk is quantifiable and manageable, different categories have their particular circumstances and the answers are not the same. It is credible to manage landslide risk without quantification, although risk quantification can undeniably aid risk management. Landslide risk quantification may not be practicable in all cases. Even if landslide risk is quantifiable, it is important not to lose sight of the degree of uncertainty involved.

1 INTRODUCTION

Landslide risk management and Quantitative Risk Assessment (QRA) have been undergoing rapid development in the past 20 years. Notable recent developments and applications of landslide QRA are described in Fell & Hartford (1997), Wong et al. (1997), Ho et al. (2000) and Wong (2005). Separately, under funding from the European Commission, the integrated research project 'SafeLand' has been conducted in Europe by 27 institutions from 13 countries, aiming at developing generic quantitative risk assessment and management tools and strategies for landslides.

The quantitative approach in landslide risk assessment and management has gained wider use, both in global and site-specific assessments, as illustrated by successful applications in Hong Kong and elsewhere.

This paper aims to discuss whether landslide risk is quantifiable and how landslide risk is being managed in practice, with and without quantification. Particular reference is made to the practice and experience in Hong Kong, which is recognised as a role model in urban landslide risk management.

2 LANDSLIDE AND SLOPE SAFETY MANAGEMENT IN HONG KONG

2.1 *Landslide problems in Hong Kong*

While landslides are widespread in many parts of the world, landslides in Hong Kong interact intensely with human activities in urban areas. Landslides pose particularly grave challenges to densely populated built-up areas like Hong Kong because:

- landslide consequences are serious due to the close proximity to and the high concentration of population and vulnerable facilities;
- urban development, when carried out without adequate geotechnical input, results in the formation of potentially unstable slopes and increases landslide frequency;
- landslide problems in an urbanised setting are aggravated by human factors, including concentrated surface water flow and localised cutting and filling; and
- relocation of existing facilities to avoid landslide hazards is often not viable, while at the same time landslide prevention and mitigation works are difficult and costly given space and access constraints.

In the early years of Hong Kong's rapid urbanisation, a large number of cut and fill slopes and retaining walls were formed to pave the way for housing and infrastructure developments. Typically formed with little geotechnical input at the time, these unengineered man-made slope features continue to pose landslide risks to the community to this day. Against this background, the Landslip Prevention and Mitigation (LPMit) Programme (known as Landslip Preventive Measures, LPM, Programme before 2010) has been implemented by the Geotechnical Engineering Office (GEO,

formally the Geotechnical Control Office) of the Civil Engineering and Development Department, with significant headway made in risk reduction.

The severe weather conditions experienced in Hong Kong and the increasing urban development close to natural hillsides have also called for attention to managing the risk of landslides originating from natural terrain.

2.2 *Slope safety management system*

Following a number of disastrous landslides with serious fatalities in the 1970s in Hong Kong, the GEO was established in 1977. Over the years, a comprehensive Slope Safety System has been developed and implemented by the GEO to combat landslide problems.

The key components of the Slope Safety System in Hong Kong together with their functions in a risk management context are summarised in Table 1. A range of initiatives are included in the System to manage landslide risk in a holistic manner.

The goals of the System are: (i) to minimise landslide risk to the community through a policy of priority and partnership for reducing landslide frequency and consequence, and (ii) to address public attitude and tolerability of landslide risk to avoid unrealistic expectations. The System also adds value to the society through averting potential fatalities and improving the built environment.

The Slope Safety System has proven successful in containing landslide risk within an As Low as Reasonably Practicable (ALARP) level, via: (i) improving slope safety standards, technology and administrative and regulatory frameworks, (ii) ensuring safety standards of new slopes, (iii) rectifying substandard Government slopes and maintaining them, (iv) ensuring that private owners take responsibility for slope safety, and (v) promoting public awareness in and response to slope safety. Besides slope safety, the improved aesthetics and ecology of engineered slopes have also contributed to enhancing the built environment.

Retrofitting of the old unengineered slopes is carried out in the pre-2010 LPM Programme and post-2010 LPMit Programme. The Programmes serve to systematically assess the stability of old man-made slopes according to their ranked

Table 1. The slope safety system in Hong Kong (based on Malone 1998).

	Primary contribution of each component to		
	Reduce landslide risk		Address public attitude and tolerability
Components of slope safety system	Reduce likelihood	Reduce consequence	
Policing			
– Checking new slope works	✓		
– Slope maintenance audits	✓		
– Recommending safety clearance of vulnerable squatters and unauthorised structures threatened by hillsides		✓	
– Exercising geotechnical control through input in land use planning		✓	
– Safety screening studies and recommending statutory repair orders for private slopes	✓		
Works projects			
– Retrofitting substandard government man-made slopes	✓		
– Natural terrain landslide mitigation and boulder stabilisation works	✓		
Research and setting standards	✓	✓	✓
Education and information			
– Slope maintenance campaigns	✓		✓
– Risk awareness programmes and personal precaution campaigns	✓	✓	✓
– Information services	✓	✓	✓
– Landslip warning and emergency services		✓	✓

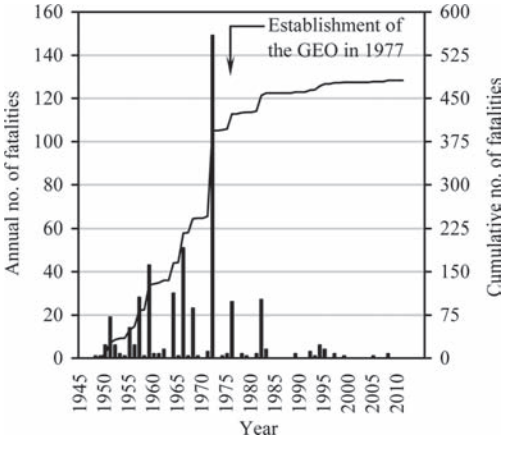

Figure 1. Historical annual landslide fatalities in Hong Kong.

order of priority and to upgrade substandard Government slopes to the required standards.

2.3 *Risk trend*

A detailed analysis of the landslide risk trend in Hong Kong is given in Wong (2009a). Two types of landslide risk trend have been assessed: historical and theoretical. They illustrate how the holistic landslide risk management framework has contributed to reducing landslide risk in Hong Kong.

Since the 1940s, documentary records have been available in Hong Kong for reliably tracing historical landslide fatalities. Figure 1 shows the annual landslide fatality figures. Although historical fatalities reflect the risk that has actually been realised, they do not necessarily represent the true (or theoretical) level of landslide risk, because such figures are affected by the actual rainfall conditions, spatial distribution of heavy rain with respect to that of existing facilities, near-miss events, etc. QRA has therefore been applied in Hong Kong to quantify the levels of theoretical landslide risk. The historical and theoretical landslide risk trends in Hong Kong are further described in Section 5.2 below.

3 CLASSIFICATION OF LANDSLIDES

Proper classification of landslides is important for risk assessment and management. Common practice is to classify landslides based on either the physical characteristics of the slope (e.g. whether man-made or natural; whether cut slope or fill slope) or the landslide mechanism (e.g. whether sliding, liquefaction or washout; whether debris flow or slide or avalanche). Proper classification prevents fundamentally different landslide types and their related data from being lumped together. As different fault trees and event trees are involved in assessing the risks of different types of landslides, mixing them together is not conducive to meaningful analysis and diagnosis of risk patterns and trends.

Factors other than physical characteristics could also be critical to landslide classification. For example, the landslide susceptibility of cut slopes formed before and after 1977 in Hong Kong is markedly different due to different levels of geotechnical input in their design and construction. Changes in slope design standards and processing systems applied to slopes should also be taken into account in the classification of slopes and landslides.

In terms of landslide classification, three notable categories of landslides have contributed to the landslide risk in Hong Kong: (i) landslides induced by construction activities, (ii) landslides triggered by heavy rain on slopes that do not meet engineering standards, and (iii) landslides under severe weather conditions, on slopes that meet engineering standards. The answers to the question about whether landslide risk is quantifiable and manageable are different for each of the categories. Their respective risk quantification and management issues for each class of landslides are explored in the following sections.

4 LANDSLIDES INDUCED BY CONSTRUCTION ACTIVITIES

4.1 *Description of problem*

Construction activities that are improperly carried out may cause failure of both temporary and permanent slopes. Slopes that are poorly designed or built may fail during or soon after its formation. Construction activities such as unauthorised excavation may also cause failure of the adjacent slopes even if the slopes have been designed to a high safety standard. Such failures could involve system deficiency (e.g. poor design guidelines and construction practice), malpractice (e.g. unauthorised construction activities), and human error (e.g. design fault).

Heavy rainfall is often one of the aggravating factors of construction-induced landslides. The most notable example in Hong Kong is the Po Shan landslide on 18 June 1972 (Fig. 2), which resulted in the collapse of the 15-storey Kotewall Court and 67 fatalities. The cause of the landslide was attributed to poorly executed site formation works which undermined the stability of the hillside and resulted in a catastrophic failure when hit by heavy rain.

Figure 2. The Po Shan landslide on 18 June 1972.

4.2 *Risk quantification*

The risk of construction-induced landslides is very difficult to quantify. Such landslides are typically the result of multiple causes that are highly variable. In many historical cases, the causes of failure are poorly documented and detailed design information is not available. As construction practice evolves with time, so do construction problems. There is often a lack of reliable data that can be consistently analysed for landslide frequency assessment. Risk quantification of this kind of failures has therefore not been conducted in Hong Kong, with the narrow exception of a preliminary review of trench excavation-induced failures by Kwong (2003). While construction-induced landslides are also commonplace in other parts of the world, to the author's knowledge, there is hardly any systematic, comprehensive risk quantification carried out.

4.3 *Risk management*

Despite the difficulty in risk quantification, the risk of construction-induced landslides is nonetheless manageable. The primary factors causing such landslides are reasonably well understood and can be regulated by improved system and practice.

This has been done in Hong Kong through the geotechnical control of Government and private developments. All permanent geotechnical works including man-made slopes and retaining walls formed under public works developments are submitted to the GEO for checking (ETWB 2002), and there is also an established independent checking system for temporary works. Geotechnical control over private developments is also exercised by the GEO through the statutory powers of the Buildings Authority. Design submissions made by developers or owners are subject to approval before construction commences.

Geotechnical control needs to be supported by regulatory and administrative systems to ensure effective enforcement. Also of importance is good professional ethics and accountability in upholding good practice in design and construction.

Given the system in place, extensive landslides triggered by construction activities are no longer expected in Hong Kong. However, the possibility of isolated incidents arising from unforeseen circumstances or exceptional irregularities at individual sites cannot be entirely ruled out. Also, smaller failures may still result from localised unauthorised construction, e.g. in squatter and village areas.

5 LANDSLIDES TRIGGERED BY HEAVY RAIN, ON SLOPES THAT DO NOT MEET ENGINEERING STANDARDS

5.1 *Description of problem*

On average, approximately 300 landslides are reported in Hong Kong every year, most of which involve failure of substandard man-made slopes triggered by rain when the Landslip Warning is in force. Issue of Landslip Warning is decided by the GEO based on rainfall forecasts from the Hong Kong Observatory and the landslide frequency-rainfall model established by the GEO using historical data. Normally three to four Landslip Warnings are issued in Hong Kong every year. The rainfall concerned is heavy, but usually not extreme.

Slopes not meeting engineering standards refer to unengineered man-made slopes formed without proper geotechnical design and control. This occurred prior to the establishment of the GEO in 1977. In those days, slopes in Hong Kong were designed and formed empirically by experience: cut slopes typically constructed to 55° and fill embankments to 35° were deemed to be satisfactory. A total of 39,000 sizeable unengineered slopes (>3 m high) have been registered in the GEO's catalogue of man-made slopes. After 1977, good practice and regulatory system were put in place, which virtually eliminated the formation of new substandard slopes. However, due to the presence of the large number of these old unengineered slopes, they are the principal source of landslide risk in Hong Kong after 1977.

A notable example of failure of unengineered slope triggered by heavy rainfall was the collapse of a fill embankment at Sau Mau Ping in 1976 where landslide debris punched through the ground floor of Block 9 of Sau Mau Ping Estate

Figure 3. Fill slope failure at Sau Mau Ping on 25 August 1976.

killing 18 people (Fig. 3). Subsequent investigation revealed that the loose sandy fill materials in the surface 3 m of the slope had undergone liquefaction failure when it became saturated in the heavy rain (Morgenstern 1978).

Natural hillsides that have marginal stability and are active in landsliding may also fall into this category. From the interpretation of the comprehensive inventory of historical aerial photographs, it is found that an average of about 300 natural terrain landslides occur on the natural terrain in Hong Kong each year. However, most of these landslides do not result in any major consequences and are not reported to the GEO.

5.2 *Risk quantification*

The landslide risk associated with this kind of slopes can be more readily quantified, provided that comprehensive data are available on:

i. historical landslides, their locations, time, scale and consequence; and
ii. the characteristics of the slopes, i.e. their type, size, gradient, etc.

The above conditions are favourably met in Hong Kong, which renders risk quantification practicable. Comprehensive and good quality failure data are available, and all existing, sizeable man-made slopes have been registered and surveyed. In Hong Kong, the instability problem of this category of slopes is principally controlled by the deficiency of empirical-based design, which displays a probabilistic pattern of failure associated with: (i) presence of geological weaknesses, and (ii) occurrence of heavy rain. Historical landslide data, together with local knowledge and information on ground and rainfall conditions, provide a good basis for analysing both of these factors, and thereby establishing the frequency of landslides. The numerous historical landslide data together with detailed inventory of slopes and the facilities affected in the event of failure also enable the development and application of landslide consequence models for quantifying the consequence of failure (Wong et al. 1997).

Global QRA has regularly been carried out to quantify the landslides risks for this category of slopes, as an integral part of landslide risk management in Hong Kong. The effect of construction activities is excluded in the quantification of rainfall-induced landslides for this category of slopes, given that landslide risk from construction activities has been largely managed.

Figure 4 shows the rolling 15-year average values of the annual fatalities, which depict the historical landslide risk trend in Hong Kong. Figure 5 presents diagrammatically the calculated

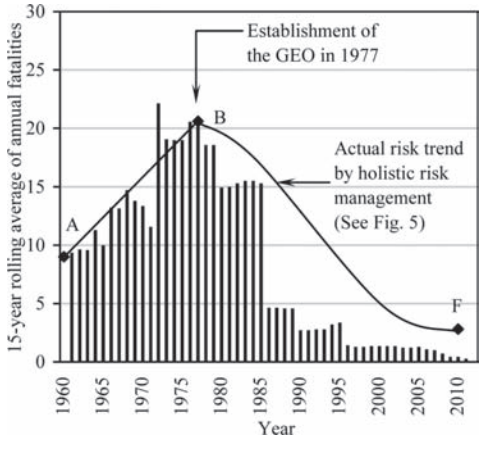

Figure 4. 15-year rolling average of historical annual landslide fatalities in Hong Kong.

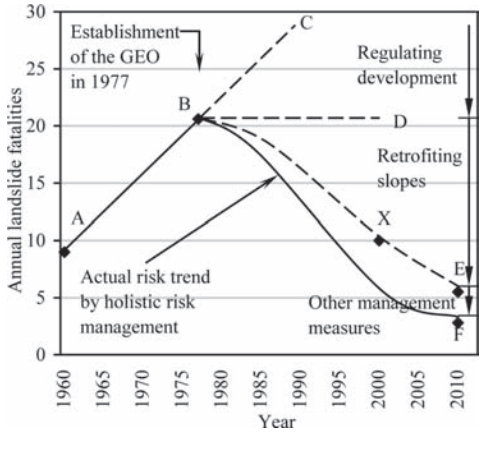

Figure 5. Landslide risk trends in Hong Kong.

landslide risk trend for this category of slopes in Hong Kong, as assessed by global QRA.

In 1977, territory-wide geotechnical control was introduced by the GEO to ensure that newly formed slopes in Hong Kong are designed and built to the required standards of safety. Since then, the increasing risk trend has levelled off, i.e. turned from line BC to line BD in Figure 5, despite that an additional more than 20,000 sizeable man-made slopes have been formed as a result of urban development in Hong Kong. Since 1977, the outcome of the retrofitting effort under the LPM Programme is progressive risk reduction along Line BE (Fig. 5). From a global QRA, the calculated overall landslide risk in year 2000 is 50% of that in 1977 (Cheung & Shiu 2000), i.e. Point X in Figure 5. It was also found that by year 2010, the retrofitting works should have brought the overall risk level to within 25% of that in 1977 (Cheng 2011), i.e. Point E.

The global QRA conducted on the unengineered slopes in Hong Kong has given results with good reliability, as is also illustrated by the good match of the calculated risk figures with the historical landslide risk trend (Fig. 4).

Wong (2005) also describes the application of QRA at individual sites in Hong Kong, for the quantification and management of the risk at site-specific level. In general, given the use of the same set of data, the reliability of the risk quantification would decrease from global to site-specific QRA. Hence, in practice, site-specific QRA normally calls for more detailed information and assessment.

5.3 *Risk management*

Hong Kong's Slope Safety System is instrumental in its success in managing landslide risks arising from old substandard slopes. This has however not come easily. The process has called for a strong commitment in resources, time and strategy. In contrast with forming new slopes that are up to standard, retrofitting existing substandard ones is resource-demanding and is subject to many other engineering, environmental and social constraints. It takes a long time to achieve notable results. A system manager, a role taken on by the GEO, is required to devise good strategy and organisation, involving the compilation of catalogues, prioritisation, systematic study and retrofitting, etc.

Global QRA has been successfully used to identify the scale of the landslide problem and to facilitate the formulation of strategy and prioritisation. It has formed the basis for resource allocation and assessment of relative priority between different slope types under the LPM and LPMit Programmes, as incorporated into the prevailing risk-based priority ranking system.

On natural terrain, the distribution of risk amongst different types of catchments has been assessed, including open slopes, topographic depression and channelised debris flow (Wong et al. 2006, Cheng & Ko 2010). These results have been instrumental in formulating the post-2010 LPMit Programme, which implements risk mitigation works for 30 natural hillside catchments annually apart from retrofitting old man-made slopes.

Global QRA has also provided useful figures on the amount of risk reduction achieved and the effectiveness of risk management effort, which aids risk communication.

Site-specific QRA, on the other hand, facilitates a rational consideration of risk tolerability and evaluation of risk mitigation strategy at a particular locality. This is where state-of-the-art quantified risk management is usefully applied. For example, a natural terrain landslide hazard study has been carried out at Sha Tin Heights, Hong Kong (Fig. 6) following six landslides in 1997, three of which developed into debris flows that affected residential buildings. QRA was used to evaluate the acceptability of risk levels (Fig. 7) and the cost effectiveness of risk mitigation strategies. Risk mitigation works were completed in 2004.

In parallel, besides landslip prevention and mitigation works, non-works measures such as public education, landslide warning, etc. have helped reduce the consequence of landslides. The GEO runs a public education and publicity campaign on slope safety to promulgate the importance of slope maintenance and educate the public on personal precautionary measures to be taken during heavy rainstorms. The GEO also provides a 24-hour emergency service to attend to landslip incidents and to advise on emergency and follow-up actions,

Figure 6. Residential buildings affected by landslide hazards at Sha Tin Heights (after Wong & Ho 2005).

such as building evacuation and road closure, to minimise the impact of landslides on the public.

The non-works initiatives form an integral part of holistic landslide risk management. They have proven to be effective in reducing the landslide risk to the ALARP level. This is shown diagrammatically as Line BF in Figure 5, reflecting a further reduction in landslide risk from the theoretical level (Line BE) that accounts only for the effect of slope retrofitting works. Over the past 20 years, the actual annual landslide fatalities in Hong Kong have been consistently less than the theoretical risk level by at least 50%. The overall risk trend suggests that the contribution of the non-works initiatives to reduction of landslide risk in Hong Kong could be fairly significant. As an illustration, in the past 20 years, the number of Landslip Warnings issued, landslide incidents reported, buildings and people temporarily evacuated, and sections of road closed as a result of the landslide emergency responses of the GEO and the community are shown in Table 2.

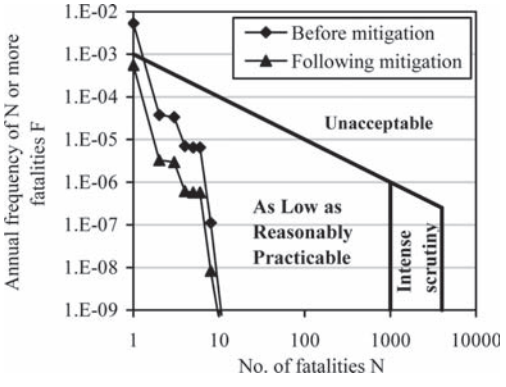

Figure 7. Comparison of societal risk in terms of F-N pairs with societal risk criteria at Sha Tin Heights. societal risk was reduced from 5.67×10^{-3} PLL/year to 4.44×10^{-3} PLL/year following the implementation of risk mitigation measures (after Fugro Maunsell Scott Wilson JV 2004).

6 LANDSLIDES UNDER SEVERE WEATHER CONDITIONS, ON SLOPES THAT MEET ENGINEERING STANDARDS

6.1 *Description of problem*

An account of the key lesson learnt from the systematic landslide investigation in Hong Kong that engineered slopes still have a finite chance of failure is given in Wong & Ho (2003). Such failures are typically related to the progressive degradation of man-made slopes under repeated rainfall conditions or to geological defects not identified in slope design by the current state of knowledge and practice.

Table 2. Breakdown of landslides affecting different facilities in Hong Kong since 1994.

Year	No. of landslip warning issued	No. of reported landslide incidents	No. of buildings* evacuated			No. of sections of road affected/closed
			Block	House	Flat/unit	
1994	4	436	4	24	207	225
1995	6	295	5	8	170	163
1996	2	153	0	7	58	87
1997	8	491	0	19	176	253
1998	1	216	0	6	43	120
1999	3	402	4	10	128	166
2000	6	322	0	3	15	184
2001	8	214	0	6	48	98
2002	3	138	0	7	5	73
2003	1	201	0	2	3	98
2004	2	69	0	0	3	18
2005	2	481	7	4	46	219
2006	4	193	0	1	8	85
2007	1	83	0	0	4	36
2008	5	849	1	22	80	420
2009	2	124	0	0	2	45
2010	3	266	0	0	7	93
2011	0	99	0	0	0	27

*A 'block' is a multi-storey building, which may comprise up to several dozen of flats/units. A 'house' is typically within 3 storeys, which comprises several flats/units.

Between 1997 and 2002, 106 landslide incidents involved man-made slopes with past geotechnical engineering input and geotechnical design submissions checked and accepted under the slope safety system, 24 of which were major failures (i.e. ≥50 m^3 in volume). All the 106 failures were subject to the GEO's detailed landslide investigation to enable a systematic diagnosis of the probable causes of failure. Of the 106 cases, 53 affected engineered soil cut slopes, 15 of which were major failures. All these 53 failures involved unsupported soil cuts, with no structural support such as soil nails or earth retaining structures. The comprehensive analysis showed such engineered man-made slopes that were formed with old technology before the 1990s, known as 'old technology slopes' in Hong Kong, are not sufficiently robust in withstanding degradation and could fail under severe rainfall conditions.

During the severe rainstorms between May and July 2008, 28 landslides occurred on engineered man-made slopes, of which two were major failures (Li et al. 2012). The one at Pak Fuk Road was an unsupported soil cut slope formed between 1976 and 1980. The one at Tsing Yi Road involved a wedge failure in its rock portion. These failures on engineered slopes are typical of the residual landslide risk problem associated with old technology slopes in Hong Kong.

Unengineered slopes have a much higher failure frequency than engineered ones, and they tend to show instability under much less intense rainfall. In contrast, the risk of failure of engineered slopes tends to become evident under severe rainfall conditions. The dire consequences of such failures can be illustrated by the following two examples:

i. The 13 August 1995 landslide at Fei Tsui Road (GEO & Knill 1996) involved a large-scale failure (14,000 m^3) of a 27 m high engineered cut slope that had no structural support (Fig. 8). A total of 370 mm rainfall was recorded at the site within 24 hours before the landslide, and the 31-day rainfall of 1303 mm exceeded the highest calendar monthly rainfall ever recorded by the rain gauge at the Hong Kong Observatory since records began in 1884. The landslide consisted of a translational failure with the detached ground mass sliding on a surface dipping gently out of the slope. Large failures of this type are unusual in Hong Kong. The post-failure investigation established that the basal slip surface of the landslide developed along a laterally extensive (>50 m) weak layer of kaolinite-rich altered tuff, which was about 15 m below the crest of the cut slope and dipping out of the slope at about 10° to 25°. The failure caused one fatality.
ii. The adverse effect of significant geological defects on slopes previously subjected to engineering studies was evident in the Shek Kip Mei landslide of 25 August 1999 (Fugro Maunsell Scott Wilson JV 2000). The 4-day rainfall before the landslide was most severe, with a total of 641 mm of rain and was the heaviest recorded since slope formation. The slope displaced forward by about 1 m at the slope toe. The total volume of the displaced mass was about 6000 m^3. A laterally-persistent (over 60 m long) discontinuity dipping at a shallow angle out of the slope formed the basal plane of the southern part of the landslide. This discontinuity was infilled with polished, slickensided kaolin and manganese oxide deposits up to 15 mm thick only (Fig. 9), which was not mapped in the past geotechnical studies. As a result of the landslide, two public housing blocks were permanently evacuated.

Figure 8. Failure of cut slope at Fei Tsui Road on 13 August 1995.

Natural terrain in Hong Kong also exhibits instability that resembles this category of landslide problem, in that natural terrain tends to respond vigorously to severe rainfall. Ko (2005) established from detailed rainfall and natural terrain landslide correlations that the density of natural terrain landslides increases exponentially with rainfall intensity (Fig. 10). Under moderate to heavy rainfall conditions, there are generally few failures on natural terrain in Hong Kong. However, when rain becomes severe, e.g. when 20% or more of the average annual rainfall is recorded within 24 hours, widespread natural terrain landslides tend to occur. For instance, in the June 2008 rainstorm, Lantau Island was subjected to a maximum of 623 mm rainfall in 24 hours, with a statistical return period of about 200 years. The 4-hour rainfall of 384 mm in the rainstorm was most severe, which measured over 1000-year return period. More than 2400 natural terrain landslides occurred during the

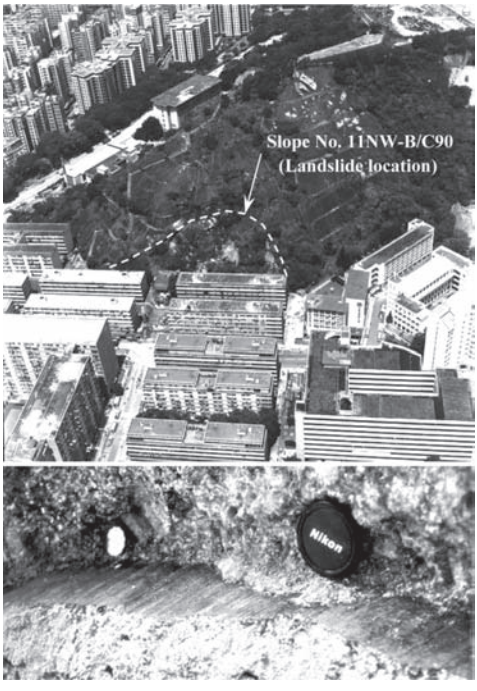

Figure 9. Failure of cut slope at Shek Kip Mei on 25 August 1999 (top); laterally persistent discontinuity infilled with slickensided kaolin and manganese oxide deposits (bottom).

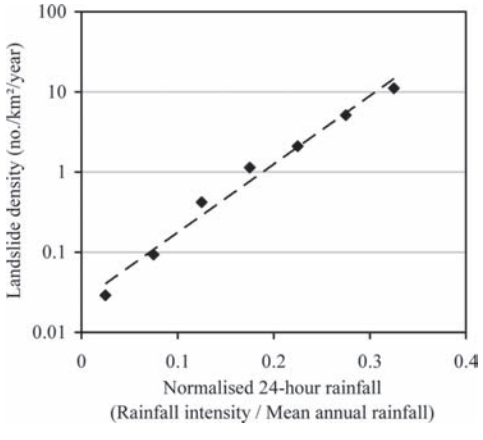

Figure 10. Correlation between rainfall and natural terrain landslide density.

rainstorm (Fig. 11). Furthermore, it was evident that the scale of the natural terrain landslides and the mobility of the landslide debris also increased drastically under such extreme rainfall (Wong 2009b).

Figure 11. Natural terrain landslides at Tung Chung, Lantau Island during the June 2008 rainstorm.

6.2 *Risk quantification*

Quantifying the landslide risk under severe weather conditions is difficult and is subject to significant uncertainty. First, only limited data are available on the landslide frequency in severe rainfall conditions, given the limited observation period for relatively rare events. For instance, the current natural terrain landslide inventory maintained by the GEO is primarily based on low-level aerial photographs which reveal historical natural terrain landslides over the past 60 years. Caution is needed when using the historical data as a basis for assessing extreme, or low-frequency-high-magnitude events by simple projections. Large and mobile landslides are potentially underrepresented.

Second, the quantification of landslides occurring during severe weather conditions requires extensive extrapolation, which increases uncertainty. There is little information available on the presence and extent of geological defects that could subvert slope stability, even for man-made slopes that have been properly engineered. The phenomenon and process of slope degradation are not well understood. There is limited knowledge of how landslide scale and mobility increase under extreme rainfall conditions.

Third, effects of climate changes could alter both the frequency of occurrence as well as the severity of extreme rainfall conditions. However, this is an area awaiting further study and analysis to ascertain the effects, their potential influence on the severity and frequency of extreme rainfall, and how slope instability would respond to such changes.

In short, risk quantification may be attempted for landslide risk under severe weather conditions but the findings should be interpreted with care and with due consideration of the significant uncertainty involved.

6.3 *Risk management*

Managing landslide risks that may be brought about by severe weather conditions poses some of the greatest challenges for the geotechnical profession today. The difficulty is two-fold. Firstly, the

uncertainties in risk quantification reflect the lack of understanding of the nature and severity of the problem, which hinders the formulation of risk management strategy and deployment of resources. Secondly, given the present state of knowledge and technology, pragmatic solutions to curb landslides in extreme weather conditions may not always be available.

For man-made slopes, robust design solutions have already been adopted in Hong Kong. This includes the use of structural support such as soil nailing and prescriptive measures such as enhanced drainage provisions. Engineered slopes formed with old technology could be vulnerable to failure in severe rainfall conditions. However, it is notable that no mobile, high consequence or major failures have occurred on soil nailed cut slopes in Hong Kong to date. This indicates the robustness of soil nailed systems in preventing large scale instability even in the face of severe weather conditions. Minor failures do occur, and these may be reduced by improved slope surface protection and drainage measures (Ng et al. 2008).

For natural terrain landslides, on the other hand, existing technology has limited capability in coping with the hazards that may arise under severe rainfall conditions. There is thus a pressing need for the development of better mitigation measures and innovative solutions. Some thoughts on enhanced risk management and mitigation strategy for natural terrain arising from observations and lessons learnt from the June 2008 rainstorm are given in Wong (2009b). For instance, in dealing with sizeable debris flows exceeding several thousand cubic metres, there may be a need to explore the use of multiple layers of debris resisting barriers rather than a single layer.

Non-works options will also continue to feature prominently in the management of landslide risk under severe weather conditions, including public education, landslip warning and emergency preparedness as discussed earlier. At the same time, closer collaboration with the meteorological profession is required in assessing the effects of climate change and its implications in slope safety.

7 CONCLUDING REMARKS ON RISK QUANTIFICATION AND MANAGEMENT

A range of factors affect the practicability of risk quantification. These need to be evaluated before deciding whether or not it is practicable to perform QRA and whether or not risk quantification can be expected to give reliable results. Even where it is possible to quantify the risk, it is important not to lose sight of the degree of uncertainty involved.

Proper classification, including consideration of both the physical and system aspects of the landslide hazards, is important in risk quantification and management. Different types of landslides should not be lumped together in analysis. The availability of good documentation and data of historical landslides and slopes are prerequisites to QRA.

The main challenge in risk quantification often lies with the assessment of landslide frequency (including the scale and mobility of failure). Consequence assessment is generally less difficult, although existing consequence models do warrant further review of their applicability and reliability under different circumstances. This is beyond the scope of this paper.

It is possible to manage landslide risks without quantification, but risk quantification can undeniably aid risk management. The problem of construction-induced landslides in Hong Kong illustrates how the multiple uncertainties involved could render risk quantification difficult, even though there are a wealth of data, good understanding of landslide mechanisms and ample experience in use of QRA.

Where risks cannot be quantified with reasonable confidence, it is difficult to apply the quantified risk assessment and management framework. However, the relevant risk assessment principles and considerations are still useful in general terms. Applied in a qualitative manner together with expert judgment, they can still facilitate management of risk.

In Hong Kong, the risk of rainfall-induced landslide on old, unengineered slopes has been reduced to a low level. As the risk level reduces, risk quantification becomes increasingly sensitive to the uncertainties involved. In the past, this category of landslides was the predominant component of the overall landslide risk in Hong Kong. Upon reduction of the risk to a relatively low level, other factors have come into play, e.g. the effect of construction activities and risk associated with extreme weather conditions, which originally would not contribute significantly to the overall landslide risk.

Therefore, it may become more difficult and unreliable to further quantify the actual risk reduction that could be achieved by a certain risk management initiative, when the risk is at a low level already and is sensitive to changes associated with other factors.

Viewed from another perspective, containing risk within the ALARP level calls for continual effort to curb various factors that may increase risk. This in turn requires risk management efforts which may not necessarily achieve a noticeable or quantifiable risk reduction.

ACKNOWLEDGEMENT

This paper is published with the permission of the Director of Civil Engineering and Development, Government of the Hong Kong Special Administrative Region. Thanks are due to Mr Eugene K.L. Wong for his assistance in preparing this paper.

REFERENCES

Cheng, P.F.K. 2011. Assessment of landslide risk posed by man-made slopes as of 2010. *GEO Special Project Report No. SPR 1/2011*. Hong Kong: Geotechnical Engineering Office.

Cheng, P.F.K. & Ko, F.W.Y. 2010. An updated assessment of landslide risk posed by man-made slopes and natural hillsides in Hong Kong. *GEO Report No. 252*. Hong Kong: Geotechnical Engineering Office.

Cheung, W.M. & Shiu, Y.K. 2000. Assessment of global landslide risk posed by pre-1978 man-made slope features: risk reduction from 1977 to 2000 achieved by the LPM Programme. *GEO Report No. 125*. Hong Kong: Geotechnical Engineering Office.

ETWB 2002. Geotechnical control for slopes and retaining walls. *ETWB Technical Circular (Works) No. 29/2002*. Hong Kong: Environment, Transport and Works Bureau.

Fell, R. & Hartford, D. 1997. Landslide risk management. In D. Cruden & R. Fell (eds), *Landslide Risk Assessment*: 51–110. Rotterdam: Balkema.

Fugro Maunsell Scott Wilson JV 2000. Report on the Shek Kip Mei Landslide of 25 August 1999. Hong Kong: Geotechnical Engineering Office.

Fugro Maunsell Scott Wilson JV 2004. Detailed study of the hillside area below Sha Tin Heights Road. *GEO Report No. 143*. Hong Kong: Geotechnical Engineering Office.

GEO & Knill, J. 1996. *Report on the Fei Tsui Road Landslide of 13 August 1995*. Hong Kong: Geotechnical Engineering Office.

Ho, K.K.S., Leroi, E. & Roberds, W. 2000. Quantitative risk assessment—application, myths and future direction. *Geotechnical and Geological Engineering GeoEng2000*; *Proc. intern. conf., Melbourne, 19–24 November 2000, vol. 1*: 269–312. USA: Technomic.

Ko, F.W.Y. 2005. Correlation between rainfall and natural terrain landslide occurrence in Hong Kong. *GEO Report No. 168*. Hong Kong: Geotechnical Engineering Office.

Kwong, J.S.M. 2003. A Study on Past Failures of Trench Excavations. *GEO Report No. 137*. Hong Kong: Geotechnical Engineering Office.

Li, A.C.O., Lau, J.W.C., Cheung, L.L.K. & Lam, C.L.H. 2012. Review of landslides in 2008. *GEO Report No. 274*. Hong Kong: Geotechnical Engineering Office.

Malone, A.W. 1998. Risk management and slope safety in Hong Kong. In K.S. Li, J.N. Kay & K.K.S. Ho (eds), *Slope Engineering in Hong Kong*; *Proc. 16th Annual Seminar of the HKIE Geotechnical Division, Hong Kong, 2 May 1997*: 3–17. Rotterdam: Balkema.

Morgenstern, N.R. 1978. Mobile soil and rock flows. *Geotechnical Engineering* 9: 123–141.

Ng, A.F.H., Lau, T.M.F., Shum, K.W. & Cheung, W.M. 2008. Review of selected landslides involving soil-nailed slopes. *GEO Report No. 222*. Hong Kong: Geotechnical Engineering Office.

Wong, H.N. 2005. Landslide risk assessment for individual facilities. *Landslide Risk Management*; *Proc. intern. conf., Vancouver, 31 May–3 June 2005*: 237–296. London: Taylor & Francis.

Wong, H.N. 2009a. Holistic urban landslide risk management—challenges and practice. *Keynote Lecture at the 7th Asian Regional Conference of the International Association for Engineering Geology and the Environment, Chengdu, 9–11 September 2009*.

Wong, H.N. 2009b. Rising to the challenges of natural terrain landslides. *Natural Hillsides: Study and Risk Management Measures; Proc. 29th Annual Seminar of the HKIE Geotechnical Division, Hong Kong, 17 April 2009: 15–53*. Hong Kong: Hong Kong Institution of Engineers.

Wong, H.N. & Ho, K.K.S. 2003. Lessons learnt from landslides. *Case Histories in Geotechnical Engineering in Hong Kong; Proc. 23rd Annual Seminar of the HKIE Geotechnical Division, Hong Kong, 9 May 2003*: 255–263. Hong Kong: Hong Kong Institution of Engineers.

Wong, H.N. & Ho, K.K.S. 2005. Landslide risk management and slope engineering in Hong Kong. *Proc. State-of-the-Practice of Geotechnical Engineering in Taiwan and Hong Kong, Hong Kong, 20 January 2005*: 97–136. Hong Kong: Hong Kong Institution of Engineers.

Wong, H.N., Ho, K.K.S. & Chan, Y.C. 1997. Assessment of consequence of landslides. In D. Cruden & R. Fell (eds), *Landslide Risk Assessment*; *Proc. intern. workshop, Honolulu, 19–21 February 1997*: 111–149. Rotterdam: Balkema.

Wong, H.N., Ko, F.W.Y. & Hui, T.H.H. 2006. Assessment of landslide risk of natural hillsides in Hong Kong. *GEO Report No. 191*. Hong Kong: Geotechnical Engineering Office.

This page intentionally left blank

3 *Geotechnical uncertainty and variability*

This page intentionally left blank

Geotechnical Safety and Risk IV – Zhang et al. (eds)
ISBN 978-1-138-00163-3

Quantifying epistemic uncertainty and aleatory variability of Newmark displacements under scenario earthquakes

W. Du & G. Wang
Department of Civil and Environmental Engineering, The Hong Kong University of Science and Technology, Clear Water Bay, Hong Kong SAR, China

ABSTRACT: Earthquake-induced slope displacement is an important parameter for safety evaluation and design of slope systems. Many Newmark displacement models have been recently developed using various ground motion databases and different intensity measures as predictors. In this study, the epistemic uncertainties among different models and aleatory variability of the predicted Newmark displacements are quantified. The epistemic uncertainty is represented by the variation between different model predictions. The standard deviation of the uncertainty is approximately 0.5–1 in natural log scale for scenario earthquakes of M_w 5.5–7.5, which is much larger than that of the ground motion prediction equations. This indicates further development of the Newmark displacement models is much needed. The total aleatory variability considering both GMPEs and displacement models is roughly 1.5–2.5 in natural log scale. The large epistemic uncertainty and aleatory variability imply that it is extremely important to account for both in seismic slope analysis.

1 INTRODUCTION

Newmark displacement model is commonly used to estimate the seismic performance of slopes during earthquake (Newmark, 1965). The Newmark displacement model assumes the sliding mass is rigid, and sliding occurs on a predefined interface. The critical acceleration (a_c) represents the resistance of the slope against sliding. It can be determined by the strength of material and the slope angle etc. Sliding is initialized when the shaking acceleration exceeds the critical acceleration, and the block displaces plastically along the interface. The permanent displacement D is calculated by double integrating the exceeded accelerations with respect to time (Fig. 1). Although the simple rigid-plastic model does not consider the deformation of the block itself during shaking, this method has been widely used to evaluate earthquake-induced displacement for natural slopes (Jibson 2007).

Empirical equation to estimate the Newmark displacement was first proposed by Ambraseys & Menu (1988) as a function of the critical acceleration ratio (critical acceleration a_c over the Peak Ground Acceleration PGA). Throughout years, many researchers (e.g., Jibson, 2007; Saygili & Rathje, 2008; Hsieh & Lee, 2011) have proposed various empirical equations using various ground motion Intensity Measures (IMs) as predictors, including Peak Ground Acceleration (PGA), moment magnitude of the earthquake (M), Peak Ground Velocity (PGV) *etc*. Arias intensity (Ia) is also an important predictors, as it incorporates cumulative effect of an acceleration time history and represent a measure of earthquake energy. Arias Intensity is calculated by the following equation (Travasarou & Bray, 2003):

$$Ia = \frac{\pi}{2g}\int_0^{t_{tot}} a(t)^2 dt \tag{1}$$

where g is the acceleration of gravity, $a(t)$ is the acceleration time history, and t_{tot} is the total duration of the time history.

Because different database and functional forms are used in developing these empirical prediction models, it is not surprising that these models would yield different predicted results. Uncertainty associated with the Newmark displacement models can be classified as two categories: epistemic uncertainty and aleatory uncertainty. Epistemic uncertainty is due to lack of knowledge. In principal, it can be reduced by using sufficient data or improved regression techniques. The epistemic uncertainty can be approximately evaluated by the variation of different model predictions. Aleatory variability, on the other hand, represents inherent randomness that can not be reduced. Aleatory variability is usually quantified by variation of the observed data against the model prediction. Recently, Douglas (2010, 2012) studied the consistency of

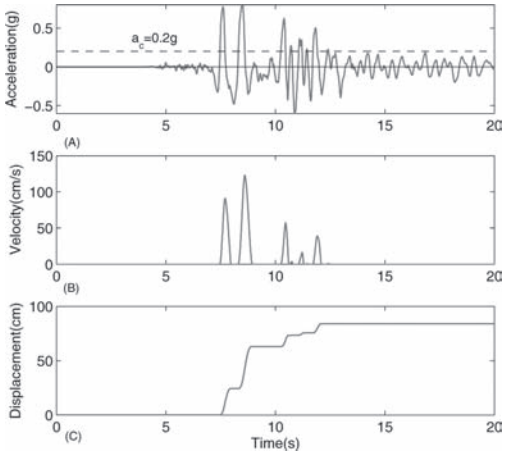

Figure 1. Illustration of Newmark displacement with critical acceleration a_c = 0.2 g. (A) Earthquake acceleration-time history. (B) Velocity of sliding block versus time. (C) Displacement of sliding block versus time.

Ground Motion Prediction Equations (GMPEs) developed in the past four decades for IMs such as PGA, PGV, Ia, etc. However, the epistemic and aleatory uncertainties of the Newmark displacement models have not yet been thoroughly investigated.

This study aims at quantifying the epistemic uncertainty and aleatory variability of Newmark displacement models. Ten recently developed Newmark displacement models are used in this study and listed as follows:

1. [PGA] RS08 model (Saygili & Rathje, 2008):

$$\ln D = 5.52 - 4.43\left(\frac{a_c}{PGA}\right) - 20.39\left(\frac{a_c}{PGA}\right)^2 + 42.61\left(\frac{a_c}{PGA}\right)^3 - 28.74\left(\frac{a_c}{PGA}\right)^4 + 0.72\ln(PGA)$$
$$\sigma_{\ln D} = 1.13 \quad (2)$$

2. [PGA, Ia] RS08 model (Saygili & Rathje, 2008):

$$\ln(D) = 2.39 - 5.24\left(\frac{a_c}{PGA}\right) - 18.78\left(\frac{a_c}{PGA}\right)^2 + 42.01\left(\frac{a_c}{PGA}\right)^3 - 29.15\left(\frac{a_c}{PGA}\right)^4 - 1.56\ln(PGA) + 1.38\ln(Ia)$$
$$\sigma_{\ln D} = 0.46 + 0.56\left(a_c/PGA\right) \quad (3)$$

3. [PGA, PGV] RS08 model (Saygili & Rathje 2008):

$$\ln D = -1.56 - 4.58\left(\frac{a_c}{PGA}\right) - 20.84\left(\frac{a_c}{PGA}\right)^2 + 44.75\left(\frac{a_c}{PGA}\right)^3 - 30.5\left(\frac{a_c}{PGA}\right)^4 - 0.64\ln(PGA) + 1.55\ln(PGV)$$
$$\sigma_{\ln D} = 0.41 + 0.52\left(a_c/PGA\right) \quad (4)$$

4. [PGA, Ia, PGV] RS08 model (Saygili & Rathje 2008):

$$\ln(D) = -0.74 - 4.93\left(\frac{a_c}{PGA}\right) - 19.91\left(\frac{a_c}{PGA}\right)^2 + 43.75\left(\frac{a_c}{PGA}\right)^3 - 30.12\left(\frac{a_c}{PGA}\right)^4 - 1.3\ln(PGA) + 1.04\ln(PGV) + 0.67\ln(Ia)$$
$$\sigma_{\ln D} = 0.2 + 0.79\left(a_c/PGA\right) \quad (5)$$

5. [PGA, M] RS09 model (Rathje & Saygili, 2009):

$$\ln(D) = 4.89 - 4.85\left(\frac{a_c}{PGA}\right) - 19.64\left(\frac{a_c}{PGA}\right)^2 + 42.49\left(\frac{a_c}{PGA}\right)^3 - 29.06\left(\frac{a_c}{PGA}\right)^4 + 0.72\ln(PGA) + 0.89(M_w - 7)$$
$$\sigma_{\ln D} = 0.73 + 0.79\left(a_c/PGA\right) - 0.54\left(a_c/PGA\right)^2 \quad (6)$$

6. [PGA] J07 model (Jibson, 2007):

$$\log_{10}(D) = 0.215 + 2.341\log_{10}\left(1 - \frac{a_c}{PGA}\right) - 1.438\log_{10}\left(\frac{a_c}{PGA}\right)$$
$$\sigma_{\log_{10} D} = 0.51 \quad (7)$$

7. [PGA, M] J07 model (Jibson, 2007):

$$\log_{10}(D) = -2.71 + 2.335\log_{10}\left(1 - \frac{a_c}{PGA}\right) - 1.478\log_{10}\left(\frac{a_c}{PGA}\right) + 0.424\,\mathrm{M}_w$$
$$\sigma_{\log_{10} D} = 0.454 \quad (8)$$

8. [Ia] J07 model (Jibson, 2007):

$$\log_{10}(D) = 2.401\log_{10}(Ia) - 3.481\log_{10}(a_c) - 3.23$$
$$\sigma_{\log_{10} D} = 0.656 \tag{9}$$

9. [PGA, Ia] J07 model (Jibson, 2007):

$$\log_{10}(D) = 0.561\log_{10}(Ia) - 3.833\log_{10}\left(\frac{a_c}{PGA}\right) - 1.474$$
$$\sigma_{\log_{10} D} = 0.616 \tag{10}$$

10. [Ia] HL11 model (Hsieh and Lee, 2011):

$$\log_{10}(D) = 0.847\log_{10}(Ia) - 10.62a_c + 6.587a_c\log_{10}(Ia) + 1.84$$
$$\sigma_{\log_{10} D} = 0.295 \tag{11}$$

Among these equations, the unit of the Newmark displacement D is cm; PGA and a_c are in the unit of g; PGV is in the unit of cm/s; and Ia is in the unit of m/s. [PGA] RS08, [PGA] J07, [Ia] J07, [Ia] HL11 models employs only a single IM as the predictor. Therefore, they are called scalar models. The other models employ a combination of more than one IMs (PGA, Ia or PGV), and they are called vector models.

2 EPISTEMIC UNCERTAINTY OF NEWMARK DISPLACEMENT MODELS

In this study, epistemic uncertainty of the above Newmark displacement models will be studied. Earthquake scenarios considered in the analysis are moment magnitude (M_w) 5.5, 6.5 and 7.5 events on a strike-slip fault. The site condition is assumed to be a stiff soil site with $V_{s30} = 400$ m/s. Four Next Generation Attenuation (NGA) GMPEs are used to predict PGA and PGV (Abrahamson & Silva, 2008; Boore & Atkinson, 2008; Campbell & Bozorgnia, 2008; Chiou & Youngs, 2008). The GMPEs proposed by Travasarou & Bray (2003), Foulser-Piggott & Stafford (2012) and Campbell & Bozorgnia (2012) are chosen for predicting Ia. In order to minimize the influence of epistemic uncertainty existed in the GMPEs, the predicted median IMs are averaged as the input to predict the median Newmark displacements. By this way, the epistemic uncertainty and aleatory variability in the GMPEs are neglected.

Figure 2 shows the predicted median sliding displacements versus rupture distances assuming a_c = 0.1 g and M_w equals 7.5, 6.5 and 5.5, respectively. It can be observed that the predicted

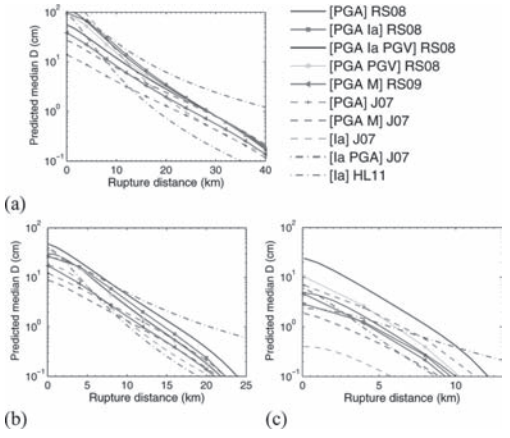

Figure 2. Median predicted displacements by various Newmark displacement models for (a) M_w 7.5 (b) M_w 6.5 (c) M_w 5.5 earthquake on a strike-slip fault. Note: for each scenario, the average of the predicted median IMs are used as input parameters.

displacements by different Newmark displacement models vary significantly for a given scenario. For example, the estimated median displacement ranges from 4 cm to 24.6 cm for M_w 7.5 at the rupture distance of 10 km. As rupture distance increases, all the predicted sliding displacement decreases as expected. Epistemic uncertainty is expected to be higher if the predicted values among these models are more scattered. From the figures, the predicted displacements (in log scale) are more scattered as rupture distance increases, especially for smaller magnitude events. This is mainly due to specific functional forms chosen by different models. Some models decays much faster as rupture distance increases. Since very small displacement values are not of engineering significance, it is more rational to focus only on large displacement amplitudes. Figure 3 shows the standard deviations of the predicted median displacements by these models for three scenarios. The standard deviations among predicted values are in the range of 0.5–1 (in natual log scale) for all three scenarios. The M_w 6.5 scenario shows the smallest epistemic uncertainty and the M_w 5.5 event has the largest uncertainty, which is constantly greater than 1 if all Newmark displacement models are considered. This is not unexpected since that the number of larger magnitude events ($M_w > 6$) is usually dominant in the ground motion databases that are used to develop the Newmark displacement models. In addition, the epistemic uncertainty among six vector models are much smaller than that of four scalar models for all cases considered, as shown in Figure 3. In general, the standard deviation of vector models is in the range of 0.4–0.6 (in natural log

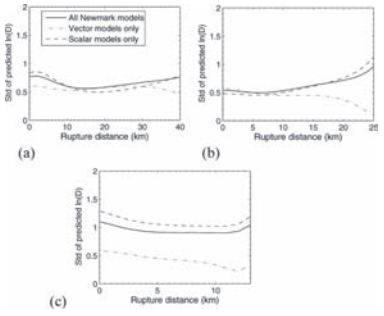

Figure 3. Standard deviations of the median Newmark displacements (in natural log scale) predicted by the ten Newmark displacement models: (a) For a M_w 7.5 strike-slip earthquake; (b) For a M_w 6.5 strike-slip earthquake; (c) For a M_w 5.5 strike-slip earthquake. Same as Figure 2, the average of the median predicted IMs by various GMPEs are used as input IMs.

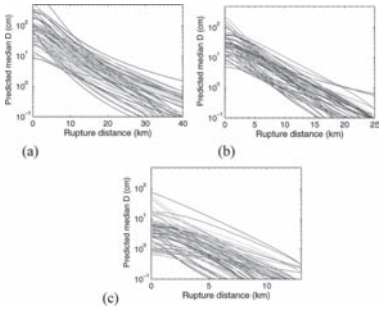

Figure 4. Variation of the displacements predicted by various GMPEs and Newmark displacement models, for (a) M_w 7.5 (b) M_w 6.5 (c) M_w 5.5 strike-slip earthquakes.

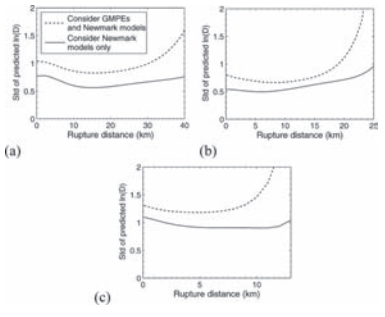

Figure 5. Standard deviations of predicted displacements in natural log scale, considering epistemic uncertainty of both GPMEs and Nemwark displacement models, or considering only epistemic uncertainty of Newmark displacement models, for (a) M_w 7.5 (b) M_w 6.5 (c) M_w 5.5 strike-slip earthquakes.

scale) for various scenarios. This reveals that the vector models can provide more consistent results by using multiple IMs. The vector IMs represent different aspects of ground motion properties and provide more information about the ground motion characteristics.

Furthermore, epistemic uncertainties of both GMPEs and Newmark displacement models are considered in the following analysis. Instead of applying the averaged median IMs to compute sliding displacements as before, the predicted median IMs are chosen from different GMPEs (one from four NGA models for PGA, PGV, and one from three GMPEs for Ia) to compute the median sliding displacement using 10 Newmark displacement model, as shown in Figure 4. All together, there are 120 ($4 \times 3 \times 10$) combinations of displacements in each subplot. The displacements are hugely scattered, indicating that selection of different GMPEs and Newmark displacement models would significantly influence the final results. For example, the estimated median displacement ranges from 2 cm to 60 cm for M_w 7.5 at the rupture distance of 10 km. Figure 5 shows the standard deviations of displacements (in natural log scale) shown in Figure 4. The standard deviations by considering both epistemic uncertainties existed in GMPEs and Newmark displacement models is generally 20% larger then the previous analysis by only considering the epistemic uncertainty of the Newmark displacement models. The standard deviation obtained from the latter is generally 20% larger than the former case. The results are consistent with recent studies on the epistemic uncertainty of IMs. The reported standard deviations of the epistemic uncertainty for PGA, PGV and Ia are approximately 0.2–0.4 in the natural log scale (Douglas, 2010; 2012). The epistemic uncertainty of the Newmark displacement models appears to be much larger than that of the GMPEs, probably due to inherent difficulty to correlate the sliding displacements with IMs using simple function forms. It calls for more research efforts to be placed to develop more advanced Newmark displacement models in the future.

3 ALEATORY VARIABILITY OF NEWMARK DISPLACEMENT MODELS

The aleatory variability of Newmark displacement models is also compared for given earthquake scenarios. Although vector models usually reported a smaller standard deviation compared with the scalar models by incorporating more predictors, inclusion of additional IMs may also induce extra variability in the IMs themselves. Therefore, the total aleatory variability of the Newmark displacement for a scenario earthquake should count for contributions from aleatory variability in GMPEs and that in Newmark ground motion models.

Monte-Carlo simulation is used to evaluate the total aleatory variability of the Newmark displacement for a given scenario earthquake. First, 100 sets of correlated vector IMs are generated for a specific scenario. The vector IMs are assumed to follow multivariate lognormal distribution with mean and standard deviation specified by GMPEs. For vector models, the joint occurrence of multiple IMs is specified by the empirical correlations between them. The correlation coefficients among PGA, PGV and Ia are specified as ρ(PGA, Ia) = 0.88, ρ(PGA, PGV) = 0.69 and ρ(Ia, PGV) = 0.74 (Campbell and Bozorgnia, 2012), respectively. Secondly, for each set of vector IMs, 100 Newmark displacement values are simulated by assuming the displacements follow a lognormal distribution. The standard deviation of the resulted 10000 displacement values is then calculated to estimate the total aleatory variability for each Newmark displacement model. It is noted that very small displacement values have to be excluded, since they are of little engineering importance but appear to be highly scattered in log scale. Figure 6 shows the obtained total standard deviations versus rupture distances for different Newmark displacement models by only considering displacement values greater than 0.001 cm. Quite similar trend can be observed for both magnitudes considered. Generally speaking, the total standard deviations (in natural log scale) fall in the range of 1.5–2.5 for different models, which implies that the displacement distribution is significantly scattered for each scenario. For example, although the reported standard deviation is 0.295 in $\log_{10}$ scale (0.68 in natural log scale) for the [Ia] HL11 model, the total standard deviation of displacements is as high as 1.5 in natural log scale, due to large standard deviation of Ia ($\sigma_{lnIa} \approx 1$).

If the cutoff displacement value is set as 1 cm, which is the recommended upper bound for negligible displacement by Bray & Travasarou (2007), the total standard deviations versus rupture distances are shown as Figure 7. In this case, the standard deviations are generally smaller compared with the values shown in Figure 6. This is expected since the scatter of larger displacement values would be inevitably smaller in the log scale. The standard deviations decreases as separation distance increases, which are approximately within the range of 1–1.5 for most models. The total aleatory variability appears to be rather consistent for all vector models and scalar models. This is a favorable result since the aleatory variability is the inherent randomness. In principle, it should not change significantly from model to model.

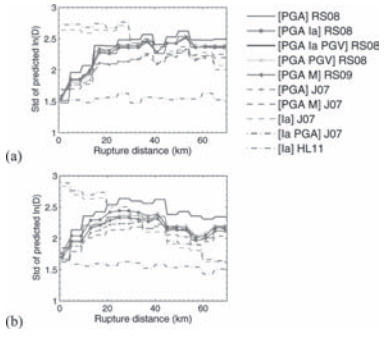

Figure 6. Standard deviations considering aleatory variability of GMPEs and Newmark displacement models, for (a) M_w 7.5 (b) M_w 6.5 strike-slip earthquakes. Cutoff displacement value is 0.001 cm.

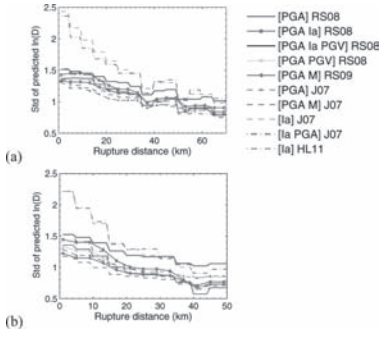

Figure 7. Standard deviations considering aleatory variability of GMPEs and Newmark displacement models, for (a) M_w 7.5 (b) M_w 6.5 strike-slip earthquakes. Cutoff displacement value is 1 cm.

4 CONCLUSIONS

In this paper, epistemic uncertainty and aleatory variability of Newmark displacement models are quantified for given scenario earthquakes. Since the Newmark displacement models are based on IMs (e.g., PGA, Ia) as predictors, the uncertainties to predict these IMs have to be considered in the analysis. The standard deviation of the epistemic uncertainty of the Newmark displacement models is within the range of 0.5–1 using the predicted median IMs as input parameters. In general, the standard deviation of epistemic uncertainty becomes 20% larger if both of the epistemic uncertainties of GMPEs and Newmark displacement models are considered. The epistemic uncertainty in the Newmark displacement is significant larger compared with that of GMPEs. It implies that it is more efforts should be placed to develop advanced Newmark displacement models to reduce the epistemic uncertainty in the future.

The total aleatory variability of the Newmark displacement model is also studied for given

scenario earthquakes. Choosing different cutoff displacement values would result in different total aleatory variabilty. Considering both aleatory variabilities of GMPEs and the Newmark displacement models, the total standard deviation of predicted displacement are 1.5–2.5 in natural log scale if the cutoff value is chosen as 0.001 cm. The total aleatory variability will be reduced if the cutoff value is chosen as 1 cm. The total aleatory variabilities are rather consistent for scalar models and vector models considered.

It is important to emphasize that vector models do not significantly reduce the total aleatory variability of the predicted displacements, due to additional sources of variability introduced by incorporating additional IMs. However, the epistemic uncertainty for vector models is generally smaller than that of the scalar models. The epistemic uncertainty of vector models tends to be consistent for all scenarios considered, since incorporating multiple IMs can better satisfy the sufficiency criterion (Saygili & Rathje, 2008), such that the model is not biased for different magnitude and distances.

In current practice, seismic slope analysis is a two-step process. First, the ground motion IMs (e.g., PGA, PGV or Ia) are estimated using GMPEs; Secondly, the estimated IMs are used as input parameters to the Newmark displacement models. Both of the epistemic uncertainties and aleatory variabilities in GEMPs and Newmark displacement models should be well considered in seismic hazard analysis of slopes. A reasonable logic tree analysis should be employed to account for epistemic uncertainties in GMPEs and Newmark displacement models. It is also envisioned that developing Newmark displacement models directly based on earthquake scenarios (magnitude and distance etc.) would reduce the inherent complexity and uncertainties in current two-step approach.

ACKNOWLEDGEMENTS

The authors acknowledge financial support from Hong Kong Research Grants Council Grant 620311, and DAG08/09.EG13, DAG11EG03G to conduct this study. Any opinions, findings, and conclusions or recommendations expressed in this material are ours and do not necessarily reflect those of the sponsor.

REFERENCES

Abrahamson N.A. & Silva W.J. 2008. Summary of the Abrahamson & Silva NGA ground-motion relations. *Earthquake Spectra* 24(1): 67–97.

Ambraseys N.N. & Menu J.M. 1988. Earthquake-induced ground displacements. *Earthquake Engineering and Structural Dynamics* 16: 985–1006.

Boore D.M. & Atkinson G.M. 2008. Ground-motion prediction equations for the average horizontal component of PGA, PGV and 5%-damped PSA at spectral periods between 0.01s and 10s. *Earthquake Spectra* 24(1): 99–138.

Bray J.D. & Travasarou T. 2007. Simplified procedure for estimating earthquake-induced deviatoric slope displacements. *Journal of Geotechnical and Geoenvironmental Engineering* 133(4): 381–392.

Campbell K.W. & Bozorgnia Y. 2008. NGA ground motion model for the geometric mean horizontal component of PGA, PGV, PGD and 5% damped linear elastic response spectra for periods ranging from 0.1 to 10 s. *Earthquake Spectra* 24(1): 139–171.

Campbell K.W. & Bozorgnia Y. 2012. A comparison of ground motion prediction equations for Arias intensity and cumulative absolute velocity developed using a consistent database and functional form. *Earthquake Spectra* 28(2): 931–941.

Chiou B. & Youngs R.R. 2008. An NGA model for the average horizontal component of peak ground motion and response spectra. *Earthquake spectra* 24(1): 173–215.

Douglas J. 2010. Consistency of ground-motion predictions from the past four decades. *Bulletin of Earthquake Engineering* 8: 1515–1526.

Douglas J. 2012. Consistency of ground-motion predictions from the past four decades: peak ground velocity and displacement, Arias intensity and relative significant duration. *Bulletin of Earthquake Engineering* 10(5): 1339–1356.

Foulser-Piggott R.F. & Stafford P.J. 2012. A predictive model for Arias intensity at multiple sites and consideration of spatial correlations. *Earthquake Engineering and Structural Dynamics* 41(3): 431–451.

Hsieh S.Y. & Lee C.T. 2011. Empirical estimation of the Newmark displacement from the Arias intensity and critical acceleration. *Engineering Geology* 122: 34–42.

Jibson R.W. 2007. Regression models for estimating coseismic landslide displacement. *Engineering Geology* 91: 209–218.

Newmark N.M. 1965. Effects of earthquakes on dams and embankments. *Geotechnique* 15(2): 139–160.

Rathje E.M. & Saygili G. 2008. Probabilistic seismic hazard analysis for the sliding displacement of slopes: scalar and vector approaches. *Journal of Geotechnical and Geoenvironmental Engineering* 134(6): 804–814.

Rathje E.M. & Saygili G. 2009. Probabilistically based seismic landslide hazard maps: An application in Southern California. *Engineering Geology* 109: 183–194.

Saygili G. & Rathje E.M. 2008. Empirical predictive models for earthquake-induced sliding displacements of slopes. *Journal of Geotechnical and Geoenvironmental Engineering* 134(6): 790–803.

Travasarou T. & Bray J.D. 2003. Empirical attenuation relationship for Arias Intensity. *Earthquake Engineering and Structural Dynamics* 32: 1133–1155.

Geotechnical Safety and Risk IV – Zhang et al. (eds)
© 2014 Taylor & Francis Group, London, ISBN 978-1-138-00163-3

Reliability analysis of 640 m long soil retaining wall for an embedded highway construction

Y. Honjo, Y. Otake, T. Kusano & T. Hara
Gifu University, Gifu, Japan

ABSTRACT: A reliability analysis of 640 m long retaining wall for an embedded highway has been carried out. The soil profile at the site mainly consists of alternation of three cohesive and cohesionless soil layers. The soil investigations have been conducted by the borings (SPT N-values) of about 100 m interval. It was found that the most dominant source of uncertainty to control the performance of the retaining wall is the thickness of the soil layers which are different from a section to another. The layers thicknesses are modeled as correlated random processes whose thicknesses are known at the location of the borings. The thickness of a layer at a certain location is estimated by Co-Kriging method and the conditional simulation based on it with quantified uncertainty. The design calculation model error is also evaluated by comparing the calculated results with laboratory model experiment results and actual site measurements. The response surfaces of the performance of the retaining wall as a function of layer thicknesses and soil property variations are obtained by extensive design calculations of the retaining wall. Finally, the reliability evaluation of the retaining wall along the excavation has been carried out by Monte Carlo Simulation (MCS). The final result takes into account the spatial variability of soil properties both soil mechanical property variation and the layer thicknesses, the statistical estimation error due to sparse soil investigations, and design calculation model errors. The quantitative contributions of each component are also presented.

1 INTRODUCTION

A reliability analysis of 640 m long retaining wall for an embedded highway has been carried out by a reliability analysis procedure proposed by the authors (Honjo, Otake and Kato, 2012; Otake and Honjo, 2012, 2013; Honjo and Otake, 2012). The main focus of this study is to introduce a method to take into account the uncertainty due to the layer thicknesses on top of uncertainties induced by spatial variability and statistical estimation error of soil properties and design calculation model error.

The procedure consists of three part, namely 1) geotechnical analysis, 2) uncertainty analysis and 3) reliability evaluation.

In geotechnical analysis, equations are developed, so called Response Surfaces (RS), which relate the inputs and the outputs in the design. In the context of the retaining wall design, the inputs are soil properties, layer configurations (*i.e.* layer thicknesses), dimensions and stiffness of the retaining wall *etc.* The outputs can be the maximum bending moment or displacement induced in the wall during the construction.

The uncertainties caused by various sources are quantified in the uncertainty analysis. The sources include spatial variability of soil properties, statistical estimation error of soil properties and layer thicknesses, and the calculation model error.

Finally, the reliability of the structure at the various locations are evaluated by combining these information and employing Monte Carlo Simulation (MCS).

2 DESCRIPTION OF THE SITE

2.1 *The retaining wall*

The structure under study is a retaining wall of an embedded highway construction which runs in an urban populated area. The total length of the excavation is 640 m where underground space of 13 m deep and 23 m wide should be retained for the highway. The retaining wall is a permanent structure.

The retaining wall is 14 to 20 m long, where the excavation depth is 11 to 13 m. The type of the retaining wall is a cast-in-site diaphragm wall by the Soil Mixing Wall (SMW) method.

2.2 *Geotechnical conditions*

The soil profile at the site is presented in Figure 1. The first layer is landfill soil (B), followed by a diluvial sand gravel layer (Dg) whose underneath

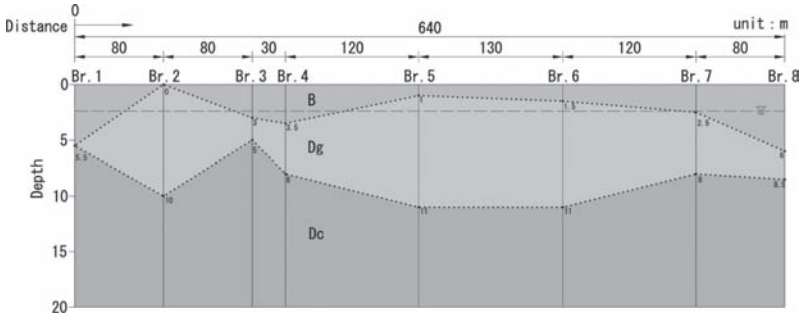

Figure 1. Soil profile at the section.

the deluvial sandy silt layer (Dc). The ground water level is 2.4 m below the ground surface. The thickness of the layer changes within the construction location.

2.3 *Performance requirements and performance criteria*

The first performance requirement for the retaining wall is the stability during and after the excavation. There is also strict requirements for the movement of the surrounding ground so as to secure the serviceability of the adjacent building and other embedded structures.

For the stability of the retaining wall, sufficient embedded depth of the wall should be secured. Also the maximum bending moment in the wall should be below the yielding limit. The maximum horizontal deformation of the wall should be limited so as to secure the serviceability of the adjacent structures.

The three performance criteria set were the stability of wall for the turnover, the maximum bending moment of the wall and the maximum horizontal displacement of the wall. The first criterion was satisfied for all cases if 3 m embedded depth is secured, which is the minimum required embedded depth by the code. The maximum bending moment is limited by the yielding strength of the wall. The criterion for the horizontal displacement is limited to 1% of the excavation depth according to the past experiences.

3 GEOTECHNICAL ANALYSIS

3.1 *Elasto-plastic method*

Elasto-plastic method first proposed by Yamagata et al (1969) is the most commonly used retaining wall design method in Japan. The method is placed as the standard method to design retaining wall for highways (JRA, 1999). In this method, the retaining wall is model as a beam on a elasto-plastic body. The active earth pressure is applied as a distributed load, whereas the passive side ground is modeled by linear elastic spring bed which yields at its passive earth pressure. The strata are model as elastic springs.

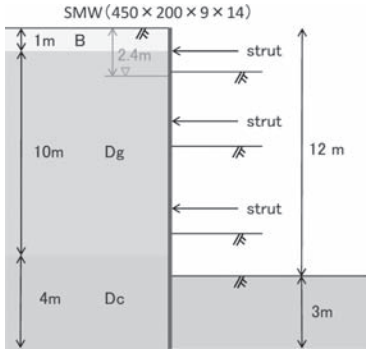

Figure 2. The section at Br.5.

Table 1. Excavation steps.

Step	Excavation depth (m)	Position of strut (m)
1	2.0	–
2	5.5	1.0
3	9.5	4.5
4	12.0	8.5

Figure 2 is the section at Br.5, where H steel pile of H-450 × 200 × 9 × 14 is used. The stepwise excavation depth and the position of struts are presented in Table 1. This section is one of the critical sections in this construction because relatively soft Dg layer is thickly deposited.

Figure 3 presents the distribution of the horizontal displacement and the bending moment in the wall at various excavation stages. The maximum horizontal displacement appears at the last stage of the excavation near the excavation bed, whereas the maximum moment at one stage before the last (3rd step) also at the same location.

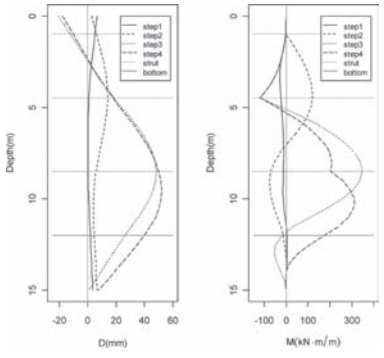

Figure 3. Result of he design calculation at Br.5.

Table 2. Results of verification.

	Unit	Calculated (C)	Allowable (A)	*C*/*A*
Plastic rate	%	62	90	0.69
Bending moment	kN·m	338	341	0.99
Displacement	mm	52	120	0.43

Table 2 summarizes the relationship between the maximum calculated values (C) and the allowable values (A). C/A for the bending moment is 0.99, and it is clear that the section is determined by this item. Other items have some extra margin of safety for the limiting values.

3.2 *Building response surfaces*

The Response Surfaces (RS) for the maximum horizontal displacement and the bending moment have been constructed. RS is a function of basic variables which indicates the performance of the structure whether it is exceeding the limit state or not. A RS function can be given as follows:

$$y = f(x_1 \ldots x_n) + \varepsilon \quad (1)$$

where $x_i (i = 1 \ldots n)$ are n basic variables, y is the response and ε residual error.

Due to the limitation of the space, no further description on the RSs is presented. We have successfully built the RSs in this study.

4 UNCERTAINTY ANALYSIS

Three types of uncertainties are analyzed in this section. Namely,

1. Spatial variation of the local average of SPT N-value, and the statistical estimation error associated in evaluating this local average value.
2. Uncertainty of the layer thickness.
3. Model uncertainty concerning the elasto-plastic method of retaining wall design.

4.1 *Spatial variability and statistical estimation error of SPT N-value*

Due to the limitation of the space, no further explanation on how the spatial variability and the statistical estimation error of SPT N-values are treated are not presented in this paper. We have developed the methodology to treat these uncertainties which has been applied to this study (Honjo, Otake and Kato, 2012; Honjo and Otake, 2012, 2013; Otake, 2012). The results of the evaluation are presented in Table 3.

4.2 *Layer thickness uncertainty*

The layer thickness changes within the site as illustrated in Figure 1. The RS functions obtained also indicate that the layer thicknesses have considerable influence on the design of the retaining wall. Thus, it is important to take the uncertainty of layer thicknesses into account.

One of the distinguished characteristics of the layer thicknesses at the site is the negative correlation between the layer thicknesses of B and Dg layer, which can be observed from the scattergram, Figure 4. The correlation coefficient between the two quantities is –0.89.

Co-Krigin is used in this study to estimate the layer thicknesses of B and Dg layers which should be interpolated from the observed points together with the statistical estimation error. To evaluate the

Table 3. Uncertainty associated with SPT N-value.

Layer	n	σ	V (m)	θ_V (m)	$\Gamma^2(V/\theta)$	A_G^2	σV
B	3	12.20	3.0	0.5	0.28	0.40	10.03
Dg	5	4.51	5.5	0.5	0.17	0.24	2.86
Dc	6	3.01	6.5	0.5	0.14	0.20	1.76

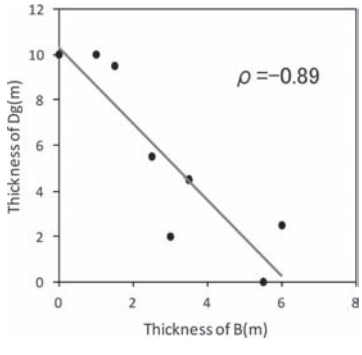

Figure 4. Scattergram of B and Dg layer thicknesses.

influence of the layer thicknesses to the performance of the retaining wall, the conditional simulation technique is used. In the conditional simulation, necessary number of random filed samples are generated that take the observed thicknesses at the observation points. Based on the generated sample layer thicknesses, the RS functions can be used to evaluate the reliability of the retaining wall.

4.2.1 *Co-Kriging*

Let the thicknesses of the two layers be $\mathbf{Z}(x) = (Z_1(x), Z_2(x))$, where x is the coordinate to show the position corresponds to "Distance" in Fig. 1). The layer thicknesses at $Z_k(\underline{x})$ is interpolated from $2n$ observed layer thicknesses at $x_1, x_2, \ldots, x_n$. Note that suffix k indicates the layer B ($k = 1$) or Dg ($k = 2$).

The basic assumptions of Co-Kriging is not different from those of Ordinary Kriging (Journel and Huijbrechts, 1978) Under the three basic assumptions, namely the linear estimator, the un-biasness and the minimum estimation variance estimator, Co-Kriging problem results to solve the following simultaneous equation to obtain the weights:

$$\begin{bmatrix} \mathbf{K}_{11} & \mathbf{K}_{12} & \mathbf{1} & \mathbf{0} \\ \mathbf{K}_{21} & \mathbf{K}_{22} & \mathbf{0} & \mathbf{1} \\ \mathbf{1}^T & \mathbf{0}^T & 0 & 0 \\ \mathbf{0}^T & \mathbf{1}^T & 0 & 0 \end{bmatrix} \begin{bmatrix} \mathbf{w}_1 \\ \mathbf{w}_2 \\ \lambda_1 \\ \lambda_2 \end{bmatrix} = \begin{bmatrix} \mathbf{k}_1 \\ \mathbf{k}_2 \\ l \\ l \end{bmatrix} \tag{2}$$

where,

$\mathbf{K}_{jj'}$: Covariance matrix of $\mathbf{Z}_j = \{Z_j(x_i)\}$ and $\mathbf{Z}_{j'} = \{Z_{j'}(x_i)\}$ where ($j, j' = 1, 2$)

$\mathbf{k}_k$: Covariance vector of $\mathbf{Z}_j = \{Z_j(x_i)\}$ and $Z_k(x)$ where ($i = 1, \ldots n$; $j = 1, 2$; $k = 1, 2$)

$\mathbf{w}_j$: Weights in the estimator $\mathbf{w}_j = \{w_{ij}\}$ ($i = 1, \ldots, n$; $j = 1, 2$)

λ_j: Lagrange multiplier ($j = 1, 2$)

$\mathbf{1}$: n – D column vector with 1

$\mathbf{0}$: n – D column vector with 0

l: = 1 (if $j = k$)
= 0 (if $j \neq k$)

i: Sampling point number ($i = 1, \ldots n$)

j: Layer number ($j = 1, 2$)

k: Estimating layer number ($k = 1$ or 2)

The estimator is given by the following linear equation where w_{ij} are the weight assigned to each observation that are obtained from Eq. (2):

$$\hat{Z}_k(x) = \sum_{i=1}^{n} \sum_{j=1}^{2} w_{ij} Z_j(x_i) \tag{3}$$

The estimation error can be also evaluated:

$$\sigma_{EV}^2 = \begin{bmatrix} \mathbf{w}_1 \\ \mathbf{w}_2 \end{bmatrix}^T \begin{bmatrix} \mathbf{K}_{11} & \mathbf{K}_{12} \\ \mathbf{K}_{21} & \mathbf{K}_{22} \end{bmatrix} \begin{bmatrix} \mathbf{w}_1 \\ \mathbf{w}_2 \end{bmatrix} \tag{4}$$

4.2.2 *The conditional simulation*

The two correlated random filed can be generated based on the fact that m dimensional normal distribution can be decomposed to m independent normal distributions by the eigenvalue decomposition of the covariance matrix.

In order to apply this procedure to the present problem, the correlation among the layer thicknesses, $Z_1(x_i)$, $Z_2(x_i)$, need to be assumed, where $x_i (i = 1, \ldots m)$ that indicates the coordinate of the location where the layer thicknesses be generated. The covariance can be calculated as follows:

$$Cov\left(Z_k(x_i), Z_l(x_j)\right) = \begin{cases} \sigma_{Z_k} \sigma_{Z_l} \rho\left(|x_i - x_j|\right) & (\text{if } k = l) \\ -0.89\, \sigma_{Z_k} \sigma_{Z_l} \rho\left(|x_i - x_j|\right) & (\text{if } k \neq l) \end{cases} \tag{5}$$

where, ($i, j = 1, 2, \ldots m$; $k, l = 1, 2$), σ_{Z_k} is the SD of layer thickness for layer k, and ρ is the autocorrelation function of the exponential function type. It is assumed that the autocorrelation distance for the two layers are the same.

Finally, the procedure of the conditional simulation is as follows:

Step 1 Generate layer thickness $s_k(x_j)$ ($j = 1, \ldots m$; $k = 1, 2$) by the procedure shown above. These generated values fulfill the statistical properties assumed for the layer thicknesses.

Step 2 Interpolate the layer thicknesses at $x_i (i = 1, \ldots m)$ by Co-Kriging based just on the generated layer thicknesses where observations are originally made. The interpolated results are denoted by $\hat{s}_k(x_j)$.

Step 3 Let the results of Co-Kriging based on the original observations be $\hat{z}_k(x_j)$. A sample by the conditional simulation can be obtained by the equation below:

$$z_k(x_j) = \hat{z}_k(x_j) + (s_k(x_j) - \hat{s}_k(x_j)) \tag{6}$$

The obtained set of layer thicknesses, $z_k(x_j)$ ($j = 1, \ldots m$; $k = 1, 2$), satisfies the statistical properties assumed and also pass through all the observed layer thicknesses at the observed points.

Step 4 Repeat step 1 to step 3 as necessary to generate required sets of sample layer thicknesses.

The statistics estimated from the observed values of the layer thicknesses are summarized in Table 4. The autocorrelation distance of the layer thicknesses, θ_H, is not clearly estimated. Thus, two cases, namely θ_H = 50 and 100 m, are set to compare the results.

4.3 *Model error*

Otake (2012) has done an extensive study on the model error of the elasto-plastic method. Due to the limitation of the space, only the results are summarized here.

Based on the collected model experiment results and actual construction case histories, the elasoto-plastic method has been tested for its accuracy. The results are presented in Table 5.

The model error is defined by (observed value)/(calculated value) so that when the error is multiplied to the calculated value, the value be transformed to the true value that is represented here by the observed value.

The model error employed in the reliability evaluation in this study adopted the results based on the model experiment.

Table 4. Estimated statistics for B and Dg layer thickness.

			θ_H (m)	
Layer	μ (m)	σ (m)	Case A	Case B
B	3.0	2.10	50	100
Dg	5.5	3.94	50	100

Table 5. Model error in the elasto-plastic method.

	Item	Mean	COV	*n*
Case histories	Max disp.	0.70	0.29	58
	Max BM	0.69	0.43	42
Model experiments	Max disp.	1.08	0.67	38
	Max BM	0.73	0.44	24

(note 1 error = (observed)/(calculated); (note 2 BM: bending moment, disp.: displacement).

5 RELIABILITY EVALUATION

5.1 *Conditions of the evaluation*

The sections are set 5 m interval for the 640 m long construction site. The reliability evaluations are made for all these sections. The RS functions can be described as follows by the basic variables:

$$D = f_D(N_B, N_{Dg}, N_{Dc}, H_B, H_{Dg}, H_{Dc}) \cdot \delta_{ME} \quad (7)$$

$$M = f_M(N_B, N_{Dg}, N_{Dc}, H_B, H_{Dg}, H_{Dc}) \cdot \delta_{ME} \quad (8)$$

The mean and COV of each basic variable are listed in Table 6.

5.2 *Results*

The reliability evaluation results for the maximum horizontal displacement are presented in Figure 5, whereas those for the maximum bending moment in Figure 6. In (a) in the both figures, the exceedance probabilities of the limiting values, P_f, are are superposed for θ_h = 50 (m) and 100 (m) for comparison. Furthermore in (b) in the both

Table 6. Statistics of the basic variables.

		μ	σ	COV
Statistical estimation	N_B	15.0	6.43	0.43
Error Γ^2	N_{Dg}	19.0	1.83	0.10
(Normal)	N_{Dc}	12.0	1.13	0.09
Spatial variability	N_B	15.0	7.69	0.51
Λ^2	N_{Dg}	19.0	2.20	0.12
(Normal)	N_{Dc}	12.0	1.35	0.11
Model error	Disp.	1.08	0.67	0.62
δ_{ME}	BM	0.73	0.44	0.60
(log normal)				

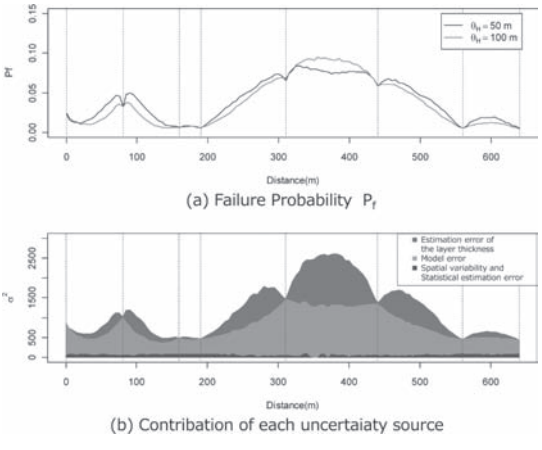

Figure 5. Results of MCS for the maximum horizontal displacement.

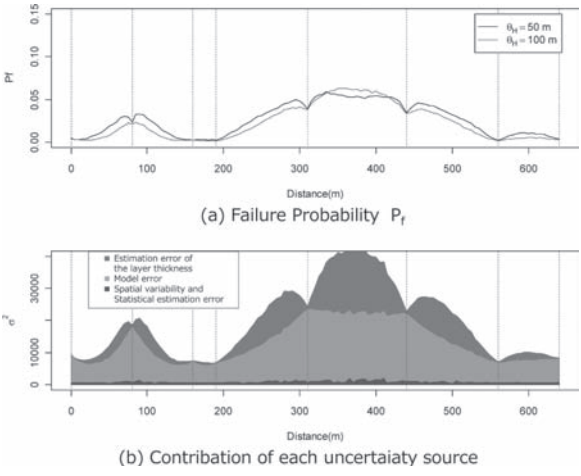

Figure 6. Results of MCS for the maximum bending moment.

figures, contribution of each uncertain source are illustrated for case $\theta_h = 100$ (m).

The following observations can be made for these cases.

1. P_f for both the maximum horizontal displacement and the bending moment takes the maximum value between distance 300 to 450 (m). In this section, the thickness of Dg layer is thicker, which makes the earth pressure lager.
2. The accuracy of the layer thickness prediction is less for $\theta_h = 50$ (m) than for 100 (m). It is also less in the area that are distanced from the observations are made. However, the difference is rather small for $\theta_h = 50$ (m) and for 100 (m).
3. The uncertainty sources that are critical are the model error and the statistical estimation error of the layer thicknesses. The spatial variability and the statistical estimation error of SPT N-value of each layer have only negligible impacts.

6 CONCLUSION

The sources of uncertainty concerning retaining wall design have been identified and quantified taking 640 m long embedded highway retaining wall as an example. The reliability analysis scheme proposed by Honjo, Otake and Kato (2012) has been applied to the reliability evaluation of the retaining wall.

The result of the evaluation has shown that the two major sources of uncertainty are the statistical estimation error of the layer thicknesses and the model error of the elasto-plastic method for retaining wall design. The impacts of the spatial variability of soil properties within each layer, and the statistical estimation error of the soil properties are quite limited on the reliability of the retaining wall.

REFERENCES

Honjo, Y.,Y. Otake & Kato H. 2012. A simpli-fied scheme to evaluate spatial variability and statistical estimation error of local average of geotechnical parameters in reliability analysis. *J. Geotechnical Engineering (JSCE)* 68(1):41–55. (in Japanese).

Honjo, Y. & Otake Y. 2012. Verification of statistical estimation error evaluation theory of local averages of geotechnical parameters. *J. Geotechnical Engineering (JSCE)* 68(3):475–490. (in Japanese).

Honjo, Y. & Otake Y. General and local estimation of local average of geotechnical parameters in reliability analysis. *Proc. APSSRA*, Phoon, K.K., Beer, M., Quek, S.T., Pang, S.D. (editors), 236–241.

Honjo, Y. & Otake Y. 2013. A Simple Method to Assess the Effects of Soil Spatial Variability on the Performance of a Shallow Foundation. *ASCE Geotechnical Special Publication No. 229, Foundation Engineering in the Face of Uncertainty (honoring Fred H. Kulhawy)*, J.L. Whithiam, K.K. Phoon and M.H. Hussein (eds.), 385–404.

Jounel, A.G. & Huijbregts C.J. 1978. *Mining Geostatistics,* Academic Press.

Otake, Y. & Honjo Y. 2012. Reliability based design on long irrigation channel considering the soil investigation locations, *Proceedings of Geo Congres*, 2836–2845.

Otake, Y. 2012. Development of geotechnicl reliability based design and chllenges in geotechnical design, PhD dissertation submitted to Gifu university, 215 pp. (in Japanese).

Vanmarcke, E.H. 1977. Probabilistic modeling of soil profiles. *J. of Geotechnical Engineering, ASCE* 103 (GT11): 1227–1246.

Geotechnical Safety and Risk IV – Zhang et al. (eds)
© 2014 Taylor & Francis Group, London, ISBN 978-1-138-00163-3

CPT-based Bayesian identification of underground soil stratigraphy

K. Huang
Department of Civil and Architectural Engineering, Shenzhen Research Institute, City University of Hong Kong, Hong Kong, China

Z. Cao
State Key Laboratory of Water Resources and Hydropower Engineering Science, Wuhan University, Wuhan, P.R. China

Y. Wang
Department of Civil and Architectural Engineering, Shenzhen Research Institute, City University of Hong Kong, Hong Kong, China

ABSTRACT: This paper aims to identify underground soil stratum and classify the soil types using Bayesian approaches and Cone Penetration Tests (CPT). The uncertainty in the CPT-based soil classification using the Robertson chart is modeled explicitly in the Bayesian approaches. The proposed Bayesian approaches contain two major components: a Bayesian model class selection approach to identify the most probable number of underground soil layers and a Bayesian system identification approach to estimate the most probable layer thicknesses and determine the soil types simultaneously. Equations are derived for the Bayesian approaches, and the proposed approaches are validated using a set of simulated CPT data. It has been shown that the proposed approaches correctly identify the underground soil stratification and classify the soil type of each layer.

1 INTRODUCTION

Determining the underground soil stratigraphy (i.e. the number of soil types/layers and their thicknesses/boundaries) is one key aspect in geotechnical site characterization, during which Cone Penetration Tests (CPTs) are widely used around the world. CPT enjoys many advantages (Mayne 2007, Robertson 2009). However, no soil sample is retrieved for visual inspection to assist in soil classification.

When performing soil classification from CPT data, the CPT reading (e.g. tip resistance and friction ratio) is linked directly to the soil types, and the Soil Behavior Type (SBT) classification is determined using soil classification charts (e.g. Robertson 1990, Jefferies & Davies 1993). Consider, for example, the soil classification chart, which is shown in Figure 1 and is frequently referred to as the Robertson chart (Robertson 1990). The soil type is determined based on two parameters (i.e. two axes in Fig. 1): the normalized friction ratio, $F_R = 100 f_s/(q_t - \sigma_{v0})$, and the normalized tip resistance, $Q_t = (q_t - \sigma_{v0})/\sigma'_{v0}$, where f_s, q_t, σ_{v0}, σ'_{v0} are the sleeve friction, corrected tip resistance, vertical total stress, and vertical effective stress, respectively. The nine areas in the chart correspond to nine different

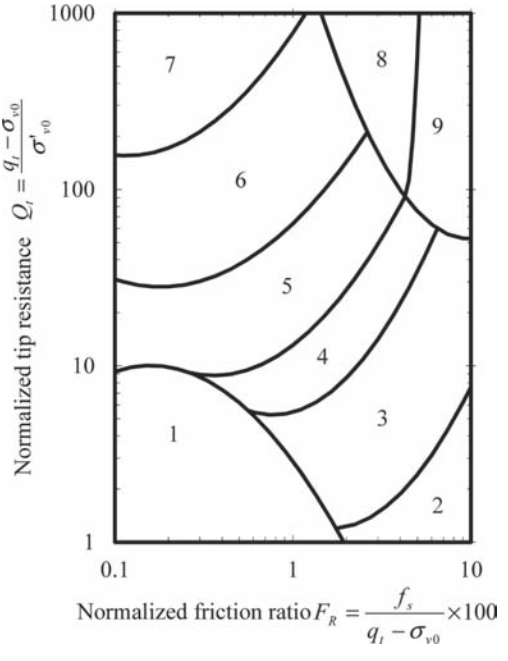

Figure 1. The Robertson soil classification chart based on CPT data (After Robertson (1990)).

Table 1. Description of soil types in the Robertson's soil classification chart (After Robertson (1990)).

Area	Soil description
1	Sensitive, fine-grained
2	Organic soils (peats)
3	Clays (clay to silty clay)
4	Silt mixtures (clayey silt to silty clay)
5	Sand mixtures (silty sand to sandy silt)
6	Sands (clean sand to silty sand)
7	Gravelly sand to sand
8	Very stiff sand to clayey sand
9	Very stiff, fine-grained

soil types, as described in Table 1. Based on which area the measured (F_R, Q_t) combination is located in, the soil type is determined accordingly. Note that the Robertson chart was developed based on past observations and engineering experience, and various uncertainties are involved inevitably, such as observation scatterness, measurement error, and transformation uncertainty. Such uncertainties can be properly dealt with by integrating the Robertson chart with probabilistic methods.

Several probabilistic soil classification approaches have been proposed (e.g. Zhang & Tumay 1999, Kurup & Griffin 2006). However, these approaches mainly focused on determining the soil type from a particular CPT data point. How to stratify the underground soil profile from a large number of nearly continuous CPT data points remains unsolved. Engineering judgment is frequently used to handle such a problem. However, inconsistencies often arise due to different judgment from different engineers. The key issue to this problem is that the uncertainty in the CPT-based soil classification and the spatial distribution of the CPT data (e.g. Wang et al. 2010) is not considered explicitly, but treated implicitly and vaguely by using engineering judgment.

This paper integrates the Robertson chart with Bayesian approaches to explicitly and properly consider the uncertainty in the CPT-based soil classification and spatial distribution of CPT data. Bayesian system identification and model class selection approaches are used to identify the most probable thicknesses and number of soil layers in a systematic and rational manner. The paper starts with the probabilistic framework for soil stratum identification and probabilistic soil classification based on the Robertson chart, followed by the proposed Bayesian system identification and model class selection approaches. Then, the application procedure for the Bayesian approaches is described. The proposed approaches are validated using a set of simulated CPT data.

2 PROBABILISTIC FRAMEWORK FOR SOIL STRATUM IDENTIFICATION

As shown in Figure 2, identifying the underground soil strata based on CPT data is to determine the layer thickness $\underline{h} = [h_1, h_2, \ldots, h_n, \ldots, h_N]$ in a soil profile containing N soil layers, where h_n is the thickness of the n-th layer. The number N in the first part of this paper (i.e. before Section 5 "The Most Probable Number of Soil Strata") is treated deterministic but unknown. It is then determined by a Bayesian model class selection approach proposed in Section 5.

Let $\underline{\xi} = [\underline{\xi}_1, \underline{\xi}_2, \ldots, \underline{\xi}_N]$ be a set of $\ln(F_R)$ and $\ln(Q_t)$ data obtained from a CPT test in a soil profile with N soil layers, in which $\underline{\xi}_n = [\underline{\xi}_{n1}(d_1), \underline{\xi}_{n2}(d_2), \ldots, \underline{\xi}_{nk_n}(d_{k_n})]$, $n = 1, 2, \ldots, N$, is a set of $\ln(F_R)$ and $\ln(Q_t)$ measured at the k_n depths $d_1, d_2, \ldots, d_{k_n}$ within the *n-th* soil layer. For a given layer number N of soil layers, the probability $P(\underline{\xi}_n | N)$ that all data points in the n-th layer belong to the same soil type can be calculated as:

$$P(\underline{\xi}_n | N) = \sum_{J=1}^{9} P_{ST_J}(\underline{\xi}_n | N) \quad n = 1, 2, \ldots, N \tag{1}$$

where $P_{ST_J}(\underline{\xi}_n | N)$ is the probability that all data points in the n-th layer belong to the same given soil type J. The $P_{ST_J}(\underline{\xi}_n | N)$ can be expressed as:

$$P_{ST_J}(\underline{\xi}_n | N) = \prod_{i=1}^{k_n} P_{ST_J}(\underline{\xi}_{n,i} | N) \quad \text{for } J = 1, 2, \ldots, 9 \tag{2}$$

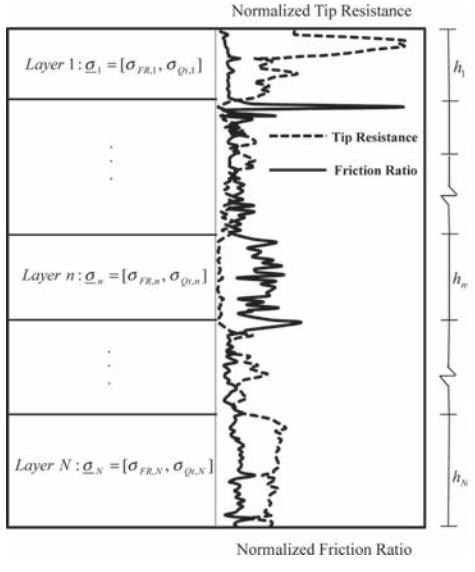

Figure 2. An illustration of the underground soil stratigraphy.

where $P_{ST_J}(\underline{\xi}_{n,i}|N)$ is the probability that a data point i in the n-th layer belongs to the soil type J. The value of $P_{ST_J}(\underline{\xi}_n|N)$ is calculated repeatedly for J varying from 1 to 9. Then, the probability $P(\underline{\xi}_n|N)$ is calculated using Equation 1, and the soil type J with the maximum value of $P_{ST_J}(\underline{\xi}_n|N)$ among the nine soil types is taken as the soil type for the n-th soil layer. The probability $P_{ST_J}(\underline{\xi}_{n,i}|N)$ is the key input variable in Equations 1 and 2, and a probabilistic model is developed in the next section to estimate the $P_{ST_J}(\underline{\xi}_{n,i}|N)$ value.

3 PROBABILISTIC SOIL CLASSIFICATION BASED ON THE ROBERTSON CHART

Consider, for example, a CPT data point i with a combination of $[\ln(F_R^i), \ln(Q_t^i)]$ value measured at a given depth during the test. Because the Robertson chart and $[\ln(F_R^i), \ln(Q_t^i)]$ are not perfect knowledge or information, there exists a plausibility (or occurrence probability) that the soil at this given depth, in fact, should be classified as any of the nine types of soil. Such a probability can be quantified through a Probability Density Function (PDF) (Wang et al. 2013), as shown in Figure 3, and be expressed as:

$$P(\ln(F_R), \ln(Q_t)|\underline{\sigma}) = \frac{1}{2\pi\sigma_{FR}\sigma_{Qt}} \times \exp\left\{-\frac{[\ln(F_R)-\ln(F_R^i)]^2}{2\sigma_{FR}{}^2} - \frac{[\ln(Q_t)-\ln(Q_t^i)]^2}{2\sigma_{Qt}{}^2}\right\} \quad (3)$$

where $\underline{\sigma} = [\sigma_{FR}, \sigma_{Qt}]$, σ_{FR} and σ_{Qt} are the standard deviation of the joint Gaussian distribution along the $\ln(F_R)$ and $\ln(Q_t)$ axes, respectively.

Then, the probability P_{ST_J} that the data point i with the measured values belongs to the soil type J is expressed as:

$$P_{ST_J} = \iint_J P(\ln(F_R), \ln(Q_t)|\underline{\sigma}) d\ln(F_R) d\ln(Q_t) \quad \text{for } J = 1, 2, ..., 9 \quad (4)$$

The two dimensional integration in Equation 4 is performed repeatedly for each soil type and each data point to obtain the $P_{ST_J}(\underline{\xi}_{n,i}|N)$. Note that, $\underline{\sigma} = [\sigma_{FR}, \sigma_{Qt}]$ are model parameters in each soil layer. As illustrated in Figure 2, for a soil profile containing N soil layers, the N sets of model parameters are defined as $\underline{\Omega}_N = [\underline{\sigma}_1, \underline{\sigma}_2, \ldots, \underline{\sigma}_N]$, in which $\underline{\sigma}_n = [\sigma_{FR,n}, \sigma_{Qt,n}]$, $n = 1,2, \ldots, N$.

It is also worthwhile point out that the parameters of real interest in the identification of underground stratification are the thickness vector

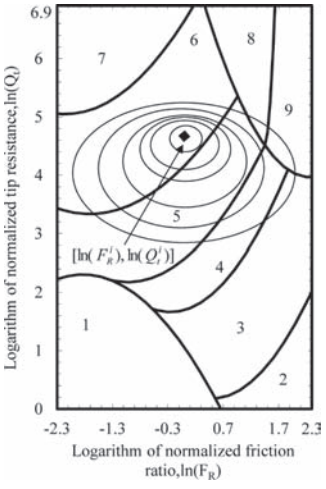

Figure 3. An illustration of the probability contour and two-dimensional joint PDF for soil classification based on a given CPT data point.

$\underline{h} = [h_1, h_2, \ldots, h_n \ldots, h_N]$, but are not $\underline{\Omega}_N$. Dividing CPT data $\underline{\xi}$ into different soil layers requires information on the boundaries that separate various soil layers. Such information is unknown and needs to be determined in site characterization. The next section presents a Bayesian system identification approach to determine the thicknesses and soil types for a soil profile with a given number N of soil layers.

4 BAYESIAN SYSTEM IDENTIFICATION OF THE THICKNESSES OF SOIL STRATA

Within the Bayesian framework, the updated rule for the estimation of the model parameters $\underline{\Omega}_N$ is given by (Cao & Wang 2013, Wang et al. 2013):

$$P(\underline{\Omega}_N|\underline{\xi}, N) = K_N P(\underline{\xi}|\underline{\Omega}_N, N) P(\underline{\Omega}_N|N) \quad (5)$$

where K_N is a constant; $P(\underline{\xi}|\underline{\Omega}_N, N)$ is the likelihood function; $P(\underline{\Omega}_N|N)$ is the prior distribution. The $P(\underline{\xi}|\underline{\Omega}_N, N)$ is expressed as (Wang et al. 2013):

$$P(\underline{\xi}|\underline{\Omega}_N, N) = \prod_{n=1}^{N} P(\underline{\xi}_n|\underline{\sigma}_n, N) \quad (6)$$

where $P(\underline{\xi}_n|\underline{\sigma}_n, N)$ is the likelihood function for the n-th layer and calculated using Equations 1–4. Note that, as the boundaries of soil layers (i.e., layer thicknesses) change, the division of CPT data also changes. Therefore, $\underline{\xi}_n$ is a function of layer

thicknesses and $P(\underline{\xi}_n|\underline{\sigma}_n,N)$ is also a function of layer thicknesses.

Similarly, the prior distribution is expressed as:

$$P(\underline{\Omega}_N|N)=\prod_{n=1}^{N}P(\underline{\sigma}_n|N) \tag{7}$$

where $P(\underline{\sigma}_n|N)$ is the prior distribution of the model parameters $\underline{\sigma}_n$ for the n-th soil layer, which is calculated using Equation 8:

$$P(\underline{\sigma}_n|N)=\begin{cases}\frac{1}{1.33}\times\frac{1}{1.99} & \text{for } \sigma_{FR}\in[0,1.33],\ \sigma_{Qt}\in[0,1.99]\\ 0 & \text{for others}\end{cases} \tag{8}$$

Interested readers are referred to Wang et al. (2013) for detailed discussions on the prior distribution in Equation 8.

Then, the most probable thicknesses of the soil layers are identified using an asymptotic technique to approximate the posterior PDF of the model parameters in Equation 5. The asymptotic technique involves approximating the posterior PDF as a Gaussian PDF (Cao & Wang 2013, Wang et al. 2013). Then, the posterior PDF for the model parameters is a joint Gaussian PDF with the mean value equal to the Most Probable Values (MPV) of the posterior PDF. The MPV, denoted by $\underline{\Omega}_N^*$, maximizes the posterior PDF. Under this approximation, maximizing $P(\underline{\Omega}_N|\underline{\xi},N)$, or for numerical convenience, minimizing an objective function $f=-\ln[P(\underline{\Omega}_N|\underline{\xi},N)]$, leads to the posterior mean for the model parameters.

Note that, because the likelihood function in Equation 6 is a function of thicknesses of soil layers, both the posterior PDF and the objective function are functions of soil layer thicknesses. Maximizing the posterior distribution, i.e. minimizing the objective function, provides not only the MPV of $\underline{\Omega}_N$ but also the MPV of layer thicknesses.

5 THE MOST PROBABLE NUMBER OF SOIL STRATA

Starting from this section, the number N of soil layers is considered as a variable k, and a Bayesian model class selection approach (Beck & Yuen 2004, Cao & Wang 2013) is used to determine the most probable value k^* among a pool of candidate model classes. A model class herein is referred to a family of stratification models that share the same number (e.g. k) of soil layers but have different model parameters (e.g., layer thickness $\underline{h}_N$ and model parameters $\underline{\Omega}_N$). Let N_{max} denote the maximum possible number of soil layers within the depth of which CPT is performed. Then, the model class number k is a positive integer varying from 1 to N_{max}. The most probable model class M_k^* is the model class with the maximum occurrence probability among all candidate model classes, given that a set of CPT data $\underline{\xi}$ is observed. The most probable layer number k^*, therefore, can be determined by selecting the one with the maximum value of $P(M_k|\underline{\xi})$ for all candidate model classes.

According to Bayes' Theorem (Beck & Yuen 2004, Cao & Wang 2013), $P(M_k|\underline{\xi})$ is written as:

$$P(M_k|\underline{\xi})=P(\underline{\xi}|M_k)P(M_k)/P(\underline{\xi}),\ k=1,2,\ldots,N_{\max} \tag{9}$$

where $P(\underline{\xi})$ is a constant; $P(\underline{\xi}|M_k)$ is frequently referred to as the 'evidence' for the model class M_k provided by the CPT data $\underline{\xi}$; $P(M_k)$ is the prior probability of the model class M_k. If no prevailing prior knowledge on the number of soil layers is available, the prior probability for each of the N_{max} candidate model classes is the same, and therefore, $P(M_k)$ can be taken as $1/N_{max}$. Then, according to Equation 9, $P(M_k|\underline{\xi})$ is proportional to $P(\underline{\xi}|M_k)$, and the most probable number of soil layer can be selected by comparing the value of $P(\underline{\xi}|M_k)$ among the N_{max} candidate model classes. The most probable number of soil layers is the one with the maximum value of $P(\underline{\xi}|M_k)$. Details of calculating the evidence $P(\underline{\xi}|M_k)$ for each model class are referred to Wang et al. (2013).

The $P(\underline{\xi}|M_k)$ is calculated repeatedly for $k=1,2,\ldots,N_{max}$, and the most probable number k^* of soil layers are determined by selecting the model class with the maximum $P(\underline{\xi}|M_k)$ value. Note that the most probable thicknesses $\underline{h}_k^*$ have been determined in the previous section. Therefore, the determination of the most probable number k^* of soil layers simultaneously leads to the determination of the most probable thicknesses $\underline{h}_{k^*}^*$.

6 APPLICATION PROCEDURE

Seven steps are involved in the application procedure of the proposed approach. Details of each step and their associated equations are summarized as follows:

1. Obtain a set of CPT data and convert them to the normalized terms;
2. Choose an appropriate maximum number N_{max} of soil layers for the CPT data;
3. Define the prior distribution for model parameters using Equations 7 and 8;
4. Compute the likelihood function using Equations 1–4;

5. Construct the objective function, and minimize the objective function (e.g., by a MATLAB function "fminsearch") and determine the most probable thicknesses $\underline{h}_k^*$ for the k-th model class. Then, compare $P_{ST_J}(\underline{\xi}_n|\underline{\sigma}_n, N)\ J = 1, 2 \ldots, 9$ for the n-th layer and determine the soil type for the soil layer;
6. Calculate the conditional probability $P(\underline{\xi}|\underline{M}_k)$;
7. Repeat steps 3–6 $N_{\max}$ times to calculate $\underline{h}_k^*$ and $P(\underline{\xi}|M_k)$ for the $N_{\max}$ candidate model classes. The model class with the maximum value of $P(\underline{\xi}|M_k)$ is selected as the most probable model class M_k^* and the corresponding $\underline{h}_k^*$ are the most probable layer thicknesses/boundaries.

Although the proposed Bayesian approach involves quite a number of equations and seems mathematically complicated, it is rather straightforward to program it as a user function or toolbox in computer software. Geotechnical practitioners only need to provide prior knowledge, if any, and project-specific CPT test data as input, and the user function or toolbox will return the underground soil classification and stratification. This significantly improves the practicality of the proposed approach.

The proposed Bayesian approaches have been shown to perform well for some real-life examples (Wang et al. 2013). In the next section, the proposed approaches will be further validated using a set of simulated CPT data.

7 SIMULATED EXAMPLE

The CPT data is simulated from a three-layer soil profile, with respective thicknesses of 3 m, 4 m, and 5 m and a depth interval of 0.1 m. The distribution of the $\ln(F_R)$ and $\ln(Q_t)$ of the simulated CPT data is shown in Figure 4. Figure 5 plots the $\ln(F_R)$ and $\ln(Q_t)$ data pairs in the Robertson chart, and the data points are mainly located within the areas 1, 3 and 5 (see Table 1 for the description of each soil type), with some scattered data points in the areas of 2, 4 and 6. Note that in practice the true boundaries of soil layers are unknown, and they are estimated from project-specific test results and prior knowledge.

Consider, for example, four candidate model classes. For all model classes, the prior distributions of model parameters are all estimated using Equations 7 and 8. Using the prior knowledge and the CPT data shown in Figure 4, the proposed Bayesian system identification and model class selection approaches are used to determine the most probable number of soil layers and identify the most probable thicknesses and soil types of the layers, as discussed in the following two subsections, respectively.

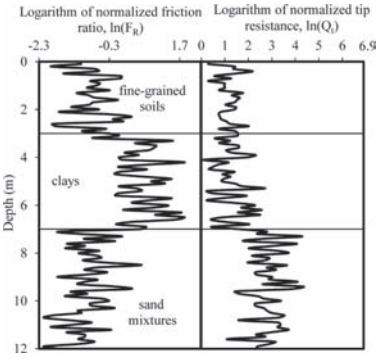

Figure 4. A set of simulated CPT data.

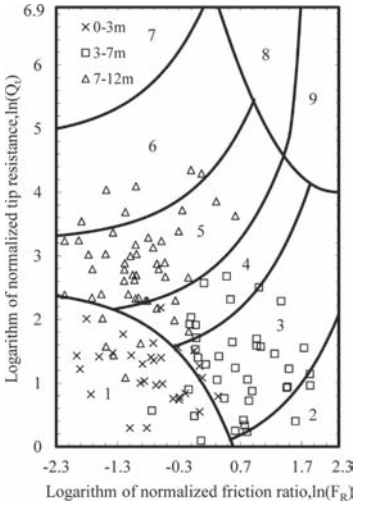

Figure 5. The distribution of the simulated CPT data points on the Robertson soil classification chart.

7.1 *The most probable number of soil strata*

Table 2 shows the logarithm of evidence (i.e. $\ln[P(\underline{\xi}|M_k)]$) in the second Column for the four candidate model classes. It increases from –218.9 to –98.4 as k increases from 1 to 3 and it then decreases from –98.4 to –102.1 as k further increases from 3 to 4. The model class with three soil layers, has the largest value of evidence among all the four model classes. Therefore, the most probable number of soil layers is three. The true number of soil layers is identified correctly.

7.2 *The most probable thicknesses or boundaries*

The most probable thicknesses (i.e. $\underline{h}_k^*$) of soil layers for the four candidate model classes are also summarized in Table 2. The most probable boundaries for the four model classes and the true boundaries

Table 2. Results of the Bayesian model class selection approach in the simulated case.

Model class	$\ln[P(\underline{\xi}\|M_k)]$	The most probable thicknesses h_k^* (m)			
		h_1^*	h_2^*	h_3^*	h_4^*
M_1	–218.9	12	–	–	–
M_2	–142.1	7.0	5.0	–	–
M_3^*	–98.4	3.2	3.9	4.9	–
M_4	–102.1	3.2	2.4	1.3	5.1

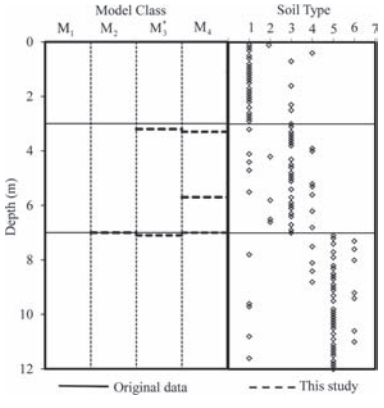

Figure 6. The most probable boundaries of soil layers for different model classes.

of the three soil layers defined in the original data are delineated in Figure 6 by dashed and solid lines, respectively. For the most probable model class M_3^*, the most probable thicknesses of these three layers are 3.2 m, 3.9 m and 4.9 m, respectively. They are consistent with the ones defined in the original data. In addition, the soil types for the three layers are classified as soil type 1, soil type 3 and soil type 5, respectively. They agree well with the true soil types defined in the original data.

8 SUMMARY AND CONCLUSIONS

This paper aimed to identify underground soil stratum and classify the soil types using Bayesian approaches and Cone Penetration Tests (CPT). It integrated the Robertson chart with Bayesian approaches to explicitly and properly consider the uncertainty in the CPT-based soil classification and the spatial distribution of the CPT data. The proposed Bayesian framework contains two major components: a model class selection approach to identify the most probable number of underground soil layers and a system identification approach to estimate the most probable layer thicknesses and classify the soil types simultaneously.

Equations were derived for the Bayesian approaches, and the proposed approaches were validated using a set of simulated CPT data. It has been shown that the proposed approaches correctly identify the underground soil stratification and classify the soil type of each layer.

ACKNOWLEDGEMENT

The work described in this paper was supported by a grant from the Research Grants Council of the Hong Kong Special Administrative Region, China (Project No. 9041550 (CityU 110210)), a grant from City University of Hong Kong (Project No. 7002695), and a grant from National Natural Science Foundation of China (Project No. 51208446). The financial supports are gratefully acknowledged.

REFERENCES

Beck, J.L. & Yuen, K.V. 2004. Model selection using response measurements: Bayesian probabilistic approach. *Journal of Engineering Mechanics* 130(2): 192–203.

Cao, Z. & Wang, Y. 2013. Bayesian approach for probabilistic site characterization using cone penetration tests. *Journal of Geotechnical and Geoenvironmental Engineering* 139(2): 267–276.

Jefferies, M.G. & Davies, M.P. 1993. Use of CPTU to estimate equivalent SPT N60. *Geotechnical Testing Journal* 16(4): 458–468.

Kurup, P.U. & Griffin, E.P. 2006. Prediction of soil composition from CPT data using general regression neural network. *Journal of Computing in Civil Engineering*, 20(4): 281–289.

Mayne, P.W. 2007.Cone penetration testing: A synthesis of highway practice. *NCHRP synthesis 368*. Washington, D.C: Transportation Research Board.

Robertson, P.K. 1990. Soil classification using the cone penetration test. *Canadian Geotechnical Journal* 27(1): 151–158.

Robertson, P.K. 2009. Interpretation of Cone Penetration Tests-a unified approach. *Canadian Geotechnical Journal* 46(11): 1337–1355.

Wang, Y., Au, S.K. & Cao, Z. 2010. Bayesian approach for probabilistic characterization of sand friction angles. *Engineering Geology* 114(3–4): 354–363.

Wang, Y., Huang, K. & Cao, Z. 2013. Probabilistic identification of underground soil stratification using cone penetration tests. *Canadian Geotechnical Journal* (accepted).

Zhang, Z.J. & Tumay, M.T. 1999. Statistical to fuzzy approach toward CPT soil classifications. *Journal of Geotechnical and Geoenvironmental Engineering* 125(3): 179–186.

Geotechnical Safety and Risk IV – Zhang et al. (eds)

Characterization of three-dimensional random crack network in soil using CT test

J.H. Li
Centre for Offshore Foundation Systems, The University of Western Australia, Perth, Australia
Harbin Institute of Technology Shenzhen Graduate School, Shenzhen, China

L.M. Zhang
The Hong Kong University of Science and Technology, Hong Kong, China

Y. Zhao
China Merchants Shekou Industrial Zone Co., Ltd., Shenzhen, China

ABSTRACT: Cracks in soils are three-dimensional (3D) and provide important preferential pathways for rainfall infiltration. The geometrical properties of 3D cracks are crucial parameters for analysis of seepage in discontinuous soils or rocks. However 3D crack planes in soils are still largely unknown because the cracks in soils are prone to disturbance and sensitive to moisture content. This paper presents a method to characterize 3D crack planes in soils by employing a nondestructive Computer Tomography (CT) test. The traces of cracks are first obtained from sections along three directions in the CT test. Then three criteria are proposed to determine a crack plane based on these crack traces. Finally the random crack network in the soil is established by assembling the planes. The probability distribution and statistical parameters can be obtained based on the obtained crack planes.

1 INTRODUCTION

Cracks in soils provide preferential flow pathways for rainfall infiltration into soil slopes, covers and clay liners. The infiltration in a cracked soil is mainly determined by the geometry of crack networks (Li et al. 2009). Many researchers studied the pattern and geometrical parameters of a crack network on soil surface (Li & Zhang 2010, 2011; Nahlawi & Kodikara 2006). However cracks normally penetrate the soil and form a three-dimensional random crack network (Li 2009). Based on assumed crack shapes and distributions some researchers have attempted to establish a three dimensional network for fractured rock. For example, a disc-shaped fracture model was proposed by Baecher (1977) and Long et al. (1985) and a polygonal fracture model was presented by Dershowitz (1985). The pattern and geometry of cracks in soils are however still largely unknown because the cracks in soils are more easily destroyed and sensitive to changes in moisture content. The objective of this paper is to present a method to characterize a 3D random crack network in an expansive soil mass. A Computer Tomography (CT) test was used to investigate the crack traces in cross sections of a soil sample without disturbing the soil. A method was then proposed to reconstruct the crack plane in three dimensions. Both the two- and three-dimensional crack geometries were obtained.

2 FIELD BLOCK SAMPLE AND CT TESTS

A block soil sample was carefully retrieved in an expansive soil slope in Zhenjiang, China. The physical properties of the soil are shown in Table 1. The soil was cut into a cube with dimensions of $0.25 \times 0.25 \times 0.25$ m. The soil sample experienced several drying-wetting cycles. The expansive soil shrinks during drying and swells during wetting. Therefore many cracks were present within the soil cube as shown in Figure 1a.

Table 1. Properties of the field soil sample.

Soil property	Value
Dry unit weight (kN/m^3)	16.7
Saturated water content (%)	30.0
Liquid limit (%)	40.4
Plastic limit (%)	15.6
Shrinkage index	13.0
Expansive index	56.0

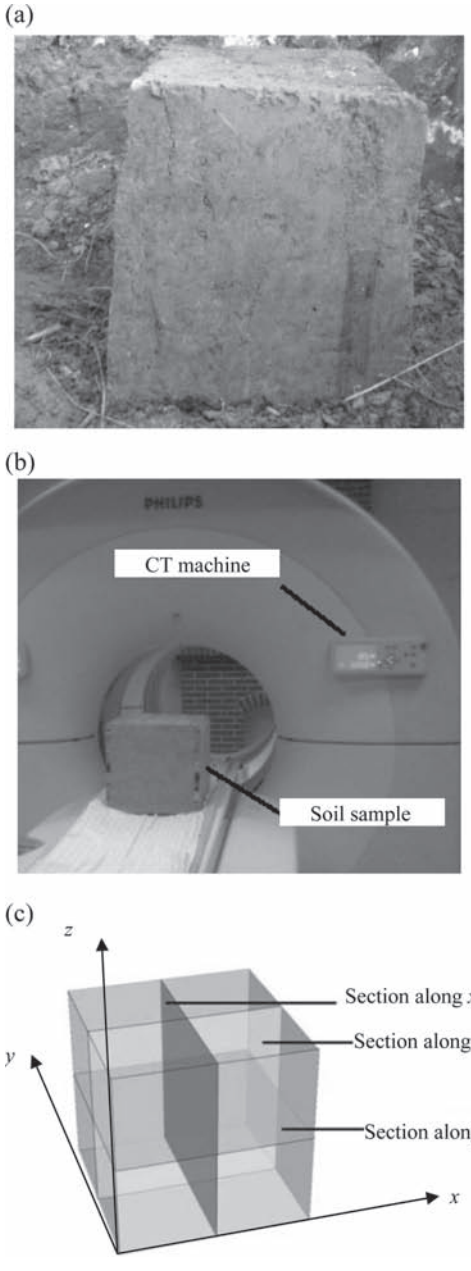

Figure 1. (a) Soil sample; (b) CT test; (c) sections of the soil sample in the CT test.

After the cracks reached a steady state it was brought to the laboratory for CT tests, as shown in Figure 1b. The cross sections of the soil sample were obtained along the x-, y-, and z-directions, respectively, as shown in Figure 1c. Along the x-direction there are 36 sections. Along the y- and z-directions, there are 38 and 50 sections, respectively. Therefore the spacing between the sections along the x direction is 6.4 mm. The spacing between the sections along the y direction is 6.6 mm. The spacing between the sections along the z direction is 5 mm.

3 TRACES IN THREE-DIMENSIONAL SPACE

When a crack plane intersected with a section there will be an intersection line in the section, which is a trace of a crack plane. A section in the CT test shows the traces of different crack planes (see Fig. 2). The crack traces show a darker color in

Figure 2. A section containing crack traces.

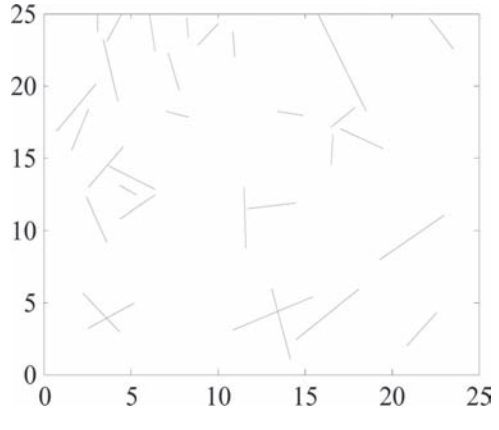

Figure 3. The crack traces on one section in Figure 2 (unit: cm).

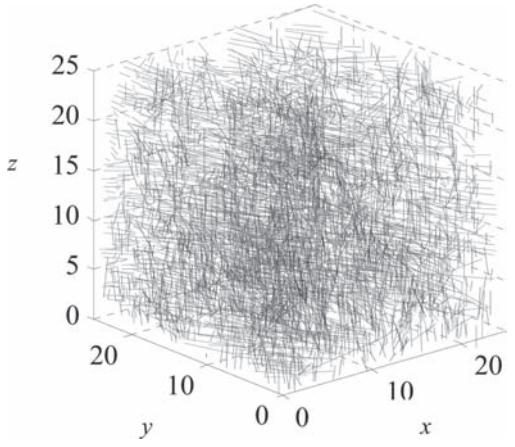

Figure 4. Crack traces in 3D space (unit: cm).

the section than that of the soil matrix. Assuming the 3D crack is a plane, a crack trace that develops along a certain direction can then be modeled as a line. The coordinates of the two ends of the crack are extracted from the section. The accuracy of the data is 0.3 mm. The crack traces in a certain section can then be obtained. Figure 3 shows the traces of the section in Figure 2. In this way the crack traces in every section can be obtained and put into a 3D space as shown in Figure 4.

4 CRITERIA TO DETERMINE THE CRACK TRACES THAT BELONG TO A PLANE

Figure 4 shows all the traces in different sections in the CT test. However difficulty lies in how to determine the 3D crack plane from the traces. In this section three criteria are proposed to determine the traces that belong to a crack plane:

1. The traces in the sections along the z-direction must be parallel to each other. Figure 5a shows a plane in the 3D space. If this plane is intersected by three sections along the z-direction (Fig. 5b), the traces of the plane in the sections along the z-direction are shown in Figure 5c. The three traces are parallel to each other. Therefore if the traces in the sections along the z-direction belong to a crack plane they should parallel to each other.
2. The spacing between the adjacent traces in sections along the z-direction is equal. As the spacing between two adjacent sections is equal (i.e., 5 mm along the z-direction) in the CT test the spacing of the two adjacent traces from a crack plane should be the same (as shown in Fig. 5c).

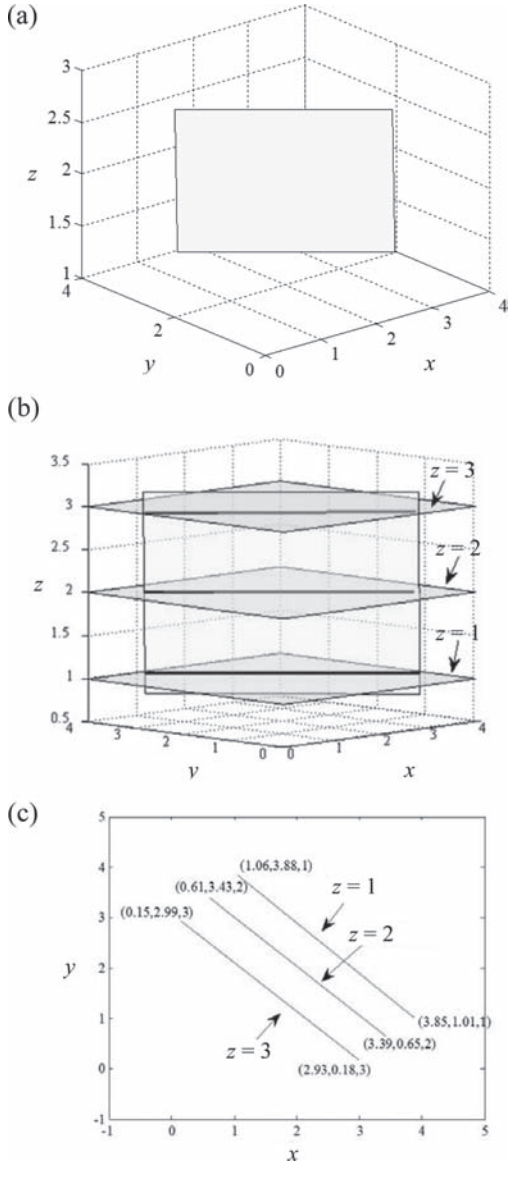

Figure 5. (a) A plane; (2) three sections along the z-direction; (c) traces between the plane and the three sections.

If the traces are parallel to each other but the spacing is different, these traces could be in different planes. Figure 6 shows two parallel planes that intersect with three sections along the z-direction. The traces of the two crack planes are parallel to each other. However the spacing between the traces from different planes is not equal (i.e., $d_1 \neq d_2$), as shown in Figure 6(b).

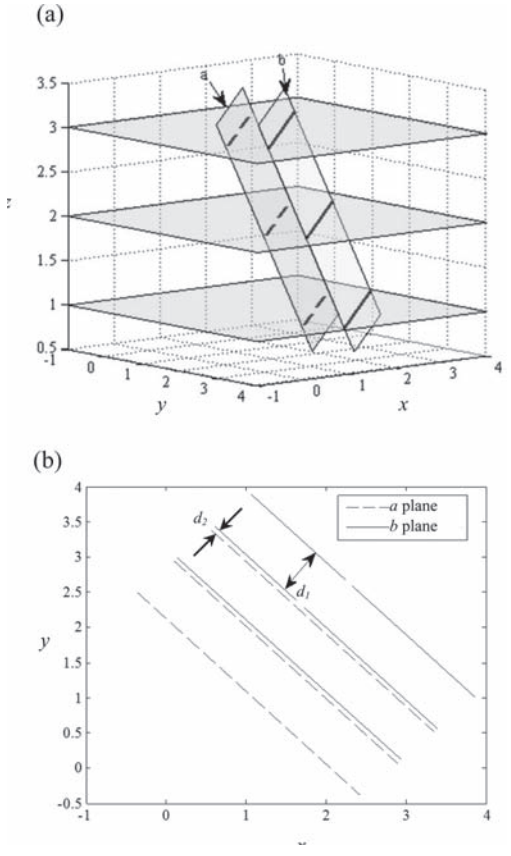

Figure 6. (a) Two parallel planes that intersect with three sections; (b) traces of the two planes.

3. The traces that satisfy the first and second criteria must be interconnected by the traces in the sections along the *x*- or *y*-direction.

There is a possibility that the traces from two different planes are parallel to each other and the spacing between them is equal, as shown in Figure 7. Figure 7a shows two different planes (CP1 and CP2) that are intersected by three sections. The traces of the two planes (as shown in Fig. 7b) are parallel to each other and have an equal spacing. However, the traces shown in solid line belong to plane CP1 and those shown in dash line belong to CP2. The traces belong to the same plane should be intersected by the traces in the sections along the *x*- or *y*-direction. Figure 7c shows the traces of plane CP1 along the *x*- and *y*-direction (the dash lines), which intersect with the traces in the sectios along the *z*-direction (the solid lines). The traces of plane CP2 do not intersect with the traces of plane in the sections along the *y*-direction. In the following analysis the

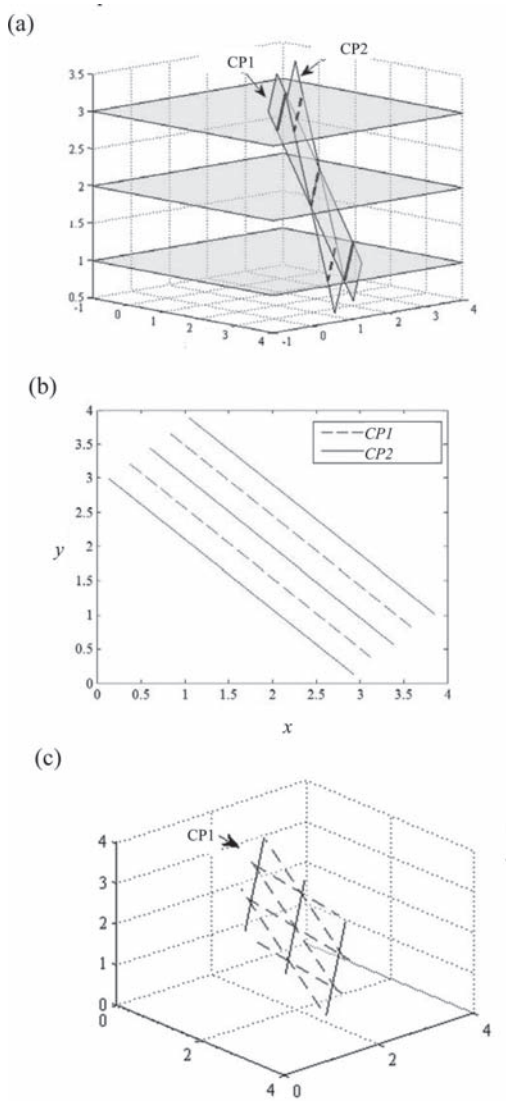

Figure 7. (a) Two planes that intersect with three sections; (b) traces of the two planes in the sections along the *z*-direction; (c) traces of plane CP1 in the sections along the *z*-direction intersected by the traces in the sections along the *x*- and *y*-direction.

three criteria are used to determine the traces that belong to a certain crack plane.

5 IDENTIFICATION OF CRACK PLANES

According to the three criteria the traces that belong to a certain crack plane can be identified. First, the traces in the sections along the *z*-direction are projected to the $x - y$ plane. Figure 8a shows the

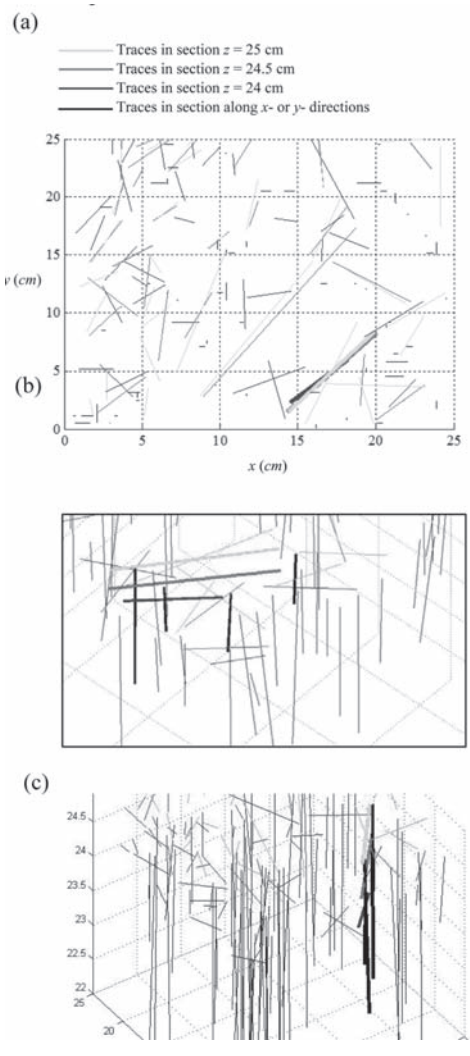

Figure 8. (a) Traces that projected on the $x - y$ plane; (b) traces on the sections along the z-direction intersecting by the traces in the sections along the x- or y-direction; (c) traces in the same crack plane (unit: cm).

traces of the soil sample in the sections along the z-direction which are projected on the $x - y$ plane. The green lines, red lines, and blue lines represent the crack traces on the sections of $z = 25$, $z = 24.5$, and $z = 24$, respectively. The black lines represent the traces on the section along the x- or y-direction. The traces those are parallel to each other and have similar spacing in the three sections are found (e.g., the three bold lines in Fig. 8a and 8b). This means the three traces satisfy the first and second criterion. The three lines are also intersected by the black lines (as shown in Fig. 8b), which means that

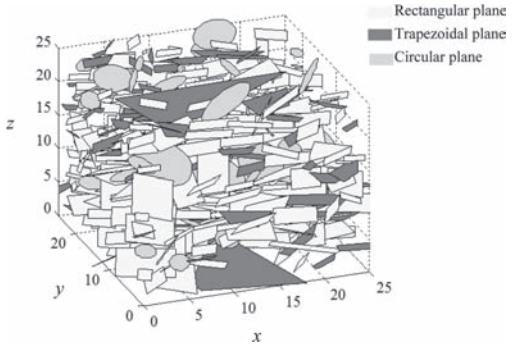

Figure 9. All of crack planes in 3D space (unit: cm).

they satisfy the third criterion. Then there will be a large possibility that the crack plane is developed according to these traces. Figure 8c shows clearly that there is a crack plane crossing these traces.

Following this method, the crack planes in the soil sample are all identified. The shape of the crack planes are further investigated by Zhao (2012). Finally the crack planes with different shapes are obtained and presented in Figure 9. There are totally 424 crack planes. The average depth of the crack plane is about 21 mm. These crack planes form a random crack network in the 3D space. The probability distribution and the statistical parameters can be obtained based on the obtained crack planes (Zhao 2012).

6 SUMMARY AND CONCLUSIONS

This paper presents a method to characterize a three-dimensional random crack network in soil using a CT test. A field block soil sample subjected to several drying-wetting cycles was retrieved to a laboratory for a CT test. The traces of the cracks in the soil sample were obtained in the sections along the x-, y-, and z-directions. Three criteria were proposed to determine a crack plane using these traces of the cracks. Finally many crack planes were established following the proposed method. It is found that the crack planes intersect with each other and form a random crack network. The average depth of the crack planes is about 21 mm. The probability distribution and the statistical parameters for the cracks can be obtained based on the obtained crack planes.

ACKNOWLEDGEMENTS

This research was substantially supported by the Natural Science Foundation of China

(Grants No. 51379053 and No. 51009043), the Doctoral Program of Higher Education of China (No. 20102302120070), and the Science, Industry, Trade and Information Technology Commission of Shenzhen Municipality.

REFERENCES

Baecher, G.B. 1977. Statistical description of rock properties and sampling. *Proceedings of the 18th U.S. symposium on rock mechanics.* Colorado: Colorado School of Mines Press.

Dershowitz, W.S. 1985. A new three dimensional model for flow in fractured rock. *Int. Assoc. Hydrogeol.* 17(7): 441–448.

Li, J.H. 2009. *Field experimental study and numerical simulation of seepage in saturated/unsaturated cracked soil*. PhD thesis. The Hong Kong University of Science and Technology, Hong Kong.

Li, J.H., Zhang, L.M., Wang, Y., & Fredlund, D.G. 2009. Permeability tensor and representative elementary volume of saturated cracked soil. *Canadian Geotechnical Journal* 46: 928–942.

Li, J.H. & Zhang, L.M. 2010. Geometric parameters and REV of a crack network in soil. *Computers and Geotechnics* 37: 466–475.

Li, J.H. & Zhang, L.M. 2011. Study of desiccation crack initiation and development at ground surface. *Engineering Geology* 123: 347–358.

Long, J.C.S. Gilmour, P. & Witherpoon, P.A.A. 1985. Model for steady fluid flow in random three-dimensional networks of disc-shaped fractures. *Water Resources Research* 21(8): 1105–1115.

Nahlawi, N. & Kodikara J.K. 2006. Laboratory experiments on desiccation cracking of thin soil layers. *Geotechnical and Geological Engineering* 24: 1641–1664.

Zhao, Y. 2012. *Reconstruction and numerical modelling of three-dimensional random crack network in soils*. MPhil thesis, Harbin Institute of Technology, Shenzhen, China.

Geotechnical Safety and Risk IV – Zhang et al. (eds)
© 2014 Taylor & Francis Group, London, ISBN 978-1-138-00163-3

Linear regression and statistical analysis of shear strength parameters

X. Li, L.H. Chen & N. Zhang
School of Civil Engineering, Beijing Jiaotong University, Beijing, China

ABSTRACT: Linear regression is often used to obtain the sample mean value that can be regarded as the population mean. A common misuse of linear regression is on the standard error of the mean, which decreases with sample number and has nothing to do with the real variance of regression parameters. Derivations are reported to calculate the "real" variance and numerical tests are used to verify these derivations. Further, linear regression is used to analyze the tri-axial test data. The results demonstrate that an equation transformed from traditional mean stress relation can lead to mean and variance values with higher accuracy in linear regression, especially under the condition of small sample size (smaller than 1000).

1 INTRODUCTION

One of the classic job and essential ability of geotechnical engineers is to evaluate reasonable values of soil parameters based on results of in situ and laboratory tests. Both the mean value and the variance of soil properties are concerned, either for determining the design values of soil properties, or using directly in reliability analysis.

Linear Regression (LR) is often used to calculate the mean and variance of soil properties. However, the linear regression all too often is used incorrectly in geotechnical engineering and the theoretical assumptions of the method are often violated (Mann 1987). For example in shear strength estimation based on triaxial test data or direct shear test data, many engineers use the standard deviation of linear regression parameters as the "real" standard deviation of shear strength and use it in design. However, this is not correct. The standard deviation of linear regression parameters only represents the variance of the estimated mean value from the linear regression analysis. In fact, the values of standard deviation of linear regression parameters will decrease with the increase of sample size (Chen 2005, Weisberg 2005) and approach zero when the sample size approaches infinite. Special variance functions should be used to calculate the variances of shear strength parameters.

In this paper, derivations are reported to calculate the "real" standard deviation. Numerical tests are also carried out to prove the misusing of standard deviation of linear regression parameters and to verify the special equation used to calculate the variance. Further, linear regression is used to analyze the tri-axial test data, searching for the best method for the determination of the mean and variance of shear strength parameters.

2 SIMPLE LINEAR REGRESSION METHOD

A Simple Linear Regression (SLR) equation for variables $\boldsymbol{Y}$ and $\boldsymbol{X}$ with n pairs of values of x_i and y_i is

$$Y = a + bX + \varepsilon \tag{1}$$

where $\boldsymbol{a}$ and $\boldsymbol{b}$ are regression coefficients, $\boldsymbol{\varepsilon}$ is a random variable. The following quantities are defined as,

$$\begin{aligned} \mu_X &= \sum x_i/n \\ \mu_Y &= \sum y_i/n \\ SXX &= \sum (x_i - \bar{x})^2 \\ SXY &= \sum (x_i - \bar{x})(y_i - \bar{y}) \\ s_0^2 &= \frac{1}{n-2}\sum (y_i - a - bx_i)^2 \end{aligned} \tag{2}$$

Assume (1) the residual $\boldsymbol{\varepsilon}$ has a mean of 0 and a small variance of var($\boldsymbol{\varepsilon}$), and (2) $\boldsymbol{X}$ is the independent variable, $\boldsymbol{Y}$ is the dependent variable. The regression coefficients $\boldsymbol{a}$ and $\boldsymbol{b}$ can be estimated as,

$$b = \mu_{\boldsymbol{b}} = SXY/SXX \tag{3}$$

$$a = \mu_{\boldsymbol{a}} = \mu_Y - b\mu_X \tag{4}$$

$$Se^2(b) = \frac{s_0^2}{SXX} \tag{5}$$

$$Se^2(a) = s_0^2\left(\frac{1}{n} + \frac{\mu_X{}^2}{SXX}\right) \quad (6)$$

$$\rho_{a,b} = -s_0^2\frac{\mu_X{}^2}{SXX} \quad (7)$$

where a, b are the sample means of ***a, b***; $Se(\boldsymbol{a})$ is the standard error of ***a***, $Se(\boldsymbol{b})$ is the standard error of ***b***, $\rho_{a,b}$ is correlation coefficient of ***a*** and ***b***; s_0 is often called as standard error of regression.

3 LIMITATION OF LINEAR REGRESSION METHOD

Giving the mean and variance of ***X***, SXX increases with the size of ***X*** (referring to Eq. 2). Giving ***a, b, ε***, the standard error of regression s_0 can be regarded as a constant. If ***a, b, ε*** are independent and follow normal distribution, s_0^2 is equal to var(***ε***) (Yan & Su 2009). Obviously, $Se^2(\boldsymbol{a})$ and $Se^2(\boldsymbol{b})$ are inversely proportional to the sample size number.

In fact, the Standard Errors of the Mean (SEM), Se(a) and Se(b) are the standard deviation of the sample-mean's estimate of a population mean. It can also be viewed as the standard deviation of the error in the sample mean relative to the true mean, since the sample mean is an unbiased estimator. Clearly, the SEMs calculated by Eqs. 5 and 6 are not the real standard deviations of a and b; they just indicate the accuracy of the mean value calculated by Eqs. 3 and 4.

3.1 *Numerical test of simple linear regression method*

Considering Eq. 1, numerical tests can be carried out to check the validity of simple linear regression. The settings of numerical tests are listed in Table 1.

Table 1. Summary of numerical test settings.

Test no.	***a***	***b***	***X***	Eq. no.	Table no.
1	N (10, 4)	N (2, 0.16)	U (0, 100)	1	2
2	N (10, 4)	N (2, 0.16)	I (0, 100)	1	3
3	N (10, 4)	N (2, 0.16)	U (0, 100)	8	4
4	N (10, 4)	N (2, 0.16)	U (0, 100)	9	5
5	N (10, 4)	N (2, 0.16)	U (0, 100)	12	5
6	N (10, 4)	N (2, 0.16)	I (0, 100)	10	6
7	N (10, 4)	N (2, 0.16)	I (0, 100)	12	6

*N(μ,σ^2) denotes a normal distribution; U(X_{min}, X_{max}) denotes a uniform distribution; I(X_{min}, X_{max}) denotes m value with the same spacing in interval [X_{min}, X_{max}].

In numerical test 1, ***a, b*** are taken as normal distributions and ***X*** as a uniform distribution with input settings: $a = 10$, $\sigma_a = 2$, $b = 2$, $\sigma_b = 0.4$, $x_{min} = 0$, $x_{max} = 100$. The test procedure for numerical test 1 is as follows:

1. Giving a, σ_a and b, σ_b for ***a, b***.
2. Generating n pairs of random numbers ***a, b*** which follow normal distributions N(a, σ_a^2) and N(b, σ_b^2).
3. Generating n random numbers for ***X***, which follow a uniform distribution on [x_{min}, x_{max}].
4. For each x_i, selecting one pair ***a, b*** and using Eq. 1 to calculate y_i.
5. Finally, n pair x_i and y_i are obtained. Calculating the sample mean and standard error using Eqs. 3~6.
6. Comparing the sample mean and standard error with the input value a, σ_a and b, σ_b.

The results of numerical test 1 are listed in Table 2. Referring to Table 2, the sample means calculated by Eqs. 3 and 4 have some difference with the input values and become closer to the input values with the increase of sample size. Referring to Figure 1, $Se^2(\boldsymbol{a})$ and $Se^2(\boldsymbol{b})$ are found to be inversely proportional to the sample size and has nothing to do with the input var(***a***) and var(***b***).

Table 2. Simple linear regression with uniform ***X*** (test 1).

Sample size n	a (Eq. 4)	b (Eq. 3)	$Se^2(\boldsymbol{a})$ (Eq. 6)	$Se^2(\boldsymbol{b})$ (Eq. 5)
10	18.75	1.742	266	0.124
50	9.37	2.02	46.83	0.01
200	5.40	2.12	10.12	0.003
1000	9.96	2.00	2.21	6.5E-4
5000	9.38	2.02	0.42	1.3E-4
20000	9.77	2.01	0.1	3.2E-5
100000	9.96	2.00	0.02	6.5E-6

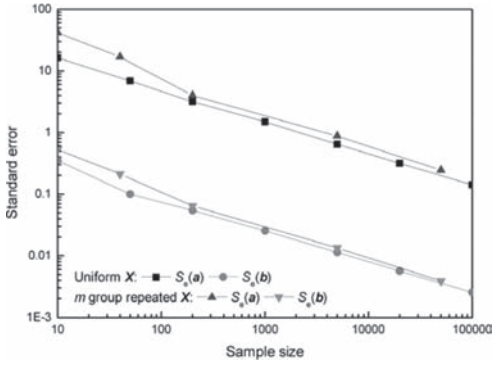

Figure 1. Standard error vs. sample size.

Sometimes, $\boldsymbol{X}$ may not follow a uniform distribution. For example, $\boldsymbol{X}$ may be the confining pressure in triaxial tests, which normally is taken as 50 kPa, 100 kPa, 200 kPa, 400 kPa, etc. To check the influence of $\boldsymbol{X}$ on simple linear regression, m groups of repeated x_i are used in Numerical test 2 (referring to Table 1). The procedure is as follows:

1. Giving a, σ_a and b, σ_b for ***a, b***.
2. Generating $n*m$ pairs of random numbers a, b which follow normal distributions $N(a, \sigma_a^2)$ and $N(b, \sigma_b^2)$.
3. Generating m numbers for $\boldsymbol{X}$ with the same spacing in the interval $[x_{min}, x_{max}]$.
4. For each x_i, selecting n pairs of a, b and using Eq. 1 to calculate y_i.
5. Finally, $n*m$ pairs of x_i and y_i are obtained. Calculating the sample mean and standard error using Eq. 3~6.
6. Comparing the sample mean and standard error with the input value a, σ_a and b, σ_b.

With input settings: $a = 10$, $\sigma_a = 2$, $b = 2$, $\sigma_b = 0.4$, the results of numerical test are listed in Table 3. The distribution of $\boldsymbol{X}$ does not have significant influence on the results calculated by Eqs. 3~6. Again, the accuracy of a, b calculated by Eq. 3 and 4 increases with the sample size. $Se^2(\boldsymbol{a})$ and $Se^2(\boldsymbol{b})$ are inversely proportional to the sample size and show no relation with var($\boldsymbol{a}$) and var($\boldsymbol{b}$). Another thing to note is that $Se(a)^2$ is much larger than $Se^2(\boldsymbol{b})$ in the upper two cases. Referring to Eq. 6, because $Se^2(\boldsymbol{a})$ is about μ_X^2, i.e. 2500 in case 1, times of $Se^2(\boldsymbol{b})$. That is to say, the b value calculated by Eq. 3 is of much higher accuracy comparing the a value calculated by Eq. 4.

Considering another form of Eq. 1

$$\frac{Y}{X} = \frac{a}{X} + b + \varepsilon \tag{8}$$

where $1/\boldsymbol{X}$ can be regarded as independent variable and $\boldsymbol{Y}/\boldsymbol{X}$ can be regarded as dependent variable. Applying SLR to Eq. 8 with the same data source used in numerical test 1, the results of the numerical test are listed in Table 4. Referring to the *a, b* values listed Table 4, if the sample size is smaller than 1000, Eq. 8 can lead to better accuracy of *a, b* comparing to Eq. 1. However, if the sample size is larger than 1000, Eq. 1 will lead to better accuracy of *a, b.* Such phenomenon is consistent with the values of standard error $Se(\boldsymbol{a})$ and $Se(\boldsymbol{b})$, i.e. the indicator of accuracy of sample mean.

Table 3. SLR with m group repeated $\boldsymbol{X}$ (test 2).

Sample size	a (Eq. 4)	b (Eq. 3)	$Se^2(\boldsymbol{a})$ (Eq. 6)	$Se^2(\boldsymbol{b})$ (Eq. 5)
n = 5, m = 2	17.12	1.89	1763	0.28
n = 20, m = 2	10.32	1.99	282	4.5E-2
n = 20, m = 10	15.24	1.87	15.92	4.1E-3
n = 100, m = 2	18.29	1.88	48.85	7.8E-3
n = 1000, m = 5	10.21	1.99	0.78	1.8E-4
n = 5000, m = 10	9.92	2.00	0.06	1.5E-5

Table 4. Simple linear regression with uniform $\boldsymbol{X}$ (test 3).

Sample size	a (Eq. 3)	b (Eq. 4)	$Se^2(\boldsymbol{a})$ (Eq. 5)	$Se^2(\boldsymbol{b})$ (Eq. 6)
n = 10	4.2	2.37	3.42	2.7E-2
n = 50	7.96	2.06	7.8E-2	3.6E-3
n = 200	10.32	1.98	2.7E-2	1.4E-3
n = 1000	10.19	2.00	3.9E-3	2.5E-4
n = 5000	9.33	2.06	1.1E-4	7.9E-4
n = 20000	10.55	1.97	1.4E-4	2.3E-4
n = 100000	12.66	1.74	1.4E-5	3.0E-4

3.2 *Summary*

In short, the numerical test results prove that:

1. $Se^2(\boldsymbol{a})$ and $Se^2(\boldsymbol{b})$ are inversely proportional to the sample number; having nothing to do with the real var($\boldsymbol{a}$) and var($\boldsymbol{b}$) but indicating the accuracy of the mean value calculated by Eqs. 3 and 4.
2. Both Eq. 1 and Eq. 8 can be used to estimate the sample mean *a, b*. The selection of Eq. 1 or Eq. 8 can be referring to the standard errors $Se^2(\boldsymbol{a})$ and $Se^2(\boldsymbol{b})$ calculated in two conditions.
3. In geotechnical engineering, the accuracy of 1% is normally acceptable for soil parameters. So according to Tables 2~4, at least dozens of data are required for the estimation of the mean of regression parameter a, b.

4 DETERMINATION OF VARIANCE

4.1 *Theory*

A common misuse of linear regression is taken the SEMs calculated by Eqs. 5 and 6 as the "real" standard deviation of ***a, b***. As SEMs decrease with the sample number, if the sample number is large, such mistake will severely underestimate the standard deviation of ***a, b***. On the contrary, if the sample number is small, such mistake will significantly overestimate the standard deviation of ***a, b***.

As discussed in section 3, the mean of ***a, b*** can be calculated correctly in SLR. The problem is to estimate the variances σ_a^2 and σ_b^2. Referring Eq. 1,

if ***a, b, ε*** are independent and follow normal distribution, the following relation is valid,

$$\mathrm{Var}(Y) - b^2\mathrm{Var}(X) = {\mu_X}^2{\sigma_b}^2 + \sigma_a^2 + \sigma_\varepsilon^2 \quad (9)$$

where b is the mean of ***b*** calculated by Eq. 3, which is considered to be of high accuracy; σ_ε is normally regarded as a negligible value. So there are two unknowns σ_a and σ_b.

If the sample is divided into n groups, and Eq. 9 is applied to each group, n equations can be obtained and used to solve the two unknowns σ_a and σ_b.

Obviously, the error of var(***X***) will affect the accuracy of the solved σ_a and σ_b. To reduce the value of var(***X***), n groups of data should be selected according to the ***X*** value, but not selected randomly. For example, σ_a and σ_b can be solved by using the following procedure:

1. dividing the sample into m groups according to the ***X*** value with an interval of $[\max(\boldsymbol{X}) - \min(\boldsymbol{X})]/m$.
2. For each group data, a pair of $[{\mu_X}^2, \mathrm{var}(\boldsymbol{Y}) - \bar{b}^2\mathrm{var}(\boldsymbol{X})]$ can be obtained and a total m pairs of data can be obtained.
3. Taking ${\mu_X}^2$ as independent variable and $[\mathrm{var}(\boldsymbol{Y}) - \bar{b}^2\mathrm{var}(\boldsymbol{X})]$ as dependent variable, ${\sigma_a}^2$ and ${\sigma_b}^2$ can be solved using linear regression (Eqs. 3 and 4).

The above procedure is valid for general cases, such as for ***X*** following a uniform distribution. If ***X*** is m groups of repeated data and m groups of data are selected according to ***X*** value, var(***X***) is 0 and Eq. 9 can be simplified as (if σ_ε is negligible),

$$\mathrm{Var}(Y) = {\mu_X}^2{\sigma_b}^2 + \sigma_a^2 \quad (10)$$

If ***a, b*** are assumed to be dependent, Eq. 7 can be written as (if σ_ε is negligible),

$$\mathrm{Var}(Y) - b^2\mathrm{Var}(X) = {\mu_X}^2{\sigma_b}^2 + \sigma_a^2 + 2\rho_{ab}\sigma_a\sigma_b\mu_X \quad (11)$$

Eq. 11 can be solved by quadratic regression, taking μ_X as independent variable and $[\mathrm{var}(\boldsymbol{Y}) - b^2\mathrm{var}(\boldsymbol{X})]$ as dependent variable.

To solve for var(***a***) and var(***b***), the following equation can be also used in LR instead of Eq. 9

$$\frac{\mathrm{Var}(Y) - b^2\mathrm{Var}(X)}{{\mu_X}^2} = {\sigma_b}^2 + \frac{1}{{\mu_X}^2}\sigma_a^2 \quad (12)$$

The choice of Eq. 9 or 12 depends on the accuracy indicated by the standard errors while applying these two equations.

4.2 *Numerical test of the estimation of variance*

Taking ***a, b*** as normal distributions and ***X*** as a uniform distribution with input settings (Tests 4 & 5 in Table 1): $a = 10$, $\sigma_a = 2$, $b = 2$, $\sigma_b = 0.4$, $x_{min} = 0$, $x_{max} = 100$, the results of numerical test are listed in Table 5. Referring to Table 5, Eq. 9 can lead to accurate var(***b***), but unreliable var(***a***), which has great difference with the input value and is of high standard error. Whereas, Eq. 12 can lead to values with higher accuracy for var(***a***) and similar accuracy for var(***b***) comparing to Eq. 9.

If ***X*** is taking as m groups of repeated data, the results of numerical tests are listed in Table 6. According to Table 6, Eq. 12 can lead to values with higher accuracy comparing to Eq. 10. Using ***X*** as m groups of repeated data instead of ***X*** with

Table 5. Estimation of variance with ***X*** of uniform distribution.

		SLR using Eq. 9 (test 4)				SLR using Eq. 12 (test 5)			
		σ_a^2		σ_b^2		σ_a^2		σ_b^2	
n*	m•	μ (Eq. 4)	Se^2 (Eq. 6)	μ (Eq. 3)	Se^2 (Eq. 5)	μ (Eq. 3)	Se^2 (Eq. 5)	μ (Eq. 4)	Se^2 (Eq. 6)
15	3	–288	18391	0.235	6.8E-3	–547	21658	0.311	7.5E-3
60	3	–195	10007	0.215	5.8E-4	25	1034	0.175	6.1E-3
100	5	153	20646	0.046	1.3E-3	6.24	217	0.124	1.9E-3
500	10	–13	6692	0.167	3.2E-4	4.12	1.38	0.164	2.1E-4
1000	10	32	1027	0.143	4.9E-5	3.69	0.39	0.156	6.7E-5
1000	50	56.7	1241	0.132	6.6E-5	4.53	2.9E-3	0.155	7.4E-5
10000	10	–2.14	132	0.163	6.7E-6	5.46	4.4E-3	0.161	6.7E-6
10000	100	0.24	296	0.162	1.5E-5	3.59	6.2E-5	0.158	8.3E-6
100000	10	8.24	7.0	0.158	3.5E-7	5.65	5.2E-3	0.159	8.9E-7
100000	100	0.161	24.8	0.161	1.2E-7	4.08	4.4E-6	0.159	7.2E-7

*Total size of sample; •number of groups.

Table 6. Estimation of variance with $\boldsymbol{X}$ of m group repeated values.

		SLR using Eq. 10 (test 6)				SLR using Eq. 12 (test 7)			
		σ_a^2		σ_b^2		σ_a^2		σ_b^2	
n*	m•	μ (Eq. 4)	Se^2 (Eq. 6)	μ (Eq. 3)	Se^2 (Eq. 5)	μ (Eq. 3)	Se^2 (Eq. 5)	μ (Eq. 4)	Se^2 (Eq. 6)
15	3	602	1.1E6	0.106	5.9E-2	–108	2.4E5	0.451	1.1E-1
60	3	–121	4.5E5	0.232	2.5E-3	24.6	1.0E3	0.161	4.5E-3
100	5	–94.9	2.5E5	0.230	1.3E-3	2.66	2.6E2	0.187	6.6E-4
500	10	–0.74	3.2E3	0.155	1.6E-4	4.90	9.1E-1	0.158	1.5E-4
1000	10	–11	3.8E3	0.163	1.9E-4	4.25	3.2E-1	0.155	5.2E-5
1000	20	–3.3	1.5E3	0.159	7.5E-5	5.46	2.8E-2	0.155	3.7E-5
10000	10	–8.5	9.4E2	0.168	4.7E-6	3.90	3.9E-2	0.161	6.3E-6
10000	20	23.7	3.5E2	0.151	1.8E-6	4.08	1.0E-2	0.161	1.4E-5
100000	10	5.77	2.8E2	0.159	1.4E-6	3.91	1.9E-3	0.160	3.1E-7
100000	25	5.67	2.7E2	0.160	1.3E-6	3.84	1.9E-4	0.160	4.9E-7

*Total size of sample; •number of groups.

a uniform distribution, the accuracy of var(a) and var(b) also increases slightly under the same sample size.

4.3 *Summary*

According to Tables 5 and 6, Eqs. 9~12 can be used to solve the variance of the regression parameters and Eq. 12 shows better performance in the numerical tests, in which μ_X is relatively large comparing to a and b. At least hundreds of data are required to obtain a meaningful variance that can be used in geotechnical engineering practice.

5 APPLICATION OF THE STATISTICAL ANALYSIS OF SHEAR STRENGTH

In geotechnical engineering, a core concern is the shear strength, which is often simply characterized by the parameters of cohesion $\boldsymbol{c}$ and friction angle $\boldsymbol{\phi}$. There are several equations in the SLR for statistical analysis of shear strength based on triaxial test data as follows:

$$(\sigma_1 - \sigma_3) = 2c\cos\phi + (\sigma_1 + \sigma_3)\sin\phi \tag{13}$$

$$\sigma_1 = 2c\tan\left(\phi/2 + \pi/4\right) + \sigma_3\tan^2\left(\phi/2 + \pi/4\right) \tag{14}$$

$$\frac{\sigma_1}{\sigma_3} = \frac{1}{\sigma_3}2c\tan\left(\phi/2 + \pi/4\right) + \tan^2\left(\phi/2 + \pi/4\right) \tag{15}$$

where σ_1 is the major effective principal stress; σ_3 is the minor effective principal stress. Denoting $\boldsymbol{f} = \tan\boldsymbol{\phi}$, $\lambda = \tan(\boldsymbol{\phi}/2 + \pi/4)$, $2\boldsymbol{c}\lambda$ as $\boldsymbol{a}$, and λ^2 as $\boldsymbol{b}$, the mean of $\boldsymbol{c}$, $\boldsymbol{f}$ can be calculated as,

$$\begin{cases} \mu_f \approx \dfrac{b-1}{2\sqrt{b}} \\ \mu_c \approx \dfrac{a}{2\sqrt{b}} \end{cases} \tag{16}$$

The standard deviation of c and f can be calculated as:

$$\begin{aligned} \sigma_c &= \sqrt{\sigma_a^2\frac{1}{4b} + \sigma_b^2\frac{1}{16}a^2b^{-3} - 0.25\rho_{ab}ab^{-2}\sigma_a\sigma_b} \\ \sigma_f &= \frac{1}{4}\sigma_b(b^{-0.5} + b^{-1.5}) \end{aligned} \tag{17}$$

In reliability analysis, the correlation between $\boldsymbol{c}$ and $\boldsymbol{f}$ is often ignored to simplify the problem. In numerical test, $\boldsymbol{c}$ and $\boldsymbol{f}$ are assumed to be independent and used to generate triaxial test data, as listed in Table 7. Numerical tests 8~10 refer to fine soil; numerical tests 11 and 12 refer to coarse soil; and numerical tests 13 and 14 refer to well compacted widely-graded soil. The numerical test results are listed in Table 8 and demonstrate that:

1. For the same series of triaxial test data, Eq. 8 and Eq. 15 can lead to the values of highest accurate among these equations.
2. If the soil cohesion c is not small, hundreds data is enough to obtain meaningful statistical characteristic for shear strength, i.e. μ_c, μ_f, var($\boldsymbol{c}$), and var($\boldsymbol{f}$). If $\boldsymbol{c}$ is small, the variance of c is also of low accuracy even when the sample size goes up to thousands. In this condition, var($\boldsymbol{c}$) is taken as an empirical value, e.g. $0.01\sim0.1\mu_c^2$, instead of the var($\boldsymbol{c}$) obtained in LR.

Table 7. Summary of numerical test settings.

Test no.	n^*	c	$\tan\phi$	σ_3	$\boldsymbol{a} = 2c\lambda$	$\boldsymbol{b} = \lambda^2$
8	40	N (50, 100)	N (0.36, 0.002)	50, 100, 150, 200	~N (142, 842)	~N (2.03, 0.029)
9	400	N (50, 100)	N (0.36, 0.002)	50, 100, 150, 200	~N (142, 842)	~N (2.03, 0.029)
10	4000	N (50, 100)	N (0.36, 0.002)	50, 100, 150, 200	~N (142, 842)	~N (2.03, 0.029)
11	800	N (10, 4)	N (0.73, 0.006)	100, 200, 300, 400	~N (39.4, 68.2)	~N (3.89, 0.236)
12	8000	N (10, 4)	N (0.73, 0.006)	100, 200, 300, 400	~N (39.4, 68.2)	~N (3.89, 0.236)
13	800	N (100, 400)	N (0.73, 0.006)	100, ..., 2000	~N (394, 6820)	~N (3.89, 0.236)
14	8000	N (100, 400)	N (0.73, 0.006)	100, ..., 2000	~N (394, 6820)	~N (3.89, 0.236)

Denote $\lambda = \tan(\phi/2 + \pi/4)$; *total size of sample.

Table 8. Results of statistical analysis of shear strength (numerical test).

Test no.	Eq. 1 and Eq. 13		Eq. 1 and Eq. 14		Eq. 8 and Eq. 15	
	$2c\tan\phi$	$\sin\phi$	$\boldsymbol{a} = 2c\lambda$	$\boldsymbol{b} = \lambda^2$	$\boldsymbol{a} = 2c\lambda$	$\boldsymbol{b} = \lambda^2$
8	N (86.2, 575)	N (0.35, 0.003)	N (151, 21.8)	N (1.94, 0.105)	N (144, 523)	N (2.02, 0.066)
9	N (81.7, 606)	N (0.36, 0.0021)	N (143, 818)	N (2.01, 0.044)	N (143, 838)	N (2.01, 0.030)
10	N (82.5, 617)	N (0.36, 0.0020)	N (144, 883)	N (2.02, 0.041)	N (144, 864)	N (2.02, 0.043)
11	N (–14.1, –39.6)	N (0.615, 0.0040)	N (41.5, –834)	N (3.88, 0.265)	N (41.3, –30.4)	N (3.88, 0.250)
12	N (–12.8, 216)	N (0.614, 0.0039)	N (42.7, 356)	N (3.88, 0.242)	N (42.4, 270)	N (3.88, 0.242)
13	N (82.2, 7490)	N (0.606, 0.0018)	N (427, –12840)	N (3.85, 0.268)	N (399, 9104)	N (3.89, 0.256)
14	N(69.4, 1458)	N(0.609, 0.0021)	N (389, 25607)	N (3.90, 0.236)	N (390, 8864)	N (3.90, 0.259)

6 CONCLUSIONS

In this paper, theoretical and numerical efforts are conducted to study the capacity of the linear regression method. The study demonstrates that:

1. A common misuse of linear regression is to take the standard errors of the mean (SEM, Eqs. 5 and 6) as the "real" standard deviations of regression parameters ***a, b***. In fact, SEMs are inversely proportional to the sample size number, have nothing to do with the real var(***a***) and var(***b***), but indicate the accuracy of the mean value *a, b* (Eqs. 3 and 4).
2. If *a* is relatively small comparing to the mean of independent variable, μ_X, Eq. 8 can improve the accuracy of regression analysis comparing to Eq. 1, especially under the condition of small sample size (smaller than 1000).
3. In the statistical analysis of shear strength based on triaxial test data, Eqs. 8 and 15 are recommended because they lead to mean and variance values with higher accuracy.

ACKNOWLEDGEMENTS

This study is supported by the State Key Development Program of Basic Research of China (Project No. 2012CB026104), a Chinese National Key Technology R&D Program of the Ministry of Science and Technology Project (2012BAH10B01), and the National Natural Science Foundation of China (Grant No. 51109003).

REFERENCES

Chen, L.H. & Chen, Z.Y. 2007. Effect of nonlinear strength of rockfill on slope stability of high earth-rock dam. *Rock and Soil Mechanics* 9(28): 1807–1810.

Mann, C.J. 1987. Misuses of linear regression in earth sciences. In W.B. Size (ed.), *Use and Abuse of Statistical Methods in the Earth Sciences*: 74–106. New York: Oxford University Press.

Weisberg S. 2005. *Applied linear regression*. Hoboken: John Wiley & Sons, Inc.

Yan, X. & Su, X.G. 2009. *Linear regression analysis-theory and computing*. Singapore: World Scientific Publishing Co. Pte. Ltd.

Geotechnical Safety and Risk IV – Zhang et al. (eds)
 ISBN 978-1-138-00163-3

Uncertainty quantification by polynomial chaos expansion for geotechnical reliability-based analysis

S.H. Marques, A.T. Gomes & A.A. Henriques
Department of Civil Engineering, Faculty of Engineering, University of Porto, Portugal

ABSTRACT: Uncertainty quantification is the process of determining the effect of input uncertainties on response metrics of interest. Many approximate methods have been developed so far for the purpose, and among these methods the polynomial chaos expansion is considered a technique with strong mathematical basis and ability to produce functional representation of stochastic variability. The approach has proven to be an efficient methodology to study several stochastic problems, considered the original form where optimal convergence for orthogonal Hermite polynomials is only achieved for gaussian stochastic processes. Regarding the developments in the stochastic response surface methodology and some heuristic and optimisation concepts, results for a design example with correlated nonnormal random variables are presented in the light of the quality of the approximate metamodels. Considered truncated full and sparse polynomial chaos expansions, the efficiency and accuracy provided by different schemes of experimental design are analysed and the convergence process is lastly discussed.

1 INTRODUCTION

Metamodelling is a very interesting research area for the replacement of simulation models when the trade-off between efficiency and accuracy is appropriate. If a model is a simplified and abstract representation of reality, a metamodel is a further abstraction, a model of a model, which is typically easier to generate and evaluate than the model itself. In fact, the use of metamodels is now established to reduce the need to run expensive simulations, as stated by Can & Heavey (2011). The selection of a suitable approach is not straightforward and should take into account the final purpose.

Considered the literature, Huang *et al*. (2009) present an Excel add-in implementation for the stochastic response surface methodology, developed for practitioners and used to analyse illustrative geotechnical examples for reliability analysis. In turn, Li *et al*. (2011) present an improved stochastic response surface methodology for reliability analysis of rock slopes involving correlated nonnormal random variables. Huang *et al*. (2009) and Li *et al*. (2011) accordingly argue that there appears to be no simple method to manage the proliferation of terms for the higher random dimensions, noted that it is possible that the order can be kept at four or below for most practical problems.

To address such problems described in recent work, Blatman & Sudret (2010a) present an adaptive algorithm that builds a sparse polynomial chaos expansion to represent the random model response. As a consequence of this sparse representation, a rather small number of polynomial chaos terms is eventually retained, which may be obtained at a reduced computational cost compared to the classical truncated full polynomial chaos approximation. In fact, the number of terms to be computed grows dramatically with the size of the input random vector, which makes the computational cost of the classical solution schemes unaffordable when the model is expensive to evaluate.

For the purpose, Blatman & Sudret (2010b) present also a methodology for the efficient computation of global sensitivity indices by using a sparse polynomial chaos expansion. Global sensitivity analysis is related to the quantification of the output uncertainty due to changes of the input parameters over their entire domain of variation. In this context, variance-based methods which rely upon the decomposition of the response variance as a sum of the contributions of each input variable are of major interest to quantify the contribution of each parameter to the output variability.

Thus, soft computing technologies have acquired increasing importance in engineering and several techniques are nowadays available. In this line of thought, Armani *et al*. (2011) present a relatively new metamodelling building technique that is able to generate explicit mathematical expressions describing the relationship between the input variables and the modelled response, the so called genetic programming. In turn, Hofwing *et al*. (2011) present a genetic algorithm used to find the terms

to be included in a proposed optimal polynomial regression model. In practice, the genetic algorithm generates the optimal set of exponents in a polynomial regression model with improved performance compared to the traditional regression model, in that for a full expanded regression model a large number of design sampling points is really required. The determination of the higher order terms that yields the most accurate regression model is indeed an optimisation problem.

Therefore, considered truncated full and sparse polynomial chaos expansions, the efficiency and accuracy provided by different schemes of experimental design are analysed in the next sections with a design example for a concrete gravity retaining structure, considered correlated nonnormal random variables.

2 MULTI-DIMENSIONAL HERMITE POLYNOMIAL CHAOS EXPANSION

Despite being an attractive technique available to the community of researchers and practitioners, the application of the stochastic response surface methodology to geotechnical reliability problems has not been extensively investigated.

The methodology involves the propagation of input uncertainties through a model to express a random output, expanded for instance in the standard normal space of uncorrelated random variables by a multi-dimensional Hermite polynomial chaos, summarised by Equations 1, 2 and 3:

$$Y = a_0 + \sum_{i1=1}^{n}\left(a_{i1}\cdot\Gamma_1\left(U_{i1}\right)\right) + \sum_{i1=1}^{n}\sum_{i2=1}^{i1}\left(a_{i1i2}\cdot\Gamma_2\left(U_{i1},U_{i2}\right)\right) + \sum_{i1=1}^{n}\sum_{i2=1}^{i1}\sum_{i3=1}^{i2}\left(a_{i1i2i3}\cdot\Gamma_3\left(U_{i1},U_{i2},U_{i3}\right)\right)+\ldots \quad (1)$$

$$\Gamma_o\left(U_{i1},\ldots,U_{io}\right) = (-1)^o\cdot e^{\left(\frac{1}{2}\right)U^T\cdot U}\cdot\frac{\partial^o}{\partial U_{i1}\ldots\partial U_{io}}e^{-\left(\frac{1}{2}\right)U^T\cdot U} \quad (2)$$

$$U=\begin{bmatrix}U_1\\U_2\\\vdots\\U_n\end{bmatrix} \quad (3)$$

where Y=model output; $a_0, a_{i1}, a_{i1i2}, a_{i1i2i3}, \ldots$=unknown coefficients to be determinated; n = number of standard normal random variables; o = order of multi-dimensional Hermite polynomial chaos expansion; $\Gamma_o(U_{i1}, \ldots, U_{io})$ = order o multi-dimensional Hermite polynomials; and U = vector of standard normal random variables.

Such technique involves the calculation of chaos expansion coefficients based on a set of response function evaluations. The regression approach uses a least-squares solution to find the complete set of coefficients that best match a set of response values obtained from a number of design sampling points. A stochastic response surface is then produced, describing the relationship between the input variables and the output, which represents the metamodel. A different order for the response surface can produce a robust estimation of the reliability index for a performance function, and usually the accuracy of the response surface increases as the order of the surface response increases. Despite the excellent convergence properties reported for general probabilistic analysis problems, there is no universal base for every problem and convergence difficulties were found when highly nonlinear behaviour was considered. In fact, even if the basic input random variables are modelled as gaussian, the response may present highly nongaussian behaviour due to the nonlinear relationship established between the basic input random variables and the system response.

However, the polynomial chaos expansion suffers yet from a set of other drawbacks. In the presence of a particular computational budget for a problem with a particular dimensionality, the primary weakness of the regression approach is the common need for a large number of sample points in the design of experiments as the order of the multi-dimensional Hermite polynomials and the number of random variables increase. Thus, the use of a multi-dimensional Hermite polynomial chaos expansion for the generation of the response surface has been hindered by the eventual high computational complexity that the technique shows. Therefore, there is great interest in presenting metamodelling techniques that are able to provide high quality metamodels at a reasonable computational complexity, introduced some heuristic and optimisation concepts. A novel approach should take into account that truncated full polynomial chaos expansions are quite far from being simpler to visualise and evaluate than the model itself, and so the replacement is not always worthwhile in that Monte Carlo simulation based on counting remains expensive. Another interesting issue is the pursuit of accuracy, considered truncated full and sparse polynomial chaos expansions.

The flowchart of procedures adopted for uncertainty quantification by polynomial chaos expansion is then presented in Figure 1. For the purpose, a simplified approach suggested by Kiureghian & Liu (1986) and described by Haldar & Mahadevan (2000) may be considered for the equivalent standard normal correlation matrix computation. The trans-

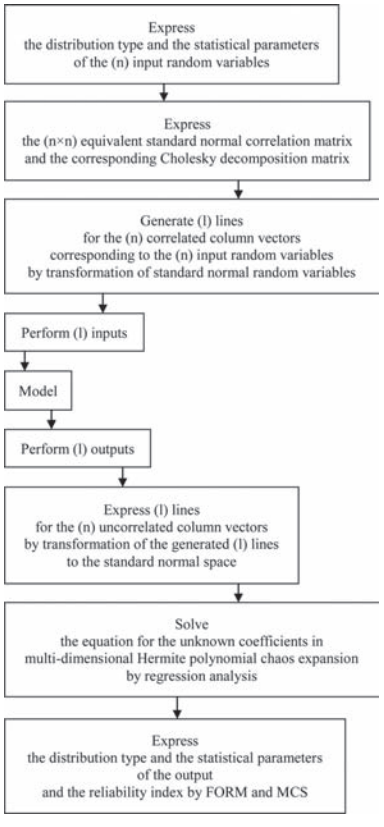

Figure 1. Flowchart of procedures adopted for uncertainty quantification by polynomial chaos expansion.

formations $xi^* = f(yi^*)$ and $f(xi^*) = yi^*$ derived by Equation 4 are further considered:

$$xi^* = F_{Xi}^{-1}\left[\Phi\left(yi^*\right)\right] \sim \Phi^{-1}\left[F_{Xi}\left(xi^*\right)\right] = yi^* \qquad (4)$$

where xi^* = random variable in the original space; yi^* = random variable in the standard normal space; F_{Xi} = cumulative nonnormal distribution function; F_{Xi}^{-1} = inverse cumulative nonnormal distribution function; Φ = cumulative standard normal distribution function; and Φ^{-1} = inverse cumulative standard normal distribution function.

Considered normal, lognormal and weibull distributions, the described transformations for representation of random variables xi^* with different distributions as a function of standard normal random variables yi^* are further detailed in Table 1.

3 DESIGN EXAMPLE

The design example is referred to the concrete gravity retaining structure on a relatively homogeneous

Table 1. Transformations for representation of random variables xi^* with different distributions as a function of standard normal random variables yi^*.

Distribution	$xi^* = f(yi^*)$
Normal	$xi^* = \mu + \sigma \cdot yi^*$
Lognormal	$xi^* = e^{(\mu 1 + \sigma 1 \cdot yi^*)}$
Weibull	$xi = sc \cdot (-\ln(1 - \Phi(yi^*)))^{(1/sh)}$
Distribution	$f(xi^*) = yi^*$
Normal	$(xi^* - \mu)/\sigma = yi^*$
Lognormal	$(\ln(xi^*) - \mu 1)/\sigma 1 = yi^*$
Weibull	$\Phi^{-1}(1 - e^{(-(xi^*/sc)sh)}) = yi^*$

$\mu 1$-log mean; $\sigma 1$-log standard deviation; sh-shape; sc-scale.
Φ-cumulative standard normal distribution function.
Φ^{-1}-inverse cumulative standard normal distribution function.

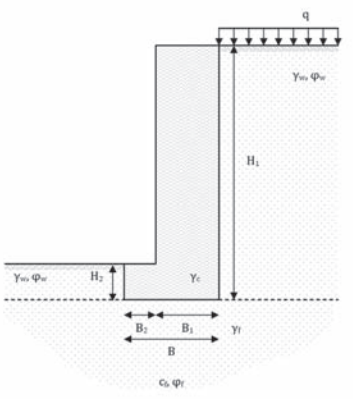

Figure 2. Concrete gravity retaining structure.

c-φ soil shown in Figure 2, wherein groundwater level is away. Considered the inclined eccentric loading problem and the calculation model for bearing capacity, the performance function may be described by the simplified Equation 5:

$$M = f\left(B_1, B_2, H_1, H_2, \gamma_c, \varphi_w, \gamma_w, c_f, \varphi_f, \gamma_f, q\right) \qquad (5)$$

where the sum of B_1 and B_2 is the foundation width B; H_1 is the wall height; H_2 is the foundation height; γ_c is the unit concrete weight; φ_w is the friction angle of the soil on the active and passive sides of the wall; γ_w is the unit soil weight on the active and passive sides of the wall; c_f is the cohesion of the foundation soil; φ_f is the friction angle of the foundation soil; γ_f is the unit weight of the foundation soil; and q is the variable load at ground surface. Other considered parameters, namely for the earth pressure coefficients, are the soil-wall interface friction

angle on the active side of the wall $\delta_w a = 2/3\varphi_w$; the soil-wall interface friction angle on the passive side of the wall $\delta_w p = 0$; and the soil-foundation interface friction angle $\delta_f = \varphi_f$; considered either a 50% reduction for passive earth pressures.

Table 2 summarises the description of basic input variables, with different distribution types. The considered coefficients of correlation between the random variables are either presented in Table 3, noted that the correlation matrices are idealised with the main purpose of creating high correlation between some of the random variables. The strength of the association is measured by a correlation coefficient in the range [–1,1], for the case that both variables vary inversely or together exactly, respectively. In a brief analysis, the correlation between the cohesion and the friction angle of the foundation soil depends particularly on the material, and the question whether the two parameters are correlated is still not clearly decided in the literature. References for negative correlation are common but regarding a sensitivity analysis for the design example, the influence of negative correlation on reliability is favourable. Thus, the hypothesis of uncorrelated random variables is probably cautious, noted that the characteristic values of soil properties are often calculated separately, neglecting the effects of correlation.

Table 2. Summary description of basic input variables.

Basic input variables	Distribution	mv	cv	Statistics
B_1 (m)	Deterministic	–	–	1.75
B_2 (m)	Deterministic	–	–	1.00
H_1 (m)	Deterministic	–	–	7.00
H_2 (m)	Deterministic	–	–	1.00
γ_c (kN/m^3)	Deterministic	–	–	24.00
φ_w (°)	Lognormal	33.00	0.10	μ1-3.4915 σ1-0.0998
γ_w (kN/m^3)	Normal	18.80	0.05	–
c_f (kN/m^2)	Lognormal	14.00	0.40	μ1-2.5648 σ1-0.3853
φ_f (°)	Lognormal	32.00	0.05	μ1-3.4645 σ1-0.0500
γ_f (kN/m^3)	Normal	17.80	0.05	–
q (kN/m^2)	Weibull	–	–	sh-3.25 sc-10.00

mv-mean value; cv-coefficient of variation.
μ1-log mean; σ1-log standard deviation; sh-shape; sc-scale.

Table 3. Coefficients of correlation between the random variables.

Correlation matrix for the bearing capacity model					
$\rho_{\varphi w\varphi w}$	$\rho_{\varphi w\gamma w}$	$\rho_{\varphi w\varphi f}$	$\rho_{\varphi wq}$	$\rho_{\varphi wcf}$	$\rho_{\varphi w\gamma f}$
$\rho_{\gamma w\varphi w}$	$\rho_{\gamma w\gamma w}$	$\rho_{\gamma w\varphi f}$	$\rho_{\gamma wq}$	$\rho_{\gamma wcf}$	$\rho_{\gamma w\gamma f}$
$\rho_{\varphi f\varphi w}$	$\rho_{\varphi f\gamma w}$	$\rho_{\varphi f\varphi f}$	$\rho_{\varphi fq}$	$\rho_{\varphi fcf}$	$\rho_{\varphi f\gamma f}$
$\rho_{q\varphi w}$	$\rho_{q\gamma w}$	$\rho_{q\varphi f}$	ρ_{qq}	ρ_{qcf}	$\rho_{q\gamma f}$
$\rho_{cf\varphi w}$	$\rho_{cf\gamma w}$	$\rho_{cf\varphi f}$	ρ_{cfq}	ρ_{cfcf}	$\rho_{cf\gamma f}$
$\rho_{\gamma f\varphi w}$	$\rho_{\gamma f\gamma w}$	$\rho_{\gamma f\varphi f}$	$\rho_{\gamma fq}$	$\rho_{\gamma fcf}$	$\rho_{\gamma f\gamma f}$
1.0	0.5	0.9	0.0	0.0	0.5
0.5	1.0	0.5	0.0	0.0	0.9
0.9	0.5	1.0	0.0	0.0	0.5
0.0	0.0	0.0	1.0	0.0	0.0
0.0	0.0	0.0	0.0	1.0	0.0
0.5	0.9	0.5	0.0	0.0	1.0

ρ-coefficient of correlation.

4 RESULTS AND DISCUSSION

The published results should be referred to the considered coefficient of variation for the friction angle of the foundation soil, one of the most important parameters concerning reliability, stated that the increased nonnormal behaviour of the bearing capacity response correlates well with the higher values of the parameter.

Considered the implementation of the foremost detailed methodology, Table 4 presents the summary description of results for the bearing capacity model, included the reliability index obtained by the first order reliability method and the Monte Carlo simulation, in conjunction with the description of some important statistical parameters as the output mean, standard deviation, skewness and kurtosis. It is noted that the differences between the reliability index obtained from both methodologies are somewhat notorious due to the important nonlinear behaviour.

The bearing capacity metamodels are built according to the schemes of experimental design drawn in Figure 3. They are derived from a number of 1000 design sampling points selected at random from the original space of random variables, noted that smaller samples are always designed from larger samples.

Table 5 summarises the number of terms in multidimensional Hermite polynomial chaos expansion

Table 4. Summary description of results for the bearing capacity model.

Reliability index β_{FORM}	Reliability index β_{MCS}		
2.484	2.529		
Output mean (kN/m)	Output standard deviation (kN/m)	Output skewness	Ouput kurtosis
1267	899.1	1.802	6.391

MCS and statistics results from 10^6 simulation steps.

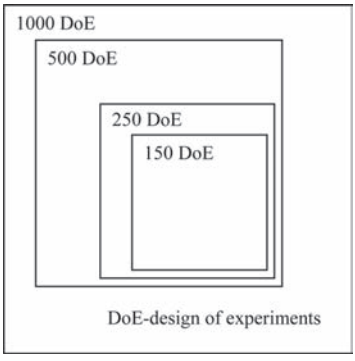

Figure 3. Schemes of experimental design.

Table 5. Number of terms in multi-dimensional Hermite polynomial chaos expansion.

n	o	Number of terms according to (n + o)!/n! × o!
6	1	7
6	2	28
6	3	84
6	4	210
6	5	462
6	6	924

n-number of standard normal random variables.
o-order of multi-dimensional.
Hermite polynomial chaos expansion.

for the case of a number of 6 standard normal random variables and different orders of multi-dimensional Hermite polynomial chaos expansion.

Considered the preliminary work, a fourth order is considered for the truncated full polynomial chaos expansion, which include a number of 210 terms. The sparse polynomial chaos expansions link a selected number of 100 terms derived from a sensitivity analysis for importance classification and a heuristic process of trial and error for a selected group of terms, considered a fourth and a fifth order.

For the purpose, the coefficient of determination evaluated on the data set for the metamodels is based on the variances of the fitted values and observed values of the dependent variable performance function, and is expressed by Equation 6, considered either a target value of 0.999 for the sparse polynomial chaos expansions:

$$R^2 = \frac{\sum_{i=1}^{1}\left(\widehat{M}_i - \bar{M}\right)^2}{\sum_{i=1}^{1}\left(M_i - \bar{M}\right)^2} \qquad (6)$$

where R^2 = coefficient of determination; l = number of observed values of the performance function; M_i = ith observed value of the performance function; $\widehat{M}$ = ith fitted value of the performance function; and $\bar{M}$ = mean of the observed values of the performance function.

Table 6. Summary description of results for the bearing capacity metamodels.

Case*	DoE	o	Polynomial chaos expansion	Relative error (%) β_{FORM}	Relative error (%) β_{MCS}
1	1000	4	Truncated full	–3.027	–4.040
2	150	4	Sparse	0.354	0.572
3	250	4	Sparse	0.274	3.238
4	500	4	Sparse	0.636	2.516
5	1000	4	Sparse	–0.209	0.903
6	150	5	Sparse	–1.377	–1.805
7	250	5	Sparse	–1.578	–3.192
8	500	5	Sparse	0.958	–1.459
9	1000	5	Sparse	1.361	–0.391

DoE-design of experiments; o-order.
MCS results from 10^6 simulation steps.
*R^2-coefficient of determination, for the different cases 1–9: 1-R^2 = 0.993579; 2-R^2 = 0.999991; 3-R^2 = 0.999958; 4-R^2 = 0.999921; 5-R^2 = 0.999902; 6-R^2 = 0.999981; 7-R^2 = 0.999961; 8-R^2 = 0.999902; 9-R^2 = 0.999897.

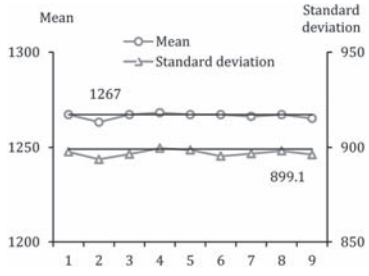

Figure 4. Model deviation for mean and standard deviation of the bearing capacity metamodels, cases 1–9, statistics results from 10^6 simulation steps.

The relative errors obtained by different reliability techniques are then presented in conjunction with the description of some important statistical parameters. For the purpose, Table 6 presents the summary description of results for the bearing capacity metamodels, included the relative errors obtained in full analysis by the first order reliability method and the Monte Carlo simulation. In addition, Figures 4 and 5 further present the model deviation of the main statistical parameters of the bearing capacity metamodels.

It is noted that the convergence is verified considering the quality of the regressions, the stability of the solutions for different design of experiments and further for different orders. The truncated full polynomial chaos expansion presents

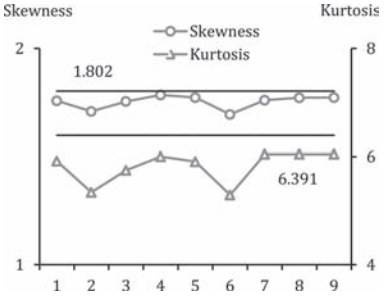

Figure 5. Model deviation for skewness and kurtosis of the bearing capacity metamodels, cases 1–9, statistics results from 10^6 simulation steps.

relative errors considered quite acceptable, but the sparse polynomial chaos expansions may present improved solutions. So, the fourth order presents higher accuracy for the first order reliability method, and the fifth order may improve in general the results from Monte Carlo simulation. The statistical description of the output for the bearing capacity metamodels is quite accurate considered the reference model, with exception to the case studies for a number of 150 design sampling points, where some differences in kurtosis are more important.

5 CONCLUSION

In the field of abstraction, metamodelling is the construction of a cluster of concepts within a certain domain, highlighting properties of the model itself. Due to the computational complexity of the analysis of current systems, metamodelling has become an indispensable tool for exploring the design space and performing sensitivity analysis, particularly useful for the implementation of numerical-based reliability techniques, to be used for design purposes and risk analysis. Therefore, there is great interest in the development of techniques that facilitate the construction of approximation models by using criteria of efficiency and accuracy.

Regarding these issues, results for a design example with correlated nonnormal random variables are presented. For the purpose it is considered an inclined eccentric loading problem referred to a bearing capacity nonlinear calculation model for a concrete gravity retaining structure, moreover a geotechnical reliability-based analysis problem.

Considered the important nonlinear behaviour of the geotechnical bearing capacity model, results show that the bearing capacity metamodels built by multi-dimensional Hermite polynomial chaos expansion may provide a general approximation statistically representative of the performance function. Compared the sparse polynomial chaos expansions versus the corresponding truncated full, the key issues gather the stability of the solutions, even as the number of required design sampling points and the accuracy shown by the derived metamodels. It is further noted that for a selected group of terms, additional data may not be required for the accuracy improvement, in that the minimum number of design sampling points may be enough to match the best solutions in the field of reliability if considered a reduced model deviation of the main statistical parameters of the derived metamodels.

REFERENCES

Armani, U., Khatir, Z., Khan, A., Toropov, V.V., Polynkin, A., Thompson, H., Kapur, N. & Noakes C.J. 2011. Control of physical consistency in metamodel building by genetic programming. In: *Proc. of the Second International Conference on Soft Computing Technology in Civil, Structural and Environmental Engineering, Chania, Crete, Greece*: Civil-Comp Proceedings 97, Paper 43, 1–18. Civil-Comp Press.

Blatman, G. & Sudret, B. 2010a. An adaptive algorithm to build up sparse polynomial chaos expansions for stochastic finite element analysis. *Probabilistic Engineering Mechanics* 25(2): 183–197.

Blatman, G. & Sudret, B. 2010b. Efficient computation of global sensitivity indices using sparse polynomial chaos expansions. *Reliability Engineering and System Safety* 95(11): 1216–1229.

Can, B. & Heavey, C. 2011. Comparison of experimental designs for simulation-based symbolic regression of manufacturing systems. *Computers & Industrial Engineering* 61(3): 447–462.

Haldar, A. & Mahadevan, S. 2000. Reliability assessment using stochastic finite element analysis. John Wiley & Sons.

Hofwing, M., Strömberg N. & Tapankov M. 2011. Optimal polynomial regression models by using a genetic algorithm. In: *Proc. of the Second International Conference on Soft Computing Technology in Civil, Structural and Environmental Engineering, Chania, Crete, Greece:* Civil-Comp Proceedings 97, Paper 39, 1–20. Civil-Comp Press.

Huang, S.P., Liang B. & Phoon, K.K. 2009. Geotechnical probabilistic analysis by collocation-based stochastic response surface method: an Excel add-in implementation. *Georisk: Assessment and Management of Risk for Engineered Systems and Geohazards* 3(2): 75–86.

Kiureghian, A.D. & Liu, P.L. 1986. Structural reliability under incomplete probability information. *Journal of Engineering Mechanics* 112(1): 85–104.

Li, D., Chen, Y., Lu, W. & Zhou, C. 2011. Stochastic response surface method for reliability analysis of rock slopes involving correlated non-normal variables. *Computers and Geotechnics* 38(1): 58–68.

4 *Influence of spatial variability on geotechnical design decisions*

This page intentionally left blank

Geotechnical Safety and Risk IV – Zhang et al. (eds)
© 2014 Taylor & Francis Group, London, ISBN 978-1-138-00163-3

Mobilized shear strength of soils with constrained slip curves

Y. Hu & J. Ching
Department of Civil Engineering, National Taiwan University, Taipei, Taiwan

ABSTRACT: A previous study by Ching et al. (2013) showed that the mobilized shear strength of a spatially variable soil is governed by two factors: (a) line averaging effect along potential slip curves; and (b) the emergent feature of the critical slip curve, i.e., the location of the critical slip curve depends on the random field realization. In the study done by Ching et al. (2013), the latter factor plays a major role as the slip curves are allowed to propagate freely without constraints. For scenarios where slip curves are constrained, e.g., the slip curve in a vertical retaining wall typically passes through the toe, it is not clear whether this latter factor will be fully suppressed. It is therefore the goal of this study to understand the behavior of the mobilized shear strength for spatially variable soils when slip curves are constrained.

1 INTRODUCTION

This study is complementary to a previous study performed by the second author (Ching et al. 2013). In this study, the mobilized shear strength of a spatially variable soil in compression and pure shear tests was simulated. Although the inclination angle of the critical slip curve is dominated by mechanics, it vertical position is not constrained and varies significantly, depending on the weak zone in the simulated random field. As a result, the spatial variability strongly influences the mobilized shear strength; the critical slip curve may seek the weak zone in the random field. However, in the present study, the slip curve is constrained: for a retaining wall problem, the slip curve must pass through the toe (see Fig. 1). Therefore, it is expected that the spatial variability should have a weaker influence on the simulated active lateral force (P_a). An important goal of this study is to understand how to quantify this weaker influence if it still exists.

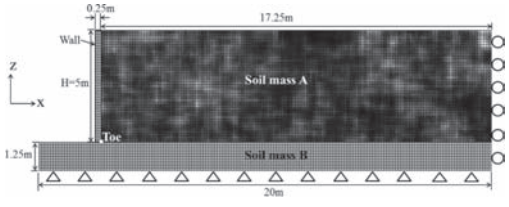

Figure 1. Finite element model for a retaining wall with spatially variable soil.

2 SIMULATION OF ACTIVE LATERAL FORCES

The shear strength at a point in soil mass A is denoted by $\tau_f(x,z)$, where x and z are the horizontal and vertical coordinates, respectively. The friction angle ϕ is taken to be 0° in this study for simplicity, i.e., $\tau_f(x,z) = c(x,z)$. The shear strength $\tau_f(x,z)$ is simulated as a stationary Gaussian random field with inherent mean $E(\tau_f) = \mu$ and inherent standard deviation $[Var(\tau_f)]^{0.5} = \sigma$. The Coefficient Of Variation (COV) of this random field is equal to σ/μ. To define the correlation structure of $\tau_f(x,z)$ between two locations with horizontal distance = Δx and vertical distance = Δz, an auto-correlation model is considered in this study: the single exponential model (SExp) (Vanmaqrcke 1977, 1984). And the two-dimensional (2D) stationary Gaussian random field $\tau_f(x,z)$ can be readily simulated by the Fourier series method (Jha & Ching 2013).

2.1 *Limit equilibrium method*

The process of simulating a random sample of P_a using the Limit Equilibrium Method (LEM) is illustrated in Figure 2. Figure 2a shows a realization of the $\tau_f(x,z)$ random field, where sections A, B, and C represent the locations of three potential slip planes (x_A, x_B, and x_C in Figure 2a characterize the horizontal daylight positions of the three potential slip planes). It is assumed that the potential slip curves are planes (straight lines). This assumption is in principle non-conservative because the actual slip curve may not be a plane. However, in a later comparison with Random

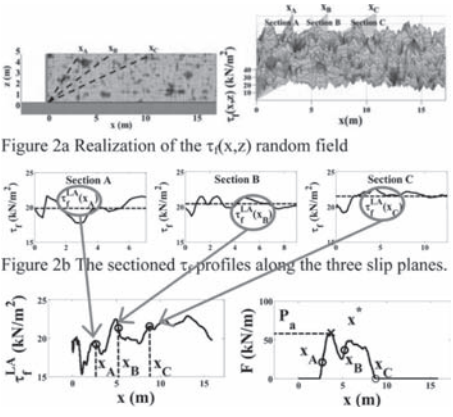

Figure 2. Process of simulating a random sample of P_a using the LEM.

Finite Element Analysis (RFEA) results, it will be clear that the actual effect of this assumption is minimal. It is also assumed that the potential slip planes pass through the toe. This is barely an assumption because the actual slip curves obtained in RFEA always pass through the toe as well. For clarity, only three of these planes are shown.

The sectioned τ_f profiles along the three potential slip planes are plotted in Figure 2b. The average of each profile (the dashed lines in Fig. 2b) is equal to the line average for each section. Let us denote the line average of $\tau_f(x,z)$ along a potential slip plane as τ_f^{LA}. This line average can be directly simulated by the Fourier series method developed in Jha & Ching (2013) (Eq. 19 in Jha & Ching (2013)).

Let us denote the line averages over the three potential slip planes shown in Figure 2a by $\tau_f^{LA}(x_A)$, $\tau_f^{LA}(x_B)$, and $\tau_f^{LA}(x_C)$. There are an infinite number of potential slip planes. Each potential slip plane has a line average τ_f^{LA}, and the resulting continuous line average process $\tau_f^{LA}(x)$ forms a One-Dimensional (1D) random field. This 1D random field is illustrated in Figure 2c. For each potential slip plane with daylight position x, force equilibrium can be used to derive the lateral force F required to support the failing soil mass. The force equilibrium of the wedge formed by the potential slip plane can be written as

$$W = N \cdot \cos(\beta) + \tau_f^{LA} \cdot L_p \cdot \sin(\beta)$$
$$F + \tau_f^{LA} \cdot L_p \cdot \cos(\beta) = N \cdot \sin(\beta)$$
$$\frac{1}{2} H \cdot x \cdot \gamma = N \cdot \frac{x}{L_p} + \tau_f^{LA} \cdot H$$
$$F + \tau_f^{LA} \cdot x = N \cdot \frac{H}{L_p}$$
$$F = \frac{1}{2}\gamma H^2 - \tau_f^{LA} \cdot \frac{L_p^2}{x} = \frac{1}{2}\gamma H^2 - \tau_f^{LA} \cdot \frac{x^2 + H^2}{x} \quad (1)$$

where β and L_p are the inclination angle and length of the potential slip, respectively; W is the weight of the wedge; N is the normal force between the wedge and potential slip plane; H is the wall height; γ is the soil unit weight; and x is the daylight position of the potential slip plane (x is also the length of the upper side of the wedge, i.e. $x = H/\tan\beta$).

Occasionally, the F is negative, which indicates that the wedge can stand on its own without the support from the wall. Thus, F will be zero in this case. Each potential slip plane corresponds to a value of F. This F is plotted as a function of x in Figure 2d. The P_a is then the maximum value in the $F(x)$ function:

$$P_a = \max_x F(x) = \max\left(\frac{1}{2}\gamma H^2 - \tau_f^{LA} \cdot \frac{x^2 + H^2}{x} \ , 0 \right) \quad (2)$$

The x position at which $F(x)$ is maximized is denoted by x^*, which is the daylight position of the critical slip plane.

Active lateral forces also can be simulated by RFEA. The first step of the RFEA is a geostatic step that builds up the in situ stress field, and in the second step a horizontal displacement is applied to the wall (away from the soil mass) to reach an active failure state. Then, the lateral force is calculated as the integration of the soil-wall contact forces in the FEA. Figure 3 shows a comparison between the P_a samples simulated by RFEA and the LEM for 100 cases. These 100 cases use wall heights in the range of [5 m, 20 m]. The random field realizations for these 100 cases have fairly wide ranges of μ, σ, δ_x, and δ_z (δ_x and δ_z are the horizontal and vertical Scale Of Fluctuation (SOF), respectively). Each case is analyzed by both RFEA and the LEM to determine the P_a values under the same random field realizations. It is clear that the P_a values simulated by both methods generally follow the 1:1 line. As mentioned earlier, although the assumption in

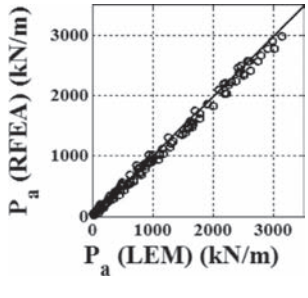

Figure 3. Comparison between the P_a values simulated by RFEA and the LEM.

LEM that the slip curve is a plane is in principle unconservative, its effect is minimal, judging from the fact that RFEA and LEM produce consistent P_a estimates (note: RFEA does not assume a slip "plane"). This is probably because the actual slip curves obtained in RFEA rarely significantly deviate from planes.

3 OBSERVED BEHAVIORS IN THE SIMULATED PA VALUES

3.1 *Effect of the COV*

The statistics of the LEM P_a samples depend on the COV of the τ_f(x,z) random field. Consider the reference case ($\gamma = 20$ kN/m^3, H = 5 m, $\mu = 20$ kN/m^2) with $\delta_x = \delta_z = 1$ m. The upper plots in Figure 4 demonstrate the P_a histograms (sample size N = 1,000). The solid vertical lines show the deterministic solution, denoted by $P_{a,d}$. It is clear that the P_a samples are more variable for larger COV's. But it is interesting to note that the P_a samples shift to the right of $P_{a,d}$ when the COV is large. As mentioned earlier, the slip plane is highly constrained because it must pass through the toe—it cannot evolve freely. It is tempting to hypothesize that the actual critical slip plane is a prescribed 45° line passing through the toe, in which case P_a is simply a random variable that depends on the average shear strength along the prescribed 45° slip plane. The mean value of τ_f^{LA} is the same as μ because line averaging along any prescribed line will not alter the mean. The consequence is that the mean value of P_a should be equal to $P_{a,d}$. However, this result is contradictory to the fact that the P_a samples shift to the right of $P_{a,d}$. As a result, the hypothesis that the actual critical slip plane is a prescribed 45° line passing through the toe is generally incorrect. The lower plots in Figure 4 show the histograms of the daylight positions (x^*) of the critical slip planes (N = 1,000). It is clear that x^* exhibits a certain variability. Thus, the critical slip plane is not a prescribed line but varies around the 45° line. When the COV is large, x^* has a large variability, possibly because there is more opportunity for the critical slip plane to find a weak path that deviates from the 45°. If a "weak path" is found, the $\tau_f^{LA}(x^*)$ has a mean value less than μ. Then, P_a histogram significantly shifts to the right of $P_{a,d}$.

3.2 *Effect of SOF*

The COV is not the only factor that affects the statistics of P_a. Consider the reference case with COV = 0.3 and $\delta_x = \delta_z \in$ (0.2 m, 1 m, 10 m, 1,000 m). The upper plots in Figure 5 present the LEM P_a histograms. The histograms with white faces show the negative P_a samples. These samples should be zero because a negative F implies that the wedge can stand on its own. It is clear that the P_a histograms for $\delta_x = \delta_z \in$ (0.2 m, 1 m) are significantly shifted to the right of $P_{a,d}$, whereas the P_a histograms for $\delta_x = \delta_z \in$ (10 m, 1,000 m) are not. This observation is consistent with those made in Fenton et al. (2005), where it was found that there is a critical SOF at which the P_a behavior becomes more complicated. The lower plots in Figure 6 show the x^* histograms: whenever the x^* variability is large, the P_a samples significantly shift to the right of $P_{a,d}$, and vice versa. This example shows that the variability of x^* depends on not only the COV but also the SOF. The $\tau_f^{LA}(x^*)$ will later be denoted by the "mobilized" shear strength (τ_f^m) because it is the shear

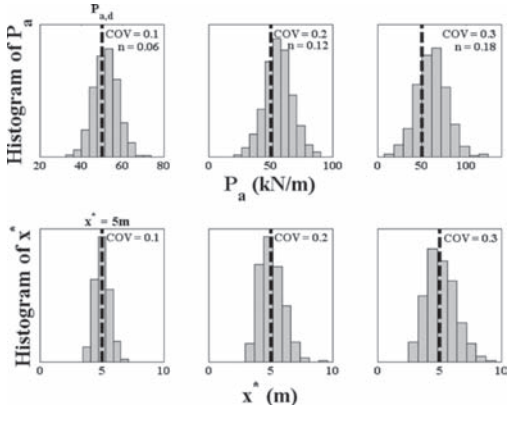

Figure 4. (Upper plots) LEM P_a histograms; (lower plots) histograms of the daylight positions (x^*) of the critical slip planes (reference case with $\delta_x = \delta_z = 1$ m).

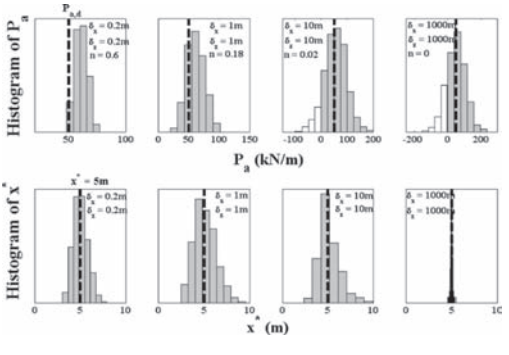

Figure 5. (Upper plots) LEM P_a histograms; (lower plots) histograms of the daylight positions (x^*) of the critical slip planes [reference case with COV = 0.3 and $\delta_x = \delta_z \in$ (0.2 m, 1 m, 10 m, 1,000 m)].

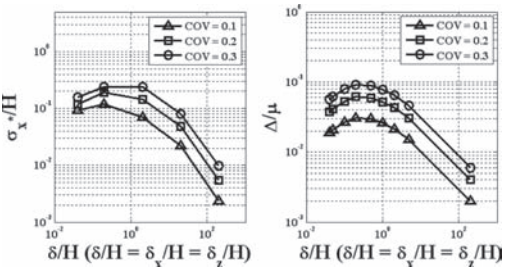

Figure 6. Variation of σ_{x^*}/H and Δ/μ with respect to δ/H (reference case with $\delta_x = \delta_z$). Figure 6a Variation of σ_{x^*}/H Figure 6b Variation of Δ/μ.

strength that is actually experienced by the retaining wall.

3.3 *More insight into the variability of x**

It is interest to gain insight into the variability in x^*. Consider 15 reference cases with COV $\in$ (0.1, 0.2, 0.3) and $\delta_x = \delta_z \in$ (0.2 m, 1 m, 10 m, 100 m, 1,000 m). For each case, 1,000 sets of LEM P_a samples and x^* samples are simulated. The variability of these x^* samples is quantified by its sample standard deviation, denoted by σ_{x^*}. Figure 6a shows how σ_{x^*}/H varies with the COV and δ/H ($\delta = \delta_x = \delta_z$). It is reasonable to observe that σ_{x^*} increases with increasing COV. It is also reasonable to see that σ_{x^*} is small for large SOFs.

3.3.1 *Connection between σ_{x^*} and the local roughness of $\tau_f^{LA}(x)$*

Recall that σ_{x^*} is large whenever the critical slip plane is able to find the weak zone. If $\tau_f^{LA}(x)$ is nearly a constant function, then there is no weak zone, and x^* will be nearly deterministic ($\approx$H) and $\sigma_{x^*} \approx 0$. If $\tau_f^{LA}(x)$ is a rough function, there are significant weak zones, and x^* will be more random, whereas σ_{x^*} will be large. It is expected that σ_{x^*} will be correlated with the roughness of $\tau_f^{LA}(x)$. Moreover, the local roughness of $\tau_f^{LA}(x)$ near the point x = H is more relevant because most x^* samples cluster around H. Let us define $x_L = H \times \tan(40°)$ and $x_R = H \times \tan(50°)$, and $[x_L, x_R]$ represents the local daylight region of interest. Let us define Δ to be the standard deviation of $[\tau_f^{LA}(x_R) - \tau_f^{LA}(x_L)]$. It is clear that when $\tau_f^{LA}(x)$ is a constant function, Δ will be close to zero. When $\tau_f^{LA}(x)$ is a rough function, Δ will be large. Therefore, Δ quantifies the local roughness of $\tau_f^{LA}(x)$ near x = H.

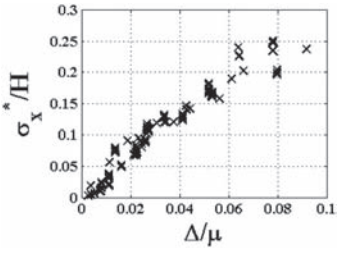

Figure 7. Relationship between σ_{x^*}/H and Δ/μ.

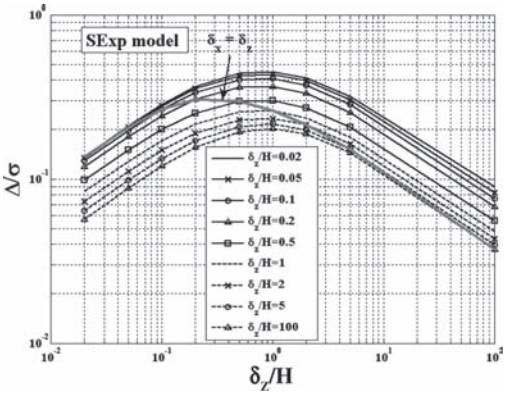

Figure 8. Relationships between Δ/σ and (δ_x/H, δ_z/H).

3.3.2 *Quantify σ_{x^*} through Δ*

It is expected that σ_{x^*} is positively correlated with Δ. Note that σ_{x^*} and Δ have different units: the former is in meters, and the latter is in kN/m^2. Therefore, it is more sensible to compare σ_{x^*}/H with Δ/μ. Figure 7 shows that σ_{x^*}/H and Δ/μ are positively correlated for 100 cases in a wide range of values for H, μ, COV, δ_x, and δ_z. The result suggests that it is possible to quantify σ_{x^*}/H through Δ/μ.

Δ/σ can be determined given the information on (δ_x/H, δ_z/H) from Figure 8. It is interesting to note that the gray line in Figure 8 has a similar shape to the three σ_{x^*}/H versus δ/H curves in Figure 6a. Figure 6b re-plots the (scaled) Δ/μ versus δ/H relationships ($\delta = \delta_x = \delta_z$) for comparison.

4 NUMBER OF INDEPENDENT POTENTIAL SLIP PLANES

Although the critical slip plane is constrained to pass through the toe, it is still able to seek the weak zone and vary locally around the prescribed 45° line. And the σ_{x^*}/H can be quantified by Δ/μ. One can imagine that there are a number of "independent"

potential slip planes, and the actual critical slip plane will be among these independent potential planes. A large Δ/μ (σ_{x^*}/H) implies that there may be many independent potential slip planes from which to seek. The number of independent potential slip planes quantifies the tendency of seeking the weak zone. This number also depends on the normalized correlation length of $\tau_f^{LA}(x)$, denoted by θ/H. If θ/H is large, the number of independent potential slip planes should be small. The notion of "correlation length" is herein adopted in regard to $\tau_f^{LA}(x)$ because the SOF of $\tau_f^{LA}(x)$ is infinity. The correlation length is defined to be the interval length at which the correlation coefficient is exactly exp(-1) (Li & Der Kiureghian 1993). If the correlation coefficient between $\tau_f^{LA}(x_L)$ and $\tau_f^{LA}(x_R)$ is exactly equal to exp(-1), the correlation length is simply the interval length $|x_L - x_R|$. x_L and x_R should be centered at x = H because x^* occurs around this location. In this study, we adopt x_L = H/r and x_R = H × r (r > 1). The ratio r is first solved, and θ is simply |H/r − H × r|. Figure 9 shows a unique mathematical relationship between θ/H and (δ_x/H, δ_z/H).

4.1 *Quantify the number of independent potential slip planes by n = (Δ/μ)/(θ/H)*

Conceptually, n = (Δ/μ)/(θ/H) quantifies the number of independent potential slip planes. It is found that the n being 'roughly proportional' to the number of independent potential slip planes. This concept is illustrated in Figure 10: Δ/μ quantifies the (normalized) daylight range for the critical slip plane, and θ/H quantifies the (normalized) correlation length in $\tau_f^{LA}(x)$. Thus, n = (Δ/μ)/(θ/H) quantifies the number of (normalized) correlation lengths of $\tau_f^{LA}(x)$ covered by the daylight range of the critical slip plane.

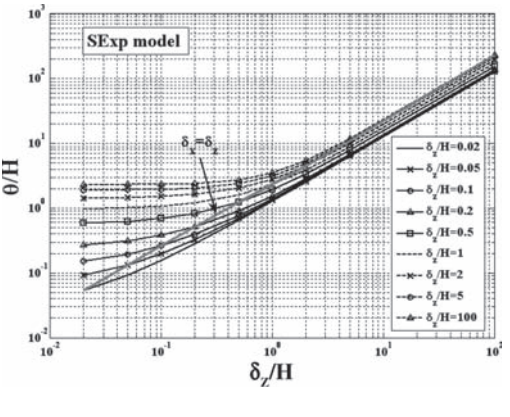

Figure 9. Relationships between θ/H and (δ_x/H, δ_z/H).

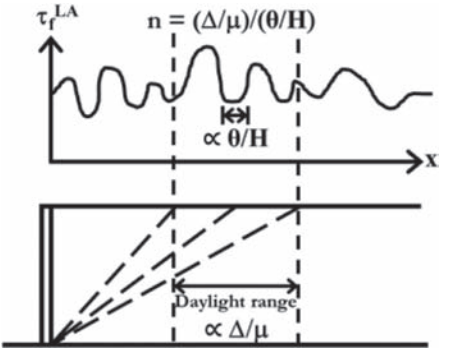

Figure 10. Illustration of the concept of n.

If n ≈ 0, the daylight range covers nearly zero correlation length, implying that $\tau_f^{LA}(x)$ is nearly constant within the daylight range. Thus, there should be a single independent potential slip plane. As a result, the critical slip plane cannot find a weaker zone, and the mean value of the resulting $\tau_f^m = \tau_f^{LA}(x^*)$ will be equal to μ; thus, the resulting P_a samples will not shift to the right of $P_{a,d}$. If n is large, the daylight range covers many correlation lengths, implying that $\tau_f^{LA}(x)$ oscillates drastically within the daylight range. Thus, there should be many independent potential slip planes from which to choose. As a result, the critical slip plane is more likely to find a weaker zone, and the mean value of the resulting τ_f^m will be less than μ; the resulting P_a samples will shift to the right of $P_{a,d}$. This result can be observed in Figures 4 and 5, where the n values are tabulated in the P_a histograms for all cases. It is clear that whenever n is large, P_a significantly shifts to the right of $P_{a,d}$.

4.2 *Observed number of independent potential slip planes*

The previous section discusses how to ***conceptually*** quantify the number of independent potential slip planes by n = (Δ/μ)/(θ/H). Nonetheless, it is possible to estimate the ***actual*** number of independent potential slip planes based on the LEM results. The factor n will be referred as the "conceptual number of independent potential slip planes". Additionally, the number of planes estimated from the LEM results will be referred as the "observed number of independent potential slip planes", denoted by n_o.

Corresponding to each LEM P_a sample, there is a simulated τ_f^m (= $\min_x \tau_f^{LA}(x)$). Each τ_f^{LA} is normally distributed with a mean value of μ and a variance of $\sigma^2 \times \Gamma^2$, where Γ^2 is the variance reduction factor. The Probability Density Function (PDF) of τ_f^m can be derived by differentiating $F(\tau)$ with respect to τ.

Given the LEM simulation results of for a sample size N ($\tau_{f,1}^{m}$, $\tau_{f,2}^{m}$, …, $\tau_{f,N}^{m}$). The estimation of (n_o, α) can be achieved through maximizing the following likelihood function L(n_o,α):

$$L(n_o,\alpha)=\prod_{i=1}^{N}\left(\frac{n_o}{\alpha\times\sqrt{\sigma^2\times\Gamma^2(n_p)}}\times\left[1-\Phi\left(\frac{\tau_{f,i}^{m}-\mu}{\alpha\times\sqrt{\sigma^2\times\Gamma^2(n_p)}}\right)\right]^{n_o-1}\times\varphi\left(\frac{\tau_{f,i}^{m}-\mu}{\alpha\times\sqrt{\sigma^2\times\Gamma^2(n_p)}}\right)\right) \quad (3)$$

where φ is the PDF of the standard normal random variable. The parameter n_p characterizes the averaging effect along the potential slip plane, n_o characterizes the number of independent potential slip planes, and α compensates for the continuous reality. Figure 11 shows the (n_o, α) values for 15 reference cases with COV ∈ (0.1, 0.2, 0.3) and $\delta_x = \delta_z \in$ (0.2 m, 1 m, 10 m, 100 m, 1,000 m). For each case, N = 1,000 samples of τ_f^{m} are simulated and used to estimate (n_o, α) using the maximum likelihood method.

Figure 12 shows the n_o versus n plot for 200 cases with a wide range of H, μ, COV, δ_x, and δ_z. For each case, N = 1,000 samples of τ_f^{m} are simulated and used to estimate (n_o, α) using the maximum likelihood method. The factor n for each case is also calculated based on its COV, δ_x, and δ_z. It is found that there is an approximately unique relationship between n_o and n. And there is also a rough relationship between α and n. It is evident that the following equations provide a satisfactory fit:

$$n_o \approx 1+12\times n \qquad \alpha \approx 1+n/(0.2+4\times n) \quad (4)$$

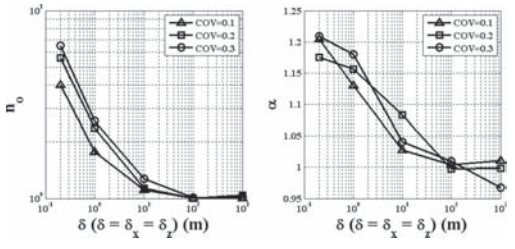

Figure 11. Variations of (n_o, α) with respect to δ (reference case with $\delta_x = \delta_z$).

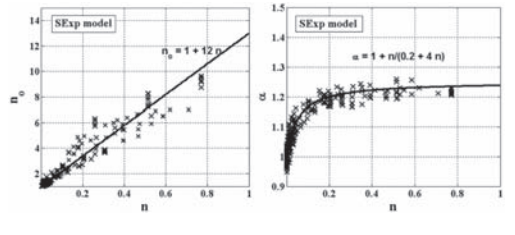

Figure 12. n_o-n and α-n relationships for the SExp model.

5 SIMULATING P_a SAMPLES USING A SIMPLIFIED PROCEDURE

The following simplified procedure can be used to simulate P_a samples (for the $\phi = 0°$ condition) without actually employing the LEM or RFEA. This simplified procedure requires knowledge of H, γ, μ, COV, δ_x, and δ_z.

1. Determine Δ/σ from Figure 8 based on H, δ_x, δ_z.
2. Determine θ/H from Figure 9 based on H, δ_x, δ_z.
3. Calculate n = (Δ/μ)/(θ/H) = (COV × Δ/σ)/(θ/H), and estimate (n_o, α) using Eq. 4.
4. Simulate a random sample U from a uniform distribution with the range [0, 1].
5. A sample of τ_f^{m} can be obtained as $F^{-1}(U)$, where F^{-1} is the inverse of the CDF F:

$$\tau_f^{m}=\mu+\alpha\times\sqrt{\sigma^2\times\Gamma^2(n_p)}\times\Phi^{-1}\left[1-(1-U)^{\left(\frac{1}{n_O}\right)}\right] \quad (5)$$

6. A sample of P_a can be obtained as

$$P_a=\max\left(\frac{1}{2}\gamma H^2-2\tau_f^{m}\times H,\ 0\right) \quad (6)$$

Repeat the above steps N times to obtain N samples.

The performance of the above procedure is illustrated for a case (Fig. 13). The top row shows the histograms of the LEM P_a samples (N = 1,000). The middle row shows the histograms of the P_a samples (N = 10,000) simulated by the simplified procedure.

The bottom row shows the histograms of the P_a samples (N = 10,000) simulated based on the hypothesis that the actual critical slip plane is the prescribed 45° line passing through the toe (x^* is fixed at H). In general, the P_a samples simulated by the hypothesis x^* = H behave very differently from LEM when the SOF is small. When $\delta_x = \delta_z = 0.2$ m, the LEM samples are clearly not centered at $P_{a,d}$ but shift to a positive value of approximately 45 kN/m.

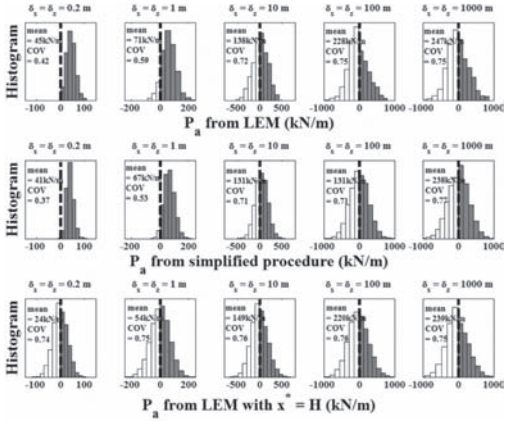

Figure 13. Histograms of the simulated P_a samples for the case in which H = 10 m, COV = 0.3, μ = 50 kN/m^2, $\delta_x = \delta_z \in$ (0.2 m, 1 m, 10 m, 100 m, 1,000 m), and the SExp model is used. (Top row) LEM samples; (middle row) samples from the simplified procedure; (bottom row) samples based on the hypothesis that $x^* = H$.

The shift is also quite obvious for $\delta_x = \delta_z = 1$ m. However, the samples in the bottom row are always centered at $P_{a,d}$; a major discrepancy exists between the LEM samples and those based on the hypothesis that $x^* = H$ when the SOF is small. But for larger SOFs [$\delta_x = \delta_z \in$ (10 m, 100 m, 1,000 m)], there is a less noticeable shift. The above observation implies that the hypothesis $x^* = H$ may be acceptable when the SOF is large but is not acceptable when the SOF is small. When the SOF is smaller than H, weak zones are more pronounced, so x^* starts to deviate from H and σ_{x^*} increases. As a result of these changes, n (n_o) increases and τ_f^m should be less than μ; thus, the samples shift to the right of $P_{a,d}$. Nonetheless, the P_a histograms simulated by the simplified procedure (middle row) behave similarly to the LEM P_a histograms, even when the SOF is small.

6 CONCLUDING REMARKS

In this study, the mobilized shear strength of soils with constrained slip curves is explored. It is found that although the actual critical slip curve is highly constrained (must pass through the toe), it is still able to seek weak zones locally when the SOFs are smaller than the height of the wall.

The main contribution of this study is to discover that the tendency of seeking weak zones can be characterized by the number of independent potential slip planes. Moreover, this study derives a set of equations and charts to facilitate the determination of such a number based on the characteristics of the random field and wall height. The determination does not require sophisticated analyses, such as the finite element method; instead, it requires only simple algebraic calculations and chart checking. Finally, a simplified procedure is proposed to simulate the P_a samples without the finite element method or LEM, and the simulated P_a samples are observed to behave similarly to the P_a samples simulated by the LEM.

REFERENCES

Ching, J. Phoon, K.K. & Kao, P.H. 2013. Mean and variance for mobilized shear strengths of spatially variable soils under uniform stress states. *Journal of Engineering Mechanics*, ASCE (accepted w/minor revision).

Fenton, G.A., Griffiths, D.V. & Williams, M.B. 2005. Reliability of traditional retaining wall design. *Geotechnique* 55(1): 55–62.

Jha, S.K. & Ching, J. 2013. Simulating spatial averages of stationary random field using Fourier series method. *Journal of Engineering Mechanics*, ASCE 139(5): 594–605.

Li, C. & Der Kiureghian, A. 1993. Optimal discretization of random fields. *Journal of Engineering Mechanics*, ASCE 119(6): 1136–1154.

Vanmarcke, E.H. 1977. Probabilistic modeling of soil profiles. *Journal of Geotechnical Engineering Division*, ASCE 103(11): 1227–1246.

Vanmarcke, E.H. 1984. *Random Fields: Analysis and Synthesis*, MIT Press, Cambridge, Mass.

This page intentionally left blank

Geotechnical Safety and Risk IV – Zhang et al. (eds)
 ISBN 978-1-138-00163-3

Reliability of heterogeneous slopes with cross-correlated shear strength parameters

T.M.H. Le

Department of Civil and Transport Engineering, Norwegian University of Science and Technology—NTNU, Norway

ABSTRACT: Spatial variabilities of the soil shear strength parameters (friction angle and cohesion coefficient) have long been recognised as an important factor influencing the reliability of geo-structures including slopes. However, these two parameters are frequently considered separately in research studies even though, in natural soils, both parameters are likely to vary simultaneously with existence of cross-correlation between them. This study stochastically investigates the reliability of a slope constructed in soil having spatially varying both friction angle and cohesion coefficient, and compares that with the scenarios where each soil parameter varies individually. The finite element method is merged with the random field theory to probabilistically evaluate the factor of safety and probability of failure of the slope *via* Monte-Carlo simulations. A simple procedure to create perfect cross-correlation is discussed. The results show that the variabilities of both friction angle and cohesion coefficient even without cross-correlation can elevate the probability of failure relative to the cases where each of them varies individually. If a perfectly positive cross-correlation exists, the probability of failure increases significantly due to increasing occurrences of local failures.

1 INTRODUCTION

Probabilistic modelling has been quite frequently employed in the geotechnical engineering discipline to deal with soil variability. Particularly, slope stability is one of a few engineering problems that is more often analysed using probabilistic approaches (Alonso 1976, Mostyn & Soo 1992, Mostyn & Li 1993, Hicks & Samy 2002, Babu & Mukesh 2004, Griffiths & Fenton 2004, El-Ramly et al. 2005, Hicks & Onisiphorou 2005, Popescu et al. 2005, Sejnoha et al. 2007, Griffiths et al. 2009, Griffiths et al. 2011). Among these studies, a number have investigated the influence of spatial variability of soil properties on Factor of Safety (FoS) and probability of failure (p_f) of slopes. Monte-Carlo simulations were used in many of these studies due to its conceptual simplicity and its ability to handle complicated geometry, loading sequence and variability patterns without over-simplified assumptions. In a Monte-Carlo simulation, random samples generated from the same input statistical parameters are repeatedly analysed. Each analysis is usually referred to as a "realizations". This method is especially attractive for complex problems without closed form solutions such as slope stability.

In describing spatial variability, a number of slope stability studies took into account the inherent characteristic that measurement of a soil property at a given location tends to be similar (i.e. correlate with) those of the same property at close locations but different from those at far locations (e.g. Mostyn & Soo 1992, Hicks & Samy 2002, Babu & Mukesh 2004, Griffiths & Fenton 2004). This characteristic is usually quantified in stochastic modelling by a correlation length (θ). The value of soil property at a given location also tends to correlate with the values of other soil properties at the same location or at close locations. This characteristic is termed "cross-correlation".

Cross-correlation between various soil properties has been reported by a few authors (Cherubini 2000, Baecher & Christian 2003). When considering problems related to failure, the influence of heterogeneity of friction angle (ϕ') and cohesion coefficient (c') and the cross-correlation between them are likely to play an important role. Cherubini (2000) suggested that the cross-correlation between ϕ' and c' might be negative (i.e. a large value of ϕ' occurs with a small value of c' at a given location or vice versa). It is however intuitively expected that a stochastic slope with negatively correlated ϕ' and c' is likely to be more stable than a slope with uncorrelated or positively correlated ϕ' and c'. The risk associated with having no correlation or ignoring an existing positive correlation between these two shear strength parameters should therefore not be

ignored. Only few studies have considered the effect of cross-correlation between different soil properties on slope stability (e.g. Popescu et al. 2005, Griffiths et al. 2009, Griffiths et al. 2011). Griffiths et al. (2009) briefly investigated a drained slope with a cross-correlation between soil c' and ϕ' and concluded that a positive cross-correlation decreased the "critical" value of Coefficient Of Variation (COV) (i.e. the value at which ignoring spatial correlation will lead to unconservative estimates).

This study presents a simple procedure to generate cross-correlation between soil shear strength parameters modelled by random fields. The procedure facilitates comparison between the effects of variability of single and multiple soil properties on both qualitative characteristics of slip surfaces and quantitative values of FoS and p_f. This procedure is then applied to probabilistically investigate the stability of a slope with spatially varying friction angles and cohesion coefficients with either zero or perfectly positive cross-correlation between them.

2 METHOD

2.1 *Numerical model*

A 1:2 slope model is used for every realization in the current study (Fig. 1). The soil behaviour is assumed to be elastic perfectly plastic, with a Mohr-Coulomb yield/failure criterion. Elastic matrix is calculated from Young's modulus and Poisson's ratio through the classical linear isotropic elasticity theory. This study adopts a non-associated flow rule with zero dillatancy. Stresses are updated by means of a viscoplastic algorithm. The model is numerically analysed with the finite element program CODE_BRIGHT (Olivella et al. 1996).

The failure mechanism is artificially mobilised by the shear strength reduction technique (Zienkiewicz et al. 1975). The displacements of ten points (located along the face, on the crest and at the base of the slope) are monitored to detect failure (Fig. 1). The FoS is estimated when

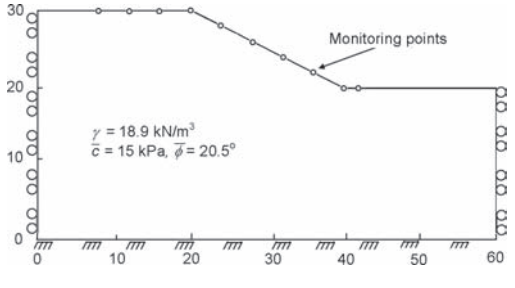

Figure 1. Slope dimensions, geometry and boundary conditions (scale in meter).

sudden increases in displacements of one or more of these points occur during the application of the shear strength reduction procedure. The points are approximately spaced between 2 to 4 m apart, which is sufficient to identify the majority of global and local failures in the current study.

In each realisation, spatial variability of ϕ' and/or c' is generated by mapping each element of the finite element mesh with a random value of ϕ' and/or c' selected from a random field. The values of $tan\phi'$ and c' are assumed to follow a log-normal distribution with mean values equal to 0.375 and 15 kPa, respectively, and a range of COV from 0.1 to 1.6. The vertical correlation length (θ_v) is investigated for the range from 1 to 16 m while the horizontal correlation length (θ_h) is assumed to be equal to two times θ_v. This range of θ_v is larger than the usual range of θ_v reported in the literature which is from 0.5 to 4 m (see, for example, Spencer (2007)). The larger range is studied to emphasise the influence of correlation length (if any) on the obtained results. The Local Average Subdivision (LAS) algorithm is selected to generate all random fields in this study because it has been suggested as being suitable for soil properties (Fenton & Vanmarcke 1990; Fenton & Griffiths 2008). The Markov correlation function is assumed to model the spatial correlation of random values.

2.2 *Cross-correlation between soil properties*

A popular method for generating cross-correlated random fields is the covariance matrix decomposition method. This method is capable of producing fields which have a defined degree of correlation (ρ) varying between −1 and 1. This study adopts a simpler approach to generate cross-correlated random fields of $tan\phi'$ and c', by assuming a simple arithmetic transformation between these two parameters. This approach has an advantage of simplifying the conceptual understanding of the effect of cross-correlated soil properties, which eases the explanation of failure mechanisms associated with the variability of each parameter.

The stability of slopes with either ϕ' or c' varying singly are compared with those having both parameters varying simultaneously with zero cross-correlation ($\rho = 0$) and with perfectly positive cross-correlation ($\rho = 1$). To facilitate this comparison, the values of $\mu(tan\phi')$ and $\mu(c')$ are kept constant in every analysis at 0.375 and 15 kPa, respectively. Four closely related scenarios are designed as follows:

a. Random $tan\phi'$ and uniform c'

A random field of $tan\phi'$ is generated by the LAS with $\mu(tan\phi') = 0.375$ and mapped onto the mesh, while the value of c' is kept spatially uniform at 15 kPa. Figure 2 conceptually illustrates the

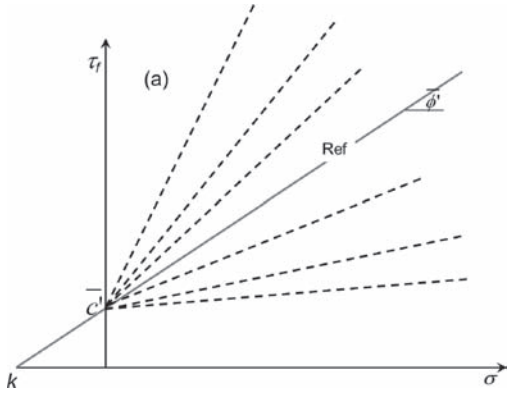

Figure 2. Variation of failure envelope corresponding to scenario (a) Random $tan\phi'$ and uniform c'.

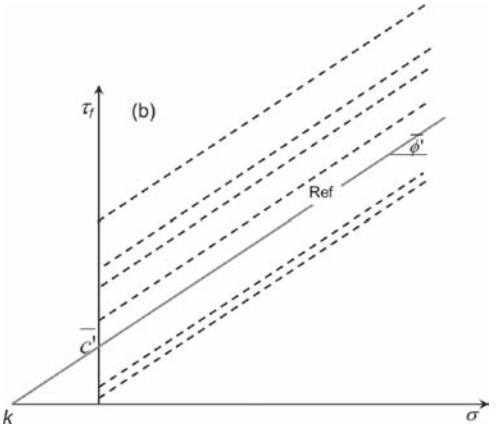

Figure 3. Variation of failure envelope corresponding to scenario (b) Random c' and uniform $tan\phi'$.

variation of the Mohr-Coulomb failure envelope relative to the reference envelope which is corresponding to the failure state with $c' = \mu(c')$ and $tan\phi' = \mu(tan\phi')$. In this scenario, the failure envelopes of different soil elements vary in gradient but always intersect the vertical axis at c'.

b. Random c' and uniform $tan\phi'$

The same field of $tan\phi'$ generated in scenario (a) is used to create a random field of c' by multiplying each random value of $tan\phi'$ with a constant $k = \mu(c')/\mu(tan\phi') = 15/0.375 = 40$ kPa. By simple arithmetics, it can be shown that this transformation leads to consistency in the variability characteristics of the $tan\phi'$ random field in (a) and the c' random field in (b) (i.e. $COV(c') = COV(tan\phi')$, $\theta(c') = \theta(tan\phi')$ and $\mu(c') = k.\mu(tan\phi') = 15$ kPa). The random c' values are mapped onto the mesh while the value of $tan\phi'$ is kept spatially uniform at 0.375 in this scenario. Therefore, the failure envelope corresponding to individual soil element shifts its position up and down but is always parallel to the reference envelope due to uniform friction angle (Fig. 3).

c. Random $tan\phi'$ and c' with zero cross-correlation ($\rho = 0$)

In this scenario, the random field of $tan\phi'$ generated in scenario (a) is first mapped onto the mesh. A second random field of $tan\phi'$ (having the same statistical parameters as the first one) is generated using the LAS generator. This second random field is then used to create a random field of c' in a similar fashion to the method described in scenario (b) above. The $tan\phi'$ and c' random fields employed in this scenario are therefore independently generated but they have similar variability characteristics (i.e. the same COV and θ while $\mu(tan\phi') = 0.375$ and $\mu(c') = 15$ kPa). The c' random field is also mapped onto the mesh and hence each finite element is

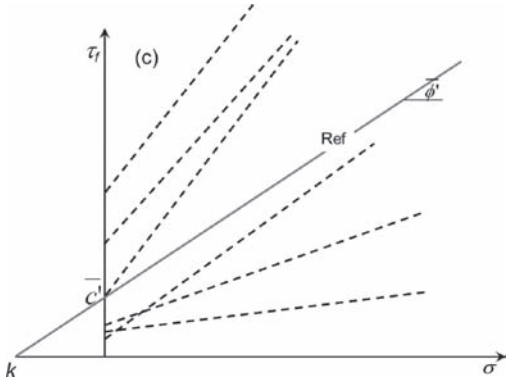

Figure 4. Variation of failure envelope corresponding to scenario (c) Random $tan\phi'$ and random c' with zero cross-correlation.

assigned with a random value of $tan\phi'$ and a random value of c'. The failure envelope of each soil element changes both gradient and position randomly with respect to the reference envelope in this scenario (Fig. 4).

d. Random $tan\phi'$ and c' with perfect cross-correlation ($\rho = 1$)

The same random field of $tan\phi'$ from scenario (a) above is used to generate a random field of c' in the same fashion as described in scenario (b). Both the random field of $tan\phi'$ from (a) and the currently generated random field of c' are used to map random values of ϕ' and c' onto the mesh. This leads to perfectly positive correlation of $tan\phi'$ and c' at every location. Because both parameters are varied and $c' = k tan\phi'$, it can be shown through trigonometry that the failure envelope of soil element

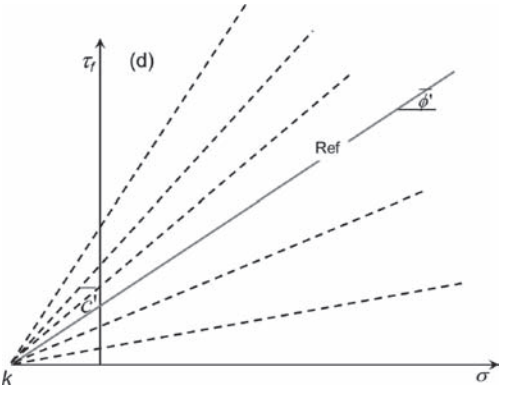

Figure 5. Variation of failure envelope corresponding to scenario (d) Random $tan\phi'$ and random c' with perfectly positive cross-correlation.

varies its gradient (due to the variability of $tan\phi'$) but always intersects the horizontal axis at the same point k similar to the reference envelope (Fig. 5).

The use of the same random field of $tan\phi'$ in all four scenarios, and hence the same configuration of shear strength variability, as described above, facilitates direct comparison between these scenarios. The reason is that, for a single realisation, it eliminates differences between scenarios caused by the discrepancy in spatial distribution of shear strength parameters. Also, it becomes possible to qualitatively compare the effect of variabilities of $\tan\phi'$ and c' on the characteristic of the slip surface for each individual realization as will be shown in the subsequent section.

3 RESULT AND DISCUSSION

3.1 *Failure mechanism*

Figure 6 illustrates typical examples of 'local' and 'global' slip surfaces for the four scenarios introduced in the previous section. These contour plots and the slip surfaces correspond to slopes having the same random configuration of $tan\phi'$ except for scenario (c) in which a second random field is required to generate the variable configuration of c'. Figures 2 and 3 show that, at high confining stresses, the failure shear strength (τ_f) corresponds to scenario (a) with random $tan\phi'$ varies over a broader range compared with scenario (b) with random c'. Conversely, at low confining stresses, the value of τ_f corresponds to scenario (b) varies over a broader range than to scenario (a). When the values of τ_f spread over a broad range, it becomes 'easier' to find a series of weak soil elements (i.e. having low τ_f) to form a shear

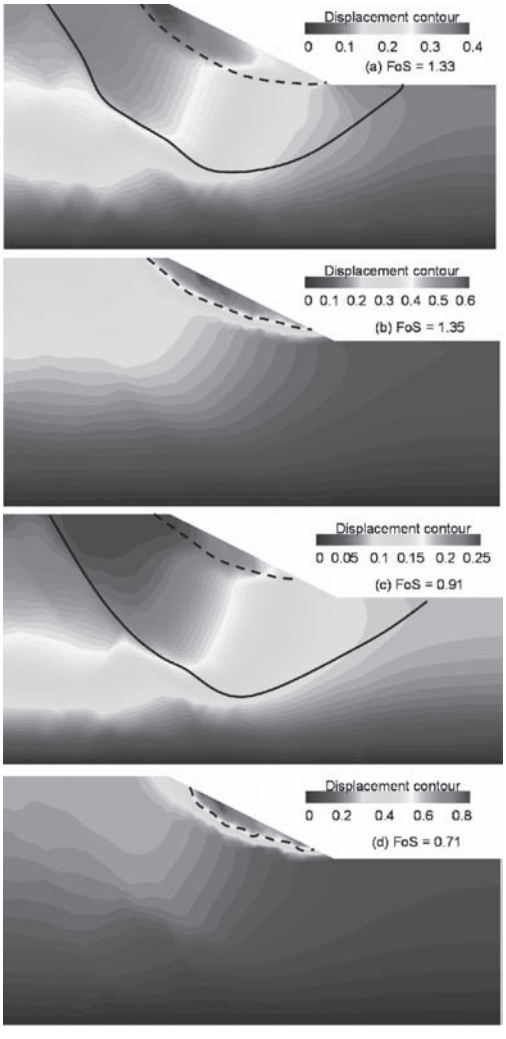

Figure 6. Typical displacement contours and possible global (continuous line) and local (broken line) slip surfaces of the four scenarios: (a) random $tan\phi'$ and uniform c' (b) random c' and uniform $tan\phi'$ (c) random $tan\phi'$ and c' with zero cross-correlation (d) random $tan\phi'$ and c' with perfectly positive cross-correlation ($\mu(tan\phi') = 0.375$, $\mu(c') = 15$ kPa, COV = 0.8, $\theta = 0.8$). Contour scales are different between scenarios.

band and mobilise a slip surface. Between the two first scenarios, even though the slope in scenario (a) has random $\tan\phi'$ and that in scenario (b) has random c', the two scenarios have the same random configuration due to the assumed perfect correlation of $\tan\phi'$ and c' used to generate the random field of c' as described earlier. Therefore, in deep soil regions (corresponding to regions of high confining stresses), the 'weakest' path is likely

to be weaker in scenario (a) than in scenario (b). Conversely, in shallow soil regions (corresponding to regions of low confining stresses), the weakest path is likely to have lower shear strength in scenario (b) than in scenario (a). Consequently, mobilisation of deep failure mechanism is more commonly observed in the case of varying tanϕ' (Fig. 6a) compared to varying c' (Fig. 6b). For the example shown in Figure 6a, both global (i.e. deep and large in extent) and local (shallow and limited in extent) slip surfaces are indeed mobilised, but the global slip surface corresponds to a lower FoS and hence dominates the failure mechanism in this case. The corresponding slipping mass of the slope having random c' (with the same random configuration) tends to be local (Fig. 6b). This difference in failure mechanisms between the two scenarios, where shear strength parameter is varied singly, is observed for numerous realizations in the current study. The FoS in scenario (a) is also frequently smaller than that in scenario (b).

For a given realisation in scenario (c), if the simultaneous but not cross-correlated variabilities of ϕ' and c' lead to a dominance of combinations of low tanϕ' with low c' in the weakest path, the stability of the slope will tend to be lower compared with the two previous scenarios (e.g. Fig. 6c). On the other hand, if these variabilities lead to a dominance of combinations of low tanϕ' with high c', the stability of the slope is likely to be improved and a higher FoS compared with other scenarios is likely to be observed. The failure mechanism can also vary widely in this scenario, from shallow local slipping mass if the weakest path is dominated by low c', to deep global slipping mass if the weakest path is dominated by low tanϕ'.

Finally, when both tanϕ' and c' vary with perfectly positive cross-correlation, in the region below the reference envelope, the failure envelope in scenario (d) is always lower than in scenarios (a) and (b) because an element with low ϕ' will also certainly have low c' (Fig. 5). As a result, the weakest path is weaker in scenario (d) than in scenarios (a) or (b) and hence slopes with perfectly positive cross-correlation have lower FoS than those with varying only ϕ' or only c'. Also, a local slip surface concentrating in a small soil region is frequently observed in scenario (d) such as in the example shown in Figure 6d. This is because the combination of low values of both tanϕ' and c' leads to regions of soil with so low shear strength that the local slip surface is mobilised much earlier than the global one.

3.2 *Factor of safety and probability of failure*

The variations of μ(FoS), COV(FoS) and p_f with the degree of variability of the strength parameters (i.e. COV) are compared between the four scenarios and for different values of θ (Figs. 7 and 8). The horizontal axes in these figures are labelled with a generic term, COV(*Shear strength*), which is equal to COV(*tan*ϕ') in (a), to COV(c') in (b) and equal to both COV(*tan*ϕ') and COV(c') in (c) and (d). Griffiths et al. (2009) concluded that if the input COV(*Shear strength*) exceeds a certain critical value, ignoring spatial variability can lead to unconservative estimates of the p_f of heterogeneous slopes. This study therefore considers a large range of values of the input COV (0.1–1.6), though the typical values of COV(*Shear strength*) are normally less than 0.5.

The most noticeable trends in Figure 7 are the decreasing value of μ(FoS) and increasing value of COV(FoS) as the degree of soil variability increases, which leads to an apparent increase in p_f with COV(*Shear strength*) for all cases (Fig. 8). Note that the logarithm of p_f and the log-scale vertical axis have been adopted to facilitate the presentation of results in Figure 8, and hence the upward

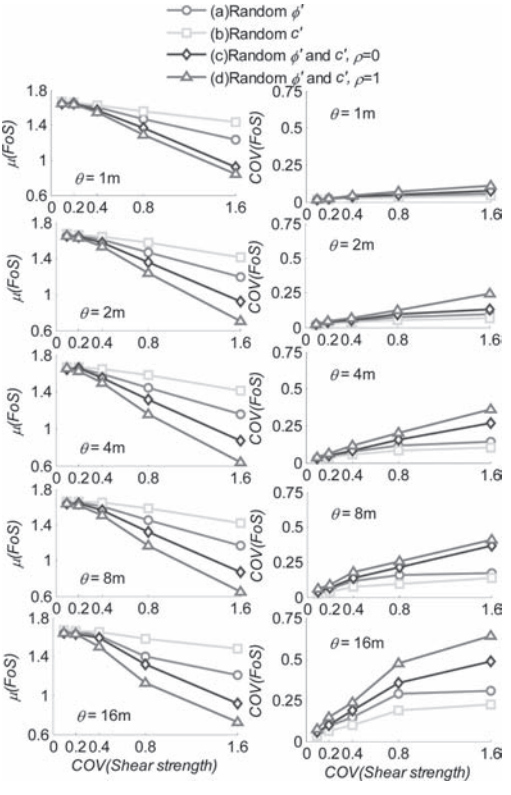

Figure 7. Variations of the μ(*FoS*) and *COV*(*FoS*) with *COV*(*Shear strength*) for four scenarios (μ(*tan*ϕ') = 0.375, μ(c') = 15 kPa, *COV*(*Shear strength*) = *COV*(*tan*ϕ') = *COV*(c'), $\theta_v = \theta$, $\theta_h = 2\theta$).

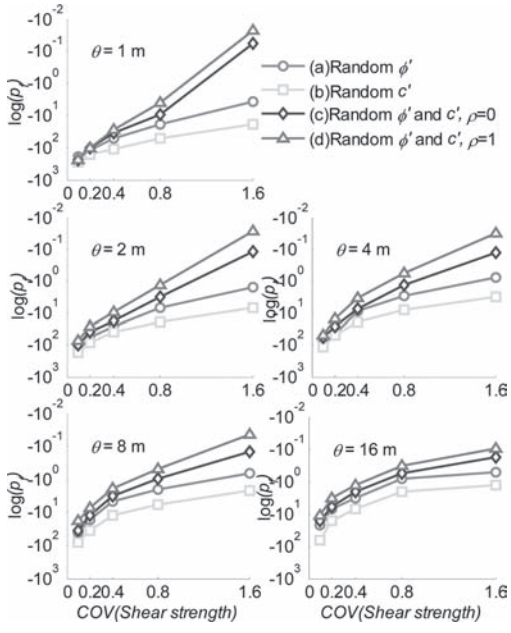

Figure 8. Variation of the p_f with COV(*Shear strength*) at different θ for four scenarios ($\mu(tan\phi')$ = 0.375, $\mu(c')$ = 15 kPa, COV(*Shear strength*) = $COV(tan\phi')$ = $COV(c')$, $\theta_v = \theta$, $\theta_h = 2\,\theta$).

direction denotes the increasing probability of failure and vice versa. The increasing value of p_f is the result of the increasing probability of soil elements with very low $tan\phi'$ and/or c' with larger degree of variability in shear strength, therefore raising the possibility of shearing a sufficient number of weak soil elements to form a slip surface. It seems that, for the slope considered, the contribution of $tan\phi'$ to the stability of the slope is more significant than the contribution of c' because the value of μ(FoS) is always larger for scenario (a) with varying $tan\phi'$ than for scenario (b) with varying c'. In addition, the scenario (b) results in smaller values of COV(FoS) than scenario (a) (Fig. 7).

In the scenarios with both shear strength parameters varying (either with or without cross-correlation), lower values of μ(FoS) and larger values of COV(FoS) are observed compared with scenarios with only one parameter varying due to the possibility of a low $tan\phi'$ occurring with a low c' in a soil element (Fig. 7). Consequently, slopes with heterogeneity of both parameters pose higher risk of failing than those with only one soil parameter being varied. If $tan\phi'$ and c' are positively correlated, the value of μ(FoS) decreases and the value of COV(FoS) increases compared slopes having zero cross-correlation between these two parameters (Fig. 7), and hence an increase in p_f is observed (Fig. 8). The reason is that, in the case of positive cross-correlation, all the soil elements with low value of $tan\phi'$ also have corresponding low value of c', while an element with low $tan\phi'$ might have low or high c' in the absence of cross-correlation.

The value of μ(FoS) changes insignificantly with the value of θ, while a very consistent increase in the value of COV(FoS) with increasing θ is observed (Fig. 7). When both $tan\phi'$ and c' varying, the value of p_f increases much more significantly with COV(*Shear strength*) for shorter θ than for longer ones. Therefore, slopes with shorter θ appear to pose lower risk of failure than those with longer θ at low values of COV(*Shear strength*) but an opposite trend is observed for COV(*Shear strength*) = 1.6 in scenarios (c) and (d) (Fig. 8). The reason is that the shear strength of a number of soil elements becomes very low when both $tan\phi'$ and c' are varied, together with the reduction in the size of region of 'correlated' soil property (with smaller θ) lead to the dominance of local failure mechanism occurring within a small region of soil over global failure mechanism (e.g. Fig. 6d). Long θ in this case causes larger and less fragmented weak soil regions compared with short θ, thus lowering the probability of occurrence of these local slip surfaces.

4 CONCLUSIONS

This paper has discussed some interesting effects of cross-correlation between soil shear strength parameters on the failure mechanism and the stability of a stochastic slope using the finite element method and the random field theory. A simple procedure to generate perfect cross-correlated random shear strengths is demonstrated, which eases the conceptual understanding of the influence of soil parameter variability on the slope performance.

The results show that, compared with slopes having only one heterogeneous shear strength parameter, the probability of failure increases when both friction angle and cohesion coefficient are varied, even with zero cross-correlation between them. If the two shear strength parameters are perfectly positive cross-correlated, the probability of failure increases significantly relative to the case where no cross-correlation exists, due to dominant occurrences of local failure mechanism over global failure mechanism.

For the slope investigated, an increase in soil variability decreases the mean however significantly increases the coefficient of variation of the factor of safety, thus resulting in an increasing probability of failure in all cases considered. If multiple shear strength parameters are varied with zero

to positive cross-correlation, the increase in the probability of failure with degree of soil variability (i.e. coefficient of variation of shear strength) is more significant at small correlation lengths than at large ones. This can lead to decreases in probability of failure with increasing correlation length at sufficiently large degrees of soil variability.

REFERENCES

Alonso, E.E. 1976 Risk analysis of slopes and its application to Canadian sensitive clays. *Géotechnique* 26(3): 453–472.

Babu, G.L.S. & Mukesh, M.D. 2004 Effect of soil variability on reliability of soil slopes. *Géotechnique* 54(5): 335–337.

Baecher, G.B. & Christian, J.T. 2003 *Reliability and statistics in geotechnical engineering,* Chichester, United Kingdom, Wiley.

Cherubini, C. 2000 Reliability evaluation of shallow foundation bearing capacity on c′, phi′ soils. *Canadian Geotechnical Journal* 37: 264–269.

El-Ramly, H., Morgenstern, N.R. & Cruden, D.M. 2005 Probabilistic assessment of stability of a cut slope in residual soil. *Géotechnique* 55(1): 77–84.

Fenton, G.A. & Vanmarcke, E. 1990 Simulation of random field via Local Average Subdivision. *ASCE Journal Engineering Mechanics* 116(8): 1733–1749.

Griffiths, D.V., Huang, J. & Fenton, G. A. 2011 Probabilistic infinite slope analysis. *Computers and Geotechnics* 38(4): 577–584.

Griffiths, D.V., Huang, J. S. & Fenton, G. A. 2009 Influence of Spatial Variability on Slope Reliability Using 2-D Random Fields. *Journal of Geotechnical and Geoenvironmental Engineering* 135(10): 1367–1378.

Hicks, M.A. & Onisiphorou, C. 2005 Stochastic evaluation of static liquefaction in a predominantly dilative sand fill. *Géotechnique* 55(2): 123–133.

Hicks, M.A. & Samy, K. 2002 Reliability-based characteristic values: a stochastic approach to Eurocode 7. *Ground Engineering* 35: 30–34.

Mostyn, G.R. & Li, K.S. 1993 Probabilistic slope analysis: state-of-play. *Proceedings of the conference on probabilistic methods in geotechnical engineering.* Canberra, Australia.

Mostyn, G.R. & Soo, S. 1992 The effect of autocorrelation on the probability of failure of slopes. *Proceedings of 6th Australia, New Zealand Conference on Geomechanics: Geotechnical Risk.*

Olivella, S., Gens, A., Carrera, J. & Alonso, E. 1996 Numerical formulation for a simulator (CODE-BRIGHT) for the coupled analysis of saline media. *Engineering Computations* 13(7): 87–112.

Popescu, R., Deodatis, G. & Nobahar, A. 2005 Effects of random heterogeneity of soil properties on bearing capacity. *Probabilistic Engineering Mechanics* 20: 324–341.

Sejnoha, M., Sejnoha, J., Kalousková, M. & Zeman, J. 2007 Stochastic analysis of failure of earth structures. *Probabilistic Engineering Mechanics* 22(2): 206–218.

Spencer, W.A. 2007 Parallel stochastic and finite element modelling of clay slope stability in 3D. *Faculty of Engineering and Physical Sciences.* Manchester, University of Manchester.

Zienkiewicz, O.C., Humpheson, C. & Lewis, R.W. 1975 Associated and non-associated visco-plasticity and plasticity in soil mechanics. *Géotechnique* 25(4): 671–689.

This page intentionally left blank

Geotechnical Safety and Risk IV – Zhang et al. (eds)
© 2014 Taylor & Francis Group, London, ISBN 978-1-138-00163-3

Finite element analysis of compression behavior of ground improvement with spatial variability

T. Namikawa
Shibaura Institute of Technology, Tokyo, Japan

ABSTRACT: The strength of cement-treated soil varies greatly owing to variability of the in-situ soil, variability of mixing effectiveness, and other factors. This paper presents the numerical experiments that investigate the effect of the spatial correlation on the behavior of cement-treated soil columns with different sizes. Finite element analyses were performed to simulate the unconfined compression behavior of the columns with three different heights. The spatial distribution of the material properties was provided by means of Monte Carlo simulation. The simulations were carried out with the samples in the presence of different degrees of spatial autocorrelation. The numerical results provide good understanding of the effects of the column height on the compression behavior of the cement-treated soil columns with spatial variability.

1 INTRODUCTION

Ground improvement by deep mixing method has been widely used for structure foundations, retaining walls and liquefaction mitigation method. In this method, it is well known that the strength of cement-treated soil varies greatly, even at a single column, owing to variability of the in-situ soil, variability of mixing effectiveness, and other factors. Therefore, to design adequately the ground improvement, it is necessary to evaluate appropriately the influence of the variability of cement-treated soil strength on the behavior of ground improvement.

The most popular statistical parameter expressing variability is the standard deviation. In practical design procedures, the mean and the standard deviation of the unconfined compressive strength of cement-treated soils have been used for determining the design strength and assessing the quality of ground improvement (e.g., Matsuo 2002, CDIT 2002). In these design procedure, the design strength is reduced with the increase in the standard deviation of the strength of cement-treated soils. However, the standard deviation is not sufficient in characterizing the variability of the strength because the spatial variation of the strength is generally correlated with each other. Therefore, it is necessary to investigate the influence of the spatial correlation of the strength on the behavior of the entire ground improvement by cement-mixing. Namikawa & Koseki (2013) conducted the Finite Element analysis (FE-analysis) with Monte Carlo Simulations (MCS) to investigate the compression behavior of full scale cement-treated columns with spatial variability. That study revealed that the spatial autocorrelation in the material properties affects significantly the overall compressive strength of the full scale column. However, since the column size was held constant in that study, the effect of spatial correlation on the behavior of cement-treated columns with different sizes has not been studied.

This paper presents the numerical experiments that investigate the effect of the spatial correlation on the behavior of cement-treated soil columns with different sizes. FE-analysis with MCS was performed to simulate the unconfined compression behavior of the columns with three different heights. The spatial distribution of the material properties was provided by means of MCS. The simulations were carried out with the samples in the presence of different degrees of spatial autocorrelation. The numerical results provide good understanding of the effects of the column height on the compression behavior of the cement-treated soil columns with spatial variability.

2 GENERATING STOCHASTIC FIELD

The spatial distribution of the strength in the sample is provided by means of Monte Carlo simulation (MCS). In the simulations, the probability characterization of cement-treated soil strength is required for generating of random fields. The type of probability distribution of the cement-treated soil strength is required in the generating

random field. In this study, the variability of the unconfined compressive strength of the cement-treated soil q_u is assumed to be characterized by the normal distribution. Moreover the stationary random field with an exponential type autocorrelation function is assumed for the spatial variability of q_u in a cement-treated column. The exponential type autocorrelation function is defined as:

$$\rho(d) = \exp\left(-\frac{d}{\theta_{qu}}\right) \tag{1}$$

where $\rho(d)$ is the correlation coefficient of q_u, d is distance between two points considered and θ_{qu} is the autocorrelation distance of q_u, In this study, the spatial autocorrelation is assumed to be isotopic for simplicity.

The stochastic field in the presence of spatial autocorrelation was generated by covariance matrix decomposition (Griffiths & Fenton 2007) in this study. Covariance matrix decomposition is a direct method of producing a random field with prescribed covariance structure. In this method, a random field vector $\boldsymbol{X}(\boldsymbol{r})$ with the mean value μ is derived as:

$$\boldsymbol{X}(\boldsymbol{r}) = \boldsymbol{\mu} + \boldsymbol{L} \cdot \boldsymbol{u}(\boldsymbol{r}) \tag{2}$$

where $\boldsymbol{L}$ is the lower triangular matrix of covariance matrix $\boldsymbol{\Sigma}$, $\boldsymbol{\mu}$ is a vector consisting of μ and $\boldsymbol{u}(\boldsymbol{r})$ is a white noise vector with a standard normal distribution. $\boldsymbol{\Sigma}$ consists of $\rho(d)$ calculated from d by Eq. (1). $\boldsymbol{L}$ satisfies

$$\boldsymbol{L}\boldsymbol{L}^T = \boldsymbol{\Sigma}. \tag{3}$$

$\boldsymbol{L}$ is obtained using Cholesky decomposition.

Using the Box-Muller method (Fushimi 1992), the normal random numbers (white noise with the standard normal distribution) were calculated from uniform random numbers generated by the M-sequences method (Fushimi 1992). The random fields with $\mu = 0$ were generated by adopting the aforementioned method. 50 realizations of the Monte Carlo process were performed for several autocorrelation distances (θ_{qu} = 0.2, 0.5, 1.0 and 2.0 m). The number of realizations is not large in this study. However, since the three-dimensional nonlinear analysis is very time consuming, the number of realizations selected was considered sufficient to investigate the effects of the column height on the compression behavior of cement-treated soil columns with spatial variability. The influence of the number of realizations on the calculated probability parameters of the overall strength of cement-treated soil columns with spatial variability was discussed in the previous paper by the author (Namikawa & Koseki 2013).

3 FINITE ELEMENT ANALYSIS

3.1 *Numerical condition*

Three-dimensional finite element analyses were performed using the finite element program developed by Shiomi et al. (1993). The unconfined compression behavior of different size cement-treated soil columns is examined in this study. The finite element meshes for the three different size columns are shown in Figure 1. The samples are modeled as a isolated column of 1 m diameter. The height of sample H is set to be 2, 3 and 4 m.

A mesh consisting of eight-node isoparametric elements was used. The majority of the elements are cubic with a length of 100 mm. The element size corresponds approximately to the standard size of cored samples. Therefore the local average process (Griffiths & Fenton 2007) has not been carried out in the analyses. The boundary condition for a sample of H = 2 m is shown in Figure 2. The boundary conditions at the top and bottom surfaces are smooth. The loading process consists of applying uniform vertical displacement at the upper surface of the sample.

The variable unconfined compressive strength value of each element q_{ui} is given by:

$$q_{ui} = \mu_{qu}(1 + x_i V_c) = \mu_{qu} + x_i \sigma_{qu} \quad (i = 1, \ldots, N_e) \tag{4}$$

where μ_{qu} is the mean of the strength, V_c is the coefficient of variation of q_u, x_i is the random variable and N_e is the number of elements. The value of x_i generated by the method mentioned in the previous section is assigned to each element in the sample in the FE-analysis. The value of mean and standard deviation of x_i are 0 and 1 respectively. Here x_i is classified into the discrete classes whose interval is

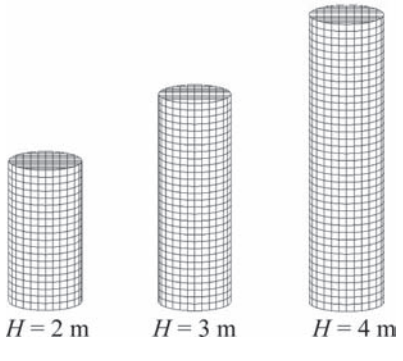

Figure 1. Mesh for three sizes of column.

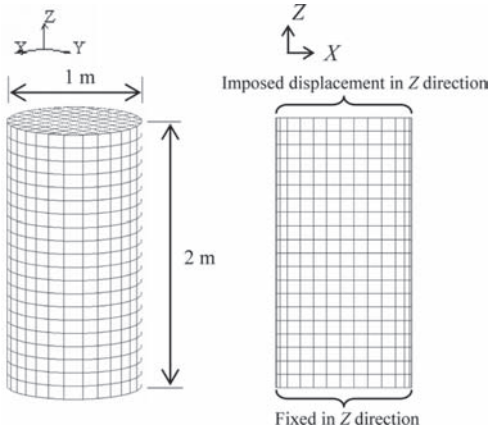

Figure 2. Boundary condition for a sample of $H = 2$ m.

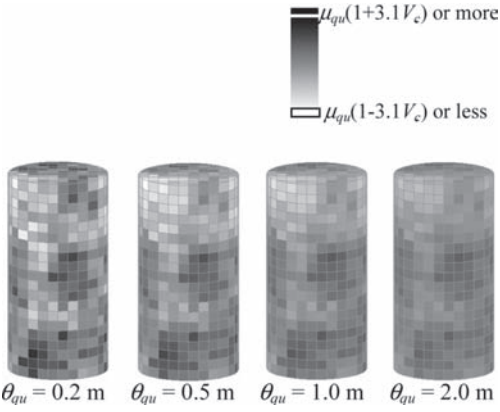

Figure 3. Typical samples for FE-analysis (H = 2 m). The darker regions indicate stronger element.

set to be 0.1. The classified x_i ranges from –3.1 to 3.1, and the value exceeding the upper and lower limits of this range is classified into the highest and lowest classes, respectively.

The mean strength μ_{qu} is held constant at 1.7 MPa and V_c is held constant at 0.3. The autocorrelation distance θ_{qu} is set to be 0.2, 0.5, 1.0 and 2.0 m. Typical samples of H = 2 m are shown in Figure 3. The samples consist of 1760 elements. Dark and light regions depict "strong" and "weak" cement-treated soil, respectively. These spatial distributions of the strength are derived from the same probability distribution, that is to say, the normal distribution with the same parameters. The difference in spatial distribution is brought about by the difference of the autocorrelation distance θ_{qu}. Figure 3 shows that a small value of θ_{qu} provides a rapidly varying field and a large value of θ_{qu} provides a smoothly varying field.

An elasto-plastic model developed for cement-treated soils (Namikawa & Mihira 2007) was used in these analyses. This model can describe appropriately tensile and shear strain-softening behaviors in the strain localization zone after the peak stress state. In this model, the smeared crack band concept (Pietruszczak & Mróz 1981) is used to avoid mesh size dependency due to the strain localization. Thus the FE-analysis with the elasto-plastic model can simulate reasonably the post-peak behavior of cement-treated soils under various boundary conditions. The performance of the used model has been verified by the simulations for several laboratory tests of cement-treated soils (Namikawa & Mihira 2007, Namikawa & Koseki 2007) and an in-situ full scale test of a cement-treated soil column (Namikawa et al. 2008).

A list of elasto-plastic model parameters used in the numerical modeling and their values are shown in Table 1. These parameters for μ_{qu} = 1.7 MPa were determined from the results of various laboratory tests in which cement-treated sand specimens with the unconfined compressive strength of 1.7 MPa were used (Namikawa & Koseki 2006, Namikawa & Mihira 2007). As indicated in Table 1, the elastic modulus E, the cohesion c, the tensile strength T_f, and the fracture energy G_f are regarded as the stochastic parameters. With the constant friction angle ϕ, the value of cohesion c is determined from the value of q_{ui}. The values of E, T_f and G_f are assumed to be proportional to the value of q_{ui}. Other parameters, Poisson's ratio ν, the hardening parameters α and e_y, the softening parameter e_r, the dilatancy coefficient D_c, the localization size t_{s0}, and the characteristics length l_c, are assumed not to vary with q_{ui}. The detailed descriptions of the material parameters and the numerical examples that can illustrate the applicability of this model are available elsewhere (Namikawa & Mihira 2007,

Table 1. Material parameters for FE-analysis.

Elastic modulus E	3000 Mpa	Stochastic
Poisson's ratio ν	0.167	Deterministic
Friction angle ϕ	30 degree	Deterministic
Cohesion c	490 kPa	Stochastic
Tensile strength T_f	380 kPa	Stochastic
Hardening parameter α	1.05	Deterministic
Hardening parameter e_y	0.0002	Deterministic
Fracture energy G_f	9.0 N/m	Stochastic
Softening parameter e_r	0.4	Deterministic
Dilatancy coefficient D_c	–0.4	Deterministic
Localization size t_{s0}	0.6 mm	Deterministic
Characteristics length l_c	100 mm	Deterministic

Namikawa & Koseki 2007, Namikawa & Koseki 2013).

3.2 *Numerical results*

Five realizations of the overall stress-strain relationship obtained from the FE-analysis with MCS are shown in Figure 4 for the case with θ_{qu} = 1.0 m. In these stress-strain relationships, the stress is calculated from the total vertical load at the upper surface and the strain is calculated from the vertical displacement of the upper surface. The stress-strain relationship of the uniform (deterministic) sample with μ_{qu} = 1.7 MPa is also plotted in these figures.

For all the sample heights H, the stress-strain relationships of the samples with θ_{qu} = 1.0 m vary widely before the peak stress state. It is also observed that most of the peak stresses are lower than the peak stress of the uniform sample. It can be seen that the axial strain at the peak stress decreases as H increases. This is because that since the size of the failure region may not depend on H, the axial displacement at the peak stress does not increase as H increases.

The overall strength Q_u is defined as the peak stress in the calculated overall stress-strain relationship in this study. The sample mean of the resulting 50 overall strengths m_{Qu} is shown in Figure 5. It can be seen that m_{Qu} varies with θ_{qu}. For all H, a minimum value of m_{Qu} is observed for θ_{qu} = 0.5 m, implying that a particular value of θ_{qu} which may depend on the sample diameter provide the minimum value of m_{Qu}. Figure 5 also shows that m_{Qu} decreases as H increases for the same θ_{qu} value. Since the possibility that the sample involves weak regions increases with the sample volume, larger values of H could lead to smaller values of m_{Qu}.

The sample standard deviation of the resulting 50 overall strengths s_{Qu} is shown in Figure 6. s_{Qu} is observed to be positively correlated with θ_{qu} for all H.

This is because, as θ_{qu} tends to become large, the field of strength tends to become uniform in a sample and the difference in m_{Qu} between the samples becomes large. From a theoretical point of view, it could be speculated that, as θ_{qu} becomes infinite, s_{Qu} returns to the σ_{qu} set for the elements. Moreover s_{Qu} decreases as H increases for the same θ_{qu} value, indicating that the standard deviation of Q_u

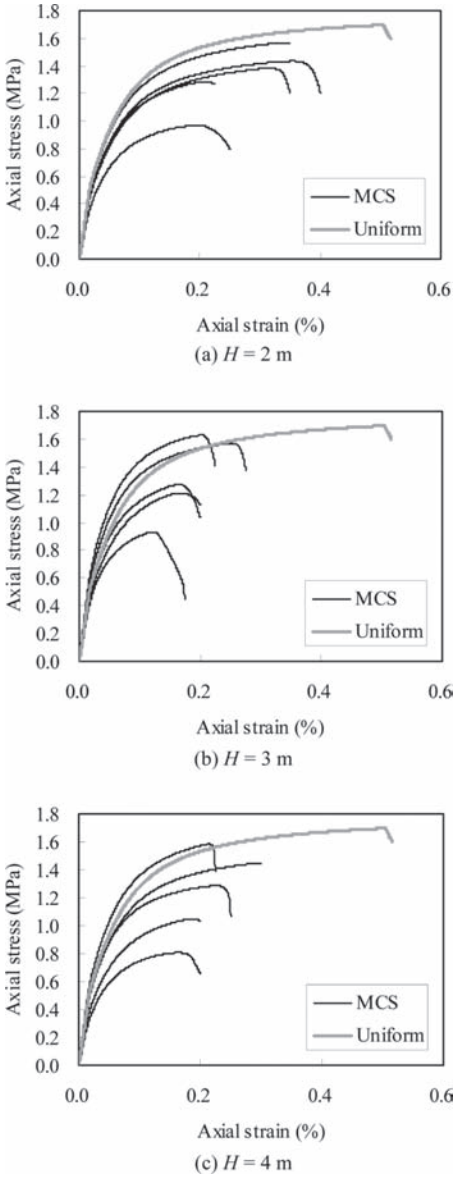

Figure 4. Typical stress-strain relationships of realizations (θ_{qu} = 1 m).

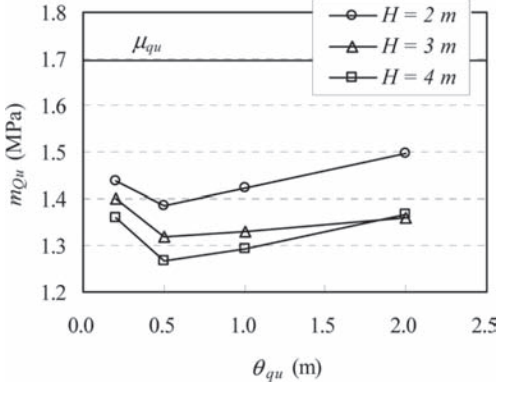

Figure 5. Sample mean of overall strength m_{Qu}.

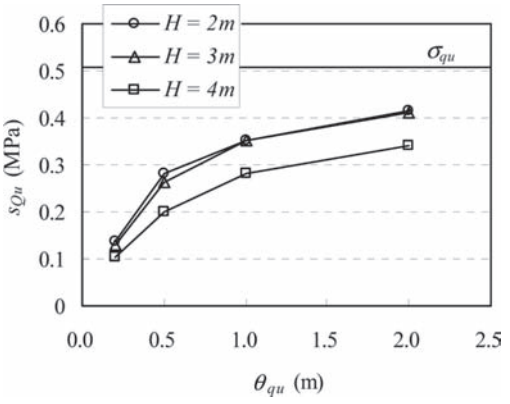

Figure 6. Sample standard deviation of overall strength s_{Qu}.

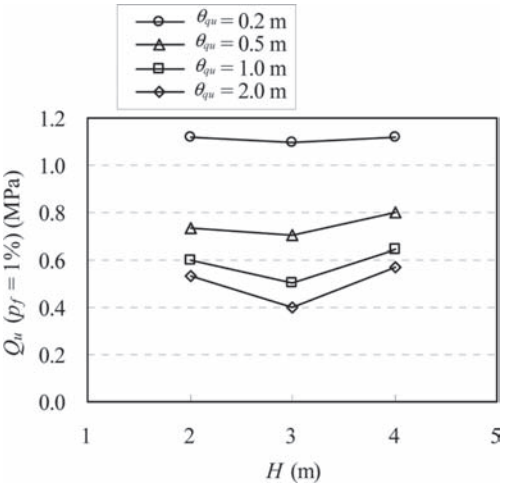

Figure 7. Overall strength for a 1% probability of failure $Q_u(p_f = 1\%)$.

depends on the volume of sample. The standard deviation of the mean strength of the elements composing the sample decreases with increasing the number of elements N_e. Since N_e is proportional to H, smaller values of s_{Qu} are obtained for larger values of H.

3.3 *Probability of failure*

In a design procedure, it is important to evaluate the probability of failure p_f of a cement-treated soil column. The type of the probability distribution of Q_u is required to evaluate p_f. Namikawa (2012) investigated the probability distribution of Q_u calculated from the FE-analysis with MCS. That study indicates that the probability distribution of Q_u corresponds to the underlying distribution of q_{ui}. Therefore, assuming the normal distribution as a reasonable fit to the probability distribution of the computed Q_u, p_f defined as occurring when exceeds a specific strength is calculated based on the computed m_{Qu} and s_{Qu}. The ISO 2394 requires $p_f = 1\%$ for some consequence of a failure and moderate relative costs of safety measures. Here the overall strength $Q_u(p_f = 1\%)$ for a 1% probability of failure is evaluated based on the computed m_{Qu} and s_{Qu}.

The evaluated $Q_u(p_f = 1\%)$ is shown in Figure 7. For all H, $Q_u(p_f = 1\%)$ deceases significantly as θ_{qu} increases. Since s_{Qu} increases as θ_{qu} increases (see Fig. 6), the low variability leads to the high value of $Q_u(p_f = 1\%)$ for the low value of θ_{qu}. Moreover, for the same reason, the value of $Q_u(p_f = 1\%)$ for $H = 4$ m is larger than those for $H = 2$ m and 3 m. For all θ_{qu}, the minimum values of $Q_u(p_f = 1\%)$ are observed when $H = 3$ m. However $Q_u(p_f = 1\%)$ is not very sensitive to H, indicating that the numerical results for the sample of $H = 2$ m or 3 m could be used to evaluate the overall strength of longer columns.

4 CONCLUSIONS

The finite element analyses with Monte Carlo Simulations (MCS) were performed to simulate the unconfined compression behavior of the columns with different heights. The simulations with the samples in the presence of different degrees of spatial autocorrelation indicate that the sample mean of the resulting 50 overall strengths m_{Qu} varies with θ_{qu}. For all the height of sample H, a minimum value of m_{Qu} is observed for $\theta_{qu} = 0.5$ m. The sample standard deviation of the resulting 50 overall strengths s_{Qu} is observed to decreases as H increases. The overall strength $Q_u(p_f = 1\%)$ for a 1% probability of failure is evaluated based on m_{Qu} and s_{Qu}. The sample height does not affect significantly $Q_u(p_f = 1\%)$, indicating that the numerical results for the sample of $H = 2$ m or 3 m could be used to evaluate the overall strength of longer columns.

ACKNOWLEDGMENTS

The author is grateful to Takenaka Corporation for their cooperation in the numerical analysis. The author acknowledges the support of the Ministry of Science and Education of Japan (Grant No. 22560505).

REFERENCES

CDIT (Costal development Institute of Technology). 2002. The deep mixing method: principle, design and construction. Balkema: Tokyo.

Fushimi, M. 1992. Analysis of Scientific Data (Basic Statistics 3), Chapter 11. Statistics Section, Department of Social Science, College of Arts and Science, University of Tokyo. University of Tokyo Press: 307–332. (in Japanese).

Griffiths, D.V. & Fenton G.A. 2007. Probabilistic methods in geotechnical engineering. Springer Wien. New York.

International Organization for Standardization. 1998. General principle on reliability for structures (ISO2394).

Matsuo, O. 2002. Determination of design parameters for deep mixing. *Tokyo Workshop 2002 on Deep Mixing*: 75–79.

Namikawa, T. 2012. Numerical study of compression behavior of cement-treated columns with strength fields following normal and lognormal distributions. *Ground Improvement and Ground Control* 2: 1193–1200.

Namikawa, T. & Koseki, J. 2007. Evaluation of tensile strength of cement-treated sand based on several types of laboratory tests. *Soils and Foundations* 47(4): 657–674.

Namikawa, T. & Koseki, J. 2013. Effects spatial correlation on compression behavior of cement-treated column. *Journal of Geotechnical and Geoenvironmental Engineering ASCE* 139(8): 1346–1359.

Namikawa, T, Koseki, K. & Suzuki, Y. 2008. Finite element analysis of a full scale bending test of cement treated soil column. *12th International Conference of the International Association for Computer Methods and Advances in Geomechanics*: 3635–3641.

Namikawa, T. & Mihira, S. 2007. Elasto-plastic model for cement-treated sand. *International Journal for Numerical and Analytical Methods in Geomechanics* 31(1): 71–107.

Pietruszczak, S.T. & Mróz, Z. 1981. Finite element analysis of deformation of strain-softening materials. *International Journal for Numerical Methods in Engineering* 17: 327–334.

Shiomi, T., Shigeno, Y. & Zienkiewicz, O.C. 1993. Numerical prediction for model No.1. Arulanandan & Scott (ed.) *Verifications of Numerical Procedures for the Analysis of Soil Liquefaction Problems*. Balkema: 213–219.

Geotechnical Safety and Risk IV – Zhang et al. (eds)
© 2014 Taylor & Francis Group, London, ISBN 978-1-138-00163-3

Stochastic finite element analysis for ground improvement by vertical drains of spatially variable soils

M. Wasiul Bari
Department of Civil Engineering, Curtin University, Perth, WA, Australia

M.A. Shams
Housing and Building Research Center, Cairo, Egypt

M.A. Shahin
Department of Civil Engineering, Curtin University, Perth, WA, Australia

ABSTRACT: A stochastic approach that investigates the effects of soil spatial variability on stabilization of soft clay via Prefabricated Vertical Drains (PVDs) is presented and discussed. The approach integrates the local average subdivision of random field theory with the Monte Carlo finite element technique. A special feature of the current study is the investigation of impact of spatial variability of soil permeability and volume compressibility in the smear zone as compared to that of the undisturbed zone, in conjunction with uncoupled 3D finite element analysis. The results of this study indicate that the spatial variability of soil properties has a significant impact on soil consolidation by PVDs; however, it is also found that the spatial variability of soil properties in the smear zone has a dominating impact on soil consolidation by PVDs over that of the undisturbed zone.

1 INTRODUCTION

Soils are highly variable from one point to another in the ground. This inherent variation of soils with respect to spatial location is known as *soil spatial variability* and is due to the uneven soil micro fabric, complex characteristics of geological deposition and stress history. Despite the fact that the impact of spatial variation of soil properties on soil consolidation has long been recognized by many researchers (e.g., Pyrah 1996; Rowe 1972), the design of soil consolidation via Prefabricated Vertical Drains (PVDs) has been traditionally carried out deterministically and thus can be misleading due to the ignorance of the uncertainty associated with the inherent spatial variation of soil properties. In general, acknowledging and quantifying the soil spatial variability in geotechnical engineering has been usually considered using probabilistic modeling techniques that treat the soil properties as random variables resulting in more realistic solutions. Unlike deterministic analyses, which are based on single best estimate (average or characteristic) values of soil properties, the probabilistic analyses explicitly take into account the variable nature of soil properties, based on their statistical characteristics.

The formulation and solution of stochastic problems are often very complicated. The review of relevant literature has indicated that although the significance of soil spatial variability in relation to ground improvement by PVDs has long been realized, little research has been made in this area. However, given the analytical and numerical complexity of the problem, available research into the consolidation of highly variable soils has been limited to the following two categories: (i) one-dimensional consolidation of vertical drainage, i.e., no PVDs, for either 1D or 2D geometries (e.g., Badaoui et al. 2007; Freeze 1977; Huang et al. 2010; Hwang & Witczak 1984); and (ii) soil consolidation by PVDs considering only the variability due to the testing errors in measuring the soil properties, while the inherent spatial variability of soil properties has not been taken into account (e.g., Hong & Shang 1998; Zhou et al. 1999). More recently, preliminary studies have been carried out by the authors (e.g., Bari et al. 2012a, b; Shahin & Bari 2012) on soil spatial variability for consolidation of soft clays by PVDs and have shown valuable insights into the impact of soil spatial variability on soil consolidation and enhanced conceptual understanding about the soil consolidation problem. However, the above mentioned works have notable limitation of either ignoring

the smear effect or considering smear effect with reference to permeability changes alone and volume compressibility have been ignored. It has to be noted that, the smear effect that develops as a consequence of mandrel installation not only reduces soil permeability, k, but also increases soil volume compressibility, m_v. The combined effect of reduced permeability and increased volume compressibility within the smear zone brings different behavior from that of the undisturbed soil. Hence, for more accurate prediction of the behavior of stabilized soil with PVDs, the changes of both k and m_v in the smear zone as well as undisturbed zone need to be considered. However, due to the non-uniform spatial distribution of soil disturbance (which decreases with the increase of distance from the center of the drain), the variability characteristics of the smeared soil may be significantly different from those of undisturbed soil. In addition, as expelled water must pass through the smear zone, the implication of variability parameters in this zone on the overall consolidation behavior may be different from that of the variability parameters in the undisturbed zone. In this paper, a parametric study is carried out to investigate the relative significance of the spatial variability of soil properties in the smear zone over undisturbed zone, where the coefficient of permeability, k, and coefficient of volume compressibility, m_v, are separately treated as random variables.

2 STOCHASTIC MODELLING OF SOIL CONSOLIDATION BY PVDS

Among several methods of modeling stochastic problems, the use of deterministic finite element analysis with random input soil parameters in a Monte Carlo framework has gained much popularity in recent years (Elkateb et al. 2003). Similar approach is adopted in the present work to investigate the effects of soil spatial variability on the behavior of soil consolidation by PVDs. The approach merges the Local Average Subdivision (LAS) method (to generate random permeability fields) and finite element modeling (to calculate soil consolidation by PVDs) into a Monte Carlo framework. For a certain problem of ground improvement by PVDs, the proposed approach can be applied using the following steps:

1. Create a virtual soil profile for the problem in hand which comprises a grid of elements that is assigned random values of soil properties different from one element to another across the grid. The virtual soil profile allows arbitrary distributions of soil properties to be realistically and economically modeled according to their statistical characteristics;
2. Incorporate the generated soil profile into a finite element modeling scheme of soil consolidation by PVDs; and
3. Repeat Steps 1 and 2 many times using the Monte Carlo technique so that a series of consolidation responses can be obtained from which the statistical distribution parameters and probability of achieving a target degree of consolidation can be estimated and analyzed.

Details of the steps used, as well as the numerical procedures, are described below.

2.1 *Generation of virtual soil profiles*

As mentioned earlier, k and m_v are considered to be random variables in the present study and are characterized in terms of their Probability Density Function (PDF) i.e., the mean, μ, standard deviation, σ (the standard deviation can also be represented by variance, σ^2, or coefficient of variation, υ, where, $\upsilon = \sigma/\mu$), and correlation length, θ. It should be noted that the spatial variation of soil properties is not entirely random and spatial dependencies also exist (Fenton & Vanmarcke 1990; Jaksa et al. 1997; Vanmarcke 1977). That is, a soil property at two separate spatial locations could be similar or otherwise, depending on the distance they are located apart and this is known as spatial correlation. Vanmarcke (1977) pointed out that adequate characterization of spatially variable soil properties requires consideration (incorporation) of such spatial correlation. The mean and standard deviation are the point statistical measures with no consideration of the spatial correlation structure of soil properties. Therefore, the correlation length, θ (also known as Scale of Fluctuation, SOF), is introduced as an additional statistic to consider the spatial correlation of soil properties. Generally speaking, a large value of θ indicates smooth spatial variation of soil property of interest, whereas a small value of θ implies erratic variation. In this study, the variability of both k and m_v is characterized by following a lognormal distribution and assumed as 3D random fields. In selecting the probability distribution of k and m_v, the authors reviewed a broad range of literature (e.g., Badaoui et al. 2007; Freeze 1977; Huang et al. 2010) and concluded that it is reasonable to assume lognormal probability distribution for both k and m_v. Since the same approach is used to generate random field of both k and m_v, only the procedure to generate the random field of k is summarized herein.

In the process of simulating the lognormally distributed random field of k, correlated local averages standard normal random field $G(x)$ are first generated with zero mean, unit variance and

a spatial correlation function using 3D LAS technique (Fenton & Vanmarcke 1990). The correlation coefficient between k measured at a point x_1 and a second point x_2 is specified by a correlation function, $\rho(\tau)$, where $\tau = |x_1 - x_2|$ is the absolute distance between the two points. An isotropic (i.e., the spatial correlation lengths in the horizontal and vertical directions are taken to be equal) exponentially decaying (Markovian) spatial correlation function is used in the current study, as follows (Fenton & Griffiths 2008):

$$\rho(\tau) = \exp\left(-\frac{2|\tau|}{\theta_k}\right) \quad (1)$$

It should be noted that the spatial correlation function in Equation 1 is assumed to be statistically isotropic, i.e., the scales of fluctuation in the horizontal (x), normal to the plane of paper (y) and vertical directions (z) are assumed to be the same (i.e., $\theta_x = \theta_y = \theta_z = \theta$). Although the correlation structures in any spatial direction are usually different (i.e., anisotropic), the reason for assuming an isotropic correlation structure for both k_h and m_v is because the scale of fluctuation is a difficult parameter to estimate in practice and assuming an isotropic condition with smaller scale of fluctuation will provide slightly conservative results (Fenton & Griffiths 2008). It is worthy to note that the spatial correlation length is estimated with respect to the underlying normally distributed random field.

Since k is assumed to be characterized statistically by a lognormal distribution, the correlated standard normal random field, $G(x)$, generated using the LAS method is then transformed into a lognormal distribution by the following transformation function (Fenton & Griffiths 2008):

$$k_i = \exp\left\{\mu_{\ln k} + \sigma_{\ln k} G(i)\right\} \quad (2)$$

where: $G(i)$ and X_i are, respectively, the local (arithmetic) average of a standard Gaussian random field $G(x)$ over the domain of the i'th element and the soil property value assigned to that element; $\mu_{\ln k}$ and $\sigma_{\ln k}$ are the mean and standard deviation of the underlying normal distribution; $\mu_{\ln k}$ and $\sigma_{\ln k}$ are obtained from the specified permeability μ_k and σ_k using the following lognormal distribution transformation functions (Fenton & Griffiths 2008):

$$\mu_{\ln k} = \ln \mu_k - \frac{1}{2}\sigma^2_{\ln k} \quad (3)$$

$$\sigma_{\ln k} = \sqrt{\ln\left(1 + \frac{\sigma_k^2}{\mu_k^2}\right)} = \sqrt{\ln\left(1 + \upsilon_k^2\right)} \quad (4)$$

where: $\upsilon_k = \sigma_k/\mu_k$ is the permeability Coefficient of Variation (COV). It should be noted that the random fields of both k and m_v are generated using the 3D free access LAS computer code available online at *http://www.engmath.dal.ca/rfem/*.

2.2 *Finite-element modeling incorporating soil spatial variability*

With the complete subsurface profile having been simulated in the previous step, the spatial variability of k and m_v is now known and can be employed as input in a Finite Element (FE) consolidation modeling of soil improvement by PVDs. In this study, all numerical analyses are carried out using a modified version of the finite element computer program "p86" from the book by Smith & Griffiths (2004) in which soil consolidation is treated as a 3D uncoupled (i.e., no displacement degrees of freedom only pore pressure degrees of freedom) problem. Originally program "p86" was for general two (plane) or three dimensional analyses of the uncoupled consolidation equation using implicit time integration with the "theta" method. The authors modified the source code of "p86" to allow for input of the volume compressibility, axisymmetric and repetitive Monte-Carlo analyses. Since a single-drain analysis is often enough to investigate the soil consolidation behavior, the effect of soil spatial variability is examined using a unit cell of soil around a single drain. The consolidation problem considered in this study implies a unit cell (axisymmetric) of actual 3D geometry of PVD system (see Fig. 1a): $L = 1.0$ m, $r_e = 0.8463$ m, $r_s = 0.2821$ m and $r_w = 0.0637$ m, where L is the maximum vertical drainage distance; r_e is the radius of equivalent soil cylinder with impermeable perimeter or the radius of zone of influence; and r_w is the equivalent radius of the drain. However for the finite-element analyses, the circular influence area of the cylindrical unit cell is transformed into an equivalent square influence area of side length S, such that $S = \sqrt{\pi} r_e^2$ (i.e., $S = 1.5$ m). The selection of square influence area instead of the equivalent circular influence area is to avoid the unfavorable mesh shape as the LAS method requires square (or rectangular) elements to accurately compute locally averaged values of k_h and m_v for each element across the grid. For the same reason, square shaped smear zone of side length $S_s = \sqrt{\pi} r_s^2$ and PVD of side length $S_w = \pi r_w/2$ are employed. It should be noted that, for simplicity, the well resistance factor which may affect the rate of consolidation is not considered in the FE analysis. This is due to the fact that the discharge capacities of most PVDs available in the market are relatively high, and hence the well resistance effect can be ignored in most practical cases (Abuel-Naga et al. 2012; Chu 2004).

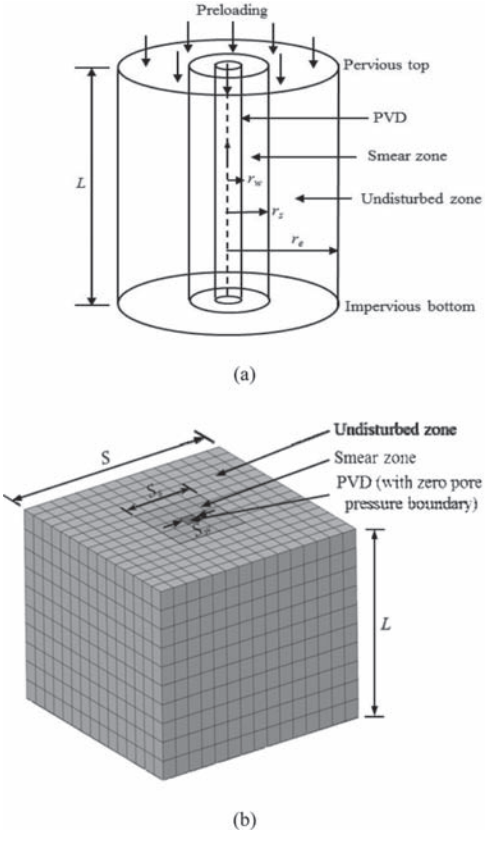

Figure 1. Schematic diagram of soil consolidation with prefabricated vertical drain: (a) cylindrical unit cell; (b) equivalent square geometry with FE mesh discretization.

In soil stabilization by PVDs, soil consolidation takes place by combined vertical and horizontal (radial) drainage of water. However, in practical sense, soil consolidation due to vertical drainage is insignificant (due to large drainage length and lower permeability in the vertical direction) compared to that of the horizontal drainage, thus, only the component of the overall consolidation resulted from horizontal drainage is considered to be random in the current study. To simulate such condition, the permeability in the vertical (z) direction, k_z is set as to zero in the FE analysis. Since the permeability variance of even one of the directions is rarely known with any accuracy, the two components of the horizontal permeability (i.e., k_x and k_y) are assumed as isotropic (i.e., $k_x = k_y$). In order to take the smear effect into consideration, two independent random fields of both k and m_v are generated separately (one for the smear zone and another for the undisturbed zone) employing the specified statistical parameters (μ, σ and θ) of each zone. Both random fields are then mapped onto the corresponding grid in the finite element mesh. As the accuracy of the finite element analysis is dependent on the mesh density, a sensitivity analysis for the problem under consideration is carried out for both the deterministic and stochastic solutions on various mesh dimensions to ensure reasonable refinement with minimal discretization error. The sensitivity analysis indicated that a mesh with element size of 0.1 m × 0.1 m × 0.1 m gives reasonable precision. Therefore, it was decided to discretize the soil domain into a mesh with an element size of 0.1 m × 0.1 m × 0.1 m (see Fig. 1b). The 3D mesh consists of 2250 eight node first order hexahedral elements.

To simulate reduced permeability condition in the smear zone during the FE analysis, the mean values of k in the undisturbed and smear zones are taken to be equal to $\mu_{k_u} = 0.03$ m/year and $\mu_{k_s} = 0.015$ m/year, respectively, which means that $\mu_{k_u}/\mu_{k_s} = 2.0$. Walker (2006) indicates that the value of the smear zone compressibility could increase by about 20% from that of the undisturbed zone. Therefore, to consider increased compressibility condition in the smear zone, the mean value of m_v in the undisturbed and smear zones are taken to be equal to $\mu_{m_{v_u}} = 8.0 \times 10^{-4}$ m^2/kN and $\mu_{m_{v_s}} = 9.6 \times 10^{-4}$ m^2/kN, respectively, which means that $\mu_{m_{v_s}}/\mu_{m_{v_s}} = 1.2$. The effect of spatially variable of k and m_v on the stochastic behavior of soil consolidation by PVDs is investigated over a range of different combinations of standard deviation, σ, and scale of fluctuation, θ. It should be noted that σ is presented herein in a normalized form as υ (i.e., coefficient of variation). The following values of υ and θ are considered for the parametric study presented in this paper:

- υ_k (%) (for both smear and undisturbed zones) = 50, 100, 200;
- υ_{m_v} (%) (for both smear and undisturbed zones) = 10, 20, 30 and
- θ (m) (for both k and m_v, and smear and undisturbed zones) = 0.25, 0.5, 1.0.

It can be noticed that, the selected range of COV of m_v is much less than that of the range selected for COV of k. This is due to the fact that soil permeability is considered to be the most significant spatially random soil property affecting soil consolidation with high COV of up to 300%, while m_v can possess a spatial variability of up to 30% (e.g., Beacher & Christian 2003; Kulhawy et al. 1991; Lee et al. 1983). However, the range of θ is assumed to be the same for both k and m_v. This assumption is reasonable because, if one thinks that the spatial correlation structure of a soil is caused by changes in the constitutive nature of the soil over

the ground, then both k and m_v would have similar correlation lengths. Since little is currently known about the typical COVs and SOFs of soils in the smear zone, the same range of υ and θ are selected for both smear and undisturbed zones. It should be noted that no cross-correlation between k and m_v is assumed in this study and this is left for future refinement. In order to identify the statistical parameters in the smear and undisturbed zones, υ and θ of k and m_v are denoted with appropriate subscripts "s" and "u" depending on whether they are specified for smear zone or undisturbed zone, where s refers to the smear zone while u refers to undisturbed zone. An initial pore water pressure of 100 kPa dissipates in a single drain is considered in all FE analyses. A single generation of a random field and the subsequent finite-element analysis of that field are termed "realization". For an individual realization, the degree of consolidation, $U(t)$, at any certain consolidation time, t, is calculated with the help of the following expression:

$$U(t) = 1 - \frac{\bar{u}(t)}{u_0} \tag{5}$$

where: u_0 = initial pore pressure; and $\bar{u}(t)$ = average pore pressures at any time of the consolidation process. It has to be emphasized that $\bar{u}(t)$ of the consolidation process is calculated by numerically integrating the pore pressure across the volume of each element at a particular time, summing the contribution of each element and dividing by the total mesh volume (element volume are also calculated by numerical integration).

2.3 *Repetition of process based on the Monte Carlo technique*

Following the procedures of the Monte Carlo technique, the process of generating random fields of k_h and m_v and performing the finite element analysis is repeated numerous times. The accuracy of the estimated statistics of the output quantities of interest is dependent on the number of realizations required in the Monte Carlo procedures. Therefore, to maintain accuracy and run time efficiency, the sensitivity of results to the number of Monte Carlo simulations is examined. The sensitivity analysis indicated that 2000 realizations are sufficient to give reasonably stable output statistics for each analysis of interest. Based on this observation, the process of generating a random field of both k and m_v and the subsequent finite element analysis is repeated 2000 times. Huang et al. (2010) also performed successful probabilistic analysis on soil consolidation using 2000 simulations. Although each k and m_v field realizations out of the 2000 realizations is generated with the same mean, standard deviation and scale of fluctuation, the spatial distribution of k and m_v varies from one realization to the next. The above repetitive process is performed for each combination of υ and θ. The obtained outputs from the suite of 2000 realizations of the Monte Carlo simulation are collated and statistically analyzed to produce estimates of the mean and standard deviation of the degree of consolidation. In this study, at any given time t, the mean of the degree of consolidation based on the excess pore water pressure, μ_U, is estimated by utilizing the geometric average (considered as the representative mean) of $\bar{u}(t)$, as follows:

$$\mu_U = 1 - \exp\left[\frac{1}{n_{sim}}\sum_{i=1}^{n_{sim}} \ln\left(\frac{\bar{u}(t)}{u_0}\right)_i\right] \tag{6}$$

The standard deviation of the average degree of consolidation at any time t defined by the pore water pressure, σ_U, is estimated as follows:

$$\sigma_U = \sqrt{\frac{1}{n_{sim}-1}\sum_{i=1}^{n_{sim}}\left[\left(U(t)\right)_i - \mu_U\right]^2} \tag{7}$$

where: n_{sim} is the number of Monte Carlo simulations; $(\bar{u}(t)/u_0)_i$ and $(U(t))_i$ are, respectively, the ratio of the average excess pore pressure to the initial excess pore water pressure and the degree of consolidation at any time t for the ith simulation (see Eq. 5). The use of the geometric average of $\bar{u}(t)$ in computing μ_U is due to the fact that, in a 2D or 3D space, compared to the 1D space, the flow of water has more freedom to avoid low permeability zones by detouring around them and therefore, the geometric average may be a better estimator (e.g., Dagan 1989) for computing the representative mean of the average excess pore water pressures. For the same reason, Huang et al. (2010) also used geometric average in determining equivalent coefficient of consolidation for a 2D system.

3 PROBABILISTIC INTERPRETATION

The estimation of the probability that a deterministic degree of consolidation overestimates the true consolidation value is one of the main objectives of the stochastic consolidation analyses. Such probability can be represented either by the probability of achieving a target degree of consolidation, U_s, (i.e., $P[U(t_s) \geq U_s(t_s)]$) at any specified consolidation time, t_s, or the probability of required time t to achieve U_s that is less than or equal to t_s (i.e., $P[t(U_s) \leq t_s(U_s)]$). In this study, the later process is

employed, i.e., $P[t(U_s) \le t_s(U_s)]$ is estimated. This is because determining probability from a set of data requires establishment of a reasonable probability distribution for the data set. However, the obtained fit using the raw data of $U(t_s)$ was typically poor while the distribution of $t(U_s)$ obtained from the suite of the 2000 realizations is reasonably fitted with lognormal distribution and gives sufficiently reasonable approximation to the $P[t(U_s) \le t_s(U_s)]$. The legitimacy of the lognormal distribution hypothesis for $t(U_s)$ is examined by the well-known Chi-square test through the frequency density plot of $t(U_s)$ data obtained from the 2000 realizations and a fitted lognormal distribution is superimposed. This process is performed for many combinations of υ and θ at several different U_s. For each of the cases considered, the goodness-of-fit p-value is found to be high enough to approve the rationality of the lognormal distribution hypothesis of simulated $t(U_s)$ data. Figure 2 illustrates a typical example of the histogram of $t(U_s)$ for the case of $\upsilon_{k_u} = 50\%$, $\upsilon_{k_s} = 200\%$, $\upsilon_{m_{v_u}} = 10\%$, $\upsilon_{m_{v_s}} = 30\%$, $\theta_{k_u} = \theta_{k_s} = \theta_{m_{v_u}} = \theta_{m_{v_u}} = 0.5$ at $U_s = 90\%$, along with their fitted lognormal distributions. The goodness-of-fit test yielded p-value of 0.4, indicating strong agreement between the histogram and the fitted distribution. Therefore, the lognormal distribution is certainly an appropriate assumption to the distribution of the simulated $t(U_s)$ data.

By accepting the lognormal distribution for t at any given U_s, the statistical moments $\mu_{t(U_s)}$ and $\sigma_{t(U_s)}$ that are representing the mean and standard deviation of the lognormally distributed t that achieves U_s are calculated from the suite of 2000 realizations using the following transformation functions:

$$\mu_{t(U_s)} = \frac{1}{n_{sim}} \sum_{i=1}^{n_{sim}} t_i(U_s) \tag{8}$$

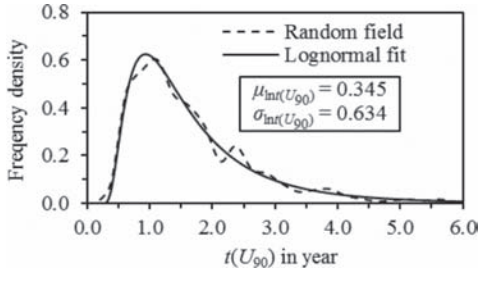

Figure 2. Typical example of frequency density histogram of simulated $t(U_{90})$ with fitted lognormal distribution for $\upsilon_{k_u} = 50\%$, $\upsilon_{k_s} = 200\%$, $\upsilon_{m_{v_u}} = 10\%$, $\upsilon_{m_{v_s}} = 30\%$, $\theta_{k_u} = \theta_{k_s} = \theta_{m_{v_u}} = \theta_{m_{v_s}} = 0.5$.

$$\sigma_{t(U_s)} = \sqrt{\frac{1}{n_{sim} - 1} \sum_{i=1}^{n_{sim}} [t_i(U_s) - \mu_{t(U_s)}]^2} \tag{9}$$

where: $t_i(U_s)$ is the t from the i'th realization (i = 1, 2, 3, …, n_{sim}) at given U_s and n_{sim} = total number of realizations = 2000. As 90% consolidation is usually acceptable for the purpose of design of any soil improvement project (Bo et al. 2003), in this study, it is assumed that the target degree of consolidation is 90% and for convenience, it is simply denoted as U_{90}. The probability that t is less than or equal to t_s that achieves U_{90} can then be obtained from the following lognormal probability distribution transformation:

$$P\left[t(U_{90}) \le t_s(U_{90})\right] = \Phi\left(\frac{\ln t_s - \mu_{\ln t(U_{90})}}{\sigma_{\ln t(U_{90})}}\right) \tag{10}$$

where: P [.] is the probability of its argument; Φ(.) is the standard normal cumulative distribution function; $\mu_{\ln t(U_s)}$ and $\sigma_{\ln t(U_s)}$ are, respectively, the mean and standard deviation of the underlying normally distributed ln $t(U_s)$ and can be estimated from $\mu_{t(U_s)}$ and $\sigma_{t(U_s)}$ with reference to Equations 3 and 4, as follows:

$$\mu_{\ln t(U_s)} = \ln \mu_{t(U_s)} - \frac{1}{2}\sigma^2_{\ln t(U_s)} \tag{11}$$

$$\sigma_{\ln t(U_s)} = \sqrt{\ln\left(1 + \frac{\sigma^2_{t(U_s)}}{\mu^2_{t(U_s)}}\right)} \tag{12}$$

Following the procedure set out above, probabilities of required time t to achieve U_s that is less than or equal to t_s can be estimated for any combination of υ and θ, and the stochastic behavior of soil consolidation by PVDs can be investigated.

4 RESULTS AND DISCUSSION

In order to investigate the relative significance of the spatially variability of the smear zone over the undisturbed zone, a series of 3D consolidation analyses are performed. The sensitivity of the statistics of the degree of consolidation and the probability of required time t to achieve U_s that is less than or equal to t_s to the statistically defined input data (i.e., υ and θ) in relation to both k and m_v is examined. For each selected set of υ and θ, 2000 Monte Carlo simulations are performed. The obtained consolidation responses are then statistically analyzed to estimate μ_U, σ_U and $P[t(U_{90}) \le t_s(U_{90})]$ using the excess pore water pressure. Since the general trends

of μ_U, σ_U and $P[t(U_{90}) \le t_s(U_{90})]$ remain unaltered over the specified range of υ and θ, only the results of a few of the tests conducted are presented in Figures 3–8, which are believed to be sufficient to demonstrate the main features of the influence of spatial variability of k and m_v on soil consolidation by PVDs. In Figures 3–8, μ_U, σ_U and $P[t(U_{90}) \le t_s(U_{90})]$ are expressed as a function of time t. Prior to placing the stochastic analyses into context, an initial deterministic solution has been performed assuming a homogeneous soil. It should be noted that the deterministic solution of this case yields

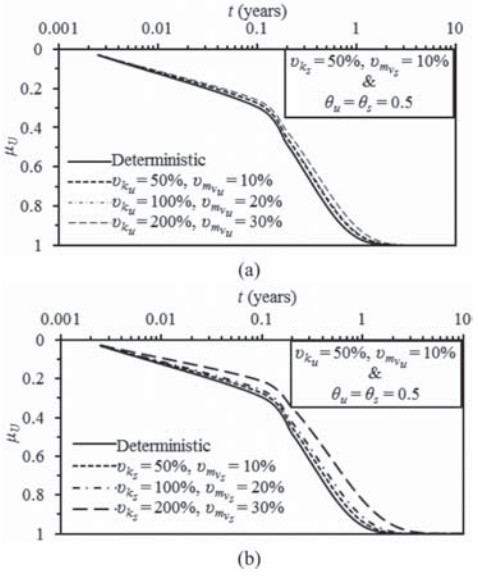

Figure 3. Effect of υ_u and υ_s on μ_U for $\theta_u = \theta_s = 0.5$.

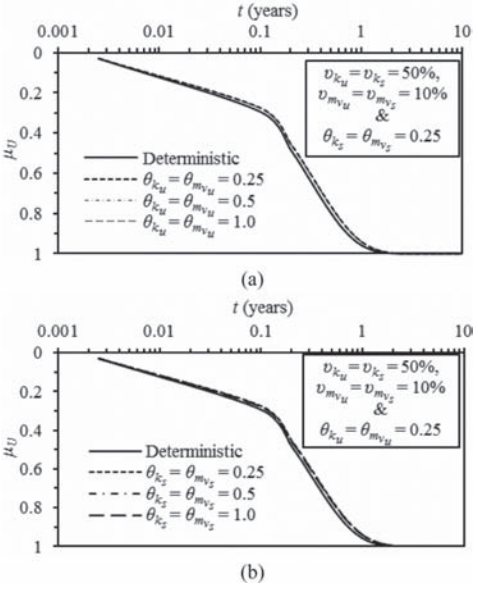

Figure 4. Effect of θ_u and θ_s on μ_U for $\upsilon_{k_u} = \upsilon_{k_s} = 50\%$ and $\upsilon_{m_{v_u}} = \upsilon_{m_{v_s}} = 10\%$.

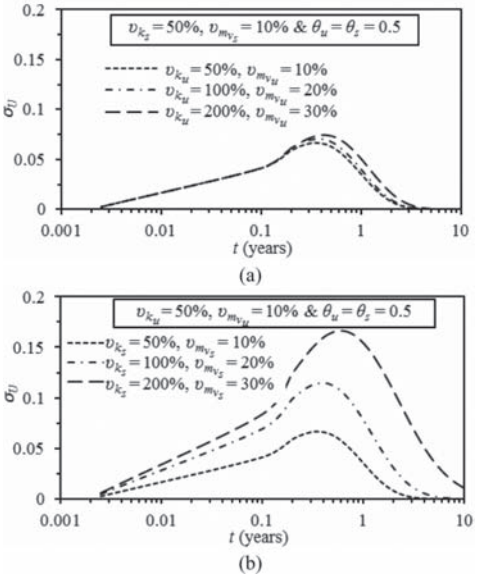

Figure 5. Effect of υ_u and υ_s on σ_U for $\theta_u = \theta_s = 0.5$.

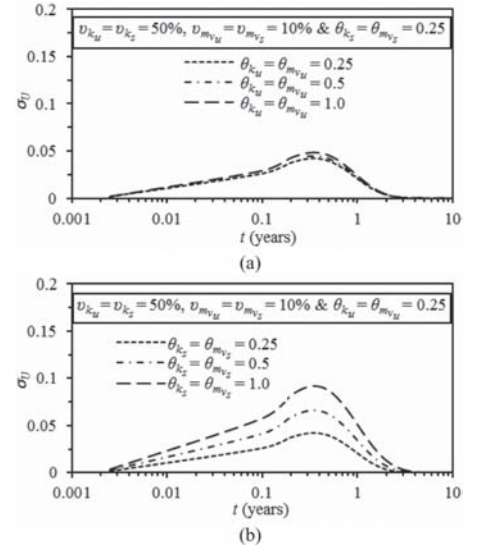

Figure 6. Effect of θ_u and θ_s on σ_U for $\upsilon_{k_u} = \upsilon_{k_s} = 50\%$ and $\upsilon_{m_{v_u}} = \upsilon_{m_{v_s}} = 10\%$.

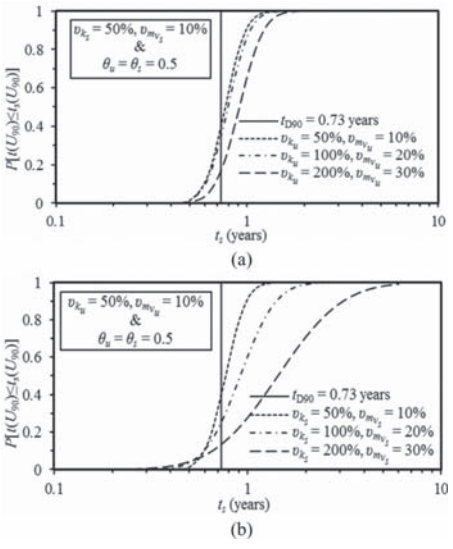

Figure 7. Effect of υ_u and υ_s on $P[t(U_{90}) \le t_s(U_{90})]$ for $\theta_u = \theta_s = 0.5$.

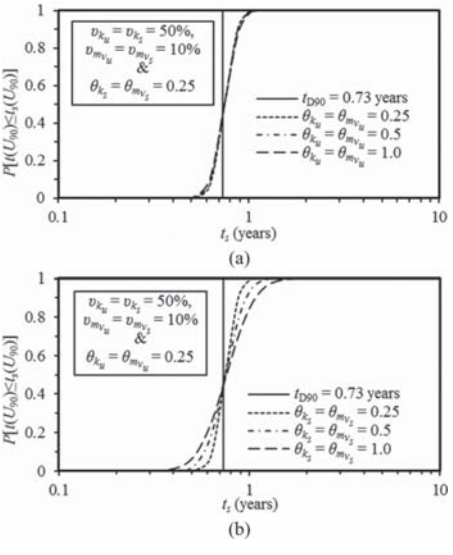

Figure 8. Effect of θ_u and θ_s on $P[t(U_{90}) \le t_s(U_{90})]$ for $\upsilon_{k_u} = \upsilon_{k_s} = 50\%$ and $\upsilon_{m_{v_u}} = \upsilon_{m_{v_s}} = 10\%$.

U_{90} at $t = 0.73$ year (i.e., $t_{D90} = 0.73$ year). The results obtained from this study are described below.

4.1 *Effect of variation of* υ *and* θ *on the mean of U*

The effects of increasing υ_u and υ_s on μ_U at fixed value of $\theta_u = \theta_s = 0.5$ is examined in Figure 3, which also includes the deterministic solution of no soil variability. It can be seen from Figure 3(a) that at any consolidation time, there is a slight reduction in μ_U for spatially varied soils compared to the deterministic case. The nearly identical curves for all cases of υ_u(υ_{k_s} and $\upsilon_{m_{v_s}}$ are fixed at 50% and 10% respectively) plotted in the figure indicate that the effect of increasing υ_u on μ_U remains marginal. The effect of υ_s on μ_U at fixed values of $\upsilon_{k_u} = 50\%$ and $\upsilon_{m_{v_u}} = 10\%$ is illustrated in Figure 3b, which shows that any change in υ_s has a significant impact on the estimated values of μ_U. At any certain consolidation time, μ_U decreases with the increase of υ_s, and the decreasing rate of μ_U consistently increases with the increase of υ_s. The comparison between Figures 3a and b reveals that the effect of υ_s on μ_U is dominating.

Figure 4 highlights the effects of increasing θ_u and θ_s on μ_U at fixed values of $\upsilon_{k_u} = \upsilon_{k_s} = 50\%$ and $\upsilon_{m_{v_u}} = \upsilon_{m_{v_s}} = 10\%$. Virtually, the identical curves of μ_U in Figure 4a for all θ_u at a fixed value of $\theta_{k_s} = \theta_{m_{v_s}} = 0.25$, indicate that μ_U is more or less independent of θ_u. Similar to θ_u, the influence of θ_s (θ_{k_u} and $\theta_{m_{v_u}}$ are fixed at 0.25) on μ_U is also marginal as can be seen in Figure 4b.

4.2 *Effect of variation of* υ *and* θ *on the standard deviation of U*

The influence of υ_u and υ_s on σ_U at a fixed value of $\theta_u = \theta_s = 0.5$ is depicted in Figure 5. For a fixed value of υ_s (υ_{k_s} and $\upsilon_{m_{v_s}}$ are, respectively, 50% and 10% in this case), increasing υ_u has a marginal effect on σ_U, as shown in Figure 5a. Figure 5b shows the effect of υ_s on σ_U at fixed values of $\upsilon_{k_u} = 50\%$ and $\upsilon_{m_{v_u}} = 10\%$, and from which it can be seen that at any certain consolidation time, σ_U increases significantly with the increase of υ_s, implying the dominant effect of υ_s on the estimated values of σ_U.

Figure 6 illustrates the effect of varying θ_u and θ_s on σ_U at fixed values of $\upsilon_{k_u} = \upsilon_{k_s} = 50\%$ and $\upsilon_{m_{v_u}} = \upsilon_{m_{v_s}} = 10\%$. In Figure 6a, it can be seen that similar to the effect of θ_u on μ_U, σ_U remains almost identical for varying θ_u with a fixed value of $\theta_{k_s} = \theta_{m_{v_s}} = 0.25$. On the other hand, the estimated σ_U for different values of θ_s is plotted in Figure 6b at a fixed value of $\theta_{k_u} = \theta_{m_{v_u}} = 0.25$, which illustrates that unlike θ_u, θ_s has a considerable impact on the estimated values of σ_U.

4.3 *Effect of variation of* υ *and* θ *on the probability of required time t to achieve* U_{90} *that is less than or equal to* t_s

The influence of the smear zone parameters over the undisturbed zone parameters in relation to the probability of required time t to achieve U_{90} that is less than or equal to t_s are investigated

in Figures 7 and 8. The deterministic time of achieving 90% consolidation, t_{D90}, is also shown in the figures by vertical solid lines that give $P[t(U_{90}) \leq t_s(U_{90})]$ at that time, for any combination of υ and θ.

The effects of υ_u and υ_s on $P[t(U_{90}) \leq t_s(U_{90})]$ at a fixed value of $\theta_u = \theta_s = 0.5$ is demonstrated in Figure 7. It can be seen from Figure 7a that, in general, the effect of increasing υ_u (υ_{k_s} and $\upsilon_{m_{v_u}}$ are fixed at 50% and 10%, respectively) on $P[t(U_{90}) \leq t_s(U_{90})]$ remains marginal. The effect of υ_s at fixed values of $\upsilon_{k_u} = 50\%$ and $\upsilon_{m_{v_u}} = 10\%$ is shown in Figure 7b, which shows that varying the values of υ_s has a considerable impact on the estimated values of $P[t(U_{90}) \leq t_s(U_{90})]$. At any certain consolidation time, $P[t(U_{90}) \leq t_s(U_{90})]$ decreases significantly with the increase of υ_s. The overall observation that can be derived from comparing the results in Figure 7 is that the effect of υ_s on $P[t(U_{90}) \leq t_s(U_{90})]$ is dominant.

Figure 8 investigates the effects of θ on $P[t(U_{90}) \leq t_s(U_{90})]$ at fixed values of $\upsilon_{k_u} = \upsilon_{k_s} = 50\%$ and $\upsilon_{m_{v_u}} = \upsilon_{m_{v_s}} = 10\%$. In Figure 8a, the influence of increasing θ_u on $P[t(U_{90}) \leq t_s(U_{90})]$ is shown at $\theta_{k_s} = \theta_{m_{v_s}} = 0.25$, and the results yield almost identical curves indicating that varying the values of θ_u has little or no impact on the probabilistic behavior of degree of consolidation. On the other hand, the estimated $P[t(U_{90}) \leq t_s(U_{90})]$ for different values of θ_s is plotted in Figure 8b at a fixed value of $\theta_{k_u} = \theta_{m_{v_u}} = 0.25$. It can be seen that unlike θ_u, θ_s has a considerable impact on the estimated values of $P[t(U_{90}) \leq t_s(U_{90})]$. The comparison between Figures 8a and b reveals that, the effect of θ_s on $P[t(U_{90}) \leq t_s(U_{90})]$ is more significant than θ_u. It is interesting to know that the deterministic solution yields $P[t(U_{90}) \leq t_s(U_{90})] < 50\%$ for all combinations of values of υ_u, υ_s, θ_u, and θ_s, as can be seen in Figures 7 and 8.

5 CONCLUSIONS

This paper has used the random field theory and finite element modeling to investigate the relative significance of soil spatially variability in the smear and undisturbed zones in soil improvement by prefabricated vertical drains. Both the coefficient of permeability, k, and coefficient of volume compressibility, m_v, were treated as independent random variables and uncoupled 3D finite element analysis was applied. The effect of coefficient of variation, υ, and spatial correlation or scale of fluctuation, θ, of the undisturbed zone on the estimated mean and standard deviation of the degree of consolidation was found to be marginal. On the other hand, the estimated statistics and probability associated with the degree of consolidation were found to be highly sensitive to υ and θ of the soil properties at the smear zone. This result indicates that the probabilistic behavior of soil consolidation is governed by the spatial variation of the soil properties of the smear zone. Since the spatial variability of the smear zone will possibly be different from that of the undisturbed zone, this observation has important implications in the sense that, modeling soil consolidation with the same υ and θ for both zones (i.e., undisturbed and smear) that are equal to the υ and θ of the smear zone does not significantly affect the final results. Overall, the results obtained from this research highlight valuable insights into the impact of soil spatial variability on soil improvement by PVDs and clearly demonstrate the potential of stochastic analyses in routine design practice.

REFERENCES

Abuel-Naga, H.M., Pender, M.J. & Bergado, D.T. 2012. Design curves of prefabricated vertical drains including smear and transition zones effects. *Geotextiles and Geomembranes* 32: 1–9.

Badaoui, M., Nour, A., Slimani, A. & Berrah, M.K. 2007. Consolidation statistics investigation via thin layer method analysis. *Transport in Porous Media* 67(1): 69–91.

Bari, M.W., Shahin, M.A. & Nikraz, H.R. 2012a. Effects of soil spatial variability on axisymmetric versus plane strain analyses of ground improvement by prefabricated vertical drains. *International Journal of Geotechnical Engineering* 6(2): 139–147.

Bari, M.W., Shahin, M.A. & Nikraz, H.R. 2012b. Probabilistic analysis of soil consolidation via prefabricated vertical drains. *International Journal of Geomechanics, ASCE*: (in press).

Beacher, G.B. & Christian, J.T. 2003. *Reliability and Statistics in Geotechnical Engineering*, John Wiley & Sons: Chichester, England.

Bo, M.W., Chu, J., Low, B.K. & Choa, V. 2003. *Soil Improvement: Prefabricated Vertical Drain Techniques*, Thomson Learning: Singapore.

Chu, J. 2004. Practical considerations for using vertical drains in soil improvement projects. *Geotextiles and Geomembranes* 22(1): 101–117.

Dagan, G. 1989. *Flow and transport in porous media*, Springer: New York.

Elkateb, T., Chalaturnyk, R. & Robertson, P.K. 2003. An overview of soil heterogeneity: Quantification and implications on geotechnical field problems. *Canadian Geotechnical Journal* 40(1): 1–15.

Fenton, G.A. & Griffiths, D.V. 2008. *Risk assessment in geotechnical engineering*, Wiley: New York.

Fenton, G.A. & Vanmarcke, E.H. 1990. Simulation of random fields via local average subdivision. *Journal of Engineering Mechanics* 116(8): 1733–1749.

Freeze, R.A. 1977. Probabilistic one-dimensional consolidation. *Journal of Geotechnical Engineering Division* 103(GT7): 725–742.

Hong, H.P. & Shang, J.Q. 1998. Probabilistic analysis of consolidation with prefabricated vertical drains for soil improvement. *Canadian Geotechnical Journal* 35(4): 666–677.

Huang, J., Griffiths, D.V. & Fenton, G.A. 2010. Probabilistic analysis of coupled soil consolidation. *Journal of Geotechnical and Geoenvironmental Engineering* 136(3): 417–430.

Hwang, D. & Witczak, M.W. 1984. Multidimensional probabilistic consolidation. *Journal of Geotechnical Engineering* 110(8): 1059–1077.

Jaksa, M.B., Brooker, P.I. & Kaggwa, W.S. 1997. Inaccuracies associated with estimating random measurement errors. *Journal of Geotechnical and Geoenvironmental Engineering* 123(5): 393–401.

Kulhawy, F.H., Roth, M.J.S. & Grigoriu, M.D. 1991. Some statistical evaluations of geotechnical properties. *Proceedings of the 6th International Conference on Applied Statistical Problems in Civil Engineering (ICASP6)*, Mexico City: 705–712.

Lee, I.K., White, W. & Ingles, O.G. 1983. *Geotechnical engineering*, Pitman: London.

Pyrah, I.C. 1996. One-dimensional consolidation of layered soils. *Géotechnique* 46(3): 555–560.

Rowe, P.W. 1972. The relevance of soil fabric to site investigation practice. *Géotechnique* 22(2): 195–300.

Shahin, M.A. & Bari, M.W. 2012. Modeling of Ground Improvement by Prefabricated Vertical Drains in Highly Variable Soils. *International Conference on Ground Improvement and Ground Control (ICGI2012)*, University of Wollongong, Australia: 321–335.

Smith, I.M. & Griffiths, D.V. 2004. *Programming the finite element method*, John Wiley & Sons.

Vanmarcke, E.H. 1977. Probabilistic modelling of soil profiles. *Journal of Geotechnical Engineering Division* 103(11): 1227–1246.

Walker, R.T. 2006. Analytical solutions for modeling soft soil consolidation by vertical drains, University of Wollongong: Wollongong, Australia.

Zhou, W., Hong, H.P. & Shang, J.Q. 1999. Probabilistic design method of prefabricated vertical drains for soil improvement. *Journal of Geotechnical and Geoenvironmental Engineering* 125(8): 659–664.

Geotechnical Safety and Risk IV – Zhang et al. (eds)
© 2014 Taylor & Francis Group, London, ISBN 978-1-138-00163-3

Regularity of the variance reduction function in Tianjin Port

Shu-Wang Yan & Lin-Ping Guo
State Key Laboratory of Hydraulic Engineering Simulation and Safety, Tianjin University, Tianjin, China

Yong-Hua Cao
CCCC-Tianjin Port Engineering Institute Ltd., Tianjin, China

ABSTRACT: In the process of reliability analysis in geotechnical engineering, the variance reduction function is the key parameter to transit the "point property" into "spatial average property". In the paper, improvement on the method to calculate the no correlation distance put forward by Yan Shu-wang and Zhu Hong-xia was made, which can greatly minimize the computation efforts. The procedure of calculation of reduction function was analyzed, and general regularity of determining reduction function through calculation of no correlation distance was obtained, which was for the first time put forward by us.

1 INSTRUCTION

Recent years, the essence of the rapidly developed reliability analysis is considering various kinds of uncertainty in engineering. In reliability analysis, the self-correlation theory is generally employed to simulate spatial variability and relativity of the soil. The soil profile random field model suggested by Vanmarcke (1977, 1983) can connect the "spatial variance" with "point property". In the theory, the reduction function of the variance is determined by the correlation distance of soil, therefore, the correlation distance is the key to the analysis (Zhu & Gao, 2003; Zhu, 2007).

The correlation function method is employed to calculate the correlation distance of typical soil layers in Tianjin port. Improvement on no correlation distance method put forward by Yan & Zhu (2007) is made, on the basis of which, reduction functions of variance of Tianjin Port are calculated. And the general regularity of determining reduction function through calculation of no correlation distance is obtained.

2 CONCEPTION AND CALCULATION METHOD OF CORRELATION DISTANCE

2.1 *Conception of correlation distance*

Vanmarcke (1977) put forward that, if:

$$\lim_{h\to\infty} h\Gamma^2(h) = 2\lim_{h\to\infty}\int_0^h \left(1-\frac{\Delta z}{h}\right)\rho(\Delta z)d(\Delta z) = 2\int_0^h \rho(\Delta z)d(\Delta z) = \delta_u \quad (1)$$

where δ_u = the correlation distance, which is a constant; Δz = sampling distance; h = depth to be averaged; $\rho(\Delta z)$ = correlation function; $\Gamma^2(h)$ = the variance reduction function. The correlation distance can be approximately written as:

$$h\Gamma^2(h) \approx \delta_u \quad (2)$$

And the variance reduction factor can be obtained as:

$$\Gamma^2(h) = \begin{cases} 1 & (h \le \delta_u) \\ \dfrac{\delta_u}{h} & (h \ge \delta_u) \end{cases} \quad (3)$$

To obtain the Eq. (3), the correlation function $\rho(\Delta z)$ in the stochastic field model should be taken as:

$$\rho(\Delta z) = \begin{cases} 1 & (\Delta z \le \delta_u) \\ 0 & (\Delta z \ge \delta_u) \end{cases} \quad (4)$$

It can be known from the theory mentioned above that the correlation distance is not a random constant. It can be regarded as an essential distance, named as "correlation distance" measuring correlation degree of two random variables. When the distance between two points is smaller than the value δ_u, they are strongly related; otherwise, they are considered as uncorrelated (Jia, 1985; Yan et al., 2006). However, the "correlation distance" is just a conception used in practical project, which is not strictly the same as perfect correlated ($\rho = 1$) or uncorrelated ($\rho = 0$) in mathematics.

It can be known from Eq. (3) that the variance reduction factor can be calculated as long as the correlation distance is obtained.

2.2 *The improved correlation function method*

There are several methods to determine correlation distance since the stochastic field model put forward by Vanmarcke (1977, 1983). Such as the space average method, correlation function method, statistical simulation method, average zero span method and half a variation coefficient method. The most specific and convenient method to obtain correlation distance is the space average method and the correlation function method (Li et al., 2003; Yan et al., 2013). In this paper, to the application of the no correlation distance, the improved correlation function method is employed to calculate the correlation distance.

The improved correlation method calculate the correlation distance through fitting the correlation function $\rho(\Delta z)$. According to the definition of correlation distance and the variance reduction function, it can be obtained:

$$\delta_u = \lim_{h\to\infty} h\Gamma^2(h) = \lim_{h\to\infty} h\cdot\frac{2}{h}\int_0^h\left(1-\frac{\Delta z}{h}\right)\rho(\Delta z)d(\Delta z)$$
$$= 2\int_0^\infty \rho(\Delta z)d(\Delta z) \qquad (5)$$

Several commonly used correlation function and corresponding expressions of correlation distance are listed in Table 1 (Peng, 1992).

The correlation distance can be obtained once the correlation function and corresponding parameters are determined. Steps are as follows:

① Take different values of i for $\Delta z = i\Delta z_0$, and calculate:

$$\rho(\Delta z) = \rho(i\Delta z_0) = E[Y(z)Y(z+\Delta z)]$$
$$= \frac{1}{n-i}\sum_{k=1}^{n-i} Y(z_k)Y(z_{k+i}) \qquad (6)$$

And a series of value for correlation function are obtained.

Table 1. Correspondence between correlation function and correlation distance.

Correlation function $\rho(\tau)$	Correlation distance δ_u
$e^{-b\|\tau\|}$	$2/b$
$e^{-(b\tau)2}$	$\sqrt{\pi}$/b
$e^{-b\|\tau\|}\cdot\cos(b\tau)$	$1/b$
$e^{-b\|\tau\|}\cdot\cos(\omega\tau)$	$(2b/b^2)+\omega^2$

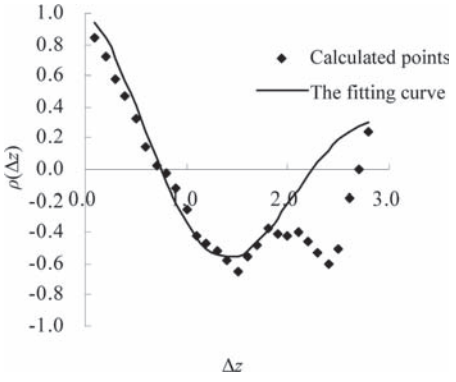

Figure 1. Fitting result of the improved correlation function method.

② plot the calculated correlation function according to Δz;
③ determine the fitting correlation function according to the plot $\rho(\Delta z) \sim \Delta z$;
④ suppose a set of parameter for the correlation function and plot the corresponding curve $\rho(\Delta z) \sim \Delta z$;
⑤ check whether the theoretical line can fit calculated points in the front part;
⑥ if not, adjust parameters, till they fit each other well in the front part (as shown in Fig. 1). And these parameters are what wanted;
⑦ the correlation distance can be obtained according to Table 1.

3 CALCULATION METHOD AND IMPROVEMENT OF NO CORRELATION DISTANCE

3.1 *Calculation method of no correlation distance*

Coefficient of reduction of variance is affected by the length to be averaged and correlation distance. Once the correlation distance is determined, the larger the value of h, the more to be reduced. Therefore, it's of vital importance to confirm the value of h and the no correlation distance. In practice, the no correlation distance can be determined by means of plotting. The correlation function should be confirmed firstly, and the $\Gamma^2(h) \sim h/\delta_u$ curve can be plotted according to Eq. (3) and Table 1. The point of intersection can be obtained, which is marked as n^*, and consider the $L^* = n^*\delta_u$, of which the L^* is the no correlation distance. The no correlation distance is half value of L^*. Regularity of no correlation distance will be discussed corresponding to different situations.

1. When the correlation function is in exponential type, the first type in Table 1, the variance reduction function is:

$$\Gamma^2(h) = \frac{2}{b^2h^2}(bh + e^{-bh} - 1) \tag{7}$$

Replace b in Eq. (7) with δ_u, and it can be obtained that:

$$\rho(\tau) = e^{-2\tau/\delta_u},$$
$$\Gamma^2(h) = \frac{\delta_u}{h} + \frac{1}{2}\left(\frac{\delta_u}{h}\right)^2 (e^{-2h/\delta_u} - 1) \tag{8}$$

The curve $\Gamma^2(h) \sim h/\delta_u$ can be plotted according to Eqns. (3) and (8), which is shown in Figure 2.

Figure 2 shows that, the intersection point is $n^* = 10$, of which the reduction coefficient is approximately 0.1 and the calculated value from Eq. (8) is 0.095, which can be approximately considered as equal.

According to Eq. (8), there can be $L^*\Gamma^2(L^*) = 0.095\ \delta_u \approx \delta_u$, meanwhile, the correlation function is $\rho(L^*) = 2.06 \times 10^{-9} \approx 0$. Therefore, the calculated L^* is the lower limit of h for $h\Gamma^2(h) \approx \delta_u$, half of which is the no correlation distance. Therefore the no correlation distance can be confirmed as $h^* = 5\delta_u$, and the reduction coefficient of variance is $\Gamma^2(h^*) = 0.18$.

2. When the correlation function is in exponential type with cosine, the third type in Table 1. The variance reduction function will be:

$$\Gamma^2(h) = \frac{2}{b^2h^2}(bh + e^{-bh} - 1) \tag{9}$$

Rewrite the correlation function and the variance reduction function with correlation distance, there can be:

$$\rho(\tau) = e^{-\tau/\delta_u}\cos\frac{\tau}{\delta_u},$$
$$\Gamma^2(h) = \frac{\delta_u}{h} - \left(\frac{\delta_u}{h}\right)^2 e^{-h/\delta_u}\sin\frac{h}{\delta_u} \tag{10}$$

The curve $\Gamma^2(h) \sim h/\delta_u$ can be plotted. According to Eqns. (3) and (10), which is shown in Figure 3.

Figure 3 shows that, the intersection point is $n^* = 4$, of which the reduction coefficient is approximately 0.25 and the calculated value from Eq. (10) is 0.251, which can be approximately considered as equal.

According to Eq. (10), there can be $L^*\Gamma^2(L^*) = 1.004\delta_u \approx \delta_u$, meanwhile, the correlation function is $\rho(L^*) = -0.012 \approx 0$. Therefore, the calculated L^* is the lower limit of h for $h\Gamma^2(h) \approx \delta_u$, half of which is the no correlation distance. Therefore the no correlation distance can be confirmed as $h^* = 2\delta_u$, and the reduction coefficient of variance is $\Gamma^2(h^*) = 0.469$.

3. When the correlation function is in exponential type with cosine, the last type in Table 1. And the variance reduction function will be:

$$\Gamma^2(h) = \frac{2}{h^2(b^2+\omega^2)^2}\left\{bh(b^2+\omega^2) + (\omega^2 - b^2) - e^{-bh}\left[2\omega b\sin(\omega h) + (\omega^2 - b^2)\cos(\omega h)\right]\right\} \tag{11}$$

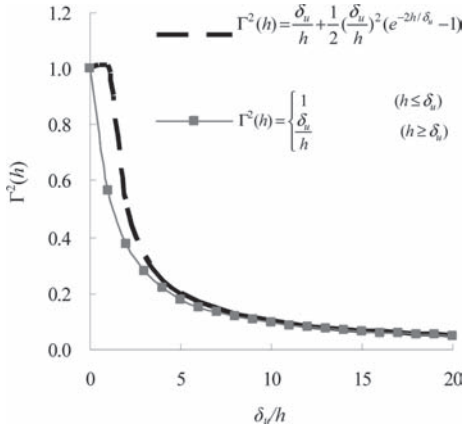

Figure 2. Reduction process of variance for correlation function in exponential type.

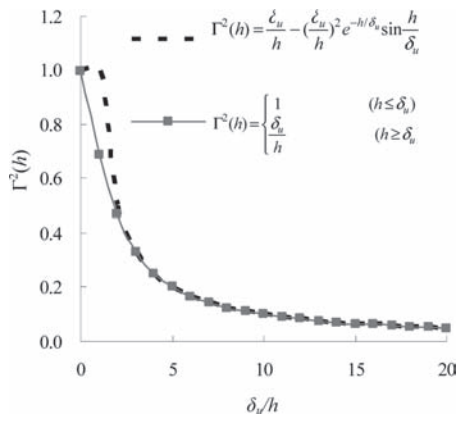

Figure 3. Reduction process of variance for correlation function in exponential type with cosine.

Table 2. No correlation distances under given conditions.

ω/b	δ_u	$\Gamma^2(h)$	h^*	$\Gamma^2(h^*)$
0.1	$1/0.505b$	$\Gamma^2(h)=\frac{\delta_u}{h}+\left(\frac{\delta_u}{h}\right)^2\left[-0.495-e^{-h/0.505\delta_u}\left(0.1\sin\frac{h}{5.05\delta_u}-0.99\cos\frac{h}{5.05\delta_u}\right)\right]$	$5\delta_u$	0.095
0.3	$1/0.545b$	$\Gamma^2(h)=\frac{\delta_u}{h}+\left(\frac{\delta_u}{h}\right)^2\left[-0.455-e^{-h/0.545\delta_u}\left(0.3\sin\frac{h}{1.82\delta_u}-0.91\cos\frac{h}{1.82\delta_u}\right)\right]$	$4.5\delta_u$	0.106
0.5	$1/0.625b$	$\Gamma^2(h)=\frac{\delta_u}{h}+\left(\frac{\delta_u}{h}\right)^2\left[-0.375-e^{-h/0.625\delta_u}\left(0.5\sin\frac{h}{1.25\delta_u}-0.75\cos\frac{h}{1.25\delta_u}\right)\right]$	$4\delta_u$	0.119
0.7	$1/0.745b$	$\Gamma^2(h)=\frac{\delta_u}{h}+\left(\frac{\delta_u}{h}\right)^2\left[0.255-e^{-h/0.745\delta_u}\left(0.7\sin\frac{h}{1.064\delta_u}-0.51\cos\frac{h}{1.0643\delta_u}\right)\right]$	$3\delta_u$	0.189
1	$1/b$	$\Gamma^2(h)=\frac{\delta_u}{h}-\left(\frac{\delta_u}{h}\right)^2 e^{-h/\delta_u}\sin\frac{h}{\delta_u}$	$2\delta_u$	0.251
1.3	$1/1.345b$	$\Gamma^2(h)=\frac{\delta_u}{h}+\left(\frac{\delta_u}{h}\right)^2\left[0.345-e^{-h/1.345\delta_u}\left(1.3\sin\frac{h}{1.035\delta_u}+0.69\cos\frac{h}{1.035\delta_u}\right)\right]$	$3\delta_u$	0.215
1.5	$1/1.625b$	$\Gamma^2(h)=\frac{\delta_u}{h}+\left(\frac{\delta_u}{h}\right)^2\left[0.625-e^{-h/1.625\delta_u}\left(1.5\sin\frac{h}{1.083\delta_u}+1.25\cos\frac{h}{1.083\delta_u}\right)\right]$	$5\delta_u$	0.096
1.7	$1/1.945b$	$\Gamma^2(h)=\frac{\delta_u}{h}+\left(\frac{\delta_u}{h}\right)^2\left[0.945-e^{-h/1.945\delta_u}\left(1.7\sin\frac{h}{1.144\delta_u}+1.89\cos\frac{h}{1.144\delta_u}\right)\right]$	$6.5\delta_u$	0.076
2	$1/2.5b$	$\Gamma^2(h)=\frac{\delta_u}{h}+\left(\frac{\delta_u}{h}\right)^2\left[1.5-e^{-h/2.5\delta_u}\left(2.\sin\frac{h}{1.25\delta_u}+3\cos\frac{h}{1.25\delta_u}\right)\right]$	$9.5\delta_u$	0.057

The two parameters b and ω should be firstly determined if the reduction function rewritten with δ_u. Regularity of no correlation distance will be discussed by means of the followed several situations, as shown in Table 2.

Curve $\Gamma^2(h) \sim h/\delta_u$ corresponding to different value of ω/b are plotted according to Eq. (3) and Table 2 as shown in Figure 4(a) and 4(b).

It can be known from Figure 4(a) and 4(b) that, with increasing of ω/b, the no correlation distance decreases when the ratio is smaller than 1, and the reduction coefficient increases; conversely, with increasing of ω/b, the no correlation distance increases when the ratio is larger than 1, and the reduction coefficient decreases. The no correlation distance is the largest and the reduction coefficient is the smallest when the ratio ω/b is 1. Regularities described above can be described as Figures 5 and 6 as scatter plots.

3.2 *Improvement of no correlation distance*

There will be a value of ω/b for each layer of each boring. The variance reduction function corresponding to each ω/b should be calculated according to Table 2, of which the process seems

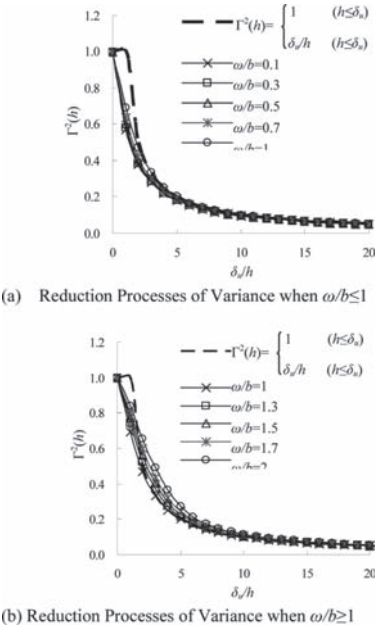

Figure 4. Reduction processes of variance with different value of ω/b.

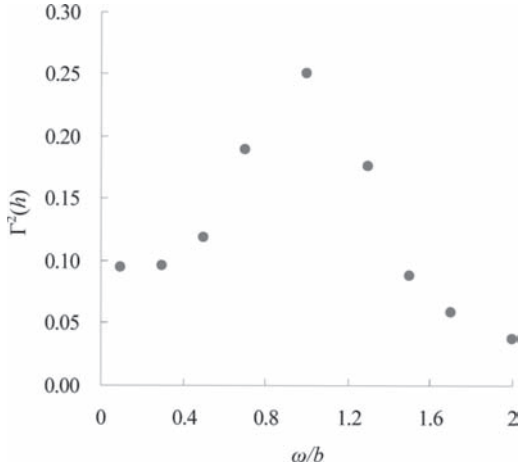

Figure 5. Change of reduction coefficient with the ratio ω/b.

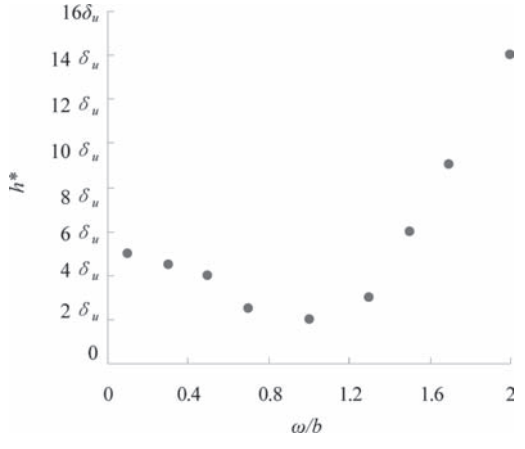

Figure 6. Change of no correlation distance with the ratio ω/b.

to be greatly complicated. Through analyzing the process mentioned above, an equation appropriate for any ratio of ω/b is obtained:

$$\Gamma^2(h) = \frac{\delta_u}{h} + \left(\frac{\delta_u}{h}\right)^2 \left[\alpha_1 - e^{-h/\alpha_2\delta_u} \times \left(\alpha_3 \sin\frac{h}{\alpha_4\delta_u} + \alpha_5 \cos\frac{h}{\alpha_4\delta_u}\right)\right] \quad (12)$$

where, $\omega/b = \alpha$, $\alpha_1 = (\alpha^2 - 1)/2$, $\alpha_1 = (\alpha^2 + 1)/2$, $\alpha_3 = \alpha$, $\alpha_4 = 2\alpha/(\alpha^2 + 1)$, $\alpha_5 = \alpha^2 - 1$.

In practical project, parameters b and ω should be determined first according to correlation function, and the correlation distance will be obtained. Secondly, plot the curve $\Gamma^2(h) \sim h/\delta_u$ and determine the no correlation distance h^*. Finally, the variance reduction function can be obtained.

Analysis mentioned above supposing that, the effective influence depth is no less than the no correlation distance. The corresponding equation for variance reduction function should be employed in case the effective influence depth is smaller than the no correlation distance.

3.3 *Principle of determining variance reduction function*

As mentioned above, reduction coefficient of variance can be determined according to Table 3.

4 CASE STUDY

Test data of the forty cone penetration tests of the Wharf engineering in Tianjin are analyzed. Correlation distances and reduction functions of variance corresponding to typical layers in Tianjin Port are obtained, which can be a reference to other projects in this area.

Table 3. Principle of determining variance reduction function.

	Variance reduction function $\Gamma^2(h)$		
Correlation function $\rho(\Delta z)$	$\delta_u \le L \le h^*$	$L \ge h^*$	
Exponential type $\rho(\tau) = e^{-b\lvert\tau\rvert}$	$\frac{2}{b^2h^2}(bh + e^{-bh} - 1)$ (where, $h = L$)	0.095	1
1. Type of exponential with Cosine $\rho(\tau) = e^{-b\lvert\tau\rvert} \cdot \cos(b\tau)$	$\frac{1}{b^2h^2}\left[bh - e^{-(bh)}\sin bh\right]$ (where, $h = L$)	0.251	1
2. Type of exponential with Cosine $\rho(\tau) = e^{-b\lvert\tau\rvert} \cdot \cos(\omega\tau)$	$\frac{\delta_u}{h} + \left(\frac{\delta_u}{h}\right)^2 \left[\alpha_1 - e^{-h/\alpha_2\delta_u}\left(\alpha_3 \sin\frac{h}{\alpha_4\delta_u} + \alpha_5 \cos\frac{h}{\alpha_4\delta_u}\right)\right]$ (where, $\omega/b = \alpha$, $\alpha_1 = (\alpha^2 - 1)/2$, $\alpha_1 = (\alpha^2 + 1)/2$, $\alpha_3 = \alpha$, $\alpha_4 = 2\alpha/(\alpha^2 + 1)$, $\alpha_5 = \alpha^2 - 1$, $h = L$)	δ_u/h^*	1

4.1 *Calculation and statistics of vertical correlation distance*

Stochastic model of the soil profile in this area possess the stationarity and ergodicity (Yan et al., 1995). Therefore, it can be analyzed by the stochastic theory put forward by Vanmarcke (1977).

Table 4. Vertical correlation distance of Tianjin Port.

Cone penetration test number	Correlation distance (m)		
	Silt	Silt clay	Silty clay
1	0.139	0.533	0.400
2	0.330	1.730	0.358
3	0.209	1.220	0.431
4	0.182	1.067	0.400
5	0.190	0.273	0.483
6	0.412	0.800	0.431
7	0.067	1.077	0.297
8	0.270	1.239	0.325
9	0.984	1.239	0.308
10	0.175	0.400	0.492
11	0.543	0.554	0.335
12	0.176	1.103	0.224
13	0.649	0.690	0.163
14	0.130	0.825	0.400
15	0.341	0.226	0.400
16	0.113	0.588	0.431
17	0.701	0.865	0.400
18	0.181	0.550	0.400
19	0.452	1.000	0.457
20	0.511	1.000	0.400
21	0.923	0.650	0.398
22	0.195	0.550	0.500
23	0.320	0.667	0.276
24	0.088	0.738	0.328
25	0.202	1.077	0.400
26	0.400	0.500	0.363
27	0.667	0.320	0.363
28	0.690	0.550	0.328
29	0.546	0.054	0.384
30	0.267	0.780	0.328
31	0.495	0.832	0.303
32	0.100	0.780	0.328
33	0.100	1.429	0.260
34	0.100	0.667	0.355
35	0.100	0.920	0.328
36	0.100	1.107	0.328
37	0.098	1.176	0.303
38	0.183	1.440	0.270
39	0.175	0.976	0.303
40	0.180	0.148	0.270
Minimum value	0.040	0.054	0.163
Maximum value	0.984	1.730	0.500
Average	0.317	0.808	0.356
Standard deviation	0.237	0.368	0.072

The cone tip resistance of CPT parameter is used to calculate the vertical correlation distance (Xu et al., 1998; Li et al., 2003; Yan et al., 2007). For preparation of the application of no correlation distance method, correlation function method is employed. Results are shown in Table 4 (Zhu, 2007).

4.2 *Variance reduction function*

Figure 7 describes laws for the reduction function with ω/b. Results of this area can be employed to prove whether the law is ubiquitous. Reduction functions of variance corresponding to the ratio ω/b are plotted in Figure 7.

It can be known from Figure 7 that the law mentioned above is ubiquitous. That is with increasing of ω/b, the no correlation distance decreases when the ratio is smaller than 1, and the reduction coefficient increases; conversely, with increasing of ω/b, the no correlation distance increases when the ratio is larger than 1, and the reduction coefficient decreases. The no correlation distance is the largest and the reduction coefficient is the smallest when the ratio ω/b is 1. To conservatively consider in practical project, the smallest ratio ω/b will be taken to determine the reduction function of the variance. In addition, the value of variance

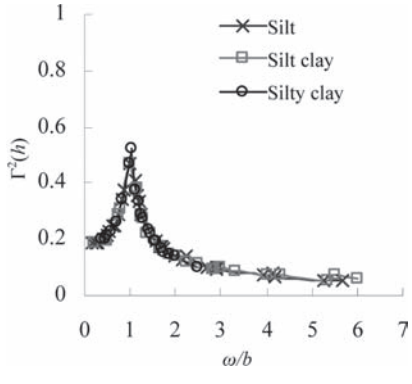

Figure 7. The change law of variance reduction function.

Table 5. Variance reduction function of typical layers in Tianjin Port.

Name of the soil	ω/b (min)	No correlation distance	Reduction function of the variance
Silt	0.17	4.75 δ_u	0.374
Silt clay	0.21	4.75 δ_u	0.312
Silty clay	0.38	4.50 δ_u	0.378

reduction function is determined only by the ratio ω/b but not the value of ω or b, which can also be known from Eq. (12).

5 CONCLUSIONS

1. An equation appropriate for any ratio of ω/b for the process of calculating no correlation distance is obtained, which can greatly minimize the computation efforts.
2. By analyzing regularity of determining variance reduction function with the method of no correlation distance, the law is obtained: with increasing of ω/b, the no correlation distance decreases when the ratio is smaller than 1, and the reduction coefficient increases; conversely, with increasing of ω/b, the no correlation distance increases when the ratio is larger than 1, and the reduction coefficient decreases. The no correlation distance is the largest and the reduction coefficient is the smallest when the ratio ω/b is 1. To conservatively consider in practical project, the smallest ratio ω/b will be taken to determine the reduction function of the variance.

REFERENCES

Jia, Xiao-li. 1985. Study on properties of stochastic field of soil profiles. Tianjin University. (In Chinese).

Li, Jing-Pei, Shu, Xiang, Ding, Shi-Jun. 2003. Discussion on characteristic parameter of self-correlation of soil index and its determining principle. Transaction of Tongji University 31(3): 287–290. (In Chinese).

Li, Xiao-Yong, Xie, Kang-He, Yu, Yan. 2003. Research of the characteristics of correlation distance on soil properties indexes. China Civil Engineering Journal 36(8): 91–95.

Peng, Da-Peng. 1992. Application of homogeneous random field to analyze indexes of soil properties. Transaction of Tianjin University 2: 118–124. (In Chinese).

Vanmareke, E.H. 1977. Probability modeling of soil Profile. J. Geotec. Eng. Division 103: 1227–1245.

Vanmarcke, E.H. 1983. Random fields: analysis and synthesis. MIT Press, Cambridge, Mass.

Xu, Bin, Wang, Da-Tong, Gao, Da-zhao. 1998. Discussion on calculation of correlation distance with cone penetration curve by correlation function method. Rock and Soil Mechanics 19(1): 55–58. (In Chinese).

Yan, Shuwang, Guo, Linping. 2013. Estimation of scale of fluctuation of soil properties indexes. Applied Mechanics and Materials. Guilin, China. 256–259: 149–152.

Yan, Shu-Wang, Jia, Xiao-Li, Guo, Huai-zhi. 1995. Test on stationarity and ergodicity of stochastic model of soil profiles. Chinese Journal of Geotechnical Engineering 17(3): 1–9. (In Chinese).

Yan, Shu-Wang, Zhu, Hong-Xia, Liu, Run, Sun, Wan-he. 2007. Study on methods for estimating correlation distance of soil layers. Rock and Soil Mechanics 28(8): 1581–1586. (In Chinese).

Zhu, Deng-Feng, Gao, Da-Zhao. 2003. Space statistical characteristics analysis of smooth stochastic field of soil characteristics. Rock and Soil Mechanics 24(3): 455–462. (In Chinese).

Zhu, Hong-xia. 2007. Study of using random field theory in soil foundation reliability analysis. Tianjin University. (In Chinese).

This page intentionally left blank

Geotechnical Safety and Risk IV – Zhang et al. (eds)
© 2014 Taylor & Francis Group, London, ISBN 978-1-138-00163-3

Seepage through anisotropic non-stationary random fields

H. Zhu & L.M. Zhang
The Hong Kong University of Science and Technology, Hong Kong, China

ABSTRACT: Natural slopes are highly heterogeneous. When inverse segregation takes place in a landslide soil deposit, the coefficient of permeability of the soil statistically decreases from the surface to the bottom of the deposit. Such material spatial variability can be characterized using non-stationary random fields. The objectives of this paper are to develop algorithms to generate non-stationary random fields for a slope with the mean coefficient of saturated permeability decreasing with depth and to carry out analysis of infiltration in an anisotropic non-stationary slope. Basic anisotropic stationary random fields with orthogonal major and minor scales of fluctuation are considered first. Non-stationary random fields are then formulated by adding a trend to the stationary random fields. The Cholesky decomposition method is applied to produce correlated random numbers following an exponential correlation structure. After generating the anisotropically heterogeneous non-stationary random fields, the steady-state pore-water pressures in each random field are obtained by solving the Richards equation. The effects of coefficient of variation of the saturated permeability and the ratio between the major and minor scales of fluctuation on the pressure bound are investigated.

1 INTRODUCTION

Natural slopes are highly heterogeneous as a result of depositional and post-depositional processes (DeGroot & Baecher 1993; Lacasse & Nadim 1997). Spatial variability can be characterized using random field theory (e.g. Vanmarcke 1977). In a random field, the variables exhibit autocorrelation, which is a tendency for soil properties at one point to be correlated to soil properties at nearby points. A classic paper that introduces the spatial correlation concept was published by Vanmarcke (1977). According to the theory, random fields are classified into two groups. A random field is called stationary if the joint probability distribution that governs the field is invariant when translated over the parameter space; a random field is noted non-stationary when a deterministic trend is added to the space. Treatment must first be given to transform a non-stationary dataset into a stationary dataset by removing the deterministic trend when analyzing spatial correlation (Dasaka & Zhang 2012). Two principal directions are defined in this study: the major principal direction along which the properties show the smoothest variation and the minor principal direction along which the properties show the rapidest variation.

Random fields have been extensively applied to geotechnical problems such as slope stability (e.g. Huang et al. 2010; Griffiths et al. 2011; Zhu et al. 2012) and bearing capacity of shallow and deep foundations (Fenton & Griffiths 2003). Stationary random fields were widely simulated in geotechnical applications. A linear trend for undrained shear strength was considered as in Lumb (1966). Hicks & Samy (2002) investigated the influence of heterogeneity on undrained clay slope stability, in which the effective shear strength parameter was treated as a non-stationary random field with the mean strength parameter increasing linearly with depth. Zhang et al. (2011) and others observed inverse segregation of particles in a giant landslide event. The observation confirms that segregation mechanism works by inverse grading, with large particles moving to the top and small particles accumulating at the bottom (Miyamoto et al. 2007). The upper zone of the landslide deposit is more permeable than that of the lower zone. Therefore, it is of great concern to treat the parameter space of saturated permeability as a non-stationary random field with the mean value decreasing from the top to the bottom of a slope, which realistically represents a landslide deposit.

The objectives of this paper are (1) to develop algorithms to generate non-stationary random fields with mean values varying with depth and (2) to figure out the extent the coefficient of saturated permeability and the ratio between the principal scales of fluctuation affects the pore-water pressures in a slope from infiltration analysis.

2 CHARACTERIZING NON-STATIONARY RANDOM FIELDS

2.1 *Random field theory*

Figure 1 shows a schematic of a One-Dimensional (1D) and a Two-Dimensional (2D) stationary random field of a variable, z, with a mean, E(z), a variance, σ^2 and a cumulative probability distribution function, F(z). These three features can be obtained by analyzing field data collected via ground investigation. The scale of fluctuation, θ, is a constant if an isotropic random field is assumed as shown in Figure 1(a). While in a 2D anisotropic random field in Figure 1(b), θ is a function of the directional angle, ϕ, and prescribed principal scales of fluctuation. Spatial correlation models are parametric relationships used to fit the experimental variograms or covariance functions from analysis of field data. Phoon & Kulhawy (1999) and Guide (2005) provided an excellent summary of common variogram models used in practice. Evaluation of correlation structures was also performed by Liu & Chen (2010). Listed below are three common correlation structures in the isotropic form (from Equations 1–3: exponential, Gaussian and spherical):

$$\rho = \exp(-2h/\theta) \tag{1}$$

$$\rho = \exp(-(h/\theta)^2) \tag{2}$$

$$\rho = 1 - 1.5(h/\theta) + 0.5(h/\theta)^3, h \le \theta;\ \rho = 0, h > 0 \tag{3}$$

where ρ is the correlation coefficient of the random variable at two locations at a separation distance of h and θ is the scale of fluctuation. This study adopts the exponential correlation structure as it fits well with geotechnical properties. The anisotropic form of exponential correlation structure can be generally written as

$$\rho = \exp\left[-2\sqrt{\frac{\Delta x^2}{\theta_1^2} + \frac{\Delta y^2}{\theta_2^2}}\right] \tag{4}$$

where Δx and Δy are the horizontal and vertical separation distances between two observations in the space, θ_1 and θ_2 denote the major and minor principal scales of fluctuation, respectively. In this case, the major direction is parallel to the horizontal axis and the minor direction is parallel to the vertical one. Let denote $\theta_h = \theta_1$ and $\theta_v = \theta_1$.

2.2 *Creating covariance matrix*

The covariance matrix is created by computing the correlation coefficient of two points spaced at any distance and in any direction in the parameter

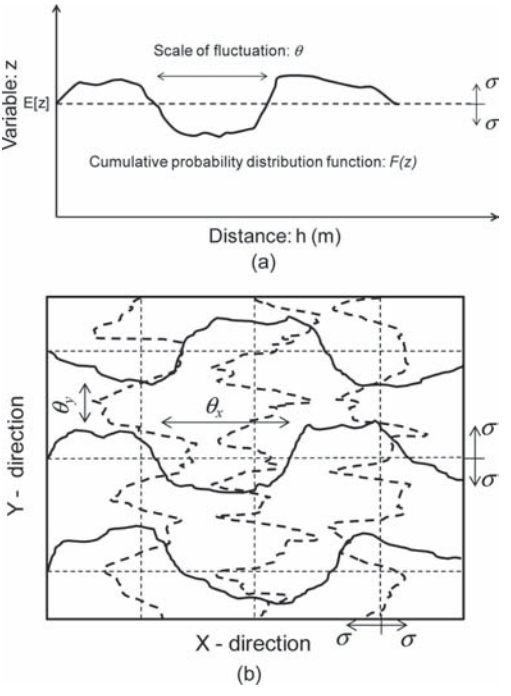

Figure 1. A realization of (a) a 1D random field and (b) a 2D random field with a mean E[z], variance σ^2, and cumulative probability function $F(z)$.

space. The coefficient of correlation in the basic anisotropy case is calculated as an example, assuming that the scale of fluctuation follows an elliptical function and the correlation structure is exponential.

Figure 2 explains the evaluation of the correlation matrix. The grid points which represent the property values in each finite element are involved in the computation of correlation coefficients. For example, if the distance between points 1 and 2 is h_x, the correlation between these two points is calculated by putting the values $\Delta x = h_x$ and $\Delta y = 0$ in Equation 4. Similarly, the correlations of point 1 with points 3, 4, 5 can be established by placing $\Delta x = 2h_x$ and $\Delta y = 0$, $\Delta x = 3h_x$ and $\Delta y = 0$, $\Delta x = 4h_x$ and $\Delta y = 0$, respectively. The correlations of point 1 with points 41, 42 and 43 can be calculated by placing $\Delta x = 0$ and $\Delta y = h_y$, $\Delta x = h_x$ and $\Delta y = h_y$, and $\Delta x = 2h_x$ and $\Delta y = h_y$, respectively. Therefore, values in the first row of the correlation matrix are the correlation coefficients between grid point 1 and other points, 1600 values in a row when the number of zones is 40×40. Hence, considering all the zones, a correlation matrix ρ_x with 1600×1600 elements can be established.

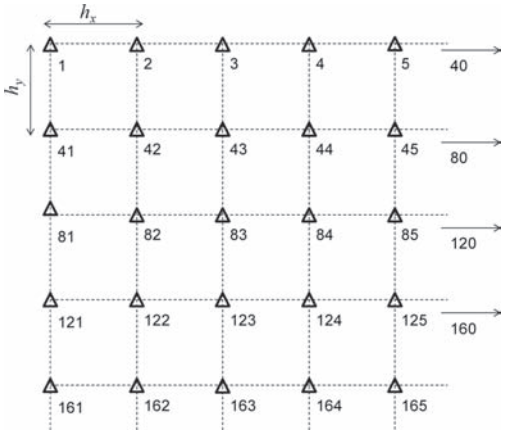

Figure 2. Discretization of a random field with 40 × 40 grid points.

2.3 *Cholesky decomposition*

The correlation matrix is decomposed into the product of a lower triangular matrix and its transpose by Cholesky's decomposition (e.g. Press et al. 2002):

$$L \cdot L^T = \rho_k \tag{5}$$

Given the matrix, L, a correlated standard normal random field is obtained as follows:

$$G_i = \sum_{j=1}^{i} L_{ij} Z_j, \quad i = 1,\ 2,\ 3,\ \ldots\ n \tag{6}$$

where Z_j is a sequence of independent standard normal random variables. A correlated lognormal random field is obtained by transforming the standard normal data.

2.4 *Adding a trend to the lognormal stationary random field*

Stationarity of the data is achieved by removing a low-order polynomial trend of order not higher than quadratic (Brooker 1991), which is usually estimated by the ordinary least squares error approach (Journel & Huijbregts 1978). In most of the studies, the trend function is simply estimated by regression analysis using either linear or polynomial curve fitting (Kulhawy et al. 1992).

Let $\mathbf{X}(x, y)$ denote the generated lognormal stationary anisotropic random field dataset at the desired location $X = x, Y = y$ in the X-Y plane. A deterministic trend $f(y)$ is added to the vertical direction of $\mathbf{X}(x, y)$. For all positions in the X-direction, the general form of $f(y)$ can be written as:

$$f(y) = a + b\left(y - Y_{\min}\right)/\left(Y_{\max} - Y_{\min}\right) \tag{7}$$

where y is the vertical coordinate of a desired position in an analysis domain; a and b are parameters in the linear function; $Y_{\max}$ and $Y_{\min}$ are the maximum and minimum Y-coordinates, respectively. Hence, the non-stationary random field dataset $\mathbf{Y}(x, y)$ can be expressed as:

$$\mathbf{Y}(x, y) = \mathbf{X}(x, y) \times f\left(y\right) \tag{8}$$

In order to better understand the trend in the non-stationary random fields simulated in this study, an example of a rectangular random field with X-coordinates ranging from 0 m to 10 m and Y-coordinates ranging from 15 m to 19 m is taken into account. Values of a and b are assumed as 1 and 10, respectively. Thereafter, $\mathbf{Y}(x, y)$ is written as:

$$\mathbf{Y}(x, y) = \mathbf{X}(x, y) \times \left(1 + 10 \times \left(y - 15\right)/4\right) \tag{9}$$

The mean of the random set in $\mathbf{X}(x, y)$ is 2×10^{-5}, and $\mathbf{Y}(x, y)$ reaches the maximum mean value of 2×10^{-5} at y = 19 m and the minimum mean value of 2.2×10^{-4} at y = 15 m.

The values for $\mathbf{X}(x, y)$ and $\mathbf{Y}(x, y)$ along an arbitrary cross section taken from one realization of random field are shown in Figure 3. The mean value of k_s for the stationary random field is assumed as 2×10^{-5} m/s. According to Equation 9, the mean values for the non-stationary random field decreases from the top (y = 19 m) to the bottom (y = 15 m). It should be noted that the coefficients of variation of k_s are implicitly assumed constant since both the mean and the standard deviation are enlarged simultaneously.

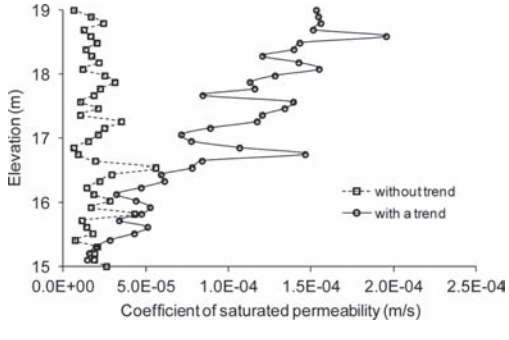

Figure 3. Random values along one arbitrary cross-section of a stationary random field and a non-stationary random field with a trend.

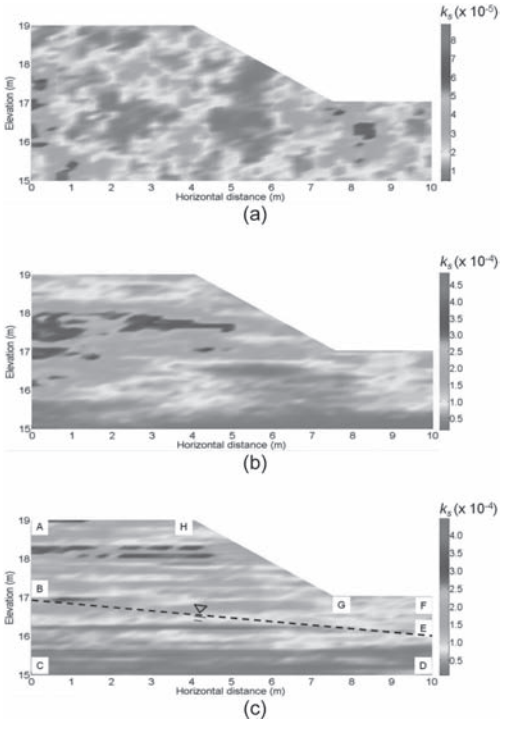

Figure 4. Realizations of non-stationary random fields: (a) stationary isotropic random field with $\mu = 2 \times 10^{-5}$ m/s, COV = 0.5, θ_h = θ_y = 1 m; (b) non-stationary random field with a trend, COV = 0.5, θ_h = 10 m, θ_v = 1 m; (c) non-stationary random field with a trend, COV = 0.5, θ_h = 10 m, θ_v = 0.1 m.

2.5 *Numerical examples of non-stationary random fields*

Typical realizations of random fields are presented in Figure 4. The mean value of coefficient of saturated permeability, k_s, for the stationary random field is 2×10^{-5} m/s. The trend form is taken flowing Equation 9. The Coefficient Of Variation (COV) of k_s is selected as 0.5 (Duncan 2000). The scales of fluctuation are selected as θ_h = 10 m, θ_v = 0.1 m, and θ_h = 10 m, θ_v = 1 m, respectively (Phoon and Kulhawy 1999).

3 PROBABILISTIC INFILTRATION ANALYSIS

In this paper, the steady-state flow in a heterogeneous unsaturated-saturated soil is described by Darcy's law in two dimensions:

$$h = \Psi + y \tag{10}$$

$$q = -k\nabla h \tag{11}$$

where h is the total head; Ψ is the pressure head; y is the elevation head; q is the flux; k is the unsaturated permeability. Considering mass conservation, the governing equation for steady-state seepage can be written as:

$$\frac{\partial q}{\partial x} + \frac{\partial q}{\partial y} = 0 \tag{12}$$

An exponential permeability equation by Leong & Rahardjo (1997) is employed:

$$k = k_s \left(\frac{\theta_w - \theta_r}{\theta_s - \theta_r} \right)^p \tag{13}$$

where θ_w is the volumetric water content; θ_s is the saturated volumetric water content; θ_r is the residual water content at which a large suction change is required to remove additional water from the soil; $(\theta_w - \theta_r)/(\theta_s - \theta_r)$ is the normalized water content; p is a constant depending on the soil type. From Equation 13, the uncertainty of permeability function is characterized by the uncertainty of k_s if p remains unchanged for points within the slope.

This paper makes use of FlexPDE (Guide 2005) to solve the seepage problem. It allows users to input variables in tabulated files by which stochastic finite element analyses are performed repeatedly. The random field grid is superimposed on the finite element mesh in such a way that their corresponding bottom right, bottom left and top left corners coincide with those of the slope. The k_s value at each grid point of the rectangular random field grid is then transferred into the finite element program as an input soil parameter. Bilinear interpolation is performed to map from the rectangular random field grid to the finite element mesh. The region that is outside of the boundary of the finite element mesh is truncated automatically in the finite element program.

Numerical modelling of seepage in a hypothetic slope with the same geometry of the slope in Figure 4(c) is conducted. The boundary conditions are considered deterministic. There is no change in hydraulic head on both sides (B–C, D–E), and the bottom boundary conditions as well as the side boundaries above the water table (A–B, E–F) are impermeable. A groundwater table is fixed at the side boundaries at points B and E. A constant flux of 2×10^{-7} m/s is applied to the surface boundaries A–H, H–G and G–F. For the soil properties in concern, the p value in the permeability function is assumed as 3 for fine sands, and the saturated water content is taken as 0.4. The COV of k_s is suggested as 0.1, 0.5 and 1.0 according to Duncan (2000). The horizontal scale of fluctuation is assumed as 10 m, i.e. five times the slope height.

Table 1. Statistics of k_s in each study case.

Case no.	Coefficient of variation	Scale of fluctuation
1	1.0	$\theta_h = 10$ m, $\theta_v = 0.1$ m
2	0.5	$\theta_h = 10$ m, $\theta_v = 0.1$ m
3	0.1	$\theta_h = 10$ m, $\theta_v = 0.1$ m
4	1.0	$\theta_h = 10$ m, $\theta_v = 1.0$ m
5	0.5	$\theta_h = 10$ m, $\theta_v = 1.0$ m
6	1.0	$\theta_h = 10$ m, $\theta_v = 0.5$ m

The vertical scale of fluctuation is assumed as 1 m, 0.5 m and 0.1 m according to Phoon & Kulhawy (1999). Since the purpose of this study is to investigate how the coefficient of variation of k_s and the ratio between the horizontal and vertical scales of fluctuation affect the pore-water pressures in the slope, Table 1 summarizes the statistics of k_s in each case of non-stationary random field.

4 RESULTS AND DISCUSSIONS OF PROBABILISTIC ANALYSIS

For each case in Table 1 together as well as an isotropic case, 1000 realizations of k_s random fields are simulated with the number of realizations sufficient to reach required computational accuracy. For each realization, the pore-water pressures are calculated by implementing the finite element method via the FlexPDE platform. The 25%, 50% and 75% quantiles of pore-water pressures above the groundwater table along the middle of slope for cases in Figures 4(a)–(c) are estimated at each elevation. Results are shown in Figures 5(a)–(c). The uncertainties in pore-water pressures are reflected by the width of pressure bound, which is defined as the difference between the 75% and 25% quantiles. A wider pressure bound implies larger uncertainty. The results regarding the bound are further interpretated as shown in Figures 6 and 7.

The effects of the COV of k_s and ratios between θ_h and θ_v on the width of pressure bound are investigated. Figure 6 shows the variation of the width of pressure bound with the COV of k_s. It implies that the pore-water pressures have a wider range of values at a higher value of COV. Figure 7 shows the changes in the width of pressure bound with the ratio between the horizontal and vertical scales of fluctuation. The horizontal scale of fluctuation is constant for all the study cases. The change in the vertical scale of fluctuation controls the rate of variation of k_s with depth. A ratio of 100 induces the rapidest variation of k_s in the study cases.

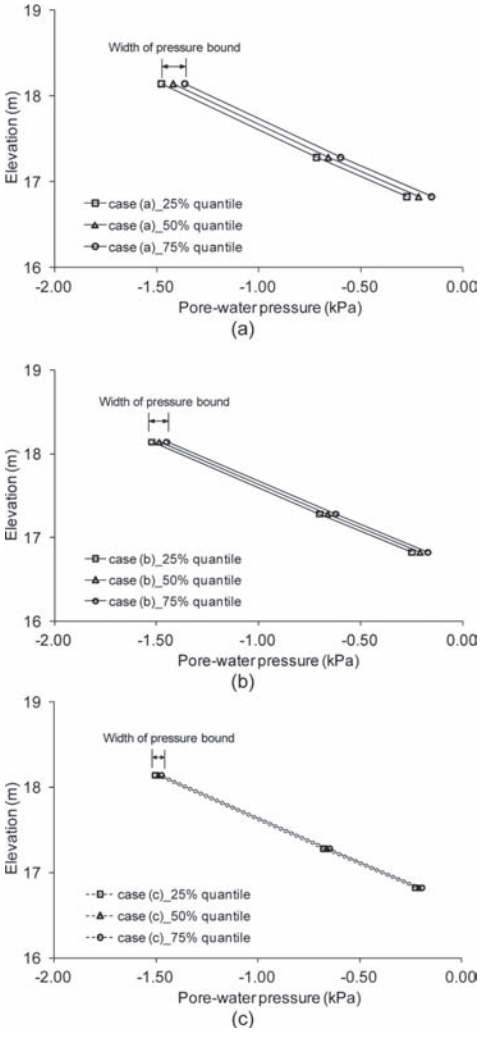

Figure 5. The 25%, 50% and 75% quantiles of pore-water pressures along the middle of the slope for cases (a), (b) and (c) in Figure 4.

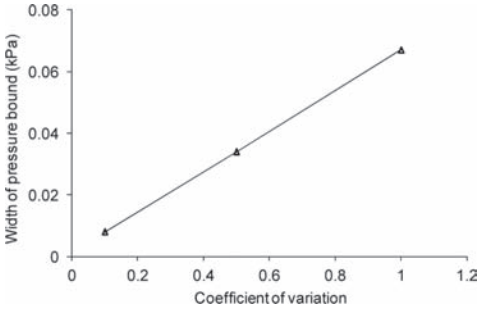

Figure 6. Variation of width of pressure bound with coefficient of variation of saturated permeability.

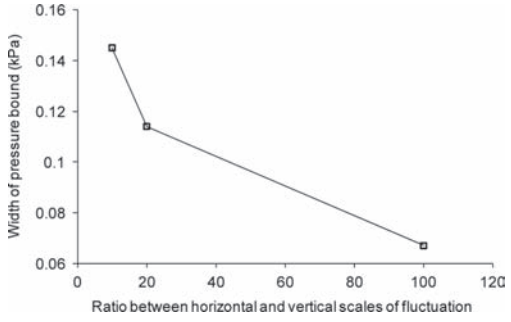

Figure 7. Variation of width of pressure bound with the ratio between horizontal and vertical scales of fluctuation.

It can be noted from Figure 7 that a more ragged distribution of k_s in the vertical direction leads to a smaller uncertainty of pressures.

5 SUMMARY AND CONCLUSIONS

Numerical algorithms were developed to model non-stationary random fields with mean values varying with depth. Steady–state analysis of seepage in the generated non-stationary random fields was carried out.

The generated profiles of pore-water pressures from infiltration analysis were further interpretated. The 25%, 50% and 75% quantiles of pore-water pressures were estimated along the depth of the slope. The width of pressure bound can be used to represent the uncertainty of hydraulic responses.

Results show that the COV of k_s and ratios between the horizontal and vertical scales of fluctuation have impacts on the pressure bounds. A wider range of pore-water pressures is expected at a higher value of COV. A more rapid variation of k_s in the vertical direction leads to a smaller uncertainty of pressures.

ACKNOWLEDGEMENTS

The work in this paper was substantially supported by the National Basic Research Program of China (973 Program) (No. 2011CB013506) and the Research Grants Council of the Hong Kong Special Administrative Region (No. HKUST09/CRF/9).

REFERENCES

Brooker, P.I. 1991. *Geostatistical Primer*, World Scientific, Singapore.

Dasaka, S. & Zhang, L.M. 2012. Spatial variability of in situ weathered soil. *Géotechnique* 62(5): 375–384.

DeGroot, D.J. & Baecher, G.B. 1993. Estimating autocovariance of in-situ soil properties. *Journal of Geotechnical Engineering* 119(1): 147–166.

Duncan, J.M. 2000. Factors of safety and reliability in geotechnical engineering. *Journal of Geotechnical and Geoenvironmental Engineering* 126(4): 307–316.

Fenton, G.A. & Griffiths, D.V. 2003. Bearing-capacity prediction of spatially random c-φ soils. *Canadian Geotechnical Journal* 40(1): 54–65.

Griffiths, D.V., Huang, J.S. & Fenton, G.A. 2011. Probabilistic infinite slope analysis. *Computers and Geotechnics* 38(4): 577–584.

Guide, F.U. 2005. *Version 5.0, PDE Solutions*. Inc., Antioch, CA, USA.

Hicks, M.A. & Samy, K. 2002. Influence of heterogeneity on undrained clay slope stability. *Quarterly Journal of Engineering Geology and Hydrogeology* 35(1): 41–49.

Huang, J.S., Griffiths, D.V. & Fenton, G.A. 2010. System reliability of slopes by RFEM. *Soils and Foundations* 50(3): 343–353.

Journel, A.G. & Huijbregts, C.J. 1978. *Mining geostatistics*, Academic press London.

Kulhawy, F., Birgisson, B. & Grigoriu, M. 1992. Reliability-based foundation design for transmission line structures. *Electric Power Research Inst.*, Palo Alto, CA; Cornell Univ., Ithaca, NY, USA.

Lacasse, S. & Nadim, F. 1997. Uncertainties in characterizing soil properties. *Publikasjon-Norges Geotekniske Institute* 201: 49–75.

Leong, E.C. & Rahardjo, H. 1997. Permeability functions for unsaturated soils. *Journal of Geotechnical and Geoenvironmental Engineering* 123(12): 1118–1126.

Liu, C.N. & Chen, C.H. 2010. Estimating spatial correlation structures based on CPT data. *Georisk* 4(2): 99–108.

Lumb, P. (1966). The variability of natural soils. *Canadian Geotechnical Journal* 3(2): 74–97.

Miyamoto, H., Yano, H., Scheeres, D.J., Abe, S., Barnouin-Jha, O., Cheng, A.F., Demura, H., Gaskell, R.W., Hirata, N. & Ishiguro, M. 2007. Regolith migration and sorting on asteroid Itokawa. *Science* 316(5827): 1011–1014.

Phoon, K.K. & Kulhawy, F.H. 1999. Characterization of geotechnical variability. *Canadian Geotechnical Journal* 36(4): 612–624.

Press, W.H., Teukolsky, S.A., Vetterling, W.T. & Flannery, B.P. 2002. *Numerical recipes*, Cambridge University Press Cambridge.

Vanmarcke, E.H. 1977. Probabilistic modeling of soil profiles. *Journal of the Geotechnical Engineering Division* 103(11): 1227–1246.

Zhang, L.M., Xu, Y., Huang, R.Q. & Chang, D.S. 2011. Particle flow and segregation in a giant landslide event triggered by the 2008 Wenchuan earthquake, Sichuan, China. *Natural Hazards and Earth System Sciences* 11: 1153–1162.

Zhu, H., Zhang, L.M., Zhang, L.L. & Zhou, C.B. 2013. Two-dimensional probabilistic infiltration analysis with a spatially varying permeability function. *Computers and Geotechnics* 48: 249–259.

5 *Geohazards*

This page intentionally left blank

Geotechnical Safety and Risk IV – Zhang et al. (eds)
© 2014 Taylor & Francis Group, London, ISBN 978-1-138-00163-3

Integrating seismic hazard analyses with geotechnical site characterization for liquefaction potential assessment in Kaohsiung area

D. Huang & J.P. Wang
Department of Civil and Environmental Engineering, Hong Kong University of Science and Technology, Kowloon, Hong Kong, China

ABSTRACT: Probabilistic Seismic Hazard Analysis (PSHA) has been widely used to estimate the ground motion intensity that should be accounted for in structure design. Here, an in-depth PSHA study for Kaohsiung, the metropolitan area in South Taiwan, is carried out. On the other hand, soil liquefaction and subsequent structural damage are usually reported in a catastrophic earthquake event, such as numerous significant incidents of liquefaction in inland alluvial areas during the 1999 Chi-Chi earthquake. A quantitative framework to evaluate earthquake-induced soil liquefaction potential is proposed herein, including earthquake hazard assessment and geotechnical liquefaction evaluation. This framework is further demonstrated with a case study for a thoroughly-investigated site in Kaohsiung. Results show that the liquefaction potential evaluated with existing methods is to some extent dependent on the earthquake hazard in terms of the occurrence probability of large-size earthquakes at the study site. Ground improvement is suggested considering severe consequences of ground failure.

1 INTRODUCTION

Soil liquefaction is one of the disasters during earthquakes. For example, soil liquefaction and subsequent structural damages were reported in many locations in Taiwan during the Chi-Chi earthquake in 1999 (Chu et al. 2004, Juang et al. 2002). Serious consequences include lateral spreading of sloping ground and settlement caused by reconsolidation of the liquefied soils (Seed & Idriss 1971). A few empirical methods have been proposed to evaluate the liquefaction potential by comparing "load" induced by one or more earthquakes with "resistance" based on the in-situ methods at the site. (Seed & Idriss 1971, Iwasaki et al. 1982, Iwasaki 1986, Tokimatsu & Yoshimi 1983).

However, most studies use deterministic methods to evaluate earthquake loading. In contrast, only a few studies consider both uncertainties from geotechnical properties and earthquake geology around the site (Lee et al. 2010, Wang & Huang 2012). As a result, the underlying scope of this study is to evaluate soil liquefaction given different durations of time, or the time-variant soil liquefaction potentials, with equal importance and effort spent to geotechnical site characteristics and earthquake geology. Both analyses are independently carried out with existing approaches, and the results are then combined to attain to the ultimate goal: Whether or not ground improvement is needed at the site. The framework is presented with a case study in Kaohsiung metropolitan area, where some important civil engineering projects are under construction or development at the site.

2 LIQUEFATION ANALYSES

2.1 *Geotechnical site characteristics*

Figure 1 shows the location of the site within Kaohsiung City (the second most important city in Taiwan), together with the seismicity since 1900 (i.e., more than 55,000 events). It is worth noting that this earthquake catalog was used for the seismic hazard analyses, as it has been analyzed for quantifying earthquake potentials for Taiwan (Wang et al. 2011, 2012a, 2012b).

The geotechnical condition at the site was intensively investigated during the construction of the mass-rapid-transit system (i.e., the subway system) of this city starting in the 1990s. The soil at the site is mainly silty sand, with SPT N-values around 4~18 at different depth (Lu 2006). Moreover, at this study site the ground water table is about 3 m below the ground surface (Lu 2006). Figure 2 shows a typical boring log at the site. Given such geotechnical information, the factor of safety of soil liquefaction was found greater than 1.0 at most depths down to 20 m below the ground.

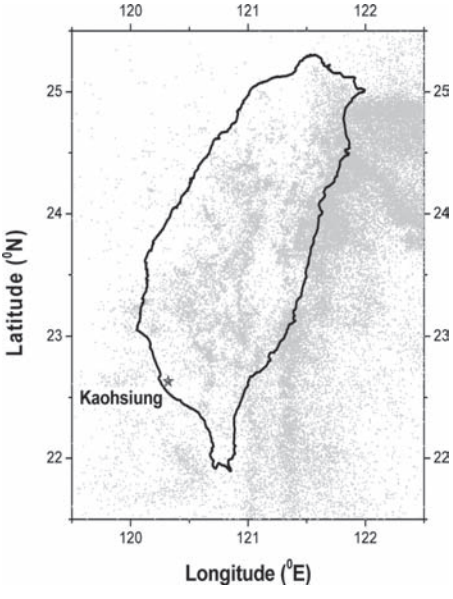

Figure 1. Spatial distribution of the seismicity around Taiwan since 1900 and the location of study site (Cheng et al. 2007, Wang et al. 2011, 2012a, 2012b).

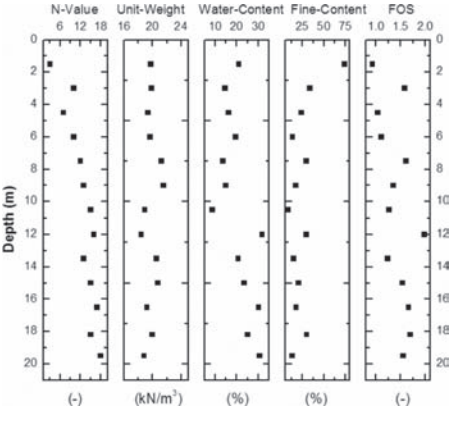

Figure 2. Geotechnical site characteristics and the factors of safety of soil liquefaction at different depths given a deterministic PGA value equal to 0.2 g.

2.2 *Empirical method for liquefaction triggering*

Given the geotechnical site condition, the liquefaction potential index (here denoted as L) proposed by Iwasaki (1986) and Iwasaki et al. (1982) can be calculated as follows:

$$L = \int_{z=0}^{20} A(10 - 0.5z)dz \tag{1}$$

where z is the depth below the ground, and A is a random variable related to the Factor Of Safety (FOS) of soil liquefaction at a given depth:

$$A = \begin{cases} 1 - FOS & FOS < 1 \\ 0 & FOS \geq 1 \end{cases} \tag{2}$$

In addition to the algorithms, Iwasaki also offered some suggestion to the messages behind this index. When L is greater than 15, the site is considered "Very High Potential" in liquefaction, followed by "Relatively High Potential" and "Relatively Low Potential" as L is in the ranges of 5~15 and 0~5, respectively. The last category is "Very Low Potential" when L is equal to zero.

It is worth noting that a few methods have been proposed to calculate the FOS for soil liquefaction. In short, it is based on the proportion of Cyclic Resistance Ratio (CSR) to Cyclic Stress Ratio (CRR). As for CRR computation, we followed the framework of Seed & Idriss (1971); as for CSR, we adopted three common methods as to account for the imperfect models or the so-called epistemic uncertainty (Ang & Tang 2007), namely the NCEER approach (National Center for Earthquake Engineering Research), JRA approach (Japan Road Association), and T & Y approach (Tokimastu and Yoshimi). Since the three approaches have been generally accepted in the community of earthquake engineering, and the underlying scope of this study is not to modify them to develop a new method, the three analyses are not elaborated in this paper, but readers can refer to the original papers or technical guideline for methodological details (Tokimatsu & Yoshimi 1983, Japan Road Association 1996, Youd & Idriss 1997).

2.3 *Liquefaction potential for the site*

With the existing liquefaction analyses, the relationship between liquefaction potential index (L) and Peak Ground Acceleration (PGA) at the study site is shown in Figure 3. Accordingly, as PGA is greater than 0.31 g in an earthquake event, the site is "Very High Potential" (i.e., $L \geq 15$) to liquefy.

However, it should be noted again that this information alone should not be enough to answer the question if the soil liquefaction will occur in a given time span. This question should only be properly managed until the earthquake potential or the probability of PGA > 0.31 g within a finite time interval of interest also becomes available.

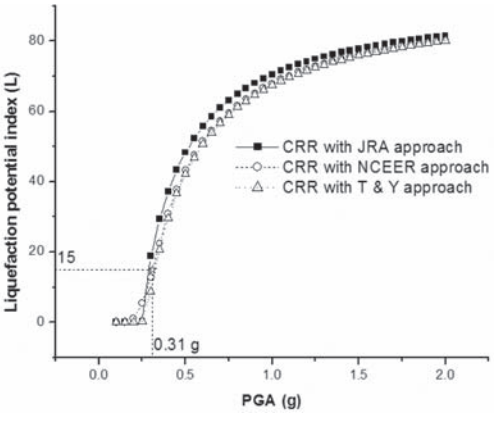

Figure 3. The relationship between liquefaction potential index L and PGA at the study site with three existing approaches; this relationship is mainly a refection to geotechnical site characteristics and to a deterministic scenario in PGA.

3 PROBABILISITC SEISMIC HAZARD ANALYSIS

3.1 *Overview of the method*

Probabilistic Seismic Hazard Analysis (PSHA) developed in the late 1960s (Cornell 1968, McGuire 1995) has become a common approach in evaluating the annual rate of site-specific earthquake motions of exceedance, e.g., PGA > 0.31 g. A number of PSHA case studies, including those for Taiwan, have been reported in the last few years (Cheng et al. 2007, Wang et al. 2013). Moreover, a recent technical guideline (USNRC 2007) prescribing the use of PSHA to develop site-specific earthquake-resistant designs for critical structures should also reflect to its general acceptance in the community of earthquake engineering.

The essence of PSHA is to account for the uncertainties of the earthquake's size, location, and motion attenuation. Its governing equation can be expressed as follows (Kramer 1996):

$$\lambda(Y > y^*) = \sum_{i=1}^{N_S} v_i \sum_{j=1}^{N_M} \sum_{k=1}^{N_D} \Pr\left[Y > y^* \mid m_j, d_k\right] \times \Pr\left[M = m_j\right] \times \Pr\left[D = d_k\right] \quad (3)$$

where $\lambda(Y > y^*)$ is the annual rate of ground motion $Y > y^*$ (Y can be PGA or a specific spectral acceleration), and the three probability terms are the underlying components of this analysis, calculating the respective probability in earthquake size (M), source-to-site distance (D), and the probability of motion of exceedance (i.e., $Y > y^*$) owing to the uncertainty of motion attenuation. Moreover, v is the annual rate of earthquakes; N_S is the number of seismic sources; N_M and N_D are the number of data bins in magnitude and distance probability functions, respectively.

After the annual rate of seismic hazard (i.e., $Y > y^*$) calculated with Equation (3), its occurrence probability in time can be computed by assuming seismic hazard is a Poissonian random variable, which makes its occurrence probability given a time span follow the exponential distribution (Kramer 1996):

$$\Pr(Y > y^* \mid \lambda, t) = 1 - e^{-\lambda t} \quad (4)$$

where λ is the mean annual rate of $Y > y^*$, and t is the time of interest.

3.2 *The recent PSHA study for Taipei*

Wang et al. (2013) recently conducted a PSHA case study for Taipei. Moreover, that specific PSHA study endeavored to follow the framework of the so-called "robust" seismic hazard analysis (Klugel 2008), with the calculation being repeatable and the inputs being traceable and verifiable. The concept of analytical "robustness" is somewhat a solution and response to the criticism of PSHA being somehow "egocentric" to those who perform the analysis, when the underlying inputs cannot be scientifically justified (Krinitzsky 2003).

As a result, the following PSHA for the study site is basically to follow the key inputs given in the most recent PSHA for Taiwan (Wang et al. 2013). It is worth noting that although the referred study focused on a site in North Taiwan, the key inputs, such as seismic source models (shown in Fig. 4),

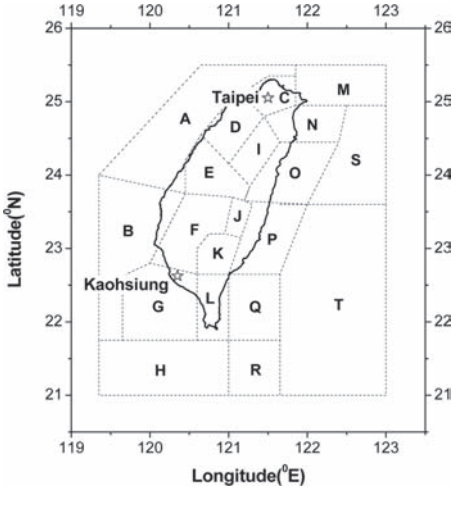

Figure 4. The up-to-date seismic source model for Taiwan (after Cheng et al. 2007, Wang et al. 2012, 2013).

model parameters (summarized in Table 1), should be generic for Taiwan, as they were calibrated with nationwide earthquake data around the region.

3.3 *Seismic hazard recurrence probability*

With the annual rate of seismic hazard (see Fig. 5), Figure 6 shows the hazard's occurrence probability in four time spans through Eq. 4.

Table 1. Summary of recurrence parameters and maximum magnitudes of each source zone (Cheng et al. 2007).

Source zone	*a*-value	*b*-value	Maximum magnitude
A	2.670	0.828	6.5
B	3.790	1.074	6.5
C	3.579	1.014	7.1
D	4.802	1.334	7.3
E	4.420	1.087	7.3
F	4.720	1.117	7.3
G	3.580	0.876	6.5
H	3.071	0.756	7.3
I	4.450	1.137	6.5
J	3.210	0.979	6.5
K	4.490	1.101	6.5
L	3.510	0.918	7.3
M	3.307	0.803	6.5
N	5.345	1.134	8.0
O	5.440	1.107	8.3
P	4.920	1.058	7.8
Q	4.170	0.898	7.8
R	3.640	0.913	7.8
S	5.104	1.036	8.0
T	4.110	0.900	7.8

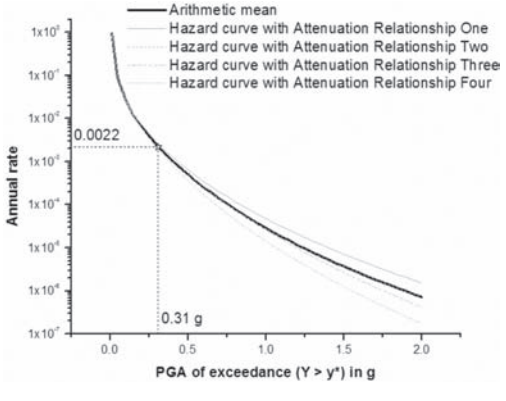

Figure 5. PSHA hazard curves at the study site with the use of four PGA attenuation relationships to account for such an epistemic uncertainty.

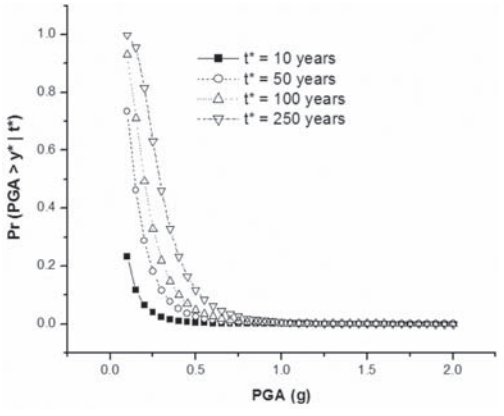

Figure 6. PGA exceedance probabilities within four time spans at the study site, given the annual rate of seismic hazard calculated from PSHA (Fig. 5).

Given PGA > 0.31 g with an annual rate of 0.0022 through PSHA, the occurrence probability for such an event is about 20% as far as a time span of 100 years is concerned. On the other hand, the occurrence probability is reduced to 2% when the time of interest is decreased to 10 years.

4 LIQUEFACTION POTENTIAL ASSESSED OVER TIME

Accordingly, at this study site we found that $L = 15$ was on the basis of PGA > 0.31 g, and we have also characterized a 20% occurrence probability for PGA > 0.31 g in 100 years, we can therefore combine the two pieces of underlying information to evaluate time-variant soil liquefaction with a new index referred to as "soil liquefaction index per unit time," denoted as $\tilde{L}_{T=t^*}$. In this instance, $\tilde{L}_{T=100\,yrs}$ is equal to 3.0 per 100 years given a unique scenario PGA > 0.31 g. Because there are infinite scenarios other than PGA > 0.31 g that can cause different levels of soil liquefaction potential, Figure 7 shows the relationships between $\tilde{L}_{T=t^*}$ and PGA given four periods of time, basically a combination of Figures 3 and 6. As a result, the integration of the curve is the resulting soil liquefaction index per unit time covering any possible scenario with a small PGA to a large PGA. For example, $\tilde{L}_{T=100\,yrs}$ is about 1.18 at the study site.

The relationship between $\tilde{L}_{T=t^*}$ and t^* at the site with repetitive calculations from $t^* = 1$ year to $t^* = 1{,}000$ years is nearly a perfect polynomial function obtained with regression analysis on the 1,000 points:

$$\tilde{L}_{T=t^*} = -0.000003\,t^{*2} + 0.0112\,t^* + 0.0887 \qquad (5)$$

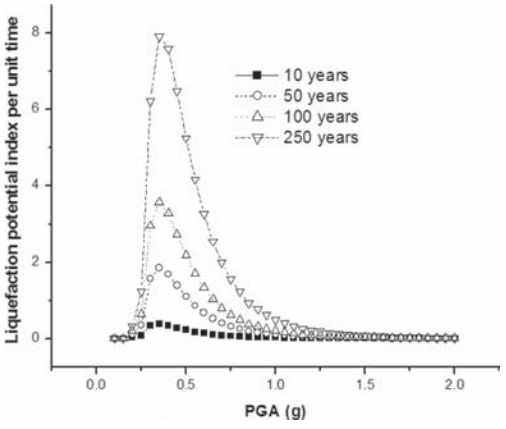

Figure 7. The relationship between liquefaction potential index per unit time and PGA at the study site.

With this time-variant relationship based on geotechnical site characteristics and regional earthquake geology, the liquefaction potential within a normal engineering time span is "Relatively Low Potential" at the site. As the time span of interest is increased to around 500 years, the site becomes "Relatively High Potential" as $L > 5$, according to the framework of Iwasaki.

5 DISCUSSIONS

5.1 *Rare events and low liquefaction potential*

As seeing the result, we were also somehow surprised learning that the study site is subject to low liquefaction potential given a normal engineering time span, because the soil at the site seems rather liquefiable. However, the result is comprehensible given the fact that large-size earthquakes are the underlying driving force to soil liquefaction, which are by all means rare, say, once in hundreds of years or longer. In other words, the low occurrence probability of "liquefaction earthquakes" is the underlying cause to low liquefaction potential within an engineering time span. In other words, no matter how liquefiable the soil would be, the liquefaction probability is still nominal within a "short" period of time (in geological scale), especially when the site is located in a geologically stable region, such as Hong Kong.

6 CONCLUSIONS

This study presents a new integrated approach from soil liquefaction evaluation, to seismic hazard assessment, to decision-making whether or not ground improvement is needed at the site. This framework was demonstrated with a case study for a site in South Taiwan. The result shows that the liquefaction potential evaluated with existing methods is rather high based on geotechnical characteristics at the study site. However, the liquefaction potential is significantly reduced given a normal engineering time span (e.g., 100 years), because of the low occurrence probability of large-size earthquakes within such a "short" geological time. This relationship between highly liquefiable soil and low liquefaction risk is comprehensible: No matter how liquefiable the soil would be, soil liquefaction at the site will not be induced due to very low probability of large magnitude earthquakes.

REFERENCES

Ang, A. & Tang, W. 2007. *Probability Concepts in Engineering: Emphasis on Applications to Civil and Environmental Engineering*. John Wiley & Sons, New Jersey.

Cheng, C.T., Chiou, S.J., Lee, C.T., Tsai, Y.B. 2007. Study on probabilistic seismic hazard maps of Taiwan after Chi-Chi earthquake. *Journal of GeoEngineering* 2:19–28.

Chu, D.B., Stewart, J.P., Lee, T.S., Tsai, J.S., Lin, P.S., Chu R.B., Hsu, S.C., Yu, M.S., Wang, C.H. 2004. Documentation of soil conditions at liquefaction and non-liquefactions site from 1999 Chi-Chi (Taiwan) earthquake. *Soil Dynamics and Earthquake Engineering* 24:647–657.

Cornell, C.A. 1968. Engineering Seismic Risk Analysis. *Bulletin of the Seismological Society of America* 58: 1583–1606.

Iwasaki, T. 1986. Liquefaction and flow during earthquakes. *Geotechnique* 43:351–415.

Iwasaki, T., Tokida, K., Tatsuoka, F., Watanabe, S., Yasuda, S., Sato, H. 1982. Microzonation for soil liquefaction potential using simplified methods. *Proc. 3rd International Conference on Microzonation, Seattle,* 3:1319–1330.

Japan Road Association, 1996. *Guidelines and Comments to Design of Roads and Bridges.* Volume V: Earthquake Resistant Design, (in Japanese).

Juang, C.H., Yuan, H., Lee, D.H., Ku, C.S. 2002. Assessing CPT-based methods for liquefaction evaluation with emphasis on the cases from the Chi-Chi, Taiwan earthquake. *Soil Dynamics and Earthquake Engineering* 22:241–258.

Klugel, J.U. 2008. Seismic hazard analysis—Quo vadis? *Earth-Science Reviews* 88:1–32.

Kramer, S.L. 1996. *Geotechnical Earthquake Engineering*. Prentice Hall Inc., New Jersey, pp. 117–133.

Krinitzsky, E.L. 2003. How to combine deterministic and probabilistic methods for assessing earthquake hazards. *Engineering Geology* 70:157–163.

Lee, Y.F., Chi, Y.Y., Juang, C.H., Lee, D.H. 2010. Annual probability and return period of soil liquefaction in Yuanlin, Taiwan attributed to Chelungpu Fault and Changhua Fault. *Engineering Geology* 114:343–353.

Lin, P.S., Lee, C.T., Cheng, C.T., Sung, C.H. 2011. Response spectral attenuation relations for shallow crustal earthquakes in Taiwan. *Engineering Geology* 121:150–164.

Lu, C.W. 2006. *Report for hazard prevention and mitigation project for Kaohsiung city*. Sub- project: Liquefaction hazard map.

McGuire, R.K. 1995. Probabilistic seismic hazard analysis and design earthquakes: closing the loop. *Bulletin of the Seismological Society of America* 85:1275–1284.

Seed, H.B., Idriss, I.M. 1971. Simplified procedure for evaluating soil liquefaction potential. *Journal of the Soil Mechanics and Foundations Division* 97:1249–1273.

Tokimatsu, K., Yoshimi, Y. 1983. Empirical correlationship of soil liquefaction based on NSPT value and fines content. *Soil Foundation* 23:56–74.

U.S. NRC, 2007. *A performance-based approach to define the site-specific earthquake ground motion*. United States Nuclear Regulatory Commission, Washington.

Wang, J.P., Brant, L., Wu, Y.M., Taheri, H. 2012a. Probability-based PGA estimations using the double-lognormal distribution: including site-specific seismic hazard analysis for four sites in Taiwan. *Soil Dynamics and Earthquake Engineering* 42:177–183.

Wang, J.P., Chan, C.H., Wu, Y.M. 2011. The distribution of annual maximum earthquake magnitude around Taiwan and its application in the estimation of catastrophic earthquake recurrence probability. *Natural Hazards* 59:553–570.

Wang, J.P., Huang, D. 2012. Comment on "Annual probability and return period of soil liquefaction in Yuanlin, Taiwan attributed to Chelungpu Fault and Changhua Fault" by Lee et al., in Engineering Geology, 114: 343–353. *Engineering Geology* 149–150:93–96.

Wang, J.P., Huang, D., Chang, S.C., Wu, Y.M. 2012b. New evidence and perspective to the Poisson process and earthquake temporal distribution from 55,000 events around Taiwan since 1900. *Natural Hazards Review-ASCE*, doi: 10.1061/(ASCE)NH.1527-6996.0000110.

Wang, J.P., Huang, D., Cheng, C.T., Shao, K.S., Wu, Y.C., Chang, C.W. 2013. Seismic hazard analysis for Taipei City including deaggregation, design spectra, and time history with Excel applications. *Computers & Geosciences* 52: 146–154.

Wang, J.P., Xu, Y. 2012. The site selection of the Longman nuclear power plant in Taiwan. *International Journal of Architecture, Engineering and Construction* 36:251–256.

Youd, T.L., Idriss, I.M. 1997. NCEER Workshop on Evaluation of Liquefaction Resistance of Soils, Nat. Ctr. Earthq. Eng. Res., State Univ. of New York at Buffalo.

Geotechnical Safety and Risk IV – Zhang et al. (eds)

Landslide considerations for low cost remedial works for the Karakorum Highway, Pakistan

A.D. Mackay
Nishimatsu Construction Company Ltd., Hong Kong, China
Formerly SMEC Asia Ltd., Hong Kong, China

ABSTRACT: The Pakistan section of the Karokorum Highway runs from Attobad in the south, crossing Pakistan's north-western frontier mountainous region to the Khunjerab Mountain Pass, in the north. This section of the highway is over 800 long and rises to a maximum elevation of about 4,700 m above sea level, making it the world's highest paved international highway. Along the majority its length the alignment follows the route of the Indus River, situated between the Himalaya and Karakorum mountain ranges. During 8 October 2005 a severe earthquake struck the region triggering landslides impacting the highway and destabilizing the natural terrain and cut slopes. This paper provides an overview of the instability of the region with particular attention specific inspections along the highway, carried out prior to 2010 impacted by the 2005 earthquake event. Details of the landslide assessment approach, particularly detailed site reconnaissance survey, are summarised for specific locations along the highway running through the Jhelan Valley. The findings of the landslide characterization and stabilization measures based on the landslide assessment are presented. The proposed stabilization measures included river erosion protection, debris removal, slope cut back and slope support.

1 INTRODUCTION

The Pakistan Karakorum Highway provides a vital connection between Pakistan's main cities and the People's Republic of China (PRC). It rises to about 4,700 m above sea level (asl) at its highest level and once connected Pakistan with the ancient Mongolian capital city of Karakorum during the 13th century. Due to the tectonic activity in the region, the effects of undercutting by the main river systems and the climate and steep terrain, the area is prone to severe instability. In particular a severe earthquake occurred on the 8 October 2005, with an epicenter located near Muzaraffarabad, devastating large areas of the Pakistan North West (NW) frontier, severely impacting the highway. This paper provides an overview of specific landslide locations along the highway impacted by the earthquake events, and outlines approaches to landslide evaluation, including site reconnaissance, involving geological mapping.

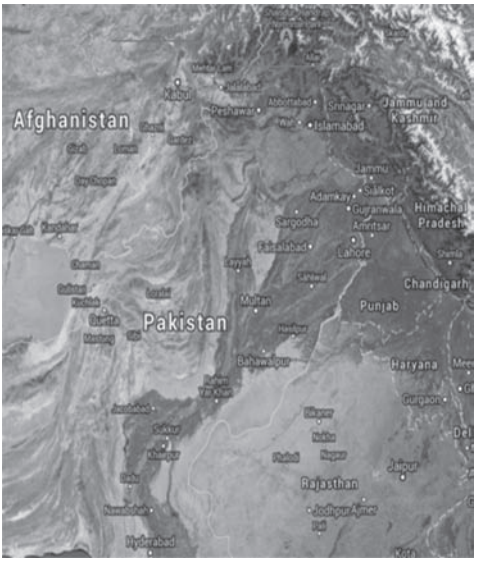

Figure 1. General location, Pakistan North West Frontier (Google Earth, 2011).

2 SETTING

2.1 *Geographical features impacting instability*

The Karakorum Highway runs through the NW Frontier of Pakistan. Refer to Figures 1 and 2 for the location.

The Highway runs to a maximum altitude of 4,700 m asl; commencing from Abbotobad to the south, running across the mountainous region to the Khunjerab Mountain Pass in the north. Refer to Figure 3 for the alignment.

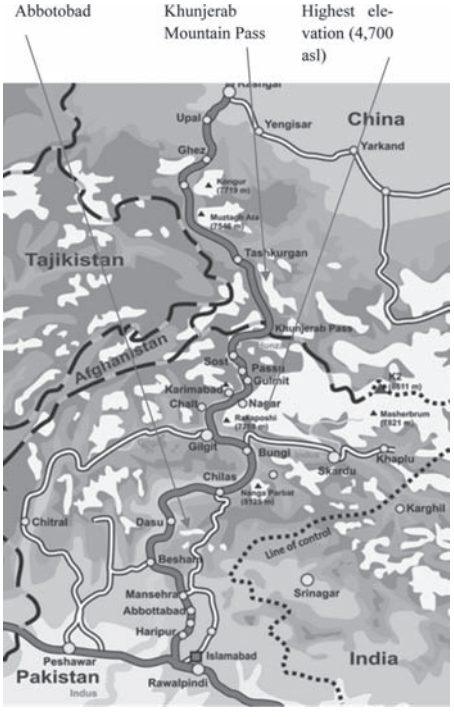

Figure 2. Karakorum Highway alignment.

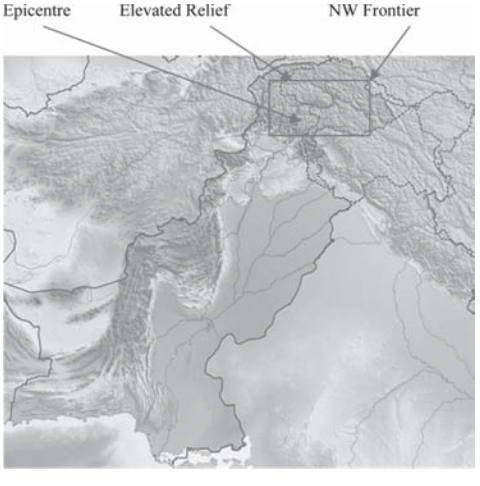

Figure 3. Pakistan relief and 2005 earthquake epicentre.

Due to the elevated and abrupt relief in northern Pakistan the annual rainfall exceeds 700 mm during the monsoon, originating from the Arabian Sea. During July to September this rainfall increases to 1000 mm annually towards the highest elevations (Muslehuddin et al., 2005). Refer to Figure 3 for the terrain relief in Pakistan.

The combination of increased annual rainfall, river erosion along the foot of the mountain ranges, steep terrain and intense tectonic activity in the region exacerbates instability, particularly sensitive locations along the Karakorum highway.

2.2 *Earthquake, 2005*

Pakistan has regions of intense tectonic activity, generally coinciding with young mountain formation. Tectonic activity is particularly intense in the NW Frontier, as presented in Figures 3 and 4.

On October 8, 2005, an earthquake of magnitude of 7.6 occurred with the epicenter located in the NW frontier of Pakistan, about 17 km north of Muzaffarbad and 100 km north-east of Islamabad. This earthquake coincided towards the end of the Pakistan monsoon in the region. About 100,000 fatalities occurred and 3 million persons were left homeless. The effects significantly altered the character of the mountain slopes and drainage basins. The earthquake intensity in the vicinity of the Karakorum Highway and main zones of settlement is shown in Figure 5.

The tectonic intensity in this region is generated from the incremental northern movement of the Indian Plate, about 40 mm/year, into the Eurasian Plate. This movement generates uplifts in excess of 7 mm/year (Coward et al., 1985). As presented

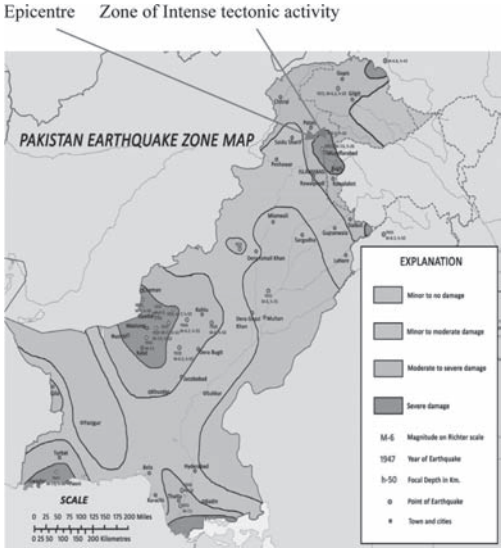

Figure 4. Pakistan earthquake intensity.

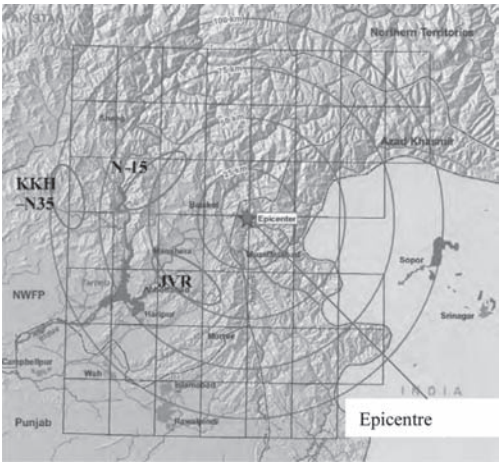

Figure 5. Pakistan earthquake intensity and epicentre.

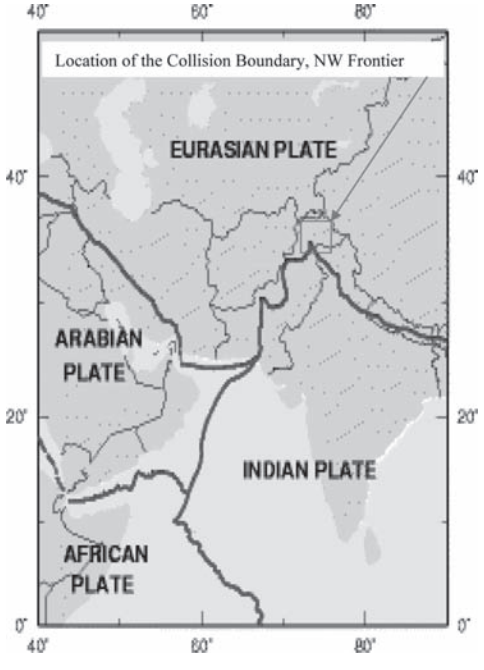

Figure 6. Continental plate locations.

in Figure 6 complications in the tectonic activity occur due to the contortion in the collision zone boundary, "syntaxis", as the plates collide (Farah et al., 1984).

The collision zone is referred to as the "Hazara-Kashmir-Syntaxis" and is associated with intense folding. The Karakorum mountain range, comprising the Kohistan, Ladahk and Karokoram Block uplifts, has occurred north of this zone and the faults, valleys, drainage catchments and major rivers systems associated with this uplift trend in similar alignment to the syntaxis. Further north the Karakorum mountain range bounds the Himalayas along the Khyber Pass, Afghanistan. The "Hazara-Kashmir-Syntaxis" is estimated to be the Miocene geological age group, ranging from about 5 to 23 Ma (Coward et al., 1985).

Figure 7. Plate collisions, NW Pakistan.

The uplifted sedimentary deposits in the region date from the middle to late Tertiary age groups, 2 to 50 Ma. This coincides with the age of the Himalayan orogeny, which has ultimately deformed all the rocks in the region. Recent deposits include alluvium and colluvium formed from debris flows, talluvium, debris fans, glacial deposits and river terrace depositions.

3 GROUND CONDITIONS

3.1 *Site investigation approaches*

A Site Investigation (SI) was initiated to assess the landslides impact to the highway. This included a literature search and site inspection, involving satellite imagery, geomorphological and geological mapping. A ground investigation, comprising boreholes with sampling and in-situ and laboratory testing was recommended based on the findings. The stability affecting the roads was generally assessed based on the interpretation from Varnes, 1978 and Hungr et al, 2001. Refer to Table 1 for a summary.

Table 1. Landslide types.

Movement type	Type of material (bedrock)	Type of material (coarse soils)	Type of material (fine soils)
Falls	Rock fall	Debris fall	Earth fall
Topples	Rock topple	Debris topple	Earth topple
Slides (rotational & translational)	Rock slide	Debris slide	Earth slide
Lateral spreads	Debris spreads	Earth spreads	Debris spreads
Flows	Rock flow (deep creep)	Debris flow (soil creep)	Earth flow (soil creep)

Complex—Combination of two or more principal types of movement.

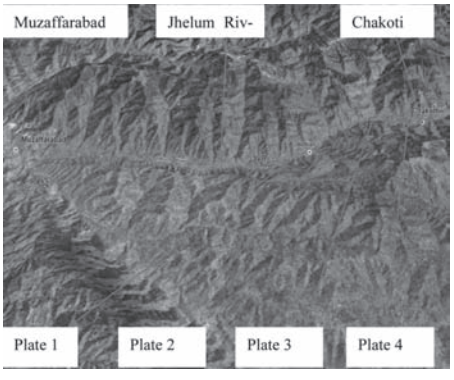

Figure 8. Inspection locations, Highway, S2, Muzaffarabad—Chakoti.

Plate 2. Rock slide.

Plate 1. Debris slide.

Plate 3. Rock fall.

Examples of the approach to the site reconnaissance along the highway are provided from the exposed geological formations and landslide types, observed along portions of the National Highway, S2, Muzaffarabad to Chakoti. The examples are summarized in the Findings.

3.2 *Findings*

The National Highway, S2, runs for about 50 km, from Muzaffarabad, at Chainage (Ch.) 0, to Chakoti, at Ch. 50, alongside the Jhelum River, Jhelum Valley (Fig. 8). Examples of the landslide

type and geological conditions are summarized below.

Debris Slide (Ch. 45.8)—Comprises recent deposition of boulders, cobbles, river terraces derived from a shale rock mass. The underlying shale bedding dips vertically and is aligned parallel to the natural dip gradient at this location. The debris slide was triggered by the 2005 earthquake in combination with river undercutting the slope toe. Refer to Plate 1.

Rock slide (Ch. 47.1)—Located near the Chinari village, comprised a mixture of debris flow and boulders released as wedges from the original rock mass. The wedges were formed from within the S shaped folds in the rock, dipping at a maximum angle of about 70 degrees with axes orientated unfavourably out of the natural slope. The S folds were formed during the intense folding associated with the uplift. Refer to Plate 2.

Rock fall (Ch. 48.2)—Rock blocks were released from persistent discontinuities, extending about 50 m vertically above the highway. The main zones of instability were derived from over-steepened, overhanging portions of the slope with increased instability. The original rock mass had experienced fracturing and disintegration from the earthquake effects increasing the opportunities for rock block release. The extent of the rock fall during the 2005 earthquake partially blocked the river flow at the base of the valley below. Refer to Plate 3.

Rock slide (Ch. 53.3)—The rock slides occurred along competent zones of inter-bedded shale and sandstone. The bedding dipped sub-vertically and was generally orientated perpendicular to the highway and river alignment. The rock mass was fractured and disintegrated, possibly resulting from the tectonic activity, which allowed release of the rock blocks. The instability was exacerbated by river erosion at the slope toe and overlying glacial deposits and sub-rounded cobbles and boulders were present. Refer to Plate 4.

Plate 4. Rock slide.

4 INTERPRETATION

To allow a rapid urgent assessment of the stabilization measures required support was assessed from the landslide type and scale, for both soil and rock type failures, as summarized in Tables 2 and 3.

5 MITIGATION MEASURES

Due to the limited available options to place the highway re-alignment was not considered. Stabilization measures for the existing highway alignment were therefore assessed based on a combination of river erosion protection, suitable surface and sub-surface drainage relief and slope stabilization measures, typically including slope debris removal and cut back, rock bolting, retaining structures, catchments or a combination of available stabilization options. Generic solutions are presented in Figures 9 to 11, including

Table 2. Proposed rock slope cut design, exceeding 7–10 m vertical height.

Rock type	Slope gradient (H:V)	Support (S./Crete; wiremesh; rockbolts)	Drainage	Benches (H/W m)
Medium jointed rock slightly weathered	1:3	Locally—30 mm; as required	Locally—50 mm dia. 6–9 m long slotted PVC	12/2.6–3
Intensively jointed rock, unfavourable discontinuities	1:2	50 mm; N/A; 25 mm dia., 4–6 m length	4 m c/c, 50 mm dia., 6–9 m long slotted PVC	12/3
Soft rock, weak, highly fractured and weathered, shale, partly disintegrated	1:1	70 mm; N/A; 25 mm dia., 6 m length	4 m c/c, 50 mm dia., 9–12 m long slotted PVC	7/3

N/A—Not applicable.

Table 3. Proposed soil slope cut design, exceeding 5–7 m vertical height.

Soil type	Slope gradient (H:V)	Support (S./Crete; wiremesh; soil nails)	Drainage	Benches (H/W m)
Conglomeratic debris, river terrace, lodgement till	2:1	30–50; locally—less cohesion; 25 mm dia., 4–6 m.	Locally—50 mm dia. 6 m long slotted PVC	12/3
Cohesive soils, colluvium and talluvium	1:1–1:1.5	50–70; N/A; 25 mm dia., 6 m	Locally—50 mm dia. 6 m long slotted PVC	7/3
Clayey-silty soil, sensitive to sliding, water saturated, landslide	2:1–1.5:1	70–100; N/A; 25 mm dia., 6 m	Locally—50 mm dia. 6 m long slotted PVC	5–7/3–5

N/A—Not applicable.

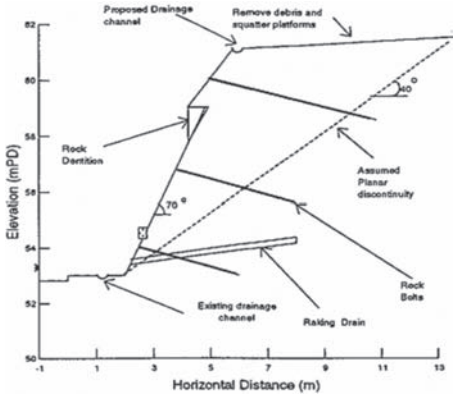

Figure 9. Slope stabilization measures.

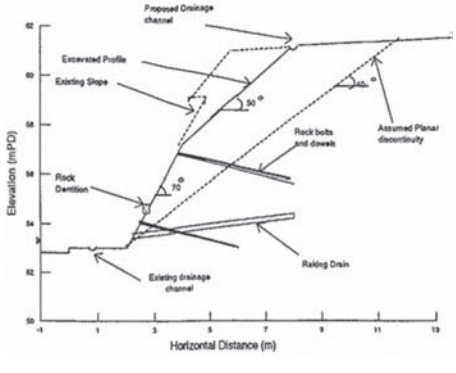

Figure 10. Slope stabilization measures with slope cut back.

rock dowel and/or soil nail and retaining walls with sub-surface drainage measures, cut back in combination with slope support measures. River erosion protection measures are presented in Plate 5.

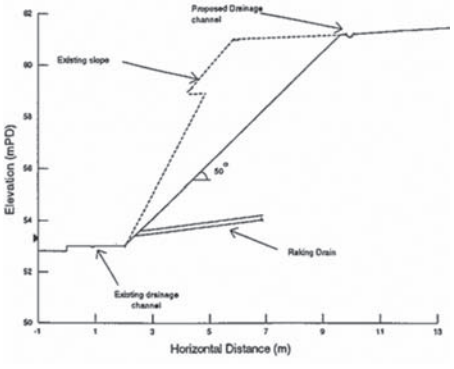

Figure 11. Slope cut back.

Plate 5. River erosion protection.

6 CONCLUSIONS

The detailed inspections assessing the ground conditions along specific landslide locations along the alignment, considering influences affecting the stability, such as the tectonic effects triggering landslides, rainfall, river erosion and the exisitngf g steep natural gradients, were considered applicable in assessing preliminary landslide mitigation proposals.

ACKNOWLEDGEMENTS

The author wishes to thank Ronald Chan in assistance in preparing this paper. The opinions expressed in this paper are those solely of the author and not of any other party.

REFERENCES

Coward, M.P. & Butler, R.W.H. (1985). Thrust tectonics and the deep structure of the Pakistan Himalayas: Geology, v. 13, p. 417–420.

Farah, A., Lawrence, R.D., & DeJong, K.A. (1984). An overview of the tectonics of Pakistan: Marine Geology and Oceanography of Arabian Sea and Coast, p. 161–176.

Google Earth (2011). Searchable map/satellite view of Pakistan.

Hungr, O., Evans, S.G., Bovis, M.J. & Hutchinson, J.N. (2001). Review of the classification of landslides of the flow type, Environmental & Engineering. Geoscience 3(3): 221–238.

Muslehuddin M., Mir H. & Faisal N. (2005). Sindh summer (June–September) Monsoon Rainfall Prediction. Pakistan Journal of Meteorology 2(4): 91.

Varnes, D.J. 1978. Slope movement types and processes. In: *Special Report 176:* Landslide*s: Analysis* and *Control* (Eds: Schuster, R.L. & Krizek, R.J.). Transportation and Road Research Board, National Academy of Science, Washington D.C., 11–33.

This page intentionally left blank

Geotechnical Safety and Risk IV – Zhang et al. (eds)
© 2014 Taylor & Francis Group, London, ISBN 978-1-138-00163-3

Landslide mitigation considerations for low cost highway remedial works, East Timor

A.D. Mackay
Nishimatsu Construction Company Ltd., Hong Kong, China
Formerly SMEC Asia Ltd., Hong Kong, China

ABSTRACT: East Timor has an extensive road network often prone to land-sliding; typically this causes disruption to its transportation system which is the island's life line. The instability impacting the roads is mainly a combination of steep terrain; high annual precipitation, typical of a sub-tropical climates, and complex ground conditions affected by the tectonic uplift and deep weathering zones common throughout the island. Other influences affecting the susceptibility include erosion sensitivity and roads being placed on poorly prepared and un-compacted ground. Remedial measures against landslides have considered optimization of road alignment corridors; the avoidance of areas of concern, were possible, and a reduction in the reliance of traditional slope stabilization measures. Traditional stabilization measures have included stone pitching and gabion boxes, which have proven insufficient to support modern transportation frequency and load impacts. Up to date landslide stability evaluation has allowed assessment of landslide susceptibility for different ground conditions. Recommendations for suitable, regular maintenance with particular attention to effective road drainage networks have been based on this. Notwithstanding effective resource, with suitable training and allocation, is required to carry out this maintenance, and allocation using suitable construction materials, sourced from suitable locations as needed. This paper provides an overview of the road network throughout East Timor and factors affecting the landslide susceptibility, such as precipitation, terrain and the geological conditions. Details of some of the landslides, representing different types of susceptibility, impacting the roads are presented, with suggested slope stability mitigation measures for each representative landslide.

1 INTRODUCTION

East Timor's road network has an extensive and large proportion of paved, surfaced roads compared with many other countries with similar capital expenditure. Notwithstanding there has been a recent increase in the transportation frequency and loading, which has impacted and/or been effected by the instability occurring along the road network. The instability is typically a result of a combination of poor road base preparation, complex geology, including tectonic uplifting and deep weathering zones, and high precipitation. To mitigate this instability initiatives have been taken to carry out remedial measures and implement more efficient road maintenance. These measures have included more robust cut and fill support along the road alignments, with particular attention to effective surface and sub-surface drainage systems, optimizing road corridors and avoiding zones susceptible to landslides were possible. This paper provides an overview of the road network, geography, climate, terrain and geology impacting the landslide susceptibility. Details of proposed stabilization initiatives for different and representative landslides encountered are presented.

2 SETTING

2.1 *Geographical features impacting instability*

Timor Island is located south of the Banda Arc Archipelago, which extends eastwards from Bali Island. East Timor occupies the north eastern portion of Timor Island. Refer to Figure 1 for the location.

Figure 1. East Timor location (Google Earth, 2011).

East Timor has mountainous terrain, rising to an altitude of 2,963 metres above sea level (asl) at Mount Tatamaiau, see Figure 2 for the general locations and Figure 3 for the relief.

The precipitation has been measured from rain gauges located throughout East Timor, with the majority located on the higher altitudes towards the west. As shown in Figure 4 the most intense annual precipitation rates exceed 2500 mm per annum, corresponding to the highest elevations.

The effect of the intense rainfall on roads with uncontrolled drainage systems is presented in Plate 1.

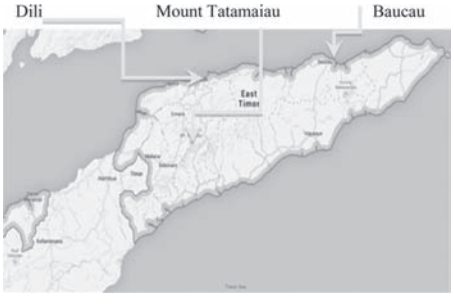

Figure 2. East Timor (Google Earth, 2011).

Figure 3. East Timor relief.

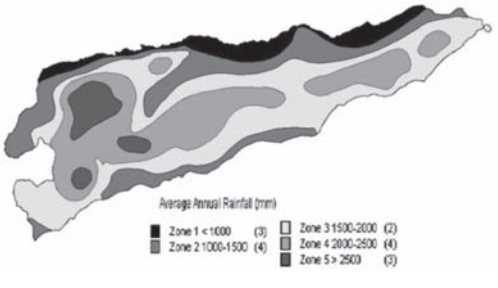

Figure 4. East Timor precipitation.

Plate 1. Uncontrolled surface drainage impacting roads.

Figure 5. Major road network, East Timor.

The high annual precipitation, changeable relief and altitude of many of the island locations contribute to the landslide susceptibility.

2.2 *Road network*

East Timor has an extensive sealed road network, which often traverses the island's steep, unstable terrain exposed to heavy rainfall. In the past the road network catered for light transport; more recently the transport loading and frequency has increased significantly, further impacting stability. Refer to Figure 5 for the main road network.

The road maintenance typically relied on labour intensive remedial measures constructed using traditional slope stabilization measures, such as masonry and gabion retaining walls. With the increased demand on the road network efficient construction of robust slope stabilization measures are necessary. Problems with slope instability impacting the roads in east Timor have typically been associated with:

Natural conditions—terrain steepness, requiring side long cut and fill placement for road formation; weak, unstable ground conditions; intense rainfall; surface water erosion and scour.

Construction—difficulties sourcing, handling and processing high quality construction material; over reliance on masonry/gabion retaining walls often founded on unstable ground; insufficient resource for emergency landslide mitigation; lack of experienced staff (designers, supervisors and contractors) and lack of suitable construction plant.

2.3 *Geological overview*

Timor Island is located between two subduction zones, along its north-west edge within the Banda Sea forming the boundary between the Australasian Continental and the Eurasian Oceanic Plates, and along to the south east along the East Timor Trench. East Timor is located at the north western boundary of the Australian Plate. The island's centre has experienced pronounced geological upthrust, with the oldest rock (Lolotoi complex of pre-Permian age) located at its core (Thompson, 2011). Refer to Figures 6 to 8 for the geological plans and section.

The lithologies and environment of formation (facies), categorized according to geological age; Oligocene-23-34Ma; Eocene-34-56 Ma; Cretaceous-66-145 Ma; Jurassic-145-200 Ma; Triassic-200-245 Ma and Permian-245-300 Ma; are summarized in Table 1.

Due to the compressive effects and island uplift between the subduction zones the island has experienced intense folding and shearing. This has influenced the competency and susceptibility to erosion and weathering of each rock formation.

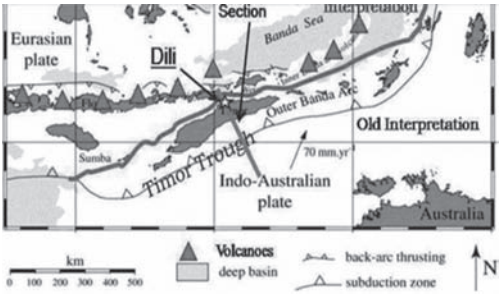

Figure 6. Banda arc plate boundaries (Thompson, 2011).

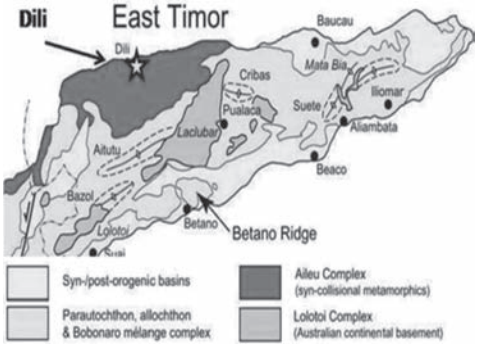

Figure 7. Geology of East Timor (Charlton, 2002).

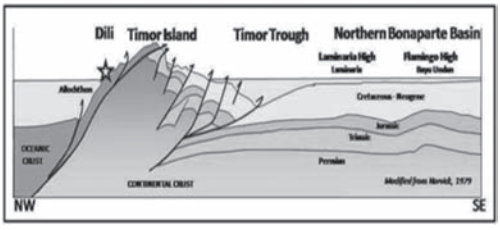

Figure 8. Sectional geology of East Timor (Norvick, 1979).

Table 1. Summary of the solid geology of East Timor (Geological research, 1994 to 1995).

Formation	Geological age	Facies/lithology (remarks)
Barique	Oligocene	Epineritic/basaltic tuffs, lavas and limestone fragments
Dartollu	Eocene	Shallow marine/limestone, calcarenite (brown colouration)
Borolalo	Cretaceous	Deep marine/massive limestone, chert and calcareous shale
Waibua	Cretaceous	Deep marine/shale, chert, calcarinite and calcirudite
Wailuli	Jurrasic	Deep marine/shale, siltstone and limestone and sandstone—lowest levels (tubidites)
Aitutu	Triassic	Epineritic/calcilutite, marl, calcareous shale and calcarenites
Cribas	Permian	Shallow marine/shale, claystone, siltstone, sandstone and calcarenites
Maubissa	Permian	Shallow marine/reefal limestone (reddish colouration)
Aileu	Permian	Shallow marine/phylite, schist, amphibolite, slate, occasional volcanics (effected by metamorphosis and deformation)
Lolitoi	Pre permian	Phylite, schist and gneisses (weak to medium effects of metamorphosis). Has experienced the relatively intense metamorphism

3 GROUND CONDITIONS

3.1 *Site investigation approaches*

A Site Investigation (SI) was initiated to assess the landslide susceptibility impacting the road network generally following the principles set out in TRL, 2005. Key considerations included the engineering properties of the classified rocks and soils, natural instability, rainfall, hydrology, topography and seismic activity. Engineering considerations included the presence and condition of existing engineering structures, such as the retaining walls; natural and man-made hazards associated with the ground conditions; the road sub-grade conditions and construction materials. Particular attention was given to the behaviour of tropical weathering effects. The SI relied on detailed inspections of landslide and rock exposure geological formations.

3.2 *Findings*

The more recent geological formations, deposited during the Pliocence (2.6 to 5.3 Ma) and Miocene (5.3 to 23 Ma) geological age series were inspected during the SI as summarized in Table 2. The inspection locations referenced are presented in Figure 9.

Table 2. Summary of the recent geology of East Timor (Geological research, 1994 to 1995).

Formation	Geological age	Facies/lithology (remarks)
Viqueque	Pliocene	Littoral/claystones, interbedded with limestone, tuffs, silts and sands
Bobonaro complex	Miocene	Deep marine/chaotic boulders in a clay matrix
Cablaci limestone	Miocene	Shallow marine/clastic Limestone (crystalline matrix)

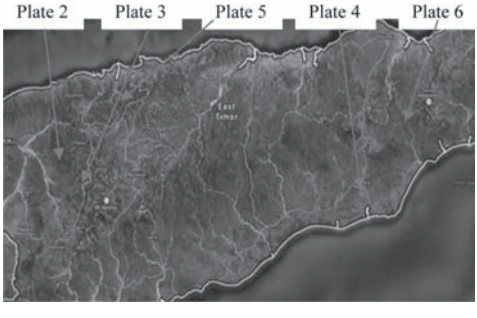

Figure 9. Site inspection locations.

The Wailuli formation tended to weather to a colluvium in steeper gradients. Due its impermeable characteristics, comprising a large proportion of fine grained weathered constituents uncontrolled surface drainage was observed (see Plate 2).

Due to the recent, un-consolidated deposition of the Bobonaro complex the formation tended to be susceptible to instability, as shown by the effects of uncontrolled drainage in Plate 3.

The Viqueque formation has been deposited recently. As a result it is highly susceptible to erosion and instability as shown by the undercutting effects of river erosion in Plate 4.

The Ailue formation is a relatively old and therefore typically stable. However Plate 5 shows a location with a reduced strength from weathering effects with colluvium covering the uppermost surface. The failure was triggered by discharge from a culvert.

Plate 6 presents a mudflow within the Cablaci limestone. The failure is located at the edge of a limestone Plateau exacerbated by erosion from a stream course, transporting the failed material away from the failure toe. As the failure is located away from roads it does not impose a hazard.

Plate 2. Wailuli formation (river flooding across road).

Plate 3. Borbanaro complex: Instability above and below road.

Plate 4. Viqueque formation: gabion wall failure above river.

Plate 5. Instability beneath road, Aileu Formation.

Plate 6. Mudflow, away from road, Cablaci Limestone.

4 INTERPRETATION

The stability affecting the roads could generally be zoned based on the general scale of instability associated with ground conditions, were information is available. A generic zoning presenting basic landslide susceptibility, is presented in Table 3.

Table 3. Ground conditions encountered in the SI.

Zone	Description
1	Coastal and alluvial plains. Stability generally not problematic unless embankments or structures are required (See Plate 7)
2	Older geological formations exhibiting competent rock standing in steep slopes. These include the Alieu and This is particularly prone to instability in more locations with more intense rainfall and deeper weathering
3	Less competent rock with minor instability
4	Moderate instability
5	Weak and unstable geological formations with potentially severe instability. In these locations retaining wall support is insufficient

Table 4. Ground conditions encountered in the SI.

Zone	Description
2	Cribas, Mabisse, Alieu
3	Lolotoi, Wailuli, Waibua, Borolalo, Dartolla limestone, Ainaro, Bancau limestone, Surebaco and Aliambata
4	Atitu, Barique, Cablaco, Lariquiti, Dilor
5	Viqueque, Barbanoro formation and complex

Plate 7. Zone 1, flat coastal and alluvial plains.

The zoning generally corresponded with the source geological conditions, the weathering intensity, natural slope gradient and precipitation. An approximate zoning corresponding with the source geological formation encountered is summarized in Table 4, as Zone 1 comprises flat recently deposited material, such as alluvium, this has not been included.

Generally instability increases with younger, uplifted geological formations; hence the inclusion of the Viqueque, and Barbanoro Formations

in Zone 5. More recent deposition in the Miocene age group also includes the Aliambata Formation in Zone 3 and the Lariquiti and Dilor formations in Zone 4.

5 MITIGATION MEASURES

Based on the findings of the instability impacting the roads more robust stabilization solutions are required. These can include:

Major realignment—This is required were severe instability impacts the road. Difficulties often occur with the land ownership and impact to existing settlements when realignments are considered

Slope stabilization: These can include combinations of shotcrete, mesh, rock dowels and bolts, catch fences, reinforced back-fill and retaining structures. Considerations should be given for free drainage, such as suitable permeable backfill and weepholes, in the shotcrete and for use of backfill behind retaining structures. Generic solutions are presented in Figures 9 to 11.

Do nothing: Due to the prohibitive expense and technical problems that may occur with some of the solutions it may be advantageous to allocate resources to for emergency maintenance and/or repair when failures occur.

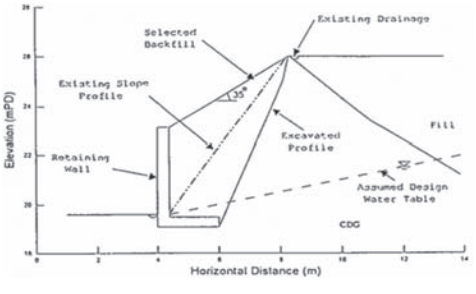

Figure 9. Retaining wall.

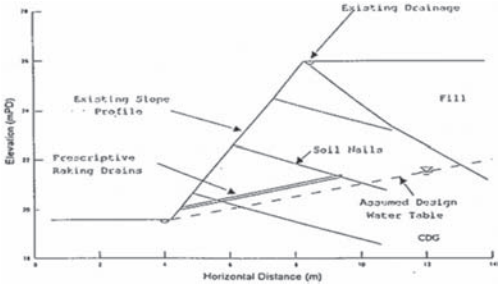

Figure 10. Skin wall with soil nails.

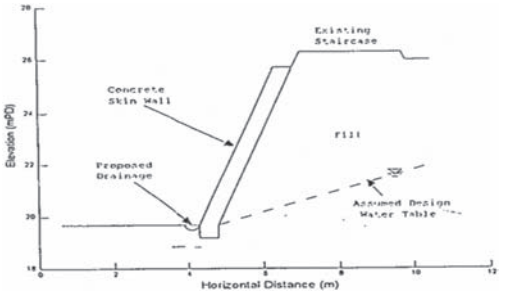

Figure 11. Skin wall.

Drainage is a requirement for all solutions ensuring surface drainage is taken away from areas susceptible to landsliding and that culverts are functioning effectively. Resource also requires allocation to ensure all roads are maintained, particularly the drainage networks.

6 CONCLUSIONS

The detailed inspections assessing the ground conditions in combination with an assessment of factors influencing the stability, such as constructions methods, natural slope gradient and annual rainfall, were considered successful in assessing preliminary landslide susceptibility. The use of these findings to categorize slope stability can be considered useful in efficient allocating resources to areas were the need is greatest and stabilization requires greatest attention.

ACKNOWLEDGEMENTS

The author wishes to thank Ronald Chan in assistance in preparing this paper. The opinions expressed in this paper are those solely of the author and not of any other party.

REFERENCES

Charlton, T.R. (2002). The Petroleum Potential of East Timor. APPEA Proceedings 32, pp 20–38.

Geological Research and Development Centre, Indonesia (1994–1995). Geological Maps and memoirs of Bacau Quadrangle, Dili Street, Atambua Sheet, 1:250,000 scale.

Norvick (1979). The tectonic history of the NBanda Arcs, Eastern Indonesia; a Review. Journal of the Geological Society, version 136, No. 5, pp 519–526.

Thompson S.J. (2011). The Geology and Soils in Timor Leste (internet).

Transport Research Laboratory (TRL, 2005). Overseas Road note, A guide to road Appraisal.

Geotechnical Safety and Risk IV – Zhang et al. (eds)
© 2014 Taylor & Francis Group, London, ISBN 978-1-138-00163-3

The landslide of Kirf: A chain of governance failures

S. Van Baars & M. Sosson
University of Luxembourg, Luxembourg

S. Jung
Dr. Jung and Lang Engineering, Germany

R. Becker
Holmalux, Luxembourg

ABSTRACT: In January 2011 a landslide occurred in the German village of Kirf, which is between the town Saarburg and the border of Luxembourg. This slope failure caused a destruction of a federal main road over 50 meters. Stability calculations were made by a geotechnical consulting company, commissioned from the Federal Road Administration, in order to design the repair works and also to find out what really had happened. These calculations showed remarkably high safety factors. Nevertheless the consulting company blamed the families of the four houses down the slope for the failure, because they had made gabion walls in the toe of the slope. A research team of the University of Luxembourg discovered that this hilly area originally was called "On the slide" and has never been stabile according to their own calculations. So, the real question is why so many apparently uncorrelated mistakes were made in a single case.

1 LANDSLIDE OF KIRF

1.1 *Slope failure*

In January 2011 a landslide occurred in the German village of Kirf, which is between the town Saarburg and the border of Luxembourg. This slope failure caused a destruction of the federal main road B407 over a length of 50 meters, see Figure 1.

Cracks had been noticed in this road since August 2010 and in October 2010 settlements of about a decimeter had been recorded. On January 7 and 8, after a time of snow melt, the slope slid and the road on this slope collapsed and had to be closed off. The families of the four houses down the slope were temporarily evacuated.

Figure 1. Landslide at the federal road B407 near Kirf.

1.2 *History*

The Federal main road B407 was first build as "Reichstrasse 327" in 1938–1939 as a strategic road connection. First in the early sixties the nearby southern part of the highway A1 was constructed and the "Reichstrasse 327" was transformed into the federal main road "Bundesstrasse 407". It is important to know that during all these years never a single stability analyses was made of the road-slope construction of the B407 near Kirf, but also never a large landslide had occurred until January 2011.

The village municipality has granted building permits for four houses at the toe of this slope. The first house (most North, with house number 16) was built in 1996. The other three houses were constructed between 2006 and 2009. All four houses have basements which were constructed in temporarily excavations at the toe of the slope. The families of the four houses ordered a constructing company in December 2009 to excavate the toe of the slope and to construct gabion walls, in order to

increase the lower part of their gardens, see also Figure 3. The constructing company did neither demand a stability calculation of the gabion wall, nor a stability calculation of the total slope.

2 RESULTS OF THE CONSULTING COMPANY

2.1 *Introduction*

For the repair works of the slope and road after the landslide, a type of crib wall were used, which is a combination of concrete beams and soil. In order to design these works and also in order to find out what really had happened, the Federal Road Administration (LBM Trier) defined one cross sections at each of the four houses, and commissioned a geo-technical consulting company to make a map of the cracks in the slope and to make slope stability calculations for the four cross sections, see Figure 2.

2.2 *Block slide calculations*

For these four cross-sections the soil layering was determined and for each soil layer the soil parameters were determined. It was said that the soil contained too many large stones for a normal soil sampling and testing. The geotechnical consulting company chose to make block slide failure calculations, since they were convinced that the slope slid as a single block over a strong and deeper soil layer. For each of the four cross sections, calculations were made. These calculations were based on a diagonal translation of a soil body. The results of the calculations, which are the safety factors (the slope strength divided by the load), are found in Table 1.

The stability calculations of the consulting company resulted in safety factors between SF = 1.55 and SF = 1.94 before the construction of the gabion walls and a strong reduction down to safety factors between SF = 1.27 and SF = 1.52 after the construction of the gabion walls. Since the safety factors were still far above SF = 1.00 (point of failure), the soil strength parameters were reduced and based on residual strength (after shearing) for additional calculations for a safe design of the crib walls.

The consulting company blamed the families of the four houses down the slope for the failure, because they had made gabion walls in the toe of the slope, see Figure 3. Especially the family of the first house (No. 16) was found responsible because they had reduced the safety factor relatively the most.

Based on these results, the Federal Road Administration charged in November 2011 the four families to pay the repair works of € 900.000—(LBM Trier, 2011). The four families feel betrayed because

Table 1. Safety Factors (SF) according to consulting company.

	Before gabions	After gabions
Safety factor	SF	SF
House No. 16*	1.94	1.39
House No. 18	1.89	1.52
House No. 20	1.64	1.44
House No. 22	1.55	1.27

*First house from the North.

Figure 2. The road, four houses, four parallel cross sections and cracks in the ground (under laying photo: Google Maps).

Figure 3. Pushed-over gabion wall at toe of slope near House No. 16.

they do feel they did neither anything wrong, nor did they know anything about soil mechanics.

3 RESULTS OF THE UNIVERSITY

3.1 *A chain of governance failures*

At the end of 2012, one of the families asked the University of Luxembourg to have a look at this case. A research team was formed consisting of the four authors of this article. They discovered a chain of mistakes in governance in this case. First of all, the geology, topography and also the vegetation show irregularities on the side, which could be a first indication of an instable slope. Besides, according to one of the maps this area is called "On the slide" (Consultancy Spoo & Pittner GmbH, 2002). The road was built already for many decades on this slope and the traffic load had risen over the years but never a stability calculation had been commissioned. The Federal Road Administration also never acquired the slope in order to protect it, nor did they warn or regulate the (new) owners of the slope. Neither did the village municipality when they granted a building permit for these houses. Also none of the architects and builders of the four houses required a stability calculation for the construction of the building pits for the basements of these houses, right next to the toe of the slope (only in one report we find a recommendation, no requirement). Also when the four families installed the gabion walls, nobody required a stability calculation. This is a clear chain of governance failure.

3.2 *Review of consulting company*

The review of the report of the consulting company revealed several major mistakes. Their assumption that the soil body of the slope slid diagonally as a block was incorrect. Detailed photos show clearly that the road and the guardrail moved vertically and the slope toe horizontally (perpendicular to the road axis), indicating that there was a rotational movement. That is why "slip circle" calculations had to be made.

The fact that their safety factors were still far above SF = 1.00, should not have immediately lead to the use of lower soil strength parameters, but to the search of the real error in their modeling. Besides, their reduction of the soil strength parameters certainly has led to a strong over dimensioning of the repair works, which means that a large part of the costs of the repair works is on the responsibility of the consulting company itself.

The consulting company concluded that the family of the first house was most accountable because here the largest reduction in safety factor was found. This reasoning is incorrect, because not the biggest reduction is important for failure, but the lowest safety factor.

The consulting company assumed also that the slope slid partly horizontally (parallel to the road axis) towards the first house, indicating that the family of this house is most responsible. There is however no evidence (measurements or photos) indicating that such a parallel movement took place, nor is this possible, since there is no energy source to compensate for the energy loss due to the frictional parallel movement, because the only source here; gravity, acts purely vertical.

3.3 *Slip circle calculations*

Remarkably, the unreduced stability calculations of the consulting company, mentioned before, proved the fitness of the slope, in spite of the occurred landslide. However, these calculations were by mistake based on "block failure". Therefore the University of Luxembourg has made new "slip circle" calculations for the four cross-sections, based on Bishop's method, both before and after the construction of the gabion walls, see Figure 4.

For the selected soil parameters see Table 2. The consulting company used an unrealistically high friction angle for the Top Loam of $\phi = 35$ degrees, which has been reduced by the authors to $\phi = 25$ degrees.

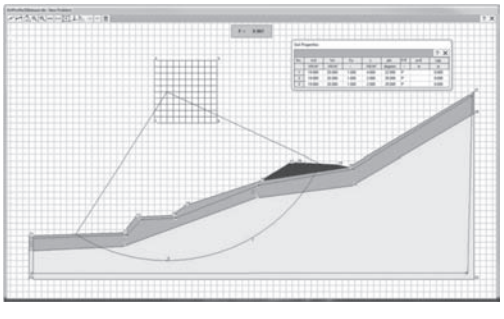

Figure 4. Slip circle calculation at cross-section House No. 20.

Table 2. Soil parameters (unit weight, friction angle and cohesion).

	γ	ϕ	c
Parameters	kN/m^3	degrees	kPa
Fill	19	35	2
Top loam	19	25*	2
Grey clay	20	27.5	10
Red clay	20	22.5	4

*The consulting company used here $\phi = 35$ degrees.

Table 3. Safety factors according to the authors.

	Before gabions	After gabions
Safety factor	SF	SF
House No. 16*	1.55	0.99
House No. 18	1.04	0.93
House No. 20	1.05	0.99
House No. 22	0.96	0.89

*First house from the North.

The calculations of the University of Luxembourg were made with a high groundwater table in order to simulate the effect of the melting snow but without traffic load.

The results of the calculations indicate that the stability factors before the construction of the gabion walls were, for the profiles of three of the four houses, between SF = 0.96 and SF = 1.05 and after its construction between SF = 0.89 and SF = 0.99, see Table 3.

4 CONCLUSIONS

The occurrence of the landslide is not a surprise since the results from the slip circle calculations show safety factors SF < 1.

However, in order to get to the condition of such a failure, the following chain of events and boundary conditions is needed:

1. There is an unstable slope.
2. A road is built on the slope.
3. No stability calculation is made before the construction of the road.
4. Never a stability calculation is commissioned during all the years of maintenance.
5. The Federal Road Administration never acquires the slope in order to protect it.
6. Nor do they prescribe anything to the slope owners, in order to protect the slope and the owners.
7. The village municipality grants building permits without any prescription for the slope.
8. The architect and builders of the houses and the excavations of the basements, never require stability calculations to be made.
9. The owners of the four houses all decide to install large gabions walls in the toe of the slope.
10. The constructor(s) of the gabion walls of all four houses does not require stability calculations to be made.

These 10 events seem rather uncorrelated. The real question which remains is; why such a chain of apparently uncorrelated mistakes could be made in a single case. The fact therefore that all 10 events were required to take place and also did take place, means that the chance of occurrence of each of the events is unfortunately too high. Therefore no other conclusion is possible than that in this case, and therefore probably also in other cases, the current requirements for good governance and risk management of earthworks were not followed by any of the stakeholders.

There are also other problems. At the first stability analysis which was performed by the consulting company after the landslide, an unacceptable high number of mistakes were made. And what is worse, they were not discovered by the normal governance system. The fact that soil strength parameters were strongly reduced in order to find failure in their calculations was unacceptable.

Finally the most unacceptable aspect of this case is the fact that the four families living at the toe of the slope were held fully accountable for the failure, and this conclusion was reached based on calculations with many errors and the lack of governance described.

REFERENCES

Clayton Environmental Consultancy GmbH, 2006. *Geotechnische bericht zum Bauvorhaben Dostert "zum Altenberg" in Kirf*, Ludwigshafen, Germany.

Consultancy Spoo & Pittner GmbH, 2002. *Bodengutachten "Im Hübel auf der Maaswies" in Kirf*, Mertesdorf, Germany.

Landesbetrieb Mobilität Rheinland-Pfalz LBM Trier, 2011, *Letter from G. Wiesel to lawyer Martini-Mogg-Vogt in Koblenz of the families houses no. 16 and 18*.

Topographical Maps *Page Koblenz 1925 and 1939 and Page Trier 1925 and 1940*.

Trierischer Volksfreund, Newspaper, http://www.volksfreund.de—Archive: 10.01.2011—*Hangrutsch bei Kirf: Bewohner verlassen Haus.*

WPW Geoconsult GmbH, 2011, *Geotechnischer Bericht "Schadensanalyse"*, Trier, Germany.

Geotechnical Safety and Risk IV – Zhang et al. (eds)
© 2014 Taylor & Francis Group, London, ISBN 978-1-138-00163-3

A risk-based active fault classification

J.P. Wang
Department of Civil and Environmental Engineering, Hong Kong University of Science and Technology, Kowloon, Hong Kong, China

ABSTRACT: Engineering risk is referred to as occurrence probability multiplied with the consequence when the event occurs. Few engineering decisions are now risk-based, using an alternative with the lowest risk as the solution to a problem. Under such a risk framework, this study develops a classification system for active faults. In addition to population at risk, this classification also considers the earthquake magnitudes and earthquake energy release. Applying such a classification to six active faults in Taiwan, we suggested that the Sanchiao Fault and Changhua Fault should be Category III active faults, the highest level in this classification system.

1 INTRODUCTION

Engineering risk is referred to occurrence probability multiplied with the consequence when the event occurs (Wang et al., 2012a). As for risk-based decision making, the decision with the lowest risk will be adopted. Few engineering decisions are now risk-based, including site selections for critical structures (Wang et al., 2012b), and earthquake early warning (Wang et al., 2012a).

Understandably, probability is used to quantify the level of uncertainty or randomness. For example, the probability in a random process that "Point One" occurs while tossing a fair dice is 1/6, which reflects the randomness of this stochastic process. Since the earthquake is hardly predictable given our limited, imperfect understanding (Geller et al., 1997), probabilistic analyses are gradually applied to evaluating earthquake potentials in terms of probability. For example, a couple of probabilistic studies (Wang et al., 2013a) were performed and suggested that indeed the earthquake's temporal occurrence follows the statistical Poisson model that has been commonly used in earthquake analyses (Wang et al., 2012c, 2013b). Another instance is the analysis evaluating large-earthquake probabilities from studying the pool of annual maximum earthquakes in Taiwan since 1900 (Wang et al., 2011).

This paper presents a risk-based classicification system for active faults. In addition to Population At Risk (*PAR*), the best-estimate earthquake magnitude and earthquake energy release are accounted for in the classicification developed. The method was then applied to six active faults in Taiwan, which is considered one of the earthquake "hot zones" in the world.

2 RISK SCORE

The risk score of an active fault in this study is referred to the relative level of risk among the faults analyzed. Note that the original score is normalized, so that the resulting risk score is dimensionless. In other words, after normalizing the units of the underlying parameters should not affect the classification.

With the concept of risk, the risk score (R_S) of an active fault in this study can be first expressed as follows:

$$R_S = \Pr(M > m^*) \times C_S \tag{1}$$

where $\Pr(M > m^*)$ is the probability of magnitude exceedance for $M > m^*$ when an earthquake occurs at an active fault; C_S denotes the consequence when such an event occurs. This expression is the underlying governing equation of this study.

2.1 *Earthquake energy release*

Earthquake energy release exponentially increases with magnitude. For example, an M 7.0 earthquake can release energy 32 times as large as an M 6.0 event (Keller, 1996). Figure 1 shows the energy release ratio on the basis of M 6.0 earthquakes. It is around a 1,000-time difference in energy release between M 6.0 and M 8.0 earthquakes.

2.2 *Earthquake energy release and consequence*

Relatively speaking, the relationship between earthquake energy release and the consequence caused by earthquake is more linear than that between earthquake magnitude and the consequence. Therefore,

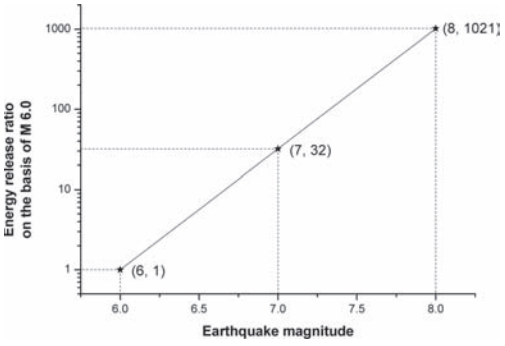

Figure 1. Earthquake energy release ratios on the basis of M 6.0 events.

we used energy release ratios as one of the factors to estimate the earthquake consequence in this study. In other words, the consequence caused by an M 7.0 is considered 32 times as severe as that caused by an M 6.0 event. Although this estimate can not be verified on a more scientific basis, it is more reasonable than considering a linear relationship between magnitude and consequence. That is, if the consequence increment is equal to 1 from M 6.0 to M 7.0 earthquakes, the increment is then equal to 2 considering the magnitude increment from 6.0 to 8.0.

2.3 *Fault location and Population At Risk (PAR)*

Understandably, the consequence caused by a large earthquake is more severe when it occurs in major cities than in remote areas. In other words, the fault's location is related to earthquake consequences. Considering human life is the most important asset to be protected, this study employed population at risk as another factor to characterize the consequence in terms of loss of life.

Therefore, with the earthquake consequence characterized by Earthquake energy Release (*ENR*) and Population At Risk (*PAR*), the governing equation (i.e., Eq. 1) to estimate the risk score of active faults can be rewritten as follows:

$$R_S = \Pr(M > m^*) \times (ENR \times PAR) \tag{2}$$

Using the ratio $R_{6.0}$ to quantify energy releases on the basis of M 6.0 events, Eq. 2 becomes:

$$R_S = \Pr(M > m^*) \times R_{6.0}(M > m^*) \times PAR \tag{3}$$

Therefore, risk score R_S is a function of magnitude m^* that appears in the first two terms, also a function of the fault's location determining the level of PAR. Note that $R_{6.0}(M > m^*)$ can by computed by the summation of $\Pr(M) \times R_{6.0}(M)$, with M from m^* to a reasonable upper-bound value (e.g., 9.0). As mentioned, the upper-bound magnitude has little influence on the resulting risk score because normalizing will be performed eventually.

3 RISK SCORE COMPUTATIONS

This study applied such a risk-based classification to six active faults in Taiwan. Figure 2 shows their locations. According to Cheng et al. (2007), the best-estimate maximum earthquake magnitudes are summarized in Table 1, with the largest one equal to M 7.6 associated with the Changhua Fault, and the smallest one of M 6.4 associated with the Hsinhua Fault. Also based on that

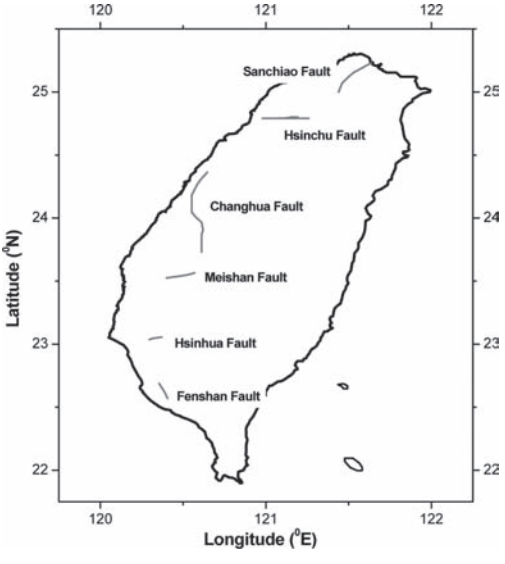

Figure 2. Locations of six active faults in Taiwan in this study.

Table 1. Summary of maximum probable earthquake magnitudes induced by the six fault in Taiwan.

Faults	Magnitude (M_w*)	COV** (%)
Sanchiao	7.0	2.9
Hsinchu	6.8	2.9
Changhua	7.6	2.6
Meishan	6.5	3.1
Hsinhua	6.4	3.1
Fenshan	6.7	3.0

*M_w: moment magnitude; **COV: coefficient of variation = standard deviation/mean.

study, the best-estimate standard deviation was reported at 0.2.

3.1 *Magnitude exceedance probability*

The first step to calculate the risk score with Eq. 3 is to compute the magnitude exceedance probability Pr($M > m^*$). However, one more piece of information is needed for this calculation, in addition to the mean values and standard deviations of maximum earthquake magnitudes available. That is, the probability distribution that can properly model this random variable.

Understandably, not too many data are available to perform statistical goodness-of-fit tests on earthquake magnitudes induced by the same fault owing to the long return periods. Alternatively, Wang et al. (2011) examined 110 annual maximum earthquakes around Taiwan since 1900, finding that the lognormal distribution can properly model the random magnitude.

Using this best-estimate information to model the distribution of maximum earthquake magnitudes induced by an active fault, Figure 3 shows the magnitude exceedance probability of the six faults. With this probabilistic analysis, the maximum earthquake magnitude exceeding 7.0 induced by the Hsinhua Fault is in probability of 0.2% (still possible), given the best-estimate mean value equal to 6.4. In contrast, the probability is near 100% for an earthquake induced by the Changhua Fault exceeding 7.0, given the best-estimate mean = 7.6.

3.2 *Estimates of Population At Risk*

This study considers the residents within a distance of 50 km from the fault are at risk. Based on the demographic data of Taiwan, Figure 4 shows the estimates of *PAR* on such a condition for the six active faults. The Sanchiao Fault located close to Taipei, the most populated city in Taiwan, results in a *PAR* in 7.5 million. In contrast, the Meishan Fault located in Chaiyi leads to a relatively low *PAR* less than one million.

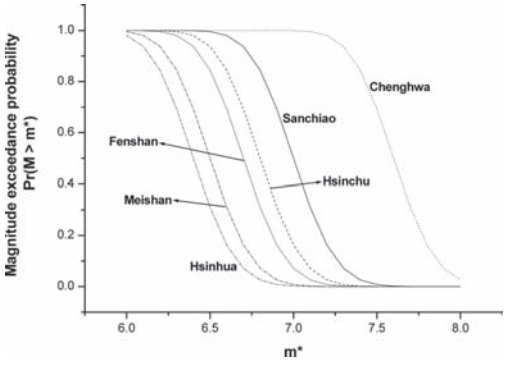

Figure 3. Earthquake magnitude exceedance probability for the six faults analyzed in this study.

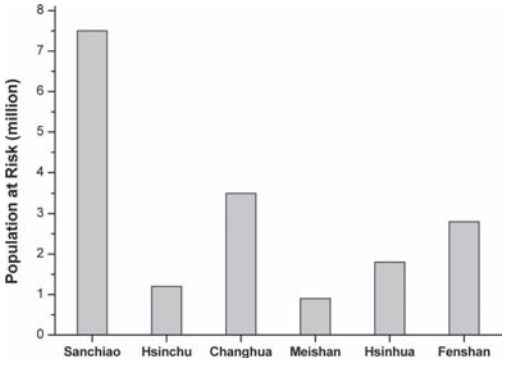

Figure 4. Population at risk for each fault considering a 50-km radius from the fault.

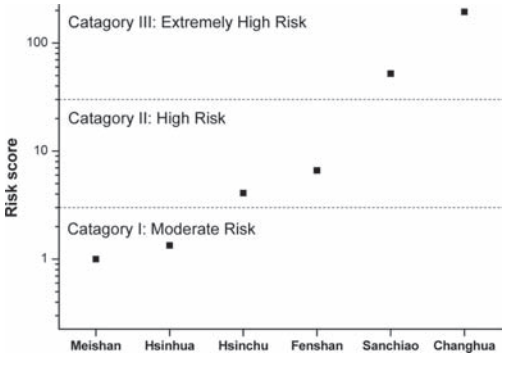

Figure 5. Risk scores and the classification for the six active faults in Taiwan.

3.3 *Risk score and fault classicification*

With the earthquake energy release ratios (i.e., Fig. 1), the best-estimate magnitude exceedance probability (i.e., Fig. 3), and the best-estimate population at risk (i.e., Fig. 4), we calculated the (normalized) risk scores for the six faults in Taiwan, as shown in Figure 5.

The result shows that the six risk scores are very distinct, ranging from 1.0 up to 200. The main causes to such a wide distribution of risk scores are that earthquake energy release that should be linearly related to earthquake consequence increases exponentially with magnitude, and that the magnitude exceedance probability at the same m^* can be distinctly different between two faults, say, 0.2% and 100% for earthquake magnitudes exceeding 7.0

induced by the Hsinhua Fault and Changhua Fault as previously mentioned.

Based on the score distribution, three categories were employed in this fault classicification: Category III Extremely High Risk; Category II High Risk; Category I Moderate Risk. The risk score ranges for each category are 1~3, 3~30, and above 30 from Category I to Category III. As a result, we considered the Sanchiao Fault in North Taiwan and Changhua Fault in Central Taiwan are Category III active faults based on this risk-based classification. In other words, a more conservative earthquake-resistant design should be employed to ensure the seismic safety of cities and townships near the two faults.

4 DISCUSSIONS

Understandably, other properties of the fault can be further integrated to this risk-based classification system, such as the return period of the fault activity or the recurred earthquake, mainly because the earthquake occurrence probability within a finite interval (e.g., 50 years) should be different if the return periods of two faults are 100 years and 1,000 years. It should not be too difficult to re-calculate the risk score with such a fault property taken into account. The issue could be the best-estimate return periods, which are better to be somewhat verifiable, otherwise the analysis is not on a scientific ground although the governing equation is more logical covering more aspects.

5 CONCLUSION

This paper presents a risk-based classification framework for active faults in a region, considering the fault's location and population at risk, the best-estimate earthquake magnitude, magnitude exceedance probability, and earthquake energy release. This new method was then applied to six faults in Taiwan. Accordingly, we considered that the Sanchiao Fault located in North Taiwan and the Changhwa Fault in Central Taiwan are Category III active faults, the highest level in this study.

REFERENCES

Cheng, C.T., Chiou, S.J., Lee, C.T. & Tsai, Y.B. 2007. Study on probabilistic seismic hazard maps of Taiwan after Chi-chi earthquake. *Journal of GeoEngineering* 2(1): 19–28.

Geller, R.J., Jackson, D.D., Kagan, Y.Y. & Mulargia, F. 1997. Earthquake cannot be predicted. *Science* 275: 1616.

Keller, E.A. 1996. Environmental Geology 7th ed. Prentice Hall, New Jersey, USA.

Wang, J.P., Chan, C.H. & Wu, Y.M. 2011. The distribution of annual maximum earthquake magnitude around Taiwan and its application in the estimation of catastrophic earthquake recurrence probability. *Natural Hazards* 59(1): 553–570.

Wang, J.P., Wu, Y.M., Lin, T.L. & Brant, L. 2012a. The uncertainty of a Pd3-PGV onsite earthquake early warning system. *Soil Dynamics and Earthquake Engineering* 36: 32–37.

Wang, J.P., & Xu, Y. 2012b. The site selection of the Lungmen nuclear power plant in Taiwan. *International Journal of Architecture, Engineering and Constructions* 1: 83–89.

Wang, J.P., Lin, C.W., Taheri, H. & Chen, W.S. 2012c. Impact of fault parameter uncertainties on earthquake recurrence probability by Monte Carlo simulation—an example in central Taiwan. *Engineering Geology* 126: 67–74.

Wang, J.P., Huang, D. & Yang, Z. 2012d. The deterministic seismic hazard map for Taiwan developed using an in-house Excel-based program. *Computers and Geoscience* 48: 111–116.

Wang, J.P., Huang, D. Chang, S.C. & Wu, Y.M. 2013a. New evidence and perspective to the Poisson process and earthquake temporal distribution from 55,000 events around Taiwan since 1900. *Natural Hazards Review ASCE* doi: 10.1061/(ASCE)NH.1527-6996.0000110.

Wang, J.P., Huang, D. & Chang, S.C. 2013b. Assessment of seismic hazard associated with the Meishan fault in Central Taiwan. *Bulletin of Engineering Geology and the Environment* doi: 10.1007/s10064-0.13-0471-x.

Wang, J.P., Huang, D. Chang, S.C. & Wu, Y.M. 2013c. A seismic hazard analysis for the region of Tehran. *Natural Hazards Review ASCE* (accepted).

Geotechnical Safety and Risk IV – Zhang et al. (eds)
© 2014 Taylor & Francis Group, London, ISBN 978-1-138-00163-3

Introducing non-stationary earthquake process concept: Including an analytical model and a case study in Central Taiwan

Y. Xu & J.P. Wang
Department of Civil and Environmental Engineering, Hong Kong University of Science and Technology, Kowloon, Hong Kong, China

ABSTRACT: From observation and experience, earthquake recurrence induced by the same fault should be influenced by "memory", or such a stochastic process should be non-stationary rather than being stationary. For instance, the same fault triggering the recent Tohoku earthquake in Japan is less likely to trigger another one in the coming few years, but the probability will be increasing with time. However, the commonly used Poisson process considers the earthquake as a stationary stochastic process, resulting in the identical probability regardless whether the next earthquake occurs in 2020~2030 or 2220~2230. As a result, based on the mechanism of faulting, this paper introduces a new analytical model to properly take the earthquake memory effect into account. A case study in Central Taiwan is given, which is considered to provide a more realistic result compared to that from the stationary stochastic process suggested by Poisson model.

1 INTRODUCTION

The Poisson process is commonly used to model the earthquake recurrence within a given time (Ang and Tang, 2007; Wang et al., 2013). Owing to the properties of the statistical model, the event of the Poisson process occurs randomly, independent of time, which is so-call "memory-less" effect or a non-stationary stochastic process (Kramer, 1996). However, a series of equivalent earthquakes induced by the same fault seem not memory-less in reality. Based on the elastic rebound theory, earthquakes occur when the shear stress reaches the shear strength of the rock along the fault, releasing the strain energy accumulated on the fault (Reid, 1911). As a result, the chances of the earthquake recurrence must relate to the time that has elapsed since the last earthquake.

Therefore, this paper introduces a new analytical framework to assess the non-stationary earthquake probability from the underlying mechanism of faulting, of which the changing probability with time is a result of time-dependent external stress accumulation and time-independent ultimate resistance on the fault plane. The method is then applied to the Meishan Fault in Central Taiwan, whose return period was best estimated at 162 years with the very last event occurring in 1906. Altogether, the overview of this fault, the development of this approach, and a case study are given in this paper.

2 OVERVIEW OF THE MEISHAN FAULT

Given the highly active seismic region around Taiwan, efforts have been spent from seismogenic characterization, to earthquake hazard analysis, to earthquake early warning system (e.g. Cheng et al., 2007; Wang et al., 2011; Wang et al., 2012a, 2012b, 2012c; Wu and Kanamori, 2005). A fault investigating program was carried out by the Central Geological Survey Taiwan (CGST), and the best-estimated return period and earthquake magnitude of 35 active faults on the island were published (Lin et al., 2008, 2009).

The Meishan Fault, located in the Central Taiwan (Fig. 1), was reportedly capable of

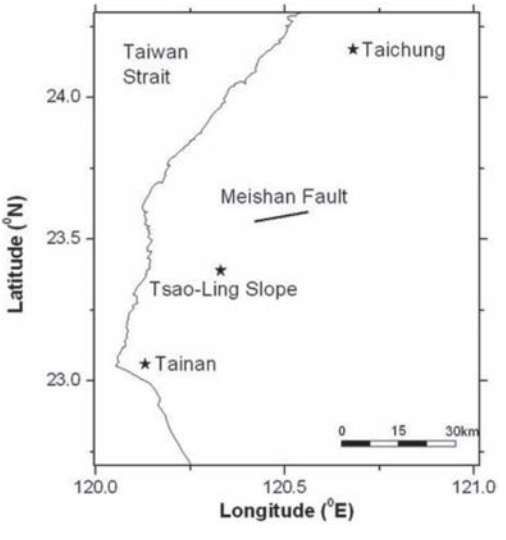

Figure 1. Meishan fault in Taiwan.

inducing a M 7.1 event every 162 years. The last occurrence in 1906 resulted in hundreds of casualties and thousands of building collapses, most of which were around the Chaiyi City (Yen et al., 2008). With the best-estimated data, the next strike caused by the Meishan Fault will be on 2068, and the Chaiyi City, lying very close to the fault, is under high earthquake risk.

3 EARTHQUAKE PROBABILITY INDUCED BY THE MEISHAN FAULT WITH THE POISSON PROCESS

To characterize the temporal distribution of the earthquake recurrence, the Poisson probability is expressed as follows (Kramer, 1996):

$$\Pr(n; t_1 \le T \le t_1 + \Delta t; \lambda) = \frac{(\lambda \times \Delta t)^n \times e^{-\lambda \times \Delta t}}{n!} \quad (1)$$

where n = the number of the event; t_1 = the starting date; Δt = time interval; and λ = the mean annual rate, respectively.

Given the occurrence probability of at least one exceedance in a specific time window can be estimated as follows:

$$\Pr(n \ge 1; t_1 \le T \le t_1 + \Delta t; \lambda) = 1 - e^{-\lambda \times \Delta t} \quad (2)$$

Therefore, if the model is considered suitable for simulating the earthquake probability induced by the Meishan Fault with the best-estimated annual rate, $\lambda = 1/162$, the probability that the earthquake could occur in 2020~2040 is 12%, identical to the likelihood in 2040~2060 given the same interval.

4 EARTHQUAKE PROBABILITY ASSESSMENT WITH A PHYSICS-BASED MODEL

4.1 *Mechanism of faulting and faulting probability*

Figure 2 shows a systematic diagram of the underlying mechanism of faulting. The model is dictated by the law that when the shear stress exceeds the strength of the rock along the fault, the faulting is initiated and leads to an earthquake (Reid, 1911). Therefore, the first boundary condition in this model is that the accumulated shear stress equals the strength of the rock when the return period is due.

Given the ground subject to a stress accumulation with time, the relationship between transient

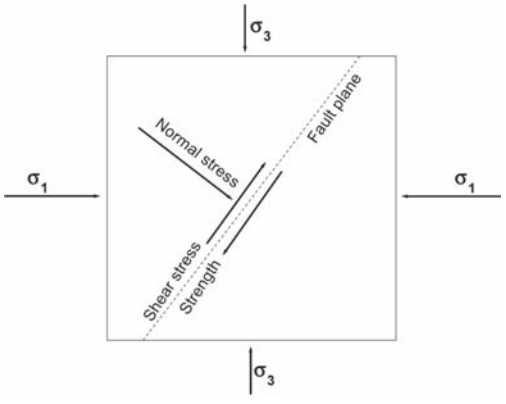

Figure 2. Systematic diagram showing the mechanism of faulting: when shear stress is greater than shear strength, the faulting should be activated. Note σ_1 and σ_3 on the figure denotes the major and minor principal stresses in horizontal and vertical directions, respectively.

stress accumulation ($\Delta\tau$) and stress accumulation (τ_t) at time t on the fault plane can be formulated as follows:

$$\tau_t = \int_{T=0}^{T=t} \Delta\tau \quad (3)$$

Applying the boundary condition derived beforehand, the relationship between the shear stress and the strength at return period R can be expressed as follows:

$$\tau_R = \int_{T=0}^{T=R} \Delta\tau = S \quad (4)$$

where $T = 0$ represents the very moment right after the latest occurrence; S = the strength of the rock.

Moreover, given the faulting governed by the simple law of physics, the probability of faulting can be expressed as follows:

$$\Pr(\textit{faulting}) = \Pr(\tau_t \ge S) \quad (5)$$

4.2 *Model verification on a deterministic basis*

On a deterministic basis, the earthquake probability is zero before the return period is due. Since the stress accumulation in every 162 years in this case is equal to the strength S, the unit stress accumulation per year is $S/162$. Therefore, the stress accumulation from 1906 to 2020 is equal to $(114 \times S)/162$, and $(134 \times S)/162$ till 2040. As a result, the earthquake probability is zero in 2020~2040 because at any moment during this time period the stress is less than the strength. Applying the calculation to evaluating the earthquake probability in

2040~2060, the same outcome (probability is zero) can be attained. As a result, it is a zero probability that the earthquake will occur before 2068 from a deterministic analysis, either it is from 2020~2040 or 2040~2060 without accounting for the uncertainty in stress accumulation.

With the two verifications, the results are robust compared to the deterministic analysis, so that this analytical model from the mechanism of faulting is reliable.

5 PROBABILISTIC ANALYSIS: THE UNCERTAINTY OF STRESS ACCUMULATION IN TIME

5.1 *The mean value of stress accumulation at time t*

Logically speaking, it is very unlikely that the earthquake really returns at the return period, which makes the deterministic analysis less realistic. One source of uncertainties in this problem is in the stress accumulation. In other words, the stress accumulation at time t is a random variable. For example, at the return period the stress accumulation should be a distribution with the mean value equal to the strength S given the return period, which can be expressed as follows:

$$E\left[\int_{T=0}^{T=R}\Delta\tau\right]=E[\tau_R]=S \tag{6}$$

where E denotes the expectation.

As a result, the mean value of stress accumulation at time t can be derived as follows (apparently t and R are constants):

$$E\left[\int_{T=o}^{T=t}\Delta\tau\right]=E[\tau_t]=E\left[\frac{t}{R}\int_{T=o}^{T=R}\Delta\tau\right]$$
$$=\frac{t}{R}\times S \tag{7}$$

5.2 *The variance of stress accumulation at time t*

Similarly, given the best-estimated standard deviation of stress accumulation at return period is equal to σ^* (i.e. constant), the variance of stress accumulation at time t can be derived as follows based on probability and statistics.:

$$VAR\left[\int_{T=0}^{T=R}\Delta\tau\right]=VAR[\tau_R]=\sigma^*$$
$$\Rightarrow VAR\left[\int_{T=0}^{T=t}\Delta\tau\right]=VAR\left[\frac{t}{R}\int_{T=0}^{T=R}\Delta\tau\right]$$
$$=\left(\frac{t}{R}\right)^2\times\sigma^* \tag{8}$$

With the mean and standard deviation of stress accumulation at time t, we can go on calculating the probability of τ_t greater than S, which is the likelihood of earthquakes based on the faulting model. It is worth noting that during such calculation the probability distribution for this variable is needed as well, no matter it is based on theory, observation, or assumption.

5.3 *Earthquake probability induced by the Meishan Fault with stress accumulation uncertainty and sensitivity analysis*

Since the variability and probability distribution of stress accumulation in Central Taiwan are not available, we carried out sensitivity analyses in the calculation of earthquake probability induced by the Meishan Fault. The levels of variability in terms of the coefficient of variation (= standard deviation/mean) are 0.5, 1.0 and 2.0, and we considered that stress accumulation is a variable following either the normal distribution or the log-normal distribution.

Figure 3 shows the earthquake probability on a variety of conditions. First of all, with the

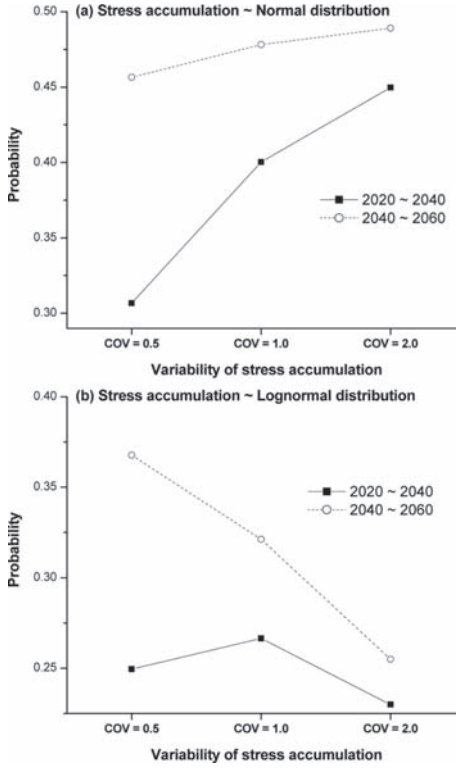

Figure 3. Earthquake probability with respect to different coefficient of variation.

new analytical model proposed, the earthquake probability induced by a specific fault is non-stationary, and it increases with the time that has elapsed in reflecting the continuing stress accumulation. Secondly, given the same period of time, the probability is substantially affected by the variability and probability distribution assigned for stress accumulation. For example, in 2020~2040, the probability can vary in a range from 23% to 44%, depending on the combination of levels of variability and probability distribution associated with the stress accumulation. In this case study, the increase in variability is not necessarily causing the increase in earthquake probability, as the calculations show an opposite trend with the normal and lognormal distributions employed to simulate this statistical attribute of stress accumulation.

From statistics and probability, such an influence in probability distribution can be fully expected and explained. Figure 4 shows the cases calculating the earthquake probability in 2040~2060. When the symmetrical normal distribution was used for modeling stress accumulation, the earthquake probability, $\Pr(\tau_t > S)$,is increased with the variability in τ_t. On the other hand, $\Pr(\tau_t > S)$ is slightly smaller with COV = 0.5 in τ_t than with COV = 2.0 when this variable is considered following the asymmetrical lognormal distribution. Therefore, as most probabilistic analyses, the underlying statistical attributes are the key factor to estimation. However, it must be noted that the characterization in the statistical attribute of this variable is not the scope of this study. An independent, comprehensive study with such a focus should be suggested to address the problem.

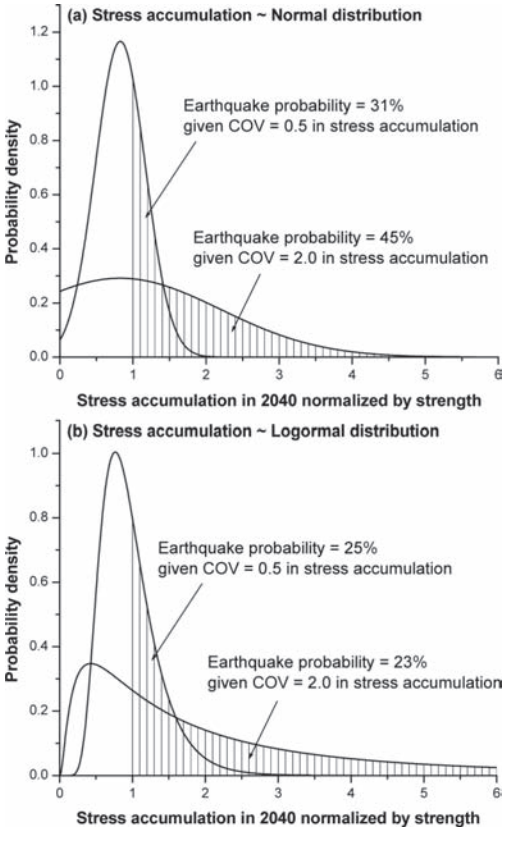

Figure 4. Earthquake probability in 2040~2060s with respect to different coefficient of variation.

6 DISCUSSIONS

Contradictory to the stationary results suggested by the Poisson process, the suggested analytical model provides a non-stationary earthquake process, which is more realistic to both the observation and the experience. However, the Poisson model is still valid in calculating the earthquake probability. The confusion comes from the underlying difference of the two problems.

For the new proposed analytical model, a specific fault with its best-estimated return period and last occurrence is required. For a specific fault, once the earthquake happens, the train energy is released. The shear stress needs time to accumulate to trigger another earthquake, so the earthquake probability drops at once when the earthquake happens and increases as the time passes by. Apparently, for a specific fault, it is a non-stationary process.

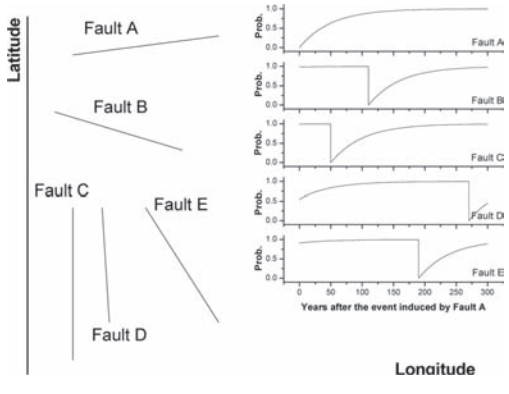

Figure 5. Systematic diagram showing the fundamental condition resulting in the memory-less effect in the Poisson model; given the region containing eight faults and the last event being triggered by Fault A, in the next few years, although the recurrence probability by Fault A is believed to be low, the increasing probability associated with other faults in the system makes up Fault A's low probability.

On the other hand, when a broad region with more active faults, say 20 faults, is taken into consideration, the individually non-stationary process becomes a robust stationary process, as suggested by the Poisson model.

To be more specific, Figure 5 shows a systematic diagram illustrating the relationship between many non-stationary processes and a stationary process after combining. Given Fault A occurring at year "zero," the overall earthquake probability in the very next moment is unchanged, or memory-less, because the earthquake probabilities induced by the other four faults keep increasing. Those probability increases compensate the "probability resetting" in Fault A, which is more believed to be a non-stationary process.

7 CONCLUSIONS

This paper introduces a new analytical model to tackle the same problem from the underlying mechanism of faulting. That is, the faulting or earthquake is induced because the strength is exceeded by the external stress on the fault plane. Using this physics-based model with some probabilistic consideration in stress accumulation, the sensitivity study shows that the earthquake probability in 2020~2040 is indeed lower than that in 2040~2060 given the same hypothetical information in the variability and probability distribution in stress accumulation. In short, the plausible non-stationary earthquake process induced by a specific fault is properly modeled by this new model proposed.

Based on the stationary Poisson process, the earthquake probability in 2020~2040 and in 2040~2060 is of no difference (=12%) given the best-estimated return period (i.e. 162 years) of the Meishan Fault and its last event in year 1906, owing to the nature of this memory-less statistical model. This stationary estimation is considered less realistic. Take the Tohoku earthquake in 2011 for example, an equivalent event induced by the same fault is less likely to recur in the coming few years, but much more probable in few hundred years. In short, such a problem is a non-stationary process, implying the earthquake memory effect.

It is worth noting that as many suggested, the customary use of the stationary Poisson model in earthquake prediction is robust from a statistical point of view. The problem is that the two situations should not be considered the same. Given a broad region where there are, say, 20 active faults, the earthquake probability in the region is a result of 20 non-stationary processes, which becomes a robust stationary process because the respective variation in faulting probability with time is canceled out owing to the nature of statistics, resulting in an overall, memory-less probability estimation with a stationary statistical model.

REFERENCES

Ang, A.H. & Tung, W.H. 2007. Probability concepts in engineering: emphasis on applications to civil and environmental engineering. 2nd edn., Wiley, N.J.

Cheng, C.T., Chiou, S.J., Lee, C.T. & Tsai, Y.B. 2007. Study on probabilistic seismic hazard maps of Taiwan after Chi-chi earthquake. *Journal of GeoEngineering* 2(1): 19–28.

Kramer, S.L. 1996. *Geotechnical Earthquake Engineering*. Prentice Hall Inc., N.J.

Lin, C.W., Chen, W.S., Liu, Y.C. & Chen, P.T. 2009. Active faults of Eastern and Southern Taiwan. *Special Publication of Central Geological Survey* 23: 178 (In Chinese with English abstract).

Lin, C.W., Lu, S.T., Shih, T.S., Lin, W.H., Liu, Y.C. & Chen, P.T. 2008. Active faults of Central Taiwan. *Special Publication of Central Geological Survey* 21: 148 (In Chinese with English abstract).

Reid, H.F. 1911. The elastic rebound theory of earthquakes. *Bulletin of the Department of Geology, University of Berkeley* 6: 413–444.

Wang, J.P., Brant, L., Wu, Y.M. & Taheri, H. 2012a. Probability-based PGA estimations using the double-lognormal distribution: including site-specific seismic hazard analysis for four sites in Taiwan. *Soil Dynamics and Earthquake Engineering* 42: 177–183.

Wang, J.P., Chan, C.H. & Wu, Y.M. 2011. The distribution of annual maximum earthquake magnitude around Taiwan and its application in the estimation of catastrophic earthquake recurrence probability. *Natural Hazards* 59(1): 553–570.

Wang, J.P., Huang, D. & Yang, Z. 2012c. The deterministic seismic hazard map for Taiwan developed using an in-house Excel-based program. *Computers and Geoscience* 48: 111–116.

Wang, J.P., Huang, D.R., Cheng, C.T., Shao, K.S., Wu, Y.C. & Chang, C.W., 2013. Seismic hazard analysis for Taipei city including deaggregation, design spectra, and time history with excel applications. *Computers and Geosciences* 52: 146–154.

Wang, J.P., Lin, C.W., Taheri, H. & Chen, W.S. 2012b. Impact of fault parameter uncertainties on earthquake recurrence probability by Monte Carlo simulation—an example in central Taiwan. *Engineering Geology* 126: 67–74.

Wu, Y.M. & Kanamori, H. 2005. Experiment on an onsite early warning method for the Taiwan early warning system. *Bulletin of the Seismological Society of America* 95(1): 347–353.

Yen, J.Y., Chen, K.S., Chang, C.P. & Boerner, W.M. 2008. Evaluation of earthquake potential and surface deformation by Differential Interferometry. *Remote Sensing of Environment* 112(3): 782–795.

This page intentionally left blank

Geotechnical Safety and Risk IV – Zhang et al. (eds)
© 2014 Taylor & Francis Group, London, ISBN 978-1-138-00163-3

Modelling techniques of submarine landslide in centrifuge

C. Zhao, W.Z. Zhang, J.H. Zhang, K.Z. Wang & Z.S. Xiong
State Key Laboratory of Hydroscience and Engineering, Tsinghua University, Beijing, China

ABSTRACT: Gas hydrate is ice-like compound consisting of mostly methane and water. It is a promising energy source but very unstable and easy to dissociate when it is disturbed. If gas hydrate in the sediments under the sea dissociates, it may trigger a submarine slide and render high risk to human beings and facilities in the sea. In this paper, modeling techniques were developed to simulate changes of strength and pore pressure in sediments caused by the dissociation of gas hydrates in a geotechnical centrifuge in order to assess the risk potential associated with submarine slides. The soft toothpaste, Kaolin paste and Kaolin paste underlying sand were used to simulate sediments containing gas hydrate. Centrifuge modeling tests were carried out on submarine landslides using the materials. The effectiveness of the methods is discussed.

1 INTRODUCTION

1.1 *Type area*

Gas hydrate is ice-like compound consisting of mostly methane and water. It is a promising energy source because of its great storage under the sea. However, gas hydrate is very unstable and easy to dissociate when it is disturbed. If gas hydrate in the sediments under the sea dissociates, it may trigger a submarine slide render high risk to human beings and facilities in the sea (Field 1990, McIver 1982, Paull et al. 1996, Mienert et al. 2005).

Theoretical and experimental investigations have been made to identify the relationship between the strength variation of sediment containing gas hydrate and the dissociation so as to assess the risk potential imposed on natural resource development, sea-floor transport and communication, coastal development and marine environment protection (e.g. Sultan et al. 2004, Xu 2006, Nixon & Grozic 2007, Winters et al. 2007). Great efforts also have been dedicated on the mechanism and consequences of submarine landslides (e.g. Locat & Lee 2002, Masson et al. 2006, Chau 2009, Brune & Ladage 2010, Sassa & Sekiguchi 2011, Xiong & Zhang 2012, Boukpeti et al. 2012). Physical modeling is one of the important approaches used to improve the understanding of the submarine landside and its influence over offshore structures such as pipelines (e.g. Gaudin et al. 2009, Boylan et al. 2009, Truong et al. 2010, Chi et al. 2011).

This paper discusses modeling techniques developed to initiate a submarine landslide in a geotechnical centrifuge. Different methods were used to simulate the changes of strength and pore pressure in sediments caused by the dissociation of gas hydrates in order to trigger submarine landslides. The purpose of the study was to develop an effective method so as to initiate a submarine landslide triggered by gas hydrate dissociation.

2 METHODOLOGY

The mechanism of the dissociation of gas hydrate affecting the stability of the submarine slope is generally considered in two ways: 1) the dissociation of gas hydrates reduces the strength of sediments and thus forming a weak layer which leads to instability of the sediments; 2) excess pore pressure generates from gas hydrate dissociation and reduces the effective stress in the sediments. The methodology of simulating sediment containing gas hydrate falls in three categories: 1) using soft materials, such as toothpaste or soft clay, to form the weak layer in sediments; 2) introducing excess pore pressure in sediments to simulate high pressures resulted from gas hydrate dissociation; 3) producing similar environment analog to the ocean (Xiong 2010, Zhang 2012, Wang 2012). Modeling techniques in a geotechnical of centrifuge were developed to simulate submarine landslides with methodology mentioned. The centrifuge tests were carried out on the 50 gt centrifuge at Tsinghua University, as shown in Figure 1.

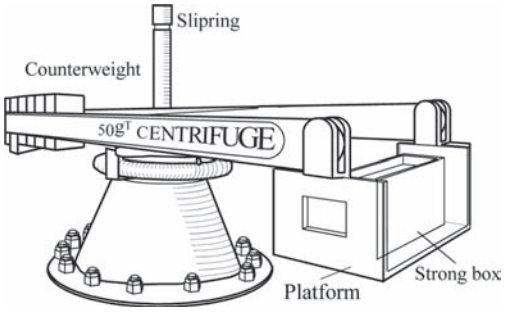

Figure 1. The 50 gt centrifuge at Tsinghua University.

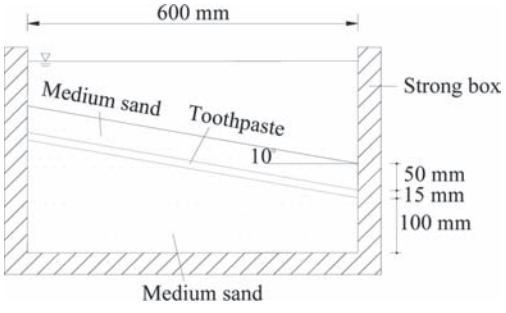

Figure 2. Centrifuge model with a layer of toothpaste.

3 TESTS AND RESULTS

3.1 *Simulation of weak layer*

A medium sand was used to simulate the sediment containing gas hydrates. A 15 mm thick layer of toothpaste forms a weak layer interlayering between two layers of medium sand. The toothpaste made in China can be bought in any supermarket. The undrained strength of the toothpaste was determined by vane shear test to be 0.5 kPa. The medium sand above the toothpaste, having a thickness of 50 mm, was prepared by sand raining method. The dry density of the sand is 1600 kg/m^3. Figure 2 shows the preparation of a centrifuge model of a slope. The strong box has an inner dimension of 600 mm in length, 500 mm in height and 200 mm in width. The slope angle was 10 degree. The toothpaste was so soft that it was manually squeezed onto the lower layer of medium sand to form the weak layer. The model was filled with tap water before being put onto the centrifuge platform.

The slope failed at a centrifugal acceleration of 10 g. Figure 3 shows the model after failure. The top sand layer moved downward along the layer of toothpaste. However, as the toothpaste was so soft that it was squeezed out and smeared on the plexiglass. The main drawback of the method was that the toothpaste was not stable as it was partially dissolved in the water and lost most of its strength, leading to conspicuous deformation in the layer in 1 g condition. If the model was soaked for a long time, the toothpaste will be squeezed out rendering sand-sand contact. Later the Kaolin clay mixed with tap water was also used, but its strength was too high after consolidation in the centrifuge. It cannot form the weak layer in sand.

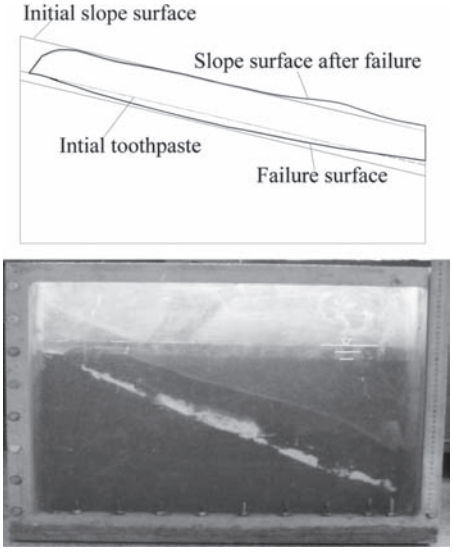

Figure 3. Centrifuge model failed at an acceleration of 10 g.

3.2 *Simulation of high pore pressure in sediment*

Gas releasing from hydrate dissociation will increase excess pore pressures in the sediment. As the gas hydrate may change from solid phase first to liquid and then to gas phase, therefore high pressure water then air was introduced within the sediment to trigger submarine slides in the centrifuge model. Figure 4 illustrates the layout of model set-up for a slope. A plexiglass plate was used to form an inclined base. Rotating the plexiglass plate around the lower end will change the slope angle. The slope consisted of Kaolin clay of 20 mm thick underlying the medium sand. Before placing the sand and clay, a set of tiny pipes were installed on the plate. High pressure water or air will flow in through the pipes to apply excess pore pressure in the sand. Three pore water pressure transducers were placed in the sand near the outlets of the pipes to monitor the variation of the pore pressure. Soil pressure cells were installed at the toe of the slope to measure the impact of the landslides on

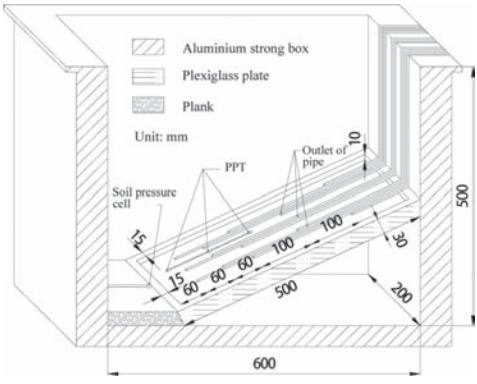

Figure 4. Layout of centrifuge model set-up.

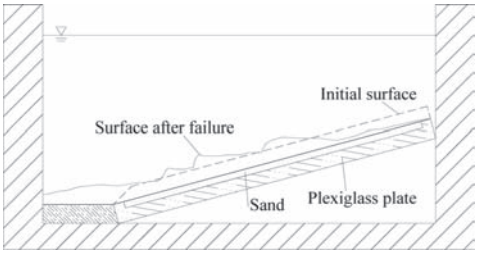

Figure 5. A model with 15° slope angle after failure.

structures, such as pipelines. The Kaolin clay was prepared as paste using tap water. After the preparation, the model was filled with tap water.

The consolidated undrained shear strength of the Kaolin clay was determined by means of triaxial tests. The clay slope will not fail at slope angles below 25° at a centrifugal acceleration of 50 g. It was the excess pore pressure rendering the failure of the gentle slope. Figure 5 shows a model with 15° slope after failure. It was found from the tests that: 1) the water or air pressure was effective to increase excess pore pressure in the sand and thus trigger a submarine landslide, 2) However, the state and strength of the clay was very sensitive to the property of water. As tap-water did not reflect the ocean environment, the Kaolin clay paste was very sticky and its dry density was greater than 1600 kg/m^3 after centrifuge test.

3.3 *Simulation of ocean water*

The ocean is composed of water with salt concentration of 3.5%. It is the basic feature of the ocean environment and highly affects the behavior of ocean sediment soil. During the preparation of the model, edible salt of sodium chlorde bought in supermarket was used to prepare the sea water

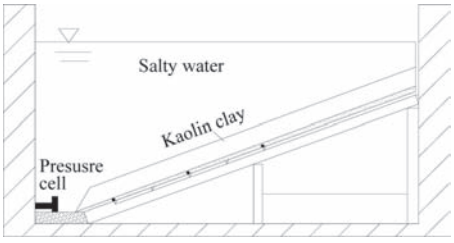

Figure 6. Centrifuge model set-up using salty water.

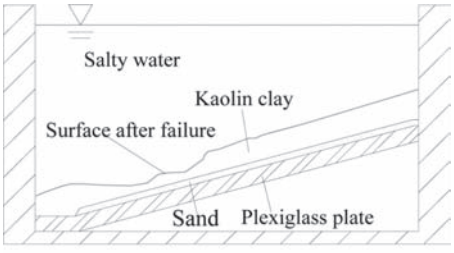

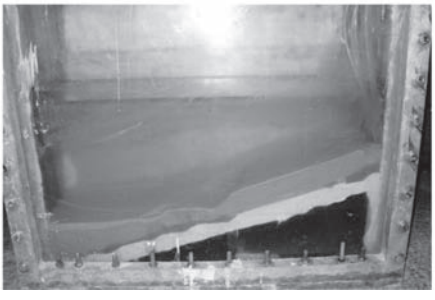

Figure 7. A model with 15° slope angle after failure.

with the concentration of 3.5% analog to the South China Sea. Figure 6 shows the model set-up. The layout of the transducers and water pipes was identical to that in Figure 4.

Due to the presence of the salt, the Kaolin was greatly dispersed and thus less sticky, featuring low cohesion strength. Tiny visible pores uniformly distributed in the clay, which rendering very different properties from that in fresh tap water. With the same preparing procedure, the dry density of the clay in the model was measured to be only 1140 kg/m^3, significantly lower than that in fresh water. Figure 7 shows a model with 15° slope failed at 50 g, however it was quite stable in fresh water owing to the cohesion strength of the Kaolin clay.

4 DISCUSSIONS AND CONCLUSIONS

The key factors influencing landslide occurrence are elevated pore pressures (leading to decreased

frictional resistance to sliding) and specific weak layers within stratified sequences. The deposit condition in ocean environment also contributes greatly to the instability of submarine sediments.

This paper discuss the modeling technique in centrifuge with the main purpose to develop an effective method so as to initiate a submarine landslide triggered by gas hydrate dissociation. In the early stage of the development of modeling technique, tap water was used to prepare Kaolin clay resulting in very strong material with high shear strength.

When using salty water was used to simulate sea water, the Kaolin clay featured low strength and low density, which was more analog to the ocean environment. High pressure water was introduced followed with high pressure air in the sediment can well simulate the sediment containing gas hydrate and its dissociation process.

The method described in the paper was effective to trigger underground landslides in the centrifuge. It provides a sound basis for assessing hazard potential related to submarine landslides.

ACKNOWLEDGEMENTS

The research work was funded by the National Natural Science Foundation of China (51038007) the National Basic Research Program of China (2013CB035902), and State Key Laboratory of Hydroscience and Engineering Project (2012-KY-04, 2013-KY-04).

REFERENCES

Boukpeti, N., White, D.J. & Randolph, M.F. 2012. Analytical modelling of the steady flow of a submarine slide and consequent loading on a pipeline. *Geotechnique* 62(2): 137–146.

Boylan, N. Gaudin, C., White, D.J., Randolph, M.F. & Schneider, J.A. 2009. Geotechnical centrifuge modelling techniques for submarine slides. *Offshore Geotechnics—Petroleum Technology* 7: 65–72.

Brune, S. & Ladage, S. 2010. Submarine landslides at the eastern Sunda margin: observations and tsunami impact assessment. *Natural Hazards* 54(2): 547–562.

Chau, K.T. 2009. Numerical simulations of submarine-landslide-induced and sea-floor-collapse-induced tsunami along coastline of South China. Prediction and Simulation Methods for Geohazard Mitigation, eds. Oka, F; Murakami, A; Kimoto, S, pp. 247–252.

Chi, K., Zakeri, A. & Hawlader, B. 2011. Impact drag forces on pipelines caused by submarine glide blocks or out-runner blocks. 5th Int. Symp. on Submarine Mass Movements and Their Consequences, eds. Yamada, Y, Kawamura, K, Ikehara, K., Kyoto, Japan, Oct 24–26, 2011. *Advances in Natural and Technological Hazards Research* 31: 429–439.

Field, M.E. 1990. Submarine landslides associated with shallow seafloor gas and gas hydrates off northern California, *AAPG Bull.* 74(6): 971–972.

Gaudin, C., White, D.J. & Boylan, N. 2009. A wireless high-speed data acquisition system for geotechnical centrifuge model testing. *Measurement Science & Technology* 20(9): 095709.

Locat, J. & Lee, H.J. 2002. Submarine landslides: advances and challenges. *Can. Geotech. J.* 39: 193–212.

Masson, D.G., Harbitz, C.B., Wynn, R.B., Pedersen, G. & Løvholt, F. 2006. Submarine landslides: processes, triggers and hazard prediction. *Philosophical Transaction Royal Society A* 364: 2009–2039.

Mienert, J., M. Vanneste, S. Bünz, K. Andreassen, H. Haflidason & H.P. Sejrup 2005. Ocean warming and gas hydrate stability on the mid-Norwegian margin at the Storegga Slide, *Mar. Pet. Geol.* 22: 233–244.

Nixon, M.F. & Grozic, J.L.H. 2007. Submarine slope failure due to gas hydrate dissociation: a preliminary quantification, *Canadian Geotechnical Journal* 44(3): 314–325.

Paull, C., W.J. Buelow, W. Ussler, & W.S. Borowski 1996. Increased continental-margin slumping frequency during sea-level lowstands above gas hydrate-bearing sediments, *Geology* 24: 143–146.

Sassa, S. & Sekiguchi, H. 2011. Dynamics of Submarine Liquefied Sediment Flows: Theory, Experiments and Analysis of Field Behavior. 5th International Symposium on Submarine Mass Movements and Their Consequences, eds. Yamada, Y, Kawamura, K, Ikehara, K., Kyoto, Japan, Oct 24–26, 2011. Submarine Mass Movements and Their Consequences, *Advances in Natural and Technological Hazards Research* 31: 405–416.

Sultan, N., Cochonat, P., Foucher, J.P., Mienert, J. 2004. Effect of gas hydrates melting on seafloor slope instability, *Mar. Geol.* 213: 379–401.

Truong, Q.H., Lee, C., Cho, G.C. & Lee, J.S. 2010. Geophysical Monitoring Techniques for Underwater Landslide in 1 g Model. *Journal of Environmental and Engineering Geophysics* 15(1): 1–19.

Wang, K.Z. 2012. Mechanism of submarine landslide considering high excess pore pressure from gas hydrate dissociation. Thesis for Master degree, Tsinghua University. (in Chinese).

Winters, W.J., Waite, W.F., Mason, D.H., Gilbert, L.Y. & Pecher, I.A. 2007. Methane gas hydrate effect on sediment acoustic and strength properties, *Journal of Petroleum Science & Engineering* 56(1–3): 127–135.

Xiong, Z.S. 2010. Mechanism of submarine landslide initiated by gas hydrate dissociation. Thesis for Bachelor degree, Tsinghua University. (in Chinese).

Xiong, Z.S. & Zhang, J.H. 2012. Effect of Dissociation of Gas Hydrate on the Stability of Submarine Slope. 31st International Conference on Ocean, Offshore and Arctic Engineering, Rio de Janerio, Brazile, Jun 10–15, 2012, OMAE2012-83190.

Xu, W. & Germanovich, L.N. 2006. Excess pore pressure resulting from methane hydrate dissociation in marine sediments: A theoretical approach, *J. Geophys. Res*., 111, B01104, doi: 10.1029/2004JB00360.

Zhang, W.Z. 2012. Initiation of submarine landslide in centrifuge. Thesis for Bachelor degree, Tsinghua University. (in Chinese).

6 *Reliability and risk analysis*

This page intentionally left blank

Geotechnical Safety and Risk IV – Zhang et al. (eds)
© 2014 Taylor & Francis Group, London, ISBN 978-1-138-00163-3

The schedule optimization for subway station construction based on critical chain

G.X. Chen
School of Civil Engineering, Tongji University, Shanghai, China
School of Civil Engineering and Architecture, Henan University of Technology, Zhengzhou, China

J.L. Song, Z.R. Xiao, J. Wang & L.F. Yue
School of Civil Engineering and Architecture, Henan University of Technology, Zhengzhou, China

ABSTRACT: Subway construction schedule management is one of the major tasks for the government departments, owner and construction units. As a new schedule management method, critical chain method is effective at shortening the project duration, optimizing the resources scheduling and economizing the project investment. Based on the analysis of basic theory and assumption of the critical chain, and combined with the characters of subway station construction, steps applying critical chain to subway project were illustrated in this paper, and methods to calculate the buffer size and activity duration were also introduced. Finally, the critical chain method is systematically used in one subway station of Zhengzhou Metro 1 route and the performance of critical chain method is satisfactory.

1 INTRODUCTION

With the positive characteristics of large capacity, fast speed, safety, punctuality, energy and land saving and so on, subway rail transit is developing with such a high speed in recent years. For example, Zhengzhou City has planned 6 subway lines with a total length of 202.53 km, including three horizontal lines, two vertical lines and one ring line, and the total investment is expected to be 100 billion Yuan. Accompanied with the construction of subway rail transit engineering, schedule management has become one of the key tasks for government departments, owner and construction units to figure out.

Along with the rapid advance of computer technology and mutual penetration of related disciplines, and combined with the decision theory and cybernetics, certain kinds of schedule management technologies such as Decision Network (DN), Graphic Evaluation and Review Technique (GERT), Venture Evaluation and Review Technique (VERT) are invented based on the network planning technology. However, as the characteristics of schedule management are changing, all the schedule management methods above are not being able to meet the needs of modern project schedule management gradually, especially for the subway project. Critical Chain Project Management, known as CCPM—presented by Goldratt in 1997 in his book named *The Critical Chain*—is considered to be a new era and stage for the project management theory (Kevin & Watson 2007). Because of its good performance in schedule management and investment control, critical chain method has been widely used in the field of manufacturing (Han & Xu 2005), software research and development (Dai & Ren 2009) and other aspects.

Starting from solving the main limiting factors of the project, CCPM overcomes the shortcomings of traditional scheduling methods in just considering the logical relationship between processes and the duration redundancy of activities, and it is especially good at schedule optimization. However, few researches are conducted applying CCPM to urban rail transit project. Considering the complexity of rail transit projects, this paper applies CCPM to the schedule management of urban rail transit project. By taking the construction of one station in Zhengzhou rail transit No.1 line for empirical research, the basic procedure of applying CCPM to rail transit project schedule management is introduced, and the critical chain method optimizes the project schedule to a certain extent. This paper provides a more comprehensive description of applying critical chain method to urban rail transit project.

2 SUBWAY PROGRESS CHARACTERISTICS AND INFLUENCE FACTORS

The construction cycle of subway project is long-period. Usually, the average construction cycle of a

single metro line in China ranges from 4 to 5 years, and it takes 10 to 20 years to build up a general line network. In the course of general line network building, difficulties such as layout of the subway line network, construction sequence and construction resource sharing are with different characteristics from traditional project schedule management. The following are the main characteristics.

2.1 *Limited time*

Subway project is a large city infrastructure project with big social impact, which is generally regarded as the landmark project of a city, representing the city's image and receiving widespread concern from the government and the public. There is almost no possibility of delaying the progress because the completion date is always announced and published to society after determined, and the rigid requirement of progress is in great demand. In addition, as an indicator of their performance, managers pursue the construction speed of subway project too much, which brings many new problems for setting schedule goals and milepost program.

2.2 *Heavy preliminary work*

The subway station is usually located at the prosperous urban area and the main road of the city. There are various kinds of preliminary difficulties including land acquisition and resettlement, afforest transplantation, pipeline move, bus line change and traffic reconciliation, which demand much work of coordination. What's more, the land acquisition and resettlement are almost the most difficult issues because there are many stakeholders involved and the procedures are cumbersome during implementing. Organizing reasonable organization structure then establishing an efficient construction team, preparing various documents submitted for approval and the implementation of specific tasks, all these include a large amount of complicated work. Therefore, the preliminary workload of rail transit project is very heavy and intricate, and we can say that the successful settlement of preliminary problems is equivalent to half the success of subway construction.

2.3 *Slow delivery of blueprint*

The schedule goals for rail transit project are tight and the design task is heavy. The time for design unit to prepare is short, and the influence of non-technological factors like route rechanneling should be taken into consideration in the design process, which can lead to the decline in drawing speed and quality of the drawings in a certain extent. Furthermore, as the standards for the quality and technology of subway project are very high, and the design units must spend some more time and energy to ensure the quality of the drawings, which will definitely result in delay of the speed of drawings. Therefore, the contractors frequently wait for the blueprint to work, resulting in the ***three simultaneities project***, namely designing while constructing and modifying simultaneously. In addition, because there are not complete and systematic drawings, it is quite easy to cause a lot of design changes later, or even lead to rework, which will also contribute to the procrastination of the construction drawings delivery.

3 THEORY AND BASIC ASSUMPTIONS OF CRITICAL CHAIN

3.1 *The basic theory of critical chain*

Known as TOC, theory of constraint is also called *bottleneck theory*, which originates from the Optimized Production Technology (OPT), and it is first generated and applied in manufacturing industry (Goldratt 1997). Goldratt, the author of CCPM held the opinion that simply pursuing the maximization of local production efficiency of each department does not necessarily lead to global optimum, and proposed the production management theory focusing on the settlement of constraint factors and bottleneck processes, namely the theory of constraint.

TOC is a systematic cyclical process including discovering, improving and eventually utilizing the constraints at the maximum. The core is to utilize the bottleneck activities and resources restricting system function, and the basic assumption is "any system exists one bottleneck at least, namely the restraining factor, which restricts the project's maximum output". What's more, Goldratt also showed clearly that in the process of project implementation, utilization rate of the resources is not balanced, and the output of a certain project is only affected by a certain kind of bottleneck resources instead of all the project resources. Therefore, we must improve the utilization of bottleneck resources in order to speed up the progress of the project (Ma & You 2007).

By applying the constraint theory to project management, Goldratt presented the critical chain project management. CCPM puts the importance of resource constraints to the same importance level with logical relationship of the processes. It introduces that the total construction period is determined by the duration of each activities, their logical relationship, resource constraints and other factors. By cutting down and conducting effective integration of the safety time to be the buffers, the

critical chain eliminates various possible uncertain factors that may delay the progress of project implementation.

3.2 *Basic assumptions*

As a new planning technique for project schedule management, the theory of critical chain project management implies some basic assumptions and principles, and to be specific, the main points are below.

3.2.1 *Progress impact factors*

There are many factors affecting the project progress, such as logical relationship of the processes, supply conditions of the resources, requirements of the construction period and other characteristics of the project. Traditional project scheduling techniques considered only the influence of logical relationship between the processes. The technique of critical chain project management based on Theory of Constraint presents that, not only the logical relationship of processes affects project schedule, but also the supply conditions of resources have a great impact on schedule. Meanwhile, critical chain method also takes the factor of human resource into consideration, such as Students Syndrome, Parkinson's Law (Zhao et al. 2009), etc, and the impact of various possible factors on project schedule is analyzed comprehensively.

3.2.2 *Estimation of the construction period*

Construction period of the process restricts the whole duration of the project. It is especially important to take an appropriate method to calculate and estimate the duration of the activities in subway project. General project schedule software obtains the estimated construction period through industrial standards and rules, or even the empirical data accumulated by the enterprise, which has a higher completion guarantee rate. However, construction period obtained through the above ways has been proved to be too long by many scholars (Chen & Guo 2010). The critical chain technique suggests that, construction period of the activities contains two parts of estimation: the necessary time and the safety time. The necessary time is considered to be the necessary estimation to complete the process, and safety time contributes less to the process completion, and the safety time is thought to be unnecessary.

3.2.3 *Buffer determining and affected factors*

There are various kinds of risks resulting in progress delays in the process of project implementation. In order to avoid the risks, the critical chain technique eliminates the safety time out of the construction period and inserts it into the distal end of critical chain or the junction of non-critical chain and critical chain in the form of time buffer. The critical chain technique presents three kinds of buffers: Project Buffer (PB), Feeding Buffer (FB) and Resource Buffer (RB), in which RB exists as an early warning indicator (Cheng et al. 2007).

At present, the frequent method to calculate the buffer size is mainly the cut-and-paste method and the square root of variance method. However, in general, there are many factors affecting the size of the buffers, such as safety time of the process, the characteristics of the project, the project manager's risk preference and complexity of the network graph, etc. Combined with the characteristics of different projects, there are some new methods suggested to calculate the buffer size by some scholars from the different points of view, which are still in the stage of theoretical research without practical application (Cao & Liu 2010).

3.2.4 *Critical chain identification*

Goldratt defined critical chain as "the longest chain constituted by activities determining the earliest completion time of the project". The critical chain is generally obtained through the following ways: Get the original project schedule through the traditional scheduling technology such as the critical path method; adjust the initial schedule based on resource constraints and time requirements then to get the adjusted schedule; circulate this process constantly to obtain the longest path, and the longest path is the critical chain.

4 PRACTICAL APPLICATIONS

This paper takes the construction of one station in Zhengzhou rail transit No.1 line for empirical research, combined with the critical chain project management technique, and studies the subway station schedule. Relevant activities, duration and logical relations of the project are shown in Table 1.

4.1 *Determination of the initial schedule*

Use network planning technology to get activity-on-node network of this project, which is shown in Figure 1.

There are a total of 8 task nodes in the civil engineering of the station, constituting 2 construction paths, which are:

Path 1: A1000-A1010-A1020-A1030-A1070;
Path 2: A1000-A1010-A1020-A1040-A1050-A1060-A1070.

Path 2 is the longest. Therefore, the critical path is Path 2. Initial scheduling of the project is shown in Figure 2.

Table 1. The activity and coefficient.

Code	No.	Name	Project duration/d	Foreground task	Logical relations
A1000	A	Building demolition	45		
A1010	B	Pipeline moving	60	A	SS+15
A1020	C	Maintenance construction	350	B	FS-15
A1030	D	Dewatering construction	20	C	FS-13
A1040	E	Foundation pit construction	50	C	FS-6
A1050	F	Main construction	280	E	FS-28
A1060	G	Gateway construction	140	F	SS+130
A1070	H	Affiliated construction	190	G	SS

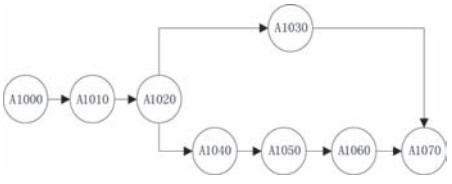

Figure 1. Activity-on-node network of this project.

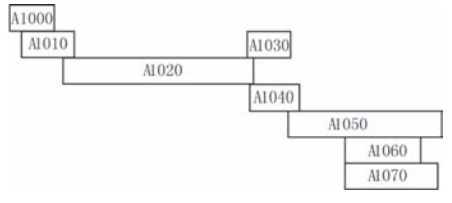

Figure 2. Initial scheduling.

Table 2. Critical chain activity duration and buffer size.

Code	No.	Name	d'	Δt_i
A1000	A	Building demolition	23	22
A1010	B	Pipeline moving	30	30
A1020	C	Maintenance construction	175	175
A1030	D	Dewatering construction	10	10
A1040	E	Foundation pit construction	25	25
A1050	F	Main construction	140	140
A1060	G	Gateway construction	70	70
A1070	H	Affiliated construction	95	95

4.2 *Activity duration and buffer size calculation*

According to the *critical chain* by Goldratt, the critical chain activity duration is half the amount of planning duration, and the buffer size is half the amount of safety time related.

$$d' = \frac{1}{2} \cdot d \tag{1}$$

$$Buffer\ size = \sum_{i=1}^{n} \left(\frac{1}{2} \Delta t_i \right) \tag{2}$$

where: d' is critical chain activity duration, Δt_i stands for safety time, n is the number of the activities. Then the critical chain activity duration and buffer size are shown in Table 2.

4.3 *Adjusting the initial scheduling*

After analyzing the actual situation of the project and optimizing the collective resources and the logical relationship of the activities, we find that pipeline relocation construction can be carried out together with building demolition. Then, adjust their logical relations as SS; adjust logical relations of pipeline relocation and maintenance construction as FS; adjust logical relations of dewatering construction and foundation pit construction as FS-6; adjust logical relations of main construction and foundation pit construction as SS+24, and other logical relations remain invariant. The logical relationship of the activities and the critical chain activity duration after adjustment are shown in Table 3.

4.4 *Determining the critical chain and the buffer*

Take the necessary time of the activities as the critical chain duration, then get PB and FB of the project using the cut & past method and insert it into the corresponding chain, which makes reasonable use of the safety time and ensures that the project can be implemented in accordance with the schedule, and the project duration is shortened as well. According to the calculation result, the

Table 3. The new coefficient of the activities.

Code	No.	Name	Foreground task	Logical relation	Buffer size
A1000	A	Building demolition			11
A1010	B	Pipeline moving	A	SS	15
A1020	C	Maintenance construction	B	FS	87
A1030	D	Dewatering construction	C	FS-13	5
A1040	E	Foundation pit construction	C	FS-6	12
A1050	F	Main construction	E	SS+24	70
A1060	G	Gateway construction	F	SS+130	35
A1070	H	Affiliated construction	G	SS	47

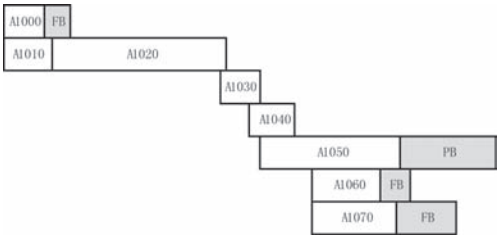

Figure 3. Critical chain scheduling.

subway station project scheduling is obtained based on critical chain, which is shown in Figure 3.

According to Figure 2, the original planned duration is 746 days. The critical chain project duration of subway station is 445 days and the buffer size is 189 days. The total duration is 634 days, less than the original planned duration 112 days. That is to say the critical chain method could effectively optimize the project schedule.

5 CONCLUSIONS

As a new method of project schedule management, CCPM is widely used in schedule planning and time optimization. However, in the present study, the critical chain method is mostly applied in part of the project, and has not been applied to the whole project schedule management systematically, which is contradictory to the theory of critical chain that local optimum does not necessarily lead to global optimum at a certain extent.

Meanwhile, critical chain emphasizes the importance of resources and supply chain management. Applying the critical chain method partly and setting various kinds of buffers are likely to have a great impact on the whole project resource scheduling, and then adversely affect the overall progress of the project, which does not achieve the purpose of optimizing the project schedule. Therefore, the utilization of critical chain method should not be limited at a small range of sub-projects or small projects. Instead, the method of critical chain project schedule management should be used systematically to achieve the optimization of project resources, scheduling and other elements.

ACKNOWLEDGMENT

The authors wish to acknowledge the support from Capital Foundation—Diaphysis Teacher's subsidy of Henan Province 2010GGJS-083.

REFERENCES

Cao, X.L. & Liu, R.H. 2010. Research on the calculation method of the buffer of critical chain project management. *Statistics and Decision* (303): 69–71.

Chen, Y. & Guo, Y.L. 2010. Flexible Management of Expressway Construction Scheduling Based on Key Chain. *Journal of Changsha University of Science & Technology (Social Science)* 25(3): 26–30.

Cheng, T.T., Li, W.B., Cheng, X. 2007. Research and Application for Critical Chain in Project's Process Management. *Microcomputer Applications* 28(5): 539–543.

Dai, Y.B. & Ren, X.L. 2009. Research on project critical chain based on Bayesian network. *Computer Applications and Software* 26(10): 127–129.

Goldratt, E.M. 1997. *Critical Chain*. New York: North River Press.

Han, W.M & Xu, X.Q. 2005. The critical chain technique and the application in production plan. *Market modernization* 453(12): 19–20.

Kevin, J. & Watson, J.H. Blackstone, Stanley C. Gardiner. 2007. The evolution of a management philosophy: The theory of Constraints. *Journal of Operations Management* 25(2): 387–402.

Ma, G.F. & You, J.X. 2007. Quantitative Analysis of Critical Chain Multiple Project Scheduling Management. *Systems Engineering-Theory & Practice*, 27(9): 54–60.

Zhao, Z.Y., You, W.Y., Lv, Q.L. 2009. Research on the Making Construction Project Schedule with Critical Chain Method. *Journal of Railway Engineering Society*, (5): 98–102.

This page intentionally left blank

Geotechnical Safety and Risk IV – Zhang et al. (eds)
© 2014 Taylor & Francis Group, London, ISBN 978-1-138-00163-3

A cell-based model for predicting runout distances of detached materials in rainfall-induced slope failures

H.X. Chen & L.M. Zhang
Department of Civil and Environmental Engineering, The Hong Kong University of Science and Technology, Clear Water Bay, Hong Kong, China

ABSTRACT: Rainfall-induced slope failures are one of the most frequent hazards in hilly terrains. This paper presents a method that adopts a distributed cell model for predicting rainfall-induced slope failures in a large area and the runout distances of detached materials. The model consists of five components; namely, a digital terrain model, a spatial rainfall distribution model, a rainfall infiltration analysis model, a slope reliability analysis model and a runout distance prediction model. A cluster of unstable cells located together are viewed as an entity and the size effect of the combined detached materials is considered. The materials move down the slopes along the steepest paths on the digital elevation map. The method predicts the locations of rainfall-induced slope failures and their depositional zones reasonably well. The material movement traces assessed by this model also offer information for the assessment of landslide and rockfall risks. The presented method shows promise for use as a module in a real-time warning system for rainfall-induced slope failures.

1 INTRODUCTION

Rainfall-induced slope failures are one of the most frequent hazards in hilly terrains, especially for those with abundant supply of loose soil materials. The 2008 Wenchuan earthquake triggered numerous landslides, leaving a large amount of loose materials in steep hill slopes and gullies. Much of the loose materials lost stability in the past few years when triggered by heavy rains. The detached materials ran down to lower locations, posing great danger to roads and people, or becoming the source materials for debris flows. A cell-based model can be a viable tool for predicting potential rainfall-induced slope failures (e.g. Crosta & Frattini 2003, Baum et al. 2008, Takara et al. 2010, Arnone et al. 2011, Chen & Zhang 2013). However, there are still some pending issues for developing a cell-based model in the Wenchuan earthquake zone. One of these issues is to assess the runout paths and distances of detached materials in a large area efficiently.

The objective of this paper is to develop a distributed cell-based stability analysis model for predicting rainfall-induced slope failures and runout distances of detached materials in regional scale.

2 STUDY AREA

The study area, including the Xiaojiagou Ravine, Pubugou Ravine and their vicinity, is only 5 km from the epicenter, Yingxiu of the 2008 Wenchuan earthquake (Fig. 1). Provincial Road 303 (PR303) goes through the study area. It has an area of 16.8 km^2, an elevation range between 1,000 m and 3,540 m, and a local relief of 2,540 m (Chen & Zhang 2013). The exposed lithology in the study area is mainly composed of four kinds of Proterozoic magmatic rocks; namely, diorite, biotitic granite, granodiorite and hornblende diorite. The maximum and mean annual precipitations within the study area are 1,225 mm and 828 mm, respectively. Approximately 68% of the total precipitation falls between June and September. Based on the surface geological characteristics, the soils and rocks in the study area are classified into four types: loose soil deposit, vegetated soil, bedrock and riverbed. Among them, the bedrock and riverbed are set to be stable.

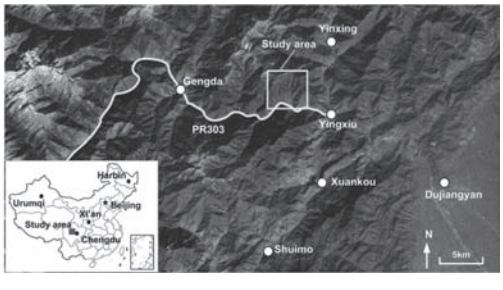

Figure 1. Locations of the study area (i.e. the box) and rain gauges (i.e. the six dotted locations).

3 MODEL FRAMEWORK

The distributed cell-based model consists of five components; namely, a digital terrain model, a spatial rainfall distribution model, a rainfall infiltration analysis model, a slope stability analysis model and a runout distance prediction model. The study area is discretized into a grid first with information for each cell assigned (e.g. the elevation, slope angle, soil depth, ground water level, soil properties, and rainfall information). The cell size is 20 m × 20 m. Based on the universal Kriging method, a spatial rainfall distribution model is used to interpolate the cumulative rainfall at each cell in the study area, which can be represented by an optimal linear combination of the rainfall records of the nearby rain gauges. The real-time hourly rainfall intensity at each cell can be then obtained. The reason why universal Kriging is used is that it does not require that the mean rainfall in the study area is constant and it reflects the topographic effect. The algorithm has been explained in detail by Olea (1999). An infiltration model for two-layer soils is then applied to compute the infiltration and runoff processes. The pore water pressure profile can be obtained. A slope stability analysis model is then used to compute the Factor of Safety (*FS*) of each cell at different times. If the factor of safety is smaller than 1, the cell is viewed as unstable. The probability of slope failure can be calculated using Monte Carlo simulation. The runout paths and distances of the detached materials are then assessed using a runout distance prediction model.

4 SLOPE STABILITY ANALYSIS

Infiltration analysis is first conducted to obtain the pore water pressure profiles in each cell. The rainfall information of each cell is obtained through universal Kriging interpolation. In the study area, soils are layered in some locations. For the vegetated land and loose soil deposit, the underlying layer is fissured rocks. The infiltration parameters for the top layer and the bottom layer may be significantly different. Hence, an infiltration model for two-layer soils is adopted to consider the heterogeneity of the soils. Analytical solutions to transient infiltration in layered soils under constant rainfall condition proposed by Srivastava & Yeh (1991) and Zhan et al. (2012) are improved using Heaviside functions based on the principle of superposition. The improved model can consider arbitrary rainfall processes. An infinite slope model is then adopted to compute the factor of safety for each of the large number of cells. The adopted analysis method is described in detail by Chen & Zhang (2013). The slip surface is assumed to be at the wetting front in this study.

The values of ϕ' and c' for the loose soil deposits are determined as 37° and 4 kPa, respectively and the value of ϕ' for the vegetated land is also 37° (Chen & Zhang 2013). According to Coppin and Richards (1990), c' can typically increase by 1–12 kPa by vegetation roots. An average value, 6.5 kPa, is adopted here for the vegetated land. Other parameters are reported by Chen & Zhang (2013).

The thicknesses of the two-layer soils are measured along the vertical direction in this study. The fissured rock layers in vegetated land and deposit zones are estimated to be 4 m based on field investigations. As the fissure rock layers have much higher shear strength, the potential slip surface is within the top soil layer. The infiltration parameters for the fissured rock layers are similar with those of the vegetated land. Field investigations also indicate that the average soil thickness in flat areas is about 10 m. The interpretation of the landslide data triggered by the Wenchuan earthquake near the study area shows that the average thickness of the deposits retained on slopes with angles larger than 35° is less than 2 m. Back analysis using the infinite slope model considering relatively dry initial soil condition indicates that a layer of 2 m thick soil can be retained on slopes as steep as 75°. Hence, it is estimated that the soil thickness of the top layer in the vegetated land and loose soil deposit linearly decreases from 10 m to 2 m as the slope angle increases from 0° to 35°, and keeps at 2 m when the slope angle is larger than 35°.

From 12 August 2010 to 14 August 2010, a storm swept Yingxiu and its vicinity. The locations of six rain gauges are shown in Figure 1. The rainfall interpolation results and the material properties of the four surface material types are reported by Chen & Zhang (2013). Figure 2 shows the results of slope stability analysis. As shown in Figure 2a, almost all the cells are stable at the beginning of the rainfall. The number of unstable cells increases sharply at about 15 hours after the rain starts (see Fig. 2b). The unstable cells increase continuously until the peak rainfall intensity occurs (see Fig. 2c). The distribution of the unstable cells when the peak rainfall intensity occurs is almost the same with that at the end of the storm event (see Fig. 2d).

A comparison between the rainfall-induced slope failures after the 2008 Wenchuan earthquake and the computed unstable cells is shown in Figure 3. Most slope failures in the inventory have been predicted successfully, which indicates that the cell-based model can predict the locations of rainfall-induced slope failures reasonably well. A small portion of slope failures are not predicted successfully and some unstable cells are located at places where there is no slope failure, which maybe due to the resolution of the digital elevation data, the cell size, and the limitation of the infinite slope stability model.

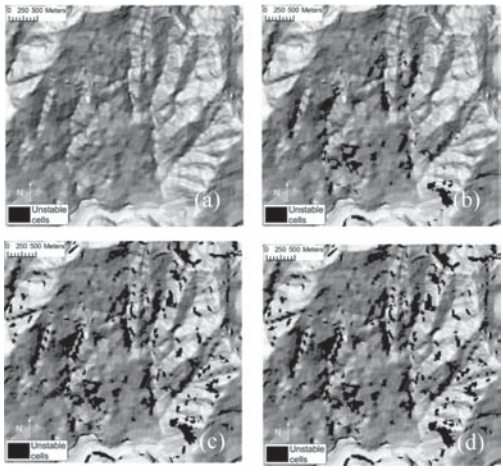

Figure 2. Computed unstable cells after the rainfall starts: a) 1 hour; b) 15 hours; c) 36 hours; d) 46 hours.

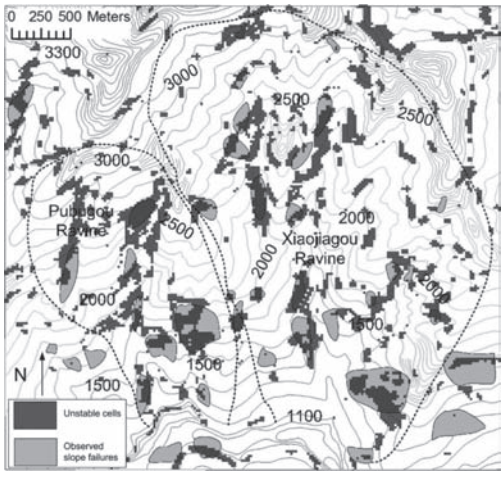

Figure 3. Comparison between rainfall-induced slope failure inventory after 14 Aug. 2010 storm and the computed unstable cells.

5 RUNOUT DISTANCE PREDICTION

Although the runout distance of detached materials has been widely researched (e.g. Corominas 1996, Dai et al. 2003, Kuo et al. 2009), a cell-based runout distance computation method is still to be developed. Simple empirical approaches can be adopted to compute the runout distances of the detached materials from failure of one cell efficiently (e.g. Arnone et al. 2011), but the size effect of the detached materials on the runout distance is not considered previously, which tends to underestimate the runout distance. A slope failure of a larger size will move farther if other conditions are the same. A method considering the size effect of the detached materials and the elevation difference between the original location and the final location of the detached materials is developed to predict the runout path and distances of the detached materials.

An empirical relationship is firstly developed to predict the runout distance as follows based on data of 31 soil slope failures in the Wenchuan earthquake zone:

$$L = 3.85\, V^{0.19} H^{0.38} \quad (1)$$

where L (m) is the runout distance; V (m^3) is the volume of slope failure; H (m) is the elevation difference. The runout distance here is defined as the length of the horizontal path between the highest point of the slope failure and the lowest point of the deposit. The R^2 coefficient for equation (1) is 0.74.

The steps for cell-based runout distance prediction considering the effect of V and H are as follows:

1. Group the unstable cells that are bounded at one or more sides, each cell belonging to a slope group and each group is viewed as an individual slope failure.
2. Compute the volume of the detached materials of each group by summing the volumes of the detached materials in the cells in that group. The volume of the detached material of each unstable cell is determined by the cell area and the depth of the slip surface.
3. Conduct analysis cell by cell, allowing the detached materials to move to lower cells along the steepest path. The steepest path is the one with the largest gradient between the cell where the detached material is located and each of the eight adjacent cells (i.e. the east, south, west, north, northeast, southeast, southwest and northwest cells). The detached material moves along the steepest path on the hill slope first. After it reaches a channel, it will move along the steepest path in the channel.
4. Compute H and L when the detached material reaches a new cell.
5. The material stops movement when L is larger than the predicted value by Equation 1.

The runout traces and deposited locations of the detached materials are shown in Figure 4. The movements of the detached materials reveal the evolution of the loose materials. In Pubugou Ravine and Xiaojiagou Ravine, a small part of the detached materials from the rainfall-induced failures move for a short distance and stay on the hillslopes; the majority of the detached materials run down for a long distance and are retained in the channels. They can block the channels, forming barrier ponds during

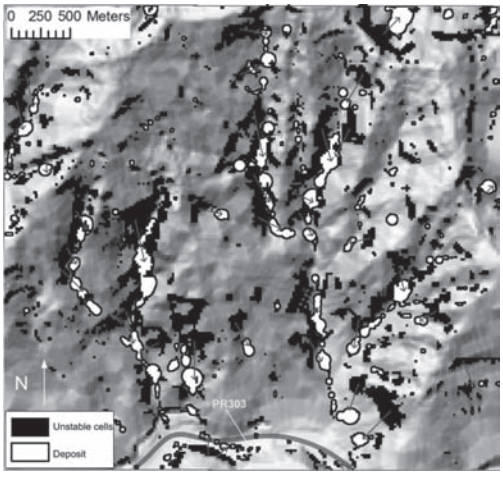

Figure 4. Runout traces and deposited locations of the detached materials at the end of the 14 Aug. 2010 storm.

the storm or simply become the source materials for channelized debris flows. Some hills lopes along the PR303 fail; part of the detached materials moves down, goes across the road or deposits on the road, which poses hazard to the people and properties. Hence, the prediction of runout distance not only provides information for assessing debris flow risks, but also directly helps assess the risk posed by the rainfall-induced slope failures along PR303.

6 CONCLUSIONS

A distributed cell-based model for predicting the runout distances of detached materials from rainfall-induced slope failures is developed in this study. The model consists of five components; namely, a digital terrain model, a spatial rainfall distribution model, a rainfall infiltration analysis model, a slope stability analysis model and a runout distance prediction model.

The slope stability and runout distances of the detached materials can be computed efficiently. The runout distance prediction model takes into account the effect of V and H.

A comparison between the slope failure inventory and the simulation results shows that the model can predict the locations of the slope failures reasonably well. The runout paths and distances of the detached materials can also be predicted successfully. The material movements assessed by this model offer information for the assessment of landslide and debris flow risks. The presented method shows promise for use as a module in a real-time warning system for rainfall-induced slope failures.

ACKNOWLEDGEMENT

The authors acknowledge the support from Sichuan Provincial Department of Transportation and Communications, the National Basic Research Program of China (No. 2011CB013506), and the Research Grants Council of the Hong Kong SAR (Grant No. 622210). The technical help from Mr. Jozsef Danka is also acknowledged.

REFERENCES

Arnone, E., Noto, L.V., Lepore, C. & Bras, R.L. 2011. Physically-based and distributed approach to analyze rainfall-triggered landslides at watershed scale. *Geomorphology* 133: 121–131.

Baum, R.L., Savage, W.Z., & Godt, J.W. 2008. TRIGRS-a Fortran program for transient rainfall infiltration and grid-based regional slope-stability analysis, Version 2.0. *U.S. Geological Survey Open-File Report* 2008 75 pp.

Chen, H.X. & Zhang, L.M. 2013. A cell-based reliability analysis model for predicting regional rainfall-induced slope failures. In Proceedings of *the 2013 Geo-Congress, Entitled Stability and Performance of Slopes and Embankments III*, San Diego, 3–7 March, 2013, 982–990.

Coppin, N.J. & Richards, I.G. 1990. Use of vegetation in civil engineering. Butterworths, London.

Corominas, J. 1996. The angle of reach as a mobility index for small and large landslides. *Can. Geotech. J.* 33: 260–271.

Crosta, G.B. & Frattini, P. 2003. Distributed modelling of shallow landslides triggered by intense rainfall. *Natural Hazards and Earth System Science* 3: 81–93.

Dai, F.C., Lee, C.F. & Wang, S.J. 2003. Characterization of rainfall-induced landslides. *International Journal of Remote Sensing* 24: 4817–4834.

Kuo, C.Y., Tai, Y.C., Bouchut, F., Mangeney, A., Pelanti, M., Chen, R.F. & Chang, K.J. 2009. Simulation of Tsaoling landslide, Taiwan, based on Saint Venant equations over general topography. *Engineering Geology* 104: 181–189.

Olea, R.A. 1999. Geostatistics for engineers and earth scientists. Kluwer Academic Publishers, Norwell.

Srivastava, R. & Yeh, T.J. 1991. Analytical solutions for one-dimensional, transient infiltration toward the water table in homogeneous and layered soils. *Water Resources Research* 27: 753–762.

Takara, K., Yamashiki, Y., Sassa, K., Ibrahim, A.B. & Fukuoka, H. 2010. A distributed hydrological–geotechnical model using satellite-derived rainfall estimates for shallow landslide prediction system at a catchment scale. *Landslides* 7: 237–258.

Zhan, T.L.T., Jia, G.W., Chen, Y.M., Fredlund, D.G. & Li, H. 2012. An analytical solution for rainfall infiltration into an unsaturated infinite slope and its application to slope stability analysis. *Int. J. for Numerical and Analytical Methods in Geomechanics* DOI: 10.1002/nag.2106.

Geotechnical Safety and Risk IV – Zhang et al. (eds)
© 2014 Taylor & Francis Group, London, ISBN 978-1-138-00163-3

Dike failure mechanisms from the perspective of risk assessment

J. Danka & L.M. Zhang
The Hong Kong University of Science and Technology, Clear Water Bay, Hong Kong SAR, China

ABSTRACT: The failure of a dike system, as a characteristic of long linear systems, is ruled by its weakest link. Meanwhile the most serious hazard in a dike section is its breaching, which can develop due to different failure mechanisms. The objective of this paper is to identify the most common failure mechanisms and evaluate them from the point of view of risk assessment. As illustrated via four case studies, the most frequent problem in the design and risk assessment is the inappropriate addressing of potential threats. The results of risk analysis are not reliable if relevant failure mechanisms are neglected, the structural behaviour of the dike-section is not understood or inadequate maintenance is provided.

1 INTRODUCTION

From the dike risk management point of view, the most serious threat is related to the breaching of the dike, which may cause the inundation of the flood zone. Meanwhile from the geotechnical engineering aspect the breaching process is governed by several failure mechanisms.

The first objective of this paper is to identify the most common failure mechanisms which may lead to breaching. This study intends to recognize serious threats from the risk assessment aspect. Even a failure mechanism occurs frequently, if it is easily noticeable and/or predictable, the risk could be lowered since in such cases warning, evacuation and countermeasures could be implemented. If the progression of a failure mechanism is hardly noticeable or the failure will develop in a less ductile way, then the time for countermeasures or warning will be limited and the corresponding risk might be high.

The second objective is to evaluate breaching cases in which different failure drivers significantly affect the risk management. Four case studies are reported in which breaching developed as a result of unexpected failure mechanisms, misunderstanding of the structural behaviour, and failure of maintenance.

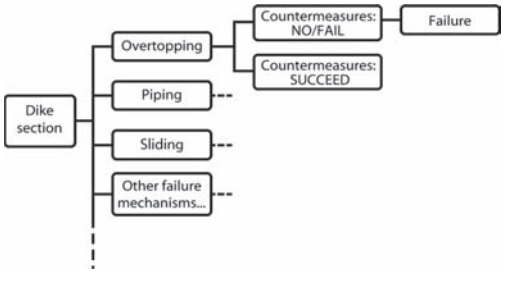

Figure 1. Illustration of an event tree related to a dike section.

Figure 1 illustrates a possible event tree for risk management purposes. The importance of the topic can be clearly identified if one of the potential failure mechanisms is considered as an "unlikely" event. In that case the risk assessment would fail to identify a threat, therefore may cause a false sense of security and potential problems during the flood event.

2 FAILURE MECHANISMS

2.1 *Historical overview*

During qualitative or quantitative risk analysis, the first step is the identification of potential hazards. Comprehensive statistical analysis on past dike breaching cases was carried out by a few researchers (Nagy 2012, Fukunari 2008, Baars & Kempen 2009). Based on their results, the most frequent failure mechanisms were determined, which may aid a rough estimation of likelihood of potential hazards. Here the results of Nagy (2012) and Baars & Kempen (2009) will be compared and evaluated, which are presented in Table 1.

The analyses of Nagy and Baars & Kempen focus on the Carpathian Basin and on the Netherlands, respectively. Their studies cover different types of dikes from a few aspects (construction material—fine and/or coarse graded materials, peat; different structural arrangements of the dike section—core, drain, puppet wall etc.; sea and river defense

Table 1. Comparison of statistics related to dike failure mechanisms from Nagy (2012) and Baars & Kempen (2009).

Nagy (2012)		Baars & Kempen (2009)	
Investigation period			
(1564–2010)		(1134–2006)	
Failure mechanism	Rel. freq.	Failure mechanisms	Rel. freq.
Not known	58.1%	Erosion of inner slope prot. & crest	67%
Overtopping	32.4%	Ice drift	11%
Human activity	2.3%	Erosion or instability of	6%
Slope failure	2.0%	outer slope prot.	
Subsoil failure	1.8%	Sliding in. slope	5%
Other known	1.2%	External (human	4%
Structural failure	1.3%	and animal)	
Wave erosion	0.6%	Sliding out. slope	3%
		Liq. of shore line	2%
		Piping	1%
		Micro instability	0.5%
		Horizontal shear	0.5%
Total	2858 cases		1735 cases

structures). Based on their results, the most frequently observed cause of dike breaching was the external erosion due to overtopping. Erosion of the outer slope, distresses caused by human or animal activities and sliding of the inner slope during flood event are the most serious threats in addition to overtopping.

2.2 *Most important failure modes*

In the historical overview it was revealed that the most probable failure scenario is the overtopping of dike section. However the external erosion might not be governed by the elevation difference between the flood water level and the dike crest, but by waves. When the erosion starts in the upstream side (e.g. the Upper Jones Tract levee breach), the failure of the riverside slope will become the most likely cause of breaching.

Although the most probable failure mechanism is the external erosion of the section it must be stated that, from risk management point of view, their assessment may not be the most challenging one. Nowadays flood water levels can be estimated with acceptable accuracy; therefore the overtopping of the section is quite predictable. Moreover, the observation of the external erosion type of failures is quite straightforward. Thus the warning of the population at risk and their evacuation from the flood zone seem to be more manageable than in the case of a less ductile failure.

The failure modes of dike sections originated from internal erosion are more deceitful since their initiations are hardly observable without a monitoring system. More likely they are only noticed in the developed phase. By then the opportunity of implementing rescue measures is limited. In Figure 2 the most common failure modes related to external and internal erosion are summarized. Moreover potential factors that may accelerate erosion are highlighted.

Additionally non-erosion related failure modes like slope failures must be evaluated both under flood conditions (the down-stream side) and under rapid draw-down conditions (the upstream side). Local slope failures caused by seepage in the inner-slope may be referred to as micro-instabilities in the literature.

Other failures might be governed by settlement, horizontal shearing (sliding), earthquakes, drifting ice or collision with floating objects. Non-erosion related failure modes are summarised in Figure 3.

2.3 *Failure modes vs. risk*

The first issue in the risk management is whether a threat is identified or not. One of the most common reasons for dike breaching is that a failure mode is considered as "unlikely", hence not included in the design or risk analysis. Once the failure unexpectedly develops, adequate countermeasures may not be well prepared.

Other possible failure scenarios occur when the potential failure modes are identified but the dike construction does not meet the design criteria.

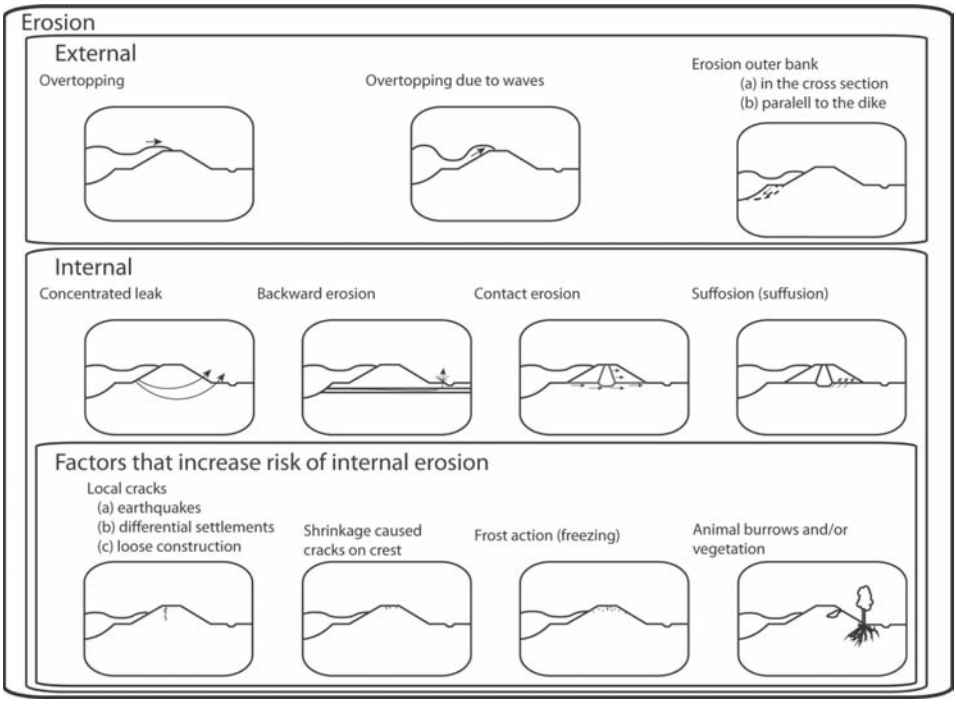

Figure 2. Most common failure modes related to external and internal erosions. (Based on Vrijling et al. 2011).

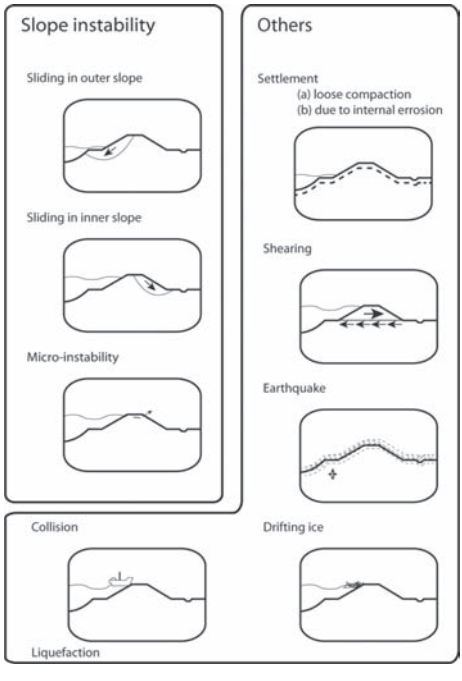

Figure 3. Non-erosion related failure modes (based on Vrijling et al. 2011).

Such events may happen due to the lack of appropriate construction or inadequate maintenance.

Finally it has to be underscored that progression time of failure is one of the most crucial factors of a successful defence. In this regards the evaluation of different structural materials and failure modes are essential: soils may behave differently (erodability, loss of strength due to water content changes etc.), hence the progression time varies in a wide range.

2.4 *Progression of failure*

The breaching probability is usually approximated as the probability of initiation of failure because of the complex mechanisms of dike breaching and the uncertainties in the development time. This approximation leads to a conservative estimate. For instance in Figure 4 a piping-caused breaching scenario is illustrated. If the piping failure is approximated by the initiation probability, then only one criterion has to be met: the hydraulic gradient during the flood event (i) must be higher than the critical gradient (i_c).

However the time factor must be considered additionally. If the duration of the flood event is short, then the time for the development of piping will be limited, hence no breaching may take place.

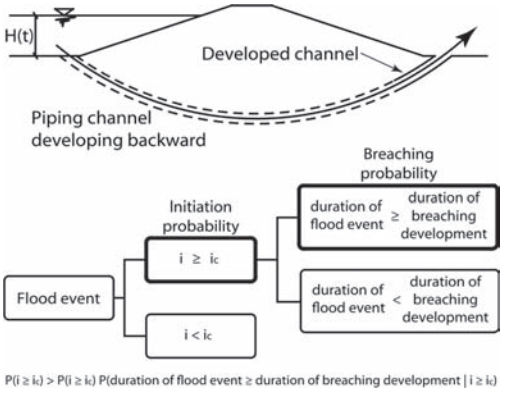

Figure 4. Illustration of differences between breaching probability and initiation probability in the case of piping.

Although the use of the initiation probability is common in quantitative risk analysis, there have been significant developments in the research of breaching processes. Relevant papers (Zhu et al. 2005, Visser et al. 2006) are published related to the overtopping erosion failure of sand and clay dikes. In their works 5 stages of breaching process are distinguished. The analysis assumes a homogeneous and trapezoidal breaching section. In the case of internal erosion, ICOLD bulletin (ICOLD 2013) and Chang & Zhang (2013) derive relevant information to access the time factor of breaching and the critical hydraulic gradients in each phase of internal erosion, respectively.

3 CASE STUDIES

3.1 *Objectives*

The investigation of potential failure modes plays an important role in both risk assessment and ordinary design process. Four case studies are introduced in this section to illustrate how unforeseen failure mechanisms (not expected during the design) and unexpected conditions (animal burrows, or gas development in the subsoil) led to breaching or failure of dike sections.

3.2 *Grand canal, Edenderry, Ireland*

In the 18th century, a canal dike was constructed close to Edenderry. The canal was formed into the crest of a peat embankment and its bed was covered with a clay layer (Pigott et al. 1992). The height of the embankment was 10 m. The height of the two dikes formed by cutting was 2 m and their crest width was 6 m. The inclination of the slopes was about 1:4.

On 15 January 1989 at 3.30 pm, a large 350 m wide breach opened in the north bank of the Grand Canal as its dike slid horizontally. The distance of sliding was 60 m at the eastern end and decreased gradually to zero in the western end of the breach. The breaching caused the water level in the canal to decrease rapidly. As a result of the rapid drawn down, 200 m of the south bank was damaged. Approximately 200,000 m^3 of materials were displaced during the failure. Based on the report of an eyewitness, a loud "tearing noise" accompanied the lateral displacement of the north bank.

Investigation was carried out including laboratory measurements, in-situ vane tests and other probes before the remedial works. Based on the analysis, the groundwater level was close to or at the ground surface, the frictional resistance of the peat was low. The most probable scenario is sliding failure as in the case of the comprehensively studied Wilnis dike breaching (Baars 2005).

It might be assumed that the sliding failure was not expected during the design of the dike. Baars & Kempen (2009) reveals that even in the Netherlands the sliding failure is considered as an "impossible failure mode" though former Dutch and New Orleans case studies highlighted the possibility.

3.3 *Foenna stream dike, Sinalunga, Italy*

A dike breach occurred in Sinalunga on the bank of the Foenna stream due to animal burrows and piping during an ordinary flood event on 1 January 2006 (Bayoumi & Meguid 2011, Camici et al. 2010). The sings of animal presence and activities were observed earlier, which led to extensive maintenance along the dike. However during the flood event an outflow was located on the downstream side of the dike, 2 m below the dike crest. On the upstream slope the inlet a flow channel was observed approximately at the same elevation. Counter-measures were applied to stop the piping process: blankets were installed on the upstream hole. Unfortunately there was not enough time to stop the internal erosion and the piping channel collapsed. Consequently the crest settled hence the section was overtopped. The formation of the trapezoidal breaching was fast; the town next to the stream was inundated in an hour.

After investigations, it was verified that porcupine burrows were responsible for the development of the internal erosion channel, even though maintenance works were finalized before the flood event.

The required maintenance and remedial works must be performed to satisfy the design conditions. However the Sinalunga case study reveals that even the potential problems (animal burrows) were tackled, neither investigation of the burrows nor

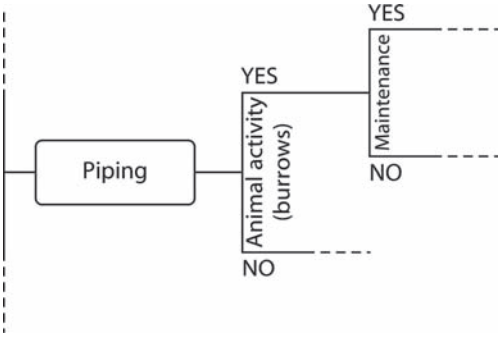

Figure 5. Development of an unexpected branch of the event tree due to animal burrows and lack of maintenance.

the maintenance was performed adequately, which led to the change in piping resistance. The burrows formed an unexpected branch of the event tree as shown in Figure 5.

3.4 *17th Street Canal, New Orleans, USA*

The inundation of the major part of New Orleans and the large number of breaches triggered a comprehensive investigation after hurricane Katrina in 2005. The final reports underscored relevant threats in different fields: potential failure mechanisms, structural behaviour, erodibility of materials etc. The case of the 17th Street Canal is presented here to improve the understanding of the structural behaviour and failure mechanism of the I-wall structures. In this case the breach was caused by the horizontal sliding of the I-wall (flood protection wall) and the embankment.

Around 6.30 am on 29 August 2005 a portion of the I-wall and embankment moved about 15 m horizontally and opened a gap of approximately 135 m. The breach released storm surge floodwater, which flooded homes and destroyed buildings in the Lakeview area. As a part of the governmental investigation, field surveys were carried out including auger borings and CPT tests. The site investigation was further supported by centrifuge tests (Steedman & Sharp 2011), the observed failure mechanism is presented in Figure 6.

Based on the centrifuge tests, when the floodwater reached the bottom of the I-wall, the failure initiated with a slight landward rotation of the I-wall. Hence a gap was formed between the foundation of the I-wall and the soil on the canal site. The gap reached the underlying clay layer in which the foundation was located. Upon formation, the gap was immediately filled with water.

When the water level rose, the passive earth resistance on the defended site had to be mobilized,

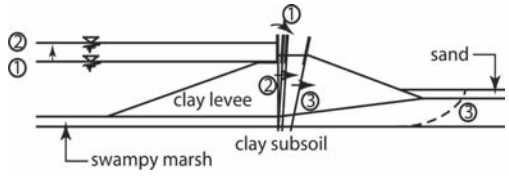

Figure 6. Development of failure in 17th Street Canal: (1) Rotation of the I-wall and development of gap; (2) Increase of water level and mobilization of the passive earth pressure; (3) Development of critical slip surface, backward progression of the slip surface and sliding/rotation of the section.

accompanied by horizontal displacements, to withstand the horizontal hydrostatic load. Mean-while on the top of the clay surface the critical slip surface was formed and extended landwards to the ground surface through the marsh layer.

Although the case study only focused on the 17th Street Canal dike, the failure mechanism was common in New Orleans. A gap between the I-wall and the soil was formed both on the London Avenue (North and South) and on the Orleans Avenue (North and South). Therefore an important threat was revealed related to I-wall type of flood defence structures.

3.5 *Bleiswijk, The Netherlands*

During August 1990 deformations were observed on the downstream slope of a polder dike in Bleiswijk, The Netherlands, which consisted of peat and clay layers. Due to the settlement of the section, the water level in the belt canal was close to the crest. Moreover, intensive piping was detected and cracks were observed. These phenomena activated immediate counteractions and investigations of the site. Fortunately breaching did not occur. The deformation mechanism was examined and the final results showed that the effect of draught, shrinking and oxidation of the peat caused higher permeability and changes in the structure of the peat material.

At another site during the survey of Bleiswijk dikes, water spurted out of a hole after the removal of a penetration cone. To stop the fountain, a standpipe was installed and after 1.5 hours the water level in the pipe started to drop. Investigation showed that expansion of gas bubble inside the subsoil caused the water spring. Gas bubbles formed during the oxidation of the peat. The origin and age of the gas could not be ascertained therefore the bubble could have developed thousands of years ago. Irrespective of the origin of the gas, its presence influenced unfavourable effective stress conditions and the pressurized gas could be responsible for significant uplift forces (Vonk 1994).

Some threats are significant not only because they have influence on one distinguished failure mechanism, but also because they may trigger other failure mechanisms. For instance the uplift force decreases the sliding resistance due to the decrease of the effective stress and hence the frictional resistance. In addition the case reveals that anomalies (gas bubble, and highly permeable soil deposits in the river) may influence or govern the failure modes.

4 SUMMARY

In the first phase of dike risk assessment, the potential threats must be identified and studied. Based on historical dike breaching cases (Nagy 2012, Baars & Kempen 2009), overtopping (external erosion) is the most common cause of breaching. The erosion of the outer slope, breaching caused by human or animal activities and sliding of the inner slope during flood event are the most serious threats in addition to the overtopping.

Different failure mechanisms have different development times, therefore the duration of the flood event cannot be neglected. Since the warning and evacuation time is an important factor in risk management, failure mechanisms must be differentiated based on the development time and on the perceptibility of the process. In this respect, external erosion type of failures is less threatening but internal erosion is more deceitful.

Case studies revealed that breaching will most likely occur due to a well-known failure mechanism. However, some of those failure mechanisms were neglected during design or risk analysis. Possible scenarios for such negligence include bad understanding of failure mechanisms/structural behaviour, and anomalies along the dike. Even though the presence of gas bubbles is unlikely, crossings with river bed with highly permeable soil deposits may be faced. The highly permeable formation may result in unexpected and extensive piping. Another relevant failure driver might be failure of maintenance, which may lead to the development of an unforeseen branch of the event tree.

Due to the rising sea level and climate changes which aggravate weather extremes, the demand on detailed risk analysis and management of dike systems is growing. Such demand is magnified by the rapid growth of elements at risk in the flood zones. Hence dike failure mechanisms must be studied more carefully to support successful coastal and flood defence and ensure the security of the inhabitants in the flood zones.

ACKNOWLEDGEMENTS

The research work was supported by the National Science Foundation of China (No. 51129902).

REFERENCES

Bayoumi, A., Meguid, M.A. 2011. Wildlife and safety of earthen structures: a review. *Journal of Failure Analysis and Prevention*, 11(4): 295–319.

Chang, D.S., Zhang, L.M. 2012. Critical hydraulic gradients of internal erosion under complex stress states. *Journal of Geotechnical and Geoenvironmental Engineering*, online, doi:10.1061/(ASCE)GT.1943-5606.0000871.

Fukunari, K. 2008. The Tone river case and others. *Safety of River Levee in Japan Conference,* PowerPoint presentation, Tokyo, Japan.

ICOLD 2013. ICOLD Bulletin on Internal Erosion of Existing Dams, Levees and Dikes, and their Foundations, Volume 1: Internal Erosion Processes and Engineering Assessment, ICOLD, Paris.

Nagy, L. 2012. Statistical evaluation of historical dike failure mechanism. *Riscuri si Catastrofe*, Ed.: Sorocovschi V., Editura Casa Cartii de Stiinta, Cluj-Napoca, X(2): 7–20.

NSF 2006. Investigation of the Performance of New Orleans Flood Protection Systems in Hurricane Katrina on August 29, 2005, online, Berkeley University, USA.

Pigott, P.T., Hanrahan, E.T., Somers, N. 1992. Major canal reconstruction in peat areas. *Proceedings of the ICE—Water Maritime and Engineering*, 96(3): 141–152.

Steedman, R.S. & Sharp, M.K. 2011. Physical modelling analysis of the New Orleans levee breaches. *Proceedings of the ICE—Geotechnical Engineering*, 164(6): 353–372.

Van Baars, S., Van Kempen, I.M. 2009. The causes and mechanisms of historical dike failures in the Netherlands. *E-Water, Official Publication of the European Water Association*, online.

Van Baars, S. 2005. The horizontal failure mechanism of Wilnis peat dyke, *Géotechnique,* 55(4): 319–323.

Visser, P.J., Thu, Y., Vrijling, J.K. 2006. Breaching of dikes. *Proceeding of the 30th International Conference on Coastal Engineering,* Sand Diego, USA. 2893–2905.

Vonk, B.F. 1994. Some aspects of the engineering practice regarding peat in small polder dikes, *Advances in Understanding and Modelling the Mechanical Behaviour of Peat, den Haan, Termaat & Edil (eds).* Balkema, Rotterdam, 389–399.

Vrijling, J.K., Schweckendiek, T., Kanning, W. 2011. Safety standards of flood defenses. *Geotechnical Safety and Risk, Proceedings of ISGSR 2011*, Bundesanstalt für Wasserbau, Münich, 67–84.

Zhu, Y., Visser, P.J., Vrijling, J.K. 2005. A model for breach erosion in clay-dikes. *Proceedings of Coastal Dynamics 2005: State of Practice*: 1–10.

Geotechnical Safety and Risk IV – Zhang et al. (eds)
© 2014 Taylor & Francis Group, London, ISBN 978-1-138-00163-3

Reliability assessment of earth pressure on rigid non-yielding retaining walls

S.M. Dasaka, T.N. Dave & V.K. Gade
Indian Institute of Technology Bombay, Mumbai, India

ABSTRACT: Pressure transducers are increasingly being used within soil mass or at soil-structure interface to monitor stresses at the point of installation. Calibration of these transducers provides unique relationship between applied pressure and measured stress. Routinely, calibration is performed by applying fluid pressure on diaphragm of transducer, however interpretation of data using fluid calibration results lead to measurement errors when transducer is used in soil for stress measurement. This paper presents comparison of calibration results of pressure transducer using fluid and soil calibration techniques. The bias factor in the earth pressure measurement using fluid calibration results are evaluated, which can be used with fluid calibration results to precisely arrive at the values of earth pressures on the retaining wall, in the absence of in-soil calibration test results.

1 INTRODUCTION

Retaining structures are integral part of various infrastructural projects to support deep excavations, or steep and deep basements. These walls withstand pressures from retained materials, surcharge pressures due to movement of vehicular traffic or loads from foundations of the adjacent buildings on their backfills and loads due to natural calamities like earthquake. A properly instrumented structure gives information about variation of stresses with time and space. Pressure transducers of different varieties are used to measure stresses within soil mass or at the interface of structure and soil.

Calibration of transducers is very important as the calibration factors obtained from calibration process would give an idea about actual stresses at the point of measurement. The calibration of pressure transducer involves the investigation of the unique relationship between the applied pressure and pressure cell output (Take 1997). Through calibration, the output from pressure transducers is related to normal stress (multiplying the output voltage (or strain) with the calibration factor will give rise to actual in-situ pressure, that converts cell's electrical output to the pressure). To obtain calibration factors, the standard procedure is to calibrate the transducer in a fluid (air, water or oil) and to analyze the unique relationship between the input and output. However, recent studies highlighted that the results of fluid calibration of Earth Pressure Cell (EPC) will be highly misleading, if the EPC are used in soil or at soil-structure interface for measurement of in-situ stresses. Hence, it is suggested that the pressure transducers should be calibrated under the conditions identical to its intended use.

2 LITERATURE REVIEW

Various approaches have been adopted in the past for laboratory fluid calibration of pressure transducers. Ramirez et al. (2010) calibrated pressure transducers by subjecting them to external oil pressure by means of dead weight calibrator. The other approaches are (I) use of centrifugal technique to calibrate pressure transducers (Take 1997, Chen & Randolph 2006), (II) use of application of fluid pressure to calibrate pressure transducer (Clayton & Bica 1993, Labuz & Theroux 2005, Ramirez et al. 2010). The fluid calibration helps in assessing instrument's physical condition; however data interpretation using standard calibration curve obtained using fluid calibration leads to measurement errors when EPC is used in soil for stress measurement. (Clayton & Bica 1993). The alternative but more complex procedure of in-soil calibration of EPC may reduce this error considerably as a more realistic calibration curve can be obtained (Selig 1980, Weiler & Kulhawy 1982, Selig 1989). The reliable measurement of stresses in soil is still difficult to achieve due to strong dependency of measurement on relationship between EPC and soil stiffness (Hadala 1967, Hvorslev 1976, Dunnicliff 1988).

Various factors affecting EPC output during in-soil calibration were broadly classified into inclusion effects, EPC-soil interaction, placement effects, environmental influence and dynamic response (Weiler & Kulhawy 1982, Dunnicliff 1988). The literature is full of examples illustrating the effect of placement method, soil density/stiffness, geometry, grain size, loading history and soil type on the calibration of EPC. Askegaard (1994) suggested to test EPC under as varied conditions as possible to get an estimate of the accuracy obtainable when the EPC are used in practice in unknown material and loading histories. In-soil calibration of EPC involves application of uniform vertical stress to the upper surface of a large soil specimen placed inside a stiff-walled chamber.

Review of literature suggested that studies related to effect of using fluid and in-soil calibration results on the measured earth pressure and statistical studies in relation to evaluation of bias factors is missing. Hence, the present study is aimed at evaluation of effect of using fluid and in-soil calibration results on the pressure cell output, and its influence on the measured earth pressures. Based on the above, bias factors are derived for earth pressure, which can be used with fluid calibration results to estimate the earth pressures on the retaining wall, in the absence of in-soil calibration test results. Bias factor is defined as the ratio of average pressure cell output using fluid calibration and that corresponds to in-soil calibration.

In the present study in-soil calibration of EPC are carried out using sand.

3 EVALUATION OF CALIBRATION FACTORS

3.1 *Fluid calibration*

In order to obtain calibration factors, a calibration device was developed by modifying a conventional triaxial apparatus suitable for testing 100 mm diameter soil specimen, as shown in Figure 1. Further details about the developed device can be seen in Dave and Dasaka (2012a). The calibration device was fully filled with de-aired water, and pressure was applied by an air-water bladder cylinder, using compressed air with an accuracy of 0.1 kPa.

The fluid pressure in the triaxial cell was increased so as to apply pressure on pressure transducer for calibration. Pressure in increments of 20 kPa was applied on transducer up to a maximum value of 180 kPa. From the maximum value, the pressure in the chamber was reduced by decreasing the fluid pressure in 20 kPa steps back to zero gage pressure. Calibration of two different transducers, medium size transducer (Haris Sensor Technologies make, India) of diameter 40 mm

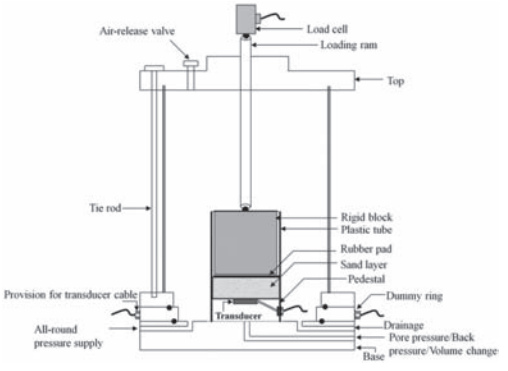

Figure 1. Details of in-house calibration device developed by modification in triaxial set up.

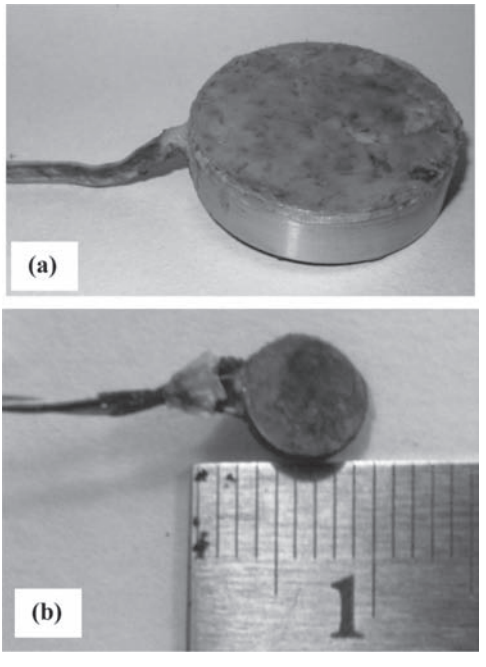

Figure 2. Pressure transducers used in present study (a) type 1 (b) type 2.

(Type 1) and miniature transducer (TML, Japan make—Model No. PDA PA) of diameter 6.5 mm (Type 2) presented in Figure 2, was carried out using the developed calibration device. A detailed specification of both the transducers is presented in Table 1. The fluid pressure in the triaxial cell was increased to a maximum of 180 kPa, in increments of 20 kPa. The transducer data was recorded in terms of the output strain from the transducer at each step of loading. Readings corresponding to

Table 1. Details of transducer used in the present study.

Terminology	Type 1	Type 2
Pressure range	0–2 kg/cm^2	0–2 kg/cm^2
Sensitivity	1.420 mV/V at FS	+946 μV/V
Non-linearity & hysteresis	0.5% of FS	0.5% of FS
Thermal sensitivity shift	0.1% of FS/°C	1%/°C
Dimensions	40 mm Φ × 10 mm	6.5 mm Φ × 1 mm

each loading were obtained once the fluid pressure had stabilized, typically in 30 seconds.

The relationship between applied pressure and acquired data (measured in terms of micro strain) and measurement non-linearity for both the transducers was obtained and presented in Table 1.

3.2 *In-soil calibration*

Effect of sand layer thickness on the performance of Type 2 transducer is observed. Same modified triaxial setup with additional plastic tube of 2.5 mm thickness and 100 mm Internal Diameter (ID) placed tightly on the brass pedestal was used with the transducer fixed flush on it. In the present study silica sand (Indian Standard sand of Grade III) was used. The typical particle size distribution curve of the sand used in the study is shown in Figure 3. Some of the physical and mechanical properties of the sand used in the present study are presented in Table 2.

Considering diameter of EPC (D_{EPC}) as reference, sand layer thicknesses of 10 mm ($0.25D_{EPC}$), 20 mm ($0.5D_{EPC}$), 40 mm (D_{EPC}), 60 mm ($1.5D_{EPC}$) and 100 mm ($2.5D_{EPC}$) were placed above the EPC to obtain relation between applied pressure and measured strain. Greased polyethylene sheets of 60 μm thickness were pasted to inner surface of plastic tube in order to reduce friction between sand particles and plastic tube surface. A rigid wooden block followed by thick rubber pad was placed on sand layer for proper transfer and uniform distribution of pressure between load cell of triaxial apparatus and transducer, as shown in Figure 1.

Air pluviation was adopted for preparation of sand layer of 16 kN/m^3 unit weight. Incremental displacements were applied manually to the triaxial base, thereby monitoring applied stress on wooden block through load cell and induced strains in the transducer. Strains were measured upto 50 kPa pressure. Results obtained from both fluid calibration and in-soil calibration of both pressure sensors

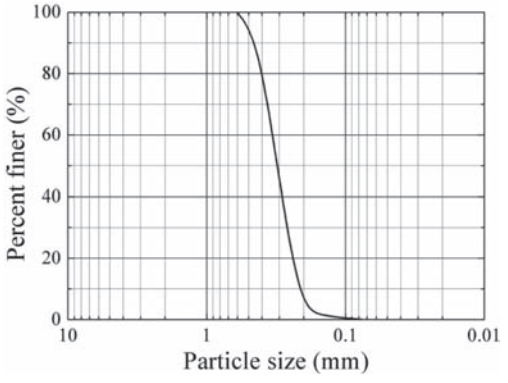

Figure 3. Particle size distribution of sand.

Table 2. Physical and mechanical properties of sand.

Property	Value
G_s	2.65
C_u	1.42
C_c	0.93
γ_{dmin} (kN/m^3)	14.58 (ASTM D4254-00)
γ_{dmax}(kN/m^3)	17.10 (Pluviator)
Cohesion, kPa (c′)*	0
Friction angle (ϕ′)*	39°

*Obtained from direct shear test at 68% relative density.

(Type 1 and Type 2) were compared, discussed in the following section.

4 RESULTS AND DISCUSSION

Calibration performances of Type 1 and Type 2 transducers in the range of 0–180 kPa for first loading-unloading cycle were obtained. Typical fluid calibration results are presented in Figure 4. The fluid calibration results of first loading-unloading cycle indicated maximum non-linearity of 0.6% of FS (full scale) and 2.64% of FS for Type 1 and Type 2 transducers, respectively.

The calibration factors obtained from fluid calibration of these two pressure cells are presented in Table 3.

In case of in-soil calibration, the relation between applied pressure and measured strain is non-uniform for sand layer thickness of 0.25 D_{EPC} and 0.5 D_{EPC}. As the pedestal body was more rigid than diaphragm of EPC, arching of sand might have caused non-uniform transfer of pressure, in line with observations by Ingram (1968). With increase in the sand layer thickness effect of arching would have been reduced, thus allowing

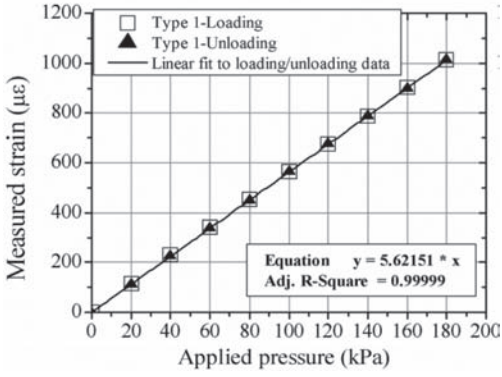

Figure 4. Typical fluid calibration results.

Table 3. Fluid calibration factors obtained using in-house calibration device (Dave & Dasaka, 2012a).

	Type 1	Type 2
Best fit equation	Y = 2.0534*X	Y = 2.4672*X
Calibration factor	0.4868	0.4053
Coefficient of determination (R^2)	0.9998	0.9999

*Where, Y = measured strain (με); X = Applied pressure (kPa).

uniform transfer of pressure from load cell to EPC, and thereby increasing output of EPC. Outputs using sand thicknesses of D_{EPC} and $1.5D_{EPC}$ were almost similar and on higher side of that obtained for $0.25D_{EPC}$ and $0.5D_{EPC}$. However, with further increase in thickness of sand layer beyond $1.5D_{EPC}$, EPC output was reduced, which may be attributed to stress dissipation inside the soil causing only a portion of applied pressure to transfer to the diaphragm of the EPC.

Figure 5 presents the fluid and in-soil calibration test results for Type 1 EPC. For any value of applied pressure the induced strains in the EPC are higher in fluid calibration.

Table 4 shows the pressure cell output corresponding to an applied pressure of 180 kPa, for both fluid and in-soil calibration of EPC (Type 1).

It is evident from the above results that higher calibration factor (≈180/372 = 0.4839) is obtained for the EPC using fluid calibration, than that obtained using in-soil calibration (in the range of 0.6962–0.8091, for sand thickness in the range of 10 mm–60 mm). Considering the fact that the optimum sand layer thickness is around $1.5D_{EPC}$, the bias factor for Type 1 and Type 2 EPC are evaluated as 1.25. It means that these EPC, if used

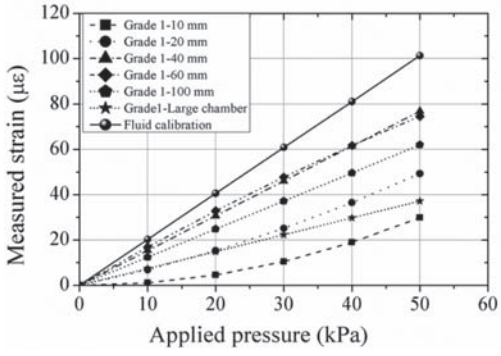

Figure 5. Comparison of fluid and in-soil calibration results.

Table 4. Results of in-soil and fluid calibration of transducers.

	Sand		
Fluid	$0.25D_{EPC}$	D_{EPC}	$1.5D_{EPC}$
372	259	298	301

with fluid calibration factors, would understand the earth pressures in sand by as much as 25%. As the pressure sensors are routinely calibrated using a fluid, either due to lack of information of their intended use, or unavailability of in-soil calibration devices, only fluid calibration factors are supplied to the user. These fluid calibration factors, if used, grossly underestimate the earth pressures on the retaining walls. In the absence of in-soil calibration results, the earth pressure measurements in sand, employing fluid calibration results, need to be scaled up by 25%, to arrive at the precise values.

It is to be noted that the bias factors developed in this study are only applicable for the grain size distribution of the sand used in this study. Bias factors may vary depending on the grain size distribution of the material. Hence, further studies in this direction are essential, involving different materials (sand, silt, and clay) with wide range of grain size distribution, to critically understand the influence of material type and its grain size distribution on the bias factors.

5 CONCLUSIONS

Interpretation of earth pressures in sand using EPC, employing the fluid calibration results, should be handled carefully, as EPC responds differently with fluid and sand. Following are

the major conclusions derived from the present studies.

Optimum sand layer thickness to be placed above the EPC during the calibration studies for Type 1 and Type 2 EPC is obtained as $1.5D_{EPC}$, where D_{EPC} is the diameter of the diaphragm of EPC.

For any value of applied pressure the induced strains in the EPC are higher in fluid calibration than that in the in-soil calibration.

The bias factor for Type 1 and Type 2 EPC are evaluated as 1.25.

Calibration factors should be obtained by in-soil calibration of EPC, under the conditions similar to that prevail at the place of intended use for obtaining reliable results.

REFERENCES

Askegaard, V. 1994. Applicability of normal and shear stress cells embedded in cohesionless materials. *Experimental Mechanics* 35(4): 315–321.

Chen, W. & Randolph, M. 2006. Measuring radial total stresses on model suction caissons in clay. *Geotechnical Testing Journal* 30(2): 1–9.

Clayton, C.R.I. & Bica, A.V.D. 1993. The design of diaphragm-type boundary total stress cells. *Geotechnique* 43(4): 523–536.

Dave, T.N. & Dasaka, S.M. 2012a. Assessment of portable traveling pluviator to prepare reconstituted sand specimens. *Geomechanics and Engineering—An International Journal*, Techno Press 4(2): 79–90.

Dave, T.N. & Dasaka, S.M. 2012b. Universal calibration device for fluid and in-soil calibration of pressure transducers. *Indian Geotechnical Journal—Springer Publishers* 42(3): 212–219.

Dave, T.N. & Dasaka, S.M. 2012c. In-house calibration of pressure transducers and scale effect on calibration factors. *Geomechanics and Engineering—An International Journal*, Techno Press 5(1): 1–15.

Dunnicliff, J. & Green, G.E. 1988. Measurement of total stress in soil. *Geotechnical instrumentation for monitoring field performance*, Wiley, New York, 165–184.

Hadala, P.F. 1967. *The effect of placement method on the response of soil stress gages.* Technical Report No. 3–803, Army Eng. Waterways Expt. St., Vicksburg, MS.

Hvorslev, M.J. 1976. *The changeable interaction between soils and pressure cells.* Tests and Reviews at the Waterways Experiment Station, Technical Report S-767, Army Eng. Waterways Expt. St., Vicksburg, MS.

Labuz, J.F. & Theroux, B. 2005. Laboratory calibration of earth pressure cells. *Geotechnical Testing Journal* 28(2): 1–9.

Ramirez, A., Nielsen, J. & Ayuga, F. 2010. On the use of plate type normal pressure cells in silos part 1: Calibration and evaluation. *Computers and Electronics in Agriculture* 71: 71–76.

Selig, E.T. 1980. Soil stress gauge calibration. *Geotechnical Testing Journal* 3(4): 153–158.

Selig, E.T. 1989. *In situ stress measurements*, State-of-the-Art of pavement response monitoring systems for roads and airfields, U.S. Army Cold Reg. Res. and Engg. Lab., Hannover, NH.

Take, W.A. 1997. *Lateral earth pressure behind rigid fascia retaining walls*, M.S. Thesis, The Uni. of New Brunswick, Canada.

Weiler, W.A. & Kulhawy, F.H. 1982. Factors affecting stress cell measurements in soil. *Journal of Geotechnical Engineering Divison* 108(12): 1529–1548.

This page intentionally left blank

Geotechnical Safety and Risk IV – Zhang et al. (eds)

Seismic damage occurrence probability in an existing estuary dam

T. Hara, M. Iwata, Y. Otake & Y. Honjo
Gifu University, Gifu, Japan

T. Kato, A. Nishida & H. Yukimoto
Japan Water Agency, Saitama, Japan

ABSTRACT: This paper presents an example of S-PSA, Seismic Probabilistic Safety Assessment, applied to an existing estuary dam. Severe damage probabilities of respective parts constituting the dam, which are estimated by reliability analysis with using geotechnical analysis (FEM) and statistical analysis of uncertainties, are described. Finally, the seismic retrofit planning based on risk is discussed.

1 INTRODUCTION

Seismic design with considering occurrence probability of larger earthquakes than the design one has been an important issue in Japan, because several large earthquakes caused tremendous damages to human and social economy, such as Kobe quake in 1995 and Tohoku quake in 2011.

Therefore, the authors have conducted a study on application of S-PSA, Seismic Probabilistic Safety Assessment (IAEA 1993, 2009), to common infrastructures except nuclear plants. In this paper, an example of S-PSA applied to an existing estuary dam is presented. Dynamic effective stress FEM analysis is adopted in order to evaluate the seismic response of the dam built on liquefiable ground during earthquake by using response surface method (Honjo 2011) in this S-PSA. In the reliability analysis, following uncertainties are considered.

Response uncertainties: Earthquake intensity based on probabilistic hazard curve at the site, reproducibility of the FEM analysis adopted in this study with respect to experimental responses of the structure built on liquefied ground, and reproducibility of the assumed response surface with respect to the seismic responses estimated by FEM analysis.

Resistance uncertainties: Strength estimation of the structural members, bearing capacity of pile foundation, spatial variation and transformation error of geotechnical parameters.

Details of the S-PSA with using FEM analysis as well as severe damage probabilities of the respective parts constituting the dam are introduced and the seismic retrofit planning based on risk is discussed in this paper.

2 TARGET STRUCTURE

The target facility is an existing estuary dam to supply city, industrial and agricultural water due to prevent running up of seawater to the river. The facility length is 192.3 m and it consists of six gates (25 m in width, 7.3 m in height) and seven hanging up structures of the gates. Figure 1 shows the external appearance of the dam. The target structure in this study is the hanging up structures of the gates. This structure is built on the liquefiable ground during earthquake with 35 steel pipe piles (600 mm in diameter, 9 mm in thickness, 25 m in length).

3 PROCEDURE FOR S-PSA

Figure 2 shows the procedure for the S-PSA in this study. At first, the uncertainty of seismic intensity is set as a probabilistic density function from the published probabilistic seismic hazard curve at the site, which corresponds to residual service term of the target facility. Then, Response Surfaces (RS)

Figure 1. External appearance of the target dam.

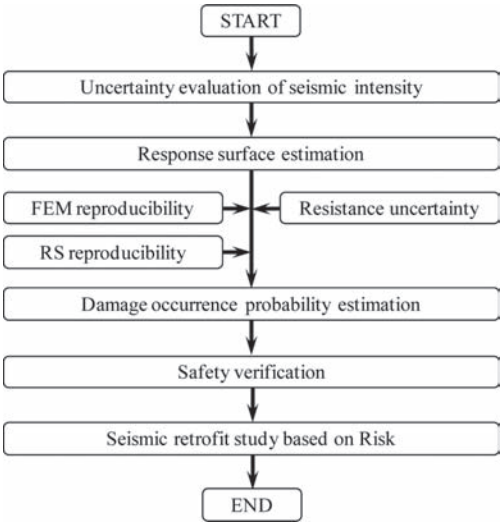

Figure 2. Procedure for S-PSA.

of respective verification points are estimated from sensitivity analyses with respect to contribution factors to each response of the points. At last, damage occurrence probabilities of the verification points are estimated by Monte Carlo Simulation (MCS) with both uncertainties of response and resistance. Safety verification is conducted from the comparison with allowable damage occurrence probability determined by one of recently built similar structures, and seismic retrofit is studied from the cost effectiveness of countermeasures, which are estimated from viewpoint of both risk reduction and cost.

4 UNCERTAINTY OF SEISMIC INTENSITY

4.1 *Uncertainty of seismic intensity*

Residual service term of the target facility, "30-year", is determined as a basic term though, "50-year" is also considered in this study from a concern of the safety in case that the term is postponed.

The probabilistic seismic hazard curve corresponding to 30- and 50-year term at the target site (J-SHIS 2010) is shown in Figure 3. Figure 4 and Table 1 present the probabilistic density function, the uncertainty of seismic intensity at the site, assumed from the hazard curve.

4.2 *Basic seismic wave*

Seismic waves with respect to several specific earthquakes, which are predicted to occur on the

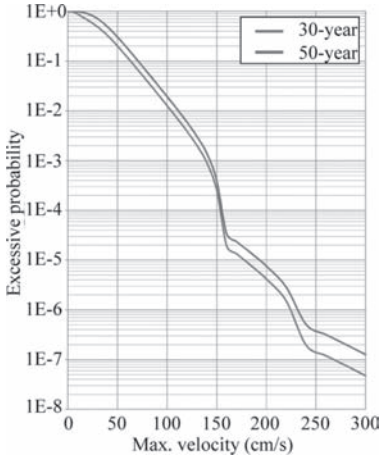

Figure 3. Probabilistic seismic hazard curve at the site.

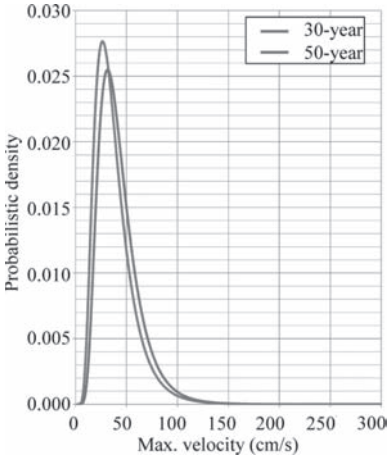

Figure 4. Uncertainty of seismic intensity at the site.

Table 1. Seismic intensity uncertainty.

Design term	Mean (cm/s)	SD (cm/s)	Distribution
30-years	34.9	19.4	Lognormal
50-years	42.6	20.2	Lognormal

engineering basement defined by shear wave velocity at each area of 250 m pitch, have been published from the government in Japan. The seismic wave caused by Tonankai-Nankai earthquake at the target site (COGJ 2006), shown in Figure 5, is adopted in this study as the basic seismic wave. Although this wave, maximum acceleration and

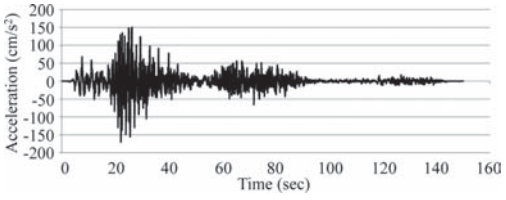

Figure 5. Basically seismic wave.

velocity are 180 cm/s^2 and 38 cm/s, is not so large, it had been adopted for seismic verification of the target facility until publishing the new wave in 2013 after occurrence Tohoku earthquake in 2011. The seismic effect in this study is considered from the basic seismic wave calibrated by the uncertainty of seismic intensity.

5 RESPONSE SURFACE (RS) ESTIMATION

5.1 *Response estimation method*

Effective stress dynamic FEM analysis, FLIP (Ver. 6.0.6), is adopted in this study, in order to evaluate the seismic response of the dam built on liquefiable ground during earthquake, by using response surface method (Honjo 2011). Figure 6 shows the FEM mesh of both river axis cross section and dam axis one. Ground condition of top three strata is presented on Table 2 and A_{s2} stratum is the liquefiable ground during earthquake.

The uncertainty of the FEM reproducibility with respect to the experimental responses of structure built on liquefied ground during earthquake, which were obtained from blind tests (JICE 2009), is shown in Figure 7. Because of blind test, the transformation error of the geotechnical parameters used in the FEM is included in the uncertainty. Although the experimental uncertainty was obtained from FEM reproducibility with respect to experimental results of river dike deformation, it was referred to one of the response estimation of pile structures as a safety evaluation in this study.

5.2 *Verification points*

A lot points have to be verified in normal seismic design though, in this study, the minimum verification points, which possess the possibility that the response corresponding to increscent seismic intensity exceeds the limit state, are selected from sensitivity analyses of responses at each point. The selected verification points are presented on Table 3.

In this paper, because of paper limitation, safety assessments of gate pier shear force in the dam axis

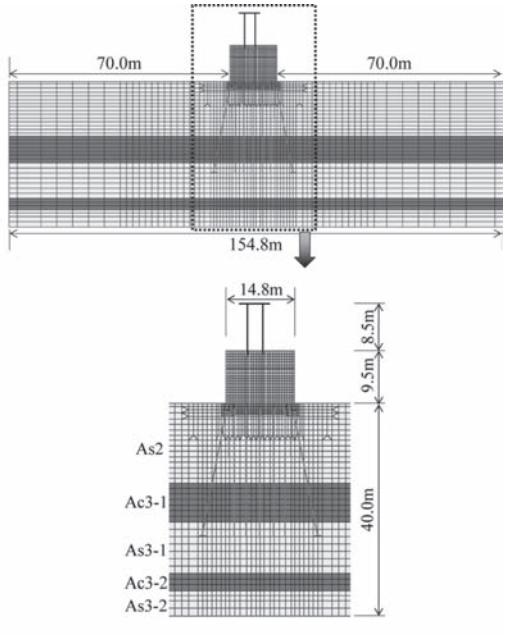

(a) River axis cross section

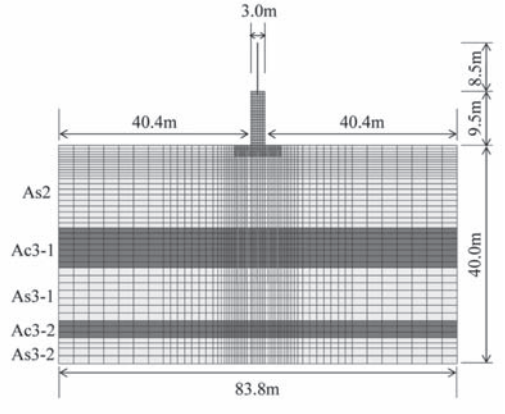

(b) Dam axis cross section

Figure 6. FEM mesh.

Table 2. Ground condition.

		SPT-N value	
	Thickness (m)	Mean	SD
A_{s2}	14.5	15.2	4.4
A_{c3}	7.0	12.4	3.0 (1.2)
A_{s3}	10.0	33.4	10.4 (4.4)

( ) in SD: converted ones for estimation of pile bearing capacity with using the proposed method by Otake & Honjo (2012).

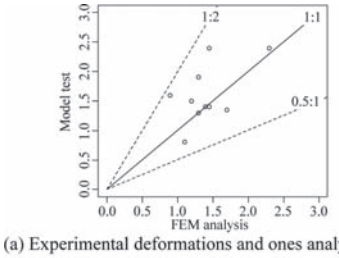

(a) Experimental deformations and ones analyzed by FEM.

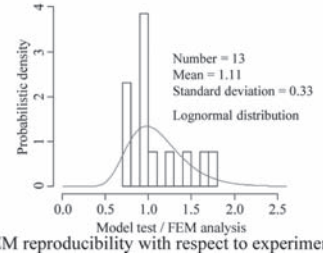

(b) FEM reproducibility with respect to experimental responses

Figure 7. Uncertainty of FEM reproducibility.

Table 3. Verification points.

		Verification section	
		River axis	Dam axis
Gate pier	Curvature	Verify	N/A
	Shear force	Verify	Verify
Dam pier		N/A	N/A
Pile	Displacement	Verify	Verify
Entirely structural inclination		Verify	Verify

cross section with respect to 30-years term is only introduced.

5.3 *Response surfaces*

It was confirmed that the uncertainty of seismic intensity is only influential one to the response of the respective verification points from sensitivity analyses with respect to uncertainties of seismic intensity, ground condition, deformation characteristic of gate pier and pile. Therefore, Response Surfaces (RSs) focused on only seismic intensity are estimated. Equation (1) and Figure 8 show RS of gate pier shear force in the dam axis cross section and its uncertainty of reproducibility with respect to the responses estimated by FEM analyses.

$$T = 1.2985 \cdot V_m + 559.95 \quad (1)$$

where, T = maximum shear force of gate pier (kN), V_m = maximum velocity of seismic wave (cm/s).

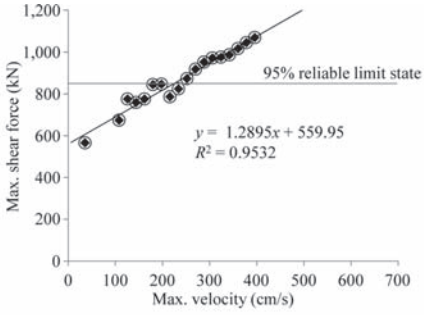

(a) Estimation of RS

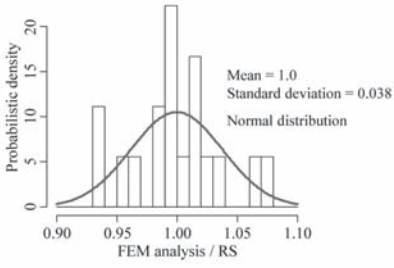

(b) Uncertainty of RS reproducibility with respect to responses estimated by FEM

Figure 8. RS of maximum shear force of gate pier.

Table 4. Uncertainty of shear strength.

Mean	SD	Distribution
1.93	0.273	Normal

6 LIMIT STATE UNCERTAINTY

The uncertainty of shear strength is presented on Table 4, which was referred from the existing research on the reproducibility of the shear strength estimated by Equation (2) to (4) with respect to experimental ones (Watanabe et al. 2007).

$$P_s = S_c + S_s \quad (2)$$

$$S_c = c_c \cdot c_e \cdot c_{pt} \cdot \tau_c \cdot b \cdot d \quad (3)$$

$$S_s = \frac{A_w \cdot \sigma_{sy} \cdot d \cdot (\sin\theta + \cos\theta)}{1.15 \cdot \alpha} \quad (4)$$

where, P_s = shear strength of reinforced concrete structure (N), S_c = shear strength boar by concrete (N), S_s = shear strength boar by reinforcing bar (N), c_c, c_e and c_{pt} = compensation coefficients concerning cyclic loading action, effective height

of the section (d) and, ratio of axial tensile reinforcing bars' area and sectional one, τ_c = mean shear stress boar by concrete (N/mm^2), b = section width (mm), A_w = area of shear reinforcing bars (mm^2), σ_{sy} = yield strength of shear reinforcing bar (N/mm^2), θ = angle of shear reinforcing bar and vertical axis (deg), α = pitch of reinforcing bars (mm).

7 DAMAGE OCCURRENCE PROBABILITY

7.1 *Reliability analysis*

Damage occurrence probability is estimated by MCS with one million runs with respect to the uncertainties of seismic intensity, reproducibility of FEM with respect to experimental responses of the structure built on liquefied ground, reproducibility of RS with respect to the responses estimated by FEM, and the limit state uncertainties.

7.2 *Shear collapse of gate column (dam axis)*

Equation 5 expresses the performance function. The shear collapse occurrence probability of gate column (dam axis) for 30-year term, 0.27%, is shown in Figure 9.

$$g = \delta_T \cdot T - \left(\begin{matrix} 1.2985 \cdot \delta_v \cdot V_m \\ +559.95 \end{matrix} \right) \cdot \delta_{FEM} \cdot \delta_{RS} \geq 0 \quad (5)$$

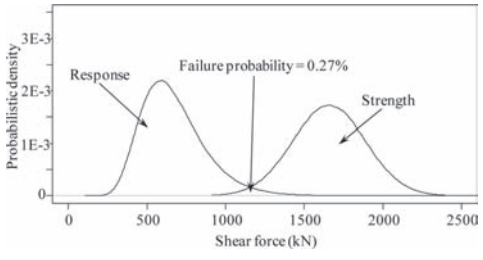

Figure 9. Shear collapse occurrence probability.

Table 5. Random variables for estimation of shear collapse occurrence probability (30-year term).

	Content	Mean	SD	Distribution
δ_T	Shear strength	1.93	0.27	Normal
δ_V	Maximum seismic velocity (cm/s)	37.6	19.4	Lognormal
δ_{FEM}	FEM reproducibility	1.11	0.33	Lognormal
δ_{RS}	RS reproducibility	1.0	0.038	Normal

where, δ_T, δ_V, δ_{FEM}, and δ_{RS} = random variables presented on Table 5, V_m = maximum seismic velocity (cm/s).

8 SAFETY VERIFICATION

8.1 *Allowable damage occurrence probability*

Damage occurrence probability of the recently built similar structures (Osumi et al. 2000, Unjo & Zhang 2009, Nakatani et al. 2009, Komori et al. 2011) is referred to specify the allowable ones for the target facility in this study.

8.2 *Safety verification*

The comparison of the allowable damage occurrence probabilities and estimated ones of all verification points is presented on Tables 6 and 7. In these Tables, the values noted in the brackets are the damage probability in 50-year term. According to the results, shear collapse occurrence probability of the gate column in dam axis cross section is only not satisfied the allowable one. Therefore, seismic retrofit for shear collapse of the gate column is studied based on risk in this paper.

Table 6. Comparison of estimated damage occurrence probabilities and allowable ones (dam axis, 30- and 50-year term).

	Damage probability (%)		
	Estimated	Allowable	Judge
Shear collapse of gate column	0.27 (0.29)	0.15	NG
Group pile displacement	2.7E-3 (3.1E-3)	0.35	OK
Residual inclination of entire structure	<1.0E-4 (<1.0E-4)	0.15	OK

Table 7. Comparison of estimated damage occurrence probabilities and allowable ones (river axis, 30- and 50-year term).

	Damage probability (%)		
	Estimated	Allowable	Judge
Flexural collapse of gate column	1.0E-4 (2.0E-4)	0.15	OK
Shear collapse of gate column	7.7E-3 (0.01)	0.15	OK
Group pile displacement	7.0E-4 (9.0E-4)	0.35	OK
Residual inclination of entire structure	1.0E-4 (1.0E-4)	0.15	OK

9 SEISMIC RETROFIT STUDY

9.1 *Risk estimation*

Damage summation cost caused by shear collapse of the gate column, which estimated by an assumption of recovery term of 120 days, is presented on Table 8. The risk with the damage, 113 million JPY, is estimated as the production of damage cost and occurrence probability of 0.27%.

9.2 *Seismic countermeasures*

Three countermeasures for seismic retrofit of the gate column, which are Wrap Reinforced Concrete, Wrap Steel Plate around the column (WRC, WSP) and Spray Polymer Cement Mortal to the column (SPM), are firstly chosen. Then residual damage probabilities after execution of each countermeasure are estimated as respective measure effects. Table 9 presents cost of each countermeasure and residual damage probability of respective countermeasures. Where, the reason why the residual damage probabilities of each countermeasure are smaller than the allowable one is to consider the minimum requirement of respective countermeasure specifications. The comparison of damage probabilities before and after execution of WRC is shown in Figure 10 for instance.

9.3 *Countermeasure selection*

Cost effectiveness (B/C) of respective countermeasures is presented on Table 10. Where, Benefit (B) is the difference of the damage risk before and after execution of each countermeasure. According to the results, WRC is desirable one for the countermeasure because of the highest cost effectiveness.

Table 8. Damage summation cost.

	Damage cost (million JPY)
Recovery cost	700
City water damage	1,750
Industrial water damage	31,200
Agricultural water damage	5,050
Summation	38,700

Table 9. Cost and effectiveness of countermeasures.

	WRC	WSP	SPM
Cost (million JPY)	60	115	92
Damage probability after execution (%)	8.0E-3 (9.0E-3)	0 (0)	0.022 (0.025)

Prob. and (Prob.): ones in 30- and (50)-year term.

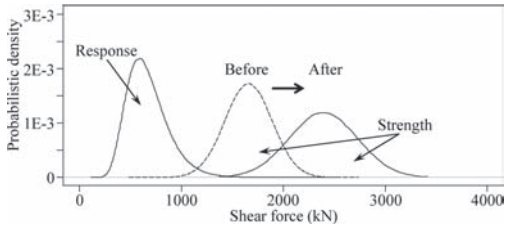

Figure 10. Comparison of damage probabilities before and after the execution of WRC.

Table 10. Cost effectiveness of respective countermeasures.

	WRC	WSP	SPM
B (million JPY)	101.9 (109.5)	105.0 (113.0)	96.4 (103.4)
C (million JPY)	60	115	92
B/C	1.70 (1.83)	0.91 (0.98)	1.05 (1.12)

B and (B), B/C and (B/C): ones in 30- and (50)-year term.

10 CONCLUSIONS

A concrete example of S-PSA application with using FEM analysis to an existing facility and seismic retrofit planning based on risk were introduced in this paper. This paper can be concluded as follows;

a. Application of S-PSA to common infrastructure is not so difficult.
b. S-PSA with using FEM analysis is possible by using response surface method.
c. The uncertainties of FEM reproducibility with respect to experimental results, RS reproducibility of responses estimated by FEM, and limit states as well as uncertainty of seismic intensity are considered in the S-PSA.
d. Seismic retrofit planning based on risk with using S-PSA result is effectiveness for countermeasure selection. This approach can be used more effectively to make priority decision for seismic retrofit planning of multiple structures despite its building region, structural type and so on.

The authors are expecting to be applied S-PSA and S-PRA to common infrastructures from the viewpoints of accountability to public and

reasonable use of limited public investment to seismic retrofit.

REFERENCES

Cabinet Office, Government of Japan (COGJ). 2006. Tonankai-Nankai seismic (acceleration) wave on engineering basement (Vs = 400 m/s): www.bousai.go.jp/jishin/chubou/.html.

Honjo, Y. 2011. Challenges in geotechnical reliability based design: Proc. of the 3rd Int. Symp. on Geotechnical Safety And Risk, 11–27, Munich, 2–3 June 2011. Germany: Bundesanstalt fur Wasserbau.

International Atomic Energy Agency (IAEA). 1993. Probabilistic safety assessment for seismic events.

International Atomic Energy Agency (IAEA). 2009. Evaluation of seismic safety for existing nuclear installations.

Japan Institute of Construction Engineering (JICE). 2002. Analysis method of seismic river dike deformation: JICE Document, Vol. 102001.

Japan Road Association (JRA). 2012. Specifications for highway bridges Part V seismic design.

Japan Road Association (JRA). 2012. Specifications for highway bridges Part IV substructures.

Japan Seismic Hazard Information Station (J-SHIS). 2010. Seismic hazard data, www.j-shis.bosai.go.jp/map/download.

Komori, N., Hoshikuma, J. & Sakai, J. 2011. A study on evaluation of seismic limit state of reinforced concrete bridge pier: Proc. of the 14th Symp. on Performance Based Seismic Design on Highway Bridges, 329–336.

Nakatani, S., Shirato, M., Kono, T., Nakamura, Y., Nomura, T., Yokomaku, K. & Iochi, H. 2009. A study on stability verification method of bridge foundation based on performance based design concept: Technical Note of Public Works Research Institute (PWRI), No. 4136.

Osumi, M., Unjo, S., Adachi, S. & Hoshikuma J. 2000. A study on seismic reliability evaluation of highway bridges: proc. of the 4th Symp. on Seismic Design Based on Ductility Design Method for Bridges: 13–16.

Otake, Y. & Honjo, Y. 2012. Verification of a simplified geotechnical reliability analysis scheme of spatial variability based on local average of geotechnical parameters: JSCE Journal C 68 (3): 475–490.

Unjo, S. & Zhang, K. 2009. A study on partial factor design for highway bridge seismic design: Report of road development research by government subsidy.

Watanabe, H., Koga, H. & Nakamura, H. 2007. A study on installation of International standard of design on concrete structure: Report of general research by government subsidy.

This page intentionally left blank

Geotechnical Safety and Risk IV – Zhang et al. (eds)
© 2014 Taylor & Francis Group, London, ISBN 978-1-138-00163-3

Probabilistic analysis of dry soil mix columns

J. Huang, R. Kelly & S.W. Sloan
ARC Centre of Excellence for Geotechnical Science and Engineering, The University of Newcastle, Australia

ABSTRACT: Analytical probabilistic analysis and Monte Carlo simulation based on elasto-plastic Finite Element Method (FEM) on dry soil mix columns are presented. It is shown that analytical method is over conservative because it ignores the supports from adjacent columns. Probabilistic FEM analysis can provide more accurate predictions, and thus lead to more economic designs. Probabilistic FEM analyses show that the effects of adjacent columns can be destructive when applied load is close to the strength. The reliability of the system of columns is analyzed by setting residual strength to zero. Results show that close spacing has more safety margin than loose spacing.

1 INTRODUCTION

Dry Soil Mix (DSM) columns are a method of ground improvement used to strengthen and stiffen soft to firm cohesive soils having an undrained shear strength of about 30 kPa or less. The strength and stiffness of the columns is a function of the ratio of water to cement and the quantity of mixing that occurs. The constructed columns do not have uniform strength within a single column or between columns due to the inherent variability of the ground along with non-uniform cement feed rates. The coefficient of variation of strength can range between 0.34 and 0.79 (Filz & Navin 2010). Experience shows that adjacent columns can have very different strengths and stiffness even though they are installed in the same ground using near identical methods. Variability is more typically controlled by specifying tight acceptance criteria for column strength and stiffness along with detailed quality control procedures in the construction documents. These requirements force the ground improvement contractor to install columns with higher strength and stiffness than required by design in order to reduce the risk of performing rework to replace non-conforming columns.

For a road or rail embankment the columns are installed individually below the crest of the embankment to control settlement and in panels or grids below the batters to provide stability. For settlement control the philosophy is the entire soil mass can be considered as having improved properties even though the columns are installed at discrete intervals. This leads to design methods where equivalent strength and stiffness parameters for the improved ground are computed using a unit cell approach and assuming equal strain conditions apply throughout the soil (e.g, Kelly & Wong 2011). Since equal strain conditions are assumed, the unit cell approach is actually a One Dimensional (1D) estimate. The advantage of this 1D estimate is that it allows a straight forward probabilistic assessment of column performance, which will be shown later in this paper. Its disadvantage is that the effects from adjacent columns are ignored, which may lead to over conservative design. In this paper we use the probabilistic finite element method (Griffiths et al. 2011) to perform preliminary assessments for the effects of DSM column variability on embankment settlement and column collapse performance.

2 DETERMINISTIC ANALYSIS

Initially, a deterministic design was performed to calculate the spacing of columns required to resist the embankment load. The DSM columns are treated as an elastic material having a constant ratio of modulus to strength (E/C_u) and have a range of strengths and centre to centre spacings in a square pattern. Assuming that the columns have a diameter of 0.8 m, a length of 10 m, the embankment has a thickness of 3 m, the fill has a unit weight of 20 kN/m^3, the columns have a stiffness to strength ratio of 200 and the spacing of the columns is controlled so that the load applied to the columns is 75% of their strength (factor of safety is 1.33). By using the unit cell method, various combinations of column strength and spacing that satisfies the design criteria are summarised in Table 1. The combination of column strength and spacing are then adopted in the probabilistic assessment.

In FEM analyses, soil fill is modelled by 20 nodes brick elements. Soil fill is assumed to be elastic with Young's modulus of 20 MPa and Poisson's ratio of 0.3. Columns are modelled as spring elements and placed beneath every corner node of brick elements. One end of the springs is connected to the brick

Table 1. Spacing by FEM and 1D estimate.

Column strength (kPa)	Spacing (m) by FEM	Spacing (m) by 1D
100	1.114	1.118
150	1.368	1.369
200	1.582	1.581
250	1.769	1.768
300	1.938	1.936
500	2.500	2.500

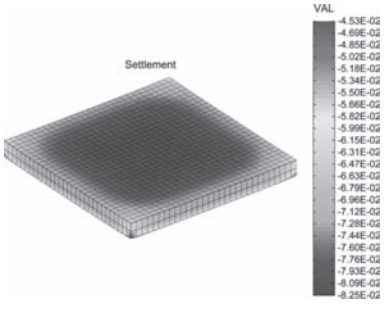

Figure 1. Deterministic settlements (column strength is 100 kPa, spacing is 1.114 m).

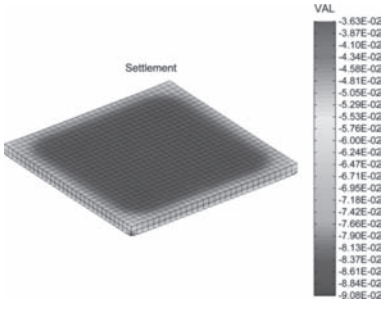

Figure 2. Deterministic settlements (column strength is 250 kPa, spacing is 1.769 m).

elements. The other end is fixed. Rollers are put at four sides. Since the performance of the column in the middle is concerned, the number of columns is decided so that the effect of boundary conditions on this column is negligible. Spacings shown in Table 1 are decided so that the settlement in the middle (S) is 0.075 m. The spacing by FEM is very close to 1D estimate, which means the boundary effects are negligible. Figures 1–3 show the settlement profiles in which soil settlements are included. It can be seen that the settlement at the boundaries are smaller than that in the middle. This is because of the reactive bending moments caused by the rollers.

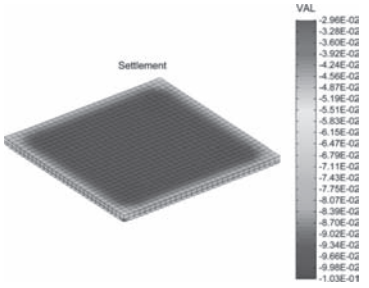

Figure 3. Deterministic settlements (column resistance is 500 kPa, spacing is 2.5 m).

3 PROBABILISTIC ELASTIC ANALYSIS

The stiffness of columns E is assumed to be a log-normally distributed random variable with coefficient of variation (V_E) of 0.5. The probability that S exceeds 0.0825 m can be estimated by 1D analysis if the effects of adjacent columns are ignored. Since the spacing was decided so that the settlement is 0.075 m, we have

$$\frac{WL}{\mu_E A} = 0.075 \tag{1}$$

where $W = \gamma HD^2$ is the applied load on the columns, L is the length of the columns, μ_E is the mean column stiffness and A is the cross sectional area of the columns.

The probability that S exceeds 0.0825 m is (e.g., Griffiths et al. 2009)

$$\begin{aligned} P(S>0.0825) &= P\left(\frac{WL}{EA}>0.0825\right) \\ &= P\left(\frac{0.075\mu_E}{E}>0.0825\right) \\ &= P\left(E<\frac{\mu_E}{1.1}\right) \\ &= \Phi\left\{\frac{\ln\left(\frac{\mu_E}{1.1}\right)-\mu_{\ln E}}{\sigma_{\ln E}}\right\} \\ &= \Phi\left\{\frac{\ln\left(\frac{\mu_E}{1.1}\right)-\ln\mu_E+\frac{1}{2}\ln(1+V_E{}^2)}{\sqrt{\ln(1+V_E{}^2)}}\right\} \\ &= \Phi\left\{\frac{\ln\left(\frac{1}{1.1}\right)+\frac{1}{2}\ln(1+V_E{}^2)}{\sqrt{\ln(1+V_E{}^2)}}\right\} \\ &= 0.51 \end{aligned} \tag{2}$$

where Φ is the cumulative standard normal distribution function.

In order to investigate the effects from adjacent columns, two thousand Monte Carlo simulations were carried out. Three typical simulations are shown in Figures 4–6. The histograms of settlements are shown in Figures 7–9.

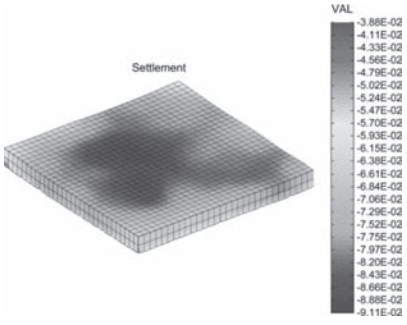

Figure 4. A typical simulation (column strength is 100 kPa, spacing is 1.114 m).

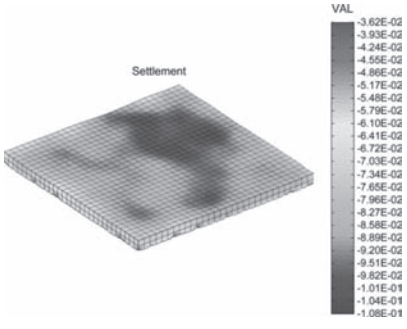

Figure 5. A typical simulation (column strength is 250 kPa, spacing is 1.769 m).

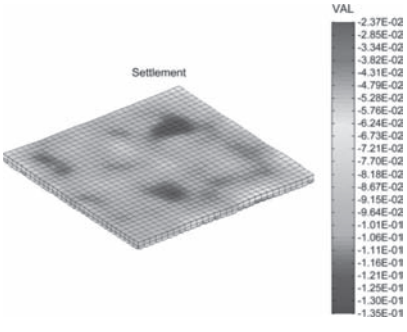

Figure 6. A typical simulation (column strength is 500 kPa, spacing is 2.5 m).

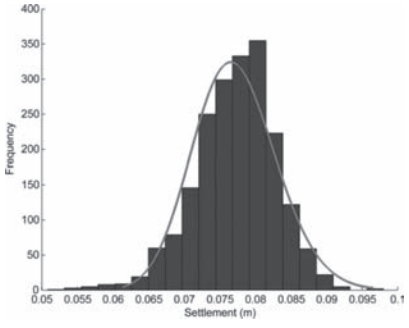

Figure 7. Histogram of settlement (column strength is 100 kPa, spacing is 1.114 m).

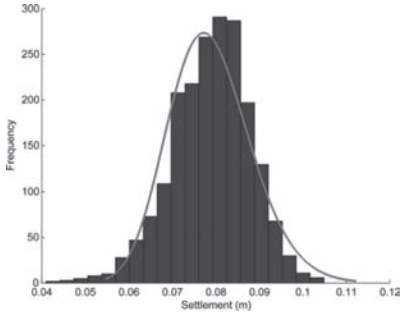

Figure 8. Histogram of settlement (column strength is 250 kPa, spacing is 1.769 m).

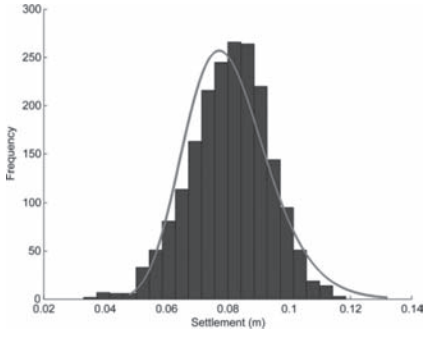

Figure 9. Histogram of settlement (column strength is 500 kPa, spacing is 2.5 m).

The probability of settlement exceeds 0.0825 m is compared to 1D estimate in Figure 10. It can be seen from Figure 10 that the probability of the settlement exceeds 0.0825 m is smaller than the 1D estimate. This is because of the supports from adjacent columns. As the spacing increases, this effect gets smaller. The probability is approaching 0.51 when the spacing is increasing as shown in Figure 10.

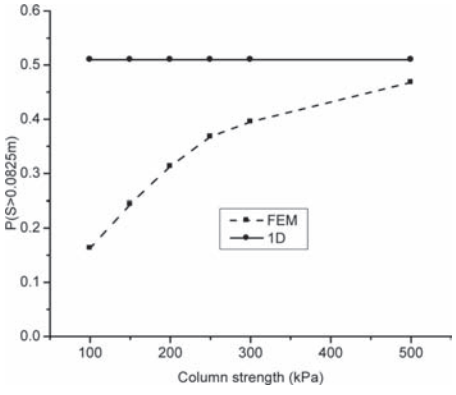

Figure 10. Probability of settlement exceeds 0.0825 m.

4 PROBABILISTIC ELASTO-PLASTICITY ANALYSIS

The strength of columns C_u is assumed to be a log-normally distributed random variable with coefficient of variation (V_{C_u}) of 0.5. The probability of column collapses can be estimated by 1D analysis. Since the spacing was decided so that the settlement is 0.075 m, assuming column stiffness is 200 times the column strength, we have

$$\frac{WL}{200\mu_{C_u}A} = 0.075 \tag{3}$$

$$\frac{W}{A} = 1.5\mu_{C_u} \tag{4}$$

If the Tresca failure criterion is used, the yield stress is

$$\sigma = \frac{W}{2A} = 0.75\mu_{C_u} \tag{5}$$

The factor of safety is 1.333. The probability of column collapse is

$$\begin{aligned} P\left(2C_u < \frac{W}{A}\right) &= P\left(C_u < 0.75\mu_{C_u}\right) \\ &= \Phi\left(\frac{\ln\left(0.75\mu_{C_u}\right) - \mu_{\ln C_u}}{\sigma_{\ln C_u}}\right) \\ &= \Phi\left(\frac{\ln(0.75) + \frac{1}{2}\ln(1+V_{C_u}{}^2)}{\sqrt{\ln(1+V_{C_u}{}^2)}}\right) \\ &= 0.35 \end{aligned} \tag{6}$$

The above estimate ignores the effects of adjacent columns, which can be analysed by probabilistic FEM. Perfect plasticity is used in probabilistic FEM analysis. For each simulation, if the column in the middle collapses, the simulation is counted as a failure, which is consistent with 1D estimation. The collapse can be caused by the overloading of the column, or by the loads redistributed by adjacent columns' yielding. The probability of column collapse is compared with 1D estimate in Table 2. The results by FEM are significantly lower than the 1D estimate. This is because of the perfect correlation between column stiffness and strength, i.e., a weak column is loaded less than a strong column.

The above results showed that the effects of adjacent columns are supportive. But this is not always true. When safety margin is small (i.e., applied load is close to mean resistance), the collapses of adjacent columns are more likely to cause the column to fail. To demonstrate this, the spacing is adjusted so that applied load is equal to the mean resistance (i.e., S = 0.1 m, FS = 1.0), and the probability of the column collapse is shown in Table 3. It can be seen from Table 3 that the probability of column collapses is much higher than the 1D estimate, which means that effects from adjacent columns are not supportive but destructive.

If perfect plasticity is used, the system of columns is stable as long as the mean strength of columns is larger than the applied load. The safety margin of the column system is not clear. It is however, possible to access system reliability by using

Table 2. Probability of column collapse.

Column strength (kPa)	Probabilistic FEM	1D estimate
100	1/2000	0.35
150	0.001	0.35
200	0.0015	0.35
250	0.0065	0.35
300	0.0165	0.35
500	0.0665	0.35

Table 3. Probability of column collapse.

Column strength (kPa)	Spacing (m)	FEM analysis	1D estimate
100	1.286	0.8770	0.59
150	1.575	0.9075	0.59
200	1.817	0.9090	0.59
250	2.031	0.9185	0.59
300	2.224	0.9175	0.59
500	2.869	0.9420	0.59

Table 4. Probability of system collapse.

Column strength (kPa)	Spacing (m)	Probability of system collapse
100	1.114	0.5e-3
150	1.368	0.55e-2
200	1.582	0.1075
250	1.769	0.3960
300	1.938	0.7390
500	2.500	0.9990

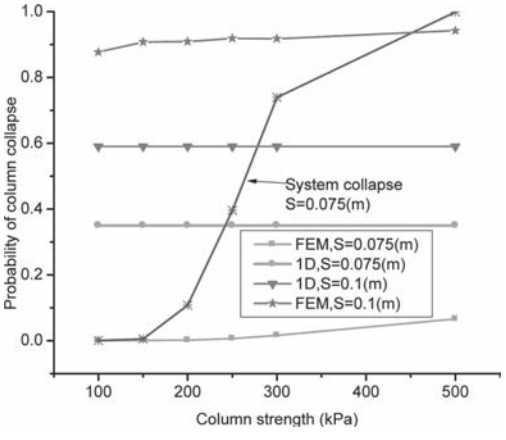

Figure 11. Comparison between 1D estimate and FEM analysis.

zero residual strength for columns after yielding. Table 4 shows the probability of system collapse.

The probabilities of column collapse by 1D estimate and FEM analyses are compared in Figure 11. It can be seen that 1D estimate is conservative when safety margin is large, but unconservative when safety margin is small. The safety margin of close spacing is larger than loose spacing.

5 CONCLUSIONS

By assuming equal strain condition, analytical method is over conservative. It would lead to very tight acceptance criteria for column strength, and in terms leads to uneconomic design. Probabilistic FEM analysis can provide more accurate prediction. The results of probabilistic FEM analyses show that the effects from adjacent columns can be destructive. It will be pursued in a future research to provide design charts for dry soil mix columns based on probabilistic FEM analyses.

ACKNOWLEDGEMENT

The authors wish to acknowledge the support of the Australian Research Council in funding the Centre of Excellence for Geotechnical Science and Engineering.

REFERENCES

Filz GM & Navin MP 2010. A Practical Method to Account for Strength Variability of Deep-Mixed Ground. GeoFlorida 2010: 2426–2433.

Griffiths DV, Dotson D and Huang J 2011. Probabilistic Finite Element Analysis of a Raft Foundation Supported by Drilled Shafts in Karst. Geo-Risk 2011: 233–239.

Griffiths DV, Huang JS and Fenton GA 2009. Influence of Spatial Variability on Slope Reliability Using 2-D Random Fields. Journal of Geotechnical and Geoenvironmental Engineering 135(10): 1367–1378.

Kelly R & Wong P 2011. Lessons learnt from design and construction of dry soil mix columns. Int. Conf. Advances in Geotechnical Engineering, Perth, Australia.

This page intentionally left blank

Geotechnical Safety and Risk IV – Zhang et al. (eds)

Soft soil subgrade's reliability and risk assessment under incomplete probability conditions

C. Liu & M. Zhao
School of Civil Engineering, Hebei University of Technology, Tianjin, China

ABSTRACT: On the basis of the interval analysis, the non-probabilistic reliability analysis method makes the reliability of slope stability and risk analysis more complete. Through the comparison between the safety factor, probability and reliability indexes and the non-probabilistic reliability index of dangerous sliding surface, the non-probabilistic reliability index's advantage is proved and a practical evaluation method is supplied for the reliability and risk assessment of geotechnical engineering.

1 INTRODUCTION

There was a highway engineering project, which was totally collapsed through gravel pile reinforcement. After the accident, we checked the coefficient of slope safety and probability reliability index. The results show that the coefficient of safety is 1.23 and the probability reliability index is 3.95, but the section and foundation around it was stable because of the tamp treatment on it in fact.

In the 1960s, the coefficient of safety method was accepted through long-term practice. But starting in the 1970s, slope engineering field began to accept the concept of uncertainty. Using reliability method was proposed as a supplement. The use of probabilistic reliability method gradually became mature at the same time. It was found that this method also had certain limitations. The nature of the soil has great variability. Soil parameter statistics belongs to the small sample problem. So in subjective distribution assumptions, the results of probability reliability calculation may be distorted. Therefore, people put forward to the non-probabilistic reliability analysis method, which can further perfect the reliability theory. The uncertainty of evaluation is more reasonable. The roadbed model is established on the bases of on finite element analysis software ABAQUS. This paper combines the finite element numerical analysis with the limits equilibrium method and conducts the probability and the interval analysis on the soil shear strength parameters and compared the differences between the safety factor, probability and non-probability indexes of reliability.

2 THE INTRODUCTION TO RELIABILITY ANALYSIS METHOD IN INTERVAL ANALYSIS

In coefficient of safety method, K means slope's stability safety, which is the ratio between skid resistance moment and sliding moment. Using simple strip method, we can get the expression of safety coefficient K:

$$K = \frac{M_r}{M_s} = \frac{\sum_{i=1}^{n} \left(\gamma b_i h_i \cos \alpha_i \tan \varphi_i + c_i l_i \right)}{\sum_{i=1}^{n} \gamma b_i h_i \sin \alpha_i} \tag{1}$$

From formulas (1):

Resistance $R = \sum_{i=1}^{n} \left(\gamma b_i h_i \cos \alpha_i \tan \varphi_i + c_i l_i \right)$,

Glide force $S = \sum_{i=1}^{n} \gamma b_i h_i \sin \alpha_i$

From probability reliability analysis's state function:

$$Z = R - S = \sum_{i=1}^{n} \left(\gamma b_i h_i \cos \alpha_i \tan \varphi_i + c_i l_i \right) - \sum_{i=1}^{n} \gamma b_i h_i \sin \alpha_i \tag{2}$$

Because b, h, α are geometric parameters, γ is physical parameter, we just put c, φ as variable. So the formula (2) can be simplified as follows:

$$Z = \gamma bh \cos \alpha \sum_{i=1}^{n} \tan \varphi_i + L \sum_{i=1}^{n} c_i - \gamma bh \sin \alpha \tag{3}$$

Spreading formula (3) at mean:

$$\sigma_z = \sqrt{\sum_{i=1}^{n}\left(n\gamma bh\cos\alpha\csc^2\mu_\varphi\sigma_\varphi\right)^2 + \sum_{i=1}^{n}\left(L\sigma_c\right)^2} \quad (4)$$

But $\sigma_z = \sqrt{\sigma_R{}^2 + \sigma_S{}^2}$ (5)

In the process of calculating the reliability index, we compare formula (4) with formula (5), and then we find that the calculation of the resistance R is considered, where the glide force R is not considered. From the code for investigation of geotechnical engineering, we can get that the value of c, is got under the situation which is a normal distribution. If we get the distribution such as Figure 1 or Figure 2 (small sample), the sample parameters probability mode will indicate a larger deviation.

From the foregoing analysis, slope's probability reliability analysis method has limitations. In the 1990's, the concept of non-probability reliability was put forward to for the first time, and then people began to develop the slope stable non-probability reliability analysis method researches on the basis of interval analysis method. Minghua Zhao, Chong Jiang and Wengui Cao applied the interval analysis non-probability reliability model to the geotechnical engineering.

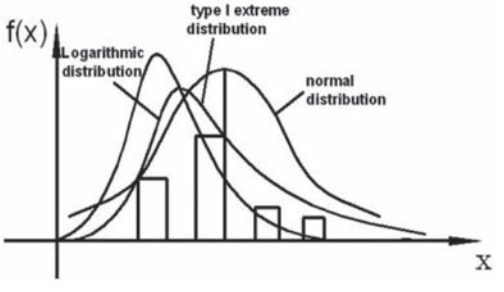

Figure 1. Normal distribution scheme estimates (small sample).

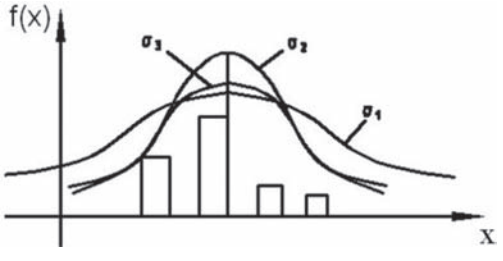

Figure 2. Normal distribution scheme estimates (small sample).

Non-probability reliability research calculation method: Taking parameters as basic interval variables, if we know the parameter's interval and monotonic, we can get the upper and lower boundary of limit state function:

$$Z^l = \min_{\delta_i \in \Delta^l} G(\delta_1, \delta_2, ..., \delta_n)$$
$$Z^u = \max_{\delta_i \in \Delta^l} G(\delta_1, \delta_2, ..., \delta_n)$$

Then we can get the non-probability reliability index by using of limit state function's upper and lower boundary and approximation formula.

$$\eta = Z^c \Big/ Z^r = (Z^u + Z^l) \Big/ (Z^u - Z^l)$$

3 CASE STUDY ANALYSIS

3.1 *Section numerical simulation*

Building the model in ABAQUS, this is shown in Figure 3.

The embankment is filled with fly ash, and the parameters are shown in Tables 1 and 2.

3.2 *The safety coefficient and probabilistic reliability analysis of section stability*

Using strength subtraction calculation, the program application result is convergent when $K = 1.3$, which can be thought of as the slope has been damaged, and the detail location of failure surface can't be got. Combined shear stress in Figure 4 ($K = 1.2$), the biggest shear describes several connecting arcs, as one of the most dangerous sliding surface, it appears within the embankment and is below a layer of soil. Then the stresses are taken from each unit in sliding surface, which is shown in Table 3.

3.2.1 *The safety coefficient and reliability index of each unit in dangerous sliding surface*

The function is

$$Z = (\tau_f - \tau)L_i = cL_i + \sigma\tan\varphi L_i - \tau L_i$$

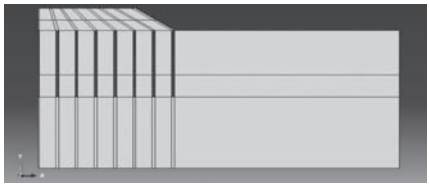

Figure 3. The ABAQUS model of the section gravel pile roadbed.

Table 1. Soil parameters of embankment.

Soil layer	Layer thinkness (m)	Weight (kN/m^3)	Cohesion (KPa)	Internal friction angle (degree)	$E_{S1\text{-}2}$ (MPa)
Fly ash	4.05	14.00	10	25	10

Table 2. The pile parameters of soil layers and gravel pile.

Soil layer	Thickness of soil layer (m)	Weight (kN/m^3)	Shear c (KPa)	Shear φ (degree)	$E_{S1\text{-}2}$ (MPa)
Muddy silty clay ②1	8.700	17.60	10.0	5.65	3.10
Sandy soil ③	5.100	19.00	0.0	20.1	19.93
Silt ④1	6.510	20.30	20.0	18.7	8.70
Pravel pile	Arrangement from	Spacing (m)	Length (m)	Diameter (m)	Weight (kN/m^3)
	Equilateral triangle	1.6	11.0	0.5	20.00

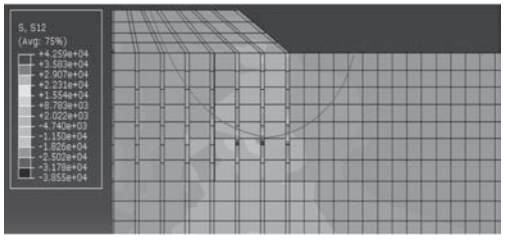

Figure 4. Shear stress.

Division of grid, make each quadrilateral element approximation for 2 m length, pile and surrounding transverse length of 0.5 m units, the soil elements between the pile lateral side length is about 2.7 m. The maximum stress and minimum stress of each unit are chosen from Figures 5 and 6. After calculation, the reliable indicators and the coefficients of safety of every unit in most likely damage surface of slope are listed in Table 3.

The Table 3 shows that the safety factor and probability reliability of embankment soil are large and the shear of muddy silty clay layer unit is large, and the safety factor through calculation of every unit is close to 1 and the probabilistic reliability index is close to zero, which tends to be damaged, and the probability reliable index of pile is not very large.

3.2.2 *The safety coefficient and reliable index of overall reliability in every soil layer*

For embankment layers τ_f and τ along the sliding surface of the integral unit length, the coefficient of safety and probabilistic reliability index can be calculated:

$$K = \frac{\sum_{i=1}^{n} \tau_f L_i}{\sum_{i=1}^{n} \tau L_i} = 181.02/89.32 = 2.03$$

$$\beta = \frac{\sum_{i=1}^{n} \mu_z}{\sqrt{\sum_{i=1}^{n} \sigma_z^2}} = 22.93/6.66 = 3.44$$

For the first embankment layer τ_f and τ along the sliding surface of the integral unit length, the safety coefficient and probabilistic reliability index can be calculated:

$$K = \frac{\sum_{i=1}^{n} \tau_f L_i}{\sum_{i=1}^{n} \tau L_i} = 752.16/666.84 = 1.13$$

$$\beta = \frac{\sum_{i=1}^{n} \mu_z}{\sqrt{\sum_{i=1}^{n} \sigma_z^2}} = 85.56/42.88 = 2$$

3.2.3 *The safety coefficient and reliability index of embankment slope's overall reliability*

We can get the coefficient of safety and probability reliability index through integrating along the

Table 3. Probability index and safety coefficient.

Soil layer	Unit	μ_c (KPa)	μ_φ (degree)	μ_z (KN/m)	σ_z (KN/m)	Probability index β	Safety coefficient K
Embankment soil	78	10.00	25.00	23.99	5.27	4.56	3.26
	77	10.00	25.00	22.30	6.05	3.69	2.09
	88	10.00	25.00	22.03	7.33	3.00	1.77
	89	10.00	25.00	23.39	7.72	3.03	1.79
Muddy silty clay and gravel pile	99	10.5	5.65	0.47	7.91	0.06	1.02
	3 (part 5)	2	45.00	–5.22	12.82	–0.41	0.93
	100	10.5	5.65	0.16	6.05	0.03	1.01
	4 (part 6)	2	45.00	6.35	16.18	0.39	1.08
	131	10.5	5.65	0.00	6.42	0.00	0.99
	5 (part 7)	2	45.00	19.43	16.20	1.20	1.31
	161	10.5	5.65	–0.50	6.76	–0.07	0.99
	5 (part 8)	2	45.00	25.06	14.71	1.70	1.51
	330	10.5	5.65	–0.44	6.72	–0.07	0.99
	5 (part 9)	2	45.00	32.96	14.21	2.32	1.84
	388	10.5	5.65	–0.59	13.44	–0.04	0.99
	389	10.5	5.65	–0.77	13.48	–0.06	0.99
	410	10.5	5.65	3.50	8.51	0.41	0.99
	431	10.5	5.65	5.16	8.13	0.63	1.09

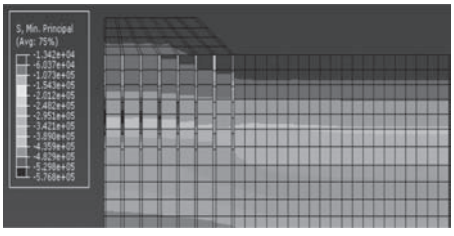

Figure 5. Maximum main stress.

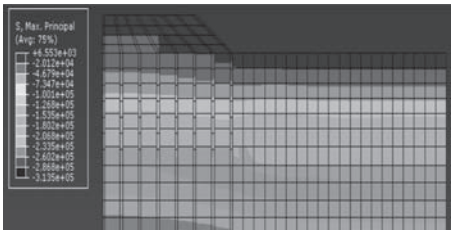

Figure 6. Minimum main stress.

whole dangerous sliding surface's each unit length about subgrade slope's τ_f and τ.

$$K = \frac{\sum_{i=1}^{n} \tau_f L_i}{\sum_{i=1}^{n} \tau L_i} = 933.17/756.16 = 1.23$$

$$\beta = \frac{\sum_{i=1}^{n} \mu_z}{\sqrt{\sum_{i=1}^{n} \sigma_z^{\,2}}} = 177.26/44.91 = 3.95,$$

The coefficient of safety of embankment slope's overall reliability is 1.23 while the probabilistic reliability index is 3.95 and the failure probability is less than 0.0001.

3.3 *The non-probabilistic reliability analysis of section stability*

3.3.1 *The non-probabilistic reliability index of each unit in dangerous sliding surface*

Because the parameters of the fly ash embankment are obtained from experience, the range of parameters is shown in Table 4, if 0.2 is chosen as the coefficient of variation value.

The function equation:

$$Z = (\tau_f - \tau)L_i = cL_i + \sigma \tan\varphi L_i - \tau L_i$$

Taking a unit of embankment as an example:

$$\sigma = 15.66 \text{ KPa}, \quad \tau = 5.3 \text{ KPa}$$

The shear strength standard values

$$c = [8,12]\text{KPa}, \quad \varphi = [20,30]^\circ$$

Table 4. The range of parameters.

Soil layer	Statistical index	Shear strength index: Cohesion c (KPa)	Shear strength index: Internal friction angle φ (degree)
Fly ash	Maximum	12	30
	Minimum	8	20
Muddy silty clay ②1	Maximum	14	8
	Minimum	6	4.3

According to the optimization method:

$Z_u = 48.26$ KN/m, $Z_l = 14.68$ KN/m

The non-probabilistic reliability index:

$$\eta = \frac{Z^c}{Z^r} = \frac{Z_u + Z_l}{Z_u - Z_l} = 3.29$$

Through calculation, the non-probability reliability indexes of each unit in the most dangerous sliding surface are shown in Table 5.

3.3.2 *The non-probabilistic reliability index of soil layers*

For embankment soil layers Z_u and Z_l along the sliding surface of the integral unit length, the non-probabilistic reliability index can be calculated:

$$\eta = \frac{Z^c}{Z^r} = \frac{\sum_{i=1}^{n}(Z_u + Z_l)dL_i}{\sum_{i=1}^{n}(Z_u - Z_l)dL_i} = 2.37$$

For the first embankment soil layer Z_u and Z_l along the sliding surface of the integral unit length, the non-probabilistic reliability index can be calculated:

$$\eta = \frac{Z^c}{Z^r} = \frac{\sum_{i=1}^{n}(Z_u + Z_l)dL_i}{\sum_{i=1}^{n}(Z_u - Z_l)dL_i} = 0.64$$

3.3.3 *The non-probabilistic reliability index of overall stability in embankment slope*

For embankment soil layers Z_u and Z_l along the sliding surface of the integral unit length, the non-probabilistic reliability index can be calculated:

$$\eta = \frac{Z^c}{Z^r} = \frac{\sum_{i=1}^{n}(Z_u + Z_l)dL_i}{\sum_{i=1}^{n}(Z_u - Z_l)dL_i} = 0.86$$

Table 5. The non-probabilistic reliability index of unit stability.

Soil layer	Unit	σ (KPa)	τ (KPa)	η
Fly ash embankment	78	15.66	5.30	3.29
	77	24.35	10.20	2.45
	88	32.97	14.35	2.02
	89	35.40	14.80	2.05
Muddy silty clay	99	43.87	14.60	0.02
	3	128.27	140.60	0.03
	100	63.84	16.71	0.04
	4	161.87	151.04	0.04
	131	107.06	21.25	0.05
	5	162.16	125.17	0.06
	161	135.86	24.27	0.06
	5	147.17	98.93	0.05
	330	132.66	23.91	0.30
	5	142.25	78.21	0.43
	388	132.54	23.80	0.41
	389	134.45	24.05	0.77
	410	103.20	18.95	1.22
	431	71.43	14.99	1.53

3.4 *The stability analysis of the section*

From each soil's the coefficient of safety and reliability index, we know that the mucky silty clay layer is more likely to be destroyed after using gravel pile to deal with the ground secsions. The mucky silty clay layer's coefficient of safety is 1.13, its probability index is 2 and its destroying probability is greater than 0.01, so the layer can not satisfy the demands. The most dangerous sliding surface's non-probability reliability index is the same as the coefficient of safety and probability reliability index. The mucky silty clay layer's non-probability is 0.64, so its reliability is low because its value is small. The whole slope's safety coefficient is 1.23, probability reliability index is 3.95, but the non-probability reliability index is 0.83. In fact, this section and the subgrade which is through gravel pile reinforcement around it are collapsing totally.

From the foregoing discussion, we can judge that the section is unstable, and the results of non-probability reliability theory conform to reality. If we use the probability reliability index,

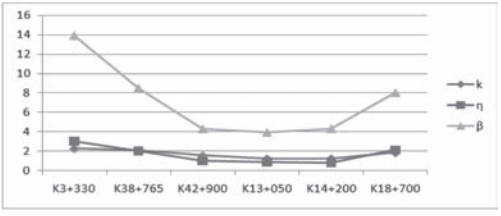

Figure 7. The relationship curve of k, β, η.

we can not get the result, because it is influenced by parameter's distribution. If the coefficient of variation is bigger, the probability reliability index will decrease. So we can say that the non-probability reliability theory is good for the slope engineering.

4 CONCLUSION

Through the analysis of engineering examples, the relationship between the three parameters is shown in Figure 7.

Figure 7 shows that the non-probabilistic reliability indexes are similar to the safety coefficient values. There are no clear provisions on the non-probabilistic reliability index, so the selecting on the value target of probabilistic reliability index can refer to the target value of safety coefficient. In addition, the quantity of soil parameters is small, so parameters distribution can only be assumed to be normal distribution, and the coefficient of variation is not accurate, when calculating the probability of slope stability reliability. Combined with project case study, the calculation of the probability reliability index cannot accurately show the stability of the section, but no matter how small the samples are, they also have the range. So the non-probabilistic reliability theory has certain advantages in small sample situation.

REFERENCES

Junqi Zhang. Non-probabilistic reliability analysis of slope stability. Hebei University of Technology, 2011.

Minghua Zhao, Chong Jiang & Wengui Cao. 2008. Non-probabilistic reliability analysis based on the the interval theory retaining wall stability.The Journal of Geotechnical Engineering 30(4): 467–472.

Ruijiao Xin & Qiang Li. 2011. Structure interval fuzzy stochastic finite element reliability analysis. Ha'erbin University of Technology, 2011.

Shengfei Yu, Zhengzhou Chen & Mingrui Zhang. Slope stability analysis based on the range of uncertainty analysis method. Journal of Engineering Geology, 1004-9665/2012/20(2)-0228.

Wengui Cao & Yongjie Zhang. 2007. Non-probabilistic fuzzy reliability analysis of slope stability based on interval method. The Journal of Civil Engineering, 2007.11.

Yong Liu & Huansheng Mu. 2011. Non-probabilistic reliability analysis of highway roadbed slope stability in soft ground conditions. Road Engineering 1002-4786 17-0096-02.

Yingying Zhang. 2011. Non-probabilistic reliability analysis based on particle swarm optimization and its application in Slope Engineering. Zhongnan University, 2011.

Zhengzhong Wang, Shengyuan Mou & Jun Liu. 2009. Calculated safety factor of slope aspect centrifugation. Rock and Soil Mechanics, 2009.9.

Geotechnical Safety and Risk IV – Zhang et al. (eds)

Localised metamodelling techniques for geotechnical reliability-based analysis

S.H. Marques, A.T. Gomes & A.A. Henriques
Department of Civil Engineering, Faculty of Engineering, University of Porto, Portugal

ABSTRACT: Metamodelling is actually a very interesting research area for the replacement of simulation models when the trade-off between efficiency and accuracy is appropriate. Several approaches have been proposed, and localised metamodelling techniques applied in reliability-based analysis may involve the search for the most probable failure point. Response surface methodology has been suggested for the approximation of functions, namely implicit limit state functions. The response surface is typically constructed from a polynomial function fitted at a number of points, but no clear guidance has been given for the effect of varying their location. Results for a geotechnical design example with correlated nonnormal random variables are presented in the light of the quality of the design point approximation. In particular, interpolation methodologies in conjunction with appropriate experimental design are suggested for extracting nonlinear response surfaces whose roughness varies substantially over the input domain, so that sequential algorithms may adapt to nonlinear features.

1 INTRODUCTION

Metamodelling techniques are actually established to reduce the need to run expensive simulations, as stated by Can & Heavey (2011). In order to reduce computational costs in reliability analysis it has been suggested to utilise approximate response functions, and one well established class of methods to deal with suitable approximations is the so called response surface methodology (Bauer & Pula 2000, Tandjiria *et al*. 2000, Babu & Srivastava 2007, Massih & Soubra 2008, Mollon *et al*. 2009, Lü & Low 2011), whose basic principles are also described by Haldar & Mahadevan (2000).

The basic idea in utilising the response surface methodology is to replace the true limit state function by an approximation whose functional values may be computed more easily. In general, a good physical knowledge of the system is very useful in deciding the appropriate order of the response surface approximation. The functions are typically chosen to be first or second order polynomials, in fact higher orders require a high number of support points, to be obtained very close to the failure surface or limit state of interest.

The response surface model should give the best possible fit to the collected data, and in general two different types of response surface models are distinguished: regression models and interpolation models (Bucher & Most 2008). By fitting the response surface to a number of design of experiments of the true limit state function, the approximated limit state function is then constructed. After that, Monte Carlo simulation based on counting may be used efficiently since the evaluation of the response surface function requires a reduced computational effort. Alternatively, the first order reliability method may be applied and corrections may be provided by the second order reliability method, otherwise different reliability techniques.

This methodology gives an approximate closed form expression, based on the selected number of design of experiments, applied to generate the training data from the decision space of the problem, and is very useful when the response has to be computed through a numerical procedure such as finite element analysis and the performance function is implicit.

Two key issues of the response surface methodology have been analysed in the literature: the polynomial degree of the response surface and the position of the sampling points. Whilst response surfaces with low degree polynomials are used in practice to reduce the number of limit state function evaluations, the approximation provided by the response surfaces is by hypothesis only local to the region where the sampling points are disposed, so a good approximation implies that the coordinates of the most probable failure point, the design point, have to be precisely discovered (Allaix *et al*. 2011).

As a general rule, the approximate closed form expression is valid only within the range of the values considered for the random variables, and extrapolation beyond the considered range may not be accurate, furthermore, the approximation may be indeed inadequate for highly nonlinear

performance functions (Haldar & Mahadevan 2000). So, regarding nonlinear analysis, different methodologies have been proposed. A very simple iterative procedure for the search of the most probable failure point is detailed next considering that the approximate function is generated in the standard normal space. For the purpose, the transformations $xi^* = f(yi^*)$ and $f(xi^*) = yi^*$ derived by Equation 1 are further considered for representation of random variables xi^* with different distributions as a function of standard normal random variables yi^*:

$$xi^* = F_{Xi}^{-1}\left[\Phi\left(yi^*\right)\right] \sim \Phi^{-1}\left[F_{Xi}\left(xi^*\right)\right] = yi^* \qquad (1)$$

where xi^* = random variable in the original space; yi^* = random variable in the standard normal space; F_{Xi} = cumulative nonnormal distribution function; F_{Xi}^{-1} = inverse cumulative nonnormal distribution function; Φ = cumulative standard normal distribution function; and Φ^{-1} = inverse cumulative standard normal distribution function.

The equivalent standard normal covariance or correlation matrix may differ slightly from the original, and for simplicity the unmodified matrix has been frequently considered in the literature. A simplified approach suggested by Kiureghian & Liu (1986) and described by Haldar & Mahadevan (2000) may be considered for the equivalent standard normal matrix computation. Considered the selected design example, the values of the correlation coefficients between the random variables are then transformed by empirical relationship according to the detailed expressions, and so the transformations are used for the computation of the resultant equivalent standard normal correlation coefficient, when the random variables are normal and lognormal, or are both lognormal. Other transformations may be considered, as the proposed Nataf's model further described by Haldar & Mahadevan (2000).

2 RESPONSE SURFACE METHODOLOGY ITERATIVE ALGORITHM

The detailed response surface methodology iterative algorithm approximates the limit state function by an explicit function of the random variables in the standard normal space, and is improved by a very simple iterative procedure based on the implementation of the first order reliability method algorithm in the standard normal space. More detail in Marques (2012). The expression considered for the approximation function is described by Equation 2, a second order polynomial with squared terms but no cross terms, suitable for nonlinear analysis:

$$H\left(A_s\right) = a_0 + \sum_{s=1}^{n}\left(a_s \cdot A_s\right) + \sum_{s=1}^{n}\left(a_{n+s} \cdot A_s^2\right) \qquad (2)$$

where n is the number of random variables; A_s is the sth random variable; and a_0, a_s, and a_{n+s} are unknown coefficients to be determined.

A brief explanation of the algorithm is summarised as follows, for schemes of experimental design of axial type, other variants in Marques (2012):

[Step 1] Set the first iteration vector $[p_1; p_2; \ldots; p_n]$ in the standard normal space for instance at zero, that means first iteration is centered in the median values for all the n random variables;

[Step 2] Construct a $(2n + 1) \times (n)$ matrix P, each column for each one of the n random variables: first line is vector $[p_1 + 0; p_2 + 0; \ldots ; p_n + 0]$; second line is vector $[p_1 + h_1; p_2 + 0; \ldots; p_n + 0]$ where h_1 is the selected distance from the center point; repeat the previous procedure for the next $(n - 1)$ lines by summing to each one of the other columns the selected number; $(n + 2)$ line is vector $[p_1 - h_1; p_2 + 0; \ldots; p_n + 0]$ where h_1 is the selected distance from the center point; repeat the previous procedure for the next $(n - 1)$ lines by subtracting to each one of the other columns the selected number; concerning efficiency the minimum number of lines is considered; the use of additional lines in regression analysis is indeed a possibility to be considered;

[Step 3] Evaluate the performance function in the standard normal space by using the points in each line of the constructed matrix P and construct the column vector R; if required use the bilateral transformation from Equation 1;

[Step 4] Construct a $(2n + 1) \times (2n + 1)$ matrix N by using a first unitary column vector, next n columns from matrix P columns, and next n columns from squared elements in previous n columns;

[Step 5] Solve the equation of the approximation function for the unknown coefficients by regression analysis expressed in $Na = R$, where a is the column vector of the unknown coefficients;

[Step 6] Express the equivalent standard normal correlation matrix and the set of random variables vector in the standard normal space, then run the first order reliability method algorithm by using the generated approximate function in the standard normal space, and estimate the reliability index β and the corresponding coordinates of the design point;

[Step 7] Set the next iteration vector $[p_1; p_2; \ldots; p_n]$ in the standard normal space at

the estimated coordinates of the design point and update matrix P;

[Step 8] Repeat steps 3 to 6 and verify the convergence to the selected tolerance criterion, for instance $|\beta_{\text{iteration i}} - \beta_{\text{iteration i-1}}| \leq 5 \times 10^{-3}$ or 5×10^{-4}, in which i is the iteration number, as the methodology may be applied beyond structural engineering; further check the convergence process for the coordinates of the design point;

[Step 9] If required, repeat steps 7 and 8 until convergence to the selected tolerance criterion, then express the final response surface, and estimate the reliability index β and the corresponding coordinates of the design point; Monte Carlo simulation based on counting is now efficient since the evaluation of the response surface function requires a reduced computational effort and input random variables are correlated in the standard normal space; it is further noted that transformations to the space of uncorrelated random variables may be considered.

Thus, the efficiency and accuracy provided by different schemes of experimental design are analysed in the next sections with a design example for a concrete gravity retaining structure, considered correlated nonnormal random variables.

3 DESIGN EXAMPLE

The design example is referred to the concrete gravity retaining structure on a relatively homogeneous $c - \varphi$ soil shown in Figure 1, wherein groundwater level is away. Considered the inclined eccentric loading problem and the calculation model for bearing capacity, the performance function is described by the simplified Equation 3, detailed in Appendix 1:

$$M = f\left(B_1, B_2, H_1, H_2, \gamma_c, \varphi_w, \gamma_w, c_f, \varphi_f, \gamma_f, q\right) \quad (3)$$

where the sum of B_1 and B_2 is the foundation width B; H_1 is the wall height; H_2 is the foundation height; γ_c is the unit concrete weight; φ_w is the friction angle of the soil on the active and passive sides of the wall; γ_w is the unit soil weight on the active and passive sides of the wall; c_f is the cohesion of the foundation soil; φ_f is the friction angle of the foundation soil; γ_f is the unit weight of the foundation soil; and q is the variable load at ground surface. Other considered parameters, namely for the earth pressure coefficients, are the soil-wall interface friction angle on the active side of the wall $\delta_w a = 2/3\varphi_w$; the soil-wall interface friction angle on the passive side of the wall $\delta_w p = 0$; and the soil-foundation interface friction angle $\delta_f = \varphi_f$; considered either a 50% reduction for passive earth pressures.

Table 1 summarises the description of basic input variables, with different distribution types.

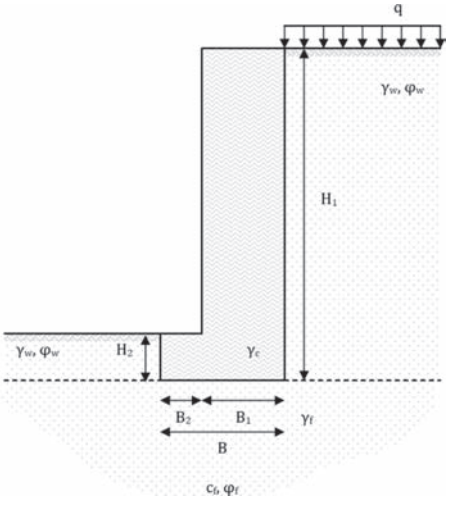

Figure 1. Concrete gravity retaining structure.

Table 1. Summary description of basic input variables.

Basic input variables	Distribution	mv	cv	Statistics
B_1 (m)	Deterministic	–	–	1.75[a] 1.85[b] 1.95[c]
B_2 (m)	Deterministic	–	–	1.00
H_1 (m)	Deterministic	–	–	7.00
H_2 (m)	Deterministic	–	–	1.00
γ_c (kN/m^3)	Deterministic	–	–	24.00
φ_w (°)	Lognormal	33.00	0.10	μ1 – 3.4915 σ1 – 0.0998
γ_w (kN/m^3)	Normal	18.80	0.05	–
c_f (kN/m^2)	Lognormal	14.00	0.40	μ1 – 2.5648 σ1 – 0.3853
			0.05[a]	μ1 – 3.4645 σ1 – 0.0500
φ_f (°)	Lognormal	32.00	0.10[b]	μ1 – 3.4608 σ1 – 0.0998
			0.15[c]	μ1 – 3.4546 σ1 – 0.1492
γ_f (kN/m^3)	Normal	17.80	0.05	–
q (kN/m^2)	Weibull	–	–	sh–3.25 sc–10.00

mv—mean value; cv—coefficient of variation.
μ1—log mean; σ1—log standard deviation; sh—shape; sc—scale.
[a]B_1 corresponding to the coefficient of variation φ_f 0.05.
[b]B_1 corresponding to the coefficient of variation φ_f 0.10.
[c]B_1 corresponding to the coefficient of variation φ_f 0.15.

Table 2. Coefficients of correlation between the random variables.

Correlation matrix for the bearing capacity model					
$\rho_{\varphi_w\varphi_w}$	$\rho_{\varphi_w\gamma_w}$	$\rho_{\varphi_w\varphi_f}$	$\rho_{\varphi_w q}$	$\rho_{\varphi_w c_f}$	$\rho_{\varphi_w\gamma_f}$
$\rho_{\gamma_w\varphi_w}$	$\rho_{\gamma_w\gamma_w}$	$\rho_{\gamma_w\varphi_f}$	$\rho_{\gamma_w q}$	$\rho_{\gamma_w c_f}$	$\rho_{\gamma_w\gamma_f}$
$\rho_{\varphi_f\varphi_w}$	$\rho_{\varphi_f\gamma_w}$	$\rho_{\varphi_f\varphi_f}$	$\rho_{\varphi_f q}$	$\rho_{\varphi_f c_f}$	$\rho_{\varphi_f\gamma_f}$
$\rho_{q\varphi_w}$	$\rho_{q\gamma_w}$	$\rho_{q\varphi_f}$	ρ_{qq}	ρ_{qc_f}	$\rho_{q\gamma_f}$
$\rho_{c_f\varphi_w}$	$\rho_{c_f\gamma_w}$	$\rho_{c_f\varphi_f}$	$\rho_{c_f q}$	$\rho_{c_f c_f}$	$\rho_{c_f\gamma_f}$
$\rho_{\gamma_f\varphi_w}$	$\rho_{\gamma_f\gamma_w}$	$\rho_{\gamma_f\varphi_f}$	$\rho_{\gamma_f q}$	$\rho_{\gamma_f c_f}$	$\rho_{\gamma_f\gamma_f}$
1.0	0.5	0.9	0.0	0.0	0.5
0.5	1.0	0.5	0.0	0.0	0.9
0.9	0.5	1.0	0.0	0.0	0.5
0.0	0.0	0.0	1.0	0.0	0.0
0.0	0.0	0.0	0.0	1.0	0.0
0.5	0.9	0.5	0.0	0.0	1.0

ρ—coefficient of correlation.

Correlation is the property in that, on average, two variables are linearly associated with one another, and the value of one provides information on the probable value of the other. The strength of the association is measured by a correlation coefficient in the range [–1,1], for the case that both variables vary inversely or together exactly, respectively. The considered coefficients of correlation between the random variables are either presented in Table 2, noted that the correlation matrices are idealised with the main purpose of creating high correlation between some of the random variables. It is further noted that the correlation between the cohesion and the friction angle of the foundation soil depends particularly on the material, and the question whether the two parameters are correlated is still not clearly decided in the literature, as stated by Fenton & Griffiths (2003). According to Marques (2012), references for negative correlation are common but regarding a sensitivity analysis for the design example, the influence of negative correlation on reliability is favourable and quite considerable when compared to the effects of positive correlation. Thus, the hypothesis of uncorrelated random variables is probably cautious and furthermore, the characteristic values of soil properties are often calculated separately, neglecting the effects of correlation, so both procedures are concordant.

4 RESULTS AND DISCUSSION

Considered the implementation of the foremost detailed methodology, Table 3 presents the summary description of results for the bearing capacity model, included the reliability index obtained by the first order reliability method and the Monte Carlo simulation, considered the different coefficients of variation for the friction angle of the foundation soil. It is noted that the differences between the reliability index obtained from both methodologies are somewhat notorious due to the important nonlinear behaviour presented by the bearing capacity model.

Table 3. Summary description of results for the bearing capacity model.

Model	Coefficient of variation φ_f	Reliability index β_{FORM}	Reliability index β_{MCS}
Bearing capacity	0.05	2.4842	2.5288
	0.10	2.2248	2.2787
	0.15	2.0410	2.0952

MCS results from 10^6 simulation steps.

The bearing capacity metamodels are built according to different schemes of experimental design of axial type, for a selected distance from the center point of 0.01, 1, 2, 3 and 4. Grouped these models, a comparative study about the convergence process is then summarised in Tables 4 and 5, for two convergence criteria and three different reference models corresponding to coefficient of variation φ_f 0.05, 0.10 and 0.15, considered the first order reliability method.

According to Haldar & Mahadevan (2000), the number of design sampling points should be kept to a minimum to increase efficiency but must be at least equal to the number of coefficients needed to define the performance function, therefore efficiency is related to the number of design sampling points and iterations, in other words the number of design of experiments. Haldar & Mahadevan (2000) refer also that the efficient location of design sampling points around the center point is essential for the accurate construction of the performance function, and increased accuracy is described in relation with an increased number of design sampling points, with the discussion of different layouts. These issues are focused hereafter.

Thus, two convergence criteria are considered in order to compare the accuracy of the models, given by the relative errors obtained by the first order reliability method, and also the efficiency from the required number of iterations. It is noted yet that the percentage errors are currently referenced in the literature to Monte Carlo simulation based on counting, although the reference is in fact the first order reliability method, used in the iterative algorithm.

From the analysis of results, it is concluded that the efficiency and accuracy of each model depend not only on the number of design sampling points and layout, but also on the distance from the center point that is considered to set the axial points, even whether the number of design sampling points and layout are

Table 4. Summary description of results for the bearing capacity metamodels.

Coefficient of variation φ_f 0.05	Model d0.01	Model d1
Tolerance criterion	5×10^{-3}	5×10^{-3}
Number of iterations	4	4
β_{FORM} model	2.48	2.48
β_{FORM} metamodel	2.48	2.48
Relative error (%)	0.00	0.00
Tolerance criterion	5×10^{-4}	5×10^{-4}
Number of iterations	4	5
β_{FORM} model	2.484	2.484
β_{FORM} metamodel	2.484	2.484
Relative error (%)	0.000	0.000
Coefficient of variation φ_f 0.10	Model d0.01	Model d1
Tolerance criterion	5×10^{-3}	5×10^{-3}
Number of iterations	4	4
β_{FORM} model	2.22	2.22
β_{FORM} metamodel	2.22	2.22
Relative error (%)	0.00	0.00
Tolerance criterion	5×10^{-4}	5×10^{-4}
Number of iterations	5	5
β_{FORM} model	2.225	2.225
β_{FORM} metamodel	2.225	2.225
Relative error (%)	0.000	0.000
Coefficient of variation φ_f 0.15	Model d0.01	Model d1
Tolerance criterion	5×10^{-3}	5×10^{-3}
Number of iterations	4	5
β_{FORM} model	2.04	2.04
β_{FORM} metamodel	2.04	2.04
Relative error (%)	0.00	0.00
Tolerance criterion	5×10^{-4}	5×10^{-4}
Number of iterations	4	5
β_{FORM} model	2.041	2.041
β_{FORM} metamodel	2.041	2.041
Relative error (%)	0.000	0.000

Table 5. Summary description of results for the bearing capacity metamodels.

Coefficient of variation φ_f 0.05	Model d2	Model d3	Model d4
Tolerance criterion	5×10^{-3}	5×10^{-3}	5×10^{-3}
Number of iterations	4	5	6
β_{FORM} model	2.48	2.48	2.48
β_{FORM} metamodel	2.49	2.49	2.51
Relative error (%)	0.40	0.40	1.21
Tolerance criterion	5×10^{-4}	5×10^{-4}	5×10^{-4}
Number of iterations	5	5	6
β_{FORM} model	2.484	2.484	2.484
β_{FORM} metamodel	2.486	2.493	2.511
Relative error (%)	0.081	0.362	1.087
Coefficient of variation φ_f 0.10	Model d2	Model d3	Model d4
Tolerance criterion	5×10^{-3}	5×10^{-3}	5×10^{-3}
Number of iterations	5	6	9
β_{FORM} model	2.22	2.22	2.22
β_{FORM} metamodel	2.23	2.23	2.24
Relative error (%)	0.45	0.45	0.90
Tolerance criterion	5×10^{-4}	5×10^{-4}	5×10^{-4}
Number of iterations	6	8	11
β_{FORM} model	2.225	2.225	2.225
β_{FORM} metamodel	2.226	2.232	2.244
Relative error (%)	0.045	0.315	0.854
Coefficient of variation φ_f 0.15	Model d2	Model d3	Model d4
Tolerance criterion	5×10^{-3}	5×10^{-3}	5×10^{-3}
Number of iterations	6	10	22
β_{FORM} model	2.04	2.04	2.04
β_{FORM} metamodel	2.04	2.05	2.07
Relative error (%)	0.00	0.49	1.47
Tolerance criterion	5×10^{-4}	5×10^{-4}	5×10^{-4}
Number of iterations	8	12	36
β_{FORM} model	2.041	2.041	2.041
β_{FORM} metamodel	2.043	2.053	2.080
Relative error (%)	0.098	0.588	1.911

similar. When this distance is reduced in order to be close to zero, the search for the design point in nonlinear analysis is improved. It is also concluded that as this distance becomes larger, the different models may present inaccurate results and important convergence problems, in particular for the tighter tolerance criterion and the higher coefficient of variation for the friction angle of the foundation soil.

The response surface methodology iterative algorithm generates nonstochastic local metamodels, in that they present statistical parameters more or less nonrepresentative of their reference models. The methodology is based on the local approximation of the coordinates of the most probable failure point, the design point, unlike the stochastic response surface methodology which may provide a general approximation statistically representative of the performance function.

5 CONCLUSION

The design of civil engineering structures relies heavily on models, abstract and simplified

representations of reality, yet accurate enough to be used for design purposes and risk analysis. Metamodelling encompasses the replacement of simulation models when the trade-off between efficiency and accuracy is appropriate. In recent years, localised metamodelling techniques have been suggested for the approximation of functions, namely the response surface methodology, particularly significant for the work with implicit limit state functions.

Regarding these issues, results for a design example with correlated nonnormal random variables are presented. For the purpose it is considered an inclined eccentric loading problem referred to a bearing capacity nonlinear calculation model for a concrete gravity retaining structure, moreover a geotechnical reliability-based analysis problem. The sensitivity of the bearing capacity model when considered different coefficients of variation for the friction angle of the foundation soil is then analysed, concluded that the increased nonnormal behaviour of the bearing capacity response correlates well with the higher values of the parameter.

Based on the degree of nonlinear behaviour and on the efficiency and accuracy provided by different schemes of experimental design of axial type, the convergence process is lastly discussed and the relative errors obtained by the first order reliability method are presented. Considered the important nonlinear behaviour of the bearing capacity model, results derived from the bearing capacity metamodels built by the response surface methodology iterative algorithm show that improved techniques for the search of the design point are required, in particular if a tighter tolerance criterion is considered. It is noted that the efficiency and accuracy of the iterative algorithm are very sensitive to the distance from the center point that is considered to set the axial points, so when this distance is reduced in order to be close to zero, the search for the design point in nonlinear analysis is improved.

Going back in history, several cases of instability have been reported in the literature regarding the use of reduced distances in schemes of experimental design, but results for the selected design example show a possibility for progression when considered the detailed response surface methodology iterative algorithm. It is noted lastly that the axial type schemes are not always the most appropriate option.

APPENDIX 1 EQUATION (3)

$$M = f\left(B_1, B_2, H_1, H_2, \gamma_c, \varphi_w, \gamma_w, c_f, \varphi_f, \gamma_f, q\right) \quad (3)$$

$$M = \left(\begin{matrix} c_f \cdot N_c \cdot s_c \cdot i_c + \gamma_w \cdot H_2 \cdot N_q \cdot s_q \cdot i_q \\ + 0.5 \cdot \gamma_f \cdot B_e \cdot N_\gamma \cdot s_\gamma \cdot i_\gamma \end{matrix}\right) \cdot B_e - Evb \quad (4)$$

$$N_q = \left(\tan\left(45 + \frac{\varphi_f}{2}\right)\right)^2 \cdot \exp\left(\pi \cdot \tan\left(\varphi_f\right)\right) \quad (5)$$

$$N_\gamma = 2 \cdot \left(N_q\left(\varphi_f\right) - 1\right) \cdot \tan\left(\varphi_f\right) \quad (6)$$

$$N_c = \left(N_q\left(\varphi_f\right) - 1\right) \cdot \cot\left(\varphi_f\right) \quad (7)$$

$$s_q = 1 \quad (8)$$

$$s_\gamma = 1 \quad (9)$$

$$s_c = 1 \quad (10)$$

$$i_q = \left(1 - \frac{Ehb}{Evb + B_e \cdot c_f \cdot \cot\left(\varphi_f\right)}\right)^2 \quad (11)$$

$$i_\gamma = \left(1 - \frac{Ehb}{Evb + B_e \cdot c_f \cdot \cot\left(\varphi_f\right)}\right)^3 \quad (12)$$

$$i_c = i_q - \frac{1 - i_q}{N_c \cdot \tan\left(\varphi_f\right)} \quad (13)$$

where the sum of B_1 and B_2 is the foundation width B; H_1 is the wall height; H_2 is the foundation height; γ_c is the unit concrete weight; φ_w is the friction angle of the soil on the active and passive sides of the wall, expressed in degrees; γ_w is the unit soil weight on the active and passive sides of the wall; c_f is the cohesion of the foundation soil; φ_f is the friction angle of the foundation soil, expressed in degrees; γ_f is the unit weight of the foundation soil; q is the variable load at ground surface; N_c, N_q, and N_γ are the bearing resistance factors; s_c, s_q, and s_γ are the foundation shape factors; i_c, i_q, and i_γ are the load inclination factors; B_e is the effective foundation width; *Evb* is the resultant vertical action for bearing capacity; and *Ehb* is the resultant horizontal action for bearing capacity.

REFERENCES

Allaix, D.L., Carbone, V.I. & Mancini G. 2011. Advanced response surface method for structural reliability. In: *Proc. of the Thirteenth International Conference on Civil, Structural and Environmental Engineering Computing, Chania, Crete, Greece:* Civil-Comp Proceedings 96, Paper 88, 1–14. Civil-Comp Press.

Babu, G.L.S. & Srivastava, A. 2007. Reliability analysis of allowable pressure on shallow foundation using response surface method. *Computers and Geotechnics* 34(3): 187–194.

Bauer, J. & Pula, W. 2000. Reliability with respect to settlement limit-states of shallow foundations on linearly-deformable subsoil. *Computers and Geotechnics* 26(3–4): 281–308.

Bucher, C. & Most, T. 2008. A comparison of approximate response functions in structural reliability analysis. *Probabilistic Engineering Mechanics* 23(2–3): 154–163.

Can, B. & Heavey, C. 2011. Comparison of experimental designs for simulation-based symbolic regression of manufacturing systems. *Computers & Industrial Engineering* 61(3): 447–462.

Fenton, G.A. & Griffiths, D.V. 2003. Bearing-capacity prediction of spatially random c – φ soils. *Canadian Geotechnical Journal* 40(1): 54–65.

Haldar, A. & Mahadevan, S. 2000. *Reliability assessment using stochastic finite element analysis*. John Wiley & Sons.

Kiureghian, A.D. & Liu, P.L. 1986. Structural reliability under incomplete probability information. *Journal of Engineering Mechanics* 112(1): 85–104.

Lü, Q. & Low, B.K. 2011. Probabilistic analysis of underground rock excavations using response surface method and SORM. *Computers and Geotechnics* 38(8): 1008–1021.

Marques, S.H.M. 2012. *Reliability-based analysis and design in geotechnical engineering: Applications to Eurocodes: Thesis Project*. Faculty of Engineering of the University of Porto.

Massih, D.S.Y.A. & Soubra, A.H. 2008. Reliability-based analysis of strip footings using response surface methodology. *International Journal of Geomechanics* 8(2): 134–143.

Mollon, G., Dias D. & Soubra, A.H. 2009. Probabilistic analysis of circular tunnels in homogeneous soil using response surface methodology. *Journal of Geotechnical and Geoenvironmental Engineering* 35(9): 1314–1325.

Tandjiria, V., Teh C.I. & Low, B.K. 2000. Reliability analysis of laterally loaded piles using response surface methods. *Structural Safety* 22(4): 335–355.

This page intentionally left blank

Geotechnical Safety and Risk IV – Zhang et al. (eds)
© 2014 Taylor & Francis Group, London, ISBN 978-1-138-00163-3

Flood simulation considering probability of heavy rains and uncertainty of soil properties of earth-fill dams

S. Nishimura & T. Shuku
Graduate School of Environmental Science, Okayama University, Okayama, Japan

H. Nagao
Naigai Engineering Corp., Kyoto, Japan

K. Fujisawa
Graduate School of Agriculture, Kyoto University, Kyoto, Japan

ABSTRACT: The risk of earth fills during heavy rains is evaluated in this research. The rainfall intensity and the variability of the numerous soil parameters of the earth-fills related to soil erosion are dealt with as probabilistic parameters. When the peak overflow head on a spillway bed becomes greater than the design overflow head, overflow occurs. The peak overflow head, is determined within 72 hours of the rainfall, and the various rainfall patterns are tested by the Monte Carlo method. Furthermore, the statistical values of the parameters for the soil erosion are assumed, and the variability of the discharge hydrographs are derived from the values. The discharge hydrographs are applied for the flood simulation as input waves. The submerged area and the head of the flood discharge in the downstream area can be predicted. Considering disaster loss, the risk to the downstream area of the earth-fill dams can be evaluated.

1 INTRODUCTION

Many earth-fill dams have been built for farm ponds in Japan. Some of the dams are getting old and decrepit, and have weakened. Every year, a number of them are damaged by heavy rains and earthquakes, and in a few worst cases, the dams are completely destroyed. To mitigate such disasters, improvement work is conducted on the most decrepit earth-fill dams. Since there is a recent demand for low-cost improvements, the development of a design method for optimum improvement work at a low cost is the final objective of this research. The previous study evaluated the risk to earth fills during heavy rains and investigated the effect of the improvement according to the total cost (Nishimura *et. al.* 2009). In this research, the probability of heavy rains and the uncertainty of the soil properties are simultaneously considered.

Firstly, the quasi-rainfall intensities are generated from random numbers, based on the statistical rainfall model considering the sequence of the rainfalls. Secondly, the inflow and discharge are estimated considering the effect of the reservoir storage. When the peak overflow head on the spillway bed, h_p, becomes greater than the design overflow head, h_d, overflow occurs. Then, the probability of overflow P_f is calculated from the number of the event, $h_p < h_d$ during the iterations of the Monte Carlo simulation. Peak overflow head h_p is determined within 72 hours of the rainfall, and the various rainfall patterns are tested by the Monte Carlo method. Furthermore, the statistical values of the parameters related to the soil erosion are assumed. The variability of the discharge hydrographs are derived from these statistical values. The discharge hydrographs are applied for the flood simulation as input waves. In this research, the shallow water equations are solved by the HLL Rieman solvers (Toro 1999), and the submerged area and the head of the flood discharge in the downstream area are predicted. From the estimated probability of overflow, and the probability of submerge in the downstream are calculated. Considering the disaster loss, the risk of the submerge is evaluated. Considering the improvement cost, including improvement of spillway, and the expected total cost is evaluated. By comparing the total costs between the original and improved states of the earth-fill dam.

2 QUASI-RAINFALL MODEL

In this research, the rainfall events continuing for 72 hours are simulated based on the annual

maximum rainfall intensities obtained from the rainfall data records in Okayama City, Japan for a span of 45 years. A dam break almost happens within 24 hours on an empirical basis. To cover all cases, the longer consecutive rainfalls for 72 hours are used. The cumulative distribution function $F_k(x)$ of rainfall intensity x (mm/h), for k (= 1~72) hours after the rain starts, is determined with the mean rank method as follows:

$$F_k(x) = m_k(x)/(N+1) \tag{1}$$

where $m_k(x)$ is the number of rainfall intensities after k hours that do not exceed x, and N denotes the number of years. Figure 1 shows an example of the cumulative distributions.

Then, rainfall intensity x (mm/h) is transformed into random variable y following the standard normal distribution as

$$y = \Phi^{-1}\left(F_k(x)\right) \tag{2}$$

where Φ is the standard normal distribution function.

Then, the correlation coefficients ρ_{ij} (i, j = 1, 2, …, 72) between probabilistic variable y after i hours and j hours can be estimated by the following equation.

$$\rho_{ij} = \frac{\sum_{I=1}^{45}(y_i - \mu)(y_j - \mu)}{\sigma^2} \tag{3}$$

Here, the set of correlation coefficients is viewed as a matrix, namely, $\mathbf{R} = [\rho_{ij}]$. Since $\mathbf{R}$ is positive definite, the lower triangular matrix $\mathbf{L}$, satisfied with $\mathbf{L}\mathbf{L}^{\mathrm{T}} = \mathbf{R}$, is obtained by the Choleky decomposition. A normal random number Y can be produced as follows:

$$Y = \mathbf{L}z \tag{4}$$

where z is standard normal random number generated by using Box-Muller method (Rubinstein 1981). Then, the normal random number Y is transformed into the random number X which has the distribution same as the actual rainfall using the following equation:

$$X = F_k^{-1}\left(\Phi(y)\right) \tag{5}$$

If X is used directly as the quasi-rainfall, the pattern causing overflows, may be fixed, because the cases of the heavy rains are very limited. To prevent it, a method that the rainfall intensity is reduced or extended, keeping the shape of hyetograph is proposed.

The Gumbel distribution is assumed for the distribution of the total rainfall T (mm/72 hours) of the annual maximum 72 hours rainfalls, $F(T)$ is determined as follows;

$$\sum_{i=1}^{72} x_i = T \tag{6}$$

$$F(T) = \exp\left(-e^{-y}\right), \quad y = a\left(T - T_0\right) \tag{7}$$

where x_i is the intensity of the annual maximum 72 hours rainfalls after i hours, and a and T_0 are the parameters employed to adjust the observed data to the theoretical distribution function (Iwai & Ishiguro 1970). Then, the random variable T' is generated as total rainfall of the from Gumbel distribution $F(T)$ shown in Figure 2.

Lastly, the adjusted rainfall intensity, X'(mm/h) is determined for each hour as following equation.

$$X' = \left(T' \Big/ \sum_{i=1}^{72} X_i\right) X \tag{8}$$

An example of a generated 72 hours rainfall series is exhibited in Figure 3.

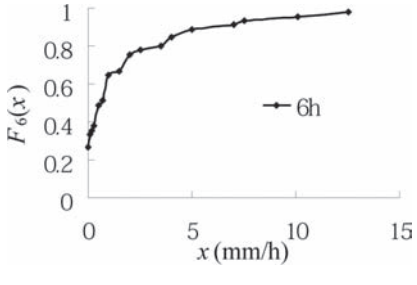

Figure 1. Cumulative probability distribution of rainfall intensity after 6 hours.

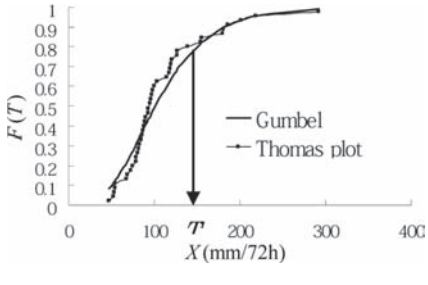

Figure 2. Cumulative distribution of maximum annual continuous precipitation.

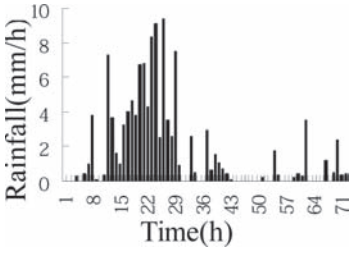

Figure 3. An example of quasi-precipitation.

3 EVALUATION METHOD FOR THE PROBABILITY OF OVERFLOW

At first, the quantity of inflow, discharge and storage are calculated. The inflow equation is defined as follows (JSIDRE 2002);

$$Q_{in} = f_p r A / 3.6 \tag{9}$$

where Q_{in} = inflow to the reservoir (m^3/s), f_p is the peak runoff coefficient, r is the quasi-rainfall intensity (mm/h) generated in chapter 2 and A is the area of the basin (km^2). Uniform random numbers are used for f_p in the 0.7 to 0.8 range (JSIDRE 2002). The discharge equation for a rectangular weir as used in this study is;

$$Q_{out} = C B_S h^{2/3} \tag{10}$$

where Q_{out} = discharge (m^3/s), C = discharge coefficient, B_s = width of spillway, and h = static or piezometric head on a weir referred to the weir crest. The storage of water in the water reservoir V_r is estimated as follows;

$$V_r = A_w h \tag{11}$$

where A_w is area of water reservoir (km^2) and h is overflow head (m). The decreasing rate of the storage V with the runoff is:

$$dV_r / dt = Q_{in} - Q_{out} \tag{12}$$

The overflow head h is determined from Equation (12), and the maximum h within the 72 hours, is defined as the peak overflow head on the spillway. When h_p becomes greater than the design overflow head h_d, the overflow occurs. Then, the probability of overflow is defined by Equation (13) as the times of $h_p < h_d$ in the iterations of the Monte Carlo simulation (Rubinstein 1981).

$$P_f = \mathrm{Prob}\left[h_d < h_p\right] \tag{13}$$

Table 1. Probability of overflow.

Earth-fill dam	Area at full water level A_w (m^2)	Water storage V (m^3)	Probability of overflow P_f (%)
A	7700	18900	0.2935
B	3100	5000	0.3334
C	3400	10800	3.4728
D	3400	15700	2.7582

The results for four dams are described in Table 1.

4 FLOOD SIMULATION

4.1 *Determination of hydrograph*

Once the event of the overflows happens, the flood simulation must be done as a next step to estimate the damage in the downstream area. The discharge hydrographs are determined to be applied for the flood simulation as input waves. An example of section of the embankments analyzed in this study is shown in Figure 4. When the overflow occurs, the embankment is supposed to be failed as in Figure 5, which shows a vertical section of an embankment. This section of the flood way is to be assumed to have a trapezoid shape. The overflow hydrograph from broken section is determined by the runoff discharge $Q_{dis.}$ is formulated as follows;

$$Q_{dis} = \sqrt{g A^3 / (\partial A / \partial h)} \tag{14}$$

$$U = Q_{dis} / A \tag{15}$$

$$dH / dt = -E / (1 - n_p) \tag{16}$$

$$E = \alpha(\tau - \tau_c) \tag{17}$$

$$\tau = \rho C_f U^2 \tag{18}$$

$$C_f = \kappa^2 / [\log\{R \cdot \exp(\kappa A_r - 1)\} / \kappa_s] \tag{19}$$

where A is the cross-sectional area of broken section (m^2), U is the flow velocity (m/s), H is the overflow head on the bottom of the failed section (m), E is the erosion rate of embankment material (m/s), n_p is the porosity of the embankment, α is the erosion rate coefficient (m/s/Pa), τ is the shear stress (Pa), τ_c is the critical shear stress (Pa), ρ is the water density (kg/m^3), κ is Karman constant, R is the hydraulic radius (m), A_r is the constants (=8.5) and κ_s is roughness height (m).To consider uncertain material values, the variabilities of the several soil parameters of the earth-fills are dealt

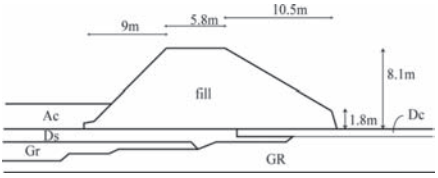

Figure 4. A section of the embankments (site C).

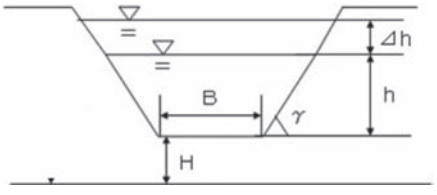

Figure 5. Assumption of failure section with overflow.

Table 2. Average and standard deviation of parameters.

	B (m)	κ_s (m)	α (m/s/Pa)	γ(rad)
Average	5.9	0.09	5.50E-05	54.226
Standard deviation	1.18	0.018	1.10E-05	17.775

with as probabilistic parameters. The normal random numbers are substituted for overflow length B, κ_s and α. The angular degree of cross-section of the failed section γ is also provided as a probabilistic variable (Francesco 2008). The average and the standard deviation of each parameter are described in Table 2. Although, essentially, parameter τ_c is a probabilistic parameter, it is dealt with as a deterministic parameter (= 0.01) for simplicity. Since the assumption means that the strength of the earthfill against the erosion is not considered, it leads the results of the flood simulation to the safe side. Since the variability of n_p is small generally, it is assumed to be constant of 0.30 in this study. At the inflow cells of flood simulation, the flow velocity U is given for the downstream direction, and the overflow head is given as the water depth.

4.2 *Flood simulation method*

As basic governing equations, two-dimensional shallow water equations are employed, in which the flow velocity is assumed to be equally distributed along the vertical axis. Furthermore, the incompressibility of water and the inclined bottom are also assumed (Yoon & Kang 2004).

$$\frac{\partial \mathbf{U}}{\partial t}+\frac{\partial \mathbf{F}}{\partial x}+\frac{\partial \mathbf{G}}{\partial y}=\mathbf{S} \tag{20}$$

$$\mathbf{U}=\begin{pmatrix} h \\ uh \\ vh \end{pmatrix}, \mathbf{F}=\begin{pmatrix} uh \\ u^2h+gh^2/2 \\ uvh \end{pmatrix}, \mathbf{G}=\begin{pmatrix} uh \\ uvh \\ v^2h+gh^2/2 \end{pmatrix} \tag{21}$$

$$\mathbf{S}=\mathbf{S}_o+\mathbf{S}_f=\begin{pmatrix} 0 \\ ghS_{ox} \\ ghS_{oy} \end{pmatrix}+\begin{pmatrix} 0 \\ -ghS_{fx} \\ -ghS_{fy} \end{pmatrix} \tag{22}$$

in which t is the time, x and y are the horizontal orthogonal axes, h is the water depth, u and v are flow velocities for x and y directions, g is the acceleration of gravity, and S_{ox} and S_{oy} are the inclinations along the x and y axes of the river bottom, S_{fx} and S_{fy} are the inclinations of friction. Inclination $\mathbf{S_o}$ is obtained from the height of the bottom, z_b, and the positive direction of inclination is defined to be downstream, namely,

$$S_{ox}=-\frac{\partial z_b}{\partial x}, \quad S_{oy}=-\frac{\partial z_b}{\partial y} \tag{23}$$

The inclinations of the friction are defined from Manning's formula,

$$S_{fx}=\frac{n^2u\sqrt{u^2+v^2}}{h^{4/3}}, \quad S_{fy}=\frac{n^2v\sqrt{u^2+v^2}}{h^{4/3}} \tag{24}$$

in which n is Manning's ratio. The equations are solved by the Finite Volume Method (Yoon & Kang 2004) (FVM), employing two dimensional rectangular cells. The FVM is the numerical method based on the integral type equation, and the analytical area is divided into finite number of cells. A group of cells objective for analysis is defined as a "control volume". An example of the control volume is exhibited in Figure 6. The cell objective for the calculation is defined as L, and surrounding cell are defined as R in the figure.

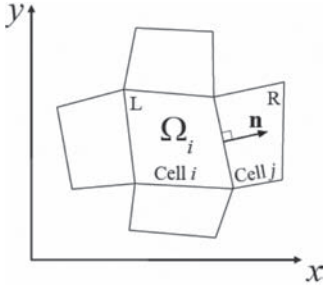

Figure 6. Typical control volume.

Following this definition, the governing equation is derived as following equation;

$$\frac{d\mathbf{U}_i}{dt} = -\frac{1}{\Omega_i}\sum_{j=1}^{4}\mathbf{E}\cdot\mathbf{n}_{ij}\Delta\Gamma_{ij} + \mathbf{S}_i \tag{25}$$

in which $\mathbf{E} = \mathbf{F} + \mathbf{G}$, $\mathbf{n}$ is unit normal outward vector, and $\Delta\Gamma$ is the length of the boundary. The numerical flux $\mathbf{E} \cdot \mathbf{n}$ is calculated by the HLL Rieman solver (Toro 1999) expressed as follows;

$$\mathbf{E}\cdot\mathbf{n} = \begin{cases} (\mathbf{E}_L)\cdot\mathbf{n} & (S_L \geq 0) \\ \dfrac{S_R(\mathbf{E}_L)\cdot\mathbf{n} - S_L(\mathbf{E}_R)\cdot\mathbf{n} + S_R S_L\left[(\mathbf{U}_R) - (\mathbf{U}_L)\right]}{S_R - S_L} & (S_L < 0 < S_R) \\ (\mathbf{E}_R)\cdot\mathbf{n} & (S_R \leq 0) \end{cases} \tag{26}$$

where $\mathbf{U}_L$ and $\mathbf{U}_R$ = reconstructions of $\mathbf{U}$ on the left and right sides, respectively, and S_L and S_R = wave speed estimates.

$$S_L = \begin{cases} \min\begin{pmatrix} \mathbf{q}_L\cdot\mathbf{n} - \sqrt{gh_L}, \\ u^* - \sqrt{gh^*} \end{pmatrix} & \text{if both sides are wet} \\ \mathbf{q}_L\cdot\mathbf{n} - \sqrt{gh_L} & \text{if the right side is dry} \\ \mathbf{q}_R\cdot\mathbf{n} - 2\sqrt{gh_R} & \text{if the left side is dry} \end{cases} \tag{27}$$

$$S_R = \begin{cases} \max\begin{pmatrix} \mathbf{q}_R\cdot\mathbf{n} - \sqrt{gh_R}, \\ u^* - \sqrt{gh^*} \end{pmatrix} & \text{if both sides are wet} \\ \mathbf{q}_L\cdot\mathbf{n} - \sqrt{gh_L} & \text{if the right side is dry} \\ \mathbf{q}_R\cdot\mathbf{n} - 2\sqrt{gh_R} & \text{if the left side is dry} \end{cases} \tag{28}$$

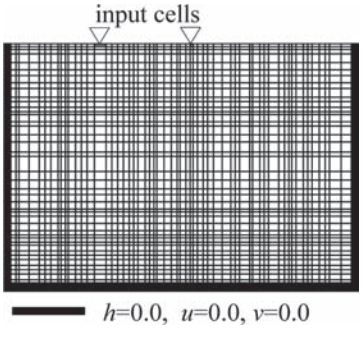

Figure 7. Boundary condition and input cells.

$$u^* = \frac{1}{2}(\mathbf{q}_L + \mathbf{q}_R)\cdot\mathbf{n} + \sqrt{gh_L} - \sqrt{gh_R} \tag{29}$$

$$\sqrt{gh^*} = \frac{1}{2}\left(\sqrt{gh_L} + \sqrt{gh_R}\right) + \frac{1}{4}(\mathbf{q}_L - \mathbf{q}_R)\cdot\mathbf{n} \tag{30}$$

in which $\mathbf{q} = \begin{bmatrix} u & v \end{bmatrix}^T$. Boundary conditions and input cells are shown in Figure 7. In input cells, h and v are obtained from hydrograph determined in 4.1.

5 RELIABILITY-BASED DESIGN

The probability of submerge in a cell i per year is defined as:

$$P_i = \sum_{jp=1}^{NE} P_{f,i,jp}\cdot P_{si,jp} \tag{31}$$

in which the subscript jp corresponds to the event, which is the combination of the failure dams, NE is number of events, P_f is probability of overflow, and P_s is the probability of submerge under the condition that the overflow happens.

The expected total cost within the lifetime period = t is given by the following equations.

$$C_T = C_0 + \sum_{i}^{M} C_{f,i}\cdot E[n_i] \tag{32}$$

$$E[n_i] = \begin{cases} \displaystyle\sum_{k=1}^{t_l}\left[P_{O,i}\left(1-P_{O,i}\right)^{k-1}\left\{1+(t_l-k)P_{I,i}\right\}\right] & \text{(Original)} \\ t_l\cdot P_{I,i} & \text{(Improved)} \end{cases} \tag{33}$$

in which M is number of cells, C_T is the expected total cost n is the frequency of overflows within a lifetime span of t (years), P_O and P_I are the probabilities of overflow a year corresponding to the original and the improved states of the embankment, respectively, C_0 is the cost of the improvement, and C_f is the damage loss due to flooding. P_O and P_I are derived from Equation (31).

In this research, the improvement of the spillway is considered, and the improvement brings about a drastic increase in the discharge ability of the spillway. In Equation (32), improvement cost C_0 is zero for the original state of the embankment, and it is assumed that when embankments are failed due to overflows, that they will be restored to the same level as the improved state of the embankment.

6 CASE STUDY

6.1 *Outline of site*

A group of earth-fill dams, A, B, C, and D, prescribed in Figure 8, is analyzed in this study. These dams were constructed in the valleys of a mountainous area. Profiles of the dams are described in Table 1. A section of the embankments of dam C is shown in Figure 4 and similar to that of the other dams. The broken sections of all ponds are same as in Figure 5.

Dams A and B and dams C and D are separated by a ridge, and are not affected by each other, while there are correlations for the probability of overflow between A and B or C and D. Since dam B is smaller than dam A, dam B is inevitably broken following the breaking of dam A. If the upstream dam, dam C, is broken, then dam D is inevitably broken. Dam D never breaks without also breaking dam C, according to the calculation results of the probability of overflow. Thus, dams C and D are denoted together as dam CD. The probabilities of overflow are expressed by Equation (34), considering the relationships among the dams.

$$P_f(A \cap B) \neq 0, P_f(\overline{A} \cap B) \neq 0, P_f(A \cap \overline{B}) = 0$$
$$P_f(C \cap D) \neq 0, P_f(\overline{C} \cap D) = 0, P_f(C \cap \overline{D}) = 0 \quad (34)$$

The symbols A, B, C, and D are the sets employed to represent the events of breaking of each dams.

6.2 *Result of flood simulation*

The example of the discharge hydrographs from the dams are shown in Figure 9. Figure 9 correspond to the case in which dam CD breaks and

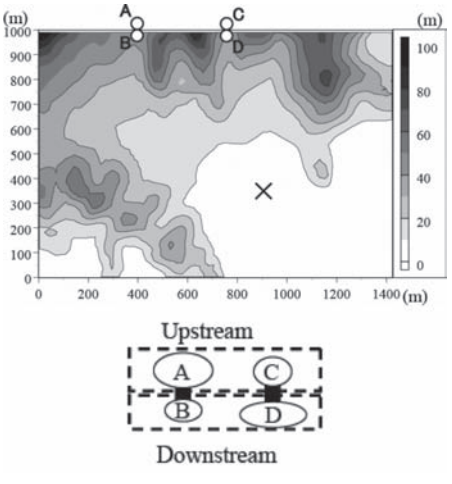

Figure 8. Locations of earth-fill dams and geography.

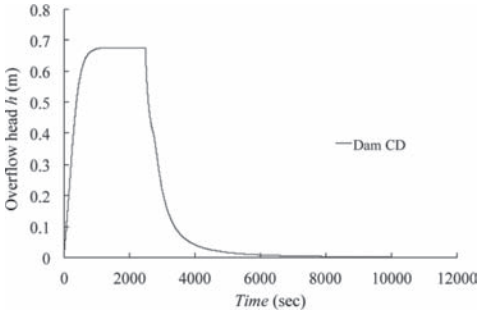

Figure 9. Hydrographs for scenario flood simulation when dams C and D break.

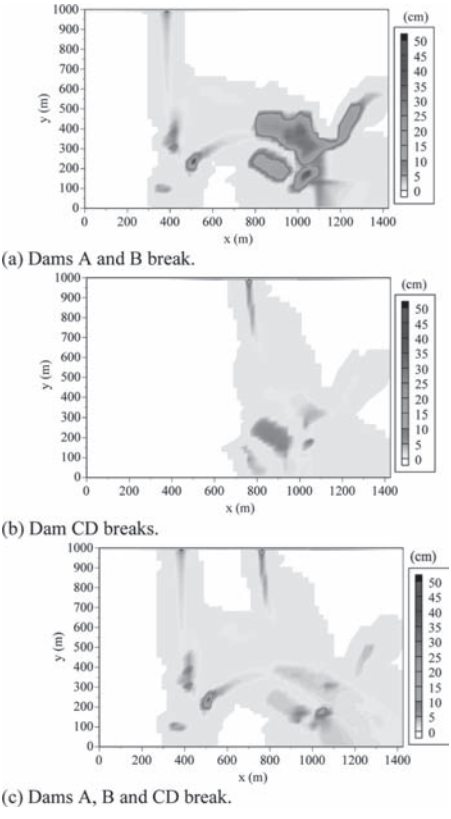

Figure 10. Head of flood discharge (cm).

the overflow depth and the velocity are shown. As Manning's ratio, the value, $n = 0.026$ is assumed.

The expected maximum head of the flood discharge is described in Figures 10(a)–(c), which correspond to the cases, in which dams A and B break, CD breaks, and dams A, B, and CD break, respectively. In the figure, submerged depths smaller than 1.0 cm are disregarded.

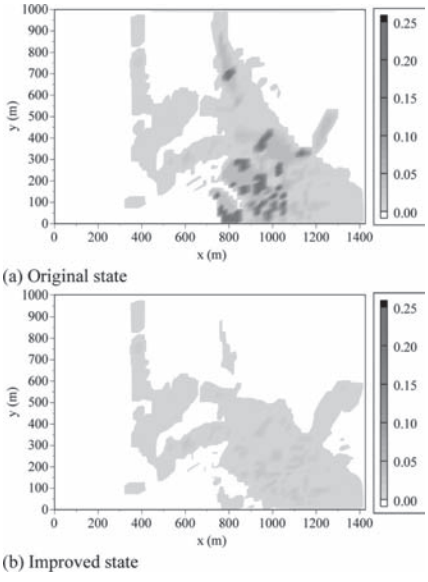

Figure 11. Spatial distributions of risk. (Unit: 1,000 JPY/m^2).

Table 3. Risks and expected total costs.

State	Improvement costs	Total risk	Total costs
Current	0	335,055	335,055
Improved	199,200	114,970	314,170

Unit: 1,000 JPY.

In comparison among Figures 10 (a), (b) and (c), the heads of discharge of (a) and (b) are greater than (c), although the volume of discharged water is greatest among the three cases. The reason is that the flow velocity affects the results. This phenomenon means that damage in the downstream area is not necessarily correlated with the depth of submergence.

Figure 11 exhibits the spatial distributions of risk corresponding to the original and improved states of earth-fills. With improvement of the spillway, the risk is reduced dramatically, since the probability of overflow is predicted to be zero for Dam CD. The total risk and the expected costs are given in Table 3. The difference between the costs of the original and improved states means the effect of the improvement works. The value is evaluated as:

335,055 – 314,170 = 20,885 (1,000 JPY)

7 CONCLUSIONS

1. A generation method for quasi-rainfall, using random numbers, has been proposed in this research. The generated rainfall events were applied to calculate the inflow from the surrounding basin into the reservoirs.
2. The probability of overflow caused by the heavy rains has been calculated for several earth-fill dams. The inflow and the discharge were estimated considering the effect of the reservoir storage. We assumed that overflows will occur when the maximum overflow head on the spillway bed becomes greater than the design overflow head. The probability of overflow was then determined by the Monte Carlo simulation. The probability of overflow of a dam in the studied site is calculated to be 3.47% in the maximum case.
3. The variability of the several soil parameters of the earth-fill dams have been dealt with as probabilistic parameters to consider uncertain material values for producing the discharge hydrograph. Normal random numbers were assigned to the overflow length, the roughness height and the erosion rate coefficient. And the angular degree of the cross-section of the failed section was also provided as a probabilistic variable.
4. The maximum head of submerge and the risk in the downstream area were estimated. Finally, the expected total costs were compared between current and improved states of the spillways, and the effect of the improvement work has been evaluated.

ACKNOWLEDGMENT

This work was partly supported by JSPS KAKENHI (23248040).

REFERENCES

Francesco M. 2008. Model for Predicting due to Earthen Dam Breaching I: Formulation and Evaluation, *Journal of Hydraulic Engineering, ASCE* 134: 1688–1969.

Iwai, S. and Ishiguro M. 1970. *Applied hydro-statistics*, Morikita (in Japanese).

Japanese Society of Irrigation, Drainage and Rural Engineering. 2002, Maintenance of irrigation tanks. *Guideline of land improvement designs (in Japanese)*: 157–162, 205–211.

Nishimura, S. and Mori, S. 2009. Risk evaluation and reliability-based design of earth-fill dams for overflow due to heavy rains. *Proc. of ICOSSAR2009*: 246–251.

Rubinstein, R.Y. 1981. *Simulation and the Monte Carlo Method,* John Wiley & Sons.

Toro, E.F. 1999. Riemann Solvers and Numerical Methods for Fluid Dynamics—*A Practical Introduction—2nd Edition, Springer*: 315–331.

Yoon, T.H. and Kang, S-K. 2004. Finite volume model for two-dimensional shallow water flows on unstructured grids. *Journal of Hydraulic Engineering, ASCE* 130: 78–688.

This page intentionally left blank

Geotechnical Safety and Risk IV – Zhang et al. (eds)
© 2014 Taylor & Francis Group, London, ISBN 978-1-138-00163-3

Reliability analysis of 20-km river dike against liquefaction failure

Yu Otake, Yusuke Honjo & Yuichi Hiramatsu
Gifu University, Gifu, Japan

ABSTRACT: The authors proposed a reliability analysis method for long continuous structures considering investigation sites to counter liquefaction failure. This method is characterized by continuously calculating the failure probability caused by liquefaction at an arbitrary point and quantifying the uncertainty concerning the investigation site. The purpose of this study is to verify its effectiveness based on application to an actual river dike that suffered liquefaction failure due to the 2011 Earthquake off the Pacific coast of Tohoku.

1 INTRODUCTION

1.1 *Purpose*

The authors have proposed a reliability analysis method for long continuous structures with consideration for investigation sites against liquefaction failure using the liquefaction index P_L-value (Otake & Honjo 2012). This index is extremely simple, and enables calculation using the SPT *N*-value and determination of particle size. This method is characterized by continuously calculating the failure probability caused by liquefaction at an arbitrary point, and quantifying the uncertainty concerning the investigation site.

The purpose of this study is to verify its effectiveness based on application to an actual river dike which suffered liquefaction failure caused by the 2011 earthquake off the Pacific coast of Tohoku. The main verification points are the possibility of extracting the high-risk collapse zone, and confirming whether the investigation intervals and quantity are adequate under the current investigational status.

1.2 *Target structure and soil conditions*

The 20-km interval between STA 25 and 45 in a first class river in Japan is targeted in this study. "STA" represents the site from the river mouth, and is measured in units of 1 km.

The soil in the levee body is sandy silt, and the dike is 3~5 m high. The dike height increases as you go downstream, and the rate of increase in height per STA is roughly constant.

Figure 1 shows a summary of the longitudinal soil profiles about the target river dike and collapsed location. Table 1 shows the soil

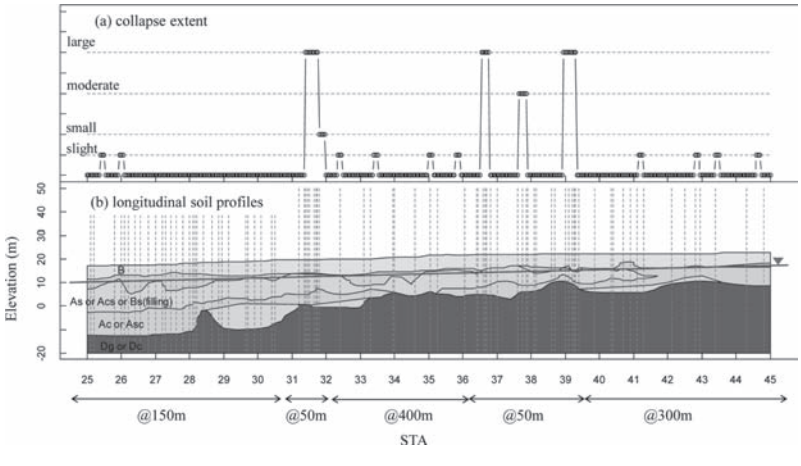

Figure 1. Longitudinal soil profiles and site of collapsed location.

Table 1. Soil parameters of each layer.

	Main soil	SPT-N (mean)	γ (kN/m²)	Fc (%)	D50 (mm)	Vs (cm/s)
Bc	Sandy silt	3.3	18	85	0.025	110
Bs	Silt sand			65	0.350	110
Ac	Silt Sandy silt	2.6	16	75	0.025	125
Acs	Silt sand	7.5	17	50	0.070	140
As	Medium sand Fine sand	18.3	18	10	0.350	150

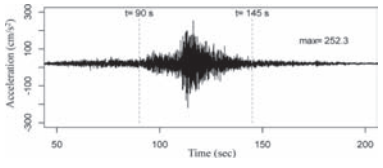

Figure 2. Temporal history of strong movement.

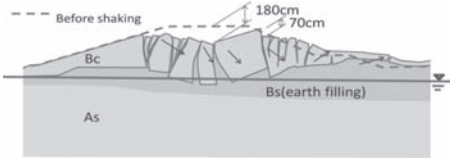

Figure 3. Collapse of river dike caused by liquefaction.

parameters for the dike body and alluvium. The river body soil is mainly sandy silt (Bc), but sandy earth filling has possibly accumulated under the Bc in the former riverbed area.

The alluvium layers under the dike body are roughly classified into two types, silt or sandy silt (Ac) (which is a non-liquefiable layer) and medium or fine sand (As) (which is liquefiable), and the total thickness of the alluvium layer is between 10 and 25 m. Furthermore, diluvium, which is regarded as engineering bedrock, has accumulated under these alluvial strata.

The soil investigations mainly consist of a Standard Penetrating Test (SPT) and determination of the particle size. There were 83 SPTs in total, but only ten particle size determinations.

1.3 *Profiles in strong movement and collapse status of target river dike*

Figure 2 shows the observed time history of acceleration at the site located on bedrock near the target river dike. The maximum acceleration of this earthquake wave was moderate by Japanese standards, but it was characterized by a very long duration.

The total duration was around 200 seconds, and during this period, the main shaking occurred between 90 and 145 seconds (i.e. for 55 s).

In addition, four points along the target river dike interval collapsed after the shaking (Fig. 1). A summary of the collapsed status is presented in Figure 3. All of the collapsed area was along the former riverbed or natural levee, and was considered to have been caused by liquefaction of earth filling Bs, which resulted in leveling of ground on the flood plain.

2 COLLAPSE RISK ASSESSMENT USING P_L-VALUE

The liquefaction risk at an arbitrary point is evaluated using the liquefaction index i.e. P_L-value, as proposed by SFHB2002 (JRA 2002). In fact, we calculated the correlation between the P_L-value and collapse risk as follows:

1. Calculation of P_L-value at all investigated sites.
2. Development of empirical fragility curve in the form of a normal distribution function using a two-value regression analysis based on information about whether the site collapsed or not.

2.1 *Calculation of P_L-value*

2.1.1 *Calculation procedures*

P_L-value at the investigation sites was basically based on SFHB2002, but there were improvements to the original method in order to take the long duration and local site of shaking amplification into consideration. The calculation procedures are described based on notations in the improvement points as follows.

Liquefaction evaluation along the depth was calculated as follows.

$$F_L = R/L \tag{1}$$

$$R = c_W R_L \tag{2}$$

where F_L is the resistance ratio of liquefaction, R is the dynamic shear resistance ratio, L is the shear stress load during strong movement, c_w is the adjusted coefficient of strong movement duration, and R_L is the dynamic triaxial resistance. R_L is defined in Equation (3), and is correlated with SPT N-value.

$$R_L = \begin{cases} 0.08822\sqrt{N_a/1.7} & (N_a < 14) \\ 0.0882\sqrt{N_a/1.7} + 1.6\times10^{-6}\cdot(N_a - 14)^{4.5} & (14 \le N_a) \end{cases} \quad (3)$$

where, N_a is the modified N-value for liquefaction evaluation considering the effective overburden stress and fine particle fraction contents.

$$N_a = c_1 N_1 + c_2 \quad (4)$$

$$N_1 = 170N/(\sigma_v' + 70) \quad (5)$$

c_1 and c_2 are adjusted coefficient correlations with fine particle fractions, and σ_V' is over effective burden stress. c_w is the adjusted coefficient for the duration of continuous shaking, which employs 1.0 for subduction zone earthquakes.

Here, since the target earthquake lasted much longer than typical subduction zone earthquakes, we use $c_w = 0.5$ for the long-duration time subduction zone earthquake as proposed by Yoshida et al. (2009).

L is defined as the ratio between the shear stress load and overburden stress. It is set as a standard value for each of the three classified soil types for ease of calculation.

Here, we improved the calculation method for L for a more rational consideration of local site effects. That is to say, in order to evaluate the shear stress distribution at different depths during shaking, we employed one-dimensional equivalent linear analysis using SHAKE (Schanable et al. 1972).

Finally, the P_L-value was calculated by weighted integration of F_L at the depths based on Equation (6). Weight is set as a linear function of the depth.

$$P_L = \int_0^{20} (1 - F_L)(10 - 0.5x)dx \quad (6)$$

Here, x is the depth from the ground surface. Note that when F_L>1, F_L is converted to 1.0.

Actually, we use the definition of Equation (7), since SPT-N is investigated each 1m over the depth.

$$P_L = \sum_{i=1}^{20} (1 - F_{Li})(10 - 0.5x_i) \quad (7)$$

2.1.2 *Calculated P_L-value*

Figure 4 shows the calculated P_L-values at all investigation sites, with the upper figure indicating the maximum acceleration at the ground surface based on response analysis. While calculated maximum accelerations were observed to have relatively large variance, these tended to decrease in the downstream part when viewed macroscopically.

On the other hand, the lower figure shows P_L (SHAKE) and P_L (Original). These differ from the calculating method for L; here the former is when using SHAKE, while the latter is in the case of simplified conventional equation in SFHFB. Hereafter, in order to confirm the difference between these indices, we continuously draw a parallel between P_L (SHAKE) and P_L (Original).

The vertical error-bar of P_L-value in Figure 4 is observation error including the soil test and the measurement of tri-axial test and SPT.

In here, observation error of P_L-value was calculated based on the assumption that the most part of regression error of Equation (3) is test and measurement error. Also, the regression error is modeled by the normal distribution, and the mean value is 0.0 and SD is 0.10 (Otake et al. 2012).

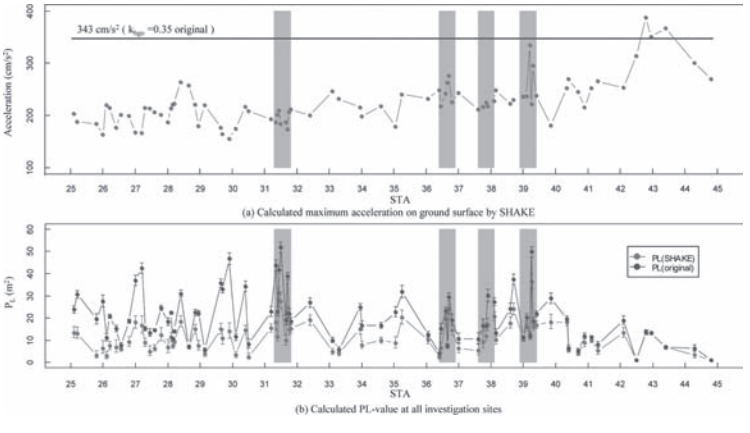

Figure 4. Results of ground response analysis in shaking and P_L-value at all investigational sites.

From the above assumption, the error is assumed as independent over the depth, it was calculated as follows. It is different value in each investigation site, but these are included the range of roughly 0.10–0.30 as COV.

$$P_L = \sum_{i=1}^{20} (10 - 0.5x_i) - \sum_{i=1}^{20} \left(\frac{10 - 0.5x_i}{L_i} \right) R_i \qquad (8)$$

$$Var[\, P_L \,] = \sum_{i=1}^{20} \left(\frac{10 - 0.5x_i}{L_i} \right)^2 Var[R_L] \qquad (9)$$

2.2 *Empirical fragility curve*

It is assumed the empirical fragility curve can be expressed in normal distribution form, and developed as a function of the P_L-value. Here, the explained variables Y are 0, i.e. un-collapsed, and 1, i.e. collapsed, and explanatory variables are calculated for P_L at all investigation sites as mentioned in subsection 2.1.2.

The likelihood function is expressed as

$$L = \prod_{i=1}^{N} [FR(\ln P_{Li})]^{\alpha_i} [1 - FR(\ln P_{Li})]^{1-\alpha_i} \qquad (10)$$

where, $F(.)$ represents the fragility curve for a specific state of damage. The symbol of "ln" represents logarithm natural. And, P_{Li} is the P_L-value, α_i depends on whether or not there is damage (0 or 1), and N is the total number of data (i.e. investigation sites).

$$FR(\ln(P_{Li})) = \Phi\left(\frac{\ln(\mu_{FR}/c)}{\xi} \right) \qquad (11)$$

$\Phi[.]$ is the standardized normal distribution function. The two parameters c and ξ are computed to satisfy the following equations to maximize ln L.

$$\frac{\partial \ln L}{\partial c} = \frac{\partial \ln L}{\partial \xi} = 0 \qquad (12)$$

Figures 5 and 6 show the calculated empirical fragility curves in each case (i.e. P_L (SHAKE) and P_L (Original))

It can be seen that P_L (SHAKE) is able to separate collapsed and non-collapsed sites than P_L (Original), so P_L (SHAKE) is considered to be an adequate parameter to evaluate the assessment of liquefaction collapse risks for river dikes. From the above, we chose the P_L (SHAKE) as the adequate index for the risk assessment against liquefaction.

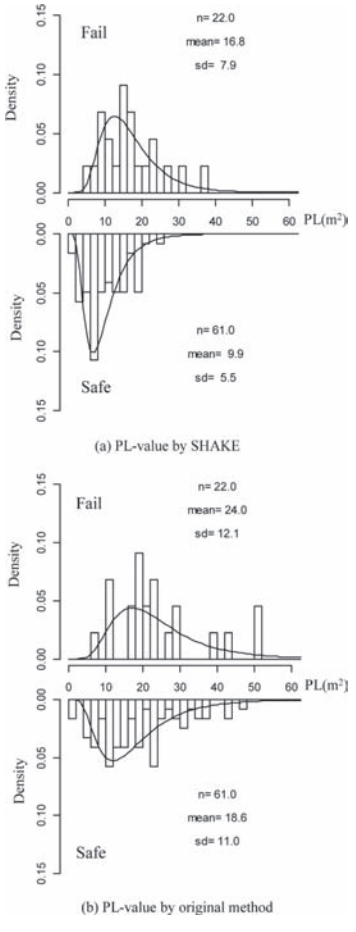

Figure 5. Histogram of P_L in each case (fail and safe).

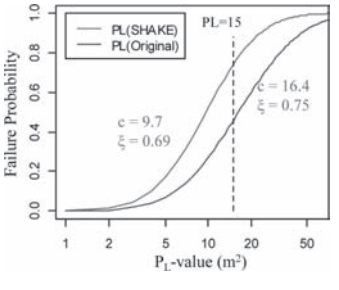

Figure 6. Calculated empirical fragility curves.

3 LIQUEFACTION RISK ASSESSMENT

3.1 *Random field modeling of P_L-values*

The lnP_L was modeled by Random Field (RF). The mean value and variance of the RF were set as the mean value and variance of the calculated

$\ln P_L$ respectively. Note that the mean value is 2.3 and variance is 0.69^2.

Then the auto-correlation function for modeling the covariance of RF was analyzed. We classified these data into two groups (i.e. Zone 1 from STA 25 to 35, and Zone 2 from STA 35 to 45) to confirm the effect of any difference in micro-topography classification. Zone 2 has extremely complex micro-topography composed mainly of the former riverbed and a natural levee, whereas Zone 1 is composed of a relatively simple micro-topography.

By considering the above, the identified results for auto-correlation distances in the case of all data, Zones 1 and 2 are shown respectively in these figures. In conclusion, we chose the Gaussian form and auto-correlation distances are identified 200 m in Zone 1, 100 m in Zone 2 respectively.

3.2 *Liquefaction risk analysis*

The probability of a river dike failing due to liquefaction is expressed as:

$$P_f = prob(g \le 0) \tag{13}$$

$$g = FR(\ln P_L) - \ln P_L \tag{14}$$

where, F_R is the fragility function and P_L is the P_L-value. In such cases, FR and P_L are assumed to be independent and modeled by normal distribution; P_f is expressed by Equation (15), and can easily be calculated.

$$P_f = \Phi\left(\frac{0-\mu_g}{\sigma_g}\right) = \Phi\left(\frac{c-\mu_{\ln P_L}}{\sqrt{\zeta^2+\sigma^2_{\ln P_L}}}\right) \tag{15}$$

where, Φ[.] is the standardized normal distribution function.

The continuous failure probabilities P_f along the river dike are shown in Figure 8. The upper figure shows the P_L-value at arbitrary points, and the filled points show the calculated values using the investigation data at that point.

The solid line is the mean value based on interpolation using the Kriging method, and the dotted line shows a range of ±1σ (i.e. standard deviation). And here, note that the hatched area is the collapsed area. Furthermore, the reason why the solid line does not pass through all data is because we independently considered the observation error in Kriging.

The middle figure shows the superimposed failure probability. As shown in this figure, the proposed method is regarded as useful, since the collapsed sites (i.e. hatched area) are regarded as high-risk zones.

The lower figure shows the contribution of uncertainty sources, in here separated P_L-value

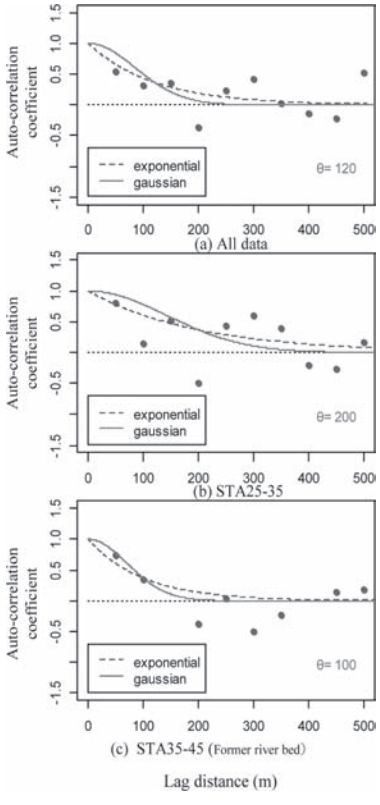

Figure 7. Identification of auto-correlation distance in case of P_L (SHAKE).

estimation error (i.e. statistical estimation error), and the precision of fragility curves (i.e. model error) at arbitrary points.

In Figure 9, the results in case of Zone 2 in same form are shown. The contribution of statistical estimation error in Zone-2 is very large all the points. The investigation in Zone-2 must be in shorter interval since the auto-correlation distance is very small for being the former riverbed area.

The results of the analysis are believed to provide useful information to manage river dikes. For example, the collapsed area (i.e. STA 31~32, STA 27.5~34, STA 37.5~34 and STA 39) characterized by small investigation intervals due to the focus on additional investigation after the shaking, the contribution of the model error indicates larger than 80%, and the statistical estimation error is very small (i.e. less than 10%). This indicates that owners should certainly plan to design countermeasures due to this being a high-risk area.

By contrast, in the case of large investigation intervals (e.g. STA 32~36 and so on), statistical estimation errors are a high contribution source (i.e. about 40%). Fortunately, the area did not collapse,

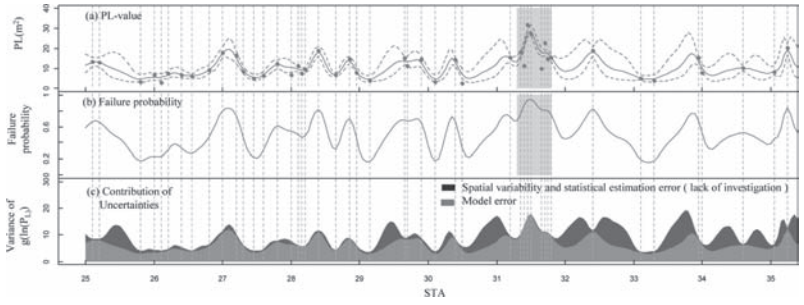

Figure 8. Estimated P_L-value, failure probability and contribution of uncertainties (Zone 1, STA 25-35).

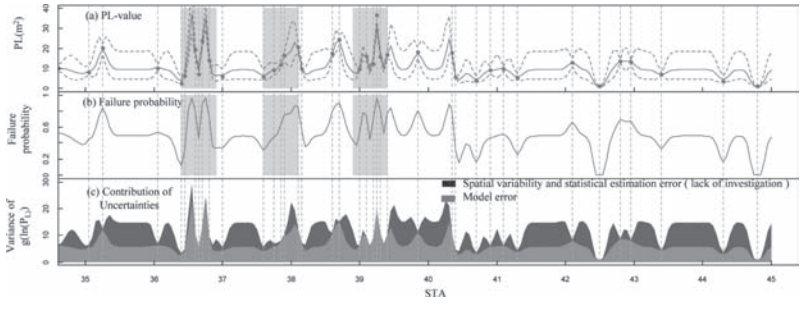

Figure 9. Estimated P_L-value, failure probability and contribution of uncertainties (Zone 2, STA 35-45).

but it was considered that additional investigations should be conducted.

4 CONCLUSION

Conducting countermeasures for a long continuous structure such as this river dike is time-consuming and costly. The information provided here is very useful for planning such a construction and determining its priorities.

It should be pointed out that the owner could obtain more information on soil properties by conducting additional soil investigations. The results from this method provide very valuable information in this regard.

REFERENCES

Japan Road Association 2002. Specifications For Highway Bridges.

Japan Institute of Country-ology and Engineering (JICE) 2009. Manuals of River Structures. (in Japanese).

Otake, Y. & Honjo, Y. 2012. Reliability based design on long irrigation channel considering the soil investigation locations. *Proceedings of Geo Congress* 2012, 2836–2845.

Otake, Y., Honjo, Y. & Koike, K. 2012. Evaluation of soil liquefaction risk on linearly structure considering the soil investigation locations, *Japanese Geotechnical Journal* 7(1): 283–293. (in Japanese).

Schnabel, P.B., Lysmer, J. & Seed, H.B. 1972. SHAKE-A computer program for earthquake response analysis of horizontally layered sites, Report EERC 72-12, Berkeley California, Earthquake Engineering Research Center, University of California.

Yoshida, N., Ohya, Y., Sawada, S. & Nakamura, S. 2009. Simplified procedure for evaluating liquefaction potential under ocean trench type long period earthquake, *Journal of JAEE* 9(3): 28–47. (in Japanese).

Geotechnical Safety and Risk IV – Zhang et al. (eds)
© 2014 Taylor & Francis Group, London, ISBN 978-1-138-00163-3

Effect of slenderness ratio on the reliability-based serviceability limit state design of augered cast-in-place piles

S.C. Reddy & A.W. Stuedlein
Oregon State University, Corvallis, Oregon, USA

ABSTRACT: This study investigated factors that control the reliability of Augered Cast-In-Place (ACIP) piles in predominately cohesionless soils under axial compression at the Serviceability Limit State (SLS). A simple probabilistic hyperbolic model was used to account the uncertainty in the load-displacement relationship using correlated bivariate curve-fitting parameters. Contrary to previous studies, the curve-fitting parameters were found to be dependent on pile slenderness ratio (D/B) and the effect of D/B and other pertinent variables (e.g., uncertainty in capacity, displacement) on SLS reliability was investigated using a First-Order Reliability Method (FORM). The D/B ratio had a considerable effect on foundation reliability, illustrating the importance of the dependence between the load-displacement behavior (i.e. curve-fitting parameters) and pile geometry and stiffness. In general, the uncertainty in the capacity model had a larger effect on reliability than that of the allowable displacement; the reliability index was found to approach an upper bound limit regardless of the level of uncertainty in allowable displacement and the pile capacity model.

1 INTRODUCTION

The behavior of geotechnical systems under loading is often difficult to predict due to the inherent heterogeneity of the geologic environment. Because the compositional and mechanical properties of soils are variable, many parameters used in geotechnical design are uncertain. Traditionally, the uncertainty associated with many geotechnical design parameters has been assessed jointly using a deterministic global factor of safety; which is frequently based on engineering judgment and experience. Reliability-Based Design (RBD) procedures can overcome many of the restrictions of traditional design checks (e.g. Allowable Stress Design [ASD]), and explicitly incorporate the uncertainty in the individual variables and their potential correlation into the overall model. The probability of failure for a prescribed limit state that results thus allows a quantitative assessment of risk. As a result, RBD is quickly becoming the preferred alternative as the demand for risk management in geotechnical engineering continues to grow.

Modern RBD codes, in which partial safety factors are calibrated with respect to a specific limit state (e.g. Ultimate Limit State [ULS], Serviceability Limit State [SLS]), are now mandated for design of bridge foundation elements (e.g. American Association of State Highway and Transportation Officials [AASHTO] Load Resistance Factor Design [LRFD]). RBD procedures for Augered Cast-In-Place (ACIP) piles (e.g., Stuedlein et al. 2012) are not yet accepted in codes.

Owing to the lack of model statistics for pile displacement, foundation reliability at the SLS is not as well understood compared to the ULS (Phoon et al. 2006). In order to assess foundation reliability at the SLS, Phoon (2006) proposed a simple probabilistic hyperbolic model that accounts for the uncertainty in the entire load-displacement relationship using a bivariate random vector consisting of hyperbolic curve-fitting parameters, which were found to be correlated and non-normally distributed. Phoon & Kulhawy (2008) describe a translational model to incorporate the correlated random variables into reliability calculations using a database of 40 loading tests on ACIP piles.

This study used an expanded database to investigate factors affecting the reliability of ACIP piles at the SLS. Contrary to Phoon & Kulhawy (2008), the hyperbolic model parameters were determined to be dependent on the pile slenderness ratio. The dependence was removed by transforming the model parameters, which were then used to assess foundation reliability for different pile geometries. In order to determine the variables which govern reliability, a parametric study was conducted by varying the mean and uncertainty of allowable displacement, uncertainty of predicted resistance, and the slenderness ratio.

2 PROBABILISTIC HYPERBOLIC MODEL AT THE SLS

To ensure that a specified level of performance of a structure is met, it is necessary to assess the likelihood of failure at both the ULS and SLS using a consistent methodology. This study focuses on reliability at the SLS, defined by one or more predefined displacements that correspond to target allowable loads.

The load-displacement behavior of ACIP piles is influenced by multiple sources of uncertainty that can be implicitly accounted for by fitting load-displacement models to date from a load test database. In this approach, the aleatory and epistemic uncertainties resulting from the uniqueness of each load test and the error associated with measurements taken during testing are combined together and statistically characterized. Although a variety of functions can be used to model the load-displacement relationship, a hyperbolic curve was chosen herein in order to remain consistent with the work pioneered by Phoon (2006). The hyperbolic curve is represented using the applied load, Q, normalized by the slope-tangent capacity, Q_{STC} (Phoon et al. 2006):

$$\frac{Q}{Q_{STC}} = \frac{y}{k_1 + k_2 y} \quad (1)$$

where y = pile head displacement, and k_1 and k_2 are fitted coefficients. The reciprocal of k_1 and k_2 is equal to the initial slope and asymptotic (or ultimate) resistance, respectively. Model parameters from the new data were calculated using ordinary least squares regression, whereas the parameters in the Chen (1998) and Kulhawy & Chen (2005) database were obtained directly from Phoon & Kulhawy (2008).

3 DATABASE

The expanded database included 87 load tests on ACIP piles constructed in predominately cohesionless soils. Forty loading tests were collected by Chen (1998) and Kulhawy & Chen (2005), 23 were compiled by McCarthy (2008), ten were reported by Stuedlein et al. (2012), ten were collected by Park et al. (2012), three were reported by Mandolini et al. (2002), and one loading test was selected from O'Neill et al. (1999). Table 1 shows the range of pile embedment depth, D, diameter, B, slenderness ratio, D/B, average SPT-N along the pile shaft, N_{avg}, and Q_{STC}.

Table 1. Range of variables observed in the database.

Variable	D (m)	B (mm)	D/B	N_{avg} (bl/0.3 m)	Q_{STC} (kN)
Minimum	7.5	300	20.0	4	367
Maximum	29.0	800	68.5	54	5300

4 RANDOMNESS OF THE HYPERBOLIC MODEL PARAMETERS

In order for foundation reliability assessments to be unbiased, k_1 and k_2 must be statistically independent from other deterministic variables in the database (e.g., SPT-N and D/B). Based on the Kendall's tau test (Daniel 1990) and adopting a 5 percent significance level ($\alpha = 5$), k_1 and k_2 are independent of average SPT-N with p-values = 0.81 and 0.93, respectively. However, convincing evidence (p-values < 0.05) suggested that both k_1 and k_2 were dependent on D/B. Figure 1 shows

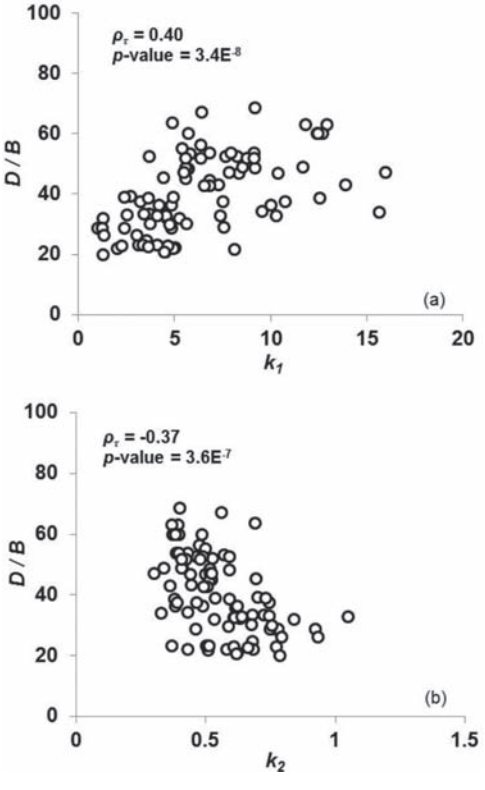

Figure 1. The dependence between slenderness ratio, D/B, and model parameters, (a) k_1 and (b) k_2 and the corresponding Kendall tau correlation coefficients and p-values.

moderately strong dependence between k_1, k_2, and D/B and the corresponding Kendall's tau correlation coefficient, ρ_τ, and p-value.

It is worthwhile to note that these correlations make physical sense in that a smaller k_1 represents a stiffer pile which corresponds to a smaller slenderness ratio; whereas a smaller k_2 indicates a larger ultimate resistance which likely relates to a larger D and D/B because of the narrow range of B in the database.

5 TRANSFORMATION OF THE MODEL PARAMETERS

In order to accurately model the uncertainty in the load-displacement relationship for the assessment of foundation reliability at the SLS, the correlation between k_1 and k_2 must be considered (Phoon & Kulhawy 2008). Figure 2a shows the inverse correlation between k_1 and k_2, and the corresponding ρ_τ and p-value, where a large (small) k_1 and small (large) k_2 indicates a slowly (quickly) decaying function and a less (more) well-defined and larger (smaller) asymptote.

In order to perform unbiased reliability analyses at the SLS, the correlation between model parameters and D/B must be considered. The dependence of k_1 and k_2 on D/B was removed by transforming the model parameters to:

$$k_{1,t} = k_1 \frac{B}{D} \tag{2a}$$

$$k_{2,t} = k_2 \sqrt{\frac{D}{B}} \tag{2b}$$

After transforming k_1 and k_2 to $k_{1,t}$ and $k_{2,t}$, the Kendall's tau correlation test between $k_{1,t}$ and $k_{2,t}$, and D/B produced p-values = 0.78, 0.56, indicating no correlation. Similarly, the model parameters remained independent of SPT-N following transformation. Figure 2b illustrates the correlation between $k_{1,t}$ and $k_{2,t}$ is slightly reduced but remains valid after transformation.

To assess foundation reliability using the translational model approach described in Phoon & Kulhawy (2008), the marginal distributions of $k_{1,t}$ and $k_{2,t}$ must be determined. Figure 3a and b shows the empirical, fitted normal, and fitted lognormal marginal Cumulative Distribution Functions (CDF) of $k_{1,t}$ and $k_{2,t}$, respectively. Also shown is the sample mean, $\bar{k}_{i,t}$, standard deviation, $\sigma_{i,t}$, and $COV_{i,t}$, defined as the standard deviation divided by the mean, of the model parameters.

Based on the Anderson-Darling goodness-of-fit test (Anderson & Darling 1952) and $\alpha = 5$ percent, there was no evidence to reject the null hypothesis of lognormality for $k_{1,t}$ and $k_{2,t}$. Therefore, $k_{1,t}$ and

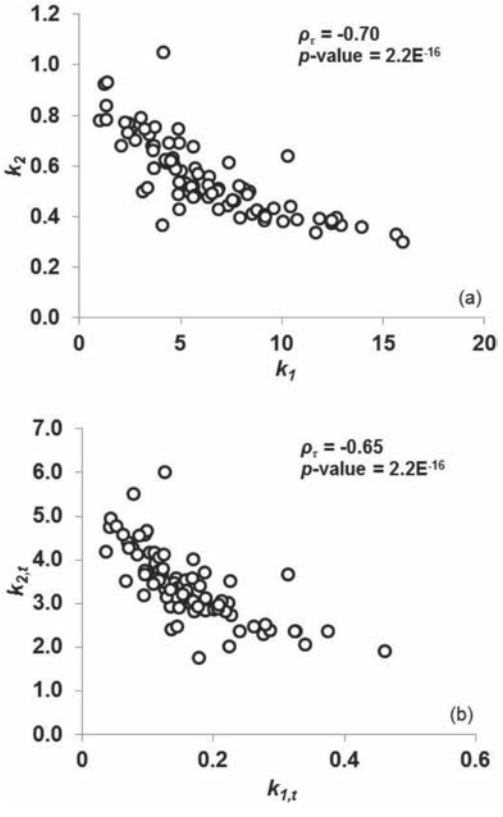

Figure 2. Correlation between model parameters (a) k_1 and k_2 and (b) $k_{1,t}$ and $k_{1,t}$ and the corresponding Kendall tau correlation coefficients and p-values.

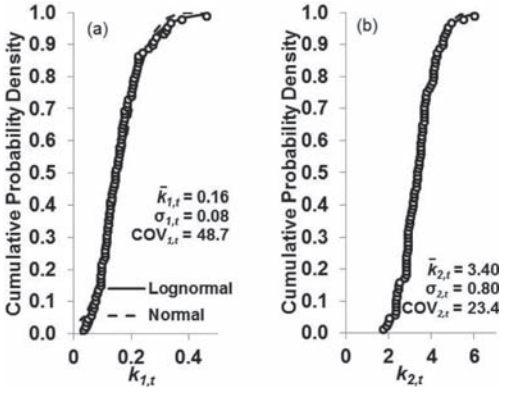

Figure 3. Empirical, lognormal, and normal marginal cumulative distributions for the transformed hyperbolic model parameters: (a) $k_{1,t}$, and (b) $k_{2,t}$.

$k_{2,t}$ were assumed to follow a lognormal distribution for the purpose of assessing foundation reliability at the SLS.

6 TRANSLATIONAL MODEL FOR BIVARIATE PROBABILITY DISTRIBUTIONS

The translational model approach for describing the marginal distributions of $k_{1,t}$ and $k_{2,t}$ requires the use uncorrelated standard normal random variables Z_1 and Z_2 (mean = 0, standard deviation = 1).

This study followed the basic procedure outlined in Phoon & Kulhawy (2008). First, Z_1 and Z_2 are converted into correlated random variables X_1 and X_2 (Phoon & Kulhawy 2008):

$$X_1 = Z_1 \tag{3a}$$

$$X_2 = Z_1\rho_{\ln} + Z_2\sqrt{1-\rho_{\ln}^2} \tag{3b}$$

where $\rho_{\ln}$ is an equivalent-normal correlation coefficient:

$$\rho_{\ln} = \frac{\ln\left[\rho\sqrt{\left(e^{\zeta_{1,t}^2}-1\right)\left(e^{\zeta_{2,t}^2}-1\right)}+1\right]}{\zeta_{1,t}\zeta_{2,t}} \tag{4}$$

and where $\lambda_{1,t}$, $\zeta_{1,t}$ and $\lambda_{2,t}$, $\zeta_{2,t}$ are the approximate lognormal mean and standard deviation of $k_{1,t}$ and $k_{2,t}$, respectively, and ρ is the standard product-normal correlation coefficient for two normally distributed variables. The second moment statistics in Equation 4 were calculated as:

$$\zeta_{i,t} = \sqrt{\ln\left(1+\sigma_{i,t}^2/\overline{k}_{i,t}^2\right)} \tag{5a}$$

$$\lambda_{i,t} = \ln\left(\overline{k}_{i,t}\right) - 0.5\zeta_{i,t}^2 \tag{5b}$$

The correlated, lognormal marginal distributions of $k_{1,t}$ and $k_{2,t}$ were thus simulated using:

$$k_{1,t} = e^{\left(\zeta_{1,t}X_1+\lambda_{1,t}\right)} \tag{6a}$$

$$k_{2,t} = e^{\left(\zeta_{2,t}X_2+\lambda_{2,t}\right)} \tag{6b}$$

In order to adequately reproduce the uncertainty in the observed load-displacement curves, $k_{1,t}$ and $k_{2,t}$ must be back-transformed into k_1 and k_2. This study calculated k_1 and k_2 using deterministic values of D/B because the uncertainty associated with pile geometry could not be evaluated from the database.

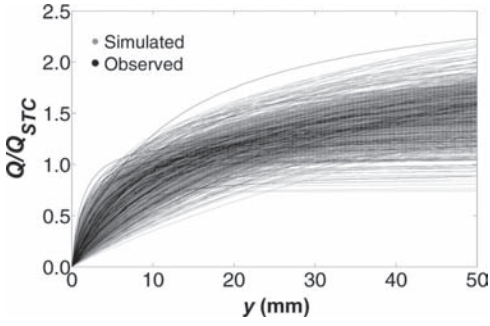

Figure 4. Observed and simulated load-displacement curves using the translational model.

Figure 4 shows the fitted load-displacement curves based on the observed loading tests and those generated using the procedure for simulating $k_{1,t}$ and $k_{2,t}$ outlined above. A sufficient number of deterministic values of D/B were used to back-transform $k_{1,t}$ and $k_{2,t}$ into k_1 and k_2 in order to adequately capture the uncertainty present in the observed load-displacement curves. In general, the observed and simulated load-displacement curves are in good agreement, and the translational model can be confidently used to assess foundation reliability at the SLS using the database herein.

7 RBD FOR THE SERVICEABILITY LIMIT STATE USING A FIRST-ORDER RELIABILITY METHOD

The SLS is reached when foundation displacement, y, equals or exceeds allowable settlement, y_a. This study followed the approach outlined in Phoon & Kulhawy (2008), where the SLS can be evaluated using a performance function, P:

$$P = y_a - y(Q) \tag{7}$$

Failure is defined as $P \le 0$, and the probability of exceeding the SLS, p_f, is:

$$p_f = \Pr\left(P \le 0\right) \tag{8}$$

By combining Equations 1, 7, and 8, and defining a deterministic mean global factor of safety, FS, the probability of failure is:

$$p_f = \Pr\left(\frac{y_a}{k_1+k_2y_a} < \frac{1}{FS}\frac{Q'}{Q'_p}\right) \tag{9}$$

where Q' and Q'_p correspond to the applied load and predicted pile capacity, respectively. In order

estimate foundation reliability at the SLS, the reliability index, β, defined as the number of standard deviations between the mean of the multivariate resistance distribution and the limit state surface, was calculated as:

$$\beta = -\Phi^{-1}\left(p_f\right) \tag{10}$$

where Φ^{-1} is the inverse standard normal function.

A First-Order Reliability Method (FORM) was used to estimate foundation reliability at the SLS. First, each random variable in the limit state function (k_1, k_2, y_a, Q', Q'_p) was transformed into a standard normal variable, such that the difference in magnitude of the random variables was eliminated (Hasofer & Lind 1974). Then the probability of failure was estimated by considering the area beneath the multivariate distribution where $P \leq 0$. The FORM approach assumes that the limit state function is linear at the failure point, and therefore may not be appropriate for situations where p_f is large. However, this approach is considered sufficient for most geotechnical applications where the target probabilities of failure are very small.

8 FACTORS AFFECTING FOUNDATION RELIABILITY AT THE SLS

This study assessed the factors which govern foundation reliability at the SLS by calculating multiple reliability indices using FORM. Each variable in Equation 9 was assumed to follow a lognormal distribution, whereas the second moment statistics for $k_{1,t}$ and $k_{2,t}$ were obtained directly from the database. The mean and COV of allowable displacement was varied from 10 to 50 mm and 5 to 85 percent, respectively. The applied load and predicted pile capacity were assumed to be unit mean variables, where COV(Q') = 20 percent based on recommendations from Paikowsky et al. (2004). The COV of the predicted pile capacity was varied from 5 to 85 percent, corresponding to different capacity prediction methods with varying degrees of uncertainty. A $FS = 3$ was selected based on that commonly adopted in current practice (Phoon & Kulhawy 2008). Slenderness ratios of 25 and 65 were selected in order to cover the range of D/B values in the database and illustrate the effect of pile geometry on β.

Figures 5a-e illustrate the effect of changing the mean y_a, COV(y_a), COV(Q'_p), and D/B on foundation reliability. Foundation reliability decreases more rapidly for increasing uncertainty in Q'_p when COV(y_a) and COV(Q'_p) are relatively small (5–45 percent) and $y_a > 20$ mm. In general, COV(Q'_p) has a larger effect on β as compared to COV(y_a),

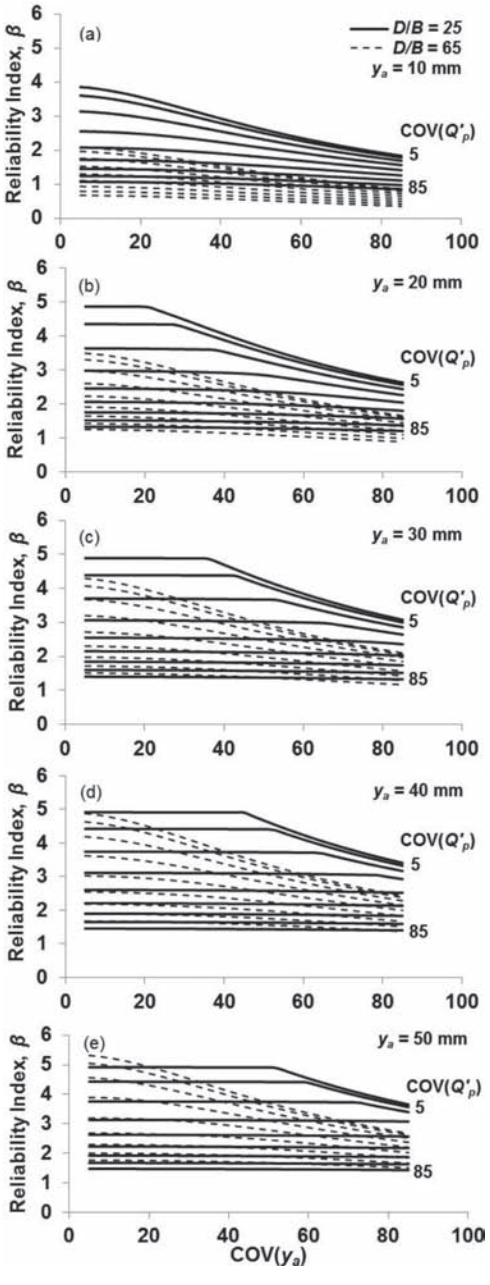

Figure 5. The effect of COV(y_a), COV(Q'_p), and D/B on β for mean y_a equal to (a) 10 mm, (b) 20 mm, (c) 30 mm, (d) 40 mm, and (e) 50 mm using $k_{1,t}$ and $k_{2,t}$ developed herein.

regardless of the level of uncertainty in Q'_p and y_a. The same general trend was observed at different levels of mean allowable displacement, where the change in β was more prominent for larger y_a. Overall, β was larger for larger mean allowable

displacements if all other variables in the performance function remained constant. At large allowable displacements (i.e. $y_a = 50$ mm), β was observed to be largely insensitive to the level of uncertainty in y_a, compared to Q'_p. This illustrates the advantage of an accurate ACIP design methodology. At large allowable displacements, β approaches an upper bound limit for each level of COV(Q'_p) as COV(y_a) decreases. For a mean $y_a < 40$ mm, β is smaller for larger D/B, whereas the opposite is true for $y_a \geq 50$ as shown in Figure 5e. Thus, accounting for the correlation between the hyperbolic model parameters and D/B is critical when estimating the reliability of ACIP piles at the SLS.

In order to illustrate the effect of slenderness ratio on foundation reliability at the SLS, reliability indices calculated herein may be compared to those reported in Phoon & Kulhawy (2008). Using the statistics for y_a and Q'_p recommended by a Phoon and Kulhawy (2008) and a $D/B = 25$, $\beta = 2.214$ ($p_f = 1.34\%$) is computed, which is in good agreement with the previously reported value (2.210). However, for longer piles, say with a $D/B = 65$, the reliability index, β, equals 1.774 ($p_f = 3.80\%$), a significantly different value than previously computed.

9 SUMMARY AND CONCLUSIONS

This paper investigated the effect of varying model statistics in reliability-based serviceability limit state design of ACIP piles installed in predominately cohesionless soils. First, a database consisting of load tests conducted on ACIP piles in cohesionless soils was compiled, and the uncertainty in the entire load-displacement relationship was reduced to a correlated bivariate vector containing the hyperbolic model parameters. Contrary to Phoon & Kulhawy (2008), both model parameters were found to be correlated to pile slenderness ratio. Subsequent analyses used transformed model parameters to avoid the undesirable effect of parameter dependence on geometric variables.

The effect of varying the mean and uncertainty of the allowable displacement and the uncertainty of the capacity prediction method on the computed reliability index was assessed. In general, changing the uncertainty in Q'_p had a larger effect on β compared to y_a. Overall, β was larger for larger mean allowable displacements when all other variables in the performance function were unchanged. At larger allowable displacements, β was found to approach an upper bound limit and shown to be largely insensitive to the level of uncertainty in y_a, compared to Q'_p. Because of the dependence of the model parameters on pile stiffness and geometry, β was found to be sensitive to D/B, and illustrates the importance of accounting for this correlation in RBD.

REFERENCES

Anderson, T.W. & Darling, D.A. 1952. Asymptotic theory of certain goodness-of-fit criteria based on stochastic processes. *The Annals of Mathematical Statistics* 23(2): 193–212.

Chen, J.R. 1998. Case history evaluation of axial behavior of augered cast-in-place piles and pressure-injected footings. M.S. Thesis. Cornell University. Ithaca, New York.

Daniel, W.W. 1990. Applied nonparametric statistics. Boston: PWS-Kent.

Hasofer, A.M. & Lind, N. 1974. An exact and invariant first-order reliability format. *Journal of Engineering Mechanics* 100(1): 111–121.

Kulhawy, F.H. & Chen, J.R. 2005. Axial compression behavior of augered cast-in-place (ACIP) piles in cohesionless soils. In C. Vipulanandan & F.C. Townsend (eds), *Advances in Deep Foundations; Proc. of GeoFrontiers Congress (GSP 132), Austin, Texas, 24–26 January 2005.* Reston: ASCE.

Mandolini, A., Ramondini, M., Russo, G. & Viggiani, C. 2002. Full scale loading tests on instrumented CFA piles. In M.W. O'Neill & F.C. Townsend (eds), *An International Perspective on Theory, Design, Construction, and Performance; Proc. of Deep Foundations (GSP 116), Orlando, Florida, 14–16 February 2002.* Reston: ASCE.

McCarthy, D.J. 2008. Empirical relationships between load test data and predicted compression capacity of augered cast-in-place piles in predominately cohesionless soils. M.S. Thesis. University of Central Florida. Orlando, Florida.

O'Neill, M.W., Vipulanandan, C., Ata, A. & Tan, F. 1999. Axial performance of continuous-flight-auger piles for bearing. *Texas Dept. of Transportation report no. 7-3940-2*, Center for Innovative Grouting Materials and Technology: University of Houston.

Park, S., Roberts, L.A. & Misra, A. 2012. Design methodology for axially loaded auger cast-in-place and drilled displacement piles. *Journal of Geotechnical and Geoenvironmental Engineering* 138(12): 1431–1441.

Paikowsky, S.G. with contributions from Birgisson, B., McVay, M., Nguyen, T., Kuo, C., Baecher, G., Ayyab, B., Stenersen, K., O'Malley, K., Chernauskas, L. & O'Neill, M.W. 2004. Load and resistance factor design (LRFD) for deep foundations. *NCHRP report no. 507,* Transportation Research Board: Washington, DC.

Phoon, K.K. 2006. Serviceability limit state reliability-based design. In M.L. Lin, C.T. Chin, H.D. Lin, Y. Honjo, K.K. Phoon (eds), *New Generation Design Codes for Geotechnical Engineering Practice; Proc. of Int. Symp., Taipei, Taiwan 2–3 November 2006.* Singapore: World Scientific Publishing Company.

Phoon, K.K., Chen, J.R. & Kulhawy, F.H. 2006. Characterization of model uncertainties for auger cast-in-place (ACIP) piles under axial compression. In R.L. Parsons, L.M. Zhang, W.D. Guo, K.K. Phoon, & M. Yang (eds), *Foundation Analysis and Design—Innovative Methods (GSP 153).* Reston: ASCE.

Phoon, K.K. & Kulhawy, F.H. 2008. *Reliability-based design in geotechnical engineering.* New York: Taylor & Francis.

Stuedlein, A.W., Neely, W.J. & Gurtowski, T.M. 2012. Reliability-based design of augered cast-in-place piles in granular soils. *Journal of Geotechnical and Geoenvironmental Engineering* 138(6): 709–717.

Geotechnical Safety and Risk IV – Zhang et al. (eds)
© 2014 Taylor & Francis Group, London, ISBN 978-1-138-00163-3

Uplifit model for the Red River dikes of Vietnam

Pham Quang Tu
Delft University of Technology, The Netherlands
Hanoi Water Resources University, Vietnam

Bui Van Truong
Hanoi Water Resources University, Vietnam

P.H.A.J.M. van Gelder
Delft University of Technology, The Netherlands

ABSTRACT: The province of Thai Binh, an area with a large population and high socio-economic status, is located at the downstream part of the Red River Delta. The area is protected by dike systems whose safety has been upgraded significantly. While overtopping was an important failure mode in the past, after raising crest levels, now piping and uplift phenomena are considered the dominant threats, having led to several dike breaches in the Red river dike system. In order to address this issue and the large uncertainties in commonly used uplift models, a series of field tests had been designed and carried out on the *Thaibinh* formation (a regional top soil layer) for determining the critical uplift pressure. A special structure is installed to increase water head artificially, by excavation through the top layers, and ground water flow is concentrated by plastic sheet piles. Phenomena are monitored and measured in an excavation, for thinning the thickness of impervious layers, during the test. The results cover critical head, uplift displacement, time series and visual observations. In this paper, the authors will perform a multivariate analysis for the field test results in order to develop statistical model for uplift mechanism. Furthermore, a proposed model of uplift has also been generated including a calibration coefficient which represents for uncertainties of both inherent and epistemic sources. The proposed model is also compared to test results and statistical model to give a better understanding of this phenomenon. The findings of the research might contribute to improving dike assessments in the Red River Delta.

1 INTRODUCTION

The province of Thai Binh, an area with a large population and high socio-economic status, is located at the downstream part of the Red River Delta. The area is protected by dike systems whose safety has been upgraded significantly. While overtopping was an important failure mode in the past, after raising crest levels, now piping and uplift phenomena are considered the dominant threats, having led to several dike breaches in the Red river dike system. In order to address this issue and the large uncertainties in commonly used uplift models, a series of field tests had been designed and carried out on the *Thaibinh* formation (a regional top soil layer) for determining the critical uplift pressure. A special structure is installed to increase water head artificially, by excavation through the top layers, and ground water flow is concentrated by sheet piles. Phenomena are monitored and measured in an excavation, for thinning the thickness of impervious layers, during the test. The test results cover critical head, uplift displacement, time series and visual observations. In this paper the author will, first, briefly present the test results, then perform a multivariate analysis to elaborate a statistic model for the uplift mechanism. Furthermore, a proposed model of uplift has been generated including a calibration coefficient. The model's results are compared together to formulate a recommendation for the uplift model of the Red River Delta.

2 STUDY ON UPLIFT PHENOMENON

2.1 *Field tests of uplift on Thaibinh formation*

2.1.1 *Introduction*

Number of phenomena and terms related to dike failure have been known in literatures, such as critical gradient, piping, heave, sand boiled, uplift, etc. To avoid confusion of those terminologies, it is necessary to remain them clearly.

Critical gradient is defined as ratio of different head and thickness of soil layers. It has been commonly confused with another hydraulic gradient which could be calculated from different

head of river and hinterland against the seepage length from foreland to observation location, see (Rijwaterstaat 1999, Sellmeijer 1988).

Uplift is a phenomenon that causes by high piezo-metric level in aquifer (often happening for river dike in flood season). The resulting cracks, vertical displacement and failure of impervious layers are common observed in combination with this phenomenon, see Figure 2.

Heave (or *sand boiled*) is phenomenon which is often visualized by sand or silt being carried out from the aquifers, see Figure 3. Heave could be understood as the first stage of piping under dikes, or we could say if there were no mitigating measures, heave will lead to piping.

Piping is the most common failure mechanism of river dikes, in which outflow discharge with buoyant sand or silt increases continuously from beginning of this mechanism. Hypothetically, continuous pipes are formed under dike embankment due to backward erosion, see (Sellmeijer 1988, van Beek et al. 2012). If the pipe is fully formed, enlargement of piping channel will elaborate and dike will collapse in hours.

Figure 1. Study location.

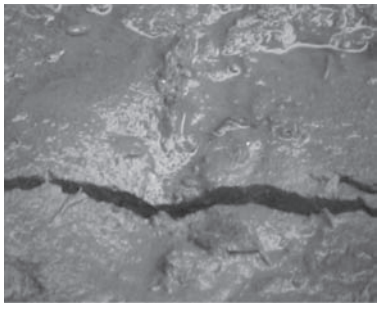

Figure 2. Crack due to uplift, from Bui (2009).

Figure 3. Heave observed during the field test, from Bui (2009).

There have been a number of studies on uplift and piping through years in Red river dikes of Viet Nam, for instance To (2002) carried out series of laboratory test on the critical head of sand boil and uplift. The test results indicated that the critical gradients is quite close to theoretical value, however small size of test equipments are one of the main limitation of this research. Recently, Bui (2009) reconsiders uplift mechanism in series of field test on *Thaibinh* formation.

The objectives of these field tests are, first, determine the critical head which leads to uplift of the impervious layers in Red River dikes system in Thai Binh; then, visualize the phenomena during the tests to give a more apprehension about the failure mechanisms. Related parameters for these failure mechanisms will also be obtained for evaluation and comparison the difference between the test results and the theoretical model. In this study, only uplift is considered experimentally and physically. The result is expected to give a better understanding for phenomena in Red River dikes.

2.1.2 *Test set up and procedures*

Critical head is created either by an excavation well or by an injection well through impervious layers. By doing so, water is supplied directly to aquifer, see Figure 4. Plastic sheet piles are installed following Ushape (see Fig. 4) to concentrate groundwater flow, which is observed in locations along the open direction of the sheet piles and forms 1D groundwater flow model.

Observation phenomena, such as uplift and heave, are monitored in an excavation which is designed with different depths for thinning the thickness of the impervious layers. Furthermore, piezometric head of groundwater flow could be measured from piezometers $H_1 - H_3$ in aquifer and $H_4 - H_7$ in top layers during tests.

Water is pumped to the wells with an adjustable discharge in order to keep water level in the well being constant in certain period of experiments.

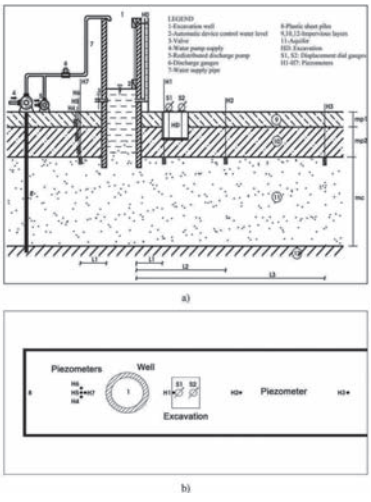

Figure 4. Schematization of field test, (a) cross section, (b) layout, adapted from Bui (2009).

After that, piezometric heads are recorded in different locations, and the next increment of water level could be started when the piezometer reading being unchanged. The procedures repeat in combination with the observation of phenomena in the excavation. Uplift is defined to be failure when crack are formed in blanket layers and water is blown out of aquifers.

At the end of the test, the impervious layers are failed including crack, sand boiled (or heave) and water blown out of the aquifer. Ground conditions could be seen in Figure 5.

2.1.3 *Test results*

Different heads corresponding to time are recorded during experiments. Phenomena included out flow discharge also be monitored. From Figure 7 it can be seen that piezometric heads in aquifer increase linearly, then it turns to non-linear relationship after cracks were observed. Afterwards, heave expands continuously with silt and sand being carried out of the aquifer. The tests have been stopped if the water head in wells could not be remained constant due to the limited supply of water and test apparatus.

It also can be noted that, pore pressure exceeding in impervious layers depends on its heterogeneous characteristics rather than consolidation process. In some cases, piezometric head raises suddenly after a period of linear increments, see Figure 6. A significantly heterogeneous characteristic could be seen that is the drought crack which could be visualized to a depth of one meter or even deeper.

Uplift displacement is also measured, see Figure 7. The magnitude of vertical displacement varies from 7 to 25 mm in experiments.

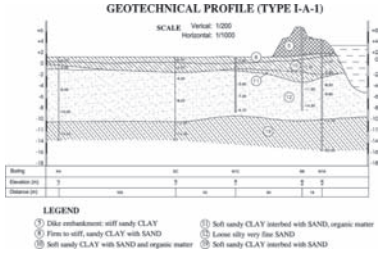

Figure 5. Geotechnical conditions in field test locations, from Bui (2009).

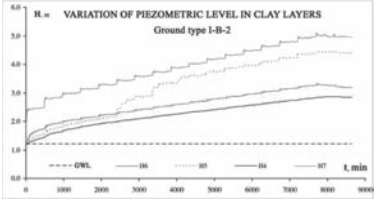

Figure 6. Sudden raise of piezometric values in impervious layers, from Bui (2009).

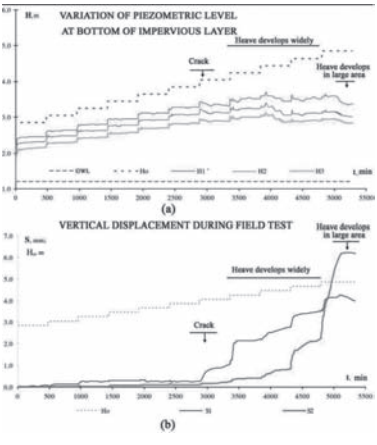

Figure 7. Critical head during the field test (a) and uplift displacement (b), from Bui (2009).

In this analysis, only critical heads of uplift are considered. Heave and piping are mentioned in other studies.

2.2 *Statistical model of uplift*

From the results of test series, a statistical model is formulated for uplift mechanism. In this study, a regression analysis is performed to figure out the relationship between critical gradient (or different head over thickness of soils) and soil's properties. The approach has been mentioned in Seber & Wild (2003) and applied successfully in Sellmeijer,

de la Cruz, van Beek, & Knoeff (2011) & van der Zee (2011). For this purpose, a framework of multivariate analysis has been developed for critical gradient from the field tests series. The linear regression could be expressed as below.

$$Y = \beta_o + \beta_1 X_1 + \beta_2 X_2 + \ldots + \beta_n X_n + \in \quad (1)$$

in which Y is target regression function; X_i is noted for measuring variable; β_i is unknown regression coefficient and $\in$ is error of estimation. Considering to field test results, a number of variables are chosen for analysis, then three following variables are considered for final calculation; they are soil density, cohesion and internal friction. A transformation of data to logarithm domain is also applied, then we have following relations.

$$i_c^{sta} = e^{\beta_o}\left(\frac{\rho}{\rho_m}\right)^{\beta_1}\left(\frac{C}{C_m}\right)^{\beta_2}\left(\frac{\phi}{\phi_m}\right) \quad (2)$$

Here, i_c^{sta} is critical uplift gradient corresponding to the statistical model; ρ and ρ_m indicate the density of soil in each test and mean value of data series respectively; C and C_m are cohesion of soil and mean value of cohesion series; ϕ and ϕ_m are noted as internal friction angle of soil and mean value of that data series.

From the calculation results, we have the following estimation of statistical model for uplift:

$$i_c^{sta} = e^{-0.182}\left(\frac{\rho}{\rho_m}\right)^{2.83}\left(\frac{C}{C_m}\right)^{0.097}\left(\frac{\phi}{\phi_m}\right)^{0.0258} \quad (3)$$

2.3 *Physical-based model of uplift*

Physically, uplift happens if piezometric head at the bottom of impervious/top layer is larger than its weight and other resistances. This phenomenon has been investigated by many researchers through century, for instance (Terzaghi 1943, Tran et al. 1988, Van et al. 2011). The basic equation for uplift design can be defined:

$$i_c^o = \frac{\rho_{sat} - \rho_w}{\rho_w} \quad (4)$$

where ρ_s is density of soil particles; ρ_w is density of water; n is porosity of soil; ρ_{sat} is saturated density of soil and i_c^o is critical gradient of uplift.

The criteria of Tezaghi in Equation 4 assumes that soil is non-cohesiveness, which is available until now even different safety factor has been used in practice, for instance critical gradient $i_o^{cri} = 0.3 - 0.8$ in (USACE 2000) or factor of safety Fs = 1.5–2 in (Rijwaterstaat 1999). In Viet Nam, safety factor of 1.5–2.0 has also been recommended for design of berm in hinterland.

From the field test results, it is suggested that the critical gradients of uplift phenomenon are much higher than which are expected. Therefore, a new model to deal with this failure mechanism for the study area has been implied. It can be seen form Figure 8 that uplift zone has a width of L due to piezometric head increasing over weight of impervious layer. In equilibrium state, all the forces in vertical direction are vanished or balance, so from Figure 9 we have:

$$H_c - P - 2(C + P' tan\phi) = 0 \quad (5)$$

Or

$$h_c = \rho' d + 2\left(C \cdot d + \frac{d^2 \cdot K_o \cdot tan\phi}{3}\right) \quad (6)$$

in which, H_c and h_c are critical piezometric level and net critical head at the bottom of top layer; $P = \rho' \cdot d$ is effective weight of top layer; P' is effective lateral earth pressure; d is thickness of top layer; C is cohesion and ϕ is internal friction angle of soil; K_o is coefficient of at-rest earth pressure, which could be found in different forms in many soil mechanics references, for instance (Das 2011, Verruijt 2010).

There are many forms of critical heads in literatures, see (Terzaghi 1943, Tran et al. 1988, Ojha et al. 2001). The differences between these approaches are basically the second term in Equation 6 which are treated elastically or plastically between relationship of stress and strain in soil, see (Chen

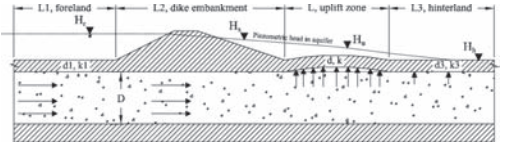

Figure 8. Uplift model for calculation.

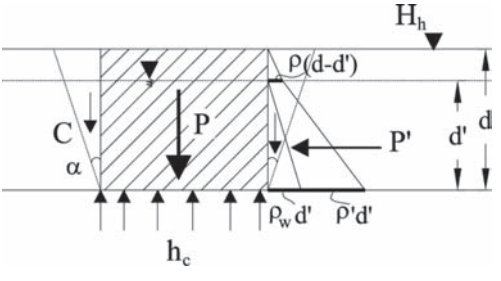

Figure 9. Uplift calculation diagram.

1975, Chen and Liu 1990) for more detail of these behaviours. A calibration coefficient, θ, has been introduced for the second term of Equation 6, in which θ represents for uncertainties of both model and soil parameters, see (van Gelder 2000, Vrouwenvelder and Steenbergen 2003, Kanning 2012) for more detail of model factor. After validation, we have the final form of critical water head for uplift in our case study as follows:

$$h_c^{pro} = \rho' d + \theta\left(C \cdot d + \frac{d^2 \cdot K_o \cdot tan\phi}{3}\right) \quad (7)$$

In this case, groundwater level is equal to the level of hinterland and parameters of foreland's blanket layers are the same as that of hinterland; h_c^{pro} c is critical uplift head of the proposed model; θ is the calibration coefficient.

Critical gradient of uplift can be calculated from Equation 7, then we have:

$$i_c^{pro} = \frac{h_c pro}{d} = \rho' + \theta\left(C + \frac{d^2 \cdot K_o \cdot tan\phi}{3}\right) \quad (8)$$

Calibration coefficient can also be figured out by:

$$\theta = \frac{3(i_c^{pro} - \rho')}{3C + d \cdot K_o tan\phi} \quad (9)$$

By fitting i_c^{pro} to uplift critical gradient from test's data series, we could elaborated the values of θ.

3 RESULTS AND DISCUSSION

3.1 *Results*

Both uplift and heave are observed during the increasing of water level indicating for flood water level. Crack was initiated first in weak spot of the blanket, then appears in many spots with sand or silt flowing out in a certain area.

There are total of fifty eight tests performs on *Thaibinh* formation for uplift and heave phenomena. The plotting of the final results of critical gradient of uplift could be found in Figure 10.

The critical uplift gradients are found to be normal distributed of mean and standard deviation equivalent to 0.836 and 0.105 respectively. From the theoretical Equation 4, the so-called theoretical critical gradient has a value of 0.758. Whereas, in the proposed model, critical gradient could be formulated in range of normal distribution with parameters N(0.8301;0.0497). It is figured out that statistical model fits quite well to normal distribution with parameters of N(0.8323;0.066).

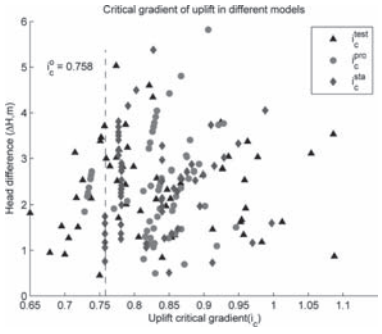

Figure 10. Critical gradient of uplift in different models.

3.2 *Discussion*

From the observation during the tests, it can be seen that uplift commences first at the weakest spot in the impervious layers, then develops widely on area if water pressure till increases continuously. The weak spots mentioned here are cracks or heterogeneous structures in soils and the drought cracks are also supposed being a main disturbed factor of the top layers in the depth from 0.8 to 1.2 m, see (Bui 2009).

After crack, heave is also visualized in all test locations and the moment of heave start is defined as end of crack developing process. Time dependent in test series may also be influenced to its results. Unfortunately, all of these issues are not included in this study.

The statistical model fitted quite well with data series of test, see Figure 8. However, it has not shown the physical relationship between parameters and its physical behaviours. It is clear from statistical analysis that, correlated coefficient of this model has a negative trend ($\rho = -5.3\%$) comparing to positive trend of two other models (ρ = 8.9–16.9%). It seem unreasonably that different heads increase lead to decline of critical gradient, following the statistical model. So that, in practice it might be incorrect if we apply the statistical model without understanding about its physical behaviours.

It also can be seen from Figure 10 that the proposed model has the smallest variation comparing to others models. Calibration coefficient has been assumed to be normal distributed and parameters are mean and standard deviation by μ_θ = 0.5519 and σ_θ = 0.746 respectively. In practice, it is recommended that θ should be chosen by 0.5 for engineering purposes.

In term of comparison between statistical to proposed model, the probability if actual critical gradient is larger than that of theoretical model could be calculated, for instance $P(i > i_c^{pro}) = P(i > 0.758)$ The final results show that exceeded probability is $P(i_c^{pro} > i_c^o) = 92.53\%$ for the proposed model and

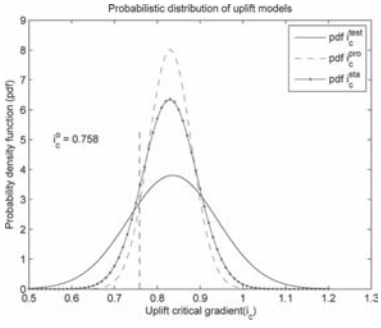

Figure 11. Probabilistic distribution of uplift models.

is $P(i_c^{sta} > i_c^o) = 86.85\%$ for the statistical model, whereas that is $P(i_c^{test} > i_c^c) = 77.06\%$ for series of field test data, see Figure 11 for more detail.

4 CONCLUSIONS

It is clear from the above results that critical gradients, which lead to uplift failure in *Thaibinh* formation of Red River dikes, are significant high comparing to current understanding of this phenomenon. Uplift failure initiates at the weakest spot, then expands to many spots in large area if piezometer levels still increase continuously.

Field test data has been fitted with both statistical and physical-based models. Calibration coefficient for supposed model (in Equation 8) has been recommended by 0.5 in practical application. It is expected that the results could be applied in flood defence assessment for the Red river dikes on *Thaibinh* formation.

Limitation: Dimensions of excavation in the field test are the same for all test series, so there is no influence of that has been taken in to account.

ACKNOWLEDGEMENTS

This paper is funded by the Project of Upgrading the Training Capacity in Coastal Engineering of the Water Resources University of Vietnam from the Royal Netherlands Embassy in Hanoi of Vietnam, and CICAT and the Department of Hydraulic Engineering of TU Delft. The authors wish to thank for their support.

REFERENCES

Bui, V.T. 2009. *Study on the failure of under seepage of lower Red river dike in Thai Binh province and field experiment-based analysis the design solutions*. Ph. D. thesis, Hanoi university of Mining and Geology, Vietnam.

Chen, W.-F. 1975. *Limits analysis and soil plasticity*. Elsevier scientific publishsing company.

Chen, W.-F. & Liu, X. 1990. *Limits analysis in soil mechanics*. Elsevier scientific publishsing company.

Das, B.M. 2011. *Principles of foundation engineering, seventh edition*. Cengage Learning.

Kanning, W. (2012). *The weakest link—Spartial variability un the piping failure mechanism of dikes*. Ph. D. thesis, Technology University of Delft, The Netherlands.

Ojha, C., Sigh, V., & Adrian, D. 2001. Influence of porosity on piping models of levee failure. *Journal of Geotechnical and Geoenvironmental Engineering* 127(12), 1071–1074.

Rijwaterstaat (1999). Technical report on piping. Technical report.

Seber, G.A.F. & Wild, C. (2003). *Nonlinear regression*. John Wiley & Sons.

Sellmeijer, J.B. 1988. *On the mechanism of piping under impervious structures*. Ph. D. thesis, Civil Engineering and Geosciences of Technical University of Delft.

Sellmeijer, H., de la Cruz, J.L., van Beek, V., & Knoeff, H. 2011. Fine-tuning of the backward erosion piping model through small-scale, medium-scale and ijkdijk experiments. *European Journal of Environmental and Civil Engineering*, 1139–1154.

Terzaghi K. 1943. *Theoretical Soil mechanics*. John Wiley & Sons.

To, X.V. 2002. *Study on the influence of seepage effect of formations in dike stability, application for a Red River dike section*. Ph.D. thesis, Ha Noi University of Mining and Geology, Viet Nam.

Tran, V.T., Tran, M.L., & Dang, Q.T. 1988. Stability of impervious layer in red river dike of ha noi. *Water Resources Bulletin, Ministry of Water Resources, Vietnam* 261(3+4), 40.

USACE. 2000. *Design and construction of levees*. Engineering manual 1110-2-1913, Army Corps of Engineer.

Van, M., Koelewijn, A., & Barends, F. 2011. *Uplift phenomenon: Model, validation and Design*. Stichting Deltares, Delft, The Netherlands.

van Beek, V., de Bruijn, H., Knoeff, J., Bezuijen, A. & Frster, U. 2012. Levee failure due to piping: A full-scale experiment. *Reliability Engineering and System Safety*, 141–150.

van der Zee, R. 2011. Influences of sand characteristics on the piping process. Master's thesis, Technical University of Delft.

van Gelder, P. 2000. *Statistical Methods for Risk-Based Design of Civil Structure*. Ph.D. thesis, Technology University of Delft, The Netherlands.

Verruijt, A. 2010. *Soil mechanics*. Delft University of Technology.

Vrouwenvelder, A. & Steenbergen H. 2003. Theoriehandleiding pc-ring, versie 4.0. deel b: Statistische modellen. Technical report.

Geotechnical Safety and Risk IV – Zhang et al. (eds)
© 2014 Taylor & Francis Group, London, ISBN 978-1-138-00163-3

Effect of rainfall on the reliability of an infinite slope

J. Yuan, I. Papaioannou, C.M. Mok & D. Straub
Engineering Risk Analysis Group, Technische Universität München, Munich, Germany

ABSTRACT: Rainfall is one of the most common factors triggering landslides, since infiltration of water into the soil has a significant impact on pore water pressure buildup that affects slope stability. In this study, the influence of the wetting front development on the reliability of an infinite slope is analyzed. The failure condition of the slope is expressed in terms of the factor of safety. Rainfall infiltration is simulated by a time-dependent model, based on the Green and Ampt assumptions. The vertical variability of the saturated hydraulic conductivity and soil strength parameters are modeled as random fields. The reliability of the slope is evaluated by Monte Carlo simulation. A numerical example demonstrates the influence of the vertical variability on the analysis results.

1 INTRODUCTION

Rainfall has a considerable influence on landslide occurrence (Polemio 1997, Corominas et al. 2002, Zêzere et al. 2008). In wet seasons, intense rainfall events often cause shallow slope failure. In such cases, the failure surface is approximately parallel to the ground surface and hence an infinite slope model can be used to represent the slope failure mechanism (Wu & Abdel-Latif 2000, Santoso et al. 2011). Since surficial infiltration is predominately driven by gravitation, the infinite slope is often simplified in practice as a column subject to vertical infiltration, unless topography is very steep. It should be noted that some authors assumed that water percolates perpendicular to the sloping surface (Chen & Young 2006, Muntohar & Liao 2010).

In this paper, rainfall infiltration is modeled by applying the Green and Ampt assumptions for one-dimensional vertical subsurface flow (Green & Ampt 1911). Hence, it is assumed that the wetting front represents a clear border between the wetted and dry (in-situ condition prior to rainfall) soil zones. Further assuming that the water table is parallel to the ground surface, the infiltration model can be combined with the classical equation for infinite slope stability analysis to evaluate the time-dependent behavior of the factor of safety of the slope.

Soil property values tend to vary in space, even within a lithologic layer that appears to be homogeneous (Phoon & Kulhawy 1999). We model the inherent vertical variability of the strength parameters and saturated hydraulic conductivity as one-dimensional statistically homogeneous random fields. Through discretization of the random fields, the soil column is represented by a multilayered system whose layers have uniform parameters described by correlated random variables. Through Monte Carlo simulation, the statistics of the wetting front development and the slope factor of safety as well as the probability of failure of the slope are estimated. Moreover, the influence of the variability of the soil properties on the analysis results is investigated.

2 TIME-DEPENDENT MODEL

2.1 *Stability of infinite slope*

Consider a slice of an infinite slope, as shown in Figure 1. Assuming that the water table and potential slip surface are parallel to the ground surface, and according to the linear Mohr-Coulomb failure criterion, the factor of safety of the slip surface is defined as (Griffiths et al. 2011):

$$FS = \frac{(\gamma H \cos^2 \beta - u)\tan\varphi' + c'}{\gamma H \sin\beta\cos\beta} \tag{1}$$

in which, γ is the average unit weight of the soil mass above the slip surface; H is the depth of the slip surface; β is the slope inclination; u is the pore water pressure at the slip surface; φ' is the

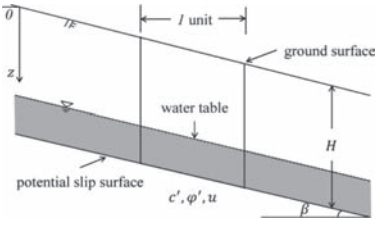

Figure 1. Typical unit slice from an infinite slope.

effective friction angle at the slip surface; c' is the effective cohesion at the slip surface.

2.2 *Stochastic model of soil parameters*

The stability of the slope depends on the shear strength of the soil at the slip surface, expressed in terms of the effective strength parameters c' and φ'. Moreover, the infiltration process, which affects the pore water pressure u during the wetting front development and the rise of the water table, is governed by the vertical saturated hydraulic conductivity K of the soil. In this study, we account for the variability of the tangent of the friction angle and the saturated hydraulic conductivity in the depth direction through a one-dimensional random field modeling.

The parameters are assumed to be log-normally distributed (Gelhar 1986). We model the natural logarithms of the parameters as homogeneous Gaussian random fields with the following exponential autocorrelation coefficient function:

$$\rho(\tau) = e^{-\frac{2\tau}{r}} \tag{2}$$

where r is the correlation length; τ is the separation between two locations in the vertical direction. The correlation length is a measure of the spatial variability of the random field. A correlation length that is much larger than the depth of the soil slice implies a uniform soil profile; in this case, the soil parameters can be modeled by random variables. In the extreme case where the correlation length is close to zero, the values of the soil parameters at each location become independent from each other.

The random fields are discretized by the midpoint method (Der Kiureghian & Ke 1988). The unit slice is divided into a number of equal layers; the randomized properties are assumed to be constant within each layer, represented by their values at the midpoints of the layers. Since homogenous fields are assumed, the mean u and standard deviation μ of the random variables corresponding to the discrete layers are constant over the entire field. The entries of the correlation matrix of the logarithms of the soil properties at each layer are evaluated with Equation (2) where τ is the distance between each pair of midpoints. Simulation of the soil parameters is performed by simulating the joint normal random variables of all layers and taking the exponential of the resulting samples. It is noted that the cross-correlation coefficient between the two parameters is set to zero in this study.

2.3 *Infiltration analysis*

We utilize the Green and Ampt assumptions to simulate the infiltration process (Green & Ampt 1911). That is, we assume that vertical infiltration causes a well-defined wetting front (see Fig. 2). Above the wetting front, the soil is fully saturated while below the wetting front it continues to have its initial moisture content.

The soil column is divided into a number of equal-thickness layers with varying saturated hydraulic conductivities as discussed in Section 2.2. We approach the problem by assuming that the wetting front development takes place in a stepwise manner, whereby the wetting front advances by one layer in each computational step. That is, in step j the wetting front is located at the bottom of the jth layer. For the sake of simplicity, the initial moisture content θ_0, soil porosity η and suction heat at wetting front S are considered to be constants within the unit slice.

This study focuses on short and intense rainfall events, during which the wetting front might not reach the water table. The infiltration process can be divided into two distinct phases (see Fig. 3): vertical infiltration during the rainfall period and plug flow driven by the saturated hydraulic conductivity of the soil until formation of the new ground water table.

During the rainfall period [Phase I, see Fig. 3(a)], the hydraulic gradient i from the ground surface to the wetting front at layer j along the vertical direction is obtained by application of Darcy's law:

$$i = \frac{z + S}{z} \tag{3}$$

where z is the depth of the wetting front at the bottom of the layer j; S is the suction head at the wetting front. Note that Equation (3) neglects the influence of the ponding water depth. We can then evaluate the infiltration rate f_{in} as follows:

$$f_{in} = K_e \cdot i \tag{4}$$

where K_e is the effective vertical saturated hydraulic conductivity, namely the harmonic mean of the vertical saturated hydraulic conductivities at the soil layers within the wetted zone (Freeze & Cherry 1979):

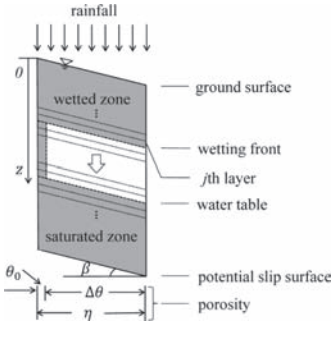

Figure 2. Green and Ampt model on the unit slice.

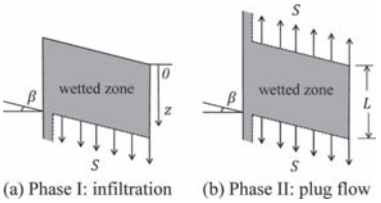

Figure 3. Infiltration process.

$$K_e = \frac{j}{\sum_{l=1}^{j} \frac{1}{K_l}} \tag{5}$$

in which K_l is the saturated hydraulic conductivity of each wetted computational layer.

We assume that the rainfall supply is larger than the infiltration capacity. Therefore the cumulative infiltration will be governed by the infiltration capacity and can be obtained by

$$F = z \cdot \Delta\theta \tag{6}$$

in which $\Delta\theta$ is the change in moisture content, given as follows:

$$\Delta\theta = \eta - \theta_0 \tag{7}$$

where η is the porosity of the soil and θ_0 is the initial moisture content (see Fig. 2). Noting that $f_{in} = dF/dt$, we can obtain the cumulative infiltration time as follows:

$$\int_0^t dt = \int_0^z \frac{\Delta\theta}{f_{in}} dz \tag{8}$$

The second phase that follows the rainfall event is governed by plug flow. It is assumed that the suction at the bottom of the wetted zone equals the one at the top [see Fig. 3(b)]. Therefore, the hydraulic gradient equals unity and the plug flow rate f_p equals the harmonic mean of the saturated hydraulic conductivities of the layers corresponding to the wetted zone:

$$f_p = K_e \tag{9}$$

Therefore, the time needed for the wetting front to reach the bottom of each layer is obtained as follows:

$$t = \begin{cases} \int_0^z \frac{\Delta\theta}{f_{in}} dz, & t \le T \\ T + \int_{z-L}^{z} \frac{\Delta\theta}{f_p} dz, & t > T \end{cases} \tag{10}$$

wherein T is the duration of the rainfall event; L is the length of wetting front exactly after rainfall stops [see Fig. 3(b)]. Equation (10) can be evaluated numerically over the computational layers as

$$t = \Delta z \cdot \Delta\theta \cdot \sum \frac{1}{f_j} \tag{11}$$

where Δz is the thickness of each layer; f_j is the flow rate at the jth computational step of either the infiltration or the plug flow phase depending on whether the time t is smaller or greater than the duration of the rainfall event T. Through Equation (11) we obtain a mapping between the cumulative time and the wetting front development.

2.4 *Pore water pressure distribution*

The pore water pressure varies with time and space within one unit slice. In this study, emphasis is on the pore water pressure within the wetted zone and below the water table.

Within the wetted zone, the spatial variability of the saturated hydraulic conductivity may introduce large hydraulic gradients that will result in variable pore water pressure. Employing the plug flow assumption given by the Green and Ampt infiltration model, we assume that the effective flow rate of the wetted zone f computed by Equations (4) and (9) equals the flow rate at each wetted layer (Liu et. al. 2008), i.e.

$$f_1 = f_2 = \ldots = f_l = \ldots = f \tag{12}$$

where f_l is the flow rate at wetted layer l, computed by

$$f_l = K_l \cdot i_l = K_l \cdot \frac{\Delta h_l}{\Delta z} \tag{13}$$

wherein i_l is the hydraulic gradient of layer l; Δh_l the change of hydraulic head within the lth layer. Combining Equations (12) and (13), we obtain:

$$\Delta h_l = \frac{f}{k_l} \cdot \Delta z \tag{14}$$

At the bottom of lth wetted layer, the hydraulic head h_l is obtained by summing the incremental heads Δh_k of each computational layer $k \le l$

$$h_l = h_0 - \sum_{k \le l} \Delta h_k \tag{15}$$

in which h_0 is the initial hydraulic head at the top of the wetted zone, i.e. $h_0 = 0$ during Phase I [Fig. 3(a)] and $h_0 = -z_0 - S$ during Phase II [Fig. 3(b)], where z_0 is the initial elevation head. Since the hydraulic head h_l consists of the pressure head ψ_l and the elevation z_l, the pressure head at the bottom of z_l th layer is evaluated as:

$$\psi_l = h_l - z_l \tag{16}$$

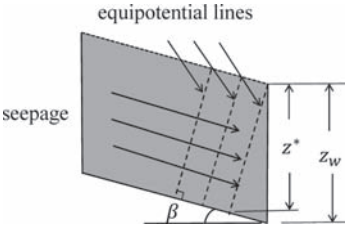

Figure 4. Hydrostatic pressure.

At the wetting front, the pressure head equals the suction head, i.e. $\psi_f = -S$. The pore water pressure can be computed as $u_l = \gamma_w \cdot \psi_f$, where γ_w is the unit weight of water.

Below the water table, the soil is subjected to hydrostatic pressure $u = \gamma_w z^* = \gamma_w z_w \cos^2\beta$, where z^* is the projection of the equipotential line in vertical direction; z_w is the depth of the soil layer under the ground water table (see Fig. 4). The hydrostatic water pressure builds up when the ground water elevation rises as the wetting front reaches the water table.

2.5 *Reliability analysis*

Slope failure occurs when the factor of safety FS is less than unity. Hence, the probability of failure of the slope is defined as

$$P_f = \Pr[FS < 1] \tag{17}$$

In this study, we estimate P_f by Monte Carlo simulation. Each realization of the random fields results in different values of the strength parameters and the saturated hydraulic conductivity at each soil layer. Based on the latter parameter value, we compute the pore water pressure distribution for each time step and each layer, as discussed in Section 2.4. We then substitute the strength parameters and pore water pressure into Equation (1) to obtain the factor of safety. Note that for each time step we evaluate the factor of safety for each potential slip surface, corresponding to the bottom of each layer. The overall factor of safety corresponds to the minimum value among all slip surfaces. The probability of failure for each time step is computed as the number of samples N_f for which FS is less than one divided by the total number of samples N:

$$P_f \approx \frac{N_f}{N} \tag{18}$$

3 EXAMPLE

We are interested in the slope stability for short and intense rainfall events. We consider a slope with a 5 m deep layer of sandy soil with zero cohesion c', subjected to a 24 h intense rainfall. The slope angle is taken as $\beta = 18°$. The tangent of the friction angle $\tan\varphi'$ and the saturated vertical hydraulic conductivity K are modeled as lognormal random fields (Table 1). The correlation length for the two parameters is identical and we assume a zero cross-correlation. The random fields are discretized into 100 layers. The water table is at a depth of 1.5 m below the ground surface. The parameter of the Green and Ampt model for sandy soil are taken from Rawls (1982) as given in Table 2. The number of Monte Carlo samples is set to 10^4, which was found to give acceptable coefficient of variations of the probability estimates for the cases considered.

3.1 *Influence of the correlation length*

The analysis is performed for two values of the correlation length r, that is 2 m and 0.5 m. Figure 5 presents the development of the mean depth of the wetting front with time. The time period of interest is 240 hr (10 days) after the start of the rainfall event.

Figure 5 shows that in the case of a smaller correlation length, the water flow will move slower towards the water table. This can be explained by the fact that a small correlation length implies a large variability within the wetted zone. The flow within the wetted zone is driven by the lower values of K, as evident from the use of the harmonic mean of the saturated hydraulic conductivity in Eq. (5); the higher the variability, the larger the likelihood of occurrence of low values.

Figure 6 shows the mean factor of safety of the slope with time. As also discussed in (Griffiths et al. 2011), the initial mean factor of safety is smaller for a smaller correlation length. A large correlation length implies a uniform soil profile and thus the most critical potential slip surface is at the base of the slope. On the other hand, a small correlation

Table 1. The values and distributions of the input variables.

Variable	Distribution	Mean μ	CV*
$\tan\varphi'$	Lognormal	0.7002	0.1
K [m/h]	Lognormal	3.6×10^{-3}	2

*CV stands for coefficient of variation (= σ/μ).

Table 2. Parameters for Green and Ampt model.

Variable	η	θ_0	S [m]
Value	0.437	0.102	0.1734

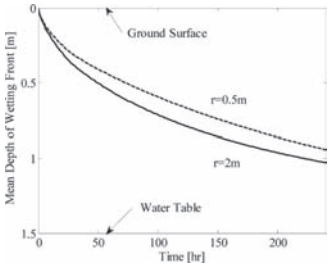

Figure 5. Development of the mean wetting front depth.

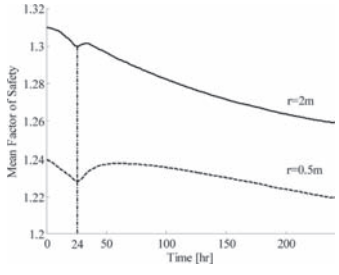

Figure 6. Influence of the correlation length on the factor of safety.

length implies vertically variable parameters and weak layers are likely to be present in most Monte Carlo realizations. The most-critical potential slip surface will likely occur in a weak layer, which will be present at a different location in each realization.

Since the pore water pressure increases due to the wetting front development, the mean factor of safety then decreases during the infiltration procedure for both cases. A faster decrease is observed for the case of the larger correlation length, since the water flow moves faster towards the water table, which causes a rise of the hydrostatic pressure.

During the rainfall event period, the mean factor of safety decreases rapidly and it reaches a transient lower value when rainfall stops. The reduction is higher for the case with a small correlation length, which implies that the likelihood of shallow slope failure is higher. A small correlation length introduces changes between large and small values of the hydraulic conductivity occurring at short distances within the wetted zone. Higher hydraulic gradients occur across the layers with low hydraulic conductivity values causing higher pressure to be built up immediately above such layers within the wetted zone. Therefore, a smaller correlation length will increase the likelihood of slip surfaces at intermediate layers above the wetting front.

After the rainfall event, the water flow transforms to plug flow [Phase II in Fig. 3(b)] and the mean factor of safety increases, since the likelihood of shallow slope failure decreases. Slope failure is now driven by the formation of the new ground water elevation that takes place when the wetting front reaches the water table. This happens faster in the case of a larger correlation length and hence the decrease of the mean factor of safety is larger in this case. A small correlation length implies that layers with low hydraulic conductivity exist in most realizations and these layers imped downward movement of infiltration water.

Figure 7 depicts the transient evolution of the point-in-time probability of failure for the two considered correlation lengths. The initial probability of failure is higher when the correlation length is smaller, which corresponds to a smaller mean factor of safety. For this case, the probability of failure increases during the rainfall event, only to decrease again until the wetting front approaches the ground water table where the probability rises once more. The case corresponding to a larger correlation length presents a different behavior: During the rainfall event, shallow slope failure will mostly occur at the wetting front as there is no localized layer with lower relative hydraulic conductivity value that impedes infiltration and leads to pore-pressure building up within the wetting front. The wetting front will move faster towards the water table and hence the likelihood that the water table is reached within one realization is higher. This results in a smooth increase of the probability of failure in terms of time since the failure will be governed by the rise of the hydrostatic pressure.

3.2 *Influence of the coefficient of variation*

We now look at the influence of the coefficient of variation of the hydraulic conductivity on the stability and probability of slope for the case of a small correlation length (0.5 m); the coefficient of variation is varied from 1 to 3. Figures 8 and 9 show the change of the mean factor of safety and the probability of failure with time.

Increasing the coefficient of variation will increase the variability within the wetted zone,

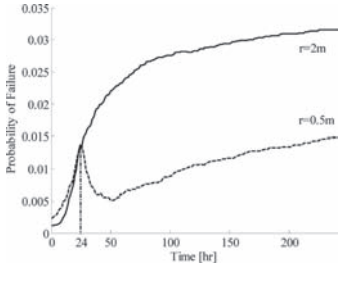

Figure 7. Influence of the correlation length on the probability of failure.

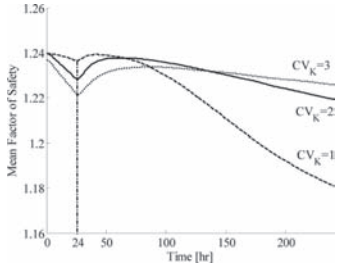

Figure 8. Influence of the coefficient of variation of the saturated hydraulic conductivity on the factor of safety for $r = 0.5$ m.

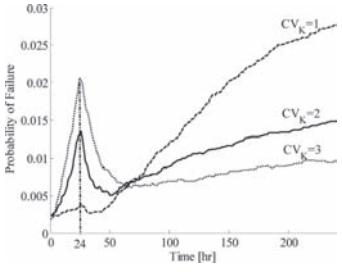

Figure 9. Influence of the coefficient of variation of the saturated hydraulic conductivity on the probability of failure for $r = 0.5$ m.

which will cause the wetting front to move slower towards the water table and therefore failure will be governed by shallow slip surfaces. Moreover, a large coefficient of variation leads to steeper changes between small and large values of the hydraulic conductivity within the wetted zone; hence the pore water pressure at layers above the wetted zone increases, which leads to a larger probability of shallow slope failure and smaller corresponding mean factors of safety.

4 CONCLUSION

In this paper, we developed a simplified time-dependent model to study the reliability of slopes subjected short-term and intense rainfall events. The model incorporates infinite slope stability analysis, one-dimensional infiltration analysis based on the Green and Ampt assumptions as well as a random field modeling of the effective friction angle and the saturated hydraulic conductivity of the soil. An example demonstrated the influence of the correlation length and coefficient of variation of the hydraulic conductivity on the development of the factor of safety and probability of failure with time. It is shown that a small correlation length and high coefficient of variation will favor shallow slope failure due to the decrease of the infiltration rate and the development of large pressure gradients within the wetted zone. In the cases with large correlation lengths and small coefficient of variation, the reliability is dominated by the rise of the hydrostatic pressure due to the fast wetting front development.

REFERENCES

Chen L. & Young M.H. 2006. Green-Ampt infiltration model for sloping surface. *Water Resources Research* 42(7): W07420.

Corominas, J., Moya, J. & Hürlimann, M. 2002. Landslide rainfall triggers in the spanish eastern pyrenees. *Proc. 4th EGS Plinius Conference*. Mallorca, Spain.

Der Kiureghian, A. & Ke, J.-B. 1988. The stochastic finite element method in structural reliability. *Probabilistic Engineering Mechanics* 3(2): 83–91.

Freeze, A.R. & Cherry, J. A. 1979. *Groundwater*. Upper Saddle River, NJ: Prentice Hall.

Gelhar L.W. 1986. Stochastic subsurface hydrology from theory to application, *Water Resources Research* 22(9): 135–145.

Green, W. H. & Ampt, G. A. 1911. Studies on soil physics, part I—the flow air and water through soils. *Journal of Agricultural Science* 4(1): 1–24.

Griffiths, D.V., Huang, J. & Fenton, G.A. 2011. Probabilistic infinite slope analysis. *Computers and Geotechnics* 38(4): 577–584.

Liu J. T., Zhang J. B. & Feng J. 2008. Green–Ampt Model for Layered Soils with Nonuniform Initial Water Content Under Unsteady Infiltration. *Soil Science Society of America Journal* 72(4): 1041–1047.

Muntohar, A.S. & Liao H. 2010. Rainfall infiltration: infinite slope model for landslides triggering by rainstorm. *Natural Hazards* 54(3): 967–984.

Phoon, K.K. & Kulhawy, F.H. 1999. Characterization of geotechnical variability. *Canadian Geotechnical Journal* 36(4): 612–624.

Polemio, M. 1997. Rainfall and Senerchia landslides, southern Italy. *Proc. 2nd COBRAE, Rio de Janeiro*.

Rawls, W.J., Brakensiek, D.L. & Saxton, K.E. 1982. Estimation of soil water properties. *Transactions of the ASAE* 25(5): 1316–1320 & 1328.

Santoso, A.M., Phoon, K., & Quek, S. 2011. Effect of 1D Infiltration Assumption on Stability of Spatially Variable Slope. *Geo-Risk 2011: Risk Assessment and Management*. 704–711.

Wu, T.H. & Abdel-Latif, M.A. 2000. Prediction and mapping of landslide hazard. *Canadian Geotechnical Journal* 37(4): 579–90.

Zêzere, J.L. Trigo, R.M. & Fragoso, M., Oliveira, S.C. & Garcia, R.A.C. 2008. Rainfall-triggered landslides in the Lisbon region over 2006 relationships with the north Atlantic Oscillation. *Natural Hazards and Earth System Science* 8(3): 483–499.

Geotechnical Safety and Risk IV – Zhang et al. (eds)
© 2014 Taylor & Francis Group, London, ISBN 978-1-138-00163-3

Influence of particle transport on slope stability under rainfall infiltration

L. Zhang & L.L. Zhang
Department of Civil Engineering, Shanghai Jiaotong University, Shanghai, China

ABSTRACT: Internal erosion and transport of fine particles are among the possible consequences of the infiltration of rainwater into a slope. The transport of fine particles may lead to local variation of soil porosity and hydraulic properties, which affects the stability of a soil slope under rainfall infiltration. In this study, the governing equation for transport of fine particles based on the conservation of mass of moving particles is coupled with the governing equation of transient seepage analysis for unsaturated soils. An internal erosion law is used to describe the relationship between the rate of eroded fine particles and the hydraulic gradient. The effect of internal erosion on change of porosity and saturated permeability is also considered. The influence of transport of fine particles on slope stability under infiltration is investigated by a finite-element analysis. The numerical results show that the rainfall infiltration can induce reduction of the density of fine particles in the shallow depth of soil slope. This can further increase the permeability and water seepage in the slope and the slope stability is reduced consequently. A parametric study is also conducted to investigate the effect of saturated coefficient of permeability on water seepage and slope stability.

1 INTRODUCTION

Slopes in natural terrain are usually composed with mixed coarse and fine particles due to deposition or weathering process. In-situ full scale and laboratory reduced scale model tests showed that under rainfall infiltration internal erosion may occur in zones with dramatic changes of seepage gradient and fine particles were observed to be transported from the upper and surface part of the slope to the toe of slope (Hu et al. 2005, Jian et al. 2005, Xu et al. 2006). When transport of fine particles occurs in a slope, the porosity and permeability may increase due to loss of fine particles. This may further lead to variation of water flow or movement of wetting front and affect the slope stability during infiltration.

Some researchers investigated particle transport in porous media. Vardoulakis et al. (1996) established a one-dimensional model of internal erosion based on mass conservation law of multiphase fluid. Sterpi (2003) developed a constitutive equation for internal erosion based on soil column tests and performed numerical analyses for internal erosion in saturated soils. Dahaghi et al. (2011) described variation of permeability coefficient considering transport and deposition of fine particles based on the conservation of mass. These studies focus on internal erosion in fully saturated soil. However, the influences of internal erosion and particle transport on unsaturated soil slope under rainfall infiltration have not been investigated. In this study, a coupled model of seepage and internal erosion in unsaturated soil is developed. The variation of porosity due to particle transport is considered. A parametric study is conduced to investigate the effect of saturate coefficient of permeability on pore water pressure distribution and slope stability.

2 SLOPE STABILITY ANALYSIS BASED ON COUPLED ANALYSIS OF SEEPAGE AND INTERNAL EROSION

2.1 *Mass-balance equations of internal erosion*

The soil is regarded as a mixture of solid and liquid which consists of the soil skeleton phase, water phase and liquefied particle phase. Liquefied particles are fine particles which are scoured by internal erosion from the soil skeleton and can move freely with water.

The liquefied fine particles satisfy mass conservation equation (Cividini & Gioda 2004, Vardoulakis & Papamichos 2005):

$$\frac{\partial \rho_{tr}}{\partial t} + div(\rho_{tr} v_i) = q_{er} \tag{1}$$

where ρ_{tr} = density of liquefied fine particles; v_i = velocity of water flow in i direction; q_{er} = volume flux of fine particles eroded. As v_i is equal to q_i/n, where q_i is Darcy velocity in i direction and n is porosity, the above equation can be written as follows:

$$\frac{\partial \rho_{tr}}{\partial t} + \frac{\partial}{\partial x}\left(\rho_{tr}\frac{q_x}{n}\right) + \frac{\partial}{\partial y}\left(\rho_{tr}\frac{q_y}{n}\right) = q_{er} \tag{2}$$

The mass conservation of soil skeleton phase can be expressed as (Vardoulakis & Papamichos 2005):

$$\frac{\partial \rho_{sk}}{\partial t} + div(\rho_{sk} v_i^{sk}) = -q_{er} \tag{3}$$

where ρ_{sk} = density of soil skeleton; v_i^{sk} = velocity of soil skeleton. The density of soil skeleton ρ_{sk} is equal to $(1\text{-}n)\rho_s$, where ρ_s is the density of soil particles. The velocity of soil skeleton phase can be assumed to be zero:

$$v_i^{sk} = 0 \tag{4}$$

Therefore, the governing equation of porosity can be obtained as follows:

$$\frac{\partial n}{\partial t} = \frac{q_{er}}{\rho_s} \tag{5}$$

2.2 *Governing equation of unsaturated flow*

The flow of water through soil is governed by the mass conservation law and Darcy's law. According to the Darcy's law, the fluid flow can be written in terms of hydraulic conductivity and hydraulic gradient as follows:

$$q_i = k_i \nabla H \tag{6}$$

where k_i = hydraulic conductivity in i direction; q_i = Darcy velocity; H = total head.

Based on the mass conservation law and the Dary's law, the governing equation for two-dimensional water flow in an unsaturated soil can be written as (Fredlund & Rahardjo 1993):

$$\frac{\partial}{\partial x}\left(k_x \frac{\partial H}{\partial x}\right) + \frac{\partial}{\partial y}\left(k_y \frac{\partial H}{\partial y}\right) = \frac{\partial \theta_w}{\partial t} \tag{7}$$

where k_x = hydraulic conductivity in x direction of the flow; k_y = hydraulic conductivity in y direction of the flow; θ_w = volumetric water content.

2.3 *Constitutive equation of internal erosion*

The constitutive equation of internal erosion describes the process in which the water phase transforms the fine particles into liquefied particle phase by erosion (Cividini & Gioda 2004):

$$q_{er}(t,v) = \beta_{er} v[\rho_f(t) - \rho_{f\infty}(v)] \tag{8}$$

where ρ_f = density of fine particle in soil; $\rho_{f\infty}$ = ultimate or long term density of fine particle; β_{er} = a parameter of erosion.

The ultimate or long term density of fine particle is a function of the flow velocity:

$$\rho_{f\infty}(v) = \begin{cases} \rho_{f0} - (\rho_{f0} - \rho^*_{f\infty})v/v^* & 0 \le v(t) \le v^* \\ \rho^*_{f\infty} - \alpha_{er}\log(v/v^*) & v^* \le v(t) \end{cases} \tag{9}$$

where v^* = initial flow velocity; ρ_{f0} = initial density of fine particles; $\rho^*_{f\infty}$ = the long term density corresponding to v^*; α_{er} = a parameter of erosion.

2.4 *Hydraulic functions of unsaturated soil*

In an unsaturated soil, water content and permeability are related with matric suction. The relation between volumetric water content θ_w and matric suction is named as Soil Water Characteristic Curve (SWCC). The relation between the coefficient of permeability and matric suction is called the permeability function. In this study, the Van Genuchten model is adopted:

$$S_r = \frac{\theta_w - \theta_r}{\theta_s - \theta_r} = \begin{cases} \dfrac{1}{\left[1 + \left[\alpha_w(u_a - u_w)\right]^{n_w}\right]^{m_w}} & u_w < 0 \\ 1 & u_w \ge 0 \end{cases} \tag{10}$$

where S_r = degree of saturation; θ_s = saturated volumetric water content; θ_r = residual volumetric water content; α_w = a curve fitting parameter inversely related to the air-entry value; n_w = a curve-fitting parameter related to the pore size distribution; $m_w = 1\text{–}1/n_w$; u_a = pore-air pressure; u_w = pore-water pressure; $(u_a - u_w)$ = matric suction.

In this paper, the unsaturated coefficient of permeability k is described as an exponential function of the matric suction (Gardner 1958):

$$k = k_s \exp[-\alpha_w(u_a - u_w)] \tag{11}$$

where k_s = saturated coefficient of permeability.

Based on the Carman-Kozeny equation, the saturated coefficient of permeability is defined as a function of porosity:

$$k_s = \frac{n^3}{(1-n)^2} \times \frac{(1-n_0)^2}{n_0^3} k_{s0} \quad (12)$$

where n_0 = initial porosity; k_{s0} = initial saturated coefficient of permeability corresponding to n_0.

2.5 *Numerical implementation*

In this study, a finite element model for the coupled governing equations [Eqs. (2), (5), and (7)] is developed in the commercial multiphysics modeling finite element program, COMSOL. In COMSOL, the Galerkin method is used to discretize the PDEs. A nonlinear differential algebraic equation solver IDA which was created by the Lawrence Livermore National Laboratory (Hindmarsh et al. 2005) is used as a time integrator for the differential algebraic system, in which the backward differentiation formulas are used to discretize the time derivative terms. As the time stepping scheme is implicit, the damped Newton method (Deuflhard 1974) is then used to solve the resulting nonlinear equations. Within each step of the Newton iteration, the most recently updated nodal values of the dependent variables are used to compute nonlinear coefficients. The nonlinear iteration at each time step is continued until the numerical solutions satisfy prescribed convergence criteria.

2.6 *Slope stability analysis*

Since slope failures induced by rainfall infiltration are usually shallow, the use of infinite slope stability analysis for the evaluation of rainfall-induced landslides is justified (Zhang et al. 2010, Santoso et al. 2011). The method used in traditional infinite slope analysis must be modified to take into account the variation of the pore water pressure profile that results from the infiltration process.

For an infinite slope with seepage parallel to the slope surface, the safety factor for the slip surface at depth h (Fig. 1) is:

$$F_s = \frac{c'}{\gamma_t h \sin\beta\cos\beta} + \frac{\tan\phi'}{\tan\beta} - \frac{h_p \gamma_w \tan\phi^b}{\gamma_t h \tan\beta} \quad (13)$$

where β = slope angle; γ_t = total unit weight of the soil; c' = effective cohesion; ϕ' = effective friction angle; h_p = pore pressure head; γ_w = unit weight of water; ϕ^b = angle indicating the rate of increase in shear strength related to matrix suction. The value of ϕ^b is generally dependent on the range of matric suction and is close to the effective friction of soil at low suction (Cho & Lee 2002).

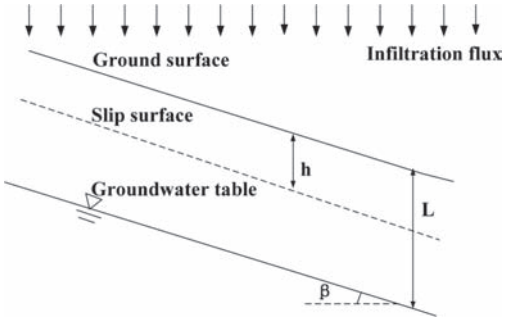

Figure 1. Typical infinite slope under rainfall infiltration.

3 AN ILLUSTRATIVE EXAMPLE

3.1 *Finite element model*

Figure 2 shows the finite element model of a hypothetical slope with a slope angle β of 35°. The slope length L is 17.5 m and the height H is 6 m. The slope is composed of residual soils. The finite element model is composed of 420 quadrilateral elements. The initial groundwater table is along BC. The initial density of liquefied fine particles is zero.

3.2 *Boundary conditions*

The boundary conditions and initial conditions for seepage and internal erosion are defined as follows. The velocity of liquefied particle phase flow is zero along the AB, BC and AD boundaries. CD boundary is free for flow of liquefied particle.

For rainfall infiltration, AB, BC and CD are fixed water level. Assume the rainfall intensity is q, the infiltration flux along the boundary AD is defined as follows.

$$flux = m_N(u_w)q + m_b(u_w)R_b(-u_w/\gamma_w) \quad (14)$$

where $flux$ = infiltration flux; m_N, m_b = complementary smoothing functions (Fig. 3); R_b = external resistance; q = rain intensity. When the pore water pressure along the slope surface AD is negative, the infiltration flux is equal to rainfall intensity q. When the pore water pressure along the slope surface AD is positive, the infiltration flux is negative to guarantee no accumulation of water available on top surface (Chui & Freyberg 2009).

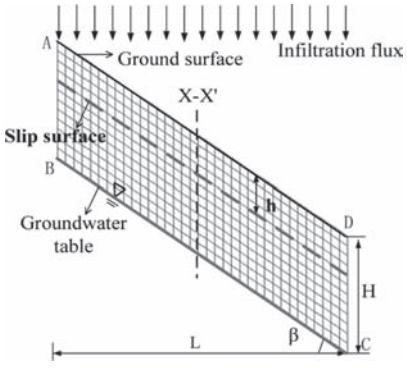

Figure 2. Finite element model of the illustrative example.

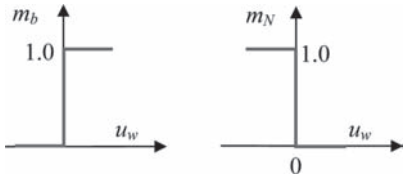

Figure 3. Function m_N and m_b.

Table 1. List of parameters for the case study.

Parameters	Value	Parameters	Value
ρ_{f0}/ρ_t	0.2	θ_r	0
$\rho^*_{f\infty}/\rho_t$	0.193	θ_s	0.395
ρ_s/ρ_t	1.184	k_{s0} (m/s)	2×10^{-5}
v^* (m/s)	3.6×10^{-7}	k_x (m/s)	k_y
α_{er}	4.76	α_w	0.2
β_{er}	6.95×10^{-3}	n_w	1.35
g (m/s^2)	9.81	β (°)	35
n_0	0.25	ϕ' (°)	34
R_b	10^3	c' (kPa)	2
q (m/s)	2×10^{-5}	ϕ^b (°)	25

3.3 *Soil parameters*

Assume the content of fine particles in the residual soil is 20%. If sufficient time is allowed, the erosion process will completely remove the fine particles ($\rho_{f0} \rightarrow \rho^*_{f\infty}$). In fact, the theoretical time necessary to complete the erosion becomes exceedingly large when the gradient value is within the range met in practical applications (Sterpi 2003). So $\rho^*_{f\infty}$ is taken about 95% of ρ_{f0}, 19.3%. The density of soil particles is 1.184 times the total density ρ_t. The values of parameters are summarized sin Table 1 (Santoso et al. 2011, Cividini & Gioda 2004).

4 RESULTS AND DISCUSSION

4.1 *Effect of internal erosion*

To analyze the influence of internal erosion on the slope stability, the results of coupled seepage with internal erosion are compared with the results of seepage analysis without considering internal erosion.

As shown in Figure 4, after 2 hours of rainwater infiltration, the depth of the wetting front is 1.4 m when considering the internal erosion. The depth of the wetting front is 1.2 m when neglecting the internal erosion. After 6 hours of rain, the depth of the wetting front is 3.5 m with internal erosion and is about 3.0 m without internal erosion. After 10 hours of rainfall, the slope is fully saturated with internal erosion.

Figure 5 shows the variation of fine particle content and porosity along cross-section X-X′. It can be seen that the decrease of fine content in soil and the increase of porosity corresponds to the advance of wetting front. Internal erosion occurs mainly in the shallow depth of the slope. The concentration of fine particles increases with depth and slightly decreases around the groundwater table. Correspondingly, the porosity decreases with depth and slightly increases around the groundwater table. The increase of porosity around ground water table is mainly because when the soil is fully saturated the flow velocity is large enough to transport the fine particles based on the constitutive model of transport in Eq. (9). Therefore, the transport of fine particles can occur in both the unsaturated zone within wetting front and the saturated zone.

Figure 6 shows the safety factor of slope along various depth of slip surface. It can be seen that the

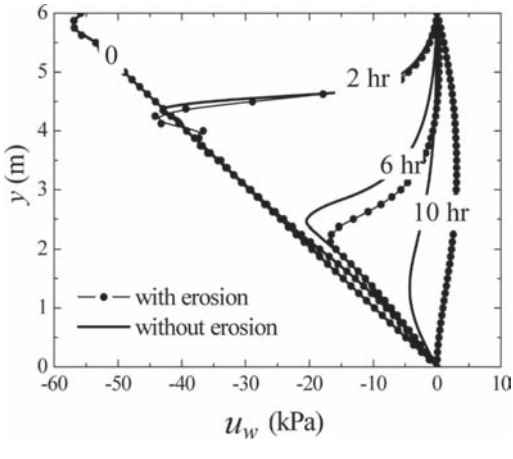

Figure 4. Variation of pore-water pressure profile along cross-section X-X′ ($k_{s0} = 2 \times 10^{-5}$ m/s).

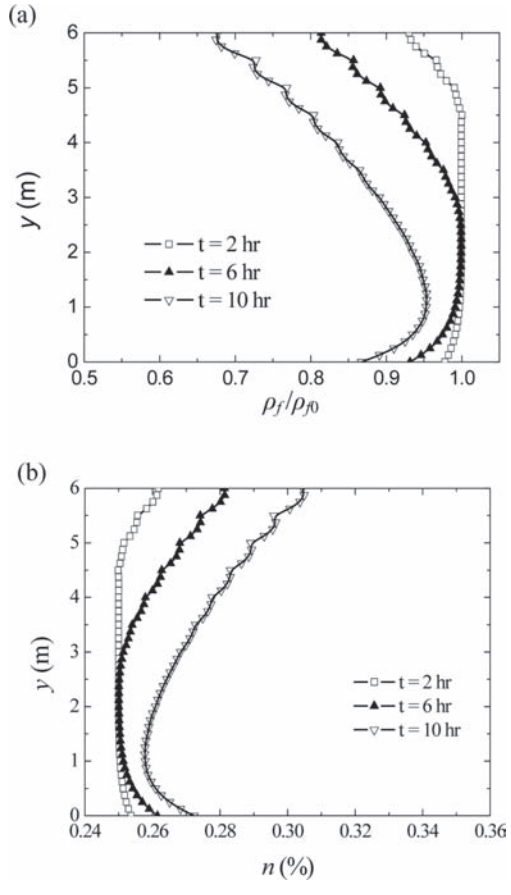

Figure 5. Variation of (a) fine particle content ρ_f/ρ_{f0} and (b) porosity with time along cross-section X-X′ ($k_{s0} = 2 \times 10^{-5}$ m/s).

soil slope reaches an unstable state more rapidly when considering the internal erosion. After 6 hours of rainwater infiltration, the depth of slip surface for a slope without erosion is around 1.5 m. However, for a slope with erosion, the critical slip surface is around 2.5 m. It implies that the consequence of a landslide may be more severe with erosion effect.

4.2 *Effect of k_{s0}*

To investigate the effect of saturated coefficient of permeability, a parametric study with different values of initial saturated coefficient of permeability k_{s0}, 5×10^{-6}, 2×10^{-5} and 8×10^{-5} m/s is conducted. The rainfall intensity is the same value, 2×10^{-5} m/s for the three cases.

Figure 7 shows that before 6 hours of rainfall the internal erosion has slight effect on pore water pressure profile and advance of wetting front for the case with k_{s0} equal to 5×10^{-6} m/s. After 6 hours, the advance of wetting front becomes faster as time increases. Figure 8 illustrates the safety factor profiles with different times. It also shows that after 6 hours the effect of internal erosion on slope stability becomes more significant.

Figure 9 presents the pore water pressure profiles when k_{s0} is equal to 8×10^{-5} m/s. It can be seen that as the saturated permeability is greater than the rainfall intensity, the slope will not be fully saturated. The internal erosion and transport of fine particles have little effect on pore water pressure distributions.

Comparing Figure 4 with Figures 7 and 9, it can be seen that when the rainfall flux is equal or greater than the saturated coefficient of permeability ($q/k_s \geq 1$), the influence of internal erosion on water infiltration and slope stability is more significant.

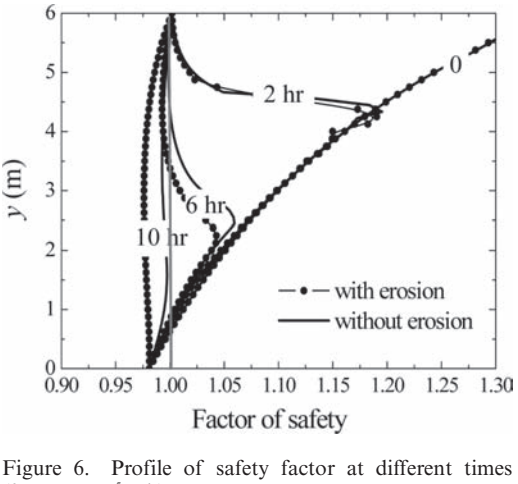

Figure 6. Profile of safety factor at different times ($k_{s0} = 2 \times 10^{-5}$ m/s).

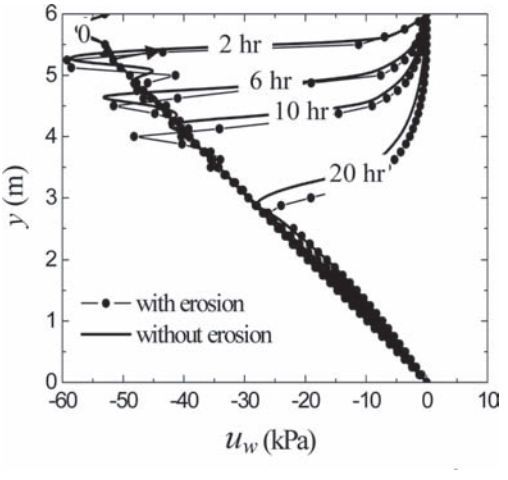

Figure 7. Pore-water pressure profiles ($k_{s0} = 5 \times 10^{-6}$ m/s).

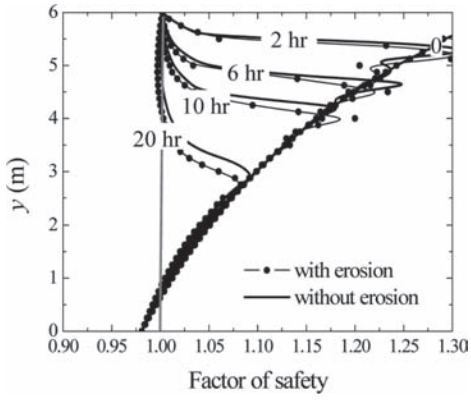

Figure 8. Profiles of factor of safety ($k_{s0} = 5 \times 10^{-6}$ m/s).

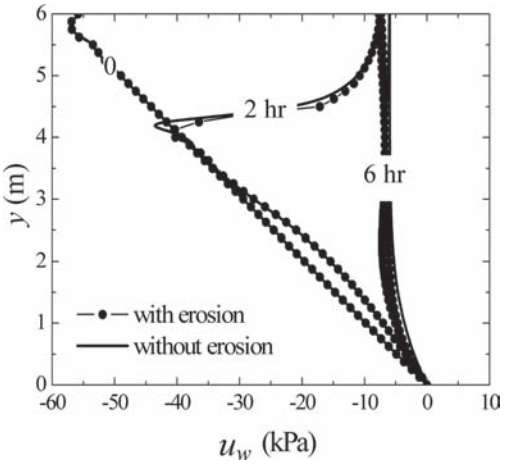

Figure 9. Pore-water pressure profiles ($k_{s0} = 8 \times 10^{-5}$ m/s).

5 CONCLUSIONS

In this study, a coupled model of seepage and internal erosion in unsaturated soil is established to investigate internal erosion on water infiltration and slope stability. The major conclusions are following:

1. The soil porosity increases with the advance of water front and process of internal erosion. The advance of wetting front in the slope is more rapid and the slope reaches an unstable state more quickly due to internal erosion.
2. With the effect of internal erosion, the slip surface of failure is deeper, which implies that the consequence of a landslide may be more severe with erosion.
3. When the rainfall flux is equal or greater than the saturated coefficient of permeability ($q/k_s \geq 1$), the influence of internal erosion on water infiltration and slope stability is more significant.

REFERENCES

Cho, S.E. & Lee, S.R. 2002. Evaluation of surficial stability for homogeneous slopes considering rainfall characteristics. *Journal of Geotechnical and Geoenvironmental Engineering* 128(9): 756–763.

Chui, T.M. & Freyberg, D.L. 2009. Implementing hydrologic boundary conditions in a multiphysics model. *Journal of Hydrologic Engineering* 14(12): 1374–1377.

Cividini, A. & Gioda, G. 2004. Finite element approach to the erosion and transport of fine particles in granular soils. *International Journal Geomechanics* 3(4): 191–198.

Dahaghi, A.K. Gholami, V. & Moghadasi, J. 2011. A novel workflow to model permeability impairment through particle movement and deposition in porous media. *Transport in Porous Media* 86(3): 867–879.

Deuflhard, P. 1974. A modified Newton method for the solution of ill-conditioned systems of nonlinear equations with application to multiple shooting. *Numerische Mathematik* 22(4): 289–315.

Fredlund, D.G. & Rahardjo, H. 1993. *Soil mechanics for unsaturated soils*. Wiley, New York.

Gardner, W.R. 1958. Steady state solutions of the unsaturated moisture flow equationwith application to evaporation from a water table. *Soil Science* 85(4): 228–232.

Hindmarsh, A.C. Brown, P.N. Grant, K.E. Lee, S.L. Serban, R. & Shumaker, D.E. 2005. Woodward CS. SUNDIALS: Suite of Nonlinear and Differential/ Algebraic Equation Solvers. *ACM Transactions on Mathematical Software* 31(3): 363–396.

Hu, M.J. Wang, R. Meng, Q.S. & Liu, G.S. 2005. Research on erosion process and features of loose gravelly soil slope. *Rock and Soil Mechanics* 26(11): 1722–1726 (in Chinese).

Jian, B.T. Lu, X.B. Wang, S.Y. Chen, X.Q. & Cui, P. 2005. The movement of fine grains and its effects on the landslide and debris flow caused by raining. *Chinese Journal of Underground Space and Engineering* 1(7): 1014–1016 (in Chinese).

Papamichos, E. & Vardoulakis, I. 2005. Sand erosion with a porosity diffusion law. *Computers and Geotechnics* 32(1): 47–58.

Santoso, A.M. Phoon, K.K. & Quek, S.T. 2011. Effects of soil spatial variability on rainfall-induced landslides. *Computers and Structures* 89(11–12): 893–900.

Sterpi, D. 2003. Effects of the erosion and transport of fine particlesdue to seepage flow. *International Journal Geomechanics* 3(1/2): 111–122.

Vardoulakis, I. Stavropoulou, M. & Papanastasiou, P. 1996. Hydro-mechanical aspects of the sand production problem. *Transport in Porous Media* 22(2): 225–244.

Xu, J.C. & Shang, Y.G. 2006. Influence of permeability of gravel soil on debris landslide stability. *Chinese Journal of Rock Mechanics and Engineering* 25(11): 2264–2271 (in Chinese).

Zhang, L.L. Zhang, J. Zhang, L.M. & Tang, W.H. 2010. Stability analysis of rainfall-induced slope failure: a review. *Geotechnical Engineering* 164(5): 299–316.

7 *Reliability- and risk-based monitoring and site investigation*

This page intentionally left blank

Geotechnical Safety and Risk IV – Zhang et al. (eds)
© 2014 Taylor & Francis Group, London, ISBN 978-1-138-00163-3

Effect of inadequate site investigation on the cost and time of a construction project

A.H. Albatal
Arab Academy for Science, Technology and Maritime Transport, Cairo, Egypt

H.H. Mohammad
Zagazig University, Zagazig, Egypt

M.E. Abd Elrazik
Arab Academy for Science, Technology and Maritime Transport, Cairo, Egypt

ABSTRACT: The appropriate information or data is the keystone of any successful design. Site investigation is one of the first steps of any construction projects. The purpose of a soil subsurface investigation is to provide data concerning the engineering properties of the soil for the proper design and safe construction of a project. The site investigation phase of any geotechnical design plays a vital role to provide the geotechnical engineer by the most appropriate data to ensure that the design data represent the investigated soil. Inadequate soil investigation may contribute to either a significantly over designed foundations, that is not cost-effective, or an under designed foundations, which may lead to potential failures. Insufficient geotechnical investigation is one of first sources of projects' delays, disputes, claims, and projects' cost overruns. This paper aims to focus on the impact of varying the scope of the site investigation process, on the financial risk of construction projects. Another goal is to compare the cost of extra site investigation with the repairing or reconstruction cost result from improper site investigation. The results of limited site investigation scope are clearly shown in a recycling factory at the 6th of October city governorate, Egypt, which suffer from cost overrun and long delays. The apparent savings due to making inadequate site investigation leads to cost overrun by about 64.2% of the project cost.

1 INTRODUCTION

Site investigation is normally carried out prior to the commencement of design of any project. Due to lack of or inadequacy of guide/code requirement regarding the extent as well as quality of site investigation work, geotechnical failures often occurred. These failures sometime lead to catastrophic disaster and imposed serious threat to public safety (Moh, 2004).

Baecher & Christian (2003) divided the characterization of ground conditions into two phases. First is a preliminary investigation or desk study, which involves collecting information about the regional geology and geological history. The second phase is a site investigation designed to obtain data based on detailed measurements of soil properties. As a result, the geotechnical data obtained from limited characterization of ground conditions can be both inadequate and/or inappropriate. This situation can lead to failure and a high level of financial and technical risk (Institution of Civil Engineers 1991, National Research Council 1984, Temple & Stukhart 1987).

Several studies have been published over the last 30 years or so that clearly demonstrate that, in civil engineering projects, the largest element of financial and technical risk usually lies in the ground (National Research Council 1984, Institution of Civil Engineers 1991, Whyte 1995).

Goldsworthy *et al.* (2007) defined the financial risk as the total cost, which includes costs associated with undertaking the site investigation, constructing, and any works required to rehabilitate the failure. Goldsworthy *et al.* (2004) mentioned that the risk of a foundation failure is heavily dependent on the quantity and quality of information obtained from a geotechnical site investigation aimed at characterizing the underlying soil conditions. Project risk is a measure of the potential inability to achieve overall project objectives within defined cost, time schedule, quality, environmental impact and technical constraints and can be estimated as the combination of the probability of a risk event occurring and its consequences for project objectives (Carlsson, 2005).

Jaksa *et al.* (2005) suggested that the site investigations that inadequately quantify the variability

of the ground can result in three possible cost outcomes:

a. The foundation is underdesigned as a result on an overly optimistic geotechnical model, and hence fails to comply with the design criteria, which can ultimately lead to some level of structural distress.
b. The foundation is overdesigned as a consequence of a pessimistic geotechnical model and/or inherent conservatism in the design process.
c. Unforeseen conditions require substantial changes to the foundation system, which also result in construction delays.

It is clear that over the last 30 years geotechnical investigation prices have been driven down, with the scope often being governed by minimum cost and time of completion (Institution of Civil Engineers 1991). As a consequence, the Institution of Civil Engineers concluded that: "*You pay for a site investigation whether you have one or not*."

The UK public accounts committee states that the average cost increase for major road projects (1988–1989) was 28% over original tender prices. The main reason was judged to be the undertaking of larger and more complex schemes that involved greater risks, particularly with ground conditions.

Despite the level of sophistication available for the determination of risk and uncertainty associated with ground work operations, a review of 5000 industrial building projects by the National Economic Development Office in the UK (NEDO, 1983) showed that 37% of the projects suffered delays due to ground related problems. When 8000 commercial buildings were examined, 50% of the samples were found to have suffered unforeseen ground difficulties (NEDO, 1988). The financial scale of the problem was confirmed by the National Audit Office (1994), in a report that recorded 210 premature failures during construction works, and that geotechnical failures were a major concern. Alhalby & Whyte's (1994) research concluded that "90% of risk to projects originates from unforeseen ground conditions which could often have been avoided by adequate and full site investigation".

The cost of site investigations in relation to the total project cost is small. Typical values in buildings projects are between 0.05% and 0.20% of total project cost, or 0.5% and 2.0% of foundations cost, and the typical values are between 0.20% and 1.50% of total project cost or 1.0% and 5.0% of foundations cost in roads projects. Site investigations should be continued until the ground conditions are known well enough for work to precede safely. Although a doubling in site investigations costs can add 1.0% to the total project cost. Unforeseen ground conditions can, and often do, raise the costs by 10% or more (Paul *et al.* 2002).

2 CASE STUDY APPLICATION

Al-Ertikaa Factory is a recycling factory at the site of Low Cost Housing project at the 6th October and includes the following buildings:

a. Administration building
b. Restaurant hall
c. Two residential buildings for technicians and labors
d. Factory building.

The main philosophy of the low cost project is to economize the used construction material. Each of the two residential buildings consists of number of adjacent units. Each unit consists of a room, hall, kitchen and bathroom. Each building consists of one floor (ground floor) only. The buildings structural system consists of wall bearing founded on reinforced concrete strip footings. Walls are constructed of red bricks and limestone blocks. The foundations are strip reinforced concrete over plain concrete. The depth of the foundation is less than 1 m below the ground surface. Information from the site indicates that there is a replacement fill placed below the foundations. The thickness of the replacement fill is about 1.5 to 2.0 m.

2.1 *Project site investigation scope*

Since the philosophy of the low cost housing is to construct the building with minimum cost, the project owner, consultant and contractor agreed to reduce the number of site investigation tests as much as possible. Site investigation boreholes have been taken randomly in the site regardless the building locations. The contractor adopted the knowledge of the geology of the area and the knowledge of the soil interpretation from previous site investigation in the project to predict the stratigraphy and properties of the soil in the factory location.

2.2 *Problem*

Directly after finishing the factory construction, cracks started to appear. The damaged structures are the two residential units for technicians and labors. The rest of the structures suffer no observed damage or cracks. Some of the cracks are dangerous especially at the middle units where concentrations of the cracks are to the extent that the ceramic are cracked and some ceramic slabs were fallen down. Figure 1 shows some cracked elements.

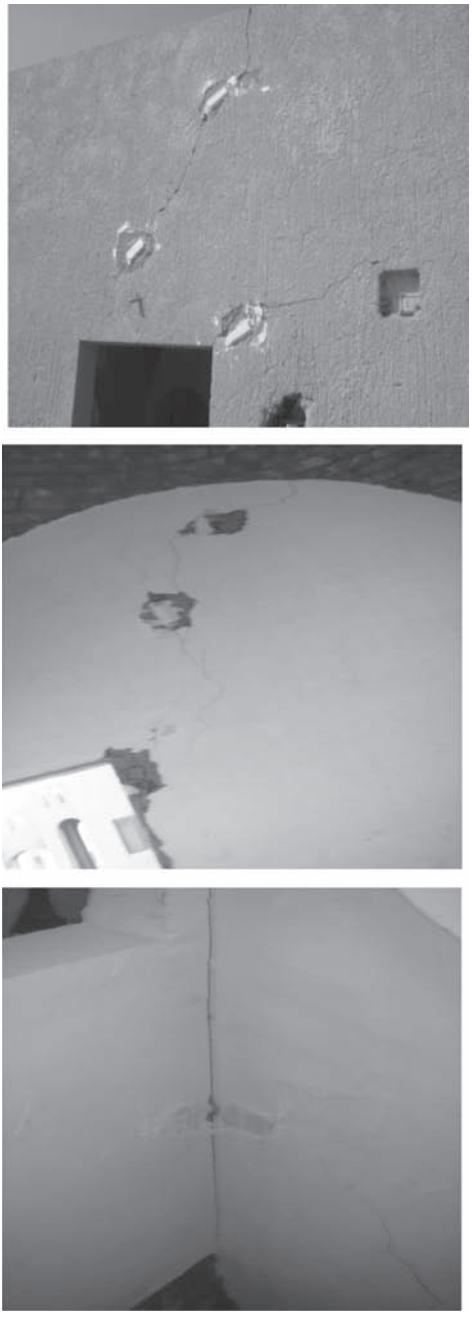

Figure 1. Buildings cracks.

According to the consulting services report, the damage reason was due to presence of swelling clay under the replacement fill under the foundations. The clay has free swell values up to 220% and one dimensional swelling pressure upon inundation of 2700 kPa. These numbers indicate high intrinsic expansiveness and swelling potential of the clay. The clay exists in the site from a depth of about 1 m and extends down to a depth of 4 to 5.5 m below the ground surface. This means that the swelling clay exists under the replacement fill that is under the foundations. Planting green areas and trees adjacent to the damaged buildings introduced water to the subsurface formation. The fact that replacement fill is sand which is permeable material facilitated the seepage of water to the swelling clay under the replacement fill. The swelling of the clay caused differential vertical displacement that caused distress to the walls and domes of the buildings.

2.3 *Problem corrective action*

The corrective action for these problems was as following.

a. Soil investigation was made to identify the cause of the buildings cracks.
b. Removing the trees adjacent to the buildings to a distance of 1.50 m from the buildings. Including changing the manholes locations and sewer lines paths.
c. Performing plastic sheets U-shape protection to prevent irrigation water from leaking to the soil under the buildings.
d. Replanting the landscape area and provide it by appropriate sprinkler irrigation system.
e. Monitoring recording of vertical displacements at Elevation Reference Points for a period of two months.
f. Fixing structural damages and replacing damaged parts. This including fixing the building cracks.

It should me mentioned that by removing the trees and protecting the building underlain soil from any source of water there is no need to make any adjustment for the soil. The building has small weight and then the stresses on the soil are low stresses.

2.4 *Rehabilitation cost for these problems*

The rehabilitation cost for the items that performed in the site were as in Table 1. These costs have been obtained from the consultant engineer in the site.

2.5 *Typical site investigation cost*

According to literature, the typical site investigation cost in residential buildings projects is between 0.05% and 0.20% of total project cost. Accordingly, site investigation cost for this project

Table 1. Rehabilitation cost for the damaged buildings.

Item No*	Unit	Rate (LE)	Quantity	Price (LE)
a	L.S.			8,750
b	m^2	150	450	67,500
d	m^2	15	700	10,500
c	m^2	250	450	112,500
e	Day	150	60	9,000
f	L.S.			25,000
Total rehabilitation cost				233,250

*From section 2.3.

should be between (LE 182), and (LE 726). While According to the Egyptian code of practice for soil mechanics, design and execution of foundations (2001), the boreholes number for such type of constructions is to be at least two boreholes if the area less than 300 m^2 and to a depth of 10 m, one extra borehole for each (300 m^2 to 500 m^2). Since the area of each building is about 222 m^2, then the number of boreholes should be four boreholes for the two buildings. The cost of the four boreholes is about (LE 3550). Accordingly, the site investigation cost for the two buildings must be at least (LE 3550).

2.6 *Comparing the rehabilitation cost with rehabilitation and construction cost*

The rehabilitation cost is (LE 233,250) which represent 65.7 times the typical site investigation cost. While the total cost for the buildings including landscape was (LE 363,150). By comparing the rehabilitation cost to the construction cost it could be concluded that the rehabilitation cost represents 64.2% of the total construction cost.

2.7 *Time delay due to the problem*

The project contract duration was 12 months. Due to the cracks, the project delivery time was 3 months more than the scheduled time. This means that the delay represents 25% of the project total duration.

3 CONTRACTUAL AND LEGAL ASPECTS OF SITE INVESTIGATION

Unforeseen site conditions may have an impact on time and cost of construction project. Sometimes they may prevent the contractors form performing the contractual obligations, and other times they only make it harder or more costly to perform the contract. The responsibility of the site investigation should be identified in the construction contracts. In it turns the construction contracts should be coinciding with the country law. On the other hand, the laws do not specify who is responsible for taking the site investigation, but most of laws identify who is the responsible for any unforeseen site conditions. By default, the responsible for the unforeseen site condition is the one who is also responsible for investigate these conditions.

3.1 *Responsibility of site investigation in the Egyptian law*

Responsibility of site investigation in the Egyptian law could be concluded from the following articles.

- Egyptian Civil Code: Article 147

The contract makes the law of the parties. It can be revoked or altered only by mutual consent of the parties or for reasons provided for by law.

When, however, as a result of exceptional and unpredictable events of a general character, the performance of the contractual obligation, without becoming impossible, becomes excessively onerous in such way as to threaten the debtor with exorbitant loss, the judge may according to the circumstances, and after taking into consideration the interests of both parties, reduce to reasonable limits, the obligation that has become excessive. Any agreement to the contrary is void.

- Egyptian Civil Code: Article 651

The engineer and contractor are jointly and severally responsible for a period of ten years for the total or partial demolition of constructions or other permanent works erected by them, even if such destruction is due to a defect in the ground itself, and even if the master authorized the erection of the defective construction, unless, in this case, the constructions were intended by the parties to last for less than ten years.

The warranty imposed by the preceding paragraph extends to defects in constructions and erections which endanger the solidity and security of the works.

The period of ten years runs from the date of delivery of the works.

This article does not apply to the rights of action which a contractor may have against his sub-contractors.

- Article 80 in Code number 98, 1989

The contractor is responsible for checking the nature of the work including any tests required for ensuring the validity of the specifications, drawings and designs. The contractor shall give notice to the owner as soon as practicable, and will be responsible for all the specifications, drawings and designs contents as like he prepare them himself.

Egyptian law is clear about bearing the contractor the whole responsibility of any unforeseen conditions. There is no argument about the contractor responsibility of any unforeseen conditions and then by default the soil investigation. Even though the Egyptian law makes the consultant jointly with the contractor responsible for any defective construction, but according to the code number 89, 1989 the contractor is responsible for any required test to check the work nature even if the owner or the consultant made these.

3.2 *Contractual aspects of site investigations*

The contract is the main reference in case of any disputes between the contract parties. Article 147 of the Egyptian Civil Code, states: "The contract makes the law of the parties". So, it is important to prepare the contracts in a way that ensure the responsibility of the site investigations. There is number of ministerial decrees that suggested comprehensive contracts between the owner and the contractor, and the owner and the consultant. These contracts are guiding contracts, and the parties have the option of follow them or choosing their own contract form. The article in these contracts concerning site investigation or unforeseen site conditions are as following.

It is mentioned in the Ministerial decree number 222 for the year 1994 about the general conditions for the construction contracts the following.

- Article 43. Boreholes and investigations: if the engineer (The consultant) or the contractor found that more soil investigation is required, then the engineer should mandate the contractor to make the required soil investigations. The extra soil investigation is to be considered as an extra work except if this work has been listed in the Bill of Quantities.
- Sub-article 24/2. Site inspection and preview: if the contractor faced any natural or artificial obstacles which may affect the project time and duration, he should inform the engineer (consultant). If the consultant is convinced that these conditions could not be discovered by an expert contractor, he should review the contractor requests to determine the extra cost that the contractor paid to face any circumstances that were not expected during tendering period. The owner should pay these expenses, and the contractor should be given an extra time to overcome these obstacles.

In the guiding contract for studies and designing, it is mentioned in the addendum 2 of the ministerial decree number 221 for the year 1994, it is one on the consultant scope of work to supervise the soil inspection and experiments, and study and evaluate the soil reports.

In the guiding contract for design and execution (by the owner funding), the ministerial decree number 246 for the year 1999, article number 4–11 under title "under-ground unexpected conditions", the following:

- If the contractor faced any under-ground unexpected conditions and he thinks that these conditions could not be discovered by an experienced contractor, the contractor should inform the owner to inspect these conditions. After inspection and exploration, the owner should agree on or decide to:

1. What is the time extension is the contractor deserve?
2. What is the extra cost that should be added to the contract price due to these conditions?

After deciding, the owner should inform the contractor what is his decision.

It is obvious that the guiding decrees are compatible with the Egyptian law. In both the contractor is the responsible for making the site investigation, while the consultant is the one who responsible for supervising the site investigations. Consultant and contractor both are responsible for making a decision if more site investigation is required. If any unforeseen site investigation faced, the owner and the consultant have the upper hand of deciding whether if the contractor deserving to be paid for overcoming these conditions or not. In the other hand the contractor and the consultant are both responsible for any consequences for the unforeseen site condition. This makes sense because the owner usually does not have experience about the right procedures to construct his structure. But such conditions make the contractor constrained to the consultant and owner willing to pay.

4 CONCLUSION

The results of the analyses conducted in this research, show that the inadequacy of the site investigation represents major factor on the construction cost and duration Due the inadequate site investigation, the extra cost represents 65.7 times the required site investigation cost. While the delay time due to the inadequacy of site investigation represents 25% of the project total duration.

The best procedure to avoid these problems is by making a proper site investigation. The proper site investigation comes in two phases. In the first phase, the owner should make a preliminary site investigation before the bidding process. Before submitting his proposal, the contractor should take into consideration, based on the preliminary site investigation, whatever if more site investigation is required or not. If more site investigation is

required, the scope of the extra site investigation should be identified. The expenses of the site investigation are minor comparing with the consequences that might happen if the site investigation ignored.

It is very important to put a clause or clauses in the contract to specify who is responsible for the unforeseen site conditions. The party who is responsible for these conditions will tend to make a proper site investigation to reduce the risk of unforeseen site condition problems. It should be taken to the consideration that the responsible here is only responsible for the cost and time delay. While the consequences of unforeseen site conditions in case of partially or total failure is restricted in the law of each country. According to the Egyptian law, the responsibility of any destruction due to the inadequate site investigation is held by the consultant and the contractor. So, they should convince the owner to make a proper site investigation if the owner underestimated its usefulness.

REFERENCES

Alhalaby, N.M. and Whyte I.L., 1994. The Impact of Ground Risks in Construction on Project Finance. Risk and Reliability in Ground Engineering Conference, London, November 11–12, 1993.

Baecher, G.B. and Christian, J.T., 2003. Reliability and Statistics in Geotechnical Engineering. John Wiley & Sons Ltd., Chichester, England.

Carlsson, M., 2005. Management of Geotechnical Risks in Infrastructure Projects. Licentiate Thesis, Division of Soil and Rock Mechanics, Royal Institute of Technology, Stockholm, Sweden.

Goldsworthy, J.S., Jaksa M.B. Kaggwa, W.S., Fenton, G.A., Griffiths, D.V. and Poulos H.G. 2004. Cost Of Foundation Failures Due To Limited Site Investigations. Proceeding of International Conference on Structural and Foundation Failures, August 2–4, 2004, Singapore, pp. 398–409.

Goldsworthy, J.S., Jaksa, M.B., Fenton, G.A., Griffiths, D.V., Kaggwa, W.S and Poulos, H.G., 2007. Measuring the Risk of Geotechnical Site Investigations. Proceedings of the Geo-Denver 2007 Symposium. K.K. Phoon et al., Eds., ASCE.

Institution of Civil Engineers, 1991. Inadequate Site Investigation. Thomas Telford, London.

Jaksa, M.B., Goldsworthy, J.S., Fenton, G.A., Kaggwa, W.S., Griffiths, D.V., Kuo, Y.L. and Poulos, H.G., 2005. Towards Reliable and Effective Site Investigations. Geotechnique Journal 55: 109–121.

Moh, Z.C., 2004. Site Investigation and Geotechnical Failures. Proceeding of International Conference on Structural and Foundation Failures, August 2–4, 2004, Singapore.

National Audit Office 1994. Quality Control of Roads and Bridge Construction. HMSO Publications, July 1994, UK.

National Economic Development Office (NEDO), 1983. Faster Building for Industry: Building E.D.C. National Economic Development Office, London.

National Economic Development Office (NEDO), 1988. Faster Building for Commerce. HMSO, London.

National Research Council, 1984. Geotechnical Site Investigations for Underground Projects. US National Committee on Tunneling Technology, Vol. No. 1, National Academy Press, Washington.

Paul, T., Chow, F. and Kjekstad, O., 2002. Hidden Aspects of Urban Planning- Surface and Underground Development. Thomas Telford Publishing, London.

Temple M.W.B. and Stukhart G., 1987. Cost Effectiveness of Geotechnical Investigations. Journal of Management in Engineering 3(1), pp. 8–19.

Whyte, I.L., 1995. The Financial Benefit from Site Investigation Strategy. Ground Engineering 10, 33–36.

Geotechnical Safety and Risk IV – Zhang et al. (eds)
© 2014 Taylor & Francis Group, London, ISBN 978-1-138-00163-3

Probabilistic characterization of Young's modulus using Markov Chain Monte Carlo simulation

Z. Cao
State Key Laboratory of Water Resources and Hydropower Engineering Science, Wuhan University, Wuhan, P.R. China

Y. Wang
Department of Civil and Architectural Engineering, Shenzhen Research Institute, City University of Hong Kong, Hong Kong, China

ABSTRACT: This paper presents a Markov Chain Monte Carlo Simulation (MCMCS)-based approach for probabilistic characterization of the undrained Young's modulus, E_u, of clay, which utilizes both the prior knowledge and project-specific SPT data to generate a large number of equivalent samples of E_u for its probabilistic characterization. The proposed approach combines the prior knowledge and project-specific SPT data systematically under a Bayesian framework and allows general choices of realistic prior knowledge (e.g. an arbitrary histogram type of prior distribution). Equations are derived for the proposed approach, and a sensitivity study is performed to explore the effects of prior knowledge on probabilistic characterization of soil properties. It is shown that the proposed equivalent sample approach integrates the information provided by different types of prior knowledge with project-specific information in a rational manner and improves significantly probabilistic characterization of soil properties by incorporating consistent prior knowledge.

1 INTRODUCTION

In the past few decades, probability analysis and Reliability-Based Design (RBD) of geotechnical structures (e.g. foundations and retaining walls) have attracted considerable attention. This has led to several probability analysis methods (e.g. Christian et al. 1994, El-Ramly et al. 2005, Wang et al. 2011b, Wang 2012) and RBD codes (e.g. Phoon et al. 1995, Honjo et al. 2010, Wang et al. 2011a, Wang 2011) in geotechnical engineering to deal rationally with various geotechnical-related uncertainties, such as the uncertainty in soil properties. These probability analysis methods and RBD codes usually require probabilistic estimations of soil properties as input, such as the statistics (e.g. mean, standard deviation, and/or lower 5% quantiles) and probability distributions (e.g. Probability Density Function (PDF) and Cumulative Distribution Function (CDF)) of soil properties. This poses a challenge in the implementation of these probabilistic analysis methods and RBD codes because the number of soil property data obtained during geotechnical site investigation is generally too sparse to generate meaningful statistics and probability distributions of soil properties for probability analysis and/or design of geotechnical structures. This problem is further complicated by fact that geotechnical site investigation is a multi-step process that relies on both site information available prior to the project (namely "prior knowledge", such as engineering experience and judgment) and site observation data obtained from test borings, in-situ tests (e.g. Standard Penetration Test (SPT)), and/or laboratory tests (e.g. Mayne et al. 2002, Cao & Wang 2013, Wang & Cao 2013). It remains a challenging task for geotechnical engineers to integrate systematically the prior knowledge and site observation data in a probabilistic manner.

To address these challenges, this paper presents a Markov Chain Monte Carlo Simulation (MCMCS)-based approach for probabilistic characterization of the undrained Young's modulus, E_u, of clay, which utilizes both the prior knowledge and project-specific SPT data to generate a large number of equivalent samples of E_u for determining the statistics and probability distributions of E_u. The proposed approach combines the prior knowledge and project-specific SPT data systematically under a Bayesian framework, in which the prior knowledge is reflected by the prior distribution. It allows general choices of realistic prior distributions (e.g. uniform prior distribution, triangular

prior distribution, an arbitrary histogram type of prior distribution, and normal prior distribution). The paper starts with development of the Bayesian framework for integrating the prior knowledge with project-specific test data and derivation of the PDF of E_u using the integrated information, followed by generating a large number of equivalent samples of E_u for its probabilistic characterization using MCMCS. Then, a sensitivity study is performed to illustrate the flexibility of incorporating various different types of realistic prior knowledge into the proposed approach and to explore the effects of prior knowledge on probabilistic characterization of soil properties.

2 BAYESIAN FRAMEWORK

The properties of geotechnical materials are inherently variable because of various factors (e.g. parent materials, weathering and erosion processes, transportation agents, and conditions of sedimentation, etc.) during their formation process (e.g. Phoon & Kulhawy 1999a). Consider, for example, the undrained Young's modulus, E_u, within a clay layer. To model explicitly its inherent variability, E_u is represented by a lognormal random variable with a mean μ and standard deviation σ. The model parameters μ and σ are unknown and need to be determined during geotechnical site investigation based on both prior knowledge and project-specific test results (e.g. SPT N values). Within a Bayesian framework, the updated knowledge about μ and σ is reflected by their joint posterior distributions based on prior knowledge and site observation data (e.g. Ang & Tang 2007, Wang & Cao 2013)

$$P(\mu,\sigma \mid Data) = KP(Data \mid \mu,\sigma)P(\mu,\sigma) \tag{1}$$

in which $K = (\int_{\mu,\sigma} P(Data|\mu,\sigma)P(\mu,\sigma)d\mu d\sigma)^{-1}$ is a normalizing constant that does not depend on μ and σ; $Data = \{\xi_i = \ln(N_i),\ i = 1, 2, \ldots, n_s\}$, where ξ_i, $i = 1, 2, \ldots, n_s$, denote n_s SPT N values obtained within a clay layer in a log scale; $P(Data|\mu,\sigma)$ is the likelihood function reflecting the model fit with *Data*; $P(\mu,\sigma)$ is the prior distribution of μ and σ that reflects the prior knowledge on μ and σ in the absence of *Data*. Calculations of the likelihood function and prior distribution are presented in the following two subsections, respectively.

2.1 *Likelihood function*

The undrained Young's modulus E_u can be estimated from SPT tests (Kulhawy & Mayne 1990, Phoon & Kulhawy 1999b). The E_u value of the tested soil is obtained by means of regression between the E_u and the N values measured during SPT tests. Consider, for example, an empirical regression between the E_u measured by pressuremeter tests and SPT N values (Kulhawy & Mayne 1990, Phoon & Kulhawy 1999b):

$$E_u/p_a = 19.3\ N^{0.63} \tag{2}$$

where p_a is the atmospheric pressure (i.e. 0.1 MPa). In a log-log scale, Equation 2 can be rewritten as:

$$\xi = \ln(N) = a\ln(E_u) + b + \varepsilon \tag{3}$$

in which $\xi = \ln(N)$ = the logarithm of SPT N value; $\ln(E_u)$ = the logarithm of E_u; $a = 1.587$, $b = -1.044$, and ε is a Gaussian random variable with a zero mean and a standard deviation $\sigma_\varepsilon = 1.352$ (Phoon & Kulhawy 1999b). The last term ε represents a modeling scatterness or transformation uncertainty associated with the regression equation. Since E_u is a lognormal random variable, $\ln(E_u)$ in Equation 3 is a normal random variable, and it can be written as (e.g. Ang & Tang 2007)

$$\ln(E_u) = \mu_N + \sigma_N z \tag{4}$$

in which z is a standard Gaussian random variable; $\mu_N = \ln\mu - \sigma_N^2/2$ and $\sigma_N = \sqrt{\ln(1+(\sigma/\mu)^2)}$ are the mean and standard deviation of $\ln(E_u)$, respectively. Combining Equations 3 and 4 leads to:

$$\xi = \ln(N) = (a\mu_N + b) + a\sigma_N z + \varepsilon \tag{5}$$

When the inherent variability is assumed to be independent of the transformation uncertainty (i.e. z is independent of ε), ξ is a Gaussian random variable with a mean of $a\mu_N + b$ and standard deviation of $\sqrt{a^2\sigma_N^2 + \sigma_\varepsilon^2}$. The project-specific SPT data (i.e. $Data = \{\xi_i = \ln(N_i),\ i = 1,2, \ldots, n_s\}$) can be considered as n_s independent realizations of the Gaussian random variable ξ. The likelihood function for the project-specific SPT data is therefore expressed as (e.g. Ang & Tang 2007, Wang & Cao 2013)

$$P(Data \mid \mu,\sigma) = \prod_{i=1}^{n_s} \frac{1}{\sqrt{2\pi}\sqrt{a^2\sigma_N^2 + \sigma_\varepsilon^2}} \exp\left\{-\frac{1}{2}\left[\frac{\xi_i - (a\mu_N + b)}{\sqrt{a^2\sigma_N^2 + \sigma_\varepsilon^2}}\right]^2\right\} \tag{6}$$

2.2 *Prior distribution*

The prior distribution can be simply assumed as a joint uniform distribution of μ and σ with

respective minimum values of μ_{min} and σ_{min} and respective maximum values of μ_{max} and σ_{max}, and it is expressed as (e.g. Ang & Tang 2007)

$$P(\mu,\sigma) = \begin{cases} \dfrac{1}{(\mu_{max}-\mu_{min})(\sigma_{max}-\sigma_{min})} & \text{for } \mu \in [\mu_{min},\mu_{max}] \text{ and } \sigma \in [\sigma_{min},\sigma_{max}] \\ 0 & \text{otherwise} \end{cases} \quad (7)$$

Note that only the possible ranges (i.e. μ_{min} and μ_{max}, σ_{min} and σ_{max}) of the model parameters are needed to completely define a uniform prior distribution herein. This requires relatively limited prior knowledge (e.g. reasonable ranges of soil properties of interest), which is commonly available in geotechnical literature (e.g. Kulhawy & Mayne 1990, Phoon & Kulhawy 1999a,b). The approach proposed in this paper is general and equally applicable for more sophisticated types of prior distributions (e.g. triangular prior distribution, an arbitrary histogram type of prior distribution, and normal prior distribution), which of course require relatively informative prior knowledge as justifications. Effects of different prior knowledge are further discussed in Section 4.

3 PROBABILITY DENSITY FUNCTION OF UNDRAINED YOUNG'S MODULUS

In this study, the undrained Young's Modulus is modeled by a random variable E_u, which follows a lognormal distribution with a mean μ and standard deviation σ. Both prior knowledge and project-specific test data (e.g. SPT N values) are used to estimate the distribution model parameters μ and σ in geotechnical site investigation. For a given set of prior knowledge (i.e. *Prior*) and project-specific SPT data (i.e. *Data*), there are many sets of possible values of μ and σ. Each set of μ and σ has its corresponding plausibility (or occurrence probability), which is defined by a joint conditional PDF $P(\mu,\sigma|Data, Prior)$. Using the conventional notation of Bayesian framework, $P(\mu,\sigma|Data, Prior)$ is simplified as $P(\mu,\sigma|Data)$ and is given by Equation 1. Using the Theorem of Total Probability (e.g. Ang & Tang 2007), the PDF of the undrained Young's modulus E_u for a given set of prior knowledge and project-specific SPT data is expressed as:

$$P(E_u \mid Data, Prior) = \int_{\mu,\sigma} P(E_u \mid \mu,\sigma) P(\mu,\sigma \mid Data, Prior) d\mu d\sigma \quad (8)$$

Combining Equations 1 and 8 leads to:

$$P(E_u \mid Data, Prior) = K \int_{\mu,\sigma} P(E_u \mid \mu,\sigma) P(Data \mid \mu,\sigma) P(\mu,\sigma) d\mu d\sigma \quad (9)$$

where $P(E_u|\mu,\sigma)$ = conditional PDF of E_u for a given set of model parameters (i.e. μ and σ). Since E_u is a lognormal random variable, $P(E_u|\mu,\sigma)$ is given by a lognormal distribution with a mean μ and standard deviation σ (e.g. Ang & Tang 2007, Wang & Cao 2013). Equation 9 is a product of the normalizing constant K and the integral term defined as $I = \int_{\mu,\sigma} P(E_u|\mu,\sigma) P(Data|\mu,\sigma) P(\mu,\sigma) d\mu d\sigma$, and it gives the PDF of E_u for a given set of prior knowledge (i.e. *Prior*) and project-specific SPT data (i.e. *Data*). In the next subsection, the Markov Chain Monte Carlo Simulation (MCMCS) method (e.g. Robert & Casella 2004) is used to generate a sequence of E_u samples whose limiting stationary distribution is the PDF of E_u (i.e. Eq. 9).

3.1 *Markov Chain Monte Carlo Simulation*

MCMCS method is a numerical process that simulates a sequence of samples of a random variable (e.g. E_u) as a Markov Chain with the PDF of the random variable (e.g. Eq. 9 for E_u) as the Markov Chain's limiting stationary distribution (e.g. Beck & Au 2002, Robert & Casella 2004). The states of the Markov Chain after it reaches stationary condition are then used as samples of the random variable with the target PDF. It provides a feasible way to generate samples from an arbitrary PDF, particularly when the PDF is complicated and is difficult to express analytically or explicitly.

In this study, the Metropolis-Hastings (MH) algorithm (e.g. Hastings 1970, Beck & Au 2002) is used in MCMCS to generate totally n_{MCMC} number of the E_u samples from Equation 9. The E_u Markov Chain starts with an arbitrary initial state, $E_{u,1}$. Then, a candidate sample, $E^*_{u,m}$, $m = 2, 3, \ldots, n_{MCMC}$, for the m-th state $E_{u,m}$ of the Markov Chain is generated from the proposal PDF $f(E^*_{u,m} \mid E_{u,m-1})$ of the Markov Chain based on its previous state $(m-1)$-th, $E_{u,m-1}$ (e.g. the initial state $E_{u,1}$ for $E_{u,2}$). Herein, the proposal PDF $f(E^*_{u,m} \mid E_{u,m-1})$ is taken as a Gaussian PDF, which is centered at the previous state $E_{u,m-1}$ and has a Coefficient of Variation (i.e. COV) equal to the mean COV of the prior knowledge (e.g. COV = $(\sigma_{max} + \sigma_{min})/(\mu_{max} + \mu_{min})$ for the uniform prior given in Eq. 7). The chance to accept the candidate sample $E^*_{u,m}$ as the $E_{u,m}$ depends on the "acceptance ratio", r_a. Using $E^*_{u,m}$, $E_{u,m-1}$, the proposal PDF, and the PDF of E_u (i.e. Eq. 9), the acceptance ratio for $E^*_{u,m}$ is calculated. Details of

the calculation of r_a are found in Wang & Cao (2013). After r_a is calculated, a random number u is generated from a uniform distribution with a range from zero to one. When u is less than r_a, E^*_{u,m_*} is accepted as $E_{u,m}$, i.e. $E_{u,m} = E^*_{u,m}$. Otherwise, $E_{u,m}$ is rejected, and $E_{u,m}$ is taken as equal to the previous state $E_{u,m-1}$, i.e. $E_{u,m} = E_{u,m-1}$. Starting from the initial sample $E_{u,1}$, the procedure described above is repeated $n_{MCMC} - 1$ times to generate $n_{MCMC} - 1$ samples of E_u, i.e. $E_{u,m}$, $m = 2, 3, \ldots, n_{MCMC}$. This leads to a Markov Chain that is comprised of n_{MCMC} E_u samples (including the initial sample). Finally, the E_u samples obtained after the Markov Chain reaches its stationary condition are considered as appropriate samples for probabilistic characterization of E_u.

3.2 *Equivalent samples*

Equation 9 shows that the PDF of E_u contains information from both project-specific site observation data (i.e. *Data*) and prior knowledge (i.e. *Prior*). The information from these two different sources is integrated probabilistically in a rational manner. The MCMCS samples that draw from the E_u PDF, therefore, contain the integrated information of both project-specific site observation data and prior knowledge. When the project-specific data is limited, the MCMCS samples mainly reflect the prior knowledge. As the amount of project-specific data increases, the effect of the project-specific data on the MCMCS samples gradually increases.

More importantly, a large amount of E_u samples can be generated conveniently by MCMCS. From a statistical point of view, these MCMCS samples are equivalent to those E_u data that are measured physically from laboratory or in-situ tests (e.g. pressuremeter tests). Therefore, this large amount of equivalent samples can be analyzed statistically, using conventional statistical methods, to estimate the required statistics (e.g. mean, standard deviation, and/or lower 5% quantiles) and probability distributions (e.g. PDF and CDF) of E_u (or $\ln(E_u)$) in probabilistic analysis and RBD of geotechnical structures.

The proposed approach integrates probabilistically the prior knowledge (e.g. previous engineering experience including regression equations) and project-specific test data (e.g. SPT test data) and transforms the integrated information into a large number, as many as needed, of equivalent samples. This allows meaningful statistics of soil properties to be obtained using conventional statistical analysis. The proposed approach effectively tackles the difficulty in generating meaningful statistics from the usually limited number of soil property data obtained during geotechnical site investigation. It has been illustrated using a set of real SPT data obtained from the clay site of the US National Geotechnical Experimentation Sites (NGES) at Texas A&M University (Wang & Cao 2013). It was shown that, based on the limited SPT data and relatively uninformative prior knowledge (i.e. reasonable ranges of soil parameters reported in the literature), the equivalent sample approach provides reasonable estimates of the statistics and probability distributions of E_u.

4 SENSITIVITY STUDY ON DIFFERENT PRIOR KNOWLEDGE

The proposed approach provides engineers with flexibility to use different types of prior distributions, which reflect the prior knowledge realistically. To illustrate such flexibility and explore the effects of prior knowledge, a sensitivity study is performed in this section using simulated SPT data that is generated from Equation 5 with $\mu_N = 2.23$ and $\sigma_N = 0.39$ (i.e. $\mu = 10.0$ MPa and $\sigma = 4.0$ MPa) and four different sets (i.e. prior knowledge I, II, III, and IV) of prior knowledge shown in Figure 1.

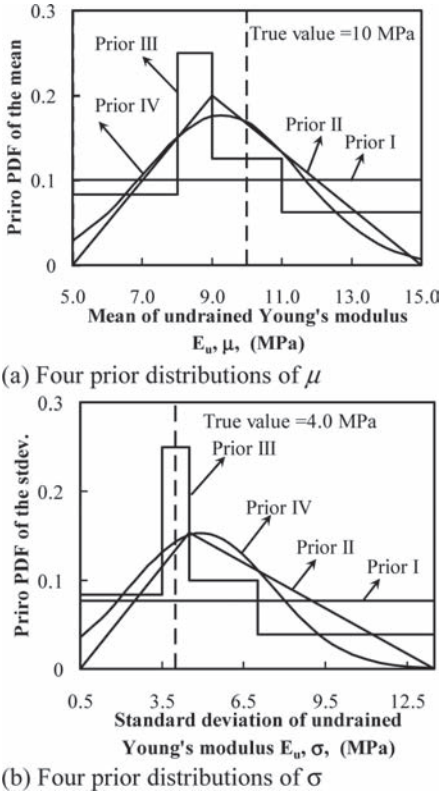

Figure 1. Prior knowledge used in the sensitivity study.

As shown in Figure 1, the prior knowledge I is a uniform prior distribution with μ_{min} = 5.0 MPa, μ_{max} = 15 MPa, σ_{min} = 0.5 MPa, and σ_{max} = 13.5 MPa.

Prior knowledge I is consistent with the typical ranges of undrained Young's modulus reported in the literature (e.g. Kulhawy & Mayne 1990, Phoon & Kulhawy 1999a, b), and it is used as the baseline case in this sensitivity study. The prior knowledge II and III follow a triangular distribution and an arbitrary histogram type of distribution, respectively. They have the same ranges of both μ and σ values as the prior knowledge I. Note that, compared with the prior knowledge I, the prior knowledge II and III have relatively large PDF values allocated close to the true values (i.e. 10MPa and 4 MPa, respectively) of μ and σ that are indicated by dashed lines in Figure 1a and 1b, respectively. Therefore, the prior knowledge II and III are slightly more informative and confident than the prior knowledge I, and it is slightly more consistent with the true values of μ and σ. The prior knowledge IV is the Gaussian best fit of the prior knowledge III, and information provided by the prior knowledge III and IV are more or less the same.

In this sensitivity study, 10 sets of simulated SPT data with 10 SPT N values in each set (i.e. data quantity n_s = 10) are generated using Equation 5. For example, Figure 2 shows a set of the simulated SPT data. Note that in practice the actual values of soil properties are unknown, and they are estimated through prior knowledge and project-specific test results.

Each set of simulated data is combined with the four different sets (i.e. prior knowledge I, II, III, and IV) of prior knowledge shown in Figure 1 to generate 30,000 equivalent samples of E_u using the proposed approach, respectively. For example, Figure 3 shows 30,000 equivalent samples of E_u generated using the set of SPT data shown in Figure 2 and prior knowledge I. Using the 30,000 equivalent samples, the statistics and probability

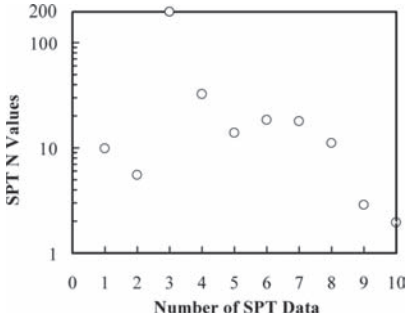

Figure 2. A set of simulated SPT data.

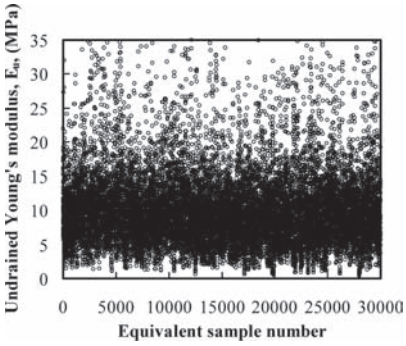

Figure 3. Scatter plot of the equivalent samples for undrained Young's modulus.

distributions of E_u (or $\ln(E_u)$) can be estimated through conventional statistical analysis. For example, the estimations (i.e. μ_N^* and σ_N^*) of μ_N and σ_N are obtained from conventional mean and standard deviation equations, and they are 2.26 and 0.54, respectively. Such a procedure described above is repeatedly performed for each combination of a set of simulated data (10 sets in total) and a set of prior knowledge (4 sets in total). This leads to 40 sets of μ_N^* and σ_N^* with 10 sets for each set of prior knowledge. In addition, for each set of the simulated SPT data, the E_u values are also directly calculated using the regression model given by Equation 2 in the absence of prior knowledge. This leads to another 10 sets of μ_N^* and σ_N^*.

4.1 *Effects on the mean of ln(E_u)*

Figure 4a shows values of μ_N^* obtained from the equivalent sample approach using prior knowledge I, II, III, and IV by open squares, crosses, open triangles, and open circles, respectively. It also includes the μ_N^* values directly estimated from the regression model (i.e. Eq. 2) without prior knowledge by solid squares. For comparison, Figure 4a also shows the true value (i.e. 2.23) of μ_N by a dashed line. In general, open squares, crosses, open triangles, and open circles (i.e. the results estimated from equivalent samples) plot more closely to the dashed line than solid squares (i.e. the results directly estimated from the regression model without prior knowledge). The μ_N^* values estimated from the equivalent samples are generally better estimations of the true value than those directly estimated from the regression model without prior knowledge. By incorporating prior knowledge, the equivalent sample approach significantly improves the estimation of μ_N in this study. Figure 4a also shows that the μ_N^* values obtained using prior knowledge II, III, and IV (see crosses,

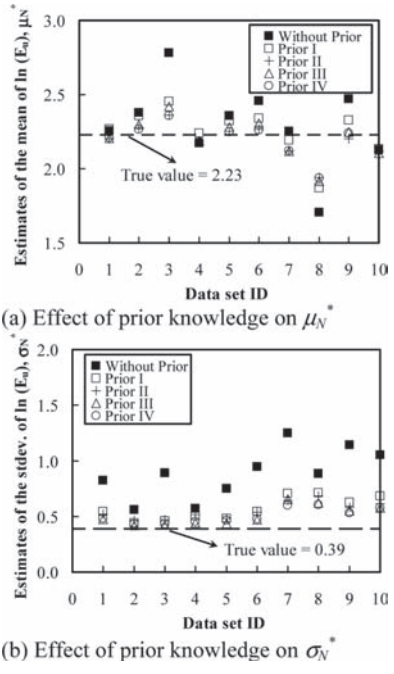

Figure 4. Effects of prior knowledge.

open triangles, and open circles, respectively) are slightly better than those obtained using prior knowledge I (see open squares). It is not surprising to see this because the prior knowledge II, III, and IV are slightly more consistent with the true value of μ_N and more informative than the prior knowledge I, as shown in Figure 1.

4.2 *Effects on the standard deviation of ln(E_u)*

Figure 4b shows values of σ_N^* obtained from the equivalent sample approach using prior knowledge I, II, III, and IV by open squares, crosses, open triangles, and open circles, respectively. It also includes the σ_N^* values directly estimated from the regression model (i.e. Eq. 2) without prior knowledge by solid squares. For comparison, Figure 4b also shows the true value (i.e. 0.39) of σ_N by a dashed line. Similar to μ_N^* values, the σ_N^* values estimated from the equivalent samples (see open squares, crosses, open triangles, and open circles for prior knowledge I, II, III, and IV, respectively) are generally better estimations of the true value than those directly estimated from the regression model without prior knowledge (see solid squares). By incorporating prior knowledge, the equivalent sample approach significantly improves the estimation of σ_N in this study. In addition, the σ_N^* values obtained using prior knowledge II, III, and IV (see crosses, open triangles, and open circles, respectively) are slightly better than those obtained using prior knowledge I (see open squares), because the information on σ_N provided by prior knowledge II, III, and IV is slightly more consistent with the true value of σ_N and more informative than that provided by prior knowledge I (see Fig. 1).

5 SUMMARY AND CONCLUSIONS

This paper presented a Markov Chain Monte Carlo Simulation (MCMCS)-based approach for probabilistic characterization of the undrained Young's modulus, E_u, of clay. The proposed approach integrates the information provided by the prior knowledge and project-specific SPT data systematically under a Bayesian framework and transforms the integrated information into a large number of equivalent samples of E_u for its probabilistic characterization using MCMCS. It effectively tackles the difficulty in generating meaningful statistics from the usually limited number of soil property data obtained during geotechnical site investigation. Equations were derived for the proposed equivalent sample approach. The proposed approach provides engineers with flexibility to use different types of realistic prior distributions, such as uniform prior distribution, triangular prior distribution, an arbitrary histogram type of prior distribution, and normal prior distribution. Such flexibility was illustrated through a sensitivity study on prior knowledge. It was shown that the proposed equivalent sample approach combines the information provided by different types of prior knowledge with project-specific information in a rational manner and improves significantly probabilistic characterization of soil properties by incorporating consistent prior knowledge.

ACKNOWLEDGEMENT

The work described in this paper was supported by a grant from the Research Grants Council of the Hong Kong Special Administrative Region, China (Project No. 9041550 (CityU 110210)), a grant from City University of Hong Kong (Project No. 7002695), and a grant from National Natural Science Foundation of China (Project No. 51208446). The financial supports are gratefully acknowledged.

REFERENCES

Ang, A.H.-S. & Tang, W.H. 2007. *Probability Concepts in Engineering: Emphasis on Applications to Civil and Environmental Engineering.* New York: John Wiley and Sons.

Beck, J.L. & Au, S.K. 2002. Bayesian updating of structural models and reliability using Markov chain Monte Carlo simulation. *Journal of Engineering Mechanics* 128(4): 380–391.

Cao, Z. & Wang, Y. 2013. Bayesian approach for probabilistic site characterization using cone penetration tests. *Journal of Geotechnical and Geoenvironmental Engineering* 139(2): 267–276.

Christian, J.T., Ladd, C.C. & Baecher, G.B. 1994. Reliability applied to slope stability analysis. *Journal of Geotechnical Engineering* 120(12): 2180–2207.

El-Ramly, H., Morgenstern, N.R. & Cruden, D.M. 2005. Probabilistic assessment of stability of a cut slope in residual soil. *Geotechnique* 55(1): 77–84.

Hastings, W.K. 1970. Monte Carlo sampling methods using Markov chains and their applications. *Biometrika* 57: 97–109.

Honjo, Y., Kikuchi, Y. & Shirato, M. 2010. Development of the design codes grounded on the performance-based design concept in Japan. *Soils and Foundations* 50(6): 983–1000.

Kulhawy, F.H. & Mayne, P.W. 1990. *Manual on estimating soil properties for foundation design*. Report EL 6800, Electric Power Research Institute, Palo Alto, 306p.

Mayne, P.W., Christopher, B.R. & DeJong, J. 2002. *Subsurface investigations—Geotechnical site characterization*. *No.* FHWA NHI-01-031, Federal Highway Administration, U.S. Department of Transportation, Washington D.C.

Phoon, K.K., Kulhawy, F.H. & Grigoriu, M.D. 1995. *Reliability-based Design of Foundations for Transmission Line Structures*, Report TR-105000, Electric Power Research Institute, Palo Alto.

Phoon, K.K. & Kulhawy, F.H. 1999a. Characterization of geotechnical variability. *Canadian Geotechnical Journal* 36(4): 612–624.

Phoon, K.K. & Kulhawy, F.H. 1999b. Evaluation of geotechnical property variability. *Canadian Geotechnical Journal* 36(4): 625–639.

Robert, C. & Casella, G. 2004. *Monte Carlo Statistical Methods*, Springer.

Wang, Y. 2011. Reliability-based design of spread foundations by Monte Carlo simulations. *Geotechnique* 61(8), 677–685.

Wang, Y., Au, S.K. & Kulhawy, F.H. 2011a. Expanded reliability-based design approach for drilled shafts. *Journal of Geotechnical and Geoenvironmental Engineering* 137(2): 140–149.

Wang, Y., Cao, Z. & Au, S.K. 2011b. Practical reliability analysis of slope stability by advanced Monte Carlo simulations in spreadsheet. *Canadian Geotechnical Journal* 48(1): 162–172.

Wang, Y. 2012. Uncertain parameter sensitivity in Monte Carlo simulation by sample reassembling. *Computers and Geotechnics* 46: 39–47.

Wang, Y. & Cao, Z. 2013. Probabilistic characterization of Young's modulus of soil using equivalent samples. *Engineering Geology* 159: 106–118.

This page intentionally left blank

Geotechnical Safety and Risk IV – Zhang et al. (eds)
© 2014 Taylor & Francis Group, London, ISBN 978-1-138-00163-3

Site investigation approaches for the proposed Ukhuu Khudag to Gashuun Sukhait Railway, South Gobi desert, Mongolia

A.D. Mackay
Nishimatsu Construction Company Limited
Formerly SMEC Asia Ltd.

N.R. Wightman
Sinclair Knight Merz (HK) Limited
Formerly SMEC Asia Ltd.

ABSTRACT: Due to the current resource demand from the People's Republic of China and the availability of these resources in the Gobi desert, Mongolia, there is a need to construct a railway to provide an efficient haulage system from the Gobi desert mines to the People's Republic of China. The proposed railway currently runs for about 225 kilometres within Mongolia from Ukhuu Khudag to the People's Republic of China border crossing facilities at Gashun Sukhait. As the Oyo Tolgoi open cast mine will also come into operation in the near future provision for haulage of these mined resources needs to be made; the alignment passes in close proximity to this location accordingly. As part of the feasibility design a preliminary site investigation was carried out, including a limited desk study, a walkover survey, a topographic survey and a basic ground investigation, including boreholes and trial pit exploration stations. The ground investigation stations were located according to geotechnical construction risks assessed from the desk study, topographic survey and walkover survey information; at this preliminary stage these included stream and river crossings, areas with considerable volumes of cut and fill, material suitability for ballast and embankment construction and areas with near surface groundwater. The ground conditions along the alignment included superficial deposits; alluvium, cemented alluvium, talluvium and aeolian (wind-blown) deposits; and solid geology; sedimentary (coal measures, shale and sandstone) and igneous (tuff, basalt, andesite and granite) rock. This paper outlines the methods adopted for carrying out the site investigation, which included considerations for the past environmental and geological history when assessing the physical characteristics relevant to construction.

1 INTRODUCTION

The Ukhuu Khudang (UKh) to Gashuun Sukhait (GS) Railway will run about 225 kilometres across the Gobi desert, Mongolia, from UKh to the north-west to the GS border crossing facilities to the south east. To ensure efficient operation stringent geometrical limitations (gradient and curvature) are required for the adopted rail alignment. Given the topographic variability of all available rail corridors across the Gobi desert considerable volumes of cut and fill will be required. A preliminary Site Investigation (SI), including a desk study, topographic survey and walkover survey data was carried out to address the construction risks. At the preliminary stage the risks included the stream and river crossings, which were generally located at topographic low points requiring considerable volumes of embankment fill, material suitability for ballast, areas with near surface groundwater and deep cuts. This paper provides a background to the railway requirements and an overview to the geological conditions in the Gobi desert in the vicinity of the proposed alignment at that time. The approach to the SI considering the implications of the environmental and geological history is provided.

2 SETTING

2.1 *Location*

The existing railway alignment is located in the south Gobi, Omnigovi province, Mongolia. Refer to Figure 1 for the general location in Mongolia.

The proposed alignment runs from the north-west, Chainage (Ch.) 0 from UKh, to the south-east, up to Ch. 225 at GS. Refer to Figure 2 for the proposed alignment across the Gobi desert.

The Gobi desert terrain typically comprises sandy and rocky soils often with sparse vegetation and a thin overlay of wind-blown deposits, comprising finer grained soil and dust particles. The proposed rail alignment descends from an altitude of about

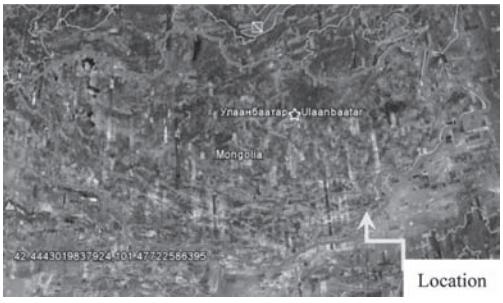

Figure 1. UG-GS Rail location (Google Earth, 2011).

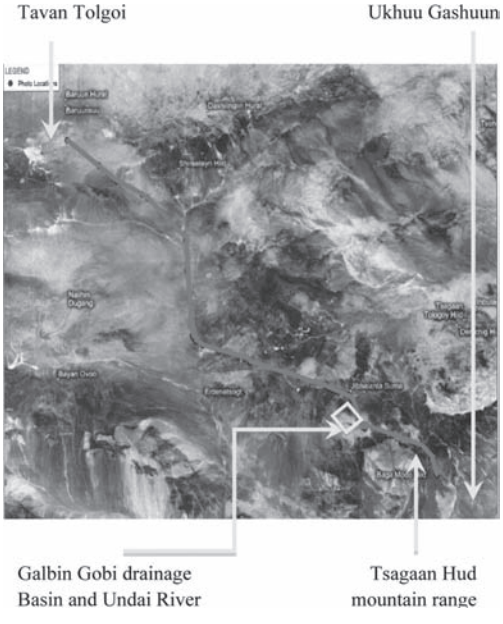

Figure 2. Rail alignment, Gobi desert (Google Earth, 2011).

1500 m above sea level (asl) at UKh decreasing to 900 m asl towards the southernmost portion. Prominent features along the alignment include the Galbin Gobi drainage basin, the major Undaii river crossing, traversing the alignment at its lowest level, and the Tsagaan Hud mountain range crossing the southernmost portion of the alignment (refer to Fig. 2).

2.2 *Rail considerations*

The commencement of the alignment, at UKh, is located near the Tavan Tolgoi coking coal open excavation mine. The GS border crossing facilities at the end of the alignment is located about 10km from the People's Republic of China (PRC) border and will facilitate transfer of the coal from the Mongolian to PRC rolling stock. Refer to Figure 2 for the locations. The maximum rail gradient for loaded trains is generally 0.6%, dependent on the type of locomotive used. At the Balloon Loop area the and marshaling yards the gradient is restricted to zero. The minimum horizontal curvature is 10km radius respectively.

To accommodate the geometrical limitations of the railway alignment and the abrupt changes in the topographic profile along all proposed alignments variable embankments and cutting heights were required ranging to a maximum of about 17 m vertically. Other important construction considerations include:

Drainage—surface drainage running into embankments require culvert installation to allow unimpeded flow beneath the alignment. Flow running into cuttings required suitable surface drainage to redirect the flow. Due to the size of the Undaii river crossing, a bridge with piled foundations was being considered.

Structural—foundations for telecom towers and towers; major culverts and accessories for the sidings and marshaling yards and accessory buildings. Suitable concrete mixes and reinforcement needed consideration for the aggressive soil conditions.

Environmental—animal crossings, including major underpasses or overpasses to allow unimpeded animal migration across the Gobi desert. Structures to accommodate oil change sump pits, latrines and groundwater abstractions were also required.

Traffic—maintenance road running alongside the alignment for its entire length. Traffic crossings are required at regular intervals.

Earthworks—ballast (250 mm thickness) is required for the entire alignment. The embankment construction required a sub-base layer (250 mm thick) and embankment layer (variable). As the marshaling yards are level a significant leveled terrace platforms were required to place the Yards. Passing sidings were proposed at approximately every 2 kms.

Refer to Figure 3 for the major railway components.

2.3 *Geological overview*

The South Gobi region has undergone continental accretion and basin range crustal extension. The area is dominated by east to west trending mountain ranges cutting the alignment, typically corresponding with dyke intrusions and faults. This suggests crustal movement from both the north and south directions in the Gobi area. A major fault, referred to as the Navin Sukhait fault, bounds the intrusive rock and sedimentary deposits; basalts and coal measures,

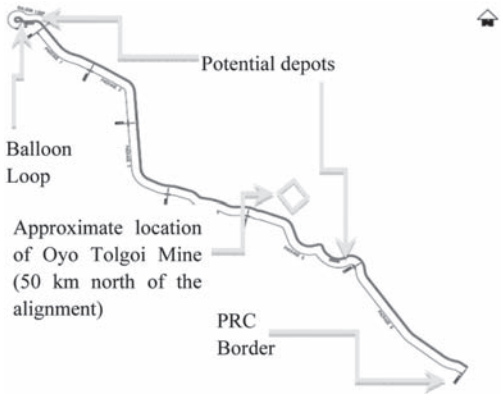

Figure 3. Rail alignment requirements.

Figure 4. Mongolia geological map.

conglomerates and sandstones, towards the northern portion of the alignment. A granitic batholith intrusion, which surfaces in areas with the granitic tor terrain, underlies the entire alignment at depth.

3 GROUND CONDITIONS

3.1 *Approach to the site investigation*

An initial Ground Investigation (GI) was carried out during 2009 and comprised boreholes (BH) positioned at about every 500 m along the proposed alignment. This prescriptive approach typically follows the traditional Russian SNiP code standards (Fookes et al. 2005), which is still often used to specify GIs in Mongolia. Generally as the geological descriptions used in Russian codes cannot be easily used to estimate geotechnical parameters for design input the data obtained was limited value for the engineering design (Mackay 2010).

To allow rapid feedback for the design preparation the "Total Engineering Geology" approach (Fookes 1997) to the SI was adopted. The premise of this approach is "that at any location the geology is the sum of its history". The aim was to maximize the amount of useful information that could be obtained during the initial literature search and walkover survey to prepare a more efficient and focused GI. Reference conditions, which group geological materials into similar engineering characteristics interpreted from SI, were estimated and refined as more information became available. This approach is compared to the traditional SI approach in Figure 4 (Baynes et al. 2005, Mackay et al. 2008).

3.2 *Terrain evaluation*

The terrain encountered along the alignment varies from undulating plains, soft hillocks, flat

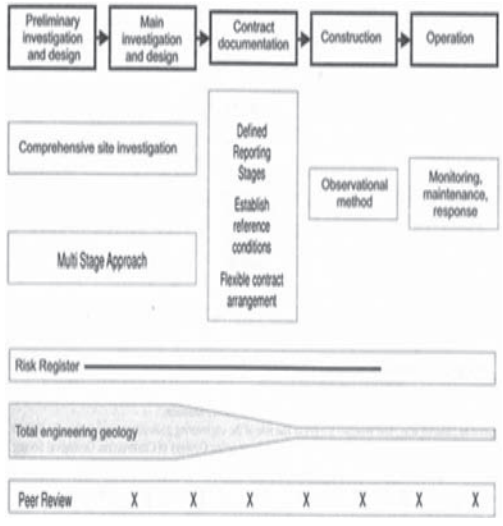

Figure 5. SI using the "Total Engineering Geology" approach (Baynes et al. 2007).

undulating plains, locally exposed rock, typically associated with abrupt changes in gradient, and granitic tor landscapes. Refer to Figure 6 for the terrain evaluation and Plates 1 to 3 for the terrain encountered.

3.3 *Ground investigation*

Following the desk study and walkover survey the GI was estimated using a risk based approach from the effects of adverse ground and groundwater conditions on the construction as outlined in Table 1.

As indicated from the risk assessments a simplified, preliminary GI was carried out including exploratory stations, pits, BHs and rock samples.

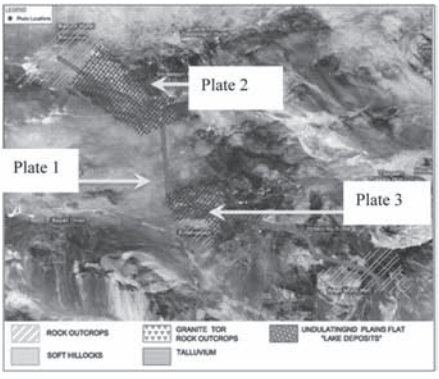

(a)

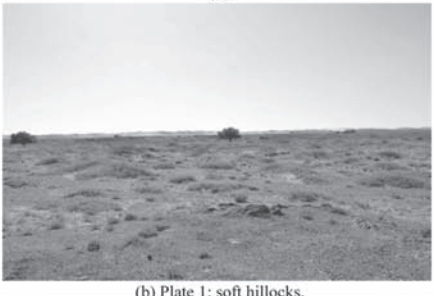

(b) Plate 1: soft hillocks.

(c) Plate 2: flat undulating plains.

(d) Plate 3: talluvium.

Figure 6. Terrain evaluation (a) and Plates 1–3 (b–d).

The BHs were advanced using undisturbed sampling and Standard Penetration Testing techniques and bulk samples and in-situ testing within the pits. Subsequent laboratory testing included particle size distribution, atterberg limit and aggregate testing. The GI specification followed international British and Eurocode standards (BS 1999) as required.

All risks referenced in Tables 1 and 2 involved further detailed walkover surveys to complement the existing walkover survey and the GI. Due to the nature of the ground, including cemented soils, which were highly sensitive to disturbance and addition of water, true undisturbed sampling was difficult to achieve.

3.4 *Findings*

The major geological units, including areas of exposed solid ground beneath the superficial deposits, generally corresponded with the terrain evaluation as follows:

Aeolian deposits—generally covering the entire area with localized increases in thickness in zones of "small hillocks" and in areas of flatter land

Talluvium—typically standing at shallow gradients beneath the rock outcrops

Alluvium and lake deposits—extensive areas of flat ground typically in the vicinity of major rivers

Sedimentary rock (sandstone, shale and coal measures)—typically undulating terrain

Igneous rock (dyke intrusions; basalt and andestite)—associated with abrupt changes in topography and surface exposure

Igneous rock (batholitic intrusions; granite)—"tor" landscape and surface exposure

The general findings of the SI, are presented in Table 2 and Figure 7.

4 INTERPRETATION

A major concern was the adequacy of the ground bearing capacity to support the embankment, paticularly placement on the recent deposits (recent to 66 Ma) identified in Table 2. The total engineering geology approach was used to assess the effects from the recent geological and environmental history on the engineering properties of the ground conditions.

4.1 *Weathering*

The relative effects of the extent of weathering in different environments are presented in Figure 8 (Fookes 1997).

As shown weathering in desert environments, such as the Gobi desert, is minimal. Relatively competent ground with an increased bearing capacity can therefore be expected near surface. As presented in Plate 5 the most recent deposits, referenced Ap-La Q111-N (Table 2), located further to the north-west, showed the weaker superficial deposits to have a minimal thickness and be present over more competent rock, as shown by the difficulty in excavation.

Table 1. Ground/groundwater risk based GI evaluation.

Risks	Effects on	SI method	Mitigation
Surface/ sub-surface water	Embankment/ cutting stability bearing capacity earthworks	Exploratory stations (pits and boreholes) in-situ permeability tests piezometric monitoring	Suitable culvert embankment/cutting protection geotextile/gravel layer suitable area identification/limit fines content in earthworks
Talluvium	Loose cutting stability	Exploratory stations (pits/boreholes, BHs)	Alignment adjustment slope support
Lake deposit/ crust	Bearing capacity	Exploratory stations (pits/BHs)	Remove if underlying rock present leave in place if underlying soil present avoid diversion of surface/subsurface water flow
Tectonic	Cut slope embankment foundations	Exploratory stations particle size distribution (laboratory tests)	Avoid fines placement in embankment add suitale factor for slope/bearing capacity design

Table 2. Ground conditions encountered in the SI.

Geological period	Ground condition
Recent (66 Ma to now)	Alluvium/lake deposits (gravel, clay and sand (key Ap-La Q111-N); talluvium; alluvium/lake deposits (gravel, clay and sand (key L-aN2) and alluvium/lake deposits (cemented granular sand and clay). (key P3).
Cretaceous (66–145 Ma)	Lake-alluvial deposits (key LaK2) and coal measures ("aleurolite"—siltstone and coal measures)
Jurassic (145–200 Ma)	Intrusive rocks (basalt, andesite and granite)
Carboniferous (300–350 Ma)	Shale with basalt and andesite intrusions
Devonian (350–417 Ma)	Sandstone with tuff and basalt and andesite intrusions

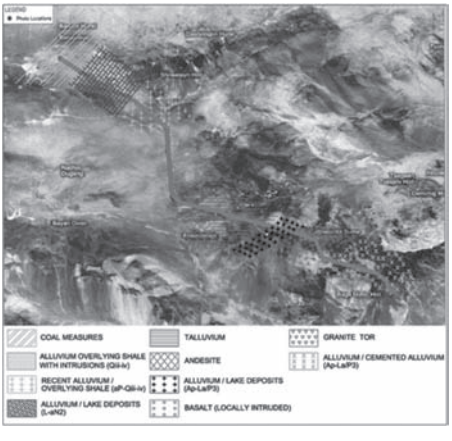

Figure 7. General locations of the ground conditions.

In contrast the older "recent" deposits, referenced P3 (Table 2), located further to the south west in the vicinity of the Galbin Gobi drainage basin towards the south east indicated influence from different environmental effects including the extent of the drainage basin, which accommodated a greater water flow than present, a variety of resistant gravel fragments, transported by past water flow and derived from source areas from a greater distance than the nearby mountain ranges, and the effects of weathering, which indicated effects of a different past weathering environment which may have been tropical (see Fig. 8). The greater extent of weathering, shown by the relative ease of excavation in Plate 6, indicates the relative extent of weathering. Due to the potential reduced bearing capacity at a greater depth consideration for excavation and replacement by selected backfill was needed.

4.2 *Cemented superficial deposits*

In general the majority of the Gobi desert had a highly competent upper crust, termed "duricrust", which is typical of many desert environments and has a high bearing capacity (refer to Fig. 9).

Duricrust is formed as a result of cementing minerals coming out of solution during the evaporation of the near surface groundwater flow. Notwithstanding due to its recent precipitation the cementing agents are highly prone to re-solution and are easily dissolved in the presence of water. Furthermore weaker material, which remained

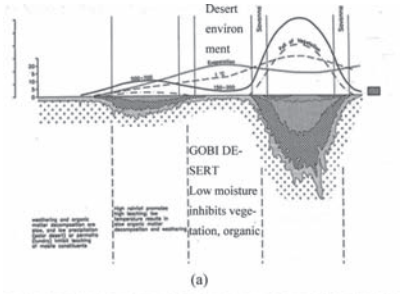

(a)

(b) Plate 5: lake deposits overlying rock

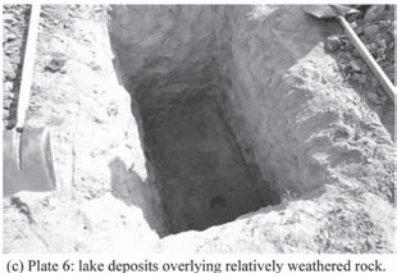

(c) Plate 6: lake deposits overlying relatively weathered rock.

Figure 8. Weathering effects in different environments (a) and Plates 5 and 6 (b & c).

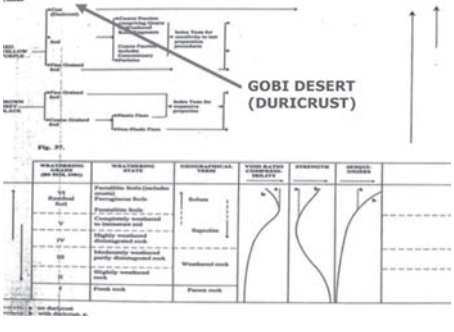

Figure 9. Geotechnical properties.

uncemented was typically present at depth beneath the duri-crust. Refer to Plate 7 on Figure 10.

The thickness of the duricrust and its vicinity to ephemeral stream course was an important consideration for estimating the bearing capacity.

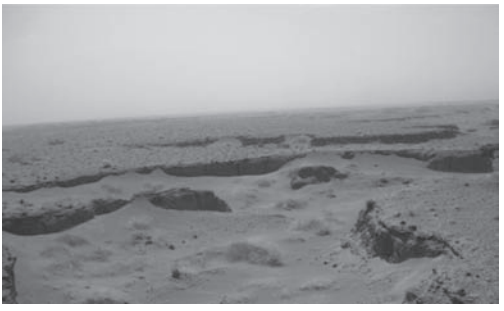

Figure 10. Plate 7: Cemented soil with overlying Aeolian deposits.

5 CONCLUSIONS

The desk study and walkover identified risks, physical properties and engineering implications at an early stage in the potential development of the railway alignment by interpreting the physical characteristics of the ground as a sum of its history. In particular the technique assisted in estimating the bearing capacity to place embankments across superficial deposits.

ACKNOWLEDGEMENTS

The authors wish to thank Ronald Chan in assistance in preparing this paper. The opinions expressed in this paper are those solely of the authors and not of any other party.

REFERENCES

Baynes, F.J., Fookes, P.G. & Kennedy, J.F. 2005. The total engineering geology approach applied to railways in the Pilbara, Western Australia. *Bulletin of Engineering Geology and the Environment* 64: 67–94.

British Standards (BS), 1999. *Code of practice for site investigations*. London: British Standards Institution (BSI).

Fookes, P.G. 1997. The 1st glossop lecture, geology for engineers: the geological model, prediction and performance. *Quaterly Journal of Engineering Geology* 30(4): 293–424.

Fookes, P.G., Hearn, G.J. & Tollin, B. 2005. Aligning oil and gas pipelines through the Makharov Mountains, Sakhalin Islands, Russia. In M. Sweeney (ed.), *Int. Conf. on Terrain and Geo-hazards Challenges Facing On-shore oil and gas pipelines, London, 2–4 June 2004*.

Mackay, A.D. 2010. The role of the civil engineer in the changing demand for space in HK. In *HKIE Civil Division Conference 2010: infrastructure solutions for tomorrow, Hong Kong, 12–14 April 2010*.

Geotechnical Safety and Risk IV – Zhang et al. (eds)
© 2014 Taylor & Francis Group, London, ISBN 978-1-138-00163-3

Bayesian model updating of a tunnel in soft soil with settlement measurements

I. Papaioannou, W. Betz & D. Straub
Engineering Risk Analysis Group, Technische Universität München, Munich, Germany

ABSTRACT: Monitoring is an essential element of modern tunneling construction. The most common monitoring method is measuring displacements, for example convergence of the tunnel opening or surface settlements. Measurement outcomes can be used to update the knowledge on material properties of the soil or other parameters that enter numerical models of the structural behavior of the tunnel. In probability theory, this process can be formalized in the concept of Bayesian updating. In this paper, we apply the Bayesian concept to update the numerical model of a tunnel in soft soil conditional on settlement measurements. The tunnel is constructed by means of the conventional tunneling method and modeled with 2D finite elements applying the stress reduction method. We assume that settlement measurements are taken at full excavation and utilize the measurements to update the material properties of the soil as well as the the relaxation factor of the stress reduction method. Updating is performed by means of BUS, a recently proposed method for Bayesian updating of mechanical models with structural reliability methods.

1 INTRODUCTION

In tunneling design, engineers establish numerical models of the tunnel excavation and conduct structural analyses to predict the stresses and deformations for the considered designs. However, there is significant uncertainty in the choice of the model parameters. Uncertainties may be related to the inherent spatial variability of the mechanical properties of the soil but also to the application of dimensionally reduced models to represent complex phenomena. A proper assessment of the safety and serviceability of the structural design involves the modeling of the uncertainties by use of probabilistic models and the evaluation of the structural reliability against the respective design requirements.

During the tunnel construction process, measurements of physical quantities such as deformations and stresses are typically conducted. Measurements can be used to compare predictions of the numerical model with the actual structural behavior, to verify the reliability of the structural design as well as to update the probabilistic description of the parameters of the numerical model. The latter is formalized in the concept of Bayesian updating. Thereby, a prior probabilistic model is updated with new data and information to a posterior probabilistic model.

Bayesian updating requires the solution of a potentially high-dimensional integral to obtain the posterior distribution of the model parameters. Commonly, Markov Chain Monte Carlo (MCMC) sampling is used to sample directly from the posterior distribution, thus bypassing the solution of the aforementioned integral (Gelman 2004). An alternative approach is based on interpreting the updating problem as a structural reliability problem (Straub and Papaioannou 2013). This approach, termed BUS, applies methods originally developed for structural reliability analysis to obtain samples from the posterior distribution.

In this paper, we apply BUS to learn the model parameters of a tunnel in soft soil using settlement measurements. The tunnel is constructed by the conventional tunneling method. We model the tunnel in 2D using nonlinear plain-strain finite elements and the 3D arching effect is approximated by application of the stress reduction method. Using assumed settlement measurements at full excavation, we update the material properties of the soil as well as the relaxation factor of the stress reduction method.

2 MODEL DESCRIPTION

2.1 *Mechanical model*

A conventional driven tunnel with a horse-shoe shaped profile is considered in this study (see Fig. 1). The problem is modeled in the SOFiSTiK Finite Element (FE) software package (SOFiSTiK AG 2012), using 2D plain strain finite elements. The numerical model has a width of 80 m and a height of 26 m. The FE mesh is shown in Figure 2.

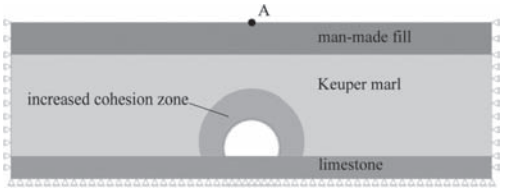

Figure 1. Ground layers considered in the model.

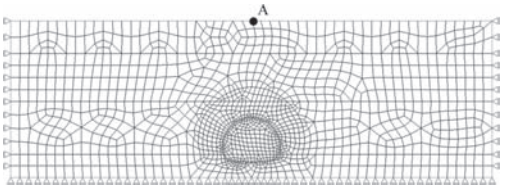

Figure 2. Finite element mesh.

In this study, we are interested in surface settlements over the tunnel center line (point A in Fig. 1). The excavation process is modeled by application of the stress reduction method (Panet and Guenot 1982). In this method, a prescribed fraction β of the initial stress is left inside the tunnel as a support pressure to approximately account for the three-dimensional arching effect. This support pressure is then removed after installation of the lining. The parameter β is termed relaxation factor.

The model consists of three different ground layers; the layers are illustrated in Figure 1. The cover layer is a man-made fill and has a depth of 5.4 m. Heavily weathered soft rock known as Keuper marl forms the second layer. The thickness of this layer is 16.8 m. We adopt a hardening plasticity soil model (SOFiSTiK AG 2012) to describe the material behavior of the first two layers. This material model allows for a realistic description of the stiffness and hardening behavior of soft soil in settlement analysis (Möller 2006). The material properties of the cover layer are as follows: elastic modulus for unloading-reloading: 30 MPa, Poisson's ratio: 0.2, specific weight: 20 kN/m^3, friction angle: 25°, cohesion: 10 kPa, oedometric stiffness modulus: 10 MPa, stiffness modulus for primary loading: 10 MPa. The exponent in the hardening law is selected as 0.5 for the first and the second layer. The angle of dilatancy is assumed as zero, corresponding to a non-associated flow rule. The soil parameters of the Keuper marl layer are modeled as random and their prior probabilistic description is discussed in Section 2.2. Strong limestone constitutes the bottom layer. The Mohr-Coulomb law is applied for this layer. The material properties are: Young's modulus: 575 MPa, Poisson's ratio: 0.2, specific weight: 23 kN/m3, friction angle: 35°, cohesion: 200 kPa. Due to the much larger stiffness of the limestone compared to the stiffness of the overlaying materials, only 3.8 m of this layer are modeled.

The height of the tunnel above the limestone layer is 6.2 m. Consequently, the tunnel is located in a depth of 16 m below the ground surface. At the intersection of the second and the third layer, the tunnel has a width of 9.16 m. In the vicinity of the tunnel the Keuper marl is reinforced with nails. This is modeled by increasing the cohesion in the affected region (see Fig. 1) by 25 kPa. Moreover, the tunnel is located above the groundwater level. The shotcrete lining is modeled using linear beam elements with a normal stiffness of 10.5 GN and a flexural rigidity of 26.78 MNm^2.

2.2 *Prior probabilistic model*

The cover layer and the limestone layer are considered as deterministic in the analysis. Since the cover layer is a man-made fill, we assume that its soil properties are well-known, and the associated uncertainties are small compared to the uncertainties in the material description of the Keuper marl layer and hence can be neglected. The limestone layer is also modeled as deterministic, because, due to its large stiffness, the contribution of this layer to the surface settlements is negligible. The probability distributions describing the uncertainties in the material parameters of the Keuper marl layer are listed in Table 1. We assume that the stiffness modulus for primary loading E_{50} equals the oedometric stiffness modulus E_{oed}. We also consider a correlation of 0.7 between E_{oed} and the elastic modulus E_{ur}. The friction angle and the cohesion are assumed to have a negative correlation of –0.5.

In conventionally driven tunnels, there is usually a large uncertainty in the choice of the relaxation factor $\beta \in [0, 1]$ of the stress reduction method (Möller 2006). In this study β is modeled as a beta-distributed random variable (see Table 1).

Table 1. Prior distribution of the parameters of the Keuper marl layer.

Parameter	Distribution	Mean	CV
Relaxation factor β	Beta (0.0, 1.0)	0.5	10%
Elast. mod. E_{ur} [MPa]	Lognormal	80.0	32%
Oedometr. mod. E_{oed} [MPa]	Lognormal	30.0	32%
Poisson's ratio ν	Beta (0.0, 0.5)	0.2	15%
Friction angle φ [°]	Beta (0.0, 45.0)	20.0	15%
Cohesion c [kPa]	Lognormal	25.0	30%
Specific weight γ [kN = m^3]	Lognormal	24.0	5%

A reliability assessment of the tunnel was presented in Ranjan et al. (2013). Therein, a two-step approach is adopted. In a first step, the reliability analysis was performed applying the First Order Reliability Method (FORM) [e.g. see (Der Kiureghian 2005)]. As a byproduct of the FORM, the influence coefficients provide information on the sensitivity of the reliability in terms of the random variables. This information was used to identify the random variables with the highest influence that, in a second step, are modeled as random fields.

Figure 3 depicts in a pie graph the squared influence coefficients obtained by the FORM. It is observed that the variable with the largest influence is the oedometric stiffness modulus E_{oed} followed by the relaxation factor β. Based on this result, we account for the inherent spatial variability of E_{oed}. Since E_{oed} is strongly correlated with the elastic modulus E_{ur}, the spatial variability of the latter parameter is also modeled. This is achieved by modeling the two parameters as cross-correlated homogeneous random fields. The joint distribution of the two fields at each pair of locations is modeled by the Nataf distribution (Der Kiureghian and Liu 1986) with lognormal marginals according to Table 1. The spatial variability depends only on the separation in horizontal and vertical direction between two locations, Δx and Δy. The following exponential autocorrelation coefficient function is chosen for both random fields:

$$\rho(\Delta x, \Delta y) = \exp\left(-\frac{\Delta x}{l_x} - \frac{\Delta_y}{l_y} \right) \tag{1}$$

where $l_x = 20$ m and $l_y = 5$ m denote the correlation lengths in horizontal and vertical direction, respectively. The cross-correlation coefficient function is:

$$\rho_{\text{cross}}(\Delta x, \Delta y) = \rho_c \cdot \rho(\Delta x, \Delta y) \tag{2}$$

where $\rho_c = 0.7$ denotes the correlation of E_{oed} and E_{ur} at the same location.

Since the random fields have the Nataf distribution, they can be expressed as functions of correlated Gaussian fields. Due to the form of their cross-correlation function, the latter fields can be transformed to independent Gaussian fields by performing the Cholesky decomposition of the 2×2 correlation matrix, whose off-diagonal terms express the correlation of the two fields at the same location. The underlying independent Gaussian fields are discretized by application of the Karhunen-Loéve expansion (Ghanem and Spanos 1991). That is, each field is represented as a truncated series of products of the eigenfunctions of its autocorrelation function and independent random variables. Each random field is dicretized with 100 random variables. Therefore the total number of random variables in the problem is 205.

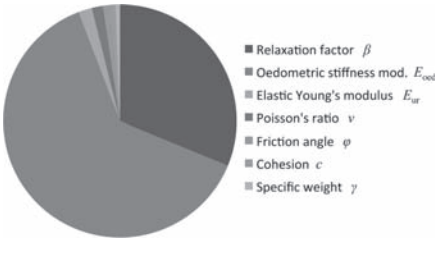

Figure 3. Squared influence coefficients obtained by FORM.

3 BAYESIAN UPDATING WITH STRUCTURAL RELIABILITY METHODS (BUS)

Let $\mathbf{X}$ denote the n-dimensional random vector representing the uncertain model parameters discussed in Section 2.2. Also, let $f(\mathbf{x})$ be the prior joint Probability Density Function (PDF) of $\mathbf{X}$. Assume that a measurement $u_{\text{A,m}}$ of the surface settlement (point A in Fig. 1) is made at full excavation. The measurement is subjected to an additive error ϵ which is described by a normal PDF f_ϵ with zero mean and standard deviation σ_ϵ. The measurement information can be described by the event $Z = \{u_{\text{A,m}} - u_{\text{A}}(\mathbf{x}) = \epsilon\}$, where $u_{\text{A}}(\mathbf{x})$ is the surface settlement evaluated by the FE program for a realization $\mathbf{x}$ of the random vector $\mathbf{X}$. The corresponding likelihood function can be expressed as follows:

$$\begin{aligned} L(\mathbf{x}) &= f_\epsilon[u_{\text{A,m}} - u_{\text{A}}(\mathbf{x})] \\ &= \frac{1}{\sigma_\epsilon \sqrt{2\pi}} \exp\left(-\frac{(u_{\text{A,m}} - u_{\text{A}})^2}{2\sigma_\epsilon^2} \right) \end{aligned} \tag{3}$$

The posterior joint PDF of $\mathbf{X}$ conditional on the measurement event Z can be obtained by application of Bayes' rule:

$$f(\mathbf{x} \mid Z) = \frac{L(\mathbf{x}) f(\mathbf{x})}{\int_{\mathbb{R}^n} L(\mathbf{x}) f(\mathbf{x}) d\mathbf{x}} \tag{4}$$

The evaluation of the n-fold integral in the denominator of Equation (4) is computationally demanding; this has motivated the application of MCMC algorithms for sampling directly from the posterior $f(\mathbf{x}|Z)$ (Gilks et al. 1998, Gelman 2004). Here, we apply an alternative approach, termed BUS, which uses methods originally developed for structural reliability analysis to obtain samples from the posterior distribution (Straub and Papaioannou 2013).

The method is based on the algorithm for reliability updating developed in Straub (2011) and applied in Papaioannou and Straub (2012) to the reliability updating of geotechnical structures.

The BUS approach introduces the following limit state function:

$$h(\mathbf{x},u_0) = u_0 - \Phi^{-1}[cL(\mathbf{x})] \tag{5}$$

where u_0 is the outcome of a standard normal random variable U_0, $\Phi^{-1}(.)$ is the inverse of the standard normal cumulative distribution function and c is a positive constant chosen to ensure that $cL(\mathbf{x}) \leq 1$. It is shown in Straub and Papaioannou (2013) that the posterior PDF $f(\mathbf{x}|Z)$ is proportional to the prior PDF $f(\mathbf{x})$ conditional on the event $Z_e = \{h(\mathbf{x}, u_0) \leq 0\}$. Hence, solving the updating problem becomes equivalent to solving the structural reliability problem of estimating the probability $\Pr(Z_e)$.

It should be noted that the constant c has considerable influence on the efficiency of the BUS approach, since its value is directly proportional to the probability $\Pr(Z_e)$ (Straub and Papaioannou 2013). A large value of $\Pr(Z_e)$ is beneficial for most structural reliability methods. Therefore, c should be chosen a large as possible, while still ensuring that $cL(\mathbf{x}) \leq 1$. For the likelihood function of Equation (3), the optimal choice is $c = [\max f_\epsilon(\in)]^{-1} = \sigma_\epsilon \sqrt{2\pi}$.

For most reliability methods, it is convenient to transform the problem from the original random variable space to a space of independent standard normal random variables. Since the distribution of the random vector $\mathbf{X}$ is described by the Nataf model, such a transformation $[U_1, \ldots, U_n] = \mathbf{T}(\mathbf{X})$ is straightforward (Der Kiureghian and Liu 1986). The limit-state function $h(x, u_0)$ can be expressed in the transformed space as $H(\mathbf{u}) = h[\mathbf{T}^{-1}(u_1, \ldots, u_n); u_0]$, where $\mathbf{T}^{-1}$ denotes the inverse transformation and $u \in \mathbb{R}^{n+1}$ is the outcome of $\mathbf{U} = [U_0, U_1, \ldots, U_n]$.

The formulation of the updating problem in terms of the limit-state function of Equation (5) allows for the application of a variety of structural reliability methods for estimation of the posterior PDF. Application of crude Monte Carlo method will lead to a rejection-acceptance scheme, with $\Pr(Z_e)$ being the acceptance probability. However, this approach becomes very inefficient for small $\Pr(Z_e)$, which correspond to cases where the posterior distribution differs considerably from the prior. In the following section, we discuss the application of BUS in conjunction with Subset Simulation (SubS), which is an adaptive Monte Carlo method for estimating small probabilities. The SubS is especially efficient in high dimensional problems, as is the case in the present application where a large number of random variables is used for the random field representation of the soil properties.

3.1 *SubS-based BUS*

The SubS method, originally developed in Au & Beck (2001), evaluates the probability $\Pr(Z_e)$ of the event $Z_e = \{H(\mathbf{u}) \leq 0\}$ as a product of larger conditional probabilities. This is achieved by expressing the event Z_e as the intersection of M intermediate events that are nested, i.e. it holds $Z_1 \supset Z_2 \supset \ldots \supset Z_M = Z_e$. The events $\{Z_i, i = 1, \ldots, M\}$ are defined as $Z_i = \{H(\mathbf{u}) \leq b_i\}$, where $b_1 > b_2 > \ldots > b_M = 0$. The probability $\Pr(Z_e)$ is then expressed as

$$\Pr(Z_e) = \prod_{i=1}^{M} \Pr(Z_i \mid Z_{i-1}) \tag{6}$$

where Z_0 denotes the certain event and $\Pr(Z_i|Z_{i-1})$ is the probability of the event Z_i conditional on the occurrence of the event Z_{i-1}. The values b_i can be chosen adaptively, such that the estimates of the conditional probabilities correspond to a given value p_0.

The probability $\Pr(Z_1|Z_0) = \Pr(Z_1)$ is computed by applying crude Monte Carlo simulation. To estimate the conditional probabilities $\{\Pr(Z_i|Z_{i-1}), j = 2, \ldots, M\}$, we need to obtain samples of $\mathbf{U}$ conditional on the occurrence of the events $\{Z_{i-1}, j = 2, \ldots, M\}$. Assume that at each subset level i, J samples $\{\mathbf{u}^{(j)}, j = 1, \ldots, J\}$ of $\mathbf{U}$ conditional on Z_{i-1} are available. The threshold b_i is set as the $(1 - p_0)$-percentile of the samples; the samples $\mathbf{u}^{(j)}$ for which $H(\mathbf{u}^{(j)}) \leq b_i$ are then used as seeds for the simulation of samples conditional on Z_i by application of an MCMC algorithm (Papaioannou et al. 2013).

For Bayesian updating, we are interested in obtaining samples conditional on Z_e. Therefore, we add one final step, which is to obtain K such samples trough MCMC starting from the samples generated at the last subset level M for which $H(\mathbf{u}^{(j)}) \leq 0$. These samples are then transformed to the original space as $\{\mathbf{x}^{(k)} = \mathbf{T}^{-1}(u_1^{(k)}, \ldots, u_n^{(k)}), k = 1, \ldots, K\}$ in order to obtain samples from the posterior distribution $f(\mathbf{x}|Z)$. In this study, the parameters of the SubS algorithm for Bayesian updating are set as follows: $p_0 = 0.1$; number of samples per level $J = 1000$; number of target samples $K = 1500$.

4 RESULTS AND DISCUSSION

We consider a measurement outcome of $u_{A,m} = 20$ mm. The prior mean of $u_A(\mathbf{X})$ is 10.5 mm, which indicates that the prior model underestimates the measured surface settlement. The updating was performed for two different values of the standard deviation σ_ϵ of the measurement error: 1 mm and

2 mm. Figures 4 and 5 show the posterior sample means of the oedometric stiffness modulus E_{oed} and the elastic stiffness modulus E_{ur}, respectively. The samples statistics of the remaining material parameters of the Keuper marl layer are shown in Table 2.

Looking at the results for σ_ϵ = 2 mm, one can observe that the posterior mean of E_{oed} at the elements within and around the tunnel is smaller than the prior. Note that E_{oed} is the parameter with the highest influence on the tunnel's reliability (see Fig. 3). Away from the tunnel, the posterior mean of E_{oed} increases and the value of its prior mean is reached at the upper left and right corners of the computational domain. Similar results are obtained for E_{ud}, which is highly correlated with E_{oed}. Due to

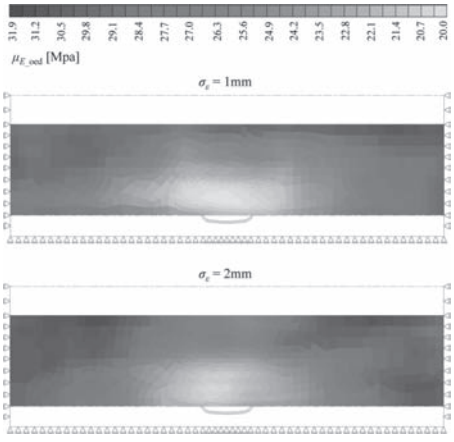

Figure 4. Posterior mean of the oedometric stiffness modulus E_{oed} of the Keuper marl layer.

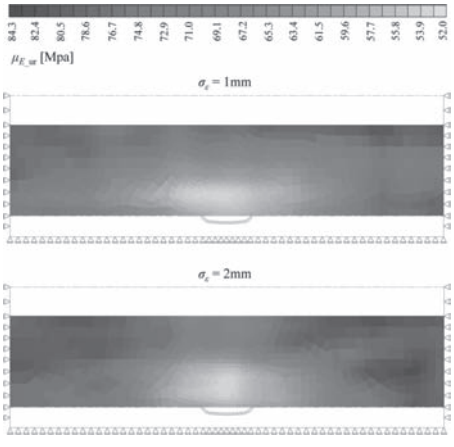

Figure 5. Posterior mean of the elastic stiffness modulus E_{ur} of the Keuper marl layer.

Table 2. Statistics of the posterior distribution of the random variables of the Keuper marl layer.

	σ_ϵ = 1 mm		σ_ϵ = 2 mm	
Parameter	Mean	CV	Mean	CV
Relaxation factor β	0.42	8.3%	0.44	8.4%
Poisson's ratio v	0.19	14.5%	0.19	15%
Friction angle φ [°]	18.5	17.2%	18.9	17.2%
Cohesion c [kPa]	29.04	30.5%	26.3	29.3%
Specific weight γ [kN/m^3]	24.2	5%	24.4	5.2%

the symmetry of the problem, it is expected that the spatial distribution of the posterior means of both E_{oed} and E_{ud} be symmetric about the vertical central axis. This result is evident in the area close to the tunnel, however away from the tunnel one can observe what seems like local random fluctuations from the expected result. This effect is attributed to sampling error and is related to the fact that in the areas away from the tunnel the influence of the values of E_{oed} and E_{ud} on the surface settlements is minor. That is, a large number of combinations of material values in these areas can justify the measurement outcome, which requires a large number of samples for the SubS algorithm to account for all the possible combinations.

The effect of the measurement is also evident in the posterior mean of the relaxation factor β of the stress reduction method, which is decreased compared to its prior. Its posterior Coefficient of Variation (CV) is also smaller than its prior, which reflects the impact of the measurement on the variable. Moreover, the initial stress for the stress reduction is computed based on the elements corresponding to the tunnel whose posterior means are much lower than their priors. This reveals the influence of the 2D modeling of the arching effect by the stress reduction method, which is consistent with the fact that most settlements will take place in the excavation phase, i.e. before the installation of the lining.

The friction angle ϕ is slightly influenced by the measurement; its posterior mean is decreased compared to the prior however its coefficient of variation is somewhat increased which indicates that the impact of the measurement on ϕ is small. The mean of the cohesion c is increased reflecting its negative correlation with the friction angle, while the influence of the measurement on the rest of the parameters is negligible.

The results for the case where the standard deviation of the measurement is decreased, i.e. when σ_ϵ = 1 mm, confirm the high impact of the measurement outcome on the stiffness variables

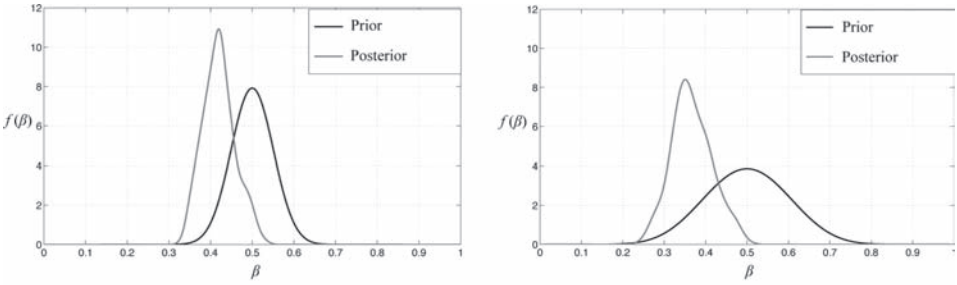

(a) Prior CV of β: 10%. (b) Prior CV of β: 20%.

Figure 6. Posterior PDF of the relaxation factor β for σ_ϵ = 1 mm.

E_{oed}, E_{ud} and the relaxation factor β. In this case, which implies higher information content of the measurement, the posterior mean of β is further decreased and the weak zone around the tunnel with low values of E_{oed} and E_{ud} is increased.

Figure 6 demonstrates the influence of the prior knowledge on the relaxation factor β. Therein, the prior and posterior PDFs of β are plotted for two different assumed prior coefficients of variation (10% and 20%) and for σ_ϵ = 1 mm. It is observed that as the prior knowledge on beta decreases, i.e. as its prior coefficient of variation increases, the influence of the measurement becomes higher. Comparing the posterior PDFs for the two cases, we see that the same measurement information leads to much lower values of β when a larger prior coefficient of variation is assumed. This result further highlights the influence of the 2D modeling of the arching effect on the surface settlements. Moreover, it shows how the confidence on the prior assumption can influence the updating results that may provide a basis for further risk and reliability assessment.

5 CONCLUSION

In this paper, we performed Bayesian updating of the parameters of a 2D numerical model of a tunnel in soft soil, conditional on settlement measurements. We applied BUS, a recently proposed method for Bayesian updating with structural reliability methods, combined with subset simulation, an adaptive Monte Carlo method that is able to handle efficiently problems with a large number of random variables. The results demonstrate the influence of the accuracy of the measurement device as well as the prior knowledge of the uncertain parameters on their posterior distributions. It was shown that the highest impact of the measurement fell on the stiffness moduli and the relaxation parameter of the stress reduction method that models the 3D arching effect of the stress distribution.

REFERENCES

Au, S.K. & Beck, J.L. 2001. Estimation of small failure probabilities in high dimensions by subset simulation. *Probabilist. Eng. Mech.* 16(4): 262–277.

Der Kiureghian, A. 2005. First- and second-order reliability methods. In E. Nikolaidis, D.M. Ghiocel, and S. Singhal (Eds.), *Engineering Design Reliability Handbook*. Boca Raton, FL: CRC Press.

Der Kiureghian, A. & Liu, P.L. 1986. Structural reliability under incomplete probability information. *J. Eng. Mech.-ASCE* 112(1): 85–104.

Gelman, A. (2004). *Bayesian data analysis*. Boca Raton, FL: Chapman & Hall/CRC.

Ghanem, R. & Spanos, P. 1991. *Stochastic Finite Elements—A Spectral Approach*. Berlin: Springer.

Gilks, W.R., S. Richarson & D.J. Spiegelhalter (Eds.) 1998. *Markov chain Monte Carlo in practice*. Boca Raton, FL: Chapman & Hall/CRC.

Möler, S. 2006. Tunnel induced settlements and structural forces in linings. Ph.D. thesis, Institut für Geotechnik, Universität Stuttgart.

Panet, M. & Guenot, A. 1982. Analysis of convergence behind the face of a tunnel. In *Proc. International Conference on Tunnelling '82*, London. IMM.

Papaioannou, I., Betz W., Zwirglmaier K. & Straub D. 2013. MCMC algorithms for subset simulation. Manuscript, Engineering Risk Analysis Group, TU München.

Papaioannou, I. & Straub D. 2012. Reliability updating in geotechnical engineering including spatial variability of soil. *Comput. Geotech.* 42: 44–51.

Ranjan, R., Betz W., Papaioannou I. & Straub D. 2013. A two-step approach for reliability assessment of a tunnel in soft soil. In *Proc. 3rd International Conference on Computational Methods in Tunnelling and Subsurface Engineering EUROTUN: 2013, Bochum*.

SOFiSTiK AG. 2012. *SOFiSTiK analysis programs version 2012*. Oberschleißheim: SOFiSTiK AG.

Straub, D. 2011. Reliability updating with equality information. *Probabilist. Eng. Mech.* 26(2): 254–258.

Straub, D. & Papaioannou I. (under review 2013). Bayesian updating of mechanical models. *J. Eng. Mech.-ASCE*.

Geotechnical Safety and Risk IV – Zhang et al. (eds)
© 2014 Taylor & Francis Group, London, ISBN 978-1-138-00163-3

A role of monitoring to reduce the uncertainty in the performance of pile foundations

Satoko Ryuo
Railway Technical Research Institute, Tokyo, Japan

Yoshiharu Asaka
Shimizu Corporation, Tokyo, Japan

Kenichi Soga
University of Cambridge, Cambridge, UK

ABSTRACT: In typical conventional foundation design, the inherent variability of soil properties, model uncertainty and construction variability are not modeled explicitly. A main drawback of this is that the effect of each variability on the probability of an unfavorable event cannot be evaluated quantitatively. In this paper, a method to evaluate the uncertainty-reduction effect on the performance of a vertically-loaded pile foundation by monitoring the pile performance (such as pile load testing or placing sensors in piles) is proposed. The effectiveness of the proposed method is examined based on the investigation of a 120-pile foundation placed on three different ground profiles. The computed results show the capability of evaluating the uncertainty-reduction effect on the performance of a pile foundation by monitoring.

1 INTRODUCTION

Most pile foundations are designed in a deterministic manner. That is, the inherent variability of soil properties, model uncertainty and construction variability are not modeled explicitly; instead some factors of safety are applied to account for the uncertainty and variability. In such conventional design method, a main drawback is that the effect of a specific variability on the probability of an unfavorable event cannot be evaluated quantitatively. A more rational design method that evaluates the uncertainties for a pile group foundation is required.

The performance of a vertically-loaded pile that considers the variation of soil properties was investigated by Phoon et al. (1990), Quek et al. (1992), Fenton and Griffiths (2003), Haldar and Babu (2008) and Wang et al. (2011). In general, these studies do not model the variability of soil properties in three dimensional conditions and do not evaluate the uncertainty for a pile group foundation.

Monitoring of a vertically-loaded pile is becoming increasingly popular in order to find the pile performance directly and to reduce uncertainly of the performance. Leung et al. (2011) proposed a method to decide the optimum locations of monitoring points based on decreasing the uncertainty in predicting the overall differential settlements. However, the effectiveness of pile monitoring on the performance of a pile group foundation from the viewpoint of improving the accuracy of the design was not addressed.

In this paper, a procedure to evaluate the uncertainty-reduction on the performance of a vertically-loaded pile foundation by monitoring is developed in the following manner. First, at the locations of the borehole, the ultimate resistance of a "virtual" pile is calculated using the borehole information and widely-used calculation formulae. Using this data, the performance of piles at actually installed locations is evaluated using the Kriging method. The uncertainty is modeled stochastically by considering the variability of soil parameters and construction. The uncertainty of monitored piles is also modeled. Then, the uncertainty of the whole pile group foundation that consists of both normal and monitored piles is modeled. To demonstrate the effectiveness of the proposed evaluation method, a hypothetical case of an end-bearing 120-pile foundation placed on three different ground profiles is considered. The computed results show good agreement with typical rules of thumb, indicating that the developed method is capable of evaluating how the uncertainty on the performance of a piled foundation can be reduced by monitoring.

2 A PROCEDURE TO EVALUATE THE UNCERTAINTY REDUCTION

2.1 *Uncertainty of individual pile*

A vertically-loaded pile is modeled by shaft resistance and base resistance. The uncertainty of an individual pile performance can then be defined by the ultimate shaft resistance and ultimate base resistance. In this paper, widely-used calculation formulae (ICE(2012)) are applied to estimate the ultimate shaft resistance and ultimate base resistance.

The ultimate shaft resistance is given as follows.

$$R_{s,cal} = \pi D \int_0^L \tau_s dz \tag{1}$$

$$\tau_s = \alpha c_u \quad \text{(for clayey soils)} \tag{2}$$

$$\tau_s = \sigma_h' \tan\delta' = K\sigma_v' \tan\delta' = \beta\sigma_v' \quad \text{(for sandy soils),} \tag{3}$$

where D = iameter of pile; L = thickness of layer which corresponds to length of pile calculating shaft resistance; τ_s = shaft resistance per unit area; α = empirically-determined reduction coefficient; c_u = undrained shear strength (cohesion); σ_v' = effective stress in horizontal direction; σ_v' = effective stress in vertical direction (effective overburden pressure); K = coefficient of lateral pressure; δ' = friction angle between pile shaft and ground; and $\beta = K \times \tan\delta'$. Apart from the variance in diameter D, the uncertainty of the ultimate shaft resistance is assumed to originate from layer thickness and undrained shear strength for clayey soils, and layer thickness, effective overburden pressure, coefficient of lateral pressure and friction angle for sandy soils.

The ultimate base resistance is computed by the following formulae.

$$R_{b,cal} = q_b A_b \tag{4}$$

$$q_b = N_c c_u \quad \text{(for clayey soils)} \tag{5}$$

$$q_b = N_q \sigma_v' \quad \text{(for sandy soils)} \tag{6}$$

where A_b = base area of pile; and N_c, N_q = coefficients of bearing capacity. The value of N_c is typically 9 and N_q is a function of internal friction angle (Berezantzev et al. (1961)). Apart from the variance in base area A_b, the uncertainty in ultimate base resistance is assumed to originate from undrained shear strength for clayey soils, and effective overburden pressure and internal friction angle for sandy soils.

In this paper, the uncertainty of soil parameters and construction are characterized by a normal distribution. Table 1 shows the variation coefficient of soil parameters used for estimating pile ultimate capacity. Based on these results, the variation coefficient of ultimate capacity resulting from uncertainty in soil parameters is assumed to be 0.3 for both shaft resistance and base resistance. It should be noted that the formulae for calculating the resistance values have also uncertainty and that there is no appropriate reference about the degree of uncertainty for the formulae themselves. In this study, the variation coefficient of ultimate resistance resulting from the uncertainty in the formulae is arbitrarily set to 0.3. Further study is needed to examine this uncertainty.

Using the values presented above, the magnitude of uncertainty (i.e. variation coefficient) in the ultimate shaft resistance and ultimate base resistance of a pile located at a borehole location is given in Table 2. The uncertainty of the ultimate shaft resistance is 0.42, whereas the uncertainty

Table 1. Soil parameters published in the literature.

Soil parameter	Variation coefficient range	References
Weight density	0–0.15	Harr (1984), Lacasse and Nadim (1997), Phoon and Kulhawy (1999a)
Undrained shear strength (UU, UC)	0.1–0.70	Harr (1984), Cherubini (1997), Lacasse and Nadim (1997), Phoon and Kulhawy (1999a, 1999b), Duncan (2000)
Internal friction angle	0.02–0.15	Harr (1984), Phoon and Kulhawy (1999a, 1999b)
SPT N-value	0.15–0.5	Harr (1984), Barker et al. (1991), Phoon and Kulhawy (1999a)
Shear modulus or Young's modulus	0.15–0.65	Phoon and Kulhawy (1999a)
DMT Horizontal stress index	0.2–0.6	Phoon and Kulhawy (1999a)
Compression index	0.1–0.37	Harr (1984), Duncan (2000)

Table 2. Magnitude of uncertainty and its factors for virtual pile.

Resistance	Variability factors	Set values of variation coefficients at borebole locations	Remarks
Ultimate shaft resistance	Layer thickness	Known	At borehole locations
	Soil parameter		
	Clayey soil	0.3	Shear strength
	Sandy soil	0.3	Unit weight, coefficient of lateral pressure, and friction angle
	Calculation formula and construction	0.3	Model uncertainty and construction variability
	Overall rating	0.42	$= (0.3^2 + 0.3^2)^{0.5}$
Ultimate base resistance	Upper layer thickness	Known	At borehole locations
	Soil parameter		
	Clayey soil	0.3	Shear strength
	N_q of sandy soil	0.3	Unit weight and friction angle
	Calculation formula and construction	0.3	Model uncertainty and construction variability
	Overall rating	0.42	$= (0.3^2 + 0.3^2)^{0.5}$

Table 3. Magnitude of uncertainty and its factors for monitored pile.

Resistance	Variability factors	Set values of variation coefficients at borehole locations	Remarks
Ultimate shaft	Sensor accuracy, variation of deformation modulus	0.05	Overall rating
Ultimate base resistance	Sensor accuracy	0.05	Overall rating

of the ultimate base resistance is also 0.42. These values of uncertainty approximately coincide with the variation coefficients of resistance calculated from field tests in previous studies (ex. Barker et al. (1991), Okahara et al. (1993), Kay (1993), Architectural Institute of Japan (AIC) (2001)). Hence it is concluded that the developed procedure for calculating uncertainty is reasonable.

For a pile that is directly monitored by instrumentation or if a pile load test was carried out, the uncertainty of the "monitored" pile is governed by the accuracy of measurement devices, the parameters used in conversion of measurement and physical quantity such as Young's modulus of concrete or steel. In this paper, for monitored piles, the variation coefficients of ultimate shaft resistance and ultimate base resistance are assumed as 0.05 (see Table 3). These values are smaller than the values assigned for non-monitored piles, which are given in Table 2.

2.2 *Uncerainty of a whole pile group foundation*

The uncertainty of a whole pile group foundation that consists of normal and monitored piles can be evaluated by the following steps.

1. First, using the borehole data, the thickness of soil layers and the soil parameter values are estimated by the Kriging method at all pile locations.
2. At borehole locations, the ultimate shaft resistance and ultimate base resistance of a "virtual" pile are calculated. Also, based on the thickness of soil layers and the soil parameter values evaluated from Step (1) above, the ultimate shaft resistance and ultimate base resistance of each pile in the actual foundation are calculated by using each borehole data.
3. A pile or piles that will be monitored are randomly selected as a given monitoring scenario. The mean value of the ultimate shaft resistance and base resistance obtained from Step (2) has a variability characterized by a normal distribution and the 95% confidence bounds is set as 0.05 for monitored piles and 0.42 for "virtual" piles. Then, 1000 data sets of shaft resistance and base resistance are randomly produced for both monitored piles and "virtual" piles.
4. From each of 1000 data sets, the ultimate shaft resistance and base resistance for each pile in the actual foundation are estimated by the Kriging method.

5. From the 1000 data set of ultimate shaft resistance and ultimate base resistance evaluated at the actual pile locations, the respective mean values are adopted as the ultimate shaft resistance and ultimate base resistance of the actual piles. Then the sum of the two resistance values is the ultimate overall resistance of the piles. Also the uncertainty value of each pile is derived from the mean of Kriging variance and the sum of the uncertainty values is called the "uncertainty" of the whole piled foundation.

Steps 3 to 5 are repeated by changing the pile(s) that will be monitored. The appropriate monitoring locations can then be decided from the degree of reduction in the overall uncertainty.

2.3 *Evaluation criterion for the uncertainty-reduction by monitoring*

From the procedure described in the previous section, the ultimate resistance and the uncertainty of a whole piled foundation that consists of normal and monitored piles are calculated. In this study, the evaluation criterion to select the most suitable pile(s) for monitoring is given as follows.

Evaluation criterion: Find the location of monitoring point(s) that minimize(s) the following equation,

$$\sum_{i\in \text{all pile}} \frac{\text{Kriging variance of pile } i}{\text{USR and UBR of pile } i} \Big/ \text{the number of piles.}$$

The estimated value is called "average of variation co-efficient" in this paper. As a separate study, other evaluation criteria for selecting the monitoring point(s) to reduce the uncertainty of piled foundation are considered and the results will be reported elsewhere in the future.

3 CASE STUDY

3.1 *Condition for calculation*

A piled foundation which has 120 single piles placed at 7-meter intervals is considered as a hypothetical case study. The plan area is composed of 7-span-49 meter × 14-span-98 meter as shown in Figure 1. Each pile is cast-in-place pile with diameter of 0.8 m and its length coincides with the thickness of clay as shown in Tables 4 to 6. The ultimate resistance is given by the shaft resistance and the base resistance considering the soil conditions. Three soil profiles are considered; (i) Case 1: two horizontally layered conditions, (ii) Case 2: two layers with an inclined interface, in which the slope angle changes at the centerline of the foundation, and (iii) Case 3:

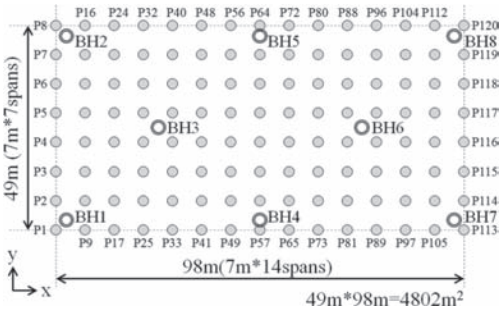

Figure 1. Layout of piles and boreholes and soil profile.

two layers with abrupt change in top layer thickness due to faulting (i.e. buried terrace structure). For each ground profile, a clayey soil layer is underlain by a sandy soil layer (see Figure 2).

Eight boreholes are deployed. Tables 4 to 6 show the soil parameters and the resistance values of a virtual pile placed at the location of each borehole. In the following discussion, the variation coefficient of c_u and q_b are assumed to be 0.3 as the uncertainty of soil parameters. Then, the uncertainty of ultimate resistances of each borehole shown in Tables 4 to 6 is modeled by assuming their variation coefficient as 0.42 and the distribution as a normal distribution.

3.2 *Computed results for one monitored pile*

The results for the cases with one monitored pile are shown in Figures 3 to 5 for the three different soil profiles. In these figures, the effectiveness of monitoring for the whole piled foundation is defined by the difference between the average of variation coefficient for whole pile foundation calculated in one monitored pile situation and that without monitoring. The differential value is computed at each monitored pile location and then a contour plot showing the spatial distribution of the differential value is generated. The location that gives the maximum value is considered to be the ideal place to monitor. Also the maximum value itself gives the value of monitoring; that is, the larger the value is, the uncertainty reduces more by monitoring.

Figure 3 shows the result for Case 1. In the case of horizontally-layered conditions, the pile located away from the borehole, especially the one near the center of the piled foundation, will be ideal in terms of reducing the uncertainty of the foundation.

The result for Case 2 is shown in Figure 4. It indicates that a pile located away from the boreholes and on the left hand side of the ground that has a moderate interface slope angle would be effective one for monitoring to reduce the uncertainty.

Table 4. Soil parameters and resistance for Case 1.

	BH1	BH2	BH3	BH4	BH5	BH6	BH7	BH8
c_u of clay (kPa)	50	50	55	55	50	50	45	45
q_b at toe (kPa)	12000	11700	11700	12300	12000	12300	12000	12000
Thickness of clay = pile length (m)	20	19.5	19.5	20.5	20	20.5	20	20
Diameter of model pile, D (m)	0.8	0.8	0.8	0.8	0.8	0.8	0.8	0.8
Adhesion factor of shaft resistance, α	0.6	0.6	0.6	0.6	0.6	0.6	0.6	0.6
Ultimate shaft resistance, USR1 (kN)	1508.0	1470.3	1617.3	1700.2	1508.0	1545.7	1357.2	1357.2
Ultimate base resistance, UBR (kN)	6031.9	5881.1	5881.1	6182.6	6031.9	6182.6	6031.9	6031.9
USR1 + UBR(kN)	7539.8	7351.3	7498.3	7882.9	7539.8	7728.3	7389.0	7389.0

Table 5. Soil parameters and resistance for Case 2.

	BH1	BH2	BH3	BH4	BH5	BH6	BH7	BH8
c_u of clay (kPa)	50	50	55	55	50	50	45	45
q_b at toe (kPa)	10200	9900	10800	12300	12000	13800	15000	15000
Thickness of clay = pile length (m)	17	16.5	18	20.5	20	23	25	25
Diameter of model pile, D (m)	0.8	0.8	0.8	0.8	0.8	0.8	0.8	0.8
Adhesion factor of shaft resistance, α	0.6	0.6	0.6	0.6	0.6	0.6	0.6	0.6
Ultimate shaft resistance, USR1 (kN)	1281.8	1244.1	1492.9	1700.2	1508	1734.2	1696.5	1696.5
Ultimate base resistance, UBR (kN)	5127.1	4976.3	5428.7	6182.6	6031.9	6936.6	7539.8	7539.8
USR1 + UBR(kN)	6408.8	6220.3	6921.6	7882.9	7539.8	8670.8	9236.3	9236.3

Table 6. Soil parameters and resistance for Case 3.

	BH1	BH2	BH3	BH4	BH5	BH6	BH7	BH8
c_u of clay (kPa)	50	50	55	55	50	50	45	45
q_b at toe (kPa)	12000	11700	11700	12300	12000	17700	18000	18300
Thickness of clay = Pile length (m)	20	19.5	19.5	20.5	20	29.5	30	30.5
Diameter of model pile, D (m)	0.8	0.8	0.8	0.8	0.8	0.8	0.8	0.8
Adhesion factor of shaft resistance, α	0.6	0.6	0.6	0.6	0.6	0.6	0.6	0.6
Ultimate shaft resistance 1, USR1 (kN)	1508	1470.3	1617.3	1700.2	1508	2224.2	2035.8	2069.7
Ultimate base resistance, UBR (kN)	6031.9	5881.1	5881.1	6182.6	6031.9	8897	9047.8	9198.6
USR1 + UBR (kN)	7539.8	7351.3	7498.3	7882.9	7539.8	11121.2	11083.5	11268.3

In Case 3, the result is given in Figure 5. Results show that monitoring in the space enclosed by BH6, BH7 and BH8 where the clayey soil layer is relatively thicker will not be effective in reducing the uncertainty. The most effective location for monitoring is at the left hand side of the ground in which the soil profile is uniform. Another effective monitoring area is the space enclosed by BH4, BH5 and BH6 where the thickness of the clayey soil layer is variable.

The efficient locations obtained from the calculations are consistent with typical rules of thumb. According to Case 2 and 3, the effective area for monitoring is located at the ground that has a moderate interface slope angle and that has uniform soil profile in large part. This is because when new information about ground profile is found to be similar to the existing ground profile, this reduces the uncertainty in the ground profile. This would increase the precision of fitting function to the ground profile, which in turn reduces the uncertainty of the whole foundation.

3.3 *Computed results for multi-monitored pile*

Based on the contour plots, the location(s) of the monitoring are determined and the effect of monitoring number in reducing the uncertainty was examined. The number of monitoring was increased up to ten and a relationship between monitoring number and the effect is shown in Figure 6. The average of variation coefficient for

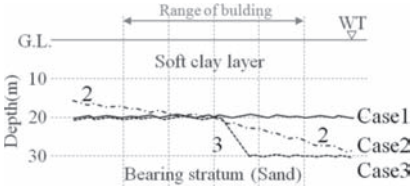

Figure 2. Pattern diagram of Cases 1 to 3.

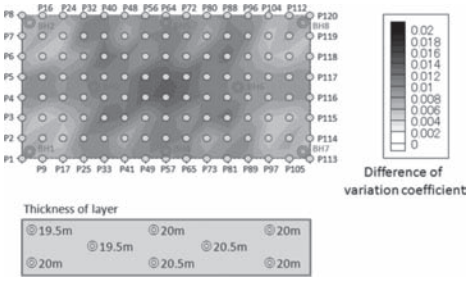

Figure 3. Effectiveness of monitoring based on Evaluation critetion 1 (Case 1: Horizontally-layered, one monitored pile).

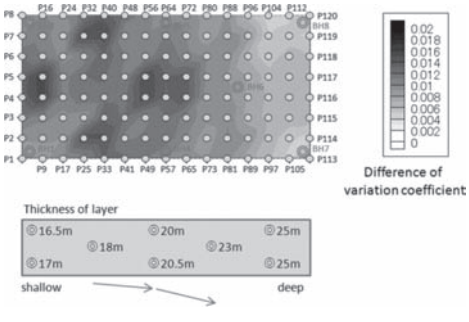

Figure 4. Effectiveness of monitoring based on Evaluation critetion 1 (Case 2: Dipping bearing stratum, one monitored pile).

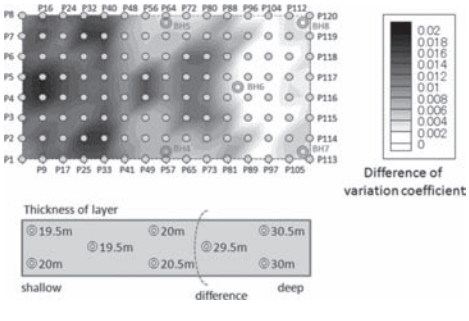

Figure 5. Effectiveness of monitoring based on Evaluation critetion 1 (Case 3: Buried terrace, one monitored pile).

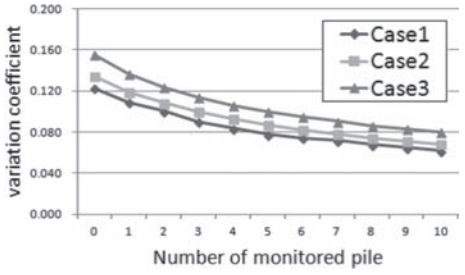

Figure 6. Effectiveness of monitoring at several locations for each ground profile.

the case of no monitoring pile is 0.123 for Case 1, 0.134 for Case 2, and 0.155 for Case 3. The value of Case 1 with uniform soil conditions is smaller than the values of the other cases, showing the effect of soil conditions on uncertainty as expected. In all cases, the degree of uncertainty decreases with increasing number of monitoring. For example, in the case of ten monitored piles placed at well-chosen locations, the uncertainty value is half of that of the non-monitored pile foundation case.

4 CONCLUSIONS

In this paper, a procedure to evaluate the uncertainty-reduction effect of pile monitoring on the performance of a pile foundation is presented. The variability of the single-loaded pile behavior was modeled by assuming their shaft resistance and base resistance as 0.42 and the distribution as a normal distribution. When the pile is monitored (or a pile test is carried out at this location), it was assumed that the variability would reduce to 0.05. The uncertainty of a whole piled foundation that consists of monitored and non-monitored piles was then evaluated. To demonstrate the effectiveness of the proposed evaluation method, a hypothetical case of 120-pile foundation placed was examined for three different ground profile conditions. The results show that the developed method gave good agreement with typical rules of thumb and could provide quantitative data to make more rational decision in carrying out pile monitoring or pile testing.

REFERENCES

Architectural Institute of Japan (AIJ) (2001). *Recommendations for Design of Building foundations*. Architectural Institute of Japan, (in Japanese).

Barker, R.M., Duncan, J.M., Rojiani, K.B., Ooi, P.S.K.,Tan, C.K. & Kim, S.G. 1991. Manuals for the design of bridge foundations. *NCHRP Report 343*.

Berezantzev, V.G., Khristoforov, V. & Golubkov, V. 1961. Load bearing capacity and deformation of piled foundations. *Proc. 5th ICSMFE 2 2*: 11–15.

Cherubini, C. 1997. Data and considerations on the variability of geotechnical properties of soils. In *Proceedings of the international conference on safety and reliability, ES-REL*, Volume 97: 1583–1591.

Duncan, J.M. 2000. Factors of safety and reliability in geotechnical engineering. *Journal of Geotechnical and Geoenvironmental Engineering 126*(4): 307–316. Fenton, G.A. & Griffiths, D.V. 2003. Bearing-capacity prediction of spatially random c-φ soils. *Canadian geotechnical journal 40*(1): 54–65.

Haldar, S. & Babu, G.L.S. 2008. Reliability measures for pile foundations based on cone penetration test data. *Canadian Geotechnical Journal 45*(12): 1699–1714.

Harr, M.E. 1984. *Reliability-based design in civil engineering*. Department of Civil Engineering, School of Engineering, North Carolina State University.

Institution of Civil Engineers (ICE) 2012. *ICE Manual of Geotechnical Engineering, Vol. II*. Geotechnical Design, Construction and Verification, Edited by Burland, J., Chapman, T., Skinner, H. & Brown, M.

Kay, J.N. 1993. Probabilistic design of foundations and earth structures. *Proceedings of Probabilistic methods in geotechnical engineering, Edited by K.S. Li & S.C.R. Lo. A.A.*: 49–62.

Lacasse, S. & Nadim, F. 1997. Uncertainties in characterising soil properties. *Publikasjon-Norges Geotekniske Institutt 201*: 49–75.

Leung, Y.F., Soga, K. & Klar, A. 2011. Multi-objective foundation optimization and its application to pile reuse. *Geotechnical Special Publication 211*: 75–84.

Okahara, M., Kimura, Y., Ochiai, H. & Matsui, K. 1993. Statistical characteristics of bearing capacity of single piles. In *proceedings of the ninth us-japan bridge engineering workshop*, Volume 3230.

Phoon, K.K. & Kulhawy, F.H. 1999a. Characterization of geotechnical variability. *Canadian Geotechnical Journal 36*(4): 612–624.

Phoon, K.K. & Kulhawy, F.H. 1999b. Evaluation of geotechnical property variability. *Canadian Geotechnical Journal 36*(4): 625–639.

Phoon, K.K., Quek, S.T., Chow, Y.K. & Lee, S.L. 1990. Reliability analysis of pile settlement. *Journal of Geotechnical Engineering 116*(11): 1717–1734.

Quek, S.T., Chow, Y.K. & Phoon, K.K. 1992. Further contributions to reliability-based pile-settlement analysis. *Journal of geotechnical engineering 118*(5): 726–741.

Wang, Y., Au, S.K. & Kulhawy, F.H. 2011. Expanded reliability-based design approach for drilled shafts. *Journal of geotechnical and geoenvironmental engineering 137*(2): 140–149.

This page intentionally left blank

Geotechnical Safety and Risk IV – Zhang et al. (eds)
© 2014 Taylor & Francis Group, London, ISBN 978-1-138-00163-3

Using head monitoring for reliability updating of levees

T. Schweckendiek
Deltares, Unit Geo-Engineering, Delft, The Netherlands
Department of Hydraulic Engineering, Delft University of Technology, Delft, The Netherlands

ABSTRACT: Backward erosion piping is an important internal erosion failure mechanism in deltaic areas. Piping is very sensitive to ground conditions, especially to the permeability of aquifers under levees. The uncertainties in these ground properties can be reduced by monitoring the hydraulic head in the piping-sensitive aquifer in order to update the probability distributions of the basic random variables influencing the geo-hydrological conditions such as the hydraulic resistance of the aquifer. This paper demonstrates how Bayesian posterior analysis can be used to incorporate head monitoring information in order to update the reliability with respect to uplift, heave and piping for river levees. The paper starts by recapping background on uplift, heave and piping reliability, before we discuss how the equality type of information involved can be used in posterior analysis by following the approach proposed by Straub (2011). The workings of the theory are illustrated by an example considering uplift (of a blanket layer) only using a simplified groundwater model for the sake of illustration. Sensitivity analysis on the example shows that the effect of reliability updating can be considerable for large prior uncertainties and for observations which are rather unlikely given the prior distributions of the random variables (i.e. far from the expected value of the measurement).

1 INTRODUCTION

Flood defense levees are crucial for flood protection, especially in riverine and deltaic areas. One of the most critical failure modes of levees is backward internal erosion or piping. In the VNK2 project (Jongejan et al. 2013) which is analyzing the reliability of all primary flood defenses in The Netherlands, piping was identified as a main contributor to the probability of flooding.

Such reliability analyses of flood defenses work with prior probabilities of relevant parameters such as the ground conditions, which are based on sparse site investigation data and/or expert judgment. The prior uncertainties in ground properties are relatively large compared to other civil engineering materials like concrete or steel. But these uncertainties can be reduced by gathering and incorporating additional information.

One source of information is monitoring of the hydraulic head in an aquifer underlying a levee and a blanket layer. It is common engineering practice to instrument levees, where the geo-hydrological conditions are rather uncertain, with observation wells to observe the response of the hydraulic head to changes in the river water level. This allows us to get an impression of not only the hydraulic resistance of the aquifer but also on the seepage length and other geo-hydrological parameters. However, the interpretation of such data is usually done by interpolation, regression analyses or expert judgment, the incorporation of which in reliability analysis is not straightforward.

In order to provide a more rigorous approach for reliability updating with such head monitoring data, this paper explores the possibilities and effects of applying Bayesian Updating. By working with Monte Carlo analysis and exact methods without approximations in the methods themselves, we will show how not only the reliability is updated but also how the posterior distributions of the basic random variables change with respect to their priors. The latter allows more detailed interpretation of the results and the plausibility of the observations.

The paper starts by recapping background on uplift, heave and piping reliability, before we discuss how the equality type of information involved can be used in posterior analysis by following the approach proposed by Straub (2011). The workings of the theory are illustrated by an example considering uplift (of a blanket layer) only using a simplified groundwater model for the sake of illustration.

2 PLIFT, HEAVE AND PIPING RELIABILITY

2.1 *Physical processes*

The conceptual model underlying piping reliability modeling in Dutch practice is illustrated in Figure 1. The typical situation addressed here is a

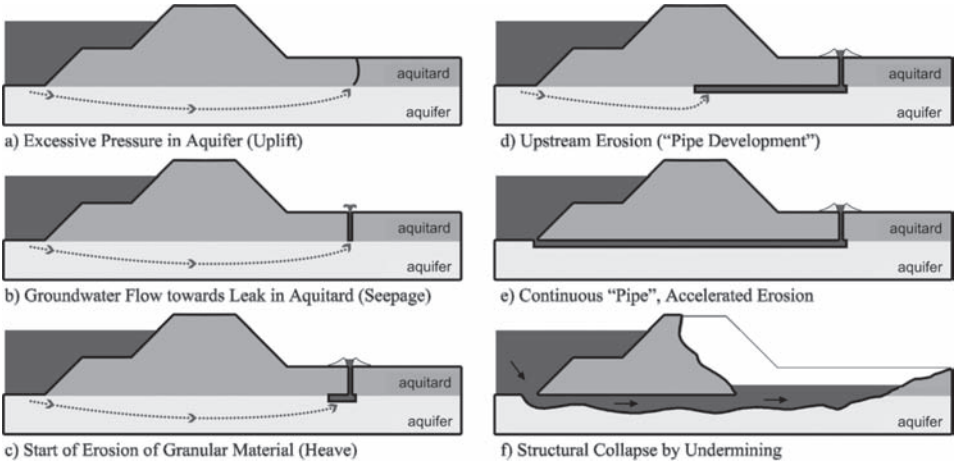

Figure 1. Phases of the piping process including uplift and heave.

relatively low permeability levee with low permeability blanket on the land-side. High floods generate high pore pressures in the relatively highly permeable aquifer underneath (Fig. 1, stage a). When and where the pressure exceeds the weight of the blanket (i.e. uplift, stage b), the latter may rupture causing accelerated upward ground water flow. If the flow exceeds a critical rate (i.e. heave, stage c), sand particles start to erode. Subsequently, the internal erosion progresses in upstream direction (i.e., towards the river) forming erosion channels—so-called "pipes" (stage d). If the piping process does not come to a halt, the levee can be "undermined" and collapse (stages e, f).

Note that the same process is often also called under-seepage or backward erosion in the literature. For sake of conciseness we will refer to the whole process as piping throughout the paper.

2.2 *Limit states*

Below we present the commonly used limit state functions for uplift heave and piping. For uplift, the head difference at the bottom of a (potential) exit point needs to exceed the weight exerted by the blanket:

$$g_u(\mathbf{x}) = m_u d\left(\frac{\gamma_{sat}}{\gamma_w} - 1\right) - \Delta\phi \tag{1}$$

where m_u is a model factor addressing the uncertainty in the critical uplift head difference, d [m] is the blanket thickness, γ_{sat} [kN/m^3] is the saturated volumetric weight of the blanket, γ_w [kN/m^3] is the volumetric weight of water and $\Delta\phi$ [m] is the head difference at the exit point (with respect to surface level), the latter to be calculated by groundwater flow analysis or to be estimated from measurements. For the sake of illustration, in the example elaborated below we will apply the following simplified approach using a damping factor λ for predicting the head difference in the aquifer at the potential exit point (see Fig. 2):

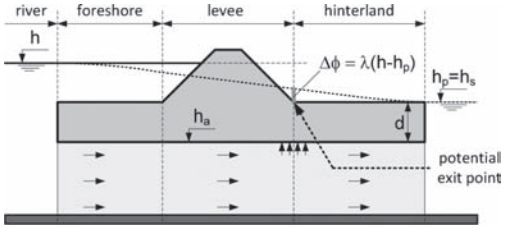

Figure 2. Definition of the damping factor for estimating the head at the critical exit point.

$$\Delta\phi = \lambda(h - h_p) \tag{2}$$

where h [m] is the (river) water level (all absolute levels are with respect to MSL = mean sea level) and h_p [m] is the phreatic level in the polder (i.e. landside of the levee). The damping factor λ can be based on expert judgment or groundwater flow analysis and is supposed to include model uncertainty.

While uplift is concerned with the breaching of the impervious boundary, heave is concerns the start of erosion; the resistance against heave is expressed in terms of a critical exit gradient i_c:

$$g_h(\mathbf{x}) = i_c - \Delta\phi/d \tag{3}$$

For piping we consider the average gradient-based equilibrium model by Sellmeijer (1988), which was revised recently (Sellmeijer, 2012) by recalibrating the coefficients in the critical piping head difference H_c [m]. The performance function is given by:

$$g_p(\mathbf{x}) = m_p H_c - (h - h_p - 0.3\,d) \tag{4}$$

where m_p is a model uncertainty factor.

2.3 *Reliability analysis*

Let the failure event F_i for failure mode i be defined as the limit state function g_i assuming negative values. The probability of failure is then given by:

$$P(F_i) = P(g_i(\mathbf{X}) < 0) = \int_{g_i(\mathbf{X})<0} f_{\boldsymbol{X}}(\boldsymbol{x})d\boldsymbol{x} \tag{5}$$

where $\boldsymbol{X}$ is the vector of random variables and $f_{\boldsymbol{X}}(\boldsymbol{x})$ its (prior) Probability Density Function (PDF).

Fragility curves are a frequently used alternative way of expressing the uncertainty in the aggregated resistance $\boldsymbol{R}$ with respect to a dominant load variable. In other words, $\boldsymbol{R}$ contains all variables in $\boldsymbol{X}$ except the dominant load variable, which for river levees is the water level h), providing the conditional probability of failure with respect to h:

$$P(F_i \mid h) = \int_{g_i(\boldsymbol{R},h)<0} f_{\boldsymbol{R}}(\boldsymbol{r})d\boldsymbol{r} \tag{6}$$

As explained in the previous section, failure can only occur if uplift precedes heave and heave precedes piping, because piping can only develop if the groundwater can flow upwards through the ruptured blanket (i.e. uplift) sufficiently to move sand particles vertically (i.e. heave). In reliability terms this relationship can be described by means of a parallel system, for which the failure set is given by:

$$F = \{g_u(\boldsymbol{x}) < 0\} \cap \{g_h(\boldsymbol{x}) < 0\} \cap \{g_p(\boldsymbol{x}) < 0\} \tag{7}$$

Note that the prior probability of failure and the fragility curves as defined above can be determined per failure mode individually (i.e. F_u, F_h and F_p) as well as for the "system" failure event F.

3 RELIABILITY UPDATING

This section provides the theory and definitions used in this study for reliability updating with information from pore pressure monitoring. We apply Bayes' rule (Bayes, 1763) to obtain the posterior (updated) probability of failure, here expressed in terms of the definition of conditional probability as in Benjamin and Cornell (1970):

$$P(F \mid \varepsilon) = P(F \cap \varepsilon) / P(\varepsilon) \tag{8}$$

where ε is the evidence, which in our application means that we monitor or measure the head ϕ at the exit point with measurement error e_m [m], resulting in the measured value of the head ϕ_m [m]:

$$\varepsilon \equiv \{\phi_m + e_m - \phi = 0\} \tag{9}$$

The well-known issues with this equality type of information are that the numerator in Eq. (8) cannot be determined by standard reliability analysis techniques and the denominator is zero by definition. Using the approach proposed by Straub (2011), however, we can re-formulate the observation space ε in terms of the following equivalent inequality domain:

$$\varepsilon_e = \left\{u - \Phi^{-1}\left[cf_{e_m}\left(\phi_m - \phi(\boldsymbol{x})\right)\right] < 0\right\} \tag{10}$$

where u is a standard Normal distributed random variable, Φ^{-1} is the inverse cumulative standard Normal distribution function, f_{e_m} is the PDF of the measurement error and c is a positive constant to be chosen such that the term in square brackets is always between zero and one. For the derivation and further details of this method we refer to Straub (2011).

This transformation allows us to compute the updated probability of failure using standard reliability analysis methods by evaluating the following expression:

$$P(F \mid \varepsilon) = \frac{P(F \cap \varepsilon_e)}{P(\varepsilon_e)} = \frac{\int_{F \cap \varepsilon_e} f_X(\boldsymbol{x})\varphi(u)du\,d\boldsymbol{x}}{\int_{\varepsilon_e} f_X(\boldsymbol{x})\varphi(u)du\,d\boldsymbol{x}} \tag{11}$$

where $\varphi(u)$ is the standard normal PDF. Notice that this way the posterior probabilities of failure for the separate failure mechanisms uplift, heave and piping can be computed as well as the posterior (parallel system) probability of failure for the whole failure mode (i.e. $P(F_u \cap F_h \cap F_p \mid \varepsilon)$).

4 EXAMPLE: UPLIFT

4.1 *Limit state*

In the following we provide a numerical elaboration for uplift failure as defined in section 2.2. The limit state function for this example is obtained by

inserting the load term (Eq. 2) in the uplift limit state function (Eq. 1) resulting in

$$g_u(\mathbf{x}) = m_u d\left(\frac{\gamma_{sat}}{\gamma_w} - 1\right) - \lambda\left(h - h_p\right) \tag{12}$$

Equating to zero and solving for the water level gives the critical uplift water level $h_{c,u}$ [m], which will is the aggregated resistance and will be used for illustration of results in terms of fragility curves:

$$h_{c,u} = m_u d\left(\frac{\gamma_{sat}}{\gamma_w} - 1\right) / \lambda + h_p \tag{13}$$

Notice that the cumulative distribution $F_{hc,u}$ is the uplift fragility curve.

4.2 *Input parameters and prior analysis*

The example parameters as presented in Table 1 are fictitious but realistic. The annual prior probability of uplift failure is $P(F_u) = 6.6 \cdot 10^{-2}$ obtained by Monte Carlo simulation, which corresponds to a reliability index of $\beta = 1.50$.

4.3 *Posterior analysis*

We suppose that monitoring during a 100-year water level of $h' = 3.9$ m has resulted in a measured head in the aquifer at the dike toe (i.e. exit point) of $\phi_m = 2.3$ m. The duration of the reached flood level is assumed sufficient for a near steady-state pore pressure response in the aquifer, which means that the applied limit state models are applicable (i.e. steady state assumption in the groundwater model). Furthermore, the measurement is assumed to be unbiased with an error e_m with zero mean and standard deviation equal to 0.1 m.

Since the failure models are computationally inexpensive, we can obtain exact results by using Monte Carlo simulation as summarized in Table 2. Incorporating the monitoring observation causes the probability of failure to decrease by an order of magnitude.

Table 1. Input parameters uplift example.

X_i	Distribution type	Parameters (mean and standard deviation)
h	Gumbel	$\mu = 2.67$, $\sigma = 0.38$
h_p	Normal	$\mu = 0.3$, $\sigma = 0.1$
d	Lognormal	$\mu = 3.0$, $\sigma = 0.5$
m_u	Lognormal	$\mu = 1.0$, $\sigma = 0.1$
γ_{sat}	Normal	$\mu = 20.0$, $\sigma = 1.0$
λ	Lognormal	$\mu = 0.8$, $\sigma = 0.1$
e_m	Normal	$\mu = 0.0$, $\sigma = 0.1$
γ_w	Deterministic	10

Table 2. Annual prior and posterior reliability.

	Probability of failure	Reliability index
Prior	$P(F_u) = 6.6 \cdot 10^{-2}$	$\beta = 1.50$
Posterior	$P(F_u \mid \varepsilon) = 4.8 \cdot 10^{-3}$	$\beta = 2.59$

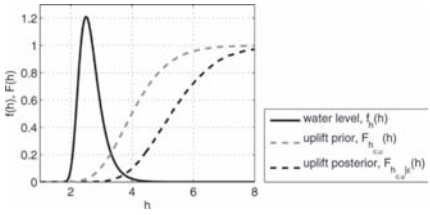

Figure 3. Water level distribution vs. prior and posterior uplift fragility curve at the exit point.

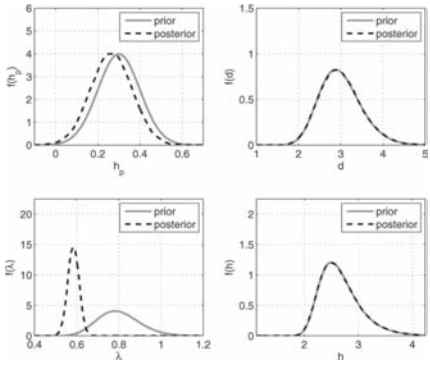

Figure 4. Posterior probability densities of selected basic random variables.

Notice that even though the prior and posterior probability are not extremely low, the posterior analysis takes a large number of Monte Carlo-realizations to converge. The reason is the numerator term in Bayes' rule, $P(F_u \cap \varepsilon)$ which can be orders of magnitude lower than $P(F_u|\varepsilon)$ itself. The large number of realizations is not so much a problem of computation time but a memory issue, especially if one wants to retain the values of all random variables for subsequent analysis and interpretation of results.

Figure 3 shows that the fragility curve of the critical water level $h_{c,u}$ changes significantly as a result of the posterior analysis. Besides fragility curves and load effect, also the posterior probability densities of some basic random variables can be obtained as shown in Figure 4. Notice that only h_p

and λ, the variables influencing the measurement, are updated. While the probability density of h_p only slightly shifts to the left, the we see a significant shift and considerable decrease of spread in the distribution of λ. Figure 5 also shows that after updating h_p and λ are correlated.

4.4 *Sensitivity analysis*

In the following we investigate the sensitivity of the outcomes to the measured head at the potential exit point (ϕ_m), the observed water level at which the measurement was obtained (h') and the measurement error (e_m).

Figure 6 is a contour plot showing the posterior reliability index for combinations of the observed water level (h') and the measured head (ϕ_m) for a given measurement error of $\sigma_{e,m} = 0.1$m. The posterior probability of failure increases with the measured head. For the (relatively large) considered range of the measured head, the posterior probability of failure varies by several orders of magnitude.

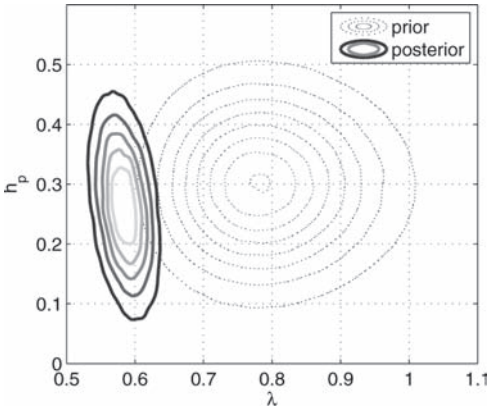

Figure 5. Prior and posterior joint posterior probability densities of λ and h_p.

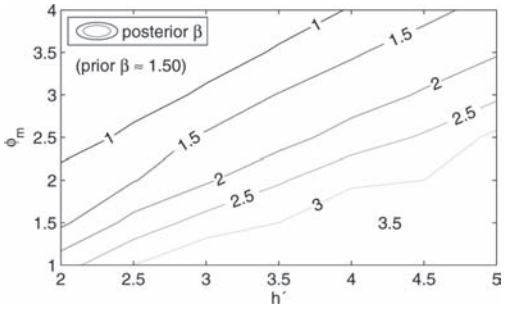

Figure 6. Posterior annual reliability as a function of the measured head ϕ_m and the observed water level h' (for a measurement error of $\sigma_{e,m} = 0.1$ m).

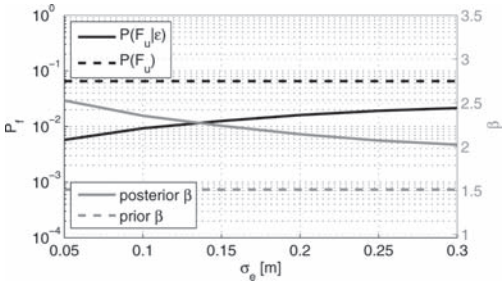

Figure 7. Sensitivity of the posterior annual reliability with respect to the measurement error $\sigma_{e,m}$ (for a measured head of $\phi_m = 2.3$ m and a 100-year flood level $h' = 3.9$ m).

For a given value of the measured head, varying the water level illustrates that the higher the observed water level, the greater the impact on the posterior reliability. The decrease of the reliability index is roughly a linear function of both, ϕ_m and h'.

Figure 7 clearly demonstrates that the updating effect vanishes with increasing measurement error.

5 CONCLUSION

The reliability updating method for equality type of information proposed by Straub (2011) enables us to do posterior analysis for structural reliability problems where we have direct measurements of one or more system characteristics (i.e. variables involved in the performance function).

This paper has discussed how head monitoring information can be used to update the reliability regarding uplift, heave and piping (i.e. underseepage) for levees using Straub's approach. The (simplified) example on uplift has demonstrated the workings of the method and illustrated that the effect of updating (i.e. the change from prior to posterior probability of failure) can be considerable, if the prior uncertainties are rather large and the observation was rather unlikely given the prior probability distributions.

An extension of the presented posterior analysis to pre-posterior and decision analysis is discussed in Schweckendiek (2013a); a more extensive case study on including uplift, heave and piping can be found in Schweckendiek (2013b), which includes more sophisticated limit state models, system reliability aspects and treatment of (discrete) stratification scenarios.

REFERENCES

Bayes, T. 1763. An essay towards solving a problem in the doctrine of chances. *Philosophical Transactions of the Royal Society of London*, 53, 370–418.

Benjamin, J. & Cornell, C. 1970. *Probability, statistics and decision for civil engineers*. New York: McGraw-Hill.

Jongejan, R., et al. 2013. *The VNK2-project: a fully probabilistic risk analysis for all major levee systems in The Netherlands*. IAHS Publication, 357: Floods: From Risk to Opportunity.

Schweckendiek, T. 2013a. Reliability updating and decision analysis for head monitoring of levees, *Georisk* 7(2), in press.

Schweckendiek, T. 2013b. On reducing piping uncertainties—a bayesian decision approach. PhD thesis, Delft University of Technology (in preparation).

Sellmeijer, J., et al. 2012. Fine-tuning of the piping model through small-scale, medium-scale and experiments. *European Journal of Environmental and Civil Engineering*, Special Issue devoted to "Erosion in geomechanics" (in press).

Sellmeijer, J. 1988. On the mechanism of piping under impervious structures. PhD-thesis, Delft University of Technology.

Straub, D. 2011. Reliability updating with equality information. *Probabilistic Engineering Mechanics* 26 (2011), 254–258.

8 *Performance evolution and risk assessment of high slopes in hydropower engineering in China*

This page intentionally left blank

Geotechnical Safety and Risk IV – Zhang et al. (eds)
© 2014 Taylor & Francis Group, London, ISBN 978-1-138-00163-3

Numerical simulation of blasting induced damage of high rock slope

Y.G. Hu, W.B. Lu, M. Chen & P. Yan
State Key Laboratory of Water Resources and Hydropower Engineering Science, Wuhan University, Wuhan, Hubei, China
Key Laboratory of Rock Mechanics in Hydraulic Structural Engineering of Ministry of Education, Wuhan University, Wuhan, Hubei, China

ABSTRACT: The capability of predicting Blasting Induced Damage (BID) in the surrounding rock mass is important to excavation of high rock slopes. A tensile-compress damage model linked to the computer code LS-DYNA through the user subroutine interface was used by introducing the consideration of compress damage and modifying the method of definition of the elastic constants based on the existed blasting damage models. To verify the rationality of the proposed model, based on the case study of the excavation of high rock slope at the Xiluodu Hydropower Station in Sichuan province of China, spatial distribution of blasting induced damage zone at the 640 m berm were determined with cross-hole sonic test. Numerical simulations of BID at the 640 m berm were implemented with tensile-compress model and other four existing blasting damage models. The damage zone obtained by the modified tensile-compressive damage model agreed with observations better than other four existing blasting damage models.

1 INTRODUCTION

During a blasting excavation, damage is induced by a combination of the effects of the blasting load and stress redistribution (Martino & Chandler 2004). Investigation of damage characteristics is most important to restrict the damage extension. The Excavation induced Damage Zone (named EDZ) is generally defined as the zone beyond the boundary where the rock has been considerably damaged or disturbed (Malmgren et al. 2006). Based on the AECL's Underground Research Laboratory, Read (2004) have got progress in the aspect of formation mechanism, mechanical property and detection technique for the damage zone in the surrounding rock mass. In support of the excavation for the permanent shiplock of Three Gorges Project, Sheng et al. (2002) investigated the deformation and the damage in the remaining rock with sonic wave detection and numerical simulation. However, compared to the study on the EDZ of underground openings, fewer attentions are paid to the formation and spatial distribution of EDZ of high rock slope.

The excavation of high rock slope is one of the biggest problems in the construction. Goodman & Kieffer (2000) pointed out that slopes and underground openings have distinctly different environments and the slope environment is generally less secure than the underground environment. It is believed that the excavation damage zone associated with the surface excavation would be larger and more complicated than that associated with the underground excavation. So for the huge high rock slope, the requirement of stability and safety in long term makes the investigation of the EDZ characteristics is important and absolutely necessary.

Researchers often get the characteristics of EDZ with the experiment and the engineering detection. But the method of full size experiment is very expensive and time-consuming. The engineering detection is after the event in the engineering, which is not good for the control of EDZ. Numerical method, derived from sound mechanical principles and validated against experimental data, indicates a promising approach to reveal the EDZ formation process. For this case, various damage models have been suggested to study the damage of rock mass under blasting. For instance, Grady & Kipp (1980), Taylor (1986) and his coworkers, Yang et al. (1996) and Liu & Katsabanis (1997) developed several widely used continuum damage models to describe the dynamic damage process of rock mass in tension. The damage variable is introduced to describe the changing state of a material. However, the damage variable is established based on the tensile strain and compressive damage is neglected in these damage models. Thus far, application of an appropriate damage model to simulate the different damage pattern is rarely found.

In the present study, based on the blasting excavation for the rock mass high slope of Xiluodu hydropower station, the outline of blasting induced damage zone of the berm at the elevation 640 m

was determined with methods of cross-hole sonic test firstly. Then a modified damage model is presented by incorporating the compressive damage into the exiting damage model. The damage of the berm at the elevation 640 m was subsequently simulated, to verify the accuracy of the model, four kinds of existed blasting damage models were used to be compared.

2 TENSILE-COMPRESS DAMAGE MODEL

The investigation of blasting damage models is represented by America Sandia National Laboratory. To predict the damage and failure, the dynamic fracture was regarded as a continuum process of damage cumulation and the relationship between the damage scalar D and the crack density was established. Several blasting damage models were put forward to describe the degradation of rock stiffness and strength caused by cracks growth under blasting (Grady & Kipp 1980, Taylor et al. 1986, Kuszmaul et al. 1987, Thorne et al. 1990, Yang et al. 1996). But in the existed blasting damage model, the damage scalar D was defined by the tensile strain, while the compressive damage was neglected. It is known that a compressive damage zone was formed by the blasting load in rock mass near the charge hole. The next section describes a tensile-compressive damage model in which the compressive damage was introduced and a modified method of definiting the elastic constants was proposed.

Based on the research of Taylor et al. (1986), the effective bulk modulus of the cracked solid is

$$\frac{\overline{K}}{K} = 1 - \frac{16}{9}\frac{(1-\overline{\mu})}{(1-2\overline{\mu})}C_d \tag{1}$$

where K and μ are the original bulk modulus and Passion's ratio for intact material, the barred quantities represent the corresponding degraded constants for damaged material, with C_d being the crack density parameter.

Following Grady & Kipp (1980), the crack density parameter is assumed to be proportional to the product of N, the number of cracks of per unit volume, is expressed as a Weibull statistical distribution function activated by the bulk strain $\varepsilon_v = (\varepsilon_x + \varepsilon_y + \varepsilon_z)/3$, according to

$$N = k(\varepsilon_v)^m \tag{2}$$

where k and m are the material constants. The average crack radius and the crack density parameter are estimated from the nominal fragment radius for dynamic fragmentation in a brittle material (Grady 1983) as Eqs. (6) and (7)

$$a = \frac{1}{2}\left(\frac{\sqrt{20}K_{IC}}{\rho c \dot{\varepsilon}_{\max}}\right)^{2/3} \tag{3}$$

$$C_d = \frac{5}{2}k\left(\frac{K_{IC}}{\rho c \dot{\varepsilon}_{v\max}}\right)^2 \varepsilon_v^m \tag{4}$$

where ρ is the mass density, c is the wave speed, and K_{IC} is the fracture toughness of the material, $\dot{\varepsilon}_{v\max}$ is the maximum volumetric strain rate experienced by the representative volume element at fracture.

Kuszmaul (1987) considered the material overlap of high density fracture zone, the decrease caused by damage was introduced into the activity ratio, and the expression of the crack density parameter was modified as:

$$C_d = \frac{5}{2}k\left(\frac{K_{IC}}{\rho c \dot{\varepsilon}_{\max}}\right)^2 \varepsilon_v^m (1 - D_t) \tag{5}$$

An expression based on the percolation theory (Englman & Jaeger 1987):

$$\overline{\mu} = \mu \exp\left(-\frac{16}{9}\beta C_d\right) \tag{6}$$

Inspection of Eq. (4) suggests that the tensile damage can be defined by

$$D_t = \frac{16}{9}\frac{(1-\overline{\mu}^2)}{(1-2\overline{\mu})}C_d \tag{7}$$

On the other hand, when the rock material is in compression, the von Misses yield condition is expressed as:

$$\Phi = \Lambda^2 - \sigma_y^2 = 0 \tag{8}$$

where $\Lambda = \sqrt{\frac{3}{2}s_{ij}s_{ij}}$ is the von Misses equivalent stress.

Based on the coupling principle of strain-rate effect in the RDA model (Furlong et al. 1990), the compressive damage D_c is expressed as:

$$\dot{D}_c = \frac{\lambda \dot{W}_p}{1 - D_t} \tag{9}$$

where λ is the sensitivity constant of D_c which is taken to be equal to 1.0×10^{-3} kg/J in this study (Sun 2002). While the plastic work W_p is computed by

$$W_p = \int \sigma_{ij} d\varepsilon_{ij}^p \tag{10}$$

There are the tensile damage scalar and the compress damage scalar in the model at the same

time. Introducing the symbol D into expressing the damage scalar and considering the biggest damage effect, the damage scalar can be get

$$D = \max(D_t, D_c) \tag{11}$$

In the exiting blasting damage models, the degraded shear modulus G and bulk modulus K for a material point can be written as

$$\overline{E} = E(1-D) \tag{12}$$

$$\overline{G} = G(1-D) \tag{13}$$

The above method of determining the elastic constants could not meet the mathematic relation between the elastic constants. Normally, the elastic constants have the following relations:

$$E = 2(1+\mu)G \tag{14}$$

$$E = 3(1-2\mu)K \tag{15}$$

The method of determining the elastic constants was modified in this study, the degraded bulk modulus and Poisson's ratio were definited as the same as the origin method.

$$\overline{K} = K(1-D) \tag{16}$$

$$\overline{\mu} = \mu \exp\left(-\frac{16}{9}\beta C_d\right) \tag{17}$$

Other elastic constants were determined by the mathematic relation:

$$\overline{G} = \frac{3(1-2\overline{\mu})}{2(1+\overline{\mu})}\overline{K} \tag{18}$$

$$\overline{E} = \frac{9\overline{K}\overline{G}}{3\overline{K}+\overline{G}} \tag{19}$$

The constitutive relations recording the damage effect could be definited with Hooke's law of increment as follow:

$$d\sigma_{ij} = \overline{K} d\varepsilon_{kk}\delta_{ij} + 2\overline{G} de_{ij} \tag{20}$$

Based on the above analysis, a tensile-compress damage model was established. LS-DYNA is a well-known general purpose commercial FEM code that has been developed for simulating the nonlinear dynamic response of structures. It has several constitutive models such as *MAT_BRITTLE_DAMAGE (Govindjee et al. 1995) and the H-J-C model (Holmquist & Johnson 1993) designed for dynamic damage analysis of brittle rock. What is important, it provides user subroutine interface to implement the userdefined model (LSTC 2010).

3 SONIC WAVE TEST AND BLASTING INDUCED DAMAGE DISTRIBUTION

To fully understand the damage distribution in the remaining rock mass near the berm, the cross-hole sonic wave test was employed to determine the extent of damage zone surrounding the berm at the 640 m elevation of the Xiluodu high rock slope. The arrangement of the testing holes was shown in Figure 1. Three groups measuring results were obtained in this test. One group of them was in the left and other two groups were in the right. The change of acoustic velocities and the damage depths are listed in Table 1.

According to the results of sonic wave test, the acoustic velocities in the remaining rock mass near the berm range from 1500 m/s to 5800 m/s. The acoustic velocities decreases form the outer flank to the inside of the berm. The minimum acoustic velocity was found at the outer flank of the berm, which means the rock mass in this part is the most serious damaged.

The outline of EDZ for rock mass near the berm was showed in Figure 2. In the vertical direction the damage depth ranges from 1.0 m to 4.0 m and decreases nonlinearity from the outer flank to inside of the berm. In the horizon direction

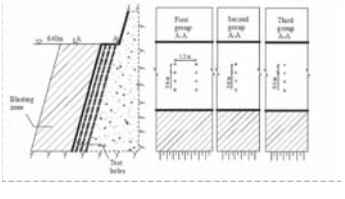

Figure 1. Schematic illustration of sonic wave test holes at the EL.640 m berm.

Table 1. The result statistics of sonic wave test.

Section No.	Rock mass	V_p	Damage before blasting	Damage after blasting	PPV
XZ640BH	III_1	3200~5500	0~0.50	1.00~4.0	18.3
XYB640B	III_2	1500~4200	0.00	0.25~1.10	8.7
XYB640C	III_1	2500~5800	1.50~3.25	1.75~4.50	9.7

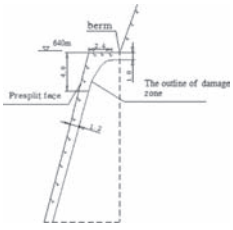

Figure 2. Extent of damage zone in remaining rock at the EL.640 m berm.

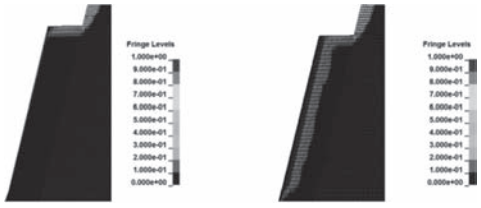

Figure 3. Damage distribution of tensile-compress damage model.

Table 2. Material constants and damage constants.

Density (kg/m^3)	Elasticity modulus (GPa)	Poison's ratio	Dynamic tensile strength (MPa)	Damage constants (k)	Damage constants (m)	K_{IC}	Damage constants (λ)
2530	25	0.228	2	2.3×10^{24}	7	0.92	0.0001

the damage radius is between 1.2 m and 3.0 m, and decreased nonlinearity from the top to the bottom of slope. The maximum vertical damage depth and the maximum horizontal damage extent are found to be at the outer flank of the berm.

It can be seen that damage degree and extent of rock mass near the berm is more serious and much larger than other parts of slope. There are three induced factors for this: firstly, the rock mass near the outer flank of the berm was affected by buffer blasting of former bench most seriously; secondly, there are two free surfaces at the top of slope, which the enlarge degree of stress redistribution and induce a more larger damage extent; thirdly, in the current bench blasting excavation, the combination of effect the shock wave and detonation gas is another main damage induced factor. To guarantee the safety of the slope, the reinforcement measure should be carried out on the top of slope in time.

4 NUMERICAL SIMULATION OF BLASTING INDUCED DAMAGE ZONE

4.1 *Numerical model*

In the present study, 3D numerical simulation of blasting induced damage was implemented with the computer code LS-DYNA. The height of blasting excavation layer is 15 m depth. Diameter of the blast holes is 110 mm. The excavation region can be divided into many same sections. One section contains five presplit holes, two buffering holes and one production hole. Considering the limit of mesh number and computation time, one section was selected to establish the numerical model. The number of nodes is 566016 and the element number is 541400.

Assuming to be isotropic and homogenous material, the damage constants used in the tensile-compress damage model for the rock mass of basalt were listed in Table 2. The material constants such as elastic modulus, Poisson's ratio et al were determined according to the geological data and field experiments. To simulate borehole blasting, a radial pressure was applied to the elements on the borehole wall. The amplitude and the duration of the pressure wave can be determined according to the method proposed by Lu et al. (2011), the density of explosive is 1000 kg/m^3 and the detonation velocity is 3200 m/s. To prevent the effects of reflected waves at the edge of the region, the transmitting boundaries were adopted in numerical simulation. Damping in the model is done through the Rayleigh classical approach by making the damping matrix equal a linear combination of the mass and stiffness matrix.

4.2 *Numerical results*

Figure 3 shows the damage distribution characteristics of the former bench and presplitting blasting of the current bench.

It can be seen that the damage depth caused by the former excavation bench is about 0.6 m. The damage degree decreases from the outer flank to the inner side of the berm. After the presplitting blasting of underlayer excavation, a columnar damage zone was formed, the degree of damage decreases with the distance to the blast hole. The rock mass close to the blast hole which was crushed by the shock wave was critical destroyed for the damage scalar equals 1.0, then the shock wave changed into stress wave and the damage degree decreases to about between 0.2 and 0.8. The maximum damage extent is located in the top face of the blast hole.

To verify the accuracy of the tensile-compress blasting damage model, other four exiting blasting

damage models were used to make a comparison. Yang et al. (1996) establishd a continuum damage constitutive model which was widely used in the numerical simulation of dynamic damage. LS-DYNA has several damage models designed for studying dynamic damage, the material Type 96 can be used to simulate the large strains, high strain states and high pressures to which the rock mass may be subjected in blasting. Especially, the accumulative plastic strain was used to describe the degree of damage which is quite different from other blasting damage models. Considering that the tensile-compressive damage model was modified based on the TCK model and KUS model, so the comparison between the MAT96, the YANG model, the TCK model, the KUS model and the tensile-compressive damage model was carried out in the next paragraphs.

The YANG model, the TCK model and the KUS model were implemented into LS-DYNA though its user subroutine interfaces with FORTRAN. For the MAT96, the viscosity constant and the fracture toughness constant which were determined as 140.35 $NM^{-1/2}$ and 0.723 $MPaS^{-1}$ according to the keyword user's manual of LS-DYNA. The calculation procedure was the same as that of the tensile-compress damage model. Figure 4 lists the results of four existing damage models.

It can be seen that the distributions of the damage zone for these damage models are overall identical, but the extents are different. The damage radius of YANG model is the largest and the TCK model takes the second place, while the KUS model and the tensile-compress model are smaller. The damage zone of MAT96 is the least.

Based on the cross-hole sonic wave result of the berm at the EL.640 m of Xiluodu as shown in Figure 2, the quantitative accuracy of numerical simulation results could be confirmed. The comparison between these blasting damage models and

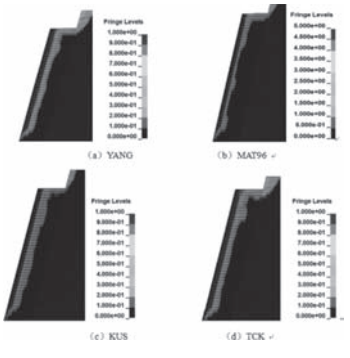

Figure 4. Damage distributions of four existing blasting damage models.

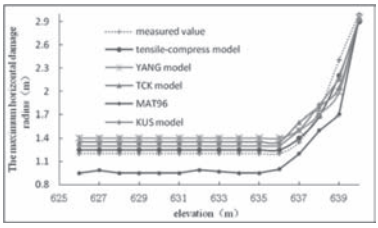

Figure 5. Damage distributions of four existing blasting damage models.

site measurement results was shown in Figure 5. The damage threshold D_{cri} is set as 0.19.

It could be obviously seen that the result of the tensile-compress damage model agrees with the test result well. The extents of the tensile-compress model, YANG model, the TCK model and the KUS model are bigger than that of sonic wave test. Respectively Errors of these models are 0.09 m, 0.123 m, 0.15 m and 0.17 m. The result of the MAT96 is smaller than that of test value and the error is as big as 0.35 m. It could be seen that the result of tensile-compress damage model agreed with the observations better than other damage models.

5 CONCLUSIONS

In the present study, the spatial distribution of EDZ near the EL.640 m berm of Xiluodu high rock slope was determined by cross-hole test. The results reveal that an approximation columnar damage zone was formed near the excavation face. The extent of EDZ and damage degree at the top of slope is much larger and more serious than other parts. The horizontal damage depth decreases non-linearly from the top to the bottom of slope, the vertical damage depth increases non-linearly from the inner side to the outer flank of the berm, the maximum horizontal damage radius and the maximum vertical damage depth are found to be at the outer flank of the berm.

Based on the exiting blasting damage models, the damage pattern of compress was introduced and the method of determining the material elastic constants was modified, and then a modified tensile compress damage model was implemented with the user subroutine interface of LS-DYNA. The damage effect induced by blasting excavation of the ET.640 berm of Xiluodu high rock slope was simulated by using the modified model and other four blasting damage models. Compared with other widely used four blasting damage models, the result of the tensile-compressive damage model agreed with the observations better than four blasting damage models.

However, the numerical simulation done in this paper is just a preliminary work. The isotropic and homogeneous damage model for the rock mass is employed in the numerical simulation for the rock damage under blasting, while the anisotropic and inhomogeneous of the rock mass in reality are ignored. The site measurement of EDZ and numerical simulations done in the present study still provide a good reference for the similar high rock slope excavation engineering.

ACKNOWLEDGEMENTS

This work is supported by Chinese National Science Fund for Distinguished Young Scholars (51125037), Chinese National Programs for Fundamental Research and Development (973 Program) (2011CB013501), Chinese National Natural Science Foundation (51279146 and 51179138) and the Fundamental Research Funds for the Central Universities (2012206020205). The authors wish to express their thanks to all supporters.

REFERENCES

Chen, S.H., Wang, G.J., Zhou, H., Wang, W.M. & Zou, L.C. 2012. Evaluation of excavation-induced relaxation and its application an arch dam foundation. *International Journal For Numerical And Analytical Methods In Geomechanics* 36(2): 166–181.

Englman, R. & Jaeger, Z. 1987. *Theoretical aids for the improvement of blasting efficiencies in oil shale and rocks*. Report of Soreq Nuclear Research Center.

Furlong, J.R., Davis, J.F. & Alme, M.L. 1990. *Modeling the dynamic load/unload behavior of ceramics under impact loading*. Final Report for U.S. ARMY RESEARCH OFFICE.

Goodman, R.E. & Kieffer, D.S. 2000. Behavior of rock slopes. *Journal of Geotechnical and Geoenvironmental Engineering* 126(8): 675–684.

Govindjee, S., Kay, G.J. & Simo, J.C. 1995. Anisotropic modeling and numerical simulation of brittle damage in concrete. *Int. J. Numer. Methods Eng.* 38(2): 3611–3633.

Grady, D.E. & Kipp, M.E. 1980. Continuum modeling of explosive fracture in oil shale. *Int. J. Rock Mech. Min. Sci.* 17(3): 147–157.

Grady, D.E. 1983. The mechanics of fracture under high-rate stress loading. In Z.P. Bazant (ed.), *Preprints of the William Prager symposium of mechanics of geomaterials: rocks, concrete and soils*: 149–188. Evanston: Northwestern University.

Hao, H., Wu, C.Q. & Zhou, Y.X. 2002. Numerical analysis of blast-induced stress waves in a rock mass with anisotropic continuum damage models part 1: equivalent material property approach. *Rock Mechanics and Rock Engineering* 35(2): 79–94.

Holmquist, T.J. & Johnson, G.R. 1993. A computational constitutive model for concrete subjected to larger strains, high strain rates and high pressure. In N. Jackson, S. Dickert (eds); *14th International Symposium on Ballistics, Quebec, 26–29 September 1993*.

Kuszmaul, J.S. 1987. A new constitution model for fragmentation of rock under dynamic loading. In L. William, D.D. Richard (eds.); *Proc. of 2nd Int. Symp. on Frag. by Blastin, Keystone, 23–26 August 1987*.

Li, H.B., Xia, X. & Li, J.C. 2010. Rock damage control in bedrock blasting excavation for a nuclear power plant. *Int. J. Rock Mech. Min. Sci.* 48(2): 210–218.

Liu, L.Q. & Katsabanis, P.D. 1997. Development of a continuum damage model for blasting analysis. *Int. J. Rock Mech. Min. Sci.* 34(2): 217–231.

LSTC, 2010. *LS-DYNA theoretical manual*. Livermore: Livermore Software Technology Corporation.

LSTC, 2010. *LS-DYNA keyword user's manual, Version 970*. Livermore: Livermore Software Technology Corporation.

Lu, W.B., Yang, J.H. & Chen, M. 2011. An equivalent method for blasting vibration simulation. *Simulation Modeling Practice and Theory* 19(9): 2050–2062.

Lu, W.B., Yang, J.H., Yan, P., Chen, M., Zhou, C.B., Luo, Y. & Jin, L. 2012. Dynamic response of rock mass induced by the transient release of in-situ stress. *Int. J. Rock Mech. Min. Sci*. 53: 129–141.

Ma, G.W. & An, X.M. 2008. Numerical simulation of blasting-induced rock fractures. *Int. J. Rock Mech. Min. Sci.* 45(6): 966–975.

Malmgren, L., Saiang, D., Töyrä, J. & Bodare, A. 2006. The excavation disturbed zone (EDZ) at Kiirunavaara mine, Sweden-by seismic measurements. *Int. J. Rock Mech. Min. Sci.* 61(1): 1–15.

Martino, J.B. & Chandler, N.A. 2004. Excavation-induced damage studies at the Underground Research Laboratory. *Int. J. Rock Mech. Min. Sci.* 41(8): 1413–1426.

Read, R.S. 2004. 20 years of excavation response studies at AECL's Underground Research Laboratory. *Int. J. Rock Mech. Min. Sci*. 41(8): 1251–1275.

Sheng, Q., Yue, Z.Q. & Lee, C.F. 2002. Estimating the excavation disturbed zone in the permanent shiplock slopes of the Three Gorges Project, China. *Int. J. Rock Mech. Min. Sci.* 39(2): 165–184.

Sun, Y.X. 2002. *Studies on penetration resistance of concrete*. Hefei: University of Science and Technology of China.

Taylor, L.M., Chen, E.P. & Kuszmaul, J.S. 1986. Microcrack induced damage accumulation in brittle rock under dynamic loading. *Computer Methods in Applied Mechanics and Engineering* 55(3): 301–320.

Thorne, B.J., Hommert, P.J. & Brown, B. 1990. Experimental and computational investigation of the fundamental mechanisms of cratering. In *Proc. of 3rd Int. Symp. on Frag. by Blasting, Brisbane, 26–31 August 1990*.

Wang, Z.L., Wang, J.G. & Li, Y.C. 2006. Numerical study on craters and penetration of concrete slab by ogive-nose steel projectile. *Computers and Geotechnics* 34(2): 1–9.

Wang, Z.L., Li, Y.C. & Wang, J.G. 2007. Numerical simulation of tensile damage and blast crater in brittle rock due to underground explosion. *Int. J. Rock Mech. Min. Sci*. 44(5): 730–738.

Yang, R., Brwden, W.F. & Katsabanis, P.D. 1996. A new constitutive model for blast damage. *Int. J. Rock Mech. Min. Sci.* 33(3): 245–254.

Geotechnical Safety and Risk IV – Zhang et al. (eds)
© 2014 Taylor & Francis Group, London, ISBN 978-1-138-00163-3

Slope reliability analysis using a non-intrusive stochastic finite element method

S.H. Jiang & D.Q. Li
State Key Laboratory of Water Resources and Hydropower Engineering Science, Wuhan University, Wuhan, P.R. China

ABSTRACT: Reliability analysis of slope stability has received considerable attention. This paper aims to propose a Non-Intrusive Stochastic Finite Element Method (NISFEM) for slope reliability analysis with an implicit performance function. This procedure is formulated on the basis of the Stochastic Response Surface Method (SRSM) and the deterministic finite element method. The probabilistic analysis of slope stability is decoupled with the deterministic finite element analysis. A global sensitivity analysis based on Sobol's indices is carried out to identify the key factors influencing the factor of safety of a slope. A practical rock slope example is presented to demonstrate the capability of the proposed method. The results indicate that the proposed method can effectively evaluate the slope reliability with an implicit performance function with a sufficient accuracy. The internal friction angles of the fault $f_{42\text{-}9}$ and the class III_2 rock mass have a significant effect on the stability of the Jinping left abutment slope.

1 INTRODUCTION

It is widely recognized that there are many uncertainties in the analysis of slope stability because of inadequate information of site characterization and inherent variability and measurement errors in geological and geotechnical parameters (Phoon & Kulhawy 1999, Baecher & Christian 2003). Traditional slope stability analysis using the factor of safety method cannot effectively account for these uncertainties in a quantitative way. In order to remove such limitations, a new perspective concerning reliability-based method is developed. On the other hand, the finite element method and finite difference method have been extensively used for slope stability analysis (Matsui & San 1992, Zou et al. 1995, Kim & Lee 1997, Farias & Naylor 1998, Griffiths & Lane 1999). In comparison with the factor of safety method, these methods can effectively represent the slope actual stress state, meet the displacement compatibility condition and account for the effect of deformation of soil and rock masses on the slope stability. In this case, the factor of slope safety obtained from finite element analysis cannot be explicitly expressed as a function of input parameters. The computational effort for complex slope stability problem is always expensive. In this respect, both First Order Reliability Method (FORM) and Second Order Reliability Method (SORM) are not applied directly due to the implicit performance function (Der Kiureghian et al. 1987). The Monte Carlo Simulation (MCS) can be used for such purpose. However, it is prohibitively expensive because a large number of finite element analyses of slope stability will be needed especially for the case of small probability level (e.g. Tamimi et al. 1989).

Recently, the Response Surface Methods (RSM) have also been applied for slope reliability analysis (Wong 1985, Cho 2009). However, an iterative calculation of factor of safety was indispensable in the RSM for reliability analysis, making it difficult to combine with the commercial finite element codes. Therefore, many attempts are made to solve the slope reliability problems using the optimization methods (Low & Tang 1997, Tang et al. 2012, Luo et al. 2012). However, the process of searching global optimization could be prohibitively expensive due to a substantial number of slope stability analysis required. Although the Stochastic Finite Element Method (SFEM) can also be used for this purpose (Ishii & Suzuki 1987, Ghanem & Spanos 1991), it requires significant modification of existing finite element codes underlying the deterministic finite element model for slope stability.

The main objective of this study is to propose a non-intrusive stochastic finite element method for slope reliability analysis with an implicit performance function. This method is formulated on the basis of the Stochastic Response Surface Method (SRSM) (Li et al. 2011, Mollon et al. 2011) and the deterministic finite element method. For illustration, the finite element stress-based method (Farias & Naylor 1998) using the software

SIGMA/W and SLOPE/W is selected to compute the factor of slope safety. The SRSM is employed to perform the probabilistic analysis of slope stability. A practical rock slope example is presented to illustrate the proposed method.

2 NON-INTRUSIVE STOCHASTIC FINITE ELEMENT METHOD

A flowchart summarizing the links between the probabilistic analyses and deterministic Finite Element Analysis (FEA) of slope stability is presented in Figure 1. Several major steps of the Non-Intrusive Stochastic Finite Element Method (NISFEM) are outlined as follows.

1. Identify the random variables and estimate their means, Coefficients Of Variation (COV), distribution types and correlations between them for the considered slope reliability problem.
2. Construct the FEA model of slope stability with the mean values of the input random variables using the software SIGMA/W and SLOPE/W.

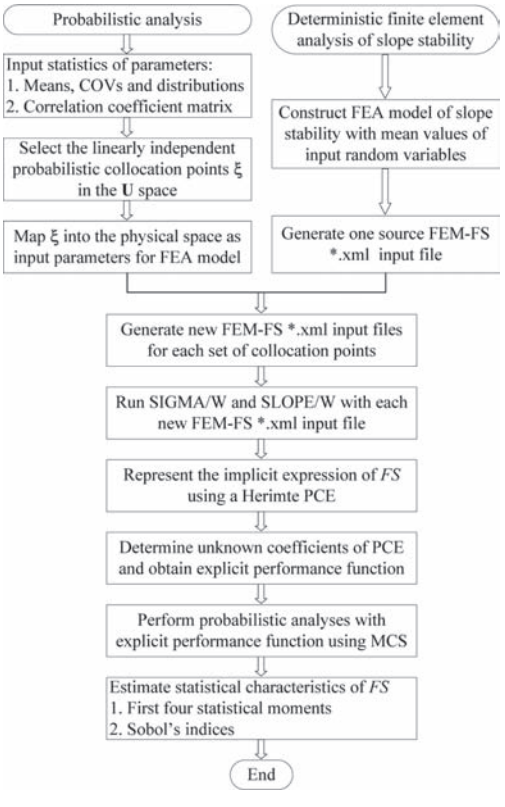

Figure 1. Flowchart of the NISFEM for slope reliability analysis.

Save the deterministic slope stability model file as one source FEM-FS *.xml input file, which can be directly viewed via the text editor.

3. The Hermite Polynomial Chaos Expansion (PCE) is adopted as a meta-model to approximate the implicit relationship between the factor of slope safety *FS* and input uncertain parameters (Li et al. 2011, Mollon et al. 2011, Mao et al. 2012):

$$FS(\boldsymbol{\xi}) = a_0\Gamma_0 + \sum_{i_1=1}^{n} a_{i_1}\Gamma_1\left(\xi_{i_1}\right) + \sum_{i_1=1}^{n}\sum_{i_2=1}^{i_1} a_{i_1 i_2}\Gamma_2\left(\xi_{i_1}, \xi_{i_2}\right) + \sum_{i_1=1}^{n}\sum_{i_2=1}^{i_1}\sum_{i_3=1}^{i_2} \boldsymbol{a}_{i_1 i_2 i_3}\Gamma_3\left(\xi_{i_1}, \xi_{i_2}, \xi_{i_3}\right) + \cdots + \sum_{i_1=1}^{n}\sum_{i_2=1}^{i_1}\sum_{i_3=1}^{i_2}\cdots\sum_{i_n=1}^{i_{n-1}} a_{i_1 i_2, \ldots, i_n}\Gamma_n\left(\xi_{i_1}, \xi_{i_2}, \ldots, \xi_{i_n}\right) \quad (1)$$

where $FS(\boldsymbol{\xi})$ is the vector of the factor of safety; $\boldsymbol{a} = (a_0, a_{i_1}, a_{i_1 i_2}, \cdots)$ are the unknown coefficients to be estimated, in which n is the number of random variables representing the uncertainties of the model inputs, and $i_1 + i_2 + \cdots + i_n \le n$; $\boldsymbol{\xi}_i = (\xi_{i_1}, \xi_{i_2}, \cdots, \xi_{in})$ is the vector of independent standard normal variables resulting from the transformation of the input uncertain parameters, $\boldsymbol{X}_i$; $\Gamma_n(\xi_{i_1}, \xi_{i_2}, \cdots, \xi_{in})$ is the multivariate Hermite polynomials of degree n. (Li et al. 2011, Mollon et al. 2011).

4. Generate and select N_c sets of collocation points in the independent standard normal **U** space, $\boldsymbol{\xi} = (\boldsymbol{\xi}_1, \boldsymbol{\xi}_2, \ldots, \boldsymbol{\xi}_{Nc})$ based on the linearly independent principle. The linearly independent Probabilistic Collocation Method (PCM) can yield accurate results with much less computational cost. The number of runs of slope stability model equals to the number of unknown coefficients in the PCE of order p, N_c, $N_c = (n + p)!/(n! \times p!)$. The reader is referred to Mao et al. (2012) for details.
5. Map the selected collocation points $\boldsymbol{\xi}$ in the independent standard normal **U** space into the collocation points **X** in the physical space. If the input random variables are correlated non-normal variables, the Nataf transformation (Nataf 1962) can be used to transform $\boldsymbol{\xi}$ into **X**. Then, the N_c sets of collocation points **X** can be obtained and taken as input parameters for the deterministic FEA model of slope stability.
6. Replace the corresponding mean values of input random variables in the source FEM-FS *.xml file generated in step (2) with the N_c sets of the collocation points **X**. Then N_c different new FEM-FS *.xml input files can be generated. Thus, no programming effort is required to modify the existing finite element codes in

contrast to the popular spectral stochastic finite element method (Ghanem & Spanos 1991).

7. Run the SIGMA/W and SLOPE/W with each new input file generated in step (6) to perform deterministic FEA of slope stability. Note that these input files can be executed automatically with the help of the Winbatch™ software. Once the solution process is finished, the corresponding result files are obtained. Then, post-processing can be carried out to extract the factor of slope safety FS, $FS = (FS_1, FS_2, \ldots, FS_{Nc})$.
8. Establish a linear algebraic system of equations in terms of the unknown coefficients $\boldsymbol{a}$ according to Eq. (1) with the $\boldsymbol{\xi}$ and FS, and solve it to obtain the unknown coefficients of PCE.
9. Once the coefficients in the PCE is obtained, the implicit performance function can be explicitly expressed by a meta-model for slope reliability analysis, $G(\boldsymbol{\xi}) = FS(\boldsymbol{\xi}) - 1$. The probability of slope failure and the corresponding reliability index can be estimated for the performance function involving the output responses represented by the Hermite PCE. The first four statistical moments and Sobol's indices can also be directly calculated using the coefficients of PCE. In this study, the direct MCS with a sample size of 10^5 is used for such purpose. It should be pointed out that the evaluation of the factor of slope safety does not involve finite element model runs, but only the evaluation of simple algebraic expressions, which is much more computationally efficient.

3 RELIABILITY ANALYSIS OF JINPING SLOPE IN CHINA WITH AN IMPLICIT PERFORMANCE FUNCTION

Jinping I hydropower station is located at the upstream of Yalong River, between Muli and Yanyuan counties in Sichuan Province, China. The double curvature concrete arch dam is 305 m in height upon completion (Wu et al. 2008). The dam site is located in a typical deeply cut V-shaped valley and the left abutment slope is very high and steep, as shown in Figure 2. The lamprophyre dike X, faults f_5, f_8 and $f_{42\text{-}9}$ and some other weak geological structural features are found in the left abutment slope. Besides, the relief fractures develop widely in the subsurface of slope, even up to 100~200 m in depth. It can be observed that the geological conditions at the dam site are extremely complicated, which lead to poor stability conditions of the left abutment slope.

A typical section, Section II_1-II_1, of the left abutment slope shown in Figure 3 is selected for reliability analysis. Note that the slope being considered here is the natural slope before excavation. For the

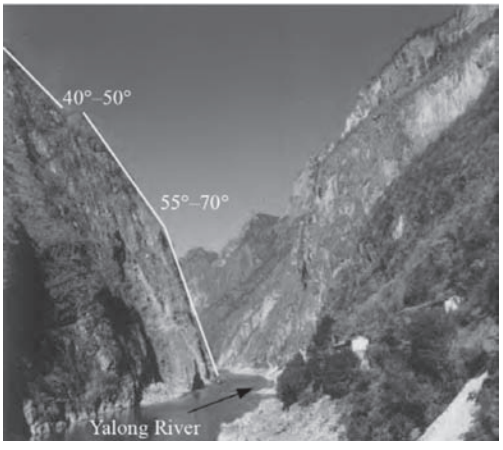

Figure 2. A deeply cut V-shaped valley at the dam site of Jinping I hydropower station.

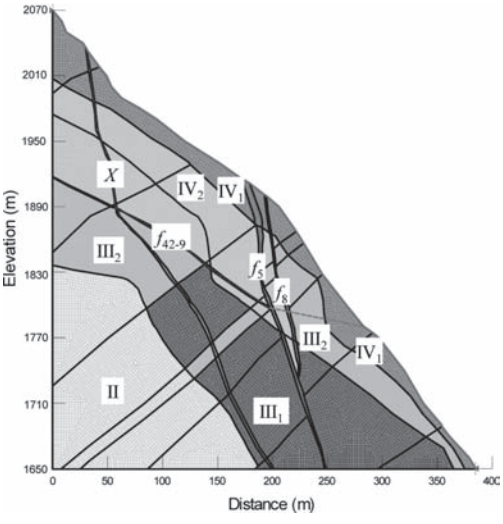

Figure 3. The FEM model for the section II_1-II_1 of natural slope at the Jinping left abutment.

slope stability model considered, the specific unit weights γ_i, Young's modulus E_i and Poisson's ratios ν_i of rock masses and structural planes as well as the parameters related to geometry are treated as deterministic quantities, their values are listed in Table 1. The cohesions and internal friction angles of the materials of some weak structural planes and rock masses closely related to the slope stability are identified and treated as random variables. The statistical parameters of 10 random variables of slope materials are summarized in Table 2. c_i and ϕ_i ($i = 1, 2, \ldots, 5$) denote the cohesions and internal

Table 1. The mechanical parameters of rock masses and weak structural planes in the Jinping left abutment slope stability model.

Materials	γ_i (kN/m^3)	E_i (GPa)	ν_i	c_i (kPa)	ϕ_i (°)
Class II rock mass	27	23.5	0.225	2000	53.47
Class III$_1$ rock mass	27	10.5	0.25	1500	46.94
Class III$_2$ rock mass	27	5.5	0.275	900	45.57
Class IV$_1$ rock mass	27	2.5	0.3	600	34.99
Class IV$_2$ rock mass	27	1.9	0.3	400	30.96
Lamprophyre dike X	25	1.0	0.2	20	16.7
Fault $f_{42\text{-}9}$	25	0.45	0.25	20	16.7
Fault f_5	25	0.45	0.35	20	16.7
Fault f_8	25	0.45	0.35	20	16.7

Table 2. Statistics of random variables in the Jinping left abutment slope stability model.

Materials	Random variables	Mean	COV
Lamprophyre dike X	c_1 (kPa)	20	0.25
	ϕ_1 (°)	16.7	0.15
Fault $f_{42\text{-}9}$	c_2 (kPa)	20	0.3
	ϕ_2 (°)	16.7	0.2
Class III$_2$ rock mass	c_3 (kPa)	900	0.15
	ϕ_3 (°)	45.57	0.08
Class IV$_1$ rock mass	c_4 (kPa)	600	0.18
	ϕ_4 (°)	34.99	0.10
Class IV$_2$ rock mass	c_5 (kPa)	400	0.2
	ϕ_5 (°)	30.96	0.12

friction angles of five types of materials, respectively. The means of the shear strength parameters are determined based on field test, laboratory test supplemented with engineering judgment, such as direct shear test and triaxial test (Wu et al. 2008). The Coefficients of Variation (COV) of the shear strength parameters are adopted from the literature (Phoon & Kulhawy 1999, Baecher & Christian 2003, Tang et al. 2012). Additionally, all random variables are assumed to be characterized statistically by a lognormal distribution. The slope stability is evaluated under two working conditions, namely natural condition and rainfall condition. For the natural condition, the groundwater table is below the slip surface of the slope. If the groundwater table is above the slip surface of the slope, the resulting load should be taken into account, which corresponds to the rainfall condition. The pore-water pressure ratio $R_u = 0.1$, a ratio of the pore-water pressure to the weight of overburden rock masses is used to account for the effect of rainfall on the stability of the left abutment slope.

In order to model the structures and the generalization of geomechanical model of the slope as well as the topography of the computational domain, the Finite Element Method (FEM) (Zou et al. 1995, Kim & Lee 1997) is used to calculate the factor of safety of the left abutment slope because this approach can account for the influence of the deformation of rock masses on the slope stability. Theoretically, a Three-Dimensional (3D) model for the slope stability problem considering spatial variability of rock masses should be employed. For simplicity, a finite element model based on 2D plane strain analysis is built in the SIGMA/W with the means of random variables, as shown in Figure 3. The analyzed domain is 420 m in height from the elevation 1650 m to the elevation 2070 m and 384.7 m in length of the direction perpendicular to the river from the centerline of rive to the within slope. The gravity loads induced by the self-weight of rock masses are applied. For illustrative purposes, a conventional elastic and perfectly plastic model based on the Mohr-Coulomb failure criterion is adopted to represent the stress-strain behavior of rock masses and structural planes. The finite element model consists of three-node triangular and four-node quadrilateral hybrid elements. There are totally 14363 zones and 14113 grid points in the mesh. With regard to the boundary conditions, the horizontal movement on the vertical left boundary of the mesh is restrained, whereas the base of the mesh is not allowed to move in both the horizontal and the vertical directions. The initial stress field is obtained using the SIGMA/W. Then, it is imported into the SLOPE/W for slope stability analysis. Based on the geological investigation, it can be expected that a potential deep sliding may occur along the lamprophyre dike X and fault $f_{42\text{-}9}$, and shear off superficial rock masses in accordance to the path highlighted with a red dashed line in Figure 3. For the left abutment slope with the prescribed slip surface, the factors of slope safety obtained from the FEM are 1.083 and 0.981 for the natural and rainfall conditions, respectively, which are consistent with 1.110 and 1.014 using

the Morgenstern-Price method. These results further demonstrate that the FEM is an effective tool for slope stability analysis.

As mentioned in Section 2, the NISFEM can effectively decouple the probabilistic analysis with the deterministic FEA of slope stability. It is employed to analyze the considered slope reliability problem with an implicit performance function. Firstly, the order of PCE is determined through comparing the differences in the probability of failure between two consecutive order PCEs. Table 3 shows the probabilities of slope failure obtained from the 2nd and 3rd order PCEs for the natural and rainfall conditions. The results of the direct MCS with a sample size of 10^5 are also provided in Table 3, which is used for the benchmark purpose. Note that both the computational accuracy and cost associated with the NISFEM increase with the order of PCE. There is a slight difference in the probabilities of failure obtained from the 2nd and 3rd order PCE. However, the number of finite element model runs for the latter is about four times larger than that for the former. In addition, the probabilities of slope failure obtained from the 2nd order PCE match well with those obtained from the direct MCS. The computational cost for the former is just 1/1515 of the latter. As for the example considered, a 2nd order PCE with less computational cost is adopted for slope reliability analysis and subsequent sensitivity analysis. Additionally, the probability of failure under the rainfall condition has been greatly increased to 61%, thus some reinforcement measures should be taken to improve the slope stability.

A global sensitivity analysis based on Sobol's indices (Mao et al. 2012) is conducted herein to determine the contribution of each random variable to the variation of factor of slope safety. The corresponding results for the natural and rainfall conditions are plotted in Figure 4. It is observed that the internal friction angle ϕ_2 of the fault $f_{42\text{-}9}$ is the most significant random variable for the slope stability under two working conditions, followed by ϕ_3, and the other random variables have a slight influence on the slope stability because their Sobol' indices are below 0.06.

Table 3. Comparison of the reliability results from the NISFEM and MCS for the left abutment slope.

Conditions	Methods	p_f (%)	$\varepsilon = \lvert p_f - p_{f,MCS}\rvert / p_{f,MCS} \times 100$ (%)
Natural	2nd order PCE (66 FE runs)	13.20	0.99
	3rd order PCE (286 FE runs)	13.17	0.77
	MCS (10^5 FE runs)	13.07	–
Rainfall ($R_u = 0.1$)	2nd order PCE (66 FE runs)	60.64	0.85
	3rd order PCE (286 FE runs)	61.03	0.21
	MCS (10^5 FE runs)	61.16	–

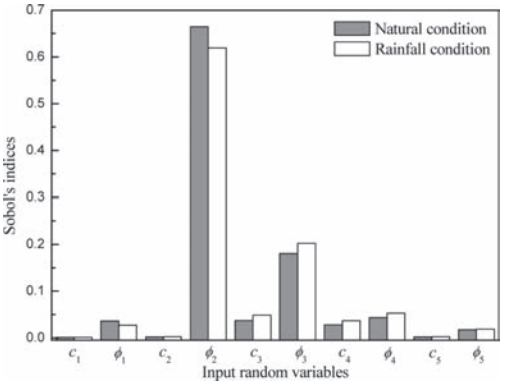

Figure 4. Comparison among Sobol's indices of input random variables for two working conditions.

4 CONCLUSION

This paper has proposed a non-intrusive stochastic finite element method for analyzing slope reliability problems with implicit performance functions. A practical rock slope example is investigated to demonstrate the validity of the proposed method. Several conclusions can be drawn from this study.

1. A non-intrusive stochastic finite element method for slope reliability analysis is proposed. The proposed method does not require the user to modify existing deterministic finite element codes, which are used as "black boxes". Moreover, the probabilistic analysis and the deterministic finite element analysis are decoupled. The proposed method provides a practical tool for reliability problems requiring complex finite element analysis.
2. The non-intrusive stochastic finite element method can efficiently evaluate the slope reliability with an implicit performance function. It can reduce the number of calls to the deterministic finite element model substantially and is much more efficient than the direct Monte Carlo simulations. For the studied example, the 2nd order PCE requiring 66 runs of the deterministic finite element model can produce sufficiently accurate reliability results.
3. The results of sensitivity analysis based on Sobol's indices indicate that the internal friction

angle of the fault $f_{42\text{-}9}$ is the most significant random variable for the slope stability, followed by that of the class III_2 rock mass, and the other random variables have a slight influence on the slope stability because their Sobol' indices are below 0.06. Therefore, the fault $f_{42\text{-}9}$ and the class III_2 rock mass should be given considerable attention in the following slope excavation and reinforcement.

ACKNOWLEDGMENTS

This work was supported by the National Basic Research Program (973 Program) (2011CB013506), the Academic Award for Excellent Ph.D. Candidates Funded by Ministry of Education of China (5052012206001) and the Fundamental Research Funds for the Central Universities (2012206020201).

REFERENCES

Baecher, G.B. & Christian, J.T. 2003. *Reliability and statistics in geotechnical engineering*. New York: John Wiley and Sons.

Cho, S.E. 2009. Probabilistic stability analyses of slopes using the ANN-based response surface. *Computers and Geotechnics* 36(5): 787–797.

Der Kiureghian, A., Lin, H.Z. & Hwang, S.J. 1987. Second order reliability approximations. *Journal of Engineering Mechanics* 113(8): 1208–1225.

Farias, M.M. & Naylor, D.J. 1998. Safety analysis using finite elements. *Computers and Geotechnics* 22(2): 165–181.

Ghanem, R. & Spanos, P.D. 1991. *Stochastic finite element: a spectral approach*. New York: Springer-Verlag.

Griffiths, D.V. & Lane, P.A. 1999. Slope stability analysis by finite element. *Geotechnique* 49(3): 387–403.

Ishii, K. & Suzuki, M. 1987. Stochastic finite element method for slope stability analysis. *Structural Safety* 4(2): 111–129.

Kim, J.Y. & Lee, S.R. 1997. An improved search strategy for the critical slip surface using finite element stress fields. *Computers and Geotechnics* 21(4): 295–313.

Li, D.Q., Chen, Y.F., Lu, W.B. & Zhou, C.B. 2011. Stochastic response surface method for reliability analysis of rock slopes involving correlated non-normal variables. *Computers and Geotechnics* 38(1): 58–68.

Low, B.K. & Tang, W.H. 1997. Efficient reliability evaluation using spreadsheet. *Journal of Engineering Mechanics* 123(7): 749–752.

Luo, X.F., Li, X., Zhou, J. & Cheng, T. 2012. A Kriging-based hybrid optimization algorithm for slope reliability analysis. *Structural Safety* 34(1): 401–406.

Mao, N., Tamara, A.B. & Soubra, A.H. 2012. Probabilistic analysis and design of strip foundations resting on rocks obeying Hoek-Brown failure criterion. *International Journal of Rock Mechanics and Mining Sciences* 49(1): 45–58.

Matsui, T. & San, K.C. 1992. Finite element slope stability analysis by shear strength reduction technique. *Soils and Foundations* 32(1): 59–70.

Mollon, G., Dias, D. & Soubra, A.H. 2011. Probabilistic analysis of pressurized tunnels against face stability using collocation-based stochastic response surface method. *Journal of Geotechnical and Geoenvironmental Engineering* 137(4): 385–397.

Nataf, A. 1962. Détermination des distributions de probabilité dont les marges sont données. *Comptes Rendus de l'Académie des Sciences* 225: 42–43.

Phoon, K.K. & Kulhawy, F.H. 1999. Characterization of geotechnical variability. *Canadian Geotechnical Journal* 36(4): 612–624.

Tamimi, S., Amadei, B. & Frangopol, D.M. 1989. Monte Carlo simulation of rock slope reliability. *Computers and Structures* 33(6): 1495–1505.

Tang, X.S., Li, D.Q., Chen, Y.F., Zhou, C.B. & Zhang, L.M. 2012. Improved knowledge-based clustered partitioning approach and its application to slope reliability analysis. *Computers and Geotechnics* 45: 34–43.

Wong, F.S. 1985. Slope reliability and response surface method. *Journal of Geotechnical Engineering* 111(1): 32–53.

Wu, F.Q., Qi, S.W., Song, S.W. & Gong, M.F. 2008. *Deformation and stability study of complicated high-steep rock slopes—take Jinping I Hydropower Station for an example*. Beijing: Science Press.

Zou, J.Z., Willians, D.J. & Xiong, W.L. 1995. Search for critical slip surfaces based on finite element method. *Canadian Geotechnical Journal* 32(2): 233–246.

Geotechnical Safety and Risk IV – Zhang et al. (eds)
© 2014 Taylor & Francis Group, London, ISBN 978-1-138-00163-3

A novel bond contact model for rock and its calibration

T. Jiang, M.J. Jiang, H. Chen, F. Liu & Z.M. Shi
Faculty of Civil Engineering, Department of Geotechnical Engineering, Tongji University, Shanghai, China
Key Laboratory of Geotechnical and Underground Engineering of Ministry of Education, Tongji University, Shanghai, China

ABSTRACT: A novel bond contact model for rocks was proposed, based on a series of laboratory tests on bonded granules idealized by two glued aluminum rods. The model was then implemented into a two-dimensional distinct element code to numerically carry out the uniaxial and biaxial compression tests on Lac du Bonnet granite. The results were compared to the experimental data and the DEM simulations using an existing Bonded-Particle Model (BPM). The results demonstrate that the proposed model can reproduce the strength envelope of Lac du Bonnet granite adequately. The slope of the strength envelope obtained from our simulation is higher than that obtained with the BPM due to higher peak shear and rolling strength in the proposed model, and that the ratio of shear and rolling failure to tension failure is also higher.

1 INTRODUCTION

The Distinct Element Method (DEM), originally developed by Cundall (1971), is a numerical simulation technique based on the discrete mechanics. The original application of the DEM was in the fields of granular material and blocky rock systems (Cundall & Strack 1979). Nowadays, DEM is widely used due to its simple principle in many aspects of geomechanics, such as granular mechanics (Thornton 2000), constitutive models for granular material (Jiang et al. 2005) and anisotropy of soil (Anandarajah 2000). In addition, DEM is also employed to model rock behavior by treating crystalline rocks as cemented granular materials. The Bonded-Particle Model (BPM) proposed by Potyondy & Cundall (2004) was widely applied to simulate mechanical behavior of rocks in the past decades. Although the BPM is able to reproduce most mechanical behavior of Lac du Bonnet granite in DEM uniaxial compression tests, the macroscopic responses of biaxial compression tests with established microscopic parameters do not match the experimental data (Cho et al. 2007). In order to improve the BPM, Wang & Tonon (2009) developed a distinct element code to model the mechanical behavior of Lac du Bonnet granite in triaxial compression; Christian et al. (2011) proposed a progressive failure model for DEM and reproduce many features of rock failure observed in published experiments. However, the bond contact models proposed by most researchers necessarily contain hypotheses lacking experimental verification.

This paper aims to propose a new bond contact model based on the experiments on the analogous cemented samples. This model was then implemented into a two-dimensional distinct element code in order to numerically carry out a series of compression tests. The proposed model was calibrated by comparing the DEM simulation results to the published experimental data.

2 A BOND CONTACT MODEL FOR ROCK

2.1 *A conceptual bond contact model*

Jiang et al. (2006) proposed a bond contact model through theoretical derivation by assuming that the bond contact width is continuously distributed with the normal/tangential basic elements. The mechanical responses are illustrated in Figure 1.

Figure 1a presents the normal mechanical response. In both tensile and compressive directions, the normal contact force F_n between two particles increases linearly with the normal displacement u_n, while in the tensile direction, after F_n reaches the tensile bond strength R_t, the bond is broken and F_n is abruptly reduced to zero. Figure 1b presents the tangential mechanical response. The tangential force F_s increases linearly with the tangential displacement u_s until the shear strength R_s is reached, then the bond breaks and F_s drops to the residual frictional shear strength. In Figure 1c, the mechanical response in the rolling contact direction is similar to that in the tangential direction, the moment M increases linearly with the rolling rotation angle θ first, and then it drops

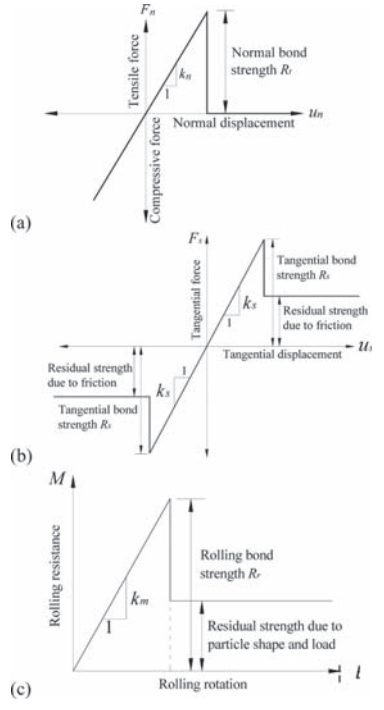

Figure 1. Schematic illustration of the mechanical responses of the bond contact model: (a) normal contact model; (b) tangential contact model; (c) rolling contact model (Jiang et al. 2006, 2012a).

to the residual strength when the rolling bond strength R_r is reached.

2.2 *Experimental setup*

In order to validate the contact law of bonded granules as well as verify the mechanical responses of the model, Delenne et al. (2004) first presented an experimental investigation on mechanical behavior of cemented granules by performing simple tests on a pair of aluminum rods glued together with epoxy resin. Taking the normal force and the bond material into account, Jiang et al. (2012a, b) conducted a series of simple and complex loading tests on a pair of aluminum rods glued with a rock-like material, cement, in addition to epoxy resin.

The analogous cemented sample adopted in the experiment is shown in Figure 2. The aluminum rods glued together with cement are 12 mm in diameter and 50 mm in length. The bond of this sample is 0.6 mm thick and 3 mm wide. Five different loading paths (tension, compression, shear under different normal forces, rolling under different normal forces and shear-rolling tests under different normal forces) were applied to characterize the mechanical behavior of the analogous cemented samples based on typical interaction relationships between particles.

2.3 *Strength envelope*

2.3.1 *Strength envelope for cemented sample with bond thickness of 0.6 mm*

Figure 3a and b presents the strength envelopes obtained from the shear tests under different normal forces and the rolling tests under different normal forces on the cemented samples with bond thickness of 0.6 mm respectively. The solid lines and dash lines shown in Figure 3 represent the peak strength and the residual strength, respectively. Figure 3 shows that the peak shear and rolling strengths depend on the applied normal force. With increasing normal force F_n, the peak shear strength R_s and the peak rolling strength R_r increase first, and then decrease until the compressive strength R_c is reached, where the peak strength envelopes intersect with the residual strength envelopes. When F_n exceeds R_c, bond is broken and the residual strength increases linearly as the normal force increases. The strength envelopes are formulated as follows:

$$R_s = \begin{cases} \mu_b \dfrac{R_c}{R_c + R_t} \cdot \left(F_{nb} + R_t\right) \cdot \left[1 + g_s \cdot \left(\ln \dfrac{R_c + R_t}{F_{nb} + R_t}\right)^{f_s}\right], & F_n \le R_c \quad (1) \\ F_n \mu_b, & F_n > R_c \quad (2) \end{cases}$$

$$R_r = \begin{cases} \dfrac{1}{6}\beta_b r \dfrac{R_c}{R_c + R_t} \cdot \left(F_{nb} + R_t\right) \cdot \left[1 + g_r \cdot \left(\ln \dfrac{R_c + R_t}{F_{nb} + R_t}\right)^{f_r}\right], & F_n \le R_c \quad (3) \\ \dfrac{1}{6} F_n \beta_b r, & F_n > R_c \quad (4) \end{cases}$$

where R_t is tensile strength; μ_b is friction coefficient of cement; β_b is rolling resistance coefficient of cement; $r = 2r_1r_2/(r_1 + r_2)$ is the common radius of two contact particles with radii of r_1 and r_2;

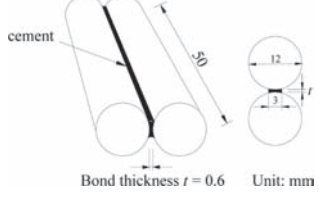

Figure 2. Analogous cemented sample used in experiments (Jiang et al. 2012a, b).

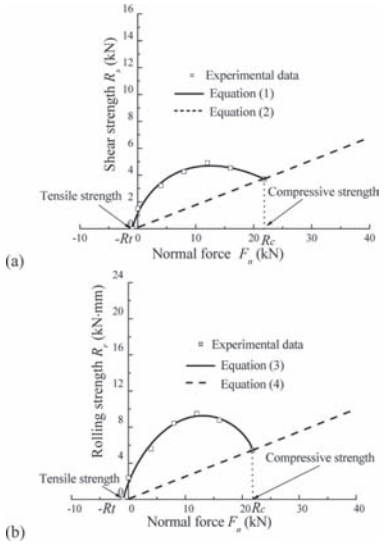

Figure 3. Strength envelopes for cemented samples with bond thickness of 0.6 mm in terms of: (a) shear strength vs. normal force; (b) rolling strength vs. normal force.

and f_s, g_s, f_r, g_r are fitting parameters that control the envelope shapes, whose values are 0.986, 2.15, 0.761 and 3.055 respectively.

2.3.2 *Strength envelope for cemented sample with zero bond thickness*

Note that the real microstructure of Lac du Bonnet granite consists of mineral grains and micro voids between mineral grains, and the distance between two contact particles is so small that it can be approximated as zero (Jiang et al. 2006, Lan et al. 2010). Thus the contact characteristics are similar to that of the cemented sample with zero bond thickness.

Due to the poor flowability of cement, it is much more difficult to prepare cemented samples with zero bond thickness in laboratory. Thus, the strength envelopes for cemented sample with zero bond thickness were obtained from the theoretical analysis based on the experimental results of cemented samples with bond thickness of 0.6 mm. The complete strength envelope for cemented sample with zero bond thickness is presented in Figure 4.

The contact in cemented samples with zero bond thickness is assumed to be composed of inter-particle contact and inter-bond contact, and they transmit the applied normal compressive force in parallel mode. Thus, the inter-particle contact force F_{np} and inter-bond contact force F_{nb} can therefore be calculated by:

$$F_{np} = F_n \cdot k_{np} / (k_{np} + k_{nb}) \tag{5}$$

$$F_{nb} = F_n \cdot k_{nb} / (k_{np} + k_{nb}) \tag{6}$$

where k_{np} is inter-particle normal contact stiffness, k_{nb} is inter-bond normal contact stiffness.

When the normal force is tensile, only inter-bond contact is present and the strength envelopes are therefore the same as expressed in Equations (1) and (2). While the normal force is compressive, the peak shear and rolling strength can be regarded as a combination of inter-bond and inter-particle strength, and can be formulated as follows:

$$R_s = \begin{cases} \mu_b \dfrac{R_c}{R_c + R_t} \cdot (F_{nb} + R_t) \\ \quad \cdot \left[1 + g_s \cdot \left(\ln \dfrac{R_c + R_t}{F_{nb} + R_t} \right)^{f_s} \right] + \mu_p F_{np}, \; 0 < F_n \le R_{cbr} \end{cases} \tag{7}$$

$$\mu_p F_{np} + \mu_b F_{nb} \qquad , \; F_n > R_{cbr} \tag{8}$$

$$R_r = \begin{cases} \dfrac{1}{6} \beta_b r \dfrac{R_c}{R_c + R_t} \cdot (F_{nb} + R_t) \\ \quad \cdot \left[1 + g_r \cdot \left(\ln \dfrac{R_c + R_t}{F_{nb} + R_t} \right)^{f_r} \right] + \dfrac{1}{6} \beta_p r F_{np}, \; 0 < F_n \le R_{cbr} \end{cases} \tag{9}$$

$$\frac{1}{6} \beta_p r F_{np} + \frac{1}{6} \cdot \beta_b r F_{nb} \qquad , \; F_n > R_{cbr} \tag{10}$$

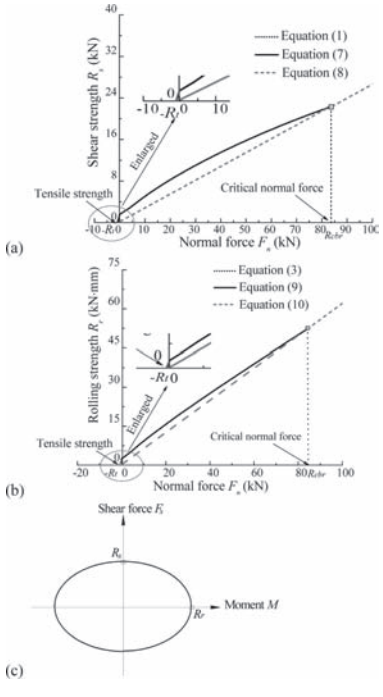

Figure 4. Strength envelopes for cemented samples with zero bond thickness in terms of: (a) shear strength vs. normal force; (b) rolling strength vs. normal force; (c) shear strength vs. rolling strength.

where μ_p is inter-particle friction coefficient; β_p is inter-particle rolling resistance coefficient; R_{cbr} is critical normal force for cemented samples with zero bond thickness which can be expressed as:

$$R_{cbr} = \frac{k_{nb} + k_{np}}{k_{nb}} R_c \tag{11}$$

Note that when F_n is compressive but less than R_{cbr}, if the strength envelopes are exceeded, the bond breaks and the shear force or rolling resistance drops to their residual strengths. When F_n exceeds R_{cbr}, the bond is already broken and the peak strength envelopes coincide with the residual strength envelopes.

In addition, if shear, rolling and normal force are present simultaneously, the strength envelope would be a three-dimensional surface, which is different with the curved lines shown in Figure 4a and b. The relationship between the peak shear strength and the peak rolling strength obtained from the shearing-rolling tests under specific normal force exhibits elliptical shape as presented in Figure 4c, and the corresponding theoretical equation is:

$$\frac{F_s^2}{R_s^2} + \frac{M^2}{R_r^2} = 1 \tag{12}$$

2.4 *Comparisons between the BPM and the proposed model*

Concerning the strength envelopes in the BPM, the peak shear strength keeps constant firstly, and then increases linearly with increasing normal force, while the peak rolling strength increases linearly with increasing normal force. In the proposed model, the peak shear and rolling strengths increase as the normal force increases in parabolic mode first, and then increase linearly with increasing normal force. Thus, under the same compressive normal force, the peak shear and rolling strengths in our proposed model are higher than that in the BPM.

In addition, bond failure modes in each model are different, namely tension and shear failure (for which peak tensile or shear strength has been exceeded respectively) in the BPM, while tension failure (for which tensile strength has been exceeded), shear and rolling failure (for which either the peak strength envelopes shown in Figure 4a and b has been exceeded) and compression failure (for which the critical normal force R_{cbr} has been exceeded) in the proposed model.

More details about the BPM can be referred to Potyondy & Cundall (2004).

3 CALIBRATION OF THE BOND CONTACT MODEL

In order to calibrate the proposed model, the bond contact model comprising the strength envelopes for cemented samples with zero bond thickness has been implemented into a two-dimensional distinct element code using C++ language. A series of uniaxial compression tests and biaxial compression tests were then simulated and the results were compared with the experimental data obtained by Martin (1993) and Martin & Chandler (1994).

3.1 *Generation of DEM rock sample*

A great number of simulations were conducted to find the appropriate microscopic parameters of material and the particle size distribution. They were eventually determined, as shown in Table 1 and Figure 5.

The multilayer undercompaction method proposed by Jiang et al. (2003) was employed for its capability of controlling homogeneity and density. The total number of particles in each numerical sample is 10000, which ensures that the macro mechanical behavior will not significantly changes with more particles. After the consolidation process, the DEM rock sample was generated, as shown in Figure 6. Note that the bonds are represented as solid lines connecting the corresponding particle centers.

Table 1. Microscopic parameters used in DEM simulations.

Parameter	Value
Particle density ρ_s (kg/m^3)	2700
Initial void ratio e	0.20
Normal stiffness of particles k_n(N/m)	1.8×10^{11}
Tangential stiffness of particles k_s(N/m)	9.47×10^{10}
Tensile strength of bonds R_t (N)	6.5×10^4
Compressive strength of bonds R_c (N)	8.0×10^7
Inter-particle friction coefficient μ_p	1.0
Inter-particle rolling resistance coefficient β_p	1.5
Friction coefficient of bonds μ_b	0.5
Rolling resistance coefficient of bonds β_b	0.5

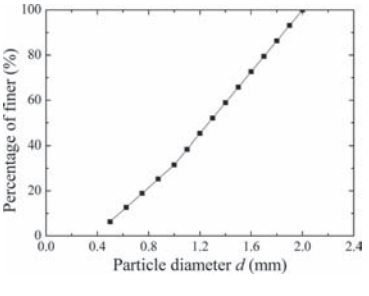

Figure 5. Particle size distribution used in the DEM analyses.

3.2 *Simulation of the uniaxial compression test*

The uniaxial compression test was simulated with the micro parameters in Table 1. Figure 7 presents the stress-strain and the number of broken bonds-strain relationships. The peak strength shown in Figure 7 is about 200 MPa, which is in consistent with the published experimental data (Martin 1993). Figure 7 also shows that, with increasing axial strain, the axial stress increases linearly up to the peak value, where the slopes of the number of broken bonds curves change obviously.

3.3 *Simulation of the biaxial compression test*

The biaxial compression tests were performed under confining pressures of 1 MPa, 5 MPa, 10 MPa, 20 MPa and 30 MPa. Figure 8 illustrates the corresponding stress-strain and number of broken bonds-strain relationships. Figure 8 shows that the axial stress increases linearly as the axial strain increases up to the peak value, where the slopes of the number of broken bonds curves change obviously. Figure 9 presents the strength envelopes obtained by laboratory tests, DEM simulations with the proposed model and with the BPM, whose micro parameters are chosen by a calibration process with Lac du Bonnet granite. It can be indicated that the peak axial stress increases linearly with increasing confining pressure, but the test results using the proposed model are more consistent with experimental data than the BPM, which cannot provide a high peak stress when confining pressure is high.

Figure 10 presents the ratio of shear and rolling-induced bond failure to tension-induced bond failure at the peak axial stress under different confining pressures. Figure 10 indicates that with increasing confining pressure, the ratio of shear and rolling failure to tension failure in the proposed model increases in a parabolic mode, while in the BPM, although the number of shear failure and tension

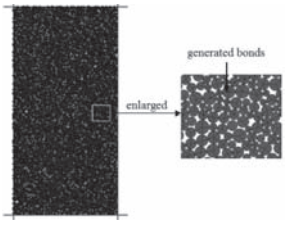

Figure 6. A DEM rock sample and generated bonds.

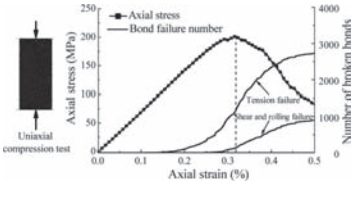

Figure 7. Stress-strain relationship accompanied with number of broken bonds-strain relationship obtained from DEM uniaxial compression test.

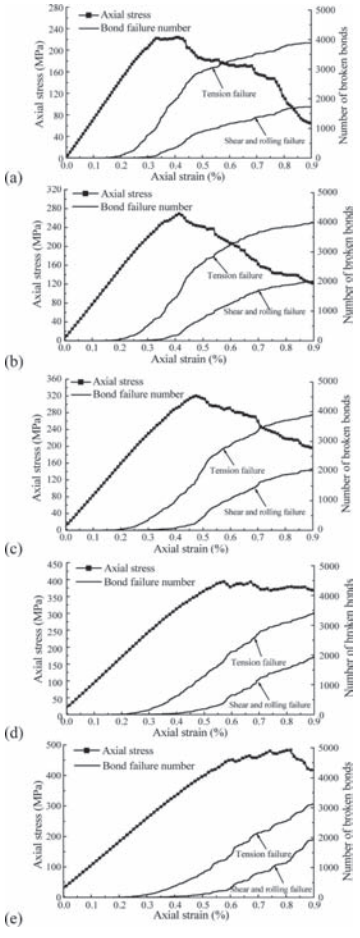

Figure 8. Stress-strain relationship accompanied with number of broken bonds-strain relationship obtained from DEM biaxial compression tests under confining pressure of: (a) 1 MPa; (b) 5 MPa; (c) 10 MPa; (d) 20 MPa; (e) 30 MPa.

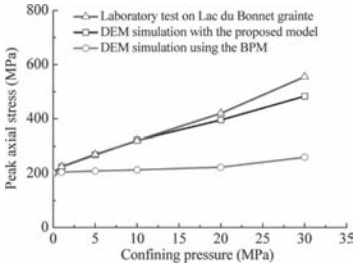

Figure 9. Strength envelopes obtained from DEM numerical simulations and laboratory tests.

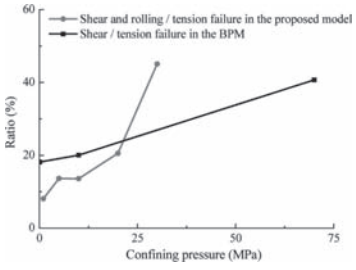

Figure 10. Ratio of shear (and rolling) failure to tension failure at the peak axial stress under different confining pressures.

failure both increase with increasing confining pressure, the ratio of shear failure to tension failure increases slowly and remains low under high confining pressure. In addition, although the tensile strength keeps constant in our DEM simulations, the shear strength and rolling strength depending on the normal force increase with increasing confining pressure. Moreover, the shear strength and rolling strength under a specific normal force in the proposed model are much higher than that in the BPM, whose shear strength is independent of normal force. Thus, the strength envelope obtained from our simulations can provide a higher slope, which is more approximate to the experimental data shown in Figure 9.

4 CONCLUSIONS

A series of experiments were conducted on a pair of cemented aluminum rods in laboratory in order to simulate the mechanical behavior of rock via DEM. Based on the experimental data, a bond contact model was developed and implemented into a distinct element code. Simulations of uniaxial and biaxial compression tests were carried out with this code, and the results were compared to the published experimental data of Lac du Bonnet granite for model calibration. The results show that the proposed bond contact model is able to model a high slope of strength envelope that is more approximate to the experimental data, and videlicet, the proposed bond contact model was successfully calibrated.

ACKNOWLEDGMENT

The research was funded by China National Funds for Distinguished Youth Scientists with Grant No. 51025932, and the Major Project of Chinese National Programs for Fundamental Research and Development (973 Program) with Grant No. 2011CB013504. All of these supports are greatly appreciated.

REFERENCES

Anandarajah, A. 2000. On influence of fabric anisotropy on the stress–strain behaviour of clays. *Computers and Geotechnics* 27(1): 1–17.

Cho, N., Martin, C.D. & Sego, D.C. 2007. A clumped particle model for rock. *International Journal of Rock Mechanics & Mining Sciences* 44(7): 997–1010.

Christian, E., Robert, S. & Peter, E. 2011. A discrete element model to describe failure of strong rock in uniaxial compression. *Granular Matter* 13(4): 341–364.

Cundall, P.A. 1971. A computer rock model for simulating progressive large scale movements in blocky rock systems. *In Proc. Int. Symp. on Rock Fracture (ISRM)*: vol. 1, 11–8. France: Nancy.

Cundall, P.A. & Strack, O.D.L. 1979. A discrete element model for granular assemblies. *Geotechnique* 29(1): 47–65.

Delenne, J.Y., Youssoufi, M.S.E., Cherblanc, F. & Benet, J.C. 2004. Mechanical behaviors and failure of cohesive granular materials. *International Journal for Numerical and Analytical Methods in Geomechanics* 28(15): 1577–1594.

Jiang, M.J., Harris, D. & Yu, H.S. 2005. Kinematic models for non-coaxial granular materials: part II: evaluation. *International Journal for Numerical and Analytical Methods in Geomechanics* 29(7): 663–689.

Jiang, M.J., Konrad, J.M. & Leroueil, S. 2003. An efficient technique for generating homogeneous specimens for DEM studies. *Computers and Geotechnics* 30(7): 579–597.

Jiang, M.J., Sun, Y.G., Li, L.Q. & Zhu, H.H. 2012a. Contact behavior of idealized granules bonded in two different interparticle distances: An experimental investigation. *Mechanics of Materials* 55: 1–15.

Jiang, M.J., Sun, Y.G., Xiao, Y. 2012b. An experimental investigation on the mechanical behavior between cemented granule. *Geotechnical Testing Journal* 35(5): 678–690.

Jiang, M.J., Yu, H.S. & Harris, D. 2006. Bonds rolling resistance and its effect on yielding of bonded granulates by DEM analyses. *International Journal of Numerical and Analytical Methods in Geomechanics* 30(8): 723–761.

Lan, H., Martin, C.D., & Hu, B. 2010. Effect of heterogeneity of brittle rock on micromechanical extensile behavior during compression loading. *Journal of Geophysical Research* 115(B01202): 1–14.

Martin, C.D. 1993. *The strength of massive Lac du Bonnet granite around underground openings*. Canada: National Library of Canada.

Martin, C.D. & Chandler, N.A. 1994. The progressive failure of Lac du Bonnet granite. *International Journal of Rock Mechanics and Mining Sciences & Geomechanics Abstracts* 31(6): 643–659.

Potyondy, D.O. & Cundall, P.A. 2004. A bonded-particle model for rock. *International Journal of Rock Mechanics & Mining Sciences* 41(8): 1329–1364.

Thornton, C. 2000. Numerical simulation of deviatoric shear deformation of granular media. *Géotechnique* 50(1): 43–53.

Wang, Y. & Tonon, F. 2009. Modeling Lac du Bonnet granite using discrete element model. *International Journal of Rock Mechanics & Mining Sciences* 46(7): 1124–1135.

Geotechnical Safety and Risk IV – Zhang et al. (eds)
© 2014 Taylor & Francis Group, London, ISBN 978-1-138-00163-3

Study on cracking risk of Jinping high and steep slope

P. Lin & X.L. Liu
State Key Laboratory of Hydroscience and Engineering, Tsinghua University, Beijing, China

ABSTRACT: By employ physical experiment and numerical simulation, this study focusses on cracking risk, the cracking stability and the reinforcement effectiveness of the high and steep left hand bank of the Jinping dam. The study results relating to the major slope at Jinping showed that: (1) The bending and toppling cracks in the unreinforced zone of the slope as well as strong relaxation and tension cracks were extended simultaneously. The rock cracking and slope failure controlling factors could be directly seen in the structurally weak rock mass. (2) The controlling failure mode for the Jinping steep and high left bank slope consists of the integral catastrophic instability mode, whereby the slope energy is totally dissipated and the slope destabilizes at a limit state. The slope cracking factor of safety and the integral stability factor of safety satisfy the stability requirements. (3) The reinforcement has been effective in keeping cracks closed in the rock, maintaining the slope stability, and increasing the slope's inherent safety factor.

1 INTRODUCTION

Slope cracking, failures occur throughout the world and contribute to economic losses and casualties. The impact of slope failures is often undervalued. Every year, the United States experiences more than $1 billion in damage and approximately 50 deaths (David 2008); worldwide, slope failures cause hundreds of billions of dollars in damage and hundreds of thousands of deaths. The Vajont reservoir slope failure disaster (Kiersch 1964), as a result a wave over topped the dam by 250 m and swept onto the valley below, with the loss of approximately 2500 lives. Many slope failures have occurred during the abutment excavation process for dams related to hydroelectric projects in China (Huang 2008). For example, the Jinlongshan landslide at the Ertan reservoir; the downstream slope failure at the Lijiaxia arch dam. The abundance of such socioeconomic losses justifies the necessary allocation of funds for slope stability research. A series of super-high arch dams, such as Jinping, Xiaowan, Xiluodu, Laxiwa et al, are being built in the alpine-gorge areas of China (Lin et al. 2011). A question which frequently arises in hydraulic engineering discussions on slope stability is how high and how steep can an excavated rock slope be (Wang et al. 2007, Pan & He 1998). How to evaluate the cracking and stability risk of a major slope after excavation for abutments has so far been a key dam design and foundation treatment issue. Poorly conducted excavation not only delays construction but also causes secondary rock mass cracking and slope failure due to the unloading of the rock mass. Such activity constitutes a hidden danger to the safety of the dam.

The Jinping hydropower station is located at a sharp bend in the Yalongjiang River at Jinping, in the middle reaches, in Sichuan province, P.R. China. The slope of the left hand bank at the Pusiluogou dam site is steep and over 1000 m high. The slope consists of relatively hard marble between El. 1900 m and El. 1690 m and relatively weak sandy slate between El. 1900 m and El. 2300 m. The maximum height of excavation at the slope reaches 200~300 m. The faults f5, f8, f42-9, SL44-1 and lamprophyre X are well developed, as seen in Figure 1. The deep fractures in the rock are especially disadvantageous to the stability of the left bank slope at the dam site, as their strikes are distributed parallel to the slope, and the steep slope is already loosened and significantly splayed. The fault f5, fault f8 lamprophyre X are relatively longer and wider being poor in property. SL44-1 is a deep tensile crack at the upstream boundary. The fault f42-9 is at the downstream boundary (bottom slide face), with lamprophyre X as the internal sliding face. These faults may produce a wedge failure mode, which controls the deformation and stability of the abutment slope.

In this study, the cracking, stability and reinforcement of the slope at the left hand abutment was analysed using the new geomechanism model test method and numerical method. The comparison of the numerical simulations and the experimental observations was carried out.

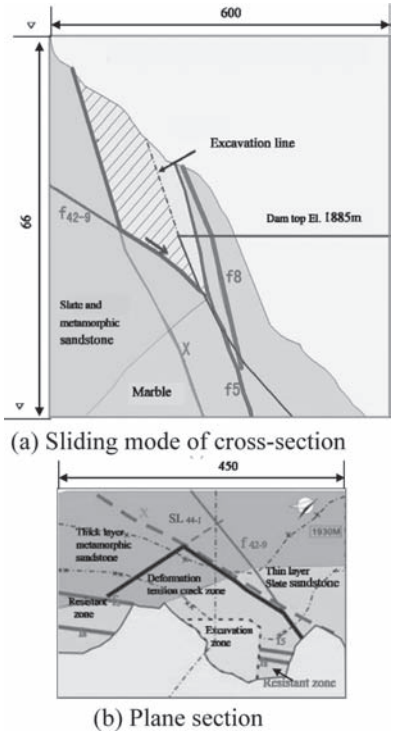

Figure 1. Schematic failure mode and simulated range of left bank slope (Unit: m).

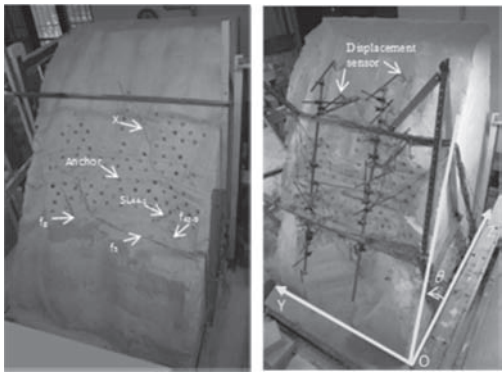

Figure 2. Schematic diagram of slope test assembly.

2 STUDY METHODS AND MODEL

2.1 *Experimental method and model*

The physical experiments were performed at the State Key Laboratory of Hydroscience and Hydraulic Engineering at Tsinghua University. It consists of a rotational structure system, a deformation monitoring, cracking and data collection system and an analysis system (Zhou 2008). The slope model is built on a rotating support system, and can be rotated to any angle of θ around the axis OY by hydraulic lift (as shown in Fig. 2). Rotation of the test platform at a velocity of 0.5°/min. When the angle reaches 5°, the excavation of the abutment groove in the model and recording of the slope deformation of every measuring point is then conducted. The testing platform is continually rotated at a velocity of 0.5°/min, until the cracks are initiated on the slope, and then coalescence is propagated until ultimate failure occurs.

The simulation scale and faults are shown in Figure 1. The model range extends 180 m upstream, 270 m downstream, and is 600 m wide, taking in left bank. The simulated elevations and heights are 1600~2250 m and 660 m, respectively, and sufficient to include the simulation of weak structure planes, lamprophyre fault veins and the deep fractures in the left hand abutment and similarity of boundary constraints. The Jinping slope geomechanical model was built by laying gypsum briquettes on to a test bed made of tamped barite powder and bentonite. The mechanical parameters of the rock mass, its faults and weak structural planes at the Jinping site are shown in Table 1. In this study, a small block masonry technique was employed for the manufacture of the Jinping slope model. As both the material and model tests are performed in a normal environment, the effect of temperature change to glue's strength is not considered.

2.2 *Numerical method and model*

FEM (Finite Element Method) was used to simulate the stability of the high and steep left hand bank of the Jinping dam in this paper. Generally, strength reduction FEM is often applied to analyze the slope stability numerically recent years. But the strength reduction FEM is not suitable to compare with the physical experiments because it is not easy to operate experiments with reduced material properties or parameters. In order to compare the numerical modeling method with the physical experiments, the same technique is used in numerical model, just like what had been done in physical modeling. That is, rotating the numerical model to some angle and calculating the stress condition of the whole model until slip surfaces occur.

Also the following equation is utilized to calculate the slope stability factor. This traditional method can be used to compare with the method developed in this paper.

$$K = \frac{F_{anti\text{-}sliding}}{F_{sliding}} \tag{1}$$

Table 1. Mechanical parameters of rock mass main faults.

Name	Width		E_0 (Mpa)		f		C (Mpa)	
	Prototype (m)	Model (cm)	Prototype $\times 10^3$	Model	Prototype	Model	Prototype	Model
II			23~31	100	1.35	1.35	2	0.007
III1			9.2~14.6	49	1.07	1.07	1.5	0.005
III2			6.4~10.2	34	1.02	1.02	0.9	0.003
IV1			2.56~1.64	9	0.7	0.7	0.6	0.002
IV2			1.4~2.4	8	0.6	0.6	0.4	0.0013
V			0.37~0.82	2.7	0.3	0.3	0.02	0
Fresh X	3.0	1.0	6.5	22	0.8~1.0	0.9	0.64	0.002
Weathered X			3.0	10	0.55~0.65	0.6	0.45	0.0015
f_5	1.0	0.33	0.4	1.4	0.3	0.3	0.02	0
	6.0	2.0	0.4	1.4	0.3	0.3	0.02	0
f_2	0.5	0.17	0.4	1.4	0.3	0.3	0.02	0
F_1	6.0	2.0	0.4	1.4	0.3	0.3	0.02	0
Compressive zone	0.3	0.1	0.4	1.4	0.3	0.3	0.02	0
SL44-1	10–15	4	2	6.7	0.45	0.45	0.1	0.0003
f42-9	0.3–1.0	0.24	0.4	1.4	0.3	0.3	0.02	0

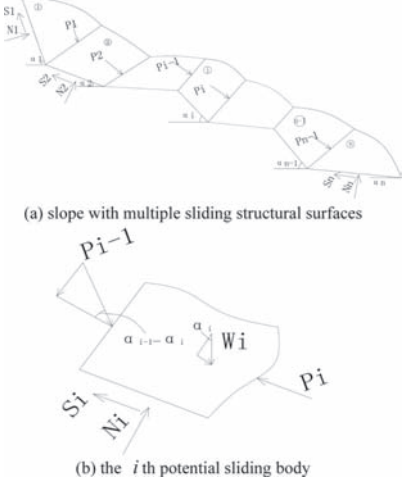

Figure 3. Slope with multiple sliding structural surfaces and the stress analysis of the *i*th potential sliding body.

where, $F_{anti\text{-}sliding}$ and $F_{sliding}$ denote the anti-sliding force and the sliding force, respectively. For a slope with multiple structural surfaces (shown in Fig. 3), the stability factor of the *i*th potential sliding body is described by the following equation

$$K' = \frac{(c_i F_i + f_i N_i) + P_i}{P_{i-1}\cos(\alpha_i - \alpha_{i-1}) + W_i \sin\alpha_i} = \frac{[c_i F_i + f_i(W_i \cos\alpha_i + P_{i-1}\sin(\alpha_{i-1} - \alpha_i))] + P_i}{P_{i-1}\cos(\alpha_i - \alpha_{i-1}) + W_i \sin\alpha_i} \quad (2)$$

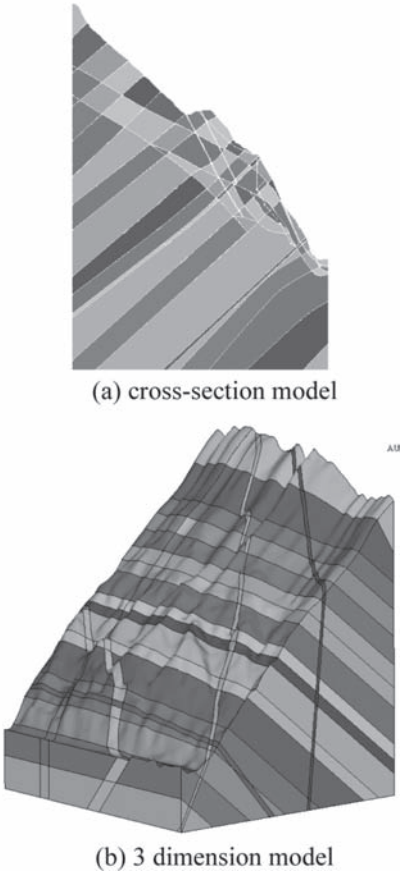

Figure 4. Numerical model of Jinping left bank slope.

where α_i denotes dip of the ith structural surface. The numerical model is shown in Figure 4.

3 THE CRACKING RISK ANALYSIS

3.1 *Experimental results*

In the experiment, the first step was to simulate excavation for the dam abutment. The excavation of the dam foundation slot was undertaken at a model rotation angle of 5 degrees. Cracking patterns and images upstream and downstream of the dam are shown in Figures 5 and 6. As shown in Fiures 5 and 6, cracking first appears along the faults and jointed rock masses above elevation 1960 m and below elevation 1885 m in those unreinforced areas upstream. When the rotation angle reaches 28°, fractures initiate, propagate and

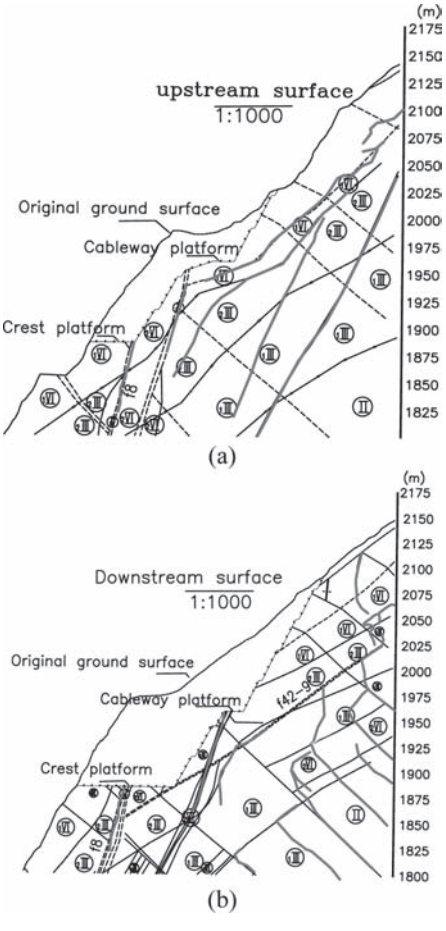

Figure 5. Schematic diagram of cracking of the up-downstream surface of slope model (red lines represent cracking).

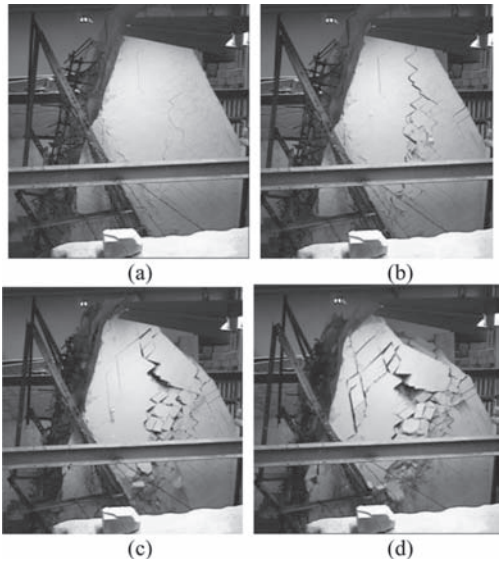

Figure 6. Crack initiation, propagation and slope failure process (view from downstream surface).

cause the slope to suddenly collapse. The fractures mainly occur in the trailing edges of reinforced zones. In the abutment slot and at the mountain top where there is no reinforcement, sliding occurs along fault lines f5. Upstream and downstream slide surfaces in two directions caused by faults SL44-1 and f42-9 and rock mass were observed (see Fig. 5b). The detailed slope failure processes are summarized below.

When the slope angle is 5 degrees, no cracking is seen. Then, during excavation of the abutment slot, no significant cracking occurs, but local cracks appear in those blocks intersected by faults f42-9 and SL44-1. When the slope angle is about 18 degree, fractures occur along fault lines and joints up and downstream of the abutment slot, where there is no reinforcement above elevation 1960 m and below elevation 1885 m (see Fig. 6a). These cracks propagate along a structurally weak plane, and at the boundary between rock masses of grade IV and grade III2, as shown in Figure 6a. They propagate downstream along strata aligned in the opposite direction and structurally weak planes, as shown in Figure 6b.

When the slope angle is between 25 and 28 degrees, multiple cracks occur in lamprophyre X in the downstream abutment slot. It then occurs along fault f5 at upstream abutment slot. Slip then occurs below EL 1885, i.e. the triangle cut by faults f42-9, and SL44-1, and ultimately it occurs along lamprophyre X and rock mass joints. When the slope angle exceeds 28°, toppling failure occurs

quickly with great release of energy. The model blocks were crushed, accompanied by a loud failure noise, as shown in Fig. 6d.

3.2 *Numerical results*

By numerical modeling, the crack initiation, propagation and slope failure process are analyzed. Figures 7 and 8 show the slide faces occur gradually when the numerical model is rotated.

The experimental and numerical results show that The bending and toppling cracks in the unreinforced zone of the slope as well as strong relaxation and tension cracks were extended simultaneously. The rock cracking and slope failure controlling factors could be directly seen in the structurally weak rock mass. The shear hole and anchor cable reinforcement system, meets the standard overall slope safety factor requirements, allowing also for losses over time to anchorage resisting forces and to initially applied prestress.

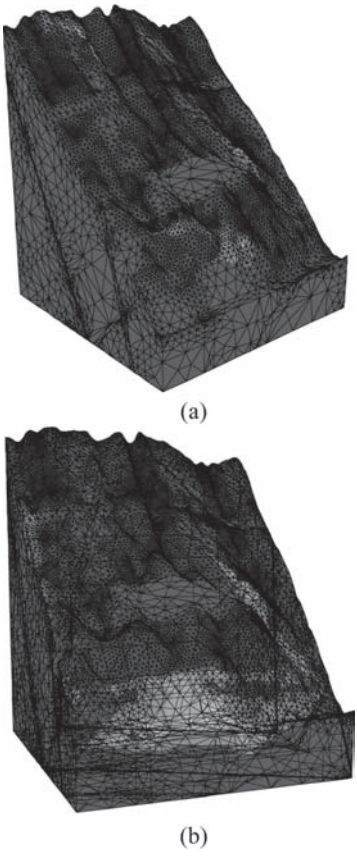

Figure 7. Crack initiation, propagation and slope failure process by 3 dimension numerical modeling.

Figure 8. Slope failure modes in different cross sections by numerical modeling.

Based on the information gained the most likely failure mode of the left hand slope above the cable machine platform is the overall slide, mainly caused by the large blocks lamprophyre X, the faults f42-9 and the deep fissures SL44-1. The test results show that the shear hole and anchor cable reinforcement systems enable the overall slope stability safety

factor to meet the standard requirements allowing for some anchorage slippage and some loss of prestress over time.

The field monitoring results indicate that the stability of the abutment has been effectively attained and the adjacent slope is stable due to the reinforcement applied. The slope deformations have settled to negligible amounts with no further significant degree of deformation at levels below 1885 m. Further slow rates of deformation were still observed after completion of the excavation of the topping slope above 1885 m elevation. Nevertheless the rate of deformation is slowing down appropriately, and converging upon an ultimate steady state.

4 CONCLUSIONS

An experimental and numerical cracking, collapse study of the Jinping Dam left hand steep and high slope adjacent to the abutment has been successfully carried out, and the following conclusions can be drawn

1. The controlling failure mode for the Jinping high left bank slope is one of overall catastrophic instability whereby the slope energy is dissipated totally and the slope destabilizes at the ultimate limit state.
2. Large areas reingforced at the abutment upper elevations to counter the unloading actions due to the excavation of rock laid above the dam platform have effectively improved the safety factor against sliding, and thus have increased overall safety factor of the slope. Deformations of this slope are converging gradually to an approximate steady state.
3. The study results show that the shear hole and anchor cable reinforcement system, meets the standard overall slope safety factor requirements, allowing also for losses over time to anchorage resisting forces and to initially applied prestress.

ACKNOWLEDGEMENTS

This research work was supported by National Basic Research Program of China (973 Program) Grant No. 2011CB013503, National Natural Science Foundation of China (No: 11272178), and Special Foundation for public welfare industry of the Ministry of Water Resources (2010001035). Special thanks to Prof. Zhou W.Y. and Yang R.Q. for experimental support.

REFERENCES

Chen, Z.Y. 2003. *Principles method and program of soil slope stability analysis*. Beijing: China Water Power Press.

David, W. 2006. *Innovative solutions for slope stability reinforcement and characterization*. Research report of PGA Iowa State University.

Huang, R.Q. 2008. Geodynamical process and stability control of high rock slope development. *Chinese Journal of Rock Mechanics and Engineering* 27(8): 1525–1544.

Kiersch, G.A. 1964. Vaiont reservoir disaster. *Civil Engineering* 34: 32–39.

Lin, P., Wang, R.K., Kang, S.Z., Zhang, H.C. & Zhou, W.Y. 2011. Study on key problems of foundation failure, reinforcement and stability for super high arch dams. *Chinese Journal of Rock Mechanics and Engineering* 30(10): 1945–1958.

Liu, X.L., Wang, E.Z., Han, G.F. & Wang, S.Y. 2012. Discontinuous deformation analysis for the slope stability in Jinping First Stage Hydropower Station, Southwestern China. *Disaster Advances* 5(4): 1481–1485.

Pan, H.Y., He, J.D. & Zhang, L. 1998. Application of material strength reserve method to the analysis of stability of high rock slope. *Chinese Journal of Sichuan Union University* 2(1): 13–18.

Tan, X.L., Xu, W.Y. & Liang, G.L. 2009. Application of extenics method to comprehensive safety evaluation of rock slope. *Chinese Journal of Rock Mechanics and Engineering* 28(12): 2503–2509.

Wang, R.K., Lin, P. & Zhou, W.Y. 2007. Cracking and stability problems of high arch dams on complicated rock foundations. *Chinese Journal of Rock Mechanics and Engineering* 26(10): 1951–1958.

Zheng, Y.Z. & Zhao, S.Y. 2006. Discussion on safety factors of slope and landslide engineering design. *Chinese Journal of Rock Mechanics and Engineering* 25(9): 1933–1940.

Zhou, W.Y., Lin, P., Yang, Q., Yang, R.Q. & Zhou, Z. 2008. Experimental research on stability of Jinping high slope with three-dimensional geomechanical model. *Chinese Journal of Rock Mechanics and Engineering* 27(5): 893–901.

Geotechnical Safety and Risk IV – Zhang et al. (eds)
© 2014 Taylor & Francis Group, London, ISBN 978-1-138-00163-3

Mechanism and numerical simulation on geological mechanical model test

X.Q. Luo, J.F. Bi & H. Shen
School of Naval Architecture, Ocean and Civil Engineering, Shanghai Jiaotong University, Shanghai, China

ABSTRACT: Reference to the principle of employing centrifugal force field to simulate gravity field, the geomechanics magnetic model test is a new test method that simulates gravity field with electromagnetic force field to study geomechanical engineering problems. Using electromagnetic method generates a magnetic field where the magnetic flux density gradient keeps a fixed nonzero value, where the mixture of ferromagnetic material and geological mechanics prototype material can get a uniform electromagnetic force. The FEM software for 3D electromagnetic field numerical simulation is used to study the influence of the electromagnetic parameters and magnetic factors to the magnetic field intensity, which provides reasonable design parameters for the production of the experimental machine. The results of simulation indicate that the geomechanics magnetic model method can effectively compensate for the landslide weight loss caused by the reduced-scale and nicely reflect the characteristics of the deformation and failure.

1 INTRODUCTION

At the beginning of the 20th century, some countries started on structural model test research, and gradually established the similarity theory. In the 1960s, experts, led by Fumagalli (1979), carried on the groundbreaking engineering geology mechanical model test research in Italy structural model test research institute. Ashby (1971) qualitatively studied the dumping slope failure mechanism and its process by adopting tilt table model technology. Soon afterwards, in Portugal, the former Soviet union, France, Germany, Britain, the United States, Japan and other countries, scholars also developed model test researches (Stewart et al. 1994, Baumgargarter & Stimpson 1979, Bray & Goodman 1981), which also get rapid and extensive development in China (Chen 1984, Shen 2001, Luo 2005). Conventional model test is a simulation test which is taken in the 1*g* gravitational field and reduces the prototype size *n* times according to the geometric similarity. However, in reality it is difficult to convert gravity stress level into 1/*n* times of prototype by no change of its physical and mechanical properties. So the test can only partly meet the geometric and mechanics similarity between the physical model and prototype, and cannot fully reflect the global deformation and failure characteristics of prototype. Although conventional model test gained great success in brittle materials (like concrete and rock) simulation test and soil (especially in soft soil) destruction test, there are a lot of difficulties in soft soil elastic-plastic model test and permeability model test considering the role of water medium. In ordinary gravitational field, the model test scale is limited, and the stress level at each point is still lower than prototype, as well as the soil stress-strain relationship, especially nonlinear relationship, in the model cannot get true embodiment, so that the reliability of the test results mainly depends on the similarity of the similar material and the dependability of the data acquisition. Domestic and foreign research results show that although the model test technology has gained greater development, due to the hardness on obtaining the similarity material of soft granular media corresponding to similarity theorem, the development of geomechanics model test technology has been severely restricted (Fumagalli 1979).

In order to overcome the geomechanics model test for the presence of these defects, in the sixties and seventies of the 20th century geotechnical centrifuge model test method has been widely used in the world, carry out a large amount of studies around the soft soil engineering, and get fruitful results (Bao 1991, Pu 1996). Geotechnical centrifuge model test is based on the principle of simulating gravity field by centrifugal force field. The centrifugal force applied to the model can make the volume-weight of the model larger, so that each point stress in the model can keep consistent with the prototype. This feature results in essential difference between the centrifugal model test and the conventional model test. At present centrifuge model test technology can improve the acceleration of the model to 400 *g* level or

higher. Prototype soil by appropriate treatment and similar material can be used for experimental research. Because *n g* simulated gravity field can be obtained in the centrifuge model tests, the requirements for the mechanical properties of the material greatly reduced compared to the conventional model test, so there is a qualitative leap in reducing the difficulty of the test and improving the reliability of the test results (Zhang & Dou 1995, Bao & Rao 1998). However, geotechnical centrifuge model test also exist some defects. First, the centrifugal inertia force field and gravitational field cannot be completely similar. The centrifugal force field is proportional to the radius of inertia, so that the acceleration, the magnitude and direction, of each point on the model is different and changing, which make the centrifugal model test cannot obtain a uniform force field. So there are some differences with the actual engineering. Secondly, the generated Coriolis acceleration in the feeding process also causes centrifugal model error. Finally, the irregular change of the stress state caused by the centrifuge accelerating and braking is also one of the problems existing in centrifuge model test method. The process of enhancing and reducing the speed of rotation will take some time, which is also not consistent with the engineering practice and causes some impact on the reliability of the test results.

The two above model test methods have achieved tremendous development, but still have some shortcomings. Centrifuge model test with the idea of using the "centrifugal force field" to simulate "gravitational field" represents the development direction of the model test. At present, the new patterns of geomechanics model test research are mainly concentrated in the "field" simulation. Tsinghua University used to investigate the drag force produced by the seepage force to increase the bulk density of the soil (Ding et al. 1994, Fang et al. 1997, Huang & Wang 1998). The principle is to use the superposition of "gravitational field" and "seepage force field" to simulate the "gravitational field", and obtained some positive results. But this method requires that the object of study must be saturated body, the permeability coefficient must reach a certain degree, and free boundary must also be plane. However, the use of "external force field" to simulate "gravity field" provides a direction for the development of the geomechanics model test theory. The core idea of the geomechanics magnetic model test is to use the similarity of the "magnetic field" and the "gravitational field", mix the particulate magnetic material in the rock-soil body to get *n g* "gravitational field" by the "magnetic field". If considering alternating electromagnetic field, we can also get *+n g* or *–n g* simulated gravitational field, making the simulation of dynamic loading easier and more convenient (Luo 2009a, b, Luo 2011). This idea is the further development of the field similarity theory of the centrifuge model tests.

The geomechanics magnetic model test is a new test method, which not only can be compared with the conventional geomechanics model test and the geotechnical centrifuge model test, but also can overcome the inherent shortcomings and deficiencies to establish a comprehensive test theory. There is a broad application prospect in structural deformation and its stability study of hydraulic engineering, civil engineering, traffic engineering, marine engineering and other areas.

2 BASIC PRINCIPLES OF GEOMECHANICS MAGNETIC MODEL TEST

The geomechanics magnetic model test is an entirely new geomechanics model test method established by using electromagnetic force to simulate gravity, and electromagnetic force field to simulate the gravitational field. The test similarity criteria can be derived based on the three basic principles of the similarity theory (Chen 1979, Chen 1980). Using the dimensional analysis and equation derivation can obtain the similarity criterion of each parameter for: $\phi^* = \epsilon^* = \mu^* = 1$, $p^* = \sigma^* = 1$, $\rho^* = 1$, $k^* = v^* = q^* = 1$, $t^* = 1$, $l^* = u^* = 1$, $g^* = 1/n$. In the model, the time t and geometric dimension l are reduced n times, the gravitational acceleration g expanded n times, while the similar ratios of other physical and mechanical parameters ($E, \mu, c, \phi, \epsilon, \sigma, k, v, q, p$) of the material are 1. If we can provide the conditions to expand g n times of the model material, we can carry out the model test by using prototype material or similar material after appropriate processing; thereby reduce the difficulty of the model test.

Magnetic material will be subjected to magnetic force in a non-uniform magnetic field. Let m stand for the mass of the magnetic substance, M_s for the saturation magnetization intensity, σ_s for the saturation magnetization intensity of unit mass, V for volume, and B for the magnetic flux density of the magnetic field, then the force for an arbitrary axial α (i.e. x, y, z) in a non-uniform magnetic field is

$$F_\alpha = M_s V \frac{\partial B}{\partial \alpha} \quad \text{or} \quad F_\alpha = \sigma_s m \frac{\partial B}{\partial \alpha} \tag{1}$$

When the magnetic force, F_α, of m (kg) material which has been magnetized to M_s in the magnetic field equals to n times of the gravity, we can get

$$F_\alpha = nmg \Leftrightarrow \frac{\partial B}{\partial \alpha} = ng \cdot \frac{m}{V} \cdot \frac{1}{M_s} \tag{2}$$

Clearly, if required F_α to be a fixed value of n times the gravity, the magnetic field gradient required to satisfy the equation (2). That is to say, the magnetic flux density B should linearly change along α direction.

As for iron powder, its saturation magnetization intensity M_s is 1703×10^3 A/m^2 under normal temperature, and density is 7800 kg/m^3. Substituting into formula (2), then:

$$\frac{\partial B}{\partial \alpha} = n \times 0.044 \left(\mathrm{T} \cdot \mathrm{m}^{-1}\right) \tag{3}$$

So if it is wanted to make iron powder be subjected to the magnetic force, n times of gravity, and the magnetic flux density gradient should be $n \times 0.044$ T/m.

Theoretically, the magnetic force F_α should be a linear relationship with $\partial B/\partial \alpha$ when the material is magnetized to saturation intensity. Increasing the value of the magnetic field gradient, the magnetic force will increase with it, and the simulated stratum stress level is also higher.

The purpose of loading or overloading can be achieved by increasing the current to enhance $\partial B/\partial \alpha$ (α axial) value, which can give the stability evaluation of the slope and dam foundation structure. As well as, by fixing the $\partial B/\partial \alpha$ (α axial) value of gradient magnetic field test area, we can research the deformation and failure mechanism of slope and dam foundation under the action of water load or excavation load.

3 IMPLEMENTATION OF UNIFORM GRADIENT MAGNETIC FIELD FOR GEOMECHANICS MAGNETIC MODEL TEST

In other to get the uniform magnetic flux density gradient magnetic field and meet the requirement of the test space, two electricity solenoids are employed with radius of 0.5 m and height of 1 m. The test equipment sketch is shown in Figure 1, and set the underside elevation 0 for convenient. In the middle of two solenoids is 1 m height test area. The coil turns of the two solenoids are same, and the current is in the same direction. The magnetic field distribution of the test area can be controlled by adjusting the current. Calculated by the finite element software, when the lower coil current is 2 times of the upper part, the magnetic flux density of test area appears obvious gradient. When the magnetic dipole moment produced by the upper coil reaches the level of the ordinary permanent magnet and the current of the lower coil is 5 times of the upper one's, the magnetic flux density gradient of the intermediate 1/3 test area reaches 2.5 T/m.

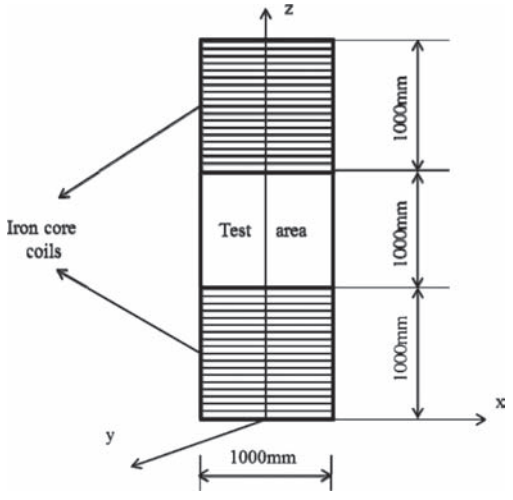

Figure 1. Test equipment sketch.

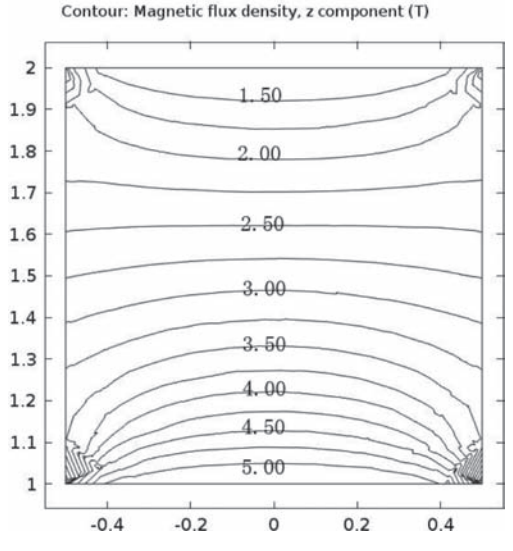

Figure 2. Magnetic flux density of test area.

According to the test need, take the lower coil current 7 times of the upper coil to simulate and analyze. Figure 2 depicts the magnetic flux density distribution of one test area longitudinal profile. The coordinates are the test area space coordinates in m. It shows that the magnetic flux density in the middle region changes uniformly by gradient of 3 T/m–5 T/m.

Magnetic flux density and its gradient along the axis of the cylindrical test area are shown in Figures 3 and 4, respectively. Figure 4 indicates the

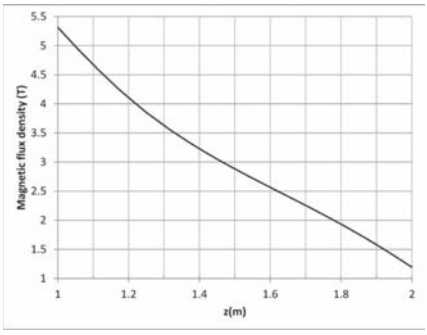

Figure 3. Magnetic flux density on the axis of the test area.

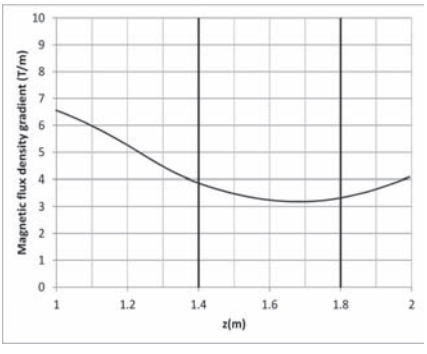

Figure 4. The magnetic flux density gradient on the axis of the test.

magnetic flux density changes greatly at both ends, i.e., the gradient is bigger corresponding to the Figure 4. In the height of 1.4 m–1.8 m, namely the distance from the test area bottom is 0.4 m–0.8 m, the change of magnetic flux density gradient is gentle, between 3.1 T/m–3.7 T/m, where can be taken for the best area for test.

4 NUMERICAL SIMULATION OF GEOMECHANICS MAGNETIC MODEL TEST OF A TYPICAL LANDSLIDE

A three-dimensional slope, on a scale of 1:100, is used for numerical simulation of geomechanics magnetic model. The geomechanics magnetic model will be restored to its original size to analyze the mechanical behavior under the action of its own gravity by finite element method and the results will be compared with the geomechanics magnetic model. According to the similarity theory, the displacement ratio should be 1:100, and stress and strain ratio should be 1:1.

The material parameters are listed in Table 1 and the shrunken model is dimensioned in Figure 5, measured in mm. The parameters of the test model will be the same as the slope body in situ.

Considering the uniformity of the magnetic force on the model, let the central axis of the test area pass through the undersurface centroid of the model. Set the model bottom level to 1.4 m, which can make the model be located in the best test area. Suppose the volume percentage of iron powder is 33.3%, and the soil volume percentage is 66.7%. Mix them well. Let μ_{rFe} donate the relative permeability of iron powder, and μ_{rSoil} donate the relative permeability of soil. The equivalent relative permeability of the mixture can be calculated by the equivalent magnetic resistance. Because of the inappreciable contribution of the μ_{rSoil}, the equivalent relative permeability can be approximately taken as $\mu_{rFe}/3$.

The body force on the mixing-material in the magnetic field equals the sum of its own gravity and the magnetic force. According to the volume percent of iron, the magnitude of the magnetic force is one third of the situation that the material is pure iron powder. The weight of the magnetic model is 776.16 N, which equals the whole volume, 0.044 m^3, times the density, 1800 kg/m^3. Applying the magnetic field shown in Figure 2 on the model, the resultant force can be calculated by using the volume integral of the body force on the model. The magnitude of the resultant force is –79472.4 N, about 102.4 times of gravity. The minus means the force direction is downward.

Figure 6 shows the distribution of the body force. It can be seen the magnetic force on the

Table 1. Material parameters.

Name	Value	Unit
Young's modulus	10e6	Pa
Poisson's ratio	0.3	1
Density	1800	kg/m^3
Cohesion	42e3	Pa
Angle of internal friction	17	Degree

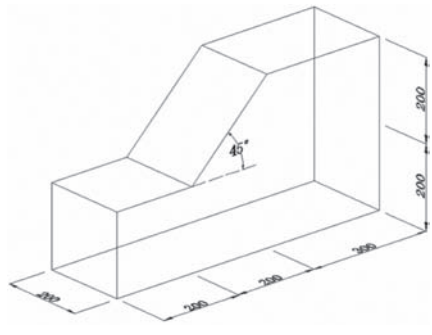

Figure 5. The dimension of slope model.

whole model is between 85 times and 115 times of gravity, as well as the area exceeding 100 times is located in middle and bottom parts, while the upper left and right parts are a little smaller, corresponding to the distribution of the magnetic flux density gradient.

Figures 7–9 are displaying the contrast of displacement, stress, and strain, respectively. Through the contrast of displacement, it can be seen that the ratio on the corresponding position of the magnetic model and prototype is 1:100. Likewise, the ratio of stress and strain is both 1:1. These all coincide with similarity theorem of model test.

The effective plastic strain, calculated based on the Drucker-Prager yield criterion, is located at the slope foot both on the magnetic model and prototype. The maximum effective plastic strain of magnetic model is about 2.5 times of the

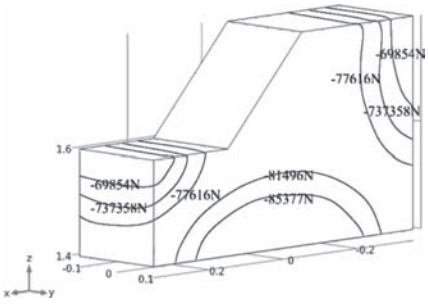

Figure 6. The distribution of body force.

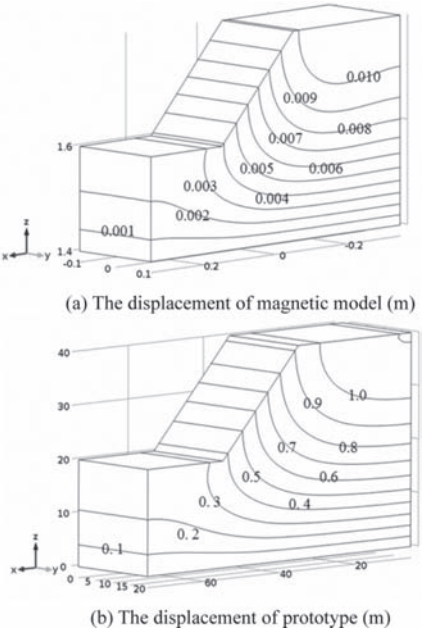

Figure 7. The contrast of displacement.

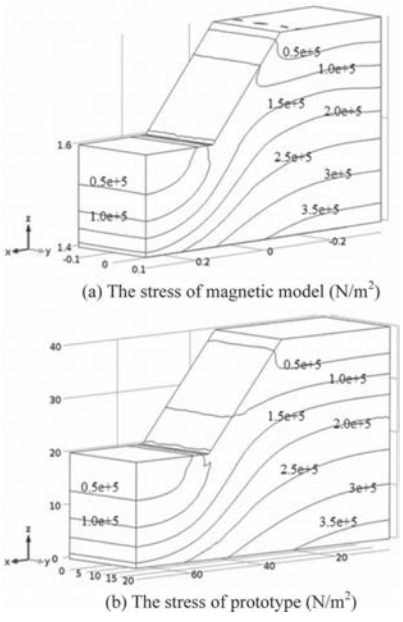

Figure 8. The contrast of stress.

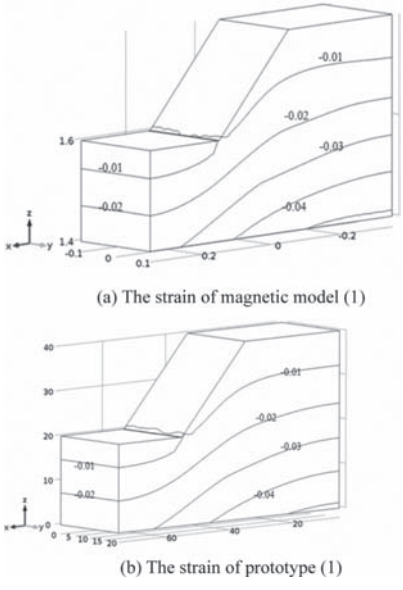

Figure 9. The contrast of strain.

prototype. The difference between the magnitudes of the two models can be blamed on the uneven distribution of the magnetic force and can get reasonable explanation from Figure 6. The magnetic force at the slope body is more than 100 times of gravity, while the ratio at the upper left corner is less than 100. Compared with the prototype, the slope body of magnetic model is in the condition

of overloading while the slope foot is unloading, which is beneficial to the development of plastic strain at the slope foot on the magnetic model.

5 CONCLUSION AND DISCUSSION

Geomechanics magnetic model test exploits the electromagnetic principle to improve the body force of the magnetic material to *n* times of its gravity. The value of *n* can be controlled by adjusting the coil current. Therefore, according to the similarity theory, the prototype can be reduced *n* times to test. It provides a new convenient and simple test mode for model test.

By means of numerical simulation, a magnetic field with high magnetic flux density gradient is produced by two energizing solenoids. The flux density gradient in the middle test area is close to be uniform, although the whole magnetic field is not ideal. The amplitude error of magnetic force on the model is less than 15% of the mean value. The finite element numerical simulation results of the magnetic model and prototype show that their mechanical behavior is similar, and the slight difference mainly comes from the non-uniformity of the magnetic force on the body. Without regard to the change of the material parameters, if the magnetic flux density gradient in the test area keeps spatially homogeneous and temporal stability, the numerical simulation results of magnetic model and prototype should be highly consistent according to the similarity theory.

It is very difficult to get a magnetic field whose magnetic flux density gradient is absolute uniform by experimental method. The best way is to deduce the solenoid parameters theoretically. How to make the magnetic flux density gradient keep uniform still need further study.

REFERENCES

Ashby, J. 1971. *Sliding and toppling modes of failure in model and jointed rock slope* [MS Thesis]. Imperial College Royal School of Mines, London.

Bao, C.G. & Rao, X.B. 1998. Principle of geotechnical centrifuge model test. *Journal of Yangtze River Scientific Research Institute* 15(2): 2–7.

Bao, C.G. 1991. The application and progress of geotechnical centrifuge model test in China. *Chinese Journal of Geotechnical Engineering* 13(6): 92–97.

Baumgargarter, P. & Stimpson, B. 1979. Development of a titable base friction frame for kinematics studies of caving at various depths. *International Journal of Rock Mechanics and Mining Sciences and Geomechanics Abstracts* 1: 265–267.

Bray, J.W. & Goodman, R.E. 1981. The theory of base friction models. *International Journal of Rock Mechanics and Mining Sciences and Geomechanics Abstracts* 18: 453–468.

Bray, J.W., Goodman, R.E., Chen, J.J., Feng, X.B. 1986. Bottom friction model theory. *Opencast Mining Technology* 3: 24–31.

Chen, B.C. 1979. Similarity Theory in Model Test. *Tractor*.

Chen, X.H. 1984. *Structure model test on brittle material*. Beijing: Water Power Press.

Ding, J.L., Tang, Q.M., Gong, Y.M. 1994. Research on saturated soil foundation load character by using water seepage force model. *Chinese Journal of Geotechnical Engineering* 16(1): 8–20.

Fumagalli, E. 1979. *Statical and geomechanical models*. Translated by JIANG Pengnian, PENG Guanglv. Beijing: Water Power Press.

Fang, L., Li, G.X., Huang, F. 1997. A new method of geotechnical model test-geotechnical model test of pile foundation water seepage force. *Geological Journal of China Universities* 3(4): 451–457.

Fumagalli, E. 1968. Model Simulation of Rock Mechanics Problem. Rock Mechanics in Engineering Practice (Stagg, K.G., Zienkiewicz, O.C., eds.). *London: J. Wiley Bulletin Ismes Nr. 38*.

Huang, F., Huang, W.F., Li, G.X., et al. 1998. Study about the resistances of piles in different loading ways by hydraulic gradient test. *Chinese Journal of Geotechnical Engineering* 20(2): 10–14.

Huang, Z.Q. & Wang, S.J. 1998. The application general situation of centrifugal model test in China. *Chinese Journal of Rock Mechanics and Engineering* 17(2): 199–203.

Luo, X.Q., Cheng, S.G., Niu, E.K. 2009a. Research on aberration correction and application in landslide geomechanical model test. *Chinese Journal of Rock Mechanics and Engineering* 28(Supp.1): 3082–3088.

Luo, X.Q., Ge, X.R., Cheng, S.G., et al. 2009b. Study of magnetic material property of geomechanical model test in electromagnet field. *Chinese Journal of Rock Mechanics and Engineering* 28(Supp.2): 3801–3807.

Luo, X.Q., Liu, D.F., Wu, J., et al. 2005. Model test study on landslide under rainfall and reservoir water fluctuation. *Chinese Journal of Rock Mechanics and Engineering* 24(14): 2476–2483.

Luo, X.Q., Cheng, S.G., Zhang, Z.H., Tang, K. 2011. Study of similarity theory of geomechanical model test in electromagnetic field. *Rock and Soil Mechanics* 32(4): 457–462.

Pu, J.L. 1996. The application and development tendency of geotechnical centrifuge model test. *Chinese Journal of Geotechnical Engineering* 18(5): 92–94.

Shen, T. 2001. Progress of geomechanical model test technology. *Journal of Yangtze River Scientific Research Institute* 18(5): 32–36.

Stewart, D.P., Adhikary, D.P. & Jewell R.J. 1994. Study on the stability of model rock slope. *In: Proceedings of the Int. Conf Centrifuge 94, Singapore: 629–634*.

Xia, X.D. 1983. Test technology research on distortion model of soil-mechanical system. *Journal of agricultural machinery* (4): 10–26.

Yu, Y.Z., Li, R.J., Li, G.X., et al. 2008. Experimental study on centrifuge model dynamic behavior of slopes with saturated subgrades during earthquakes. *Journal of Tsinghua University* 48(9): 1422–1425.

Zhang, W.M. & Dou, Y. 1995. Development of geotechnical centrifuge modeling technique. *Hydro-Science and Engineering* (3): 294–301.

Geotechnical Safety and Risk IV – Zhang et al. (eds)
© 2014 Taylor & Francis Group, London, ISBN 978-1-138-00163-3

Time-dependent behaviour modeling of geomaterials using a discrete thermodynamic approach

W. Wang
Key Laboratory of Ministry of Education for Geomechanics and Embankment Engineering, Hohai University, Jiangsu, Nanjing, P.R. China
Geotechnical Research Institute, Hohai University, Jiangsu, Nanjing, P.R. China

J.F. Shao
Key Laboratory of Ministry of Education for Geomechanics and Embankment Engineering, Hohai University, Jiangsu, Nanjing, P.R. China
Geotechnical Research Institute, Hohai University, Jiangsu, Nanjing, P.R. China
Laboratory of Mechanics of Lille, UMR 8107 CNRS, Cité Scientifique, France

Q.Z. Zhu & W.Y. Xu
Key Laboratory of Ministry of Education for Geomechanics and Embankment Engineering, Hohai University, Jiangsu, Nanjing, P.R. China
Geotechnical Research Institute, Hohai University, Jiangsu, Nanjing, P.R. China

ABSTRACT: A discrete thermodynamic approach is presented for the modeling of coupled anisotropic viscoplastic and damage behaviour in cohesive-frictional geomaterials. The idea is to extend the anisotropic coupled elastoplastic damage model to the anisotropic one using a discrete approach. The viscoplastic strain is induced by frictional sliding along weakness planes randomly distributed in the elastic matrix. The evolution of induced damage is controlled by the evolution of weakness planes in connection with the propagation of microcracks. Perzyna's viscoplastic theory is applied to formulate the macroscopic viscoplastic strain. The modified Coulomb-type plastic viscoplastic potential function and damage evolution criterion proposed by Mazars are given for each family of weakness planes. The effective elastic modulus of damaged material is determined by the damage variable associated with each family of weak sliding planes. The proposed model is applied to a typical geomaterial (e.g. sandstone) for the modeling of time-dependent behaviour. The comparison between numerical prediction and experimental data is shown. The validity of the proposed model is verified by the good fitting of strain-time curves obtained by the multi-step triaxial creep tests for sandstones.

1 INTRODUCTION

In rock engineering, time-dependent behaviour of rocks should be taken into consideration for many problems, such as long-term stability analysis of foundations, rock slopes and underground constructions (e.g. tunnels and caverns), feasibility study of nuclear waste disposal, appropriate design and performance assessment prediction of oil and gas storage. Plastic deformation and induced damage by microcracks are two main mechanisms of inelastic deformation and progressive time-dependent failure in geomaterials like concrete and rocks. It is generally accepted that the plastic deformation is mainly related to frictional sliding of microcrack surfaces while the damage evolution is directly related to propagation of these microcracks. It is clear from micromechanical analysis that plastic flow and damage evolution are inherently coupled each other (Zhu et al. 2008a). Classically, continuous phenomenological models have been developed for modelling of plastic deformation and induced damage, either separately or in coupled way (Dragon and Mroz 1979, Ju 1989, Hayakawa & Murakami 1997, Chiarelli et al. 2003, Shao et al. 2006). In such models, scalar and tensorial internal variables are used to represent isotropic and anisotropic spatial distribution of microcracks and plastic hardening variables. However, it is not easy to accurately describe actual distribution of damage and plastic hardening state even with high order tensors. Moreover, the mathematical description becomes very complex when accounting for anisotropic plasticity and damage

coupling and unilateral effects. On the other hand, micromechanical damage models based on fracture mechanics and linear homogenization techniques have also been developed for the description of brittle behaviour of geomaterials (Kachanov 1982, Gambarotta & Lagomarsino1993, Zhu et al. 2008a, b). However, most of these models focused on the modelling of elastic brittle materials. The capability to describe coupled anisotropic plastic damage behaviour in quasi brittle materials is still not well demonstrated.

Concerning time-dependent modeling, the viscoplastic theory is generally used (Lemaitre & Chaboche 1998) and most viscoplastic models for geomaterials are based on the overstress concept proposed by Perzyna (1996). Various specific models have been proposed for rocks (Cristescu 1986, Shao 1995, Maranini & Yamaguchi 2001). Other approaches (Shao et al. 2003, Pietruszczak 2004) have been developed for the description of time-dependent behaviour in rocks. The time-dependent deformation is seen as a consequence of progressive degradation of material due to physical–chemical reactions.

Based on these previous works, we propose in the present study to develop a new thermodynamics discrete approach for modeling coupled visco-plastic damage behaviour in cohesive-frictional geomaterials. The discrete thermodynamic framework for plastic modeling is firstly proposed by Zhu et al. (2008c). It is first assumed that the material contains a random distribution of Weakness Sliding Planes (WSPs) subject to frictional sliding and propagation under applied stresses. A suitable system of orientations is then chosen to discretize the continuous distribution of weakness sliding planes. Each orientation represents one family of weakness planes. Overall (total) plastic strains are obtained by the determination of frictional sliding along each weakness plane. Appropriate yield function, plastic potential, plastic hardening law and damage evolution criterion are determined for each family of weakness planes. The frictional sliding and crack propagation are inherently coupled leading to coupled macroscopic plastic damage behaviour. The effective elastic properties of damaged material can be deduced as functions of discrete damage variable related to each family of weak planes. For the modeling of time-dependent behaviour of sandstone, the elstoplastic model is extended to a viscoplastic one. The viscoplastic strain is induced by frictional sliding along weakness planes randomly distributed in the elastic matrix. Perzyna's viscoplastic theory is applied to formulate the macroscopic viscoplastic strain. The proposed model is applied to a typical quasi brittle rock material (sandstone), and comparisons between numerical simulations and experimental data are presented.

2 PRESENTATION OF THE MODEL

2.1 *Discrete representation of variables*

In the present study, we adopt the discrete thermodynamic framework proposed by Zhu et al. (2008c) and apply this method to the visco-plastic damage modelling. The assumption of small strains and isothermal conditions are adopted in the present work. The total macroscopic strain is first decomposed into an elastic part $\mathbf{E}^e$, a plastic part $\mathbf{E}^p$ and a viscoplastic one $\mathbf{E}^{vp}$:

$$\mathbf{E} = \mathbf{E}^e + \mathbf{E}^p + \mathbf{E}^{vp} \tag{1}$$

In our study, for the sake of simplicity, a simplified specific version of the model is presented for modelling mechanical behaviour of a typical quasi-brittle rock. It is assumed that the material damage may be considered in an average way and as a consequence there is an isotropic distribution of damage in all orientations.

The total free energy function is then simplified as follows:

$$\Psi = \frac{1}{2}\left(\mathbf{E} - \mathbf{E}^p - \mathbf{E}^{vp}\right) : \mathbb{C}(d) : \left(\mathbf{E} - \mathbf{E}^p - \mathbf{E}^{vp}\right) + \Psi^p + \Psi^{vp} \tag{2}$$

The state equations are obtained by the standard derivation of the total free energy Ψ with respect to elastic strain tensor $\mathbf{E}^e \left(= \mathbf{E} - \mathbf{E}^p - \mathbf{E}^{vp}\right)$:

$$\sum = \frac{\partial \Psi}{\partial \mathbf{E}^e} = \mathbb{C}(d) : \left(\mathbf{E} - \mathbf{E}^p - \mathbf{E}^{vp}\right) \tag{3}$$

2.2 *Discrete form of damaged elastic tensor*

In order to formulate discrete plastic damage model in general loading conditions, we first propose to develop a general methodology for projections of stress tensor and other variables onto each family of WSPs. For this purpose, the following two fourth order tensorial operators are introduced, $\mathbb{N}$ and $\mathbb{T}$, both functions of the unit normal vector $\underline{n}$ and with the components, respectively:

$$\begin{aligned} N_{ijkl} &= n_i n_j n_k n_l \\ T_{ijkl} &= \frac{1}{2}\left(\begin{matrix}\delta_{ik} n_j n_l + \delta_{il} n_j n_k + \delta_{jk} n_i n_l \\ + \delta_{jl} n_i n_k - 4 n_i n_j n_k n_l\end{matrix}\right) \end{aligned} \tag{4}$$

Invoking the classic isotropic damage theory, only the shear modulus is affected by damage in

the case of closed cracks. Let $k(d)$ and $\mu(d)$ be the bulk and shear modulus of damaged material, respectively, one can write:

$$k(d) = k^s, \mu(d) = \mu^s(1 - \tilde{\kappa} d) \tag{5}$$

The effective elastic stiffness tensor of damaged material can be written in the following general form:

$$\mathbb{C}(d) = 3k^s \mathbb{J} + 2\mu^s(1 - \tilde{\kappa} d)\mathbb{K} = \mathbb{C}^s - 2\mu^s \tilde{\kappa} d \mathbb{K} \tag{6}$$

In (6), $\mathbb{C}^s$ denotes the initial elastic tensor of undamaged (sound) material. Two fourth order isotropic tensors $\mathbb{J}$ and $\mathbb{K}$ verify the relation: $\mathbb{J} + \mathbb{K} = \mathbb{I}$, with the components:

$$I_{ijkl} = \frac{1}{2}\left(\delta_{ik}\delta_{jl} + \delta_{il}\delta_{jk}\right), \text{ and } J_{ijkl} = \frac{1}{3}\delta_{ij}\delta_{kl} \tag{7}$$

However, in the case of random distribution of weakness sliding planes, the damage state is generally anisotropic in nature due to propagation of microcracks in some preferred orientations. For the description of this anisotropic damage, it is proposed to replace the isotropic damage variable d by a damage distribution function $\omega(\underline{n})$. In addition, it is shown that the fourth order tensor $\mathbb{T}(\underline{n})$ is directly related to the degradation of the shear modulus (Walpole 1981). Thus, the term $d\mathbb{K}$ can be generalized in the following integral form:

$$d\mathbb{K} = \zeta \frac{1}{4\pi} \int_{S^2} \omega(\underline{n}) \mathbb{T}(\underline{n}) \mathrm{d}S$$
$$\int_{S^2} \mathbb{T}(\underline{n}) \mathrm{d}S / 4\pi = 2\mathbb{K}/5 \tag{8}$$

It follows, from the case of isotropic damage distribution, i.e. $\omega(\underline{n}) = d$, that $\zeta = 5/2$. The effective elastic stiffness tensor $\mathbb{C}$ can be rewritten into the form:

$$\mathbb{C}(\omega(\underline{n})) = \mathbb{C}^s - 2\mu^s \kappa \frac{1}{4\pi} \int_{S^2} \omega(\underline{n}) \mathbb{T}(\underline{n}) \mathrm{d}S \tag{9}$$

with $\kappa = 5\tilde{\kappa}/2$, and in discrete form:

$$\mathbb{C}(\omega(\underline{n})) = \mathbb{C}^s - 2\mu^s \frac{\kappa}{15} \sum_{i=1}^{15} \omega^i \mathbb{T}^i$$
$$= 3k^s \mathbb{J} + 2\mu^s \left(\mathbb{I} - \frac{\kappa}{15} \sum_{i=1}^{15} \omega^i \mathbb{T}^i \right) : \mathbb{K} \tag{10}$$

2.3 *Characterization of plastic flow*

Plastic flow is coupled with induced damage in each family of weakness planes. It is assumed that the induced damage is fully responsible for material softening due to propagation of various defeats. Further, as for most geomaterials, a non-associated plastic flow rule is required. In this model, a Coulomb-type plastic yield function including plastic hardening and softening is used. The macroscopic stress tensor Σ is projected on the normal vector to each family of weakness sliding planes using the general projection operators given in (4). The plastic flow in each weakness sliding plane is controlled by the shear and normal stresses applied to this plane. The plastic yield function $f^{p,r}$ is then expressed as:

$$f^{p,r}\left(\sigma_t^r, \sigma_n^r, \gamma^{p,r}, d\right) = \sigma_t^r + (1 - \zeta d)\alpha^{p,r}\left(\sigma_n^r - c\right) \le 0 \tag{11}$$

The parameter c is related to material cohesion. The function $\alpha^{p,r}$ defines the plastic hardening law and depends on the plastic hardening variable $\gamma^{p,r}$. The hardening variable $\gamma^{p,r}$ is expressed as:

$$\gamma^{p,r} = \int \left(\mathrm{d}\underline{\gamma}^r . \mathrm{d}\underline{\gamma}^r \right)^{1/2} \tag{12}$$

which is seen as the cumulated equivalent plastic distortion in weakness sliding planes. Based on experimental data obtained on typical geomaterials, the following particular form is proposed:

$$\alpha^{p,r} = \alpha_f^p - \left(\alpha_f^p - \alpha_o^p\right) e^{-b_1 \gamma^{p,r}} \tag{13}$$

Physically, the hardening function defines the current mobilized frictional coefficient along weakness sliding planes. α_o^p and α_f^p are respectively the initial and asymptotic values of the hardening function. The parameter b_1 controls its kinetics.

In order to define a non-associated plastic flow rule, the following expression is used as plastic potential $g^{p,r}$:

$$g^{p,r}\left(\sigma_t^r, \sigma_n^r, d, \gamma^{p,r}\right) = \sigma_t^r + (1 - \zeta d)\eta^{p,r}\sigma_n^r = 0 \tag{14}$$

In which $\eta^{p,r}$ is a coefficient related to plastic volumetric strain for undamaged material. In order to describe the transition from plastic compressibility to dilatancy observed in geomaterials; $\eta^{p,r}$ is defined as a function of plastic hardening variable $\gamma^{p,r}$ and expressed as follows:

$$\eta^{p,r} = \eta_f^p - \left(\eta_f^p - \eta_o^p\right) e^{-b_2 \gamma^{p,r}} \tag{15}$$

The current value of $\eta^{p,r}$ is usually called as current value of plastic dilatancy coefficient. Therefore, the two parameters η_o^p and η_f^p denote respectively the initial and asymptotic value of dilatancy coefficient.

The plastic flow rule in each family of planes is defined through plastic potential as in classic plasticity:

$$\mathrm{d}\mathbf{E}^{p,r} = \mathrm{d}\lambda^{p,r}\frac{\partial g^{p,r}}{\partial \Sigma} = \mathrm{d}\lambda^{p,r}\left(\overset{s}{\underline{t}^r}\otimes\underline{N}^r + (1-\zeta d)\eta^{p,r}\underline{N}^r\otimes\underline{N}^r\right), \mathrm{d}\lambda^{p,r}\geq 0 \tag{16}$$

On the other hand, one obtains the following relation:

$$\mathrm{d}\mathbf{E}^{p,r} = \mathrm{d}\beta^r\underline{N}^r\otimes\underline{N}^r + \mathrm{d}\underline{\gamma}^r\overset{s}{\otimes}\underline{N}^r \tag{17}$$

The comparison of (16) with (17) gives:

$$\mathrm{d}\underline{\gamma}^r = \mathrm{d}\lambda^{p,r}\underline{t}^r,\ \ \mathrm{d}\beta^r = \mathrm{d}\lambda^{p,r}(1-\zeta d)\eta^{p,r} \tag{18}$$

2.4 *Characterization of damage evolution*

The damage evolution is physically related to propagation of microcracks and defeats in various orientations. Generally, the propagation is not uniform in space orientation. However, an isotropic damage is adopted in this simplified version, and the essential consequence of damage is material softening behaviour due to material degradation. Further, it is assumed that the damage evolution is mainly controlled by plastic sliding along surfaces of microcracks and defeats. Thus, the driving force for damage evolution is taken as the averaged value of equivalent plastic shear strain $\gamma^{p,r}$ such as:

$$\bar{\gamma}^p = \frac{1}{15}\sum_{r=1}^{15}\gamma^{p,r} \tag{19}$$

Inspired by some previous works on damage modelling of geomaterials, an exponential function similar to that used by Mazars (1986) for concrete is used as the damage criterion:

$$f_d = d - d_f\left[1 - e^{-b_3\left(\bar{\gamma}^p - \bar{\gamma}_0^p\right)}\right] \leq 0 \tag{20}$$

The parameter d_f defines the asymptotic value of damage variable related to residual strength of damaged material; $\bar{\gamma}_0^p$ is the initial threshold of damage and b_3 controls the kinetics of damage evolution.

2.5 *Viscoplastic characterization*

The viscoplastic loading surface is considered as the delayed plastic yield surface. The evolutions of instantaneous plastic yield surface and viscoplastic loading surface are related to the same internal variable, for instance, the equivalent plastic shear strain. As the viscoplastic flow is delayed compared with the plastic deformation, the evolution of viscoplastic loading surface is then slower than that of plastic yield surface. However, the both are described by the same mathematical function. Thus, the viscoplastic loading surface for each family of weakness sliding planes is given by:

$$f^{vp,r}\left(\sigma_t^r, \sigma_n^r, \gamma^{p,r}, d\right) = \sigma_t^r + (1-\zeta d)\alpha^{vp,r}\left(\sigma_n^r - c\right) \leq 0 \tag{21}$$

The function $\alpha^{vp,r}$ defines the current internal friction coefficient of the viscoplastic loading surface. Therefore, it controls the evolution of the viscoplastic flow. The expression of hardening function for viscoplastic flow is given by:

$$\alpha^{vp,r} = \alpha_f^p - \left(\alpha_f^p - \alpha_o^p\right)e^{-b_1\gamma^{p,r}} \tag{22}$$

The same function is proposed for the viscoplastic potential:

$$g^{vp,r}\left(\sigma_t^r, \sigma_n^r, d, \gamma^{p,r}\right) = \sigma_t^r + (1-\zeta d)\eta^{p,r}\sigma_n^r = 0 \tag{23}$$

Based on Perzyna's viscoplastic theory (Perzyna, 1996), the viscoplastic flow rule is determined by:

$$\dot{\mathbf{E}}_{vp,r} = \gamma\left\langle\frac{f^{vp,r}}{c}\right\rangle^n\frac{\partial g^{vp,r}}{\partial\sigma} \tag{24}$$

where γ, n are the viscosity coefficients.

2.6 *Parameter identification*

The proposed model contains 16 parameters: two elastic constants for initial (undamaged) state of material, E^s and v^s; four parameters involved in plastic yield function α_m^p, α_o^p, b_1 and c; three parameters in plastic potential η_f^p, η_o^p and b_2; three parameters characterizing the damage evolution d_f, b_3, and $\bar{\gamma}_0^p$; the parameter $\tilde{\kappa}$ for describing the degradation of shear modulus and the parameter ζ for the description of damaged-related material softening, two viscosity parameters γ, n characterizing the time-dependent behaviour.

The initial elastic constants may be determined from the linear part of stress-strain curves before the initiation of plastic yielding and damage evolution. The parameters α_0^p and c are concerned with the initial yield condition and therefore can be determined by drawing up the initial plastic yield surface. Due to the fact that the damage evolution

is coupled to plastic flow and affects both plastic yield function and plastic potential, the explicit determination of all the parameters involved in plastic flow and damage evolution is generally difficult. The method used here is based on a best fitting algorithm using a series of conventional triaxial compression tests performed under different confining pressures. The viscosity parameters are determined by the best fitting method using the triaxial creep tests.

3 NUMERICAL SIMULATION

In this section, the proposed model is applied to the modelling of time-dependent behaviour of sandstone. Note that due to the damage evolution during visco-plastic flow, the material strength reduces with time. As a consequence, if the applied stress state is close to the long-term failure surface, the material failure can be produced by accelerated creep process. The model can predict three stages of creep process. An example of simulation of creep behaviour is shown in Figure 1.

The emphasis here is modelling of time-dependent deformation of sandstone. A series of creep tests under different stress states have been conducted. The purpose is to check the performance of the model in predicting the time-dependent behaviour of sandstone. The samples were cored from intact blocks of sandstones located in the underground cavern of Xiangjiaba hydropower station in the southwest of China. The off-white fine grain rocks are mainly composed of feldspar, quartz and rock debris. The sandstone has an average porosity of 2.64% and dry density of 2.62 g/cm^3. The creep tests were carried out following a multi-step loading procedure. A detailed description of test method and test result can be found in Wang et al. (2009). Based on these tests as well as short-term triaxial compression tests, the typical values of main parameters have been identified and shown in Table 1.

Figure 2 shows the result of simulation of triaxial creep tests on the sandstone under a confining pressure of 3 MPa with six different values of stress deviator. In general, the time-dependent response of material is well predicted by the proposed model. The creep rate is increasing when the stress deviator is higher.

In Figures 3 and 4, a sensitivity study of two main viscoplastic parameters r and n is presented. Here, we simulate a creep test at the first loading under the confining pressure of 5 MPa and with the deviatoric stress of 120 MPa. We can notice the influence of two parameters controlling the viscoplastic deformation r and n, on the long-

Table 1. Parameters of the model for the triaxial creep test of sandstone.

E^s (MPa)	ν^s	α_m^p	α_o^p	b_1	c (MPa)	η_f^p	η_o^p	b_2
23900	0.2	0.7	0.1	1000	6	0.3	0.1	200
d_f	b_3	$\bar{\gamma}_0^p$	$\tilde{\kappa}$	ζ	γ (h^{-1})	n		
1.0	2000	0.0	1.0	1.0	10^{-7}	0.1		

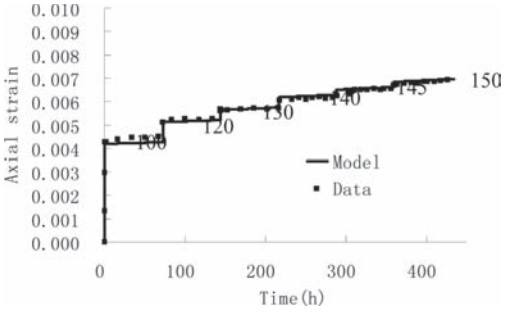

Figure 2. Simulation of a triaxial creep test with six deviatoric stress (the number on the line indicate the deviatoric stress).

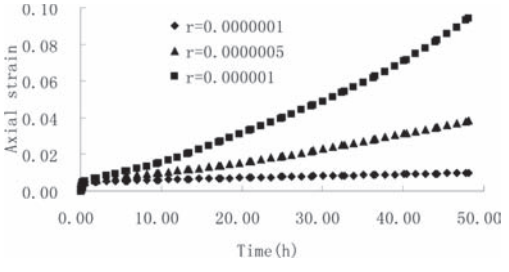

Figure 3. Influence of r on creep deformation of sandstone.

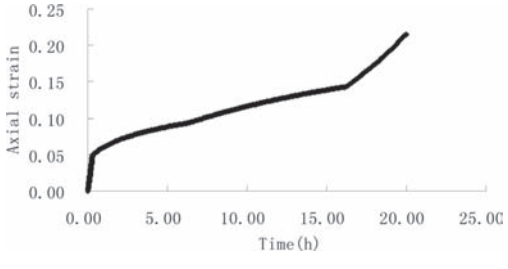

Figure 1. Example of simulation of three stages of creep behaviour of sandstone.

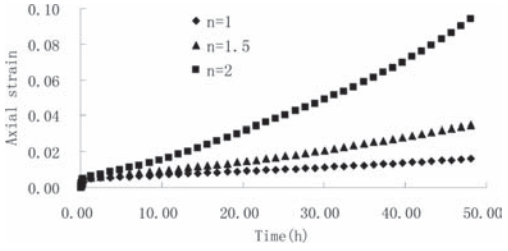

Figure 4. Influence of *n* on creep deformation of sandstone.

term response of sandstone. It seems that *n* has a stronger influence on long-term behaviour than *r*.

4 CONCLUSION

In this study, we propose a discrete approach for visco-plastic damage modelling of cohesive-frictional geomaterials. Compared with classic models, the discrete modelling allows taking into account physical mechanisms involved in viscoplastic deformation and damage evolution. For instance, macroscopic plastic strains in geomaterials are generally generated by frictional sliding along surfaces of microcracks and defeats while damage evolution is associated with the propagation of these weakness sliding planes. Further, using the proposed discrete approach, it is easier to describe induced anisotropy in plastic flow. However, a specific simplified version is proposed by using an isotropic damage description. The elastoplastic damage model can be extended into a viscoplastic model by using the Perzynas viscoplastic theory. Consequently, the time dependent behaviour of sandstone can be described by considering viscous sliding of weakness planes and sub-critical propagation of defeats. A good accord between simulation and test data verify the validity of the model. A further application of the model will be carried out in the future.

ACKNOWLEDGEMENT

This work is supported by National Program on Key Basic Research Project (973 Program) (2011CB013504) and National Science Foundation of China (51109069, 11272114).

REFERENCES

Chiarelli, A.S., Shao, J.F., Hoteit, N. 2003. Modeling of elastoplastic damage behavior of a claystone. *International Journal of Plasticity* 19(1): 23–45.

Cristescu, N. 1986. Damage and failure of viscoplastic rock-like materials. *Int J Plast* 2(2): 189–204.

Dragon, A. & Mroz, Z. 1979. A continuum model for plastic-brittle behaviour of rock and concrete, *International Journal of Engineering Science* 17(2): 121–137.

Hayakawa, K. & Murakami, S. 1997. Thermodynamical modeling of elastic-plastic damage and experimental validation of damage potential, *International Journal of Damage Mechanics* 6(4): 333–363.

Ju, J.W. 1989. On energy based coupled elastoplastic damage theories: constitutive modeling and computational aspects, *International Journal of Solids and Structures* 25(7): 803–833.

Kachanov, M. 1982. A microcrack model of rock inelasticity—Part I: frictional sliding on microcracks; Part II: propagation of microcraks. *Mechanics of Materials* 1: 19–41.

Lemaitre, J. & Chaboche, J.L. 1998. *Mechanics of solid materials*. Cambridge: Cambridge University Press.

Maranini, E. & Yamaguchi, T. 2001. A non-associated viscoplastic model for the behaviour of granite in triaxial *compression. Mechanics of Materials* 33(5): 283–293.

Mazars, J. 1986. A description of micro- and macroscale damage of concrete structures. *International Engineering Fracture Mechanics* 25(5–6): 729–737.

Perzyna, P. 1996. Fundamental problems in viscoplasticity. *Advances in Applied Mechanics* 9: 243–377.

Pietruszczak, S., Lydzba, D., Shao, J.F. 2004. Description of creep in frictional materials in terms of microstructure evolution. *Journal of Engineering Mechanics* 130(6): 681–690.

Shao, J.F., Dahou, A., Bederiat, M. 1995. Experimental and numerical investigations on transient creep of porous chalk. *Mechanics of Materials* 21(2): 147–158.

Shao, J.F., Jia, Y. Kondo, D., Chiarelli, A.S. 2006. A coupled elastoplastic damage model for semi-brittle materials and extension to unsaturated conditions. *Mechanics of Mechanics* 38(3): 218–232.

Shao, J.F., Zhu, Q.Z., Su, K. 2003. Modeling of creep in rock materials in terms of material degradation. *Computers and Geotechnics* 30(7): 549–555.

Walpole, L.J. 1981. Elastic behavior of composite materials: theoretical foundations. *Advances in Applied Mechanics* 21: 169–242.

Wang, W., Xu, W.Y., Li, L.Q., Jiang, Z.Y. Experimental study on the time-dependent behaviour of Xiangjiaba Sandstone. In Erich Bauer (ed.), *Proc. 2nd International Conference on Long Term Behaviour of Dams (LTBD09), 12–13 October 2009*. Graz University of Technology.

Zhu, Q.Z., Kondo, D., Shao, J.F. 2008a. Micromechanical analysis of coupling between anisotropic damage and friction in quasi brittle materials: role of the homogenization scheme. *International Journal of Solids and Structures* 45(5): 1385–1405.

Zhu, Q.Z., Kondo, D., Shao, J.F., Pensee, V. 2008b. Micromechanical modelling of anisotropic damage in brittle rocks and application. *International Journal of Rock Mechanics and Mining Sciences* 45(4): 467–477.

Zhu, Q.Z., Shao, J.F., Kondo, D. 2008c. A discrete thermodynamic approach for modeling anisotropic coupled plasticity-damage behaviour in geomaterials. *Comptes Rendus Mecanique* 336(4): 376–383.

Geotechnical Safety and Risk IV – Zhang et al. (eds)
© 2014 Taylor & Francis Group, London, ISBN 978-1-138-00163-3

Study of time-dependent behavior of rocks with polycrystalline approach

T. Zeng & J.F. Shao
College of Civil and Transportation Engineering, Hohai University, Nanjing, China
University of Lille I, LML, UMR 8107, Cité Scientifique, Villeneuve d'Ascq, France

ABSTRACT: A completely new constitutive model is proposed for describing the viscoplastic behavior of cohesive geological material—granite, which essentially possesses the morphology of granular texture. Based on micromechanics consideration, the local inelastic deformation is attributed to the sliding along specified direction on certain crystallographic (weakness) planes within each granular. The corresponding macro deformation is obtained with the classical homogenization approach. The special features of geomaterial, e.g. pressure sensitivity and plastic dilatancy, are taken into account by introducing Mohr-Coulomb type yield criterion and non-associated plastic potential. Comparisons between model's predictions and test data have been carried out to check the validity of proposed model.

1 INTRODUCTION

In certain practical engineering applications, appropriate constitutive models are necessary to describe mechanical behaviors of various geomaterials (soils, rocks and concretes). Generally, two kinds of models have been proposed to treat this problem, i.e. phenomenological model and micromechanical model. Phenomenological models, generally formulated within the framework of thermodynamics of irreversible processes, have been largely developed and applied. It usually has strong experiment support and is easy to be implemented into commercial finite element software. Therefore, it is suitable for structure analysis. However, such model does not take into account physical mechanisms involved at pertinent material scales. It usually contains high number of empirically based internal state variables, which results in the difficulty of identification process for model's parameters.

In fact, most geomaterials are heterogeneous materials at different scales. From microscopical point of view, they are aggregate with different constituents cemented together. The special microstructures, for instance, pores and interface, play an important role in material's macroscopic responses. Inelastic deformation and failure process of geomaterials are directly related to the evolution of these microstructures. Therefore, the micromechanical model provides a completely new way to explore the properties of geomaterials.

Until now, two kinds of micromechanical model have been proposed and their capabilities have been proved. One kind is microcrack induced damage in brittle geomaterials (Pensée 2002, Zhu et al. 2008). The other one is plastic deformation in ductile porous materials (Shen et al. 2012). For those micromechanical models, the morphology is generally represented by matrix-inclusion system. Such morphology is acceptable only when certain phase is dominate and intact. However, when the texture of geomaterial is discrete and granular, the choice of matrix system may be not that obvious. Therefore, it is necessary to define a more reasonable morphology.

Certainly, the matrix-inclusion system will not be completely abandoned. Each granular (inclusion or grain) is now embedded in a so-called Homogeneous Equivalent Medium (HEM), which is an imaginary medium and its properties equal to the overall response of aggregate. The special features of the morphology here is that the property of HEM is unknown in advance. It is coupled with property of each granular and can be only obtained at the end of calculation through SC (Self-Consistent) method (Hill 1965). However, for the sake of simplicity and as a first stage of development, the KBW model, which is initially proposed by Kröner, Budiansky and Wu (Budiansky 1962), is adopted in this paper. It assumes that the elastic interaction applies not only in elastic range but also in plastic range. Although such simplification will results in too stiff response when plastic deformation is large, it will greatly reduce the numerical work.

The inspirations of my research are from the widely used polycrystal model for metallic materials.

To adopt the polycrystalline model, we made the following assumptions and simplifications. Each granular contains many weakness planes. To consider its distribution, we introduce the conception of crystallography planes in FCC crystal structure. Moreover, the distribution of granular is assumed random and therefore, the response of polycrystal is isotropy. The local inelastic deformation is attributed to the sliding along specified direction on certain crystallographic (weakness) planes. However, due to some special features of geomaterials, the classical Schmid's law and associated plastic potential of each slip system are replaced by a Mohr-Coulomb type criterion and non-associated plastic potential. A general hardening law is adopted to depict the self-hardening and cross-hardening behavior of each slip system.

Throughout this paper, lower case letters represents local fields while capital letters are overall (macroscopic) fields. First order tensor, second order tensor and forth order tensor are denoted as $\underline{a}$, $\underline{\underline{a}}$ and $\mathbb{A}$, respectively. The operations between tensors are as follows: $\underline{a}\cdot\underline{b}=a_ib_i$, $\underline{\underline{a}}:\underline{\underline{b}}=a_{ij}b_{ij}$, $\mathbb{A}:\underline{\underline{b}}=A_{ijkl}b_{kl}$, $\underline{a}\otimes\underline{b}=a_ib_j$.

2 KBW MODEL FOR GEOMATERIAL

2.1 *Scale decomposition*

The polycrystalline model in following study generally decomposed into three different levels: macroscopic (Representative Element Volume (REV)–aggregate of granular or grains), mesoscopic (granular or single crystal), and microscopic (Crystallographic Slip System, CSS), as Figure 1 shows.

2.2 *Grain/matrix interaction law*

Imaging a polycrystalline aggregate subjected to a macroscopic stress or strain, the local stress or stain varies not only from crystal to crystal, but also from point to point within each single crystal. Many methods have been proposed to determine

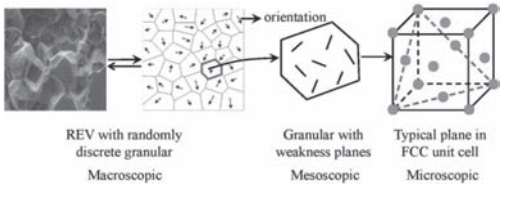

Figure 1. Schematic representations of REV, weakness planes and typical crystallographical plane in FCC unit cell. The microscopic photograph of granite is from (Soulié et al. 2007).

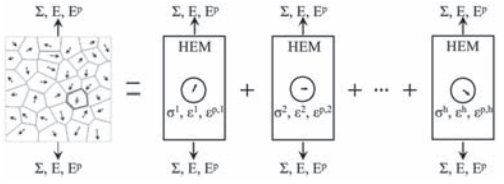

Figure 2. Schematic representation of one-site self-consistent models.

the local values. The most widely used one is the so-called one site self-consistent scheme, as Figure 2 shows. The strain or stress in a single crystal is approximately obtained by solving a spherical single crystal embedded in an infinite deformed matrix. HEM (Homogeneous Equivalent Medium) is an imaginary matrix, whose represents are identical to the overall response of the polycrystalline aggregate.

However, it is not easy to determine the properties of HEM. Some approaches have been proposed to avoid this difficulty. The most widely used KBW model—KBW assumes the elastic interaction between each single crystal and HEM, which applies to case when deformation is not too large.

Considering a polycrystalline aggregate subjected to macroscopic stress at remote boundary, the local stress within each single crystal can be determined with Equation 1

$$\dot{\underline{\underline{\sigma}}}=\dot{\underline{\underline{\Sigma}}}-k(1-c)\left(\dot{\underline{\underline{\varepsilon}}}_v^{in}-\dot{\underline{\underline{E}}}_v^{in}\right)-2\mu(1-d)\left(\dot{\underline{\underline{\varepsilon}}}_d^{in}-\dot{\underline{\underline{E}}}_d^{in}\right) \quad (1)$$

This is the general interaction law of KBW model, which takes into accounts the influence from volumetric strain. The parameters k and u, respectively, being the bulk and shear modulus of each granular. The subscripts v and d represent the volumetric and deviatoric components of the corresponding tensor. For the spherical inclusion embedded in an infinite elastic medium

$$c=\frac{3k}{3k+4\mu} \quad \text{and} \quad d=\frac{6}{5}\frac{k+2\mu}{3k+4\mu} \quad (2)$$

2.3 *Single crystal constitutive relations*

To reflect the pressure sensitivity of geomaterials, the classical Schmid law for each slip system is replaced by a Mohr-Coulomb type yield criterion as Equation 3 shows

$$f^{\alpha}\left(\underline{\underline{\sigma}},R^{\alpha}\right)=\left|\underline{\underline{\sigma}}:\underline{\underline{m}}^{\alpha}\right|+\mu_f H\left(-\sigma_n^{\alpha}\right)\underline{\underline{\sigma}}:\underline{\underline{N}}^{\alpha}-\left(\tau_c^{\alpha}+R^{\alpha}\right) \quad (3)$$

where

$$\underline{\underline{m}} = \frac{1}{2}\left(\underline{n}^{\alpha} \otimes \underline{s}^{\alpha} + \underline{s}^{\alpha} \otimes \underline{n}^{\alpha}\right) \quad \text{and} \quad \underline{\underline{N}}^{\alpha} = \underline{n}^{\alpha} \otimes \underline{n}^{\alpha} \tag{4}$$

where u_f = the frictional coefficient. n^{α} = normal of crystallographic plane. s^{α} = slip direction on the corresponding plane. In crystal theory, they are predefined and are expressed by Miller index. σ_n^{α} = the normal stress act on each slip system. τ_c = initial resistance stress. The introduction of Heviside function $H(\cdot)$ indicates that the normal stress has no effect on the yield function unless the normal stress is compressive.

Another characteristic of geomaterials is dilatancy due to plastic flow. To reflect this feature, the associated plastic potential is modified as a non-associated one

$$F^{\alpha}\left(\underline{\underline{\sigma}}, R^{\alpha}\right) = \left|\underline{\underline{\sigma}} : \underline{\underline{m}}^{\alpha}\right| + v_F H\left(-\sigma_n^{\alpha}\right)\underline{\underline{\sigma}} : \underline{\underline{N}}^{\alpha} - \left(R^{\alpha} - bq^{\alpha}R^{\alpha}\right) \tag{5}$$

where v_f reflects the roughness of each slip system. b reflects the hardening rate. q^{α} and R^{α} is a couple of internal state variables describing transgranular isotropic hardening

$$q^{\alpha} = \frac{1}{b}\left(1 - \exp\left(-b\lambda^{\alpha}\right)\right) \tag{6}$$

$$R^{\alpha} = Q\sum h_{\alpha\beta}\left(1 - \exp\left(-b\lambda^{\beta}\right)\right) \tag{7}$$

where $h_{\alpha\beta}$ is the interaction matrix allowing the introduction of cross influence of β^{th} slip system on the hardening of α^{th} slip system. If there is no cross hardening or latent hardening, $h_{\alpha\beta}$ is an identity matrix.

2.4 *Determination of slip rate* $\dot{\lambda}^{\alpha}$

For time-dependent (viscoplastic) model, the slip rate is explicitly expressed as the function of $\underline{\underline{\sigma}}$ and R^{α} as follows

$$\dot{\lambda}^{\alpha}\left(\underline{\underline{\sigma}}, R^{\alpha}\right) = \begin{cases} \dfrac{1}{\eta}\left(\left(\dfrac{f^{\alpha}}{\tau_c^{\alpha} + R^{\alpha}} + 1\right)^{\frac{1}{p}} - 1\right) & \text{if } f^{\alpha} > 0 \\ 0 & \text{if } f^{\alpha} \le 0 \end{cases} \tag{8}$$

where η is a viscosity-related material constant, whose dimension is time, while p is a rate-sensitive material constant without dimension. Usually, these two parameters must be strictly positive.

When the slip rate (or plastic multiplier) is determined, the local inelastic deformation is the summation of all active slip systems within each granular

$$\dot{\underline{\underline{\varepsilon}}}^{vp} = \sum \dot{\lambda}^{\alpha} \frac{\partial F^{\alpha}}{\partial \underline{\underline{\sigma}}} \tag{9}$$

2.5 *Polycrystal constitutive relations*

At macroscale, the macroscopic viscoplatic strain is calculated by an averaging procedure

$$\dot{\underline{\underline{E}}}^{vp} = \left\langle \dot{\underline{\underline{\varepsilon}}}^{vp} \right\rangle = \sum_{h=1}^{N_g} f_h \dot{\underline{\underline{\varepsilon}}}^{vp,h} \tag{10}$$

where f_h = relative volume fraction. Owing to the randomly distribution, each single crystal possesses the same relative weights, i.e. $f_h = 1/N_g$. N_g = the number of discrete grains (orientations). For FCC single crystal, 40 grains are enough to represent the polycrystal with isotropic behavior. The macro Cauchy stress can be easily determined by Hooke's law

$$\dot{\underline{\underline{\Sigma}}} = C : \left(\dot{\underline{\underline{E}}} - \dot{\underline{\underline{E}}}^{vp}\right) \tag{11}$$

3 NUMERICAL SIMULATION

3.1 *Representation of the model*

The constitutive equations can be combined with any commercial finite element software, e.g. ABAQUS, without any difficulty. From microscopic point of view, each integration point is regarded as a polycrystal, which associates with a large number of randomly distributed grains. The stereographic projection of those 40 grains is as Figure 3 shows.

3.2 *Parameters calibration*

The predictive capacity of the modified KBW polycrystalline model for geomaterials is now

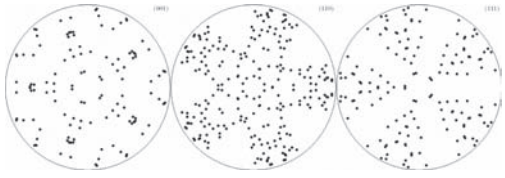

Figure 3. <0 0 1>, <1 1 0> and <1 1 1> pole figures of 40 discrete grains with cubic symmetry.

checked through the simulation of laboratory tests on a quasi-brittle rock, Lac du Bonnet granite. The experimental data of triaxial compressions and creep tests are taken from (Martin 1997) and (Lajtai 1987), respectively. These data are used to determine the model's parameters and validations. The detail procedure for parameters identification can be found in (Zeng 2012). After a back-analysis procedure, the final parameters for simulation are listed in Table 1.

3.3 *Short term response*

For short term response, the strain rates applied in the simulations are corresponding to laboratory tests. With the calibrated parameters given in Table 1, the final simulations results are given in Figures 4 and 5.

3.4 *Long term response*

The long term responses of brittle rocks are briefly depicted in dry conditions. Due to the insufficiency of experiment data, the simulations will be rather qualitative than quantitative. The comparison is given in Figure 6, which is obtained by keeping the specimen strained under $\Sigma_{33} = 143$ Mpa for 70 days.

Table 1. Parameters for simulation of time-dependent mechanical behavior.

E (MPa)	v	u_f	v_f	η (s)	p	τ_c (MPa)	$h_{\alpha\beta}$	b	Q (MPa)
68000	0.21	0.4	0.6	10^9	0.9	35	1	400	40

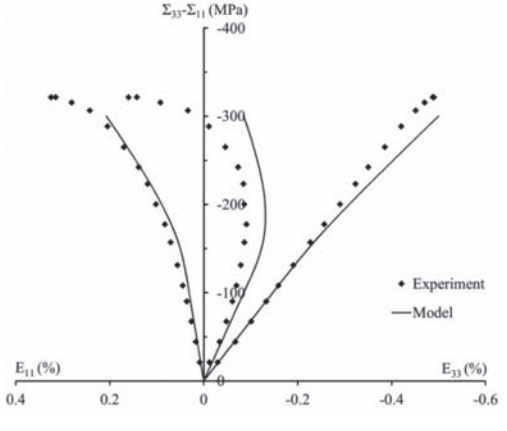

Figure 4. Comparison between experiment data and polycrystal model predictions–triaxial compression with confining pressure 10 MPa.

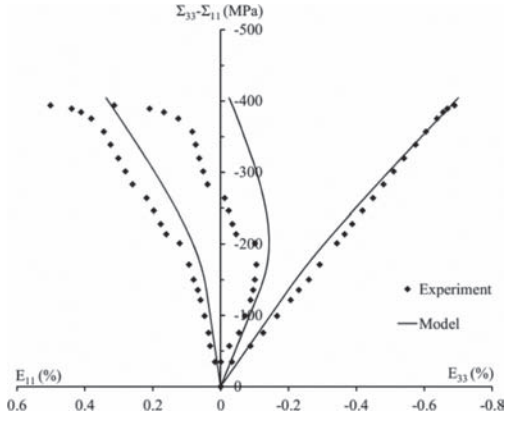

Figure 5. Comparison between experiment data and polycrystal model predictions–triaxial compression with confining pressure 20 MPa.

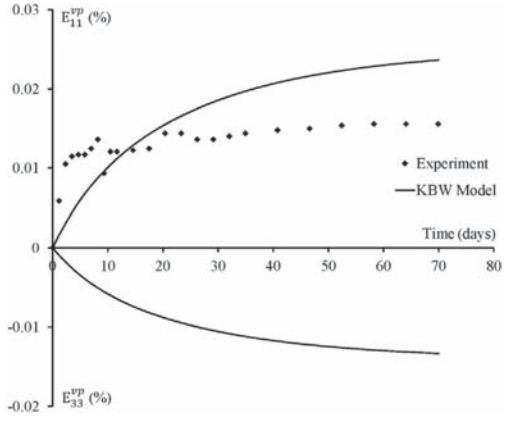

Figure 6. Comparison between experiment data and polycrystal model predictions–uniaxial creep test in dry conditions.

ACKNOWLEDGEMENT

The present work is jointly supported by the China Scholarship Council (CSC) for the first author and the Chinese state 973 program with the grand 2011CB013504.

REFERENCES

Budiansky, B. & Wu, T.T. 1962. Theoretical prediction of plastic strains of polycrystals. *Proc. 4th U.S. Congress on Applied Mechanics* 1: 1175–1185.

Hill, R. 1965. Continuum micro-mechanics of elastoplastic polycrystals. *Journal of the Mechanics and Physics of Solids* 13: 89–101.

Lajtai, E.Z., Schmidtke, R.H., Bielus, L.P. 1987. The effect of water on the time-dependent deformation and fracture of a granite. *International Journal of Rock Mechanics and Mining Sciences* 24: 247–255.

Martin, C.D., Read, R.S., Martino, J.B. 1997. Observations of brittle failure around a circular test tunnel. *International Journal of Rock Mechanics and Mining Sciences* 34: 1065–1073.

Pensée, V., Kondo, D., Dormieux, L. 2002. Micromechanical analysis of anisotropic damage in brittle materials. *Journal of Engineering Mechanics* 128: 889–897.

Shen, W.Q., Shao, J.F., Kondo, D., Gatmiri, B. 2012. A micro-macro model for clayey rocks with a plastic compressible porous matrix. *International Journal of Plasticity* 36: 64–85.

Soulié, R., Mérillou, S., Terraz, O., Ghazanfarpour, D. 2007. Modeling and rendering of heterogeneous granular materials: granite application. *Computer Graphics Forum* 26: 66–79.

Zeng, T. 2012. Modélisation multi-échelle des comportements plastiques et viscoplastiques des géomatériaux polycristallins. *Ph.D. thesis*. Université Lille 1.

Zhu, Q.Z., Kondo, D., Shao, J.F., Pensée, V. 2008. Micromechanical modeling of anisotropic damage in brittle rocks and application. *International Journal of Rock Mechanics and Mining Sciences* 45: 467–477.

This page intentionally left blank

9 *Reliability-based design and limit state design in geotechnical engineering*

This page intentionally left blank

Geotechnical Safety and Risk IV – Zhang et al. (eds)
© 2014 Taylor & Francis Group, London, ISBN 978-1-138-00163-3

Serviceability limit state design of lime-cement columns—a reliability-based design approach

N. Bergman, R. Ignat & S. Larsson
Division of Soil and Rock Mechanics, KTH Royal Institute of Technology, Stockholm, Sweden

ABSTRACT: Deep mixing with lime-cement columns is a ground improvement method used to improve the strength and deformation properties of soft cohesive soils. Due to the complex manufacturing process, the variability in the strength and deformation properties is normally high. A rational approach to include variability in the design process is by introducing Reliability-Based Design (*RBD*). This paper presents a reliability-based design approach for Serviceability Limit State (*SLS*) design of soil improved by lime-cement columns using the First-Order Reliability Method (*FORM*). The paper further presents the impact of uncertainties, reliability indices and area replacement ratios on the relationship between the characteristic value and the design value with respect to the column modulus of elasticity.

1 INTRODUCTION

Deep Mixing (*DM*) using lime-cement columns is a ground improvement method that is used to improve the deformation and strength properties in soft soils. Because of the complexity of the soil-binder mixing process, soils improved by lime-cement columns often show a large variability with respect to their strength and deformation properties (Larsson 2005). The large variability makes it difficult to predict the properties in advance; and it is thus essential to verify the properties after installation. This is normally done by penetration test methods and laboratory tests on samples taken from the columns.

In current design practice, it is assumed that the effects of variability and uncertainties on the reliability of a mechanical system are taken into consideration by using an adequate total factor of safety. A more rational way to deal with uncertainties is by including them as parameters in the design model. In fact, Eurocode 7 (Eurocode 7: Geotechnical design—Part 1: General rules 2004) states that the selection of characteristic values for geotechnical parameters shall take into consideration the variability of the measured property values. This can be accomplished by using a Reliability-Based Design (*RBD*) approach. The need for *RBD* in *DM* has previously been address by Honjo (1982), Kitzume (2004), Larsson et al. (2005), Liu et al. (2008), Zheng et al. (2009), Babu et al. (2011), Al-Naqshabandy et al. (2012), Al-Naqshabandy & Larsson (2012, 2013), Bergman et al. (2013). Among these studies, only the study by Zheng et al. (2009) included reliability analyses for the Serviceability Limit State (*SLS*) and presented the relationship between the area replacement ratio (α) and the reliability indices (β). They did not however study the impact of column characteristic uncertainties on the relationship between the characteristic value of the column modulus of elasticity (E_k) and the design value of the column modulus of elasticity (E_d).

The present paper presents a *RBD* approach for the *SLS* design of soils improved by lime-cement columns. Uncertainties related to inherent variability, measurement errors, statistical errors and model and transformation errors are considered and put into context with the evaluation of the design value of E_d. Finally, the First-Order Reliability Method (*FORM*) is used to analyze the impact of uncertainties on the *SLS* design of an embankment founded on lime-cement columns.

The *SLS* design of a lime-cement-column-supported embankment is normally based on an assumption of E_d. In the present paper, using *FORM* analyses and considering the assumed E_d, uncertainties and reliability indices, a corresponding value of E_k was evaluated. Present paper also presents and discusses the relationship between E_d and E_k, and gives an illustrative example of how this relationship can be used as support for the design.

2 METHODS

This section gives a description of the statistical methods used in this study. It also shows how a simple and well established deterministic design model can be incorporated in a *RBD* methodology.

2.1 *Uncertainties*

Using a *RBD* approach, a statistical quantification of the stochastic variables included in the design model is needed. In the present study, the average evaluated column modulus of elasticity ($\bar{E}_{col}$) and the average evaluated clay oedometer modulus ($\bar{M}_{soil}$) are considered and treated as stochastic variables. Bergman et al. (2013) quantified the variability of $\bar{E}_{col}$, in terms of the total coefficient of variation ($COV^2_{\bar{E},TOT}$) evaluated from penetration test data (q_c), as:

$$COV^2_{\bar{E},TOT} = (COV^2_{qc} - COV^2_{m,qc})\left(\frac{1}{N} + \Gamma^2\right) + \frac{COV^2_{m,q_c}}{N} + COV^2_{tr,\bar{E}} \quad (1)$$

where COV_{qc} is the evaluated coefficient of variation of the penetration test data, COV_{m,q_c} is the coefficient of variation associated with random measurement noise, $COV_{tr,\bar{E}}$ is the coefficient of variation associated with transformation model bias, N is the number of uncorrelated tests and Γ^2 is the variance reduction factor. The variance reduction factor can be described as the reduction in the standard deviation due to spatial correlation, and is further described in Bergman et al. (2013).

Values of COV_{qc} are normally obtained from penetration test data, while COV_{m,q_c}, $COV_{tr,\bar{E}}$ and Γ^2 are obtained from experience and literature, thus giving an estimation of $COV_{\bar{E},TOT}$ (Bergman et al. 2013). In the following analysis, a wide range of $COV_{\bar{E},TOT}$ are studied.

2.2 *Distributions*

Soil parameters are often modeled as log-normally distributed variables since they are strictly non-negative. Al-Naqshabandy et al. (2012) and Bergman et al. (2013) found that q_c was either normally or log-normally distributed. As a consequence, two different analyses were made. One analysis in which E_{col} and M_{soil} were considered to be normally distributed parameters, and a second analysis in which they were considered to be log-normally distributed.

2.3 *Design values*

Thoft-Christensen & Baker (1982) defined the design value (x_d) of a normally distributed variable as:

$$x_d = \frac{x_k}{\gamma_m} = m + \alpha\beta\sqrt{s^2} \quad (2)$$

where x_k is the characteristic value, γ_m is a partial factor, m is the sample mean value, s^2 is the sample variance, α is a sensitivity factor derived from the reliability analysis and β is the reliability index given in standards and design practices.

For a log-normally distributed variable, the design value ($x_{d,log}$) can be described as:

$$x_{d,\log} = \frac{x_{k,\log}}{\gamma_m} = e^{(\mu_{lnx} + \alpha\beta\sigma_{lnx})} \quad (3)$$

where $x_{k,log}$ is the characteristic value, μ_{lnx} is the mean value of the transformed variable and σ_{lnx} is its standard deviation.

In present paper, the characteristic value was considered to correspond to an evaluated or assumed average value.

2.4 *Serviceability limit state design*

For simplicity, a simple and well established model was adopted for the serviceability limit state analysis. The total settlement (S_{emb}) of an embankment founded on normally consolidated clay, improved by end-bearing lime-cement columns (Fig. 1), can be expressed by an equal strain (Voigt) model (Broms 1999, TK Geo 2011):

$$s_{emb} = \sum \frac{h_j \cdot h_{emb} \cdot \gamma_{emb}}{a \cdot \bar{E}_{col} + (1-a) \cdot \bar{M}_{soil}} \quad (4)$$

where h_j is the height of layer j, h_{emb} is the height of the embankment, γ_{emb} is the unit weight of the embankment and a is the area ratio of the lime-cement columns.

2.5 *First Order Reliability Methods (FORM)*

Reliability analysis makes it possible to quantify how close a system is to failure (Baecher & Christian 2003). In *SLS* design, failure can be defined as an unacceptable difference between

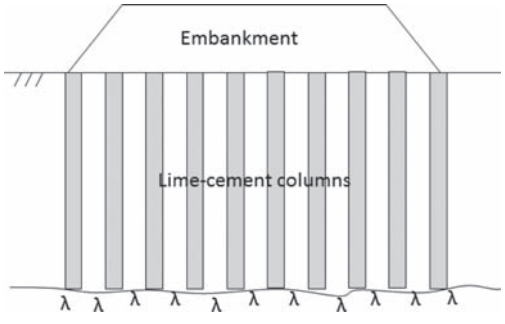

Figure 1. Embankment founded on end-bearing lime cement columns.

observed and allowed performance. To assess the reliability of a geotechnical structure, a limit state function ($g(X)$) is defined at $g(X) = 0$. In the present study, $g(X)$ was defined as:

$$g(X) = \delta_{max} - \delta(x_1, x_2, \ldots, x_n) = 0 \quad (5)$$

where δ_{max} is the maximum allowed settlement and $\delta(X)$ is the estimated settlement calculated from design properties $x_1, x_2, \ldots, x_n$. A value of $G(X) > 0$ indicates an acceptable difference between allowed and observed performance. Combining Equations (2), (4) and (5), the limit state function can be rewritten as:

$$g(\bar{E}_{col}, \bar{M}_{soil}) = \delta_{max} - \sum h_j \cdot \frac{h_{emb} \cdot \gamma_{emb}}{a \cdot \left(\mu_{\bar{E}_{col}} - \alpha_{\bar{E}_{col}} \cdot \beta \cdot \sigma_{\bar{E}_{col}}\right) + (1-a) \cdot \left(\mu_{\bar{M}_{soil}} - \alpha_{\bar{M}_{soil}} \cdot \beta \cdot \sigma_{\bar{M}_{soil}}\right)} \quad (6)$$

where $\mu_{\bar{E}_{col}}$ is the mean value of $\bar{E}_{col}$, $\alpha_{\bar{E}_{col}}$ is the evaluated sensitivity factor, $\sigma_{\bar{E}_{col}}$ is the standard deviation of $\bar{E}_{col}$, $\mu_{\bar{M}_{soil}}$ is the mean value of $\bar{M}_{soil}$, $\alpha_{\bar{M}_{soil}}$ is the evaluated sensitivity factor and $\sigma_{\bar{M}_{soil}}$ is the standard deviation of $\bar{M}_{soil}$. The sensitivity factors $\alpha_{\bar{E}_{col}}$ and $\alpha_{\bar{M}_{soil}}$ were determined by an iterative process described by Rackwitz & Fiessler (1978) and Baecher & Christian (2003).

3 INPUTS AND ASSUMPTIONS

Input parameters used in the reliability analysis are summarized in Table 1.

The *FORM* analyses were performed using the input parameters given in Table 1. In the analyses, E_k was altered with changing $COV_{\bar{E},TOT}$ in order to keep β constant at 1.0 and 1.5. The value of $\beta = 1.5$ was provided by Eurocode 0 and $\beta = 1.0$ was adopted for comparative analyses. From these analyses, the quotient E_k/E_d was evaluated. This is a relationship that can serve as a basis for the design process, as is shown in the illustrative example below. Analyses were made assuming both normal and log-normal distributions of $\bar{E}_{col}$ and $\bar{M}_{soil}$. Moreover, the following assumptions were made:

- The influence of curing time is not considered
- The composite material (soil and lime-cement column) was assumed to be uniformly strained
- $\bar{E}_{col}$ and $\bar{M}_{soil}$ are assumed to be constant throughout the soil profile
- Loads are assumed to be only vertically distributed.

4 RESULTS

The outcome of the *FORM* analysis, using the parameters values presented in Table 1, is illustrated in Figure 2, where E_k/E_d is plotted against $COV_{\bar{E},TOT}$.

When $\bar{E}_{col}$ and $\bar{M}_{soil}$ were modeled as normally distributed parameters and with $\beta = 1.0$, E_k/E_d ranged from 1.04 to 2.53. For $\beta = 1.5$, E_k/E_d ranged from 1.06 to 9.98. When $\bar{E}_{col}$ and $\bar{M}_{soil}$ were modeled as log-normally distributed parameters and with $\beta = 1.0$, E_k/E_d ranged from 1.04 to 2.03. For $\beta = 1.5$, E_k/E_d ranged from 1.06 to 2.67.

Table 1. Summary of input parameters.

Parameters	Value	Comments/References
Reliability index (β)	1.0 and 1.5	Adopted value and Eurocode 0, Honjo et al. (2010)
Maximum allowed settlement (δ_{max})	15 cm	Adopted value
Characteristic value of column modulus of elasticity (E_k)	Varying	Parameter is altered with different values of $COV_{\bar{E},TOT}$ considering acceptable value of β
Characteristic value of clay oedometer modulus ($\bar{M}_{soil}$)	500 and 1500 kPa	Adopted values. Normally consolidated clay
Unit weight embankment (γ_{emb})	20 kN/m^3	TK Geo (2011). In the present study γ_{emb} is considered and treated deterministically
Height embankment (h_{emb})	4 m	Adopted value
$COV_{E,TOT}$	5–60% (altered in 5% intervals)	Adopted range
$COV_{M,soil}$	30%	Adopted value
Column length (L)	10 m	Adopted value
Lime-cement column area replacement ratio (a)	0.1, 0.2 and 0.4	Adopted values

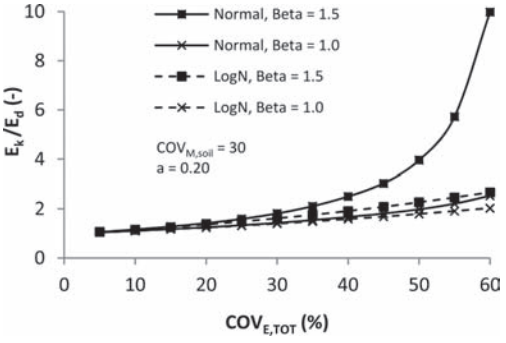

Figure 2. The quotient E_k/E_d plotted against $COV_{\bar{E},TOT}$ with different values of β.

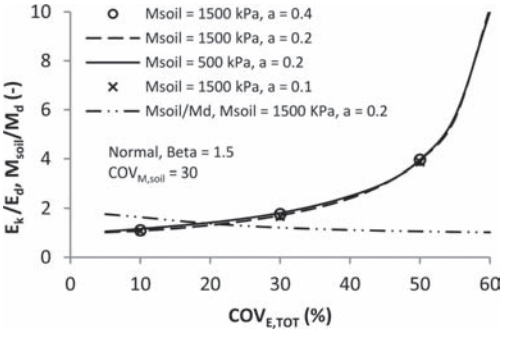

Figure 3. The quotients E_k/E_d and $\bar{M}_{soil}/M_d$ plotted against $COV_{\bar{E},TOT}$ with different values of $\bar{M}_{soil}$ and a.

With low $COV_{\bar{E},TOT}$ and $\beta = 1.5$, the difference between E_k/E_d for the normal and log-normal cases is small, only 4% at $COV_{\bar{E},TOT} = 20\%$. This difference becomes greater with increasing $COV_{\bar{E},TOT}$, the difference being 74% at $COV_{\bar{E},TOT} = 50\%$. For β = 1.0, the difference between E_k/E_d for the normal and log-normal cases is much smaller, only 1% at $COV_{\bar{E},TOT} = 20\%$ and 11% at $COV_{\bar{E},TOT} = 50\%$.

Figure 3 shows the impact of $\bar{M}_{soil}$ on E_k/E_d, when $\bar{M}_{soil}$ increased from 500 kPa to 1500 kPa. As can be seen in the figure, the impact was low, only 6% at $COV_{\bar{E},TOT} = 30\%$ and less than 1% at $COV_{\bar{E},TOT} = 50\%$. The figure also shows the impact of a on E_k/E_d. At $COV_{\bar{E},TOT} = 30\%$, the difference in E_k/E_d when a as increased from 0.1 to 0.4 was 6%. In practice, the small impact of $\bar{M}_{soil}$ and a on E_k/E_d means that E_k/E_d is almost entirely governed by $COV_{\bar{E},TOT}$. Figure 3 also shows the quotient $\bar{M}_{soil}/M_d$ plotted against $COV_{\bar{E},TOT}$. For $COV_{\bar{E},TOT} = 20\%$, $\bar{M}_{soil}/M_d$ equals 1.4, but it approaches 1.0 with increasing $COV_{\bar{E},TOT}$.

5 DISCUSSION INCLUDING AN ILLUSTRATIVE EXAMPLE

The use of Figure 2 as a design aid is best presented with an illustrative example.

If E_{col} is assumed to be normally distributed and E_d is assumed to be 20 MPa, with $COV_{\bar{E},TOT}$ evaluated to 50%, E_k must exceed 20 * 1.98 = 39.6 MPa for $\beta = 1.0$. For $\beta = 1.5$, the minimum value of E_k is 20 * 3.96 = 79.2 MPa. If $\bar{E}_{col}$ is less than the required E_k, the designer has several options: (1) to reduce $COV_{\bar{E},TOT}$, by making additional tests or by decreasing $COV_{tr,\bar{E}}$ by performing tests with an additional test method (e.g. Ching et al. 2010) (2) to add columns to the design (3) to wait and perform tests on a later occasion when E_k may have increased or (4) to investigate whether the obtained β is good enough for the structure and client.

As shown in Figure 3, changes in $\bar{M}_{soil}$ and a have only a small impact on E_k/E_d, and in practice this means that it is almost entirely governed by $COV_{\bar{E},TOT}$. However, it must be noted that Figures 2 and 3 are valid only for this particular serviceability limit state model and only within specified ranges of $\bar{M}_{soil}$ and a.

Although a value of β = 1.5 is suggested by Eurocode 0, the authors believe that it may be a too conservative value for many *DM* applications. A value of β = 1.5 corresponds to 6.7% risk of failure. In the authors' opinion, for structures where potential failure is of minor consequence, a value of $\beta = 1.5$ cannot always be economically justified. For these structures, a wider range of β could be allowed, where β is decided by balancing the cost of making higher quality columns and additional tests against the cost of structure maintenance.

6 CONCLUSION

The *RBD* methodology is considered to be a rational approach to include strength and deformation parameter variability in *DM* design. If it is adapted and presented in the context of its particular area of application, the *RBD* methodology can become a useful design aid (cf. Fig. 2) for the *DM* industry. However, it must be noted that Figures 2 and 3 are valid only for this particular serviceability limit state model and only within specified ranges of $\bar{M}_{soil}$ and a.

For small values of $COV_{\bar{E},TOT}$, the impact of different distributions (normal or log-normal) and β on the quotient E_k/E_d is small, but the differences become substantial as $COV_{\bar{E},TOT}$ increases.

In *SLS* design, Eurocode 0 suggests β = 1.5. However, it is the authors' belief that a wider range of β could be allowed for structures whose potential failure is of minor consequence. Here β

should be decided by balancing the cost of making higher quality columns and additional tests against the cost of structure maintenance.

7 NOTATION

a	Lime-cement column area replacement ratio
h_j	Height of layer j
h_{emb}	Height of the embankment
m	Sample mean value
q_c	Cone tip resistance
s_{emb}	Embankment settlement
s^2	Sample variance
x_d	Design value of a normally distributed variable
$x_{d,log}$	Design value of a log-normally distributed variable
x_k	Characteristic value of a normally distributed variable
$x_{k,log}$	Characteristic value of a log-normally distributed variable
$COV_{\bar{E},TOT}$	Total coefficient of variation of $\bar{E}_{col}$
COV_{m,q_c}	Coefficient of variation associated with random measurement noise
$COV_{\bar{M},soil}$	Coefficient of variation of $\bar{M}_{soil}$
COV_{qc}	Coefficient of variation of penetration test data
$COV_{tr,\bar{E}}$	Coefficient of variation associated with transformation model bias
DM	Deep mixing
$\bar{E}_{col}$	Average column modulus of elasticity evaluated from in-situ or laboratory tests
E_d	Assumed design value of the column modulus of elasticity
E_k	Characteristic value of the column modulus of elasticity evaluated from *FORM* analyses
$FORM$	First-order reliability method
L	Length of lime-cement columns
M_d	Design value of clay oedometer modulus
$\bar{M}_{soil}$	Characteristic value of clay oedometer modulus evaluated from in-situ or laboratory tests
N	Number of uncorrelated tests
RBD	Reliability-based design
SLS	Serviceability limit state
α	Sensitivity factor
$\alpha_{\bar{E}_{col}}$	Evaluated sensitivity factor of $\bar{E}_{col}$
$\alpha_{\bar{M}_{soil}}$	Evaluated sensitivity factor of $\bar{M}_{soil}$
β	Reliability index
γ_m	A partial factor
δ_{max}	Maximum allowed settlement
μ_{lnx}	Mean value of the transformed variable x
$\mu_{\bar{E}_{col}}$	Mean value of $\bar{E}_{col}$
$\mu_{\bar{E}_{soil}}$	Mean value of $\bar{M}_{soil}$
σ_{lnx}	Standard deviation of the transformed variable x
$\sigma_{\bar{E}_{col}}$	Standard deviation of $\bar{E}_{col}$
$\sigma_{\bar{M}_{soil}}$	Standard deviation of $\bar{M}_{soil}$
γ_{emb}	Unit weight of the embankment
Γ^2	Variance reduction factor

ACKNOWLEDGEMENT

The authors acknowledge the support of the Development Fund of the Swedish Construction Industry, Skanska Sverige AB and the Swedish Transport Administration.

REFERENCES

Al-Naqshabandy, M. & Larsson, S. 2013. Effect of uncertainties of improved soil shear strength on the reliability of embankments. *ASCE Journal of Geotechnical and Geoenvironmental Engineering* 139(4): 619–632.

Al-Naqshabandy, M. & Larsson, S. 2012. Partial factor design for a highway embankment founded on lime-cement columns. Proc. *ISSMGE—TC 211 International Symposium on Ground Improvement IS-GI Brussels*.

Al-Naqshabandy, M., Bergman, N. & Larsson, S. 2012. Strength variability in lime-cement columns based on CPT data. *Ground Improvement* 165 (1): 15–30.

Baecher, G.B. & Christian J.T. 2003. *Reliability and Statistics in Geotechnical Engineering*. England: Wiley and Sons Ltd.

Babu, G.L., Sivakumar., Srivastava, Amit & Sivapulliah, P.V. 2011. Reliability analysis of strength of cement treated soils, *Georisk: Assessment and Management of Risk for Engineered Systems and Geohazards* 5 (3–4): 157–162.

Bergman, N., Al-Naqshabandy, M. & Larsson, S. 2013. Strength variability in lime-cement columns evaluated by CPT and KPS. *Georisk* 7(1): 21–36.

Broms, B. 1999. Keynote lecture: Design of lime, lime/cement and cement columns. *International Conference on Dry Mix Methods: Dry Mix Methods for Deep Soil Stabilization*. Stockholm.

Ching, J., Phoon, K. & Chen Y. 2010. Reducing shear strength uncertainties in clays by multivariate correlations. *Canadian Geotechnical Journal* 47(1): 16–33.

Eurocode 0: *Basis of structural design*. EN 1990:2002.

Eurocode 7: *Geotechnical Design—Part 1*: General rules. 2004. PrEN 1997-1:2004:E.

Honjo, Y. 1982. A probabilistic approach to evaluate shear strength of heterogeneous stabilized ground by deep mixing method. *Soils and Foundations* 22 (1): 23–38.

Honjo, Y., Hara, T. & Kieu Le, T.C. 2010. Level III Reliability Based Design of Examples set by ETC10. *Proceedings of 17 SEAGC*, *Taiwan*.

Kitazume, M. 2004. Approach to reliability based design on deep mixing improved ground. *Proceedings of DFI's 29th Annual Conference on Deep Foundation*, *Vancouver*.

Larsson, S. 2005a. State of Practice Report Session 6: Execution, monitoring and quality control. *Proceedings of the International Conference on Deep Mixing*, *Stockholm*.

Larsson, S., Stille, H. & Olsson, L. 2005. On horizontal variability in lime-cement columns in deep mixing. *Géotechnique* 55 (1): 33–44.

Liu, Y., Zheng, J. & Guo, J. 2008. Statistical evaluation for strength of pile by deep mixing method. *Proceedings of GEDMAR08, Nanjing*.

Rackwitz, R. & Fiessler, B. 1978. Structural reliability under combined random load sequences. *Computers and Structures* 9: 489–494.

Thoft-Christensen P. & Baker M.J. 1982. *Structural reliability and its application*. Berlin: Springer-Verlag, Berlin.

TK Geo 2011. *Swedish Design Guidelines*, Trafikverket, Borlänge (In Swedish).

Zheng, J., Liu, Y. & Xu, Z. 2009. Reliability-based Design Applied to Multi-column Composite Foundations. *In Advances in Ground Improvement: Research to Practice in the United States and China: Proceedings of the US-China Workshop on Ground Improvement Technologies, Orlando, Florida*.

Geotechnical Safety and Risk IV – Zhang et al. (eds)
© 2014 Taylor & Francis Group, London, ISBN 978-1-138-00163-3

Cost-effective framework for simplified geotechnical reliability-based design

J.Y. Ching
Department of Civil Engineering, National Taiwan University, Taipei, Taiwan

K.K. Phoon
Department of Civil and Environmental Engineering, National University of Singapore, Singapore

ABSTRACT: Reliability-Based Design (RBD) is known to provide a rational basis for incorporating uncertainties in the design environment explicitly into geotechnical design. In principle, RBD should be able to translate site investigation efforts into design savings. However, the constant partial factor approach prohibits such translation. This study shows that the combination of two recent developments made by the authors allows such translation. The first development is the multivariate probability distribution of soil parameters. Such a multivariate distribution provides a solid basis that can translate site investigation efforts into smaller parameter variability, e.g. smaller Coefficient Of Variation (COV). The second development is called the Quantile Value Method (QVM). The QVM adopts constant quantile values as the design values, so the resulting partial factors scale with the parameter COV—when parameter COV is small, partial factors are closer to one. The combination of the above two novel developments is a cost-effective framework that is able to translate site investigation efforts into smaller parameter COVs and in turn translate into partial factors that are closer to one.

1 INTRODUCTION

More economical geotechnical designs can be achieved by reducing uncertainties through site investigation, in particular, by reducing uncertainties in soil parameters. While it is theoretically correct that reduction in uncertainties should translate to design savings, practical questions such as "how many meters of reduction in pile length?" and "is pile length reduction worth the engineer's time/money to collect more site information?" cannot be answered in a general theoretical sense. These questions can only be answered empirically by applying Reliability-Based Design (RBD) to actual design problems where the amount of site information can be varied systematically.

Ching & Phoon (2012a) showed that rigorous RBD (direct probability-based design method) is able to link site investigation efforts to final design savings. They demonstrated that site investigation (as an illustration of "information") is not only a cost item but also an investment item, because reduction of uncertainties through more and/or better tests can translate directly to design savings through rigorous RBD. However, practicing engineers may not be familiar with the procedures of rigorous RBD. The partial factors or load and resistance factors associated with these simplified RBD methods are used to obtain conservative design values for soil parameters or resistances. Although these simplified RBD methods can produce familiar "look and feel" design codes that do not require engineers to perform probabilistic calculations, they are unable to achieve the desired target reliability index under all design scenarios, namely, the translation from site investigation to final design savings may not be satisfactory.

This study shows that the combination of two recent developments made by the authors allows such translation. The first development is the multivariate probability distribution of soil parameters (e.g., Ching et al. 2010, Ching & Phoon 2012b). Such a multivariate distribution provides a solid basis that can translate site investigation efforts into smaller parameter variability, e.g. smaller Coefficient Of Variation (COV). The second development is called the Quantile Value Method (QVM) (Ching & Phoon 2011, Ching & Phoon 2013). The QVM adopts constant quantile values as the design values, so the resulting partial factors scale with the parameter COV—when parameter COV is small, partial factors are closer to one. The combination of the above two novel developments is a cost-effective framework that is able to translate site investigation efforts into smaller parameter COVs and in turn translate into partial factors that are closer to one.

2 COST EFFECTIVE FRAMEWORK FOR RBD

2.1 *Multivariate probability distribution of soils parameters*

A database of OCR (overconsolidation ratio), s_u (undrained shear strength), $q_T - \sigma_v$ (net cone resistance), and N_{60} (SPT N corrected for energy efficiency) is compiled in Ching et al. (2010). This database was used to construct the multivariate probability distribution of (OCR, s_u, $q_T - \sigma_v$, N_{60}). Given the multivariate probability distribution, the Bayesian analysis is taken to derive some useful equations for the (updated) mean and COV of s_u given information such as OCR, s_u, $q_T - \sigma_v$, and N_{60}. It is concluded that the updated COV decreases with increasing information. Ching & Phoon (2012b) presented another clay database containing multivariate LI (Liquidity Index), s_u, s_u^{re} (remolded undrained shear strength), σ'_p (preconsolidation stress), and σ'_v (effective vertical stress) data points. This database was used to construct the multivariate probability distribution of (LI, s_u, s_u^{re}, σ'_p, σ'_v). It is also concluded that the updated COV of s_u decreases with increasing information. In summary, a multivariate probability distribution provides a solid basis that can translate site investigation efforts into smaller parameter variability, e.g. smaller Coefficient Of Variation (COV).

2.2 *Quantile value method*

The first framework (multivariate probability distribution) alone does not guarantee the link from site investigation efforts to final design savings. To elaborate on this, consider a simple pile design problem involving two lognormal random variables, the resistance/capacity Q and the action F. Let δ_Q be the COV of the resistance. Let scenario A be a case where very detailed site investigation has been conducted (e.g. OCR, $q_T - \sigma_v$, and N_{60} are simultaneously known). As a result, δ_Q is small and equal to 0.2. Scenario B is a case where the site investigation is cursory. As a result, δ_Q is large and equal to 0.45. Let us consider the strategy of implementing a constant partial factor for Q, e.g. $\gamma_Q = 0.6$, for both scenarios. This implies that $Q_d = Q_k \times 0.6$ (Q_k is the characteristic (mean) value of Q, and Q_d is the design value) will be taken for the design calculations of both scenarios. For scenario A, there is a very small chance that the actual $Q < Q_d$, but for scenario B, this chance becomes much larger (Fig. 1). It is quite unlikely that the same design value of $Q_d = Q_k \times 0.6$ can maintain a uniform target reliability index over these two disparate scenarios.

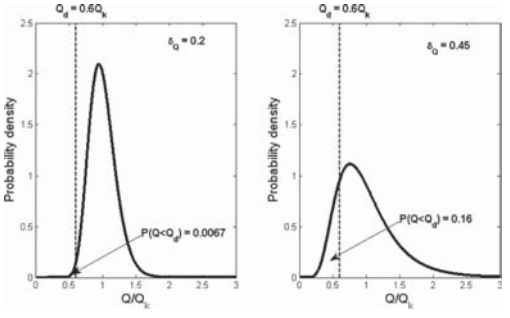

Figure 1. Probability density functions of resistance Q for scenarios A (left) and B (right); the vertical dashed lines indicate the design value Q_d with the constant partial factor $\gamma_Q = 0.6$.

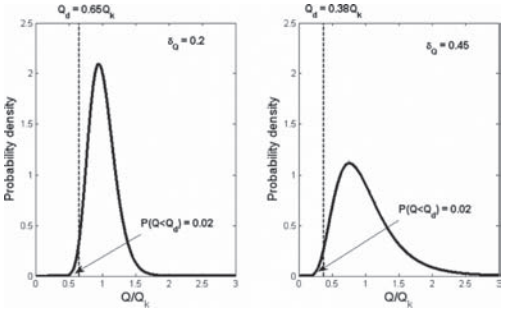

Figure 2. Probability density functions of resistance Q for scenarios A (left) and B (right); the vertical dashed lines indicate Q_d with constant probability threshold = 0.02.

Ching & Phoon (2011) showed that for problems with variable COVs, it may be possible to maintain better uniformity with fixed quantiles. The strategy of fixed quantiles is formally named the Quantile Value Method (QVM) in Ching & Phoon (2013) and can be explained in Figure 2 for the same example. The QVM adopts design values for resistance Q corresponding to fixed quantiles, e.g. 0.02 quantiles, for both scenarios A and B. For the action F, the $1 - 0.02 = 0.98$ quantile is taken to be the design value because it is a destabilizing variable. The number 0.02 is called the "probability threshold η'' in Ching & Phoon (2011). For scenario A, the resulting Q_d is the 0.02 quantile = $Q_k \times 0.65$, but for scenario B, the 0.02 quantile becomes $Q_k \times 0.38$. Note that the fixed quantile strategy implies different partial factors should be used for scenarios with different COVs. The above 0.02 probability threshold is just for illustration. In reality, the probability threshold η should be calibrated by the reliability theory developed in Ching & Phoon (2011) to achieve a prescribed target reliability index β_T.

2.3 *ETC10 example for pad foundation design*

The pad foundation example adopted in this paper was developed by ETC10 (Eurocode 2011). The square pad foundation with width B is embedded at a depth of 0.8 m. It is designed to support the following loads: (a) permanent vertical L, and (b) variable horizontal load Q_h and variable vertical load Q_v. All loads are assumed to be (statistically) independent of each other. The soil consists of the Boulder Clay, with undrained shear strength of s_u and a bulk unit weight of 21.4 kN/m^3. The concrete unit weight γ_c is 25 kN/m^3. The ground water table is assumed to be deeper than B below the depth of embedment. Hence, it has no influence on the bearing capacity of the foundation.

There are four random variables $\{s_u, L, Q_v, Q_h\}$, and their distributions and statistics are listed in Table 1. For simplicity, the characteristic values of $\{s_u, L, Q_v, Q_h\}$ are assumed to be equal to their respective mean values, i.e. $s_{u,k} = \mu_{su}$, $L_k = \mu_L$, $Q_{v,k} = \mu_{Qv}$, and $Q_{h,k} = \mu_{Qh}$. The ratio between the mean variable load to mean dead load is $r_{QL} = \mu_Q / \mu_L = (\mu_{Qv}^2 + \mu_{Qh}^2)^{0.5}/\mu_L$, and the angle α of the variable load is defined to be $\tan^{-1}(\mu_{Qh}/\mu_{Qv})$.

This study focuses on the Ultimate Limit State (ULS) requirement. We adopt the equation recommended in Eurocode 7 [Eq. (D1) in page 157, BS EN 1997-1:2004 (British Standards Institute 2004)] for calculating q_u:

$$q_u = (\pi+2)s_u \cdot s_c \cdot i_c + q = 0.6(\pi+2)\left[1+\sqrt{1-\frac{Q_h}{B^2 s_u}}\right]s_u + 17.12 \quad (1)$$

where s_c = 1.2 for the square foundation, $i_c = 0.5[1 + (1 - Q_h/B^2/s_u)^{0.5}]$, and q = total surcharge pressure = 0.8 × 21.4 = 17.12 kN/m^2. The performance function can be written as

$$g(X,B) = q_u B^2 - L - Q_v - W_p \quad (2)$$

where X denotes the collection of all random variables $\{s_u, L, Q_v, Q_h\}$, and $W_p = \gamma_c \times B^2 \times 0.8 = 20\,B^2$ kN is the weight of the foundation. The RBD requirement is to enforce the reliability constraint

$$P[\,g(X,B) < 0\,] \le p_T = \Phi(-\beta_T) \quad (3)$$

where $\Phi(\cdot)$ is the cumulative density function of the standard normal random variable; p_T is the target failure probability; β_T is the target reliability index. The Partial Factor Design (PFD) requirement is to enforce

$$B^2\left(0.6(\pi+2)\left[1+\sqrt{1-\frac{\gamma_{Q_h} r_{QL}\mu_L \sin(\alpha)}{B^2\gamma_{s_u}\mu_{s_u}}}\right]\gamma_{s_u}\mu_{s_u} + 17.12\right) \ge \gamma_L\mu_L + \gamma_{Q_v} r_{QL}\mu_L\cos(\alpha) + 20\times B^2 \quad (4)$$

where γ's are the partial factors.

2.4 *Simplified RBD codes for pad foundation in clays*

For the calibration of simplified RBD codes, partial factors must be calibrated with respect to a wide range of design scenarios rather than a specific design scenario. The range of the design scenarios considered in this study are listed in Table 2. There are six design parameters: B, μ_{su}, δ_{su}, μ_L, r_{QL}, and α. The range for μ_L is not specified, as it has no effect on the calibrated partial factors. The partial factors for L, Q_v, and Q_h are chosen to be γ_L = 1.1, γ_{Qv} = 1.5, and γ_{Qh} = 1.5 to be consistent with the structural codes. As a result, the only partial factor to be calibrated is γ_{su}. The target reliability index β_T is chosen to be 3.2.

Two simplified RBD formats are calibrated:

a. (constant PF) The design value of s_u is equal to the characteristic value of s_u multiplied by γ_{su}, and a single γ_{su} is calibrated to cover all design scenarios. This code format is adopted in most current design codes (e.g. AASHTO and Eurocode 7). A set of m = 360 cases with (B, μ_{su}, δ_{su}, r_{QL}, α) randomly drawn from the

Table 1. Statistics and characteristic values of the random variables.

Variable	Description	Distribution	Statistics: Mean	Statistics: COV	Characteristic value
s_u	Undrained shear strength	Lognormal	$\mu_{su}\,\delta$	$\delta_{su}\,\mu$	μ_{su}
L	Permanent vertical load	Gaussian[1]	$\mu_L\,\delta$	$\delta_L = 10\%$[1]	μ_L
Q_v	Variable vertical load	Gumbel[1]	$r_{QL}\mu_L\cos(\alpha)$	$\delta_{Qv} = 20\%$[1]	$r_{QL}\mu_L\cos(\alpha)$
Q_h	Variable horizontal load	Gumbel[1]	$r_{QL}\mu_L\sin(\alpha)$	$\delta_{Qh} = 20\%$[1]	$r_{QL}\mu_L\sin(\alpha)$

[1]According to Sørensen (2002).

ranges given in Table 2 are adopted as the calibration cases. For the i-th calibration case with (B_i, $\mu_{su,i}$, $\delta_{su,i}$, $r_{QL,i}$, α_i), the "actual" reliability index, denoted by $\beta_{A,i}$, depends on the selected value of γ_{su} in Eq. (4). $\beta_{A,i}$ can be estimated using Monte Carlo simulation. It is impossible to find a perfect γ_{su} so that $\beta_{A,i} = \beta_T$ for all m = 360 calibration cases, but a reasonable value of γ_{su} can be found by solving the following optimization problem:

$$\min_{\gamma_{su}} \sum_{i=1}^{m} \left[\beta_{A,i}(\gamma_{su}) - 3.2 \right]^2 \tag{5}$$

b. (QVM) The design value of s_u is equal to the η-quantile of s_u, and a constant η is calibrated to cover to all design scenarios. This is the code format associated with QVM (Ching & Phoon 2011, 2013). The same 360 cases with random (B, μ_{su}, δ_{su}, r_{QL}, α) are taken as the calibration cases. For the i-th calibration case, a probability threshold η_i is calibrated to achieve the target reliability β_T. The details for the calibration of η_i are presented elsewhere in Ching & Phoon (2011, 2013). The final η is taken to be the average of η_1, …, η_{360}. With this average η value, the design value $s_{u,d}$ of a future design case is simply its η-quantile, denoted by s_u^{η}. Equivalently, the required partial factor γ_{su} is equal to $s_u^{\eta}/s_{u,k}$.

Table 2. Ranges of the design parameters selected for code calibration.

Parameter	Description	Range
B	Foundation width	[2 m, 4 m]
μ_{su}	Mean value of s_u	[25 kN/m^2, 200 kN/m^2]
δ_{su}	COV of s_u	[0.1, 0.7]
L	Mean value of L	–
r_{QL}	Live to dead load ratio = μ_Q/μ_L	[0.1, 1.0]
α	Average inclination angle of the variable $\tan^{-1}(\mu_{Qh}/\mu_{Qv})$	[0°, 40°]

Because s_u is assumed to be lognormally distributed, γ_{su} can be expressed as:

$$\gamma_{s_u} = \frac{s_u^{\eta}}{s_{u,k}} = \exp\left[\sqrt{\ln\left(1+\delta_{s_u}^2\right)} \times \Phi^{-1}(\eta)\right] \Big/ \sqrt{1+\delta_{s_u}^2} \tag{6}$$

It is critical to note that the resulting partial factor γ_{su} depends on the COV of s_u (δ_{su}) of the future design case, i.e. γ_{su} depends on the site investigation efforts of the future design case.

Table 3 shows the calibrated γ_{su} for the constant PF method and the calibrated η for QVM with target reliability index β_T = 3.2. Note that the partial factors γ_L = 1.1, γ_{Qv} = 1.5, and γ_{Qh} = 1.5 are not calibrated and are fixed at values suggested in structure codes.

3 COMPARISONS AMONG CODE FORMATS FOR A DESIGN IN A VIRTUAL SITE

3.1 *A clay virtual site*

Table 3 was calibrated over a wide range of design scenarios, not for a single design case. The purpose of this section is to examine which of the two codes performs better in linking site investigation efforts to final design savings for a specific design. In this section, site investigation efforts are varied systematically using the concept of a virtual site developed for clays by Ching & Phoon (2012a). This clay "virtual site" can produce consistent reduction in δ_{su} as a function of the type and number of field tests. The design goal of this design case is to determine the width B for a pad foundation in this virtual site to fulfill the target reliability index β_T = 3.2. The values of (μ_{su}, δ_{su}, μ_L, r_{QL}, α) for this specific design are summarized below: μ_L = 1000 kN, r_{QL} = 0.59, and α = 33.7°. The values of (μ_{su}, δ_{su}) depend on the site investigation efforts. The clay is assumed to be overconsolidated with OCR uniformly distributed between 5 and 24. Based on the above information, important soil parameters can be simulated.

Table 3. Calibrated γ_{su} for the constant PF method and calibrated η for constant QVM.

Calibrated γ_{su}				
Constant PF	Constant QVM	γ_L	γ_{Qv}	γ_{Qh}
γ_{su} = 0.331	η = 0.0083 $\gamma_{s_u} = \exp\left(\sqrt{\ln\left(1+\delta_{su}^2\right)} \times \Phi^{-1}(0.0083)\right) \Big/ \sqrt{1+\delta_{su}^2}$	1.1	1.5	1.5

The simulation is based on the graphical model developed in Ching et al. (2010) which is deemed to adequately model the correlations among (OCR, s_u, N_{60}, $q_T - \sigma_v$). The equations used in the simulation steps summarized below are taken from Eqs. (4), (10), and (15) in Ching et al. (2010):

a. Simulate a MCS sample of OCR from the uniform distribution over the interval [5, 24].
b. Simulate a $\ln(s_u)$ sample from the following equation:

$$\ln(s_u) = 0.64 \times \ln(OCR) + \ln(\sigma'_{v0}) - 0.874 + 0.237 \times Z_1 \quad (7)$$

where 0.237 is the standard deviation of the transformation uncertainty, and Z_1 is standard normal. The average vertical effective stress $\sigma'_{v0} = 2.3 \times 21.4 = 49.22$ kN/m^2.

c. Given the $\ln(s_u)$ sample from step (b), simulate a $\ln(N_{60})$ sample from the following equation:

$$\ln(N_{60}) = 1.633 \times \ln(s_u) - 0.403 \times \ln(\sigma'_{v0}) - 3.845 + 2 \times 0.456 \times Z_2 \quad (8)$$

where 2×0.456 is the transformation uncertainty, and Z_2 is standard normal.

d. Given the $\ln(s_u)$ sample from step (b), simulate a $\ln(q_T - \sigma_v)$ sample from the following equation:

$$\ln(q''_T) = \ln(s_u) + 2.54 + 0.34 \times Z_3 \quad (9)$$

where 0.34 is the transformation uncertainty, and Z_3 is standard normal.

e. Apply exponential to the $\ln(s_u)$, $\ln(N_{60})$, and $\ln(q_T - \sigma_v)$ samples to get the (s_u, N_{60}, $q_T - \sigma_v$) samples.

Repeat the above steps for $n = 10^6$ times to obtain $n = 10^6$ samples of (OCR, s_u, N_{60}, $q_T - \sigma_v$).

A variety of site investigation efforts are produced by systematically changing: (1) the number of test types and (2) the test precision. Four scenarios are considered for the number of test types: (T1) only the range of N_{60} is known; (T2) the ranges for N_{60} and $q_T - \sigma_v$ are both known; (T3) the ranges for N_{60} and OCR are both known; and (T4) the ranges for N_{60}, $q_T - \sigma_v$, and OCR are all known. Scenario T1 is considered as the basic case with the least effort, while T4 contains the most information in terms of number of test types. Five scenarios (P0 to P4) are considered for test precision. The ranges in Table 4 represent the bounds for OCR, N_{60}, and $q_T - \sigma_v$ based on the assumption that more precise information on each test type measurement is available perhaps by increasing the number of tests and boreholes. For instance, P0 means no site-specific tests are conducted and information bounds are purely estimated from general literature appropriate for "clay". This scenario is the cheapest, because no site investigation is conducted. P4 means that sufficiently extensive tests are conducted to narrow the ranges. There are 20 possible scenarios for site investigation efforts in terms of number of test types and precision of information measured. For instance, the scenario T2-P1 means two test types are available (N_{60} and $q_T - \sigma_v$) and the information for each test type is known with reasonable precision, $N_{60} = 3$~18 and $q_T - \sigma_v = 730$~2040 kN/m^2. Samples of (OCR, s_u, N_{60}, $q_T - \sigma_v$) have been simulated from the virtual site using the procedure presented in the previous section. Based on the information bounds for a given scenario, the conditional samples of s_u can be easily obtained. For example, in the case of T2-P1, samples satisfying $N_{60} = 3$~18 and $q_T'' = 730$~2040 kN/m^2 simultaneously can be filtered out from the population at large. The s_u values associated with this filtered set are therefore the conditional s_u samples. In this study, the number of conditional samples is chosen to be $n = 10^6$ for all 20 scenarios. Table 5 lists the statistics of the conditional s_u samples, including conditional mean and conditional COV. It is clear that μ_{su} and δ_{su} indeed depend on the site investigation efforts and that δ_{su} decreases with increasing site investigation efforts.

Table 4. The information bounds for various precision scenarios.

	Precision scenario	Information bounds based on site investigation		
		OCR	N_{60}	q_T'' (kN/m^2)
P0	Zero precision	[1, 50]	[0, 100]	[200, 6000]
P1	Poor precision	[5, 25]	[3, 18]	[730, 2040]
P2	:	[7.5, 16.7]	[5, 12]	[940, 1580]
P3	:	[8.5, 14.6]	[6, 10]	[1030, 1450]
P4	Excellent precision	[9.5, 13.1]	[7, 9]	[1100, 1350]

3.2 *Rigorous RBD for virtual site*

The rigorous RBD can be taken to determine the required width B under each scenario that exactly achieves the target reliability β_T. This can be easily done by MCS—based on the $n = 10^6$ conditional samples of s_u for each scenario and $n = 10^6$ independent sets of samples of (L, Q_v, Q_h), one can solve for B such that $P[g(X,B)<0] = P[q_u \times B^2 - L - Q_v - W_p < 0] = \Phi(-\beta_T)$. Table 5 shows the required B for rigorous RBD. It is clear that the required B reduces from 3.33 m for P0 (zero site investigation effort) to 2.84 m for T4-P4 (significant effort). Site investigation efforts can be perfectly linked to final

Table 5. Statistics of conditional s_u samples under various scenarios.

	Conditional mean in kPa (conditional COV) (final design dimension for rigorous RBD)			
	T1	T2	T3	T4
P0		115.8 (0.35) (3.33 m)		
P1	111.3 (0.32) (3.21 m)	107.3 (0.27) (3.04 m)	111.3 (0.32) (3.21 m)	107.3 (0.27) (3.03 m)
P2	111.4 (0.31) (3.19 m)	105.7 (0.25) (2.94 m)	102.4 (0.25) (3.02 m)	100.4 (0.21) (2.87 m)
P3	111.3 (0.31) (3.16 m)	105.5 (0.24) (2.91 m)	99.9 (0.24) (2.98 m)	99.0 (0.20) (2.81 m)
P4	112.0 (0.31) (3.17 m)	105.3 (0.24) (2.88 m)	99.5 (0.23) (2.93 m)	98.1 (0.19) (2.84 m)

Table 6. Final design dimensions (deviation in B to the rigorous RBD)/β_A for the constant PF method.

	T1	T2	T3	T4
P0		3.61 m (0.28 m)/3.72		
P1	3.68 m (0.47 m)/4.14	3.75 m (0.71 m)/4.75	3.68 m (0.47 m)/4.10	3.75 m (0.72 m)/4.75
P2	3.68 m (0.49 m)/4.16	3.78 m (0.84 m)/4.75	3.84 m (0.82 m)/≥4.75*	3.88 m (1.01 m)/≥4.75*
P3	3.68 m (0.52 m)/4.16	3.78 m (0.87 m)/≥4.75*	3.88 m (0.90 m)/≥4.75*	3.90 m (1.09 m)/≥4.75*
P4	3.67 m (0.49 m)/4.16	3.78 m (0.90 m)/≥4.75*	3.89 m (0.96 m)/≥4.75*	3.92 m (1.08 m)/≥4.75*

Table 7. Final design dimensions (deviation in B to the rigorous RBD)/β_A for the QVM.

	T1	T2	T3	T4
P0		3.21 m (–0.12 m)/2.96		
P1	3.14 m (–0.07 m)/3.05	3.02 m (–0.02 m)/3.16	3.14 m (–0.07 m)/3.04	3.01 m (–0.02 m)/3.16
P2	3.10 m (–0.08 m)/3.04	2.94 m (–0.00 m)/3.20	3.02 m (0.00 m)/3.21	2.89 m (0.02 m)/3.26
P3	3.10 m (–0.06 m)/3.08	2.92 m (0.01 m)/3.22	2.99 m (0.01 m)/3.21	2.84 m (0.03 m)/3.28
P4	3.08 m (–0.09 m)/3.01	2.91 m (0.03 m)/3.27	2.97 m (0.03 m)/3.29	2.84 m (0.00 m)/3.21

design savings rationally using the rigorous RBD. However, practicing engineers may not be comfortable with the rigorous RBD. The design table in Table 3 developed by the two simplified RBD methods is more likely to be used in practice.

3.3 *Constant PF*

Table 6 shows the required width B based on the calibrated partial factor $\gamma_{su} = 0.331$ given in Table 3. To find the required B for each information scenario, one only needs to solve Eq. (4) for B with

$\gamma_{su} = 0.331$, $\mu_L = 1000$ kN, $r_{QL} = 0.59$, and $\alpha = 33.7°$. The mean undrained shear strength, μ_{su}, is extracted from Table 5 for each information scenario. Note that δ_{su} in Table 5 is not used in the constant PF method. The discrepancy between the required B determined by the constant PF method and the one determined by the rigorous RBD shown in Table 5 is listed in the parenthesis (·). If all discrepancies are small, the constant PF method is nearly as effective as the rigorous method in linking the site investigation efforts to design outcomes, and vice versa. Another way of verifying the effectiveness is to find the actual reliability index β_A for each required B, which can be easily calculated by MCS with sample size $n = 10^6$. It is clear that the constant PF method is not very effective because the discrepancy in B is often large, and β_A often significantly deviates from the target value 3.2.

3.4 * *No failure sample in MCS with $n = 10^6$ QVM*

Table 7 shows the required width B based on the calibrated $\eta = 0.0083$ shown in Table 3. This probability threshold η was also calibrated for a wide range of design scenarios shown in Table 2. Note that the resulting partial factor is not a constant: for P0 ($\delta_{su} = 0.35$), $\gamma_{su} = 0.418$ is rather small due to the large COV, and for P4-T4 ($\delta_{su} = 0.19$), $\gamma_{su} = 0.626$ is large due to the small COV. The smaller deviation in B from the rigorous RBD shows that the QVM is more effective than the constant PF method. In fact, the required B shows the same trend as the rigorous RBD—the largest for P0 and the smallest for T4-P4. As a result, the actual reliability index β_A for the QVM method is more uniform and closer to the target value 3.2 than the constant PF method.

It is evident that the QVM behaves similarly to the rigorous RBD (the required B reduces with increasing site investigation efforts), indicating that the QVM is effective in linking the site investigation efforts to design savings. This is not an easy task at all—remember that Table 3 was NOT calibrated with respect to any specific design case with any particular site investigation effort but were calibrated with respect to a very wide range of design scenarios. The constant PF method cannot link the site investigation efforts to design savings at all. The inability to link to site investigation efforts is a severe disadvantage as it nullifies a strong practical motivation to adopt RBD in the first place.

4 CONCLUSIONS

It is well accepted that site investigation efforts may reduce the uncertainties in the design soil parameters. However, whether uncertainty reduction due to the site investigation efforts can be linked to final design savings using simplified Reliability-Based Design (RBD) methods has not been clarified in literature quantitatively with a sound theoretical basis. The link can be easily established using the rigorous RBD method, but practicing engineers are generally not comfortable with the rigorous RBD to date. The most widely adopted compromise in existing RBD codes is to use simplified methods containing reliability calibrated partial factors that have the same look and feel as the global factor of safety method.

According to the analysis results in this paper, such a link for simplified RBD methods is possible if: (a) the methods are sufficiently responsive to a wide range of geotechnical information, and (b) the mean and COV of the soil parameters are properly updated using appropriate correlation models and Bayesian analysis. It is concluded that the constant partial factor format that is adopted in many current codes (e.g. AASHTO and Eurocode 7) fails to establish this crucial link. The design method based on QVM seems to be able to link site investigation efforts to final design savings in a more effective way.

REFERENCES

British Standards Institute 2004. Eurocode 7: *Geotechnical Design—Part 1: General Rules*. BS EN 1997-1:2004, London.

Ching, J., Phoon, K.K. & Chen, Y.C. 2010. Reducing shear strength uncertainties in clays by multivariate correlations. *Canadian Geotechnical Journal* 47(1): 16–33.

Ching, J. & Phoon, K.K. 2011. A quantile-based approach for calibrating reliability-based partial factors. *Structural Safety* 33: 275–285.

Ching, J. & Phoon, K.K. 2012a. Value of geotechnical site investigation in reliability-based design. *Advances in Structural Engineering* 15(11): 1935–1945.

Ching, J. & Phoon, K.K. 2012b. Modeling parameters of structured clays as a multivariate normal distribution. *Canadian Geotechnical Journal* 49(5): 522–545.

Ching, J. & Phoon, K.K. 2013. Quantile value method versus design value method for reliability-based code calibration. *Structural Safety* 44: 47–58.

Eurocode 2011. Geotechnical design ETC10 Design Example 2.2. Pad foundation with inclined eccentric load on boulder. http://www.eurocode7.com/etc10/Example%202.2/index.html.

Sørensen, J.D. 2002. Calibration of partial safety factors in Danish Structural Codes. Workshop on Reliability Based Code Calibration. *Swiss Federal Institute of Technology*, ETH Zurich, Switzerland, March 21–22: 2002.

This page intentionally left blank

Geotechnical Safety and Risk IV – Zhang et al. (eds)
© 2014 Taylor & Francis Group, London, ISBN 978-1-138-00163-3

Reliability index of pile foundations designed to SANS 1016-5

M. Dithinde
Department of Civil Engineering, University of Botswana, Botswana

J.V. Retief
Department of Civil Engineering, University of Stellenbosch, South Africa

ABSTRACT: In accordance with international trends in development of geotechnical codes, South Africa has converted to limit state design philosophy through the publication of SANS 10160: 2010. Within this suite of standards, Part 5 (SANS 10160-5) is devoted to basis of geotechnical design and actions. Although SANS 10160 set of standards is formulated on the basis of reliability principles, the resistance partial factors prescribed in SANS 10160-5 were not developed on the basis of calibration studies but were adopted from the UK National Annex to EN 9197-1. In lieu of the calibration process, the critical question is what is the reliability index of piles design to SANS 1060-5? The paper uses resistance statistics from a comprehensive pile load tests database in conjunction with partial resistance factors and the model factor prescribed in SANS 10160-5 to compute reliability indices (β-values) for various pile classes designed to this code. It was found that the β values for all pile classes are above the target β of 3.0 for the reference class of structures as specified in SANS 10160-1 indicating that the resistance factors in SANS10160-5 adopted from BS EN1997-1 are conservative and uneconomical for Southern Africa.

1 INTRODUCTION

SANS 10160:2010 is essentially a loading code and presents the general principles, requirements for design of buildings and industrial structures in accordance with the limit state design approach in South Africa. The procedures are deemed to achieve acceptable levels of structural performance in terms of safety, functionality and economy. It consists of eight self-contained parts, each dealing with a specific action type. Accordingly SANS 10160-5 set out the basis of geotechnical design and gives guidance on the determination of geotechnical actions on buildings and industrial structures. The actions include vertical earth loading, earth pressure, ground water and free water pressure, as well as actions caused by ground movement. However, due to the absence of geotechnical limit state code in the country, SANS 10160-5 also provides guidance on geotechnical design aspects of structures within the scope of SANS 10160 including pile foundations.

Although SANS 10160-5 have the same basis and design format as that for structural parts, in general there is lack of analytical calibration and verification. The resistance partial factors for pile foundations have been adopted from BS EN1997-1. It is important to note that calibration of partial factors is dependent on local design practice, experience and environment such as local geology, soil type and conditions, site investigation practices (extend, methods, standards, equipment advances). Since these factors generally differ from one country to another, values developed for a specific country cannot be simply adopted by another country. The need to calibrate geotechnical resistance factors for different applications utilising local databases was further emphasised in a study to review developments of limit state design or LRFD methods in Canada, Germany, France, Denmark, Norway and Sweden (DiMaggio et al. 1999). For the same reason, EN1997-1 leaves the calibration of partial factors to individual countries.

In lieu of the calibration process, the critical question is what is the reliability index of pile foundations designed to SANS 1060-5? To answer this question, this paper uses resistance statistics from a comprehensive pile load tests database for Southern Africa (Dithinde et al. 2011) in conjunction with partial resistance factors and the model factor prescribed in SANS 10160-5 to compute reliability indices (β-values) for various pile classes designed to this code.

2 PILE DESIGN TO SANS 10160-5

2.1 *Design approach adopted by SANS 10160-5*

EN 1997-1 provides three design approaches for design of substructures or structural

members involving geotechnical actions. These are: (a) Design Approach 1, (b) Design Approach 2, and (c) Design Approach 3. These three design approaches differ in the way they distribute the partial factors on actions and ground resistances/properties. The attributes of the three design approaches have been discussed by many commentators (e.g., Driscoll & Simpson 2001, Orr 2002, Orr 2006, Frank 2002, Schuppener & Frank 2006). The selection of a particular design approach is a matter for national determination. Accordingly SANS10160-5 has selected Design Approach 1 for two main reasons (Day & Retief 2009): (i) partial factors are applied directly to the source of uncertainty (i.e. actions, calculation models, and material properties), (ii) the results obtained using this approach agree reasonably with the current South African practice based on the overall factor of safety approach.

2.2 *Pile design methods and procedure*

SANS 10160-5 recognises that piles can be designed using one of the following methods: (i) Full scale pile load tests, (ii) Empirical analysis by directly using standard field tests results (e.g. SPT and CPT), (iii) Static analysis using engineering properties of the soil as determined from laboratory or in-situ field testing and (iv) Dynamic driving resistance (Pile driving formulae and Wave equation). In contrast to EN 1997-1 in which the predominant pile design methods are the full scale pile load tests and empirical methods, the main design method in SANS10160-5 is the static analysis. Accordingly the analysis presented in this paper is based on the static analysis.

The static analysis entails directly determining the characteristic base resistance (q_{bk}) and shaft resistance (q_{sk}) using the static formula. Hence the characteristic resistance ($R_{c,k}$) is given by:

$$R_{c,k} = R_{b;k} + R_{s;k} \tag{1}$$

The design resistance (R_d) then given by:

$$R_d = R_k/\gamma_M\gamma_t \tag{2}$$

The design load (F_d) is given by:

$$F_d = \gamma_G \cdot G_k + \gamma_Q \cdot Q_k \tag{3}$$

where γ_M is the model factor, γ_t is the relevant resistance partial factor from Table 1, γ_G is the permanent action partial factor, G_k is the characteristic permanent action, γ_Q is the partial factor on variable action and Q_k is the characteristic variable action.

The partial factors to be used in Eqs. 2–3 are presented in Table 1. It is important to note that values of the partial factors presented in Table 1 were developed for application in conjunction with the correlation actors (ξ). Accordingly these partial factors are not sufficiently large to be used alone in the analytical approach. Therefore for the static analysis method, the partial factors need to be corrected by a model factor (γ_M) larger than 1. In this regard SANS 10160-5 recommend a model factor of 1.5.

Table 1. Partial factors for pile foundations.

Parameters	Limit states			
1. Partial factors for actions	STR	STR-P	GEO	
Permanent (unfavourable)	1.2	1.35	1.0	
Variable (unfavourable)	1.6	1.0	1.3	
Permanent (favourable)	0.9	0.9	1.0	
Variable (fafourable)	0	0	0	
2. Partial material factors			*	**
Shearing resistance (tanϕ)	1.0	1.0	1.0	1.25
Effective cohesion (c)	1.0	1.0	1.0	1.25
Undrained strength (c_u)	1.0	1.0	1.0	1.4
Weight density (γ)	1.0	1.0	1.0	1.0
3. Partial resistance factors				
Compression piles	1.0	1.0	1.6	
Tension piles	1.25	1.25	1.7	

*Applies for the resistance of piles and anchors.
**Applies for unfavourable actions on piles owing to negative skin friction or lateral loading.

Furthermore, in accordance with Design Approach 1, two combinations need to be considered as follows:

Combination 1 (STR/STR-P)
The design resistance (R_d) is:

$$R_d = R_k/\gamma_M\,\gamma_t = R_k/1.5 \times 1.0 = R_k/1.5$$

Combination 2 (GEO)

$$R_d = R_k/\gamma_M\,\gamma_t = R_k/1.5 \times 1.6 = R_k/2.4.$$

3 RELIABILITY ANALYSIS

3.1 *Performance function and basic design variables*

In accordance with the algorithm for the computations of reliability index β, the first step is the formulation of the performance function. In this regard the limit state function is given by:

$$R - D - L = 0 \tag{4}$$

where R, D, and L are random variables defined as follows: R = measured resistance; D = measured permanent load and; L = measured variable load.

Usually the measured load and resistance are presented in terms of their respective predicted values and mean model factors as follows:

$$R = M_R R_n;\ D = M_D D_n;\ L = M_L L_n \tag{5}$$

where: M_R = mean model factor for resistance, M_D = mean model factor for dead load, M_L = mean model factor for live load and the other symbols are as previously defined.

Substituting Eq. 5 into Eq. 4, the performance function becomes:

$$M_R R_n - M_D D_n - M_L L_n = 0 \tag{6}$$

In Eq. 6, M_R, M_D, and M_L are now the random variables following specific probability distributions while R_n, D_n, and L_n are deterministic values.

3.2 *Load and resistance statistics and their probability models*

In reliability index computations for the performance function in Eq. 6, the statistics (mean, standard deviation and coefficient of variation) as well as the type of distribution that best fit the load and resistance are required. With regard to load statistics, values assumed in the previous South African loading code (SABS 0160:1988) reported by Kemp et al. (1987) were adopted and reproduced here as Table 2. The distribution followed by each load type is also shown.

The resistance statistics based on a pile load test database from the Southern African geological setting and pile design practice reported by Dithinde & Retief (2013) have been adopted and are presented in Table 3. The complete set of 174 cases was further classified in terms of four theoretical principal pile design classes based on both soil type and installation method. These fundamental set of classes include: (i) Driven piles in Non-Cohesive soil (D-NC) with 29 cases, (ii) Bored pile in Non-Cohesive soil (B-NC) with 33 cases; (iii) Driven piles in Cohesive soils (D-C) with 59 cases, and (iv) Bored pile in Cohesive soils (B-C) with 53 cases. These principle four data sets were further combined into various practical pile design classes considered in design codes such as SANS 10169-5:2011 and EN 1997-1:2004. The additional classification schemes include:

1. Classification based on pile installation method irrespective of soil type. This is the classification adopted in EN 1997-1:2004 and it yields: 87 cases of driven piles (D) and 83 cases of bored piles (B).
2. Classification based on soil type. This classification system is supported by the general practice where a higher factor of safety is applied to pile capacity in clay as compared to sand. This combination results in 58 cases in Non-Cohesive soil (NC) and 112 cases in Cohesive soil (C).
3. All pile cases as a single data set irrespective of pile installation method and soil type. This is the practical consideration presented in SANS 10160-5:2011 where a single partial factor is given for all compressive piles. The scheme yields 174 pile cases (ALL).

Table 2. Load statistics (Kemp et al. 1987).

Type of load	Code	Mean load/ nominal load	Coefficient of variation	Type of distribution
Permanent load	SABS 0160	1.05	0.10	Lognormal
Live (office): lifetime max.	SABS 0160	0.96	0.25	Type 1

Table 3. Resistance statistics (after Dithinde & Retief 2013).

M	n	Mean (m)	Std. dev (s_M)	COV	Skewness	Kurtosis
D-NC	28	1.11	0.36	0.33	0.35	–1.15
B-NC	30	0.98	0.23	0.24	0.14	–0.19
D-C	59	1.17	0.3	0.26	–0.01	–0.74
B-C	53	1.15	0.28	0.25	0.36	0.49
D	87	1.15	0.32	0.28	0.1	–0.95
B	83	1.09	0.28	0.25	0.41	0.47
NC	58	1.04	0.30	0.29	0.55	–0.37
C	112	1.16	0.29	0.25	0.15	–0.29
ALL	170	1.1	0.31	0.28	0.24	–0.75

Based on the analysis carried by Dithinde & Retief (2013), a lognormal distribution was adopted for resistance. The analysis concluded that although at the customary 5% confidence level, the chi-square goodness-of-fit test results indicate that both the Normal and Lognormal distributions are valid, the Lognormal distribution has a slight edge, particularly towards the lower tail.

3.3 *Limit state design equation*

To facilitate the computation of reliability index using the spreadsheet, the limit state design equation in addition to the performance function is required. As already alluded to, limit state design approach entails applying partial factors to both the actions and resistance. Accordingly, the design equation is given by:

$$\frac{R_k}{\gamma_R \gamma_M} = \gamma_G G_k + \gamma_Q Q_k \tag{7}$$

where R_k = characteristic predicted pile capacity; γ_R = partial resistance factor; γ_M = model factor; G_k = characteristic permanent action; γ_G = partial factor for permanent action; Q_k = characteristic variable action; and γ_Q = partial factor for variable action.

For the GEO limit state, the values of γ_G, γ_Q, γ_R, and γ_M are 1.0, 1.3 and 1.6, and 1.5 respectively. Therefore Eq. 7 becomes:

$$\frac{R_k}{1.6x1.5} = 1.0G_k + 1.3Q_k \tag{8}$$

For simplicity the calculation was done in the load space which entails expressing L_n in terms of D_n. By so doing, it is not necessary to deal specifically with pile diameter and length as design situations are now represented by the L_n/D_n ratio. When L_n is expressed in terms of D_n, Eq. 8 becomes:

$$\frac{R_k}{2.4} = G_k\left(1 + \frac{1.3Q_k}{G_k}\right) \tag{9}$$

From Eq. 9, the expressions for G_k and Q_k are as follows:

$$G_k = \frac{R_k}{2.4\left(1 + 1.3Q_k/G_k\right)} \tag{10}$$

$$Q_k = \frac{1}{1.3}\left(\frac{R_k}{2.4} - G_k\right) \tag{11}$$

The design equation, the performance function, and the load and resistance statistics were then set on a spread sheet to compute β for the various pile classes. As already mentioned, the calibration points were defined by the L_n/D_n ratio. Typical range of L_n/D_n ratios are 0.5–1.5 for concrete structures and 1–2 for steel structures (Melchers 1999). Based on this information, a practical range of L_n/D_n ratio of 0.5 to 2 was adopted.

Reliability index β computations were carried out using an excel spread sheet developed by Low & Tang (2007).

4 RESULTS AND DISCUSSIONS

β values were sensitive to the variation in L_n/D_n ratio and not the variation in the nominal resistance, implying that the calibration points are only defined by the L_n/D_n ratio. Accordingly beta values were calculated for a range of L_n/D_n ratio. The resulting β values for the GEO limit state as a function of the L_n/D_n ratio are shown in Figure 1.

Further analysis of Figure 1 indicates that:

The shapes of the curves follow a characteristic pattern in which for permanent load dominated structures (i.e. $L_n/D_n < 1$), β values increase with the increase in the L_n/D_n ratio. Conversely as live loads become significant (i.e. $L_n/D_n > 1$), β values decreases with the increase in the L_n/D_n ratio. The scenario is caused by loading and in SANS 10160 it has been accounted for by the introduction of STR-P (see Table 1) to cater for permanent load dominated structures.

The β values vary with pile classes as well as with individual cases represented by the L_n/D_n ratios within the same pile class. This suggests that despite that SANS 10160-5 provides a single resistance partial factor and model factor for all the pile classes, it does not produce a consistent level of reliability across different design situations and even within the same design situation. This scenario is not surprising as the partial factors prescribed in SANS10160-5 were not determined on the basis of reliability calibration capturing the distinct soil types for the geologic region of Southern Africa as well as the local pile design and construction experience base.

Piles in cohesive materials (D-C, B-C, and C) depict higher reliability irrespective of installation method compared to piles in non-cohesive materials (D-NC, B-NC, and NC). The scenario is attributed to the variability exhibited by piles in non-cohesive materials as demonstrated by standard deviations or coefficient of variations in Table 3. Dithinde & Retief (2013) attributed the scenario to the fact that in cohesive materials the undrained shear strength derived from the SPT measurement is directly used in the computation of pile capacity while in non-cohesive materials,

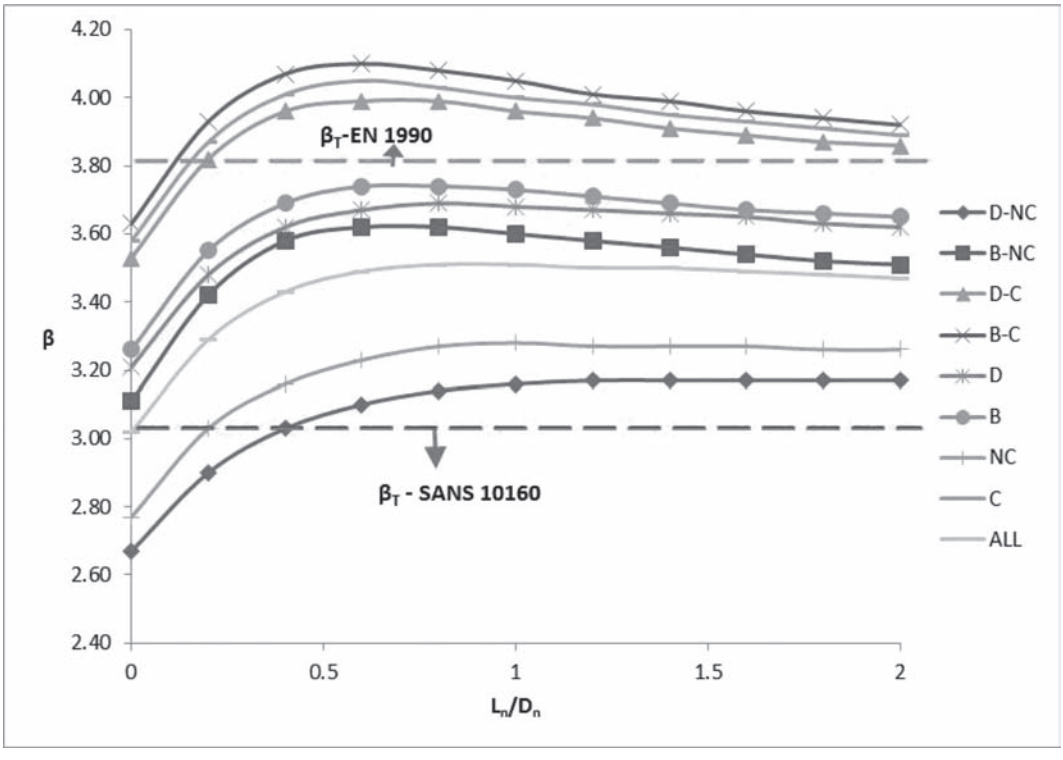

Figure 1. Variation of beta values with L_n/D_n ratio.

the angle of friction obtained from the SPT measurement is not directly used. Instead the key pile design parameters in the form of bearing capacity factor (N_q), earth pressure coefficient (k_s) and pile-soil interface friction (δ) are obtained from the derived angle of friction on the basis of empirical correlation and thus introducing some additional uncertainties.

With piles in none-cohesive soils, there is a significant difference in β values between bored and driven piles. In this regard β values for bored piles are higher than that for driven piles. Again this attributed to the higher uncertainty depicted by driven piles relative to bored piles presented in Table 3. Dithinde & Retief (2013) further explains that this implies that the densification of the soil surrounding the pile emanating from the pile driving process is not well captured in the selection of the soil design parameters and hence current practice is conservative in selecting design parameters for driven piles.

Comparing β values for all piles in Cohesive materials (C) versus all piles in Non-Cohesive (NC), shows distinctively different level of reliability suggesting the two broad classes based on soil type should be treated separately in calibration studies. Nonetheless, the relatively lower β values depicted by NC are mainly due to the data set from D-NC which has the lowest β. It appears that D-NC significantly diverges from the rest of the dataset and therefore warrants further investigations in future studies.

A comparison of all Bored (B) versus all Driven (D) piles irrespective of soil type indicates very little difference in terms of β values. This suggests that pile installation method has little influence on β values. Therefore from reliability perspective, pile design should be classified on basis of soil only. This further implies that resistance partial factors and model factors should be differentiation on basis of soil properties. Further differentiation into pile installation method is just a refinement and elaboration.

Generally the β values for all pile classes are above the target β of 3.0 for the reference reliability class R2 for which reliability procedures are specified in SANS 10160. When taking into account the redundancy due to group and system effects, the β values will increase appreciably. Therefore for pile groups (which is the common practice), SANS 10160-5 yields β values that are significantly higher than the target β of 3.0 for class R2. Conversely,

in exception of piles in cohesive materials β values for all other pile classes are below target β of 3.8 for the reference class of structures as specified in EN 1990. Even for piles in cohesive materials, the β values are quite close to that target β in EN1990. Perhaps this is an indication that the resistance factors in SANS10160-5 adopted from BS EN1997-1 are conservative and uneconomical for Southern Africa. Even with Eurocodes, the determination of levels of safety, including aspect of durability and economy remains within the competence of individual member states. Therefore it appears that in implementation of limit state design, local calibration studies are inevitable.

5 CONCLUSIONS

Using resistance statistics generated from local pile load tests, load statistics from the previous South African loading code (SABS 0160), and partial factors prescribed in SANS10160-5 the paper evaluated reliability indexes of pile foundations designed to SANS10160-5. The key conclusions drawn from the analyses and discussions are as follows:

1. SANS10160-5 does not achieve a consistent level of reliability as β values vary with pile classes as well as with individual cases represented by the L_n/D_n ratios within the same pile class. This is attributed to lack of rigorous calibration of partial factors capturing the distinct soil types for the geologic region of Southern Africa as well as the local pile design and construction experience base.
2. The obtained β values are influenced by the soil type and not pile installation methods. This implies that resistance partial factors and model factors should be differentiated on basis of soil properties.
3. β values for all pile classes are above the target β of 3.0 for the reference class of structures as specified in SANS 10160-1. If redundancy due to group and system effects is accounted for, the β values will become significantly higher than the target β of 3.0 indicating that the resistance factors in SANS10160-5 adopted from BS EN1997-1 are conservative and uneconomical for Southern Africa. Therefore it appears that in implementation of limit state design, local calibration studies are inevitable.

REFERENCES

Day, P.W. & Retief, J.V. 2009. *Provision for geotechnical design in SANS10160. Background to SANS 10160*. SunMedia, Stellenbosch.

DiMaggio, J., Saad, T., Allen, T., et al. 1999. *Geotechnical engineering practice in Canada and Europe*. Report No. FHWA–PL-99-013, Federal Highway Adminstration, Washington, DC.

Dithinde, M., Phoon, K.K., De Wet, M., et al. 2011. Characterization of model uncertainty in the static pile design formula. *Journal of Geotechnical and Geoenvironmental Engineering* 137(1): 70–85.

Dithinde, M. & Retief, J.V. 2013. Pile design practice in southern Africa I: Resistance statistics. *Journal of the South African Institution of Civil Engineering* 55(1): 60–71.

Driscoll, R. & Simpson, B. 2001. EN 1997 Eurocode 7: Geotechnical design. *Proceedings of ICE*.

EN 1997: 2004. *Eurocode 7: geotechnical design—Part 1: General rules*. European Committee for Standardization (CEN), Brussels.

Frank, R. 2002. Development and feature of Eurocode 7—Geotechnical design. *Proc. of Foundation Design Codes and Soil Investigation in View of International Harmonization and Performance-Based Design, Kamakura, Japan.*

Holický M. 2009. *Reliability analysis for structural design.* Stellenbosch: SUNMeDIA Press.

Kemp, A.R., Milford, R.V. & Laurie, J.P.A. 1987. Proposal for a comprehensive limit states formulation for South African structural codes. *The Civil Engineer in South Africa* 29(9): 351–360.

Low, B.K. & Tang, W.H. 2007. Efficient spreadsheet aligirithm for FORM. *Journal of Engineering Mechanics* 133(12): 1378–1387.

Melchers, R.E. 1999. *Structural reliability: Analysis and prediction*. Chichester, New York: John Wiley & Sons.

Orr, T.L.L. 2002. Selection of characteristic values and partial factors in geotechnical designs to Eurocode 7. *Computers and Geotechnics* 26(3–4): 263–279.

Orr, T.L.L. 2006. Development and implementation of Eurocode 7. *Proc. of the International Symposium on New Generation Design Code for Geotechnical Engineering Practice, Taipei, Taiwan.*

SANS 10160-5:2010. *Basis of structural design and actions for buildings and industrial structures—Part 5: Basis for geotechnical design and actions.* SABS Standards Division, Pretoria.

Schuppener, B. & Frank, R. 2006. Eurocode 7 for geotechnical design—basic principles and implementation in the European member states. *Proc. of the International Symposium on New Generation Design Code for Geotechnical Engineering Practice, Taipei, Taiwan*.

Geotechnical Safety and Risk IV – Zhang et al. (eds)
© 2014 Taylor & Francis Group, London, ISBN 978-1-138-00163-3

Codified reliability-based design of shallow foundations in Shanghai

J.P. Li
Department of Geotechnical Engineering, Tongji University, Shanghai, China

S.N. Liu & S.N. Hou
Shanghai Xiandai Architectural Design Co., Ltd., Shanghai, China

J. Zhang
Department of Geotechnical Engineering, Tongji University, Shanghai, China

ABSTRACT: As part of the worldwide efforts for implementing reliability-based design in geotechnical engineering, Shanghai also calibrated the resistance factors for design of shallow foundations using reliability theory. This paper introduces how the resistance factors are determined in Shanghai. A typical shallow foundation is assumed to be constructed on 142 sites in Shanghai. The mean values of cohesion and friction angle are determined based on the site-specific data. The Coefficients Of Variation (COV) of the cohesion and friction angle are determined based on regional experience considering variance reduction due to spatial correlation of soil properties. The first order reliability method is then used to determine the partial factors for each site. It is found that if the notional Factor Of Safety (FOS) is 2.5, the reliability indexes of the 142 foundations are in the range of 2.3–4.2 with a mean of 3.35. If the target reliability index is 3.35, the partial factor for cohesion for the 142 sites have a mean of 2.76 and a standard deviation of 0.32, and the partial factor for friction angle has a mean of 1.17 and a standard deviation of 0.07. It is then recommended that the partial factors for cohesion and friction angle be 2.7 and 1.2, respectively. The adopted partial factors produce design bearing capacity predictions consistent with local experience.

1 INTRODUCTION

Although the global Factor Of Safety (FOS) method has been successfully used for many years, its disadvantage is obvious in that it does not explicitly consider the level of uncertainty involved in a design. As a result, designs with the same FOS may in fact correspond to different levels of safety. To overcome the disadvantage of the global FOS method, probabilistic methods can be used to model uncertainty explicitly, through which the safety in a design can be controlled by limiting the chance of unsatisfactory performance to a sufficiently low level. In the past decades, extensive researches have been conducted to develop partial factors for design of foundations based on the reliability theory (e.g., Barker et al. 1991; McVay et al. 2000; Honjo et al. 2002; AASHTO 2004; Paikowsky et al. 2004; Foye et al. 2009; Zhang et al. 2009a,b; Zhang & Chu 2009a, 2009b).

As part of the worldwide efforts for implementing reliability-based design in geotechnical engineering, the resistance factors for design of shallow and deep foundations were also calibrated in Shanghai, China using the reliability theory with a semi-empirical procedure when revising the local foundation design code (SUCCC, 2010). The objective of this study is to introduce how the resistance factors in Shanghai are determined for design of shallow foundations. This paper is organized as follows. First, the local bearing capacity prediction model is introduced. Then, the methodology for partial factors calibration is described. Finally, the calibration results are interpreted, analyzed, and verified with previous experience.

2 BEARING CAPACITY MODEL

Experience in Shanghai indicates that Hassan's bearing capacity model (Hassan, 1970) can often produce bearing capacity predictions with reasonable accuracy. Thus, the bearing capacity is often calculated based on the Hassan model adjusted with local field test data as follows (Li & Hou 2009)

$$R_u = 0.5\psi N_\gamma \zeta_\gamma \gamma B + N_q \zeta_q \gamma_0 D + \psi N_c \zeta_c c \qquad (1)$$

where B = width of the foundation (m); D = embedded depth of the foundation; c = cohesion of the soil (kPa); γ = effective unit weight of the soil beneath the foundation (kN/m^3); γ_0 = effective unit weight of the soil above the foundation bottom (kN/m^3); ζ_γ, ζ_q, ζ_c = shape factors; N_γ, N_q, N_c are bearing capacity factors; and Ψ = a model correction factor calibrated based on results from 38 field tests carried at Shanghai (Li & Hou 2009). The expressions for calculating Ψ, bearing capacity factors and shape factors are summarized as follows

$$\psi = \begin{cases} 0.9 & \varphi \le 20^0 \\ 0.053\varphi - 0.166 & 20^0 < \varphi \le 32^0 \end{cases} \tag{2}$$

$$N_q = 2.0 \sim 3.0 \tag{3}$$

$$N_c = \left[e^{\pi \tan\varphi} \tan^2\left(45° + \frac{\varphi}{2}\right) - 1 \right] \cot\varphi \tag{4}$$

$$N_\gamma = 1.5\left[e^{\pi \tan\varphi} \tan^2\left(45° + \frac{\varphi}{2}\right) - 1 \right] \tan\varphi \tag{5}$$

$$\zeta_\gamma = 1.0 - 0.4B/L \tag{6}$$

$$\zeta_q = 1.0 + B\sin\varphi/L \tag{7}$$

$$\zeta_c = 1.0 + 0.2B/L \tag{8}$$

where L = width of the foundation (m) and φ = friction angle of the soil (°).

3 DESIGN EQUATION

Supposing only live and dead loads are present, the limit state function in the foundation design problem can be written as follows

$$R_u - S_L - S_D = 0 \tag{9}$$

where S_L = live load; and S_D = dead load. In the above equation, the uncertain variables include c, φ, S_L, and S_D. For ease of presentation, we define $R_u(c, \varphi)$ as follows

$$R_u(c,\phi) = 0.5\psi N_\gamma \zeta_\gamma \gamma B + \psi N_c \zeta_c c + N_q \zeta_q \gamma_0 D \tag{10}$$

Substituting Eq. (10) into Eq. (9) yields

$$R_u(c,\phi) - S_L - S_D = 0 \tag{11}$$

The design equation can then be written as follows

$$R_u\left(\frac{c_n}{\gamma_c}, \frac{\varphi_n}{\gamma_\phi}\right) - \gamma_L S_{nL} - \gamma_D S_{nD} = 0 \tag{12}$$

where γ_c, γ_φ, γ_D, and γ_L = partial factors for c, φ, S_L, and S_D, respectively; and c_n, φ_n, S_{nL}, and S_{nD} = nominal values of c, φ, S_L, and S_D, respectively.

For an uncertain variable x, its nominal value x_n is often related to its mean value μ_x through the use of a bias factor λ_x as follows (e.g., Ang & Tang 1984)

$$x_n = \frac{\mu_x}{\lambda_x} \tag{13}$$

In Shanghai, the shear strength parameters are often measured using undrained direct shear tests. When the peak values of cohesion and friction angle of the soil measured in the undrained direct shear tests are reduced by 20%, the predictions from the bearing capacity model as introduced above are most consistent with the measured bearing capacity for a large number load tests in Shanghai (Li & Hou, 2009). Thus, for the design of shallow foundations, $\lambda_c = \lambda_\varphi = 1.25$ are adopted.

4 METHOD OF CALIBRATION

In principle, the partial factors of the foundation design can be calculated using the first order reliability method by comparing the coordinates of the design point with the nominal values of the random variables. One feature in geotechnical design is that, its load factors are pre-specified, which are usually different from those obtained directly based on reliability theory. According to the national design code in China (MHURD, 2002; MHURD, 2011), the load factors for design of foundations should be 1.0, i.e., $\gamma_L = \gamma_D = 1.0$. In such cases, the resistance factors obtained directly using the reliability theory cannot be straightforwardly used in geotechnical design.

In this study, reliability analysis is performed considering only c and φ as random variables. The values of partial factors of γ_L and γ_D are taken as 1.0. Thus, the limit state function in used in reliability analysis for calibrating resistance factors is as follows

$$R_u(c,\varphi) - S_{nD} - S_{nL} = 0 \tag{14}$$

Let c* denote the value of c at the design point. The partial factor for c can be determined using the following relationship

$$\gamma_c = \frac{c_n}{c^*} \tag{15}$$

γ_φ can also be determined using the same procedure.

Traditionally, shallow foundations are designed based on the global FOS approach. Let K denote the notional FOS adopted in a design as defined below

$$S_{nL} + S_{nD} = \frac{1}{K} R_{nu} \tag{16}$$

$$R_{nu} = R_u\left(c_n, \varphi_n\right) \tag{17}$$

Let ρ denote the ratio of live load to dead load,

$$\rho = \lambda_L / \lambda_D \tag{18}$$

Substituting Eq. (18) into Eqs. (16) and (17), the mean values of live and dead loads can be calculated as follows

$$S_{nD} = \frac{R_{nu}}{\left(1+\rho\right) K} \tag{19}$$

$$S_{nL} = \frac{\rho R_{nu}}{\left(1+\rho\right) K} \tag{20}$$

Given the values of c_n, φ_n, ρ and K, Eqs. (19) and (20) can be used to determine the values of S_{nD} and S_{nL} based on which the reliability index corresponding to a specific K can be found out using Eq. (14) as the limit state function. If one knows the target reliability index, one can adjust the values of S_{nD} and S_{nL} in Eq. (14) subjected to the constraints set by Eqs. (19) and (20) until the target reliability index is satisfied, which can then be used to determine the partial factors corresponding to the target reliability index.

To calibrate the resistance factors for design, consider a strip foundation with $B = 3$ m, $D = 1$ m. In Shanghai, the typical design FOS is $K = 2.5$. As the soil data may vary with site, the foundation is assumed to rest on 142 different sites in Shanghai to obtain a set of robust partial factors that can be generally used in Shanghai. At a site, while the mean values of soil properties are relatively easier to determine, the Coefficients Of Variation (COV) are much hard to estimate based on limited site-specific data. Thus, the mean values of the cohesion and friction angle take the site-specific values, and the COV values of the cohesion and friction angle take the regional values. In Shanghai, the COV of cohesion of the clay at shallow depths is in the range of 0.42–0.55, and the COV of the friction angle is in the range of 0.16–0.25 (Li & Gao 2001). For calibrating the resistance factors for regional design, the upper bound values of COV are adopted, which is on the conservative side. Considering the spatial correlation of the soil properties (Li & Gao, 2001), a variance reduction factor of 0.27 is applied to cohesion and friction angle. Thus, the COV values of the cohesion and friction angle adopted in the reliability analysis are 0.21 and 0.09, respectively. It is assumed that both cohesion and friction angle are lognormally distributed and statistically independent. Sensitivity analysis indicates that the calibrated partial factors are not sensitive to the value of ρ adopted, which is consistent with previous findings (Barker et al. 1991; McVay et al. 2000; Zhang 2004). In this study, $\rho = 0.2$ is adopted.

5 CALIBRATION RESULTS

5.1 *Current level of reliability and target reliability index*

Figure 1 plots the calculated reliability indexes and mean values of cohesion for the 142 sites. The reliability indexes are in the range of 2.3–4.2 with a mean of 3.35. For comparison, Phoon et al. (2003) reported that the reliability index of existing drilled shafts under compression to support transmission line structures in North America is in the range of 2.4–3.6. Figure 2 plots the calculated reliability indexes and mean values of friction angle for the 142 sites. Comparing Figures 1 and 2, there are less scatter in the relationship between reliability index and the friction angle, probably because the reliability indexes of the foundation are more affected by the friction angle.

The target reliability index is often determined with reference to the reliability index of existing buildings (e.g., Allen 1975; Phoon 2003) or

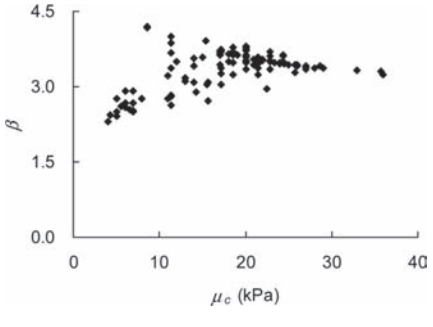

Figure 1. Relationship between cohesion and reliability index for the 142 sites.

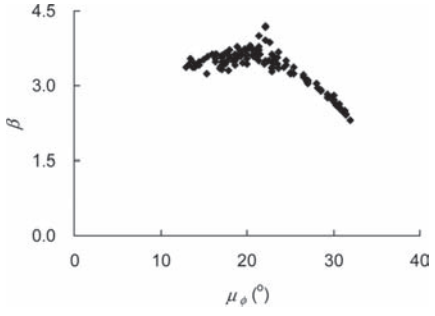

Figure 2. Relationship between friction angle and reliability index for the 142 sites.

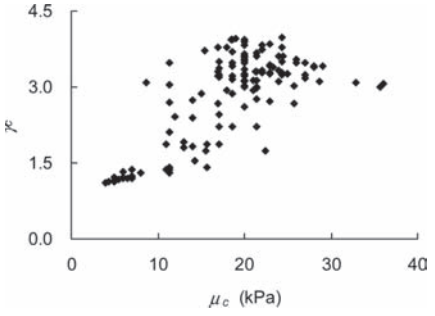

Figure 3. Relationship between γ_c and μ_c for the 142 sites.

with reference to experience in other regions. As the mean reliability index of the foundation at 142 sites is 3.35, 3.35 is taken as the target reliability index. Becker (1996) suggested the reliability index for design of shallow foundations against bearing capacity failure be 3.5.

5.2 *Recommendation of partial factors*

Figures 3 and 4 show the relationships between γ_c and μ_c and the relationship between the γ_φ and μ_c for the 142 sites, respectively. While γ_c tends to increase with the cohesion, γ_φ tends to decrease with the cohesion. This is deemed reasonable, since a larger cohesion implies increased importance of cohesion in foundation design, and hence a larger resistance factor should be applied to maintain the same level of safety. For comparison, Figures 5 and 6 show the relationships between the γ_c and μ_φ and the relationship between γ_φ and μ_φ, respectively. Comparing Figures 3–6, there are large scatter in the relationship between the resistance factors and the cohesion, probably because the relationship between cohesion and reliability index is more uncertain, as shown in Figure 1. It is attempting to suggest partial factors based on regression analysis of the data in Figures 5 and 6. However, considering the tradition of using fixed FOS and fixed partial factors in the profession, it is decided that fixed partial factors be used in design of shallow foundations.

Table 1 summarizes the statistics of the reliability indexes, γ_c and γ_φ of the shallow foundation when it is constructed at the 142 sites in Shanghai. The recommended resistance factors of γ_c and γ_ϕ in design are 2.7 and 1.2, respectively, which are close to their mean values.

5.3 *Verification of the recommended partial factors*

The national design code suggests the nominal value of the bearing capacity can be calculated using the following equation (MHURD, 2010):

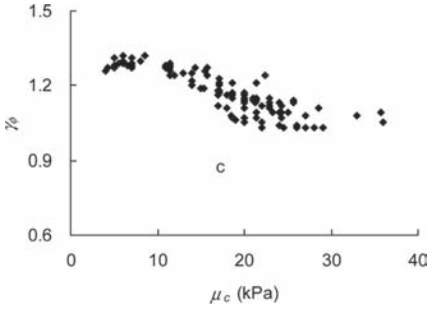

Figure 4. Relationship between γ_ϕ and μ_c for the 142 sites.

$$R_n = M_B \gamma B + M_D \gamma + M_c c \tag{21}$$

where M_B, M_D, and M_c are bearing capacity factors summarized in Table 2. In Eq. (21), B should be reduced to 6 m when the foundation width is larger than 6 m, and when the foundation is resting on the sandy ground, the value of B should be increased to 3 m if the foundation width is smaller than 3 m. In a design, it is required that R_n should not be smaller than the summation of the nominal live and load loads, i.e., $S_{nD} + S_{nL}$. Compared with the requirement indicated in Eq. (9), it indicates that the bearing capacity predicted using Eq. (10) using soil parameters factored with the calibrated partial factors should be comparable with that produced using Eq. (20). As a rule of thumb, the values c and φ used in a design are often 70% of their mean values when Eq. (21) is used in Shanghai for shallow foundation design.

Let R_{ns} denote the bearing capacity calculated using according to Shanghai code with cohesion and friction angle factored by the partial factors recommended in this study. Let R_{nn} denote the bearing capacity calculated according to the national code with cohesion and friction angle being 0.7 of their mean values. Figure 7 shows the values of R_{ns} and μ_φ for the 142 sites. The values of R_{ns} are in the range of 50–200 kN. As expected,

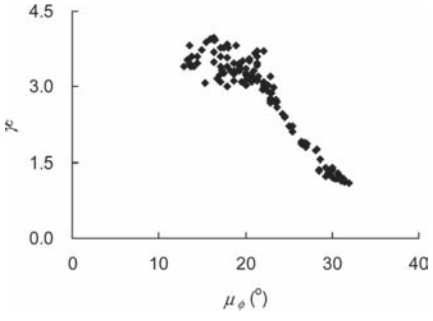

Figure 5. Relationship between γ_c and μ_ϕ for the 142 sites.

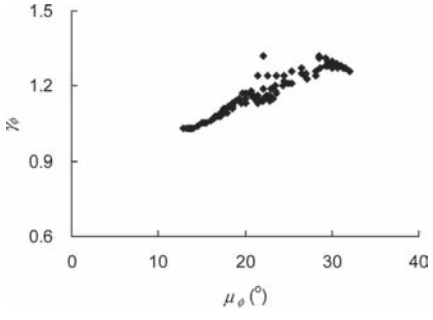

Figure 6. Relationship between γ_ϕ and μ_ϕ for the 142 sites.

Table 1. Summary of calibration results of the 142 sites.

	β	γ_c	γ_φ
Mean	3.35	2.76	1.17
COV	0.12	0.32	0.07

R_{ns} tends to increases with μ_φ. However, the relationship between R_{ns} and μ_φ is not unique because R_{ns} is also affected by the cohesion, which varies from sites to sites. Figure 8 shows the relationship between the notional FOS (i.e., K) and μ_φ for the 142 sites. The notional FOS values of the foundation at the 142 sites are in the range of 2.0–3.0, which is largely consistent with the local experience for adopting a K value of 2.5 in shallow foundation design. Figure 9 shows the relationship between R_{ns}/R_{nn} and μ_φ for the foundation at each site. When the mean friction angle is smaller than 20°, the predicted bearing capacity from the two approaches are largely consistent. When the friction angle is larger than 20°, the predicted bearing capacity based on Eq. (21) is larger. It is known that Eq. (21) tends to underestimate the bearing capacity when the soil has a larger friction angle (Li & Hou 2009).

Table 2. Values of bearing capacity factors recommended in MHURD (2002).

φ (°)	M_B	M_D	M_c
0	0	1	3.14
2	0.03	1.12	3.32
4	0.06	1.25	3.51
6	0.1	1.39	3.71
8	0.14	1.55	3.93
10	0.18	1.73	4.17
12	0.23	1.94	4.42
14	0.29	2.17	4.69
16	0.36	2.43	5
18	0.43	2.72	5.31
20	0.51	3.06	5.66
22	0.61	3.44	6.04
24	0.8	3.87	6.45
26	1.1	4.37	6.9
28	1.4	4.93	7.4
30	1.9	5.59	7.95
32	2.6	6.35	8.55
34	3.4	7.21	9.22
36	4.2	8.25	9.97
38	5	9.44	10.8
40	5.8	10.84	11.73

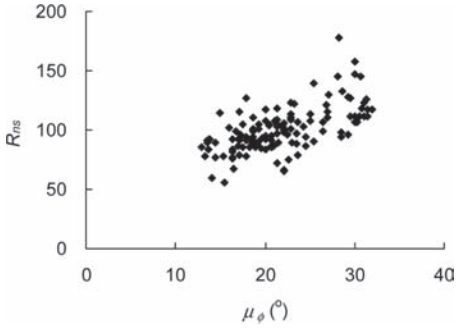

Figure 7. Relationship between R_{ns} and μ_φ for the 142 sites.

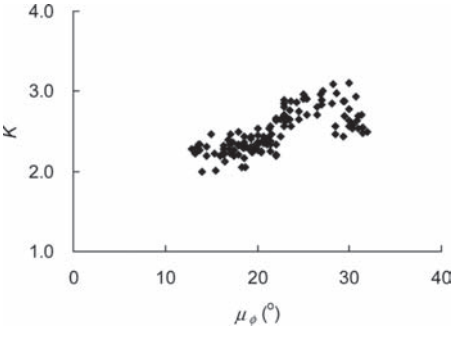

Figure 8. Relationship between K and μ_φ at the 142 sites.

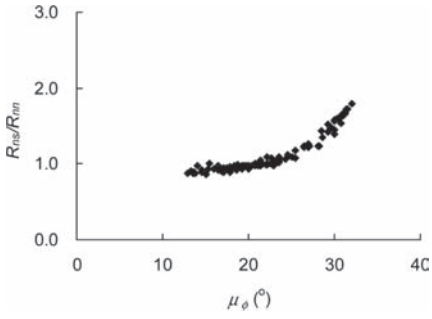

Figure 9. Relationship between R_{ns}/R_{nn} and μ_φ at the 142 sites.

6 SUMMARY AND CONCLUSIONS

The research reported in this paper can be summarized as follows:

1. The semi-empirical procedure adopted in calibrating partial factors for design of shallow foundation is described.
2. For the hypothetical shallow foundation, its reliability index is in the range of 2.3–4.2 when resting on 142 different sites at Shanghai.
3. To achieve a target reliability index of 3.35 and for the 142 sites considered, the partial factor for cohesion has a mean of 2.76 and a standard deviation of 0.32, and the partial factors for friction angle has a mean of 1.17 and a standard deviation of 0.07.
4. Adopting 2.7 and 1.7 respectively as partial factors for cohesion and friction angle can produce bearing capacity predictions consistent with local experience in Shanghai.

ACKNOWLEDEMENT

This research was substantially supported by the Natural Science Foundation of China (Project No. 41272288).

REFERENCES

AASHTO. 2004. *LRFD Bridge Design Specifications*, 3rd Ed. Washington, D.C.: American Association of State Highway and Transportation Officials.

Allen, D.E. 1975. Limit states design—a probabilistic study. *Canadian Journal of Civil Engineering* 2(1): 36–49.

Ang, A.H.-S. & Tang, W.H. 1984. *Probability concepts in engineering planning and design: design, risk and reliability,* Vol. 2. New York: Wiley.

Barker, R.M., et al. 1991. *Manuals for the Design of Bridge Foundations, NCHRP Report 343*. Washington, D.C.: Transportation Research Board, National Research Council.

Becker, D.E. 1996. Eighteenth Canadian geotechnical colloquium: limit states design for foundations. Part II: Development for the national building code of Canada. *Canadian Geotechnical Journal* 33(6): 984–1007.

Foye, K.C., Abou-Jaoude, G., Prezzi, M. & Salgado, R. 2009. Resistance factors for use in load and resistance factor design of driven pipe piles in sands. *Journal of Geotechnical and Geoenvironmental Engineering* 135(1): 1–13.

Hassen, J.B. 1970. *A revised and extended formula for bearing capacity*. Copenhagen: Danish Geotechnical Institute.

Honjo, Y., Suzuki, M., Shirato, M. & Fukui, J. 2002. Determination of partial factors for a vertically loaded pile based on reliability analysis. *Soils and Foundations* 42(5): 91–109.

Li, J.P. & Gao, D.Z. 2001. Study of Variable Behavior of Soil Index. *China Harbour Engineering*, 6: 26–30. (In Chinese).

Li, J.P. & Hou, S.N. 2009. Discussion on the formula of the ultimate bearing capacity of foundation in Shanghai region. *Journal of Geotechnical Investigation & surveying* 37(4): 6–9. (In Chinese).

McVay, M.C., Birgisson, B., Zhang, L.M., Perez, A. & Putcha, S. 2000. Load and Resistance Factor Design (LRFD) for driven piles using dynamic methods—A Florida perspective. *Geotechnical Testing Journal* 23(1): 55–66.

Ministry of Housing and Urban-Rural Development (MHURD). 2002. Code for design of foundations. Beijing: China Construction Press. (In Chinese).

Ministry of Housing and Urban-Rural Development (MHURD). 2011. Code for design of foundations. Beijing: China Construction Press. (In Chinese).

Paikowsky, S.G., et al. 2004. *Load and resistance factor design (LRFD) for deep foundations. NCHRP Rep. No. 507*. Washington, D.C.: Transportation Research Board, National Research Council.

Phoon, K.K., Kulhawy, F.H. & Grigoriu, M.D. 2003. Development of a reliability-based design framework for transmission line structure foundations. *Journal of Geotechnical and Geoenvironmental Engineering* 129(9): 798–806.

Shanghai Urban Construction and Communications Commission (SUCCC). 2010. *Foundation Design Code* (DGJ 08-11-2010). Shanghai.

Zhang, L.M. & Chu, L.F. 2009a. Calibration of methods for designing large-diameter bored piles: Ultimate limit state. *Soils and Foundations* 49(6): 883–896.

Zhang, L.M. & Chu, L.F. 2009b. Calibration of methods for designing large-diameter bored piles: Serviceability limit state. *Soils and Foundations* 49(6): 897–908.

Zhang. J., Zhang, L.M. & Chu, L.F. 2009b. Resistance factors for ultimate limit state design of large-diameter bored piles in Hong Kong. International *Journal of Engineering under Uncertainty: Hazards, Assessment, and Mitigation* 1(3–4): 141–152.

Zhang, J., Zhang, L.M. & Tang, W.H. 2009a. Reliability based design of pile foundations considering both parameter and model uncertainties. *Journal of GeoEngineering* 4(3): 119–127.

Zhang, L.M. 2004. Reliability verification using proof pile load tests. *Journal of Geotechnical and Geoenvironmental Engineering* 130(11): 1203–1213.

Geotechnical Safety and Risk IV – Zhang et al. (eds)
 ISBN 978-1-138-00163-3

Development and reliability of a pile driving formula for the MnDOT

S.G. Paikowsky
University of Massachusetts Lowell (UML), Lowell, Massachusetts, USA
GeoDynamica, Inc., Newton, Massachusetts, USA

C.M. Marchionda
Nobis Engineering, Inc., Lowell, Massachusetts, USA
Previously UML, MA, USA

S. Amatya
Golder Associates Pty Ltd., Richmond, Victoria, Australia
Previously UML, MA, USA

M.C. Canniff
GeoDynamica, Inc., Newton, Massachusetts, USA

A.S. Budge
Minnesota State University Mankato, Mankato, Minnesota, USA

ABSTRACT: Driven piles are the most common foundation solution used in bridge construction (Paikowsky et al., 2004). Their safe use requires to reliable verification of their capacity and integrity. Dynamic analyses of driven piles are methods attempting to obtain the static capacity of a pile, utilizing its behavior during driving. Dynamic equations (aka pile driving formulas) are the earliest and simplest forms of dynamic analyses. The development and the examination of such equation tailored for given demands are presented. After establishing the bridge pile construction practices of MnDOT, a database of driven pile case histories relevant to these practices was built. The databases were utilized to investigate previous MnDOT (and other) dynamic formulas and use object oriented programming for linear regression to develop a new formula that was then calibrated for LRFD methodology and evaluated for its performance. A standalone control database and a database of dynamic measurements enabled independent evaluation of the formula leading to the final stage in which the equation was adjusted for field application and past experience. Though developed for MnDOT, its use is universal for driven piles within the provided limitations.

1 BACKGROUND

1.1 *Overview*

Minnesota Department of Transportation (MnDOT) used its own pile driving formula; however, its validity and accuracy had never been thoroughly evaluated. With the implementation of Load Resistance Factor Design (LRFD) in Minnesota in 2005, and its mandated use by the Federal Highway Administration (FHWA) in 2007, the resistance factor associated with the use of the MnDOT driving formula needed to be determined. Paikowsky et al. (2009, 2010) addressed this need by establishing the bridge pile construction practices of MnDOT and building up a database of driven pile case histories relevant to these practices. The databases were utilized for the investigation of the MnDOT (and other) dynamic formulas, the evaluation of the uncertainty of their performance and thereby calculating the resistance factor required for a consistent level of safety in the bridge foundations. The results of the study suggested that the formula in use is inaccurate and inefficient and the development of an alternative formula was, therefore, required.

1.2 *MnDOT state of practice*

1.2.1 *Objectives and method of approach*

Data relevant to the subsurface conditions and practices of substructure design and construction in Minnesota were collected and summarized. This compilation of data ensures the relevance of the pile performance database to the needs of the MnDOT. The following steps were used in developing the state of design and practice: (a) a detailed

questionnaire distributed as part of NCHRP project 12-66 (Paikowsky and Canniff, 2004) and completed by Mr. Dave Dahlberg of the MnDOT, (b) review of MnDOT bridge construction manual, (c) review of local construction records of 28 bridges, and (d) interviews of contractors, designers and DOT personnel. Details of the data and its relevant analyses are presented by Paikowsky et al. (2009), while the following section provides a short summary.

1.2.2 *Summary of findings*

a. Majority of bridge foundations are based on Closed Ended Pipe (CEP) and H piles.
b. CEP piles range in diameter from 12 to 20" (0.30 to 0.51 m) and comprise 85% of the driven piles.
c. Most common CEP piles used are 12" × 0.25" (0.30 m × 6.4 mm) and 16" × 0.3125" (0.41 m × 7.9 mm), installed as 40% and 25% of the total foundation length, respectively (based on 28 bridge projects).
d. H piles comprise 15% of the driven pile foundations with sizes ranging between 10 × 42 and 14 × 73 (HP 250 × 63 to HP 360 × 109).
e. Typical (average) driven pile length is 66 feet (20 m) with a load of 186 kips (827 kN). More specific categorization includes for example CEP 12" × 0.25" (0.30 m × 6.4 mm) pile length is 77 feet (23 m) and it carries 155 kips (689 kN) design (factored) load.
f. Diesel hammers are most commonly used for driving piles ranging in size from D 19-32 (42.4 kip-ft or 57.5 kN-m) to D 30-32 (75.4 kip-ft or 102.2 kN-m).
g. Over 90% of the piles are driven beyond the easy driving resistance zone of 4 bpi (16 b/10 cm), hence allowing more accurate capacity evaluation when utilizing the dynamic methods. Fifty percent (50%) of the piles were driven to a final penetration of 8 or more bpi (31 b/10 cm).

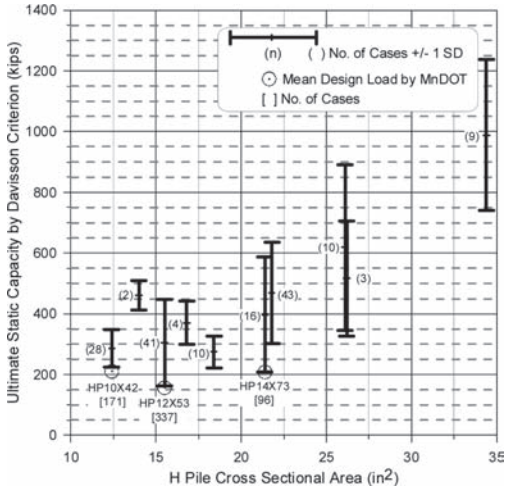

Figure 1. Range of pile capacity based on static load test (mean +/– 1 S.D.) and MnDOT mean factored design loads sorted by H pile type and cross-sectional area.

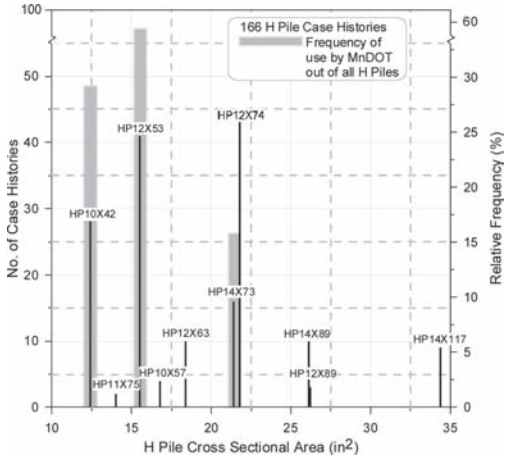

Figure 2. Distribution of database MnDOT/LT H-piles by pile area cross-section along with the frequency and pile type used by MnDOT.

2 DATABASES

2.1 *Overview*

Two new robust databases of H and pipe piles driven and statically load-tested to failure were compiled to address the specific needs of Minnesota DOT aforementioned pile foundation practices.

2.2 *MnDOT/LT-H-Piles*

Figures 1 and 2 present graphically some of the important features of MnDOT/LT 2008 H Piles database along with a comparison of data reflecting the MnDOT foundation practices. The information in Figure 1 provides mean static load-test failure load (+/– 1 standard deviation) for each pile type/size category comprising the database, along with the number of cases related to that information. In addition, the mean LRFD factored (design) load for the MnDOT for the applicable pile cases is presented along with the number of piles it is based upon. For example, 41 case histories of the database are related to HP12X53. The mean failure load of these cases (applying Davisson's failure criterion) was 305 kips +/– 142 kips (1 SD). The mean factored load of this type of pile by the

MnDOT is 157 kips based on 337 HP12X53 piles. These data suggests that the mean safety margin of the MnDOT is 1.943 +/– 0.904 in comparison with the database information (not including the load factor) or the covering of approximately 1 S.D range (lower value of resistance is 163 kips compared to a load of 157 kips) translates to a target reliability of $\beta = 1$ and a probability of failure $p_f = 15.9\%$. The information in Figure 2 presents the distribution of the case histories in the database based on the pile sizes in comparison with the distribution of use of the same pile by MnDOT. To be relevant, the frequency of use of the H-Piles by the MnDOT, presented in Figure 2, reflects the use of the particular pile type out of the H-Piles only and not out of all driven piles. For example, 41 pile cases of HP12X53 are available in the database (24.7% of all cases), while the MnDOT uses this pile in 55.5% of the cases where H-Piles are being used.

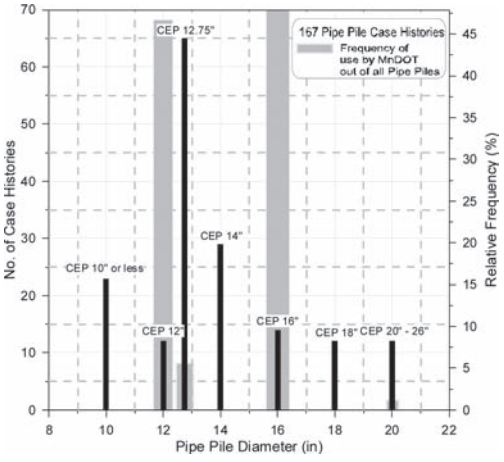

Figure 4. Distribution of database MnDOT/LT pipe piles by pile area cross-section along with the frequency and pile type used by MnDOT.

2.3 *MnDOT/LT-Pipe-Piles*

Figures 3 and 4 present graphically some of the important features of MnDOT/LT 2008 Pipe Piles database along with a comparison of data reflecting the MnDOT foundation practices as presented earlier in section 1. The information in Figure 3 provides mean failure load (+/– 1 standard deviation) for each pile type/size category (by pipe pile diameter) comprising the database, along with the number of cases related to that information. In addition, the mean LRFD factored (design) load for the MnDOT for the applicable pile cases is presented along with the number of piles it is based upon. For example, 12 and 65 case histories of the database are related to 12.00 and 12.75 inch diameter piles, respectively. The mean failure load of these cases was 388 +/– 173 kips and 372 +/– 195 kips (1 SD) for the 12 and 12.75 inch diameter piles, respectively. The mean factored load of the 12 and 12.75 inch piles by the MnDOT is 155 and 120 kips, based on 1055 and 116 piles, 12.0 and 12.75 inch diameter pipe piles, respectively. These data suggests that the mean safety margin of the MnDOT 12 and 12.75 inch diameter piles is 2.503 +/– 1.116 and 3.100 +/– 1.625 in comparison with the database information (not including the load factor) or the covering of approximately 1.3 S.D range (lower value of resistance is 1.29 and 1.35 standard deviations from the mean, hence approximately taken as 1.3) translates to a target reliability of $\beta = 1.3$ and a probability of failure $p_f = 9.8\%$. The information in Figure 4 presents the distribution of the case histories in the database based on the pile sizes in comparison with the distribution of use of the same pile by MnDOT. To be relevant, the frequency of use of the pipe piles by the MnDOT, presented in Figure 4, reflecting the use of the particular pile type out of the pipe piles only and not out of all driven piles. For example, 77 pile cases of 12 and 12.75 inch diameter piles are available in the database (46.1% of all cases), while the MnDOT uses these diameter piles in 50.0% of the projects where pipe piles are being used. The major difficulty of the database as presented in Figure 4 is evidently related to the 16 inch diameter closed ended pipe piles. This type of piles are used by the MnDOT in 22.9% of all

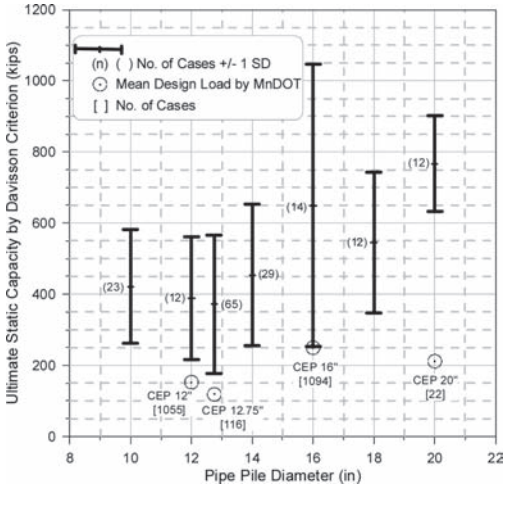

Figure 3. Range of pile capacity based on static load test (mean +/– 1 S.D.) and MnDOT mean factored design loads sorted by pipe pile type and pipe pile diameter.

projects and 26.9% of all pipe piles but only 10 closed ended and 4 open ended 16 inch diameter piles are available at the database.

3 DEVELOPMENT OF A NEW MNDOT DYNAMIC EQUATION

3.1 *Plan of action*

a. Developing an independent equation for the needs of the MnDOT using object oriented programming.
b. Examine the new MnDOT dynamic equations by the following steps: (1) evaluate the ultimate pile static capacity of all tested piles using Davisson's failure criterion (Davisson, 1972), (2) evaluate the pile capacity of the database case histories using the developed new equation, (3) evaluate the bias of the method as the ratio between measured (stage 'a') to calculated (stage 'b') capacity, and (4) examine the statistical parameters of the bias.
c. Conduct an in-depth evaluation to the new MnDOT equation by examining subsets of various conditions.
d. Examine the new MnDOT distribution functions fit to LRFD calibration.
e. Develop the resistance factors associated with the different conditions, using both FOSM and MC simulation methods.
f. Examine the recommended resistance factors in comparison to the performance of the traditional MnDOT and other dynamic equations. This examination includes the use of a control databases the data of which not included in the development of the equation and the use of dynamic measurements data from MnDOT projects.
g. Adjust the equation for the practice of field observations by MnDOT field inspectors.
h. Examine the equation for use with timber and concrete driven piles.
i. Develop final recommendations now implemented by the MnDOT.

3.2 *Principle*

A regression analysis can provide parameters that connect the major factors affecting the pile capacity (e.g. energy, driving resistance, etc.) and allow the development of a dynamic equation. A limited attempt was made in that direction, but most obtained equations had no engineering "feel" (or "logic") to them and are constructed of arbitrary terms and parameters.

A different approach was then taken. Recognizing the unique success of the Gates equation (Gates, 1957) in associating the pile capacity to the square of the hammers' nominal energy, and the simplicity in using logarithm of the blow count, a linear regression analysis of the data was performed looking for the best fit parameters to the anticipated formulation. This process is outlined in the following section.

3.3 *Method of approach*

S-Plus is a commercial advanced statistics package sold by Insightful Corporation of Seattle, Washington. It features object oriented programming capabilities and advanced analytical algorithms. To develop the New MnDOT Dynamic Equation, a linear regression was performed using the S-Plus program. Static capacity and Gates parameters (which are square root of hammer energy and log of 10 times the blow count) were provided as input parameters into an S-Plus worksheet. Linear regression was then performed for each of the eight (8) different examined cases. The coefficient for the New MnDOT Dynamic Equation and the coefficient of determination, r^2 of the proposed relationship were calculated, as well as Cook's Distance graph, enabling to identify the data outliers.

Cook's Distance is a commonly used estimate of the influence of a data point when doing least squares regression. Cook's distance measures the effect of deleting a given observation. Data points with large residuals (outliers) and/or high leverage may distort the outcome and accuracy of a regression. Points with a Cook's distance of 1 or more are considered to merit closer examination in the analysis. Cook's distance is a measurement of the influence of the *i*th data point on all the other data points. In other words, it tells how much influence the *i*th case has upon the model. The formula to find Cook's distance, D_i, is, (Cook, 1979):

$$D_i = \frac{\sum \left(\hat{Y}_j - \hat{Y}_{j(i)} \right)^2}{p \bullet MSE} \quad (1)$$

where $\hat{Y}_j$ is the predicted (fitted) value of the *i*th observation; $\hat{Y}_{j(i)}$ is the predicted value of the *j*th observation using a new regression equation found by deleting the *i*th case; *p* is the number of parameters in the model; and *MSE* is the Mean Square Error.

Using the F distribution to compare with Cook's distance, the influence that the *i*th data point has on the model can be found. Values in the F distribution table can be used to express the percentage of influence the *i*th data point has. A percentage of 50% or more would indicate a large influence on the model. The larger the error term implies that the D_i is also larger which means it has a greater influence on the model.

The new MnDOT equation was developed in two stages described in the following sections. The most generic form is described in section 3.4 and is investigated in section 3.5. A more specific form is described in section 3.6 and is investigated in section 3.7. The final adoption of the equation to field application is described in section 5.

3.4 *The general new MnDOT dynamic equation development*

Table 1 presents a summary of the results, obtained by applying the analysis to all cases and EOD cases only for H and pipe piles suggesting the following:

a. For both pile types under all data selection criteria, the recommended coefficient varied between 34.5 and 37.1.
b. All regressions resulted with a coefficient of determination greater than 0.85. As a lower coefficient means a more conservative evaluation and the scatter of the pipe piles predictions is higher than that for the H-piles, it is reasonable to use one coefficient, 35.

Table 1. Summary of S-PLUS linear regression analysis results for the new general MnDOT dynamic equation.

Pile type	Condition	# of cases	Searched coeff.[1]	Coeff. of determ. r^2
H	All cases	135	35.814	0.880
H	All excluding Cook's outliers	132	35.170	0.896
H	EOD only	125	35.660	0.896
H	EOD excluding Cook outlier's	123	34.550	0.914
Pipe	All cases	128	35.866	0.861
Pipe	All excluding Cook's outliers	125	34.875	0.877
Pipe	EOD only	102	37.142	0.851
Pipe	EOD excluding Cook outlier's	99	35.866	0.868

[1]Searched coefficient for the equation R_u = Coeff. $\sqrt{E_h} \bullet \log(10\ N)$.

c. The final equation recommended as the new MnDOT dynamic equation for the most general case (all hammers, all conditions) is therefore:

$$R_u = 35\sqrt{E_h} * \log\ (10 * N) \tag{2}$$

where R_u = predicted pile capacity in kips, E_h = rated hammer energy kips · ft, and N = Blows Per Inch (PBI) at the End of Driving (EOD).
d. Based on the data presented in Table 2, the recommended preliminary resistance factors for equation 13 are $\phi = 0.55$ for H-piles and $\phi = 0.35$ for pipe piles.

3.5 *Investigation of the new general MnDOT dynamic equation*

Initial examination of the uncertainty of the proposed new equation and the associated resistance factors is summarized in Table 2. Figures 5 and 6 present the scatter of the new equation in the form of static (measured) capacity vs. predicted capacity for H and pipe piles, respectively. The obtained results suggest a consistent higher performance of the equation for H piles (efficiency factor of about 53% to 54%) and a resistance factor of 0.55. The results also suggest the highest performance of the equation for pipe piles (36%) with a recommended resistance factor of 0.40. Further in-depth investigations of the new equation are presented by Paikowsky et al. (2009). Section 3.6 follows the more restrictive MnDOT pile driving conditions in examining the applicability of the equation or a variation of it.

3.6 *The development of a detailed new MnDOT dynamic equation*

The approach and method of analysis presented in sections 3.1 to 3.5 were used for searching an optional new MnDOT equation that would (if possible) better fit the specific conditions than the general case of equation 2 presented earlier. Table 3 presents a summary of the results obtained by applying the

Table 2. Statistical parameters and LRFD calibration for the developed equation (2) for H piles and pipe piles, EOD condition only.

Pile type	# of cases (n)	Mean bias measured/ calculated (m_λ)	Stand. dev. (σ_λ)	Coeff. of var. (COV_λ)	Best fit line equation (least square)	Coeff. of determination (r^2)	Resistance factor ϕ $\beta = 2.33$, $p_f = 1\%$, redundant			ϕ/λ Efficiency factor (%)
							FOSM	MC[3]	Recom.	
H	125	1.0163	0.3599	0.3542	$R_u = 0.880 * R_s$	0.896	0.495	0.542	0.55	54.1
Pipe	99	1.1089	0.5955	0.5370	$R_u = 0.805 * R_s$	0.849	0.364	0.385	0.35	31.6

Note: [1]MC—Monte Carlo simulation for 10,000 simulations.

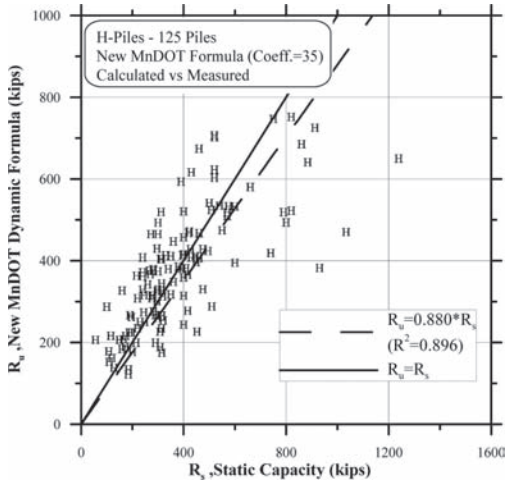

Figure 5. Measured static capacity vs. new general MnDOT dynamic equation prediction for 125 EOD cases.

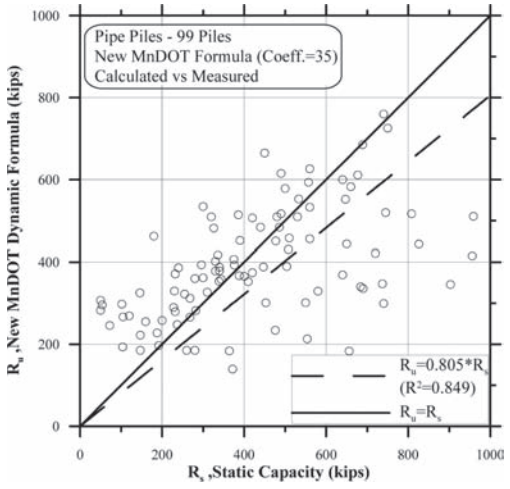

Figure 6. Measured static capacity vs. new MnDOT dynamic equation prediction for 99 EOD cases.

Table 3. Dynamic equation predictions for H piles and pipe piles EOD condition only.

Pile type	Condition	# of cases	Searched coeff.[1]	Coeff. of determ. r^2
H	EOD only	125	35.637	0.896
H	EOD only, Excl. Cook's outliers	122	34.151	0.925
H	EOD, diesel hammer, B.C. ≥ 4 BPI	39	33.527	0.907
H	EOD, diesel hammer, B.C. ≥ 4 BPI, Excl. Cook's outliers	38	32.126	0.935
H	EOD, diesel hammer, MnDOT energy[2], B.C. ≥ 4 BPI	13	34.401	0.870
H	EOD, diesel hammer, MnDOT energy[2], B.C. ≥ 4 BPI, Excl. Cook's outliers	12	31.181	0.924
Pipe	EOD only	99	36.746	0.850
Pipe	EOD only, Excl. Cook's outliers	97	35.839	0.859
Pipe	EOD, diesel hammer, B.C. ≥ 4 BPI	41	30.532	0.918
Pipe	EOD, diesel hammer, B.C. ≥ 4 BPI, Excl. Cook's outliers	38	29.983	0.946
Pipe	EOD, diesel hammer, MnDOT energy[2], B.C. ≥ 4 BPI	16	33.294	0.974
Pipe	EOD, diesel hammer, MnDOT energy[2], B.C. ≥ 4 BPI, excluding Cook's outliers	14	33.146	0.989

Notes: [1]Searched coefficient for the equation R_u = Coeff. $\sqrt{E_h} \bullet \log(10\ N)$, [2]MnDOT energy range contains hammers with rated energies between 42.4 and 75.4 k-ft.

analysis under the various sub-categorizations to the EOD cases only. The obtained results summarized in Table 3 suggest the following:

a. For both pile types under all EOD data selection criteria (with or without the outliers), the recommended coefficient varied between 34.2 to 36.7 reaffirming the coefficient of 35 recommended for the general equation as appeared in equation 2.
b. All regressions resulted with a coefficient of determination greater than 0.85 suggesting good performance of the proposed format and obtained coefficients.
c. When restricting the EOD data to diesel hammers only and a blow count of equal or greater to 4 BPI (with or without the outliers) the recommended coefficients are 32.1 to 33.5 for the H piles and 30.0 to 30.5 for the pipe piles. Both subsets contain significant number of cases (38 H piles and 38 pipe piles when eliminating outliers).
d. When further restricting the conditions described in (c) above by looking at the energy

range of the diesel hammers typically used in MnDOT practice, the subsets decrease to 13/12 H pile cases and 16/14 pipe pile cases, with and without outliers, respectively. These are marginal size sets that result with coefficients varying between 31.2 to 34.4 for H piles and 33.1 to 33.3 for pipe piles.

e. Close examination of the most restrictive subsets described in (d) above (i.e. 13 H piles and 16 pipe piles before removing the outliers) show that in both subsets a relatively (to the subset size) large group of cases are of different piles of the same size tested at the same site (e.g. 7 out of the 16 pipe piles are 14" diameter piles from Deer Island project in Massachusetts and 6 of the H piles are 12 × 53 from site no. 37 in Canada). As such, the data are too biased as not only the set is marginal in size, but about 50% of the cases are related to the same project. The statistics and coefficient obtained from that subset should, therefore, cautiously be applied.

f. As a lower coefficient means a more conservative capacity evaluation, the above discussion and the observations presented in (c) should serve as the guideline for the new MnDOT dynamic equation that suits better to MnDOT pile driving practice of diesel hammers and a Blow Count (BC) ≥ 4 BPI.

g. The equation recommended as the new MnDOT dynamic equation for the specific practice (diesel hammers) is therefore:

$$R_u = 30\sqrt{E_h} * \log(10 * N) \tag{3}$$

h. The associated recommended preliminary resistance factors for equation 3 are $\phi = 0.60$ for H-piles and $\phi = 0.45$ for pipe piles. Further details and discussion of these recommendations are presented in Paikowsky et al. (2009) and section 3.7.

3.7 *Investigation of the detailed new MnDOT dynamic equation*

Table 4 presents the statistical details of the new MnDOT dynamic equation (equation 3) applied to H piles. For the most generic case of EOD with all piles, the statistics of both equations (2 and 3) are presented in Table 4. This is done so to examine the applicability of using the detailed equation (3) under all driving conditions.

The presented information suggests that the performance of equation (3) is consistent and reliable for all H piles driven with diesel hammers regardless of the energy range. The use of equation (3) for all type of hammers at EOD and all

Table 4. Statistical parameters and resistance factors of the new detailed MnDOT dynamic equation for H piles.

Case no.	# of cases (n)	Coeff.	Condition	Mean bias measured/ calculated (m_λ)	Stand. dev. (σ_λ)	Coeff. of var. (COV_λ)	Best fit line eq. (least sq.)	Coeff. of determ. (r^2)	Resistance factor ϕ $\beta = 2.33, p_f = 1\%$, redundant			ϕ/λ Efficiency factor (%)
									FOSM	MC[3]	Recom	
1	125	35	EOD only	1.0163	0.3599	0.3542	$R_u = 0.888\ R_s$	0.896	0.495	0.542	0.55	54.1
		30	EOD only	1.1856	0.4199	0.3542	$R_u = 0.754\ R_s$	0.896	0.578	0.632	0.60	50.6
2	39	30	EOD, diesel, BC ≥ 4 BPI	1.0760	0.3417	0.3176	$R_u = 0.812\ R_s$	0.907	0.566	0.628	0.60	55.8
3	38	30	EOD, diesel, BC ≥ 4 BPI w/o outliers	1.0458	0.2888	0.2762	$R_u = 0.873\ R_s$	0.935	0.598	0.674	0.65	62.2
4	13	30	EOD, diesel, MnDOT energy, C ≥ 4 BPI	1.1419	0.4531	0.3968	$R_u = 0.759\ R_s$	0.870	0.508	0.553	0.55	48.2
5	12	30	EOD, diesel, MnDOT energy, BC ≥ 4 BPI w/o outliers	1.0518	0.3297	0.3135	$R_u = 0.889\ R_s$	0.924	0.558	0.620	0.60	57.0

Notes: Calculated capacity using MnDOT new dynamic equation R_u = Coeff. $\sqrt{E_h} \bullet \log(10\ N)$, R_s is the static capacity of the pile examined by Davisson's failure criterion, MC—Monte Carlo Simulation for 10,000 simulations.

Table 5. Statistical parameters and resistance factors of the new detailed MnDOT dynamic equation for pipe piles.

Case no.	# of cases (n)	Coeff.	Condition	Mean bias measured/ calculated (m_λ)	Stand. dev. (σ_λ)	Coeff. of var. (COV_λ)	Best fit line eq. (least sq.)	Coeff. of determ. (r^2)	Resistance factor ϕ $\beta = 2.33, p_f = 1\%$, redundant			ϕ/λ Efficiency factor (%)
									FOSM	MC[3]	Recom	
1	99	35	EOD only	1.1089	0.5955	0.5955	$R_u = 0.805\ R_s$	0.849	0.364	0.385	0.35	31.6
		30	EOD only	1.2937	0.6947	0.5370	$R_u = 0.694\ R_s$	0.850	0.424	0.450	0.45	34.8
2	41	30	EOD, diesel, BC ≥ 4 BPI	0.9519	0.4078	0.4284	$R_u = 0.902\ R_s$	0.918	0.396	0.427	0.40	42.0
3	38	30	EOD, diesel, BC ≥ 4 BPI w/o outliers	0.9071	0.3149	0.3472	$R_u = 0.946\ R_s$	0.946	0.449	0.492	0.45	49.6
4	16	30	EOD, diesel, MnDOT energy, BC ≥ 4 BPI	1.1284	0.2051	0.1818	$R_u = 0.878\ R_s$	0.974	0.766	0.905	0.85	45.3
5	14	30	EOD, diesel, MnDOT energy, BC ≥ 4 BPI w/o outliers	1.1065	0.1273	0.1151	$R_u = 0.895\ R_s$	0.988	0.825	1.012	0.90	81.3

Notes: Calculated capacity using MnDOT new dynamic equation R_u = Coeff. $\sqrt{E_h} \bullet \log(10\ N)$, R_s is the static capacity of the pile examined by Davisson's failure criterion, MC—Monte Carlo Simulation for 10,000 simulations.

driving resistances naturally would provide a safer evaluation compared to that of equation (2) that was developed for that situation specifically. The greater mean bias obtained when using equation (3) allows, therefore, to select a consistent resistance factor of $\phi = 0.60$ to be used for all the cases when applying equation (3). This conclusion was further examined and reaffirmed against an independent control database.

Table 5 presents the statistical details for the new MnDOT dynamic equation (equation 3) applied to pipe piles. For the most generic case of EOD with all piles, the statistics of both equations (2 and 3) are presented in Table 5. This is done to examine the applicability of using the detailed equation (3) under all driving conditions.

The presented information suggests that equation (2) provides accurate predictions for all cases (mean about 1.0), however, due to the larger scatter associated with the capacity prediction of pipe piles, the coefficient of variation is typically higher than that for the H piles, and hence, the associated resistance factors are lower. Exception to that are the cases of the most restrictive subsets, matching closely the MnDOT practice by the hammers energy range in addition to diesel hammers and BC ≥ 4 BPI. These subsets result with an under-prediction and, hence, a bias greater than 1.0 along with low coefficients of variation, resulting with very high resistance factors. The reasons for that behavior were previously discussed, as the small subset is biased due to large number of piles from the same site, the use of these parameters is, therefore, not safe. A consistent resistance factor of 0.45 could be used when applying equation (3) for all pipe pile cases.

4 EVALUATION OF THE DEVELOPED EQUATION

4.1 *Overview*

Following the above described process and development, three additional stages took plac: (a) evaluation of equation (3) via a control database, (b) evaluation of equations (2) and (3) via a MnDOT database of dynamic measurements, and (c) adjustment of the equation to field practices, local procedures and past experience.

4.2 *Re-evaluation of equation (3) and recommended resistance factors*

An independent control database was assembled beyond the one described in section 2 and not being part of the data originally used to develop equations (2) and (3). The control database included 24 H piles of which 20 cases related to EOD with blow counts greater or equal to 4 bpi (BC ≥ 4 bpi).

Equations (2) and (3) were examined to the general driving conditions and appropriate resistance factors were developed as summarized below.

Figure 7 summarizes the resistance factors developed for H piles using the original and the control databases. Figure 7 presents the findings leading to the conclusion that the appropriate resistance factors to be used for H piles under MnDOT practices (and all conditions as well) would be $\phi = 0.60$ assuming redundant pile use.

Figure 8 summarizes the findings regarding resistance factors developments for pipe piles with the use of relevant databases. The small datasets associated with the best match to the MnDOT practices has several sets of identical piles from a small number of sites and hence result with a reduced variability (i.e. COV) and increased resistance factor. Figure 8 expresses this trend showing a consistent increase in the resistance factor with the decreased number of cases in the database (or more accurately, with an increased alliance of the database with MnDOT practices).

In summary, the recommendations of the resistance factors for the new dynamic equation proposed to be used by the MnDOT (equation 3) was investigated leading to the conclusion that the appropriate resistance factors to be used for pipe piles under MnDOT practices (and all conditions as well) would be $\phi = 0.45$ assuming redundant pile use.

The difference in the behavior of the two pile types is evident. While H piles are predominantly small displacement piles, closed-ended pipe piles are large displacement piles and would be, therefore, more sensitive to soil inertia effects expressed via blow count and hammer type and energy. As a result, it is unwise to rely on the smaller subsets that provide resistance factors of $\phi = 0.80$ to 0.90. A unique resistance factor is therefore recommended to be used with the new MnDOT dynamic equation (equation 3) for all H and Pipe Piles, driven by Diesel hammer to EOD BC ≥ 4 BPI being $\phi = 0.60$ for H piles and 0.45 for pipe piles.

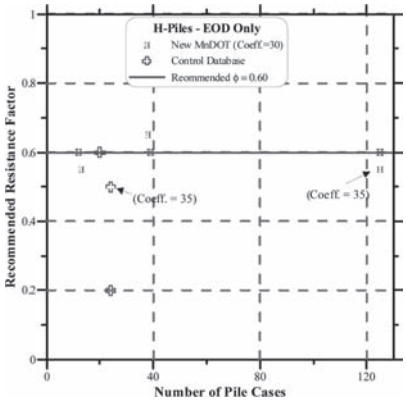

Figure 7. Developed and recommended resistance factors as a function of H piles' database and its subsets for existing and proposed MnDOT dynamic equations.

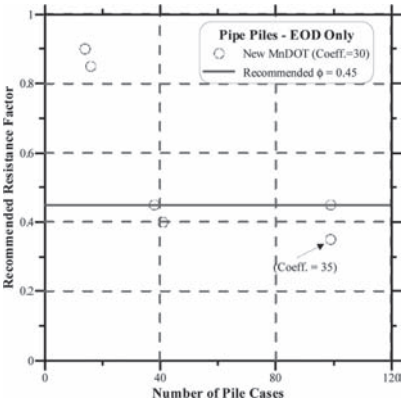

Figure 8. Developed and recommended resistance factors as a function of pipe piles' database and its subsets for existing and proposed MnDOT dynamic equations.

4.3 *Evaluation of the developed equation via dynamic measurements database*

4.3.1 *Overview*

MnDOT had not accumulated its own database of load tested piles as the process was not part of the common practice. As such, the above described equation was developed by tailoring a generic database to the practices of MnDOT.

A local database containing dynamic measurements and signal matching analyses was developed by the MnDOT. The database was compiled and provided by Messrs. Ben Borree and Derrick Dasenbrock of the MnDOT Foundations unit. The database consists of accumulated PDA data from various projects with supplemented DOT data (stroke, blow count, etc.), and was entered into formatted spreadsheets provided by UML. The compiled database contains 126 pipe-pile cases including hammer type and rated energies that match for the most part the MnDOT practice as previously established. 95 cases included signal matching analyses (CAPWAP) and sufficient data to evaluate the new equation. The dataset did not include any static load test information and 50% of it was assessed to relate to bridges within one square mile area of Minneapolis/St. Paul (Rowekamp, 2011). The evaluation of the data was aimed at comparing the performance of the signal matching analyses to various dynamic equations including the above described newly developed MnDOT equation.

4.3.2 *Comparison results*

The comparison between the signal matching analyses (CAPWAP) and the various selected dynamic equations is described in detail by Paikowsky et al. (2013). Figures 9 and 10, and the statistical parameters provided in Table 6 present comparisons between the signal matching analyses and equations (2) and (3), respectively.

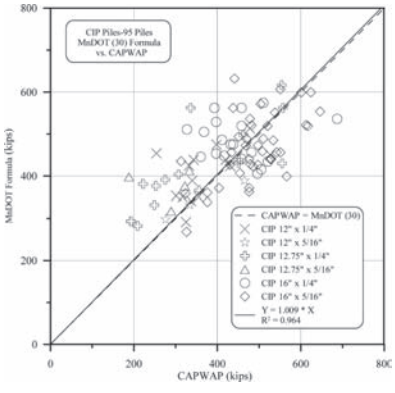

Figure 9. CAPWAP vs. new MnDOT formula (coefficient 30) all CIP piles.

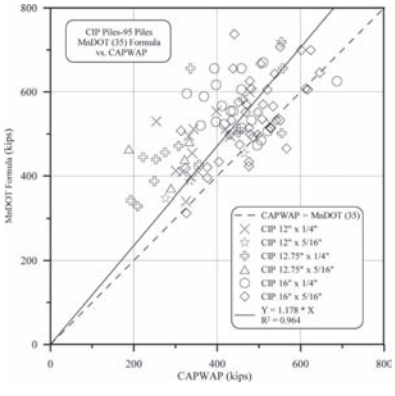

Figure 10. CAPWAP vs. new MnDOT formula (coefficient 35) all CIP piles.

4.3.3 *Conclusions*

Noting that the analyses are not compared to a benchmark (i.e. SLT) capacity, the analyses presented lead to the following observations and conclusions:

a. The CAPWAP values to which the new equations are compared most likely represents a typical conservatism of CAPWAP at EOD. Previous analyses of static load test ultimate capacity over CAPWAP capacity prediction (377 cases of EOD and BOR) resulted with a ratio of 1.368 (Paikowsky et al., 2004).
b. The proposed new MnDOT equation (3) designated for Diesel hammers, EOD and BC > 4 bpi (coeff = 30) performed the best of all examined dynamic formulas with a mean ratio of 1.0 compared to CAPWAP.
c. The general proposed new MnDOT equation (2) designed for all hammers, all piles, all cases (coeff = 35) provided the second best ratio compared to CAPWAP. A bit on the unsafe side but probably considering CAPWAP conservatism, very close to what one could expect in a SLT.

5 EQUATION ADJUSTMENT AND FINAL FORMULATION

5.1 *Overview*

The equations presented above were found to best predict pile capacity when examined with separate data not related to its development. Several additional developments were required in order to finalize the equation format to be used by the MnDOT. These developments include the following:

Table 6. Summary of statistical analysis and best fit line correlation.

Relations	Figure no	Category	No. of cases n	Statistics			Best fit line	Coeff. of determ. (r^2)
				Mean	S.D.	COV		
CAPWAP/ proposed MnDOT (35) E_n	10	All piles	95	0.8260	0.1632	0.1976	$R_u = 1.178 * R_c$	0.964
		EOID	40	0.8438	0.1591	0.1886	–	–
		BOR	55	0.8131	0.1664	0.2047	–	–
		EOID & BC ≥ 4 BPI	33	0.8314	0.1533	0.1843	–	–
CAPWAP/ proposed MnDOT (30) E_n	9	All piles	95	0.9637	0.1904	0.1976	$R_u = 1.009 * R_c$	0.964
		EOID	40	0.9844	0.1857	0.1886	–	–
		BOR	55	0.9486	0.1941	0.2047	–	–
		EOID & BC ≥ 4 BPI	33	0.9700	0.1788	0.1843	–	–

Notes: R_u is the calculated capacity using each of the dynamic formulae. R_c is the Capacity determined by CAPWAP.

a. Modify hammer energy to rely on ram's stroke measurements by field inspectors.
b. Scrutinize the database for specific case histories to be examined as to their applicability to MnDOT practices (e.g. pile size, soil type, driving conditions, etc.).
c. Design, construction, and cost ramifications when moving from past practice to the use of the new equations.
d. Examine the equation applicability for analyzing the driving of concrete and timber piles.
e. Configure the equation's format to resemble existing field practices.

The detailed procedures of the above developments are beyond the scope of the present paper and are presented in details by Paikowsky et al. (2013). The following sections provide a brief description of the work done tracking the above list and concluding with the equations adopted for current use by the MnDOT.

5.2 *Field observations*

While equations (2) and (3) were developed using nominal hammer energy, the actual developed energy (in particular for diesel hammers) depends on the resistance to penetration and the fuel-pump setting. As such, inspector's field observations, albeit difficult and of limited accuracy, can greatly help in assessing the actual hammer's energy. This value is typically 75% of the nominal energy, but can vary significantly especially during easy driving. Examination of those values and the adjustment of the equations to $E_h = W_r \cdot h$, i.e. hammer energy equal to the ram's weight times the stroke, was performed including statistical data based on existing observations and limiting values to prevent unreasonable values.

5.3 *Database outliers of common MnDOT practice*

As the databases described in section 2 do not include case histories from Minnesota, different cases (of high and low biases) were examined by the MnDOT research panel and unrelated cases were excluded. These cases included, for example, very short piles, piles of easy driving, piles designed for loads out of range, etc.

5.4 *Ramification of change in practice*

Data for a large number of piles observed during bridge construction were assembled and the previous practice was compared to the proposed practice. The change was examined; i.e. the acceptability of a pile under previous practice vs. under the proposed new practice, and then the reason for the difference. Overall, it was found that under normal driving conditions, the recommended new equation results with equal or better economic outcome. However, under unrestricted high driving resistance, it was found that past practice resulted with an economic advantage. This, however, was a result of using a dynamic equation that had an almost linear increase in capacity with increase in blow count, resulting with unsafe high capacity prediction under refusal.

5.5 *Equation examination for concrete and timber driven piles*

Expansion of the work previously described included the assembly of two additional databases for timber and Prestressed Precast Concrete (PPC) piles. These databases included 137 PPC and 28 timber cases for which static load tests were carried out. The equations were examined for their performance and for statistical parameters to allow LRFD resistance factors to be developed.

5.6 *Equation format*

Final stage of development included restructuring of the equations to be compatible with MnDOT field practices, e.g. using ton rather than kips in capacity evaluation, weight of ram in pounds and the use of penetration per blow.

5.7 *Final formulation*

The following final formulation known as MPF12 (Minnesota Pile Formula 2012) was adopted for use:

$$R_n = 20\sqrt{\frac{W \times H}{1{,}000}} \times \log\left(\frac{10}{s}\right) \tag{4}$$

where R_n = nominal resistance (tons), H = stroke (height of fall) (ft), W = weight of ram (lbs), s = set (pile permanent displacement per blow) (inch). The value of the energy ($W \cdot H$) used in the dynamic formula shall not exceed 85% of the manufacturer's maximum rated energy for the hammer used considering the settings used during driving. Equation (4) is to be used with the following Resistance Factors (RF) in order to obtain the factored resistance:

$$R_r = \phi \cdot R_n \tag{5}$$

– for pipe and concrete piles, $\phi = 0.50$, $2 < BC \leq 15$
– for H piles, $\phi = 0.60$, $2 < BC \leq 15$ BPI

and for timber piles:

$$R_n = 10\sqrt{\frac{WH}{1000}}\log\sqrt{\frac{10}{S}} \quad (6)$$

where $\phi = 0.60$.

See http://www.dot.state.mn.us/bridge/docs down.html.

Although the equation was developed for hammers with $E_h \leq 165$ kip-ft (224 kN-m), its use should be applicable for hammers with higher energies but this was not verified directly in the study.

ACKNOWLEDGEMENTS

The presented research was supported by Minnesota Department of Transportation (MnDOT) via a grant to Minnesota State University at Mankato and is presented in detail by Paikowsky et al. (2009, 2013). The Technical Advisory Panel (TAP) is acknowledged for its support, interest, and comments. In particular we would like to mention, Mr. Paul Rowekamp and Mssrs. Richard Lamb, Gary Person, Dan Mattison and Derrick Dasenbrock of the Foundations Unit, and Mssrs. Paul Pilarsky, Dustin Thomas, Dave Dahlberg, Kevin Western, Bruce Iwen, and Paul Kivisto of the Bridge Office.

The research presented in this manuscript makes use of a large database specifically developed for MnDOT purposes. This database makes use of data originally developed for a Federal Highway Administration (FHWA) study by Paikowsky et al. (1994) followed by an updated database denoted as PD/LT 2000 presented by Paikowsky and Stenersen (2000), which was also used for the LRFD development for deep foundations (presented in NCHRP Report 507, see Paikowsky et al., 2004). The contributors for those databases are acknowledged for their support as detailed in the referenced publications. Mssrs. Carl Ealy and Albert DiMillio of the FHWA were constructive in support of the original research studies and facilitated data gathering via FHWA sources. Significant additional data were added to those databases, most of which were provided by six states: Illinois, Iowa, Tennessee, Connecticut, West Virginia, and Missouri. The data obtained from Mr. Leo Fontaine of the Connecticut DOT was extremely valuable to enlarge the MnDOT databases to the robust level presented in this study. In addition, the data provided by Ms. Betty Bennet of the Ontario ministry of Transportation were invaluable for developing the timber piles database.

Previous students of the Geotechnical Engineering Research Laboratory at the University of Massachusetts Lowell are acknowledged for their contribution to the aforementioned databases and various studies, namely: John J. McDonell, John E. Regan, Kirk Stenersen, Colin O'Hearn, Jorge Fuentes and Christopher Jones.

REFERENCES

Cook, R.D. 1979. Influential Observations in Linear Regression. *Journal of the American Statistical Association* 74, 169–174.

Davisson, M. 1972. High Capacity Piles. In *Proceedings, Soil Mechanics Lecture Series on Innovations in Foundation Construction*, ASCE, Illinois Sect., Chicago, pp. 81–112.

Gates, M. 1957. Empirical formula for predicting pile capacity, *Journal of the Soil Mechanics and Foundations Division*, ASCE 27(3): 65–66.

Paikowsky, S.G. with contributions by Birgission G., McVay M., Nguyen T., Kuo C., Baecher G., Ayyub B., Stenersen K., O'Mally K., Chernauskas L., and O'Neill M. 2004. *Load and Resistance Factor Design (LRFD) for Deep Foundations*, NCHRP Report 507, Transportation Research Board, National Research Council, Washington, DC., pp. 134 (not including Appendices), http://onlinepubs.trb.org/onlinepubs/nchrp/nchrp_rpt_507.pdf.

Paikowsky, S.G., and Canniff, M.C. 2004. AASHTO LRFD Specifications for Serviceability in the Design of Bridge Foundations, Appendix A: Questionnaire. Interim Report Appendix A submitted for the research project NCHRP 12-66 to the National Academies, Geosciences Testing & Research, Inc., N. Chelmsford, MA.

Paikowsky, S.G., Canniff, M.C., Robertson, S.O., and Budge, A.S. 2013. *Load and Resistance Factor Design (LRFD) Pile Driving Project—Phase II Study.* Final report submitted to Minnesota State University Mankato, University of Massachusetts Lowell, Lowell, MA.

Paikowsky, S.G., Marchionda, C.M., O'Hearn, C.M., Canniff, M.C., and Budge, A.S. 2009. *MnDOT Research Project: Developing a Resistance Factor for MnDOT's Pile Driving Formula.* Final Report submitted to Minnesota State University Mankato, October 29, pp. 209, website: http://www.lrrb.org/pdf/200937.pdf.

Paikowsky, S.G., Marchionda, C.M., O'Hearn, C.M., Canniff, M.C., Budge, A.S., Dasenbrock, D., Person, G. and Dahlberg, D. 2010. The reliability of MnDOT pile driving formula—new equation and resistance factors. *Proc. University of Minnesota 58th Annual Geotechnical Eng. Conf.*, University of Minnesota, St. Paul, Feb. 26, pp. 79–99.

Rowekamp, P. 2011. Email communication Monday, April 11, 2011 to A. Budge and S. Paikowsky.

Geotechnical Safety and Risk IV – Zhang et al. (eds)
© 2014 Taylor & Francis Group, London, ISBN 978-1-138-00163-3

On the validation of reliability and partial safety factors for axially loaded piles in dense sand

K.A. Schmoor & M. Achmus
Institute for Geotechnical Engineering, Leibniz University of Hannover, Germany

ABSTRACT: By designing mainly axially loaded offshore foundation piles in North Sea conditions, two commonly used design methods, the β-method and the ICP-method, were used. Thereby the required minimum embedded pile length may vary a lot. The actual safety which is achieved with a certain pile length and the corresponding prescribed partial safety factors is not known. For general assumed pile and soil conditions it could be determined that a reliability index between β = 3.5 and β = 4.1 is established. Further it could be shown that the prescribed partial safety factors should be decreased for the β-method, where an increase for the ICP-method should be considered. By performing reliability based design also a more accurate determination of the required pile length for a specified safety is possible.

1 INTRODUCTION

One of the main reasons for the increase of renewable energy in Germany over the last years is the continued extension of wind energy. For the next years additionally several offshore wind farms are planned to be built in the North Sea. Since many projects at the German North Sea sites are going to be realized outside of the 12 sea mile border, water depths greater than 30 m are often faced. For such water depths jacket and tripod supporting structures with mainly axially loaded foundation piles are mostly used.

Thereby the pile resistance can be calculated by applying the well known β-method (also known as API-method) recommended in the guideline of the American Petroleum Institute (API 2007). In the course of publishing errata and supplements for the existing guideline, new simplified CPT-based design methods were introduced following the recommendation of the corresponding research groups, like the ICP-method introduced by Jardine et al. (2005).

For many design cases the ICP-method leads to considerably differing resistances compared with the API-method. This affects also the deterministic design, where this deviation leads to a strong variation of the required embedded pile length. For practical applications it is of interest which method is more reliable for determining the pile length and which method should be used, respectively? In addition it is also unknown which safety level—measured by the reliability index β—is finally achieved by applying one of these methods with the corresponding partial safety factors in a deterministic design.

2 DESIGN METHODS

The tension bearing capacity of mainly axially loaded piles consists basically of the mobilized friction between the pile outer shaft area and the surrounding soil. Additionally if an open ended pile is used two different condition states "plugged" or "unplugged" have to be considered. In the unplugged case also the friction resistance between the inner pile shaft area and the inner soil can be taken into account. By assuming a plugged condition the effective weight of the inner soil plug can be added to the bearing capacity.

Generally it can be observed that in almost all design cases the tension limit state is the controlling one with regard to the required pile length. Therefore only tensile capacity is considered here. The pile resistance for the unplugged or plugged condition can be computed by applying Equation 1:

$$R_t = A_o \int f_t(z)\,\mathrm{d}z + \min[A_i \int f_t(z)\,\mathrm{d}z ; G'_p] \qquad (1)$$

where A_o = outer pile shaft area; $f_t(z)$ = skin friction for tension loading; A_i = inner pile shaft area; and G'_p = effective weight of the inner soil plug.

Following the API-method the skin friction of offshore foundation piles in sand for tension conditions can be computed by Equation 2. Thereby the friction is basically determined by multiplying the effective vertical stress with a β-value. Further a limitation of the skin friction is included. Both, the shaft friction factor as also the limiting friction value, only depend on the relative density of the soil and may vary with depth. The additional

factor of 2/3 is not recommended by the API, but is regularly used in practice since it is prescribed by certification companies like the Germanischer Lloyd (GL 2010). It is not clearly indicated whether the reduction factor should also be applied to the limit value. However, here the approach is used in that way.

$$f_t(z) = \tfrac{2}{3}\,\beta\,\sigma'_v \le \tfrac{2}{3} f_{t,\max} \tag{2}$$

where β = shaft friction factor from Table 1; σ'_v = effective vertical stress; and $f_{t,max}$ = limit skin friction from Table 1.

To determine the relative density from the results of a CPT test, the approach proposed by Jamiolkowski et al. (API 2007) according to Equation 3 is recommended by the API.

$$D_r = \frac{1}{2.93}\ln\left(\frac{q_c}{205 p'^{\,0.51}_m}\right) \tag{3}$$

where q_c = measured cone tip resistance in kPa; and p'_m = effective mean in-situ soil stress in kPa.

The ICP-method stated in API (2007) assumes a plugged condition for the determination of the tension pile resistance. Also no additional resistance by the inner soil plug is taken into account. The skin friction for non-cohesive soils according to the ICP-method can be determined by applying Equation 4. Therefore the trend of the skin friction is mainly influenced by the measured cone tip resistance.

$$f_t(z) = 0.016\, q_c \left(\frac{\sigma'_v}{p_a}\right)^{0.1} \times A_r^{\,0.2}\left(\max\left[\frac{L-z}{D_o};\nu\right]\right)^{-0.4} \tan\delta_{cv} \tag{4}$$

where p_a = atmospheric pressure = 100 kPa; A_r = effective area ratio $A_r = 1 - (D_i/D_o)^2$; D_i = pile inner diameter; D_o = pile outer diameter; L = embedded pile length; ν = dimensionless parameter $\nu = 4(A_r)^{0.5}$; and δ_{cv} = interface friction angle.

Table 1. Design parameters for the API-method (API 2007).

Relative density		β (–)	$f_{t,max}$ (kPa)
Medium dense	(D_r = 0.36–0.65)	0.37	81
Dense	(D_r = 0.65–0.85)	0.46	96
Very dense	(D_r = 0.85–1.00)	0.56	115

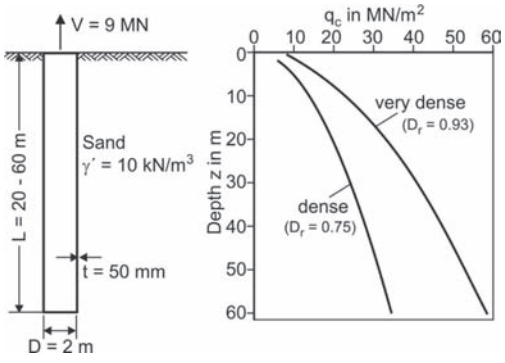

Figure 1. Considered pile system.

3 PILE SYSTEM UNDER CONSIDERATION

For the performed study typical site conditions for the North Sea and typical ranges for the foundation pile properties were assumed.

Since the subsoil in the German North Sea mostly consists of dense sands with only limited intermediate cohesive layers, two idealized CPT profiles for homogeneous dense (D_r = 0.75) and very dense (D_r = 0.93) sands were considered. The effective unit weight was assumed to be 10 kN/m³, since this value represents a reasonable estimate for both soil densities.

The choice of pile properties depends on the type of foundation, the water depth and the subsoil condition at the desired location. In general it can be said that pile slenderness ratios (embedded length to diameter) between L/D = 10 and L/D = 40 are used. Thereby the pile outer diameter is varying between D = 1 m and D = 3 m, where the pile embedded length is commonly chosen to be between L = 20 m and L = 60 m. For the considered range of the load in this study a diameter of D = 2 m was chosen. The regular pile wall thickness which is commonly used can approximately be determined by t = D/40.

A characteristic load of V_k = 9 MN for a pile foundation with a supporting structure for a 5 MW windmill in the German North Sea with a water depth of 30 m was considered. Therefore typical 50-year extreme environmental values were assumed (Achmus et al. 2007). Figure 1 shows the considered boundary conditions.

4 DETERMINISTIC DESIGN

The partial safety factors for the deterministic design of an offshore pile foundation in Germany are defined by the Eurocode 7 with the

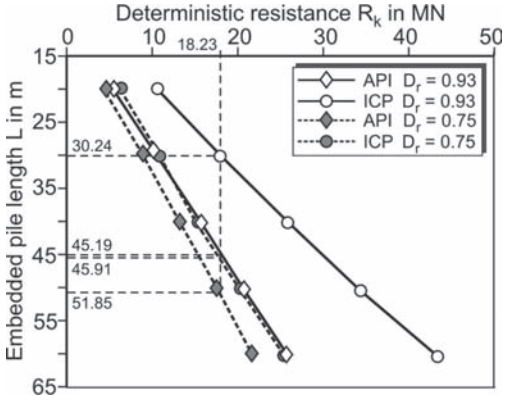

Figure 2. Deterministic resistances for the API and ICP method with increasing pile length.

national supplementary code DIN 1054. Here a 50-year extreme event is studied. Thereby the corresponding partial safety factor for the load is defined as $\gamma_L = 1.35$. For the tension resistance of a pile a partial safety factor of $\gamma_R = 1.5$ according to DIN 1054 is applied. Together a product of partial safety factors—indicating the global factor of safety—of 2.03 is applied.

For the assumed CPT profiles with their corresponding relative densities the two introduced design methods were evaluated. Figure 2 shows the development of the characteristic resistance with increasing pile length. For very dense soil conditions a strong deviation between the methods must be noticed.

By assuming the characteristic load and partial safety factors a characteristic resistance of $R_k = 18.23$ MN is required to fulfill the deterministic design proof according to Equation 5. The corresponding pile lengths for the different methods and densities can be obtained from Figure 2. Also Table 4 summarizes the deterministically determined pile lengths.

$$V_k \gamma_L \gamma_R \leq R_k \tag{5}$$

where V_k = characteristic load; γ_L = partial safety factor for the loading; γ_R = partial safety factor for the resistance; and R_k = characteristic resistance.

5 RELIABILITY BASED APPROACH

5.1 *Stochastic subsoil model*

Since soil properties are subject to spatial variation, a certain volume has to be considered. For most geo-technical applications which affect a local soil area, soil properties could be approximated by applying only one single random variable. In case of a pile where properties along the vertical axis are varying much more, a random field could be applied to get a more reliable subsoil model.

The soil model used for the performed study mainly bases on a 1-D autocorrelated field for the cone tip resistance. Therefore the two CPT profiles for constant densities were specified as trend functions and a random component was added to represent uncertainties from inherent variability w_{qc} and measurement errors e_{qc}.

To account for the genesis of the soil additionally an autocorrelation was taken into account. This implies that the properties of two points which are close together are more related as the properties of two points which are far away from each other. This relation can be expressed by an autocorrelation function. Equation 6 shows the applied single exponential function. Thereby the autocorrelation length describes how strong the correlated field is.

Since only a 1-D field was simulated the correlation structure was computed by applying the Cholesky technique (Fenton & Griffiths 2008).

$$\rho(\tau) = e^{-\left(\frac{\tau}{\theta}\right)} \tag{6}$$

where τ = distance between two points; and θ = autocorrelation length.

Figure 3 elucidates one realization of the simulated CPT profile with the presumed trend function for the very dense soil condition.

5.2 *Model error*

A model error can be determined by comparing measured properties with calculated ones. In this way a model error is an indicator how reliable a calculation method is.

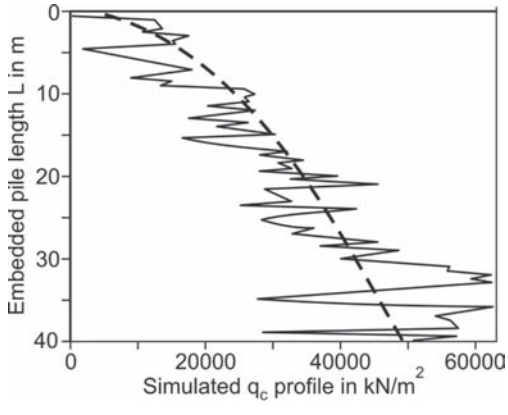

Figure 3. One realization of a simulated CPT profile.

Table 2. Model error (R_m/R_c) for ICP and API-method.

Method	μ (–)	σ (–)	COV (–)
ICP-method, all pile tests	1.01	0.28	0.28
API-method, all pile tests	1.15	0.58	0.50
ICP-method, only related tests	1.16	0.19	0.16
API-method, only related tests	1.26	0.14	0.11

Jardine et al. (2005) obtained a model error for both methods where the following pile tests were considered: Closed-ended and open-ended piles, tension and compression test, steel and concrete piles and loose to very dense soil state.

Altogether 81 pile tests were evaluated. The statistical values are shown in Table 2. Therein the model error is defined as the ratio of the measured to the calculated resistance.

Achmus & Müller (2010) compared measured with calculated results for the API and the ICP-method only with pile tests which are closely related to the boundary conditions in the North Sea (see section 3). By this it can be seen how reliable these methods are to a special boundary sector. In detail the following pile tests were considered: Open-ended piles, tension test, steel piles, dense to very dense soil state and slenderness ratios between 10 and 40.

By taking into account only pile tests within a range of 95% confidence interval, only 6 pile test for the ICP-method and only 4 pile tests for the API-method could be found. The mean and standard deviations for these related tests are summarized in Table 2 and should be seen as rough approximations of the real values.

As it can be seen the overall model error for the ICP-method is smaller in mean and standard deviation compared to the overall model error for the API-method. By comparing the model error only for the related tests, it can be said that in average both methods underpredict the resistance. The standard deviation seems also to be closer related to each other as in the overall case.

5.3 *Stochastic variables and simulation*

For each performed simulation with a certain pile length 6 million realizations within a plain Monte-Carlo Simulation (MCS) were computed.

The inherent variability of the cone tip resistance w_{qc} was assumed to be constant with depth. By applying a standard deviation of 6 MN/m² the COV is varying between 0.75–0.20 for dense and 0.40–0.10 for very dense soil conditions. According to Phoon & Kulhawy (1999) the COVs were thereby in a typical range of 0.81 and 0.10.

Table 3. Parameters used for all Monte-Carlo simulations.

Basic variables	Notation	μ	σ	Type*
Unit weight	γ' in kN/m³	10	1	N
Inherent variability q_c	w_{qc} in MN/m²	0	6	N
Measurement error q_c	e_{qc}	1	0.15	N
Transformation error φ	e_φ in °	0	2.8	N
Model error API	m_{API}	1.26	0.14	N
Model error ICP	m_{ICP}	1.16	0.19	N
Pile diameter	D in m	2	–	D
Pile wall thickness	t in m	0.05	–	D
Pile length	L in m	20–60	–	D
Axial loading	V in MN	5.4	1.89	G

*N = Normal distributed; D = deterministic value; and G = Gumbel distributed.

The vertical autocorrelation length for the cone tip resistance is indicated to be between 0.1 m and 2.2 m. Hence, the value of $\theta = 0.6$ m was chosen for all simulations.

The buoyant unit weight γ', the measurement error for the cone tip resistance e_{qc} and the transformation error for the internal friction angle e_φ were modeled as uncorrelated and normally distributed random fields with typical values for the mean and standard deviation. The stochastic formulation for the load was chosen according the recommendation by Holicky et al. (2007) for a 50-year extreme environmental event.

All applied variables with their corresponding stochastic moments are summarized in Table 3.

6 OBSERVED RESULTS

6.1 *Impact of uncertainties*

For the computed data sets first the COVs of the resistance distributions are evaluated. Additionally the corresponding parts which arise from the model error and soil uncertainties were estimated, as depicted in Figure 4 for very dense soil condition.

For both methods the total variation of the resistance is much lower than of the load. For the API-method almost 11% and for the ICP-method about 17% were obtained. Further the model error is almost exclusively responsible for the variation of the resistance, especially for the API-method. Also it can be noticed that the deviation arising from soil uncertainties is decreasing with embedded pile

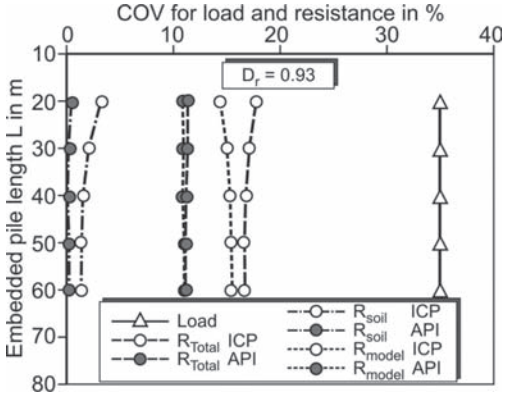

Figure 4. COV for the resistance and load with increasing pile length.

length, since an averaging effect becomes more dominant.

6.2 *Safety*

The safety of a system can be described in terms of a reliability index β corresponding to Equation 7. In the following, β is also termed safety.

In the Eurocode 0 three reliability classes with the corresponding safeties were proposed. Further it is remarked that the partial safety factors are construed for the second reliability class and therefore a safety of β = 3.8 should be established in a design system. However, offshore pile foundations may also be associated to the first reliability class which demands a safety of β = 3.3.

$$\beta = \Theta^{-1}(1 - pf) \tag{7}$$

where Θ^{-1} = inverse of the cumulative standard deviation; and pf = failure probability.

For the computed pile lengths the derived reliability index is shown in Figure 5. Table 4 also presents the corresponding safeties for the deterministic required pile lengths.

Therefore it can be generally said that by applying the usual partial safety factors a safety of β = 3.5 according to the ICP-method and about β = 4.1 according to the API-method is achieved. Nevertheless, it should also be noticed that the API-method indeed yields a longer embedded pile length.

For a certain embedded pile length or safety it could be generally assumed that the real established safety or required pile length is between the computed values corresponding to these methods, respectively.

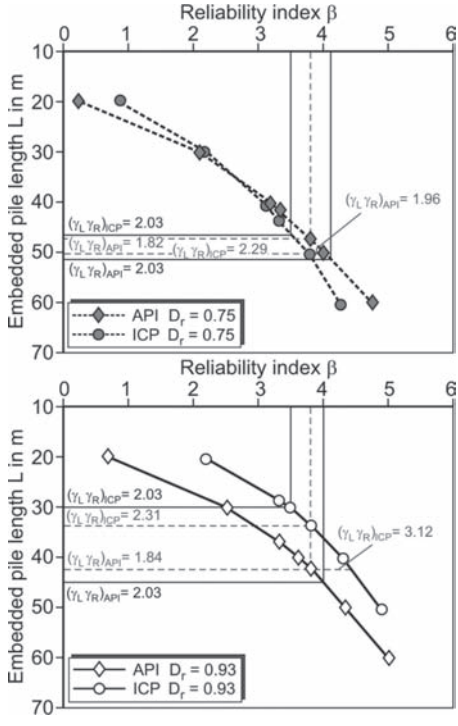

Figure 5. Evaluated safety with increasing pile length.

Table 4. Required deterministic pile lengths with corresponding reliability index.

	$D_r = 0.75$		$D_r = 0.93$	
Design method	API	ICP	API	ICP
Deterministic length	51.85	45.91	45.19	30.24
Reliability index	4.1	3.5	4.0	3.5

6.3 *Partial safety factors*

Figure 6 elucidates the sensitivity values depending on safety. It can be seen that the sensitivity for the load is much higher than for the resistance. Generally the values are getting more uniform for higher reliability values and more dense soil conditions.

The corresponding partial safety factors which should be used for a given safety are shown in Figure 7. For the API-method a resistance partial safety factor lower than one was computed. This uncommon result is achieved due to applying model uncertainty in combination with nonuniform COVs. However, the product of both partial safety factors affects the safety within the deterministic design proof. In contrast both partial

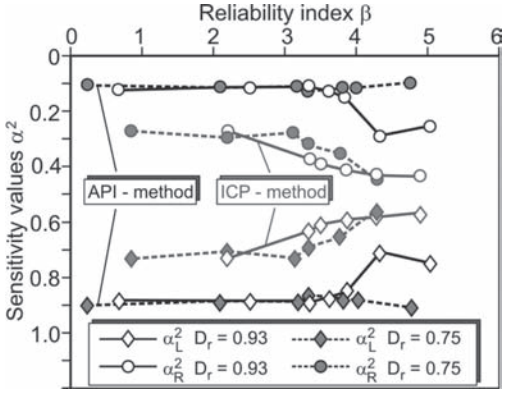

Figure 6. Load and resistance sensitivity values with increasing safety.

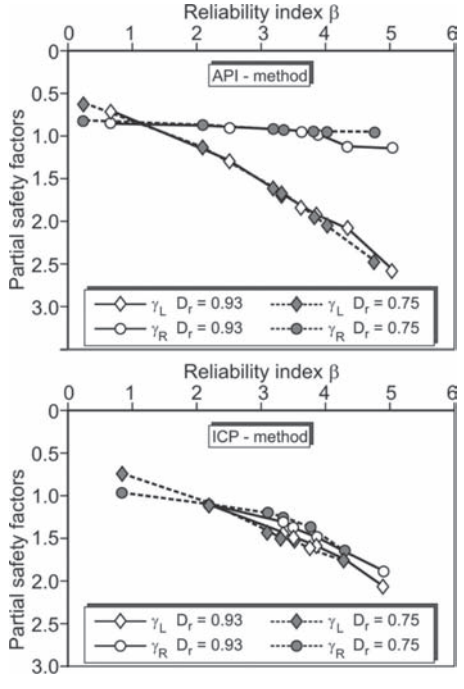

Figure 7. Partial safety factors required to achieve a certain safety.

safety factors for the ICP-method are increasing continuously, where for very dense sand condition the partial safety factors tend to be more uniform, like also the sensitivity values.

Table 5 shows the products of partial safety factors which should be used within a deterministic design to achieve the given safeties according to the minimum of both methods. Comparing to the deterministic values, generally a decrease for the API-method and an increase for the ICP-method should be applied. Single partial safety factors as also the product can be estimated for a desired safety from Figure 7.

Table 5. Product of partial safety factors for a safety according to the minimum of both methods.

Design method	$D_r = 0.75$		$D_r = 0.93$	
	API	ICP	API	ICP
$\gamma_L\ \gamma_R$				
$\beta = 3.3$	1.59 (1.52)*	1.86	1.55	2.60 (1.87)*
$\beta = 3.8$	1.96 (1.82)*	2.29	1.84	3.12 (2.31)*

*Corresponding partial safety factors product by not taking into account the minimum of both methods.

Table 6. Comparison of the separation of required pile lengths for different designs.

	ΔL ($D_r = 0.75$)	ΔL ($D_r = 0.93$)
For deterministic design	5.94	14.95
For reliability $\beta = 3.3$	1.46	8.61
For reliability $\beta = 3.8$	3.12	8.77

6.4 *Deterministic design vs. reliability based design*

By performing reliability based design the same safety can be aspired as also more information, like a model error, can be taken into account. This leads to a more robust determination of the required pile length. Therefore Table 6 summarizes the separation according to deterministic design and two reliability indexes. As it can be seen the gap between the obtained pile lengths via reliability based design is decreased about 61% for dense and 41% for very dense soil conditions.

7 CONCLUSIONS

It could be determined that the use of partial safety factors according to DIN 1054 for mainly axially loaded foundation piles of offshore wind turbines leads in case of the API-method to a safety of $\beta = 4.1$, where in case of the ICP-method a safety of $\beta = 3.5$ was detected. Based on that, it generally can be assumed that the real safety is in the range of these values.

Also it was found that the variation for the resistance arises mainly from the model error and

that the soil uncertainty is of much lower effect than it would be expected.

According to the computed results the partial safety factors should be decreased for the conservative API-method, where an increase for the ICP-method is recommended.

A more specific determination of the pile length by applying reliability based design is possible, since more information is evaluated.

REFERENCES

Achmus, M., Abdel-Rahman, K. & Tom Wörden, F. 2007. Geotechnical design of piles supporting foundation structures for offshore wind energy converters. *Proceedings of the 17th (2007) International Offshore and Polar Engineering Conference (ISOPE 2007): Held in Lisbon, Portugal, July 1–6, 2007*. Lisbon: ISOPE.

Achmus, M. & Müller, M. 2010. Evaluation of pile capacity approaches with respect to piles for wind energy foundations in the North Sea, In S. Gourvenec, D.J. White (eds), *Frontiers in Offshore Geotechnics Two*, CRC Press: Balkema

API 2007. Errata and Supplement 3—API Recommended Practice 2A-WSD, Recommended Practice for Planning, Designing, Constructing Fixed Offshore Platforms—Working Stress Design.

DIN1054 2010. Baugrund-Sicherheitsnachweise im Erd und Grundbau, Berlin: Deutsches Institut für Normung.

Eurocode 0, 2010. DIN EN 1990: Eurocode: Grundlagen der Tragwerksplanung, Berlin: Deutsches Institut für Normung.

Eurocode 7, 2009. DIN EN 1997: Eurocode 7: Entwurf, Berechnung und Bemessung in der Geotechnik—Teil 1: Allgemeine Regeln, Berlin: Deutsches Institut für Normung.

Fenton, G.A. & Griffiths, D.V. 2008. *Risk assessment in geotechnical engineering*. Hoboken: Wiley & Sons.

GL G.L. *Rules and Guidelines, IV Industrial Services, Guideline for the Certification of Offshore Wind Turbines*. Germanischer Lloyd Wind Energie GmbH, Hamburg/Germany, Edition 2005.

Holicky, M., Markova, J. & Gulvanessian, H. 2007. Code Calibration Allowing for Reliability Differentiation and Production Quality. In Kanda, Takada & Furuat (eds), *Application of Statistics and Probability in Civil Engineering: Proceedings of the 10th International Conference*, *London*. Taylor & Francis.

Jardine, R., Chow, F.C., Overy, R. & Standing, J. 2005. *ICP design methods for driven piles in sands and clays*. London: Thomas Telford.

Phoon, K.K. & Kulhawy, F.H. 1999. Characterization of geotechnical variability. *Canadian Geotechnical Journal* 36(4): 612–624.

This page intentionally left blank

Geotechnical Safety and Risk IV – Zhang et al. (eds)
© 2014 Taylor & Francis Group, London, ISBN 978-1-138-00163-3

Reliability-based evaluation of vertical bearing capacity of piles using FORM and MCS

A. Teixeira & A. Gomes Correia
University of Minho—C-TAC, Guimarães, Portugal

A.A. Henriques
University of Porto—LABEST, Porto, Portugal

ABSTRACT: This paper aims to show reliability concepts for axial pile foundations' design and safety aspects, revealing that reliability analysis do not imply a significant increased effort when compared to the traditional design methodologies. In fact, calculations using reliability concepts provide very useful information, such as the uncertainty that mostly influence the probability of failure. Therefore, the most used reliability methods, FORM and MCS, are here presented and used to evaluate the safety of the bearing capacity of an axial bored pile considering the geotechnical uncertainties and different load values. For the application example presented, the physical uncertainties of actions, the inherent soil variability and model error (pile's resistance) were determined by experimental *in situ* tests (SPT) or collected from bibliography.

1 INTRODUCTION

The new regulation codes and social concerns, such as the sustainability or the economy, are imposing geotechnical engineers to increase their ability to deal with uncertainty in a direct and more rational way. Designs should be economic, sustainable and reliable at the same time. Concerning the reliability part of design, different approaches can be done, but the most important thing to keep in mind is the simplicity of the tools and applied methods. To prevent loss and intuitive understanding of the problem it is necessary to fully understand what is being done, regarding data collection task, uncertainties characterisation and the reliability calculation itself.

Because in geotechnical practice these tools are not as present as they are in the structural engineering, this paper aims to show simple reliability concepts for axial pile foundations' design and safety aspects. It is also shown that calculations using reliability concepts provide very useful tools to model the uncertainties and to quantify and give information about the ones that mostly influence the behaviour under study. The most used and simple reliability methods are FORM (First Order Reliability Method) and MCS (Monte Carlo Simulations). These methods denote different reliability levels. FORM is an approximate method, while MCS is a pure probabilistic method with higher accuracy, and it is used as reference method. Therefore, a simple reliability-based approach is presented, using both FORM and MCS to evaluate the safety of the bearing capacity of a pile concerning different load values. Finally, an application example of a vertically loaded pile foundation, a bored pile (reinforced concrete) installed in a residual soil of granite, illustrates the applicability of the proposed reliability-based approach and the consistency between the FORM and MCS results.

2 RELIABILITY

Reliability Analyses (RA) have the intention of assessing the probability of a particular behavior by introducing randomness of the variables.

2.1 *RA levels*

Usually, the RA levels considered are five—Table 1:

- RA level zero: deterministic methods, the Random Variables (RV) involved are taken as deterministic and uncertainties taken into account by a global Safety Factor (SF);
- RA level I: semi-probabilistic methods, where deterministic formulas are applied and the representative values of RV (statistically determined) are multiplied by partial SF (calibrated by RA level II or III);
- RA level II: approximate probabilistic methods, where the RV are characterised by their statistical

Table 1. Levels of reliability.

	Zero	I	II	III	IV
Geotechnical parameters					
Calculation method (deterministic)					
Design parameter (statistical basis)					
Variability of parameters:					
– mean and SD					
– PDF					
Costs/consequences					
Type of analysis:	Global SF	Partial SF	e.g. FORM	e.g. MCS	Risk

parameters—mean and Standard Deviation (SD) or coefficient of variation (COV = SD/mean);
– RA level III: full probabilistic analyses, it takes into account all the probabilistic characteristics of the RV—mean, SD and Probability Distribution (PDF) and when the problem is complex simulations methods are used;
– RA level IV: risk analyses, where the consequences of failure are also taken into account and the risk is used as a measure of the reliability.

2.2 *RA methods*

One of the first attempts to solve this kind of problems involving probabilities and statistics, with non-normal variables and complex integral calculations, was the First Order Second Moment (FOSM) proposed by Cornell (Cornell 1969) that first introduced the concept of reliability index. FOSM ignores the shape of the PDF, using only the mean and SD of the RV, and the calculation model is linearized using Taylor's expansion. Next, other authors (e.g. Hasofer & Lind 1974) continued to develop the method, and FORM was proposed, solving the invariance problem of FOSM and being nowadays one of the basic tools for RA level II. These are called first and second order methods and are approximation techniques.

For more accurate calculations (RA level III) the simulation methods are used, these methods can be applied to RV with non-normal distribution and complex performance functions (e.g. requiring nonlinear functions or finite element methods). RA level III use all the statistical information about the RV and the most known and method of reference is the MCS. To MCS it is possible to add reduction of variance techniques, such as Stratified sampling, Latin hypercube or Importance sampling, with the goal of reducing calculation time, by selecting only points near failure, or selecting specific groups to be represented in calculations (Phoon & Honjo 2005, Phoon 2008, Zhang et al. 2011).

A full account of the reliability methods development and evolution can be found in Manohar & Gupta (2005) and Baecher & Christian (2003).

2.3 *RA-based safety evaluation*

In order to carry the reliability-based safety evaluation, the following procedure is used for both FORM- and MCS-based RA:

– definition of the significant failure modes and formulation of their functions $\rightarrow g(X_i)$:

$$M = R - E = g(X_i) \tag{1}$$

where M is the safety margin, R denotes the resistance, E denotes the action, g is the performance function, and X_i are the random variables;
– identification of the random and deterministic variables $\rightarrow X_i$;
– description and characterisation of the RV, namely the statistical parameters—mean, SD, COV and PDF type—as well as identification of the dependencies among them (if existent);
– selection of the target reliability index $\rightarrow \beta_T$ and correspondent probability of failure $\rightarrow pf$.

The target depends on many factors, such as the type of structure, the social tolerance for non-compliance, among others. Its selection can be based on previous similar construction projects that met predefined requirements or on recommendations in design codes—β_T for ultimate limit state design should be 3.3 to 4.3 (CEN 2002a) or 1.3 to 4.3 (ISO 2394, 1998). These values correspond to pf of approximately 10^{-1} and 10^{-5}, as shown in Figure 1.

For safety evaluation of the bearing capacity, the problem main characteristics are fixed, such as dimensions and materials, and probabilities of failure (reliabilities) are calculated for different load values.

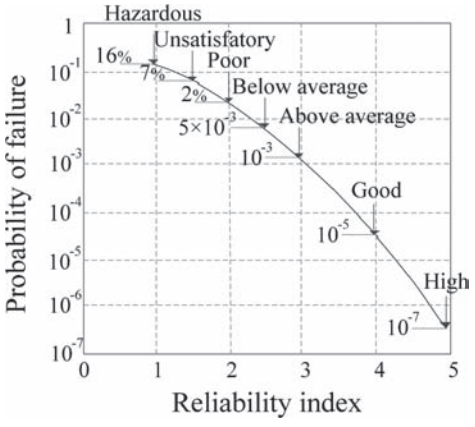

Figure 1. Probability of failure vs. reliability index.

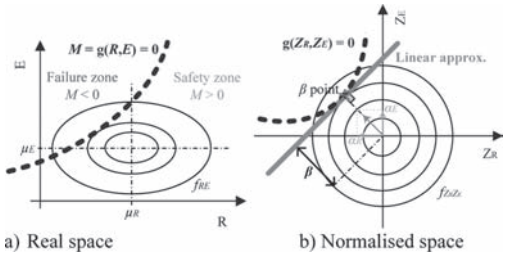

Figure 2. Graphical representation of FORM.

2.4 *FORM*

RA level II using FORM is based on successive linear approximations to a nonlinear performance function (Fig. 2) (Henriques et al. 1999). Following the previously described steps, a RA using FORM is accomplished as follows:

- transforming all RV into standard normalised RV $\rightarrow Z \sim N(0,1)$;
- rewriting the performance function with normalised RV $\rightarrow g(Z_i)$;
- selecting the design point $\rightarrow Z^*$, that is, the one closest to the origin in the normalised space;
- evaluating β as the distance between the origin and the design point Z^*.

This method includes sensitivity factors (α), determined as shown in Figure 2b (for the case of two RV, E and R), that help to evaluate the influence of each RV in the result.

2.5 *MCS*

Simulation methods are RA level III. They can be applied to more complex RV and performance characteristics Once again, after following the general steps previously described, RA using MCS is accomplished as follows:

- based on the desired β select the number of simulations $\rightarrow n$;
- generate n values for each RV based on the variability information (mean, SD or COV and PDF) by applying existing correlations;
- compute the value of the performance function for each generation;
- determine pf as the sum of the simulations that fail ($g(X_i) < 0$) divided by n.

The total number of simulations n must be chosen carefully. Its stability should be studied by analysing the fluctuation of the final results of different n (Teixeira 2012).

2.6 *Uncertainties*

Uncertainties are associated with the RV. Mostly, RV are continuous variables and uncertainties characterised by their statistical moments, mean and SD or COV, and PDF. Very commonly this PDF is assumed to be Normal or Lognormal. The uncertainties are usually divided as follows:

- physical uncertainties, are the inherent uncertainties of the material;
- modelling uncertainties, come from the theoretical approaches (transformations and models);
- statistical uncertainties, include the uncertainty associated with the finite size and fluctuations in the samples (always present);
- human errors (usually not considered in geotechnical RA, however its influence can be reduced by an adequate quality control during design and construction);
- and spatial variability.

Gathering all RV and uncertainties may be a consuming task, because there is a great number of variables, but only the variability of the most important and influent ones are worth considering (Baecher & Christian 2003, Teixeira et al. 2012). For that purpose, sensitivity analyses can help evaluate the relative influence of the uncertainty associated with each RV on the final result. However, the knowledge of the important and influent uncertainties is sometimes limited. Data from the specific site in study may not be available or may not be sufficient to estimate variability, in this cases, uncertainty can be characterized by COV observed in similar sites. Kulhawy & Mayne (1990), Phoon & Kulhawy (1999a, 1999b) and Uzielli et al. (2007) did a literature review for the COV of inherent variability, scale of fluctuation (soil spatial correlation), and COV of measurement error. Also, typical values of COV for soil properties and *in situ* test results have been compiled and

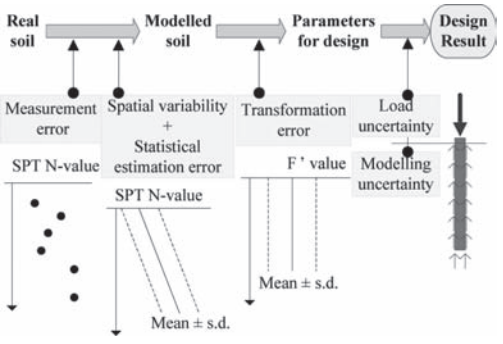

Figure 3. Methodology and uncertainties considered in RA (adapted from Honjo et al. 2010).

reported by Phoon et al. (1995), Jones et al. (2002), and more recently by Phoon (2008). Geotechnical variability is so great that sometimes none of these references can be applied. Finally, some RV in geotechnical problems, vary continuously over a space or time. These variables are referred as random fields, and autocorrelation between variables in space or time can and should be considered (Vanmarcke 1977). The spatial variability is normally ignored because of the difficulties in practical application. But when introduced, spatial correlation of variables can reduce the variances. It could be said that it is a conservative choice, but it is technically incorrect to perform probabilistic analyses without considering spatial correlation (Lacasse & Nadim 1996, Kulhawy & Phoon 1996, Honjo et al. 2007). In Figure 3 are depicted the uncertainties that will be taken into account in this paper, for pile foundations.

3 APPLICATION EXAMPLE

3.1 *Case study*

The case study pertains to an experimental site in the north of Portugal (Viana da Fonseca & Santos 2008). Residual soil from granite is found at this site. The site is characterised geologically by an upper layer of heterogeneous residual (saprolitic) granite soil of varying thickness, overlying a relatively weathered granite in contact with high-grade metamorphic rocks. Bedrock is found at a depth of approximately 20 m, and the ground water line is found at a depth of approximately 10 m. An extensive *in situ* and laboratory investigation was conducted, but because the SPT is one of the most commonly used *in situ* tests for geotechnical design and soil characterisation, SPT results were used for the calculations performed. The pile considered is a reinforced concrete bored pile (id: E9) that is 6 m in length and 0.6 m in diameter. The ultimate capacity of the pile, measured under static loading to failure, was 1350 kN.

Since the case study is an experimental pile designed according to the available resources and sponsorships, the actions values were not available. Therefore, the permanent and variable loads range (considered equal in magnitude) was determined based on the prediction of the vertical bearing capacity and using partial safety factors proposed by Eurocodes (CEN 2002b, 2007).

3.2 *Bearing capacity*

Throughout the world, the SPT is the most common method of soil investigation and often is the only available source of information for pile design. Also, the major specifications pertaining to piles have also adopted pile bearing capacity estimation formulas based on the N value obtained from the SPT. As such, the vertical bearing capacity of the pile is evaluated by an SPT based empirical method from the Specifications of Highway Bridges of Japan (JRA 2001, Honjo et al. 2002, Teixeira et al. 2012). This method was selected because it has statistical information about the model error associated with the bearing capacity values predicted (Okahara et al. 1991).

Considering the result of the static load test, and also considering that the permanent and variable loads were equivalent in magnitude, E (total $G_k + Q_k$) for the RA-based safety evaluation it was assumed to be between 400 and 1400 kN.

3.3 *Performance function*

The basic formula for the performance function presented in Equation 1, is transformed into Equation 2 when using an empirical method for the evaluation of the pile vertical bearing capacity.

$$M = \left(R_{tip} + R_{side}\right) - \left(G + Q\right) = \left(\delta_t \times Q_{tip} + \delta_f \times F_{side}\right) - \left(\delta_G \times G_k + \delta_Q \times Q_k\right) \quad (2)$$

where M is the safety margin, R_{tip} the tip resistance of the pile, R_{side} the side resistance of the pile, G is the permanent action, Q is the variable action, δ are the factors to take into account the uncertainties (δ_t for model error uncertainty on tip resistance, δ_f for model error uncertainty in side resistance, δ_G for permanent actions uncertainties and δ_Q for variable actions uncertainties), Q_{tip} is the predicted tip resistance, F_{side} is the predicted side resistance, G_k the permanent characteristic actions and Q_k the variable characteristic actions.

3.4 *Uncertainties*

The uncertainty sources considered taking into account the Equation 2 were:

- the modelling uncertainty (or model error) in the evaluation of resistance by an empirical method, both side and tip components, δ_f and δ_t;
- the inherent soil variability (spatial and estimation error) considered through the number of blows (N) of SPT or other soil test, both side and tip components, $N_{SPT,side}$ and $N_{SPT,tip}$;
- and the physical uncertainties of actions (permanent and variable), δ_G and δ_Q.

Note that all uncertainties were considered as independent and the values for each uncertainty are presented in Table 2.

As referred before, uncertainties for model error were gathered from Okahara et al. (1991), while for actions, the studies made by JRA (2001) and Holicky et al. (2007) were used. The SPT trend was fitted to the SPT data at the site, presented in Figure 4. The soil variability is therefore, taken into account with this information (trend and residuals) and by a normal distribution for the residuals. A graphical method (probability plot, also known as Q-Q plot) was used to assess this approximation. The reduction of SD of the soil uncertainty/variability was based on Vanmarcke's principle of autocorrelation (Vanmarke 1977, Honjo & Setiawan 2007, Honjo et al. 2011).

3.5 *Results*

Recall that the safety evaluation approach assumes a fixed length and diameter of the pile while it calculates the probabilities for different load values. Safety evaluation approach was carried out for the following load values $E = G_k + Q_k$ = [400; 600; 700; 750; 800; 850; 900; 1000; 1200; 1400] kN. FORM

Table 2. Uncertainties values for application example.

Uncertainties	Mean	SD	PDF type
Model			
– tip	1.12	0.706	Lognormal
– side	1.07	0.492	Lognormal
Soil			
– $N_{SPT,tip}$	10.26.1.91 z	4.6*	Normal
– $N_{SPT,side}$		4.6**	Normal
Actions†			
– permanent	1.0	0.10	Normal
– variable	0.6	0.21	Gumbel

*Will be reduced taking into account the influence zone on the pile tip (3 × diameter) as averaging over the thickness. **Will be reduced taking into account the length of the pile as averaging over the thickness. †Considered $G_k = Q_k$.

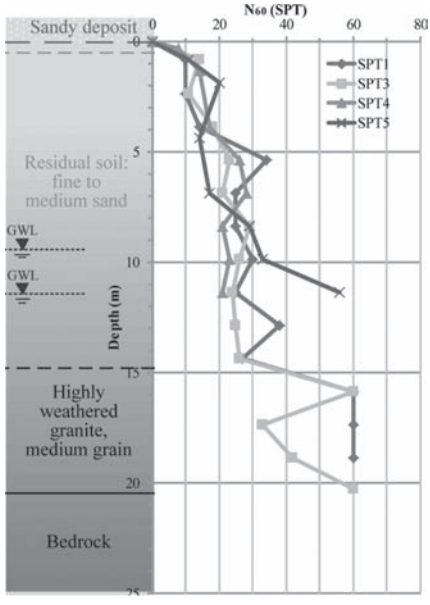

Figure 4. SPT data from application example.

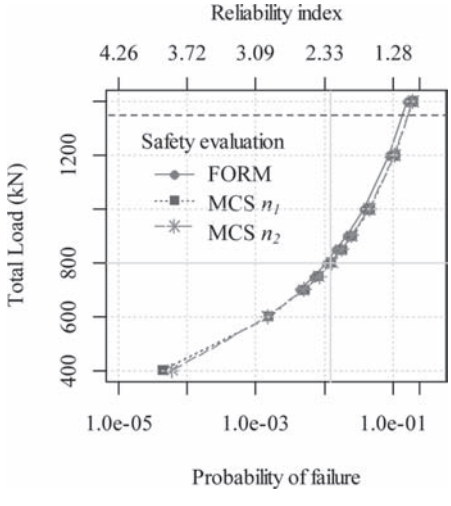

Figure 5. Reliability-based safety evaluation of vertical bearing capacity of application example.

and MCS results are presented in Figure 5. MCS using n_1 = 200,000 and n_2 = 1,000,000 are presented to see that the number of simulations stabilizes from n > 200,000. Figure 5 also depicts a light line marking the hypothetical/considered design load (total of 800 kN) and the load test result (1350 kN). Moreover, Figure 6 presents the obtained values for α factors (FORM).

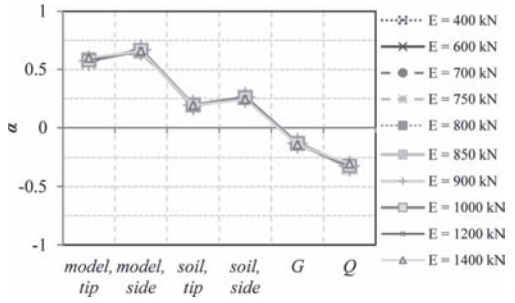

Figure 6. FORM sensitivity factors for the application example.

It is possible to conclude that:

- for MCS with n_1 and n_2 the results are consistent;
- FORM results give very acceptable approximations to MCS results;
- the results also show a clear relationship (exponential type) between the reliability and the load;
- if one considers the hypothetical action (800 kN) it is possible that it does not meet the requirements, that usually recommend a reliability index between 2.5 and 4.0;
- and it is also possible to see that the uncertainty that has more influence in the reliability is the model error, being the other uncertainties considerably less important.

4 CONCLUSIONS

This paper presented a simple methodology for a reliability-based safety evaluation of an axial pile foundation, based on FORM and MCS. These are believed to be easy methodologies and following the trend of reliability-based assessments. They can help support the design of pile foundations and also try to eliminate the possible confusions and difficulties that traditional reliability methodologies used in structures can cause to geotechnical designers in practice. This paper also presented an application example, for which calculations were repeated for different loads. One of the main results is the relationship between probability of failure and the load value and the high influence of the model error in these results. Furthermore, the actions uncertainties were demonstrated to have not an important role in the reliability. This type of reliability-based assessments allows a more rational way to deal with uncertainties of a problem, instead of just introducing safety factors into the calculation.

ACKNOWLEDGEMENTS

The authors wish to thank to "Fundação para a Ciência e a Tecnologia" (FCT) for the financial support under the strategic project PEst-OE/ECI/UI4047/2011 and the doctoral grant SFRH/BD/45689/2008. Also, authors wish to thank the contributions of Professor Yusuke Honjo and Doctor Kieu Le Thuy Chung for their contributions and ideas.

REFERENCES

Baecher, G.B., & Christian, J.T. 2003. *Reliability and statistics in geotechnical engineering.* Chichester, UK: John Wiley & Sons.

CEN. 2002a. European Committee for Standardization. Eurocode 0: Basis of Structural Design. EN 1990.

CEN. 2002b. European Committee for Standardization. Eurocode 1: Actions on Structures. EN 1991.

CEN. 2007. European Committee for Standardization. Eurocode 7: Geotechnical Design. EN 1997.

Cornell, A.C. 1969. A probability-based structural code. *Journal American Concrete Institute* 66(12): 974–985.

Hasofer, A.M. & Lind, N.C. 1974. Exact and invariant second-moment code format. *Journal of the Engineering Mechanics Division, ASCE* 100(EM1): 111–121.

Henriques, A.A., Calheiros, F. & Figueiras, J.A. 1999. Probabilistic modelling of nonlinear behaviour of concrete structures. In Schueller, & Kafka (Ed.), *Proc. ESREL, '99 (pp. 495–500) Munich, Germany: A. A. Balkema*.

Holicky, M., Markova, J. & Gulvanessian, H. 2007. Code calibration allowing for reliability differentiation and production quality. *Proc.10th International Conference on Applications of Statistics in Civil Engineering*, *Tokyo, Japan*. Taylor & Francis.

Honjo, Y. & Setiawan, B. 2007. On conditional estimation accuracy of spatial average of soil proprieties and sample size. *Proc.10th International Conference on Applications of Statistics in Civil Engineering*, *Tokyo, Japan*. Taylor & Francis.

Honjo, Y., Suzuki, M., Shirato, M. & Fukui, J. 2002. Determination of partial factors for a vertically loaded pile based on reliability analysis. *Soils and Foundations* 42(5): 91–109.

Honjo, Y., Jliati, M.N. & Ishino, J. 2007. Effects of spatial variability and statistical estimation error in prediction of settlement of shallow foundation. *Proc.10th International Conference on Applications of Statistics in Civil Engineering, Tokyo, Japan*. Taylor & Francis.

Honjo, Y., Hara, T. & Kieu Le, T.C. 2010. Level III reliability based design of examples set by ETC10. *Proc. 2nd International Workshop on the Evaluation of Eurocode 7, Pavia, Italy*.

ISO. 1998. International Organization for Standardization. ISO 2394: General principles on reliability for structures.

Jones, A.L., Kramer, S.L. & Arduino, P. 2002. *Estimation of uncertainty in geotechnical properties for performance-based earthquake engineering.* Pacific Earthquake Engineering Research Center, University of Washington, USA.

JRA. 2001. Japan Road Association. Specifications for Highway Bridges.

Kulhawy, F.H. & Mayne, P.W. 1990. *Manual on estimating soil properties for foundation design*. Electric Power Research Institute, Cornell University, USA.

Kulhawy, F.H. & Phoon, K.K. 1996. Engineering judgment in the evolution from deterministic to reliability-based foundation design. *Uncertainty in the Geologic Environment: From Theory to Practice, Geotechnical Special Publication, ASCE*, 58: 29–48.

Lacasse, S. & Nadim, F. 1996. Uncertainties in characterising soil properties. *Proc. UNCERTAINTY'96, Madison, USA*. ASCE.

Manohar, C.S. & Gupta, S. 2005. Modeling and evaluation of structural reliability: current status and future directions. In K.S. Jagadish. & R.N (eds). Iyengar, *Recent Advances in Structural Engineering*: 90–187. Indian Institute of Science, Bangalore, India.

Okahara, M., Takagi, S., Nakatani, S. & Kimura, Y. 1991. A study on bearing capacity of as single pile and design method of cylinder shaped foundations. Technical Memorandum of PWRL.

Phoon, K.K., Kulhawy, F.H. & Grigoriu, M.D. 1995. *Reliability-based design of foundations for transmission line structures*. Electric Power Research Institute, Cornell University, USA.

Phoon, K.K. & Kulhawy, F.H. 1999a. Characterization of geotechnical variability. *Canadian Geotechnical Journal* 36(4): 612–624.

Phoon, K.K. & Kulhawy, F.H. 1999b. Evaluation of geotechnical property variability. *Canadian Geotechnical Journal* 36(4), 625–639.

Phoon, K.K. & Honjo, Y. 2005. Geotechnical reliability analyses: towards development of some user-friendly tools. *Proc. 16th ICSMGE*: *2845–2848*, *Osaka, Japan*.

Phoon, K.K. 2008. *Reliability-based design in geotechnical engineering: computations and applications*. London and New York: Taylor & Francis.

Teixeira, A., Honjo, Y., Gomes Correia, A. & Henriques, A.A. 2012. Sensitivity analysis of vertically loaded pile reliability. *Soils and Foundations* 52(6): 1118–1129.

Teixeira, A. 2012. *Reliability and cost models of axial pile foundations.* PhD Thesis. Dep. Civil Engineering, University of Minho, Portugal.

Uzielli, M., Lacasse, S., Nadim, F. & Phoon, K.K. 2007. Soil variability analysis for geotechnical practice. *Proc. 2nd Int. Workshop on Characterization and Eng. Properties of Natural Soils. 3. Singapore*: Taylor & Francis.

Vanmarcke, E.H. 1977. Probabilistic modeling of soil profiles. *Journal of the Geotechnical Engineering Division, ASCE* 103(GT11): 1227–1246.

Viana da Fonseca, A. & Santos, J.A. 2008. *International Prediction Event. Behaviour of CFA, Driven and Bored. ISC'2 Experimental Site*. FEUP, Porto and IST, Lisboa.

Zhang, J., Zhang, L.M. & Tang, W.H. 2011. Kriging numerical models for geotechnical reliability analysis. *Soils and Foundations* 51(6): 1169–1177.

This page intentionally left blank

Geotechnical Safety and Risk IV – Zhang et al. (eds)
© 2014 Taylor & Francis Group, London, ISBN 978-1-138-00163-3

Reliability-based design for the serviceability state design of an excavation with cross walls in clays

S.H. Wu & J. Ching
Department of Civil Engineering, National Taiwan University, Taipei, Taiwan

C.Y. Ou
Department of Construction Engineering, National Taiwan University of Science and Technology, Taipei, Taiwan

ABSTRACT: Cross walls are commonly used for constraining the excavation-induced deformations as well as the subsequent building damages in Taiwan. Based on the real case histories, a regression model that is capable of predicting maximum wall displacements for excavations with or without cross walls is proposed. With the consideration of uncertainties in the proposed model, a simplified Reliability-Based Design (RBD) method in the form of partial factors for the Serviceability Limit State (SLS) design of excavations is developed. The partial factors are calibrated by rigorous reliability theory and are verified to produce design outcomes that meet the target reliability index. The use of cross walls which is extremely effective in achieving the target reliability level is highlighted.

1 INTRODUCTION

Large deformations induced by excavations would cause serious damage to adjacent buildings, especially for excavations in soft clay. In Taiwan, cross walls are known to be extremely effective for constraining the excavation-induced deformations in soft clay (Lin 2010, Ou et al. 2011). A cross wall is a wall connecting opposite diaphragm walls, as shown in Figure 1. Cross walls are constructed prior to excavation and behave as the lateral support with large axial stiffness. An important feature of cross walls is that it develops wall displacement behavior similar to the corner effect of diaphragm walls (Lin 2010, Ou et al. 2011).

Wu et al. (2013) developed a regression model for predicting the maximum wall displacement that is applicable to excavations with or without cross walls. They concluded that the use of cross walls is fairly effective in reducing wall displacements in a qualitative way, but the effectiveness of cross walls was not verified in a quantitative way in that study, i.e. how the reliability index would increase after the use of cross walls? To address this quantitative question, quantifications of uncertainties are required. For instance, the regression model developed in Wu et al. (2013) is not 100% accurate, i.e. there are transformation and parameter uncertainties. These uncertainties must be taken into account for the purpose of reliability-based design.

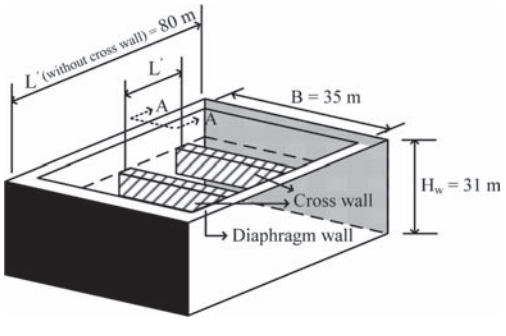

Figure 1. Schematic diagram of cross walls.

In this paper, the uncertainties associated with this model will be quantified and a simplified Reliability-Based Design (RBD) methodology based on partial factors will be developed for the SLS design in excavations—these partial factors are calibrated by reliability theory rather than specified by judgments and experiences. A design example is illustrated for the application. The effectiveness of cross walls in achieving the target reliability level will be demonstrated in the design example.

1.1 *Review of the regression model*

Based on the 11 cases with cross walls (all are cast in-situ prior to excavation) and another 11 cases without cross walls in Taipei, Wu et al. (2013) developed a regression model for predicting maximum wall displacement δ_m^* (in mm) for

the A-A section in Figure 1 for braced excavations in soft clay:

$$\ln\left[\delta_m^*(mm)\right] \approx a_0 + a_1\mathrm{B} + a_2\ln(H_e) + a_3\ln\left(s_u/\sigma_v'\right) + a_4\ln(\mathrm{L}') + a_5\ln(\mathrm{K}) + a_6\left[\ln(H_e)\right]^2 + a_7\left[\ln(\mathrm{L}')\right]^2 + a_8\left[\ln(\mathrm{K})\right]^2 + a_9\ln\left(s_u/\sigma_v'\right)\ln(\mathrm{L}') + a_{10}\ln(\mathrm{L}')\ln(\mathrm{K}) \quad (1)$$

where L′, B, and H_e (in meters) are respectively the spacing between the two cross walls, excavation width, and excavation depth (see Fig. 1 for the definition of L′ and B); s_u/σ_v' is the normalized undrained shear strength based on isotropic Consolidated Undrained Compression (CIUC) test; K (in kN/m) is the system stiffness; coefficients are $a_0 = 11.1908$, $a_1 = -0.0048$, $a_2 = -0.0168$, $a_3 = 1.5855$, $a_4 = -0.5071$, $a_5 = -1.1914$, $a_6 = 0.2354$, $a_7 = -0.0691$, $a_8 = 0.0390$, $a_9 = -0.8365$, and $a_{10} = 0.0196$. Note that Equation 1 is applicable to cases with or without cross walls. For cases with cross walls (e.g. Fig. 1), if the maximum wall displacement at the A-A section in Figure 1 is of concern, L′ is the spacing between the two cross walls, whereas for cases without cross walls (i.e. the hatched cross walls in Figure 1 do not exist), L′ is the spacing between the two diaphragm walls. The system stiffness K can be modeled as an in-series system consisting of the following two stiffnesses: (a) the flexural stiffness of the diaphragm wall (k_2) and (b) the stiffness of the parallel sub-system consisting of the axial stiffness of the cross walls (k_1) and the axial stiffness of the lateral supports (struts) (k_3):

$$\mathrm{K} = \frac{k_2 \times (k_1 + k_3)}{k_1 + k_2 + k_3} \quad (2)$$

For cases without cross walls, k_1 should be calculated as the axial stiffness of the diaphragm walls in dark and grey (see Fig. 1). The details for the calculations of K can be found in Wu et al. (2013).

Based on the results in Wu et al. (2013), the use of cross walls was found to be fairly effective in reducing wall displacements. Nonetheless, it is not clear how the use of cross walls can effectively increase the reliability index and how to design the spacing L′ to meet the target reliability level. This is the main objective of this study.

2 MONTE CARLO SAMPLES OF δ_M^*

The reliability-based design method adopted in this paper requires the simulations of Monte Carlo samples of δ_m^*. As seen in Equation 1, δ_m^* depends on s_u/σ_v', K, H_e, L′, and B. Among them, H_e, L′, and B are treated as deterministic parameters, but the values of s_u/σ_v' and K are treated as random variables. Furthermore, Equation 1 is not exact, and the random model error is characterized by an error term ε in the following:

$$\ln\left[\delta_m^*(mm)\right] = a_0 + a_1\mathrm{B} + a_2\ln(H_e) + a_3\ln\left(s_u/\sigma_v'\right) + a_4\ln\left(\mathrm{L}'\right) + a_5\ln(\mathrm{K}) + a_6\left[\ln(H_e)\right]^2 + a_7\left[\ln\left(\mathrm{L}'\right)\right]^2 + a_8\left[\ln(\mathrm{K})\right]^2 + a_9\ln\left(s_u/\sigma_v'\right)\ln\left(\mathrm{L}'\right) + a_{10}\ln\left(\mathrm{L}'\right)\ln(\mathrm{K}) + \varepsilon \quad (3)$$

where ε is the model error. The regression model error ε is modeled as a zero-mean normal random variable. The STD of ε is determined to be roughly 0.33 based on the 22 cases given in Wu et al. (2013).

As mentioned earlier, in real application the value of s_u/σ_v' may not be exactly known due to measurement and transformation errors. Only the measured (or nominal) value of s_u/σ_v', denoted by $(s_u/\sigma_v')_m$, may be known. The relation to the measured value is assumed to be

$$\ln\left(s_u/\sigma_v'\right) = \ln\left[\left(s_u/\sigma_v'\right)_m\right] + e_1 \quad (4)$$

where the error e_1 is modeled as a zero mean normal distribution with Standard Deviation (STD) in the range of 0.1–0.5 [the STD of e_1 is roughly the same as the Coefficient of Variation (COV) of s_u/σ_v'; the range of 0.1–0.5 is consistent to the low to medium variability summarized in Phoon & Kulhawy (2008)].

The value of K is also treated as a random variable. It depends on the values of the more fundamental input parameters, such as the Young's moduli of the concrete (E_c) for the diaphragm wall, cross walls, and concrete floor slabs as well as the Young's modulus for the steel struts (E_{st}) [see Wu et al. (2013) for the detailed formulas for K]. These concrete Young's moduli (E_c) depend on the concrete compressive strengths (f_c):

$$\ln\left(E_c\right) = \ln\left[4700\sqrt{f_c}\right] + e_2 \quad (5)$$

where e_2 is the transformation error, modeled as a zero mean normal random variable with STD in the range of 0.1~0.3. The transformation errors of the E_c's (namely, e_2's) for the diaphragm walls, cross walls, and concrete floor slabs are considered to be independent. Finally, the f_c in the above equation is related to the measured value $(f_c)_m$ by

$$\ln\left(f_c\right) = \ln\left[\left(f_c\right)_m\right] + e_3 \quad (6)$$

where e_3 denotes the measurement error, modeled as zero mean normal random variables with STD in the range of 0.1~0.2. Again, the measurement errors of the f_c's (namely, e_3's) for the diaphragm walls, cross walls, and concrete floor slabs are considered to be independent. The struts Young's modulus (E_{st}) for the steel struts is related to its measured value by

$$\ln\left(E_{st}\right) = \ln\left(E_{st}\right)_m + e_4 \tag{7}$$

where e_4 denotes the measurement error, modeled as a zero mean normal random variable with STD in the range of 0.1~0.3.

In summary, the system stiffness K can be simulated as a function of $\{(f_c)_m, (E_{st})_m, e_2, e_3, e_4\}$ and the s_u/σ_v' can be simulated as a function of $\{(s_u/\sigma_v')_m, e_1\}$. One also needs to know the dimension parameters {B, L′, H_e} and needs to simulate a sample of ε. A Monte Carlo simulation (MCS) sample of δ_m^* can be then computed by Equation 3. Repeating the above steps to yield N samples of δ_m^*, and the failure probability (P_f) of exceeding a prescribed limiting displacement δ_L can be estimated to be N_f/N, where N_f is the number of samples that satisfy $\delta_m^* > \delta_L$, and the reliability index $\beta = -\Phi^{-1}(P_f)$, where $\Phi^{-1}(.)$ is the inverse cumulative density function of standard normal distribution. Note that the above calculation of P_f or β can be conducted at any excavation stage—one needs to replace (H_e, K) by the depth and stiffness of the current excavation stage.

3 SIMPLIFIED RELIABILITY-BASED DESIGN

Although cross walls are effective in increasing reliability level, it is not clear at this point how to design a real case (e.g. select the cross wall spacing L′) in order to meet the target reliability level because L′ is highly related the amount of wall displacement (Wu et al. 2013). This is the main purpose of this section.

In this study, a simplified RBD design equation in the form of partial factors will be developed. The First Order Reliability Method (FORM) (Ang & Tang 1984) was commonly used for calibrating partial factors in major design codes (e.g. AASHTO codes & Eurocode), however, based on the recent study given by Ching & Phoon (2011), they indicated that the partial factors calibrated by the quantile approach is more sensible and robust than FORM. This approach is formally called the Quantile Value Method (QVM) in Ching & Phoon (2013). Therefore, QVM is used in this study for calibrating the partial factors. What follows will only present the basic idea of QVM without mentioning the technical details. The technical details of QVM are given in Ching & Phoon (2011, 2013).

The main idea of QVM is to reduce stabilizing random variables to their η quantiles (η is small) and the increase destabilizing ones to their 1 – η quantiles. For Equation 3, stabilizing random variables include s_u/σ_v' and K, and destabilizing random variables include ε. Taking K as an example, its η quantile, denoted by K_η, satisfies

$$\mathrm{P}\left(\mathrm{K} < K_\eta\right) = \eta \tag{8}$$

For example, if K is a normally distributed random variable, the 5% quantile, $K_{0.05} = \mu_K(1 - 1.645\delta_K)$, where μ_K and δ_K are the mean and COV of K, respectively. This definition is appropriate for stabilizing factors, because the design value is typically a conservative value less than the mean. For destabilizing factor such as ε, the (1 – η) quantile is applied:

$$\mathrm{P}\left(\varepsilon < \varepsilon_{1-\eta}\right) = 1-\eta \qquad \text{or} \qquad \mathrm{P}\left(\varepsilon > \varepsilon_{1-\eta}\right) = \eta \tag{9}$$

The probability of ε larger than $\varepsilon_{1-\eta}$ is 100η%. If ε is normally distributed, the (100 – 5)% = 95% quantile of ε is $\varepsilon_{0.95} = \mu_\varepsilon\ (1 + 1.645\delta_\varepsilon)$, where μ_ε and δ_ε are the mean and COV of ε, respectively, which is a conservative value larger than the mean. Therefore, the RBD in the form of QVM can be achieved by first calculating a conservative design value for $\ln(\delta_m^*)$. This can be done by inserting the η quantiles of s_u/σ_v' and K and the 1 – η quantile of ε into the right hand side of Equation 3:

$$\begin{aligned}\ln\left[\delta_{m,d}^*(mm)\right] &= a_0 + a_1\mathrm{B} + a_2\ln\left(H_e\right) \\ &+ a_3\ln\left[\left(s_u/\sigma_v'\right)_\eta\right] + a_4\ln\left(\mathrm{L}'\right) + a_5\ln\left(\mathrm{K}_\eta\right) \\ &+ a_6\left[\ln\left(H_e\right)\right]^2 + a_7\left[\ln\left(\mathrm{L}'\right)\right]^2 \\ &+ a_8\left[\ln\left(\mathrm{K}_\eta\right)\right]^2 + a_9\ln\left[\left(s_u/\sigma_v'\right)_\eta\right]\ln\left(\mathrm{L}'\right) \\ &+ a_{10}\ln\left(\mathrm{L}'\right)\ln\left(\mathrm{K}_\eta\right) + \varepsilon_{1-\eta}\end{aligned} \tag{10}$$

where $\delta_{m,d}^*$ is the design value for δ_m^*. If the design value $\delta_{m,d}^*$, is less than the limiting value δ_L, the design is satisfactory, and vice versa. Apparently, a design dimension that satisfies $\delta_{m,d}^* \le \delta_L$ is a conservative design, because the random variables s_u/σ_v', K, and ε are taken conservative quantile values in order to determine $\delta_{m,d}^*$.

Equation 10 may not yet be convenient for practical engineers because it requires the knowledge for the definition of quantiles. Practical engineers are familiar with the deterministic RBD design equation in the form of partial factors.

Equation 10 can be readily converted to the form of partial factors:

$$\delta^{*}_{m,d}(mm) = \exp\left\{\begin{array}{l} a_0 + a_1 \mathrm{B} + a_2 \ln(H_e) \\ + a_3 \ln\left[\gamma_{s_u} \times \left(s_u/\sigma_v'\right)_m\right] + a_4 \ln(\mathrm{L}') \\ + a_5 \ln(\gamma_K \times K_m) + a_6 \left[\ln(H_e)\right]^2 \\ + a_7 \left[\ln(L')\right]^2 + a_8 \left[\ln(\gamma_K \times K_m)\right]^2 \\ + a_9 \ln\left[\gamma_{s_u} \times \left(s_u/\sigma_v'\right)_m\right] \ln(\mathrm{L}') \\ + a_{10} \ln(\mathrm{L}') \ln(\gamma_K \times K_m) \end{array}\right\} \times \gamma_\delta \quad (11)$$

where γ's are the partial factors: $\gamma_\delta = \exp[\varepsilon_{1-\eta}]$ is for the model uncertainty; $\gamma_{su} = (s_u/\sigma_v')_\eta / (s_u/\sigma_v')_m = \exp[(e_1)_\eta]$; $\gamma_K = K_\eta/K_m$, where K_m is the nominal K evaluated based on $\{(E_{st})_m, (f_c)_m\}$. Because ε and e_1 are zero-mean normal random variables with STDs equal to σ_ε and σ_1, γ_δ and γ_{su} have the following analytical forms:

$$\gamma_\delta = \exp(\varepsilon_{1-\eta}) = \exp\left[\sigma_\varepsilon \times \Phi^{-1}(1-\eta)\right]$$
$$\gamma_{s_u} = \exp\left[(e_1)_\eta\right] = \exp\left[\sigma_1 \times \Phi^{-1}(\eta)\right] \quad (12)$$

However, γ_K does not have the analytical form, as K is not a random variable of well-known type, hence K_η does not have an analytical form. However, K_η can be obtained by MCS with a large sample size—n samples of K can be obtained from MCS, and $K_\eta \approx$ the 100η% sample quantile of K, which is simply the $n \times 100\eta$% ordered statistics (sorted from small to large K samples) of the n samples of K. Once K_η is obtained, γ_K is simply K_η/K_m.

Based on the theory developed in Ching & Phoon (2011), the $\eta - \beta_T$ relations can be calibrated. Figure 2 shows the calibrated $\eta - \beta_T$ relation. It is found that the calibrated $\eta - \beta_T$ relation is fairly unique with respect to various construction methods (bottom-up or top-down methods), various design dimensions (B ranging from 15 m to 85 m; L′ ranging from 10 m to 136 m; H_e ranging from 1.5 m to 35 m), various typical values of $\{(f_c)_m, (E_{st})_m, (s_u/\sigma_v')_m\}$, and various choices of STDs of $\{e_1, e_2, e_3, e_4\}$. The only exception is when 7.5 m < L′ < 10 m, the calibrated $\eta - \beta_T$ relation somewhat changes (see Fig. 2). The lower bound 7.5 m is a possible practical bound for L′ for the BU construction method.

Given the prescribed β_T, the required η can be checked from Figure 2, and Equation 12 can be subsequently used to derive the required partial factors γ_δ and γ_{su}, while γ_K can be determined by MCS. Figure 3 shows the resulting calibrated

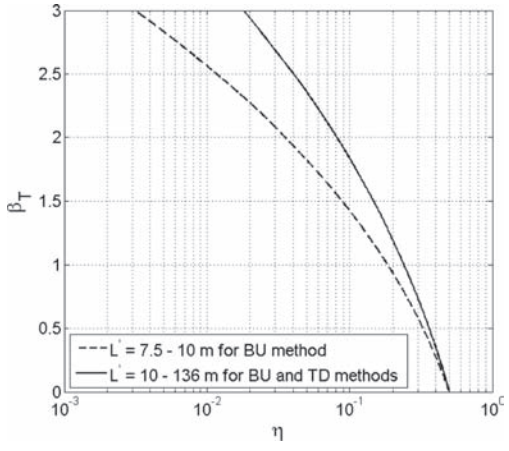

Figure 2. Relations between η and β_T for BU and TD methods.

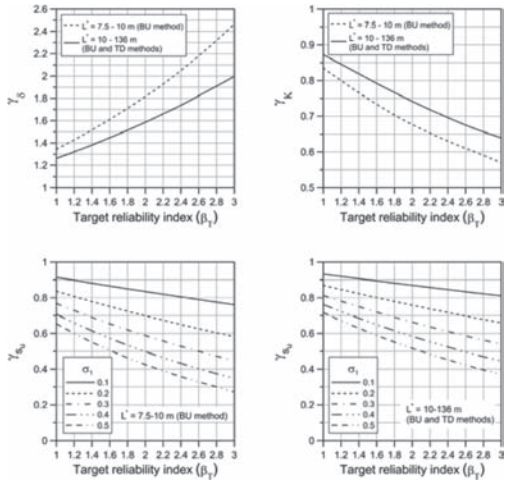

Figure 3. Relations between target reliability index (β_T) and partial factors (γ_i).

$\beta_T - \gamma$'s relations. Note that these calibrated relations do not depend on the choice of δ_L. It is noteworthy mentioned that five sets of $\beta_T - \gamma_{su}$ relations are calibrated (see Fig. 3) for five different STD's of e_1 (0.1, 0.2, …, 0.5). The practical engineers should choose the appropriate $\beta_T - \gamma_{su}$ relation based on the STD of e_1. The practical engineers can check the required partial factors $\{\gamma_\delta, \gamma_{su}, \gamma_K\}$ from this figure and implement these factors in Equation 11 to obtain $\delta_{m,d}{}^*$. If $\delta_{m,d}{}^* \le \delta_L$, the design should roughly satisfy $\beta \ge \beta_T$. Verification (not shown herein) indicates that these partial factors can indeed achieve the target β_T fairly accurately—the actual reliability

indices of the designs based on these partial factors are reasonably close to the target value.

4 DESIGN EXAMPLE

A design example is taken to illustrate the use of the partial factor charts (Fig. 3) and the effectiveness of cross walls. Suppose a rectangular excavation area in Figure 1 (B = 35 m, the total length of the excavation area = 80 m) to be constructed by the bottom-up method with the following parameters: final H_e = 16.6 m, and $(s_u/\sigma_v')_m$ = 0.325 with σ_1 = 0.2 (COV = 0.2). The total depth and thickness of the diaphragm wall (H_w) are 31.0 m and 0.8 m, respectively. There are five levels of steel struts with 4 m horizontal spacing. The nominal compressive strength of concrete $(f_c)_m$ = 27.5 MPa. The nominal Young's modulus of the steel struts $(E_{st})_m = 2.1 \times 10^8$ kPa. The design target is to ensure the maximum wall displacement at the A-A section is less than δ_L = 60 mm at the final excavation stage with target reliability index β_T = 1.5.

Let us first consider the design without cross walls (the hatched walls in Fig. 1 are absent). In this case, B = 35 m and L' = 80 m. Recall that the input parameters for Equation 11 are $\{H_e$, B, L′, $(s_u/\sigma_v')_m$, K_m, γ_δ, γ_{su}, $\gamma_K\}$. The nominal K (K_m) is computed to be 2.44×10^4 kPa based on $\{(f_c)_m, (E_{st})_m\}$ and problem dimensions (thickness of the walls, cross sections of the struts, total depth of the diaphragm wall, etc.). Because there is no cross wall, k_1 in Equation 2 is the axial stiffness of the diaphragm walls in dark and grey. The partial factors $\{\gamma_\delta, \gamma_{su}, \gamma_K\}$ can be checked from Figure 3 for β_T = 1.5—they are 1.415, 0.812 and 0.805, respectively.

Once all input parameters $\{H_e$, B, L′, $(s_u/\sigma_v')_m$, K_m, γ_δ, γ_{su}, $\gamma_K\}$ are obtained, the design maximum wall displacement ($\delta_{m,d}^*$) at the A-A section is computed to be 196.6 mm by the right hand side of Equation 11. It should be noted that the $\delta_{m,d}^*$ calculated above is a conservative value, since $(s_u/\sigma_v')_m$ and K_m are multiplied by its corresponding reduction factors, i.e. γ_{su} = 0.812, and γ_K = 0.805, and the resulting δ_m^* is multiplied by an amplification factor, i.e. γ_δ = 1.415, that accounts for the model error. Without such conservatism ($\gamma_{su} = \gamma_K = \gamma_\delta = 1$), $\delta_{m,d}^*$ is 84 mm. The design value $\delta_{m,d}^*$ = 196.6 mm is greater than δ_L = 60 mm, indicating that the serviceability is not satisfied for the requirement of β_T = 1.5 at the final excavation stage. As a result, cross walls are needed.

To reduce the wall displacement at the A-A section, cross walls (the hatched wall in Fig. 1) are introduced. Assume that the cross walls are to be constructed from 3 m below ground surface to the bottom of the diaphragm wall. Note that when computing k_1 in Equation 2, the cross section area of the cross walls should not be computed based on the initial height of the cross walls (H_w – 3.0 = 28 m) but should be computed based on the height at the final stage the height (H_w – final H_e = 14.4 m) because the cross wall portion above the excavation depth will be dismantled.

It is desirable to determine the spacing of the cross walls (L′) to fulfill $\delta_{m,d}^* \le \delta_L$ = 60 mm at the final excavation stage. The introduction of the cross walls will reduce L′ from 80 m to a smaller value. This reduction in L′ will affect k_1, k_2, and k_3 in Equation 2 and consequently K. Moreover, it will also change the L′ value input to Equation 11. The parameters $\{H_e$, B, $(s_u/\sigma_v')_m\}$ will not change, and the required partial factors $\{\gamma_\delta, \gamma_{su}, \gamma_K\}$ also remain the same. As a result, the process of determining L′ is iterative. It is found that the spacing L′ corresponding to $\delta_{m,d}^* = \delta_L$ = 60 mm is about 20 m. This indicates that the spacing L′ is required to be less than 20 m in order to meet the design target of δ_L = 60 mm with β_T = 1.5. A simple MCS shows that the actual reliability index for this design spacing is 1.47, fairly close to the target value of 1.5. The simplest way to fulfill this L′ ≤ 20 m requirement is to divide the site into four subzones with same geometry, i.e. L′ can be taken to be 80/4 = 20 m.

4.1 *Effectiveness of cross walls for RBD*

The aforementioned design example only illustrated a case where δ_L = 60 mm and β_T = 1.5. In this section, sensitivity analysis is taken to demonstrate the RBD for other choices of δ_L and β_T.

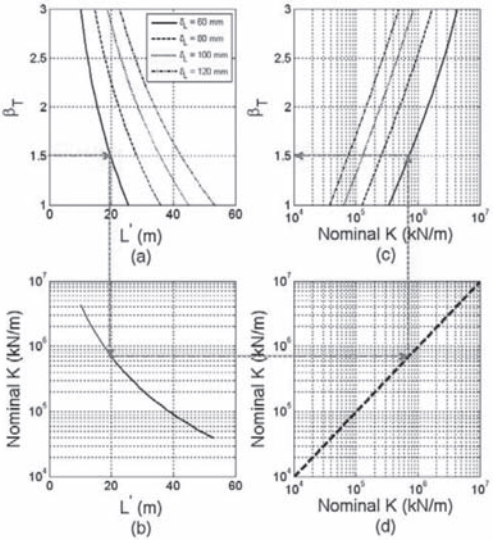

Figure 4. Design example illustration.

Figure 4(a) shows how the required L′ changes with respect to δ_L values and β_T requirement for the A-A section, while Figure 4(b) shows the relation between L′ and K. Figure 4(c) is developed based on Figure 4(a), (b). The red dashed line in Figure 4 corresponds to the design outcome demonstrated previously for $\beta_T = 1.5$ and $\delta_L = 60$ mm. It is clear from Figure 4(a) that reducing L′ is fairly effective for increasing β_T. For instance, for a fixed $\delta_L = 60$ mm, reducing L′ from 20 m to 15 m leads to an increase of β_T from 1.5 to 2.1 (P_f from 0.067 to 0.018). This is because reducing L′ is very effective for increasing K, as shown in Figure 4(b). Sensible trends are observed in Figure 4(a): for a fixed β_T smaller δ_L results in smaller L′ and larger K, because the reduction in L′ leads to the reduction of wall displacement.

5 CONCLUSIONS

Based on the regression equation proposed by Wu et al. (2013), this study further developed a simplified RBD method for the serviceability limit state design of excavations. Easy-to-implement charts for the calibrated partial factors are produced. These partial factors are rigorously calibrated by the Quantile Value Method (QVM) recently developed by Ching & Phoon (2011, 2013). Strictly speaking, the proposed method should be only applicable to Taipei cases that are mostly dominated by soft clays, because the regression model was calibrated based on these cases. The Taipei soft clays are with Liquidity Index (LI) = 0.5~1.0, Plasticity Index (PI) = 7~20, and s_u/σ_v' (CIUC) = 0.3~0.37. Nonetheless, the proposed method may be still applicable to non-Taipei cases that are dominated by soft clays with properties similar to the Taipei soft clays. Finally, the proposed method should only be applied to cases that are retained by diaphragm walls and constructed by either the Bottom-Up (BU) or Top-Down (TD) method using steel struts and concrete floor slabs as lateral supports.

Finally, a design example is used to illustrate for the use of the partial factor charts developed in this study and to show the effectiveness of cross walls. The design outcomes show that reducing the cross wall spacing L′ is very effective to the increase of the reliability index.

REFERENCES

AASHTO. 1997. *LRFD highway bridge design specifications*. AASHTO, Washington, D.C.

Ang, A.H.S. & Tang, W.H. 1984. *Probability Concepts in Engineering Planning and Design, Vol. II—Decision, Risk and Reliability*. New York: Wiley.

CEN (European Committee for Standardization) 2001. *Eurocode 7 Part 1: Geotechnical Design: General Rules*. CEN, Brussels.

Ching, J. & Phoon, K.K. 2011. A quantile-based approach for calibrating reliability-based partial factors. *Structural Safety* 33(4–5): 275–285.

Ching, J. & Phoon, K.K. 2013. Quantile value method versus design value method for reliability-based code calibration. *Structural Safety* (in press).

Lin, Y.L. 2010. *The Effect of Cross Walls on the Movements of Excavations in Clay*. Ph.D. Dissertation, National Taiwan University of Science and Technology, Taipei, Taiwan.

Ou, C.Y., Hsieh, P.G. & Lin, Y.L. 2011. Performance of excavations with cross walls. *Journal of Geotechnical and Geoenvironmental Engineering* ASCE 137(1): 94–104.

Phoon, K.K. & Kulhawy, F.H. 2008. Serviceability limit state reliability-based design. In Phoon, K.K. (ed.), *Reliability-based Design in Geotechnical Engineering: Computations and Applications*: 344–384. London: Taylor & Francis.

Wu, S.H., Ching, J. & Ou, C.Y. 2013. Predicting wall displacements for excavations with cross walls in soft clay. *Journal of Geotechnical and Geoenvironmental Engineering* ASCE 139(6): 914–927.

10 *Risk assessment and management in geotechnical engineering and infrastructural projects*

This page intentionally left blank

Geotechnical Safety and Risk IV – Zhang et al. (eds)
© 2014 Taylor & Francis Group, London, ISBN 978-1-138-00163-3

Indicator Kriging for locating risk zones: An application to buildings at risk in the Barcelonnette Basin

S.A. Arnaouti, S. Fotopoulou, K. Pitilakis & Th. Chatzigogos
Civil Engineering Department, Aristotle University of Thessaloniki, Thessaloniki, Greece

A. Puissant
Laboratoire Image, Ville, Environnement, CNRS and University of Strasbourg, Strasbourg, France

J.-P. Malet
Laboratoire Image, Ville, Environnement, CNRS and University of Strasbourg, Strasbourg, France
Institut de Physique du Globe de Strasbourg, CNRS and University of Strasbourg, Strasbourg, France

ABSTRACT: In this study, landslide risk to buildings is assessed through an index-based, semi-quantitative approach by integrating information obtained from multiple sources: landslide inventory and susceptibility maps; information concerning the exposed buildings and their vulnerability. Once the risk value of the individual buildings have been determined, a methodology based on the geostatistical technique of Indicator Kriging (IK) is proposed in order to cluster the exposed buildings into zones of equal risk. Each risk zone consists of the areas where the probability of exceedance of the risk zone value—that is produced through geostatistical analysis—is greater than a given threshold. The final risk zone map is produced by the synthesis of each risk zone. The proposed methodology is applied to the Barcelonnette Basin, where areas of low, moderate and high landslide risk zones are determined. The risk zone map produced objectively can provide useful guidelines for risk management design.

1 INTRODUCTION

An efficient landslide risk assessment, which allows integration of the hazard analysis, information on the elements at risk and their vulnerability, is always required for the sustainable development of mountainous areas and the safety of the citizens. Index-oriented, semi-quantitative approaches have been widely used at medium scales (1:50,000–1:10,000) for mapping landslide risk due to their flexibility and their ability to combine a vast amount of diverse information into a simpler, more usable form (e.g., Puissant et al. 2006, Puissant et al. 2013).

Even though landslide hazard and susceptibility zoning is an everyday practice in landslide risk assessment, this is not the case for spatially non-continuous parameters, such as vulnerability or risk, whose spatial extent is constrained within the area of the exposed elements. However, at the same time, van Westen et al. (2005) points out the need of integrated risk information for emergency management purposes, which is the main purpose of risk analysis in meso-scales (1:50,000–1:10,000). In the same spirit, Puissant et al. (2006) note that at these scales the final goal of risk analysis is the determination of the most sensitive areas.

Two studies, those of Maquaire et al. (2004) and Ferlisi & Pisciotta (2007), cluster the exposed buildings to units of equal vulnerability. The first authors present a semi-automatic procedure using Hierarchical Ascending Classification to aggregate the buildings at risk based on their geometrical and contextual characteristics. Their methodology is compared with an expert's vulnerability zonation and the two results are in accordance for the majority of the buildings. Also, Ferlisi & Pisciotta (2007) homogenized the buildings at the Lazio and Abruzzo regions in Central Italy according to their use in order to reduce the time for data collection in a working scale of 1:25,000. Each homogeneous unit consists of buildings with specific use (residential, commercial and industrial) whose distance between them does not exceed 100 m. In terms of loss index, Kappos et al. (2009) estimated the risk in urban blocks; buildings that belong to the same urban block form a cluster and the loss index of this cluster is the average of the loss indexes of each building weighted upon the built area.

In this context, the present work first provides an index-based, semi-quantitative approach to assess landslide risk of individual buildings at medium scales. Then, a statistical methodology is proposed based on indicator kriging to cluster buildings in

units of equal risk. Especially in meso-scales, this risk clustering is the spatial information necessary to the local authorities to easily establish efficient management strategies since it highlights the areas where the high-risk buildings are concentrated and thus immediate action at those areas should follow the landslide event. Further, the risk zonation can trace the sensitive areas where a more detailed risk analysis should be conducted. The proposed methodology is implemented in the Barcelonnette Basin (South East France), an area highly susceptible to landslide activity.

2 GEOSTATISTICAL FRAMEWORK

Geostatistics is an interpolation method that allows the estimation of a regionalized variable $R(x)$ at an unsampled location. The Indicator Kriging (IK) approach presented by Journel (1983) applies the geostatistical principles to the indicator function $I(x)$. For a specific threshold R_o, the indicator function is defined as:

$$I\left(x;\, R_o\right) = \begin{cases} 1, \text{ if } R(x) < R_o \\ 0, \text{ if } R(x) \geq R_o \end{cases} \quad (1)$$

By assuming that $R(x)$ has second order stationary indicators, the IK predictor $I(x_o, R_o)$ at location x_o, that is actually an estimate of the probability $P(R(x_o) < R_o)$, can be determined by following the ordinary kriging equations (Cressie, 1993):

$$\hat{I}\left(x_o;\, R_o\right) = \sum_{i=1}^{n} \lambda_i \cdot I\left(x_i;\, R_o\right) \quad (2)$$

where $I(x_i; R_o)$ is the known value of the indicator function at the x_i location given the R_o threshold, n is the number of the I known values in the field and λ_i is the weight of this value.

According to the kriging theory, the estimator $\hat{I}$ should be unbiased and of minimum square error. Based on those two criteria, the equations to estimate weights λ_i are respectively:

$$\sum_{i=1}^{n} \lambda_i = 1 \quad (3)$$

$$\sum_{i=1}^{n} \lambda_i \cdot \gamma_{R_o}\left(x_{ij}\right) + m\left(R_o\right) = \gamma_{R_o}\left(x_{io}\right),\ j = 1, \ldots, n \quad (4)$$

where x_{ij} the distance between locations x_i and x_j, $m(R_o)$ a Lagrange multiplier and $\gamma_{Ro}(x)$ the variogram that corresponds to the R_o threshold.

The variogram describes the difference between measurements of distance h in respect to that distance and its determination is based on the n known values of the parameter under study, here the indicator function I. By physical intuition, γ is expected to increase as h increases, since close measurements tend to show similar results while measurements that lie far apart exhibit greater discrepancies.

3 METHODOLOGY

3.1 *Landslide risk assessment of buildings*

The process of risk estimation integrates the hazard analysis with the elements at risk and their vulnerability in the form of the generic equation (Varnes, 1984):

$$\text{Risk} = \text{Hazard} \times \text{Vulnerability} \times \text{Elements at risk} \quad (5)$$

This simple equation allows identifying separately the principal factors contributing to landslide risk. These include the probability of occurrence of a hazardous landslide of a given intensity within a given period of time (i.e. hazard), the degree of loss to an element or set of elements exposed to a landslide of given type and intensity (i.e. vulnerability) and the valued assets at risk (i.e. elements at risk).

Within the framework of this study, a semi-quantitative procedure fully implemented in a GIS environment is suggested to assess landslide risk. The study is focused herein on the risk assessment of buildings but the procedure is quite flexible and can be easily adjusted to different assets.

The proposed framework includes four main steps that are shortly outlined below:

- The collection of the susceptibility and hazard information based on the characteristics of the landslide inventory.
- The identification of the buildings at risk and of the main factors influencing their vulnerability (e.g. construction material, number of floors, state of maintenance etc.). The value of the exposed buildings that is associated to their function and thus to their importance to the local community should also be specified.
- The vulnerability assessment of the buildings by weighting the different contributing factors using engineering judgment based on the framework proposed by Papathoma et al. (2007). A different score is assigned to each category of the given factors and the total vulnerability value is calculated for each building by means of a Weighted Linear Combination Method (e.g., Papathoma et al. 2007, Mousavi et al. 2011).

– The risk estimation integrates information on the hazard, the vulnerability and the value of the element (see Eq. 5). Both hazard and vulnerability values are given in standardized terms. Landslide risk can be finally assessed either qualitatively or semi-quantitatively expressed on a scale from 0 to 1.0.

The proposed procedure, although it involves some degree of subjectivity, is generally compatible with the availability and quality of data taking also into account the scale of the analysis (1:10,000). In addition, this index-based semi-quantitative approach allows treating on a hierarchical basis the level of risk supporting, in this way, effective risk management and decision making processes.

3.2 *Indicator Kriging for locating risk zones*

Indicator Kriging can be used to cluster the exposed elements in groups of equal risk. The whole procedure that can be totally implemented in a GIS environment is summarized in the following steps.

Once the risk value, either quantitative or qualitative, of the buildings has been determined, the risk $R(x)$ at location x ($x \in$ D, D the study area) can be considered as a regionalized variable whose value is equal to the building's risk value inside the building's area and zero otherwise.

The number of the desired risk zones n_k forming the risk zone map has to be selected, along with the risk value $R_{o,k}$ of each zone. For the kth risk zone, the indicator function $I(x; R_{o,k})$ and the variogram γ_k that corresponds to its spatial variation is determined. Then, by applying the kriging equations at different locations x_o of the field, an estimate of the indicator function $I(x_o; R_{o,k})$ at the whole study area can be calculated. At this point it should be noted that in order to provide monitonicity, a single variogram—that of the median of thresholds—can be used for the whole analysis (Cressie 1993) instead of estimating different variograms for each risk zone. Also, the kriging estimations equal the input data values. To produce more smooth risk zones that can include exposed buildings of different risk value this property of kriging should be relaxed. Thus, a nugget effect n_e, i.e. an offset at the origin, fully attributed to measurement errors should be added to the variogram.

According to the geostatistical theory, the indicator function $I(x_o; R_{o,k})$ is an estimate of the probability of the R(x) not to exceed the threshold R_o at that point. However, the risk zones should contain all the areas where $R(x)$ is equal or greater than R_o, so, it is the complementary event that is actually of interest. Thus, a map with the probability of exceedance $Q(x; R_{o,k})$ regarding the R_o threshold can be produced according to the equation:

$$Q(x; R_{o,k}) = 1 - I(x; R_{o,k}) \quad (6)$$

To produce the kth risk zone from the probability $Q(x; R_{o,k})$ map, a probability threshold Q_b is required—common for all risk zones—that will define the boundary of the risk zone. Indeed, areas of the probability exceedance map that exhibit probability $Q(x; R_{o,k})$ greater than Q_b form the kth risk zone.

Finally, the risk zone map is produced by superposition of each risk zone.

4 IMPLEMENTATION TO THE BARCELONNETTE AREA

4.1 *The study area*

The test site (Fig. 1) is located on the north-facing hillslope of Barcelonnette Basin extending over an area of about 100 km^2 and it is representative of the climatic, lithological, geomorphological and landcover conditions common to several regions of the South French Alps. Barcelonnette Basin is a highly landslide prone area characterized by a large variety of slope movements (e.g., Maquaire et al. 2003, Malet et al. 2005, Thiery et al. 2007),

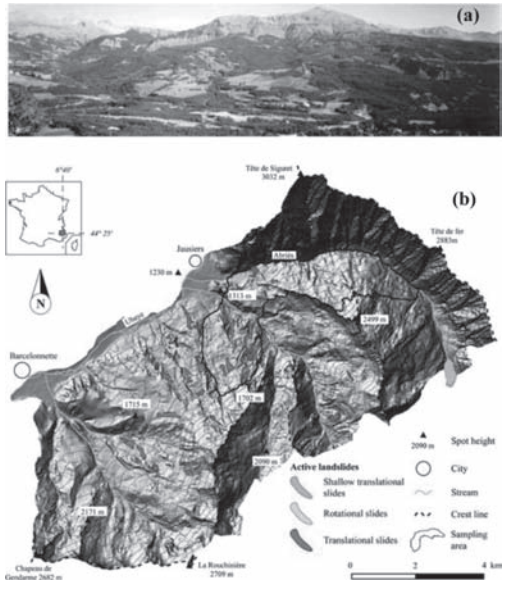

Figure 1. (a) Typical landscape of the north-facing hillslope of the Barcelonnette Basin and (b) shaded relief map and distribution of landslides (Thiery et al. 2007).

some of which directly affect the local community causing considerable physical damage and economic losses.

4.2 *Landslide risk assessment of buildings*

The proposed framework for assessing landslide risk is implemented to the buildings of the Barcelonnette Basin that have been repeatedly affected by different landslide hazards. Information on the susceptibility classes for the active landslides type of the North-facing slope and the corresponding landslide susceptibility map at 1:10,000 scale has been taken from previous published work (Thiery et al. 2007)—see Figure 2. It should be noted that information on the magnitude-frequency relationships of the potentially damaging landslides of different types was not made available and thus, only a preliminary hazard analysis based on its spatial component (i.e. susceptibility) was possible. In addition, a database of the exposed buildings in Barcelonnette area including their structural characteristics and their urban function (Puissant et al. 2006) has been provided in GIS format for the purpose of this study.

Table 1 presents the description of the various factors considered for the vulnerability assessment of the buildings in Barcelonnette Basin as well as their relevant scores defined by expert knowledge and judgment. Different weightings are assigned to each of the factors on the basis of their relative importance in the vulnerability assessment. Table 2 presents the various functions of the exposed buildings and the corresponding values assigned for each function.

Finally, Figure 2 illustrates the estimated risk of each individual building in the Barcelonnette Basin in qualitative terms (low, moderate, high). It is seen that the higher risk buildings are generally concentrated in highly susceptible areas.

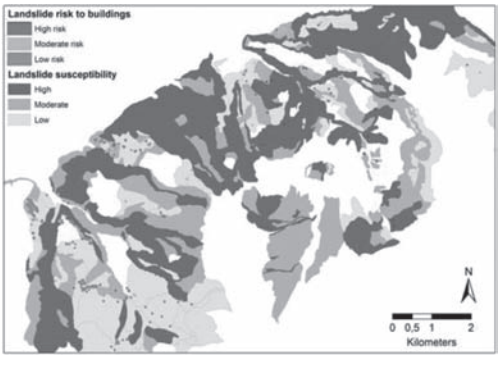

Figure 2. Landslide risk to individual buildings in the Barcelonnette Basin.

Table 1. Factors contributing to building vulnerability to landslides, the score of each category and their relevant weightings.

Factor	Categories	Score	Weighting
Construction material	Masonry	0.6	4
	RC	0.3	
	Steel	0.3	
	Wood	0.8	
	Mixed	0.7	
Number of floors	1	0.5	1
	2–3	0.3	
	≥4	0.1	
Outdatedness	Good	0.1	4
	Average	0.3	
	Bad	0.6	
	Destroyed	0.9	
Age	Before 1900	0.9	3
	1900–1950	0.7	
	1950–1970	0.5	
	1970–1990	0.3	
	1990–2000	0.1	
	After 2000	0	

Table 2. Function and the corresponding value of the building.

Function	Value of the building (E)
Residential	1
Commercial	1.1
Industrial and craft	1
Agricultural	1
Leisure and sportive	1.1
Hotel	1.1
Place of religious worship	1.2
Private service	1.2
Public service	1.3
Education	1.3
Civil service	1.3
Urgency service	1.3

4.3 *Indicator Kriging for characterising risk zones*

Three risk zones ($n_k = 3$), that of low, intermediate and high risk, were selected for the present analysis, in accordance with the qualitative terms used in buildings' risk assessment.

The indicator function changes sharply near the buildings' limits since non-null risk values at the building's area exist adjacent to null values outside of it. To take account of the non-smoothness of the I function, the exponential model was adopted for the variogram (Kitanidis 1997). The variogram parameters selected for the median risk threshold (moderate risk) were sill = 0.10 and range = 70 m.

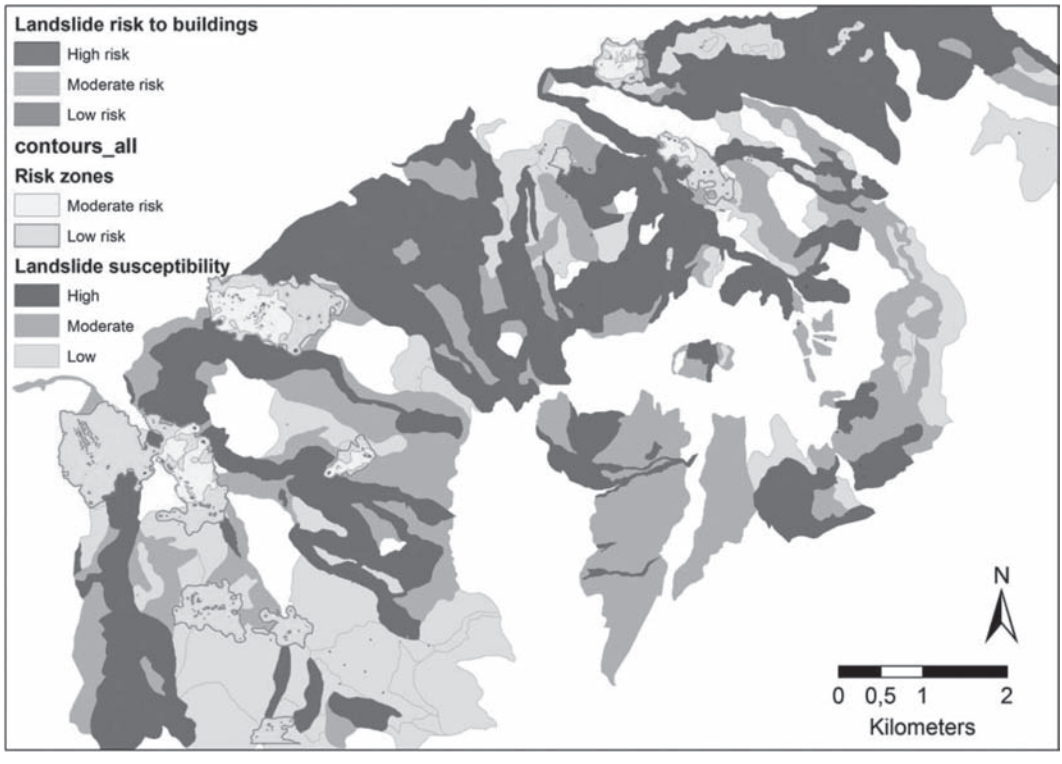

Figure 3. Landslide risk zone map in Barcelonnette Basin.

To validate the selected parameters, a 10% of the input data was randomly selected and excluded from the analysis. The selected exponential variogram was used with the remaining data to predict the indicator function at the excluded locations. The very small value of the mean absolute error (0.03) verifies the efficiency of the adopted variogram and, in general, the legitimacy of the use of geostatistics for the determination of the risk zones. Also, to allow for a more smooth risk zone, a nugget effect n_e equal to 50% of the sill parameter is artificially added to the selected variogram. The same variogram is used for all three risk zones.

To finally determine the risk zones, a value of Q_b equal to 0.2 was selected.

The risk zones are illustrated in Figure 3. No high risk zone exists because the buildings that exhibit high risk are few and spatially scattered. Six moderate risk zones—the larger one at the North-West side of the Barcelonnette Basin covers an area of about 445,000 m^2—and multiple low risk zones are formed. The risk zone map highlights the prone areas on the basin. Indeed, in the Barcelonnette Basin, the South-West moderate risk zone encloses a vast area where the most severe and densely-spaced damages are expected to occur. So, an emergency plan should include extra caution for this area in case of a landslide event.

5 CONCLUSIONS

The present paper provides an index-based, semi-quantitative approach for spatial analysis of landslide risk at medium scales by combining information on hazard analysis with the characteristics and function of the elements at risk as well as their vulnerability. The proposed approach is quite general in concept and depends primarily on data availability and the expertise of the user.

Once the risk value of each individual element at risk (building in our case) is assessed, this study presents a geostatistical framework based on indicator kriging equations, which offers an automatic procedure to objectively cluster the elements at risk in zones of equal risk. Although the procedure has been applied to landslide hazard, it can be easily extended to other hazards as well. The whole procedure can by fully implemented in an ArcGIS environment.

The resulting risk zone map offers an integrated risk representation necessary for efficient

emergency strategies since it highlights the most sensitive areas where high risk elements are concentrated.

ACKNOWLEDGMENT

A special acknowledgement is due to Mr. Bouchounas and the MDS Marathon Data Systems Co. for their technical support on ArcGIS.

REFERENCES

Cressie, N.A.C. 1993. *Statistics for spatial data.* N.Y.: John Wiley and Sons, Inc.

Ferlisi, S. & Pisciotta, G. 2007. A preliminary study of landslide induced property damages towards consequence analysis. In Schuster, Schuster, Turner (eds), *First North American Landslide Conference*; *Proc.*, *Vail (Colorado), 3–9 June 2007.* AEG Publication n.23.

Kappos, A.J., Stylianidis, K.C., Sextos, A.G., Papanikolaou, V.K., Panagopoulos, G., Kouris, L. & Goutzika, E. 2009. Seismic risk scenarios for the building stock in Grevena. *16th Hellenic conf. on Concrete, Paphos, Cyprus, 2009.* Paper no. 111108.

Journel, A.G. 1983. Nonparametric estimation of spatial distribution. *Mathematical Geology* 15(3): 445–468.

Kitanidis, P.K. 1997. *Introduction to geostatistics: applications to hydrology.* Cambridge: Press Syndicate of the University of Cambridge.

Malet, J.-P., Van Asch, T.W.J., van Beek, R. & Maquaire, O. 2005. Forecasting the behaviour of complex landslides with a spatially distributed hydrological model. *Natural Hazards and Earth System Sciences* 5: 71–85.

Maquaire, O., Malet, J.-P., Remaître, A., Locat, J., Klotz, S. & Guillon, J. 2003. Instability conditions of marly hillslopes: towards landsliding or gullying? The case of the Barcelonnette Basin, South East France. *Engineering Geology* 70: 109–130.

Maquaire, O., Thiery, Y., Malet, J.-P., Weber, C., Puissant, A. & Wania, A. 2004. Current practices and assessment tools of landslide vulnerability in mountainous basins—identification of exposed elements with a semi-automatic procedure. In Lacerda, Ehrlich, Fontoura and Sayão (eds), *Landslides: Evaluation and Stabilization; Proc. of the IX intern. symp. on Landslides, Rio de Janeiro, 2004.* Taylor & Francis Group, London.

Mousavi, M.S., Omidvar, B., Ghazban, F. & Feyzi, R. 2011. Quantitative risk analysis for earthquake-induced landslides - Emamzadeh Ali, Iran. *Engineering Geology* 122(3–4): 191–203.

Papathoma, K., Neuhauser, B., Ratzinger, K., Wenzel, H. & Dominey-Howes, D. 2007. Elements at risk as a framework for assessing the vulnerability of communities to landslides. *Natural Hazards and Earth System Sciences* 7: 765–779.

Puissant, A., Malet, J.-P. & Maquaire, O. 2006. *Mapping landslide consequences in mountain areas: a tentative approach with a semi-quantitative procedure*. In Weber and Gancarski (eds), *Proc. intern. conf. on Spatial Analysis and Geomatics SAGEO, Strasbourg, 2006.*

Puissant, A., Van Den Eeckhaut, M., Malet, J.-P. & Maquaire, 0, 2013. Landslide consequence analysis: a region-scale indicator-based methodology. *Landslides* (in press).

Thiery, Y., Malet, J.P., Sterlacchini, S., Puissant, A. & Maquaire, O. 2007. Landslide susceptibility assessment by bivariate methods at large scales: application to a complex mountainous environment. *Geomorphology* 92: 38–59.

van Westen, C.J., van Asch, T.W.J. & Soeters, R. 2005. Landslide hazard and risk zonation—why is it still so difficult? *Bulletin of Engineering Geology and the Environment* 65(2): 167–184.

Varnes, D.J. 1984. Landslides hazard zonation: A review of principles and practice. UNESCO, Paris.

Geotechnical Safety and Risk IV – Zhang et al. (eds)
© 2014 Taylor & Francis Group, London, ISBN 978-1-138-00163-3

Development of a probabilistic model for the prediction of building damage due to tunneling induced settlements

Carles Camós & Climent Molins
Universitat Politècnica de Catalunya, Barcelona, Spain

Olga Špačková & Daniel Straub
Engineering Risk Analysis Group, Technische Universität München, Munich, Germany

ABSTRACT: Tunnel construction can cause deformations of the surrounding ground, which endanger buildings and other structures located in the vicinity of the tunnel. The prediction of these deformations and the damages to the buildings is difficult due to limited knowledge of the geotechnical conditions and uncertainty in the response of the structures to the settlements. This paper presents a probabilistic model for prediction of the damage to buildings due to tunneling, which combines the volume loss method with the equivalent beam model. It furthermore proposes a probability-based method for determination of the limiting value of settlement that is used for control purposes during the tunnel construction. Updating of the limiting settlement with measurements gathered during the construction is described. The proposed methodology is applied to a masonry building affected by the construction of the L9 metro line tunnel in Barcelona.

1 INTRODUCTION

The prediction of damages to buildings caused by underground constructions such as tunnels entails uncertainty due to our limited knowledge of the geotechnical conditions and the response of the structures subjected to differential settlements. Prediction of damages is important as a basis for the design, the selection of the construction technology and for setting allowable limits on settlements. These limiting values of settlement are then used in the construction phase for control purposes: if the measured settlement exceeds the limiting values, the construction is stopped or additional safety measures must be taken.

At present, settlement profiles and resulting damages in buildings are commonly modeled deterministically. Settlement profiles are typically predicted by means of 2D Finite Element (FE) models combining the soil, the tunnel and the foundations of a given building. Alternatively, the volume loss method (Peck, 1969; Attewell et al., 1986) can be used for approximation of the subsidence trough. The volume loss method is an empirical approach to determining the settlement profile; this empirical approach is computationally more efficient than 2D FE simulation and it is fully sufficient for many engineering applications. Once the settlement profile is calculated, it is possible to predict damages in buildings by means of empirical methods such as the equivalent beam method (Burland & Wroth, 1974; Boscardin & Cording, 1989), which is widely used in tunnel engineering. This method determines the maximum tensile strain in the building by modeling it as a linear elastic beam subjected to a given deflection ratio. This strain value is then compared with limiting strain values, which define different categories of damage according to the severity of affection. An iteration process is performed in order to assess the limiting value of settlement that leads to damages below an acceptable level.

This paper proposes a computationally efficient probabilistic model for the estimation of building damage due to tunneling, combining the volume loss method for approximation of the subsidence trough and the equivalent beam method for modeling the response of the building (Sec. 2). The parameters of the volume loss method are usually selected based on expert judgment. The uncertainty connected to the choice of these parameters is typically high. The proposed methodology allows taking into account these uncertainties as well as the uncertainty in the building response.

The paper further proposes a novel methodology for the determination of the limiting settlement value on a probabilistic basis (Sec. 3). The limiting settlement is here defined as a settlement, for which the probability of damage to the building is acceptably low. Two approaches for setting

this limiting value are proposed: (1) a simple approximate approach using a plot of the results of the probabilistic analysis, (2) an advanced approach based on reliability updating (Straub, 2011). Additionally, a procedure for updating the limiting values with observations gathered during the tunnel construction is described.

The proposed methodology is applied to a case study of masonry buildings affected by the construction of the L9 metro line in Barcelona.

2 PROBABILISTIC MODEL OF BUILDING DAMAGE DUE TO TUNNELING

The shape of the settlement profile in a plane, which is close to perpendicular to the tunnel axis, can be modeled by means of a Gaussian curve (Peck, 1969). The settlement at the distance y from the tunnel axis then equals:

$$s(y) = S_{max} \exp\left(-\frac{y^2}{2i^2 \cos\theta}\right) \tag{1}$$

where i is the location of the inflection point (horizontal distance from tunnel axis), θ is the angle between the modeled plane and the perpendicular plane and S_{max} is the maximum settlement in the center of the Gaussian curve, i.e. above the tunnel axis. S_{max} can be calculated as:

$$S_{max} = f_1(V_L, K) = \frac{V_L \cdot d^2}{3.192 \cdot K \cdot z_0} \tag{2}$$

where d and z_0 are the diameter and depth of the tunnel, respectively, V_L is the expected volume ground loss (i.e., the ratio between the area of the settlement trough and the cross-section area of the tunnel), which is dependent on the tunneling technology, and K is a shape parameter of the curve which depends on the type of soil. The product $K \cdot z_0$ determines the location of the inflection point i of the Gaussian curve with respect to tunnel centerline. V_L and K are modeled as random variables (RVs). The model error is considered as described later in Eq. (12).

Knowledge of the shape of the settlement trough allows determining the deflection ratios Δ/L that are affecting the building, where L is the distance between two reference points and Δ is the relative deflection between these two points.

The response of the building is modeled using the equivalent beam method, which represents the building by means of a weightless linear elastic rectangular beam. The aim is to calculate the tensile strains in the beam for a given deflected shape. The distribution of strains in the beam depends on the mode of deformation. Therefore, extreme modes of bending and shear are analyzed separately. The extreme fiber strains in bending and shear are given by the following equations:

$$\varepsilon_{br} = f_2\left(V_L, K, \frac{E}{G}\right) \cdot E_{\varepsilon_{br}} = (\varepsilon_{bmax} + \varepsilon_h) \cdot E_{\varepsilon_{br}} \tag{3}$$

$$\varepsilon_{dr} = f_3\left(V_L, K, \frac{E}{G}\right) \cdot E_{\varepsilon_{dr}} = \left[\varepsilon_h\left(1 - \frac{E}{4G}\right) + \sqrt{\frac{\varepsilon_h^2}{16}\left(\frac{E}{G}\right)^2 + \varepsilon_{dmax}^2}\right] \cdot E_{\varepsilon_{dr}} \tag{4}$$

where E/G is the ratio between the Young and shear moduli of the building material, which is modeled as a RV, $E_{\varepsilon_{br}}$ and $E_{\varepsilon_{dr}}$ represent the model errors and ε_h is the horizontal strain at the base of the beam, which is obtained as the derivative of the horizontal displacements u:

$$u(y) = \frac{s(y) \cdot y}{z_0} \tag{5}$$

$$\varepsilon_h(y) = \frac{du(y)}{dy} \tag{6}$$

The model errors $E_{\varepsilon_{br}}$ and $E_{\varepsilon_{dr}}$ are considered as multiplicative RVs with mean value equal to 1. They result from the assumption of linear elasticity, the position of the neutral axis and the omission of the presence of openings.

Maximum bending (ε_{bmax}) and shear (ε_{dmax}) strains in the equivalent beam are calculated as:

$$\varepsilon_{bmax} = \frac{\frac{\Delta}{L}}{\left(\frac{L}{12t} + \frac{3I}{2aLH}\frac{E}{G}\right)} \tag{7}$$

$$\varepsilon_{dmax} = \frac{\frac{\Delta}{L}}{\left(1 + \frac{HL^2}{18I}\frac{G}{E}\right)} \tag{8}$$

where H is the beam height, I is the inertia per unit length, t is the assumed position of the neutral axis and a is the location of the fiber where strains are calculated.

The calculation of Eqs. (3)–(8) is performed separately for the zone of the building undergoing sagging deflection (upwards concavity) and for the zone undergoing hogging deflection (downwards concavity). The errors of the equivalent beam model in sagging, $E_{\varepsilon_{br}}^{sag}$, $E_{\varepsilon_{dr}}^{sag}$, and hogging, $E_{\varepsilon_{br}}^{hog}$, $E_{\varepsilon_{dr}}^{hog}$, are assumed to be independent. In case of sagging deflection, the neutral axis is assumed to be at middle

Table 1. Classification of damage (Burland et al., 1977).

Category of damage	Normal degree of severity	Typical damage	Limiting tensile strain (ε_{lim})(%)
0	Negligible	Hairline cracks less than 0.1 *mm*	0–0.050
1	Very slight	Fine cracks up to 1 *mm*	0.050–0.075
2	Slight	Cracks easily filled up to 5 *mm*	0.075–0.150
3	Moderate	Cracks from 5 to 15 *mm*	0.0150–0.300
4	Severe	Extensive repair work. Cracks from 15 to 25 *mm*	> 0.300
5	Very severe	Partial or complete rebuilding. Cracks > 25 *mm*.	

height ($t = H/2$). In case of hogging deflection, the neutral axis is assumed to be at the top fiber ($t = H$). Strains are calculated in the most critical fiber from the position of the neutral axis, so that $a = t$ in both cases. The damage on the buildings is determined depending on the maximum strain $\varepsilon_{\max}$:

$$\varepsilon_{max} = \max\left[\varepsilon^{sag}_{\varepsilon_{br}}, \varepsilon^{sag}_{\varepsilon_{dr}}, \varepsilon^{hog}_{\varepsilon_{br}}, \varepsilon^{hog}_{\varepsilon_{dr}} \right] \tag{9}$$

where $\varepsilon^{sag}_{\varepsilon_{br}}, \varepsilon^{hog}_{\varepsilon_{br}}$ are the maximum bending strains in sagging and hogging respectively, both obtained using Eq. (3), and $\varepsilon^{sag}_{\varepsilon_{dr}}, \varepsilon^{hog}_{\varepsilon_{dr}}$ are the maximum shear strains in sagging and hogging respectively, both obtained using Eq. (4).

Based on ε_{max}, one can estimate the size of the cracks in the building. The approach of Burland et al. (1977) is used in this paper for classification of the damage magnitudes as shown in Table 1.

The different damage categories can be used for the definition of system failure $F_{\varepsilon_{lim}}$. Failure occurs if the maximum strain (ε_{max}) obtained from Eq. (9) exceeds a given limiting tensile strain value ε_{lim} for a target category of damage according to Table 1. For example, if cracks with a width larger than 0.1 mm are considered inacceptable, the limiting strain defining the failure is $\varepsilon_{lim} = 0.05\%$.

The Limit State Function (LSF) is then defined as

$$g(\mathbf{X}) = \varepsilon_{lim} - \varepsilon_{max} \tag{10}$$

where $\mathbf{X}$ is the vector of variables that are considered to be random. The LSF determines the failure domain $\Omega_F = \{g(\mathbf{x}) \leq 0\}$. The probability of failure then equals the probability of $\mathbf{X}$ taking a value within the failure domain:

$$\Pr(F_{\varepsilon_{\lim}}) = \Pr(\mathbf{X} \in \Omega_F) \tag{11}$$

Note that this definition of LSF is suitable when applying sampling methods for the computation of probabilities. If methods such as First-Order Reliability Method (FORM) were used, separate LSFs for $\varepsilon^{sag}_{\varepsilon_{br}}, \varepsilon^{sag}_{\varepsilon_{dr}}, \varepsilon^{hog}_{\varepsilon_{br}}, \varepsilon^{hog}_{\varepsilon_{dr}}$ should be defined and the failure event should be described as a series system.

3 DETERMINATION OF LIMITING SETTLEMENT

The measured maximal settlement above the crown of the tunnel S_m equals:

$$S_m = S_{max} + E_f + E_m = S_{max} + E_E \tag{12}$$

where S_{max} is the maximal settlement calculated using Eq. (2), E_f is the model error representing the deviation of the real settlement from the idealized Gaussian shape described by Eqs. (1) and (2), E_m is the error of measurement on site, which reflects imprecision of the instruments, human errors, effect of temperature changes, etc., and $E_E = E_f + E_m$.

The goal is to find the limiting value of settlement s_{lim} from the following condition:

$$\Pr(F_{\varepsilon_{\lim}} \mid S_m = S_{lim}) = p_T \tag{13}$$

p_T is the required (target) safety level. A measured settlement $S_m > s_{lim}$ thus implies an unacceptably high probability of failure $F_{\varepsilon lim}$ and would trigger further actions.

In the following, the value of s_{lim} will be determined using two different approaches. In Sec. 3.1, an approximate approach based on engineering judgment is utilized. In Sec. 3.2, the exact value of s_{lim} will be determined using a reliability-based approach. Finally, Sec. 3.3 describes the updating of the limiting settlement based on observations gathered during the tunnel construction.

3.1 *Approximate approach*

An approximate estimate of the limiting settlement s_{lim} can be determined based on evaluation

of the probabilistic model described in Sec. 2 using Monte Carlo (MC) simulation. For each sample of the input variables **X**, the settlement trough is evaluated according to Eqs. (1) and (2). Based on the estimated settlement, the maximal tensile strain in the building is calculated using Eqs. (3) to (8).

For simplification, the error terms are disregarded and only V_L, K and E/G are considered as RVs. Eq. (12) then reduces to $S_m = S_{max}$. The limiting settlement is approximately determined from a scatter plot of the maximum tensile stains ε_{max} against the maximal settlement S_{max} as is shown later in Figure 4. The value is determined visually from the plot using engineering judgment.

3.2 *Reliability-based approach*

The conditional probability of Eq. (13) can be determined by means of Bayesian updating techniques with equality type information as proposed in Straub (2011) and applied to geotechnical safety in Papaioannou and Straub (2012). With this approach, all the model and measurement errors are included.

First, the likelihood of V_L and K for given measured settlement s_m is calculated:

$$L(v_L,k) \propto \Pr(s_m = s_m \mid V_L = v_L, K = k) = f_E(s_m - f_1(v_L,k)) \tag{14}$$

where f_E is the Probability Density Function (PDF) of the error E_E in Eq. (12). Following Straub (2011), this likelihood function can be expressed by a LSF:

$$h(v_L,k,u) = u - \Phi^{-1}[cL(v_L,k)] \le 0 \tag{15}$$

where u is the realization of a standard Normal RV, Φ^{-1} is the inverse standard normal CDF and $c = \sigma_{E_E} \cdot \sqrt{2\pi}$ is a scaling constant chosen to ensure that $cL(v_L, k) \le 1$ for all v_L, K. This LSF defines the observation domain $\Omega_0 = \{h(\mathbf{x}, u) \le 0\}$ in a space that contains the original RVs $\mathbf{X} = (V_L, K\ E/G)$ and the standard Normal variable U. With this approach, the conditional probability of failure $F_{\varepsilon lim}$ for a given observed settlement s_m is computed as:

$$\Pr(F_{\varepsilon_{\lim}} \mid S_m = S_m) = \frac{\Pr(F_{\varepsilon_{\lim}} \cap S_m = S_m)}{\Pr(S_m)} = \frac{\Pr([\mathbf{x},u] \in \Omega_0 \cap \Omega_F)}{\Pr([\mathbf{x},u] \in \Omega_0)} \tag{16}$$

This probability can be evaluated using a MC simulation for different values of s_m. The limiting settlement value s_{lim} ensuring Eq. (13) is then found iteratively.

3.3 *Updating with the measurements gathered during construction*

After the construction starts, N measurements of the settlements $\mathbf{s} = (s_1, s_2, \ldots s_N)$ are obtained along the tunnel. These measurements can be used for updating the probabilistic model and the value of the limiting settlement. The measurements are carried out in the same quasi homogeneous geotechnical section of the tunnel, where also the analyzed building is located.

The uncertain geotechnical conditions in this quasi-homogeneous section, characterized by volume loss V_L and shape parameter K, are now described as stationary spatial stochastic processes with constant autocorrelation functions $R_K(l) = \rho_K$ and $R_{VL}(l) = \rho_{V_L}$ where l is the distance between two locations within the section. In other words, K has the same marginal distribution at any location within the section and the values of K at any two locations are correlated with correlation coefficient ρ_K, independent of the distance between them. The same holds for V_L. This simple correlation model was selected based on a preliminary analysis of data from a constructed tunnel; its validity should be tested in the future based on a more detailed analysis. The new measurements at locations 1, …, N can be expressed by separate likelihood functions L_1, …, L_N following Eq. (14). For each likelihood function L_i, one can find the corresponding observation domain Ω_i defined by means of a LSF $h_i(v_{L,i}, k_i, u_i)$ as described in Eq. (15). Here, $v_{L,i}$ and k_i are the realizations of the random processes K and V_L at the location of measurement i.

To update the limiting value of settlement for S_m conditional on the existing measurements **s**, the failure probability conditional on S_m and on **s** is computed (compare with Eq. (16)):

$$\Pr(F_{\varepsilon_{\lim}} \mid S_m = S_m, \mathbf{S} = \mathbf{s}) = \frac{\Pr(F_{\varepsilon_{\lim}} \cap S_m = S_m \cap \mathbf{S} = \mathbf{s})}{\Pr(S_m = s_m \cap \mathbf{S} = \mathbf{s})} = \frac{\Pr([\mathbf{x},u,u_1,\ldots u_N] \in \Omega_F \cap \Omega_O \cap \Omega_1 \cap \ldots \cap \Omega_N)}{\Pr([\mathbf{x},u,u_1,\ldots u_N] \in \Omega_O \cap \Omega_1 \cap \ldots \cap \Omega_N)} \tag{17}$$

Analogous to the procedure in Sec. 3.2, this conditional probability is evaluated for different values of s_m. The updated limiting settlement value s^*_{lim} ensuring Eq. (13) is found iteratively.

4 CASE STUDY

The proposed method is applied to a case study of the L9 metro line construction in Barcelona. The damage produced by the tunnel construction to a complex of masonry buildings from the late

1920's located in the *Bon Pastor* area is studied. An equivalent beam analysis of the buildings was already performed in Camós et al. (2012), showing the validity of this model. The location of the building and the tunnel is shown in Figure 1.

4.1 *Model parameters*

The tunnel diameter d in the studied section is 12 m, the depth of the tunnel is z_0 = 23 m. The length of the building complex is L = 46 m, the angle between the building wall and the plane perpendicular to the tunnel axis is $\theta = 26°$, the building height is H = 3 m and thus, the inertia per unit length of the cross-section of the building is equal to $I = 2.25$ m^4/m. The parameter t equals 1.5 m in the sagging zone and 3 m in the hogging zone and $a = t$ for both zones.

The probabilistic model is summarized in Table 2. The shape parameter of the settlement profile K usually varies from 0.2 to 0.3 for granular soils to 0.4 to 0.5 for stiff clays to values as high as 0.7 for soft silty clays (Burland, 2008). The ground in the analyzed tunnel section is formed by typical alluvial soil with coarse sand, limes and a small quantity of gravel. K is likely to be in the interval from 0.2 to 0.4, which is thus assumed to be a 90% confidence interval. The mean is assumed to be 0.3 and coefficient of variation (c.o.v.) is assumed equal to 0.2. K is non-negative and the lognormal distribution is thus an appropriate model for this RV.

Experience from tunneling constructions in similar conditions (TYPSA, 2003) shows that the expected interval of volume loss V_L is in the range 0.1% to 0.6%. Nevertheless, the uncertainty on these values is high due to many unpredictable factors that influence ground losses (unexpected geological units, technical problems of the TBM, human errors, etc.). The interval of 0.1–0.6% is thus assumed to be a 90% confidence interval and the c.o.v. is supposed to be 0.4. V_L is modeled by a lognormal distribution.

A value equal to 2.5 is typically assumed for the ratio E/G of masonry buildings. Uncertainty is also present in this parameter due to the variety of orthotropic materials composing a building, yet this uncertainty is relatively small. Therefore, it is here modeled by a Beta distribution defined on the interval 2.4 to 2.6. The measurement error E_m and the model error E_f are represented with normal distribution with zero mean and standard deviations 0.5 mm. The multiplicative model errors of the equivalent beam model $E^{sag}_{\varepsilon_{br}}, E^{sag}_{\varepsilon_{dr}}, E^{hog}_{\varepsilon_{br}}, E^{hog}_{\varepsilon_{dr}}$, are described by lognormal distributions with mean equal to 1.

4.2 *Results of the probabilistic analysis*

The results of the MC simulation of the model described in Sec. 2 are presented here. They show the influence of the different uncertain parameters on the assessment of maximum strain ε_{max} calculated following Eq. (9) and on the associated damage category as defined in Table 1.

Table 2. Random parameters of the model.

Parameter [units]	Distribution	Mean	St.dev.
K [-]	Lognormal (–1.22, 0.20)	0.3	0.06
V_L [%]	Lognormal (–0.99, 0.39)	0.4	0.16
$\frac{E}{G}$ [-]	Beta (2,2, [2.4, 2.6])	2.5	0.045
E_m, E_f [mm]	Normal (0.0, 0.5)	0.0	0.50
$E^{sag}_{\varepsilon_{br}}, E^{sag}_{\varepsilon_{dr}}, E^{hog}_{\varepsilon_{br}}, E^{hog}_{\varepsilon_{dr}}$ [-]	Lognormal (0.0, 0.05)	1.0	0.05

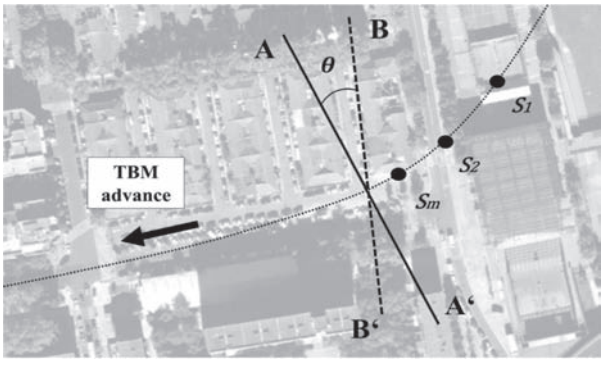

Figure 1. Location of buildings and tunnel track.

Figure 2 shows the influence of the volume loss V_L on the maximum strain ε_{max}. A positive linear correlation is observed; higher values of volume loss are likely to lead to more severe damages on the building. Figure 3 displays the influence of the shape parameter K on ε_{max}. Higher values of K produce flatter settlement troughs, which cause smaller tensile strains in the building and thus lead to milder damages. The relationship is clearly nonlinear.

The a-priori probability of the building damage being in category 0, which corresponds to negligible damages, is 0.6. The probability of only aesthetical damages, corresponding to categories 0–2, is 0.95.

4.3 *Approximate determination of the limiting settlement value*

The limiting settlement s_{lim} is determined using the approximative approach described in Sec. 3.1. Only a negligible damage (category 0) is acceptable, as is usual in tunneling construction. More severe damages to buildings are considered as a failure, therefore the limiting tensile strain is set to $\varepsilon_{lim} = 0.05\%$. Figure 4 shows the scatter plot of settlement S_{max} and maximum strain ε_{max} obtained from the MC simulation. An approximate value of the limiting settlement is determined $s_{lim} = 22$ mm.

4.4 *Exact reliability-based determination of the limit value of settlement*

The reliability based approach shown in Sec. 3.2 is used to find the limiting settlement s_{lim} that satisfies Eq. (13) for $p = 0.05$ and $\varepsilon_{lim} = 0.05\%$ (the failure event is defined in accordance with the previous Sec. 4.3.). Figure 5 displays the conditional probability of failure for different values of measured settlement s_m from 20 to 30 mm (denoted as prior estimate). The limiting settlement is determined as $s_{lim} = 23$ mm.

4.5 *Results of updating with observations from monitoring instruments*

The prior estimate of the limiting settlement described is now updated with the measurements gathered during the construction process, following the procedure described in Sec. 3.3. Two measurement of the settlement in the same quasi-homogeneous section are utilized: $s_1 = 14$ mm, $s_2 = 19$ mm. Correlation coefficients of the underlying normal distributions of shape parameter and volume loss are estimated by expert judgment: The shape of the settlement trough (described by parameter K) is dependent on the geotechnical conditions. A high correlation is therefore assumed within a geologically homogeneous section and $\rho_K = 0.7$. On the contrary, the volume

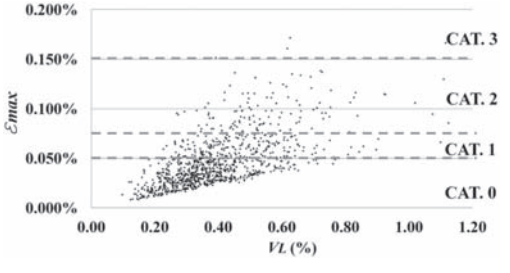

Figure 2. Scatter plot of volume loss V_L and max. strain ε_{max}.

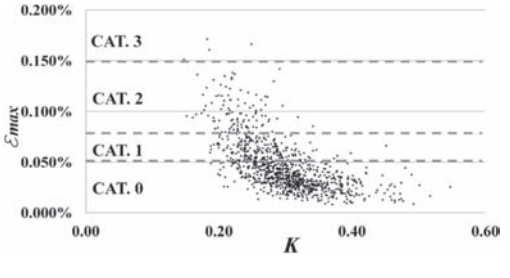

Figure 3. Scatter plot of parameter K and max. strain ε_{max}.

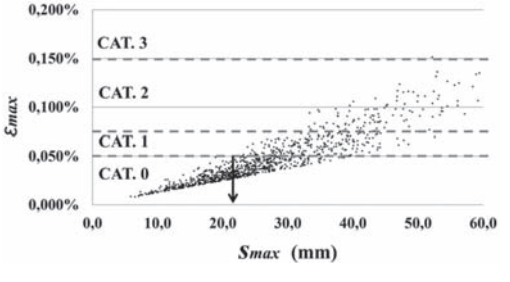

Figure 4. Scatter plot of settlement S_{max} and max. strain ε_{max}.

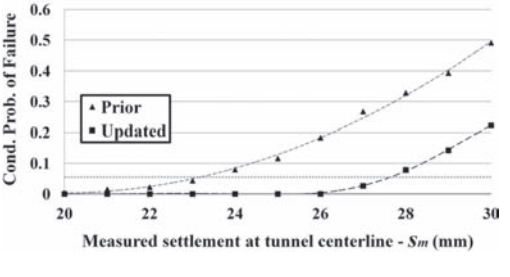

Figure 5. Conditional probability of failure for different values of measured settlement, $\Pr(F_{\varepsilon_{\lim}=0.050\%} \mid s_m)$.

loss V_L is strongly influenced by the construction process and it is typically highly variable within one homogeneous section. It is therefore assumed to be uncorrelated and $\rho_{V_L} = 0$. The updated conditional probabilities of failure for different values of the settlement measured at the vicinity of the building, s_m, are depicted in Figure 5. The updated value of limiting settlement is $s^*_{lim} = 27$ mm.

5 CONCLUDING REMARKS

The paper presented a computationally efficient model for probabilistic prediction of building damage due to tunnelling that is applicable in engineering practice (Sec. 2). Further, a novel method for determining the limiting settlement was presented (Sec. 3), which is a more systematic and traceable reliability-based approach with an explicit rationale than the deterministic methodology typically used in practice. Additionally, the reliability-based approach allows to incorporate measurements made during the construction. The proposed procedure was demonstrated on a case study of a tunnel construction in Barcelona (Sec. 4). First, the influence of the uncertainty in the model parameters (volume loss, shape parameter of the settlement through, Young and shear moduli of the building material) on the estimated damage was presented. Second, the value of the limiting settlement was determined with the approximate approach as 22 mm. Third, the limiting settlement was determined more precisely using an advance realiability-based approach as 23 mm. Both approaches provide similar values and the simpler method appears to be satisfactory for practical applications. Both of these values are more strict than the value that was used in the real case, where a settlement of up to 24 mm was considered to be safe. The reason for this difference is the fact that in the real case, the uncertainties in the ground parameters and building parameters were not considered and some unfavorable values of these parameters were thus not taken into account. Finally, the value of the limiting settlement was updated with observations gathered during the construction. The updated limiting settlement is 27 mm and is thus higher that the prior value determined during the design phase. The increase of the the limit is possible thanks to the reduction of uncertainty after including the additional measurements.

REFERENCES

Attewell, P.B., Yeates, J. and Selby, A.R. (1986) *Soil movements induced by tunneling and their effects on pipelines and structures*. Blackie Academic & Professional.

Boscardin, M.D. and Cording, E.J. (1989) Building response to excavation-induced settlement. *Jour of Geo. Eng.* 115(1–21).

Burland, J.B. (2008) The assessment of the risk of damage to buildings due to tunnelling and excavations. J.T. Payma Cotas: *Mov. de edificios inducidos por excavaciones*. p. 3.

Burland, J.B., Broms, B. and De Mello, V.F.B. (1977) Behaviour of foundations and structures. *Proc. 9th Int. Conf. on Soil Mech. and Found. Eng*., 2, 495–546.

Burland, J.B. and Wroth, C.P. (1974) *Settlement of buildings and associated damage*. London: Pentech Press.

Camós, C., Molins, C. and Arnau, O. (2012) A case study of damage on masonry buildings produced by tunneling induced settlements. *Int. Jour. of Architectural Heritage*.

Papaioannou, I. and Straub, D. (2012) Reliability updating in geotechnical engineering including spatial variability of soil. *Computers and Geotechnics* 42: 44–51.

Peck, R.B. (1969) *Deep excavations and tunneling in soft ground*. SOA Report, 7th Int. Conf. SM&FE.

Straub, D. (2011) Reliability updating with equality information. *Probabilistic Engineering Mech. 2*6: 254–258.

TYPSA. (2003) Análisis de los movimientos del terreno producidos por la excavación mecánica del túnel de la L9 en la zona de Santa Coloma de Gramanet. *Projecte de construcció de la Línia 9 de metro de Barcelona. Tram 4t Bon Pastor—Can Zam. Infraestructura i Estacions.* Annex 8.

This page intentionally left blank

Geotechnical Safety and Risk IV – Zhang et al. (eds)
© 2014 Taylor & Francis Group, London, ISBN 978-1-138-00163-3

A three-level framework for multi-risk assessment

Z.Q. Liu & F. Nadim
Norwegian Geotechnical Institute/International Centre for Geohazards, Oslo, Norway

ABSTRACT: Many regions of the world are exposed to and affected by several natural hazards. Implementation of effective risk management strategies in these areas requires that all relevant threats are assessed and considered. Compared to single-risk analysis, the examination of multiple risks poses a range of additional challenges due to the different characteristics of hazards. This paper summarizes previous research on multi-risk assessment and proposes a new three-level framework for multi-risk assessment that could account for the possible interactions among the threats. The framework is developed as part of the EU FP7 Collaborative Research Project MATRIX. The first level is a simple flow chart that guides the user in whether a multi-hazard, multi-risk approach is required for the problem at hand. The second level is a simplified, semi-quantitative approach to explore if a detailed assessment is needed. The third level is a detailed quantitative multi-risk analysis based on Bayesian networks. The key components of this framework, such as assessment of cascading hazards, time-dependent vulnerability estimation, and the choice of the required level of sophistication are addressed in the paper. The multi-risk assessment procedure outlined in the paper integrates the results of risk posed by each threat, cascade effect, and appropriate consideration of uncertainties, to provide a rational estimate of multiple risks. Simple examples that demonstrate the application of the method are presented in the paper.

1 INTRODUCTION

Many regions of the world are exposed to and affected by several types of natural hazard. The assessment and mitigation of the risk posed by multiple natural and man-made threats at a given location requires a multi-risk analysis approach that could account for the possible interactions among the threats, including possible cascade events. Performing quantitative multi-risk analysis using the methodologies available today presents many challenges (e.g., Kappes et al. 2012, Marzocchi et al. 2012). The risks associated with different types of natural hazards such as volcanic eruptions, landslides, floods, and earthquakes are often estimated using different procedures and the produced results are not comparable. Furthermore, the events themselves could be highly correlated (e.g., floods and debris flows could be triggered by an extreme storm event), or one type of threat could be the result of another (e.g., a massive landslide that is triggered by an earthquake, so-called cascade effect).

It is obvious that a mathematically rigorous approach to multi-risk assessment that addresses all the challenges named above, as well as the uncertainties in all steps of the analysis, will be complicated and require resources and expertise. On the other hand, in many situations the decision-maker in charge of risk management can identify the optimum alternative among those options available without doing a detailed, rigorous multi-risk analysis. Therefore, the framework recommended in this study is based on a multi-level approach where the decision-maker and/or the risk analyst will not need to use a more sophisticated model than what is required for the problem at hand, or what would be reasonable to use given the available information.

2 THE RECOMMENDED THREE-LEVEL FRAMEWORK FOR MULTI-RISK ASSESSMENT

The recommended multi-risk assessment framework is a multi-level process which assumes that the end-user (decision-maker or risk analyst) has identified the relevant threats and has carried out an assessment of the risk(s) (at the level of sophistication required for the problem at hand) associated with each single hazard(s). Figure 1 shows the general steps of the multi-risk assessment framework. The overall multi-risk assessment process comprises the following stages: (1) risk assessment for single hazards, (2) Level 1: qualitative multi-risk analysis, (3) Level 2: semi-quantitative multi-risk analysis, and (4) Level 3: quantitative multi-risk analysis. The details are described below.

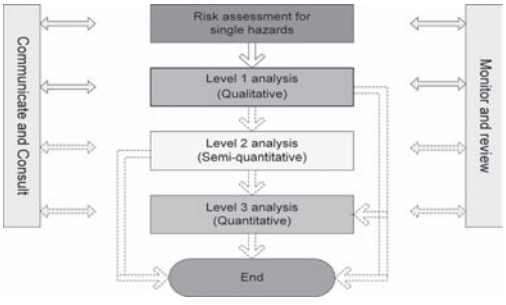

Figure 1. Schematic view of the steps followed in the proposed multi-risk assessment framework.

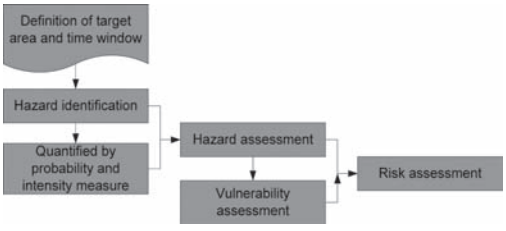

Figure 2. Stages of risk assessment for single hazard.

In the first step, it is assumed that the risk assessment for the single hazard(s) roughly follows the classical approach that is comprised of the following stages (Fig. 2):

- Definition of space/time assessment window (target area, time window) and the risk metric quantifying the expected losses.
- Threat(s) identification (e.g., earthquake, volcano, landslide, etc.).
- Single hazard assessment (e.g., rate of occurrence, pathway, intensity measure, etc.).
- Assessment of the vulnerability of the elements at risk (e.g., people, buildings, etc.).
- Assessment of the consequences in terms of the chosen metric (e.g., loss of life, economic losses, environmental degradation, etc.).

Once the results of the single-hazard risk assessment(s) are available, the user embarks on a three-level process, which becomes more detailed and rigorous as the user moves from one level to the next. The user moves to a higher level analysis only if the problem at hand requires a more accurate risk estimate and, equally important, if the data needed for doing the more detailed analysis are available. The selection of which of these three levels is to be used depends on the outcome of the preliminary risk assessment for single hazard(s).

3 LEVEL 1 ANALYSIS

The Level 1 analysis comprises a flow chart type list of questions that guides the end-user as to whether or not a multi-type assessment approach, which explicitly accounts for cascading hazards and dynamic vulnerability within the context of conjoint or successive hazards, is required. Each question will be supplied with an exhaustive list of answers that the user should choose from. This process is shown schematically in Figure 3.

The flow chart will include, for example, these questions:

- What is the purpose of the risk assessment exercise? (answers: identifying the most critical risk scenarios and choosing the optimal risk mitigation measures, assessing the adequacy of resources and level of preparedness for post-event response, etc.).
- Which natural threats are relevant for your area of interest? (answers: earthquake, landslide, volcanic eruption, tsunamis, wildfire, winter storm, storm surge and coastal flood, fluvial flood, snow avalanche, other perils, etc.).
- (If the user has chosen only one natural hazard from the list) How likely is it that the dominant natural threat could happen more than once during the time window of concern with an intensity that will cause significant loss? (answers: very likely, likely, unlikely, very unlikely, virtually impossible).

Note: At this stage, if the user has chosen only one natural hazard from the list and chooses very unlikely or virtually impossible as the answer to the above question, then there is no need to go any further and a more detailed multi-risk assessment is irrelevant.

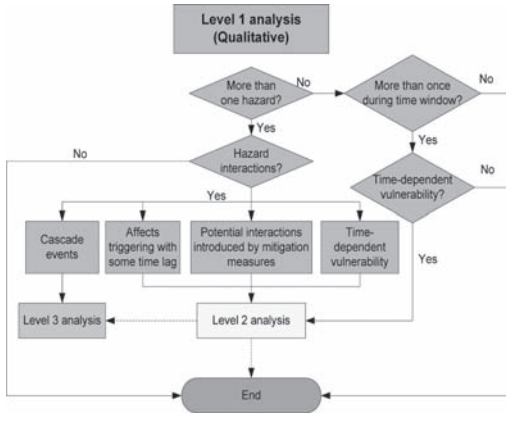

Figure 3. The steps involved in the Level 1 multi-risk analysis.

- Cascading events: Could a hazard trigger another hazard in your list (example: an earthquake triggering a landslide, landslide debris blocking a river and causing flooding when the landslide dam breaks, earthquake causing collapse of flood defence structures and leading to flood, etc.)? (answers: yes or no).
- Conjoint events: Could several hazards in your list occur simultaneously because they are caused by the same external factors (example: earthquakes and volcanic eruptions are both caused by tectonic processes, winter storms and storm surges, fluvial floods and debris flows caused by extreme precipitation events, ..)? (answers: yes or no).

Note: The user will be provided with some guidance and examples for questions such as the previous two, which may not be straightforward.

- Dynamic vulnerability: Could the occurrence of one of the hazards in your list significantly influence the vulnerability of some of the elements at risk to another event of the same type or to other hazards (example: a building partially damaged by an earthquake has a higher vulnerability to the next earthquake or to floods and landslides, ash fall from a volcanic eruption on roof tops will increase the mass and hence may increase the seismic vulnerability of the building, etc.) ? (answers: yes or no).
- Dynamic hazard: Could the occurrence of one of the hazards in your list significantly influence the occurrence probability of other hazards (example: a strong earthquake could weaken the soil in a slope and increase the probability of landslide during extreme precipitation events, etc.)? (answers: yes or no).

Additional questions may, of course, be added, depending upon the situation at hand. If the Level 1 results strongly suggest that a multi-type assessment is required, then the end user moves on to Level 2 to make a first-pass assessment of the effects of dynamic hazard and time-dependent vulnerability (see Fig. 4). If cascading events are potentially a concern, the user goes directly to the Level 3 analysis.

4 LEVEL 2 ANALYSIS

In Level 2 analysis, the interactions among hazards and dynamic vulnerability are assessed approximately using semi-quantitative methods. The steps involved in the Level 2 analysis are shown in Figure 4.

To consider hazard interactions and time-dependent vulnerability, the suggested method in multi-risk Level 2 analyses is a matrix approach based on system theory. This kind of matrix has been used in various fields, including environmental issues (Simeoni et al. 1999, de Pippo et al. 2008), rock engineering (Hudson 1992) and natural hazard assessment (Kappes et al. 2010). The assumption of this approach consists of the comprehension and description of the relationships among agents and processes in the evolution of system.

Figure 4 shows an example to explain this approach. Firstly, a matrix is developed by means of the choice of a couple of hazards, considered as the basic components of the system (Fig. 5a). It will be followed by a clockwise scheme of interaction (Fig. 5b), with the description of the mutual influence between different hazards (Fig. 5c). More specifically, each element of the row, which crosses one of the hazards in the mean diagonal, shows the influence of this hazard on the system, thus indicating the cause of the phenomena; whereas each element of the column, which crosses the same hazard analysed, shows the influence of the system

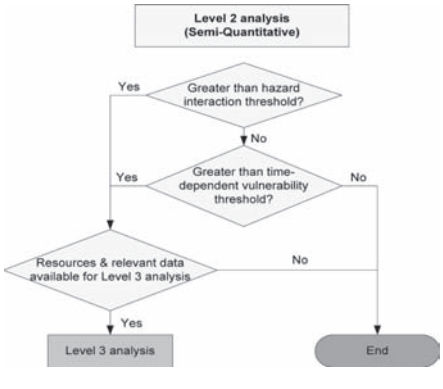

Figure 4. The steps involved in the Level 2 multi-risk analysis.

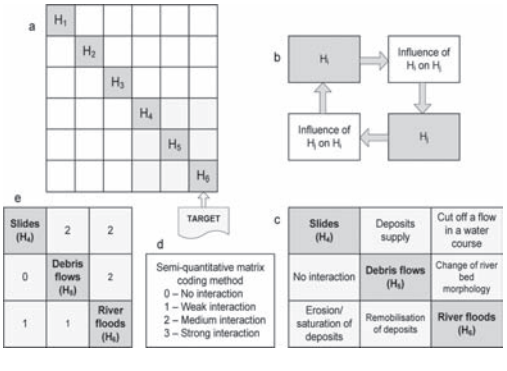

Figure 5. Matrix approach for the identification of the interactions between hazards in Level 2 analysis (Modified after de Simeoni et al. 1999 and Kappes et al. 2010).

on this hazard, thus focusing on the effect of the phenomena. After the descriptions contained in the matrix, they are assigned numerical codes varying between 0 (No interaction) and 3 (Strong interaction) with intervals of 1, as a function of their degree of the interaction intensity (Fig. 5d, 5e). Once all the hazards in the matrix are filled, it is possible to verify the degree of the impact of each hazard on the others and the effect from other hazards. In order to avoid the excessive weighting of a single hazard, the sum of the codes for the row and the column is considered. Table 1 shows the coding result for each hazard.

It can be seen that slides are the dominant hazard caused by other hazards because they have the maximum number of causes. On the other hand, river floods are the hazards most sensitive to the influence of other hazards, with the maximum number of effects.

In the scoring system above, the maximum possible value of each off-diagonal cell in Figure 5a is 3. Therefore the maximum possible value for the total sum of each row is $3 \cdot (n - 1)$, where n is the number of hazards. Likewise, the maximum possible value for the total sum of each column is $3 \cdot (n - 1)$. This means that the maximum possible value for the total sum of causes and effects is:

$$H_{I,max} = 2 \cdot 3 \cdot n \cdot (n-1) = 6 \cdot n \cdot (n-1) \quad (1)$$

where n is the number of hazards and H_I is the hazard interaction index.

Therefore, the maximum possible value for the hazard interaction index is $H_{I,max} = 6 \cdot 3 \cdot 2 = 36$ for the example considered in Table 1. Given the uncertainties and possible excessive or moderate weighting of single hazards, a threshold hazard interaction index H_I equal to 50% of $H_{I,max}$ is recommended for considering a more detailed Level 3 analysis. If the hazard interaction index is less than this threshold, Level 3 analysis is not recommended because the additional accuracy gained by the detailed analyses is most likely within the uncertainty bounds of the simplified multi-risk estimates. Otherwise, Level 3 analysis is recommended. In the example above, the threshold hazard interaction index calculated by Equation 1 is $H_I = 18$ (50% of 36), while the total value of causes and effects is 16, hence we do not need to do Level 3 analysis.

Table 1. Coding of each hazard in the system.

Number	Hazard	Causes (rows)	Effects (columns)	Causes + effects
1	Slides	4	1	5
2	Debris flows	2	3	5
3	River floods	2	4	6
Total		8	8	16

5 LEVEL 3 ANALYSIS

In Level 3 analysis, the interactions among hazards and dynamic vulnerability are assessed quantitatively with as high accuracy as the available data allow.

A new quantitative multi-risk assessment model based on Bayesian networks (BaNMuR) is introduced to both estimate the probability of a triggering/cascade effect and to model the time-dependent vulnerability of a system exposed to multi-hazard. The flexible structure and the unique modelling techniques offered by Bayesian networks make it possible to analyze cascade effects through a probabilistic framework. Furthermore, the interactions between hazards and the uncertainties involved may be captured using a Bayesian network. The uncertainties in each hazard/vulnerability and their interrelationships are represented with probabilities. The prior (conditional) probabilities can be updated with information of specific cases by Bayes' theorem. Therefore, the uncertainties would become smaller and the updated multi-risk results would become more reliable based on the new information. In particular, this methodology is well suited for treating uncertainties associated with hidden geodynamic variables, which are not directly observable from the Earth's surface (e.g., model uncertainty in causal relationships between unobservable volcanic processes and surface manifestations or monitoring data).

The probabilities of hazardous events are updated on the basis of any new information gathered. This framework shows how the updating of probabilities due to the interaction of hazards helps to update the vulnerability and total risk quantitatively and how mitigation measures influence the multi-risk consequences.

A conceptual Bayesian network multi-risk model may be built as shown in Figure 6. To determine the whole risk from several threats, the network takes into account possible hazards and vulnerability interactions. This would include the events:

1. Independent but threatening the same elements at risk with or without chronological coincidence (the column marked in deep orange color in Fig. 6);
2. Dependent on one another or caused by the same triggering event or hazard; this is mainly the case of 'cascading events' (the column marked in green color in Fig. 6).

Figure 6. Bayesian network for quantitative multi-risk assessment.

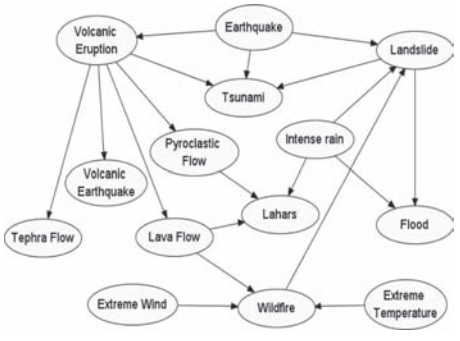

Figure 7. Possible scenarios of multi-hazard interaction as considered in the MATRIX project.

This network consists of two main sub-networks for (1) multi-hazard and (2) time dependent vulnerability, as detailed in the following sections.

5.1 *Multi-hazard analyses*

A number of possible scenarios of single hazards and cascade events have been identified for the MATRIX (EU FP7 Project: New Multi-HAzard and MulTi-RIsK Assessment MethodS for Europe) case studies (Garcia-Aristizabal et al. 2012). A Bayesian network may therefore be built as shown in Figure 7 to describe the interactions between hazards. It is obvious that one hazardous event could trigger other hazardous events.

5.2 *Time-dependent vulnerability assessment*

Predicting the damage of elements at risk (e.g., buildings) is critical for the evaluation of economic losses and should be estimated with an acceptable degree of credibility in order to determine the potential losses that are dependent upon the performance of elements at risk subjected to various hazard excitations. Fragility curves represent the cumulative distribution of damage, which specify the continuous probability that the indicated damage-state has been reached or exceeded, and could provide graphical information on the distribution of damage.

The Limit State (LS) probability for a structure exposed to a single hazard can be expressed in terms of discrete random variables as follows:

$$P_f = \sum_{i=0}^{\infty} P\left[LS \middle| I = i\right] P\left[I = i\right] = \sum_{x=0}^{\infty} P\left[D > C \middle| I = i\right] P\left[I = i\right] \quad (2)$$

where I is the intensity measure of the hazard and LS (limit state) is the condition in which the load demand D due to the hazard is greater than the capacity C. The conditional probability $P[\,LS \mid I = i\,]$ is the probability of reaching LS at a given hazard intensity level, $I = i$. The term $P[I = i]$ is the marginal hazard probability. For continuous random variables, Eq. (2) can be expressed as

$$P_f = \int_{i=0}^{i=\infty} F_r(i) g_I(i)\, di \quad (3)$$

where $F_r(i)$ is the fragility function in the form of a cumulative distribution function and $g_I(i)$ the hazard function in the form of a probability density function.

In the case of a structure subjected to a multi-hazard situation involving additive load effects (e.g., earthquake + landslide), the convolution concept must be expanded. This multi-hazard form is calculated as

$$P_f = \sum_{i_1=0}^{\infty} \sum_{i_2=0}^{\infty} \ldots \sum_{i_n=0}^{\infty} P\left[LS \middle| I_1 = i_1 \cap I_2 = i_2 \cap \ldots \cap I_n = i_n\right] \times P\left[I_1 = i_1 \cap I_2 = i_2 \cap \ldots \cap I_n = i_n\right] \quad (4)$$

Eq. (3) can also be expressed in terms of continuous random variables as

$$P_f = \int_{i_1=0}^{i_1=\infty} \int_{i_2=0}^{i_2=\infty} \ldots \int_{i_n=0}^{i_n=\infty} F_r(i_1, i_2 \ldots, i_n) g_{I_1}(i_1) g_{I_2}(i_2) \ldots g_{I_n}(i_n)\, di_1 di_2 \ldots di_n \quad (5)$$

An example of the seismic fragilities, including the combination of probabilistic debris flow load (additional seismic weight), are presented

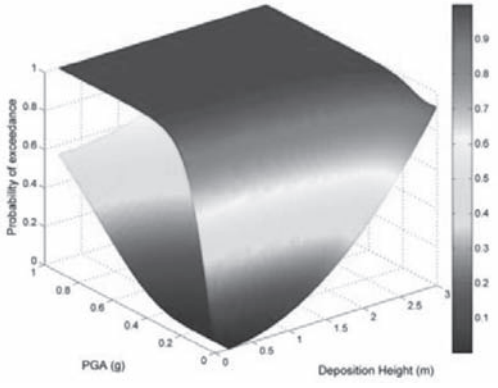

Figure 8. Fragility surface for a scenario involving a seismic event and debris flow for a low rise, low code RC building.

over three-dimensions, where the x-axis is the peak ground acceleration, the y-axis the deposition height, and the z-axis the fragility (see Fig. 8).

6 CONSLUSIONS

Quantification of all the natural and anthropogenic risks that can affect an area of interest is a basic factor for the development of a sustainable environment, land-use planning, and risk mitigation strategies. In this study, we put forward a consistent framework for multi-risk assessment. The developed procedure consists of three levels: (1) Level 1: qualitative analysis, (2) Level 2: semi-quantitative analysis, and (3) Level 3: quantitative analysis. In this way, multi-risk assessment can be performed step by step. At the same time, the interactions among different threats are considered in a systematic structure, and the uncertainties in the different stages can be accounted for in the recommended framework.

ACKNOWLEDGEMENT

The research leading to these results has received funding from the European Community's Seventh Framework Programme [FP7/2007-2013] under Grant Agreement n 265138 New Multi-Hazard and Multi-Risk Assessment Methods for Europe (MATRIX).

REFERENCES

de Pippo, T., Donadio, C., Pennetta, M., Petrosino, C., Terlizzi, F. & Valente, A. 2008. Costal hazard assessment and mapping in Northern Campania, Italy. *Geomorphology* 97: 451–466.

Garcia-Aristizabal, A. & Marzocchi, W. (with: Woo G., Reveillere A., Douglas J., Le Cozannet G., Rego F., Colaco C., Fleming K., Pittore M., Tyagunov S., Vorogushyn S., Nadim F., Vangelsten B.V., and ter Horst W.) 2012. Review of existing procedures for multi-hazard assessment, Deliverable D3.1. *New methodologies for multi-hazard and multi-risk assessment methods for Europe (MATRIX), contract No. 265138.*

Hudson, J.A. 1992. *Rock engineering system*. Ellis Horwood Ltd., Chichester.

Kappes, M.S., Keiler, M., Glade, T. 2010. From single- to multi-hazard risk analyses: a concept addressing emerging challenges. In Malet, J.-P., Glade, T. & Casagli, N. (Eds.), *Mountain Risks: Bringing Science to Society. Proceedings of the International Conference, Florence. CERG Editions, Strasbourg*: 351–356.

Kappes, M.S., Keiler, M., von Elverfeld, K. & Glade, T. 2012. Challenges of analysing multi-hazard risk: a review, *Natural Hazards* 64(2): 1925–1938.

Marzocchi, W., Garcia-Aristizabal, A., Gasparini, P., Mastellone, M.L. & Di Ruocco, A. 2012. Basic principles of multi-risk assessment: a case study in Italy. *Natural Hazards* 62(2): 551–573.

Simeoni, U., Calderoni, G., Tessari, U., Mazzini, E. 1999. A new application of system theory to foredunes intervention strategies. *Journal of Coastal Research* 15(2): 457–470.

Geotechnical Safety and Risk IV – Zhang et al. (eds)
 ISBN 978-1-138-00163-3

Rockfall risk management based on survey data of real slopes

S. Moriguchi
Tohoku University, Sendai, Miyagi Prefecture, Japan

Y. Otake, M. Iwata, Y. Honjo, A. Takagi, F. Kurauchi, T. Hara, K. Sawada & A. Yashima
Gifu University, Gifu, Gifu Prefecture, Japan

N. Asano
Chubu University, Kasugai, Aichi Prefecture, Japan

ABSTRACT: This paper presents a framework of risk management of rockfall using real survey data. Hida area located in Gifu prefecture in Japan is selected as a target area. In the evaluation process of rockfall provability, relative probability is calculated based on results of the survey data using the logistic regression analysis. Then, absolute probability is calculated using history data of occurrence of rockfall in the target area. In the evaluation process of the economic loss, road closure induced by rockfall is considered. Direct and indirect losses are taken into consideration. A trial calculation with different strategies were conducted based on calculated risk, and then it was summarized the obtained results are useful information for rockfall risk management.

1 GENERAL INTRODUCTION

Rockfall is one of the serious slope disasters. Once rockfall take place, it has potential to cause damage on infrastructures and loss of human lives. Japanese governments, researchers, and engineers have been making effort to minimize the damages. There are however still huge numbers of dangerous slopes that has high risk of rockfall in Japan. Furthermore it is becoming difficult to construct new countermeasures due to the budget cut of public works, and maintenance cost of existing countermeasures is becoming larger year by year. It is therefore quite important to develop a method which realizes a strategic decision making of the maintenance and new construction of countermeasures.

In order to overcome the problem mentioned above, this study presents a framework of risk management of rockfall. Risk of rockfall is calculated based on real survey data. In this paper, first, setting conditions, such as definition of risk, study area, and assumptions are explained, then calculation procedures of risk of rockfall are explained. This paper finally shows a result of a trial calculation is shown. Based on the result, effectiveness of the proposed framework is discussed.

2 SETTING CONDITIONS

2.1 *Target area*

Hida area, northern part of Gifu prefecture in Japan (Fig. 1), is selected as a target area. In the area, mountain areas are widely distributed, and

Figure 1. Study area.

there are a lot of slopes that has high risk of rockfall. The reason why the area is selected is that detailed survey data of slopes and accident data of rockfall has been accumulated by local government.

2.2 *Definition of risk and risk event*

Risk is defined as the product of the economic loss and the probability of risk event as follows,

$$R = P\sum D \tag{1}$$

where R is risk, D is the economic loss and P is the probability of risk event. Road closure induced by rockfall is defined as the risk event.

2.3 *Assumptions*

Following assumptions are used in this study.

a. Risk event occur independently. Thus, condimental occurrence of risk event is not considered.
b. Effects of disturbances such as earthquakes and rainfalls are not considered directly. This means these effects are not considered directly in calculations of the risk. However, because the effects should be included in rockfall accident data, a part of the effects is reflected indirectly.
c. Degradation of countermeasures is not taken into consideration. Therefore, once a countermeasure constructed, it is assumed that risk of slope is zero for eternity.
d. Effect of size of rockfall is not considered. It is therefore assumed that the road closure always occurs when rockfall takes place.

There are two reasons why the assumptions are used in this study. First reason is shortage of survey data. Large amount of survey data are accumulated, but it is difficult to build a database because of partial lack of data. Second reason is to simplify the calculation conditions. Although it is better to consider real condition, in this case, it becomes difficult to understand calculation results. Because the objective of this study is to build a framework of risk management of rockfall, we tried to build the framework under the assumptions. It is however important to remove the assumptions in future study.

3 PROBABILITY OF RISK EVENT

As mentioned in subsection 2.2, the road closure induced by rockfall is defined as risk event. In addition, as mentioned in subsection 2.3, we identify the occurrence of rockfall with the occurrence of road closure. Therefore, the probability of occurrence of rockfall can be treated as the probability of the road closure.

The probability is calculated based on a survey data. An intensive slope survey was carried out in 1996. A total of 3023 slopes were investigated by skillful engineers in target area. The slopes were separated into two failure types, rockfall and rock failure. In this study, rock failure is treated as a kind of rockfall. The slopes are also classified into three levels, namely Measures Required (MR), Observation (OB) and No Measures (NM). In addition, information of each slope, such as geological characteristics and geometric configuration, were accumulated.

The flow of the evaluation process of rockfall probability is shown in Figure 2. Based on the survey data, relative rockfall probability is firstly calculated using the logistic regression analysis. Then the absolute probability is calculated by calibrating the relative probability using the accident data of rockfall. The accident data has also been accumulated in target area. Number of slopes and rockfall accidents are summarized in Table 1. As shown in the table, the target area includes three regions, Gero, Takayama and Furukawa. Different models are built for each region in consideration of the rationality. Histograms of annual absolute rockfall probability are shown in Figures 3–5. It is found the probability of Furukawa region is higher than other two regions.

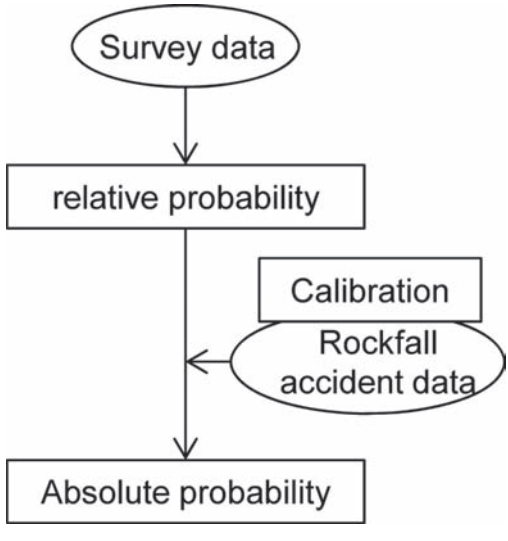

Figure 2. A flow of evaluation process of rockfall probability.

Table 1. Number of slopes and rockfall accidents.

Region	Evaluated level	Numbers of slopes		Number of rockfall accidents	
		Rockfall	Rock failure	Investigated	Uninvestigated
Gero	MR	186	51	5	7
	OB	399	68	12	
	NM	204	10	0	
Takayama	MR	275	109	7	17
	OB	517	380	7	
	NM	133	36	0	
Furukawa	MR	277	36	11	16
	OB	126	20	5	
	NM	186	11	3	

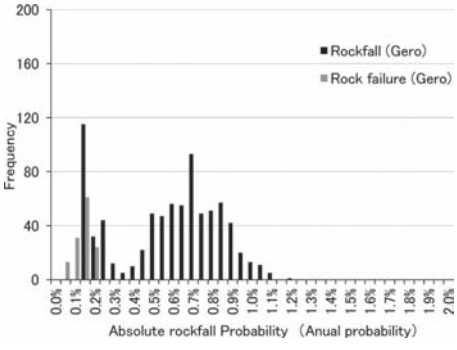

Figure 3. Histogram of rockfall probability (Gero).

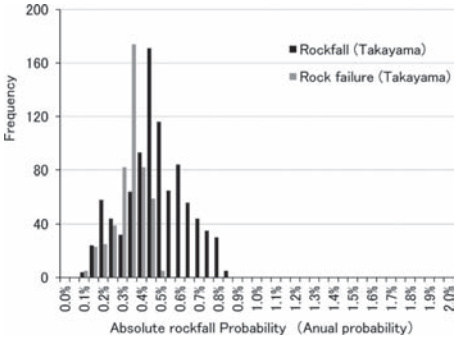

Figure 4. Histogram of rockfall probability (Gero).

4 ECONOMIC LOSS

4.1 *Items of economic loss*

As shown in Figure 6, the economic losses considered in this study are separated into two categories; direct loss and indirect loss. The direct loss includes the economic loss from traffic accidents (D_1) and the restoration cost (D_2), and the indirect loss includes the circumvention loss (D_3) and the emergency medical service loss (D_4). Thus equation 1 can be described using the economic losses as below,

$$R = P\left(D_1 + D_2 + D_3 + D_4\right) \tag{2}$$

Detailed information of each economic loss is explained in following subsections.

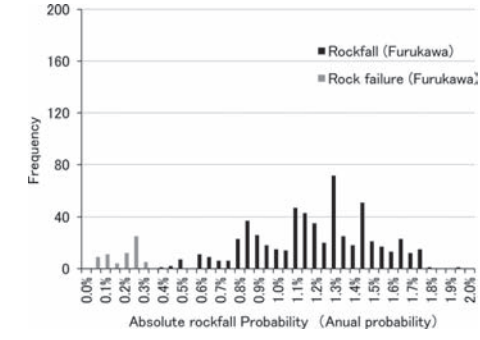

Figure 5. Histogram of rockfall probability (Gero).

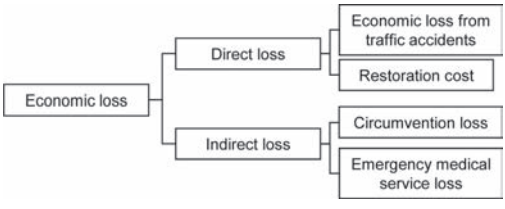

Figure 6. Economic losses.

4.2 *Economic loss from traffic accidents*

The economic loss from traffic accidents means the loss related death and injury induced by rockfall.

In other words, the loss is calculated based on a supposition that drivers or passengers are injured or killed due to the rockfall directly. Although much of discussions have been made about the definition of risk in terms of human life, but at least in Japan, confronting at various natural disasters, the value of human life is generally considered explicitly to quantify the benefit of infrastructure investment. Public Works Research Institute (PWRI) (2004) proposed a concept of the economic loss from traffic accidents. Figure 7 shows an image of the concept. The value of the economic loss from traffic accidents is evaluated based on trapezoid distribution. Height of the trapezoid means the value of the human life. The value of the human life (242 million Japanese Yen) is originated from a report published by Japanese government (2007).

4.3 *Restoration cost*

The restoration cost is evaluated from history data of rockfall accidents. 115 cases of restoration cost data are used and the averaged cost (410,000 JPY) is employed as the restoration cost in this study. Although it is better to evaluate the cost depending on size of rockfall and level of importance of road, these effect is not considered in this study, thus we used the averaged value for all cases.

4.4 *Circumvention loss*

The circumvention loss is calculated by following equation.

$$D_3 = CT \tag{3}$$

where C and T are amount of change of the consumer surplus and number of days of road closure, respectively. Number of days of road closure is assumed as 1 day. Although this is also big assumption, but the number of days is strongly depends on degree of damage of road and size of rockfall and level of importance of road, thus we assumed the number of days in consideration of past tends. C is calculated from increments of travel time and travel distance. These are calculated using a using a user equilibrium traffic assignment.

$$C = \alpha\left(t_1 - t_0\right) + \beta\left(l_1 - l_0\right) \tag{4}$$

where α is unite amounts of the talue of time, β is unite amounts of the travel cost, t is travel time and l is travel distance. Subscripts 0 and 1 indicate states before and after road closure, respectively. The values of α and β are obtained from a manual published by The Ministry of Land, Infrastructure, Transport and Tourism (2008).

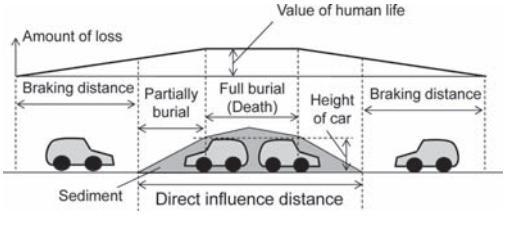

Figure 7. Image of economic loss from traffic accidents of slope (PWRI, 2004).

4.5 *Economic medical service loss*

The Emergency medical service loss relates to death of emergency patients induced by road closure. Fatality rate of emergency patients is strongly depends on travel time of ambulances. Hashimoto et al. (2002) reported a relation between the fatality rate and the travel time. In their study, brain hemorrhage, subarachnoid hemorrhage, acute myocardial infarction, acute cardiac failure, pneumonia, cardiopulmonary arrest, and brain infarction are employed as target diseases. The diseases and the model proposed by Hashimoto et al. (2002) are used in this study. Onset probability of each disease and averaged travel time are obtained using a medical data accumulated in hospitals and fire departments in the target area. These information are shown in Tables 2 and 3.

Table 2. Onset probabilities of diseases in study area.

Disease	Hida ($\times 10^{-4}$/day)	Takayama ($\times 10^{-4}$/day)	Gero ($\times 10^{-4}$/day)
Brain hemorrhage	6.2	10.5	5.4
Subarachnoid hemorrhage	4.7	12.4	1.9
Acute myocardial infarction	6.2	14.3	8.2
Acute cardiac failure	5.5	11.4	6.0
Pneumonia	9.9	0.0	9.8
Cardiopulmonary arrest	7.3	40.9	4.9
Brain infarction	14.6	33.3	11.2

Table 3. Averaged time required for transportation to hospital.

Region (number of data)	Avaraged time required
Hida (979)	28 min. 18 sec.
Takayama (346)	32 min. 29 sec.
Gero (1311)	24 min. 00 sec.

5 RISK MANAGEMENT

5.1 *Definition of B/C*

In this section, results of evaluated risk are shown. Because the cost-benefit ratio (B/C) is frequently used, the definition of B/C is described here. Generally, B/C is defined as follows,

$$(B/C) = \frac{\Delta R}{C} \tag{5}$$

where ΔR is a decrease in risk and C is cost of countermeasure. In this study, it is assumed the risk of slope is zero after taking countermeasure. Because degradation of countermeasures is not considered in this study, we employed this assumption. But in the future study, it is important to check the effect of this assumption. Based on the assumption, amount of risk change equal to risk as follows,

$$(B/C) = \frac{R}{C} \tag{6}$$

The cost of countermeasure C is obtained from the database of the survey data, because information of assumed cost is recorded in the data.

5.2 *Results of evaluated risk*

Figures 8 and 9 show histograms of risk and B/C. As mentioned before, the slopes are categorized into 3 levels, required (MR), Observation (OB) and No Measures (NM). Total of 1706 slopes that are grouped in MR and OB are described. As shown in Figure 9, values of B/C are over 1.0 in 288 slopes. It is therefore considered from the view point of the efficiency that there are still a lot of slopes that should be taken countermeasures.

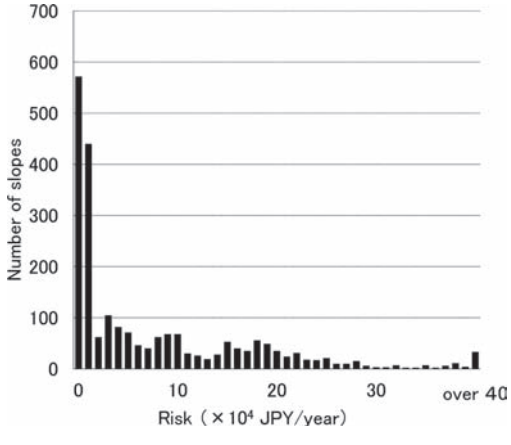

Figure 8. Evaluated economic loss.

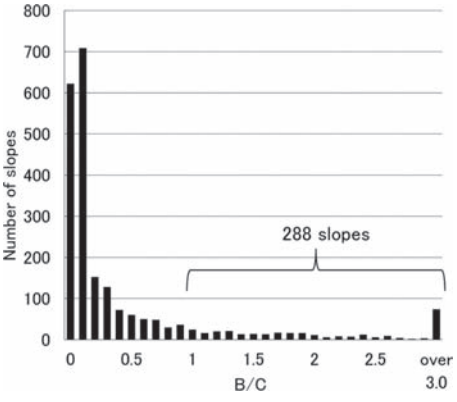

Figure 9. Evaluated economic loss.

Figure 10 shows values of risk of top 100 slopes. Values of B/C of each slope are also described in the figure. As we can understand from the figure, high risk slopes don't always have high values of B/C. This indicates that it is necessary to make decision of taking countermeasures using both risk and B/C.

5.3 *A trial calculation of risk management*

A trial calculation was carried out to validate the effectiveness of calculated results in this study. Following three different strategies of taking countermeasures were considered in this validation.

Plan A
Information of risk and B/C obtained in this study are not used. Generally, decision making of taking countermeasure should strongly depend on the results of the survey and the traffic volume. Thus priority of taking countermeasure is made based on levels of survey results (MR, OB, NM) and traffic volume in this plan.

Plan B
Results obtained in this study are efficiently used in this plan. Priority of taking countermeasure is determined based on B/C evaluated in this study.

Plan C
Results obtained in this study are used in this plan. Priority of taking countermeasure is determined based on amount of risk evaluated in this study.

Figure 11 shows a relation between residual risk and amount of investment. Results of each plan mentioned above are shown in the figure. As we can see in the Figure, plans B and C can remove the residual risk much more effectively than plan A. This indicates evaluated risk and B/C in this study are effective information for decision making of taking countermeasure. Here, let us discuss about the result of plans B. Plan B can remove risk most

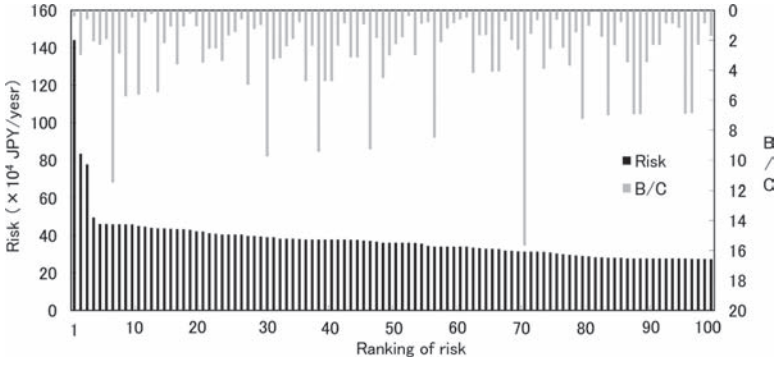

Figure 10. Risk top 100 and B/C.

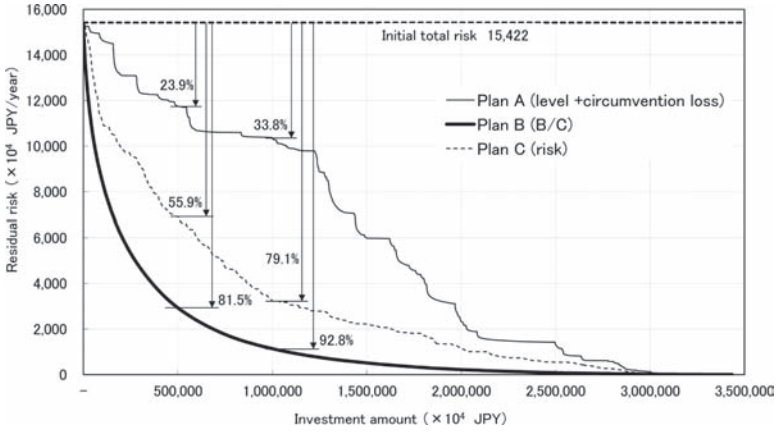

Figure 11. A relation between residual risk and investment.

effectively, but the strategy of plan B is not best solution of risk management. The reason is that the strategy depends on only economic efficiency, and other viewpoints, such as fairness, are not considered. It is therefore important to introduce another indexes in future study.

6 CONCLUSION

This paper presents a framework of risk management of rockfall risk using real survey data. Road closure is defined as risk event, and the provability of occurrence and economic losses are calculated. Finally, the trial calculation with different strategies of taking countermeasure was shown. According to the result of the trial calculation, it could be summarized the obtained results are useful information for risk management of rockfall.

Although effectiveness of the proposed framework was validated, some important viewpoints, such as fairness, are not considered in proposed framework. In addition, as mentioned in this paper, some big assumptions are still included. It is therefore necessary to develop the framework in the future works.

REFERENCES

Cabinet office (Japanese Government), *A report of economic analysis of damage of traffic accident*, 2007. (in Japanese)

Hashimoto, T., Kurihara, M., Inoue, K., Iwasaki, Y. & Fujimoto, A. 2002. Relationship between the carrying time and the survival rate in emergency medical service. *Journal of Japanese Society for Emergency Medicine* 5: 285–292. (in Japanese)

Public Works Research Institute (PWRI), *A manual of risk analysis and risk management* (draft version), Records of PWRI, No. 3926, 2004. (in Japanese)

The Ministry of Land, Infrastructure, Transport and Tourism, *A manual of cost-benefit analysis*, 2008. (in Japanese)

Geotechnical Safety and Risk IV – Zhang et al. (eds)
© 2014 Taylor & Francis Group, London, ISBN 978-1-138-00163-3

Implementing geo risk management in a client organization

M.Th. van Staveren
VSRM, Breda, The Netherlands

P.P.T. Litjens & J.J. Heerema
Rijkswaterstaat, Ministry of Infrastructure and the Environment, The Netherlands

ABSTRACT: Rijkswaterstaat, the largest public client organization for infrastructural projects in The Netherlands, is responsible for the design, construction, management, and maintenance of the main civil infrastructure in The Netherlands. Their key success factor is realizing infrastructure projects, not only within time, budget, safety and quality standards, but also with a minimum of hindrance for the public during construction. For these reasons, Rijkswaterstaat initiated the Dutch Geo-Impuls programme for reducing geotechnical failure. Consequently, this public organization embraced Geotechnical Risk Management (GeoRM) as the leading geotechnical working method and is serious about implementing GeoRM in its own organization. This paper presents the selected approach for the GeoRM implementation process, which includes embedding GeoRM in existing formal working procedures and empowering geotechnical engineers and managers to adopt and apply GeoRM in their day to day activities. The main hurdles encountered and solutions applied are discussed. Finally, the paper draws the main conclusions for implementing GeoRM in public client organizations in the construction industry.

1 INTRODUCTION

Rijkswaterstaat is the executive organisation that manages and develops the main national infrastructure facilities on behalf of the Dutch Minister and State Secretary for Infrastructure and the Environment. Rijkswaterstaat is responsible for the design, construction, management, and maintenance of the main infrastructure in The Netherlands. This makes Rijkswaterstaat the largest public client organization for infrastructural projects in The Netherlands. Realizing these projects, not only within time, budget, safety and quality standards, but also with a minimum of hindrance for the public during construction, is a key success factor.

For these reasons, Rijkswaterstaat is the initiator of the Dutch Geo-Impuls programme for reducing geotechnical failure. This joint industry programme aims to strengthen the geotechnical community by substantially reducing geotechnical failures in all types of construction projects (Cools 2011). Over 200 geotechnical engineers and managers from some 40 Dutch organizations, including client organizations, contractors, engineering firms, and knowledge institutes, work closely together in this programme that runs from 2009 up to 2015.

The Geo-Impuls participants embraced Geotechnical Risk Management (GeoRM) as the leading geotechnical working method. GeoRM is an explicitly structured and well-communicated way of dealing with geotechnical risks that is executed in all project phases, in order to achieve project objectives effectively and cost-efficiently. GeoRM is a new name for the GeoQ process for geotechnical risk management (van Staveren 2006). The process of geotechnical risk management is similar to the process of project risk management and involves the same sequence of steps. Therefore, GeoRM fits well in any sort of project risk management. The difference is that GeoRM is a more specific and in-depth approach of project risk management, for giving geotechnical risk the attention it requires in all phases of engineering and construction projects.

As initiator of the Geo-Impuls program, Rijkswaterstaat is serious about implementing GeoRM in its own organization. This paper presents the selected approach for the GeoRM implementation process and its results to date. First, the GeoRM implementation objectives of the public organization will be presented. Next, the selected GeoRM implementation approach is introduced, by the three dimensions of method, organization and people. Then each dimension is explored in more detail, including the main hurdles that were encountered and the actions that were executed. Finally, the paper draws the main conclusions for implementing GeoRM in public client organizations in the engineering and construction industry.

2 GeoRM IMPLEMENTATION OBJECTIVES

Before starting any GeoRM implementation activities, an organization should establish a set of clear implementation objectives. These objectives provide the rationale for the entire implementation process.

The main GeoRM implementation objective for Rijkswaterstaat is to embed GeoRM and its supporting tools in all relevant working processes and developments within the entire organization. Well-implemented GeoRM should contribute to the organizational objectives of realizing infrastructure projects within time, budget, safety and quality standards, with a minimum of hindrance for the public during construction. The GeoRM implementation is initiated by the Rijkswaterstaat top management and executed by a working group of geotechnical engineers within Rijkswaterstaat. There are two types of members of these working group.

The first type of members are engineers who are actually working in projects, by supporting and facilitating geotechnical activities within these projects. Examples of these activities are geotechnical reviews of the scope of site investigations, specification of geotechnical boundary conditions, and reviews of geotechnical reference designs. Specific GeoRM implementation objectives for these engineers are being able to apply GeoRM activities in the most complex projects of Rijkswaterstaat, and being able to delegate GeoRM activities to other professionals within Rijkswaterstaat, as well as to subcontract GeoRM activities to engineering firms.

The second type of members of the working group responsible for GeoRM implementation are engineers who are not directly working in projects. Specific GeoRM implementation objectives for these engineers are expanding the motivation and commitment to routinely applying the GeoRM working method, by using their networks. Also, these engineers monitor and steer the execution of GeoRM related topics within research development programmes within Rijkswaterstaat, with knowledge institutes and universities, as well as with similar organizations abroad, including the US Corps of Engineers in the United States.

Finally, all members of the geotechnical working group should participate in at least one working group of the Geo-Impuls development program.

3 GeoRM IMPLEMENTATION APPROACH

The applied GeoRM implementation approach acknowledges three implementation dimensions of (1) method, (2) organization and (3) people (van Staveren 2009). These implementation dimensions are inter-related and their organization-specific balance will allow effective implementation of GeoRM in an organization. This can be a client organization, but also a project organization, or an organization of a contractor or engineering company. Figure 1 presents these GeoRM implementation dimensions.

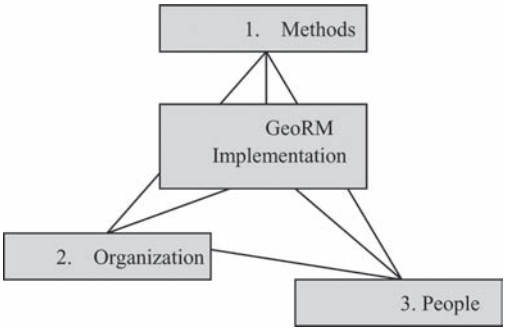

Figure 1. The three GeoRM implementation dimensions.

Given the previously mentioned implementation objectives, an implementation plan has been derived. The members of the GeoRM working group have been interviewed in order to acknowledge their views, expectations, and concerns regarding the GeoRM implementation, which will have an effect on their working routine. Moreover, the actual organizational conditions for the GeoRM implementation have been identified and discussed with the working group members. All these activities resulted in personalized implementation objectives of the working group members, as presented in the previous section.

Based on the organizational and personal objectives, as well as the identified organizational conditions for the GeoRM implementation, a series of activities have been defined for the implementation dimensions of method, organization and people. At the moment of writing of this paper, these activities are being executed and the first results are gained. These activities and results are presented in the next three sections, including any hurdles encountered and the solutions applied to overcome these hurdles.

4 THE GeoRM METHOD DIMENSION

The GeoRM method dimension includes the procedure and the supporting tools for applying it in an effective and cost-efficient way. The GeoRM procedure has been summarized in a thin guideline and is similar to the GeoQ approach for geotechnical risk management (van Staveren 2006).

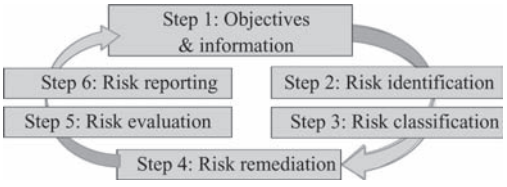

Figure 2. The GeoRM structure in six cyclic steps.

Van Staveren (2013) provides an summary in English of this Dutch guideline. The GeoRM process fits well in the ISO risk management process (ISO 2009) and also in the RISMAN process for project risk management (van Well-Stam et al. 2004). This latter process is widely applied in The Netherlands.

Figure 2 presents the structure of the GeoRM procedure, with six cyclic risk management steps.

Two types of tools can be distinguished that proved to be useful in several phases of infrastructure projects: (1) *conventional* geotechnical tools that can be applied in a risk-driven way and (2) s*pecific* GeoRM tools.

Examples of the first type of conventional tools are geological, geohydrological, and geotechnical maps and databases, geotechnical data reports, geotechnical modelling software for providing sensitivity analysis, risk-driven site and laboratory investigations, risk-driven geotechnical monitoring, and, not to forget, specialist geotechnical knowledge and judgement of well-experienced geotechnical experts.

Examples of specific GeoRM tools are of course geotechnical risk checklists and risk registers. Other tools are well-structured processes for geotechnical risk identification, risk classification and risk remediation sessions, that can be supported by specific software in so-called electronic board rooms for dealing effectively with different risk perceptions (van Staveren 2006). Another useful instrument is the GeoRiskScan (Bles et al. 2009) for appraising the GeoRM quality. Finally, a well-defined process for the communication of geotechnical risk towards stakeholders of projects proved to be valuable.

5 THE GeoRM ORGANIZATION DIMENSION

An *organization* can be defined as a stable and structured social system, where individuals work together to achieve one or more joint goals (Rogers 2003). Organizations include different types of sub-organizations, such as units, projects and teams. An example is a design team realizing the geotechnical design for a deep foundation. To be effective and cost-efficient, all organizational members need to agree on their formal tasks and responsibilities. This creates some sort of formal organizational *structure*. Such a structure may stimulate and support, or frustrate and even obstruct the implementation of geotechnical risk management.

In addition to this structure each organization has also some sort of informal way of working, behaving and talking: an organizational *culture*. However, an organizational culture is not tangible. It is "the way we are working here", with the shared convictions of the people working within an organization (Cameron & Quinn 1998). The organizational culture will to an considerable degree determine whether the formalized part of geotechnical risk management will be turned into action, or just stay on paper.

Due to the widely accepted importance of the concepts of organizational structure and culture in the organization sciences, the GeoRM dimension *organization* has been be divided into the organizational *structure* and the organizational *culture*.

5.1 *GeoRM and organizational structure*

For becoming embedded, it is important that the GeoRM method, its processes and supporting tools, fits well within the *formal* work procedures of the organization. Otherwise GeoRM would be considered as "unofficial" and therefore not becoming applied in a routine way of working within all projects. Within Rijkswaterstaat a formal project management procedure for realizing infrastructure projects is used. This procedure distinguishes three main project phases: (1) the definition phase, (2) the development phase and (3) the realisation phase. In each of these phases a number of formal documents have to be developed. Specific reviews are applied to allow the project to proceed to the next phase.

Specifically for the formal project management procedure, a formal and organization-specific GeoRM guideline has been developed by a number of members of Rijkswaterstaat's geotechnical group. This guideline presents the core elements of GeoRM, by providing definitions of geotechnical risk and its management, a description of the GeoRM process, and the presentation of the GeoRM principles. In addition, the guideline defines for each of the three project phases which GeoRM activities need to be performed and reported in which formal document. As a result of these activities these documents will benefit, in order to fulfil the requirements of the formal project management procedure of Rijkswaterstaat.

For example, during the *project definition phase*, the first four GeoRM process steps of sampling project information, identifying geotechnical risk, classifying geotechnical risk, and remediation geotechnical risk can be applied in order to support the costs estimations of the project with a required degree of accuracy. Tools applied are for instance geotechnical risk checklists for the specific type of project (a tunnel, a road, a railway, and so on) and databases with geological, geotechnical and geohydrological information in the neighbourhood of the project location. The resulting GeoRM product is a cost assessment of geotechnical risk remediation. This product can become part of the cost estimation report of the formal project management procedure.

During the *project development phase*, Rijkswaterstaat has to define and procure for instance location specific ground information that is needed for reference designs and contracting. The risk-driven definition and execution of a site investigation is a GeoRM tool that is for instance useful in this phase. By using the formal GeoRM guideline, Rijkswaterstaat is able to subcontract the execution of risk-driven site investigations with a scope that satisfies the geotechnical risk profile of the project. A tunnel project adjacent to an existing tunnel in poor soil conditions has typically a higher risk profile than the same tunnel in isolation in better soil conditions. Consequently, the risk-driven scope of the site investigation for the first tunnel would be more extensive than that for the second tunnel. Quite obvious for a geotechnical engineer, however, by applying the GeoRM approach the need for more or less site investigations becomes also clear for less geotechnically educated project managers and decision makers.

Finally, during the *project realization phase* for example contractual management of geotechnical risk becomes important for controlling the budget and planning of the project. The Rijkswaterstaat specific GeoRM guideline provides clear suggestions on how to deal with the contractual allocation of geotechnical risks, for instance by using the concept of the geotechnical baseline report (Essex 1997).

5.2 *GeoRM and organizational culture*

In addition to the *formal* part of GeoRM implementation, by developing the organization-specific GeoRM guideline that is part of the formal project management procedure, also the *informal* part of the organizational culture needs attention. This is a combination of adapting GeoRM to the existing organizational culture and trying to change the existing organizational culture in favour of routinely applying GeoRM. Regarding the latter aspect, for a considerable number of years Rijkswaterstaat transforms from a rather technically-oriented to a more project management-oriented organization. The well-structured GeoRM process suits well in the organizational culture of risk-driven project management and control. Over the years, many technically-oriented managers developed towards more process-oriented managers, who increasingly recognize and appraise the process structure of GeoRM. In addition, project risk management is a key topic in Rijkswaterstaat and GeoRM is in fact the risk-driven and geotechnical specialism of project risk management.

Nevertheless, on-going attention is needed to communicate the benefits of applying GeoRM in Rijkswaterstaat projects to project managers, technical managers and contract managers, because it changes the way of dealing with geotechnical engineering in a project from rather implicit and reactive towards more explicit and pro-active ways of working. For this reason, best practice flyers have been provided. These flyers summarize the GeoRM process in only one brief text block, make the link with the formal project management approach and give examples of GeoRM steps taken, GeoRM tools applied, and the results for the projects in terms of cost savings, avoided delays, improved quality and higher satisfaction of stakeholders in the projects.

Furthermore, specific flyers have been developed for the technical managers, contract managers and project teams. These flyers summarize the proven GeoRM benefits for these specific roles within the project. An example of these benefits for the *technical manager* are the execution of additional risk-driven site investigations in a motorway expansion project in The Netherlands, which proved the feasibility of embankments in a conventional way and saved a lot of money. An example of GeoRM benefits for the *contract manager* was the application of a geotechnical baseline report in a large bridge construction, which settled the occurrence of differing site investigation effectively and efficiently, without delaying the project. The entire *project team* benefitted for instance from the results of a GeoRiskScan (Bles et al. 2009) in a project for broadening a canal, which revealed in time a gap in essential yet lacking ground information which has been filled by hiring specific geotechnical expertise.

6 THE GeoRM PEOPLE DIMENSION

The third dimension for GeoRM implementation is about the people who need to have the motivation and competencies to apply geotechnical risk management in their work processes. Obviously,

the people dimension and cultural part of the organization dimension are closely coupled, as organizational culture is developed by interactions between individuals. The people dimension has a focus in the individual, and in particular on the motivation and competencies to apply GeoRM. For this reason, in the current phase of geotechnical risk management implementation at Rijkswaterstaat the people dimension concerns especially the members of the geotechnical working group.

In order to identify their view on GeoRM, as well as the hurdles they encounter when trying to apply GeoRM in their project, six interviews were held with members of the geotechnical group. Questions included the expectation and results of GeoRM, as well as hurdles and solutions for routinely applying GeoRM. There revealed wide consensus about the GeoRM objective of supporting the realization of successful projects by effectively, cost-efficiently and continuously managing geotechnical risk. In particular explicit communication about geotechnical risk was considered new and valuable.

However, also a few hurdles arose. First of all, how to put the GeoRM process in the practice of projects appeared rather difficult for some of the engineers. Also, the selection and allocation of GeoRM tasks between the geotechnical engineers of Rijkswaterstaat acting as client of public projects, engineering firms performing design and contractual services, and contractors realizing projects, appeared to be not always clear.

In general, engineers of engineering firms seem to hesitate to apply GeoRM, perhaps because of a lack of awareness of the need for it and a lack of knowledge about what Rijkswaterstaat is expecting from them. Moreover, within the organization of Rijkswaterstaat some of the engineers encountered difficulties to communicate the need and benefits of GeoRM with non-technical project managers, contract managers, and other project team members.

For the latter hurdle, development of earlier introduced best practice flyers and specific flyers for the project managers and teams have been developed. Regarding outsourcing of GeoRM activities to engineering firms, guidance is in development. A procedure how to outsource risk-driven site investigations within the GeoRM process for road projects to engineering firms has already been developed and applied successfully.

Regarding the hurdle of putting the GeoRM process in the practice of projects, in combination with outsourcing GeoRM tasks to engineering firms and contractors, so-called inter-vision meetings are held every two months. During these meetings of about one day each, one of the members of the geotechnical working group presents his or her GeoRM hurdle in his or her project. The other members reflect on the problem and provide possible solutions from their own practice by brainstorming. It is in fact a sort of action learning or learning by doing and reflection, in combination with training on the job, according to the concepts of Argyris & Schön (1978).

In the next meeting, some two months later, the experiences with the solution of the previous meeting is discussed and also a GeoRM hurdle of another team member is considered. Also, the overall progress of the GeoRM implementation within the entire Rijkswaterstaat organization is discussed in each session.

7 CONCLUSIONS

This paper presents the selected approach for the GeoRM implementation process within a large Dutch public client organization, Rijkswaterstaat. This implementation process involves embedding GeoRM in existing formal working procedures, as well as empowering geotechnical engineers during inter-vision sessions to adopt and apply GeoRM in their day to day activities.

Rijkswaterstaat is the largest public client organization for infrastructural projects in The Netherlands, with a responsibility for the design, construction, management, and maintenance of the main civil infrastructure in The Netherlands. As such, Rijkswaterstaat is front-running with implementing GeoRM in all phases of its project management activities in order to contribute to successful project results in terms of budget, planning, quality, safety, and user-friendliness. The GeoRM strategy of this client organization is expected to result into a boost of GeoRM applications by engineering firms and contractors, who work for Rijkswaterstaat. In addition, other important public client organizations in The Netherlands, such as the municipalities of large cities and the organizations that are responsible for flood protection, are already following Rijkswaterstaat in the application of GeoRM in their most complicated projects.

It proved to be essential to formalize GeoRM in the existing project management procedures, in order to be taken seriously and applied within the projects of Rijkswaterstaat. For this reason, the development of the organization-specific GeoRM guideline, which entirely fits in the formal project management procedures, proved to be a necessary step. Developing this guideline resulted in clarifying the required GeoRM steps, the targeted GeoRM results and the available GeoRM tools in the subsequent project phases.

In addition to this organization-specific implementation of the GeoRM method in the

organizational *structure*, it was also necessary to pay attention to the organizational *culture* and the people dimension. Writing GeoRM best practice flyers, as well as specific flyers for project managers and project teams, proved to be valuable for revealing the GeoRM benefits in an explicit way to non-geotechnical professionals. Technical managers, contract managers, and project teams have now specific examples of why and how GeoRM contributes to their own tasks and responsibilities for realizing successful projects, within the inherent limitation of budgets that are funded by public money. In conclusion, the combination of paying attention to methods, organizational structure, organizational culture, and people works, when implementing geotechnical risk management in a large public client organization.

ACKNOWLEDGEMENTS

The authors are grateful to all members of the geotechnical working group within Rijkswaterstaat, as well as to all project managers, technical managers, contract managers and other managers who dare to apply the still rather new concept of GeoRM in their day to day practices.

REFERENCES

Argyris, C. & Schön, D. 1978. *Organizational learning: a theory of action perspective*. Boston: Addison-Wesley.

Bles, T.J., van Staveren, M.Th., Litjens, P.P.T. & Cools, P.M.C.B.M. 2009. Geo risk scan: getting grips on geotechnical risks. In Y. Honjo et al. (eds.), *Geotechnical Risk and Safety; Proc. 2nd Int. Symp., Gifu, 11–12 June 2009*. London: Taylor and Francis.

Cameron, K.S. & Quinn, R.E. 1998. *Diagnosing and Changing Organisational Culture*. Boston: Addison-Wesley.

Cools, P.M.C.B.M. 2011. The geo-impuls programme reduc-ing geotechnical failure in The Netherlands. In N. Vogt et al. (eds.), *Geotechnical Safety and Risk; Proc. 3rd Int. Symp., Munich, 2–3 June 2011*. Karlsruhe: Bundesanstalt fur Wasserbau.

Essex, R.J. 1997. *Geotechnical baseline reports for underground construction*. Danvers: American Society of Civil Engineers.

ISO, 2009. *International organization for standardization 31000:2009 risk management: principles and guidelines.* Geneva: ISO.

Rogers, E.M. 2003. *Diffusion of innovations (5th edition)*. New York: Free Press.

van Staveren, M.Th. 2006. *Uncertainty and ground conditions: a risk management approach.* Oxford: Elsevier.

van Staveren, M.Th. 2009. *Risk, innovation & change: design propositions for implementing risk management in organizations.* Köln: Lambert Academic Publishing.

van Staveren, M.Th. 2013. Geotechnics on the move: guidance for a risk-driven way of working. *Georisk* (accepted).

van Well-Stam, D., Lindenaar, F., van Kinderen, S. & van den Bunt, B.P. 2004. *Project risk management: an essential tool for managing and controlling projects*. London: Kogan Page.

Geotechnical Safety and Risk IV – Zhang et al. (eds)
© 2014 Taylor & Francis Group, London, ISBN 978-1-138-00163-3

Implementing geo risk management in the construction industry

M.Th. van Staveren
VSRM, Breda, The Netherlands

P.P.T. Litjens & P.M.C.B.M. Cools
Rijkswaterstaat, Ministry of Infrastructure and the Environment, The Netherlands

ABSTRACT: Geotechnical Risk Management (GeoRM) aims to contribute to successful infrastructural and other types of construction projects by effectively and cost-efficiently dealing with inherent uncertain ground conditions. GeoRM has been adopted as the leading geotechnical working method by over 200 participants of 40 organizations that participate in the Geo-Impuls geotechnical development program. This is a Dutch industry wide program that aims to strengthen the geotechnical community by substantially reducing geotechnical failures in all types of construction projects. Routinely applying GeoRM in projects requires embedding GeoRM in organizations. This paper presents some of the efforts the Dutch geotechnical community is currently making for implementing geotechnical risk management. The main results of three industry wide work-shops about organizational key conditions for routinely applying GeoRM are presented. Representatives of client organizations, engineering firms, and contractors assessed the presence of these key conditions and identified 36 pragmatic actions for strengthening their organizational GeoRM conditions.

1 INTRODUCTION

1.1 *Why geo-risk management?*

Applying Geo Risk Management (GeoRM) in construction projects becomes more and more a key success factor. It is because GeoRM aims to contribute to successful infrastructural and other types of construction projects.

Successful projects are by definition completed within budget and planning, as well as according to pre-set safety and quality standards. In addition, these projects fulfill the expectations and needs of its end users and other stakeholders. However, still too often unexpected ground conditions or behavior reduce project success or even creates project failure.

1.2 *Geo-Impuls development program*

Geo-Impuls is a Dutch industry-wide geotechnical development program. It aims to strengthen the geotechnical community by substantially reducing geotechnical failures in all types of construction projects. Over 200 geotechnical engineers and managers from some 40 Dutch organizations, including client organizations, contractors, engineering firms, and knowledge institutes, work closely together in this program that runs from 2009 up to 2015 (Cools 2011).

The Geo-Impuls participants embraced geotechnical risk management (GeoRM) as the leading geotechnical working method. The two key objectives of the Geo-Impuls program are (1) a completed GeoRM toolbox, including the process, tools, guidelines, and best-practices, and (2) in total 100 projects that demonstrate appropriate GeoRM application by 2015. This requires embedding GeoRM principles and practices in organizations. Therefore, the implementation of GeoRM in (project) organizations is a key issue in the Geo-Impuls program. The quality of GeoRM application in these projects will be validated by an update of the GeoRiskScan (Bles et al. 2009).

There are three central development themes within the Geo-Impuls program: (1) contracts for dealing with legal issues, (2) geo-engineering for dealing with technical issues, and (3) project communication for paying attention to differences in risk perception by the human factor. For each theme, the by the Dutch geotechnical community considered most important topics are worked out in 12 Working Groups.

Examples of these working groups are risk-based soil investigation planning (contracts theme), guidance for the application of the Observational Method (geo-engineering theme), and a protocol for communicating geotechnical risk to communities (project communication theme). Moreover, international knowledge exchange, education, and training are part of the Geo-Impuls program.

1.3 *Paper set up*

This paper presents some of the efforts the Dutch geotechnical community is currently making for implementing geotechnical risk management in their organizations.

First, the concept of GeoRM will be briefly presented, including its so-called Geo-Principles. The core of this paper consists of presenting the execution and results of three industry-wide GeoRM implementation workshops. These have been executed for the three main players of client organizations, engineering firms, and contractors. In these sessions, the presence of four organizational key conditions for routinely applying GeoRM in the different types organizations were identified, classified, and thoroughly discussed. This resulted in 36 pragmatic actions for strengthening these four organizational key conditions for effective GeoRM.

Finally, the paper will draw the main conclusions and remaining challenges for implementing GeoRM in organizations in the construction industry.

2 GeoRM CONCEPT & PRINCIPLES

2.1 *GeoRM concept*

Before explaining the GeoRM concept, it may be helpful to define the term geotechnical risk. According to ISO31000 (2009), a risk is the effect of uncertainty on realizing objectives. Similarly, a geotechnical risk can be defined as the effect of geotechnical uncertainty on realizing objectives, such as settlements or horizontal deformations within pre-set limits. Geotechnical uncertainty may result from randomness, fuzziness, incompleteness, or simply incorrect geotechnical information (van Staveren 2006). A geotechnical risk has a probability of occurrence, one or more geotechnical causes, and usually a number of different effects when happening, such as damage, cost overruns and delay.

GeoRM is an explicitly structured and well-communicated way of dealing with geotechnical risk. It should be executed in all project phases, in order to achieve project objectives effectively and cost-efficiently. GeoRM is a new name for the GeoQ process for geotechnical risk management (van Staveren 2006). The process of geotechnical risk management is similar to the process of project risk management and involves the same sequence of steps. Therefore, GeoRM fits well in any sort of project risk management. The difference is that GeoRM is a more detailed and in-depth approach of project risk management, for giving geotechnical risk the attention it requires in all phases of engineering and construction projects. Figure 1 presents the six cyclic GeoRM steps.

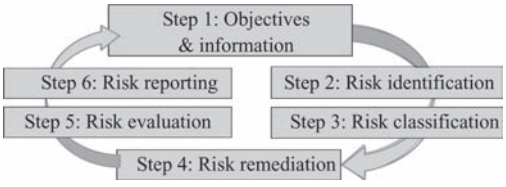

Figure 1. The GeoRM process in six cyclic steps.

2.2 *GeoRM principles*

Basically, there are two main routes of doing risk management: *rule-based* and *principle-based*. The rule-based approach is using rules and results into one best way for managing risk. This is not appropriate for GeoRM, because of the large diversity of engineering and construction projects in complexity, size, location, and ground conditions. For this reason the Geo-Impuls takes the principle-based route for allowing fit-for-purpose geotechnical risk management. Based on the eleven generic risk management principles from ISO31000 (2009), eight specific geotechnical or GeoRM principles have been defined by a number representative of Geo-Impuls participants.

By definition, principles are abstract and need a translation into activities. Such a translation can be done for specific projects and even for specific project phases, again in a fit-for-purpose way. By this approach GeoRM is a mean for realizing project objectives, and not an end in itself. Table 1 presents the eight GeoRM interrelated principles and a number of examples of related actions in the format of a simple checklist.

3 GeoRM WORKSHOPS

3.1 *Why GeoRM implementation workshops?*

Managing risk is difficult. Applying risk management is more difficult. Implementing risk management in organizations is the most difficult (van Staveren 2009b). The Geo-Impuls program provides a lot of guidelines and tools for executing GeoRM. However, routine application of these guidelines and tools, in other words its *implementation*, requires serious attention. Experiences, as well as research, teaches that this is not a spontaneous process in many (project) organizations (van Staveren 2009b). For this reason, the implementation of GeoRM within the organizations and projects of the Geo-Impuls participants started already during the program, parallel to the development of guidelines and tools. The Geo-Impuls implementation target is to apply GeoRM in 100 Dutch projects by 2015.

Table 1. GeoRM principles in a checklist format.

No.	GeoRM principles	Examples of GeoRM actions	Done	
			Yes	No
1	Generate and protect value	Make all geotechnical risks in each project phase explicit, including risk effects and risk remediation measures		
2	Participate in decision making in all project phases	Make a geotechnical risk file from the start of the project and use it for decision making		
3	Make geotechnical uncertainty explicit	Include geotechnical sensitivity analyses with margins in project reports		
4	Work systematically, structured, and in time	Include GeoRM explicitly in the project planning and reserve resources for it		
5	Use all available information	Work from a general level to a detailed level, from using geological maps to geotechnical monitoring		
6	Work transparently together with all stakeholders	Indicate and communicate any dependencies of geotechnics with other disciplines in the project		
7	Include the role of the human factor	Make differences in organizational culture of all involved project parties visible and feasible		
8	Use experiences and lessons for continuous improvement	Use all available and relevant project evaluations, risk checklists, and experiences from professionals		

A first series of three workshops focussed on the application of GeoRM in three large Dutch tunnelling projects in different phases: one in the development phase, one in the design phase and one in the construction phase. These workshops resulted in fine-tuning of the Geo-Impuls activities within the themes contracts, geo-engineering and project communication. The next year, a second series of workshops were executed with a focus on the implementation of GeoRM in the participating client organizations, engineering firms and knowledge institutes, as well as contractors. This second series of workshops are presented in more detail in this paper.

3.2 *Workshop objective and participants*

The objective of the three workshops was to identify what should be done in the organizations of the Geo-Impuls participants in order to shape the right organizational conditions for implementing the GeoRM way of working in their organizations.

The participants consisted of geotechnical engineers and (project) managers who are working for client organizations, engineering firms and knowledge institutes, as well as contractors. In total over 40 persons of more than 20 different organizations participated in the three workshops. In order to learn as much as possible from organizations with more or less the same role in projects, these workshops were held separately for the client organizations, the engineering firms together with the knowledge institutes, and the contractors.

3.3 *Workshop execution*

The three workshops were held in the LEF Future Centre of Rijkswaterstaat. This is a special accommodation for working with groups that want to change their routines. Implementing GeoRM in (project) organizations requires some sort of organizational and individual change, because dealing with inherent geotechnical uncertainties becomes well-structured and well-communicated in an explicit way.

The interactive workshop program of one morning or afternoon each consisted of three parts. The *first* part consisted of an introduction, in which the participants indicated their own degree of GeoRM implementation. Also, the core definitions of geotechnical risk and its management were shared, to work on a shared language of risk management. The *second* part was a quick audit, in which the participants assessed the degree of presence of four key conditions for GeoRM implementation in their organizations. During the *third* part of the workshop, the participants defined and discussed their most appropriate individual actions that were based on the assessed degree of presence of the key conditions. In other words, what should they do by themselves, within their (project)organizations, in order to realize quick wins with regards to GeoRM implementation?

4 GeoRM WORKSHOP RESULTS

4.1 *GeoRM positioning*

During the first part of the workshop the participants should indicated their own degree of GeoRM

implementation. They were literally asked to take their position on a line of one to ten. The number one position indicated no GeoRM implementation at all, while the ten number ten position indicated perfectly implemented GeoRM within the activities of the particular workshop participant.

This exercise provided a wide array of different GeoRM implementation positions. The participants of the client organizations took positions ranging from 2,5 to 8. The positions of the participants of engineering firms and knowledge institutes varied between 3,5 and 8,5, while the positions of the contractors ranged from 4 to 8.

It became paramount that the degree of GeoRM implementation is still highly dependent on the persons involved. Even within the same organization, different persons took sometimes entirely different positions with regard to the degree of GeoRM implementation. This situation indicated that GeoRM was not yet implemented in the entire (project)organization, but at best in a number of parts of the organization.

During the discussion that followed a number of points of attention were raised for implementing GeoRM more widely in organizations. These included making the benefits of applying GeoRM clear (expressed in terms of quality, positive financial effects, stronger professional reputation), developing a shared risk management language, rewarding the application of GeoRM, relating risks to expectations, communicating geotechnical risks effectively to clients and their clients (who do not always want to hear about risk), persisting as geotechnical engineers in making geotechnical risk and their potential effects explicit, acknowledging the inherent subjective role of the human factor in risk assessments, and finally considering also the positive side of uncertainty, being opportunities with favourable effects on project results.

4.2 *GeoRM conditions*

During the second part of the workshop the participants completed a quick audit on the presence of four key conditions for GeoRM implementation in their organizations. These key conditions, which are derived from van Staveren (2009b), include (1) an uniform and shared understanding of GeoRM within the entire (project) organization, (2) an inter-disciplinary application of GeoRM (such as involving contracts and planning departments in GeoRM), (3) a formally embedded GeoRM in the working procedures of the organization, and (4) a GeoRM cooperation with external parties, including project stakeholders, subcontractors, suppliers, and so on. The results of the audit on the presence of these four key conditions are presented in Table 2.

From Table 2 a few remarkable observations can be made. Key condition number 1, a uniform and shared GeoRM understanding, seems present for some 25% to 75% in all of the three types of organization.

With regard to key condition number 2 about the inter-disciplinary application of GeoRM, there is considerable variation within the client organizations and between the contractors and the clients, engineering firms and knowledge institutes. The contractors showing almost no inter-disciplinary GeoRM application (assessment of 0% to 25%) explained the score by stating that in their organizations there is no cooperation between geotechnical engineering and other disciplines with regard to explicitly applied geotechnical risk management.

Table 2. Results of quick scan on GeoRM key conditions.

	Assessment of degree of presence			
GeoRM key conditions	0–25%	25–50%	50–75%	75–100%
1. There is uniform & shared GeoRM understanding		Cl EK Co	Cl EK Co	
2. There is interdisciplinary GeoRM application	Cl Co	Cl EK	Cl EK	Co
3. GeoRM is formally embedded in working procedures	Cl EK	EK Co	Co	
4. GeoRM is cooperated with external party involvement	EK Co	Cl	Cl EK Co	

Legend:
Cl: Client Organisation
EK: Engineering forms & Knowledge institutes
Co: Contractors.

The contractors have already a reasonable degree of formally embedded GeoRM in their work procedures, as expressed by their assessment of key condition number 3. The client organizations not yet started with it, similar to the engineering firms and knowledge institutes.

Finally, regarding the cooperation of GeoRM with external parties, the client organisations are front-running, as do part of the engineering firms, knowledge institutes and contractors. In addition, some of these latter organizations nearly did not cooperate at all with external parties, when applying GeoRM.

In conclusion, a number of the participating organisations, either clients, engineering firms, knowledge institutes or contractors, have already some of the GeoRM key conditions present to a considerable degree. Nevertheless, for all of the participating organizations there is still some, or even a lot, of opportunity to increase the level of presence of key conditions, which will support the GeoRM implementation in their organizations. Therefore, the next task during the workshop was to identify and discuss appropriate actions for increasing the degree of presence of the GeoRM key conditions.

4.3 *GeoRM actions*

During the third and final part of the workshops each participant identified at least one individual and pragmatic action for increasing the degree of presence of one of the GeoRM key conditions. Obviously, key conditions with a relatively low degree of presence should be prioritized.

The participants wrote their action(s) on a postcard, which they received three weeks later as a kind reminder of taking action. In total 36 pragmatic actions were identified and discussed. These actions are summarized, slightly adapted when required for clarification purposes, and presented in Table 3 up to and including Table 6. In total 17 actions for establishing or strengthening key condition number 1 about the uniform shared GeoRM understanding are presented in Table 3.

In total 5 actions for establishing or strengthening key condition number 2 about the inter-disciplinary application of GeoRM are presented in Table 4.

Table 3. Actions for establishing key condition number 1.

No.	Action
1	Apply GeoRM in a uniform way.
2	Explicitly mentioning geotechnical risks during project management meetings.
3	Include geotechnical risk in project presentations.
4	Communicate geotechnical risk in the terminology of lawyers and non-technical decisions makers.
5	Share GeoRM knowledge and experiences in the entire organization.
6	Take a strong position as a geotechnical engineer in the project team in order to take care of GeoRM.
7	Make project team members and colleagues aware of the GeoRM need by organizing internal workshops.
8	Establish checklists with geotechnical risks.
9	Integrate GeoRM in the education program of structural engineers.
10	Integrate GeoRM in internal project management courses.
11	Stimulate GeoRM thinking and acting within your department.
12	Put GeoRM on the agenda of strategy meetings.
13	Invite external GeoRM experts for sharing their knowledge in the organisation.
14	Develop GeoRM best practices that show the GeoRM successes and use these best practices.
15	Draw attention to effective attitude and behaviour when applying GeoRM.
16	Explain differences in applying GeoRM for different types and scopes of projects.
17	Stimulate learning about GeoRM by reading GeoRM books and papers.

Table 4. Actions for establishing key condition number 2.

No.	Action
1	Give specific attention to geotechnical risks during project risk management sessions.
2	Organize internal and interdisciplinary GeoRM workshops for a number of projects.
3	Demonstrate to the internal organization how to apply interdisciplinary GeoRM, including its benefits.
4	Make geotechnical risks, including its inter-disciplinary remediation actions, explicit in the project risk registers.
5	Provide internal checklists for geotechnical risks that demonstrate their inter-disciplinary character.

In total 10 actions for establishing or strengthening key condition number 3 about formally embedding GeoRM in work procedures are presented in Table 5.

Finally, in total 4 actions for establishing or strengthening key condition number 4 about the coordinating GeoRM with the external project environment and stakeholders are presented in Table 6.

Together, all these individual actions demonstrate how geotechnical engineers and (project) managers are able to give their own appropriate attention to implementing GeoRM in their organisations. On the one hand, participants representing client organizations, as well as engineering firms and knowledge institutes, dedicated their actions in particular to developing an uniform and shared GeoRM understanding and to formally embedding GeoRM in work procedures. On the other hand, the contractors focussed their actions on increasing internal and external cooperation during the application of GeoRM.

4.4 *Examples of GeoRM implementation*

As initiator of the GeoImpuls program, Rijkswaterstaat is very serious about implementing GeoRM in its own organization (van Staveren et al. 2013). Parallel to embedding GeoRM in existing work procedures, Rijkswaterstaat used several tools within different types of projects. This resulted in successful examples of GeoRM implementation, as presented in Table 7.

Table 7 shows also the main GeoRM key conditions that were realized within these projects. Using the GeoRM tools proved to be helpful for the geotechnical engineer to communicate the impact of subsoil risk in terms of money and time effects, as well as reputation consequences.

Therefore, geotechnical risks became a specific topic of interest for the project management team members. This resulted in dedicated risk control activities, such as gathering missing subsoil information linked to geotechnical risks, specific

Table 5. Actions for establishing key condition number 3.

No.	Action
1	Apply internal lobby activities in the organization for getting GeoRM embedded in existing processes.
2	Include geotechnical engineering with GeoRM in primary process descriptions.
3	Provide a clear internal protocol for applying GeoRM.
4	Include the GeoRM process in the formal quality management protocol.
5	Formally embed GeoRM in the geotechnical department.
6	Consider together with the geotechnical consultancy team how to formalize GeoRM in projects.
7	Formally apply the relevant GeoRM tools in projects.
8	Design and apply formal GeoRM reporting structures.
9	Organize formal sessions about the GeoRM embedment in the organization.
10	Develop a formal scan for deriving the top 3 geotechnical risks in each project.

Table 6. Actions for establishing key condition number 4.

No.	Action
1	Make non-technical decision makers enthusiastic by presenting the specific GeoRM benefits for them.
2	Identify geotechnical risks with the entire project environment and stakeholders at the start of the project.
3	Integrate geotechnical risks systematically and explicitly in contract between project parties.
4	Show to the project environment and stakeholders the need for and specific benefits of GeoRM.

Table 7. Examples of GeoRM implementation in projects.

Type of project	Type of GeoRM tool applied	GeoRM key condition
Waterway	GeoRiskScan Third Party Expertise	1, 4
Motorway	Risk-based soil investigation	1, 3
Bridge construction	Geotechnical baseline report	1, 2
Tunnelling	GeoRM Communication protocol	1, 4

contractual statements for managing these risks, early requests of necessary licences for groundwater extraction, and strategies for communicating geotechnical complexity to local residents who live near the project.

The projects mentioned in Table 6 are now used as Best Practices within Rijkswaterstaat. In this way, these projects help in further formalising and applying GeoRM within this major client organization.

5 CONCLUSIONS

The three Dutch and industry-wide workshops, as presented in this paper, demonstrate that the *status* of GeoRM implementation, as well as the ways to *increase* the degree of GeoRM implementation, is rather organization specific. Between and within organizations, quite different degrees of GeoRM implementation emerged by applying the quick scan on the degree GeoRM key conditions presence. Obviously, similar types of workshop can be easily organized in other countries with similar programs for reducing geotechnical failure, or within individual companies for strengthening their GeoRM implementation capabilities and effects.

The results and examples in this paper demonstrate that a lot of pragmatic actions for embedding GeoRM are readily available. Therefore, it is simply up the responsible engineers and managers to apply the quick scan for assessing the degree of presence of GeoRM key conditions in their organizations, and to select and apply suitable actions for strengthening any yet underdeveloped key conditions. By doing so, considerable steps can be made with implementing GeoRM in client organizations, engineering firms, knowledge institutes, and contractors. These organizations all have their stake in realizing successful construction projects, against reasonable costs.

ACKNOWLEDGEMENTS

The authors would like thank all participants of the Geo-Impuls workshops for sharing their precious insights and experiences with GeoRM.

REFERENCES

Bles, T.J., van Staveren, M.Th., Litjens, P.P.T. & Cools, P.M.C.B.M. 2009. Geo risk scan: getting grips on geotechnical risks. In Y. Honjo et al. (eds.), *Geotechnical Risk and Safety; Proc. 2nd Int. Symp., Gifu, 11–12 June 2009*. London: Taylor and Francis.

Cools, P.M.C.B.M. 2011. The Geo-impuls programme reducing geotechnical failure in The Netherlands. In N. Vogt et al. (eds.), *Geotechnical Safety and Risk; Proc. 3rd Int. Symp., Munich, 2–3 June 2011*. Karlsruhe: Bundesanstalt fur Wasserbau.

ISO 2009. International organization for standardization 31000:2009 risk management—principles and guidelines. Geneva: ISO.

van Staveren, M.Th. 2006. *Uncertainty and ground conditions: a risk management approach.* Elsevier, Oxford.

van Staveren, M.Th. 2009a. Extending to geotechnical risk management. *Georisk* 3(3): 174–183.

van Staveren, M.Th. 2009b. *Risk, innovation & change: design propositions for implementing risk management in organizations.* Köln: Lambert Academic Publishing.

van Staveren, M.Th., Litjens, P.P.T. & Heerema, J.J. 2013. Implementing geo risk management in a client organization. In *Geotechnical Risk and Safety; Proc. 4th Int. Symp., Hong Kong, 2–4 December 2013* (in press).

This page intentionally left blank

Geotechnical Safety and Risk IV – Zhang et al. (eds)
© 2014 Taylor & Francis Group, London, ISBN 978-1-138-00163-3

The buildup and assessment of environmental indices for storm induced disaster prone areas

M.-H. Wu
Department of Civil and Environmental Engineering, National University of Kaohsiung, Kaohsiung, Taiwan

J.P. Wang
Department of Civil and Environmental Engineering, Hong Kong University of Science and Technology, Hong Kong, China

H.-R. Liao & Y.-R. Chen
Department of Civil and Environmental Engineering, National University of Kaohsiung, Kaohsiung, Taiwan

ABSTRACT: In recent years, global warming has resulted in serious extreme climate events. Natural disasters occur more frequently world widely, and the corresponding impacts are more and more serious, for example of the tragedy of Hsiaolin Village, Kaohsiung due to the impact of Typhoon Morakot in 2009. In this research, the study areas are primarily those who were suffering from typhoon storm-related disasters and are characterized with high disaster potential. A series of field reconnaissance works were conducted in flood and slopeland disaster-prone areas in Kaohsiung city in order to analyze the causative factors of the hazards. There are ninety eight communities and ninety nine villages under investigation for flood and slopeland disaster potential analyses. With the environmental index buildup and assessment, the districts of Shanlin, Namaxia, Meinong, Maolin, Taoyuan and Liugui are categorized as high slopeland disaster-prone districts, and the causative factors are existence of serious landslides and poor vegetated bare slopes. The districts of Yongan, Mituo, Gangshan, Qiaotou, Nanzi, Dashe and Renwu are classified as high flood disaster-prone districts, and the causes are abundant rainfall and poor drainage system. The results obtained from this study will contribute to keep abreast of high disaster-prone areas and to promote the corresponding disaster prevention and preparedness tasks.

1 INTRODUCTION

Natural hazards are threatening events, capable of producing damage to the physical and social space in which they take place not only at the moment of their occurrence, but in the long-term, due to their associated consequences. When these consequences have an impact on society and/or infrastructure, they become natural disasters (Irasema 2002). In average, there are four typhoons per year around the region of Taiwan. They usually bring a huge amount of rainfall that occasionally causes natural hazards such as floods, landslides, and debris flows. In recent years, due to extreme climate condition caused by global warming, there come more frequent natural disasters with aggravating impacts around the world. Disaster reduction becomes an important issue. Disaster reduction strategies include an assessment of vulnerability and risk, as well as assessment of institutional capacities describing an operational framework (ISDR 2004). But vulnerability research, if it is to contribute to wider debates on resilience and adaptation faces significant challenges, in measurement, in handling perceptions of risk, and in governance (Adger 2006). The diversity and apparent lack of convergence over time are, in many ways, a reflection of the divergent objectives of the research and the phenomena being explained (Janssen 2006). A comprehensive theory of vulnerability to global change therefore needs to account for a range of risks, thresholds and institutional responses and resources, given that vulnerability will manifest itself differently at different scales (Kasperson & Kasperson 2001).

The City of Kaohsiung in Taiwan suffered serious typhoon induced disasters in 2009 and 2010, including Typhoon Morakot in 2009 causing a massive landslide burying a village and killing most villagers as many as 474 people. As a result, more attention is placed on the environmental vulnerability of 38 individual districts of the city.

Figure 1. Flow chart of study procedure.

The assessment of vulnerability essentially includes the characteristics of critical facilities, social and economic infrastructure, the use of effective early warning systems, and the application of scientific, technical, and other skilled abilities (UNDP 2004). To develop environmental index assessment, we carry out an investigation for environmental characteristics in this research. Vulnerability has two elements: exposure and susceptibility (ADPC 2006). Exposure is the nature and degree to which a system experiences environmental or socio-political stress (Adger 2006). The characteristics of these stresses include their magnitude, frequency, duration and areal extent of the hazard (Burton 1993). Susceptibility takes into account those social, economic, political, psychological and environmental variables that work together in producing susceptible impacts amongst people within the same exposure (DFID 2004).

This study investigated the hazard prone areas including those with frequent disaster history or those with high disaster potential in the near future, in order to understand the spatial distribution and causative factors of the storm induced disasters. A series of reconnaissance works were conducted in the sites with typhoon induced flooding and slopeland disaster history. The information was collected and integrated to build up the disaster database, so as to facilitate the pre-warning analysis and interpretation of emergency response operations during typhoon events. Moreover, not only qualitative but also quantitative analyses were carried out the assessment of environmental indices. The study's procedure is shown in Figure 1. With the analyses, it is more efficient to establish the assessment method and to master the risks of villages for the use of foundation of emergency response strategies.

2 FLOODING & SLOPELAND DISASTER PRONE AREA INVESTIGATIONS

The flooding and slopeland disaster-prone area investigations were mainly conducted with field reconnaissance and literature review. As for flooding prone site investigations, the team went to the field and surveyed flood attributes at the site including elevations, flood heights, and the factors such as if the site is close to water ways or reservoirs,

Table 1. Survey form of flooding prone sites.

2012 Reconnaissance for Environmental Indices of Flood Prone Area		
City :	District :	Village :
Description of the scope of flood prone areas (Address, Road, Building, etc) :		
River Basin :	Drainage System :	
Reconnaissance Date :	Investigator(s) :	

Flood History in Five Years			
Flood Event & Year	Flooding Duration (hours)	Average Flood Depth (meters)	Maximum Flood Depth (meters)
Event 1 :			
Event 2 :			
Event 3 :			
Event 4 :			
Event 5 :			

Flood Inducing Factors : (Multiple Choice)

☐ Excessive Rainfall ☐ Seawater Intrusion ☐ Reservoir Spillway ☐ Poor Drainage
☐ Pumping Station Failure ☐ Ground Subsidence ☐ Pumping Delay
☐ Upstream Overdevelopment ☐ Stream Overflow ☐ Dike Breaching
☐ Dike Construction Gap ☐ Watergate Open ☐ Stream Silting ☐ River Blocking
☐ Embankment Effect ☐ Road construction ☐ Earthquakes ☐ Landslides
☐ Lack of Remediation ☐ Debris Flows ☐ Others ( )

Flooding Environmental Characteristics and Disaster Potential of Flooding			
Assessment Items	Yes	No	Description
1. Lowland or Ground Subsidence Area			
2. Near rivers, drainage system or coast			
3. Stream Silting or River Blocking			
4. Downstream of Reservoir Spillway			
5. Dike Construction Gap			
6. Flood Prevention Plan Delineation Area			
7. Approved Flood Prone Area			
8. Flood Potential Zone			
9. Lack of Water Conservancy Facilities			
10. Others			

Table 2. Survey form of slopeland disaster prone sites.

2012 Reconnaissance for Environmental Indices of Slopeland Disaster Prone Area

Site	City	District	Village
Name of Cluster			
Cluster Scale	☐ Under 20 household ☐ 20~40 households ☐ 40~60 households ☐ Over 60 household		
Coordinate(TW97)	X :	Y :	
Date			
Investigators			

1. Disaster Potential nearby Cluster :

Situ Type	Yes	No	Remark
1. Slopeland			
2. River Terrace			
3. Stream Valley (including Alluvial Fan)			
4. Potential Debris Flows Creek			
5. Dip-Slope			
6. Debris Slide			
7. Rock Slide			
8. Rock Fall			
9. Slope Gradient .> 30 degrees			
10. Seismic Faulting Zone			

2. Assessment of Disaster Characteristics nearby Cluster

Assessment Item	Existence		Description
	Yes	No	
Disaster History			
1. Serious Landslide			
2. Strata Slide			
3. Occurrence of Debris Flow			
Slopeland Disaster Characteristics			
4. Slope Face Seepage			
5. Crack of Slope Surface			
6. Building Foundation Subsidence			
7. Crack of Retaining Wall			
8. Poor Vegetation			
9. Cluster nearby Dangerous Slope			
10. Headwater Erosion			
11. Riverbank Erosion			
Traffic Conditions			
12. Frequent Observation of Crack on Access Road and Rock Fall on Up Slope			
13. No Substitute Access Road			

and if there are draining facilities around the site. Slopeland disaster attribute includes geological conditions such as if the site on the dip-slope or seismic fault zone, and geographical conditions such as if the site is on the stream terrace and the slope gradient. Moreover, some observed characteristics such as slope seepage, crack of retaining wall, and poor vegetation were reported. In this study, 99 villages of the 30 districts and 96 clusters within 7 districts of Kaohsiung City were selected for site investigations of flooding and slopeland prone areas, respectively. The surveying forms are shown in Tables 1 and 2.

3 DATA CLASSIFICATION AND STATISTICAL ANALYSIS

3.1 *Data classification*

In this study, the environmental assessment indices (factors) are divided into categories of exposure, environmental sensitivity and disaster prevention measures, as shown in Figure 2.

3.2 *Statistical analysis*

According to the aforementioned classification, each factor is given up to 1 point, and the score for each cluster or village would be calculated by summarized the total factors (points) applied to them, namely the environmental score. Through the analysis of each cluster's (village's) environmental score, the levels as well as the corresponding environmental indices are established for flooding and slopeland disaster prone clusters or villages. The levels included high vulnerability, medium vulnerability and insensitivity.

In terms of district vulnerability, the district hazard environmental score is obtained by the following equation:

$$\text{District environment score} = \frac{\text{Number}_{HVV} \times 4 + \text{Number}_{MVV} \times 3 + \text{Number}_{IV} \times 1}{\text{Number}_{RVD}} \quad (1)$$

where HVV = high vulnerability villages, MVV = medium vulnerability villages, IV = insensitive villages and RVD = reconnaissance villages in the district. Through the calculation of the equation, the levels as well as the corresponding environmental indices are established for flooding and slopeland disaster prone districts. The classification of district vulnerability is as follows: ≦3 points for medium vulnerability and >3 points for high vulnerability.

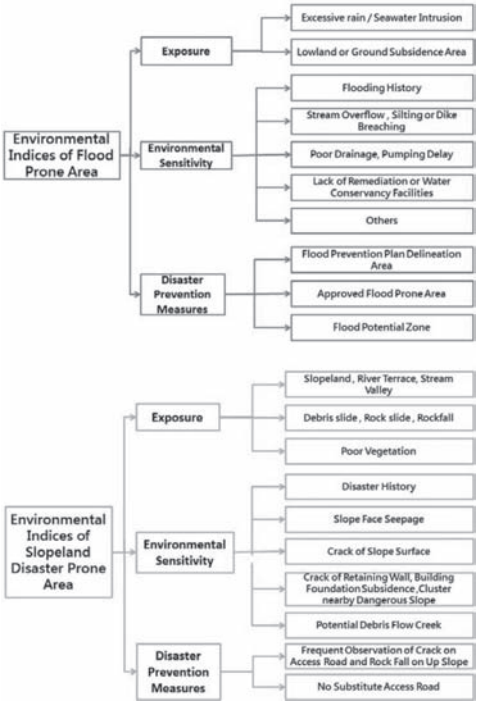

Figure 2. Classification of environmental indices.

4 RECONNAISSANCE AND ANALYSIS RESULT

In recent five years, Typhoon Morakot in 2009 and Typhoon Fanapi 2010 are two principal events inducing serious flooding and slopeland disasters. Typhoon Morakot, which coupled with Southwest Monsoon, in total brought a rainfall of 2792 mm in four days, about 150% of the annual rainfall in Kaohsiung. The disasters resulted in serious landslides and debris flows in mountainous districts, killing 523 people, 17 people missing (Ministry of the Interior); Typhoon Fanapi brought a rainfall of 321 mm in Kaohsiung within 3 hours, resulting in serious flooding in plain areas, and railway or highway traffic tie-up.

This study investigated the areas with disaster history within the two principal typhoon events, along with referencing to the scope of "2010 Kaohsiung City Preservation Plan of Flooding Hazard Potential Areas" and "2010 Investigation and Analysis of Vulnerability Factors for Kaohsiung City Disaster-Prone Area". The sites under investigation and analysis are shown in Figure 3.

This study categorized the environmental indices (factors) into three groups, which are exposure, environmental sensitivity and disaster prevention

Figure 3. Distribution of reconnaissance sites.

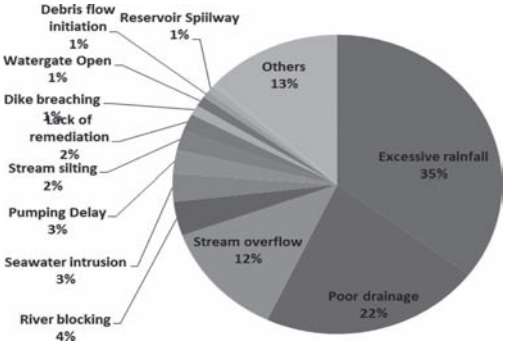

Figure 4. Statistical chart of flood inducing factors.

measures. According to the reconnaissance report, each site would be given a score from summarizing the points of its environmental factors. Based on analysis of the scores, the environmental indices for regional (village and district levels) were determined.

4.1 *Flooding reconnaissance result*

The analysis shows that the main reason for flooding disaster in Kaohsiung should be the excessive rainfall, followed by poor drainage and river embankment overflow, as shown in Figure 4.

The survey also found that among the past flooding events, the primary environmental characteristics of flooding areas are near rivers, drainage systems or coast (75%), followed by lowland or ground subsidence area (70%), as shown in Figure 5.

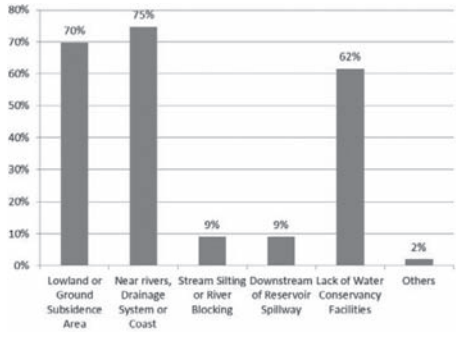

Figure 5. The variation of environmental characteristics of flood hazard areas.

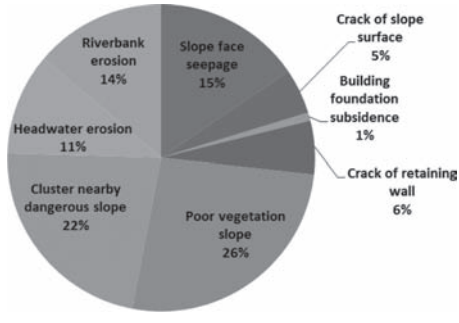

Figure 6. Statistical chart of slopeland disaster inducing factors.

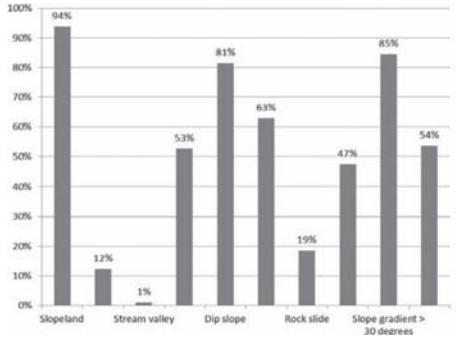

Figure 7. The variation of environmental characteristics of slopeland hazard areas.

4.2 *Slopeland reconnaissance result*

Among the 96 clusters under reconnaissance in this study, 71% of those have landslides nearby, and 64% have suffered debris flow disasters. The statistical analysis of disaster inducing factors is shown in Figure 6. Poor vegetation and cluster close to

Table 3. Village flooding indices grading form.

District	Village	Excessive rainfall, seawater intrusion, reservoir spillway	Lowland or ground subsidence	Flooding history	Stream overflow, silting or blocking	Poor drainage, pumping dalay	Lack of remediation or water conservancy facility	Others	Flood prevention plan area	Approved flood prone area	Flood potential zone	Total score
Yong An	Sin Gang	1	1	1	0	1	0	1	1	1	1	8
	Wei Sin	1	1	1	0	1	1	1	1	1	1	9
Mituo	Tadi	1	1	1	0	1	1	1	0	1	1	8
	Jiugang	1	1	1	0	1	0	1	1	1	1	8

dangerous slope are the main features. Besides, the study also reported that all of the mountainous clusters have no substitute access roads, which means once the main roads are interrupted, the clusters would be isolated.

The statistical analysis for geographical features of slope hazard prone areas showed that 81% of the sites have more than one sensitive geological characteristic, for example of dip slope, rockfall, debris slides and rock slides, and 53% of the sites nearby potential debris flow creeks, shown in Figure 7.

4.3 *Flooding indices assessment result*

In recent five years, the flooding disasters which resulted in live and property loss in the villages were primarily in Morakot and Fanapi typhoon events in 2009 and 2010, respectively. Observed from the analysis, the minimum score of these villages with flooding depth below 0.5 meters is 4.0, and the mean is 6.8. Therefore, the village flooding disaster

Table 4. District flooding vulnerability assessment.

District	District environmental score	Vulnerability
Yong An	4	High
Mi Tuo	4	
Gang Shan	4	
Hu Nei	4	
Yan Chao	4	
Lu Jhu	4	
A Lian	4	
Da She	4	
Ren Wu	4	
Cian Jin	4	
Cian Jhen	4	
San Min	4	
Ling Ya	4	
Mei Nong	4	
Zih Guan	4	
Nan Zih	3.9	
Ciao Tou	3.8	
Da Shu	3.8	
Cie Ding	3.7	
Niao Song	3.5	
Tian Liao	3.3	
Da Liao	3.3	
Fong Shan	3.3	
Ci Shan	3.2	
Gu Shan	3	Medium
Ci Jin	3	
Liou Guei	3	
Sin Sing	3	
Zuo Ying	2.8	
Yan Cheng	2.5	

Table 5. Village slopeland indices grading form.

District	Village	No. of households	Slopeland, stream terrace or valley	Debris slide, rock slide, rockfall	Disaster history	Slope seepage	Slope surface crack	Building foundation subsidence, retaining wall crack, near dangerous slope	Poor vegetation	Potential debris flow creek, dip slope	No subsitute access road	Total score
Shan Lin	Ji Lai	0.2	1.0	1.0	1.0	0.0	0.0	1.0	0.0	1.0	1.0	6.2
Na Ma Sia	Maya	1.0	1.0	1.0	1.0	1.0	1.0	1.0	1.0	1.0	1.0	10
Mei Nong	Guanglin	0.2	1.0	1.0	1.0	0.0	1.0	0.0	1.0	1.0	1.0	7.2

Table 6. District slopeland vulnerability assessment.

District	District environmental score	Rank
Na Ma Sia	4	High
Mei Nong	4	
Mao Lin	4	
Tao Yuan	3.8	
Shan Lin	3.6	
Jia Sian	3.1	
Liou Guei	3.1	

prone classification is determined as follows: less than 3.0, 3.1~6.9 and 7.0~10 represent insensitivity, medium vulnerability, and high vulnerability, respectively. The grading method is sorting the factors into 10 items, and allocating 1 point to each item, as shown in Table 3. The village vulnerability assessment was completed. Moreover, in terms of district vulnerability, through the Equation (1), it was found that 84% of the 30 districts with flooding history in Kaohsiung were categorized as high vulnerability, and 16% of them were classified as medium vulnerability, as shown in Table 4.

4.4 *Slopeland indices assessment result*

After analysis, it is observed that the minimum score of the reconnaissance clusters is 3.7, and the mean score is 7.0. Therefore, the village slopeland disaster prone classification is determined as follows: less than 3.6, 3.7~6.9 and 7.0~10 represent insensitivity, medium vulnerability, and high vulnerability, respectively. The grading method is grouping the factors into 10 items, and allocating 1 point to each item, as shown in Table 5. The village vulnerability assessment was completed. Moreover, in terms of district vulnerability, through the Equation (1), it was found that all of the 7 districts with slopeland disaster history in Kaohsiung were categorized as high vulnerability, as shown in Table 6.

5 CONCLUSIONS

In recent five years, Typhoon Morakot in 2009 and Typhoon Fanapi 2010 are two principal events inducing serious flooding and slopeland disasters in Kaohsiung City. In this study, a series of reconnaissance works were conducted on the investigation of 99 villages with flooding disaster history and 96 clusters with slopeland disaster history in Kaohsiung within five years. From the observation

of the result, the primary inducing factors for flooding disaster are excessive rainfall (97%), poor drainage system (60%) and stream overflow (34%). As far as geographical characteristics are concerned, 75% of flooding villages are located in lowland areas, and 75% of them are close to river. The environmental indices assessment shows that among the investigated villages, 68% of them are classified as high vulnerability and 28% as medium vulnerability. With regard to the 30 districts with flooding disaster history, 80% of them are categorized as high vulnerability and 20% as medium vulnerability. The study also reports that all of the 96 clusters under slopeland hazard investigation have no substitute access road, which would encounter threat of isolation in slopeland disasters. Among them, 66% are located close to poor-vegetated slopeland, and all of the seven districts are classified with high vulnerability.

The results obtained from this study will provide the reference of high disaster-prone areas in Kaohsiung City, and contribute to disaster prevention and preparedness tasks.

ACKNOWLEDGEMENTS

This study was possible through the "2012 Kaohsiung City Disaster-Prone Areas Environmental Reconnaissance & Assessment" sponsored by National Science and Technology Center for Disaster Reduction (NCDR). Special thanks to Dr. Chih—Hsin Chang in NCDR.

REFERENCES

Adger, W.N. 2006. Vulnerability. *Global Environmental Change* 16: 268–28.

ADPC (Asian Disaster Preparedness Center), 2006. *Critical guidelines: community-based disaster risk management*. Bankok: Asian Disaster Preparedness Center.

Burton, I., Kates, R.W. & White, G.F. 1993. *The environment as hazard (second edition)*. New York: Guilford.

DFID (Department for International Development), 2004. *Disaster risk reduction: a development concern*. Norwich: Overseas Development Group, School of Development Studies, University of East Anglia.

Irasema, A.A. 2002. Geomorphology, natural hazards, vulnerability and prevention of natural disasters in developing countries. *Geomorphology* 47: 107–124.

ISDR (International Strategy for Disaster Reduction), 2004. *Living with risk: a global review of disaster reduction initiatives*. Geneva.

Janssen, M.A., Schoon, M.L., Ke, W. & Börner, K. 2006. Scholarly networks on resilience, vulnerability and adaptation within the human dimensions of global environmental change. *Global Environmental Change* 16(3): 240–252.

Kasperson, J.X. & Kasperson, R.E. 2001. G*lobal environmental risk*. London: Earthscan and UNU Press.

Mohammed, S.I., Mohammad S.H.S. & Shamim M.H. 2013. Disaster risk index: How far should it take account of local attributes? *International Journal of Disaster Risk Reduction* 3: 76–87.

UNDP (United Nations Development Programme), 2004. *Reducing disaster risk: a challenge for development, a global report.* New York.

This page intentionally left blank

11 *Geotechnical applications and case studies*

This page intentionally left blank

Geotechnical Safety and Risk IV – Zhang et al. (eds)
© 2014 Taylor & Francis Group, London, ISBN 978-1-138-00163-3

Ultrasound as a new approach for the prediction of collapsible soils

K. Abbeche
Department of Civil Engineering, Laboratory LARHYA, University of Batna, Batna, Algeria

M.S. Laouar Mohamed Salah
Department of Civil Engineering, University of Tebessa, Tebessa, Algeria

ABSTRACT: Collapsible soils types are found in natural unsaturated soils, which are characterized by a metastable structure, and undergo an abrupt collapse when they are flooded (with or without loading), which causes important damages. Based on the structural composition of these soils, samples made up of various proportions of sand and fine particles were reconstituted. The first phase of work consists in the experimental determination of the geotechnical characteristics of these samples. It is thereafter proposed a test program based primarily on the use of the cone penetrometer and the ultrasonic apparatus as the approaches for the prediction of the factors which influence collapse. The results obtained clearly show the influence of certain parameters such as; water content and the energy of compaction on the collapse potential and the ultrasonic speed.

Keywords: collapsible soils, collapse potential, cone penetrometer, ultrasonic speed

1 INTRODUCTION

Collapsible soils are metastable soils of loose open structure, unsaturated nature, being in deposits form. In the dry state, a natural cementing between the grains confers an important inter-granular connection and can support very high loads. However, saturation, even without additional loading, causes the disintegration of the connections giving a denser structure followed by a sudden collapse of the soil particles. Among the causes of saturation there is the raise of the ground water, water infiltration and canalization leaks. Because of the important collapse potentials and serious consequences which can occur in the construction, this type of soil is considered unstable where foundations sit. These soils are primarily localized in the arid and semi arid region. They relate to a significant number of countries in particular those of the northern hemisphere located between the 30th and 55th parallels as well as countries of South America (Abelev 1988). The cycles of prolonged dryness which occurred these last years on several occasions and in several regions of the world modify the parameters governing the behavior of the soil and give rise to new collapsible soils zones. The following are considered as collapsible soils: the alluvial and eolian deposits, flows mud, residual grounds, volcanoes rejections, loesses, and embankments slightly compacted or compacted in the dry slope of the compaction curve.

The collapse of Cheria in Eastern of Algeria which occurred in 2009 constitutes a good example. In the latter, a great collapse was recorded, in which tens of constructions were inserted of more than two meters and half in the ground. While waiting to achieve measurements of the technical expertise, the preliminary report charges this catastrophe to a movement in the ground water. A geotechnical study made by Batna (2000), within the scope of the realization of a natural gas station in Hassi Messaoud shows that the site is composed of two layers of collapsible nature, the adopted solution is substituting the first layer and taking measures to avoid the infiltration of water to the second layer. In addition, degradations of several residence buildings which took place in Biskra (2002) are due to water infiltrations. A building of three floors with Xining, Qinghai, was destroyed beyond repair because of collapse Qian & Lin (1988). This problem occurred because the loess beneath the foundations underwent a structural collapse when it was flooded. Experimental and theoretical studies aiming to understanding the great number of uncertainties implied in the phenomenon of collapse are currently undertaken. The literature revealed that the majority of research was devoted to the collapse mechanisms and the identification methods, of treatment and prediction.

Dudley (1970) qualitatively described that the collapse phenomenon for cemented structures does not depend on dampness, it occurs only when the

cementing connections are broken by mechanical constraints. In revenge, if the ground is a mixture of grains and fine particles which induce important connections due to suction or cementing, dampness lead to the cancellation of suction what decreases cohesion and supports collapse. This result was confirmed by Cui & Magnan (2000), Morgenstern & De Matos (1975) and Ganeshan (1982), who affirmed that the cause of collapse lies in the low water contents. Booth (1975) and Ting (1979) explained that collapse depends on the initial dry density, the void ratio and the degree of saturation. Markin (1969) propose an interval of degree of saturation between 60% and 65% beyond which collapse does not appear any more. The same result is confirmed by Ganeshan (1982), Booth (1977) and Lawton (1989), who observed that for a given dry density the overload which causes collapse is inverse proportion to the natural moisture content of the soil. The destruction of the capillary forces can explain the sudden collapse by flooding the ground. The suctions developed in the clay connections can be different from those developed between the silt grains. Up to our days, there is no means to measure these differences (Fredlund & Rahardjo 1993). The examination of the macroscopic and microscopic aspects of the sudden collapse is recommended (Feda 1994). Abrupt collapse occurs when the dry density and the initial moisture content are low (Cui et al. 1999; Cui et al. 1998). If the relative density is higher than 0.65% and the moisture content is close to the optimum of Proctor there is no risk of collapse (Abbeche et al. 2005). In spite of having a great range of ultrasonic equipment and a large use of this process in various fields, the literature reveals that, except geotechnical marine and some applications, little attention was granted to this technique regarding soil mechanics problems. This experimental work presents the results of three series of tests. In addition to the compression tests, a series of tests using the cone penetrometer and the first time of the original experimental, curves of the non-destructive tests with the ultrasounds are put in parallels, in the objective to propose a predicting method of the collapsible soils based on ultrasonic tests.

2 CHARACTERISTICS OF MATERIALS

The tests were carried out on six reconstructed soils made up of sands and of kaolin in various proportions for which the application of the various criteria of collapse, reported by Ayadat & Bellili (1995), shows that those are collapsible.

Two types of sands lesser than 2 mm of diameter are used for the soils reconstruction; sand of Dunes of Oum Ali region and sand of stream extracted from Melag stream of El Aouinet region washed and dried at 105 °C during 24 hours. In view of the

Table 1. Characteristics of materials.

Materials	Characteristics						
Sand of dunes	Sand equivalent: 73.26% Grain size distribution ranged between 0.08 and 2 mm with 1.36% of particles < 80 μm Coefficient of uniformity: 3.91 Coefficient of curvature: 1.33						
Sand of stream	Sand equivalent: 68.69% Grain size distribution ranged between 0.08 and 2 mm with 3.01% of particles < 80 μm Coefficient of uniformity: 2.19 Coefficient of curvature: 0.94						
Kaolin	% <2 μm 43% Liquid limit: 65.83% Plastic limit: 39.64% Specific density of grains Gs 2.42						
Reconstructed soils	Label	S1	S2	S3	S4	S5	S6
	% Kaolin	15	35	50	20	30	40
	% Sands of dunes	85	65	50	–	–	–
	% Sands of stream	–	–	–	80	70	60
	G_S	2.65	2.59	2.46	2.62	2.56	2.48
	ω_L%	16.47	26.63	35.37	18.47	28.97	33.42
	ω_p%	11.03	5.37	20.87	11.95	14.77	19.03
	γ_{dmax}(g/cm^3)	2.04	1.95	1.84	1.95	1.82	1.75
	ω_{opt}%	8.62	9.43	13.88	12.82	14.67	117.82
	% <2 μm	4.91	1.73	16.74	7.03	9.84	14.12

small percentage of fine particles that they contain, these two types of sands are used for the concretes making. The kaolin used (<80 µm) is extracted from of Hamame Debagh Mine of Guelma region it has white color and is used generally in the manufacture of the fine porcelain, pottery and ceramic products. The soils S1, S2 and S3 are reconstructed with sands of Dunes and kaolin, while the soils S4, S5 and S6 are reconstructed with sands of stream and kaolin. The geotechnical characteristics of sands, kaolin and reconstructed soils are presented in Table 1. The gradation curves of the reconstructed soils are presented in Figures 1 and 2.

2.1 *Characteristics of consistency of the soils*

The literature revealed that a soil is expected to collapse if at least, one of the following criteria is checked (Ayadat & Ouali 1999): $A_C < 1$, $I_L < 0$, $I_P \leq 20$, $I_C > 1$, $I_W \leq 1$.

The results presented in Tables 2, show that these soils are expected to collapse and that the characteristics of consistency of the reconstructed soils depend basically on the initial moisture content.

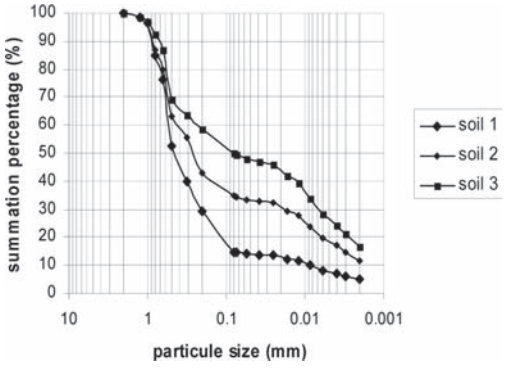

Figure 1. Grains size distribution curves (Soils 1, 2 and 3).

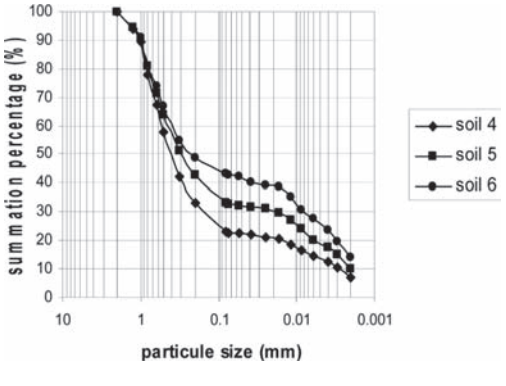

Figure 2. Grains size distribution curves (Soils 4, 5 and 6).

Table 2. Characteristics of consistency of soils.

Soil	W_0	A_C	I_P	I_L	I_C	I_W
Soil 1	2	1.11	5.44	–1.66	2.66	0.37
	4			–1.29	2.29	0.73
	6			–0.92	1.92	1.10
	8			–0.56	1.56	1.47
Soil 2	2	0.96	11.26	–1.19	2.19	0.18
	4			–1.01	2.01	0.35
	6			–0.83	1.83	0.53
	8			–0.65	1.65	0.71
Soil 3	2	0.87	14.5	–1.30	2.30	0.14
	4			–1.16	2.16	0.27
	6			–1.02	2.02	0.41
	8			–0.89	1.89	0.55
Soil 4	2	0.93	6.52	–1.53	2.53	0.31
	4			–1.22	2.22	0.61
	6			–0.91	1.91	0.92
	8			–0.61	1.61	1.23
Soil 5	2	1.44	14.2	–0.90	1.90	0.14
	4			–0.76	1.76	0.28
	6			–0.62	1.62	0.42
	8			–0.48	1.48	0.56
Soil 6	2	1.02	14.39	–1.18	2.18	0.14
	4			–1.04	2.04	0.28
	6			–0.90	1.90	0.42
	8			–0.77	1.77	0.55

3 USED MATERIALS

3.1 *Oedometric tests*

The odometer whose essential elements are:

- Oedometer Mold of 50.4 mm diameter and 20 mm height.
- Frame of consolidation of lever arm of 1/10.
- Set of weights.

The compaction tamper Figure 3 which is conceived especially at the laboratory for the compaction of the soil in the oedometer ring. Entirely manufactured of steel, it is consists of:

- A base of 48.42 mm diameter and 3 mm thickness attached to a column of guidance of 280 mm length, through which a piston slips. A sliding stopper along the rod makes it possible to adjust drop height of the hammer.
- A hammer in circular shape of dish of 84.422 mm diameter and 8.40 mm thickness. Its weight is de121g, having a centered drilling of 8.45 mm diameter.

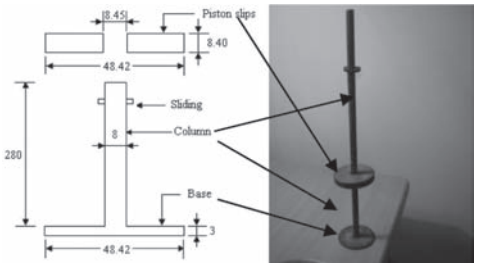

Figure 3. Compaction tamper.

Figure 4. Cone penetrometer.

Figure 5. Ultrasonic analyzer.

3.2 *Penetration tests*

The manual cone penetrometer. Figure 4 is made up of:

- A stainless steel cone, 30 degrees of opening surmounted by a rod. The weight of the mobile system is of 80 g.
- A dial gauge of 36 mm/0.01 mm.
- A metal dish with a diameter of 53 mm and 36.4 mm height. Its mass is about 56.2 g.

3.3 *Ultrasonic tests*

The equipment Figure 5 includes:

- An analyzer for velocity measurement of the ultrasonic waves.
- A calibration bar.
- A set of two transducers of 54 kHz with cables, acting differently as transmitter or receiver.
- Paste pot of contact.

4 TEST PROGRAM

Three series of principal tests were carried out on six reconstructed soils; Table 3 illustrates the program of these tests.

5 TEST PROCEDURE AND REALIZATION

5.1 *Oedometric tests*

The test soil consists of sand and kaolin according to the proportions mentioned above. The soil is brought to the required moisture content by addition of distilled water; the set soil-water must be well homogenized in a porcelain mortar. The mix of soil is then poured in the mold of the odometer then compacted using the compaction tamper.

The compaction of the soil consists in dropping the hammer which slides through the rod of the Tamper from a height H = 15 cm, which will strike the dish that transmits the shock to the specimen. To make it perfectly plane, the higher face of the sample must be leveled using a rigid blade.

The compression tests with the oedometer are made according to Jennings & Knight (1975) procedure which consists to succeeding application of the following loads: 25, 50, 100, and 200 kPa. Then, proceeding to the flood of the sample and recording the new settlement value, afterward increasing the loading up to 400 kPa. During the test the readings of settlement are noted at 15s, 30s, 1 min, 2 min, 5 min, 10 min and 24 h.

5.2 *Penetration tests*

They are achieved with a cone penetrometer provided with a metal dish. The soils reconstruction, the mix filling and the compaction in the dish are carried out in the same manner as for the compression tests. The cone, with its rod, is placed in contact with the upper face of the soil sample. The penetration of the cone in the soil is measured with the dial gauge. The Δh penetrations of the cone are carried forward relating to the selected parameters.

5.3 *Ultrasonic tests*

This series of tests starts with the calibration of the analyzer, by measuring the speed transmission of the wave through the calibration bar. The velocity of an ultrasonic wave train, which crosses soil

Table 3. Tests program.

Test type	Selected parameters	Test #	Observation
Odometric tests	Moisture contents: 2%, 4%, 6% and 8%. Compaction degrees: 10, 25, 40 and 60 blows.	96	Realized according to Jennings and Knight procedure.
Penetration tests	Moisture contents: 2%, 4%, 6%, 8%, 10%, 12% and 14%. Compaction degrees: 10, 25, 40 and 60 blows.	168	Realized with the cone penetrometer.
Ultrasonic tests	Moisture contents: 2%, 4%, 6% and 8%. Compaction degrees: 10, 25, 40 and 60 blows.	96	Led to the ultrasonic analyzer.

specimens, produced in the oedometric mold, is measured, according to the procedure of the compression tests. To ensure a good transmission of the waves in the body of the specimen and before adjusting the system of measurement, thin layers of contact grease to the two faces of the transducers (transmitter and receiver) are applied.

On the screen of the analyzer are represented, the time or the transit speed of the wave, that according to the configuration of the analyzer.

6 TEST RESULTS AND INTERPRETATION

The results of this experimental work are presented in two parts; the first concerns the standard tests (Tables 1 and 2) (characteristics of materials and characteristics of consistency), necessary to the geotechnical identification of used materials and the reconstructed soils. The second is distributed as follows.

6.1 *Oedometric tests*

6.1.1 *Depiction of the collapse of the soil*

The variation of the moisture contents and energies of compaction are made in the purpose to check whether these soils have the properties of collapsible soils. The variation of moisture content and energies of compaction allow controlling the collapse potential. The curves obtained are similar to that of Jennings and Knight (1975).

The Collapse Potential CP (%) is calculated by the relation:

$$CP = \frac{\Delta e_c}{1 + e_0} \times 100\% \quad (1)$$

where:
$\Delta e_c = e_1$ (200 kPa) – e_2 (200 kPa, flooded)
e_0: Initial void ratio

The results of these tests show that the collapse potential CP varies for;

- Soil S1: from 0.52% to 7.54%
- Soil S2: from 0.59% to 8.34%

Table 4. Classification.

CP	Degree of problem
0% to 1%	No risk
1% to 5%	Moderate trouble
5% to 10%	Trouble
10% to 20%	Severe trouble
>20%	Very severe trouble

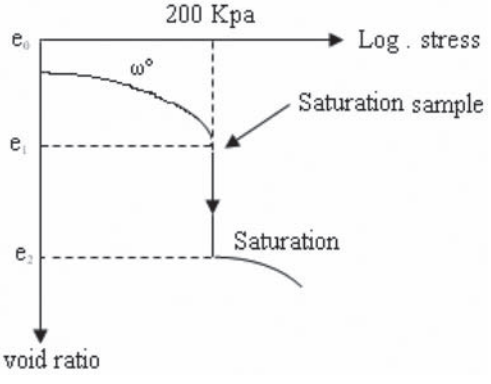

Figure 6. Typical oedometric curve of a collapsing soil (Knight and Jennings, 1975).

- Soil S3: from 0.83% to 8.92%
- Soil S4: from 0.66% to 7.61%
- Soil S5: from 0.74% to 7.84%
- Soil S6: from 0.77% to 7.90%.

According to the classification suggested by Jennings and Knight (1975), (Table 4), these results correspond to the headings going from "No risk" to "Troubles".

6.1.2 *Influence of the water content and the energy of compaction*

The high collapse potentials are noted for low initial moisture contents. For a given initial water contents the collapse potential is decreasing with the increase in the energy of compaction.

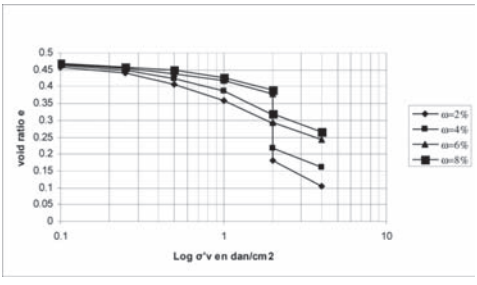

Figure 7. Oedometric curve Soil 1 ($E = 10$ blows).

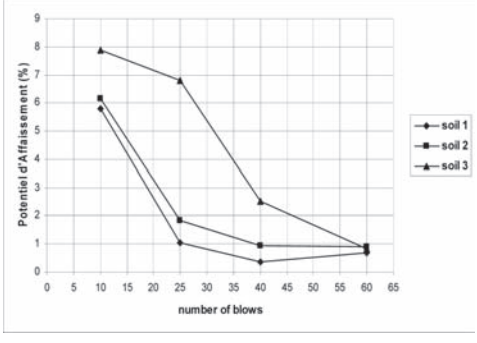

Figure 8. Variation of collapse potential with number of blows ($\omega = 6\%$).

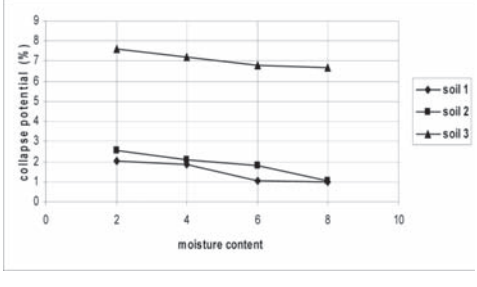

Figure 9. Variation of collapse potential with moisture content ($E = 25$ blows).

The decrease of collapse is more obvious that the moisture content increases. In the same conditions of compactness and moisture content of the soil containing the greatest percentage of kaolin exhibit greatest collapse potential.

These results agree with those of Lawton et al. (1989) and Ayadat et al. (1998) and confirm the observations of Abbeche et al. (2007). One can conclude that the reconstructed soils at the laboratory hold a similar behavior to those met in situ, therefore suitable for the series of tests suggested.

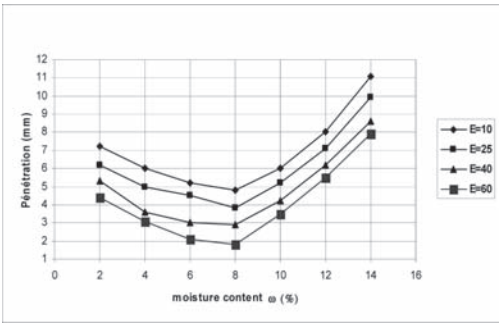

Figure 10. Variation of penetration with moisture (Soil 1).

6.2 *Penetration tests*

6.2.1 *Interpretation of the penetrations versus the initial moisture content ω_0*

The moisture contents between $\omega = 2\%$ and $\omega = 8\%$ do not give a clear idea on the behavior of the studied soils; thus the increase in the water contents is increased up to 14%.

The curves obtained are divided into two slopes Figure 10. In the first, collapse decreases gradually with the increase in the moisture content until a lower limit when the moisture content approaches the Proctor optimum. In the second slope it is noted an opposite behavior in which collapse increases with the growth of the moisture content.

Considering its speed and its convenience compared to the Proctor test, it can be more practical for the compaction projects of the collapsible soils to use the test of the cone penetrometer for the determination of the limit penetration and the corresponding moisture content which divide the penetration curve into two slopes, the first is dry and the second is wet. This is analogue to Proctor test that the optimum separates also the curves into two slopes, dry and wet. A similar performance is noted for all tested soils. One can deduce on collapsible soils, that there is an opposite relationship between the penetration test and the Proctor test, the first being used to determine the limit penetration and the second the maximum dry density.

6.2.2 *Interpretation of the penetrations versus ω_{opt}/ω_0*

Collapsible soils are characterized by the condition $\omega_{opt}/\omega_0 > 1$, (Holtz & Hilf 1961). Analysis of the penetration curves versus the ratio ω_{opt}/ω_0, Figure 11 confirm the existence of two distinct behaviors and separated by the line $\omega_{opt}/\omega_0 = 1$. On the left of this line, the penetration knows a gradual decrease for then growing in a roughly regular way as one moves away from the limit separating the collapsible soils ($\omega_{opt}/\omega_0 > 1$) of the non

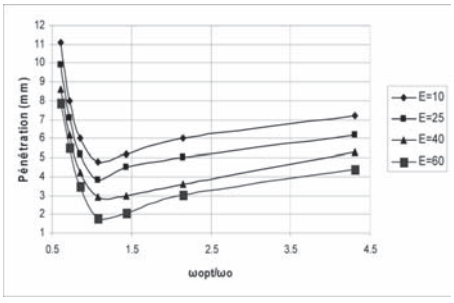

Figure 11. Variation of penetration with ω_{opt}/ω_0 (Soil 1).

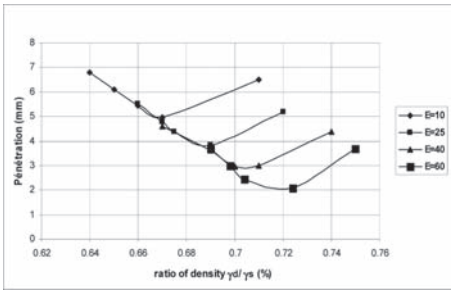

Figure 12. Variation of penetration with γ_d/γ_s (Soil 5).

collapsible soils. This limit corresponds to the limit penetration indicated by P_{lim}.

6.2.3 *Interpretation of the penetrations versus* γ_D/γ_S

The same statement is visualized in the representation of the penetration against the ratio of density γ_d/γ_s, Figure 12. We notice a gradual decrease of the penetration up to a limit value corresponding to the straight line separating the two states from soils for then knowing a phase of progressive increase with the growth of this ratio.

Similarity of previous curves illustrates the existence of a similar behavior of the collapsible soils with respect to the penetration and that a limit characteristic value separates the collapsible soils of the non collapsible soils.

6.3 *Ultrasonic tests*

6.3.1 *Influence of the moisture content and the energy of compaction*

The results of the ultrasonic tests show that ultrasonic speed varies according to variation of the energy of compaction and/or moisture content the Figures 13 and 14. For the same value of the energy of compaction, whatever the soil, the ultrasonic speed is increasing with the growth of the moisture content.

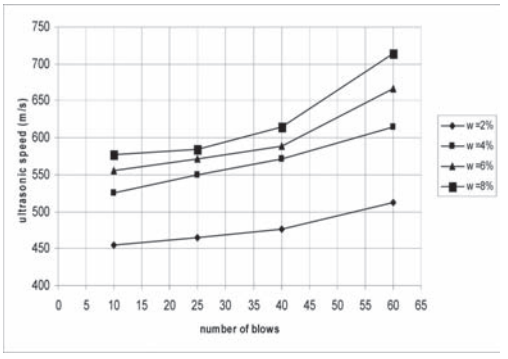

Figure 13. Variation of ultrasonic speed with number of blows (Soil 4).

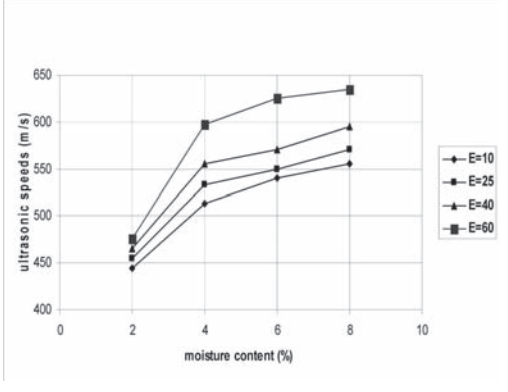

Figure 14. Variation of ultrasonic speed with moisture content (Soil 1).

The growth of compaction contributes to the increase of speeds, especially when the moisture content comes close to the Proctor optimum. Let us note that curves corresponding to 60 blows present more important speed values compared to other energies of compaction, especially with the increase in the moisture contents. This proves a good state of compactness due to the humidification and the rearrangement of the grains; it is the case of non collapsible soils.

6.3.2 *Prediction of collapse by ultrasonic test*

Figures 15 and 16 concretize a vital relationship between ultrasonic speed and potential collapse; the decrease of one is synchronized with the increase of other. In Figure 15, curves have the same shape. They pass by three phases, in the beginning parallel straight lines representing an important fall of the CP with very close speed values. Then, two successive slopes of the curves are noted; in the first, a reduction of the CP corresponds to an increase

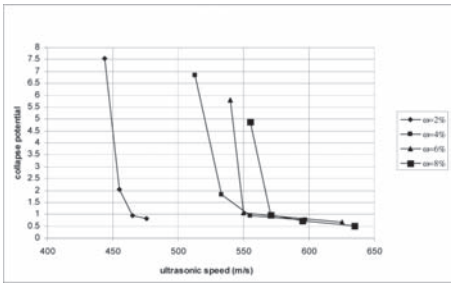

Figure 15. Variation of collapse potential with ultrasonic speed for w% (Soil 1).

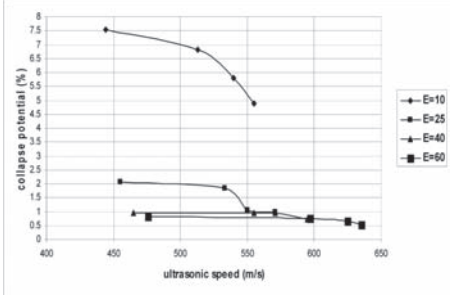

Figure 16. Variation of collapse potential with ultrasonic speed for E (Soil 1).

speeds, in the second, the stabilization of collapse is explained by great values speeds and very close collapse potentials.

The curves of collapse potential according to speed show that the compaction and the water content take part with the reduction of collapse and the increase of ultrasonic speeds. Figure 16 shows that the energy of compaction contributes more effectively than the water content to the reduction of collapse. For a higher energy of compaction, making the non collapsible soils, it is noted a low variation in the state of compactness soil, this for various proportions of water content, while speeds variation is more important.

From these observations, values of ultrasonic speeds are compared against various water content and energy of compaction values. Since the questioned soils have the possibility of collapsing when they are in a loose state; one propose a prediction method of collapsible soils based on ultrasonic tests (non destroyed), fast and easy to realize.

Values of ultrasonic speed are limited as follows:

- $V \leq 400$ m/s $\rightarrow$ Collapse appears;
- 400 m/s $< V <$ 1000 m/s $\rightarrow$ Collapse can occur.
- $V >$1000 m/s $\rightarrow$ Risk of Collapse is not likely to occur.

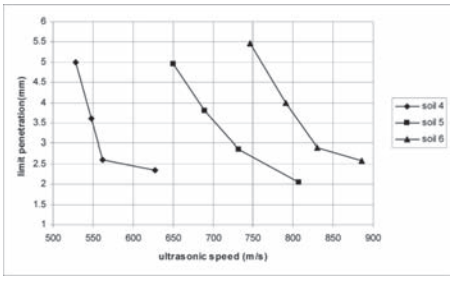

Figure 17. Variation of limit penetration with ultrasonic speed.

In the second case the susceptibility of collapse depends on the water content and the state on compactness on the soil. This procedure can be applied to the restructured or intact soil, at the laboratory and even on site. Considering its advantages, the results of the ultrasonic sounding can be generalized with various types of collapsible soils such as the loesses and other unsaturated soils.

6.3.3 *Relation limit penetration ultrasonic speed*

Results of the compression tests using the oedometer show that the energy of compaction which corresponds to 60 blows makes the soils non collapsible, whatever the percentage of the fine particles and the water content. This deduction agrees with the representation of the limit penetrations against the ultrasonic speeds (Fig. 17), where it is noted that the reduction of limit penetrations is increasing with the increase of ultrasonic speeds. For energies of compaction varying between 10 and 40 blows, the soils remain likely to collapse and the lines have almost the same slope and the same tendency equations. A remarkable slope of these slopes is visualized by applying energy of compaction equal to 60 blows; which explains the existence of a similar behavior specific to the collapsible soils and which differed from the behavior of the non collapsible soils.

7 CONCLUSIONS

The principal conclusions which one can draw from this study can be summarized as follows:

1. The suggested experimental program allows to characterize in a satisfactorily manner the behavior of the collapsible soils.
2. Collapsible soils can be reconstructed in the laboratory by mixing with various proportions kaolin, such fine particles with sand, led to water contents lower than the optimum of Proctor and than compacted to moderate energies of compaction.

3. The results obtained clearly show the influence of certain parameters such as; kaolin content, water content and energy of compaction on the collapse potential, the limit penetration and the ultrasonic speed.
4. The collapse potential can be excessive if the initial water content is low. For water content lower than the optimum of Proctor, there is an energy of compaction beyond which collapse does not occur.
5. The use of the cone penetrometer as an identification mean of the collapsible soils is possible. This makes it possible to follow the evolution of collapse and to propose a limit penetration, separating the collapsible soils from the noncollapsible soils.
6. A new experimental approach of prediction of collapsible soils based on ultrasonic tests, easy and fast, is proposed. The results obtained depend on grains size distribution, state of compactness of the soil and water content. Ultrasonic speeds are limited as follows:
   – V ≤ 400 m/s, then collapse appears;
   – V >1000 m/s, then the risk of collapse is isolated.
   – Between these two limits collapse can occur, it depends then on the water content and the state of compactness.
7. The ultrasonic test can be carried out in the laboratory or in situ, on intact or altered samples of an unspecified form.
8. The ultrasonic speed of metastable soils gives an idea of the state of compactness; it is inverse proportion with the potential of depression.

REFERENCES

Abbeche K., Mokrani L., Boumekik A. 2005. Contribution à l'identification des sols effondrables. *Revue Française de Géotechnique* 110:85–90.

Abbeche K., Hammoud F., Ayadat T. 2007. Influence of Relative Density and Clay Fraction on Soils Collapse. *Experimental Unsaturated Soil Mechanics*. *Springer Proceedings in Physics,* 112:3–9.

Abelev M.Y. 1988. Loess and its Engineering Problems in the USSR, *Proc. of the Int Conf. Engineering Problems of Regional Soils*. Beijing, China.

Ayadat T., Ouali S. 1999. Identification des sols affaissables basée sur les limites d'Atterberg. *Revue française de géotechnique.*

Ayadat T., Bellili F. 1995. Sols susceptibles d'affaissement: Identification mécanique et traitement. *Revue Algérie Equipment,* no. 20, p. 18–23.

Ayadat T., Belouahri B., Ait Ammar R. 1998. La migration des particules fines comme approche d'explication du mécanisme de l'effondrement des sols. *Revue Française de Géotechnique* 83:1–9.

Booth A.R. 1975. The Factors Influencing Collapse Settlement in Compacted Soils. In: *Proceedings of the 6th Regional Conference for Africa on Soil Mechanics and Foundation Engineering.* Dublin, South Africa, 57–63.

Booth A.R. 1977. Collapse Settlement in Compacted Soils. *CSIR Research Report 321 NITRR, Pretoria, South Africa, Bulletin 13*.

CTC Biskra 2002. Intervention du directeur du CTC de Biskra. *2eme Colloque Maghrébin de Génie Civil, Biskra, Algérie. 10,11 Decembre*.

Cui Y.J., Delage P., Alzoghbi P. 1998. Microstructure and Collapse Behaviour of Loess from Northern France. In: *Proceeding of Unsat 98, Beijing,* Vol. 1 31–36.

Cui Y.J., Delage P., Schlosser F., Wonarowcz M. 1999. Etude du comportement volumique d'un lœss du nord de la France. *Xlléme congrès Européen de Mécanique des sols et de Géotechnique Amsterdam,* Vol. 1 p. 337–342.

Cui Y.J., Magnan J.P. 2000. Affaissement locaux dus à l'infiltration d'eau en géomécanique environnementale. *Chapitre n°6 «Risques naturels et patrimoine». Ed. Hermes* 139–164.

Dudley J.H. 1970. Review of Collapsing Soils [J]. *Journal of Soil Mechanics and Foundation Div ASCE* 96(3): 925–947.

Feda J. 1994. Mechanisms of collapse of soil Structure. In Derbyshire (ed) Genisis and properties of collapsible soils. NATO Series C. *Mathematical and Physical Sciences,* Vol. 468 pp. 149–172. Dordrecht: Kluwer.

Fredlund D.G., Rahardjo H. 1993. Soil mechanics for unsaturated soils. New York, John Wiley and Sons, Inc.

Ganeshan V. 1982. Strength and Collapse Characteristics of Compacted Residual Soils. *Thesis (M.E), Asian Institute of Technology Bangkok Thailand.*

Holtz W.G., Hilf J.W. 1961. Settlement of Soil Foundation due to Saturation In: *Proceeding 5th International Conference on Soil Mechanics and Foundation Engineering*, Vol. 3 673–679.

Jennings J.E., Knight K. 1975. The Additional Settlement of Foundation due to Collapse of Sandy Soils on Wetting. In: *Proceeding. 4th International Conference on Soil Mechanics and Foundation Engineering,* 316–319.

Lawton E.C., Fragaszi R.J., James H. 1989. Collapse of Compacted Clayey Sand. *Journal of Geotech. Eng ASCE, Vol.* 155(9):1252–1267.

LNHC 2000. Projet Extension des Gazoducs à Hassi Messaoud. Rapport de reconnaissance de sol. *Laboratoire National de l'Habitat et de la Construction de Batna, Algérie.*

Markin B.P. 1969. Discussion on standard criteria of Sag in Loess soils. *Soil Mechanics and Foundations Engineering,* no. 2, p. 137.

Morgenstern N., De Matos M. 1975. Stability of slopes in residual soils. *Proc. 5th. Pan American Conf. on soil Mech. and Found Eng. Buenos Aires Argentina*. 3, p. 367–383.

Qian H.J., Lin Z.G. 1988. Loess and its Engineering Problems in China. In: *Proceeding of the International Conference Engineering Problems of Regional Soils.* Beijing, China, 136–153.

Ting W.A. 1979. Consolidation of a partilly saturated residual soil. *Proc. 6th Asian Reg. Conf. on Soil Mech. and Found. Eng.,* Singapore, vol. 1, p. 95–98.

This page intentionally left blank

Geotechnical Safety and Risk IV – Zhang et al. (eds)
© 2014 Taylor & Francis Group, London, ISBN 978-1-138-00163-3

Effect of riverbed scouring on bridge piles during earthquake

Z.H. Khan, M.R.I. Khan, M.F. Raiyan & K.M. Amanat
Bangladesh University of Engineering and Technology, Dhaka, Bangladesh

ABSTRACT: This study represents an approach for investigating the effect of riverbed scouring on piles of a reinforced concrete bridge in the event of an earthquake. A finite element model of box girder bridge with 9 spans was developed for analysis of this phenomenon. Loading was generated due to earthquake in along the traffic and perpendicular to the traffic direction. Scouring depth of the pier and rived bed scour percentage with main river width are taken as parameter of the study. Flexural stress in pile increases by 137% and axial stress was found increasing by 11% about original no scoured condition for earthquake along the traffic direction while the flexural stress increases by 87% and axial load increases by 5% about original no scoured condition for earthquake in parallel direction of traffic.

1 GENERAL INTRODUCTION

Numerous current studies have indicated that only static analysis is not enough to provide required structural safety of any structure. So structural response for dynamic disturbance must be evaluated with static disturbance of the structure. In safety assessment, the effect of bridge pier scouring on pier design parameters such as moment and axial load is observed for the event of earthquake. Excessive scouring leads to rapid increase in pier moment reducing the factor of safety of the structure. A screening and evaluation program in the United States reports that, of a total of almost 500,000 bridges, there are more than 26,000 scour-critical and more than 26,000 scour-susceptible bridges (Pagàn-Ortiz 2003). Again in recent years, in Bangladesh, Meghna Bridge situated on the most important route of the country (National Highway N1), was detected to be severely scoured threatening to cripple the economic trade route of the country with the outside world. Therefore it is necessary to assess the effect of scouring in the overall integrity of the bridge structure. Generally in most of the bridge design it is assumed that the riverbed level will remain within the level of pile-cap. For this support condition, relevant formulas in AASHTO bridge design were used and the member size and shape of the structure was calculated with some factor of safety. But with large amount of scouring in around any pier increases its unsupported length and also changes the design parameters. With these changes in moment or axial load if earthquake is induced it might have some negative consequences on the structure. This study tries to focus on this phenomenon exclusively.

2 OBJECTIVES AND SCOPES

The major objective of this study and analysis is to enhance our knowledge about pier scouring and relevant changes in the design parameters in the event of an earthquake.

The salient features of this study are briefly mentioned below.

I. To model a reinforced concrete cantilever box girder bridge with nine continuous spans using beam element.
II. To apply earthquake in perpendicular direction to the traffic and in the parallel direction to the traffic of the bridge.
III. Perform modal analysis and single point response spectrum analysis with 5% damping ratio.
IV. To observe the changes in the axial load and moment in piles by varying the scouring depth and number of piers scoured.

3 THE MEGHNA BRIDGE

Bangladesh is a riverine country and different parts of this country are divided from each other by a number of small and large rivers. Meghna is one of the large rivers, which has divided the southeast part from the other parts of the country, especially from the central part.

Meghna Bridge was constructed between 1986–1991 (Figs. 1 and 2). It is a prestressed concrete cantilever box section bridge with hinges at the middle of every span. The overall length of the bridge is 930 m. The Bridge is situated on the 25th Km of Dhaka-Chittagong highway N1 (Latitude 23°36'20.98"N and Longitude 90°36'50.32"E). The Bridge not only connects the capital city Dhaka with port city Chittagong but also acts as a gateway of other countries of South-Asia through Myanmar.

3.1 *Present scenario of Meghna Bridge*

Construction of Meghna bridge was completed in 1991 to contemporary Bangladesh seismic standards. From the relevant documents of the bridge, it was found that, for design, seismic horizontal loading was taken as a static load equivalent to 5% of the vertical dead loads. The seismic zoning map in the Bangladesh National Building Code (BNBC) was revised in 1994, which reflects an updated assessment of the magnitude of a 1 in 200 year seismic event. The area in which Meghna Bridge is situated is classified as zone 2 in the BNBC zoning map. Before the BNBC revision the corresponding ground acceleration of zone 2 was 0.05g and after the revision the value was updated to 0.15g. This represents a threefold increase in seismic ground accelerations on the structure compared with the values adopted in the original design. The amount of confining reinforcements currently provided in the bridge piers also do not comply with the requirements of the AASHTO standard specifications 16ED. Details in this regard can be found at Final design Report on Rehabilitation of Existing Meghna Bridge, Roads and Highways Department (RHD), 2011.

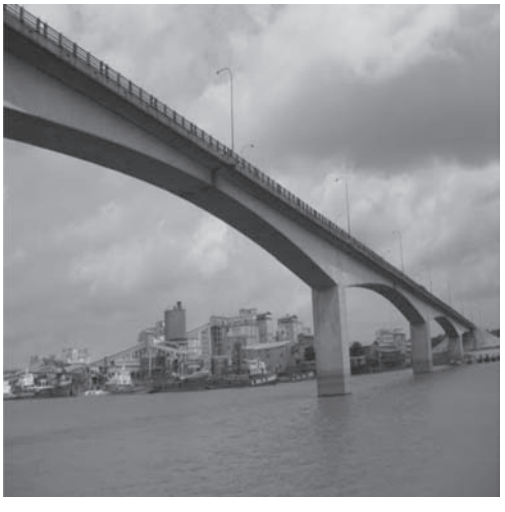

Figure 1. The Meghna Bridge.

Toll collection and Operation and Maintenance Operator currently responsible for the regular maintenance of the bridge.

They have reported that due to the last three consecutive floods riverbed erosion has taken place.

Underwater survey conducted in May 2010 revealed severe scouring of bridge foundation, especially in pier locations P5 to P10 of Meghna bridge with more than 15 m of scouring at P8.

Scouring is directly related to the shear stress or velocity. As per the past report the velocity for 1 in 50 and 1 in 100 year flood event are 1.31 and 1.36 m/s at the vicinity of the Meghna bridge. According to FAP 9B, design roughness and the gradient between Bhairab Bazar and Meghna bridge location was determined and these were Manning's coefficient $K_m = 40$ and slope $S = 2.5 \times 10^{-5}$. Using these values, for maximum water level of 22.5 m at the Meghna bridge location of 5.20 m PWD, the velocity was calculated to be 1.58 m/sec.

Water level variation of Meghna Bridge along the year is shown in Figure 3.

However detailed bathymetric surveys show that near the Meghna bridge water depth is over 35 m, which results in a flow velocity of 2.15 m/sec. So this increased velocity is one of the reasons behind this pile scouring.

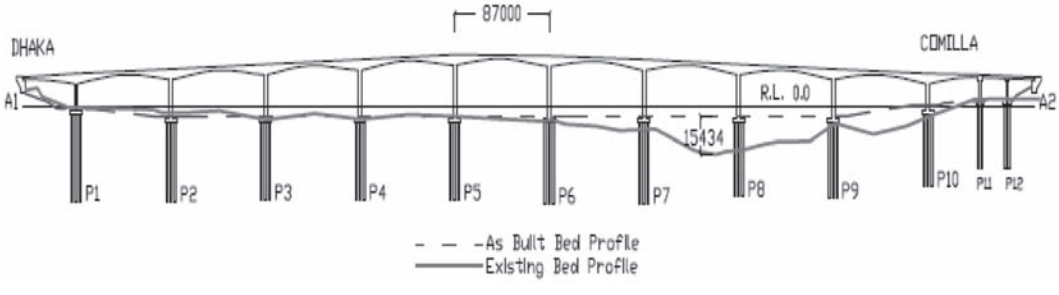

Figure 2. Bed profile of Meghna Bridge (all dimensions are in mm).

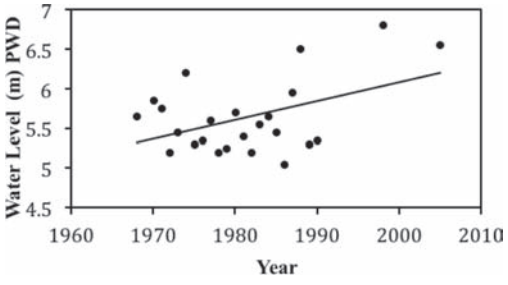

Figure 3. Maximum water level at Ferry Ghat Station of the Meghna Bridge.

4 METHODOLOGY

Finite element analysis and engineering simulation software ANSYS 11.0 was used for the complete analysis in this study. A model of nine spans of box girder cantilever reinforced concrete bridge, with simply support condition at both ends was developed using this software. Earthquake load was applied in perpendicular direction to the traffic and in the parallel direction to the traffic of the bridge by means of single point response spectrum analysis with 5% damping ratio. As a prerequisite to the single point response spectrum analysis, modal analysis of the structure was also performed. With these loading conditions, scouring depth of the pile along with number of scoured pier was varied to observe the change in pile design forces.

4.1 *Assumptions*

The investigation was carried out on the basis of some assumptions to avoid complications. These assumptions are as follows:

I. Materials involved in the study were elastic.
II. Only lateral force that was encountered by the structure is the Earthquake.
III. In analysis for earthquake only dead load of the structure was considered. No live load was taken into consideration.
IV. Linearly increasing soil subgrade modulus was considered.
V. Soil scouring profile around the bridge piers was assumed to be parabolic.
VI. All the calculations were made on the basis of pure loading. No scaling of load was done for single point response spectrum analysis.

5 MODEL DEVELOPMENTS

In this study, a balanced cantilever bridge with similar attributes like Meghna Bridge was developed. Meghna Bridge is 930 m long with a width of 9.2 m. It is a prestressed concrete box girder bridge with total thirteen spans. The first two spans of the bridge are 48 m long while the next nine are 86.840 m long. The rest two spans are 24 m long. Typical deck slab of the bridge is hinged on both sides. The deck slab portion of the Meghna bridge is curved at the bottom, with its dimension thickest near the pier and thinnest at the hinge side. For simplicity a model was developed with 9 equal spans each having a length of 87 m. Pier height and pile length were also assumed to be of uniform dimension. Pier height of 27 m and pile Length (L) of 48 m were chosen for the developed model. To incorporate the curved architectural feature of the deck slab portion of the bridge, the deck slab was divided into 10 equal segments on both sides of the each pier. A typical cross section of the deck slab near the pier location is shown in Figure 4. For creation of the model, beam type element was used for deck slab portion and pier. Shell type element was used for pile cap and pipe type element was used for pile creation.

The effect of earthquake on the bridge structure was assessed for the dead load of the structure only. The necessary material property used in the model is given in Table 1.

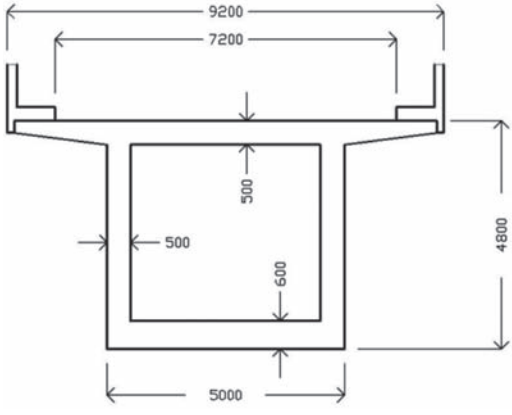

Figure 4. A typical cross section of deck slab (all dimensions are in mm).

Table 1. Material property.

Poison's ratio	Modulus of elasticity, E (N/mm^3)	Density (Ton/mm)	Soil subgrade modulus, k (N/mm^3)
0.2	20000	2.4×10^{-9}	0.02

5.1 *Boundary condition*

Like the support condition in the Meghna Bridge, the abutments in the both ends of the developed model were simply supported. The piles were fixed supported but fixing length of the pile had to be identified. In Figure 5 it can be seen that both free and fixed headed pile are subjected to a lateral load H_u, in these circumstances, piles act as a simple cantilever. Here e is the height from the ground surface to the point of application of the load and z_f is the depth to virtual fixity. Together $(e + z_f)$ is called equivalent height. With the increase in riverbed scouring, the value of e will increase and so will the unsupported length. To calculate the value of z_f two stiffness factors will be required, depending on whether the soil modulus is constant or increases linearly. For constant soil modulus, stiffness factor R is used and for linearly increasing soil modulus, stiffness factor T is used.

$$\text{Stiffness factor, } R = \sqrt[4]{\frac{EI}{kB}} \tag{1}$$

In stiffness factor R, k is the soil modulus.

$$\text{Stiffness factor, } T = \sqrt[5]{\frac{EI}{n_h}} \tag{2}$$

In stiffness factor T, n_h is the coefficient of horizontal subgrade reaction.

ACI recommends that for long pile the value of zf can be taken either $1.4R$ or $1.8T$. But for granular soils and normally consolidated clays, generally, the best practice is to assume linearly increasing soil modulus. That is why to calculate the value of z_f $1.8T$ has been adopted. For the developed model, the coefficient of the horizontal subgrade reaction was assumed to be 0.01078 N/mm^3.

Table 2 shows the relation between pile type and soil modulus. The formula that was used as per ACI to calculate z_f is for long elastic piles. So it is important to make sure that the pile in the model was a long and elastic one. From the developed model it was observed that $L \geq 4T$.

The vertical and lateral Degrees of Freedoms at both ends of the balanced cantilever portion were

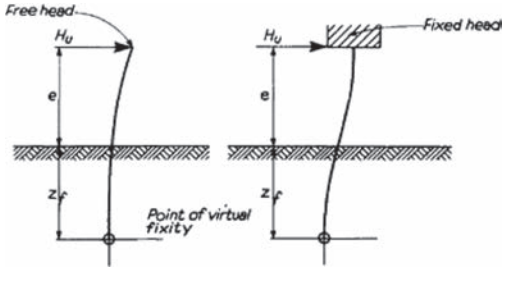

Figure 5. Piles under horizontal loads are considered as simple cantilevers.

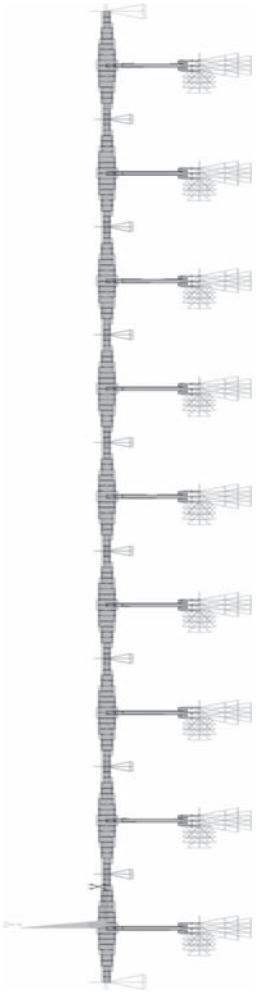

Figure 6. Fully developed model with proper boundary condition in no scouring condition.

Table 2. Relation between soil modulus and pile type.

	Soil modulus	
Pile type	Linearly increasing	Constant
Rigid (free head)	L ≤ 2T	L ≤ 2R
Elastic (free head)	L ≥ 4T	L ≥ 3.5R

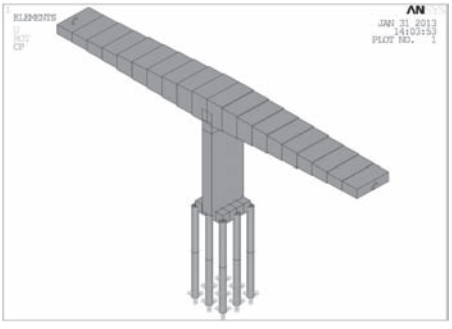

Figure 7. Segments of bridge deck slab (isometric view).

Table 3. Parametric change employed in the study.

Parameter name	Parametric change	Consequence
Percentage of riverbed scoured (as a percentage of river width)	10%	One pier scoured
	40%	Three piers scoured
	60%	Five piers scoured
For each percentage of scoured river width		
Scoured depth	0 m, 3 m, 6 m, 9 m, 12 m, 15 m and 18 m	Change in the fixing length of pile

coupled with the adjacent deck slabs. In Figure 7, the small red portion indicates the coupled DOF's. Coupling of DOF's in vertical and lateral direction means any displacements in those directions, between the adjacent deck slabs, occur together but the displacement is free in longitudinal direction of the bridge.

6 STUDY PARAMETERS

For this particular study and model, some parameters were chosen to evaluate their impact on the structure on an occasion of earthquake. The parameters that were studied summarized in Table 3.

7 STUDY OBSERVATION

7.1 *Moment variations in corner pile*

First the flexural variation in the corner pile of the maximum scoured pier will be discussed. Figure 8 is for earthquake in parallel direction of traffic and Figure 9 is for earthquake in perpendicular direction of traffic. The Black, Golden and Blue graphs are for 10%, 40% and 60% riverbed scouring respectively. Peak moment in the pile is achieved at different scouring depths in case of earthquake in parallel direction of traffic. With no scouring condition, the moment is around 1500 kN-m and maximum value of moment is around 2800 kN-m at 12 m scoured depth for 60% river bed scouring. The percentage increment is around 87%. At 18 m of scouring depth, the value of moment becomes almost same regardless the percentage of riverbed scoured. For earthquake in perpendicular direction of traffic, moment increases with the increment of scouring depth. In this condition, maximum moment for 10% riverbed scouring is achieved at 12 m scouring depth and for 40% of the riverbed scouring, the maximum moment is achieved at 15 m of scoured depth. Among the moments for earthquake in perpendicular direction of traffic, maximum value is found to be at 18 m of scoured depth

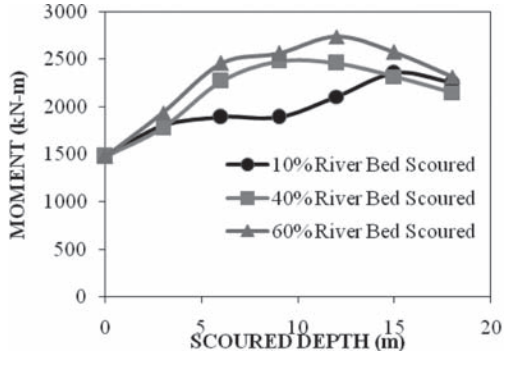

Figure 8. Moment variation for earthquake in parallel direction of traffic.

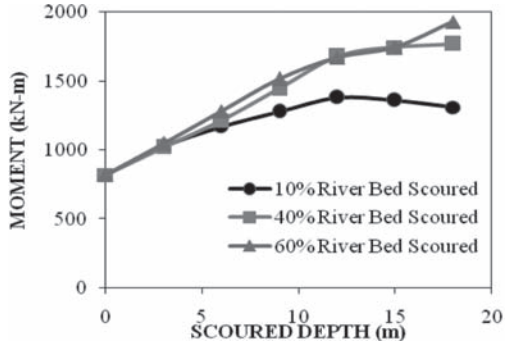

Figure 9. Moment variation for earthquake in perpendicular direction of traffic.

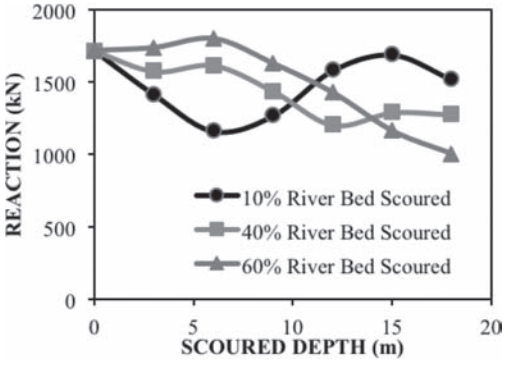

Figure 10. Axial load variation for earthquake in parallel direction of traffic.

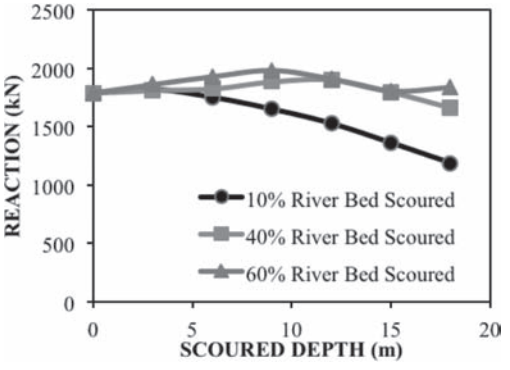

Figure 11. Axial load variation for earthquake in perpendicular direction of traffic.

for 60% of the riverbed scouring and the value is almost 1850 kN-m. With no scouring condition the moment is around 820 kN-m and the percentage increment of moment is 137%. Although the percentage increment of moment is more in earthquake in perpendicular direction of traffic but earthquake in parallel direction of traffic is more vulnerable because of the higher moment value in the latter case.

7.2 *Axial load variation in corner pile*

Figures 10 and 11 shows axial load variation, in corner pile of maximum scoured pier, for earthquake in parallel direction of traffic and for earthquake in perpendicular direction of traffic respectively. It has been found that for 10% and 40% of riverbed scouring, axial load in pile decreases for earthquake both in perpendicular and parallel direction of traffic. For 60% of riverbed scouring, axial load in pile increases by a small margin. The increment percentage is about 5% for earthquake in parallel direction traffic and 11% for earthquake in perpendicular direction of traffic about the axial load in original no scouring condition.

From the above numerical results, it can be inferred that there is a relation between the riverbed scouring and the change in moment and axial load in the piles. As the riverbed scouring progresses, the fixing length of the pile also moves downward making the bridge more susceptible to lateral loading. For that reason, in the event of an earthquake with scoured riverbed condition, the moment in the pile increases and the axial load decreases.

8 CONCLUSIONS

From above results and discussions it can be concluded that bridge pier scouring incorporated with earthquake will have adverse effect in the overall integrity and health of the structure. So proper protective measures should be taken for the soils around the bridge piers to prevent scouring.

REFERENCES

Pagán-Ortiz, J.E. 2003. *Scour program update*. Proc., Midwestern Hydraulic Engineering Conf., U.S. Department of Transportation, Federal Highway Administration, Washington, D.C.

Tomlinson, M.J. 1994. *Pile Design and Construction Practice*. 4th Edition, E & FN Spon.

Geotechnical Safety and Risk IV – Zhang et al. (eds)
© 2014 Taylor & Francis Group, London, ISBN 978-1-138-00163-3

Risk minimization by an adapted dewatering scheme at the construction of the new ship lock in Minden

H. Montenegro, B. Odenwald & R. Kauther
BAW German Federal Waterways Engineering and Research Institute, Karlsruhe, Germany

ABSTRACT: The excavation design for the new ship lock in Minden resulted challenging due to the immediate vicinity of the 14 m deep excavation pit to existing structures and surface water bodies. An alternative to a fully braced variant consisted of anchored support walls and slopes to the opposite side. The hydrogeological setting consists of fill materials and Quaternary sands above bed-rock. Borehole pulse and pumping tests revealed preferential flow along a system of fissures in the claystone in which river stage fluctuations can propagate very fast. The excavation design in a setting with a fair hydraulic connection to the river demanded an effective groundwater containment system and a robust dewatering. In order to minimize the level of risk an active-passive dewatering scheme was developed. The excavation design proved to be robust and yielded significant cost savings compared to a fully braced support walls variant.

1 INTRODUCTION

The Midland Canal traverses the Weser Valley near Minden in Westphalia, Germany. At the crossing point, the water table of the canal lies about 13 m above the mean water level of the Weser. The rising and the lowering for shipping is currently being managed by a ship lock, which was constructed in 1914. In the course of the adaptation of the Weser Valley to larger vessels, the lock is being replaced by a new structure. Benchmark data for the new ship lock are the length of 139 m, the width of 12.5 m and the 4 m access way depth. Figure 1 shows the setting of the existing lock, the excavation site for the new ship lock as well as the adjacent water surfaces of the Weser and the upper pool which connects to the Midland Canal.

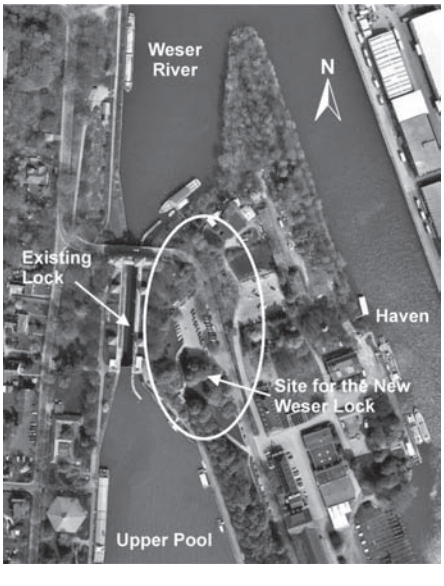

Figure 1. Aerial view of the existing lock in Minden and the construction site for the new lock.

The new excavation site is no longer situated on "a wet meadow", which was the case during the construction of the lock, but is rather in the immediate vicinity of existing facilities. Therefore it had to be ensured that the existing lock and the ongoing navigation would not be affected or impaired due to the adjoining excavation. This required profound examinations of soil-structure-interactions as well as proof of serviceability of the existing lock during any excavation stage. As the pit cuts into the surface water of the upper pool and the Weser (13 m–18 m above the pit base), any leak in the canal lining of the upper pool as well as potential leakages from ship impact at the pit walls need to be considered explicitly.

2 GROUND CHARACTERIZATION

The ground in the planned excavation site can be divided into three strata. Directly under the ground surface there are up to 12 m natural fill material. Those underlie alluvial silt and loam as well as sands and gravels of a predominantly high density of up to 3.5 m layer thickness. Below these

Quaternary layers lies tertiary claystone in a thickness beyond the target depth of the ground exploration. The claystone belongs to the group of weak rocks and has a distinctive orthogonal system of discontinuities. This consists of steep joints with an inclination between 45° and 90° and a low dipping bedding. The strength parameters for the compact rock and the rock and interfaces were determined on the basis of in-situ and laboratory shearing tests (uniaxial compressive strength on average 7.7 MN/m² in vertical and 9.2 MN/m² in horizontal direction).

3 HYDROGEOLOGICAL CONDITIONS

In the hydrogeological analysis of deep excavations in close proximity to rivers the appropriate estimation of effective conductivity and hydraulic connectivity to adjacent surface water bodies is essential. The analysis of pore pressure measurements in the claystone revealed variations in response to the filling and emptying of the existing lock, even at a considerable distance (see Fig. 2). The rapid (in relation to the conductivity of the claystone) changes of effective stress due to the filling and emptying of the chamber induce an immediate rise in pore pressure beneath the lock which can effectively propagate in space to the installed pressure transducers. These observations suggested fissured flow in the claystone.

Hydraulic properties of the claystone had to be determined at the appropriate scale. Borehole pulse tests and pumping tests revealed preferential flow along a system of fissures. The effective hydraulic conductivity of the claystone was characterized with correspondingly large values in the range of 10^{-5} m/s. Responsible for such unanticipated high values is the spatially varying fissure interconnectivity.

The hydraulic conductivity of the quaternary sediments was determined on the basis of laboratory tests in the expected range of 10^{-3} m/s. These results led to the conclusion that a fair hydraulic connection to the Weser was present, not only in the permeable Quaternary sediments but also through the fissured claystone.

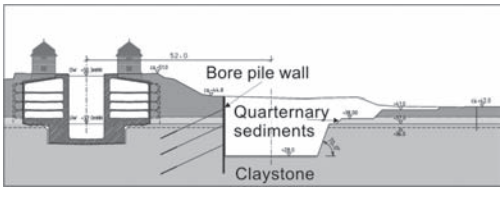

Figure 2. Cross section of the excavation pit for the new ship lock in Minden.

4 EXCAVATION PIT CONCEPT

With the objective to control extensive excavation-induced deformations and to avoid any damage in the adjacent structures the pit design evolved around braced or anchored excavation support walls. First calculations revealed however limited anchor forces in the claystone. An alternative to a fully braced variant consisted of anchored support walls and slopes to the opposite side. This alternative demanded a robust control of groundwater inflow by an effective dewatering.

On basis of preliminary groundwater flow calculations an excavation concept was developed. Rigid excavation support walls were established on the western side as a bored pile wall anchored back fourfold. At the opposite side the pit was sloped with an inclination of 70° in the claystone. The Quaternary soil layers above were sloped at an angle of 1:1.5 to 1:2 as shown in Figure 2.

5 GROUNDWATER CONTAINMENT SYSTEM

Inflows from adjacent surface waters through the permeable Quaternary sands was limited by the construction of a impervious containment cutting

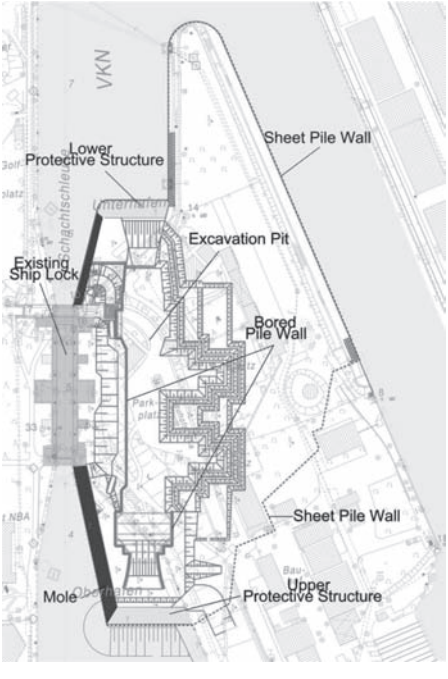

Figure 3. Arrangement of the containment system around the excavation pit.

into the claystone surrounding the excavation pit. Components of the containment system are the existing lock (based in the claystone), the sheet-pile walls of the cofferdams for the prospective mole and the upper and lower protective structures and a surrounding sheet-pile wall.

The map in Figure 3 shows the arrangement of the components of the containment system, the existing ship lock, the bored pile wall on the western side, the slopes on the eastern side and the protective cofferdam structures in the ponds.

The fissure system of the claystone in which river stage fluctuations can propagate very fast demanded required an effective and robust groundwater lowering system. Different dewatering approaches were studied to reliably control groundwater heads and reduce actions from pore pressure on the pile wall and seepage forces on the slopes.

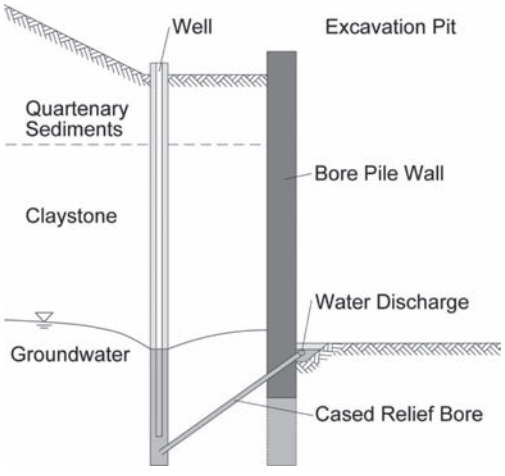

Figure 5. Schematic illustration of the dewatering system during passive operation.

6 DEWATERING SCHEME

Due to the limited anchor forces of 1000 kN acceptable groundwater heads (according to the static loading design of the bored pile wall) had to be met. There are essentially two approaches to control actions from groundwater on excavation support walls. On the one hand, "actively" by means of groundwater lowering through wells outside the excavation pit, and on the other hand, "passively" discharging the groundwater into the excavation pit taking advantage of the groundwater head difference outside and inside the pit. The groundwater discharge and so the lowering can be considerably enhanced if groundwater inflow is short-circuited through the bored pile wall. Figures 7 and 8 show schematically the active and passive dewatering approach respectively.

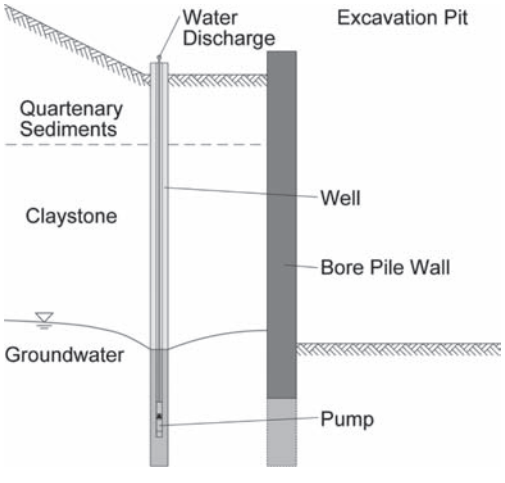

Figure 4. Schematic illustration of the dewatering system during active operation at the final excavation level.

The passive operation has a considerable advantage in the case of failure of the pump system (e.g. by lightning strike etc.) as no inadmissible head differences can build up behind the pile wall. In the worst case the pit is inundated in contrast to the active operation mode where a pumping breakdown can result in a rapid rise of groundwater heads and loadings on the excavation support walls.

Further, a passive dewatering provides operational benefits since no redundant pump system and permanent monitoring is needed as is the case during active groundwater lowering to minimize the risk of inadmissible static heads/loading behind the support wall due to unanticipated failure of the pumps.

On the other hand a passive dewatering scheme right from the start of the excavation on was not appropriate. This would require groundwater discharge through the bored pile wall at several excavation levels. Therefore an active dewatering based on vertical extraction wells (see Fig. 6) was established during the excavation. After reaching the final excavation level, the dewatering was shifted from active to passive operation. To short-circuit groundwater through the pile wall inclined boreholes were drilled from the excavation base to the vertical extraction wells and supplied with a casing. Taking advantage of the head difference outside and inside the pit, groundwater flows is captured outside the pit by the vertical wells, discharged through the wall in the obliquely-installed

Figure 6. Installation of the vertical extraction wells for the groundwater lowering during active dewatering.

casings and ultimately conducted to the drainage system at the base of the excavation. Both dewatering operational modes were examined based on spatial groundwater flow calculations.

7 GROUNDWATER FLOW CALCULATIONS

The necessary control of extensive deformations in the existing structures demanded for reliable groundwater flow and pore water pressure calculations, particularly behind the pile walls and in the slopes. For this purpose, groundwater flow models at different scales and spatial resolutions were built. At first, the effects of the containment system on the regional groundwater flow were calculated in a 2D-model (large-scale model, see Fig. 7). Then the above outlined excavation pit and a series of extraction wells required for the active dewatering was modeled in a 3D-model (excavation pit model see Fig. 8). Finally, detailed calculations along relevant cross sections in 3D-models of high spatial resolution were performed to design the dewatering system as well as to calculate the actions from pore water pressure and seepage forces on the pile wall and the slopes. Within this modelling approach, the detailed model represents a cut-out from the excavation pit model and the latter, in turn, corresponds to a snippet from the large-scale model. Such a method has the advantage that the initially unknown boundary conditions can be adopted from the respectively larger scaled model (Montenegro & Kauther 2010).

Though the topography was captured in detail in the excavation pit model (see Fig. 8), the spatial resolution and so the accuracy of the results were not satisfactory as the radial components of groundwater flow in the vicinity of the extraction wells cannot be adequately represented (Montenegro & Odenwald 2009). These limitations demanded for the detailed models of higher spatial resolution (see Fig. 9).

Figure 7. 2D-large-scale model (green) and the 3D-model (red). Lines in the area of the excavation pit: calculation sections.

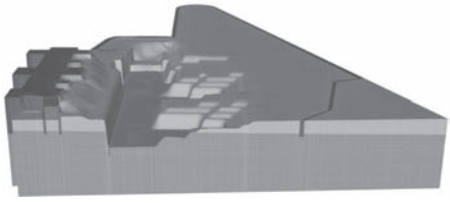

Figure 8. Cross section of the 3D-excavation pit model. Ochre: Quaternary sediments, blue: claystone, violet: groundwater containment system.

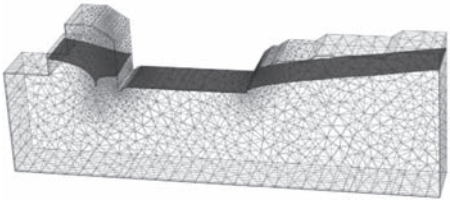

Figure 9. 3D-detailed model for the dewatering design. Blue: groundwater surface during active dewatering.

8 DEWATERING SYSTEM DESIGN

The dewatering system during both active and passive operation was designed according to the static loading in terms of heads/pore pressure distributions on the pile wall. Calculations considered a 100-year flood by applying the corresponding river stage as boundary condition. Further damage of

the protective structure in the upper pool by ship collision was taken into account by specifying leaks along the water-side sheet pile wall in the excavation pit model (see Fig. 8).

Based on the detailed models (see Figs. 9 and 10) seepage forces behind the bored pile wall and in the slopes of the eastern side were calculated at relevant cross sections. For different excavation stages pore water pressure distribution at the corresponding slip surfaces were evaluated. The groundwater heads halfway between two wells are design relevant because the potentials are higher there as compared to the position of the wells where the largest draw down occurs. Finally failure of single pumps was considered which led to an extraction well distance of 8 meters.

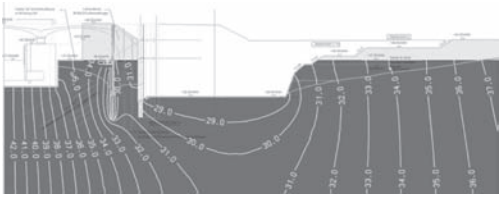

Figure 10. Groundwater flow at a well during active operation (groundwater surface: blue, groundwater head distribution: yellow) from detailed model 3D-computations.

The arrangement of the extraction wells and the withdrawal rate [m³/h] at the beginning of active operation (well drawdown in all extraction wells at NN+27 m) is shown in Figure 11. The irregular distribution of withdrawal rates indicates higher inflows in the northern area which is reasonable due to the shorter distance to the river. The extraction wells behind the short eastern bored pile wall show higher withdrawal rates as well which can be ascribed to the comparably larger catchment area of those 8 wells compared to the 27 wells on the western side.

Due to the fundamental importance of the groundwater lowering for the static loading of the anchored bored pile walls a redundant pumping system was mounted consisting of two independent pumps in each extraction well.

Figure 11. Initial withdrawal rates [m³/h] at the start of active dewatering. Well drawdown at NN+27 m.

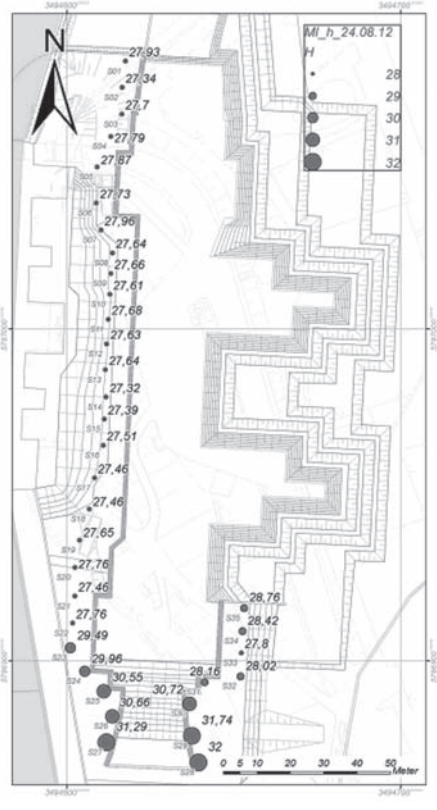

Figure 12. Well drawdown [NN+m] at the start of the passive operation.

Figure 13. Aerial view of the pit for the new ship in Minden at the final excavation stage.

Further a groundwater monitoring system was installed in every well and at other relevant stations to supervise the groundwater lowering. Measurement were instantly available via a server application. For selected stations warning and alert groundwater heads were established and automatic alarms via E-mail and SMS message were set up.

After 6 months the final excavation level was reached and dewatering mode was shifted to passive operation establishing so a much lower risk level. Observed water levels in the wells after the transition to passive operation are depicted in Figure 12. The drawdown in the wells reflects the level in the drainage system at the base of the pit maintaining so the heads behind the wall significantly below the established limit values for that particular excavation stage. Only near the southern gate increased drawdown values appear as in that sector no relief casings were installed due to lacking static necessity. A view of the excavation at the final stage just after changing to passive mode is shown in Figure 13.

9 SUMMARY

The design of the 14 m deep excavation pit for the new ship lock in Minden resulted demanding due to the immediate vicinity of the pit to existing structures and to surface water bodies. In order to control extensive excavation-induced deformations and to avoid any damage in the adjacent structures the pit design evolved around fully braced excavation support walls. An alternative consisted of anchored support walls and slopes to the opposite side.

The particular hydrogeological setting consists of fill materials and Quaternary sands above bedrock. Pore pressure measurements and hydraulic tests in the claystone revealed that river stage fluctuations can propagate very fast and may increase groundwater heads even at large distances due to flow along a system of fissures. The pit design in a setting of permeable sands above fissured claystone, both in fair hydraulic connection to the river demanded an effective groundwater containment system and a robust dewatering design.

An extensive groundwater flow analysis at varying scales was carried out. Groundwater head distributions for relevant design situations were predicted based on a 3D model of the entire excavation pit. Based on detail models at a higher spatial resolution the arrangement of vertical extraction wells was optimized considering admissible groundwater heads behind the bored pile wall.

In order to minimize the level of risk during excavation an active-passive dewatering scheme was developed. The excavation design proved to be robust and yielded significant cost savings compared to a fully braced support walls variant.

REFERENCES

Montenegro, H. & Odenwald, B. 2009. 3D groundwater flow modelling at the excavation pit for a ship lock in Minden, Germany. In *14th Danube-European Conference on Geotechnical Engineering DECGE 2010, Bratislava, 2–4 June 2010*.

Montenegro, H. & Odenwald, B. 2009. Analysis of spatial groundwater flow for the design of the excavation pit for a ship lock in Minden Germany. In *2nd International FEFLOW User Conference, Potsdam, 14–18 September 2009*.

Montenegro, H. & Kauther, R. 2010. A multi-scale approach for the consideration of spatial groundwater flow in the stability analysis of a large excavation pit. In *7th European Conference on Numerical Methods in Geotechnical Engineering NUMGE 2010, Trondheim, 2–4 June 2010*.

Geotechnical Safety and Risk IV – Zhang et al. (eds)
© 2014 Taylor & Francis Group, London, ISBN 978-1-138-00163-3

Geotechnical instrumentation monitoring for the construction of the West Kowloon Terminus of the Express Rail Link

A.K.O. So, P.W.L. Ko & V.K.W. Man
MTR Corporation Limited, Hong Kong, China

ABSTRACT: In Hong Kong, it is a statutory requirement to provide a monitoring plan where the construction works may affect any nearby building, structure, land, street or services. The traditional use of the triple-A response values has many drawbacks when the projects are large and complicated. A modified instrumentation monitoring plan is therefore proposed. Instruments are grouped to serve two purposes. The first grouping is for the protection of the external sensitive receivers. They are categorized into types for different response actions as different sensitive receivers can tolerate different extent of settlement and angular distortion. The second grouping is for the performance review of the excavation and lateral support systems. Another set of response values are determined from the predicted movements of the systems at various critical stages. Failure mechanisms are identified from the geological models and PLAXIS analysis. Mitigation and contingency measures are considered in advance.

1 INTRODUCTION

In Hong Kong, it is a statutory requirement that a monitoring plan is to be provided where the construction works may affect any nearby building, structure, land, street or services (BD 2004). Monitoring check points for the ground settlement, pavement settlement, utility settlement, building and structure settlement and tilting, and geotechnical instruments such as various types of piezometers, extensometers and inclinometers are installed. These check points and instruments are monitored against three triggering or triple-A (AAA) levels for response actions. They are to be approved by the Buildings Department (BD) and Geotechnical Engineering Office (GEO) based on the distance of the sensitive receivers from the construction works. In the case of the first A level is reached, the Contractor shall inform the Engineer within 24 hours of exceedance of the first A level and shall increase the monitoring frequency and/or monitoring check points and instruments. When the second A level is reached, the Contractor shall review the construction method in order to mitigate the detrimental effects arising from the ground settlements and/or movements. If the third A level is reached, the construction works have to cease and a thorough investigation report with an action plan shall be submitted to the Engineer and BD/GEO before resumption of the works.

Before February 2012, BD only required the third A level for a particular type of service to be agreed with the relevant government department or utility company and to be based on the amount of movement that services could tolerate (BD 2004). However, the response levels imposed by the relevant government department or utility company are generally conservative and engineers are obliged to follow, aiming for easy approval by the BD/GEO. In February 2012, BD provided details of the monitoring requirements in APP-18 and APP-137 in the Practice Notes for Authorized Persons (AP), Registered Structural Engineers (RSE) and Registered Geotechnical Engineers (RGE) or the PNAP. The AAA levels are defined as "Alert, Alarm and Action". Reference example of contingency measures for piling works for each level to be carried out by the RSE and Registered Specialist Contractor is given (PNAP APP-18). Ground settlement limits resulting from the piling and similar operations are recommended (Appendix B in PNAP APP-137). Reference AAA values for the ground settlement markers, services settlement markers and building titling markers are given based on serviceability requirements. As different structures will have different tolerance in accommodating the movements of their foundations, acceptance of estimated ground settlements should be considered on a case-by-case basis with respect to their integrity, stability and functionality of the supported structure.

The traditional use of AAA values and the recent monitoring requirements given in the PNAP APP-18 and APP-137 are generally acceptable for

small projects. However, they have many drawbacks if the projects are large and complicated, like the West Kowloon Terminus (WKT) of the Express Rail Link constructed by the MTR Corporation Limited, which are to be discussed as follows.

2 THE WEST KOWLOON TERMINUS

As shown in Figure 1, the Express Rail Link provides an efficient means of mass transport between Hong Kong and the Futian Station of Mainland China. The Hong Kong section of the link comprises an underground terminus (the WKT), an approach tunnel and about 26 km of tunnel. The WKT site is located on a reclaimed land surrounded by the Austin Station on the east, Victoria Harbour on the south, Kowloon Station and the above-station development on the west and Jordan Road on the north.

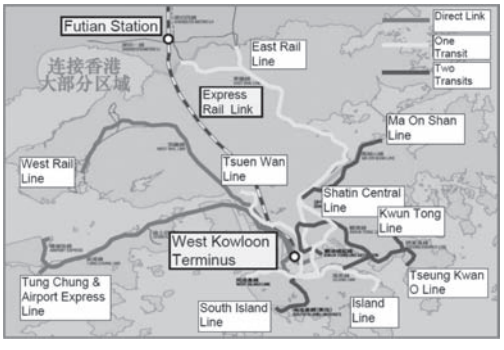

Figure 1. Geographical location of WKT.

The site has a complex history of reclamation and use. Figure 2 shows the geological stratigraphy of the site. The ground is generally flat with an existing ground level at about +4 mPD to +5.5 mPD and a groundwater level varying at about +0.8 mPD to +1.8 mPD. However, the groundwater level close to the Harbour is influenced by tidal fluctuations. The geological stratigraphy comprises a reclamation fill overlying the marine deposits, alluvium and residual soils (completely and highly decomposed granite).

Figure 3 shows the cross section and schematic construction of the WKT station structure which is about 550 m long, 250 m wide and 30 m deep. A partial top down construction at the central and full top down at the two ends of the station is adopted. Bulk excavation takes place with a cut slope supporting the diaphragm wall with a slope of 1 in 2. Once the final excavation level is

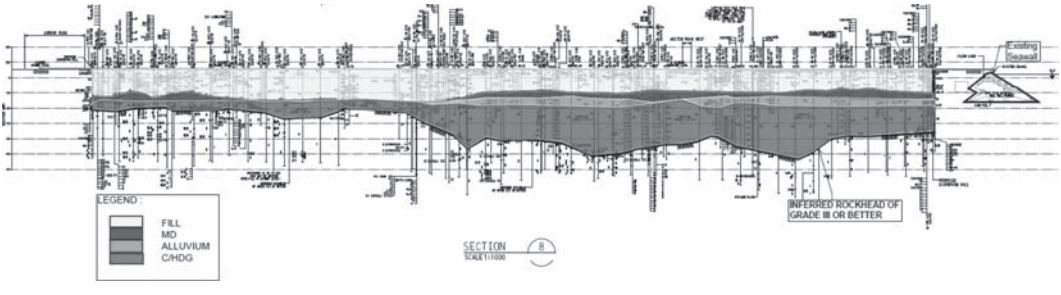

Figure 2. Geological stratigraphy of the site (N-S direction).

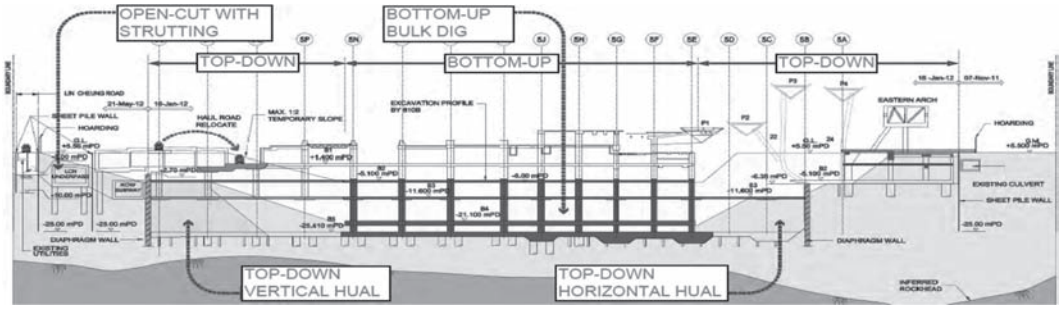

Figure 3. Cross section across the station (W-E direction).

reached, construction of the central portion of the WKT structure takes place by the bottom-up method. Progressive top-down construction of the remaining WKT structure then takes place with the floor slabs providing lateral support to the diaphragm wall.

3 PROBLEMS PROBABLY ENCOUNTERED IN TRADITIONAL USE OF AAA VALUES

As the construction of the WKT station structure was commenced in March 2011, the traditional use of AAA values would be followed because detailed monitoring requirements in the PNAP APP-18 and APP-137 were not available at that time. Because of the size and complication of the project, over 1,000 monitoring check points and instruments have to be installed. This becomes a very demanding daily task for the project team to interpret the monitoring data, check the behaviour of the Excavation and Lateral Support (ELS) systems and validate the design assumptions and design parameters. Due to the variance in the ground geology, the great depth and extent of the excavation, the nature and interfaces of the construction works, large settlements of ground and movements of ELS systems are anticipated. This may imply that an extensive amount of investigation reports are to be submitted to BD/GEO with many suspensions of works and reviews of ELS performance. Furthermore, the AAA values for the ground settlements are set traditionally as 15 mm, 20 mm and 25 mm respectively before the revision of the PNAP APP-18 and APP-137 in February 2012. These AAA values do not bear any direct relationship with the predicted settlements and are quite misleading to use as the control levels. Likewise, the estimated ELS system movements and the associated ground settlements in the ELS design are normally governed by the strength and serviceability requirements. They may not bear any direct relationship with the AAA values traditional adopted for the ELS system movements and ground settlements. Despite many check points and instruments could have far exceeded the traditional third A level, the works are repeatedly permitted to continue construction after performance reviews. As a result of this large number of exceedance of AAA levels, the alertness of the project team to watch over the monitoring readings may be reduced.

In order to overcome these drawbacks, a modified instrumentation monitoring plan is introduced. This modified plan supplements the site impact assessment report and is accepted by the BD/GEO and the concerned utility companies in advance. In this paper, the modified instrumentation plan is explained and illustrated with practical examples.

4 THE PROPOSED INSTRUMENTATION MONITORING PLAN

4.1 *Basic concept*

MTR is very proactive in instrumentation monitoring. According to the standard Material and Workmanship Specification, the AAA values are defined as "Alert, Action and Alarm". The Contractor is required to submit a Generalized Plan of Action Plan within 45 days of the date for commencement of the Works. This Plan is a plan of action determined in advance by the Contractor and approved by the Engineer for general response actions to be taken by the Contractor in the case of response levels being reached for each instrument type and certain groups of instruments and key locations. It shall include emergency response actions (i.e. Contingency Plan) to be taken by the Contractor in case of Alarm level is being reached. A Detailed Plan of Action based on the Generalized Plan of Action may be requested by MTR at Alert level before reaching Action level status. However, these requirements may still be impractical for a large and complicated but fast track project. Thus, MTR has streamlined the procedures so that some of the information as required by the Generalized Plan of Action can be submitted through design submissions and method statements when the construction activities become apparent. Furthermore, MTR has carried out more critical design checking in advance which is to be explained as follows.

Prior to the implementation of the modified instrumentation monitoring plan, the Engineer has carried out detailed assessment of the construction effect to the external sensitive receivers such as the existing buildings, structures, facilities, pavements, ground and utilities based on the method of construction, ground geology and geotechnical design. The movements of the external sensitive receivers and ELS systems are predicted. In different to the traditional instrumentation monitoring plan, AAA levels are set based on the predicted values for the response actions. The instruments are grouped to serve two main purposes. One group is for the protection of the external sensitive receivers and the other group is for the performance review of the ELS systems (could be extended to pile driving and similar operations). Prescribed mitigation measures are provided if the tolerable limits of the ground settlements and ELS system movements are exceeded. This modified instrumentation monitoring plan is introduced and supplements the site impact assessment report for the approval by the BD/GEO.

Table 1. Categories of sensitive receivers and response actions.

Sensitive receivers		Response actions for exceedance of AAA	
Categories	Examples	Settlement	Angular distortion
Category A (important structures)	Buildings/structures on piles and the seawall	Investigation reports and mitigation measures if required	Investigation reports and mitigation measures if required
Category B (semi-flexible utilities)	Gas main, fresh and salt water main Storm water main and sewer	No investigation reports or mitigation measures except at junctions to buildings	Investigation reports and mitigation measures if required
Category C (flexible utilities and pavements)	Cables such as electricity, telephone and cable TV	No investigation reports or mitigation measures except at junctions to buildings	No investigation or mitigation measures unless the change is abrupt
	Carriageway and footpath	Investigation report and resurfacing if the change is abrupt	Investigation report and resurfacing if the change is abrupt

4.2 *For the protection of the external sensitive receivers*

For the external sensitive receivers, settlements and angular distortions are the basic criteria for the AAA values, which are the same as the traditional AAA system and that recommended in the PNAP APP-137 (February 2012 revision). However, different types of sensitive receivers can tolerate different extent of settlement and angular distortion, and require different response actions. They can be categorized as in Table 1.

4.3 *For the performance review of the ELS systems*

In most situations, the estimated ground settlement caused by the movement of the ELS system may not bear any direct relationship with the traditional AAA values for the ground settlements. If, for example, the adjacent ground is bare or the utilities are supported, the tolerable limit of ground settlement can be larger than the traditional third A level, and the excavation can still be carried out in a safe manner. Despite this, investigation reports with mitigation measures are still required to be submitted to BD/GEO and a new third A level has to be approved before resumption of the Works.

In the modified instrumentation monitoring plan, the concept of minimum expected value, most probable value, and maximum expected value in the MTR Practice Note PIM/PN/11-22 is extended such that a new set of AAA values for design review are set from the predicted movements at several critical stages. This is similar to the tolerable ground settlement limits given in the PNAP APP-137 (February 2012 revision). All probable failure mechanisms are identified, and mitigation and contingency measures are provided in advance by the Contractor and approved by the Engineer and BD/GEO. During excavation, the design assumptions and design parameters are validated. Monitoring instruments along a design section are grouped for easy interpretations. Should the monitored ELS system movements and ground settlements deviate from the predicted trends, mitigation measures are implemented. Should the monitored ELS system movements and ground settlements reach the tolerable limits, contingency measures are implemented and the Work is ceased immediately. More thorough investigation report with further action plans are submitted to BD/GEO for approval before resumption of the Works.

5 MANAGEMENT OF THE INSTRUMENTATION MONITORING

5.1 *Management team*

In order to safeguard the unawareness of probable catastrophic failure, it is the contract requirement to establish a joint monitoring team. The team comprises the instrumentation team, geotechnical engineers, and the designer if necessary, of the Contractor, and the geotechnical engineers, construction engineers and detailed design consultant from the Client, and an Independent Monitoring Consultant (IMC).

5.2 *Management process*

During construction, the Contractor would measure the instrument readings and upload them to a unified web-based instrumentation database daily at a specified format agreed with

the IMC. The IMC would carry out a guarantee check to ensure all the uploaded monitored data are correct. Should there be any exceedance of the AAA value, a message would be sent to the responsible persons. The geotechnical engineers of the Contractor, the geotechnical engineers of Client and the IMC would meet on Monday and Wednesday to have a quick review of the monitored data. The joint monitoring team would meet on Friday to have a more thorough review of the monitored data and the weekly geotechnical instrumentation monitoring report prepared by the Contractor. The geotechnical engineer of the Contractor would report the main areas of concern of the report. Mitigation actions would be confirmed to implement if the measured data exceeded the Action level is reached. Works would be suspended temporary if the measured data exceeded the Alarm level. The RGE and BD/GEO would be notified immediately. Remedial measures would be proposed by the Contractor, reviewed by the Client, RGE and BD/GEO and implemented before resumption of the Works.

5.3 *Management reports*

All monitoring results would be uploaded daily by the Contractor to the unified web-based instrumentation database which is assessable by the joint monitoring team and designated persons. Detailed investigation reports would be submitted by the Contractor for any AAA exceedances. A weekly geotechnical instrumentation monitoring report as described in the previous section would be submitted by the Contractor to the Client for review. A weekly summary report would be prepared by the Technical Competent Person (TCP) grade T5 in the RGE Stream (RGE's T5) to the top management of the Client, the key TCPs and BD. A monthly report would be prepared by the RGE's T5 to the RGE, RSE and BD/GEO as traditionally required.

6 ILLUSTRATIVE EXAMPLES

In the WKT site, over 1,000 instruments, including ground settlement markers, utility settlement markers, standpipes, piezometers, inclinometers in diaphragm walls, slopes and Jet Grout Columns (JGC), were installed to monitor the construction effects to the adjacent sensitive receivers. They were named and grouped according to their locations for easy review and reporting. Furthermore, an Automatic Deformation Monitoring System (Tse & Luk 2011) was also installed to monitor the MTR tunnel which is not to be discussed in this Paper.

6.1 *Monitoring for the protection of the external sensitive receivers*

The works along a carriageway are chosen for illustration. These involved the installation of diaphragm walls, temporary cutting of a JGC stabilized slope, shoring and deep excavation for the station structure and the installation of socket H-piles, sheet piles, shoring and deep excavation for the taxi lay-by. External sensitive receivers affected by the construction were given in Table 2.

For the instruments monitoring the Austin Station, they were interpreted in traditional manner. However, for the instruments monitoring the fresh water main, they were grouped in string to determine the angular distortion. As shown in Figure 4, despite the settlement at a utility marker increased with time and reached 36 mm, the angular distortion at that point was 1:4712 only which is still within the tolerable limit. Thus, submission of the investigation report to BD and implementation of mitigation measure are not necessary. As a result, there was no interruption to the works and the BD was notified by RGE instantly through email and then by RGE's T5 weekly and monthly reports. For the instruments monitoring the carriageways and pedestrian footpaths, their surfaces were maintained regularly to avoid any abrupt change in levels, and the measured readings could therefore be reset and maintained within the tolerable limit all the time. Likewise, submission of the investigation report to BD is not required. As a result, there was no interruption to the works and the BD was notified by RGE instantly through email and then by RGE's T5 weekly and monthly reports.

Table 2. Sensitive receivers at the selected carriageway.

Category	Sensitive receivers
A	Austin station and MTR tunnel
B	200 mm diameter fresh water main
C	Road D1 and D1A carriageway and a pedestrian pavement

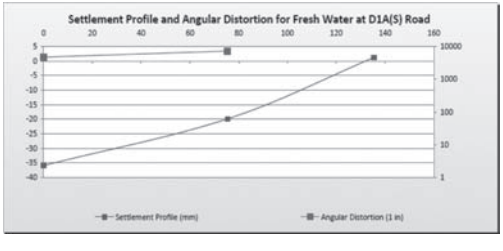

Figure 4. String of instruments to determine the angular distortion of the utility.

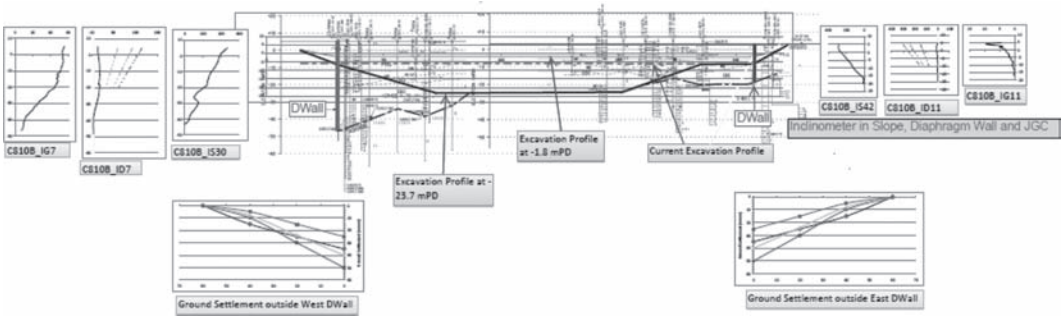

Figure 5. Group of instruments to study the performance of the ELS system.

6.2 *Monitoring for the performance review of the ELS system*

The bulk excavation for the construction of the station structure is chosen for illustration. As shown in Figure 5, instruments at each design section were grouped to study the performance of the ELS system which involved the interactions of the diaphragm wall, JGC and slope. The movements of the diaphragm wall, JGC, slope and the settlements of surrounding grounds, roads, footways, buildings, utility services and other features that would occur at each and every critical stage of works were estimated for monitoring.

Inclinometers in diaphragm wall at each design sections are chosen as bench marks for close monitoring and weekly reporting. In principle, the Alarm level at a location is taken as the maximum movement or settlement predicted in the ELS design and associated settlement analysis. AAA values are set as 50%, 80% and 100% of the prediction corresponding to the excavation level with a factor of safety not less than 1.2. For traditional projects, they are normally set as discrete values corresponding to the final excavation depth and profile for simplicity.

As shown in Figure 6, because of the scale and complexity in this project, they were set as discrete values corresponding to 4 critical excavation depths and profiles; i.e. –9 mPD, –17 mPD, –23 mPD and –32.6 mPD. For intermediate stages, they should be the interpolated values represented by the yellow, green and red curves respectively. The measured deformed profile of the diaphragm wall is also examined. If the measured profile deviates very much from the predicted profile, the geological design parameters and model have to be reviewed. For example, the trend of the maximum wall movement at an inclinometer was found increasing rapidly to 80.7 mm and approaching the Alarm level (i.e. 100% of the prediction) for –17 mPD. Excavation in front of the east slope stopped immediately.

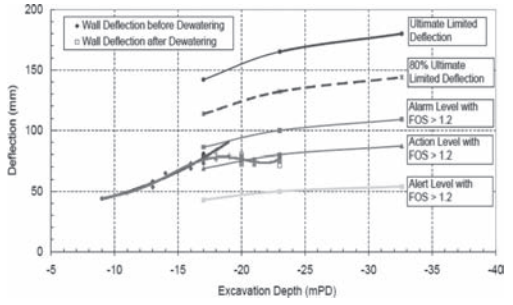

Figure 6. Plotting of deflection against excavation at an inclinometer.

Investigation and design review were carried out. Mitigation measures including lowering the water table at the back of the wall were implemented and excavation in front of the east slope could be resumed within a short period. The maximum wall movement was found reducing from the original of 80.7 mm at excavation depth of –17 mPD to later 71.3 mm at excavation depth of –23 mPD, which is below the Action level corresponding to this excavation depth.

7 CONCLUSIONS

A modified instrumentation monitoring plan was proposed following the concept of the Generalized Plan of Action and Detailed Plan of Action in the MTR Standard Material and Workmanship Specification. Instruments are grouped to serve two purposes. The first grouping is for the protection of the external sensitive receivers. They are categorized into types for different response actions as different sensitive receivers can tolerate different extent of settlement and angular distortion. The second grouping is for the performance review of the ELS systems. A new set

of AAA levels are determined from the predicted movements of the ELS systems at various critical stages. Probable failure mechanisms are identified from the geological models and PLAXIS analysis such that mitigation and contingency measures can be considered in advance. The daily task for the project team to interpret the monitoring data, check the behaviour of the ELS systems and validate the design assumptions and design parameters is alleviated. The amount of investigation reports to be submitted to the BD/GEO with many suspensions of works and performance reviews are reduced. Large deviation from the prediction can be rectified at early stage with lesser efforts and little interruption to the work progress.

REFERENCES

BD, 2004. *Code of practice for foundations*. Buildings Department, Hong Kong Government.

BD, 2012a. *PNAP APP-18-Requirements for an excavation and lateral support plan building (administration) regulation 8(1)(bc)*. Buildings Dep., Hong Kong Government.

BD, 2012b. *PNAP APP-137-Ground-borne vibrations and ground settlements arising from pile driving and similar operations.* Buildings Department, Hong Kong Government.

MTR, 2009. *Section 23-geotechnical instrumentation*. Materials and Workmanship Specification for Civil Engineering Works, Volume 3, MTR Corporation Limited.

MTR, 2010. *PIMS/PN/11-22/A1-Reporting of exceedances in instrumentation monitoring readings to senior management.* Project Integrated Management System PIM Practice Note, MTR Corporation Limited.

Tse, C. & Luk, J. 2011. Design and implementation of automatic deformation monitoring system for the construction of railway tunnel: a case study in West Island Line. In *Proceeding of Joint International Symposium on Deformation Monitoring*, Session 3H-02.

This page intentionally left blank

Geotechnical Safety and Risk IV – Zhang et al. (eds)
© 2014 Taylor & Francis Group, London, ISBN 978-1-138-00163-3

The impact of geometry bedding toward slope stability in coal mining

Supandi
Mining Engineering Department, STTNAS University, Yogyakarta, Indonesia

H. Hidayat
Geotechnical Department, PT Borneo Indobara, South Kalimantan, Indonesia

ABSTRACT: Bedding geometry is important in supporting the slope stability, particularly on low-wall part of coal mining. Elements that are part of geometry are bedding slope, slope height and bedding ratio. The key to this analysis is inserting geology conditions mainly bedding geometry. Bedding ratio value is calculated based on modeling geology in which more detailed modeling geology factor can be identified better analysis in slope stability. Slope stability analysis is assembled based on correlation between dip of bedding, bedding height and factor of safety. The result from this study is increasing bedding ratio value will be followed by increasing the factor of safety and bedding height. Changes in dip of bedding slope will impact on the slope stability and respond changes on factor of safety and bedding height. The final of the study is providing geo-mechanic parameters purposed for mine planning design based on site characteristic geology.

1 INTRODUCTION

Slope stability analysis is done routinely in mining, where it has some excavation and dumping activities. Analysis needs to be done by an appropriate method based on characteristics and the existence of geology conditions to facilitate geometry of the slope on which the design can be optimum. In general the purposed of slope stabilities analysis are:

1. Determining slope stability;
2. Defining the landslide mechanism;
3. Evaluating the support system and stabilization;
4. Optimizing the existing resources with a safety.

Geotechnical investigation must be done to support the parameter to improve quality analysis. One of the components that should be investigated is the geological condition in which the lithology and structural geology factor became an important component in the slope stability analysis.

The limit equilibrium concept is to compare between the driving force and resisting force. Driving force is controlled by slope geometry, in which material load, and resisting force is controlled by rock mechanics properties. Refers to this condition, it is important to determine the mechanical properties of the constituent stratigraphic along the slope. The performance of Geological structure and sedimentary structures is also important to know in order to determine the orientation from discontinue and daylight structure.

Through the structure of the sediment, it appears the term bedding. Bedding is similar to a layer of rock, in which two contact areas in the two layers confine bedding. Both of contact layers could be a thin layer that has important role in the slope stability. Generally, the contact material is at plastic material and it has a bad geo-mechanic properties. While the material forming the layers, the potential experience became thinning and thickening, thus leading to the form of bedding ratio. Each material has its optimum bedding height.

Through lithology factor, weak zone or carbonaceous zone, slope geometry and optimum bedding height information, drive in doing this analysis so that all components are correlated into a single unit in the slope stability. With a unity slope stability analysis, the value of slope stability in specified conditions is important in delivering this study.

2 BATULAKI BACK LIMIT EQUILIBRIUM ANALYSIS

Analysis was performed on the mining concession of PT Borneo Indobara—(Golden Energy Mine) located in the Barito basin formation Warukin in southern Borneo. In general, mudstone, clay stone, sandstone and coal materials dominate the material with hardness <1 MPa. Groundwater levels tend to be high and almost up to the surface (~3 m below surface). In the open mine mainly on coal mining, there are two terms high-wall and

low-wall (Fig. 1). High-wall slope is perpendicular to the layers and low-wall is in line to rock layers (bedding). Mining activities conducted at PT Borneo Indobara with open pit mine system by mining along the bedding dip. This study focuses on the slope stability analysis at the low-wall part of open pit coal mine.

Slope failure is occurred at the low-wall part at Batulaki pit in early May 2012. The failure occurs throughout the 200 m long, 40 m high and 5 m thick of mudstone with around 80 Kton material slides from low-wall part (Fig. 2). No injury, fatality and damage caused by it. Contact areas between carbonaceous zones about 20 cm of thickness with a 20 degrees dip of bedding control this failure. Another thing that encourages to the failure is the depletion downward where the obtained value bedding ratio <1.

To determine the slope stability at other locations, then carried back analysis based on these incidents. From the available data, there are several factors appear, that are dip of bedding, bedding height, bedding ratio and carbonaceous. According to those factors, back analysis is done so it can be used as improvement in the future analysis and design. Back analysis is done by involving all components above with slip surface in the contact area of the two materials. Back analysis conducted using the Slides 6.0 with limit equilibrium-based, it can be calculated the actual value of the material's mechanical properties. Based on the acquired properties,

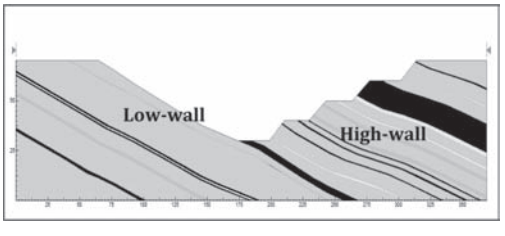

Figure 1. Overview definition low-wall & high-wall.

Figure 2. Failure analysis back area for this study.

geo-mechanic test material was resulted 18 kN/m^3 unit weight, cohesion of 87 KPa and friction angle of 22 degrees. Due to the fact that the failure occurred at the carbonaceous zone but because of the limitation of thickness it is hard to do testing so this value is not included in previous analyzes. With the landslide, it is carried the bulk sampling to the carbonaceous material and doing the geo-mechanic test. The test results on this material and the back analysis results obtained carbonaceous geo-mechanic properties are Cohesion = 0, Phi = 15^o and unit weight = 13 kN/m^3.

In addition to the material properties factor used for subsequent analysis performed also an analysis of the slope geometry. From the results of field measurement data showed that the landslide occurred at the height of 40 m and no instability occurs at a height below 40 m. Under these conditions, the correlation between the bedding geometry to slope stability is important. With reference to the conditions, in order to redesign and to review the slope stability at the site and surround, the analysis and modeling is applied to improve slope stability analysis on other location.

3 SLOPE STABILITY ANALYSIS

Slope stability analysis is done based on characteristic geo-mechanics properties based on laboratory test and back analysis results. Samples taken by drilling method and take bulk samples after the incident so that the geo-mechanic parameters are sufficient in this analysis. In concern, geological conditions in this analysis are dip of bedding, bedding height and bedding ratio. It is driven by the slip surface pattern using full specified on the carbonaceous zone, which assumed as a field delimiter in the bedding ratio calculation. Based on the explanation above, there are three main components in this analysis: dip of bedding, bedding height and bedding ratio.

Analysis is done based on existing geological condition, which relatively in common has similar dip of bedding. However, in some places obtained higher dip of bedding so the analysis conducted with another dip of bedding value. Modeling carried out on any dip of bedding so each of that can be obtained at the optimum value of bedding ratio. Bedding ratio used in the analysis was 1.5, 1 and 0.5.

The first modeling is done to make any correlation to bedding ratio toward factor of safety and bedding height. Any changes would have impact to other condition, so that it needs to do modeling in order to facilitate differences deviate from existing geological condition. Other modeling applied to discover optimum geometry where the optimum geometry is calculated at factor of safety 1.2 so

that all the information is in the model reflects the optimum factor of safety. Modeling applied to the optimum value to discover the correlation of dip of bedding, bedding ratio and bedding height. When creating the designs with existing field conditions, it can refer to both of this model so it can be used as guidance in the slope design.

Analysis is done is to discover the optimum height for each slope value which in any bedding slope was analyzed for each ratio. In one bedding ratio is analyzed 3 times by changing the bedding height. The bedding height used for this study in the analysis for all ratios are every 20 m, 35 m and 50 m. From the differences bedding height will get different factor of safety so it can be predictable the optimum bedding height for another condition. This analysis was repeated for each distinct bedding ratio value using the same analysis method to produce charts as Figures 3–5.

From the images above obtained information that the larger bedding ratio the greater factor of safety and the smaller bedding ratio followed by the decline of the factor of safety. One bedding ratio value can be obtained the correlation toward factor of safety and bedding height where the higher bedding height obtained the down of factor of safety. Based on the analysis contained in Figures 3–5, it shows the optimum bedding height for any bedding ratio. If using the stability optimum values at 1.2, it can be obtained at any bedding height for each bedding ratio in Table 1.

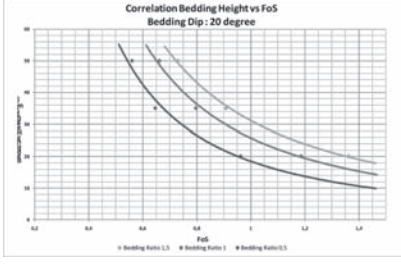

Figure 3. Correlation slope height vs FoS for 20° of dip.

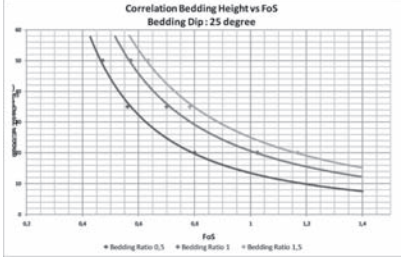

Figure 4. Correlation slope height vs FoS for 25° of dip.

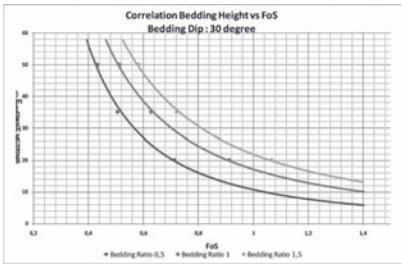

Figure 5. Correlation slope height vs FoS for 35° of dip.

Table 1. Summary optimum bedding height and bedding ratio.

Bedding ratio 0,5		Bedding ratio 1,0		Bedding ratio 1,5	
Height (m)	Dips (degree)	Height (m)	Dips (degree)	Height (m)	Dips (degree)
14	20	19	20	24	20
10	25	16	25	19	25
8	30	13	30	17	30

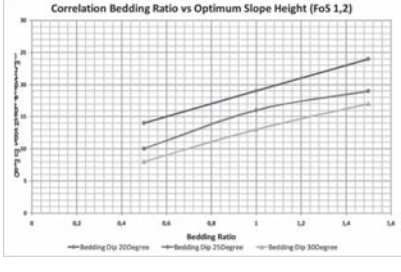

Figure 6. Correlation dip of bedding vs. optimum bedding height for factor of safety 1.2.

From the above table, it can be used as a basis model that correlates between bedding ratio and the bedding height on each slope. On this modeling chosen at factor of safety optimum so that the values are not optimum excluded from modeling. The final result is obtained by using factor of safety value of 1.2 so that all information contained in the model shows the value of factor of safety 1.2. From the data in Table 1 can be made the model shown in Figure 6.

Figure 6 shows the bedding ratio value on the x and the bedding height on the y. The lines shown in the model show the slope bedding value at the optimum conditions (factor safety 1.2). Based on the picture, it is concluded that the increasing bedding ratio responded by the greater bedding height.

The greater dip of bedding driven decreasing bedding height and the greater dip of bedding push down the factor of safety.

4 APPLICATION MODEL

Sediment-layered material made failure patterns that exist at the low-wall tend to be controlled by the contact zone. Contact layer usually as a formed of carbonaceous so that when the stratigraphic profile encounter this layer, then must be careful in determining the slip surface. The carbonaceous field stands as the interface between layers so that the overall stability low-wall built by individual bedding.

On the fact, many lithology of rock layers and carbonaceous zones where there is thickening below, thinning above and parallel layers. All gave impact on slope stability and should be considered in slope analysis. When doing slope stability analysis, first thing to do is making the geologic cross section based on geologic model. From the cross section will appear stratigraphy and slope geometry. After getting the stratigraphic profile, the main thing to do is identifying the contact zone or carbonaceous. In this case both materials referred to a weak zone.

Weak zones identified then proceed to calculate the thickness of the layer where the weak zone is underneath. Measurement is done perpendicular to the layer or bedding and performed at top and bottom of the layer/bedding. The upper part measured on crest and the lowest point measured at the location to be mined. The lowest point to be mined has many of factors that should be done based on the mining plan. From the thickness calculation of the top and the bottom will obtain the ratio bedding value. Bedding ratio 1 is the layer thickness should be equal between the top and the bottom. Bedding ratio <1 indicates the thickness of the bottom is smaller than the top while the ratio >1 indicates the thickness in the bottom is greater than the top.

Based on the explanation above, it should be considered in found bedding ratio is <1. It is based on rock mechanic concept that pressure will get greater at the toe to sustain more loads. Bedding ratio <1 had a greater risk because it receives a greater pressure for a particular area.

By knowing bedding ratio <1, it is known that there is a risk to the slope stability so that at the analysis should pay attention to this condition. Slip surface field followed the weak zones so that the analysis must apply the fully specified in order to force slip surface in this zone. Each layer in a particular slope at a certain point has optimum bedding height, so that applying the analysis and modeling can help providing guidance in geotechnical risk or provide mine design parameters.

Modeling simply in predicting the slope stability value based on the geology characteristics. From the geology data obtained from the field or from the geological model can be put in the model in order to obtain the optimum geometry to give optimum bedding height guidance for each layers or bedding. Model is effective in efforts to translate technical language into geo-mechanic common language which easy to understand.

5 CONCLUSION

Research conducted on the sedimentary basin with consist same rock formations that have relatively the same geo-mechanic and geology conditions. In this study tended to emphasize the relationship between the dip of bedding, bedding height and bedding ratio. The three factors have greatly effect to the slope stability. Each material in specific slope has optimum bedding height which to be considered in the mining design.

Analysis was conducted to determine the correlation between the factor of safety value towards the bedding height and dip of bedding at a certain bedding ratio. From the study, it is concluded that the increase of bedding ratio followed by a declining the factor of safety value, while the higher of bedding height reducing the factor of safety value. With those influence, it is necessary to find the optimum conditions.

The optimum conditions obtained from the modeling based on the analysis outcomes. The first model is performed to find the correlation between bedding ratio value toward dip of bedding slope and optimum bedding height. Other model is finding the optimum geometry using a factor of safety 1.2 decreasing from the previous model that is doing the correlation between dip of bedding toward bedding ratio and bedding height.

From the existing modeling assist a lot in identifying mining risk and can be used as guidance in constructing mining design. The field data or geology model data obtained can be put in the model so that it can quickly gather the geotechnical risk.

REFERENCES

Eberhardt E. 2003. *Rock slope stability analysis-utilization of advanced numerical techniques.* Geological Engineering, UBC, Vancouver.

Hoek, E. & Bray, J.W. 1981. *Rock slope engineering, third edition*. Institution of Mining and Metallurgy, Vancouver.

Hoek, E., Carranza-Torres, C. & Corkum, B. 2002. Hoek-Brown failure criterion. Vancouver.

Geotechnical Safety and Risk IV – Zhang et al. (eds)
© 2014 Taylor & Francis Group, London, ISBN 978-1-138-00163-3

Risk identification and mitigation for construction of a subway transfer station in Beijing

H. Wang & Z. Wu
Ranken Railway Construction Group Co., Ltd., Chengdu, China

D. Wang
Tianjin Institute of Urban Construction, Tianjin Key Laboratory of Soft Soil and Engineering Environment, Tianjin, China

ABSTRACT: More risks associated with subway transfer station construction than typical excavations due to larger depth and more interactions. Besides elaborate design and careful arrangements for constructions, monitoring is a critical process to control, predict and mitigate risks emerging possibly during construction, as well provides updated information to revise the design in a timely manner. This paper introduces a famous subway construction project-Jiaomen West Station, a transfer station for the existing subway Line 4 (M4) and the proposed new subway Line 10 (M10) in Beijing. Based on the project information, this paper identifies the risks associated to the project, introduces the methods to reduce and mitigate the risks; monitoring data are presented and discussed in association with the mitigation methods. Information presented in this paper and lessons learned from this case study are useful to the similar projects.

1 INTRODUCTION

Since the excavation depth and the intensive interactions with existing buildings, tunnels and other human-built environment, subway transfer station construction has more risks associated than interim station and the tunnel construction with Tunnel Boring Machine (TBM). Ground movement control is the principle factor to be considered in design and construction phases for reliable prediction of ground settlement; other issues, which are more or less related to the ground movement, such as the deflection of diaphragm walls, the consequent risk of the collapse of excavation as well as the damage to the existing structures are also important to the project.

Numerous literatures studied the risks associated with tunneling and subway station excavations. Sejonaha et al. (2009) categorized four types of failure, namely, (1) cave-in collapse; (2) significant exceeding of expected deformation of the tunnel tube; (3) exceeding of acceptable progress subsidence trough and (4) disturbance of water regime of in the surroundings. Gatti & Cassani (2007) studied the measures to control the ground loss in EPB (Earth Pressure Balance) TBM tunneling excavations. Hulme et al. (1990) reported and analyzed the ground settlement caused by construction of Singapore MTR, and classified the settlement to immediate component (ground loss) and the consolidation component. In order to reduce the traffic congestion in metropolitan areas, China is experiencing substantial development of subways or so-called Mass Transit Railways (MTR). Due to the complex of the project and the numbers of the undergoing projects, it is not surprised to see many accidents reported. Deng et al. (2010) conducted a research to statistically analyze the numbers, frequencies and patters of the subway construction accidents based on a total of 126 subway construction accidents which occurred in China from 1999 to 2008. Their statistical analysis indicates that the numbers of the accidents in China increased 5 times in 2008 from 1999, and the occurrence rate in January and July is the highest among the twelve months. Analysis by Li et al. (2006) indicated that the frequency of factors causing risk accidents in China is: 16.4% (complex or unrevealing geological and geotechnical conditions), 29.1% (poor design), 36.4% (casual construction), 1.8% (poor monitoring and supervising), 6.4% (poor management) and 10% (other reasons).

Based on a real and complex case study, this paper indentifies the potential risks associated with a famous subway construction project-Jiaomen West Station, which is a transfer station proposed for the existing Beijing Subway Line 4 (M4) and the new Subway Line 10 (M10). This paper introduces

the corresponding risk mitigation measures adopted in the project, such as dewatering, stabilization, pre-support measures and excavation sequences as well as the construction monitoring plans. Finally, monitoring data are presented and discussed to validate such measures. Information presented in this paper with respect to this case study is useful to the similar projects.

2 RISKS IN CONSTRUCTION A SUBWAY TRANSFER STATION IN BEIJING

As shown in Figures 1 and 2, the subway transfer station, Jiaomen West, is located in the intersection of Majia Pu West Road and Jiahe Road, Beijing. It was proposed to build for Beijing Subway Line 4 (M4), which is extended from north to south, and Beijing Subway Line 10 (M10), which is extended from east to west. The main structure for M4 is located below the intersection of the surface roads, and the new proposed covered undercutting for M10 needs to be constructed below the station of M4. High-rising residential and commercial buildings are congested around the corners of the transfer station. Moreover, a lot of utility pipelines were crossed over the excavation pit.

2.1 *Project description*

Station halls were designed at the two end sides of the stations both for M4 and M10, while the middle parts were proposed utilizing covered undercutting. Jiaomen West station for M4 was already built using a large span tri-arch cross section with a width of 22.1 m, the depth is about 8 m (to the top) and 18 m (to the bottom) below the ground surface (bgs). The proposed bottom slab of Jiaomen West Station for M10 is 27 m bgs, and a twin tunnels with a dimension of 10.25 m (width) by 9.15 m (height) will be excavated below the station for M4. The length of the covered undercutting is 35.1 m. Three transfer passages with different lengths were also to be excavated using covered undercutting technique.

The geological conditions of the site were shown in Figure 2 and summarized in Table 1 with more details. According to the geological investigation report of the project, the ground surface elevation is about 40.0 m, stable groundwater level varies greatly for each layer. Layers ④ and ⑤ are aquifers, layers $④_1$ and $⑤_1$ are aquitards. Fortunately, the groundwater in layers ④ and ⑤ is phreatic water.

2.2 *Risk identification*

Based on the project documents, the potentials of the risks for this project were studied. The following factors are identified as the sources to potentially cause problems during construction:

1. Geologic conditions
   The excavation depth requires the design performed correctly based on the reliable geologic data, the construction methods and risk mitigation measures evaluated accordingly. Moreover, the layers ④ and ⑤ consist of highly permeable cobbles with a very highly risk of water leaking during excavation and uplifting the bottom ground. Such leaking/uplifting may raise additional construction difficulties, or cause the stability problems of the bracing systems and the bottom ground of the excavation pit.
2. Engineering work
   The structural design is not risky as it is very mature already, the risks may exist on excava-

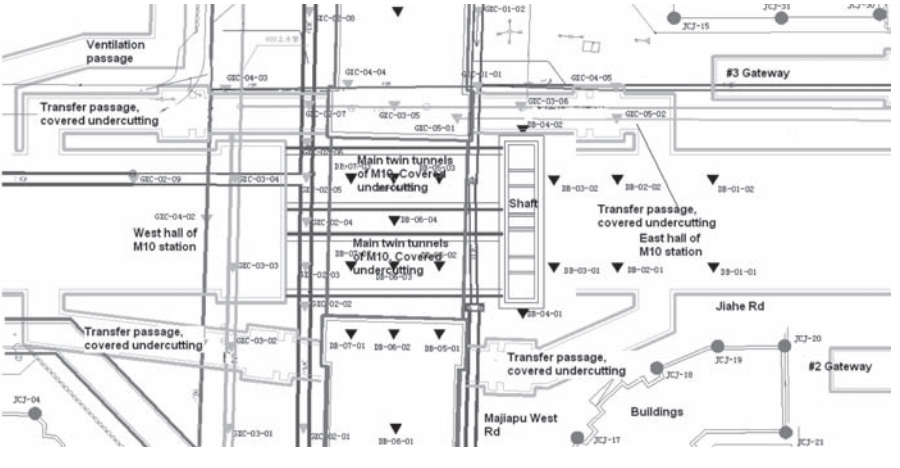

Figure 1. Jiaomen West Station for Beijing Subway M4 and M10.

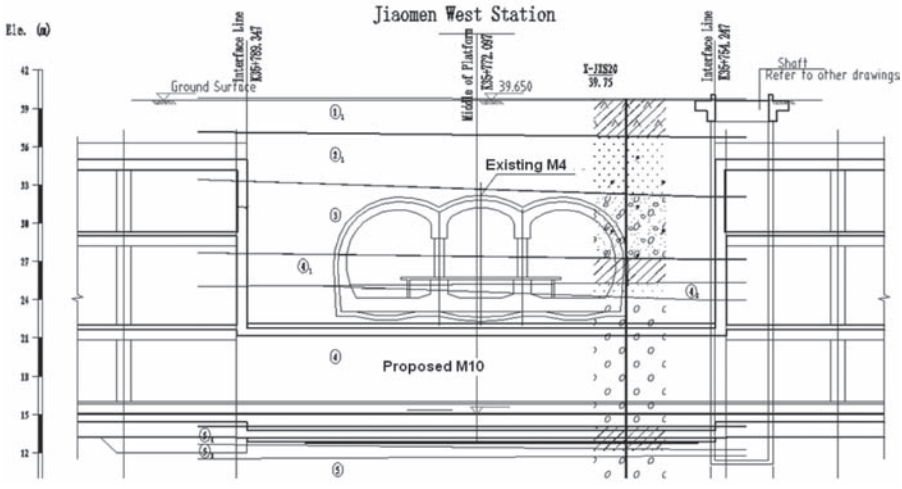

Figure 2. Cross-section of M4 and longitudinal section of M10.

Table 1. The geological conditions of Jiaomen West transfer station.

Layer	Descriptions
①$_2$	Backfill, clay mixed silt, bricks, cobbles, loose and inhomogeneous
②$_2$	Silty clay, yellow-brown, soft to stiff, wet, highly compressible
③	Cobble and gravels mixed with fine sands, medium dense, wet, size 2–5 cm, max. size 10 cm,
④$_1$	Clayey silt and silty clay, yellow, medium stiff, medium dense, medium compressible
④$_2$	Fine to medium sands, yellow, dense, wet, low compressible
④	Cobbles mixed with fine and medium sands, mixed color, dense, wet, low compressible. Size 2–6 cm, max. size 10 cm,
⑤$_1$	Clayey silt and silty clay, yellow, medium stiff, wet, low to medium compressible
⑤$_2$	Fine to medium sands, yellow, dense, saturated, low compressible
⑤	Cobbles mixed with fine and medium sands, mixed color, dense, wet to saturated, low compressible, size 4–8 cm, max. size 10 cm

tion bracing system design, strut selection and design as well as dewatering, particularly, the work mentioned above are more associated with geological and geotechnical conditions as well as construction workmanship.

3. Construction experience and workmanship
These involve in every process of the project construction. Particularly, the construction workmanship for the engineering work mentioned in item 2 is more important, even critical, to the entire project.
4. Construction management and supervision
Poor construction management may destroy a good project. Not only it is likely to reduce the project profits but also may cause project accidents or failure. Good supervision, however, may prevent this happening.
5. Construction monitoring
Underground work has high potential to cause settlement of ground, displacement of vertical strut, deflection of bracing system, damage to the utility pipes, etc. Rigorously monitoring is very helpful to indentify and control such risk, finally may make them avoidable. However, poor monitoring would not achieve the expected role.

3 MITIGATION MEASURES: CONSTRUCTION AND MONITORING PLANS

3.1 *Construction plans*

Bench-cutting method was proposed to undercut the soils below the bottom slab of Jiaomen West Station for M4. The maximum progress length for each excavation cycle was limited to 4 m. In order to stabilize and facilitate the soil excavation, the site was dewatered with stages described below; a shaft in east side of the station was built to provide construction space and mobilize personnel and equipment to the designed ground level; surroundings soils were then stabilized by grouting cement-silicate mortar into the ground along the long PVC sleeve valve pipes and pre-support systems, utilizing short perforated pipes to form umbrella vault, were installed. The details of the construction plan are described below:

1. Dewatering
   Three dewatering areas were scheduled: 1) Dewatering for shaft and covered undercutting construction below the station for M4; 2) Dewatering for excavation of east hall of the station, and 3) dewatering for excavation of west hall of the station. The depth of the wells uses 36 m bgs evenly with a spacing of 6 m along the circumferences of the excavations.
2. Shaft construction
   A shaft was proposed to provide the construction space and mobilize personnel and equipment to the designed ground level for undercutting. The shaft is 26.5 m deep and is in a rectangular shape with a dimension of 25.9 m by 9.6 m. The bracing system for the shaft consists of bored piles, horizontal struts and a capping beam which was designed in conjunction with those designed for excavation of the east and west halls of the station.
3. Stabilizing the surrounding soils
   Prior to undercutting the soils below the station for M4, grouting techniques are proposed to stabilize the soils surrounding the tunnels of M10. The area of the stabilization is shown in Figure 3. PVC sleeve valve pipes with a diameter of $\phi = 56$ mm and varying lengths from 10 to 13 m are used to pressure cement-silica mortar materials into ground. As shown in Figure 5, the spacing of such long PVC pipes utilized 1.0 m by 1.0 m and applied perpendicularly to the cross-section of the undercutting. The designed 3-day unconfined compressive strength of cement-silica-soil material is no less than 1.0 MPa with a permeability coefficient less than 0.1 m/day.
4. Bench-cutting sequence and pre-support system
   After the soils surrounding the tunnels for M10 are stabilized, excavation proceeds with bench-cutting method. As shown in Figure 4, the sequence of bench-cutting is as follows: 1) Proceed with the right tunnel, install umbrella vault system using grouting technique with small perforated pipes to pre-support excavations, cut the improved cement-silica-soil material in area I; 2) cut the cement-silica-soil material in area II, and install the preliminary lining and steel trusses; steel trusses were locked to the locking anchor pipes which were inserted and grouted to the ground; 3) cut the cement-silica-soil material in Area III, install the preliminary lining and steel trusses; 4) apply and repeat the above construction sequence for areas IV, V and VI respectively; 5) apply and repeat the above procedures for the left tunnel.

   The length of the bench used in above procedure is about to 5–10 m so that the progress for each construction cycle is limited to 4 m. The excavation for the right and left tunnels shall be apart at least 10 m along the longitudinal direction to avoid interactions during excavation.

As shown in Figure 5, umbrella vault system was installed to provide pre-support for bench-cutting each area of the cross section. Grouting materials utilized 1:1 cement-silica mortar and the mortar were pressured into the soils via the perforated pipes with a diameter of 32 mm. Such pipes were installed with different upward angles (45°and 15°) due to the limitations of the bottom slab of the station for M4 and the short PVC sleeve valve pipes. The spacing for small perforated pipes utilizes @ = 1000 mm in longitudinal direction while @ = 400 mm along the circumference of the undercutting.

3.2 *Monitoring plans*

Monitoring the construction is important as it can predict potential risks such as excessive settlement, horizontal deflections and collapse, etc, as well provide the data in a timely manner to modify the

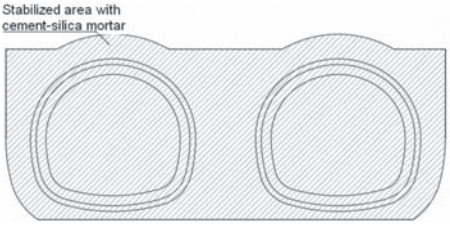

Figure 3. Stabilizing the soils surrounding the twin tunnels for M10.

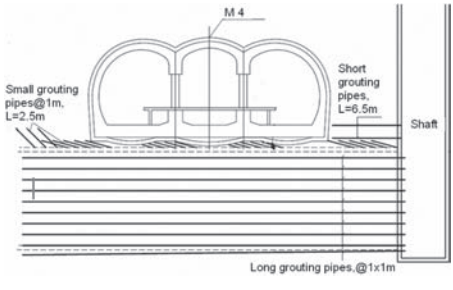

Figure 4. Bench-cutting sequence and umbrella vault installed with excavation progressing.

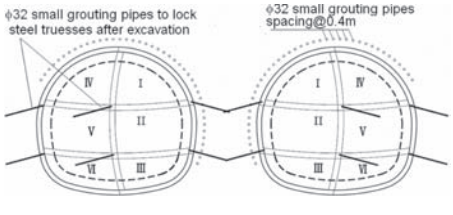

Figure 5. Umbrella vault system and soil stabilization (longitudinal section view).

Table 2. Monitoring items and the control criteria.

No.	Classification	Monitoring targets	Monitoring item	Accuracy	Control criterion
1	Environment around the undercutting	Buildings around the station	Settlement of buildings	1.0 mm	20 mm
2		Utility pipes, including ϕ 1000 and ϕ 1800 storm sewer pipes, ϕ 1000 sewage pipes, ϕ 400 gas pipes and ϕ 400 water supply pipes, etc	Settlement of the pipelines	1.0 mm	Water and gas pipes: 10 mm; storm and sewage pipes: 20 mm; rate: 2 mm/d
3		Roads and ground surface	Settlement of ground surface	1.0 mm	30 mm; rate 2 mm/d
4		Structures of existing station for M4	Vertical and horizontal displacements in structures	0.3 mm	10 mm (absolute); 5 mm (differential)
5			Vertical and horizontal displacements in track-bed structures	0.3 mm	10 mm (absolute); 5 mm (differential)
6			Deformation of deformation joints in structures	0.1 mm	3 mm
7			Distance of rail tracks	1.0 mm	+4 mm, –2 mm
			Geometry of rail tracks	1.0 mm	4 mm
8			Geometry of seamless rail track	0.3 mm	2 mm
9		Connecting passage and gateways for M4	Settlement of interface structures	1.0 mm	3 mm
10			Settlement of gateway structures	1.0 mm	5 mm
11	Bracing system	Excavation pits for main structures and auxiliary structures	Deflection of bracing pile heads	1.0 mm	30 mm
12			Deflection of bracing piles	1.0 mm	30 mm
13			Forces in struts	1.0% F·S	–

design. Table 2 summarizes the items to monitor and the control criterion utilized for monitoring in construction. Due to the length limitation of the paper, the plan of the monitoring points is shown in Figure 1 partially. In the plan, DB means the points monitoring the settlement of ground, JCJ means the points for monitoring the building settlement and GXC means the points for monitoring the settlement of the utility pipes.

Project management classified the monitoring data to three levels to issue alarm warning, 1) yellow; 2) orange; and 3) red. The classification is based on the absolute value and the rate of the monitored data. Table 3 summarizes the criterion of the three levels for warning issuance.

Table 3. Criteria for alarm warning issuance.

Alarm warning level	Criterion for alarm warning issuance
Yellow	Both absolute value and the rate of the monitored data exceeding 70% of the control criterion, or one of them exceeding 85% of the control criterion.
Orange	Both absolute value and the rate of the monitored data exceeding 85% of the control criterion, or one of them exceeding 100% of the control criterion.
Red	Both absolute value and the rate of the monitored data exceeding 100% of the control criterion, or the rate of the monitored data varies dramatically.

4 MONITORING DATA EXCEEDING CRITERION

The monitoring work was performed in accordance with the frequency requirement associated with the construction progress. Table 4 summarizes the monitoring data that exceeds the control criterion or alarm warning levels. During the constructions, alarm warnings at different levels were issued in these monitoring points and construction measures were taken accordingly, and the trend of the deformation thus suspended.

When excavating for shaft and covered undercutting for the twin tunnels, ground surface shows

Table 4. Monitoring items for main structures of the station exceeding the control criterion.

No.	Item description	Location description (monitoring point #)	Accumulative deformation (mm)	Monitoring conclusions
1	Settlement of ground surface	Above the undercutting (DB-05-03)	–24.6	Exceeding the alarm warning level
2	Deformation of track bed structures	Right alignment stationing (K1+536.2)	–15.2	Exceeding the control criterion
3	Distance of tracks	Right alignment stationing (K1+563.0)	–3.0	Exceeding the control criterion
4	Settlement of ground surface	Northwest transfer passage (DB-44-01)	–27.5	Exceeding the alarm warning level
5	Settlement of utility pipelines	Northeast transfer passage (GXC-37-02)	–16.8	Exceeding the control criterion

subsidence accordingly, the maximum settlement occurred right behind the cutting face at point DB-05-3, which is above the right twin tunnel. Monitored data also shows the subsidence of ground around the east and west exaction pit. However, the rate of the settlement around excavation is small and the maximum settlement occurred at DB-13-03 (east part of the excavation pit of the east hall), but not exceeding the control criterion. Analysis indicated that the backfill behind the bracing system is not compacted well and is more influenced by the excavation, the consolidation of the backfill also contributed to the settlement observed. As for the movement of track and track bed structures, it was caused by the subsidence of the soils surrounding the twin tunnels. Such movement is probably inevitable as long as the ground loss occurred, and probably, the control criterion for such movement will govern the stabilization design for the covered undercutting.

One of the interests is the monitoring data for transfer passage (which was not shown in Fig. 1 due to length limitation of this paper) exceeds the criterion. The dimension of the cross-section, the treatment and excavation methods for the transfer passage are similar with those applied in twin tunnels, except the overburden depth is almost half of the covered undercutting for the twin tunnel. Thus, the reasonable explanations could be 1) shallower overburden depth lead to more obvious ground subsidence observations and 2) poorer construction quality lead to more subsidence observed.

5 CONCLUSIONS

This paper identifies the risks associated with a subway transfer station construction in Beijing. Mitigation plans are introduced and the monitoring data are presented. Conclusions are made from the project that 1) elaborate design and careful construction arrangement are important to a safe and successful project; 2) monitoring is a critical process to construction; 3) covered undercutting has more risk potential that may lead to more ground subsidence than open excavations; and 4) with respect to covered undercutting, construction quality and overburden depth may play a role for ground subsidence. Lessons learned from this project are: 1) every underground project is unique, even in the same project, covered undercutting for transfer passage and twin tunnels may lead to different settlement; 2) attention should be paid to more details no matter how small the project is. Actually, auxiliary parts of the project may deserve more attention though people usually do to big and main part.

REFERENCES

Deng, X.P., Li, Q.M. & Zhou, Z.P. 2010. Statistical analysis of the accidents of subway construction in China. *Chinese J. Statistics and Decision* 9: 87–89.

Gatti, M.C. & Cassani, G. 2007. Ground loss control in EPB TBM tunnel excavations. In J. Bartak, I. Hrdina, G. Romancov & J. Zlaml (eds), Underground Space-the 4th Dimension of Metropolis; *Proceedings of the World Tunnel Congress 2007 and 33rd ITA/AITES Annual General Assembly, Prague, May 2007*. London: Taylor and Francis Group.

Huang, M.T. 2011. Dewatering practice for a deep subway station excavation. *Chinese J. Modern Urban Transit* 3: 58–61.

Hulme, T.W., Shirlaw, J.N. & Hwang, R.N. 1990. Settlement during the underground construction of the Singapore MTR. In *Proc. 10th South East Asian Geotechnical Conference, Taipei, 1990*.

Li, T., Xu, L.P., Chen, H. & Gu, G.R. 2006. Quantitative Analysis of risks of foundation excavations. *Chinese J. Geotech. Eng.* 11(28): 1917–1920.

Sejonaha, J., Jaruskova, D., Spackova, O. & Novotna, E. 2009. Risk quantifications for tunnel excavation process. *World Academy of Sciences, Engineering, and Technology* 58: 393–401.

Geotechnical Safety and Risk IV – Zhang et al. (eds)

Ground anchor considerations for crane footings adjacent deep rock excavations

N.R. Wightman
Sinclair Knight Merz (HK) Limited
Formerly SMEC Asia Ltd.

A.D. Mackay
Nishimatsu Construction Company Limited
Formerly SMEC Asia Ltd.

ABSTRACT: To increase power output from the Magat Pumped Storage Power Station, Luzon Island in the Philipines, additional power generating equipment will be installed immediately adjacent to the existing pump storage system. A concept design for the open cut excavation needed to install the equipment involved rock excavation to an average of 60 m below the existing ground level with a 22 m span. To allow equipment placement and future maintenance access into the excavation a 325 tonne load capacity gantry crane spanning the excavation was proposed. The crane will run on rails placed onto rock with sufficient bearing capacity to support the dead and live loads exerted during operation. Based on a site inspection, literature search and preliminary ground investigation the rock mass bearing capacity will depend upon the presence and characteristics of the rock joints. These included potentially persistent joints, continuing the length of the excavation, with calcite coating and an adverse orientation with respect to the excavation, trending parallel to the sides of the excavation and dipping about 60 degrees into the excavation. The calcite potentially reduces the joint surface shear strength to a friction angle of about 20 degrees. To increase the shear resistance it is intended to install six high strength proprietary rock anchors (each with 16 strand multi-core tensioned cables and capable of imposing loads over 2,200 kN) perpendicular to the joint orientation. This paper summarizes the anticipated ground conditions, the potential bearing capacity of the ground supporting the crane and the ground anchor installation proposed to improve the rock mass strength.

1 INTRODUCTION

The Magat Pumped Storage Power Station comprises an existing dam, spillway and penstocks constructed in 1976. Due to the increased power demand in the area additional power generation is now required which will be provided by additional power generating equipment to be accommodated in an open cut rock excavation. The current proposal is to install the power house equipment into the excavation using a 325 tonne gantry crane spanning the excavation. In order to reduce the additional volume of reinforced concrete required to support the gantry crane and keep space for power station operation, it is proposed to place the crane rail footings onto competent rock away from the excavation perimeter. The regional geology comprises volcanic rock, with pyroclastic breccia and lapilli tuff inclusions and a fault zone running through the proposed excavation location. The joints anticipated during the excavation are adversely orientated with respect to the excavation gradient and alignment. As part of the concept design the rock mass stability, supporting the gantry crane footings, will be improved by the installation of six proprietary high capacity multi-strand cables beneath the rail footings. The installations will increase the frictional resistance against sliding along the joints.

2 POWER STATION SETTING

2.1 *Location*

The existing power station is located at Magat, north Luzon in the Philippines. Refer to Figures 1 and 2 for the general location.

It is intended that the additional power generation plant will be a stand-alone structure located in close proximity to the existing powerhouse accommodated in an open cut excavation. Refer to Figure 3 for the Dam location.

2.2 *Geology*

The geology at Magat comprises volcanic rock from the Lower Miocene to Upper Miocene geological

Figure 1. Magat, Philipines (Google Earth, 2011).

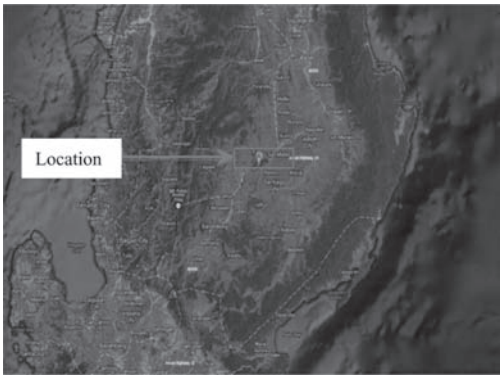

Figure 2. Magat, Luzon Island (Google Earth, 2011).

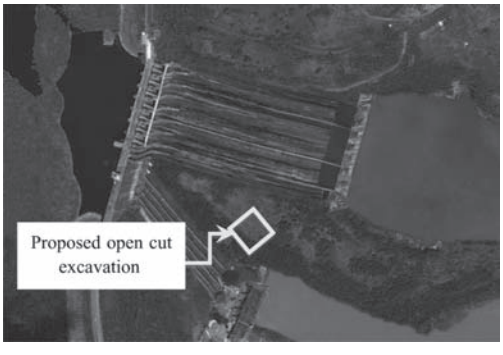

Figure 3. Aerial view of the existing power station and proposed site location.

periods (Geological map, Mines and Geoscience Bureau, Philippines, 2010). The volcanic rock comprises 'Agglomerate'. This mainly includes "pyroclastic breccia", which is very coarse grained and coloured dark grey to greenish grey with clast sizes up to 150 mm diameter in a welded matrix, and "Agglomeratic Sandstone", which is a biotitic crystalline lapilli ash tuff, comprising welded volcanic and igneous rock fragments from silt 0.06 mm up to about 4 mm.

Figure 4. General view of the dam looking north west.

Figure 5. Regional active fault locations (Mines and Geoscience Bureau, Philippines, 2010).

The structural geology includes faults and shear zones. Major structural features which have influenced the surrounding area include the active Major Philippines Fault, located about 75 km to the west of the site, trending North-North-East (NNE) to South-South-West (SSW), and a large active transverse fault, trending West-North-West (WNW) to East-North-East (ENE), located 50 km to the south of the site.

2.3 *Engineering requirements*

A pre-requisite for the construction of the additional power generation plant was that no disruption to the on-going power generation operations would be allowed. Of the available options the cable anchor installation was preferred to stabilise the ground beneath the crane footing. This provided a reduction in the quantity of concrete required for the gantry crane footing and, as a result, a reduction in the excavation quantity, which was the main anticipated cause of disruption to the power generation operation. The open cut

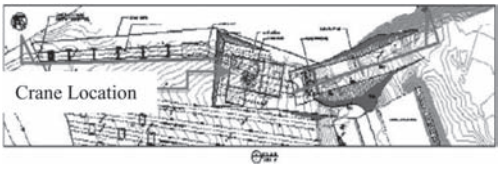

Figure 6. General layout plan of the planned extension (SMEC, 2011).

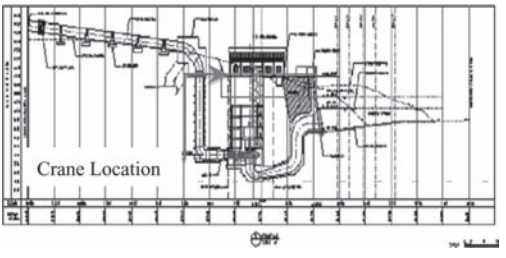

Figure 7. General layout section of the planned extension showing crane location (SMEC, 2011).

excavation was therefore positioned with sufficient space to allow the installation of the cable anchors. Figures 6 and 7 present the proposed open cut excavation in relation to the existing dam.

2.4 *Ground conditions*

The rock condition in the vicinity of the gantry crane footings was determined by site inspection and a preliminary ground investigation.

These revealed the presence of inter-bedded pyroclastic breccia and lapilli tuff rock with discontinuities comprised bedding and closely spaced joints. The average major joint set orientations were revealed to be 32°, N166° and 56°, N214°. These approximately corresponded with the two main faults identified west of the site, trending NNE to SSW, and south of the site, trending WNW to ENE, respectively. The joints also exhibited slickensiding and calcite deposits along the surfaces. Major zones of jointing, identified during the site inspection are presented in Figure 8.

The rock mass was moderately strong to strong (British Standard, BS5930:1999 and A2:2010, 2010) and, based on laboratory testing, had unconfined compressive strength values ranging from 13.4 to 92.0 MPa, averaging 40.4 MPa (moderately strong). Frictional resistance along rock joints with rock surface contact, with a rough undulating profile, typically range from 42° to 45° (Hencher et al., 2011 & Richards & Cowland, 1982). However, due to the presence of calcite veining and slickensiding, "polishing" along the

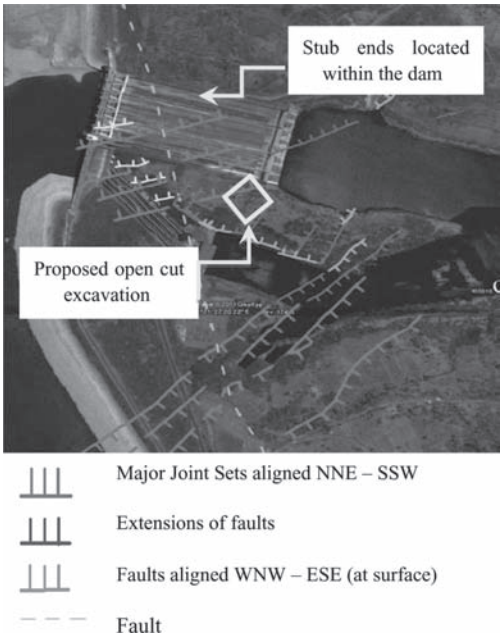

Figure 8. Areas of major jointing in the vicinity of the site.

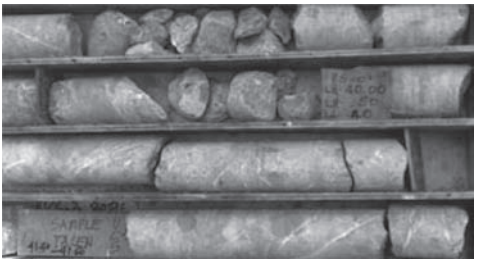

Plate 1. Calcite veining in fresh volcanic rock.

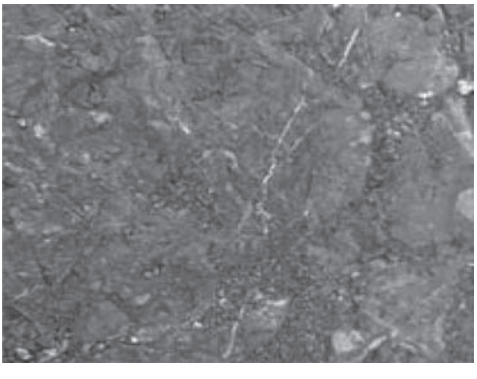

Plate 2. Calcite veining at outcrop.

joints (refer to Plates 1 and 2) the estimated joint frictional resistance was reduced to 22° (Lembo Fazio et al., 1990). As a result of this reduced frictional resistance robust stabilization measures were needed to improve the shear strength resistance along the joint surfaces.

3 CABLE SUPPORT TO CRANE FOOTINGS

3.1 *Position of crane footings*

The proposed crane footings are to be positioned either side of the open cut excavation, see Figure 9. To support the loading exerted from the crane the footings will be keyed into the rock with additional support provided by the installation of ground anchors immediately beneath the footings. The ground anchor heads will be incorporated into the reinforced concrete footings to ensure a robust tie back of the concrete block into the rock mass.

3.2 *Anchor support to the crane footings*

The aim of the rock anchor installation will be to increase the load across the joint surface thereby increasing the shear strength. To ensure the load capacity and long-term rock anchor strength is achieved, proprietary ground anchors with a 16 strand multi-core cable anchoring system, were proposed in the concept design. Based on the data available 6 No. anchor cables, each loaded to approximately 1,500 kN and increased to 2,165 kN to account for the factor of safety (BS8081, 1989), will be required. Based on the manufacturer's proprietary literature each anchor would need to have a diameter of 115 mm and a 200 mm formed hole to allow anchor installation. Each anchor had an estimated total length of 30 m, a minimum anchor length of 10 m (allowing for full rock to grout contact) and minimum sheathed length of 7 m (See Figure 10).

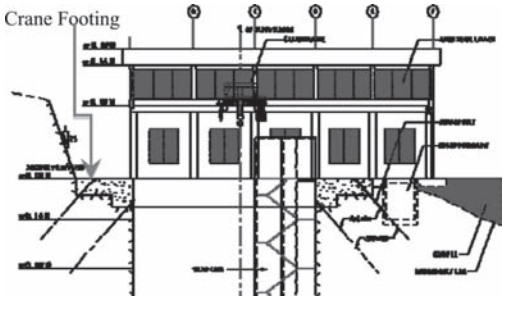

Figure 9. Location of crane footings and grouted multi-strand cables.

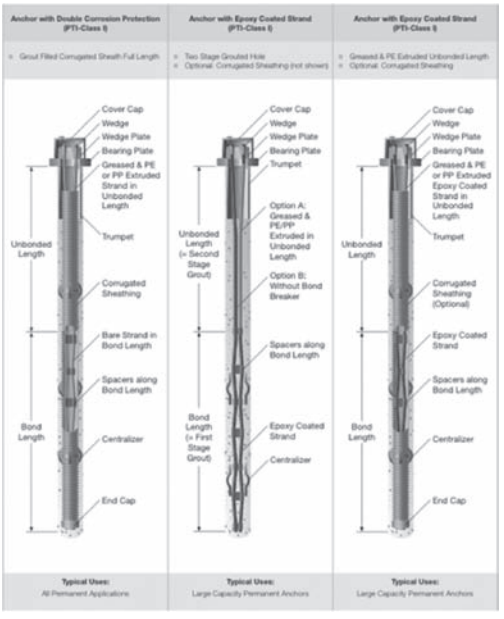

Figure 10. Permanent anchors example by Dywidag (2012).

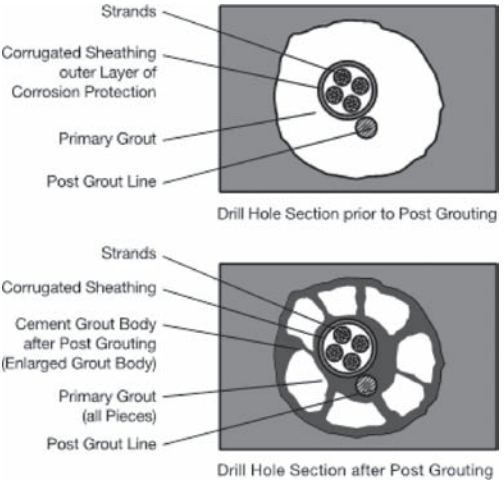

Figure 11. Grouting of permanent anchors (Dywidag, 2012).

Following rock anchor installation post grout tensioning devices, jacking off and bearing onto heavily reinforced sections of the crane footings, are anticipated. Figure 10 shows a typical multi-strand cable system (Dywidag, 2012), with corrosion protection by epoxy coating for long-term anchor installation. Figure 11 (Dywidag, 2012) shows a schematic of the anticipated two phase

grout injection to ensure the rock to anchor bond is complete following installation of the anchor.

The crane will be positioned on solid ground at the end of the crane rail alignment, away from the excavation when not in use. This avoids continual loading of the ground anchors when the crane not in operation.

4 CONCLUSIONS

The use of high strength anchors provided a solution to the potential foundation instability along adversely orientated joints beneath the gantry crane footings at the Magat power station site. The solution reduced the excavation required to form the concrete footings thereby reducing disruption to on-going power generating operation. Based on the available data, six high capacity proprietary multi-core cable anchor, with approximately 16 no strands in each anchor for each footing will be required. A maximum load capacity of 2,165 kN is required for each multi-strand cable anchor. This provids sufficient resisting force to increase the shear strength across the rock joints.

ACKNOWLEDGEMENTS

The authors wish to thank the SMEC design team, particularly Mr. Andreas Neumaier for feedback on the submission and the project sponsor SN Aboitiz. The opinions expressed in this paper are those solely of the authors and not of any other party. The authors would like to thank Ronald Chan for his assistance in the presentation.

REFERENCES

British Standards (BS) 5930:1999 + A2:2010 (2010). Code of Practice for Site Investigations. British Standards Institution (BSI). London. 147p.

BS8081:1989 (1989). Code of practice for ground anchorages. British Standards Institution (BSI). London. 180p.

Dywidag Systems International (2012). Dywidag Strand Anchors Systems brochure.

Google Earth (2011). Searchable map/satellite view of the Republic of the Philippines.

Hencher, S.R., Lee, S.G., Carter, T.S. & Richards, L.R. (2011). Sheeting Joints: Characterisation, Shear Strength and Engineering. Rock. Mech. Eng., 44:1–22, Springer.

Lembo Fazio, A., Ribucchi, R. & Tommani, P. (1990). Sheared bedding joints in rock. engineering: Two case histories in Italy. Rock Joints, Barton & Stephansson (eds) A.A. Balkem, Rotterdam, pp. 83–90.

Mines & Geoscience Bureau, (2010). Geology of the Philippines (Second Edition), Mines and Geoscience Bureau, Department of Environment and Natural Resources, Quezon City, Pilippines, 532p.

Richards, L.R. & Cowland, J.W. (1982). The effects of surface roughness on field shear strength of sheeting joints in Hong Kong Granite. The Engineer, Vol. 10, No. 10, pp. 39–43.

SMEC (2011). Feasibility Design Report, Magat Pumped Storage Project, July 2011.

This page intentionally left blank

Geotechnical Safety and Risk IV – Zhang et al. (eds)
© 2014 Taylor & Francis Group, London, ISBN 978-1-138-00163-3

Upper bound finite element method for seismic stability limit analysis of rockfill dams

X.G. Yang & S.C. Chi
School of Hydraulic Engineering, Dalian University of Technology, Dalian, China

ABSTRACT: In this study, an upper bound limit analysis Finite Element Method (FEM) is developed to study the seismic stability of rockfill dams. Considering the large value of the internal friction angel and the non-linear shear strength parameters of rockfill materials, a static form, which is corresponding dual Second-Order Cone Programming (SOCP) problem of the upper bound limit analysis, is formulated with constraints based on the yield criterion, flow rule, boundary conditions and the energy-work balance equation. The upper bound solution of critical seismic coefficient is then obtained by a state-of-the-art interior-point algorithm iteratively. Compared with the limit equilibrium method, the proposed method is applied to the seismic stability problem of a typical rockfill dam. The results demonstrate the correctness and practical value of the proposed method. From the displacement field obtained by solving the SOCP, we can predict the failure surface of the dam slope easily.

1 INTRODUCTION

Numbers of rockfill dams are built in the southwest area of China, which is also an earthquake-prone zone. Since Wenchuan earthquake, the safety assessment of rockfill dams in earthquakes has attracted growing concern and wide attention of geotechnical engineering.

Landslide is a common failure mode of rockfill dams in earthquakes. For this reason, the analysis of seismic stability of dam slopes is a very important issue. Many researchers are attempting to elaborate and develop new calculation methods to analyze the seismic stability problems. However, the conventional pseudo-static approach is still widely used in engineering design (Loukidis et al. 2003). In this study, the seismic stability of the dam slope is expressed in terms of a single parameter, the critical (or yield) seismic coefficient, k_c. The critical seismic coefficient, k_c, is the ratio of the seismic acceleration, a_c, yielding a factor of safety equal to unity, to the acceleration of gravity g (= 9.81 m/s^2). For the rockfill dam, a_c is also the maximum anti-seismic capability.

The pseudo-static approach is traditionally implemented in limit equilibrium methods to assess the seismic stability of the slope. However, neither static nor kinematic admissibility is necessarily satisfied in limit equilibrium. Limit analysis, as an alternative approach, has been a powerful tool that provides rigorous lower and upper bounds to the exact collapse load in recent years. Sloan and his cooperators (Sloan 1988, Sloan 1989, Sloan & Kleeman 1995) have made significant progress in developing the Finite Element (FE) limit analysis for stability and bearing capacity problems. In order to solve the mathematical programming easily and conveniently, a Linear Programming (LP) problem of lower or upper bound limit analysis is formulated based on the linearization of the yield function in their works. However, the error of calculation caused by the linearization increases with the value of the internal friction angle φ. Therefore, the LP mathematical model of the limit analysis is suitable for the state of $\varphi = 0$ or smaller φ. For the simplicity, the linear approximation of the failure envelope has been widely accepted for over half a century in which the shear strength of a material is described by two parameters, namely the cohesion and friction angle. It has been argued that due to the nonlinearity, these two parameters are not independent of stress level and consequently not constant (Li & Cheng 2012).

Unfortunately, a substantial number of experiments (Indraratna et al. 1993, Yamaguchi 2008) have clearly shown that the rockfill materials process two main properties: the large value of the internal friction angle φ; and the nonlinear nature of the shear strength parameters, which are commonly expressed in terms of stresses. Consequently, the FE limit analysis of the stability problems of rockfill dam slopes can't be formulated as an LP problem.

During the last decade there has been considerable progress in the application of nonlinear programming, which allows the yield function to

be treated in its native form. Recent research by Makrodimopoulos & Martin (2006, 2007a, b) has concentrated on FE limit analysis using Second-Order Cone Programming (SOCP) to solve stability or bearing capacity problems with the native form of the yield function. Based on the work by Makrodimopoulos & Martin (2007a), this paper develops an upper bound FEM to analyse the seismic stability of rockfill dams. With the native form of the yield function, the error caused by the large value of the internal friction angle can be reduced. Moreover, a static form, which is corresponding dual SOCP problem of the upper bound limit analysis, can be formulated. This means we can get the stress field of the dam in a weak sense, which can be used to determine the nonlinear shear strength parameters of rockfill materials iteratively.

2 UPPER BOUND THEOREM

Consider a rigid, perfectly plastic construction V with boundary S; according to the upper bound theorem, when the structure collapses, there exists a kinematically admissible displacement field such that energy dissipation is no more than the work of external force:

$$\int_V \boldsymbol{\sigma} : \boldsymbol{\varepsilon}(\mathbf{u}) \mathrm{d}V \le \mathbf{q}^{\mathrm{T}}\mathbf{u} \tag{1}$$

where $\mathbf{q}$ are equivalent nodal loads; $\mathbf{u}$ should satisfy the boundary conditions of S, $\mathbf{u} = \mathbf{u}_0$; $\boldsymbol{\sigma}$ should satisfy yield function, $\forall \boldsymbol{\sigma} \in F = \{\boldsymbol{\sigma} | f(\boldsymbol{\sigma}) \le 0\}$. Because displacement discontinuities between elements do not exist, the power to be dissipated by plastic deformation is only permitted to occur within each triangular element. The energy-work balance condition in Equation 1 can be written as

$$D_{\mathrm{p}}(\boldsymbol{\varepsilon}) \le \mathbf{q}^{\mathrm{T}}\mathbf{u} \text{ and } \varepsilon(\mathbf{u}) \in E \tag{2}$$

where

$$D_{\mathrm{p}}(\boldsymbol{\varepsilon}) = \int_V d_p(\boldsymbol{\varepsilon}) \mathrm{d}V \tag{3}$$

$$d_p(\boldsymbol{\varepsilon}) = \sup_{\sigma \in F} \sum \boldsymbol{\sigma} : \boldsymbol{\varepsilon} \tag{4}$$

and the set of plastically admissible strains is

$$E = \left\{ \boldsymbol{\varepsilon} : d_{\mathrm{p}}(\boldsymbol{\varepsilon}) < +\infty \right\} \tag{5}$$

The plastically admissible strains are those that satisfy the associated flow rule. We divide equivalent nodal loads into two parts: collapse loads $\mathbf{q}_1$, e.g. the seismic loads in this paper; and constant loads $\mathbf{q}_0$, e.g. the gravity and other loads in this paper. Thus, an upper bound on k_c of the dam slope can be calculated by solving the following optimisation problem:

$$\begin{aligned} \min \quad & D_{\mathrm{p}}(\boldsymbol{\varepsilon}) - \mathbf{q}_0^{\mathrm{T}}\mathbf{u} \\ \text{s.t.} \quad & \boldsymbol{\varepsilon}(\mathbf{u}) \in E \text{ in } V \\ & \mathbf{u} = \mathbf{u}_0 \text{ on S} \\ & \mathbf{q}_1^{\mathrm{T}}\mathbf{u} = 1 \end{aligned} \tag{6}$$

The six-node triangle finite element with straight sides that is used in the upper bound analysis is shown in Figure 1.

Because the nodal displacement field can be expressed as a quadratic form within a triangular element, any strain component may vary linearly. Moreover, if the element sides are straight, the strain tensor at any point within the triangle can be expressed as a combination of those at three vertices, i.e.,

$$\varepsilon(\mathbf{x}) = \sum_{i=1}^{3} L_i(\mathbf{x})\varepsilon_i,\ 0 \le L_i(\mathbf{x}) \le 1,\ \sum_{i=1}^{3} L_i(\mathbf{x}) = 1 \tag{7}$$

where the coefficients $L_i = A_i/(A_1 + A_2 + A_3)$ are area coordinates. Because any strain tensor can be expressed by ε_i at the vertices, if the flow rule is enforced at the three vertices of the element, it holds at all points within the elements. Thus, the flow rule constraint only needs to be enforced at a finite number for it to hold throughout the structure.

As mentioned by Makrodimopoulos & Martin (2007a), the main restriction of the proposed method is that the yield function must be expressed as a conic quadratic form. The Mohr-Coulomb criterion in plane strain conditions is a typical example of a yield restriction with a conic quadratic form. It can be written in the following form:

$$\left\| \mathbf{s}^{\mathrm{red}} \right\| + a\sigma_m - k \le 0 \tag{8}$$

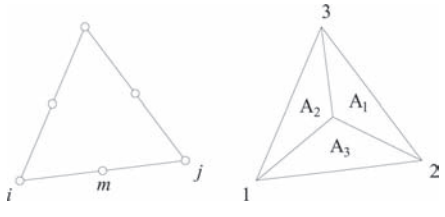

Figure 1. Six-node linear strain element for upper bound analysis.

where

$$\left\|\mathbf{s}^{\text{red}}\right\| = \begin{bmatrix} s_{11} & s_{12} \end{bmatrix}^{\text{T}} \tag{9}$$

$$\sigma_m = \frac{1}{D}\sum_{i=1}^{D}\sigma_{ii}, \quad s_{ij} = \sigma_{ij} - \sigma_m\delta_{ij} \tag{10}$$

where D is the dimension of the tensors and δ is Kronecker's δ. For plane strain conditions of the Mohr-Coulomb criterion, $D = 2$, $a = \sin\varphi$, and $k = c\cos\varphi$, where c is the cohesion and φ is the internal friction angle.

3 FEM FORMULATION FOR UPPER BOUND LIMIT ANALYSIS

Considering a plane strain structure divided into NE finite elements, the optimisation problem Equation 6 can be transformed as follows:

$$\begin{aligned} \min \quad & \sum_{i=1}^{\text{NE}}\int_{A_i} k\lambda \mathrm{d}A_i - \mathbf{q}_0^{\text{T}}\mathbf{u} \\ \text{s.t.} \quad & \lambda_i \geq \left\|\mathbf{e}_i^{\text{red}}\right\| \ (\text{i} = 1, \ldots, \text{NE}) \\ & a_i\lambda_i = \mathbf{B}_{\text{m},i}\mathbf{u} \ (\text{i} = 1, \ldots, \text{NE}) \\ & \mathbf{e}_i^{\text{red}} = \mathbf{B}_{\text{d},i}\mathbf{u} \ (\text{i} = 1, \ldots, \text{NE}) \\ & \mathbf{q}_1^{\text{T}}\mathbf{u} = 1 \end{aligned} \tag{11}$$

where

$$\theta_i = \mathbf{B}_{\text{m},i}\mathbf{u} \tag{12}$$

$$\begin{bmatrix} 2e_{xx} & 2e_{xy} \end{bmatrix}^{\text{T}} = \mathbf{B}_{\text{d},i}\mathbf{u} \tag{13}$$

The matrices $\mathbf{B}_{\text{m},i}$ and $\mathbf{B}_{\text{d},i}$ can easily be obtained from the typical strain-displacement relations. In geotechnical engineering, the displacement boundary is typically that $\mathbf{u} = 0$ on S. For conciseness, we assume that the above-mentioned conditions have already been satisfied in Equation 11 and in what follows.

As mentioned above, the flow rule only needs to be enforced at the three vertices of each six-node triangular element to ensure that it holds throughout the element. For this reason, we take the vertices of each triangle as flow rule points. Thus, for an NE-element structure, the total number of the flow rule points must be NP, where NP = 3NE. Now, Equation 11 can be formulated as follows, and more details can be found in the work by Makrodimopoulos & Martin (2007a):

$$\begin{aligned} \min \quad & \sum_{i=1}^{\text{NP}}\mathbf{c}_i^{\text{T}}\mathbf{z}_i - \mathbf{q}_0^{\text{T}}\mathbf{u} \\ \text{s.t.} \quad & \mathbf{z}_i \in K_i \qquad (\text{i} = 1, \ldots, \text{NP}) \\ & \mathbf{A}_i\mathbf{z}_i - \mathbf{B}_i\mathbf{u} = 0 \quad (\text{i} = 1, \ldots, \text{NP}) \\ & \mathbf{q}_1^{\text{T}}\mathbf{u} = 1 \end{aligned} \tag{14}$$

where

$$\begin{aligned} & \mathbf{c}_i \in \Re^3 \ \mathbf{c}_i^{\text{T}} = \begin{bmatrix} \bar{k}_i & 0 & 0 \end{bmatrix} \\ & \mathbf{z}_i \in \Re^3 \ \mathbf{z}_i^{\text{T}} = \begin{bmatrix} \lambda_i & (\mathbf{e}_i^{\text{red}})^{\text{T}} \end{bmatrix} \\ & \mathbf{A}_i \in \Re^{3\times 3} \ \mathbf{A}_i = \text{diag}\begin{bmatrix} a_i & 1 & 1 \end{bmatrix} \\ & \mathbf{B}_i \in \Re^{3\times \text{NZ}} \ \mathbf{B}_i = \begin{bmatrix} \mathbf{B}_{\text{m},i} & \mathbf{B}_{\text{d},i} \end{bmatrix}^{\text{T}} \end{aligned} \tag{15}$$

NZ is the total number degrees of freedom and $\mathbf{z}_i \in K_i$ is the second-order cone constraint. Sets K_i are quadratic cones of the following form:

$$K = \{\mathbf{x} \in \Re^d : \left\|\mathbf{x}_{2:d}\right\| \leq x_1, x_1 \geq 0\} \tag{16}$$

Equation 14 is a standard SOCP problem, which can be transformed into the corresponding dual problem as follows:

$$\begin{aligned} \max \quad & k_c \\ \text{s.t.} \quad & (y_{\text{m},i}, s_i^{\text{red}}) \in K_i \ (\text{i} = 1, \ldots, \text{NP}) \\ & y_{\text{m},i} + a_i\sigma_{\text{m},i} = k_i^* \ (\text{i} = 1, \ldots, \text{NP}) \\ & \sum_{i=1}^{\text{NP}}\mathbf{G}_{\text{m},i}\sigma_{\text{m},i} + \sum_{i=1}^{\text{NP}}\mathbf{G}_{\text{d},i}\mathbf{s}_i^{\text{red}} - \beta\mathbf{q}_1 = \mathbf{q}_0 \end{aligned} \tag{17}$$

where

$$\begin{aligned} & \mathbf{G}_{\text{m},i} = \eta_i\mathbf{B}_{\text{m},i}^{\text{T}} \\ & \mathbf{G}_{\text{d},i} = \eta_i\mathbf{B}_{\text{d},i}^{\text{T}} \\ & k_i^* = \bar{k}_i / \eta_i \\ & \eta_i = A_{\text{e},i} / 3 \end{aligned} \tag{18}$$

It has been shown that the dual formulation Equation 17 can be considered as a static form of upper bound analysis by Makrodimopoulos & Martin (2007a). The main advantages of solving the dual problem of the upper bound limit analysis are not only the dual form is robust and stability but also the stress distribution of structure can be obtained, which is used to describe the nonlinear failure criterion of rockfill materials.

At present, large-scale SOCP problems can be solved effectively using the interior-point method. Based on this method, various state-of-the-art algorithms are developed by researchers in

mathematical programming. In this paper, we use the algorithm software SDPT3 (Tütüncü et al. 2003) to solve SOCP problems. The LP/SOCP/SDP algorithm SDPT3 employs an infeasible primal-dual predictor-corrector path-following method. It has proven to be robust and efficient because various techniques to improve efficiency and stability are incorporated. Moreover, the basic code of SDPT3 is written in MATLAB (MATLAB 2011), so it is extremely simple and convenient to use by YALMIP (YALMIP 2012), which is a modelling language implemented as a toolbox for MATLAB for advanced modelling and solution of convex and nonconvex optimisation problems.

4 UPPER BOUND ANALYSIS BASED ON THE NONLINEAR SHEAR STRENGTH

Considered cohesionless soils, rockfill materials naturally evidence a nonlinearity of failure criterion with $c = 0$. As clearly shown by triaxial tests (Indraratna et al. 1993; Yamaguchi 2008), rockfill materials are susceptible to particle breakage under high confining pressure, which leads to the redistribution of intergranular stress and a decrease in the internal friction angle. Consequently, for rockfill materials, the Mohr-Coulomb envelopes are typically curved, and their variation can be expressed in the form described by Duncan et al. (1978)

$$\varphi = \varphi_0 - \Delta\varphi \lg(\sigma_3/Pa) \tag{19}$$

where φ_0 is the friction angle at the unit atmospheric pressure Pa of confining pressure σ_3, and $\Delta\varphi$ is the reduction in φ for a 10-fold increase in σ_3. We apply iterative approach to upper bound analysis in order to consider the nonlinearity of the failure criterion. Combined with Section 3, the calculating procedures for upper bound limit analysis using nonlinear failure criterion are as follows:

Step 1: Set the initial value of φ_{ini} for each element.

Step 2: Assemble the constraint data in Equation 17 and formulate the data as a dual SOCP problem.

Step 3: Solve the problem using the algorithm SDPT3 and obtain the stress field of the dam.

Step 4: According to the stress field, determine φ_{sec} by Equation 19 and compare it to φ_{ini}. If $|\varphi_{\text{sec}} - \varphi_{\text{ini}}| \le \zeta$ for 99.9% of the total element numbers, then go to next step; otherwise, set $\varphi_{\text{ini}} = \varphi_{\text{sec}}$ and go to Step 2, where ζ is the tolerance.

Step 5: Obtain the exact upper bounds and output the results.

Generally, converged rigorous upper bounds can be obtained after several iterations.

5 NUMERICAL EXAMPLES

Consider the seismic stability problem of a completed rockfill dam in an earthquake with dam height $H = 100$ m, gradient $n = 1{:}1.4$, and width of the dam crest $D_c = 8$ m. It is suggested by *Specifications for seismic design of hydraulic structures* (DL5073-2000) in China that the seismic stability of rockfill dams can be analysed by a pseudo-static approach. The concept of the pseudo-static approach relies on the representation of the earthquake-induced loading by statically applied inertial forces. Meanwhile, to assess the distribution of the response acceleration along the height of dams, the pseudo-static loads are calculated in terms of the dynamic distribution coefficient α_i, which is suggested by the specifications mentioned above. As shown in Figure 2, when the seismic design intensity is of degrees VII, VIII, and IX, the maximum dynamic distribution coefficient α_m on the top of the dams is 3.0, 2.5, and 2.0, respectively. Thus, the horizontal seismic loads acting on each element can be calculated as

$$Q = k_h \xi \alpha_i W \tag{20}$$

where ξ is the seismic reduction coefficient (generally $\xi = 0.25$), W is the weight of each element, and k_h is the horizontal seismic coefficient, which is the ratio of the horizontal seismic acceleration a_h to the acceleration of gravity g (= 9.81 m/s^2): $k_h = a_h/g$. The vertical seismic loads V can be determined as 2/3 of horizontal seismic loads approximately:

$$V = 2/3Q \tag{21}$$

In this paper, we assume the design intensity is of degree IX. The critical seismic coefficient k_c ($k_c = k_h$ in this paper) of the dam slope can be obtained by maximising Equation 17 for the upper bound analysis.

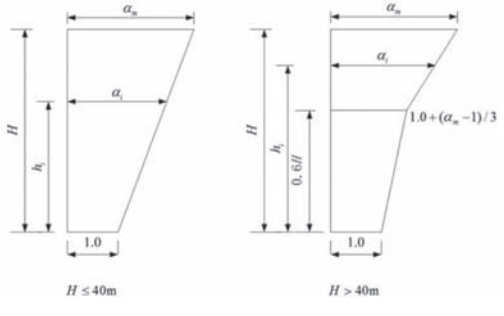

Figure 2. Dynamic distribution coefficient α_i.

Three projects is considered in this paper: Project 1, consider the horizontal seismic loads only; Project 2, consider the horizontal and vertical seismic loads and assume the direction of the vertical seismic loads is upward; Project 3, consider the horizontal and vertical seismic loads and assume the direction of the vertical seismic loads is downward. In these three projects, we assume the direction of the horizontal seismic loads is downstream. The nonlinear shear strength parameters can be set as $\varphi_0 = 52.3^\circ$ and $\Delta\varphi = 11.0^\circ$ (Chen & Chen 2007). The mesh of the dam is shown in Figure 3, and the results are presented in Table 1.

From results, we see that the solutions of k_c obtained by upper bound FEM is close to those obtained by Bishop's simplified method (Bishop 1955). The average relative difference of k_c obtained by the writers is 3.8% and 2.8% larger using coarse and fine mesh respectively than Bishop's method. It is noted that we can still get much more rigours upper bound solution by formulating the corresponding dual SOCP problem of the upper bound limit analysis, though rockfill materials process larger internal friction angel. Because of the high-order element type, the solutions are not very sensitive to mesh density. By determining the internal friction angle iteratively, the nonlinear shear strength properties of the rockfill materials are considered in the proposed method. From the displacement field, the failure surface is predicted easily. The comparison of failure surface obtained from Bishop's simplified method and the proposed method (fine meth) is shown in Figure 4. It is noted from Figure 4 that the failure surfaces predicted by the two mentioned methods are very close.

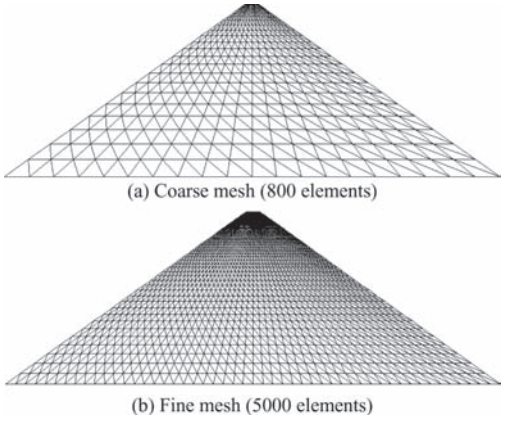

Figure 3. Mesh of the rockfill dam.

Table 1. Results of critical seismic efficient k_c.

	k_c		
	Project 1	Project 2	Project 3
Coarse mesh	1.139	0.948	1.369
Fine mesh	1.128	0.945	1.349
Bishop's method	1.09	0.92	1.32

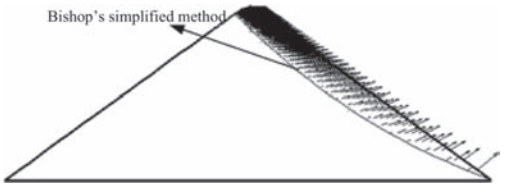

Figure 4. Failure surface and displacement field.

6 CONCLUSIONS

In this paper, an upper bound limit analysis FEM is developed to study the seismic stability of rockfill dams. In order to reduce the errors caused by the linearization of the yield function, the upper bound limit analysis is based on the native form of the Mohr-Coulomb criterion and formulated as a second-order cone programming program. It is noted that though the value of internal friction angle of the rockfill materials is very large, we still get rigorous upper bound solutions. Moreover, the nonlinear shear strength properties of the rockfill materials are also considered by using an iterative approach for the friction angle. The influence of mesh density on solutions is also studied. The results show that the solutions are not very sensitive to mesh density. This means the solutions can still be accuracy even though the finite element mesh is coarse. Comparisons of Bishop's simplified method illustrate the correctness and the practical value of the proposed method.

ACKNOWLEDGMENT

The authors gratefully acknowledge the financial support provided by the National Nature Science Foundation of China through Grants Nos. 50979014 and 51179024.

REFERENCES

Bishop, A.W. 1955. The use of the slip circle in the stability analysis of slopes. *Géotechnique* 5(1): 7–17.

Chen, L. & Chen, Z. 2007. Effect of nonlinear strength of rockfill on slope stability of high earth-rock dam. *Rock and Soil Mechanics* 28(9): 1807–1810.

Duncan, J.M., Byrne, P.M. & Wong, K.S. 1978. *Strength stress-strain and bulk modulus parameters for finite element analysis of stress and movements in soil masses,* Berkeley University of California, Berkeley.

Indraratna, B., Wijewardena, L.S.S. & Balasubramaniam, A.S. 1993. Large-scale triaxial testing of greywacke rockfill. *Géotechnique* 43(1): 37–51.

Li, D. & Cheng, Y. 2012. Lower bound limit analysis using nonlinear failure criteria. *Procedia Earth and Planetary Science* 5: 170–174.

Loukidis, D., Bandini, P. & Salgado, R. 2003. Stability of seismically loaded slopes using limit analysis. *Géotechnique* 53(5): 463–479.

Makrodimopoulos, A. & Martin, C.M. 2006. Lower bound limit analysis of cohesive-frictional materials using second-order cone programming. *International Journal for Numerical Methods in Engineering* 66(4): 604–634.

Makrodimopoulos, A. & Martin, C.M. 2007a. Upper bound limit analysis using simplex strain elements and second-order cone programming. *International Journal for Numerical and Analytical Methods in Geomechanics* 31(6): 835–865.

Makrodimopoulos, A. & Martin, C.M. 2007b. Upper bound limit analysis using discontinuous quadratic displacement fields. *Communications in Numerical Methods in Engineering* 24(11): 911–927.

MATLAB 2011. *The Mathworks*, Natic, MA, USA.

Standard of Ministry of Electric. Power, PRC. 2001. *Specifications for seismic design of hydraulic structures (DL5073-2000)*. Beijing: China Electric Power Press.

Sloan, S.W. 1988. Lower bound limit analysis using finite elements and linear programming. *International Journal for Numerical and Analytical Methods in Geomechanics* 12(1): 61–77.

Sloan, S.W. 1989. Upper bound limit analysis using finite elements and linear programming. *International Journal for Numerical and Analytical Methods in Geomechanics* 13(3): 263–282.

Sloan, S.W. & Kleeman, P.W. 1995. Upper bound limit analysis using discontinuous velocity fields. *Computer Methods in Applied Mechanics and Engineering* 127: 293–314.

Tütüncü, R.H., Toh, K.C. & Todd, M.J. 2003. Solving semidefinite-quadratic-linear programs using SDPT3. *Mathematical Programming* 95(2): 189–217.

Yamaguchi, Y. 2008. Strength evaluation of rockfill materials considering confining pressure dependency. *Journal of Japan Society of Dam Engineers* 8(3): 166–181.

Geotechnical Safety and Risk IV contains the contributions presented at the 4th International Symposium on Geotechnical Safety and Risk (4th ISGSR, Hong Kong, 4-6 December 2013), which was organised under the auspices of the Geotechnical Safety Network (GEOSNet), TC304 on Engineering Practice of Risk Assessment and Management and TC205 on Safety and Serviceability in Geotechnical Design of the International Society of Soil Mechanics and Geotechnical Engineering (ISSMGE). **Geotechnical Safety and Risk IV** covers six themes:

(1) Geotechnical uncertainty and variability
(2) Geohazards such as landslides, earthquakes and climate changes
(3) Reliability and risk analysis
(4) Reliability-based design and limit-state design in geotechnical engineering
(5) Risk assessment and management in geotechnical engineering and infrastructural projects, and
(6) Practical applications.

Geotechnical Safety and Risk IV is an excellent source of reference on the latest developments and practices of geotechnical risk and safety, and will prove to be invaluable for civil engineers (particularly geotechnical engineers), geologists, and natural hazards reduction agencies.

ISGSR IV is a continuation of a series of symposiums and workshops on geotechnical risk and reliability, starting with LSD2000 (Melbourne, Australia), IWS2002 (Tokyo and Kamakura, Japan), LSD2003 (Cambridge, USA), Georisk2004 (Bangalore, India), Taipei2006 (Taipei, Taiwan), 1st ISGSR (Shanghai, China, 2007), 2nd ISGSR (Gifu, Japan, 2009) and 3rd ISGSR (Munich, Germany, 2011).

CRC Press
Taylor & Francis Group
an informa business
www.crcpress.com

6000 Broken Sound Parkway, NW
Suite 300, Boca Raton, FL 33487
Schipholweg 107C
2316 XC Leiden, NL
2 Park Square, Milton Park
Abingdon, Oxon OX14 4RN, UK

ISBN 978-1-138-00163-3

an informa business